PROCEEDINGS

of the

THIRTEENTH INTERNATIONAL SYMPOSIUM ON

SPACE TERAHERTZ TECHNOLOGY

Tuesday – Thursday, March 26 – 28, 2002

Maxwell-Dworkin Building
Harvard University
Cambridge, Massachusetts

Organized by: Harvard-Smithsonian Center for Astrophysics

Organizing Committee

Raymond Blundell, Harvard-Smithsonian Center for Astrophysics
Edward Tong, Harvard-Smithsonian Center for Astrophysics

PREFACE

The Thirteenth International Symposium on Space Terahertz Technology was held on the campus of Harvard University, Cambridge, Massachusetts, on March 26 – 28, 2002. The Symposium was attended by about 130 scientists and engineers, from all over the world. The Symposium was organized into 10 oral sessions and an interactive forum for poster presentation. In all, 70 papers, distributed into the following broad categories, were presented:

Hot Electron Bolometers	16
SIS Mixers	14
Local Oscillator Technology	14
Optics	9
Equipment and Components	6
Sub-millimeter Systems	6
Direct Detectors	5

Included in these proceedings are 64 of the papers presented at the symposium and the 6 missing papers are represented by the accepted abstracts. Finally, we have also included one paper from the Twelfth Symposium, on request from last year's editor.

The Symposium was made possible largely through the effort of the staff members of the Submillimeter Receiver Laboratory of the Harvard-Smithsonian Center for Astrophysics (CfA). We thank Joanne Reynolds who was key in all organizational aspects of the symposium, and in preparing and editing the proceedings. We also thank Professor Irwin Shapiro, Director of the CfA, for supporting the symposium, and Dr. Venkatesh Narayanamurti, Dean of Engineering and Applied Sciences, for his support through the use of the Robert and Naida Lessin Forum. Finally, we would like to thank the session chairs, presenters, and participants for making this Thirteenth International Symposium on Space Terahertz Technology, a success.

Edward Tong
Raymond Blundell

Front cover: Photograph of the Terahertz telescope to be deployed in Northern Chile by the Submillimeter Receiver Lab of CfA in September 2002. Also shown is a spectral line of CO (J = 9-8) at 1.037 THz recorded by our HEB receiver operating at the Sub-Millimeter Telescope, in Arizona, January 2000.

THIRTEENTH INTERNATIONAL SYMPOSIUM ON SPACE TERAHERTZ TECHNOLOGY

Tuesday - Thursday, March 26-28, 2002

Maxwell-Dworkin Building
Harvard University
Cambridge, Massachusetts

Organized by: Harvard-Smithsonian Center for Astrophysics

Day 1: TUESDAY, MARCH 26

Opening Session/Remarks — **Raymond Blundell**

Session 1: SIS I — **Chair: Raymond Blundell**

Day 2: WEDNESDAY, MARCH 27

Session 5: Sources I **Chair: Antti Räisänen**

Session 6: Signal Generation via Optical Mixing **Chair: Jonas Zmuidzinas**

Session 8: Interactive Forum Continued **(held in Phillips Auditorium)**

Session 8: Interactive Forum Continued **(held in Phillips Auditorium)**

Session 8: Interactive Forum Continued **(held in Phillips Auditorium)**

Day 3: THURSDAY, MARCH 28

Session 9: Sources II — **Chair: Neal Erickson**

Session 10: Circuits & Optics — **Chair: Urs Graf**

Fixed-tuned waveguide 0.6 THz SIS Mixer with Wide band IF

A. Baryshev [1], E. Lauria [2], R. Hesper [1], T. Zijlstra [3], W. Wild [1]

[1] SRON-Groningen, Groningen, NOVA, University of Groningen, the Netherlands
[2] National Radio Astronomy Observatory, Charlottesville, VA 22903
[3] Department of Applied Physics (DIMES), Delft University of Technology

ABSTRACT

The Atacama Large Millimeter Array (ALMA) requires low noise SIS receivers for frequencies from about 80 GHz to 950 GHz with a very large IF bandwidth (8 GHz SSB upper or lower sideband, 8 GHz DSB or 4 GHz dual sideband, upper and lower sideband). Since there will be a large number of antennas in the array (currently 64), additional requirements such as high reliability, low cost, and the production of a relatively large number of mixers have to be addressed.
In this paper we report the results of a waveguide mixer with a fixed backshort for ALMA band 9 (602 – 720 GHz). The mixer is based on standard Nb/AlO_x/Nb SIS junction technology. This mixer was tested with a wide band IF amplifier with and without isolator. Mixer measurement results for different LO frequencies across a wide IF band (4-8 GHz) will be presented. DSB Receiver noise across the both RF and IF band was measured, and receiver noise as low as 136 K at 650 GHz was demonstrated over the wideband IF. Finally, the possibility of a small production series of such a mixer is discussed with results on a first batch of mixer-blocks will be presented.

INTRODUCTION

The Atacama Large Millimeter Array (ALMA) requires low-noise SIS receivers for frequencies from about 80 GHz to 950 GHz with very large IF bandwidth (4-12 GHz). ALMA will be built in the Atacama Desert (Chili) at the altitude of more than 5 km. The atmospheric conditions for mm-wave astronomical observations at this site are among the best in the world. The array will consist of at least 64 antennas, each with a diameter of 12 m.
The Alma frequency band is divided into ten subbands. These bands coincide with regions where the atmosphere is relatively transparent and astronomical observations are possible. The receivers for the different subbands will be mounted in a common cryostat supporting three temperature levels: 4.3 K, ~10 K and 80 K. Each subband receiver is contained in an independent "cartridge" that can be mounted in the receiver cryostat without disturbing other subbands. This cartridge contains a complete receiver system including SIS mixers, LO subsystem, IF amplifiers and all necessary optical components.
The remoteness of the site and the large number of receivers impose additional requirements on the receiver design such as absence of moving parts, an as simple as possible layout, low cost, and the possibility of series production.
In this paper we report mixer designs based on standard Nb/AlO_x/Nb SIS junction technology in a waveguide mixer block for ALMA band 9 (602 – 720 GHz). The mixer

does not contain moving parts e.g., a backshort. We present results on the extension of the IF bandwidth from 1.1-1.7 GHz to 4-8 GHz and 4-12 GHz by using an NRAO wide-band IF amplifier and PamTech 4-8 GHz and 4-12 GHz isolators. We will also present our approach to small series production of such a mixer.

MECHANICAL DESIGN OF THE MIXER

Fig. 1 shows the design of an ALMA band 9 single-ended double sideband (DSB) waveguide mixer. Similar designs have already been implemented in other mixers [1]. The design goal was best possible performance combined with simplicity and series fabrication possibility. The mixer consists of several parts:

- a horn (1),
- a centering ring (2) aligning the horn with the backpiece,
- a mixer backpiece (3) which holds the SIS tunnel junction and the IF connector,
- a threaded cap to hold horn and backpiece together (4),
- a magnet consisting of a coil (not shown) and two pole shoes (5),
- a mounting structure (not shown).

The parts of the mixer which are most critical to the performance are the horn, the backpiece and the substrate with the junction and the tuning structures. The diagonal horn is used for experimental mixers, but the design easily allows it to be replaced with an appropriate corrugated feedhorn. The main idea in the design is to machine all critical surfaces to such an accuracy that mutual alignment between the different parts of the mixer occurs automatically upon assembly. This design also achieves a good coupling of the magnetic field flux from the coil to the junction, which is critical for Josephson noise suppression at these frequencies. The distance between pole pieces is only 1 mm with the junction at the center. The DC/IF connection is made by means of a standard miniature SMP-type connector. This is one of the smallest connectors available, allowing us to decrease the transmission line length between the junction and any other IF components, facilitating amplifier-mixer integration. The mechanical design does not incorporate an external bias-tee. However, in certain configurations, a standard Radiall bias-tee was used.

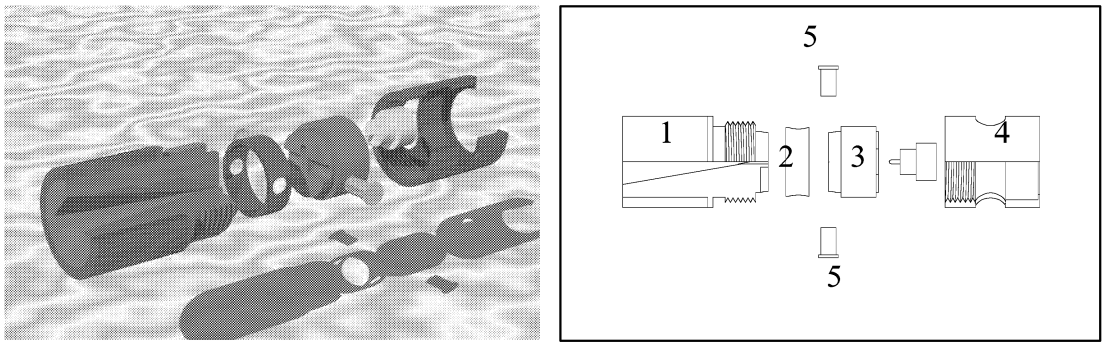

Figure 1: Mechanical design of the mixer.

For the magnet we use a coil of about 6000 turns of 63.5 micron diameter Cu-cladded Nb wire. For the core of the magnet and the pole pieces we use VacoFlux 50, which has a maximum permeability of 9000 and a saturation polarization of 2.35 T.
The waveguide has a cross-section of 100 x 400 μm. The cross-section of the substrate channel in the backpiece is 70 x 100 μm and the backshort cavity is about 200 μm deep. The backshort cavity is produced by stamping it in the copper block.
The substrate is 2.1 mm long, 50 μm thick and 70 μm wide and it contains a Nb-based SIS tunnel junction. It is glued in the channel and contacted with silver paint.

MIXER CHIP LAYOUT

A photograph of a mixer chip glued into the substrate channel is shown in fig. 2. The substrate material is fused quartz. Standard Nb technology was used for making the thin film layer structure. Optical lithography was used in all definition steps including the patterning of the 1 μm^2 SIS junction. The RF design of the coupling between the waveguide TEM mode and the SIS junction is similar to the one used earlier, for instance in [2] and [3]. The energy is coupled to a bow-tie waveguide probe and transferred via a Chebyshev type two-stage impedance transformer to the junction-tuner combination. This transformer is formed by two microstriplines connected in series. The bottom electrode of this microstripline is formed by the bottom part of the bow-tie probe. The junction is located at the end of the tuner section of the microstripline. A choke structure is used to prevent RF signals from leaking into the IF/DC bias leads. A low impedance λ/4 line is used to provide a virtual short circuit between the waveguide probe and the waveguide wall at RF.
The junction's R_nA value is about 35 $\Omega\mu m^2$ and its normal resistance R_n about 34 Ω. The thickness of the Nb is about 200 nm for the bottom layer and about 600 nm for the top layer. The thickness of the SiO_2 insulator is about 250 nm.

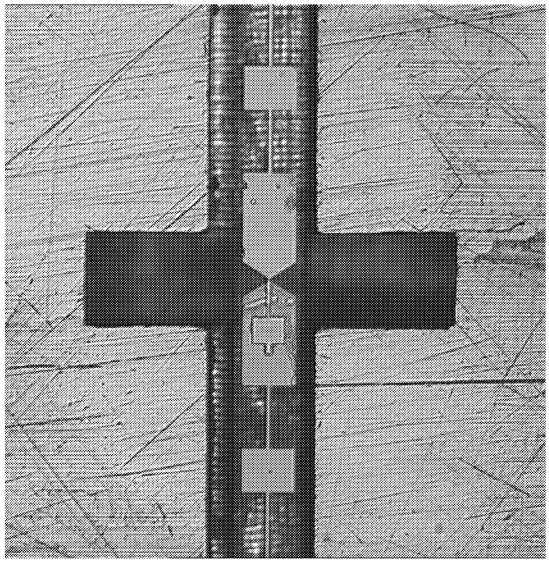

Figure 2: Photograph of a mixer chip glued into a back piece, looking straight into the backshort cavity.

WIDE-BAND IF AMPLIFIER AND ISOLATORS

Throughout the experiment, a wide band 4-12 GHz IF amplifier provided by the NRAO Central Development Laboratory (CDL) was used. This amplifier is identical to the design used in experiments done at the CDL, where a single-ended SIS mixer was directly connected to its IF amplifier [4]. The gain of the amplifier is about +34 dB, and its equivalent noise temperature (at a physical temperature of 12 K) is about 4-7 K across the IF band. The total DC power dissipation is about 8mW. This is important to prevent heating of the mixer junction, and to reduce the heat load on the 4 K stage. A mixer bias-tee is incorporated into the amplifier which facilitates integration with the SIS mixer. The amplifier was designed to be unconditionally stable, since the mixer's IF impedance seen on the input of the amplifier can vary greatly from a low impedance to a high (and even negative) impedance, depending on the LO frequency. The input return loss of the amplifier is better than 10 dB from 5 to 10.5 GHz. This is important to assure a nominal value for the mixer gain and input RF return loss to the mixer.
Two types of isolators were used for experiments: a commercially available 4-8 GHz isolator from Passive Microwave Technologies (PamTech) [5] and the development model of a cryogenic 4-12 GHz isolator also being developed at PamTech. The photograph of both isolators is presented in fig. 3. Despite its increased dimensions, the 4-12 GHz isolator may present sufficient advantages to be used in ALMA receiver cartridges because it allows mixer and amplifier to be disconnected, and provides a clear 50 Ω interface between them. The mass of 4-12 GHz isolator is about 120 grams. Preliminary cryogenic measurements of this isolator at a temperature of 4 K show its insertion loss to be below 1 dB across the 5-13 GHz band.

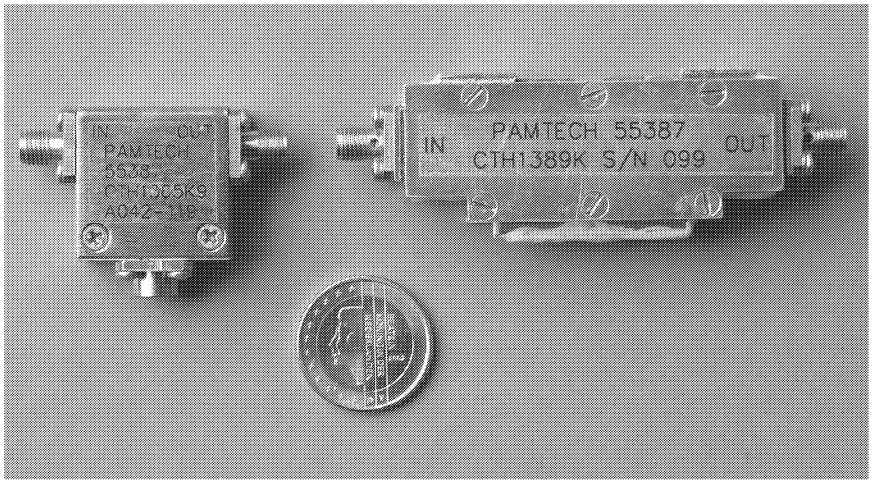

Figure 3: Photograph of a commercially available 4-8 GHz PamTech isolator (left) and the 4-12 GHz development prototype (right).

EXPERIMENTAL SETUP

We used a standard Y-factor measurement technique to determine receiver noise temperature. The mixer was mounted inside the vacuum space of a liquid helium cryostat at 4.2 K. A high-density polyethylene lens was used to refocus the wide angle beam from

the diagonal horn onto an external hot/cold load. The Mylar film of 125 μm thickness was used as vacuum window. A GoreTex sheet (expanded Teflon) of 3 mm thickness at liquid nitrogen temperature was used as an infrared radiation filter. A Mylar sheet of 12-15 μm thickness was used for local oscillator (LO) injection. A Gunn oscillator followed by a diode doubler and a diode tripler was used as an LO. Black body absorbers at 300K and 77 K were used for receiver calibration. All presented noise temperatures are uncorrected for beamsplitter loss, and a Callen/Welton formula [6] was used to obtain black body radiation temperatures.
Several mixer-amplifier configurations are shown in fig. 4. A comparison between these options was made, keeping other components of the receiver the same.

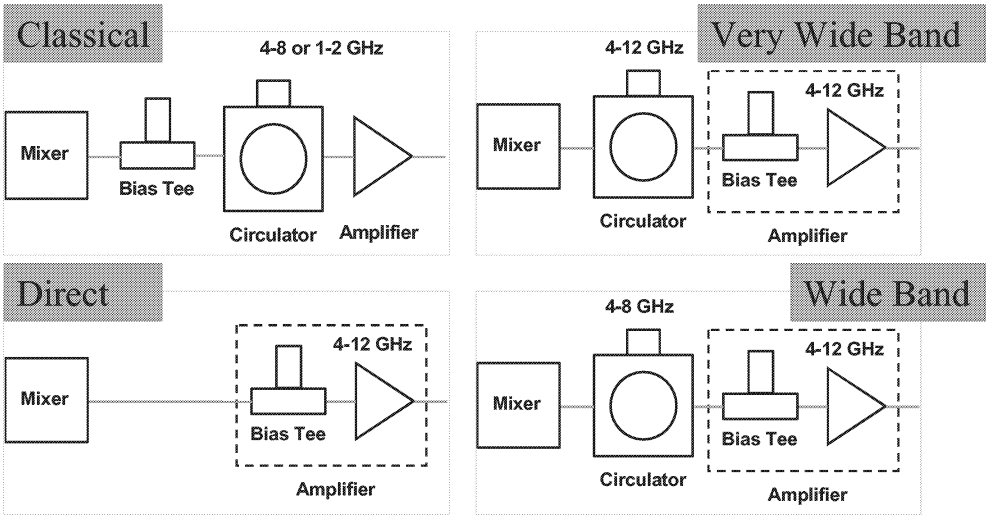

Figure 4: Measurement schemes.

The "classical" option was used to test the mixer with a conventional L-band amplifier (1.1-1.7 GHz). A Radiall bias-tee was used between mixer and circulator.
In the "wide band" and "very wide band" options a isolator was used between mixer and amplifier. It was possible to use the bias-tee integrated in the amplifier because both isolators allow biasing the SIS mixer through them.
Since the amplifier design allows it to be used with any input impedance without oscillations, a "direct" option was also tried as an intermediate step to integration of an SIS mixer and an IF amplifier. In directly connecting the mixer to the amplifier, it is important to point out that no optimization was done between the mixer and amplifier. An approximate 2 cm length of semi-rigid coax cable was connected between the mixer and IF amplifier. This experiment was done to "just see what happens", and by no means should not be taken as a final comparison between direct integration and using an isolator between the mixer and amplifier.

MEASUREMENT RESULTS AND DISCUSSION

A typical I-V curve and output IF power bias dependences are shown in fig. 5 (left). The measurements were done by using a 6-8 GHz band-pass filter in the warm IF amplifier chain, consisting of two room temperature IF amplifiers of 30 dB gain each. The curves

in fig. 5 show that the Josephson noise can be suppressed and that no artifacts are introduced by the large IF bandwidth. The receiver noise temperature measured for different IF amplifier connection options is presented in fig. 5 (right). One can see that all of them have a comparable noise temperature. The increase in noise temperature for options with high IF frequency compared to the L-band case is due to the fact that at these LO frequencies the upper sideband already hits the upper edge of the receiver band. The IF output power and noise temperature vs. IF frequency for different options is shown in figs. 6 to 8. The power curves were all taken at the same optimum bias point while changing the receiver input from 300 K to 77 K. The IF output power ripple for the "wide band" option (fig. 6) is less than 2 dB per 2 GHz, which is within the ALMA specification. The noise temperature variation across the IF band is also sufficiently small.

Similar receiver quality can be seen in the "very wide band" case (fig. 7). The dip in output power at around 7 GHz can probably be attributed to one of the SMA connectors used in the 4-12 GHz circulator. The decline in the noise temperature at the higher end of the band (frequency more than 11 GHz) is due to parasitic capacitance of the mixer tuning structures and parasitic inductance due to long choke-structures used in this particular mixer design.

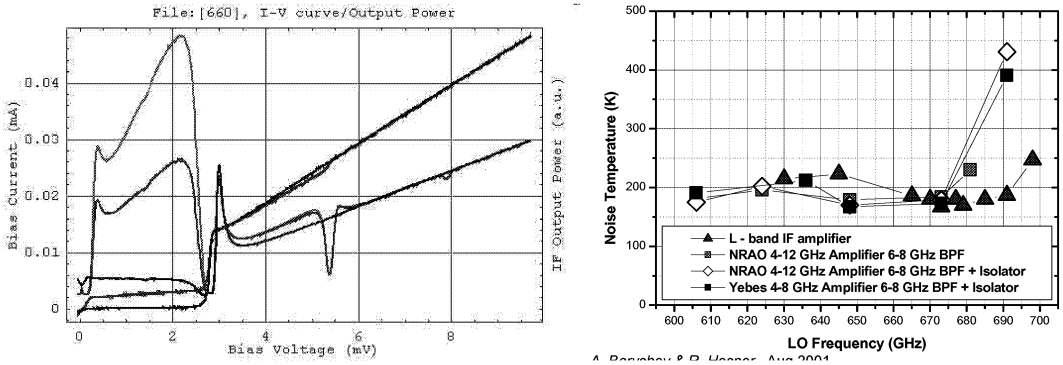

Figure 5: Typical I-V curves and IF output power (left) and summary of receiver noise temperatures for different mixer-amplifier coupling options (right).

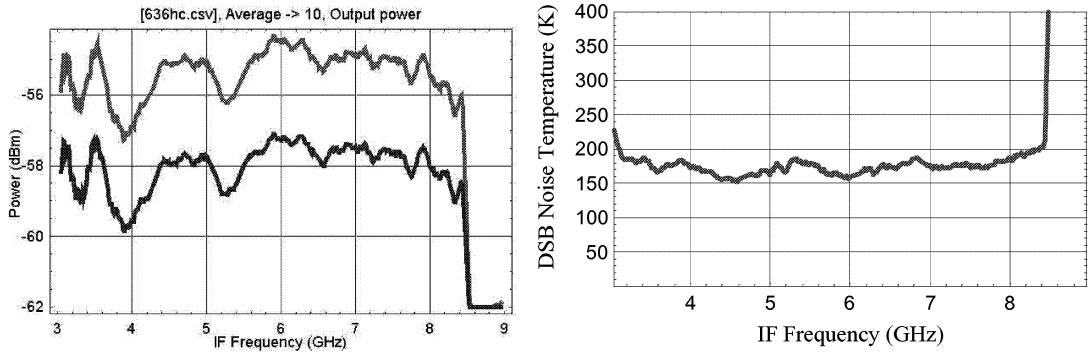

Figure 6: Receiver response with the 4-8 GHz system with isolator ("Wide band" option).

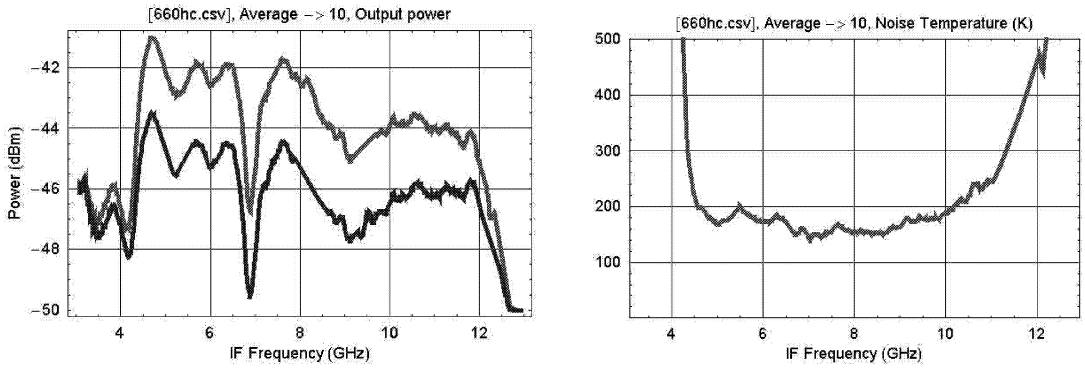

Figure 7: Receiver response with the 4-12 GHz isolator ("Very Wide band" option)

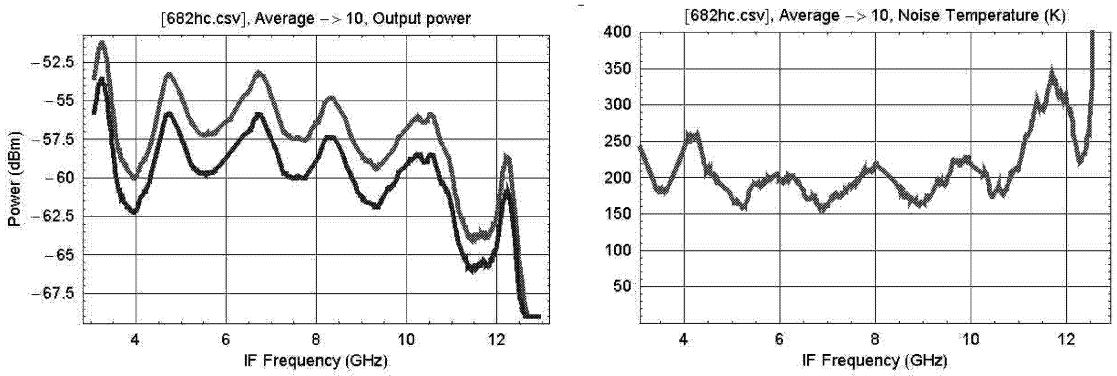

Figure 8: Receiver response without isolator ("direct" connection via 2 cm semi-rigid cable)

We expect that mixer performance can be improved at higher IF frequencies by minor design modifications. The lower boundary of the IF band is shifted upwards because of the shift in the 4-12 GHz circulator operation band.
The results for the "direct connection" case are shown in fig 8. An IF output power ripple of 8 dB was observed. A noise temperature ripple of the order of 25% is also visible. No parasitic oscillations were observed in the IF amplifier during the measurements. This option requires further optimisation of the mixer and amplifier designs to reduce the amplitude of these ripples.

SMALL SERIES PRODUCTION

One of the goals of the current mixer design is the feasibility of series production. To investigate this a collaboration was set up with a company specialized in fine-mechanical machining, Witec B.V. (Ter Apel, Holland), to fabricate the mixer backpiece (the most difficult part) on their CNC milling machines with as little human intervention as possible. Several test runs were conducted, transferring the SRON expertise of manual production to the computer-controlled method in an iterative way. Because self-alignment of the different parts of the mixer structure is a central requirement of the design, special attention was paid to the accurate positioning of the backshort cavity with respect to the reference circle, as well as to the depth of the stamped cavity, which plays a large role in tuning the receiver.

After a few iterations, during which the tooling was perfected, all important alignments had converged to within about 10 μm, which should be enough to provide good mixer performance, while the machining time had dropped to less than one hour per backpiece. The latter should be contrasted to the time it took a skilled technician to produce a backpiece by manual means, which was of the order of a week.
One of the CNC-produced backpieces was tested together with a diagonal horn, and its performance turned out to be very comparable to the classical hand-made backpieces.

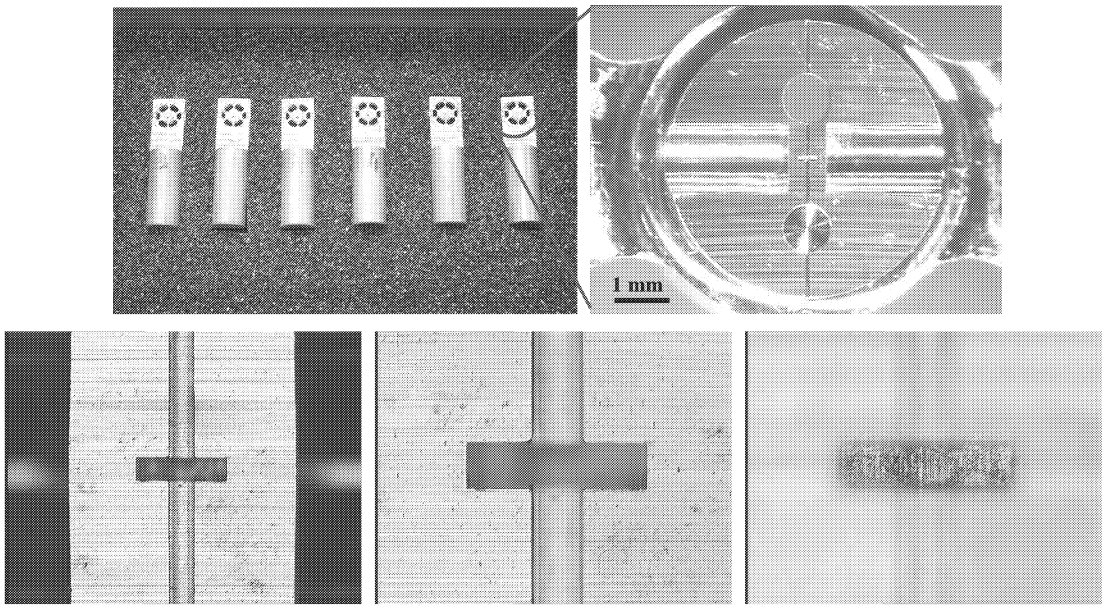

Figure 9: The small series of backpieces and photographs demonstrating the cavity quality. The middle and the right photographs at the bottom series are focused on the top and bottom of the cavity, respectively.

CONCLUSION

A compact and efficient waveguide mixer design for ALMA band 9 was demonstrated. Four different IF amplifier connection schemes were evaluated experimentally. Wide band (4.5-11 GHz) IF operation was achieved with the development model of a 4-12 GHz isolator, giving a sufficiently good performance to be used in low noise receiver systems. Series production of this mixer design with sufficiently tight tolerances has been demonstrated.

ACKNOWLEGEMENTS

The authors would like to thank Gerrit Gerlofsma and Duc van Nguen for technical assistance, Harry Shaeffer for his help in mechanical design and Herman van de Stadt for useful discussions.

REFERENCES

[1] Baryshev *et al.*, "Development of a 0.6 THz SIS Receiver for ALMA", Proc of 12th Int. Symp. on Space Terahertz Technology, pp. 581-591, 2001

[2] Blundell *et al.*, "A wideband fixed-tuned SIS receiver for 200-GHz operation," *IEEE Trans. Microwave Theory Tech.*, vol. 43, pp. 933-937, Apr. 1995.

[3] J. W. Kooi, *et al*., "230 and 492 GHz low noise SIS waveguide receivers employing tuned Nb/A10$_x$/Nb tunnel junctions," *Int. J. IR and MM Waves,* vol. 16, pp. 2049-2068 1995.

[4] Lauria, E.F., *et al.,* "A 200-300 GHz SIS Mixer-Preamplifier with 8 GHz IF Bandwidth," ALMA memo #378, http://www.alma.nrao.edu/memos/html-memos/alma378/memo378.pdf

[5] PamTec, Passive Microwave Technology Inc, 4053 Calle Tesoro, Suite A, Camarillo, CA 93012

[6] H. B. Callen and T. A. Welton, "Irreversibility and generalized noise," *Phys. Rev.*, vol. 83, pp. 34-40, July 1951.

Saturation by Noise and CW Signals in SIS Mixers

A. R. Kerr
National Radio Astronomy Observatory[1]
Charlottesville, VA 22903, USA

ABSTRACT

In ALMA Memo 321, Plambeck points out that saturation (gain compression) is likely to be a significant factor limiting the calibration accuracy of ALMA observations. In this paper, saturation by broadband noise and CW signals is analyzed for representative SIS receivers operating at different frequencies. Many SIS mixers in current use are expected to exhibit a significant degree of gain compression when connected to a room-temperature source. Previous analyses of saturation in SIS mixers have applied only to CW signals. To analyze saturation by noise, the statistics of the output voltage are derived from those of the input signal. A single constant, applicable to all SIS mixers, is determined experimentally by fitting the predicted CW gain compression curve to measured data.

Keywords: Superconductor-Insulator-Superconductor mixers, saturation, gain compression, dynamic range.

1. INTRODUCTION

Saturation (gain compression) can be a serious problem in SIS mixers not designed with appropriate input power levels in mind. Plambeck points out [1] that gain compression is likely to be a significant factor limiting the calibration accuracy of ALMA observations. SIS receivers have been reported with substantial gain compression at source temperatures as low as 50 K (1.4 dB compression [2]) and 300 K (1.7 dB compression [1]), while others have been capable of observing the sun (~6000 K) with only 0.6 dB gain compression [3]. Previous analyses of saturation in SIS mixers have considered only saturation by CW (sinusoidal) input signals. For amplifiers, it is well known that a given degree of saturation occurs at a lower input power level with noise than with a CW signal, and similar behavior is expected in SIS mixers. This memo describes a method for analyzing saturation by noise or CW signals in SIS mixers, and gives generalized saturation curves and representative results for mixers at several frequencies.

The established phenomenological theory of saturation by CW signals in SIS mixers is reviewed in Section 2, and shown to agree quite well with experimental data, even at gain compression levels as high as 3 dB.

When saturation is caused by broadband noise, a different approach is required, as described in Section 3, which allows the statistics of the output noise to be deduced from those of the input noise. The conclusion, not surprisingly, is that small and moderate degrees of gain compression are produced by noise powers several dB lower than the CW power required to produce the same gain compression. Many SIS mixers in current use are expected to exhibit a significant degree of gain compression when connected to a room-temperature source. It is noted that the linearity of a partly saturated SIS receiver to a small CW test signal can lead to the erroneous conclusion that the SIS mixer is not saturated by room-temperature input noise.

---

[1]The National Radio Astronomy Observatory is a facility of the National Science Foundation operated under cooperative agreement by Associated Universities, Inc.

2. ANALYSIS OF SATURATION BY A CW SIGNAL

For an SIS mixer with a well developed quantum response, the small signal power gain is a function of the bias voltage; this is evident in Fig. 1. Smith and Richards [4] argued that the large signal power gain could be considered as an average value of the small signal gain over an IF cycle.

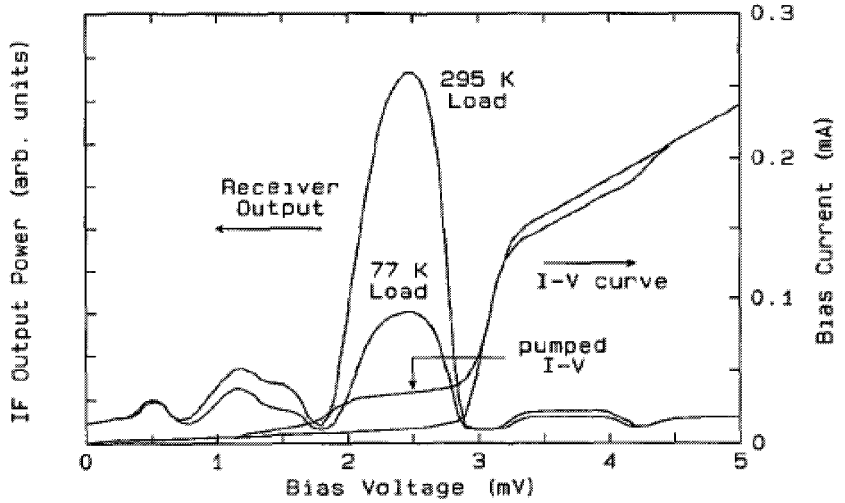

Fig. 1. I-V characteristics and output power vs. bias voltage curves for a 270 GHz SIS receiver. From [5].

The small signal power gain can be expanded as a Taylor series about the bias voltage V_0 [6]:

$$G(v) = G(V_0) + (v - V_0)^2 G''(V_0)/2 \,. \tag{1}$$

If a CW input signal produces an output voltage $v = V_0 + V_{IF}\sin(\omega_{IF} t)$, the time-averaged gain is then

$$G = G_0 + V_{IF}^2 G_0''/4 \,. \tag{2}$$

The IF power delivered to load R_L is $P_{IF} = \dfrac{V_{IF}^2}{2R_L} = P_{in} G$, from which it follows that [7]

$$G = G_0\left(1 + \frac{P_{sig}}{P_{sat}}\right)^{-1} \,, \tag{3}$$

where $P_{sat} = -2/G_0'' R_L$. Because the degree of saturation of an SIS mixer depends only on the magnitude of the IF output voltage relative to the width of a photon step, *i.e.*, $(G R_L P_{in})^{1/2}$ relative to Nhf/e, where N is the number of junctions in series and f is the LO frequency, P_{sat} can be written in the form

$$P_{sat} = K_{sat}^2 \left(\frac{hf}{e}\right)^2 \frac{N^2}{G_0 R_L} = C_{sat} \frac{N^2 f^2}{G_0 R_L} \,, \tag{4}$$

where K_{sat}^2 and C_{sat} are constant *for all SIS mixers*. K_{sat}^2 has been evaluated in [6] from experimental data which gives $K_{sat}^2 = 0.10$, corresponding to $C_{sat} = 1.7\text{e-}30$.

Figs. 2 and 3 show the results of saturation measurements on two SIS mixers using CW signals [7]. The saturation curve according to eq. (3) (the solid line) is seen to fit the measured data well. The value of P_{sat} is chosen to give the best fit to the data.

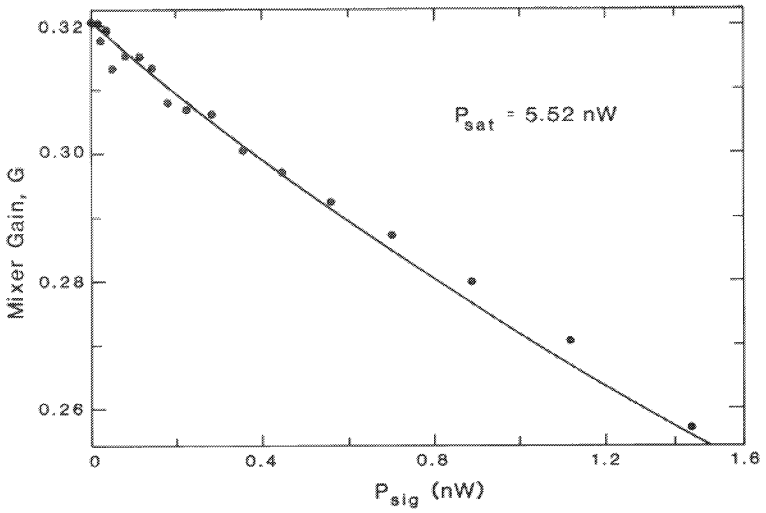

Fig. 2. Measured CW saturation for a 2-junction Pb/Ox/Nb SIS mixer at 115 GHz, from [7]. The solid curve is from eq. (3) with the value of P_{sat} chosen to give the best fit to the measured data.

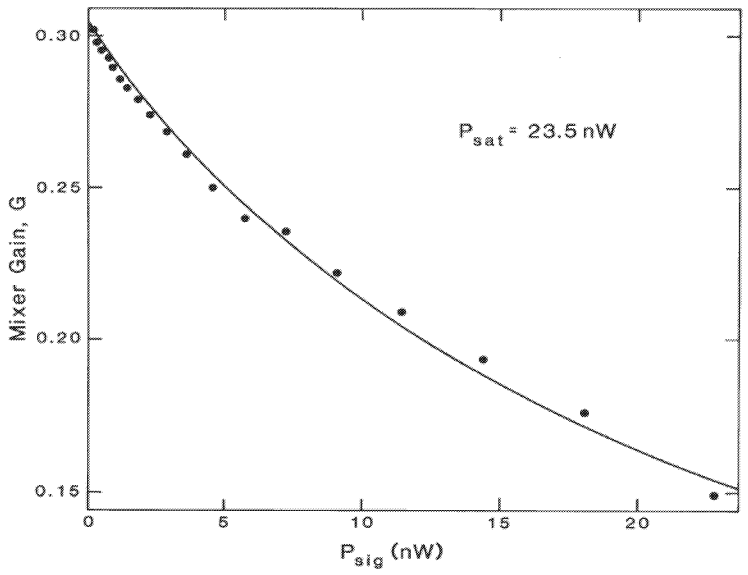

Fig. 3. Measured CW saturation for a 4-junction Nb/Al-AlOx/Nb SIS mixer at 115 GHz, from [7]. The solid curve is from eq. (3) with the value of P_{sat} chosen to give the best fit to the measured data.

Table I shows the values of C_{sat} obtained from measurements of the CW saturation power of four different SIS receivers. It is clear that the values of C_{sat} are reasonably close to the value 1.7e-30 above. Table II shows, for the same four SIS receivers, the CW signal power required to produce a gain compression of 1 dB and 1%.

Table I — C_{sat} evaluated for four SIS mixers

	LO GHz	Type	N	R_n	L_{SSB} dB	R_L	P_{sat} nW	C_{sat}
Pan *et al.* [8]	115	Pb-Nb	2	60	4.9	50	6.2	1.90E-30
Feldman *et al.* [7]	115	Pb-Nb	2	60	5.0	50	5.5	1.64E-30
Feldman *et al.* [7]	115	Nb	4	60	5.0	50	24	1.79E-30
Tong *et al.* [5]	270	Nb	1	18	3.0	50	6.4	2.20E-30

Table II — CW saturation powers for the mixers in Table I

	LO GHz	N	L_{SSB} dB	R_L	P_{1dB} nW	$P_{1\%}$ nW
Pan *et al.* [8]	115	2	4.9	50	1.6	0.062
Feldman *et al.* [7]	115	2	5	50	1.4	0.055
Feldman *et al.* [7]	115	4	5	50	6.2	0.240
Tong *et al.* [5]	270	1	3	50	1.7	0.064

3. ANALYSIS OF SATURATION BY BROADBAND NOISE

The previous section considered saturation caused by a sinusoidal RF input signal. When the RF input is noise, different saturation characteristics are expected. Because of the statistical nature of noise, the instantaneous amplitude of the signal at times exceeds the peak value of a CW signal having the same power, so gain compression begins at a lower power level than with a CW signal. To analyze gain compression by noise, it is convenient to consider the *voltage* gain of an SIS mixer rather than the *power* gain which was the focus in the previous section. If the probability density function of the input noise voltage is known, and also the nonlinear voltage characteristic of the gain compression mechanism, a new probability density function can be computed which characterizes the compressed output signal. In this section, this approach is applied to saturation by noise and CW signals — the latter case giving results in close agreement with those in the previous section.

The SIS mixer is characterized in Fig. 4 as a non-saturating mixer in series with a saturating IF element. The non-saturating mixer has gain and impedance characteristics, at all input power levels, identical to those of the actual mixer when operated under small signal conditions. The saturating element has an input impedance equal to the IF load impedance, R_L, an output impedance equal to that of the mixer, Z_m, and unity small-signal voltage gain when connected to the IF load. Hence, under small-signal and moderately large-signal operation, the circuit of Fig. 4 is indistinguishable from the real mixer.

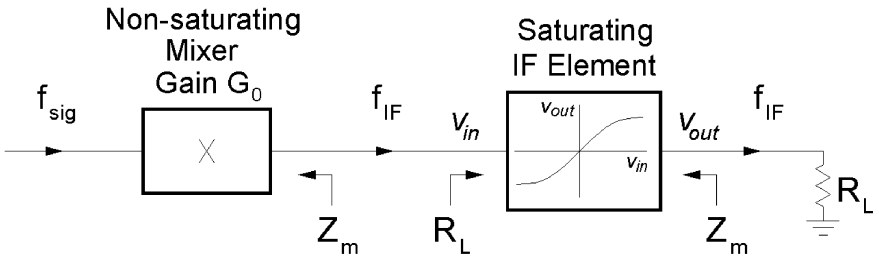

Fig. 4. Representation of the SIS mixer as a non-saturating mixer in series with a saturating IF element. The non-saturating mixer has gain and impedance characteristics identical to those of the actual mixer when operated under small signal conditions. The saturating IF element has unity small signal gain, an input impedance equal to the IF load impedance, R_L, and an output impedance equal to that of the mixer, Z_m.

The saturating element in Fig. 4 is characterized by its nonlinear voltage characteristic $v_{out}(t) = f(v_{in}(t))$, measured with the mixer and IF load in place. Note that v_{in} and v_{out} are the instantaneous values, not amplitudes, of the IF voltages at the input and output of the saturating IF element, as indicated in Fig. 4. When the mixer is biased near the middle of a photon step at the small-signal gain maximum, v_{out} is approximated by an odd function of v_{in}, and the differential gain of the saturating element is an even function of v_{in} which can be written, to first order, as[2]

$$A = \frac{dv_{out}}{dv_{in}} = \frac{1}{1 + A_3^2 v_{in}^2} \,. \tag{5}$$

Since the degree of saturation of an SIS mixer depends only on the magnitude of the IF output voltage relative to the width Nhf/e of a photon step, it is convenient to use normalized input and output voltages:

$$V_{in} = \frac{e}{Nhf} v_{in} \qquad \text{and} \qquad V_{out} = \frac{e}{Nhf} v_{out} \,. \tag{6}$$

[2] Other even functions could be chosen to approximate $A(v_{in})$, for example, the truncated Taylor expansion $(1 + Bv^2)$, which would give a good approximation to saturation in the real mixer for small values of v. It was found that the form of eq. (5), $1/(1 + Bv^2)$, gave good agreement with measured data even at levels of gain compression as high as 3 dB.

Then, in (5),

$$A(V_{in}) = \frac{dv_{out}}{dv_{in}} = \frac{dV_{out}}{dV_{in}} = \frac{1}{1 + C_3^2 V_{in}^2}, \tag{7}$$

where C_3 is a constant, independent of N and f, for all SIS mixers. The instantaneous (large signal) normalized output voltage is then

$$V_{out}(t) = \int_0^{V_{in}} \frac{dV_{in}}{1 + C_3^2 V_{in}^2(t)} = \frac{1}{C_3} \arctan\left(C_3 V_{in}(t)\right), \tag{8}$$

and the instantaneous large-signal voltage gain is

$$A_{LS}(t) = \frac{v_{out}}{v_{in}} = \frac{V_{out}}{V_{in}} = \frac{\arctan\left(C_3 V_{in}(t)\right)}{C_3 V_{in}(t)}. \tag{9}$$

When saturation is caused by broadband noise, eq. (9) allows the probability density function of the output noise to be computed from that of the input noise. The probability density of a Gaussian noise signal of mean square voltage σ^2 is given by

$$p(v) = \frac{1}{\sigma\sqrt{2\pi}} \exp\left(-\frac{v^2}{2\sigma^2}\right). \tag{10}$$

For the circuit of Fig. 4, if σ_{in} is the RMS voltage at the input of the nonlinear element whose input impedance is R_L, then the power delivered to the nonlinear element $P_{in} = G_0 P_{sig} = \sigma_{in}^2/R_L$. The output power delivered to the IF load R_L is

$$P_{out} = G P_{sig} = \frac{1}{R_L} \int_{-\infty}^{\infty} v_{out}^2 \, p(v_{in}) dv_{in}, \tag{11}$$

where $v_{out}(v_{in})$ is given by eq. (9). Therefore,

$$\frac{G}{G_0} = \frac{1}{\sigma^2} \int_{-\infty}^{\infty} v_{out}^2 \, p(v_{in}) dv_{in}. \tag{12}$$

Normalizing voltages to Nhf/e as in eq. (6), and defining the normalized RMS voltage at the input of the saturating element as $S_{in} = \frac{e}{Nhf}\sigma_{in}$, eqs. (8), (10) and (12) give

$$\frac{G}{G_0} = \frac{1}{\sqrt{2\pi}\, C_3^2 S_{in}^3} \int_{-\infty}^{\infty} \arctan^2\left(C_3 V_{in}\right) \exp\left(-\frac{V_{in}^2}{2S_{in}^2}\right) dV_{in}. \tag{13}$$

Since $S_{in}^2 = \left(\frac{e}{Nhf}\right)^2 \sigma_{in}^2 = \left(\frac{e}{Nhf}\right)^2 G_0 P_{sig} R_L$, eq. (13) allows G/G_0 to be computed as a function of P_{sig}, G_0, R_L, f, and N. If the input noise is from a broadband source with noise temperature T_{sig} at the input of the receiver, then $P_{sig} = 2kT_{sig}B_I$, the factor 2 accounting for the noise received in both upper and lower sidebands of the receiver. Determination of the constant C_3 is described in the next section, and the appropriate value of the effective IF bandwidth B_I is discussed in Section 4.

Determination of C_3

To determine the constant C_3, saturation by a CW signal was analyzed using (9), and C_3 adjusted to fit the experimental results given in the previous section.

A CW RF input signal of power P_{sig} delivers power $P_{in} = G_0 P_{sig}$ to the input resistance R_L of the saturating element in Fig. 4. If the voltage at the input of the saturating IF element is $v_{in}(t) = a\sin(\omega_{IF} t)$, then

$$P_{in} = G_0 P_{sig} = a^2/2R_L \,. \tag{14}$$

The instantaneous output power delivered to the IF load is $P_{out}(t) = v_{out}^2(t)/R_L$, which has an average value over the IF period

$$P_{out} = G\,P_{sig} = \frac{1}{R_L}\frac{1}{\tau_{IF}}\int_0^{\tau_{IF}} v_{out}^2(t)\,dt \;. \tag{15}$$

From eqs. (14) and (15):

$$\frac{G}{G_0} = \frac{2}{a^2}\frac{1}{\tau_{IF}}\int_0^{\tau_{IF}} v_{out}^2(t)\,dt \,. \tag{16}$$

Using normalized voltages, as in eq. (6), eq. (8) gives

$$\frac{G}{G_0} = \frac{2}{A^2 C_3^2}\frac{1}{\tau_{IF}}\int_0^{\tau_{IF}} \arctan^2\left(C_3 A\sin\left(\omega_{IF} t\right)\right)dt \,, \tag{17}$$

where $A = \dfrac{e}{Nhf}a$ is the normalized amplitude of v_{in}. Eq. (17) describes saturation by a CW signal in any SIS mixer. Since $A^2 = 2\left(\dfrac{e}{Nhf}\right)^2 R_L\, G_0\, P_{sig}$, eq. (17) allows G/G_0 to be computed as a function of P_{sig}, G_0, R_L, f, and N.

To determine the constant C_3, saturation by a CW signal was analyzed using (17), and C_3 adjusted to fit the experimental results given in the previous section. A good fit to the measured data at low saturation levels is obtained with $C_3 = 3.3$. Fig. 5 shows the agreement between eq. (3) with $P_{sat} = 23.5$ nW, which closely fits the measured saturation data for the 115 GHz 4-junction mixer, and the saturation characteristic given by eq. (9) with $C_3 = 3.3$.

In the above approach, the degree of gain compression was determined from the mean power delivered to the IF load (eqs.(15)-(17)). It could also be determined using the fundamental Fourier component of the power delivered to the IF load. We found that these two methods of calculation had negligible difference for gain compression levels up to ~50%.

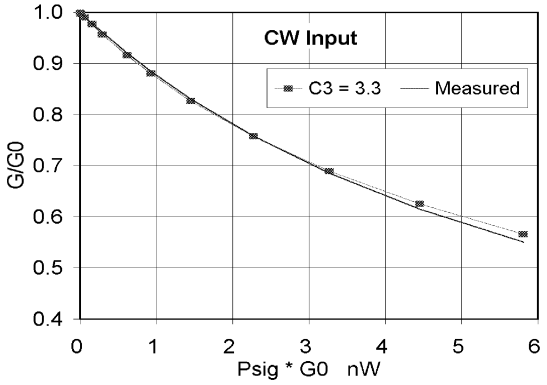

Fig. 5. The graph shows the close agreement between eq. (17) with C_3 = 3.3 and Eq. (3) with P_{sat} = 23.5 nW. Eq. (3) was shown to be an excellent fit to the measured gain compression curve for a 115 GHz 4–junction SIS mixer [7] (see Fig. 3).

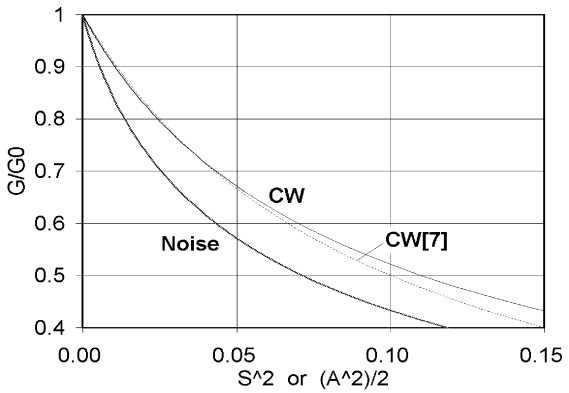

Fig. 6. Saturation by noise and CW signals. For noise, S^2 is given by eq. (18), and for CW, $A^2/2$ is given by eq. (19). The curve labeled CW[7] is computed from eq. (3) as in [7].

Comparison of Saturation by Noise and CW

A comparison of saturation by broadband noise and CW signals of equal powers is possible using eqs. (13) and (17). For noise, the signal power (in both sidebands) P_{sig} is related to S_{in} by

$$S_{in}^2 = \left(\frac{e}{Nhf}\right)^2 G_0 P_{sig} R_L \,, \tag{18}$$

and for a CW signal P_{sig} is related to A by

$$\frac{A^2}{2} = \left(\frac{e}{Nhf}\right)^2 G_0 P_{sig} R_L \,, \tag{19}$$

where N is the number of SIS junctions in series, G_0 is the small-signal gain of the mixer, and R_L is the IF load resistance. Fig. 6 shows G/G_0 as a function of S_{in}^2 (for noise) and $A^2/2$ (for CW). Also shown for comparison is the saturation curve computed from eq. (3) as in [7], which has been shown to fit experimental data well in the range $0.5 \le G/G_0 \le 1$ (see Figs. 2 and 3).

Examples

To illustrate the degree to which gain compression is likely to affect SIS receiver calibration when using a room-temperature calibration load, we make the following assumptions: (i) The mixer input bandwidth is B_I in each sideband, with B_I equal to 20% of the LO frequency. Roughly, this corresponds to a receiver which downconverts all frequencies within the full RF waveguide band, half in the LSB and half in the USB, to an extended IF band from 0 to B_I Hz. (ii) The IF load on the mixer is taken as R_L = 50 ohms over the extended IF band $0 < f < B_I$, an approximation which will be discussed below. An IF impedance of 50 ohms is used because this is the nominal input impedance of many low noise IF preamplifiers, including the present NRAO 4–12 GHz HFET preamplifier [9]. We assume the mixer and preamplifier are connected directly together with no intervening impedance transformer. (iii) The small-signal gain has a constant value G_0 over the full input band $0.8 f_{LO} < f < 1.2 f_{LO}$. Under these assumptions, Fig. 7 shows the expected gain compression caused by a room-temperature calibration load for SIS mixers at four LO frequencies. The gain compression

produced by a CW input signal of the same power as the noise input is shown for comparison. It is seen from Fig. 7 that mixer receivers satisfying assumptions (i)-(iii), with small signal gain $G_0 = 6$ dB SSB and a single SIS junction, can be expected to have a gain compression due to a room-temperature source of 16% at 115 GHz and 5% at 460 GHz. With four junctions, the gain compression is 1.4% at 115 GHz and 0.4% at 460 GHz.

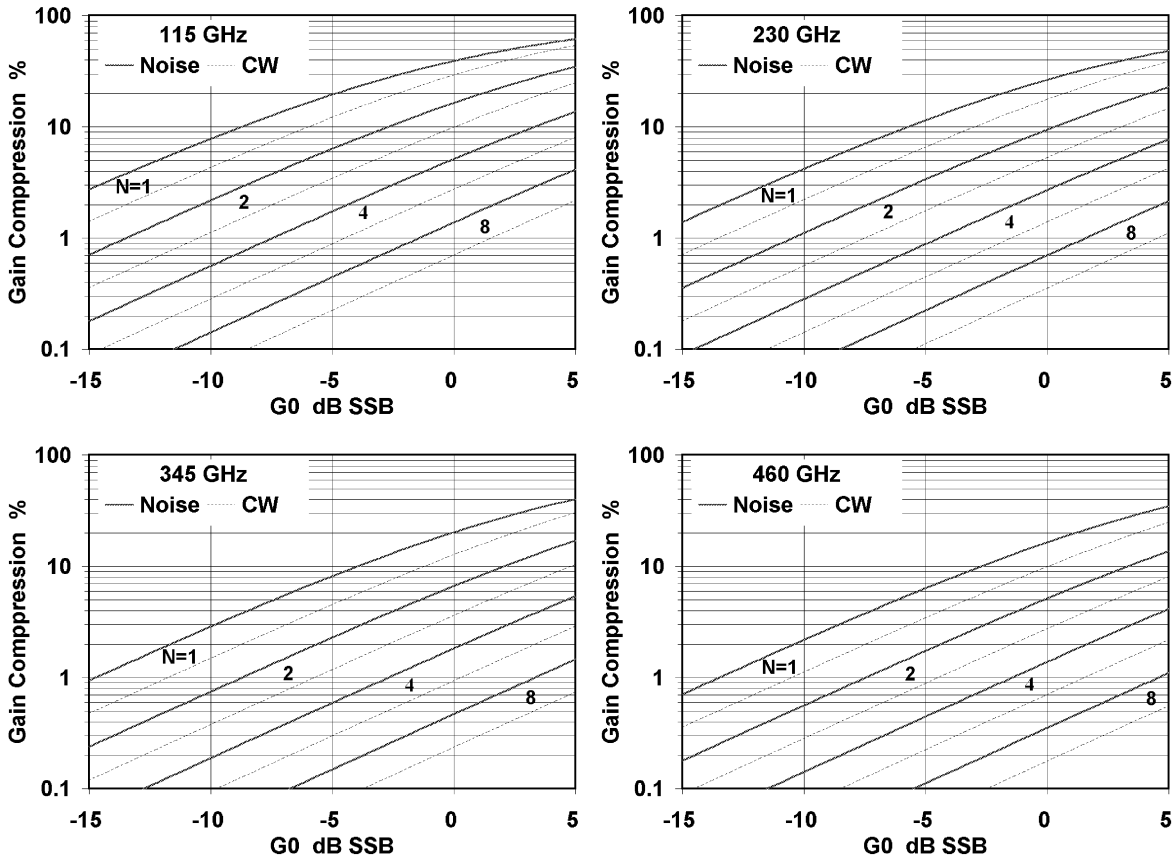

Fig. 7. Curves of gain compression caused by a 300 K source (solid red lines), as a function of small-signal mixer gain, G_0, for SIS mixers at four frequencies. The parameter *N* is the number of junctions in series. In all cases: (i) the input noise bandwidth B_I in each sideband is equal to 20% of the LO frequency, (ii) the IF load impedance is 50 ohms over the extended IF band $0 < f_{IF} < B_I$, and (iii) the small-signal gain is constant over $0.8\ f_{LO} < f_{sig} < 1.2\ f_{LO}$. Shown for comparison is the gain compression by a CW signal of the same power (dotted black line).

4. DISCUSSION

It is clear from the simulations in Section 3 that noise and CW signals of equal power produce different degrees of saturation in SIS mixers. Furthermore, it is apparent that a room-temperature source may cause significant gain compression in many practical SIS receivers, a phenomenon which affects the accuracy of astronomical observations made with an SIS receiver calibrated using a room-temperature source.

Bandwidth and IF Load Impedance

The noise saturation results in Fig. 7 are based on the following major assumptions: (i) the input noise bandwidth B_I in each sideband is equal to 20% of the LO frequency, (ii) the IF load impedance R_L = 50 ohms over the frequency range 0 to B_I, and (iii) the small-signal gain G_0 is flat over $0.8\,f_{LO} < f_{sig} < 1.2\,f_{LO}$. The frequency range $0.8\,f_{LO} < f_{sig} < 1.2\,f_{LO}$ corresponds approximately to a standard waveguide band when f_{LO} is at the band center. A typical broadband waveguide to TEM mode transducer has poor coupling outside the waveguide band, and thus acts to some extent as a band-limiting filter. However, as saturation in SIS mixers is primarily determined by the magnitude of the output voltage, the behavior of the embedding impedance $Z_e(f_{IF})$ over $0 < f_{IF} < B_I$ seen by the SIS junction(s) is the major determinant of the saturation behavior. In the analysis, it has been assumed that $Z_e = R_L$ at all frequencies, whereas in reality Z_e depends on the RF choke circuit of the mixer, any circuit elements between the mixer and IF amplifier, and the input impedance of the IF amplifier itself. The importance of Z_e over this extended IF range has been pointed out in [10].

Improving the Dynamic Range

Are there ways to improve the dynamic range of an SIS receiver? It is clear, from eqs. (3) and (4) in the case of CW signals, and eqs. (6) and (9) in the case of noise, that the dynamic range of an SIS mixer can be increased by: (i) increasing the number N of junctions in series, (ii) reducing the transducer gain G_0, or (iii) reducing the IF load resistance R_L (which also affects G_0). If saturation is caused by broadband noise, a bandpass or lowpass IF filter immediately following the SIS mixer could reduce the RMS IF noise voltage at the mixer output if the filter were designed to have low impedance at all frequencies above the desired IF band. This has been suggested in [10] but is difficult to implement unless the filter is incorporated into the SIS mixer chip. In [11], a 200-280 GHz SIS mixer is described in which $|Z_e| < 50$ ohms over 0 to 150 GHz when the IF amplifier has an impedance of 50 ohms over that band (in reality, of course, the impedance of the IF amplifier is unlikely be 50 ohms at frequencies far from the nominal IF band). Fig. 8 shows $Z_e(f)$ for that mixer, including the effects of the RF choke, junction capacitance, and all the RF circuit elements. The decrease of $|Z_e|$ with frequency reduces the IF voltage at the mixer output due to a broadband noise input, and thereby reduces the degree of saturation compared with a mixer in which the IF embedding impedance is largely in the high impedance region of the chart.

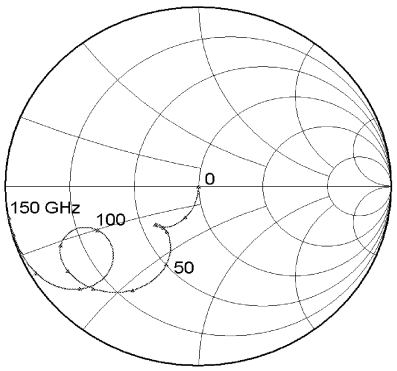

Fig. 8. Embedding impedance $Z_e(f)$ seen by the SIS junctions in a low-parasitic 200-280 GHz SIS mixer [11]. $Z_e(f)$ includes the RF choke and all the RF circuit elements, and assumes that the input impedance of the IF amplifier is 50 ohms at all frequencies. Z_e is plotted on a 50-ohm Smith chart over the frequency range 0-150 GHz with markers every 10 GHz.

In principle, the dynamic range of an SIS mixer can be increased by increasing the junction area by a factor M (> 1) while reducing the embedding impedance at all frequencies by the same factor M; for example, the larger junction could be connected to the same embedding circuit through an ideal transformer with impedance ratio M at all frequencies. A given degree of gain compression occurs in both the original mixer and the modified mixer when each has the same IF voltage at the junction. However, the modified mixer has an IF load impedance (seen from the junction) lower by factor M than the original mixer, so the IF power delivered to the load is larger by factor M, and the RF input power is therefore also larger by a factor M.

Measurement of Gain Compression using a CW Signal in the Presence of Broadband Noise

It is of interest to consider the response of an SIS mixer, partly saturated by broadband noise, to a small CW test signal. The test signal produces a response with a small-signal gain which is a function of the total input power (test signal + noise). The gain is not substantially affected by the test signal as long as its power is small compared with the noise input power, and the small-signal response is then linear. Only when the test signal power approaches that of the broadband input noise power in RF bandwidth $2B_I$ (B_I is the effective IF noise bandwidth as defined above, and the factor 2 accounts for the two RF sidebands in a DSB mixer) will it contribute substantially to saturation, which will be evident from the nonlinearity of the curve of test signal output power *vs* test signal input power.

It is sometimes assumed that a linear curve of test signal output power *vs* test signal input power implies that a receiver is not saturated by broadband noise accompanying the test signal. This is the assumption in [5], for a receiver with a room temperature input load in which no gain compression was measured at low CW powers. It was concluded that *"...the receiver is still highly linear when subjected to radiation from an ambient load...."* If one applies the noise saturation analysis of Section 3 to the mixer used in [5], assuming an extended IF noise bandwidth B_I of 15 GHz, a room temperature black body source is predicted to produce ~5% gain compression — this is consistent with the other data given in [5].

To determine the degree of gain compression produced by broadband input noise, a small CW test signal can be used as an indicator. The small-signal gain curve (test signal output power *vs* test signal input power) is measured first, in the presence of the high level broadband noise source (*e.g.*, a room temperature load), and a convenient signal level in the linear region of this curve is chosen. Then, the high level noise source is replaced with a low level noise source (*e.g.*, a liquid nitrogen load) and the test signal output level re-measured. Any gain compression caused by the high level noise source will be indicated by an increase in the test signal output when the high level noise source is replaced with the low level noise source.

Balanced and Sideband Separating Mixers

In balanced mixers and sideband-separating mixers, the input power is divided equally between two unit (double-sideband) mixers. The power required to produce a given degree of gain compression is therefore twice that required to produce the same gain compression in a single unit mixer connected to the same signal and IF embedding impedances. In the case of a balanced sideband-separating mixer, the input power is divided between four unit mixers, so the saturation power is four times that of the unit mixer.

ACKNOWLEDGMENTS

The author thanks Shing-Kuo Pan of NRAO and Charles Cunningham of HIA for their valuable discussions on saturation in SIS mixers and comments on the manuscript.

REFERENCES

[1] R. L. Plambeck, "Receiver amplitude calibration for ALMA," ALMA Memo 321, August 27, 2000. Available at http://www.alma.nrao.edu/memos/.

[2] L. R. D'Addario, "An SIS Mixer for 90-120 GHz with Gain and Wide Bandwidth," *Int. J. Infrared Millimeter Waves*, vol. 5, no. 11, pp. 1419-1442, 1984.

[3] E. S. Palmer, T. Dame, private communication, November 2001. The mixer used two SIS junctions in series and was tuned for SSB operation using its two waveguide tuners.

[4] A. D. Smith and P. L. Richards, "Analytic solutions to SIS quantum mixer theory," *J. Appl. Phys.*, vol. 53, no. 5, pp. 3806-3812, May 1982.

[5] C.-Y. E. Tong, R. Blundell, S. Paine, D. C. Papa, J. Kawamura, J. Stern, and H. G. LeDuc, "Design and Characterization of a 250-350 GHz Fixed-Tuned Superconductor-Insulator-Insulator Receiver," *IEEE Trans. Microwave Theory Tech.*, vol. MTT-44, no. 9, pp. 1548-1556, Sept. 1996.

[6] M. J. Feldman and L. R. D'Addario, "Saturation of the SIS direct detector and the SIS mixer," *IEEE Trans. Magnetics*, vol. MAG-23, no. 2, pp. 1254-1258, March 1987.

[7] M. J. Feldman, S.-K. Pan, and A.R. Kerr, "Saturation of the SIS mixer," *International Superconductivity Electronics Conference Digest*, Tokyo, pp. 290-292, Aug. 1987.

[8] S.-K. Pan, A. R. Kerr, M. J. Feldman, A. Kleinsasser, J. Stasiak, R. L. Sandstrom, and W. J. Gallagher, "An 85-116 GHz SIS receiver using inductively shunted edge-junctions," *IEEE Trans. Microwave Theory Tech.*, vol. MTT-37, no. 3, pp. 580-592, March 1989.

[9] E. F. Lauria, A. R. Kerr, M. W. Pospieszalski, S.-K. Pan, J. E. Effland, and A. W. Lichtenberger, "A 200-300 GHz SIS Mixer-Preamplifier with 8 GHz IF Bandwidth," *2001 IEEE International Microwave Symposium Digest*, pp. 1645-1648, May 2001. Available as ALMA Memo 378 at http://www.alma.nrao.edu/memos/.

[10] L. R. D'Addario, "Saturation of the SIS mixer by out-of-band signals," *IEEE Trans. Microwave Theory Tech.*, vol. MTT-26, pp. 1103-1105, no. 6, June 1988.

[11] A. R. Kerr, S.-K. Pan, A. W. Lichtenberger and H. H. Huang, "A Tunerless SIS mixer for 200–280 GHz with low output capacitance and inductance," *Proceedings of the Ninth International Symposium on Space Terahertz Technology*, pp. 195-203, 17-19 March 1998. Available as ALMA Memo 205 at http://www.mma.nrao.edu/memos/.

Quantum-limited Mixing in a Transformer-coupled SIS Resonator for the 600 GHz Frequency Band

Cheuk-yu Edward Tong, Raymond Blundell
Harvard-Smithsonian Center for Astrophysics, 60 Garden Street, Cambridge, MA 02138.

Krikor G. Megerian, Jeffrey A. Stern, Henry G. LeDuc
Jet Propulsion Lab, California Institute of Technology, 4800 Oak Grove Drive, Pasadena, CA 91109.

Abstract

Quantum-limited mixer noise temperature has been achieved in Superconductor-Insulator-Superconductor (SIS) resonant mixer in the 600 – 720 GHz frequency range. Our mixer employs a single full-wave Nb/AlN/Nb tunnel junction resonator, fed by a quarter-wave transformer. The devices have low critical current density (~ 5 kA/cm^2). The mixers were tested in a fixed-tuned waveguide mixer mount. Double-side-band receiver noise temperatures equivalent to a few quanta have been measured for a number of different devices. Using a 0.55 x 25 μm resonator, a noise temperature of 141 K was recorded at an LO frequency of 700 GHz with the mixer at 4.2 K. The noise temperature dropped to 111 K when the helium bath was pumped down to 2.8 K. High sensitivity has attained over reasonably wide RF bandwidth, ~17%. The IF bandwidth of these mixers has also been investigated.

I. Introduction

The introduction of distributed mixing in Superconductor-Insulator-Superconductor (SIS) junctions is an important development in low-noise receiver technology for sub-millimeter wavelengths [1,2]. The earliest distributed mixers employed fairly long superconducting tunnel junctions, about 2 wavelengths long. The long junction acts as a lossy transmission line in which mixing occurs along the whole length of the line. This class of receiver has demonstrated sensitivities close to the quantum limit. A noise temperature of

3hv/k was recorded at 460 GHz [1], where $h\nu$ is the photon energy and k is the Boltzmann constant.

In a subsequent developemnt, Belitsky [3] proposed that distributed mixing could also be implemented in SIS resonators. One advantage of resonant distributed mixing is that the resonator can achieve a higher impedance level compared to simple long superconducting transmission lines which generally have very low characteristics impedance. Uzawa [4] performed experiments with resonant distributed mixers incorporating a niobium nitride SIS resonator in the 800 GHz frequency band. Finally, in 2001, Matsunaga [5] implemented distributed mixing using dual SIS resonators connected in series through impedance transformers, employing standard Nb/Al/AlOx/Nb SIS junctions fabricated with optical lithography. That mixer exhibited high sensitivity, with a measured noise temperature of 185 K at 630 GHz.

Following this encouraging result, we have developed resonant mixers based on Nb/AlN/Nb junctions fabricated with electron-beam lithography at Jet Propulsion Lab. In this paper, we demonstrate that the sensitivity of 0.6 μm wide full-wave SIS resonators can reach quantum-limited performance in the 600 GHz band, at frequencies that approach the band gap frequency of niobium.

II. Modeling of the SIS Resonator

Fig. 1 shows the cross-section of the SIS non-linear transmission line, which reduces to a simple microstrip line when the width of the tunnel barrier, W_j, is zero. Such a linear superconducting microstrip line can readily be modeled by various approaches. We have employed the analysis described in [6], using frequency dependent surface impedances from the Mattis-Bardeen Theory [7]. Let Z_0 and γ_0 be the characteristics impedance and complex propagation constant of the line respectively for $W_j = 0$. If W_j is much smaller than the width of top conductor of the microstrip, W_s, we can write down the per unit length series impedance of the

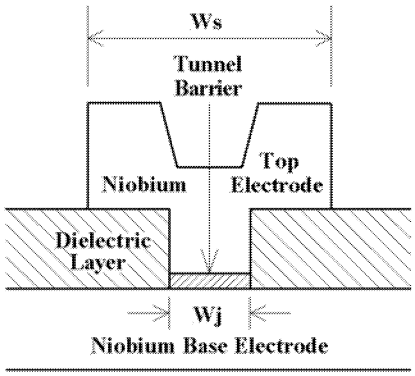

Fig. 1 Cross-sectional view of an SIS non-linear transmission line. In our mixers, the tunnel barrier is Aluminum Nitride (AlN) and the dielectric layer is 250 nm thick of Silicon Oxide (SiO). The width of the wiring layer, *Ws*, is 4 μm.

transmission line as:

$$Z_s = \gamma_0 Z_0 (1 - W_j / W_S) , \quad (1)$$

and the per unit length parallel admittance as:

$$Y_p = \frac{\gamma_0}{Z_0}.\left(1 - \frac{W_j}{W_s}\right) + j\omega.C_{sp}.W_j + \xi\frac{W_j}{R_N A} \quad (2)$$

where C_{sp} is the specific capacitance of the tunnel junction per unit area, R_NA is the product of normal state resistance and area of the junction and ξ is a signal mixing factor. In equation (2), the second term represents the contribution of the geometrical capacitance of the tunnel junction and the third term represents the mixing conductance due to the tunneling quasiparticle current, G_{qp} [3].

From Tucker's quantum theory of mixing [8], we can write down an expression for ξ:

$$\xi = G_{qp}R_N = \frac{eR_N}{2h\nu}.\sum_{n=-\infty}^{\infty}\left[J_{n-1}^2(\alpha) - J_{n+1}^2(\alpha)\right]I_{dc}(V_0 + \frac{nh\nu}{e}) \quad (3)$$

where $\alpha = eV_{LO}/h\nu$ is the normalized voltage impressed by the Local Oscillator (LO) across the junction, $I_{dc}(V)$ is the DC current-voltage characteristic of the junction and V_0 is the DC bias voltage at the operating point. From our simulation, we find that a niobium based SIS resonator should operate well with $\alpha \sim 0.7$ and $V_0 \sim 1.5$ mV for $\nu \sim 660$ GHz. Under these conditions, equation (3) gives $\xi \sim 0.8$. By assigning a constant value to ξ, we assume that the distributed mixer may be described by a linear model [1].

Once Z_s and Y_p are known, we can evaluate the key parameters of the non-linear transmission line, including the characteristic impedance, Z_c, the complex propagation constant, γ, and the guided wavelength, λ_g .

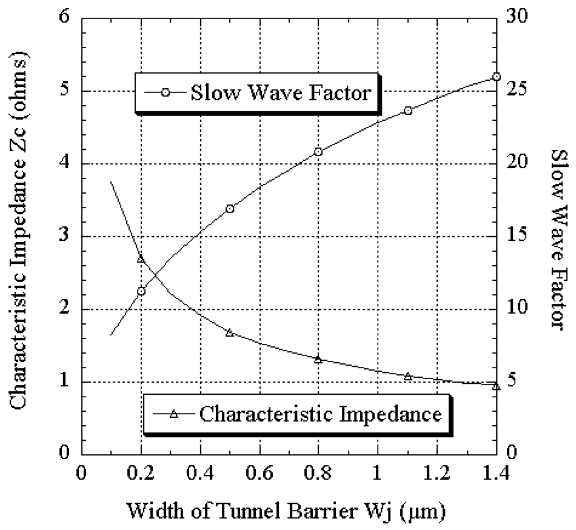

Fig. 2 Variation of Characteristic Impedance, Z_c, and Slow Wave Factor, λ_0/λ_g, as a function of W_j for our mixers at a frequency of 660 GHz. We have taken W_s = 4 μm, C_j = 65 fF/μm^2 and R_NA = 40 Ω μm^2.

$$Z_c = Z_s / Y_p \tag{4}$$

$$\gamma = \sqrt{Z_s . Y_p} \tag{5}$$

$$\lambda_g = \frac{\lambda_0}{2\pi} . \mathrm{Im}(\gamma) \tag{6}$$

The characteristic impedance and the slow wave factor, λ_0 / λ_g , for our mixer as a function of the width of the tunnel barrier, W_j , are plotted in Fig. 2. From the figure, it can be seen that Z_c is not a strong function of W_j for W_j > 0.4 μm. However, λ_g is strongly dependent on the width of the tunnel junction.

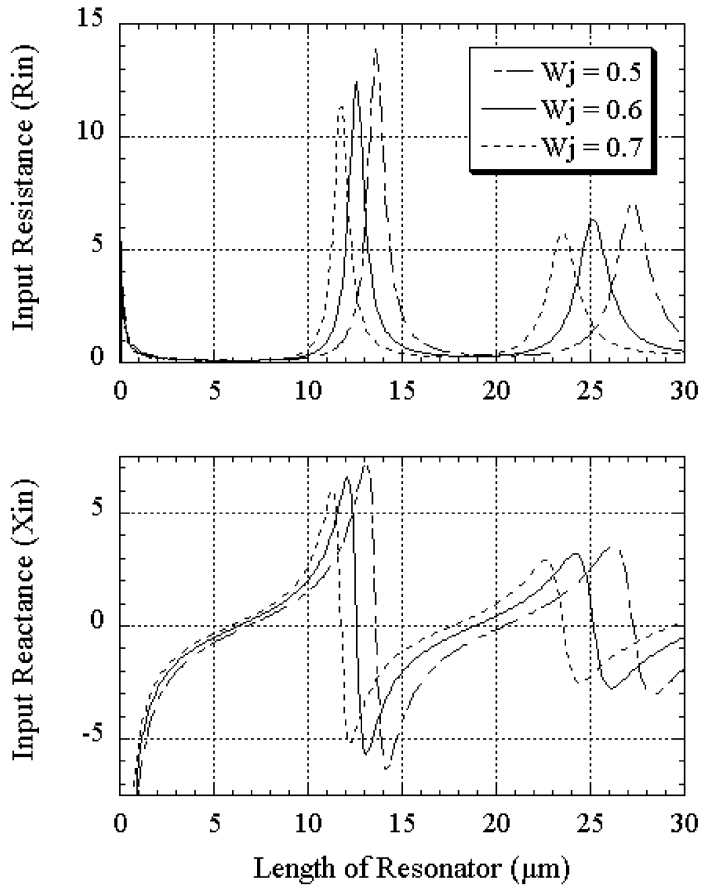

Fig. 3 Input impedance of SIS Resonator at 660 GHz as a function of resonator length for W_j = 0.5, 0.6 and 0.7 μm. R_{in} is the real part and X_{in} is the imaginary part of the input impedance, where $R_{in} + j\,X_{in} = Z_c(W_j).\coth(\gamma(W_j).L_j)$ and L_j is the length of the resonator.

In fig. 3 we display the input impedances of 3 SIS resonators with different junction widths. The length for half-wave resonance is about 12 μm and full-wave resonance occurs around 25 μm. As discussed above, the resonant impedance level is not a strong function of W_j. However, for a given length of resonator, the resonant frequency is quite sensitive to the junction width.

In our experiments, we have chosen to work with full-wave resonators rather than half-wave resonators because the value of dX_{in}/df is smaller at full-wave resonance, hence a larger impedance bandwidth can be achieved.

III. Mixer and Receiver Design

In order to match the low input resistance (~6 Ω) at the full-wave resonance of the non-linear SIS resonator, we use a 3 μm wide niobium microstrip transformer section to couple the signal power from our fixed-tuned waveguide mixer mount [9,10]. The layout of the center of the mixer chip is shown in Fig. 4. Since the resonant frequency is highly dependent on the exact width of the junction, we have fabricated chips with different junction widths and lengths about the nominal dimensions of 0.6 x 25 μm. We had a target current density of 5 kA/cm^2, which corresponds to R_NA = 40 Ω μm^2.

The mixer is tested in a laboratory test dewar, the details of which have been described elsewhere [5,11]. In all the experiments, we have used an IF center frequency of 3 GHz and the signal and LO input to the dewar are combined using a wire grid polarizer as a beam splitter in front of the cryostat vacuum window. The receiver IF output is measured by a power meter, over the band 2.4 – 3.6 GHz. Fig. 5 shows a photo of the set-up of our measurement bench.

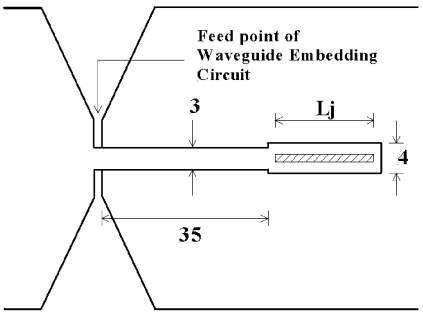

Fig. 4 Line drawing of mixer chip layout, showing the microstrip transformer section and the SIS resonator. The drawing is not to scale and the dimensions are in μm.

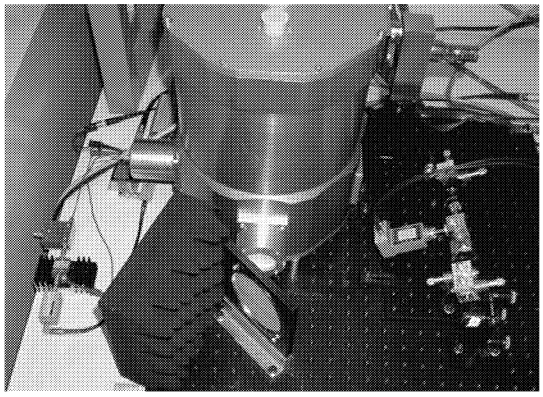

Fig. 5 Set-up of laboratory receiver measurement. LO unit is located on the right. The LO beam is focused by a 90° parabolic mirror and is injected into the dewar by a wire grid polarizer. The 3 GHz room temperature IF chain is on the left.

IV. Receiver Performance

The receiver noise temperature of was measured using the standard Y-factor method with ambient (295 K) and liquid-nitrogen cooled (77 K) loads.

We have tested a number of different mixer chips, and fig. 6 shows the current-voltage

and power-voltage characteristics of a 0.55 x 25 μm resonator, and the variation of Y-factor with bias voltage, when driven by a 700 GHz LO. The gap voltage is 2.85 mV at a bath temperature of 4.2 K. The mixer is, therefore, operating close to its gap frequency of 690 GHz. The tunneling current at 4 mV bias is about 1.4 mA, which corresponds to a normal state resistance of about 2.8 Ω. The sub-gap leakage current at 2 mV bias is about 66 μA, which corresponds to a sub-gap leakage resistance of about 31 Ω. A small magnetic field is applied so that the IF power output is minimized at 1.45 mV bias, where the first Shapiro step occurs.

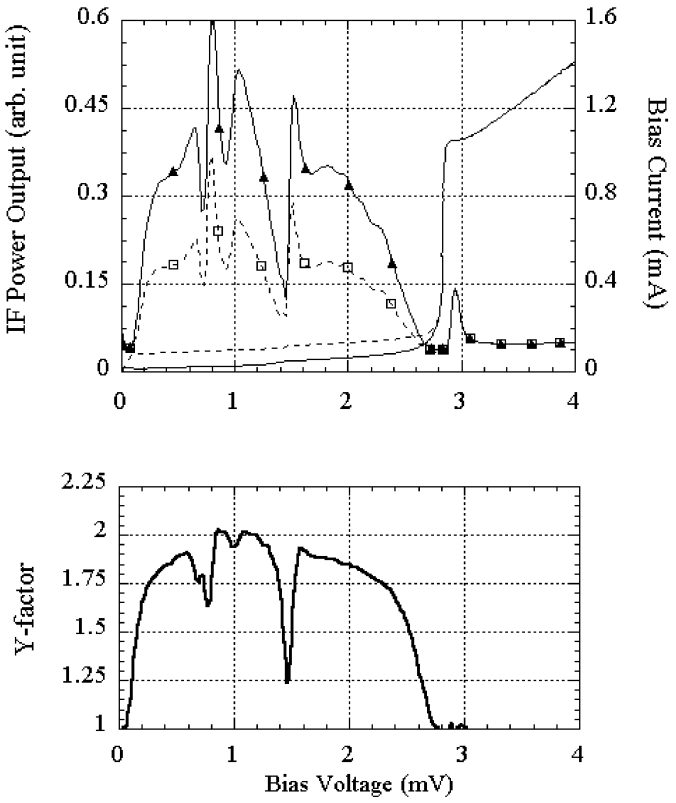

Fig 6 The top figure shows the Current Voltage Characteristics of a 0.55 x 25 μm resonant mixer without LO (solid line) and in the presence of LO power at 700 GHz (dotted line). On the same figure, the receiver IF power output is also displayed. The solid line with markers ▲ gives the response to a 295 K load, and the dotted line with markers □ gives the response to a 77 K load. The bottom figure shows the variation of Y-factor as a function of bias voltage. The bath temperature was 4.2 K.

A Y-factor of 2 was observed at a bias setting of 1.1 mV and 0.1 mA, corresponding to a double-side-band (DSB) Rayleigh-Jean noise temperature of 141 K. In spite of the high value of dP_{out}/dV at this bias setting, the receiver was found to be very stable. The estimated DSB conversion loss was about 7.5 dB. At a bias of 1.7 mV, the Y-factor was 1.92, improving to 1.95 when the LO power was slightly increased. The Y-factor showed a dip at a bias of 0.75 mV. We believe that this was caused by Josephson oscillation at about 360 GHz, the frequency at which the mixer becomes a half-wave resonator.

When the helium bath temperature was reduced to 2.8 K, the sub-gap leakage current decreased to 54 μA. Conversion loss was decreased by about 1 dB and the Y-factor measured at

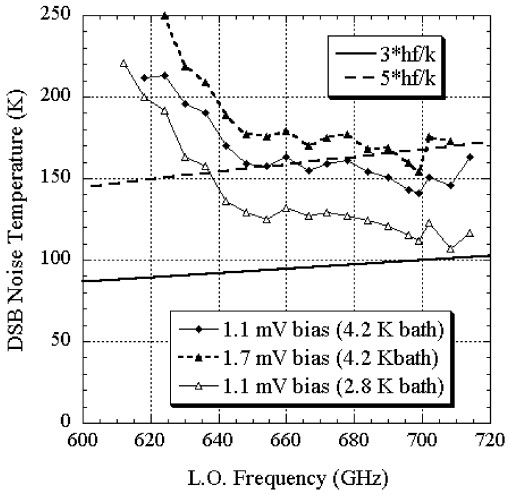

Fig. 7 Noise temperature of 0.55x25 μm SIS resonator as a function of L.O. frequency. Noise temperature is calculated from measured Y-factor in the Rayleigh-Jeans regime, by Tn = (295-77Y)/(Y-1).

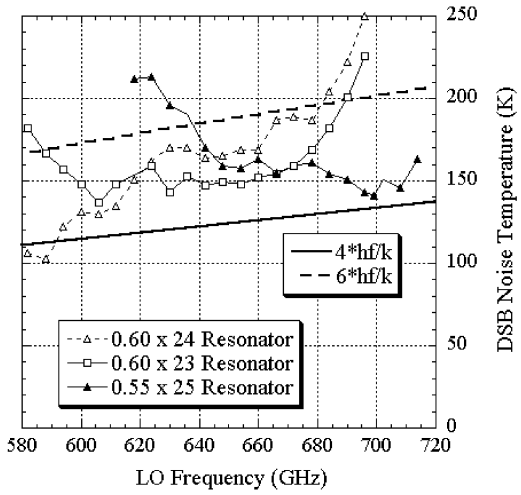

Fig. 8 Performance of different mixers biased at 1.1 mV with a 4.2 K helium bath. Also shown are the noise temperature corresponding to 4 and 6 photons.

1.1 mV bias point jumped to 2.16, corresponding to a DSB Rayleigh-Jean noise temperature of 111 K. This noise temperature is equivalent to 3.3 *hv/k*, which implies that the sensitivity is quantum-limited. The decrease in receiver noise temperature of about 30 K is mainly due to a reduction of leakage current. The gap voltage only changed by 0.05 mV and should only have a small impact on sensitivity. We expect that if lower leakage devices become available, we would be able to measure noise temperatures in the 3 *hv/k* range even with a 4.2 K helium bath.

In figure 7, plot the receiver noise temperature as a function of LO frequency for different bias conditions and different helium bath temperatures. Low noise operation is achieved up to 714 GHz, the highest frequency of our LO unit. Measurements with Fourier Transform Spectrometer indicate that the receiver should have reasonable performance up to 730 GHz.

In Fig. 8 we display frequency dependence of the sensitivity of 3 different mixers in our test receiver. The 0.60 x 23 μm resonator has a noise temperature below 200 K between 580 and 690 GHz, corresponding to a bandwidth of about 17%. These data shows that the frequency response of these resonant mixers is controlled mostly by the width of the resonator, rather than by the length. For example, the 0.60 x 23 μm resonator is centered at a

lower frequency than the 0.55 x 25 μm resonator. This is consistent with the results of the calculations shown in Fig. 3.

V. IF Bandwidth

One concern about distributed SIS mixers is their large geometrical capacitance which may limit the useful IF bandwidth. For example, in the 0.55 x 25 μm resonator, the device capacitance is estimated to be about 0.9 pF, considerably higher than other lumped element designs, which typically have a total of 0.3 pF output capacitance [6,9,10]. We have made detailed measurement of the IF performance of our mixer using a 2 – 4 GHz amplifier and a 4 – 8 GHz amplifier. The noise temperature of both amplifiers is in the 3 – 4 K range and we incorporate a circulator cooled to 4.2 K between the mixer and IF amplifier. The measured data is summarized in Fig. 9.

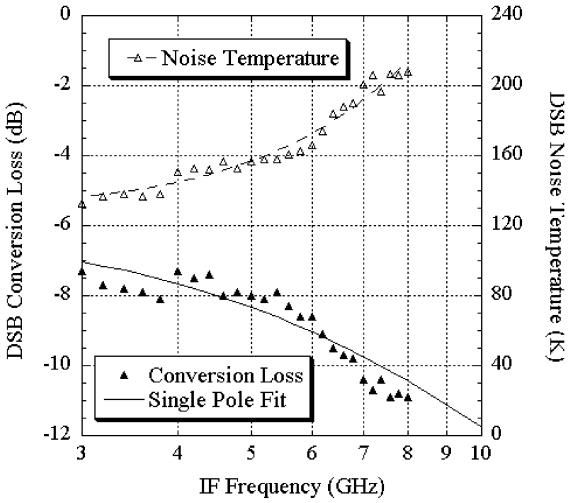

Fig. 9 IF Response of a 0.55 x 25 μm resonator. The conversion loss data has been fitted with a single pole roll-off model that has a 3-dB roll-off at about 6 GHz.

The data confirms that the receiver performance degrades with increasing IF. Using a single pole roll-off model, we derive a 3-dB IF bandwidth of 6 GHz from the experimental data. At an IF of 6 GHz, the conversion loss is about –9 dB versus –7 dB at around 3 GHz, and the noise temperature is 170 K versus 140 K at 3 GHz. From the sensitivity point of view, this mixer will be useful up to an IF frequency of 8 GHz, at which point, the noise temperature is about 1.4 times the noise temperature at lower IF, which corresponds to a doubling of integration time needed to obtain the same signal-to-noise ratio when a faint signal is being received.

The IF roll-off can be understood by considering the equivalent output circuit of the mixer as shown in Fig. 10. In this circuit, R_{out} is the output resistance of the

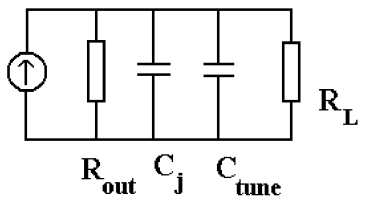

Fig. 10 Equivalent Output Circuit of SIS Mixer

device given by *dV/dI* on the current-voltage characteristic of the device in the presence of LO drive. C_j is the junction capacitance and C_{tune} is any parasitic capacitance introduced by any matching circuit. In the case of the resonant mixer, C_{tune} is introduced by the transformer section and it is much smaller than C_j . Assuming that the mixer output is connected to a constant load, R_L , the 3-dB IF bandwidth as a result of this RC circuit can simply be written as:

$$F_{3-dB} = \frac{R_{out} + R_L}{2\pi . R_{out} . R_L . (C_j + C_{tune})} = \frac{(1 + \frac{R_{out}}{R_L})}{2\pi . r . (R_N A).(1 + \chi) C_{sp}} \qquad (7)$$

where $r = R_{out} / R_N$ and $\chi = C_{tune} / C_j$. In our mixer, $R_L = 50\ \Omega$, $R_{out} \sim 45\ \Omega$ and $\chi << 1$, and we have $F_{3\text{-}dB} \sim 7.5$ GHz. This is close to the fitted value of 6 GHz.

It is clear from equation (7) that when $R_{out} \sim R_L$, the IF bandwidth limitation is imposed not so much by the large junction capacitance but by a large value of *r*, the ratio between the output resistance and the normal-state resistance. In this example, we have $r > 10$. However, this seems unavoidable at high operating frequency where the quasi-particle tunneling step is very wide and the step is more likely to be flat, giving rise to relatively high values of R_{out} . This does not seem to be unique to resonant mixers. We also note that the IF bandwidth depends on the $R_N A$ product. Clearly, we may improve the IF bandwidth by increasing the current density of the tunnel junction. However, at higher current density, C_{sp} slowly increases, so that the gain in bandwidth may be limited.

Equation (7) can be applied to all other types of SIS mixers. In many lumped element mixer designs, the tuning circuit may involve a large capacitance, making $\chi > 1$, In which case, equation (7) predicts that the IF bandwidth will be smaller than resonant mixers.

The above discussion assumes a constant IF load. An IF matching circuit can always be designed to reduce the impact of the IF roll-off effect. The large geometrical capacitance of the distributed mixer does not seem to impose a fundamental limit on the IF bandwidth of the mixer.

VI. Conclusion

A near Quantum-limited sensitivity has been achieved in the 600 – 720 GHz frequency band using an SIS resonant mixer receiver. The tunnel junction resonators in our mixer design can be modeled easily through a simple linear transmission line equations. Using transformer-coupled full wave Nb/AlN/Nb resonators, we have measured noise

temperatures as low as 141 K at 700 GHz with the mixer cooled to 4.2 K and 111 K with the mixer cooled to 2.8 K. The mixers exhibit a 17% RF bandwidth, have a measured 3-dB IF bandwidth of 6 GHz and useful sensitivities up to an IF bandwidth of about 8 GHz.

References

[1] C.E. Tong, R. Blundell, B. Bumble, J.A. Stern, and H.G. LeDuc, "Quantum-limited heterodyne detection in superconducting nonlinear transmission lines at sub-millimeter wavelengths," *Appl. Phys. Lett.,* vol. 67, pp. 1304-1306, Aug. 1995.

[2] C.E. Tong, L. Chen, and R. Blundell, "Theory of distributed mixing and amplification in a superconducting quasi-particle nonlinear transmission line," *IEEE Trans. Microwave Theory Tech.,* vol. 45, pp. 1086-1092, July 1997.

[3] Y.V. Belitsky, and E.L. Kollberg, "Superconductor-insulator-superconductor tunnel strip line," *J. Appl. Phys.,* vol. 80, pp. 4741-4748, 1996.

[4] Y. Uzawa, A. Kawakami, S. Miki, and Z. Wang, "Performance of all-NbN quasi-optical SIS mixers for the terahertz-band," *IEEE Trans. Appl. Supercond.,* vol. 11, pp. 183-186, 2001.

[5] T. Matsunaga, C.E. Tong, T. Noguchi, R. Blundell, "Fabrication and characterization of a 600 GHz resonant distributed SIS junction for fixed-tuned waveguide receiver," *Proc. 12th Int. Symp. Space THz Tech.,* pp. 571-580, I. Mehdi, ed, San Diego, CA, Feb. 2001.

[6] C.E. Tong, R. Blundell, S. Paine, D.C. Papa, J. Kawamura, X. Zhang, J.A. Stern, and H.G. LeDuc, "Design and characterization of a 250-350 GHz fixed-tuned Superconductor-Insulator-Superconductor receiver," *IEEE Trans. Microwave Theory Tech.,* vol. 44, pp. 1548-1556, Sept. 1996.

[7] D.C. Mattis, and J. Bardeen, "Theory of the anomalous skin effect in normal and superconducting metals," *Phys. Rev*., vol. 111, pp. 412- 418, July 1958.

[8] J.R. Tucker, and M.J. Feldman, "Quantum detection at millimeter wavelengths," *Rev. Mod. Phys.,* vol. 57, pp. 1055-1113, Oct. 1985.

[9] R. Blundell, C.E. Tong, D.C. Papa, R.L. Leombruno, X. Zhang, S. Paine, J.A. Stern, and H.G. LeDuc, "A wideband fixed-tuned SIS receiver for 200 GHz operations," *IEEE Trans. Microwave Theory Tech.,* vol. 43, pp. 933-937, 1995.

[10] C.E. Tong, R. Blundell, D.C. Papa, J.W. Barrett, S. Paine, X. Zhang, J.A. Stern, and H.G. LeDuc, "A fixed-tuned low noise SIS receiver for the 600 GHz frequency band," *Proc. 6th Int. Symp. Space THz Tech.,* pp. 295-304, J. Zmuidzinas, ed, Pasadena, CA, Mar. 1995.

[11] J. Kawamura, R. Blundell, C.E. Tong, D.C. Papa, T.R. Hunter, S.N. Paine, F. Patt, G. Gol'tsman, S. Cherednichenko, B. Voronov, and E. Gershenzon, "Superconductive hot-electron-bolometer mixer receiver for 800 GHz operation," *IEEE Trans. Microwave Theory Tech.,* vol. 48, pp. 683-689, 2000.

Design and characterization of 225–370 GHz DSB and 250–360 GHz SSB full height waveguide SIS mixers

A.Navarrini, B.Lazareff, D.Billon-Pierron, and I.Peron

IRAM (Institut de Radio Astronomie Millimétrique)
300, rue de la Piscine – 38406 St. Martin d'Hères Cedex – France

Abstract

We describe the design, construction, and characterization of two SIS mixers: a DSB mixer for the band 275–370 GHz, intended for band 7 of the ALMA frontend, and a SSB mixer, backshort tuned, intended for IRAM's Plateau de Bure interferometer, and covering the band 260–360 GHz. These two mixers share various common design features, such as a wideband single ended probe transition from full height waveguide to microstrip, and they use the same mixer chip. A significant challenge, especially for the SSB mixer, has been to achieve not only low noise, but also stable operation over the design band. The receiver noise for the DSB mixer is found to be below 50 K over 100 GHz of RF bandwidth, with a minimum as low as 27 K (uncorrected) at 336 GHz. The SSB receiver has a measured image rejection of order –14dB over the design band, and its noise remains below 80 K (effectively a SSB receiver noise value).

1 Introduction

The frontend for the ALMA project comprises ten frequency bands, among which band 7 (275–370 GHz), whose baseline specification is for a DSB, fixed-tuned mixer, with a maximum noise temperature of $5h\nu/k$ (66 K at 275 GHz). Therefore, our first goal has been to develop a low-noise DSB mixer with stable operation over that band.

A significant element of the system noise in a mm-wave frontend is the atmosphere's radiation in the image band. The new receivers being developed for IRAM's Plateau de Bure interferometer include a channel covering the band 260–360 GHz; it is foreseen to reject the image band with an adjustable backshort, as in current IRAM receivers. Therefore, the second goal of our work has been to develop such an SSB mixer, again with low noise and stable operation.

2 Design

In the section we review the main design features of the two mixers, referring the reader to Navarrini *et al* [1], where the design of the SSB mixer is presented in more detail.

2.1 Full height waveguide to microstrip transition

One of the goals of the design is to achieve an efficient coupling of the available RF energy to the SIS junction. Rather than attempting a global optimization, we have, as a first step, optimized the coupling of the waveguide TE_{10} mode to a TEM port with real and suitably low impedance. We chose to use full height waveguide for these mixers, because, compared with reduced height waveguide, it has lower losses and is easier to fabricate.

2.1.1 Wideband probe transition

Yassin and Withington [2] have shown that a very good match can be obtained between a full-height waveguide and the driving point impedance of a radial probe, with a real

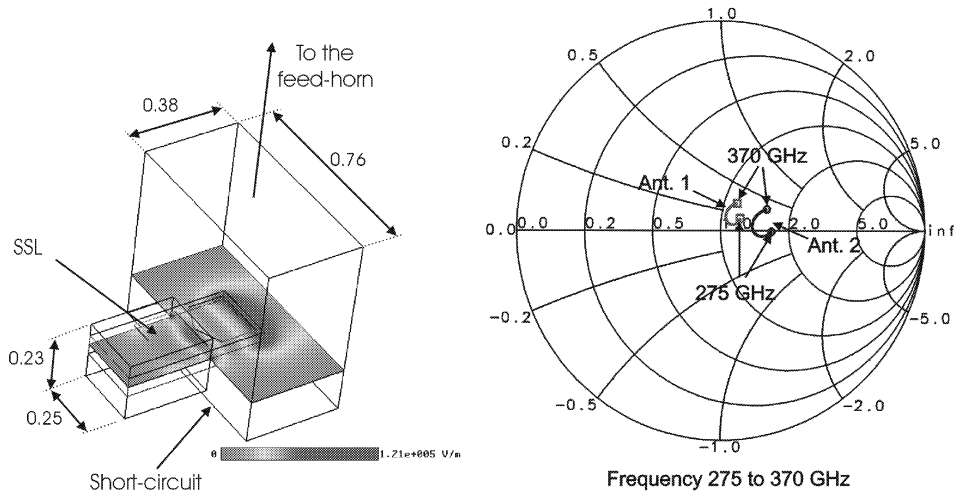

Fig.1a *Left)* Wideband probe transition. Fig. 1b *Right*) Driving point impedance found in FDTD simulations; Ant1 and Ant2 differ by the opening angle at the base, which is 130° for Ant1, and 90° for Ant2. While Ant1 delivers a lower impedance, Ant2 was preferred for the SSB application (see section 2.4).

and relatively low value (≈50 Ω) over a full waveguide band. In a practical implementation, the antenna drives a microstrip line whose ground plane is a suspended stripline RF choke sitting on a dielectric substrate, itself housed in a channel perpendicular to the waveguide (see Fig. 1a).

We modeled this configuration using the FDTD package Microwave Studio from CST [3]. We obtained for the driving point impedance the results shown on Fig. 1b, with the following parameters: waveguide dimensions 760 µm×380 µm, substrate fused quartz, width 250 µm, thickness 80 µm, 100 µm air above, 50 µm air below, probe (and substrate) extending 200 µm into the waveguide, opening angle at probe base 90°. The fixed backshort is located at 210 µm behind the plane of the probe metallization, approximately ¼ λ_g. An impedance close to 75 Ω is obtained over the band 275-370 GHz. While Yassin and Withington show that good results can be obtained with the probe either in the longitudinal plane or perpendicular to the waveguide, we chose the latter orientation in order to decouple the TE_{10} mode of the waveguide from an odd-symmetry mode of the suspended stripline, whose cutoff frequency falls within the operating band.

2.1.2 Image rejection by reactive termination.

If the electrical distance between the probe and the backshort is an integer multiple of ½ λ_g, the probe is shorted, and the junction sees a reactive termination; if that distance is an odd multiple of ¼ λ_g, a match is obtained for the probe, and for the junction, provided that a proper matching circuit is present (will be discussed further down). For given values of the signal and image frequencies, ν_S and ν_I, the two conditions can be met (approximately) for the same backshort position l_{bs} (see [1]):

$$l_{bs} = \frac{c}{8\nu_{IF}}\sqrt{1-\left(\frac{\nu_c}{\nu_{LO}}\right)} \qquad (1)$$

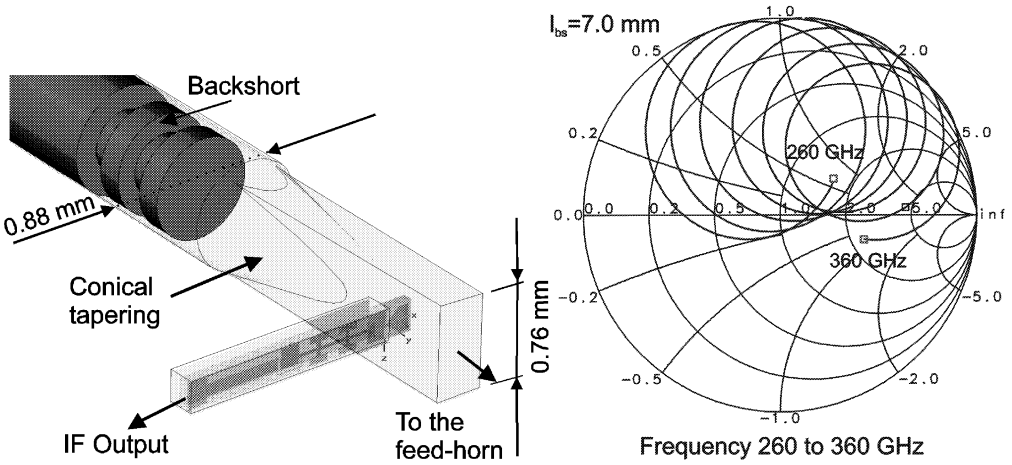

Fig 2a *Left)* Structure of the SSB mixer, with an adjustable backshort. Fig. 2b *Right)* Driving point impedance of the probe in the frequency interval 260–360 GHz, for a fixed backshort position 7 mm away from the probe. At regular frequency intervals of ≈ 8GHz, the probe impedance alternates between a real value $Z_M \approx 75\ \Omega$ and a pure reactive mismatch.

For an IF center frequency of 4 GHz, $l_{bs} \approx 7$ mm. Figure 2 shows the structure of the SSB mixer, and the modeled probe impedance as function of frequency for an arbitrary backshort position. Equation (1) only gives an approximate value for l_{bs}, the precise value is chosen to have maximum rejection at ν_I (and a near optimum match at ν_S).

2.2 Stability

2.2.1 DSB case

In the DSB case, the LSB and USB ports of the junction see equal terminations (actually, in the formalism of Tucker's theory, because $\nu_L \equiv \nu_{-1} = \nu_{IF} - \nu_{LO}$ is negative, $Y_{-1}=Y_1^*$). The output impedance at the junction's IF port, defined by (using standard notations):

$$Y_{IF} = Z_{00}^{-1} - Y_0 \qquad (2)$$

is actually independent of Y_0. If the mixer is to be stable for arbitrary passive IF load admittance Y_0, the real part of Y_{IF} must be positive. Fixing the bias voltage at the middle of the photon step: $V_{DC}=V_g-h\nu_{LO}/2e$, and the pumping parameter $\alpha=1$, leaves as the only free parameter the RF impedance Y_1 seen by the junction. The region of stability, that depends only weakly on the LO frequency, is shown on Fig. 3a. This problem had already been discussed by D'Addario [4].

2.2.2 SSB case

In the SSB case, to keep the discussion manageable, we *assume* that the junction sees on the signal port a source impedance $Z_S = R_N$. As discussed above, the rejection of the image frequency is achieved by presenting a pure reactive termination Z_I on that port, whose value is the only free parameter in this case. The stability condition (again weakly dependent on frequency) is more restrictive at the low end of the operating range; at 275 GHz, the stable region is given by:

$$-3.27 \le \frac{Z_I}{jR_N} \le +0.12 \qquad (3)$$

This portion of the $\Gamma = 1$ circle is shown on Fig.3b.

2.3 Junction parameters

To achieve the RF tuning bandwidth of ≈100 GHz, we chose a $R_N \times A$ product of 25Ω×μm^2. With a specific capacitance of 75 fF×μm^{-2}, this corresponds to a quality factor $Q = R_{RF} C\omega = 2.6$ at mid-band, based on a small-signal RF impedance $R_{RF} = 0.75 \times R_N$ at 310 GHz. A junction area of 1 μm^2 was chosen as a compromise between the technological difficulties of fabricating small area junctions with a good accuracy, and the problem of matching the junction's RF impedance to the higher driving point impedance of the waveguide probe. The junction definition was realized by E-beam lithography.

2.4 Matching circuit

The matching circuit is realized by a combination of microstrip lines patterned in the Nb wiring layer over a 200 nm SiO_2 (ε=4.2) insulation, and sections of coplanar waveguide patterned in the base Nb of the trilayer. The junction capacitance is tuned out by a short (≈λ/8) length of microstrip line terminated to a virtual ground provided by a radial stub. The resulting near-real impedance is matched to the waveguide probe by a λ/4 transformer, realized as a capacitively loaded coplanar waveguide, comprising two coplanar sections. The probe with a 90° opening angle was chosen (see Fig.1) despite the higher transformation ratio to 75 Ω, because it allows to better fulfill the stability criterion for the SSB mixer.

The design was performed by computing the S-parameters of the probe coupling structure (including the suspended substrate microstrip line choke) with CST Microwave Studio [1], and of the planar circuit discontinuities with Sonnet [5], and then importing these into ADS [6] where the optimization of microstrip and coplanar transmission line lengths was performed. As can be seen on Fig. 3, this circuit provides

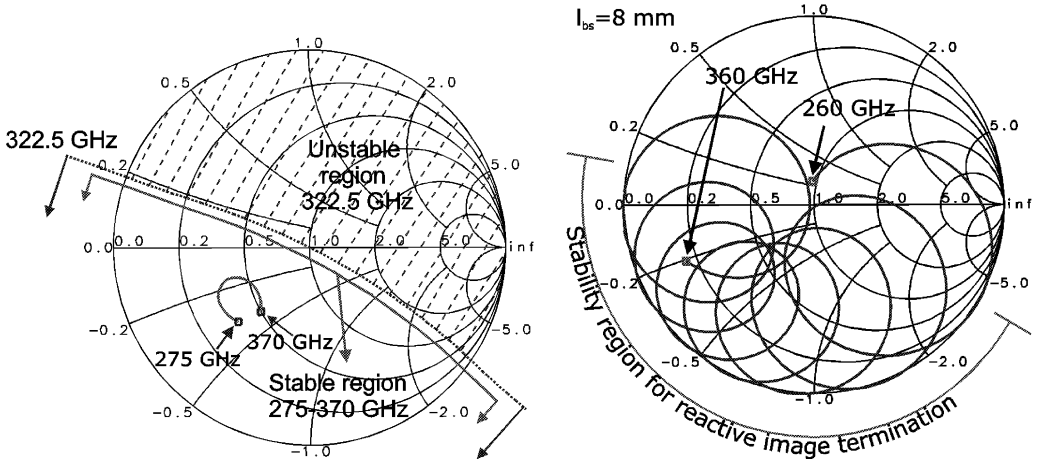

Fig. 3a *Left)* The stability region in the DSB case, and the RF impedance seen by the junction in the DSB mixer model. Fig. 3b *Right)* Similar data for the SSB case. See text. Each of the Smith Charts is normalized to the small signal RF impedance of the junction R_{RF} ≈18 Ω for R_N = 25 Ω.

a broadband match for the DSB mixer, a good match at the signal frequency for the SSB mixer, and fulfils the respective stability criteria for either type of mixer.

3 Experimental results

The main parts of both DSB and SSB mixer blocks are made of brass and are split in two parts (Fig. 4). The front block is identical in the two mixers and includes the full height waveguide realized by spark erosion. Anti-cocking bosses and alignement pins are used the front blocks. Both mixers include magnetic circuits for the suppression of the Josephson current.

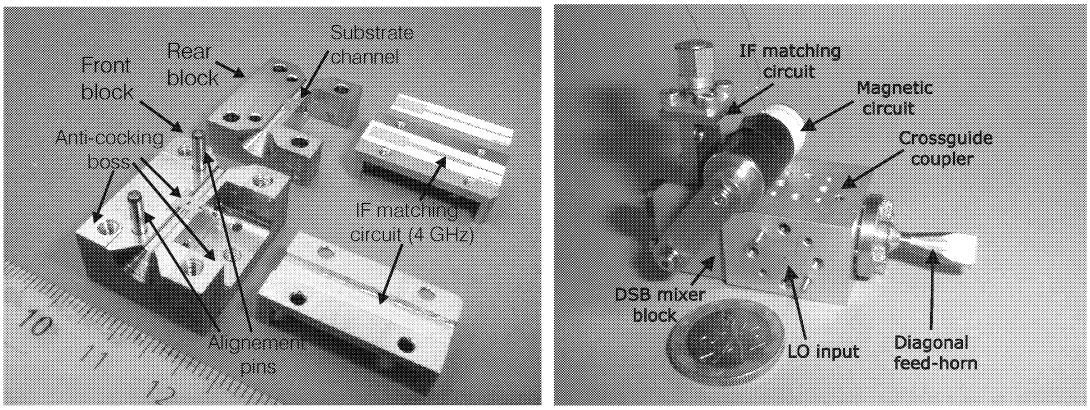

Fig. 4: *Left)* Photograph of the internal parts of the DSB mixer block and of the IF matching circuit. *Right)* DSB mixer integrated with its IF matching and magnetic circuits. A crossguide coupler and a diagonal feed-horn are also shown.

The receiver noise was obtained by the standard method placing ambient temperature and cold (77 K) loads in front of the receiver. We assumed the effective temperature of the radiating loads to equal the physical temperature (Rayleigh-Jeans approximation). This also corresponds with very good approximation to the Callen&Welton effective radiating temperature [7] that excludes quantum vacuum fluctuation from the receiver noise.

The mixer under test is installed in a two stage liquid helium/liquid nitrogen cryostat for laboratory noise measurements. A 1.78 mm thick grooved HDPE vacuum window and a IR filter realized with a 8.15 mm polystyrene foam are located on the signal path before a corrugated feed-horn with HDPE grooved phase correcting lens. A 3.5-4.5 GHz IF HEMT amplifier with noise $T_{IF}\approx 5$ K and gain $G_{IF}\approx 34$ dB is cascaded with the mixer. A Gunn oscillator followed by a frequency multiplier (3× or 4×) provides the necessary local oscillator (LO) power over the test band. The mixers have been tested by using LO injection both with *a)* a wire grid located outside the cryostat *b)* a –16 dB branch-guide coupler.

3.1 Characterization of the DSB mixer

The pumped current-voltage characteristic with LO frequency $\nu_{LO}=320$ GHz, as well as the receiver output power as a function of bias in response to hot/cold loads are shown in Fig. 5. The receiver noise measured in front of the injection grid at this particular

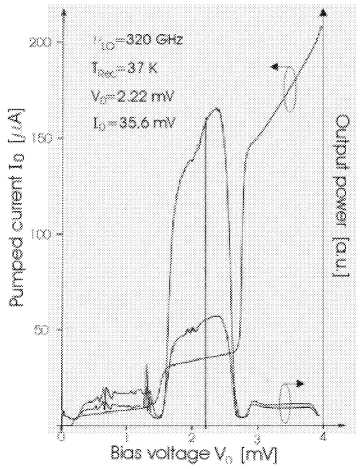

Fig. 5: Pumped IV characteristic and receiver output in response to hot/cold loads versus bias voltage for LO frequency ν_{LO}=320 GHz.

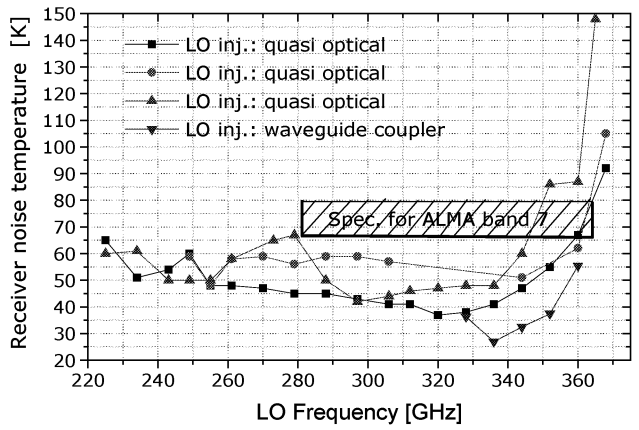

Fig. 6: Measured DSB receiver noise temperature versus frequency for different DSB mixers. The local oscillator was injected by using both a quasioptical systems and a branch-guide coupler.

frequency was 37 K. Fig. 6 shows the measured receiver noise temperature plotted against LO frequency for various chip-DSB block combination over the 225-368 GHz band. The T_{rec} measurement are uncorrected for optics and injection losses. The first three measurements were obtained with quasi-optical injection: the receiver noise is below 60 K over more than 100 GHz of band. The relative bandwidth of the mixer of approximately 50 % is one of the widest ever reported. The increase of noise in the upper part of the band is believed to be caused by the junction area being 35 % larger than specified. Even with that increase the specification for the RF coverage of ALMA band 7 is met.

A further test of the mixer using a branch-guide coupler [8] gave superior performance in terms of noise temperature over a narrower bandwidth, with minimum of (uncorrected) T_{rec}=27 K at 336 GHz; to our knowledge this is the lowest receiver noise ever reported at this frequency.

3.2 Characterization of the SSB mixer

Setting the mixer for SSB operation at the signal frequency ν_S is a two-step process. First, the LO is set at the image frequency ν_I, and the junction dc pumped current is plotted versus backshort position l_{bs}. A position that gives minimum current corresponds to minimum coupling of the junction at ν_I. Actually, several positions are found, spaced at regular intervals of $\lambda_g/2$, as shown on the experimental result plotted in Fig. 7. Mixer modelling calculations are used to select the position l_{bs} that gives near-optimum coupling at the signal frequency. Then the LO is set at the proper ν_{LO} for SSB operation at ν_S without changing l_{bs}. The narrow resonances observed in the plot of

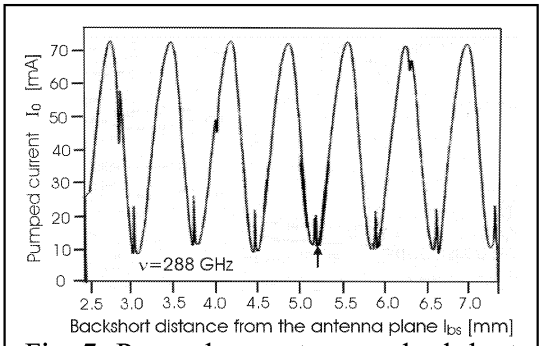

Fig. 7: Pumped current versus backshort distance from the antenna plane l_{bs} for LO pumping frequency ν=288 GHz.

the pumped current versus I_{bs} curve are believed to be caused by the second polarization of the TE_{11} mode that can propagate in the circular waveguide. We believe that the second TE_{11} mode is coupled by an off-axis displacement of the circular backshort and is trapped between the backshort and the transition. The narrow resonances can degrade the image rejection at particular frequencies. Therefore, it is foreseen to replace the circular cross-section backshort with a new choke type rectangular backshort that can be moved in an uniform rectangular waveguide.

The image band rejection has been measured by using a Martin-Puplett Interferometer (MPI) that provides sideband filtering (Fig. 8). The MPI is tuned to reject successively the signal and image band. Then, the difference of the receiver output powers in

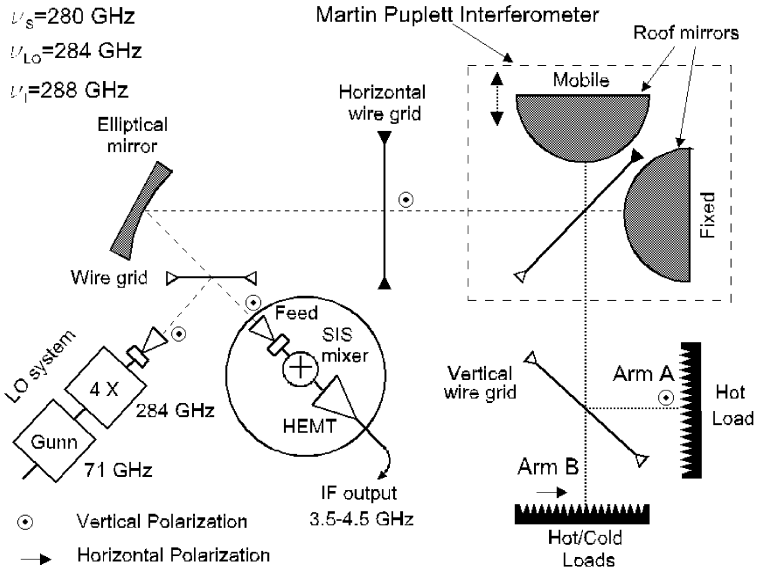

Fig. 8: Setup for the measurement of the image band rejection.

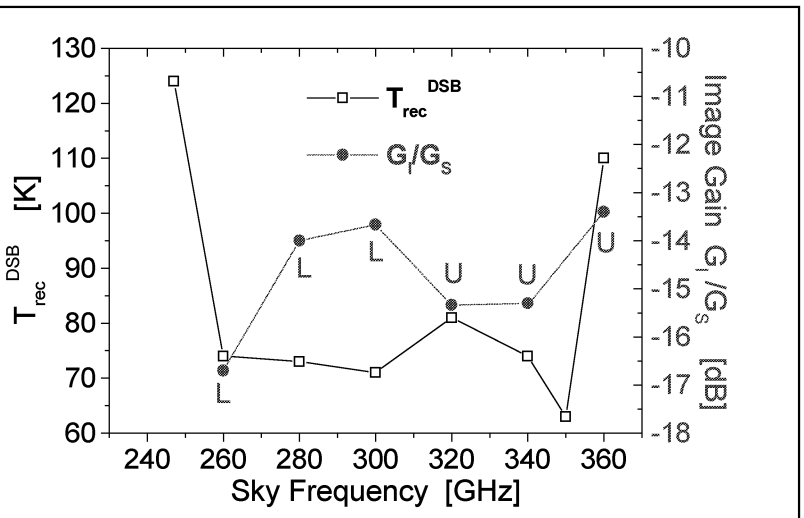

Fig. 9: Measured receiver noise temperature and sideband rejection versus frequency. The image gain was measured by using the MPI.

response to hot/cold loads located in the arm B are measured. The sideband rejection is obtained as the ratio of these differences.
The results of characterization of the SSB mixer are shown in Fig. 9. A DSB receiver noise temperature of the order of 80 K (uncorrected) is obtained over most part of the band (left scale) with an image rejection around –14 dB (right scale). Given the high image rejection, the plotted receiver noise is an SSB receiver noise temperature apart from a factor $(1+G_I/G_S)\approx 1.04$.

4 Conclusions

Two SIS mixers in full height waveguide have been designed. They use the same mixer chip. One is a fixed tuned DSB mixer, designed for ALMA band 7 (275-370 GHz). Its operation has been demonstrated over 225–370 GHz, with a DSB noise temperature below 50 K over a 100 GHz RF band, the minimum being 27 K at 336 GHz. The second one is a SSB mixer designed for IRAM's Plateau de Bure interferometer, with an RF band 260–360 GHz, and where the rejection of the image band and the matching of the signal band are simultaneously achieved by an adjustable backshort. The measured rejection is of order –14dB; the (quasi-SSB) receiver noise is below 80 K over 90% of the design band.

References

[1] A. Navarrini, D. Billon-Pierron, K.F. Schuster, and B. Lazareff, "Design of a 275-370 GHz SIS mixer with sideband rejection and stable operation", 12th International Symposium on Space Terahertz Technology (2001).

[2] G. Yassin and S. Withington, "Analytical expression for the input impedance of a microstrip probe in waveguide", Int. J. Infrared and Millimetre Waves, **17**, 1685-1705, 1996.

[3] CST, Darmstadt, Germany. http://www.cst.de

[4] L.R. D'Addario. "Noise parameters of SIS mixers" IEEE Trans. Microwave Theor. Tech., **36**, 1196-1206, 1988

[5] Sonnet Software, http://www.sonnetsoftware.com

[6] ADS, Agilent Technologies, http://eesof.tm.agilent.com/products/adsoview.html

[7] A.R.Kerr, "Suggestions for revised definitions of noise quantities, including quantum effects", IEEE Trans. Microwave Theor. Tech., **47**, 325-329, 1999

[8] S. Claude, "Branch-Guide –16 dB LO directional couplers", IRAM Technical Report N. 263.02, Jan. 2002

Detailed Characterization of Quasi-Optically Coupled Nb Hot Electron Bolometer Mixers in the 0.6-3 THz Range

W.F.M. Ganzevles[1], P. Yagoubov[2], W.J. Vreeling[2],
J.R. Gao[2], P.A.J. de Korte[2] and T.M. Klapwijk[1]

[1]Department of Applied Physics and DIMES, Delft University of Technology,
Lorentzweg 1, 2628 CJ Delft, The Netherlands

[2]Space Research Organization of the Netherlands, Sorbonnelaan 2, 3584 CA Utrecht,
The Netherlands

Abstract

Two type of Nb diffusion-cooled HEB mixers have been studied. One uses a twin-slot antenna designed for 700 GHz, and has a bridge length of 200 nm. This device is fabricated using an *in situ*-process for the interface between the bridge and the cooling pads. An uncorrected receiver noise temperature of 1200 K at 640 GHz and an IF bandwidth of 5 GHz have been measured. The second device uses a log-periodic antenna designed for a wide RF bandwidth. However, there is a misalignment of the Nb bridge with respect to the Au cooling pads. Receiver noise temperatures at 0.64, 1.9, and 2.5 THz have been measured. We are able to link the geometry feature to the measured properties.

1. Introduction

Superconducting Nb diffusion-cooled hot electron bolometer mixers have shown promising performance such as high sensitivity, large intermediate frequency bandwidth, and low local oscillator power. They are the most promising mixers for frequencies beyond 1 THz. Several research groups[1-5] are working on such devices and report good performance. However, extensive experimental data concerning the RF performance is still lacking. It is believed that the difficulty comes from the fact that the performance of such devices is very sensitive to the fabrication processing steps, the detailed geometry, and the test environment. In this work, we show that by changing one fabrication step defining the interface between the Nb bridge and Au cooling pads in-situ, good performance in terms of IF bandwidth and sensitivity can be achieved. We will also show that the DC and RF performance can strongly depend on the device geometry, as observed from a device having a misalignment of the bridge with respect to its cooling pads.

2. Mixers

Two type of quasi-optical mixer designs have been explored in this work. One uses a twin slot antenna in combination with transmission line (CPW) for 700 GHz and 2.5

THz[5]. Although the final goal is to develop devices operating at 2.5 THz, unfortunately, only those designed for 700 GHz work from two batches using a new fabrication process that will be described shortly. Details of the device *IS 1_2 G4* are listed in Table 1. An SEM micrograph of a similar device is shown in fig. 1.

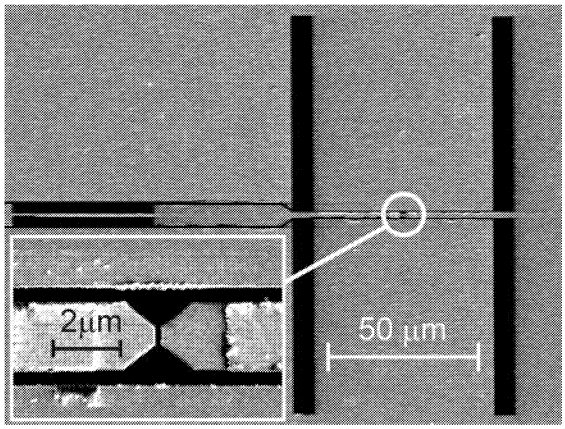

Fig. 1 SEM micrograph of a quasi-optical Nb HEB mixer with a twin-slot antenna , designed for 700 GHz. The device is similar to IS 1_2 G4. The inset shows a zoom of the CPW/bridge area.

Table 1. Details of device IS 1_2 G4. L, w and s are the antenna slot length, width and separation, respectively. a and b are the slot-- and center line width in CPW transmission lines. $Z_{hi,low}$ are filter sections having high and low impedance.

frequency	0.7 THz
Antenna	twin slot, L=137μm, w=6.9μm , s=68.5μm, metal Au layer: 300nm
CPW line	a=1.2 μm, b=2.0 μm
Filter	Z_{low}: a=1.2 μm, b=6.6 μm, Z_{hi}: a=3.9 μm, b=1.2 μm
Nb bridge	Thickness = 14 nm, length = 200 nm, width = 250 nm (nominal)
Resistance	$R_{10\,K}$ = 40 Ω, $R_{4\,K}$ = 7 Ω (series R) , $R_{300\,K}$ = 104 Ω
Substrate	Si, 300 μm thick, one-sided polished (not on purpose)

The second type of mixer is based on a log-periodic antenna (2×15 teeth), which should have a wide RF bandwidth. The antenna has a self-complimentary design and its impedance is relatively high. Since the Nb devices usually have a low impedance, there is always a considerable mismatch between the antenna and the bolometer, causing degradation of noise performance. So such a antenna is not the optimum choice for the HEB to obtain the maximum performance. However, the wide band allows us to verify the frequency dependence of the HEBM sensitivity. The SEM micrograph of the device reported in this work is shown in fig. 2. It is important to note that there is a misalignment of the bridge with respect to the cooling pads (about 150~nm), that is partly due to an error in the e-beam lithography and partly due to the fact that this device is designed for having a narrow cooling pads. The relevant parameters are; 300 nm separation between the cooling pads, 400 nm Nb bridge width, 22 Ω normal state resistance.

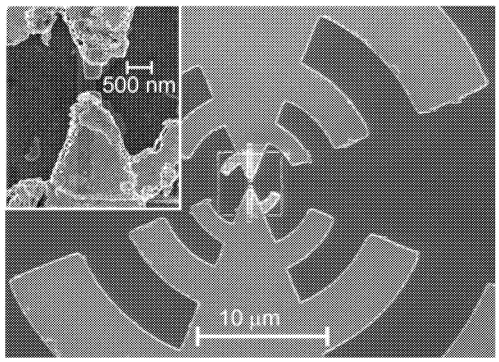

Fig. 2. SEM micrograph of device IS 1_4 F3. The inset shows the Nb nanobridge contacted by Au cooling pads. The length and width of the bridge are 300 nm and 400 nm, respectively. Clearly, the bridge is misaligned with respect to the cooling pads.

3. Fabrication.

The fabrication process is different from the one described in ref. 5, in essentially two aspects. a) the interface between the Nb bridge and Au cooling pads is realized in situ, so no vacuum breaking. This is realized by depositing thin Nb and a thin Au cap layer in situ. After defining the Au cooling pads, the Au cap layer will be etched away; b) we use a thin Al strip as an etching mask to define the bridge width.

4. RF measurement set-up

The noise temperature measurements are performed by a standard Y-factor technique with 300/77 K loads in the receiver signal path. All measurements are taken at an IF of 1.4 GHz . We use a Mylar beam splitter with a thickness of 15 μm to couple the LO into the mixer. A number of BWOs and Carcinotrons covering the frequency range from 0.3 to 1.2 THz serve as a local oscillator. Above 1 THz an optically pumped FIR ring laser in our lab is used. The output lines at frequencies of 1.6 THz, 1.9 THz and 2.5 THz are now available.

IF bandwidth measurements are done using a pair of submillimeter sources at frequencies around 650 GHz. A Miteq 0.1-8 GHz cryo-amplifier is used as the first stage amplification. It is followed by a room temperature amplifier and further by a spectrum analyzer.

5. Measurement results of a twin-slot antenna coupled HEB mixer designed for 700 GHz

5.1 DC measurements

We start with a twin slot antenna-coupled device labeled as IS 1_2 G4. The critical temperature T_c of the Nb nanobridge is 7.4 K, which equals to the larger films on the same wafer. The T_c of the Nb under the Au cooling pads (110 nm thick) is 6.2 K, thus the difference between the two T_c amounts to 1.2 K. This difference is nearly the largest observed so far in our Nb HEBMs, indicating a strong suppression of superconductivity by the Au cooling pads due to the proximity effect[6]. So one can expect a Nb/Au interface with a high transmissivity. Both the high transparent interface and the strong suppression of superconductivity of the Nb under the cooling pads are favorable for diffusion cooling. The critical current I_c is 160 μA at 4.2 K and increases to 260 μA at 3.2 K. The normal state resistance R_N measured above T_c is 40 Ω (as given in table 1), which is higher than expected. Based on the nominal geometry and square resistance measured in a larger structure, we expect the value to be around 12 Ω. We suspect that the deviation from the nominal value is partly due to over-etching while defining the Nb nanobridge. This may cause the bridge to be narrower than the nominal size. However, since SEM micrograph of this particular device is not available, we cannot make a hard conclusion. The serious resistance of 7 Ω is due to the filter structure.

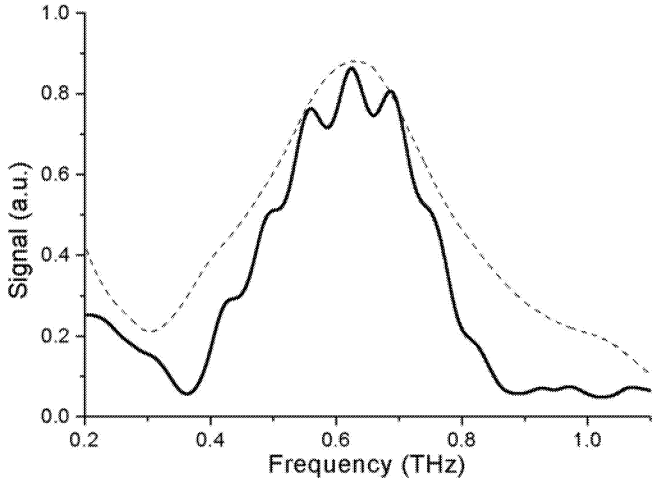

Fig. 3. Measured direct response of a twin slot antenna coupled Nb HEB mixer. The thick line gives measured data and the thin line indicates the simulation.

5.2 Direct response

Fig. 3 shows the direct response of the device as measured by FTS. The thick solid line indicates the measured curve. We calculate the FTS response for this specific device (real geometry) using the model described in ref. 5. The result is shown as a dashed line in Fig. 3. This curve includes the effect of all the optics, so we can compare it directly to the measurement. The peak frequency is well explained, however, the measured bandwidth is ~20% smaller than the predicted one. It is worthwhile to mention that other samples from the same batch show a better agreement. So it depends strongly on device

differences. We present however the data from this device because it is completely characterized regarding its noise and IF bandwidth.

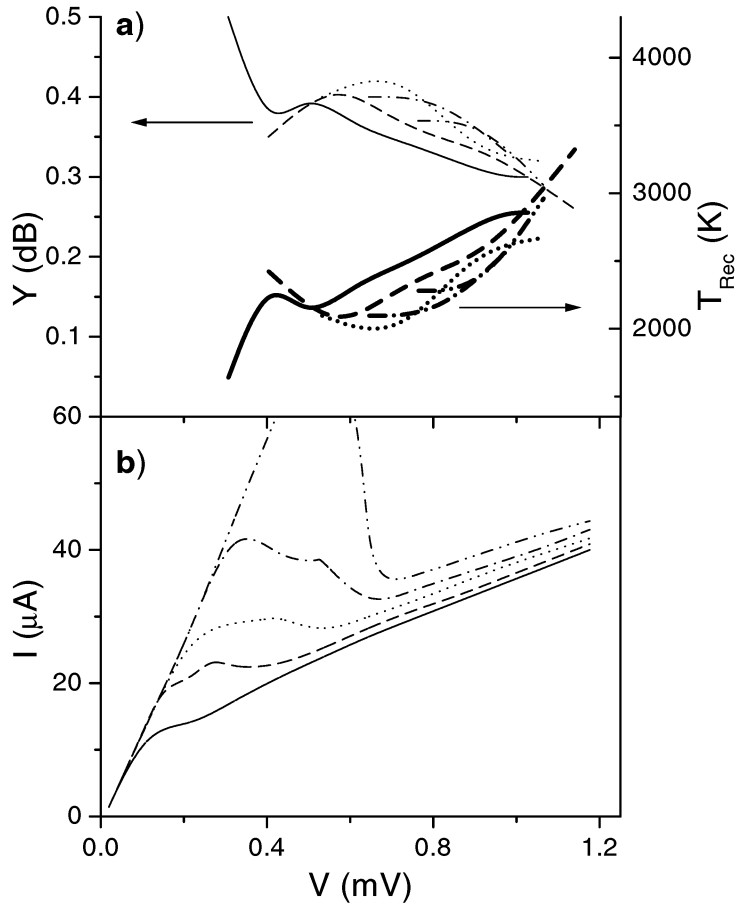

Fig. 4. In the upper panel, Y-factor (thin lines) and T_{rec} (thick lines) vs bias voltage for the device IS 1_2 G4 with several LO levels at 0.64 THz; in the lower panel, corresponded pumped IV curves are also given. The correspondence is indicated by the line style, e.g. all the dashed lines have the same LO power. These data are taken at 4.2 K.

5.3 Receiver Noise Temperature

The Y-factor and thus the receiver noise temperature of the same device(IS 1_2 G4) have been systematically measured as a function of bias voltage for different LO power levels at the bath temperatures of 4.2 and 3.2 K. Fig. 4 shows the Y-factor and the deduced receiver noise temperature as a function of bias voltage at four different pumping levels, together with their corresponding pumped IV curves, taken at a T_{bath} of 4.2 K. At this temperature, the best Y-factor of 0.5 dB has been measured manually (not included in the figure), corresponding to a receiver noise temperature of 1600 K (DSB). Note that all noise figures given in this paper have not been corrected for any loss in the signal path, e.g. beam splitter.

We now try to look at this result more closely. Two features are worthwhile to mention. First of all, for a given bias voltage, e.g. at 0.8 mV, T_{rec} decreases with increasing LO power (means starting from less pumped IV curves), passes a minimum and eventually increases again. Secondly, for a fixed LO power, T_{rec} has a minimum between low and high voltages. So these features clearly demonstrate that there is a region where the mixer has the lowest noise if one adjusts LO power and the bias voltage. Such features have been reported in NbN phonon cooled mixers[7], but rarely reported in Nb mixers. Furthermore, the highest Y-factor does not occur at the lowest bias voltage, at which the dynamical resistance starts to be negative, that is favorable for the real application. The LO power absorbed by the mixer for the case of the lowest noise is estimated to be 30 nW.

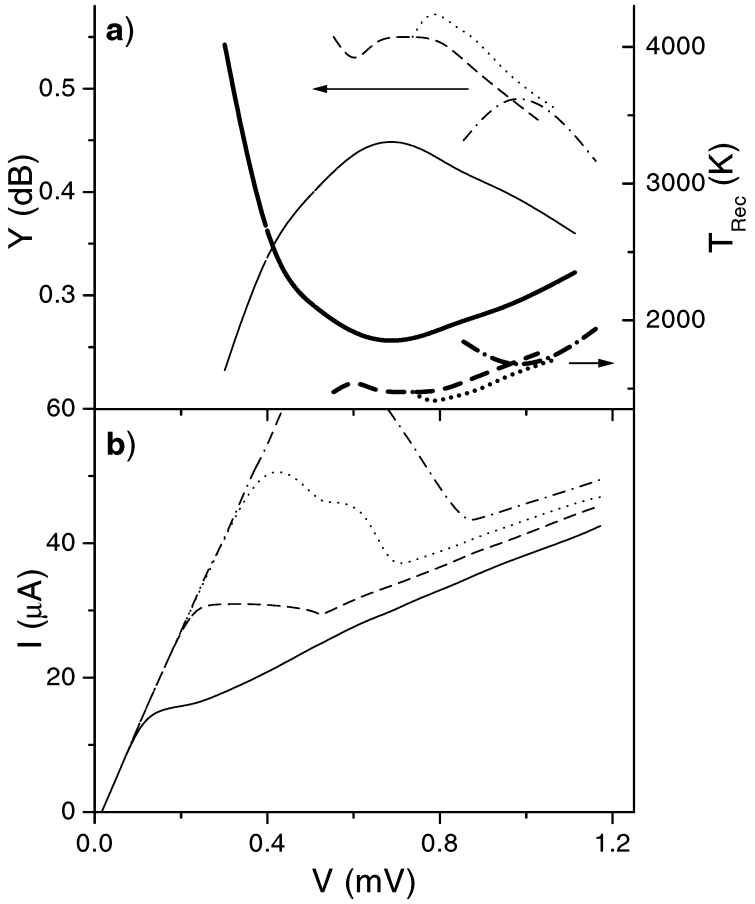

Fig. 5. In the upper panel, Y-factor (thin lines) and T_{rec} (thick lines) vs bias voltage for the same device as in fig. 4 with several LO levels at 0.64 THz. in the lower panel, corresponded pumped IV curves are also given. The correspondence is indicated by the line style, e.g. the dashed lines mean the same LO power. These data are taken at 3.2 K.

We repeated the measurement by lowering the bath temperature to 3.2 K. The result is given in fig. 5. In general, we see similar behavior of Y-factor vs the bias voltage for different LO powers. However, overall Y-factor increases at this temperature. Now

the highest Y-factor goes up to 0.65 dB (not included in the figure). This gives a receiver noise temperature of 1200 K. We also notice that it requires in general more LO power to pump the device.

The best receiver noise temperature decreases by ~26 % upon decreasing the temperature to 3.2 K. Similar improvement has also been observed in our waveguide Nb HEB mixers and by other groups. Attempts have been made to understand whether this is due to an increase of mixer gain or a decrease in mixer output noise[8]. Unfortunately, the issue is still not fully resolved.

We also measure the receiver gain in order to determine the mixer gain. The IF output power of the device has been measured by changing hot/cold loads. We find the maximum DSB receiver gain to be -20 dB. Using Table 2, which summarizes all other losses in the receiver, we deduce a DSB mixer gain G_{Mix} to be –16 dB. We can only present the mixer gain at 4.2 K, but not at 3.2 K since in the latter case no such IF power data have been recorded.

Although there is no well-established model to predict the mixer gain of a diffusion-cooled mixer, for curiosity, we calculate this value by using the electronic hot-spot model[8,9] with inputs of the experimental IV curves and the device parameters. We find the maximum mixer gain to be –12 dB. So, the difference is not considerably large.

Table 2. Balance of the receiver losses at 0.64 THz, including also a loss due to a slight off from the antenna peak frequency. We did not include the effect of roughness on one side polished substrate.

Elements	Loss(dB)
Splitter	0.4
Window	1.0
Zitex filter (x2)	0.2
Lens (reflection)	1.5
Lens (absorption)	0.3
Antenna offset	0.2
One side-polished Si	?
Total	3.6

5.4 IF bandwidth

The IF bandwidth of an HEBM is an important practical parameter, which is defined as the frequency at which the conversion gain drops by 3 dB. We measure this bandwidth for the same device (IS 1_2 G4). We start with a low bias voltage (0.65 mV), at which the minimum noise temperature has been obtained. The conversion gain as a function of IF frequency is presented in fig. 6. The one-pole Lorentzian fit to the data gives the IF bandwidth of 3.2 GHz. By increasing the bias voltage to a high value (~ 3mV), we repeat the measurement and find the IF bandwidth of 4.5 GHz. Several other devices with the same bridge length from the same batch have been evaluated, showing the IF bandwidth to be in a range of 4-5 GHz at high bias voltages. An example is given in fig. 7. This is measured in another device labeled as IS 1_2 B9 and the bandwidth is 5 GHz. To make a

comparison, the data from a similar device but produced by non in-situ process is also included. For this device, the IF bandwidth obtained is only 2 GHz.

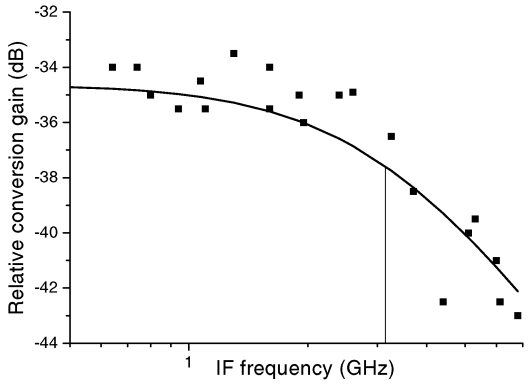

Fig. 6. The measured relative conversion gain as a function of IF frequency for the device (IS 1_2 G4) at a bias voltage of 0.65 mV for which the best sensitivity was obtained (in the optimal bias point). The one-pole fit gives a roll-off frequency of 3.2 GHz. This device has a nominal length of 200 nm.

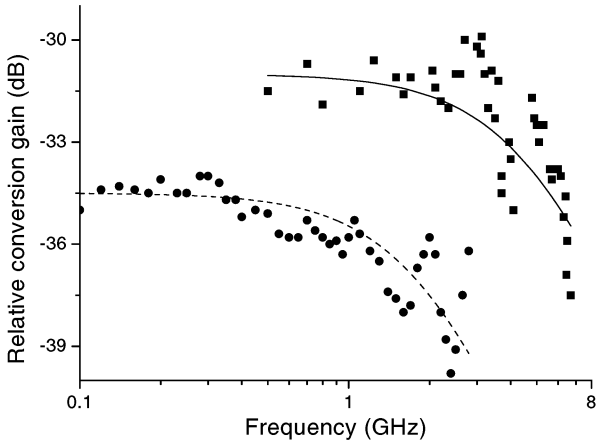

Fig. 7. The relative conversions gain as a function of IF frequency, measured on a device (IS 1_2 B9) made in-situ (squares) and one made ex-situ ES 2_2 (dots). The nominal bridge length for the both devices is 200 nm. The in-situ device gives an IF bandwidth of 5 GHz and the other one 2 GHz.

In general IF bandwidth of such a device should increase with increasing the bias voltage[10]. This is because at low bias voltages, only a part of the superconducting bridge is driven to be normal. At high bias voltages one can view the superconducting bridge just as a metallic strip. So the IF bandwidth should increase and approach to what predicted by the diffusion-cooling expression:

$$IF_{roll\text{-}off} = \pi D/2L^2$$

where D is the diffusion constant and L the bridge length. We calculate this value by taking the nominal length 200 nm and using a diffusion constant of 2.1 cm^2/s, which is deduced from a value measured in thin Nb film[8], taking the sheet resistance of our film into account. Using these values, we find the IF bandwidth of 8.3 GHz, which is higher than the observed one.

5.4. Discussions

We have evaluated three similar devices in the RF setup and obtained very similar noise performance. The noise figure presented in this paper is the lowest among the tested quasi-optical mixers in our lab. They are in general better than the devices produced in the non in-situ fabrication process. Unfortunately we can only compare the data at 640 GHz, but not at 2.5 THz because we did not have devices designed for 2.5 THz using the new process. To have a comparison, we also summarize sensitivity measurements based on devices produced by the non in-situ process. Several batches of the devices have been produced and a considerable amount of them have been tested in order to evaluate the noise performance. The DSB noise temperatures vary between 1.500-2.000 K at 640 GHz and 4.500-10.000 K at 2.5 THz. These data have not been corrected for the losses in the signal path, which we estimate to be about 4-5 dB (beamsplitter, dewar window and reflections at the air/Si lens interface).

Can we further improve the sensitivity? There must be room for if we simply compare to the best result obtained in the waveguide mixers in our lab, that was 900 K (uncorrected) at 700 GHz [8]. In order to push the noise temperature further down, more specifically the following aspects need to be improved. a) our Si lens does not have any anti-reflection coating. This gives rise to a 1.5 dB loss due to reflections from the lens surface; b) our dewar window is optimized for 2.5 THz. An improvement of about 0.4 dB can be made in optimizing the dewar window for 0.7 THz; c) This particular batch is produced on single-sided polished Si substrate. The backside has an RMS roughness of about 20 μm, being a considerable fraction of the wavelength. This can give a negative contribution to the sensitivity measurement, but it is hard to be quantified; d) The bath temperature of 3.2 K is still not lower enough.

6. Measurement results of a log-periodic antenna coupled HEB mixer designed for a wide RF band

In this section, we will summarize the key measurement data from the log-periodic antenna coupled device (IS 1_4 F3). The motivation to present such data has two folds. 1) this is one of very few devices in which we can perform systematic measurements such as DC characterization, FTS, Y-factor and the gain as a function of bias with different LO powers, and also IF bandwidth. For this device, we could in the end take the SEM micrograph; 2) we see the correlation between the measured properties and its geometric anomaly.

Here are the key observations from this device:

- Resistance vs temperature curve has additional structure, differing from a well-defined HEB device
- Un-pumped and in particular pumped IV curves differ pronouncedly from the calculated curves using the electronic hot-spot model.
- The IF bandwidth has only 0.8 GHz, which is much smaller than 4 GHz, as expected for a separation of cooling pads (300 nm) and the diffusion constant. The relative conversion gain vs IF deviates from the Lorentzian behavior.
- For the optimized operation, this device requires a LO power of 100-150 nW, which is 1.5-2 times more than a usual Nb HEB mixer. This suggests that LO power is not only absorbed in the Nb between the cooling pads, but also the Nb next to them.

Apart from those observations, we study the FTS response, which starts from 0.3 THz to 3 THz, confirming that it is indeed a wide band receiver. We also measure Y-factor and thus DSB receiver noise temperature at 0.64, 1.9 and 2.5 THz. Those values together with the mixer noise temperature and mixer gain estimated from the balance of receiver losses are listed in table 3. Note these noise data are certainly not the best if we compare them to the data given in section 5.4.

Table 3. The Y-factor and receiver noise temperature (DSB, uncorrected) of a log-periodic antenna coupled Nb HEB mixer at three different frequencies. The estimated mixer properties are also given. T_{Mix}, G_{Mix} , and G_{opt} are the mixer noise temperature, mixer gain, and the gain of the optical signal path, respectively.

f (THz)	Y-factor	T_{rec}	T_{mix}	$G_{mix}(dB)$	$G_{opt}(dB)$
0.64	0.35	2400	600	-12.7	-6.8
1.9	0.13	6900	920	-11.8	-7.1
2.5	0.10	8900	900	-12	-9.0

7. Conclusions

In conclusion, we have designed and fabricated quasi-optical Nb diffusion-cooled HEBMs to operate in the frequencies up to 2.5 THz. The IF bandwidth of the devices with a 200 nm long bridge produced using the in-situ fabrication process is as high as 5 GHz. The best receiver noise figure is 1200 K at 640 GHz. Through the systematic measurements we have confirmed that Nb HEB mixers in principle work and demonstrated reasonably good performance. However, we emphasis that the detailed fabrication process steps and also the device geometry can affect the overall performance. Unresolved problems in our case are a good control over fabrication process with respect to both reproducibility and yield.

Acknowledgements: The authors thank Dr. E. W.J.M v.d. Drift and T. Zijstra for their support and help on the fabrication. This work is supported by the European Space Agency (ESA) under Contract No. 11653/95/SRON STS-TDG-99/014 and by the

Nederlandse Organisatie voor Wetenschappelijk Onderzoek (NWO) through the Stichting voor Technische Wetenschappen (STW).

References

1. An example of JPL group, B.S. Karasik, M.C. Gaidis, W.R. McGrath, B. Bumble, and H.G. LeDuc, Appl. Phys. Lett. 71, 1567 (1997).
2. M. Frommberger, F. Mattiocco, P. Sabon, M. Schicke and K.F. Schuster, Proc. of the 11 th Int. Symp. on Space THz Techn., Ann Arbor MI, May 1-3, pp. 489-500 (2000).
3. J. Stodolka and K. Jacobs, Proc. 12th Int. Symp. Space THz Techn., San Diego, California, Feb. 14-16, 2001, p47
4. D. Wilms Floet, J.R. Gao, T.M. Klapwijk, W.F.M. Ganzevles, G. de Lange, PA.J. de Korte, Proceedings of 10th Int. Symp on Space Terahertz Technology, Charlottesville, USA, March 16-18, 1999, p228.
5. W.F.M., Ganzevles, L.R. Swart, J.R. Gao, PA.J. de Korte, and T.M. Klapwijk, Appl. Phys. Lett., **76**, 3304(2000).
6. D. Wilms Floet, J. J. A. Baselmans, T.M. Klapwijk, and J.R. Gao, Appl. Phys. Lett. 73, 2826 (1998).
7. P. Khosropanah. H. Merkel, S. Yngvesson, A. Adam, S. Cherednichenko, and E. Kollberg, 11 th Int. Symp. on Space THz Techn., Ann Arbor MI, May 1-3, pp. 474 (2000).
8. D. Wilms Floet, "Hotspot Mixing in THz Niobium Superconducting Hot Electron Bolometer Mixers", Ph.D. thesis, Delft University of Technology (2001).
9. D. Wilms Floet, E. Miedema, T.M. Klapwijk and J.R. Gao, Appl. Phys. Lett. **74**, 433 (1999).
10. D. Wilms Floet, T.M. Klapwijk, J.R. Gao and P.A.J. de Korte, Appl. Phys. Lett. **77**, 1719 (2000).
11. W.F.M. Ganzevles "A Quasi-optical THz Mixer Based on a Nb Diffusion-cooled Hot Electron Bolometer", Ph.D. thesis, Delft University of Technology, May, 2002.

A Hot Spot Model for HEB Mixers Including Andreev Reflection

Harald Merkel
Chalmers University of Technology , SE 412 96 Göteborg , Sweden

Abstract

A device model for HEB mixers is described that takes two additional effects into account: Andreev reflection at the hot spot boundaries and critical current variations on the bridge. This model is capable to predict IV curves even in the unstable areas with acceptable accuracy. Based on these large signal results a more accurate small signal expansion has been developed: In the framework of this model heating due to a small signal current change acts differently from a small signal voltage change at IF.The small signal model allows accurate predictions of the conversion gain and the mixer noise including thermal fluctuation, Johnson and quantum noise.

Introduction

Hot spot models for HEB mixers have been proposed in recent years resulting in a substantial improvement in HEB modelling and understanding of the device physics. Such models require the solution of an one-dimensional heat balance. The occurrence of a DC resistance and the device's mixing capabilities are explained by the formation of a hot spot, i.e. a normal conducting zone wherever the quasiparticles exceed the critical temperature. Depending on the applied heating powers a certain temperature profile is obtained on the HEB bridge resulting in a certain hot spot length. Applying a superposition of a strong LO source and a weak RF signal results in a time-averaged RF heating and in a small beating term oscillating at the difference frequency (IF). The latter causes a tiny change of the hot spot length. This yields a small resistance change at IF which creates small signal currents and voltages through the bridge and finally gives rise to conversion gain of the HEB. Unfortunately none of these hot spot models is capable to predict gain and noise simultaneously with acceptable accuracy without introducing additional empirical parameters or by requiring parameter values being in conflict with experimental results. A popular empirical parameter is the local resistive transition width [1] assuming that the film smoothly turns normal around Tc. This reduction of the resistance slope "helps" to fit the conversion gain but still too much heating power is predicted. Required values for this transition are about 800mK whereas experiments reveal some 50mK. For Nb the case is even worse [2]. There are strong indications that some physical effects are not covered by a simple hot spot based device model. In this paper two additional effects are discussed in order to explain at least part of the discrepancies. These additional effects are due to critical currents and due to Andreev reflection. Throughout this model, **strong localization** is assumed. This applies to quasiparticle and phonon temperatures, the critical current and the quasiparticle bandgap.

Critical current effects on the HEB bridge

In previous models a normal zone is formed wherever the quasiparticle temperature exceeds the critical temperature. This holds only for zero bias current. Otherwise the

normal zone is created wherever the bias current density exceeds the critical current density which is the case at a lower temperature. In the framework of this model, a reduced critical temperature is defined which corresponds to a critical current density equal to the current density caused by the bias current.

Andreev reflection

In simple hot spot models the HEB bridge is assigned a temperature-depending lateral thermal conductivity of exponential or polynomial form [1],[2]. Due to Andreev reflection at the boundary between the hot spot and the superconducting rest of the HEB bridge, only electrons which energy is large enough the overcome the quasiparticle bandgap participate in heat transport. Andreev reflection provides good thermal insulation of the hot spot. As a direct consequence the electron temperature within the hot spot is now more or less constant. The electron temperature profile and the resulting bandgap distribution is summarized in Figure 1:

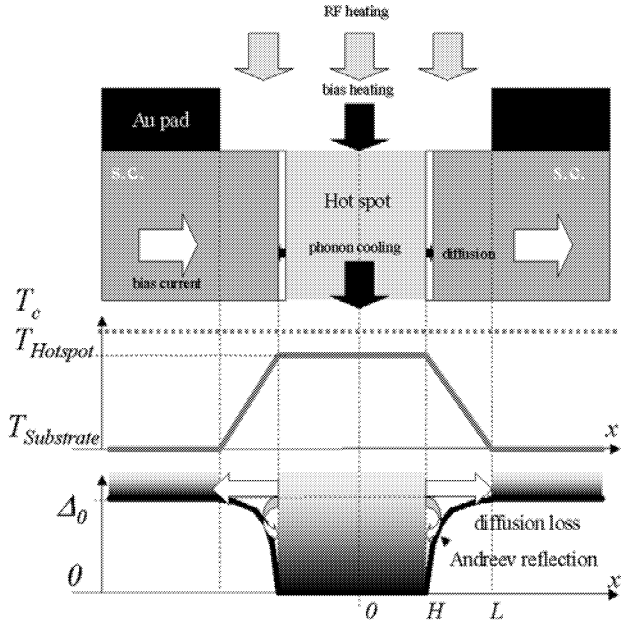

Figure 1: Schematic of a HEB bridge. The whole bridge is heated by RF, the bias heating acts only on the hot spot where superconductivity is suppressed. The electrons are cooled by phonon escape to the substrate and by outdiffusion to the pads. Outdiffusion is reduced by Andreev reflection at the hot spot boundary.

Model assumptions

The HEB device model presented here is based on a set of assumptions. All parameters used here are summarized in Table 1 at the end of the paper including typical values for the calculations presented here:

1: Localization and immediate thermalization

The correlation length is of the order of the film thickness. All superconducting parameters are localized. The film properties in vertical direction are homogenous. Besides that one assumes instantaneous thermalization of the heating powers by electron-electron interaction. Then electrons and phonons are described by effective electron and phonon temperatures.

2: Heating by superposition

The HEB is heated by LO power being the linear superposition of a local oscillator (LO) signal and a weak RF source. This superposition results in a power deposited in the HEB bridge at the intermediate frequency (IF) of the form:

$$p_{IF} \propto 2\sqrt{P_{LO}P_S}$$

In time average the HEB bridge is heated by the mean value of the LO power and DC power.

3: A model for the critical current density on the HEB bridge

Operating a HEB as a mixer requires a substantial bias current to be carried by the HEB bridge. Therefore the superconductivity on the HEB bridge is suppressed wherever the local critical current is exceeded. The theoretical temperature dependence of the local critical current density $j_c(T,x)$ is given by Ginzburg-Landau theory [3]. Performing a nonlinear best fit a simplified and more convenient relation is obtained (the parameters are explained in Table 1):

$$j_c(T,x) = j_c(0)\cdot\left[1-\frac{T(x)}{T_c}\right]^{\gamma} \qquad (1)$$

Here γ denotes a best fit coefficient set to 0.408. For T_c ranging from 8.5K to 11.5K this yields a more accurate model than the "usual" setting [3] of γ=1.5 for low temperatures and 0.5 for large temperatures. Solving (1) for the quasiparticle temperature, a "reduced" critical temperature is obtained for voltage bias:

$$T_{c,eff,V}(V_0,x_0) = T_c\cdot\left[\left(\frac{V_0}{j_c(0)\cdot A\cdot R_N\cdot\frac{x_0}{L}}\right)^{\frac{1}{\gamma}}-1\right]\le T_c \qquad (2)$$

The results for the reduced critical temperature for voltage bias for a voltage of V_0=0.8mV (1.0mV and 1.2mV) are summarized in Figure 2.

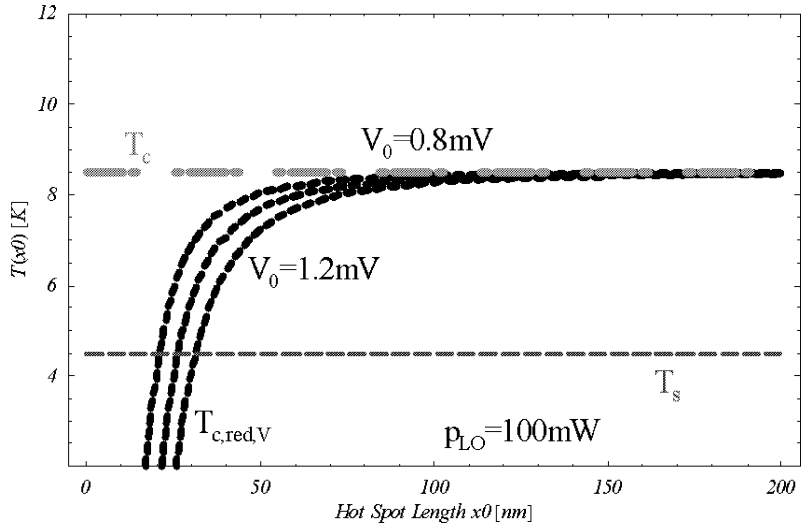

Figure 2: Reduced critical temperature for a bias voltage of V_0=0.8mV (1.0mV and 1.2mV , the black dotted curves) with a substrate temperature of 4.2K and a critical temperature of 8.5K.

4: Almost perfect Andreev reflection at the hot-spot boundaries

A hot spot is formed wherever the bias current exceeds the critical current. The remaining parts of the bridge are in perfect Meissner state. The hot spot is heated by the absorbed bias power and the uniformly absorbed LO power. The quasiparticles in the hot spot are cooled by electron-phonon interaction and the heat is removed from the film by phonon escape. At the NS interfaces Andreev reflection [4] determines the amount of heat being able to leave the hot spot by diffusion. In the ideal case (perfect Andreev reflection) no heat transfer will occur across the interface and the whole cooling power is carried by the phonon path. In reality only the fraction of "normal" electrons with the energy of the quasiparticle levels in the superconductor will be able to carry heat across the NS interface. As a first order approximation we neglect the fact that the quasiparticle bandgap opens slowly on a length given by the thermal healing length and assume the bandgap to be its coldest value reached at substrate temperature immediately. This is an acceptable assumption since we are only interested in the net heat loss of the hot spot to the antenna pads – at some point in the superconductor all electrons with energies smaller than the local bandgap will be reflected and only those being able to overcome the highest bandgap will remove heat laterally from the hot spot. The fraction of electrons transporting heat α across the hot spot boundary is estimated using a Fermi-Dirac distribution function for the electron density $n_E(E)$ [5]:

$$\alpha = \frac{\int_{\Delta}^{\infty} n_E(E)\,dE}{\int_{0}^{\infty} n_E(E)\,dE} = \frac{kT\ln\left(1+e^{\frac{\Delta(T)}{kT}}\right)-\Delta(T)}{kT\ln 2},\quad \Delta(T)=\Delta_0\left[1-\frac{T}{T_c}\right]^{\gamma} \qquad (3)$$

Calculations show that typical values of the Andreev transmission for critical temperatures around 10K and pad temperatures of the order 5K are in the range 1% to 10% providing good thermal isolation of the hot spot. It is important to note, that this model assumes the antenna pads of the HEB to be in perfect Meissner state. Using this model for HEB configurations with normal conducting antenna pads, the maximum value of the quasiparticle bandgap needs to be changed appropriately. In the next section, the hot spot size is calculated based on the previous model assumption by approximating the solution of an one-dimensional heat transport equation.

Solving for the temperature and the size of the hot spot

The quasiparticle temperature on a hot spot of given (but yet unknown) length $2x_0$ is determined by an equilibrium between electron-phonon cooling P_P, RF and bias heating and cooling due to net outdiffusion through the NS interfaces P_D. One obtains then [6]:

$$P_P + P_D = \frac{P_{LO} + \dfrac{V_0^2}{R_N \dfrac{x_0}{L}}}{2 \cdot x_0 \cdot D \cdot W} \qquad (4)$$

The net heat loss due to heat conduction from a hot spot with temperature $T_{c,eff,V}$ is determined by the gradient of the quasiparticle temperature between the hot spot and the antenna pads:

$$P_D = 2\alpha \cdot \lambda \cdot \frac{A}{V} \cdot \frac{T_s + T_{c,eff,V}}{(x_0 - L)} = 2\alpha \cdot \lambda \cdot \frac{T_s + T_c\left[\left(\frac{L \cdot V_0}{j_c A R_N x_0}\right)^{\frac{1}{\gamma}} - 1\right]}{x_0 \cdot (x_0 - L)} \qquad (5)$$

For the electron-phonon interaction one is left with the "usual" expression [6]:

$$P_P = \sigma_E\left(T^n - T_p^n\right) \qquad (6)$$

The power being transferred to the phonons heats the film phonons that is cooled by phonon escape to the substrate. The heat transport by phonons in direction of the film is neglected. Then a heat balance for the phonons becomes:

$$\sigma_E\left(T^n - T_p^n\right) = \sigma_P\left(T_p^m - T_S^m\right) \approx \delta \cdot \sigma_E\left(T_p^n - T_S^n\right) \qquad (7)$$

Inserting (7) in (6) and subsequently in (5) and (4) the temperature of a hot spot T for a given length x_0 is obtained by:

$$\frac{\delta \cdot \sigma_E}{1+\delta}\left(T^n - T_s^n\right) + 2\alpha \cdot \frac{T_s + T_c\left[\left(\frac{L \cdot V_0}{j_c A R_N x_0}\right)^{\frac{1}{\gamma}} - 1\right]}{x_0 \cdot (x_0 - L)} = \frac{P_{LO} + \frac{V_0^2}{R_N \frac{x_0}{L}}}{2 \cdot x_0 \cdot D \cdot W} \qquad (8)$$

For (8) a closed form analytical solution is available. A typical result for the quasiparticle temperature is shown in Figure 3. Note that with perfect Andreev reflection (i.e. no diffusion losses) the hot spot will violate the boundary condition under the antenna pads.

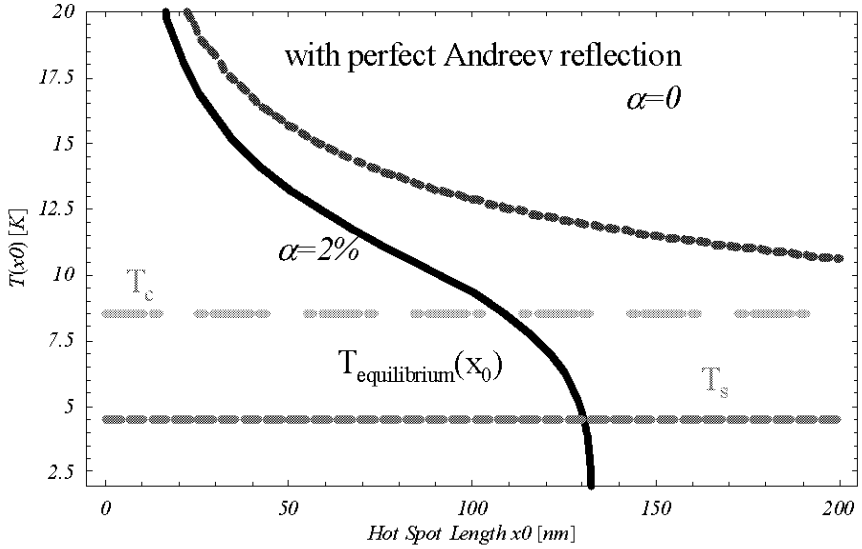

Figure 3: Equilibrium temperature of a hotspot with variable length (for a device length of 2 x 200nm) with 2% Andreev transmission (solid black line) and perfect Andreev reflection (dotted dark gray line) together with the substrate temperature T_s and the critical temperature T_c.

Obviously the temperature in the hot spot (and therefore also at the end of the hot spot) must be equal to the quasiparticle temperature required to break superconductivity for the given bias current. From this the hot spot length is calculated. A graphical solution for a single operating point is shown in the following Figure:

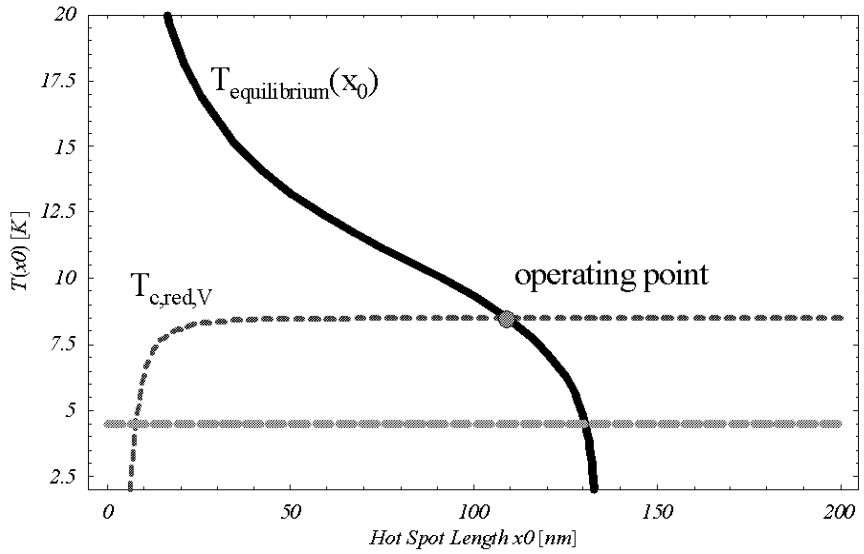

Figure 4: Solving for a hot spot length at 0.3mV bias voltage and 100nW LO power. T_c is 8.5K and the substrate is at 4.2K. The device length is 400nm, its width is 4μm and the thickness is 50Å.

Figure 5 shows a comparison between theory (thin and partially dotted curves) and experiment (thick curves) for various LO powers. The topmost curve is obtained for no RF heating at all and the lowest one for 300nW. The curves in between are obtained in steps of 25nW. For the measured curves, the topmost is obtained at about 25nW LO power and the lowest at about 300nW.

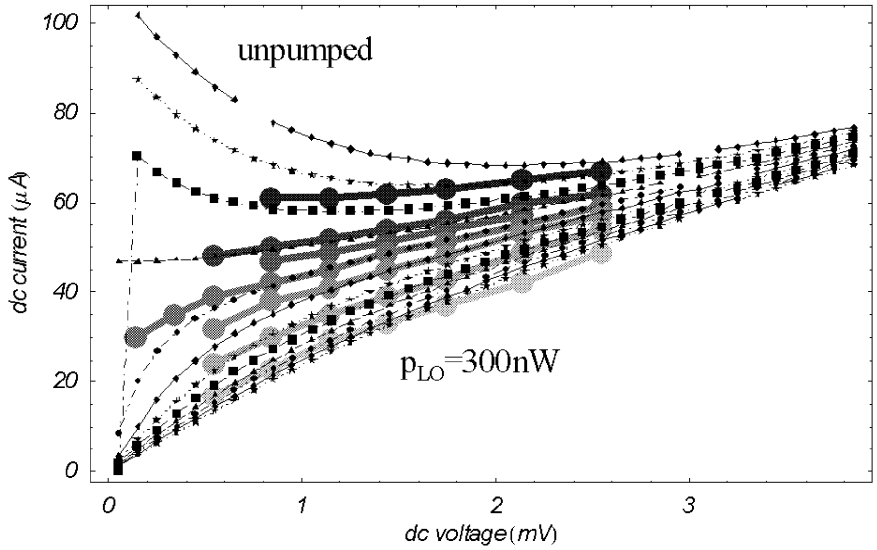

Figure 5: Measurement and theoretical results for the IV curve for a NbN HEB on MgO with the dimensions 400nm x 4μm x 55Å measured at 2.5THz. The measured points are connected by thick gray lines. The black curve is an unpumped curve, the light gray is pumped with about 300nW LO power according to a standard isothermal method applied far away from the optimum point for large bias voltages. The calculated values are obtained for 0nW up to 300nW LO power with a step size of 25nW.

Small signal model

The HEB mixer topology is shown in Fig. 6. It is similar to the topology from [7] where the biasing resistor has been replaced by a large inductance serving as RF coil:

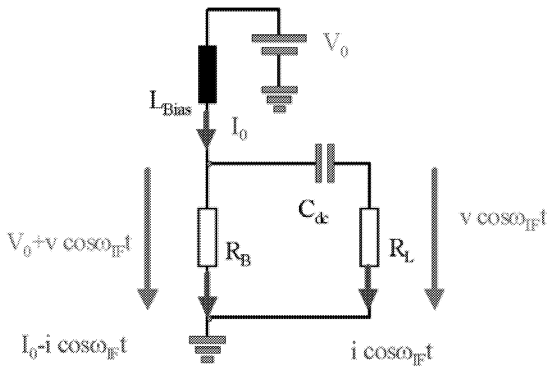

Figure 6: Mixer topology for a typical HEB application – the inductance ensures proper voltage biasing for choosing a proper DC operating point. For IF signals, the inductance poses an open circuit and the IF signal is coupled to the load resistance by a DC block capacitor. ω_{IF} denotes the intermediate frequency i.e. the difference frequency between the LO and the RF signal.

In this model, the large signal relations are behave differently in current and voltage. This is contrasted by older models [1],[7],[8] where only heating powers are considered. Let us assume that the bolometer resistance given by the hot spot length depends on LO heating power, bias current and bias voltage. Then the small signal resistance change in the bolometer r_B is modelled by:

$$r_B = C_{rf}\sqrt{P_{LO}\cdot P_S} + C_V v\cdot I_0 - C_I i\cdot V_0 \qquad (9)$$

From this, the power in the load resistance can be calculated and one obtains for the conversion gain:

$$G = \frac{P_L}{P_S} = \frac{2\cdot I_0^2}{(R_B+R_L)^2}\cdot\frac{C_{rf}^2\cdot P_{LO}}{\left[1-I_0^2\cdot\dfrac{C_I R_B - C_V R_L}{R_B+R_L}\right]^2} \qquad (10)$$

Values for the conversion loss of a HEB and comparison with measurements are indicated in Figure 7.

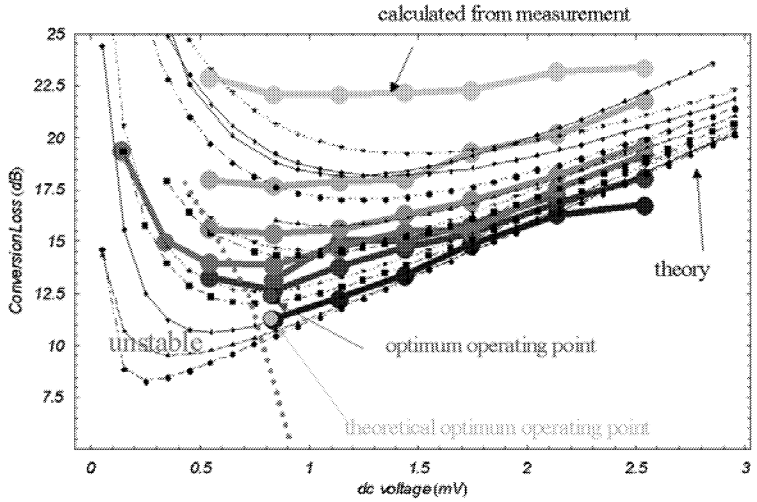

Figure 7: Calculated intrinsic conversion gain based on measurements (thick gray curves) and theoretical results (dashed and dotted curves) for the intrinsic conversion loss for a NbN HEB on MgO with the dimensions 400nm x 4μm x 55Å measured at 0.6THz. The measurement data have been obtained at an IF frequency of 1.5GHz.

HEB Noise

Noise in the HEB is caused by Johnson noise since the hot spot forms a resistor with a certain temperature $T_{Hotspot}$. The noise contribution at the mixer output T_J^{out} is given by [9],[10]:

$$T_J^{out} = \frac{4 \cdot R_L \cdot R_B \cdot T_{Hotspot}}{(R_B + R_L)^2} \cdot \frac{1}{1 - I_0^2 \dfrac{C_V R_L - C_I R_B}{R_B + R_L}} \tag{11}$$

Any system of a given temperature with a given thermal coupling to a cold reservoir and a certain volume exhibits thermal fluctuations [9] resulting in noise. For a hot spot this results in [10]:

$$T_{TF}^{out} = \frac{I_0^2 R_L}{(R_B + R_L)^2} \cdot \frac{1}{1 - I_0^2 \dfrac{C_V R_L - C_I R_B}{R_B + R_L}} \cdot \left[\left. \frac{\partial R}{\partial T} \right|_{T=T_{hotspot}} \right]^2 \cdot \frac{4 T_{hotspot}^2 \tau_{e,relax}}{C_e \cdot V \cdot \dfrac{x_0}{L}} \tag{12}$$

A third noise contribution is caused by quantum noise [11],[12]:

$$T_Q^{out} = 2G \cdot \left(L_{optics} L_{optics\,4K} \left[\frac{R_B}{R_S} + 1 \right] - 1 \right) \cdot \frac{h\nu}{2k} \tag{13}$$

Adding up all the contributions and transferring them to the mixer input, the DSB input noise temperature T_{in} is obtained [11]:

$$T_{in} = L_{optics} \frac{T_{TF}^{out} + T_J^{out} + T_{IF} + T_Q^{out}}{2G} + (L_{optics} - 1) \frac{h\nu \cdot B}{e^{\frac{h\nu}{kT_{optics}}} - 1} \tag{14}$$

Results for the DSB receiver noise temperature are summarized below:

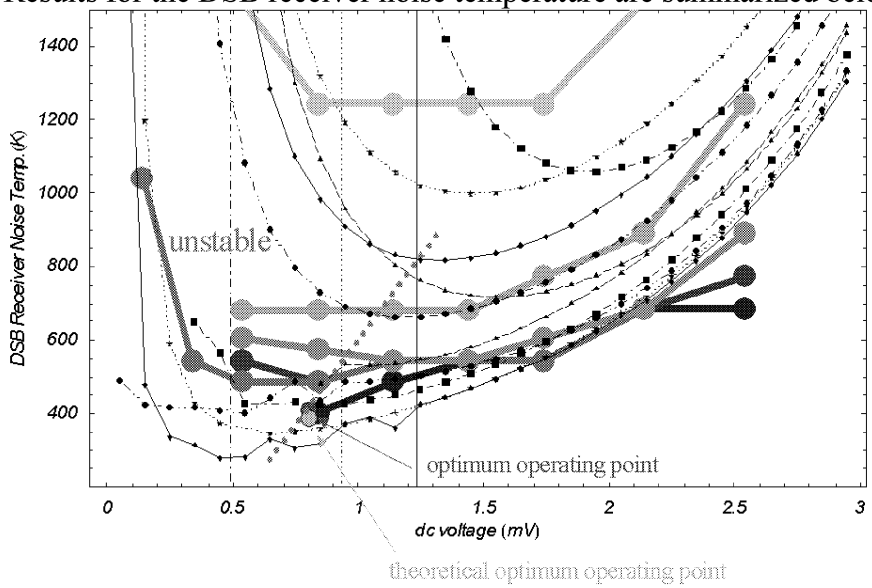

Figure 8: Measured receiver noise (thick gray curves) and theoretical results (dashed and dotted lines) for the DSB receiver noise temperature for a NbN HEB on MgO with the dimensions 400nm x 4μm x 55Å measured at 0.6THz.

The noise measured at the IF output of the HEB is a collection of the warm load at the input T_{lab} of the HEB collected in both sidebands, the fluctuation, Johnson and quantum noise contributions and the contribution of the optics losses at a given temperature of the optics:

$$T_{out} = T_{lab} \cdot 2G + T_{TF}^{out} + T_J^{out} + T_Q^{out} + \left(L_{optics} - 1\right) \frac{h\nu \cdot B}{e^{\frac{h\nu}{kT_{optics}}} - 1} \cdot 2G \qquad (15)$$

Results for the output noise temperature is summarized below for the same device as in Fig. 5.

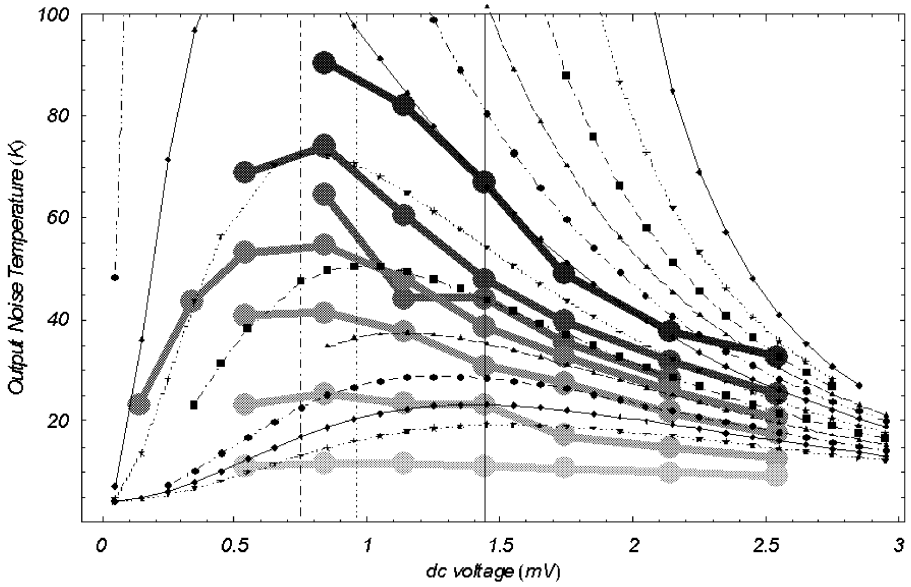

Figure 9: Measurement (thick, gray curves) and theoretical results (dashed and dotted lines) for the output noise temperature for a NbN HEB on MgO with the dimensions 400nm x 4μm x 55Å measured at 0.6THz.

Conclusion

A HEB model including critical current effects and Andreev reflection at the hot spot ends together with a small signal model where heating due to RF, IF currents and voltages is treated differently improves the quality of performance predictions by HEB device models substantially. In addition complete relations for the quantum noise in HEB receivers are now available (c.f. the contribution of K.S.Yngvesson and E.L.Kollberg in this issue) and have already been introduced in the model presented here. The model describes IV curves with satisfying accuracy and yields reasonable conversion gain and noise figures within the accuracy of the measurements. The device model has been successfully tested on various NbN HEBs with different geometries ranging from 120nm x 1μm to 400nm x 4μm. More tests on NbN on a larger geometry range and HEBs based on other materials have to be done to yield conclusive results about the overall model quality.

Model Parameters

Parameter	Description	Value used for model calculation
A	Film cross section	$A = D \cdot W$
α	Transmissivity of the s-n interface due to leaky Andreev reflection	$\alpha \approx 0.02$ typical
B	RF antenna bandwidth	$B = 500GHz$

C_E	Electron thermal capacity	$C_E = 1600 \frac{Ws}{m^3 K}$ at T_c
C_I	HEB resistance change due to a small current change at IF	$C_I = \frac{R_N}{2L \cdot V_0} \cdot \frac{\partial x_0}{\partial i}\Big\|_{P_{LO}=const, v=const}$
C_{rf}	HEB resistance change due to a small change of the RF heating power at IF	$C_{rf} = \frac{R_N}{2L} \cdot \frac{\partial x_0}{\partial P_{LO}}\Big\|_{v=const, i=const}$
C_V	HEB resistance change due to a small voltage change at IF	$C_V = \frac{R_N}{2L \cdot I_0} \cdot \frac{\partial x_0}{\partial v}\Big\|_{P_{LO}=const, i=const}$
D	Film thickness	$D = 35 Å$
δ	Phonon to electron efficiency ratio	$\delta \approx 0.2$
$\Delta(T)$	Quasiparticle bandgap as a function of quasiparticle temperature	
Δ_0	Quasiparticle bandgap extrapolated to 0K	$\Delta_0 = 800 GHz$
G	Conversion gain of the HEB	
γ	Exponent in the temperature dependence of the critical current , obtained by best fit to Ginzburg-Landau expression	$\gamma = 0.408$
h	Planck's constant	
I_0	Bias current (DC) across the HEB bridge	$I_0 = \frac{V_0}{R_B}$
i	Small signal current (IF) across the HEB bridge	
$j_c(T,x)$	Local critical current density , function of quasiparticle temperature	
$j_c(0)$	Maximum critical current density at 0K, related to maximum critical current by division by bridge cross section	$j_c = \frac{I_c}{D \cdot W}$ $I_c = 160\ \mu A$
k	Boltzmann's constant	
λ	Lateral thermal conductivity	$\lambda = 1 \frac{W}{Km}$
λ_{eff}	Lateral effective thermal conductivity across the s-n boundary	
$2 \cdot L$	HEB bridge length (Length between the pads , contact zone under the pads not taken into account)	$L = 200 nm$
L_{optics}	Loss of the optics at room temperature	$L_{optics} = 1.3$
$L_{optics\,4K}$	Loss of the optics at cryogenic (substrate) temperature	$L_{optics\,4K} = 1.7$
m	Exponent for the temperature dependence of phonon escape	$m = 4.0$
n	Exponent for the temperature dependence of electron-phonon interaction	$n = 3.6$
ν	RF frequency	$\nu = 1600 GHz$
P_D	Power leaving the hot spot by electron diffusion	
p_{IF}	Power absorbed by the HEB at the intermediate frequency	
P_L	Power delivered to the load at IF	
P_{LO}	Local oscillator power absorbed by the HEB	variable

P_P	Power leaving the hot spot by phonon cooling	
P_S	RF signal power absorbed by the HEB	
r_B	Small signal HEB resistance change due to IF beating	
R_B	Resistance of the HEB in the operating point	
R_L	Load resistance	$R_L = 50\Omega$
R_N	Normal resistance of the HEB bridge (at 20K)	$R_N = 65\Omega$
R_S	Antenna impedance (Real part)	$R_S = 100\Omega$
σ_E	Electron-phonon cooling efficiency	$\sigma_E = \frac{C_e}{3.6T^{2.6}\tau_{e\to p}}$
σ_P	Phonon escape efficiency	$\sigma_P \approx \delta\sigma_E$
$\tau_{e\to p}$	Electron- phonon interaction time constant	$\frac{1}{\tau_{e\to p}} = 8GHz$
$\tau_{e,relax}$	Electron energy relaxation time constant	$\frac{1}{\tau_{e,relax}} = 5GHz$
$T(x), \quad T$	Local quasiparticle temperature	
$T_{equilibrium}$	Hypothetic hot spot temperature, where heating and cooling powers are equal	
T_c	Critical temperature of the HEB bridge	$T_c = 8.5K$
$T_{c,effI}$	Reduced critical temperature due to critical current effects under current bias conditions	
$T_{c,effV}$	Reduced critical temperature due to critical current effects under voltage bias conditions	
$T_{hotspot}$	Hot spot temperature in a given operating point	
T_{IF}	Noise temperature constribution of the IF amplifier	$T_{IF} = 7K$
T_{in}	Noise temperature at the input of the receiver, DSB receiver noise temperature	
T_J^{out}	Noise temperature at the output of the mixer due to thermal (Johnson/ Nyquist) noise	
T_{lab}	Room temperature in the surrounding laboratory	$T_{lab} = 292K$
T_p	Temperature of the phonons in the hot spot	
T_Q^{out}	Noise temperature at the output of the mixer due to Quantum noise	
T_s	Substrate temperature under the HEB bridge	$T_s = 4.5K$
T_{TF}^{out}	Noise temperature at the output of the mixer due to Thermal Fluctuation noise	
V	HEB bridge volume	$V = D \cdot W \cdot L$
v	Small signal voltage (IF) across the HEB bridge	
V_0	Bias voltage (DC) across the HEB bridge	variable
$2 \cdot x_0$	Length of the hot spot	
W	Film width	$W = 4\mu m$

Table 1: List of used parameters with their abbreviations and model values for the calclation presented in the paper

References

[1] H.F. Merkel, P. Khosropanah, D. Wilms Floet, P. Yagoubov, E.L. Kollberg, "Conversion Gain and Fluctuation Noise of Phonon Cooled Hot Electron Bolometers in Hot Spot Regime", IEEE-Trans. MTT, 14 Apr. 2000, **48**(4), pp.690-699

[2] D. Wilms Floet, J. J. A. Baselmans, T. M. Klapwijk, J. R. Gao " Resistive transition of niobium superconducting hot-electron bolometer mixers", APL, **73**(19), pp. 2826-2828, November 9, 1998

[3] C.P. Poole, H.A. Farach, R.J. Creswick "Superconductivity", Academic Press 1995

[4] A.F. Andreev, Zh. Eksp. Teor. Fiz. **46**, 1823 (1964), Sov. Phys. JETP **19**, 1228 (1964).

[5] N.W. Ashcroft, N.D. Mermin "Solid State Physics", Saunders College Publishing 1976

[6] E.M. Gershenzon, G.N. Gol'tsman, A.M. Lyulkin, A.D. Semenov, A.V. Sergeev," Electron-
phonon interaction in ultrathin Nb films", Sov. Phys JETP. **70**(3). pp 505-511 (1991)

[7] F. Arams, C. Allen, B. Peyton, E. Sard, Proceedings of the IEEE **54**(3) 308-318 (1966)

[8] H.F. Merkel, P. Khosropanah, K. S. Yngvesson, S. Cherednichenko, M. Kroug, A. Adam, E.L. Kollberg, "An Active Zone Small Signal Model for Hot Electron Bolometric Mixers", Proc. 12 ISSTT, San Diego, March 2001

[9] B.S. Karasik, A.I. Elantev, "Noise Temperature Limit of a Superconducting Hot-Electron Bolometer Mixer", Appl. Phys. Lett. **68**, pp. 853-855, 1996

[10] P. Khosropanah, H.F. Merkel, K.S. Yngvesson, A. Adam,
S. Cherednichenko, E.L. Kollberg, "A Distributed Device Model for Phonon-cooled HEB Mixers Predicting IV Characteristics, Gain, Noise and IF Bandwidth", Proc. 11.th ISSTT U.Mich. Ann Arbor MI, May 2000

[11] E.L. Kollberg, K.S. Yngvesson "Quantum Noise Contribution to the Receiver Noise Temperature of HEB THz Heterodyne Receivers", this issue

[12] A.R. Kerr, "Suggestion fo Revised Definition of Noise Quantities Including Quantum Noise", IEEE Trans. MTT **47**(3) pp.325-329, March 1999

The sensitivity and IF bandwidth of waveguide NbN Hot Electron Bolometer mixers on MgO buffer layers over crystalline quartz

Denis Meledin, C.-Y. Edward Tong, Raymond Blundell

Harvard-Smithsonian Center for Astrophysics, 60 Garden St, Cambridge, MA, 02138, U.S.A.

Natalia Kaurova, Konstantin Smirnov, Boris Voronov, and Gregory Goltsman

Moscow State Pedagogical University, 1 M. Pirogovskaya St., Moscow, 119891, Russia.

We have developed and characterized waveguide phonon-cooled NbN Hot Electron Bolometer (HEB) mixers fabricated from a 3-4 nm thick NbN film deposited on a 200nm thick MgO buffer layer over crystalline quartz. Double side band receiver noise temperatures of 900-1050 K at 1.035 THz, and 1300-1400 K at 1.26 THz have been measured at an intermediate frequency of 1.5 GHz. The intermediate frequency bandwidth, measured at 0.8 THz LO frequency, is 3.2 GHz at the optimal bias point for low noise receiver operation.

Introduction

Receivers with large intermediate frequency gain bandwidth are very important for practical radio astronomy applications. This is especially true for the observation of distant galaxies, where spectral linewidths are large. Furthermore, when a low power solid state source is used in conjunction with a Martin-Puplett interferometer (MPI) to couple signal and local oscillator (LO) to the mixer, it is desirable to operate at relatively high intermediate frequency (IF) to maximize the usable IF bandwidth.

In the past decade the hot-electron bolometric (HEB) mixer has emerged as the mixer of choice for low noise heterodyne receivers operating above 1 THz.[1,2] The strong need for sensitive, broadband receivers operating at THz frequencies for ground based, air-

and space borne observatories, has helped to stimulate the development of HEB mixers, and rapid progress in their development has been made.[1,2,3]

Quasioptical NbN HEB mixers integrated with a planar antenna typically employ Si, MgO, or sapphire, as the substrate material. Using a thin 3 nm thick NbN film these mixers exhibit high critical temperature 9-11 K, and relatively good acoustic transparency to the substrate.[3,4] As a result, wide IF bandwidths, up to 5 GHz have been reported.[5] However, it is considerably more difficult to optimally couple the emergent beam of the planar antennas to a telescope than to couple that from a scalar feed, typical of waveguide-based mixer.

Due primarily to its low dielectric constant, and ease of processing and handling, traditional waveguide-based THz mixers employ quartz as the substrate of choice. However, for phonon-cooled NbN HEB mixers made from 3-4 nm NbN film deposited directly on crystalline quartz, the IF bandwidth is limited to about 2 GHz.[2]

It has been established that in NbN HEB mixers the electron energy relaxes through interaction with phonons that escape from the film to the substrate. Consequently, the IF bandwidth is a function of film parameters, the thickness d, critical temperature T_c, and acoustic match, α, between film and substrate. In the past few years a systematic study of phonon-cooled HEB elements based on film deposited on silicon and sapphire substrates, has shown that phonon escape time (τ_{esc}) is equal to $12d$ ps/nm,[4] and for MgO substrates a phonon escape time of $6d$ ps/nm has been established.[6]

In order to increase the IF bandwidth of waveguide-based HEB mixers, we have investigated the use a buffer layer which may improve the acoustic match between the NbN film and the crystalline quartz substrate. Since MgO has the same crystalline structure as the NbN film,[7] a number groups have reported on the use of MgO as a buffer layer for Si, sapphire,[8,9] and quartz[10] substrates. The introduction of a MgO buffer layer could potentially improve the acoustic match between the film and substrate material and then reduce $\tau_{esc} \propto d/\alpha$. In this paper, we report on the experimental results of sensitivity and IF bandwidth of NbN based HEB waveguide mixers with MgO buffer layers.

The mixers elements and experimental setup

In our experiments we used mixer elements made from high purity 3-4 nm thick NbN film. The NbN films are deposited using reactive magnetron sputtering in an argon-nitrogen gas mixture on a 200 nm thick MgO buffer layer deposited on top of a z-cut crystalline quartz substrate. The critical temperature (T_c) of these films is about 8 K and the transition width is about 0.8 K. The films are patterned by optical and e-beam lithography to give 1-2 μm wide single bolometric elements. The 80-150 nm long mixer elements are formed across two overlaid Au-Ti electrodes, which also act as coupling antennas to the waveguide. After deposition, the wafer is first diced into small blocks about 5 mm square, which are then lapped and polished to a thickness of 30 μm for 0.6-0.8 THz operation, and 23 μm for 1-1.26 THz operation. The blocks are then diced into individual HEB mixer chips: 120 μm wide × 2000 μm long and 90 μm wide×1500 μm long for 0.6-0.8 THz and 1-1.26 THz operation respectively. We have tested devices with normal-state resistance, R_N, between 80 and 170 Ω, and critical currents between 110 and 160 μA.

For tests, the individual mixer chips are mounted into a suspended microstrip channel across a reduced-height waveguide mixer block. The block is installed in a liquid helium dewar and signal input to the mixer provides via a corrugated waveguide feed horn and a 90° off-axis parabolic mirror.

For our measurements we are able to provide sufficient LO power using a solid-state LO units, which generally consist of a Gunn oscillator followed by two stages of frequency multiplication. These units allow us to make measurements continuously from 1.017 to 1.035 THz and at 1.267 THz, and deliver 5-7 μW and 2 μW respectively. The beam from the LO assembly is collimated using a 90° off-axis parabolic mirror, a MPI positioned in front of the cryostat window is used to combine signal and LO at the cryostat input.

DC bias is applied to the mixer via the third port of a circulator inserted between the mixer and a low noise cryogenic HEMT amplifier. After a second stage of room temperature amplification, the IF signal passes through a 100 MHz wide bandpass filter,

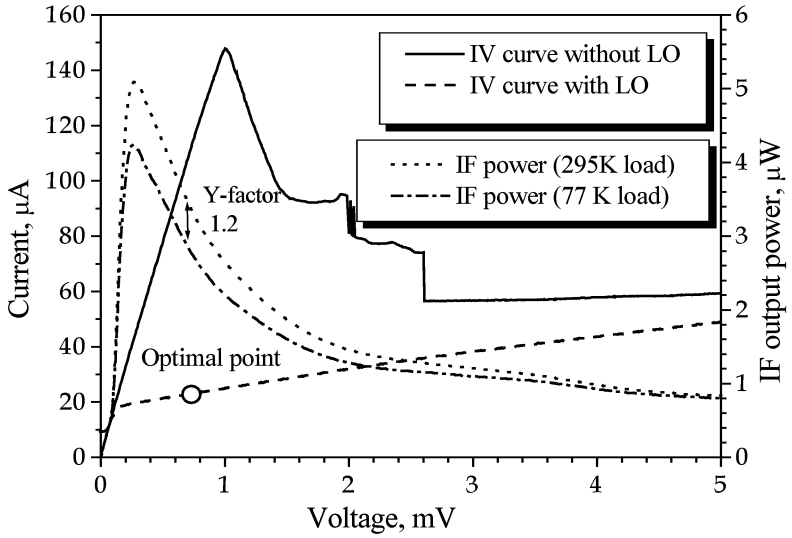

Fig.1 The I-V curves of the HEB mixer at the operating point with and without LO drive at 1.035 THz Also shown is the IF output power in response to hot (295K) and cold (77K) loads placed at the receiver input. The optimal bias point is shown by the open circle, and the measured Y factor is 1.2.

centered at 1.5 GHz, to a calibrated power meter which is used to measure the IF power output.

Experimental results and discussion

The current-voltage characteristics of one of the devices with and without LO power at 1.035 THz are shown in Fig.1, the receiver output in response to hot and cold loads is also shown. Optimal sensitivity is achieved at a bias voltage of 0.7 mV and a bias current of 23 μA. At this operating point the measured receiver noise temperature is about 1000 K, and the conversion efficiency is estimated to be -14 dB. From the figure we see that the noise performance and the mixer conversion efficiency go down strongly towards higher bias voltage. In our measurements the mixer was not influenced by direct detection: the bias current change in passing from a cold to an ambient input was less than 0.2%. The

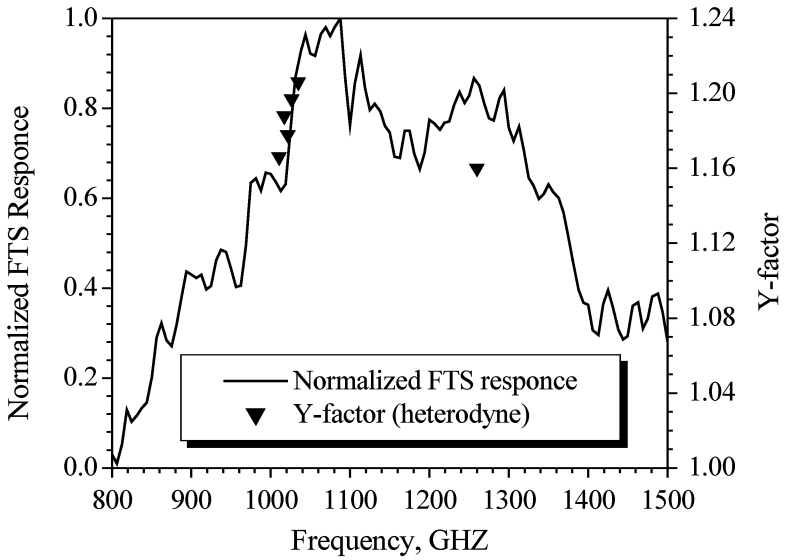

Fig.2. Spectral response of the HEB mixer measured by FTS in direct detection mode (solid curve) and heterodyne mode using Y-factor method (triangle points) as a function of frequency.

receiver also demonstrates reasonable amplitude stability, and output power fluctuations are less than 2% over a 15 min time interval.

In addition to heterodyne measurements, we have also used the Fourier Transform Spectrometer (FTS) to measure the spectral response of the same mixer. In this case the mixer was operated as a direct detector at an elevated bath temperature. The operating bias point was set at the same as for heterodyne operation, even though the general shape of the response was found to depend only weakly on the bias point. The FTS response is shown in Fig.2, solid line. From the graph we estimate that the input bandwidth is about 400 GHz. The dip around 1.15 THz might be explained by a strong atmosphere water absorption line. Other mixers have been measured using the FTS, they all demonstrate a similar bandwidth, however the center frequency shifts, by ~10%, depending on the length of backshort and the detailed layout of IF filter. The measured Y-factor from heterodyne measurements, as function of LO frequency, is also shown in Fig.2. There is reasonable correlation between the direct and heterodyne responses. For example, in general the measured receiver noise

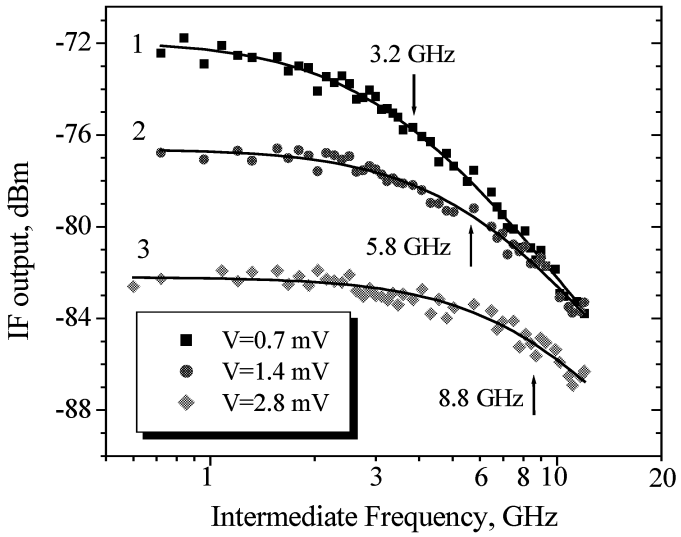

Fig.3. IF bandwidth measurements at f_{LO} =0.8 THz for different bias voltage operating points at constant LO power level. Optimal noise performance is obtained at 0.7 mV bias. Data points are fitted to the curve $1/[1+(f_{IF}/f_{3dB})^2]$. Arrows indicate f_{3dB} for the different curves.

temperature is approximately 1K/GHz, which is comparable to that of HEB mixers, which are based on NbN film directly deposited on crystalline quartz.[2] The measured Y-factor at 1.26 THz LO frequency was 1.16, which corresponds to noise temperature of about 1300 K.

IF bandwidth measurements have been performed at an LO frequency (f_{LO}) of around 0.8 THz. The receiver output as function of IF for one of the mixers is displayed in Fig.3. The experimental data are fitted to $1/[1+(f_{IF}/f_{3dB})^2]$, where f_{3dB} is the 3dB cut-off frequency. At the optimal bias setting for low noise performance, 0.7 mV, f_{3dB} is about 3.2 GHz (curve 1). This is significantly higher than the IF bandwidth of HEB mixers with no buffer layer.[2] Curves 2 and 3 are from measurements at bias voltages of 1.4 and 2.8 mV respectively, with the same LO power as at 0.7 mV bias. At high bias, 2.8 mV, the fitted f_{3dB} strongly increased up to 8.8 GHz, confirming results reported by others groups. [3,11] Although high IF bandwidth can be obtained at high bias voltage, figs. 1 and 3 clearly

demonstrate that this is obtained at the expense of noise performance and conversion efficiency. Furthermore, there is a fundamental instantaneous bandwidth limit, which is set by the electron-phonon interaction time $\tau_{e\text{-}ph}$, which has been measured for thin NbN films as [12]

$$\tau_{e-ph} = 500 \cdot T^{-1.6} \text{ [ps]},$$

where T is physical temperature in Kelvin. At T_c=8 K, this equation yields $\tau_{e\text{-}ph} \sim 18$ ps which corresponds to 3dB cut-off frequency of about 9 GHz. If thin NbN films can be made with T_c approaching the bulk value then it may be possible to have low noise heterodyne operation with instantaneous bandwidth in excess of 20 GHz using NbN thin film technology.

In conclusion, the employment of a MgO buffer layer has allowed us to increase the IF bandwidth of NbN waveguide HEB mixers without degrading their noise performance. Specifically, we have extended the IF bandwidth of our NbN HEB mixers to 3.2 GHz.

References

[1] A. Semenov, H. Huebers, J. Schubert, G. Goltsman, A. Elantiev, B. Voronov, and E. Gershenzon, Appl. Phys. Lett. **88**, 6758 (2000).

[2] J. Kawamura, E.Tong, R. Blundell, D.C. Papa, T. Hunter, F. Patt, G. Gol'tsman, and E. Gershenzon, IEEE Trans. Appl. Superconduct. **11**, 952 (2001).

[3] M. Kroug, S. Cherednichenko, H. Merkel, E. Kollberg, B. Voronov, G. Goltsman, H.W. Hübers, and H. Richter, IEEE Trans. Appl. Superconduct. **11**, 962 (2001).

[4] S. Cherednichenko et al., 8th Int. Symp. on Space THz Technology, Cambridge, USA, 245, (1997).

[5] P. Yagoubov et al., Superond. Sci. Technol. **12**, 263 (1999).

[6] P. Yagoubov et al., Europe Conf. on Applied Supercond., Barselona, Spain, 65, (1999).

[7] Z. Wang, A. Kawakami, Y. Uzawa, and B. Komiyama, J. Appl. Phys. **79**, 7837 (1996).

[8] S. Cherednichenko et al., 13th Int. Symp. on Space THz Technology, Cambridge, USA, (2002), in publication.

[9] Yu. Vachtomin et al, 13th Int. Symp. on Space THz Technology, Cambridge, USA, in publication, (2002).

[10] M. Frommberger, Ph. Sabon, M. Schicke, F. Mattiocco and K. Schuster, IEEE Trans. Appl. Superconduct. **11**, 566 (2001).

[11] D. Wilms Floet, T.M. Klapwijk, J.R. Gao, and P.A.J. de Korte, Appl. Phys. Lett. **77**, 1719 (2000).

[12] Yu. Gousev, G. Goltsman, A. Semenov, and E. Gershenzon, J. Appl. Phys. **75**, 3695 (1994).

QUANTUM NOISE CONTRIBUTION TO THE RECEIVER NOISE TEMPERATURE OF HEB THZ HETERODYNE RECEIVERS

Erik Kollberg
Microwave Electronics Laboratory, Department of Microelectronics, Chalmers University of Technology, Gothenburg, Sweden

and

Sigfrid Yngvesson
Department of Electrical and Computer Engineering, University of Massachusetts, Amherst, MA 01003, USA

Abstract

In this paper we discuss the quantum limit of bolometric mixer receivers. The importance of the optics attenuation is emphasized. Based on a simple bolometer model we predict that the *system* and *receiver* quantum noise limits referred to the input of a double-sideband hot-electron bolometer mixer receiver are, respectively, 2(*hfB*) and 1(*hfB*). The quantum limit to the DSB receiver noise temperature is *hf/2k*, in agreement with what has previously often been assumed. We suggest that an image-rejection single-sideband version of the HEB mixer would have a system quantum noise limit of 1(*hfB*). We also suggest that at a frequency of several THz the quantum noise may indeed be responsible for about half the total receiver noise temperature in a typical HEB receiver system.

1. Introduction

Quantum noise is the well-known ultimate limiting noise of any receiver system and has been treated by many authors [1, 2, 3, 4, 5]. Essentially, a perfect receiver will at the output show fluctuations even if the input is just terminated by a matched load at zero Kelvin. Referred to the receiver input, this output noise power fluctuation is equal to *(hfB)*. Of course, quantum noise is of particular importance at THz frequencies. For example, the minimum quantum noise power corresponds to a noise temperature of 48 K at 1 THz.

In this paper we discuss how to analyze the noise performance (including quantum noise) of a THz receiver, which has optical coupling losses, as well as a lossy circuit between the antenna and a Hot-Electron Bolometer (HEB) mixer. Experimental HEB mixer receivers have been described as having total DSB receiver noise temperatures of the order of ten to twenty times the quantum noise limit, defined as *hf/2k* (see e.g. [6,7]). Using a simple model we predict in this paper that at the higher THz frequencies (about 5 THz) as much as one half of the receiver noise temperature may be traced to the quantum noise.

2. Quantum noise from the input circuit

The total noise power from a matched load including the quantum-noise equivalent power according to Callen-Welton [1] is

$$P_{CW}(T_0) = \frac{hfB}{\exp\left(\frac{hf}{kT_0}\right)-1} + \frac{hfB}{2} = P_{Planck}(T_0) + \frac{hfB}{2} \qquad (1)$$

Referring to Fig 1, this is the noise "power" from a source delivered to a matched load. Notice that even if T_0=0, the source will radiate a noise power of $(hfB)/2$. Since this power will be radiated as well by the load at zero Kelvin this means that the quantum noise part, $(hfB)/2$, cannot be extracted as a real power [3].

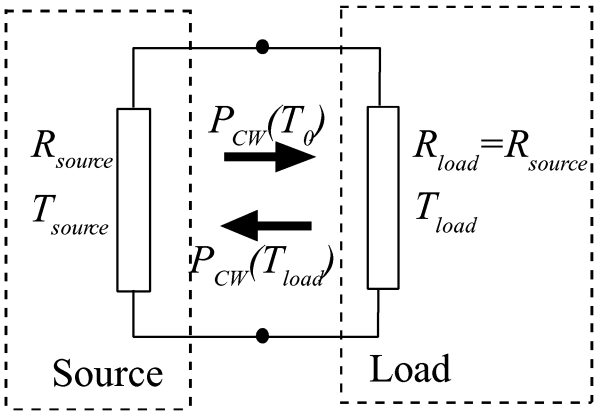

Fig. 1. Noise from a matched load (i.e. "Source") according to Callen-Welton [1]

The noise power of Eq. (1) can be transformed into an equivalent noise temperature

$$T_{CW} = T_0 \cdot \left[\frac{\frac{hf}{kT_0}}{\exp\left(\frac{hf}{kT_0}\right)-1} \right] + \frac{hf}{2k} = \left(P_{Planck}(T_0) + \frac{hfB}{2} \right) \cdot \frac{1}{kB} \qquad (2)$$

However, it is most convenient to perform our calculations in terms of noise power, and then convert this to noise temperature as the final step.

3. System noise vs Receiver noise

In order to analyze the bolometer mixer receiver, we have to make clear the difference between **System** (T_{syst}), **Receiver** (T_{Rec}), **Mixer** (T_{mixer}) and **IF amplifier** (T_{IF}) noise (see Fig. 2).

In the ***System noise*** is included the noise power from the source (R_{Source}), which is $[P_{Planck}(T_{source})+hfB/2]$ at each sideband. Concerning the minimum ***System noise*** **temperature** for a mixer receiver, references [2,3,5] are in agreement with the following statements:

For a linear amplifier and for a mixer used in SSB measurements, using either SSB or DSB receivers, the ***minimum*** *system noise temperature is hf/k.*

*For broadband continuum measurements using a DSB receiver the **minimum** (DSB) system noise temperature is hf/2k.*

The ***Receiver noise*** does not include the noise from the source. It does, however, include noise from the **optics**, the **mixer** and the **IF** amplifier**.** The **mixer** noise is generated in the bolometer at both RF and IF. Until now only the contribution from the IF side (Johnson noise and thermal fluctuation noise) has been included as shown in all standard treatments of HEB noise [8,9].

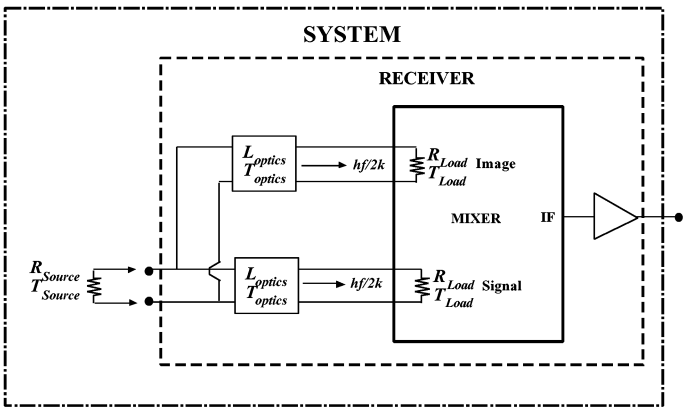

Fig. 2. Definition of Mixer, Receiver, and System.

4. The noise introduced by the optical losses

To analyze the noise from the optics we first consider one channel only (upper or lower sideband). The optics circuit is represented by a two-port matched to both the antenna and to the receiver (Fig. 3). We will now let the "**Load**" in Figure 1 represent one sideband of the *mixer*; specifically the mixer terminals are the terminals of an antenna, which couples the input optics quasi-optically to the mixer. The optical circuit introduces an attenuation L_{optics} and has the physical temperature T_{optics}. If $T_{Source}=T_{optics}$ the noise power transmitted to the mixer (P_{in}) must then be identical to the noise power $P_{CW}(T_{Source})$ from the source. The situation is described in Fig. 3

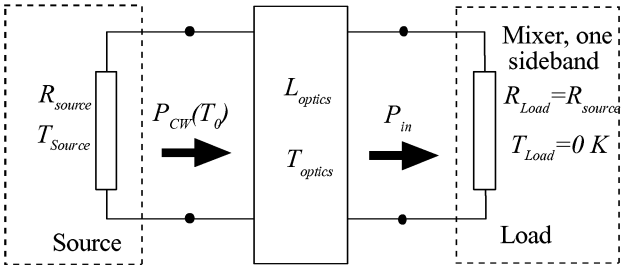

Fig. 3 A simplified model circuit for a THz mixer receiver, one sideband.

Next consider T_{Source}? T_{optics}. Then referring to Eq. (3) below, the contribution to P_{in} from the source is $P_{CW}^{source}(T_{source})\cdot 1/L_{optics}$ whereas the contribution from the lossy two-port must be $P_{CW}^{optics}(T_{optics})\cdot\left(1-1/L_{optics}\right)$. Adding these, we have:

$$\begin{aligned} P_{in} &= P_{CW}^{source}(T_{source})\cdot\frac{1}{L_{optics}} + P_{CW}^{optics}(T_{optics})\cdot\left(1-\frac{1}{L_{optics}}\right) = \\ &= P_{Planck}(T_{source})\cdot\frac{1}{L_{optics}} + P_{Planck}(T_{optics})\cdot\left(1-\frac{1}{L_{optics}}\right)+\frac{hfB}{2} \end{aligned} \tag{3}$$

As expected, the ideal receiver still receives the same quantum noise equivalent power of (hfB)/2. Adding noise power from the "load" itself, P_{Load} (including all mixer and IF contributions) the total noise power entering the "load" is:

$$P_{total,in} = \frac{1}{L_{optics}}\left[P_{Planck}(T_{source}) + P_{Planck}(T_{optics})\cdot\left(L_{optics}-1\right)+ L_{optics}\cdot\frac{hfB}{2} + L_{optics}\cdot P_{Load}\right] \tag{4}$$

The noise power within the parenthesis […] is the total noise power referred to the source. To determine the receiver noise referred to the source, we measure the Y-factor in the ordinary way by using two physical temperatures of the source, T_{Hot} and T_{Cold}. The Y-factor is measured as

$$Y = \frac{P_{total,in}^{Hot}}{P_{total,in}^{Cold}} \tag{5}$$

where

$$P_{total,in}^{Hot} = \left\{P_{Planck}(T_{Hot})+\frac{hfB}{2}\right\}+ P_{Planck}(T_{optics})\cdot\left(L_{optics}-1\right)+\left(L_{optics}-1\right)\cdot\frac{hfB}{2}+L_{optics}\cdot P_{Load} \tag{6}$$

and

$$P_{total,in}^{Cold} = \left\{P_{Planck}(T_{Cold})+\frac{hfB}{2}\right\}+ P_{Planck}(T_{optics})\cdot\left(L_{optics}-1\right)+\left(L_{optics}-1\right)\cdot\frac{hfB}{2}+L_{optics}\cdot P_{Load} \tag{7}$$

We obtain the ***receiver noise temperature*** as

$$T_{Rec} = \left\{\left(P_{Planck}(T_{optics})+\frac{hfB}{2}\right)\cdot\left(L_{optics}-1\right)+ L_{optics}\cdot P_{Load}\right\}\cdot\frac{1}{kB} = \frac{T_{CW}^{Hot}-Y\cdot T_{CW}^{Cold}}{Y-1} \tag{8}$$

If there is no attenuation in the coupling circuit, i. e. L_{optics}=1, the quantum noise contribution to the receiver noise temperature

$$P_{QN,Rec} = \left\{L_{optics}-1\right\}\cdot\frac{hfB}{2} \tag{9}$$

disappears. This term includes only the quantum noise (QN) contribution from the optics and not the QN from the source (hot and cold loads). In reference [4] it is argued that the QN should be referred to the source and not to the receiver. However, in this case when

optics losses are part of the receiver we need the QN contribution from the optics according to Eq. (9) in order to meet the requirement that the "receiver" should see a matched source emitting QN of *(hfB)/2*. So far we have also not considered the QN from the bolometer itself.

5. RF noise from the bolometer

Let us first try analyzing RF noise generated in the bolometer itself. The device in the hot-electron bolometer (HEB) mixer is essentially a temperature dependent resistance, which should add noise not only at the IF, which has normally been assumed, but also at the input frequency.

Since we assume that the RF frequency is well above the superconducting bandgap frequency in the entire bolometer, the bolometer should appear uniformly resistive to the RF power. However, the IF resistance change for a small change in RF absorption is not necessarily the same along the bridge. In Fig 3 an approximate model accounting for such a situation is described by two resistances (compare Merkel et al.[10]). R_P represents the passive RF resistance zones of the bolometer, and R_A the zones, which are actively converting RF power to IF power. We expect that we can use Eq. (1) to predict the amount of RF noise produced by any part of the bolometer. Only the active zones of the bolometer convert RF power (including noise power) to the IF, however, and we must therefore consider the active and the passive zones separately in our noise analysis. The passive zones are not only the central Hot-Spot zone, but also the zones between the hot-spot and the contacts that are superconducting and have essentially zero resistance at lower frequencies. The active zones are located at the transition from the central hotspot to the "low frequency" superconducting regions**.** Adding these two resistances together we get $R_P+R_A=R_N$, i. e. the normal resistance of the device.

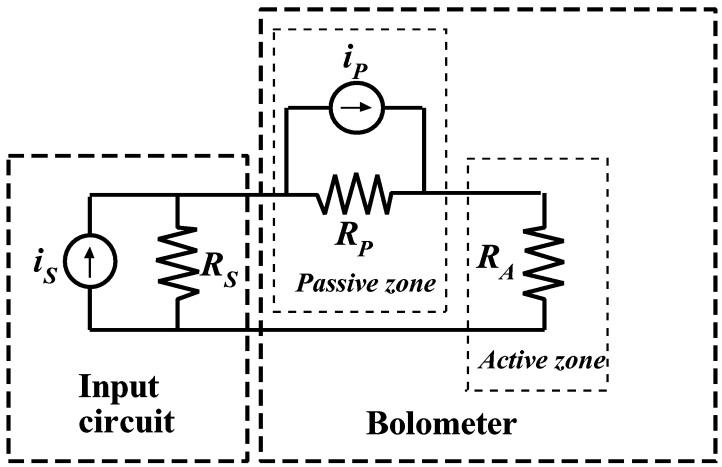

Fig 4 Equivalent circuit of a receiver including noise sources of R_P and R_S. Concerning the noise contribution from R_A, see the text below.

Referring to Fig. 4, noise currents are obtained as

$$\left(\frac{i_S}{2}\right)^2 \cdot R_S = P_{CW}(T_S) \qquad \left(\frac{i_P}{2}\right)^2 \cdot R_P = P_{CW}(T_P) \tag{10}$$

where $P_{CW}(T_S)$ etc. are the Callen-Welton noise powers according to Eq.(1). The thermal noise generated by R_A and dissipated in R_A is calculated by dividing R_A into a large number of series coupled elements ΔR_A ($\sum \Delta R_A = R_A$), which each contribute the same amount of noise current $\sqrt{\delta i_A^2}$ in the circuit viz.

$$\left(\frac{\delta i_A}{2}\right)^2 \cdot \Delta R_A = P_{CW}(T_A) \tag{11}$$

The currents i_S, i_P and all the $(\delta i_A)^2$ are completely uncorrelated. The noise current $i_{A,S}$ generated in the circuit by i_S and consequently also in the active part of the bolometer, R_A, is determined from

$$i_{A,S}^2 = i_S^2 \cdot \left(\frac{R_S}{R_S + R_P + R_A}\right)^2 \tag{12}$$

A similar noise current contribution is obtained from R_P as well as from R_A (the latter obtained as a summation of all contributions from ΔR_A). Each resistance in Fig. 4 contributes to the total noise current in the circuit and delivers noise power to R_A. Any ***signal*** from the antenna, which reaches the active zone of the bolometer, will mix with noise in the active zone. In particular, the local oscillator signal will mix with the RF-noise and produce noise power at the IF output.

We obtain the total noise power dissipated in R_A as

$$P_{tot,A} = \frac{4R_A}{\left(R_s + R_A + R_p\right)^2}\left[P_{CW}(T_s)\cdot R_s + P_{CW}(T_p)\cdot R_p + P_{CW}(T_A)\cdot R_A\right] \tag{13}$$

Considering that the bolometer mixer has two sidebands (Fig. 2) we notice that Eq. (13) applies to <u>each sideband separately</u>. It can be pointed out that Eq. (13) can also be derived using resistances in series with voltage noise sources $v^2 = 4R \cdot P_{CW}$, with the same result.

Let us investigate the case when the bolometer is matched at the RF, i. e. $R_P+R_A \equiv R_B=R_S$. We obtain

$$P_{tot,A} = P_{CW}(T_S)\cdot\frac{R_S R_A}{R_S^2} + P_{CW}(T_P)\cdot\frac{R_P R_A}{R_S^2} + P_{CW}(T_A)\cdot\frac{R_A R_A}{R_S^2} \tag{14}$$

which for the quantum noise part yields

$$P_{QN,A} = \left(\frac{R_S R_A}{R_S^2} + \frac{R_P R_A}{R_S^2} + \frac{R_A R_A}{R_S^2} \right) \cdot \frac{hfB}{2} = hfB \cdot \frac{R_A}{R_S} \qquad (15)$$

Referring this noise to the *bolometer input terminals*, we multiply (15) by R_S / R_A, and obtain

$$P_{QN,in} = hfB \qquad (16)$$

for each sideband.

Notice that the quantum noise contribution according to Eq. (16) is *hfB* and not (*hfB*)/2. The reason is that the bolometer resistance(s) contribute with (*hfB*)/2 and the source another *(hfB)*/2.

We conclude that in this model the bolometer itself contributes to the receiver RF-noise with

$$P_{CW}(T_c) \approx P_{Planck}(T_c) + (hfB)/2 \approx (hfB)/2 \qquad (17)$$

in one sideband. In (17) we have introduced the physical temperature of the bolometer, which is close to T_c, the critical temperature of the superconductor. At THz frequencies and T_c=10K $P_{Planck}(T_c)$ can be neglected.

It is reasonable to assume that there is no correlation of the noise in the two sidebands what so ever. Hence the noise to be downconverted from RF to IF originates from the two sidebands and thus is twice the noise we have considered so far. In this **matched case** the total QN at the bolometer input is *2hfB*. This noise is to be added to the noise of the mixer, i. e. at the input of the bolometer we have,

$$T_{Syst}^{SSB} \approx \frac{2hf}{k} + L_{conv.loss}^{SSB} \cdot \left(T_{mixer}^{out} + T_{IF} \right) \qquad (18)$$

where $L_{conv\,loss}^{SSB}$ is the internal SSB conversion loss of the bolometer, i. e. the loss counted from the bolometer input terminals to the IF output. $T_{mxer\,(mixer)}^{out}$ represents the noise output power from the mixer, which is due to Johnson noise and thermal fluctuation noise, and originates in the bolometer itself. Further, T_{IF} is the noise temperature of the IF amplifier.

Since half of *2hf/k* comes from the bolometer itself and the other half from the source, we have

$$T_{Rec}^{SSB} = \frac{hf}{k} + L_{conv.loss}^{SSB} \cdot \left(T_{mixer}^{out} + T_{IF} \right) \qquad (19)$$

The DSB noise temperature becomes half of the SSB noise temperature.

Adding the influence of the optics attenuation, which is assumed the same for both sidebands, and referring the noise temperature to the input of the optics, we get

$$T_{Rec}^{DSB} = L_{optics} \cdot \frac{1}{2} \left(\frac{hf}{k} + L_{conv.loss}^{SSB} \cdot \left(T_{mixer}^{out} + T_{IF} \right) \right) + \left(L_{optics} - 1 \right) \cdot \left(T_{optics}^{Planck} + \frac{hf}{2k} \right) \qquad (20)$$

Since each sideband produces the same amount of noise power, the double sideband noise temperature becomes half the single sideband noise temperature. The SSB noise

temperature is again twice the DSB noise temperature. Adding the two quantum noise terms, we can write (20) as

$$T_{Rec}^{DSB} = \left(L_{optics} - 1\right) \cdot \left(T_{optics}^{Planck}\right) + \left(L_{optics} - \frac{1}{2}\right) \cdot \left(\frac{hf}{k}\right) + L_{optics} \cdot \frac{1}{2}\left(L_{conv.loss}^{SSB} \cdot \left(T_{mixer}^{out} + T_{IF}\right)\right) \quad (21)$$

6. Comparison with experimental noise measurements

In a typical system, some optical losses are at roughly room temperature ("L_{optics}^{300K}"), and some at 4 K ("L_{optics}^{4K}"). Then we find,

$$T_{Rec}^{DSB} = \left(L_{optics}^{300K} - 1\right) T_{Planck}^{300K} + \left(L_{optics}^{300K} L_{optics}^{4K} - \frac{1}{2}\right)\frac{hf}{k} + \left(T_{mixer}^{out} + T_{IF}\right)\frac{L_{conv.loss}^{SSB}}{2} \cdot L_{optics}^{300K} L_{optics}^{4K} = \quad (22)$$
$$= T_{optics}^{300K} + T_{QN} + T_{Rec.mixer}$$

T_{Planck}^{300K} is the "Planck Temperature" of the optics. At low frequencies, this is simply the physical temperature (300 K or 295 K), but at THz frequencies we use the Planck formula to find the actual "Planck noise power" and equate that to $kT_{Planck}^{300K}B$. We can neglect the Planck Temperature for components at 4K.

In an experiment performed by the Chalmers group at 1.6 THz [11], it was estimated that L_{optics}^{300K} due to a mylar beam splitter and a polyethylene window was 1.1. Losses at 4 K due to a Zitex thermal filter, the silicon lens (with a parylene matching layer), and the antenna were estimated to be 1.33. The total optical loss was thus 1.44. For this mixer the measured T_{Rec}^{DSB} was 800 K . It was also estimated that T_{mixer}^{out} = 54 K, T_{IF} = 6 K, and $L_{Conv.loss}^{SSB}$ = 12.4 dB, by calibrating the IF system through further measurements in which the HEB device was brought to the superconducting state (a standard method). The bolometer was close to being matched to the antenna impedance. Here, $L_{Conv.loss}^{SSB}$ includes all loss effects (SSB) in the HEB from the THz antenna terminals to the IF terminals. We can now estimate all three terms in Eq. (22)

$$T_{Rec}^{DSB} = 40 \text{ K} + 70 \text{ K} + 690 \text{ K} = 800 \text{ K} \quad (23)$$

We then see that even at such a moderately high frequency as 1.6 THz, about 14 % of the receiver noise temperature is due to the optical loss at 300 K (T_{optics}^{300K}), plus the quantum noise (T_{QN}). The part of the receiver noise temperature traceable to the QN is about 9 % of the total receiver noise temperature. Note that without this more careful analysis of the QN term, a typical statement would have been "the quantum noise limited noise temperature at 1.6 THz is $hf/2k$ = 38 K, or about 5 % of the total receiver noise temperature".

The fraction of the receiver noise temperature due to QN is expected to become greater as the frequency is increased, as we will show below. In estimating the receiver noise temperature at higher frequencies, we make the following assumptions:

1) The optical losses increase linearly with frequency
2) The intrinsic conversion loss does not depend on the frequency

3) The mixer output noise temperature does not depend on the frequency

Assumption 1) agrees with estimates in [9] and [10]. Assumption 2) is reasonable based on our present knowledge of HEB models, but has not been carefully tested in experiments. It can be tested through direct conversion loss measurements, which we are planning to perform with two laser sources and/or a laser LO and a sideband generator. Assumption 3) has been verified in at least a few experiments [7,11] and appears to be true for typical NbN HEB mixers.

Figure 5 now shows calculations of T_{Rec}^{DSB} for a matched HEB mixer as a function of frequency up to 10 THz, based on an extrapolation of our measured data at 1.6 THz, and using the above three assumptions. The calculated curve is reasonably consistent with other measured data on the same device at 2.52 THz (T_{Rec}^{DSB} = 1,500 K [11]). The top curve is the total receiver noise temperature, the next one down the QN term (term T_{QN} in Eq. (22), and the smallest term the noise due to optical losses at room temperature (term T_{optics}^{300K} in Eq. (22)). **Note that the QN term rises much faster with frequency than the room temperature optics loss term, and that it approaches 50 % of the total receiver noise temperature.**

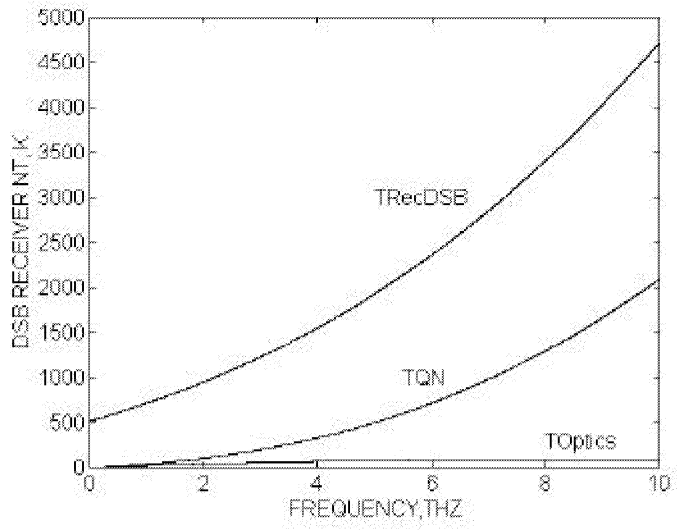

Fig. 5. DSB receiver noise temperature and the contributions from optics and quantum noise.

The question naturally arises: Can we distinguish the two main terms T_{QN} and $T_{Rec,mixer}$ through experimental measurements? There is a fundamental difficulty with doing this due to the fact that both terms depend on the optical losses in almost the same way; the minor difference being that a factor of 1/2 is subtracted from the optical losses in the QN case. It would be important to attempt to measure $L_{conv\,loss}^{SSB}$ at different LO frequencies independently, in order to determine the relative size of T_{QN} and $T_{Rec,mixer}$. The RF power

from a sideband or laser source *actually absorbed in the bolometer* can be measured by the isothermal method, and together with a measurement of the IF power will yield the conversion loss based on *absorbed power*. There is a difference between the absorbed RF power in the bolometer, and the power delivered to the bolometer terminals, however, as is clear from the earlier discussion and the equivalent circuit we have assumed (see Figure 4). The above measurement therefore does not yield $L^{SSB}_{conv\,loss}$ as used in our receiver noise temperature calculations. Measuring the conversion loss based on absorbed power at different LO frequencies would still allow us to test the important assumption 2) above, if one assumes that R_P/R_A does not vary with frequency. An *absolute* conversion loss measurement requires calibrating the RF power which reaches the bolometer terminals. This test is more difficult to perform accurately, but should also be attempted. It will also yield data on the frequency-dependence of the optical losses.

7. Discussion and Conclusion

We have analyzed the contribution of quantum noise to the system and receiver noise temperatures of THz HEB mixer receivers. The basic model we propose, and the corner stone of our analysis, is that HEB devices appear *uniformly resistive* to the THz radiation, once the radiation frequency is above the superconducting bandgap frequency. It then appears that the Callen-Welton version of the fluctuation dissipation theorem [1] is sufficient to describe the quantum noise aspects of the bolometer. The quantum noise in the bolometer resulting from the input source (the "vacuum fluctuations"), and the bolometer itself, is down-converted to the IF. No further noise sources are assumed on the RF side of the bolometer, or for the actual down-conversion process. These assumptions appear similar to those made by Kerr et al. [3]. Specifically, these authors discuss quantum noise in SIS mixers, with contributions from (1) the input source (R_S in our paper), and (2) the quantized shot noise in the SIS junction, which is down-converted to the IF. No further quantum noise due to the down-conversion process is assumed. Since our present understanding of PHEB models has led to the conclusion that the bolometer has a substantial *passive zone*, as well as an *active, frequency-converting zone*, we have analyzed how noise contributions from these different zones contribute to the total noise. We find that the division of the bolometer into one active and one passive part does not affect the contributions of Planck and quantum noise from the bolometer; rather, it is the total resistance R_B that matters. Of course, the ratio R_A/R_B affects the conversion loss $L^{SSB}_{conv\,loss}$ and therefore the receiver noise contributions related to $T^{out}{}_{mixer}$ and T_{IF} [10]. We have also used the Callen-Welton theorem to analyze the contributions to the receiver noise temperature from the optical components preceding a quasi-optically coupled bolometer. The overall conclusion is that, given the present level of performance of THz HEB receivers, we predict that close to 50 % of the total receiver noise temperature may be traced to quantum noise phenomena, for frequencies in the 5-10 THz range. This represents a larger fraction of the total noise than has previously been claimed.

The first two terms in (22) also have an effect on receiver noise bandwidth measurements, an estimated increase of about 17 % at a frequency of 5 THz, and an increase of 30 % at 10 THz, compared with the lowest THz frequencies.

Quantum noise analyses of receivers have either been carried out for a general "linear amplifier" [2] or for specific types of receivers, such as SIS mixers [3,4,5], maser and laser amplifiers [12], or photo-diode mixers [13,14]. Our analysis is of yet another specific type of receiver, and the question again arises: do the results obtained in this specific case violate limitations derived for linear amplifiers in Caves' extended sense, which also includes mixers. Caves concludes that a linear amplifier amplifies the input $hfB/2$ QN from the source and adds another contribution $hfB/2$ referred to its input, leaving us with a total of hfB as the *system* quantum noise limit. The other papers mentioned above agree with this conclusion regarding the minimum system noise. In the matched bolometer case, we predict 2(hfB) as the QN limit. The extra factor of two is due to the fact that both sidebands contribute to the noise independently. We can draw the conclusion that the *general* system quantum noise limit can be interpreted to be *hfB per independent channel*. The specific cases of the (two-channel) SIS mixer and the photo-diode mixer yield the lower limit of 1(hfB) due to cancellation of the shot-noise contributions from the two sidebands (i.e. the two channels are *not independent* in this case). We propose that it may be possible to design an HEB mixer with the same lower QN limit of 1(hfB) by configuring it as an image rejecting mixer, which allows only one sideband to convert RF to the IF. The analysis of QN in an image-rejection SIS mixer by Kerr et al. [3] also finds a minimum total QN at the input of 1(hfB).

It is possible that some further QN source has been overlooked in the model used in this paper. A system noise less than 1(hfB) seems to result when analyzing an *unmatched* bolometer in an image reject mixer in the same way as suggested in this paper. This (potential) disagreement with the accepted general limit for linear amplifiers (and mixers) of 1(hfB) due to Caves mainly represents a theoretical point unless the performance of HEB mixers in terms of intrinsic mixer noise improves very substantially, however. We may also note that all other receivers analyzed in terms of QN so far have been *matched to the input source.* If the down-conversion process is also required to produce hfB/2 of QN, then the above (potential) disagreement with Caves disappears. If an additional noise contribution due to the down-conversion process exists, our results *underestimate* the total QN. This may therefore be a hypothesis which can be tested experimentally more easily, since it increases the coefficient in front of the QN term. Further investigation will be necessary in order to prove or disprove this and other assumptions we have made in our analysis.

8. Acknowledgements

We would like to acknowledge Jonas Zmuidzinas and Anthony Kerr for fruitful discussions during the symposium. One of us (SY) would like to acknowledge support from NASA contract NAS1-01058 with the NASA Langley Research Center for this work.

9. References

[1] H. B. Callen and T. A. Welton, "Irreversibility and Generalized Noise", Phys. Rev. vol. **83**, no. 1, pp. 34-40, July 1951.

[2] C. M. Caves, "Quantum Limits on Noise in Linear Amplifiers", Phys. Rev. D, vol. **26**, No. 8, pp. 1817-1839, October 1982.

[3] A.R. Kerr, M. J. Feldman, and S. –K. Pan, "Receiver Noise Temperature, the Quantum Noise Limit, and the Role of the Zero-Point Fluctuations," in Proc. 8th Int. Nat. Symp. Space Terahertz Technology, March 25-27, 1997, pp. 101-111. Available: URL: http://colobus.aoc.nrao.edu/memos as MMA Memo 161.

[4] A. R. Kerr, "Suggestion for Revised Definition of Noise Quantities, Including Quantum Noise", IEEE Transactions on Microwave Theory and Techniques, vol. **47**, No. 3, pp. 325-329, March 1999.

[5] J. R. Tucker and M. J. Feldman, Quantum Detection at Millimeter Wavelengths," Rev. Modern Physics, vol. **57**, no. 4, pp. 1055-1153, Oct. 1985.

[6] A.D. Semenov et al., "Design and Performance of the Lattice Cooled Hot-Electron Terahertz Mixer," J.Appl.Phys. vol. **88**, p.6758, 2000.

[7] Gerecht et al., "NbN Hot Electron Bolometric Mixers - A New Technology for Low-Noise THz Receivers," IEEE Trans, Microw. Theory Techniques, vol. **47**, pp. 2519-2527, December 1999.

[8] B.S. Karasik and A.I. Elantiev, "Noise Temperature Limit of a Superconducting Hot-Electron Bolometer Mixer," Appl.Phys.Lett., vol. **68**, pp. 853-855, 1996.

[9] S.Yngvesson and E. Kollberg, "Optimum Receiver Noise Temperature for NbN HEB Mixers According to the Standard Model," 10th Intern. Symp. Space THz Technol, Charlottesville, VA, March 1999, pp. 566-582.

[10] H.F. Merkel, P. Khosropanah, K.S. Yngvesson, S. Cherednichenko, M. Kroug, A. Adam, and E.L. Kollberg, "An Active Zone Small Signal Model for Hot Electron Bolometric Mixers," 12th Intern. Symp. Space THz Technol, San Diego, CA, Febr. 2001, pp. 67-74.

[11] S. Cherednichenko, et al., "1.6 THz Heterodyne Receiver for the Far Infrared Space Telescope", accepted for publication in Physica C, 2002.

[12] H.A. Haus, "Noise Figure Definition Valid From RF to Optical Frequencies," IEEE J. Selected Topics in Qu. Electronics, vol. **6,** pp.240-247, 2000.

[13] B.M. Oliver, "Thermal and Quantum Noise," Proc. IEEE, vol. **53**, pp. 438-454 1965.

[14] M.J. Wengler and D.P. Woody, "Quantum Noise in Heterodyne Detection," IEEE J. Qu.Electronics, vol. **QE-23**, 613-622,1987.

A BROADBAND TERAHERTZ HETERODYNE RECEIVER WITH AN NbN HEB MIXER.

S. Cherednichenko, M. Kroug *, P. Khosropanah, A. Adam, H. Merkel, E. Kollberg

Department of Microwave Electronics, Chalmers University of Technology, Gothenburg, S-412 96, Sweden

D. Loudkov, B. Voronov, G. Gol'tsman

Department of Physics, Moscow State Pedagogical University, Moscow, 119435, Russia

H. Richter, H.-W. Hübers.

Institute for Space Sensor Technology DLR, Berlin, Germany

* Delft University of Technology, DIMES, Delft, The Netherlands

We present a broadband and low noise heterodyne receiver for 1.4-1.7 THz designed for the Hershel Space Observatory. A phonon- cooled NbN HEB mixer was integrated with a normal metal double- slot antenna and an elliptical silicon lens. DSB receiver noise temperature Tr was measured from 1 GHz through 8GHz intermediate frequency band with 50 MHz instantaneous bandwidth. At 4.2 K bath temperature and at 1.6 THz LO frequency Tr is 800 K with the receiver noise bandwidth of 5 GHz. While at 2 K bath temperature Tr was as low as 700 K. At 0.6 THz and 1.1 THz a spiral antenna integrated NbN HEB mixer showed the receiver noise temperature 500 K and 800 K, though no antireflection coating was used in this case. Tr of 1100 K was achieved at 2.5 THz while the receiver noise bandwidth was 4 GHz.

1. Introduction

Extension of radio astronomical observations above 1 THz has happened during the last years. It was motivated by the big progress in the areas of both mixers and local oscillators. A number of ground based, such as TREND (1.5 THz, South Pole), air- and space born (SOFIA, Herschel) observatories are now under construction. For these applications the main orientation is made on hot electron bolometer (HEB) mixers [1, 2]. An operation of these types of mixers up to 5 THz was experimentally shown in references [3]. Both quasi- optically, QO, (planar antenna integrated) and wave- guide, WG, (feed horn with a fixed tuned or tunable mixer block) coupled receivers designs were used by different groups [4]. Due to the relative technological simplicity of the lithographical fabrication technique, QO HEB receivers have been quoted much more often in the literature. However, certain advantages are associated with WG type of receivers. The radiation mode purity and probably (however, no experimental evidence has been obtained, to our knowledge) beam pattern quality are among of them.

Two types of HEB mixers are distinguished. First, phonon-cooled HEB mixers (NbN and NbTiN superconducting films based), where the hot electrons are cooled via inelastic scattering by phonons and consecutive hot phonons escape into the substrate. For thin NbN films the electron- phonon scattering time was measured to be about 10 ps at 10 K and the temperature dependence $\tau_{e\text{-}ph} \propto \theta^{-1.6}$ was observed [5]. The escape time depends on film thickness (d) and acoustic transparency (α) of the film-substrate interface, $\tau_{esc} \propto d/\alpha$. The detailed investigation of the NbN HEB mixers gain bandwidth for the wide range of NbN film thickness has been done in [6]. $\tau_{esc}=12d$ was estimated for silicon and sapphire substrates, where τ_{esc} is in ps and d is nm. While $\tau_{esc}=6d$ was found for MgO substrates [7]. For 3.5 nm thick NbN film the gain bandwidth of 3.5-4.5 GHz was found in the minimum mixer noise temperature bias point. Extension of the gain bandwidth up to 7-9 GHz has been observed for NbN HEB mixers at higher bias voltages, however the noise temperature increases in this case. Gain bandwidth of 2-2.5 GHz was measured for NbN HEB mixers on quartz substrate, which are used for WG receivers. The choice of quartz is made due to the relative small dielectric constant and ability to fabricate small and thin mixer chips for integration into terahertz mixer blocks. Recently, the gain bandwidth of NbN HEB mixers on quartz was extended up to 3.2 GHz by application a buffer layer of MgO [8].

In short Nb bridges (less then 0.5 μm long) the electron out- diffusion from the bolometer into the contact pads is the dominant cooling process for hot electrons. The electron diffusion time is $\tau_{diff} \propto \sqrt{L}$. For 0.1 μm long bolometer the mixer gain bandwidth as wide as 9 GHz was reported in reference [9]. Effect of the bias voltage on the gain bandwidth, similar to the NbN HEB mixers, has been reported in reference [10].

In this paper we report a quasioptical phonon- cooled NbN HEB mixer on silicon substrates. The main purpose is the development of a low noise mixer for the Herschel Space Observatory (Band 6L, 1.4-1.7 THz). We describe the technology used for fabrication of the HEB mixers, receiver noise temperature measurements in the 1-8 GHz IF band for LO frequencies 0.6 THz, 1.1 THz, 1.6 THz and 2.5 THz. FTS measurements of a double slot antenna integrated NbN HEB mixer is also presented.

2. Sample description and set- up.

NbN film was deposited on high resistive silicon (≥3000 Ohm, 100- crystal orientation) substrates by dc reactive magnetron sputtering [6]. The substrate temperature during deposition was 850°C and the background pressure was $3x10^{-6}$ mbar. The Ar pressure was $9x10^{-3}$mbar and N pressure was $2x10^{-4}$mbar. The discharge current was 300 mA what provided the deposition rate of 0.45 nm/sec. For 3.5 nm thick films the sheet resistance was 400-500 Ohm/sqr, Tc=8.5-10 K. The gold antenna structure (either double- slot or logarithmic spiral) was made in 4 steps of e-beam lithography plus lift- off. The NbN film etching was done by the Ar ion- milling (400 V, 200 mA). The double- slot antenna integrated HEB mixer is shown in Fig.1. The bolometer size was 4 μm wide and 0.4 μm long.

For the mixer noise characterization, the standard Y-factor technique was used. The mixer was attached to the back side of 12 mm elliptical silicon lens. The

mixer block, bias- T, isolator and IF amplifier were mounted into a LHe vacuum cryostat. The cryostat with 1-2 GHz IF chain has a Zitex G108 IR filter and HDPE (1mm thick) window. The cryostat with 4-8 GHz IF chain has the Zitex G108 IR filter and Teflon (1mm thick) window. A tunable from 1 GHz to 10 GHz Yig- filter with 30-50 MHz band was used after the room amplification stage. 12 μm Mylar beam splitter was 20 cm away from the cryostat window. The measurements are done at room conditions.

At 0.6 GHz and 1.1 THz two BWOs were used as LO sources, while at 1.6 THz and 2.5 THz an optically pumped FIR laser was applied.

The optimal LO power was dependent on the critical current and was at the level of 150-250 nW. The bias voltage was set to 1 mV, where the maximum Y factor was observed.

For the receiver noise temperature evaluation we used Callen- Wellton formula of the noise power radiated by a black body. The physical temperature of the hot and cold loads were 295 K and 77 K (LN).

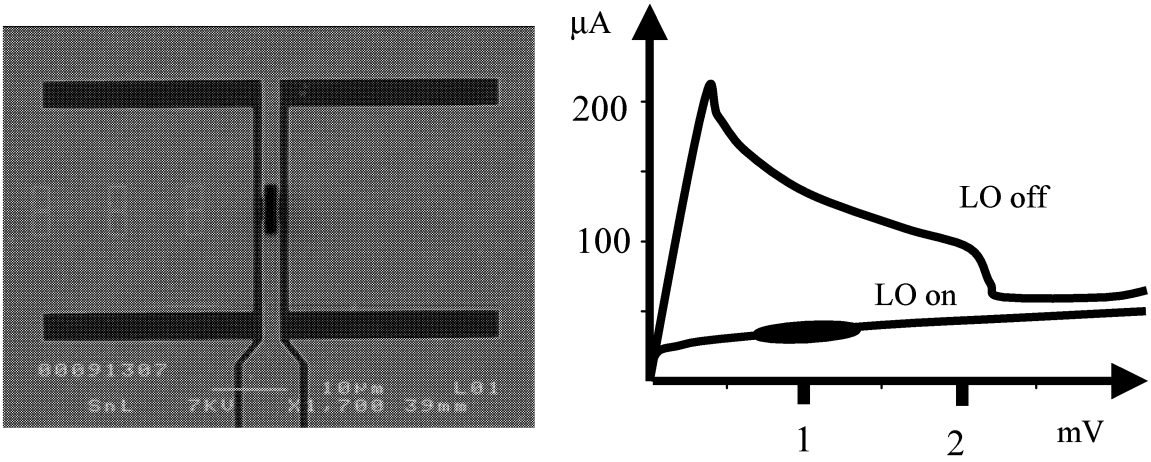

Fig.2. Typical IV- curves of a 4x0.4mm^2 NbN HEB mixer. The marked area points the minimum noise temperature bias points.

The double slot antenna (DSA) geometry was: the slot length is $0.3\lambda_0$, the slot separation is $0.17\lambda_0$, and the slot width is $0.02\lambda_0$, where λ_0 is the free space wave length of the middle of the antenna band. The coupling of the slots to the bolometer occurs via a CPW line (4 μm center conductor with 2 μm slots). RF block filter in the IF line contains 3 high impedance and 3 low impedance 1/4 λ_0 sections (not shown in the picture).

Two typical IV- curves at 4.2 K, one without and one with LO power, are shown in Fig.2. The optimal bias point (marked in the figure) was chosen in terms of the lowest mixer noise temperature and stability of the mixer output noise. The typical bias voltage is about 1 mV for all 4 μm wide and 0.4 μm long bolometers. The bias current in the optimal point depends on the mixer critical current (LO is off). For the critical current in the limits 190 μA to 400 μA the optimal bias current is from 30 μA to 50 μA.

3. 1.6 THz receiver.

In this chapter we report on the NbN HEB mixer sensitivity at 1.6 THz LO frequency, which is roughly in the middle of the Band 6L of the heterodyne instrument of the Herschel Space Observatory. The choice of this frequency for the test was made because of the availability of the strong laser generation line (LO source). Tunable LO sources in this frequency band are still under investigation [11, 12].

A compact (envelope of 32x32x45mm^3), light- weight (<75 g) quasioptical mixer block was designed (see Fig.3) , which contains a low noise filter circuitry, ESD protection, IF readout, DC bias input.

However, the results presented here were obtained still with a prototype mixer block, described in the Chapter 2.

An investigation of the coupling efficiency to double slot antenna integrated Nb diffusion cooled HEB mixers has been reported in [13]. A discrepancy between the center frequency calculated from the quasi-static approach and the measured one was observed above 1 THz. The discrepancy increased towards higher frequencies.

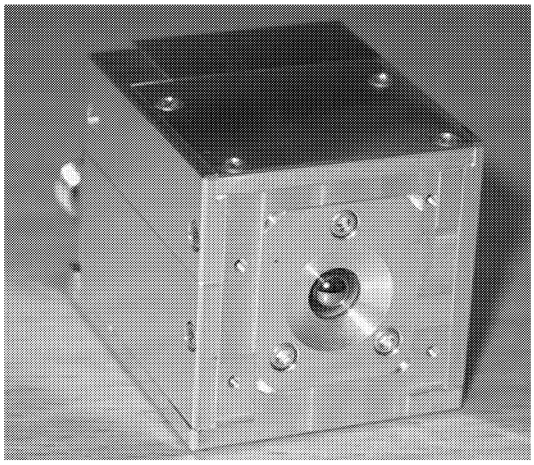

Fig.3. 1.4-1.7 THz NbN HEB mixer for the Herschel Space Observatory. The complete structure is made of aluminum. 5 mm Si lens is visible on the front side.

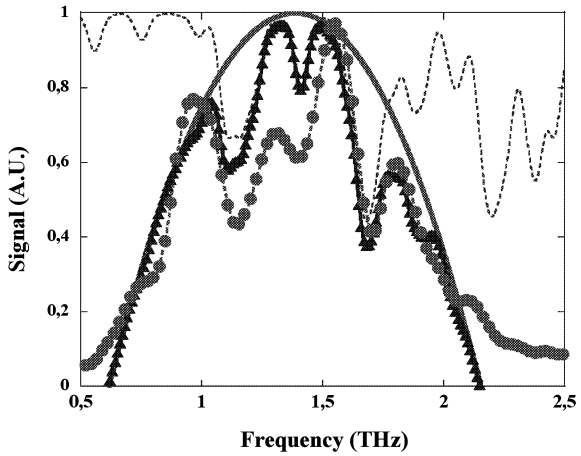

Fig.4. Direct response of 1.6 THz double-slot antenna integrated NbN HEB mixer

However, there has not been any data reported about NbN HEB coupling to DSAs. In Fig.4 (circles) we present a direct response of an NbN HEB mixer obtained with a Fourier Transform Spectrometer (FTS). Details of the measurements are presented in [14]. The antenna geometry used in the experiment is described in Chapter 2. Impedance of each slot in the second resonance is 45 Ohm [15] and is transformed to 55+7j Ohm via the CPW line down to the bolometer, positioned in the middle between the slots. The slots are connected in series with the bolometer. Therefore, the antenna embedding impedance at the bolometer terminals is 114+14j Ohm. Since the bolometer impedance is real ($\nu > 2\Delta/h$, where Δ is the superconducting energy of the NbN film under the strong LO radiation) and is about 100 Ohm, the efficient radiation

coupling occurs in a wide frequency range. Since the FTS measurements were carried out in the air, the antenna response is strongly affected by the water vapor absorption. Although vacuum measurements are necessary for correct antenna bandwidth estimations, certain conclusions can be made from the existing data. First, the atmosphere transmission of 30 cm path length have been calculated (22 °C, 30 % humidity) with 70 GHz resolution (Fig.4, dashed line). Assuming the antenna response spectrum to be parabolic (solid line), centered at 1.4 THz, and interpolating it with the atmosphere transmission spectra, we obtain a good correspondence between the resulted curve (triangles) and the measured one (circles). Then, 3 dB full bandwidth can be estimated to be 1.1 THz, i.e. 80 %. At 1.3 THz the measured response was not possible to approximate with a simple parabolic response of the antenna. A possible reason of this distortion can be a more complicated HEB response spectra then a simple parabola. For example, a secondary response peak at around 1 THz with a more sharp peak around 1.5 THz. More investigation is necessary to clarify this issue.

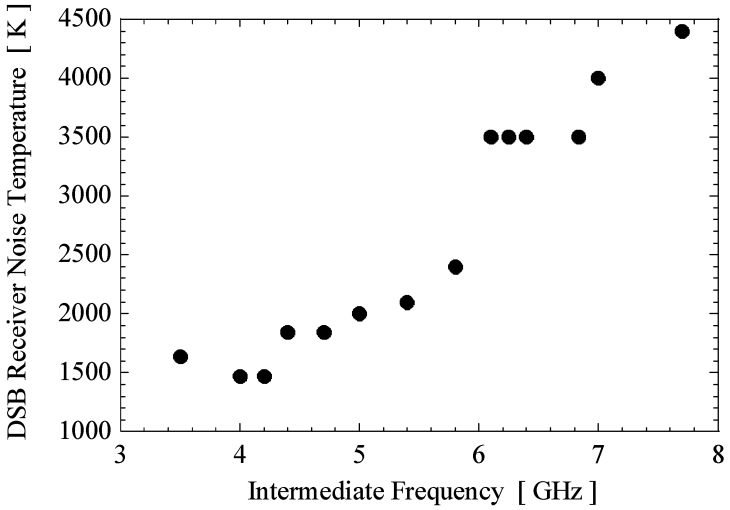

Fig.5 NbN HEB receiver DSB noise temperature at 1.6 THz LO frequency, from 3 GHz to 8 GHz.

The DSB receiver noise temperature was measured in the 3-8 GHz IF band. The lowest Tr value in this band is 1450 K at 4.2 K bath temperature. 28 μm thick Parylene was deposited onto the silicon lens as an antireflection coating [16]. The rise of the noise temperature from 4 GHz to 8 GHz is caused by the decrease of the HEB mixer gain. It has been shown at 600 GHz LO frequency, that the 3 dB gain roll- off frequency for HEB mixers made of 3.5 nm NbN film on silicon substrate [6] is 3.5 GHz. It means, that at 4 GHz there is 3 dB loss more than at 1.5 GHz, where the noise temperature of 700 K we have reported in the reference [16].

The HEB receiver noise bandwidth f_{oN} , which is defined as the intermediate frequency where the receiver noise temperature increases twice from its value at low IF, can be estimated as $f_{oN} \approx f_0 \cdot \sqrt{\frac{T_{out} + T_{IF}}{T_J + T_{IF}}}$ [17], where $T_{out}=T_{fl}+T_J$. T_{fl} and T_J are the

electron temperature fluctuation noise and Johnson noise contributions to the mixer output noise, f_0 is 3 dB gain drop frequency, T_{IF} is the noise temperature of the IF chain. T_{IF} is about 5-6 K. Using the Nyquist theorem one can show that T_J approximately equals the electron temperature, which is close to T_c [17]. From the measured data for T_{out} (about 60 K [18]) one ends up with the ratio $f_{oN}/f_o \approx 2$ for these HEB mixers. Therefore, the receiver noise temperature of 1500 K shall be expected at around 7 GHz. However, from Fig.5 one can see that at 7GHz Tr is 3500 K, i.e. at least twice higher of the expected value.

As it was described in Chapter 2, the cryostat window in the 3-8 GHz receiver cryostat was Teflon, which is more lossy in the terahertz range than the HDPE window, used in the 1-2 GHz receiver. However, about 2000 K of the rise of the noise temperature (3500 K- 1500 K) can be explained only with L additional loss at 300 K physical temperature: 300x(L-1)+ 1500 K x L=3500 K, i.e. L= 2.1 (3 dB) . 3 dB is a significant increase of the input loss to be attributed just to the Teflon window.

Thus, does the HEB mixer gain bandwidth decrease as LO frequency growths? The answer can be given only by direct gain bandwidth measurements at terahertz frequencies.

4. Spiral antenna integrated NbN HEB receiver

A direct comparison of the NbN HEB mixer performance in wide both RF and IF bands was done with a mixer, integrated with a logarithmic spiral antenna [19] on silicon substrate. The SEM image of the sample is given in Fig. 6. RF bandwidth of the spiral antennas in the terahertz range has been discussed in [20]. The upper and the lower frequencies are determined by the inner and the outer cut- off radii of the spiral. In our case it is about 10 μm and 100 μm correspondingly.

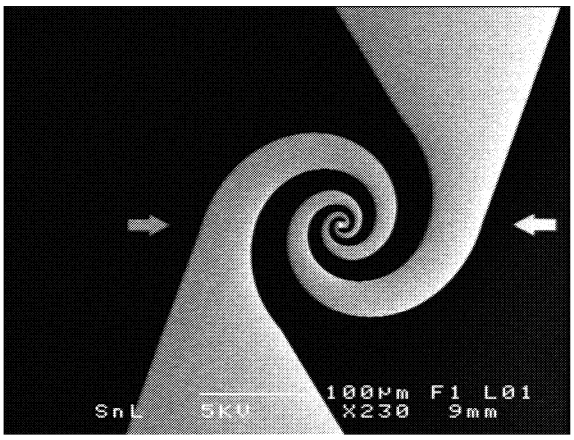

Fig. 6 SEM image of a logarithmic spiral antenna integrated HEB mixer on silicon. Dark area is the silicon surface, while the gray area is the gold antenna structure.

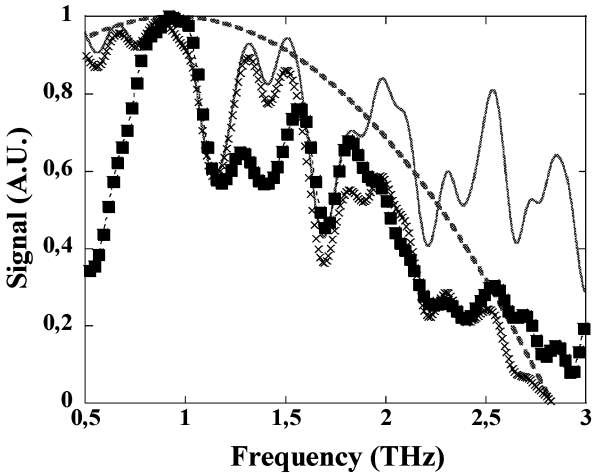

Fig.7. Direct response of the spiral antenna integrated NbN HEB mixer (squares), calculated transmission of the atmosphere between the FTS and the cryostat (solid), simplified parabolic spiral antenna response (dashed) and the interpolation of the parabola with the atmosphere transmission curve (crosses).

Although spiral antennas have been extensively used with HEB mixers during last years, to our knowledge there has been no experimental investigation done of their input bandwidth. In Fig. 7 we present a direct response of the spiral antenna integrated NbN HEB mixer from 0.5 THz to 3 THz obtained with a Fourier Transform Spectrometer (FTS). As for the double slot antenna FTS measurements, the response spectrum in Fig. 7 is modified by the water vapor absorption. Approximating the spiral antenna response by a simple parabola (Fig.7, dashed line) (the same as we did in Chapter 3), and by interpolating it with the atmosphere transmission curve, we obtain a curve (Fig.7, crosses) which is in a good agreement with the measured one (squares) from 1 THz up to 2.5 THz. Sharp roll- off of the response below 1 THz can be associated with the lower cut-off of the spiral antenna band. At higher frequencies the response decays slowly, what can be rather determined by the antenna conductive losses and the large dispersion of the terahertz waves in the spiral antenna structure. The higher frequency cut- off, caused by the spiral discontinuity in the antenna apex, seems to occur at frequencies above 3 THz, where the detected signal was already below the noise level of the measurement system. Regardless of the air loss effect, the efficiency of the presented antenna is quite low above 2 THz. We continue the planar antennas investigation in the terahertz range and the result will soon presented.

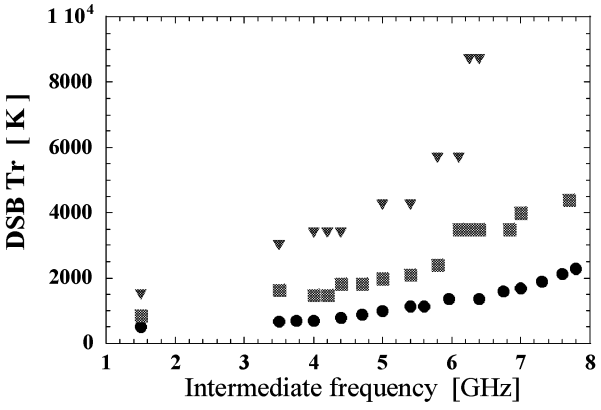

Fig.8 DSB receiver noise temperature of the NbN HEB mixer at 0.6 THz (circles), 1.62 THz (squares) and 2.5 THz (triangles) LO frequencies. Bath temperature is 4.2 K).

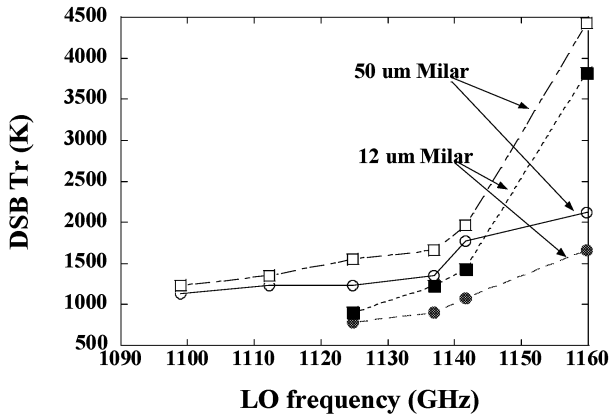

Fig.9 DSB receiver noise temperature at 1.5 GHz IF with 12 μm (filled) and 50 μm (open) Mylar beam splitters. Circles correspond to the 30 cm optical path length, while squares correspond to the 60 cm optical path length.

Fig. 8 shows the DSB receiver noise temperature for 4x0.4 μm size HEB mixer integrated with the spiral antenna in the intermediate frequency band from 1 GHz to 8 GHz. The minimum Tr values were 500 K, 800 K and 1500 K at 0.6 THz, 1.62 THz and 2.5 THz LO frequencies. The measurements were done at 4.2 K bath temperature. For the measurements at 1.6 THz and 2.5 THz silicon lenses were coated with 28 μm and 19 μm thick Parylene layers correspondingly. The noise bandwidth can be estimated from Fig.8 as 5 GHz at 0.6THz and 1.6 THz, and 4 GHz at 2.5 THz.

The frontier of the SIS and HEB heterodyne receivers falls to roughly 1.1-1.2 THz. This is the highest frequency, where an SIS receiver operation has been reported [21]. Nb- SIS mixers with Al tuning circuit has shown 840 K of the DSB noise temperature at 1.042 THz. Recently, the noise temperature of 380 K at 1.13 THz was achieved [22] for Nb/AlN/NbTiN SIS mixers with an all-Au tuning circuit. Therefore, it was interesting to compare directly two existing technologies. We used the same HEB mixer (with the spiral antenna), that we discussed in this Chapter, to perform noise measurements at 1.1 THz. The lowest DSB noise temperature in this range was 780 K (Fig.9, filled circles). We should note, that Si lens did not have any antireflection coating during these measurements, what introduced about 1 dB reflection loss on the lens surface. A sharp increase of the noise temperature towards 1.16 THz is caused by the water absorption line, since the measurements were done in the air. With a withdrawal of the hot/cold load 30cm further from the cryostat, the influence of the water absorption increases drastically. Below 1.125 THz the output power of the LO was not enough to pump the mixer to the optimal point with a 12 μm thick Mylar beam splitter. Therefore, we exchange it for a 50 μm thick Mylar beam splitter. While the receiver noise temperature was higher in this case, it was still lowering down to 1.10 THz (open circles). Since there is already another water line at 1.1 THz which we do not observe in Fig. 9, we conclude that we have an error in the LO frequency estimation. The wavelength- meter, used for the frequency estimation, seemed to have about 60 GHz up- shift and, in fact, the frequencies in the Fig.9 might be about 60 GHz higher of the actual radiation frequency. Receiver noise temperatures with the 50 μm thick Mylar beam splitter and 60 cm of the optical path length are shown with the open squares.

5. Conclusion.

Quasioptical NbN HEB mixers, discussed in this paper, showed very good performance from subMM to terahertz frequencies. In Fig. 10 we summarize the obtained DSB receiver noise temperatures quoted in the present paper as a function of the LO frequency. These data include all input losses and the IF chain noise. The solid line represents the 10 hν/k noise level, where h is the Plank constant, ν is the LO frequency, k is the Boltzman constant. With the introduction of the AR coating the noise level at 0.6 THz -1.1 THz range is expected to drop to the level marked with the dashed line. As we have shown, at terahertz frequencies the planar antenna performance deviates from the calculations given by the quasi-static approach. Specifically for DSA integrated NbN HEB mixers the measured center frequency is lower than calculated one, as it has been shown for Nb diffusion cooled HEB mixers. Now we can conclude that the reason of the down- shift of the center frequency is caused not by the bolometer geometry, as it was suggested, but by the antenna structure itself. The spiral antenna performance, used in the investigation, is not optimized for the frequencies above 2 THz either. The FTS investigation of the downscaled spiral antennas (with smaller inner radius) performance has to be performed for the 2.5 THz receiver.

From 0.6 THz to 1.6 THz the receiver noise bandwidth is about 5 GHz for NbN HEB mixers on silicon substrate, which is about 2 GHz lower than it was expected from the gain bandwidth data. At 2.5 THz the receiver noise bandwidth is 4 GHz. One possible explanation of that can be higher input losses during

measurements in the 3-8 GHz IF band comparing to the measurements in the 1-2 GHz band.

We conclude that optimization of the planar antennas will lead to an improvement of HEB mixers performance above 1 THz.

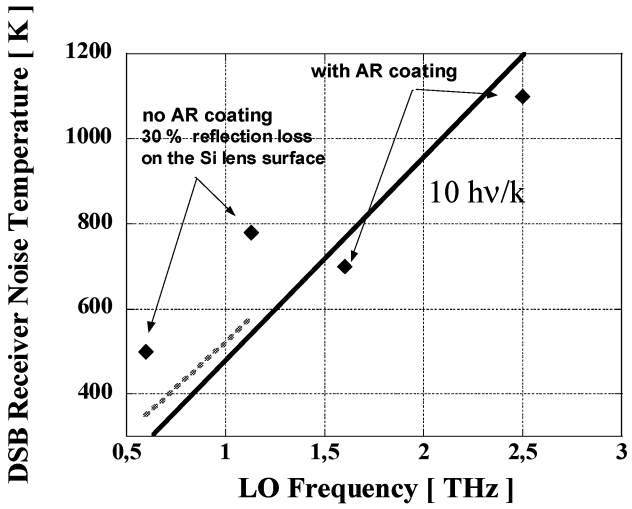

Fig.10 Summary of NbN HEB mixer performance versus LO frequency. The solid line notes the 10 hν/k noise level. Dashed line represents the expected noise temperatures in the 0.6-1.1 THz band with introduction an AR coating for Si lens.

Acknowledgements: The authors would like to thank Dr. Scott Paine for making his program for the atmospheric transmission available. We would like to acknowledge the Swedish National Space Board, and the Swedish Research Council and the European Space Agency for financial support.

References

1 E. M. Gershenzon, G. N. Gol'tsman, I. G. Gogidze, A. I. Elant'ev, B. S. Karasik and A. D. Semenov, "Millimeter and submillimeter range mixer based on electronic heating of superconducting films in the resistive state", Sov. Phys. Superconductivity, 3, 1582, 1990.

2 D.E. Prober, Appl. Phys. Lett. 62, 2119 (1993).

3 A.D. Semenov, H.W. Huebers, J. Schubert, G. Gol'tsman, A.I. Elantiev, B. Voronov, and G. Gershenzon, "Design and performance of the lattice cooled hot-electron terahertz mixer", J.Appl.Phys. **88** (11), p.6758, 2000.

4 J. Kawamura, C.-Y. E. Tong, R. Blundell, D. C. Papa, T. R. Hunter, G. Gol'tsman, S. Cherednichenko, B. Voronov, and E. Gershenzon, "An 800 GHz NbN Phonon-cooled Hot-electron Bolometer Mixer Receiver", IEEE Trans. on Appl. Superconductivity, vol. 9, No 2, 3753, 1999.

5 Yu. P. Gousev, G. N. Gol'tsman, A. D. Semenov, E. M. Gershenzon, R. S. Nebosis, M. A. Heusinger, and K. F. Renk, "Broadband Ultrafast Superconducting NbN Detector for Electromagnetic Radiation", J. Appl. Phys., vol.75, No 7, 3695, 1994.

6 S. Cherednichenko, P. Yagoubov, K. Il'in, G. Gol'tsman and E. Gershenzon, "Large bandwidth of NbN phonon cooled hot-electron bolometer mixers on sapphire substrates", *Proc. 8th Int. Symp. on Space Terahertz Technology*, Cambrige, MA, 245, 1997.

7 P. Yagoubov, M. Kroug, H. Merkel, E. Kollberg, J. Schubert, H.-W. Huebers, S. Svechnikov, B. Voronov, G. Gol'tsman, and Z. Wang, "Hot Electron Bolometric Mixers Based on NbN Films

Deposited on MgO substrates", *Proc. Europ. Conf. on Appl. Superconductivity (EUCAS'99),* Barcelona, 14-17 September, 1999.

8 D.Meledin, et al, "Sensitivity and IF bandwidth of waveguide NbN phonon-cooled HEB mixer based on a crystalline quartz substrate with an MgO buffer layer", *Proc. 13th Int. Symp. on Space Terahertz Technology*, Cambrige, MA, 2002, this issue.

9 R. Wyss, B. Karasik, W. McGrath, B. Bumble, H. LeDuc, "Noise and Bandwidth Measurements Of Diffusion-Cooled Nb Hot-Electron Bolometer Mixers at Frequencies Above the Superconductive Energy Gap", *Proc. 10th Int. Symp. on Space Terahertz Technology*, Charlottesville, VA, 214, 1999.

10 D. Wilms Floet and T. M. Klapwijk, J. R. Gao and P. A. J. de Korte, Appl. Phys. Lett. vol. 77, Issue 11, pp. 1719-1721

11 N. Erickson et al, "1.5 THz all- planar multiplied source", *Proc. 13th Int. Symp. on Space Terahertz Technology*, Cambrige, MA, 2002, this issue

12 A. Maestrini et al, "1400- 1900 GHz membrane based Schottky diode triplers ", *Proc. 13th Int. Symp. on Space Terahertz Technology*, Cambrige, MA, 2002, this issue

13 R. Wyss, A.Netto, W. McGrath, B. Bumble, H. LeDuc, "Submillimeter- wave spectral response of twin- slot antennas coupled to hot electron bolometers", *Proc. 11th Int. Symp. on Space Terahertz Technology*, Ann Arbor, MI, 379, 2000.

14 Loudkov et al*, Proc. 13th Int. Symp. on Space Terahertz Technology*, Cambrige, MA, 2002, this issue

15 G.V.Eleftheriades and G.M.Rebeiz, "Self and mutual admittance of slot antennas on a dielectric half-space", Int. J. Infrared and MM Waves, vol.14, No.10, 1993, pp.1925-1946.

16 M.Kroug, S.Cherednichenko, H.Merkel, E.Kollberg, B.Voronov, G.Gol'tsman H.-W.Huebers, H.Richter "NbN HEB mixer for terahertz heterodyne receivers", IEEE Trans. on Appl. Supercond. Vol.11, n.11, pp. 962-965, 2001

17 B.S.Karasik and A.I.Elant'tev, "Noise Temperature limit of a Superconducting Hot Electron Bolometer Mixer," App.Phys.Lett., vol.68, pp.853-855,1996.

18 S. Cherednichenko, M. Kroug, P. Khosropanah, A. Adam, H. Merkel, E. Kollberg, D.Loudkov, B. Voronov, G. Gol'tsman, H.-W. Huebers, H. Richter, "1.6 THz HEB mixer for far infrared space telescope (Hershel)", *accepted to* Physica C, Aug. 2001.

19 J.D.Dyson, "The equiangular spiral antenna", IRE Trans. Ant.Prop., 7, 181, 1959.

20 P. Yagoubov, M. Kroug, H. Merkel, E. Kollberg, J. Schubert, H.-W. Huebers, "NbN hot-electron bolometric mixers at frequencies between 0.7 THz and 3.1 THz", Supercond.Sci.Technol.12 (1999), 989-991.

21 M. Bin, M. C. Gaidis, J. Zmuidzinas, and T. G. Phillips, H. G. LeDuc, "Low-noise 1 THz niobium superconducting tunnel junction mixer with a normal metal tuning circuit"Appl.Phys.Lett **68** (12), 1714-1716, 1996.

22 A. Karpov et al, *Proc. 13th Int. Symp. on Space Terahertz Technology*, Cambrige, MA, 2002, this issue

Recent Progress on Photon-Counting Superconducting Detectors for Submillimeter Astronomy

J. D. Teufel[3], T. R. Stevenson[1], W.-T. Hsieh[1], M. J. Li[1] , C. M. Stahle[1], E. J. Wollack[2], D. E. Prober[3], and R. J. Schoelkopf[3]

[1]*NASA Goddard Space Flight Center, Detector Systems Branch, Code 553, Greenbelt, MD 20771*
[2]*NASA Goddard Space Flight Center, Infrared Astrophysics Branch, Code 685, Greenbelt, MD 20771*
[3]*Dept. of Applied Physics and Physics, Yale University, P.O. Box 208284, New Haven, CT 06520-8284*
(e-mail address: rob.schoelkopf@yale.edu)

We are developing superconducting direct detectors (the Single Quasiparticle Photon Counter, or SQPC) for submillimeter astronomy that can in principle detect individual photons. These devices operate by measuring the quasiparticles generated when single Cooper-pairs are broken by absorption of a submillimeter photon. This photoconductive type of device could yield high quantum efficiency, large responsivity, microsecond response times, and sensitivities in the range of 10^{-20} Watts per root Hertz. The use of antenna coupling to a small absorber also suggests the potential for novel instrument designs and scalability to imaging or spectroscopic arrays. We will describe the device concept, recent results on fabrication and electrical characterization of these detectors, issues related to saturation and optimization of the device parameters. Finally, we have developed practical readout amplifiers for these high-impedance cryogenic detectors based on the Radio-Frequency Single-Electron Transistor (RF-SET). We will describe results of a demonstration of a transimpedance amplifier based on closed-loop operation of an RF-SET, and a demonstration of a wavelength-division multiplexing scheme for the RF-SET. These developments will be a key ingredient in scaling to large arrays of high-sensitivity detectors.

1. Introduction

To take advantage of very low background photon rates, space-based far infrared or submillimeter-wave interferometers will require large advances in detector sensitivity and speed. Integration of photon-counting detectors with low power readout electronics to make large-format arrays is desired. The Single Quasiparticle Photon Counter (SQPC) is a type of superconducting direct detector, which has been proposed (Schoelkopf *et al.* 1999) to meet these requirements. This paper gives an overview of operation principles of the SQPC, the current state of development of this device, and its potential advantages.

2. Detector Concept and Fabrication

The SQPC is an antenna-coupled Superconducting Tunnel Junction (STJ) detector with integrated Radio Frequency Single-Electron Transistor (RF-SET) readout amplifier. (See Fig.1). STJs have been used for energy-resolving detection of single photons at visible to x-ray wavelengths (Peacock *et al.* 1996). In an STJ detector, a superconducting-insulating-superconducting tunnel junction is biased below its superconducting gap. At temperatures well below the superconducting transition temperature, very little current flows since most

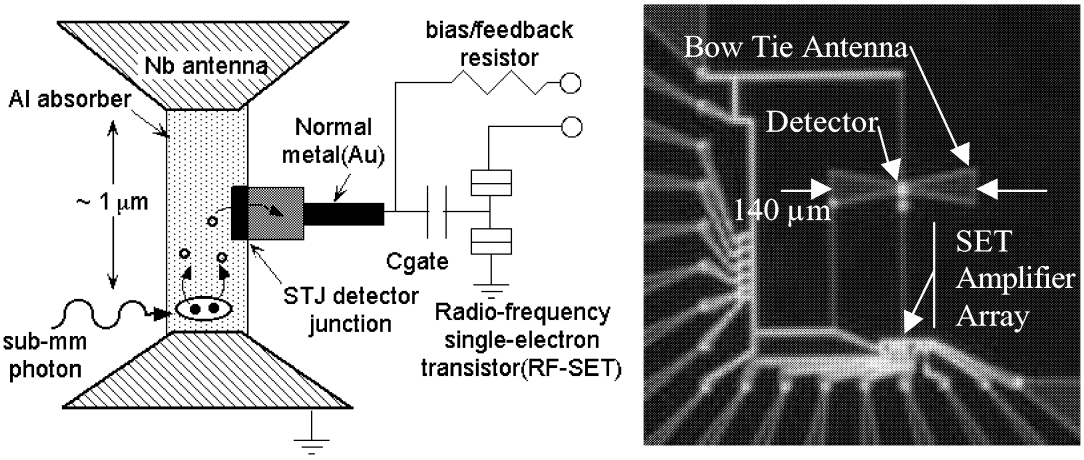

Fig. 1. Single Quasiparticle Photon Counter (SQPC): A niobium bow-tie antenna provides coupling to submillimeter radiation. Absorption of a submillimeter photon breaks Cooper pairs in the aluminum strip joining the halves of the bow-tie, and gives a current pulse through a tunnel junction connected to an RF-SET readout amplifier.

electrons are bound in Cooper pairs. The number of thermally-generated unbound quasiparticles, and hence also the dark current and detector noise, decrease exponentially as the operation temperature is lowered. For aluminum junctions, operating temperatures of ~ 250 mK or less are used.

When a photon is absorbed in one of the superconducting electrodes of the tunnel junction, or in a superconducting absorber film linked to a junction electrode, then much of the photon's energy goes into breaking Cooper pairs, and the quasiparticles released give a current pulse. The integrated charge in the pulse is a measure of the photon energy. At high count rates, overlapping pulses give a photocurrent proportional to the absorbed optical power. The tunneling time which sets the detector speed can be quite fast (~ 1 μs) since the response is a non-equilibrium effect, and not limited by long thermal phonon relaxation times at low temperatures.

2.1 Use of an STJ detector for low energy photons

Figure 1 shows how an STJ is adapted for detection of millimeter or submillimeter-wave photons in an SQPC. The optimal volume of the STJ detection electrode scales in proportion to the maximum photon energy (see Sec. 4). For submillimeter detection, dimensions of the absorber and junction need to be submicron. Efficient coupling of long-wavelength radiation to the small absorber is provided by an antenna structure. Sensitive and high-bandwidth readout of photocurrents through the small, high-impedance tunnel junction is provided by an integrated RF-SET, as described below.

In our devices, in Fig. 2, we make the STJ using aluminum films for the electrodes and absorber, and we fabricate the antenna from niobium. For photon frequencies between the superconducting gap frequencies of aluminum (100 GHz) and niobium (700 GHz), the aluminum absorber strip appears to have its normal-state resistance, and can present a

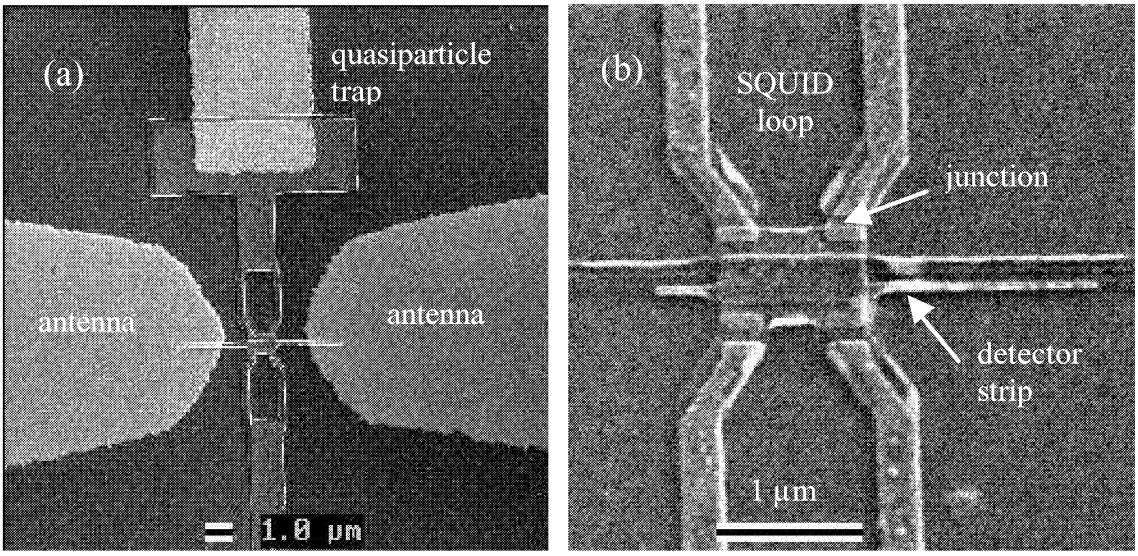

Fig. 2. (a) SQPC detector strip and tunnel junctions are located between two halves of a niobium bow-tie antenna for coupling to submillimeter radiation. A gold quasiparticle trap is included here in the wiring to just one of two dual detector SQUIDs. (b) Close-up view of detector strip and tunnel junctions made by double-angle deposition of aluminum through a resist mask patterned by electron beam lithography. Pairs of junctions form dc SQUIDs, and critical currents can be suppressed with an appropriately tuned external magnetic field.

well-matched impedance for absorbing energy at the center of the superconducting niobium bow-tie antenna.

Figures 1 and 2a show an additional feature: a normal metal (gold) section in the bias lead near the detector junction. This acts a quasiparticle trap which aids rapid diffusion of collected quasiparticles away from the junction after tunneling. This prevents the backtunneling effect (Wilson *et al.* 2001) which may otherwise slow the detector response time. Figure 2b shows that instead of one junction we actually use two junctions in parallel to form a dc Superconducting Quantum Interference Device (SQUID). This allows the critical current of the combined junctions to be suppressed nearly to zero, which is necessary for bias stability, and essential for achieving the lowest dark currents (Sec. 3).

2.2 Integrated Readout Amplifier

At detector readout frequencies (<< 100 GHz), the aluminum is superconducting, and the tunnel junction has a subgap differential resistance of 100 M? or higher, and a capacitance of a femtofarad or less. A standard readout circuit for a high impedance photoconductor is the transimpedance amplifier (see Fig. 3). An ideal amplifier for implementing this readout circuit for an SQPC is the RF-SET (Stevenson *et al.* 2001). A Single Electron Transistor (SET) is a very high performance electrometer based on the Coulomb blockade effect (Fulton & Dolan 1987) with sub-femtofarad input capacitance. An RF-SET integrates the SET with a LC circuit resonant at ˜ 1 GHz to impedance match

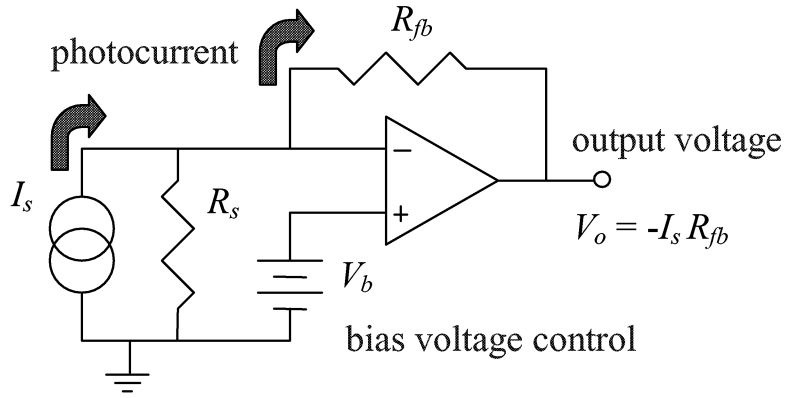

Fig 3. Measuring photocurrent with a transimpedance amplifier: feedback draws photocurrent out through a (cold) feedback resistor, keeping constant bias voltage across the detector.

the typical 50 k? SET output impedance to a 50 ? High Electron Mobility Transistor (HEMT) (located at 4K). Signal bandwidths of 100 MHz can be obtained.

To make an RF-SET transimpedance amplifier, we feed the room temperature output voltage of the RF-SET amplifier system back to the input gate of the SET via a cryogenic, high-value (100 M?) resistor integrated at the detector bias point (see schematic in Fig. 1). Although we have not yet done so, we intend to use electron beam lithography to fabricate a feedback resistor on-chip with physical dimensions small enough to not limit the readout bandwidth with stray capacitance.

2.3 Fabrication Process

We use optical lithography and thin-film processing techniques to fabricate substrates for SQPCs and SETs. The substrates include the antenna, inductors and capacitors for the rf circuits, and device contacts.

We use electron-beam lithography to fabricate both SETs and the SQPC detector in one process. Figure 4 shows one of our transistors, and a sketch of the self-aligned process used to form the small tunnel junctions required both for SET and detector. We use a standard SET fabrication process using a resist bilayer (Dolan 1977). The bottom resist layer is more sensitive to electron-beam exposure than the top, high-resolution layer. Consequently, development of the resists results in undercuts which can be made to merge and form free-standing bridges of the top resist. Evaporating aluminum films onto the substrate at two angles allows junctions to be formed under the resist bridge, as shown in Fig. 4a. A room temperature thermal oxidation step between deposition of the two aluminum layers forms an Al_2O_3 tunnel barrier in the junction area defined by the overlap of the layers.

We have refined this fabrication process with the goal of achieving the reproducibility needed for large-format arrays. By monitoring and controlling the sensitivity of the lower resist layer, we have recently attained large improvements in device yield. We now make chips with 20 or more functional SETs, and small (5 element) arrays of SETs with junction resistances clustered within 10% of a target value. We are continuing to study and make improvements in device yield, uniformity, and long term stability.

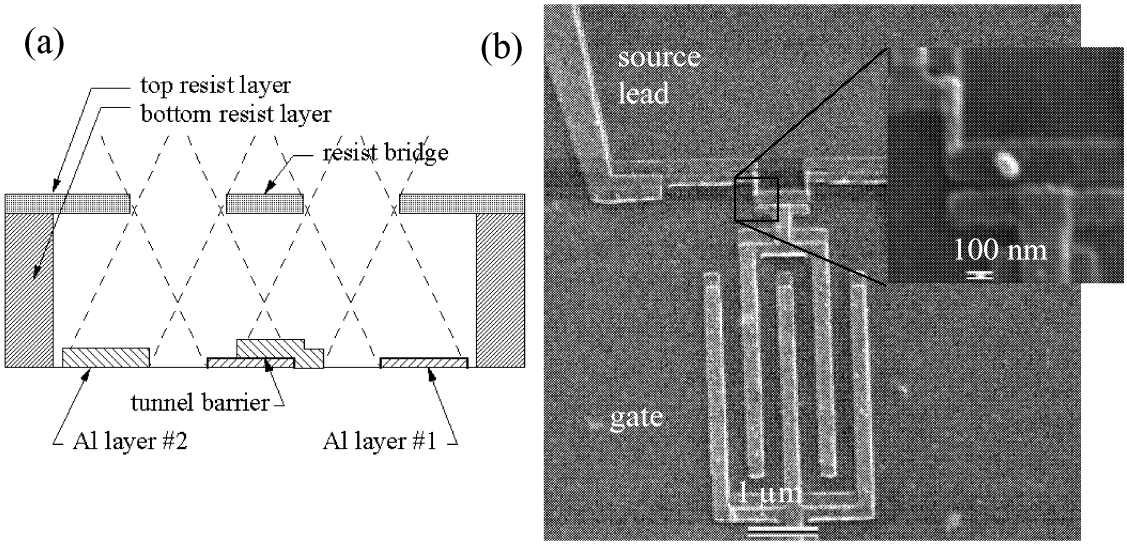

Fig. 4. (a) Double-angle deposition process used to form the self-aligned junctions for the SQPC and SET. (b) An SET with 0.5 fF input gate capacitor. Source and drain leads are connected to island via ultra-small tunnel junctions. Inset shows close up of a 60 nm x 60 nm junction.

3. Optimization of Device Parameters and Experimental Results

Apart from efficiency of antenna coupling, the fundamental factors determining SQPC sensitivity are: (i) detector responsivity, (ii) shot noise on the dark current, (iii) noise of the RF-SET expressed as an equivalent voltage noise at its input, (iv) Johnson noise in the feedback resistor, and (v) impedance of the detector in parallel with the feedback resistor. We have investigated each of these issues, and predict Noise Equivalent Power (NEP) ~ 1×10^{-19} W/vHz could be obtained with our existing SQPC prototypes based on the demonstrated levels of performance measured for each factor.

3.1 Detector Responsivity

The responsivity of the SQPC is ideally equal to *e/?*, where *?* is the energy gap of the absorber material and *e* is the electronic charge. For aluminum, *e/?* ~ 5000 A/W. Efficient collection of photon-generated quasiparticles as a tunneling current depends on making the tunneling time short by confining the quasiparticles to a small absorber or trap volume, and on avoiding sources of quasiparticle recombination other than recombination with the thermal equilibrium concentration of quasiparticles. At low operating temperatures, thermal recombination rates are orders of magnitude slower than our 1-10 µs tunneling times. Using the dual detector SQUID structure shown in Fig. 2b, we have used one SQUID in a pair to electronically inject a quasiparticle current into the common absorber strip. We see a strong response in the subgap tunneling current of the second SQUID. While we have yet to complete analysis, we believe the observed response indicates good confinement and collection in our devices.

3.2 Dark Currents

We have investigated dependence of dark current on device parameters. We found initial prototype detectors with ~ 1 k? junctions deviated from BCS predictions for thermally-generated dark current below ~ 300 mK. The temperature-independent dark current was proportional to the square of the (magnetic-field dependent) critical current of the SQUID, and was explainable as "rectification" of the Josephson oscillations occurring at a non-zero dc bias voltage (Holst 1994). Since the minimum critical current of a dc SQUID is limited to non-zero values by self-inductance, and by asymmetry between junctions, we could not fully suppress the critical current with a magnetic field as is done for UV/optical or x-ray STJ detectors.

Instead, we were motivated to try junctions with smaller areas and higher resistance-area products. For junctions with a Josephson energy $E_J = I_c\Phi_0 /2p$ smaller than kT, we observed extra suppression of the critical current by thermal fluctuations. The dark current at bias less than *?/e* was then greatly improved. Several different detectors were cooled in a pumped He^3 refrigeration system to temperatures as low as 250 mK. Preliminary tests focused on carefully quantifying the dark current and its response to variation in temperature and magnetic field. First, we were able to show that the supercurrent can be suppressed to less than 0.1% on its initial value with a few Gauss of magnetic field on the device. This shows both that the fabrication process can yield sufficiently symmetric SQUID geometries and that we can robustly quench the supercurrent contribution to the dark current.

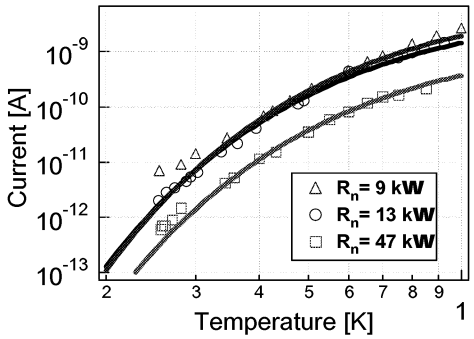

Fig. 5. Data and theory for dark currents of three different detector junctions.

The next step in our characterization of the junctions was to demonstrate how small the dark current could be and see how this compares with theoretical predictions. BCS theory predicts that the subgap current due to thermally excited quasipartcles should decrease exponentially with temperature. So far, our measurements have shown that the subgap current corresponds to the BCS value and that it continues to scale exponentially at the lowest temperatures at which it has been measured. At 256 mK, we measured a dark current less than 1 pA (Figure 5). This implies that a shot noise limited detector would have an NEP of less than 10^{-19} W/rt.Hz. This sensitivity should continue to improve as the temperature decreases. While it remains to be seen how low this dark current can be made, it is highly encouraging that such a low dark current has been demonstrated and that its value fits so closely with theory.

3.3 RF-SET voltage noise

Nearly quantum-limited charge noise ~ 10^{-6} *e*/vHz has been demonstrated for RF-SETs with small input gates (Aassime 2001). However, just as for dc SQUIDs, it is difficult to maintain quantum-limited sensitivity while providing strong coupling to an input signal. For SQPC readout, the figure of merit is the voltage noise, equal to the charge noise divided by the input gate coupling capacitance. As gate capacitance is increased, the voltage noise at first drops, but then levels off or increases as the charge noise of the RF-SET starts to degrade due to co-tunneling effects (Stevenson 2001). We have obtained record SET voltage noise of 30 nV/vHz with a 0.5 fF gate, and have been able to maintain a voltage noise close to this value during closed-loop transimpedance amplifier operation (Segall 2002).

3.4 Predicted Detector Sensitivity

Table I summarizes the noise budget for an SQPC detector using demonstrated parameters. We assume our 0.5 pA device is used with a 100 M? integrated feedback resistor at 250 mK, with higher subgap impedance for the biased detector.

Table I. Detector sensitivity for demonstrated parameters.

Noise source	**Parameters**	**Effective current noise**
Dark current	0.5 pA at 250 mK	0.4 fA/vHz
RF-SET noise	30 nV/vHz	0.3
Johnson noise in Rfb	100 M? at 250 mK	0.4
Total current noise		0.6
NEP		1.2×10^{-19} W/vHz

4. Modeling of Detector Performance for Various Absorbed Power Levels

The maximum power level the SQPC can tolerate, and the expected background count rates in a space environment, will determine the maximum fractional bandwidth allowed for the incident radiation. As the absorbed power is increased, the peak or steady-state concentration of quasiparticles in an SQPC absorber strip will grow, and the rate of self-recombination of particles will increase. When the self-recombination rate per quasiparticle equals or exceeds the tunneling rate, then the efficiency of charge collection drops. We have performed Monte Carlo simulations of the effects on signal and noise in this case, and have found that the saturation of the detector is really quite gradual and weak.

Preliminary results calculated for a device like our prototype with 0.5 pA dark current. The self-recombination and tunnel times become equal at an absorbed power of 3 fW. Above that power, the photocurrent grows as square-root of power, and the time constant of the response drops with the self-recombination time. The total NEP degrades very slowly, and remains close to the photon shot-noise limit until the power reaches 0.1 pW.

With the expected background for space observations (Mather *et al.* 1998), this SQPC model allows background limited sensitivity for incident bandwidths of 0.1% to 100%. Only at powers above a pW will the device saturate "hard," when quasiparticle concentrations grow large enough to supress the superconducting gap and drive the aluminum normal. We consider weak saturation one advantage of the SQPC.

5. Design of Antenna Coupling and Calibration

We have an experiment currently underway to attempt to measure for the first time the photoresponse of an SQPC to radiation. For this purpose, we have made a calibrated 200 GHz source with calculable coupling to the SQPC antenna.

5.1 STJ/Antenna Coupling

At this stage of sensor development, we employ a bow-tie antenna on a dielectric substrate to optically couple the device. This simple scheme has minimal impact on processing and will allow basic characterization of the device properties. In order to integrate the detector to the antenna, the impedance, field configuration, and interaction of the bias network topology with the radiating structure need to be considered.

We estimate the bow-tie antenna's input impedance by treating the structure as a radial transmission line in the quasi-static limit (Rutledge & Muha 1982). For the geometry used for the prototype devices, we estimate an input impedance of ~130 ? . The rf impedance presented by a typical SQPC-SET sensor is 20~50 ? . This impedance mismatch will be addressed in subsequent sensor iterations.

For an antenna on a substrate, the power radiated into the dielectric is greater than the power radiated into the vacuum by a factor of $e_r^{-1.5}$. For the silicon substrate in use, we note that ~97.5% of the power resides in the dielectric portion of the half-space. A quarter-wave-matching layer is employed between the dielectric and freespace to improve the coupling efficiency for the component of the radiation propagating away from the antenna into the dielectric. A substrate lens can also be employed to limit conversion of trapped rays into surface waves on an electrically thick substrate.

The beam efficiency, the ratio of the main beam-to-total beam solid angle, for a bow tie is relatively low. For this reason, we plan to transition to antenna structures with improved sidelobe control. This will enhance compatibility of the device development effort with needs of precision radiometric applications. Given the sensor's planar topology, processing requirements and RF impedance levels; dual slot and taper slotline configurations are presently under consideration to meet these demands.

5.2 200 GHz Calibration Source Development

A quasi-optical calibration scheme was chosen to allow maximum flexibility during sensor characterization. For the initial measurements, a quasi-optically coupled "reverse bolometer" will be used as a thermal source in the sensor's field of view to produce a calculable radiometric flux. The absorber physical temperature and emissivity as a function of frequency effectively control the source bandwidth.

The calibrator was fabricated as follows: The absorber was formed by evaporation of Pd/Au to realize ~400 ? /? on an electrically thin silicon substrate at the anticipated

operational temperature. This layer is held in a silicon frame at a spacing of ~410 microns, roughly a quarter wavelength, from a smooth oxygen free copper backshort. The emitter is supported on micro-machined conductive legs, which provide electrical connections for the thermometry and thermal isolation. Provisions are provided in the design to reconfigure the calibrator for use as a mount in WR05 waveguide for verification of the coupling efficiency via standard waveguide metrology techniques.

6. Multiplexing for Arrays

An advantage we see for the SQPC detector system is the multiplexing capability of RF-SETs. Multiplexing schemes will be crucial to the development of large-format arrays of SQPCs, or other low-temperature detectors.

RF-SETs have a natural wavelength division multiplexing capability, as shown in Fig. 6a. Each RF-SET is connected to one coaxial line by an rf tank circuit with a unique resonance frequency. A directional coupler allows rf carriers to be applied at each resonance frequency and reflected powers to be monitored by a single HEMT following amplifier at 4 K. RF-SETs can be individually or simultaneously powered and read out. We have made a two-channel rf multiplexing demonstration using discrete inductors for the rf tank circuits (Stevenson *et al.* 2001). The two input signals were successfully reconstructed with little cross-talk. Lithographic versions of the rf circuits (Fig. 6b) had measured parameters in agreement with electromagnetic modeling, with reduced cross capacitance and inductance. We have designed a 50-channel system with components based on measured parameters of our lithographic circuits (Stevenson *et al.* 2002).

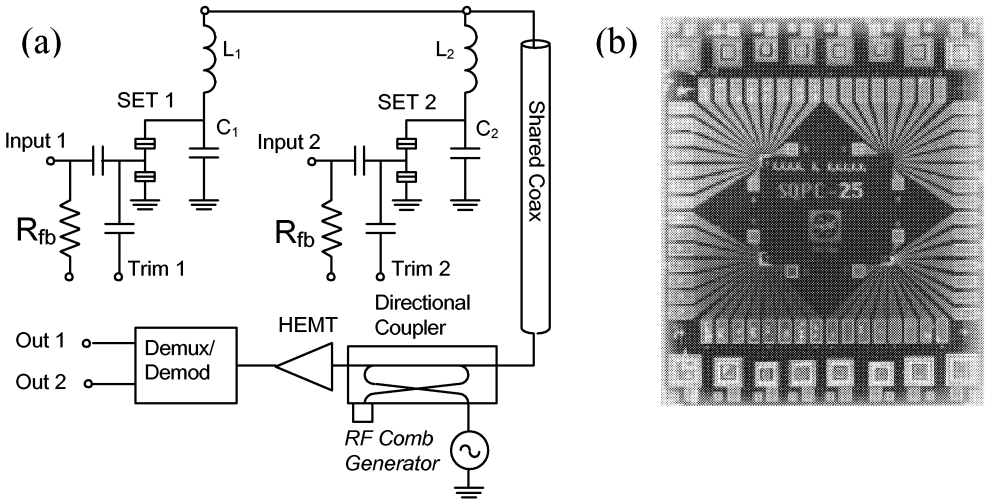

Fig. 6. (a) WDM multiplexing scheme. All inductors are connected to one coax running from subkelvin chip to components at 4K. Multiple carrier frequencies pass through directional coupler to excite tank circuits. Reflected power is directed to HEMT amplifier. Outputs are demultiplexed and demodulated at room temperature, and fedback to resistors for transimpedance operation. Detector bias can be changed using trim gates. (b) 8 mm x 10 mm chip with 16 lithographically defined tank circuit inductors.

The wavelength division multiplexing scheme still requires two wires for each pixel which is being read out simultaneously: one wire for connection to the transimpedance feedback resistor, and one for a weakly coupled SET trim gate. Combining wavelength division multiplexing with some form of time-division, or other, multiplexing will be required in to implement large arrays; however, the 50-fold reduction in output connections seems quite valuable.

7. Conclusion

We have refined a fabrication process for SQPC detectors and RF-SET amplifiers with the goal of achieving the reproducibility needed for large-format arrays, and have recently attained large increases in device yield. With proper device design, we have attained subpicoamp dark currents, and record RF-SET voltage noise levels, which allow sensitivities of 1×10^{-19} W/vHz at temperatures as high as 250 mK. There is potential for even better sensitivity at lower temperatures, and the expected detector saturation behavior and multiplexing capability of RF-SETs enhance the potential for application of the SQPC in space-based submillimeter-wave interferometers.

8. Acknowledgments

This work has been funded by GSFC Director's Discretionary Funds, NASA Explorer and CETD Programs, NASA Codes S & R, NASA NSG-8589.

9. References

Aassime A, Gunnarsson D, Bladh K, Delsing P, and Schoelkopf R, 2001, Appl. Phys. Lett. 79, 4031.

Dolan GJ, 1977, Appl. Phys. Lett. 31, 337.

Fulton TA and Dolan GJ, 1987, Phys. Rev. Lett. 59, 109.

Holst T, Esteve D, Urbina C, and Devoret MH, 1994, Physica B 203, 397.

Mather JC, Moseley SJ, Leisawitz D, *et al.*, 1998, astro-ph/9812454.

Peacock A, Verhoeve P, Rando N, van Dordrecht A, Taylor BG, Erd C, Perryman MAC, Venn R, Howlett J, Goldie DJ, Lumley J, and Wallis M, 1996, Nature 381 135.

Rutledge DB and Muha MS, 1982, IEEE Trans. Antennas Propag., AP-30 535.

Schoelkopf RJ, Moseley SH, Stahle CM, Wahlgren P, and Delsing P, 1999, IEEE Trans. Appl. Supercond. 9 2935.

Segall K, Lehnert KW, Stevenson TR, and Schoelkopf RJ, 2002, in preparation.

Stevenson TR, Aassime A, Delsing P, Schoelkopf S, Segall K, and Stahle CM, 2001, IEEE Trans. Appl. Supercond.11, 692.

Stevenson TR, Pellerano, FA, Stahle CM, Aidala K, and Schoelkopf RJ, 2002, Appl. Phys. Lett., accepted.

Wilson CM, Frunzio L, Segall K, Li L, Prober DE, Schiminovich D, Mazin B, Martin C, and Vasquez R, 2001, Trans. Appl. Supercond. 11, 645.

Spectral Sensitivity and Temporal Resolution of NbN Superconducting Single-Photon Detectors

A. Verevkin, J. Zhang[1], W. Slysz[2], and Roman Sobolewski[3]
Department of Electrical and Computer Engineering and Laboratory of Laser Energetics
University of Rochester, Rochester, NY 14627-0231
A. Lipatov, O. Okunev, G. Chulkova, A. Korneev, K. Smirnov, G.N. Gol'tsman
Department of Physics, Moscow State Pedagogical University, Moscow 119435, Russia
A. Semenov
DLR, Berlin

Abstract

We report our studies on spectral sensitivity and time resolution of superconducting NbN thin film single-photon detectors (SPDs). Our SPDs exhibit an experimentally measured detection efficiencies (DE) from ~ 0.2% at λ=1550 nm up to ~3% at λ=405 nm wavelength for 10-nm film thickness devices and up to 3.5% at λ=1550 nm for 3.5-nm film thickness devices. Spectral dependences of detection efficiency (DE) at λ=0.4 –3.0 μm range are presented.

With variable optical delay setup, it is shown that NbN SPD potentially can resolve optical pulses with the repetition rate up to 10 GHz at least. The observed full width at the half maximum (FWHM) of the signal pulse is about 150-180 ps, limited by read-out electronics. The jitter of NbN SPD is measured to be ~35 ps at optimum biasing.

Introduction

NbN ultrathin film superconducting single-photon detectors (SPDs) are promising for their fast response time and ultimate sensitivity from ultraviolet to near infrared ranges [1-4]. Simultaneously, with the quantum-counting property, dark counts of the detector are negligibly low under the cryogenic operation environment [5,6]. As the result, superconducting NbN SPDs offer some obvious advantages over any modern semiconductor single-photon detectors [6].

The single photon counting property of NbN SPDs has been investigated thoroughly, and a model of hot-spot formation process has been introduced to explain the photon-counting mechanism of NbN SPDs [7, 8].

However, it is of great interest to study spectral sensitivity characteristics and time characteristics of NbN SPD. Another very important time-related characteristic is the time jitter. The last characteristic is responsible for an accuracy of photon event registration in time scale.

---

[1] Also at: Materials Science Program, University of Rochester, NY, 14627.
[2] Also at: the Institute of Electron Technology, PL-02668 Warszawa, Poland.
[3] Also at: the Institute of Physics, Polish Academy of Sciences, PL-02668 Warszawa, Poland.

SPD's fabrication and experimental setup

The devices used in our experiments are meander-structured NbN superconducting stripes with thickness of d = 10 nm and 3.5 nm, and width of w ~200 nm. The T_c of the devices is about 10.5 K for 10-nm thickness film, and about 10 K for 3.5-nm thick film devices, with critical current density j_c at 4.2 K up to 5×10^6 A/cm^2. The fabrication process of NbN SPDs is as follows: first of all, the ultra-thin NbN films are deposited on double-side polished sapphire substrates by reactive dc magnetron sputtering method in the Ar + N_2 gas mixture. The maximum values of the critical film parameters (T_c and j_c) are reached at the partial Ar pressure of $5\text{x}10^{-3}$ mbar, the partial N_2 pressure of $9\text{x}10^{-5}$ mbar, the discharge current value of 300 mA, the discharge voltage of 300 V and the substrate temperature of 850 ^{o}C. Next, the film is patterned into a meander-type stripe occupying an area of ~10 μm ×10 μm or 4 μm ×4 μm by e-beam lithography after the outer Ti-Au contact pads are fabricated by lift-off optical photolithography. Thereafter the NbN film is removed from the whole surface of the substrate except the meander-type structure and contact pads by ion milling in Ar atmosphere through supplementary Ti mask, which is created on the surface of NbN meander-type and contact pads. Finally, the last process is to remove Ti mask in diluted hydrofluoric acid. SEM image of the device with 10μm × 10μm working area is shown in Fig.1.

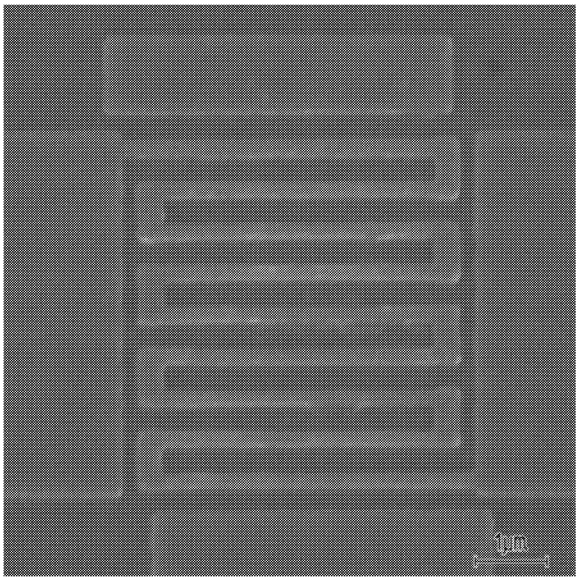

Fig. 1. SEM image of Meander-structured NbN SPD fabricated by the magnetron sputtering method with covered area of 4 μm × 4 μm, average stripe width w = 210 nm.

Typical I-V curve of the 10-nm-thick SPD at 4.2 K is shown in Fig. 2. We bias the SPD at currents below critical current I_c (e.g., point A on superconducting branch). After the absorption of the photon the resistive barrier across the full width of NbN stripe appears, and detector is switched from superconducting state (point A in Fig. 2) to meta-stable state (point B in Fig. 2) with a voltage signal generated.

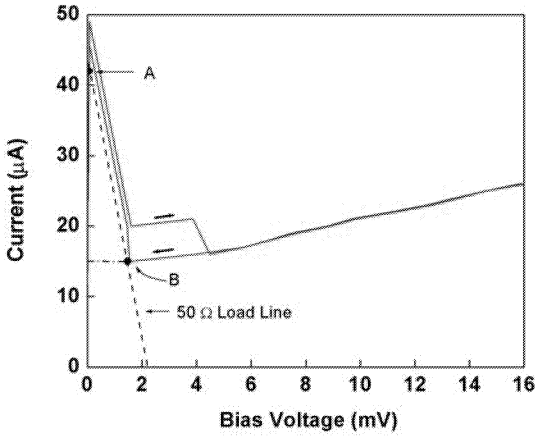

Fig. 2. I-V curve of 10-nm-thick, 4 μm × 4 μm area NbN SPD at 4.2 K.

Experimental setup

The schematic diagram of our experimental setup is shown in Fig. 3. The device is wire-bonded to a microstripe line and then connected to the bias and output circuits through a bias tee. The vacuum cryostat that holds the SPDs is cooled by liquid helium and maintained at 4.2K. Optical sources were either 100-fs-wide pulses with a 82-MHz repetition rate at 405 nm, 810 nm, and 1.55-μm wavelengths from a self-mode-locked Ti-sapphire laser, coupled with the parametrical optical amplifier, or CW laser diodes. The intensity of incident radiation was attenuated using banks of neutral density filters. In addition, the wavelength dependency of SPD's detection efficiency (DE) was measured using a grating spectrometer and a CW blackbody radiation source.

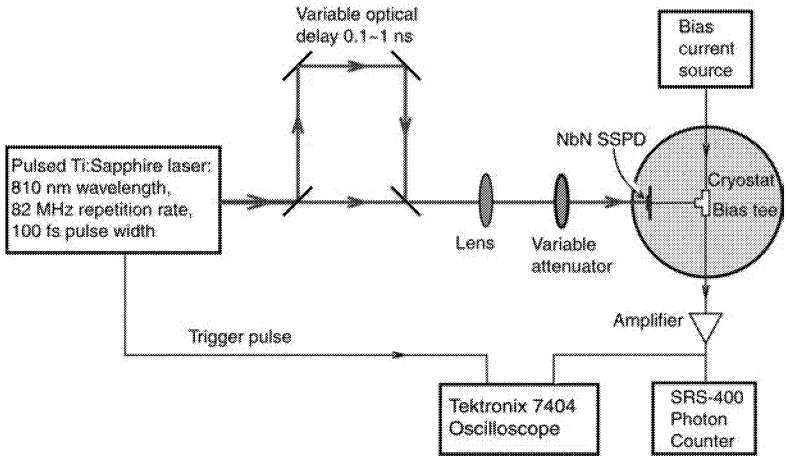

Fig. 3. Experimental setup with variable optical delay stage.

In order to measure the time-resolving ability of NbN SPDs, we have set up an adjustable optical delay stage. The laser beam is firstly split into two beams, and then one

of the beams is delayed by the optical delay stage and then merged back into the original beam by the second beam-splitter. The minimum amount of the delay is 100 ps. The voltage signal generated by the incident photon in the SPD is amplified by a room-temperature amplifier and then fed to the Tektronix 7404 single-shot digital oscilloscope (synchronously triggered by the Ti:Sapphire laser) or counted by SR400 photon counter, the room temperature amplifier and oscilloscope have bandwidths of 0.01-12 GHz and 0-4 GHz, respectively.

Experimental results

Spectral sensitivity

The DE spectral dependences for some 4x4 μm^2 and 10x10 μm^2 10-nm film thickness SPDs at λ=0.4 –3.0 μm range are presented in Fig. 4. We notice here that DE is a global parameter referring to the number of photons registered by the detector, normalized only to the incident beam size. The DE dependences have an activated-type character with DE ~ exp(-E_g/hν), where E_g is the activation energy [4]. The activation character of DE and E_g value looks similar for all the tested devices with the same thickness. We observed some noticeable variations of the spectral sensitivity dependence slope with the stripe width, but it is a subject of more detail future study.

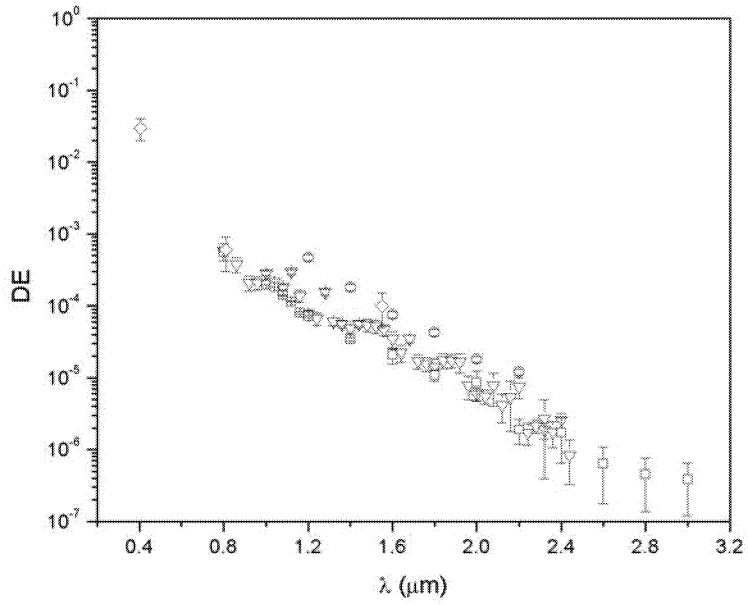

Fig. 4. Spectral dependences of detection efficiency for 10x10 μm^2 (diamonds), and some of 4x4μm^2 SPDs (circles, triangles, and squares) obtained with CW radiation source.

The preliminary results for 3.5-nm-thick devices show significantly smaller activation energy value, which is in agreement with prediction of hot-spot model. It makes thinner devices more promising for near-infrared and middle-infrared ranges.

Our 10-nm-thick SPDs exhibit an experimentally measured detection efficiencies (DE) from ~ 0.2% at λ=1550 nm up to ~3% at λ=405 nm wavelength. The devices with the film thickness of 3.5-nm shows DE up to 3.5% at λ=1550 nm. The intrinsic quantum efficiency of these devices is close to 100% at 1.2 μm wavelength (see notice above about definition of DE).

Time resolution

With the variable time delay setup, we have taken the single shots of the pulse-shape with Tektronix 7404 oscilloscope (100 ps rise time). The results are shown in Fig. 5. Signal pulse itself has a FWHM of about 150 ps, and rise time of ~100 ps. When the optical delay is adjusted to be 100 ps (Fig. 5b), pulse shape by oscilloscope is evidently wider than the pulse shape without delay, and the signature of the second delayed pulse can be detected. For comparison, pulses for the delays of 330 ps, 650 ps, and 1080 ps are shown in Fig. 5c, d, and e. Obviously, the superconducting state should be recovered for to detect next photon. As the result, we can make a conclusion that the device is capable to detect photons with 10-GHz counting rate.

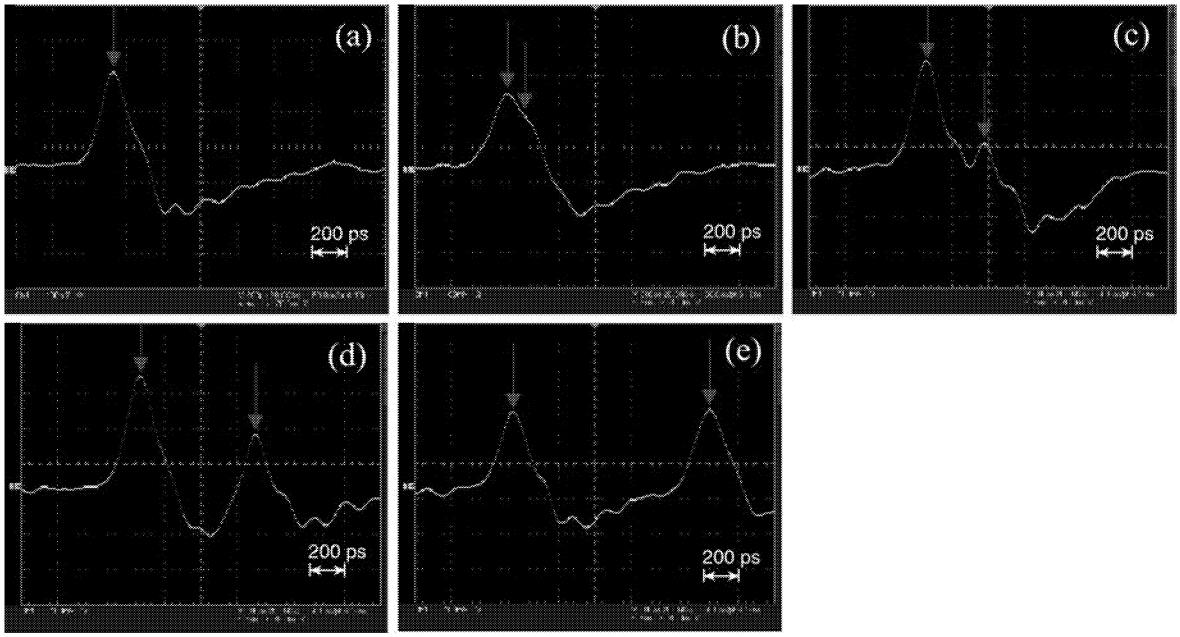

Fig. 5. Pulse patterns at different optical delays: (a) delay = 0, (b) delay = 100 ps (we can see the signature of the delayed pulse), (c) delay = 330 ps, (d) delay = 650 ps, (e) delay = 1080 ps.

The signal pulse from our NbN SPD has an extremely small jitter. With the analysis of pulse shape by standard histogram method, we can find that the total system jitter is about 35 ps (as shown in Fig. 6) at the relatively high flux. This value of jitter includes jitters from the laser system (~4 ps), the output circuits and the oscilloscope performance, thus,

the intrinsic device jitter is expected to be smaller.

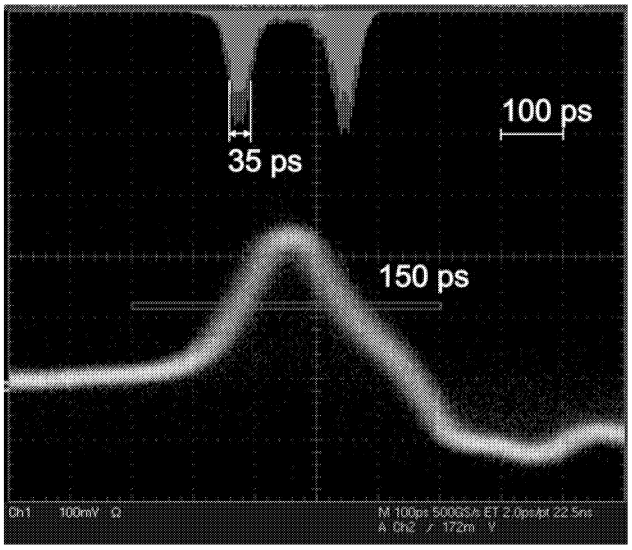

Fig. 6. Pulse shape at incident flux level of 1000 photons per second, with FWHM of about 180 ps, and jitter of about 35 ps.

Conclusions

NbN SPDs are sensitive to UV, visible, and IR radiation. Obviously, 3.5-nm film thickness devices are already in competition with the best semiconductor single-photon detectors at 1.55-micron communication wavelength.

The experimental results of optical pulse delay have shown that our NbN SPDs can resolve pulse trains with optical delay of about 100 ps. This ultra-fast responsive property makes NbN SPDs to be very promising detectors in a lot of application fields, such as fiber-optics communication and even Earth-satellites communication. Measured jitter of detectors is about 35 ps which makes our devices very promising for ultrafast applications.

Acknowledgements

This work was supported by the AFOSR grant F49620-01-0463 and by the Schlumberger SS, San Jose, CA. We are very thankful to K. Wilscher, W. Lo., S. Kasapi, and S. Somani for fruitful discussions.

Reference:

1. G. N. Gol'tsman, O. Okunev, G. Chulkova, A. Lipatov, A. Semenov, K. Smirnov, B. Voronov, A. Dzardanov, C. Williams and R. Sobolewski, Appl. Phys. Lett. **79**, 705 (2001).
2. K. S. ll'in, M. Lindgren, M. Currie, A. D. Semenov, G. N. Gol'tsman, R. Sobolewski, S. I. Cherednichenko and E. M. Gershenzon, Appl. Phys. Lett. **76**, 2752 (2000).

3. K.S. ll'in, I. I. Milostnaya, A. A. Verevkin, G. N. Gol'tsman, E. M. Gershenzon and R. Sobolewski, Appl. Phys. Lett. **73**, 3938 (1998).
4. A. Verevkin, J. Zhang, R. Sobolewski, G. Chulkova, A. Korneev, A. Lipatov, O. Okunev, A. Semenov, and G. N. Gol'tsman, Appl. Phys. Lett. (Accepted).
5. G. Gilbert, M. Hamrick, *Practical Quantum Cryptography: A comprehensive analysis,* MTR00W0000052, Mitre Technical Report, 2000.
6. S. Somani, S. Kasapi, K. Wilsher, W. Lo, R. Sobolewski and G. Gol'tsman, J. Vac. Sci. Technol. B **19**, 2766 (2001).
7. A. M. Kadin, and M. W. Johnson, Appl. Phys. Lett **69**, 3938 (1996).
8. A. D. Semenov, G. N. Gol'tsman, A. A. Korneev, Physica C **351,** 349 (2001).

KINETIC INDUCTANCE THZ MIXER FOR SPACE APPLICATIONS

Andrei V. Sergeev [a] and Vladimir V. Mitin
Wayne State University, Detroit, MI 48202

Boris S. Karasik and William R. McGrath
Jet Propulsion Laboratory, California Institute of Technology, Pasadena, CA 91109

We consider a new type of hot-electron mixer that employs a kinetic-inductance response in a superconducting film near superconducting transition. The significant advantage of this mixer over the resistive one is that the intermediate frequency bandwidth and the local oscillator power can be adjusted independently. The intermediate frequency bandwidth is determined by the inverse quasiparticles multiplication time. The local oscillator power is determined by the electron cooling time, which is the electron-phonon relaxation time for phonon-cooled mixers. Our modeling has shown that the intermediate frequency bandwidth can be as large as 50 GHz along with the local oscillator power of about 10 nW and the conversion efficiency ~ 0.01.

Currently, hot-electron superconducting bolometer (HEB) mixers are the most sensitive heterodyne detectors at THz frequencies. Both the diffusion and the phonon cooled HEB mixers demonstrate very good noise characteristics [1,2]. The achieved noise temperature in practical mixers is approximately 10 times higher than the quantum limit, $T_Q = h\nu/k_B$. The intermediate frequency (IF) bandwidth, B_{IF}, is given by the inverse electron cooling time, τ_c, i.e., $B_{IF} = 1/(2\pi\tau_c)$. The maximum IF bandwidth of ~ 9 GHz has been demonstrated in an ultrashort diffusion-cooled Nb mixer [3]. The local oscillator (LO) power of an HEB mixer is $P_{LO} \approx C_e T_c/\tau_c \propto T_c^2/\tau_c$, where C_e is the electron heat capacity. Typical low values for the LO power are in the range 20-100 nW [3]. A further decrease of the LO power in HEB mixers can be achieved by using superconductors with lower critical temperature [4].

In the current work, we analyze a new type of hot-electron mixer, which employs a kinetic-inductance response in a superconducting film in the vicinity of the superconducting transition. This mixer allows for substantial increase of the IF bandwidth and simultaneous decrease of the LO power.

The kinetic inductance response to the electromagnetic radiation near the superconducting transition has been studied in many works [5,6,7,8]. The radiation

[a] E-mail address: sergeev@ciao.eng.wayne.edu

quanta create large number of excited quasiparticles in a superconducitng film. Electron-electron scattering ensures effective avalanche-like multiplication of photoexcited quasiparticles. Increase of the number of quasiparticles (decrease of the number of Cooper pairs) leads to a change of kinetic inductance which can be detected via a change of the ac voltage across the current biased superconducting bridge. In impure superconductors, the electron-electron scattering time, τ_{ee}, is significantly shorter than the electron-phonon time, $\tau_{e\text{-}ph}$, and on the time scale longer than τ_{ee} one can describe the electron kinetics by the electron temperature, θ, in the same way as in the resistive state:

$$\delta\theta = \frac{P}{C_e} \frac{\tau_{e-ph}}{1+i\omega\tau_{e-ph}} \exp(i\omega t), \qquad (1)$$

where P is the electromagnetic power absorbed in a superconducting bridge.

The kinetic inductance, L_k, is a function of the electron temperature, so the responsivity of the kinetic-inductance detector may be presented as

$$S_\omega = I\frac{\partial L_k}{\partial\theta}\frac{\omega\theta_\omega}{P_\omega} = \frac{I}{C_e}\frac{\partial L_k}{\partial\theta}\frac{i\omega\tau_{e-ph}}{1+i\omega\tau_{e-ph}}, \qquad (2)$$

where I is the biased current, and ω is the modulation frequency; the subscript ω denotes the corresponding Fourier component.

In general, the dependence of the responsivity on the modulation frequency has a shape shown in Fig. 1. At low frequencies, the inductive signal is proportional to the frequency. Then, at $\tau_{e\text{-}ph}^{-1} < \omega < \tau_{ee}^{-1}$ the frequency dependence has a plateau, which can be used for mixing. At higher frequencies, a 1/ω decrease of the signal with frequency is expected. Here, the variations of the electromagnetic field are so fast that the quasiparticle multiplication cannot follow and, as a result, the kinetic inductance does not change much. Experiment [8] has demonstrated the presence of the linear and the frequency independent parts of the dependence $S_\omega(\omega)$. The high-frequency region above τ_{ee}^{-1} could not be observed in view of instrumentation bandwidth limitation.

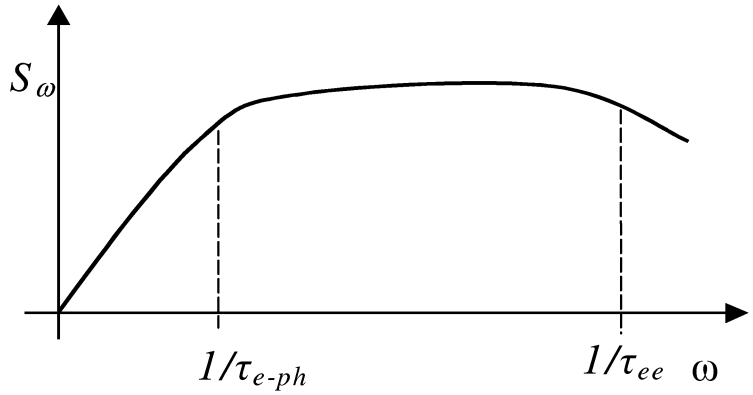

Fig. 1. Dependence of the responsivity on the modulation frequency

The electron-electron scattering rate in an impure superconductor near the transition is given by [9]:

$$\frac{1}{\tau_{ee}} = \frac{e^2 R_\square T_c}{2\pi\hbar^2} \ln\left(\frac{\pi\hbar}{e^2 R_\square}\right), \qquad (3)$$

where $R_\square$ is the sheet resistance. Typical values of τ_{ee} in disordered films at helium temperatures are 2-7 ps. Thus, the kinetic-inductance mixer would allow for an IF bandwidth

$$B_{IF} = 1/(2\pi\tau_{ee}) \simeq 50 \text{ GHz}. \quad (4)$$

For the proposed kinetic inductance mixer, the IF bandwidth and the LO power are controlled by different electron processes and do not have to be traded off. In order to minimize the LO power, the mixer should work in the phonon-cooled mode. Then, the LO power will be given by :

$$P_{LO} \cong C_e T_c / n\tau_{e-ph}, \quad (5)$$

where n=4-6 is the exponent in the temperature dependence in the electron energy loss function. Choosing the volume of the superconducting bridge, one can adjust the LO power to a required value. For example, for Nb bridge of 10nm×0.1μm×1μm and T_c= 5.5K the LO power is expected to be ~10nW.

Let us now consider the responsivity near the superconducting transition. In this region the temperature dependence of the kinetic inductance is [10]

$$L_K = \frac{2\hbar R k_B T}{\pi(\Delta(T))^2} \propto (1-T/T_c)^{-1}, \quad (6)$$

where $\Delta(T)$ is the superconducting gap, and R is the normal state resistance. The kinetic-inductance response is proportional to the biased current, which is limited by the critical Ginzburg-Landau current,

$$I_{GL} = \frac{8\sqrt{2\pi^5}}{21\sqrt{3}\,\zeta(3)} \frac{(k_B T)^{3/2}}{(\hbar D)^{1/2}} \frac{L}{eR} (1-T/T_c)^{3/2}, \quad (7)$$

where D is the diffusion coefficient, and L is the length of the bridge.

Assuming that the biased current is a times smaller than the critical current and combining Eqs. 2, 6 and 7, we obtain the responsivity

$$S \approx \frac{0.1}{a} \frac{(\hbar D)^{1/2}}{(k_B T)^{3/2}} \frac{eR}{L} (1-T/T_c)^{-1/2}. \quad (8)$$

Choosing a = 2 and $(1\text{-}T/T_c)^{-1/2}$ = 6, for a 10nm thick and 0.1μm wide superconducting Nb bridge with T_c = 5.5K, resistivity of 5×10^{-5} Ω cm, and the diffusion constant D = 1 cm^2/s, we get the responsivity of $5\cdot10^3$ A^{-1}.

The mixer conversion efficiency is given by

$$\eta = \frac{2S^2 P_{LO}}{R_L}, \quad (9)$$

where R_L = 50 Ω is the IF load resistance. With S = 5000 A^{-1} and P_{LO} = 10nW, we expect the conversion efficiency to be of the order of 10^{-2}. With a typical LHe cooled HEMT amplifier (noise temperature 2-5 K) the mixer noise temperature of several hundred Kelvin can be expected.

In summary, we propose a new type of low-noise hot-electron mixer based on the kinetic-inductance response in the superconducting state. The IF bandwidth of this mixer

is given by the rate of the electron-electron scattering processes and it can be as large as 50 GHz. The LO power is independently controlled by a relatively slow electron cooling process and can be separately adjusted to the required low values.

References

1. P.J. Burke, R.J. Schoelkopf, D.E. Prober et al., *J. Appl. Phys.* **85**, 1644 (1999).
2. A.D. Semenov, G.N. Gol'tsman, and R. Sobolewski, *Supercond. Sci. Technol.* **15**, R1 (2002).
3. R.A. Wyss, B.S. Karasik, W.R. McGrath, B. Bumble, and H. LeDuc, *Proc. 10th Int. Symp. on Space Terahertz Technology, UVa, Charlottesville, VA,* March 16-18, 1999, pp. 215.
4. B.S. Karasik, W.R. McGrath, and R.A. Wyss, *IEEE Trans. on Appl. Supercond.* **9**, 4213 (1999); A. Skalare, W.R. McGrath, P.E. Echternach et al., *IEEE Trans. on Appl. Supercond.* **11**, 641 (2001).
5. E.N. Grossman, D.G. McDonald, and J.E. Sauvageau, *IEEE Trans. Magn.* **27**, 2677 (1991).
6. N. Bluzer, *Phys. Rev.* **B 44**, 10222 (1991); *J. Appl. Phys.* **71**, 1336 (1992).
7. F.A. Hegmann and J.S. Preston, *Phys. Rev. B* **48**, 16023 (1993).
8. I.G. Gogidze, P.B. Kuminov, A.V. Sergeev, A.V. Elantev, A.I. Menshcikov, and E.M. Gershenzon, *Sov. Phys. - Tech.Phys.* **43**, 1193 (1998); I.G. Gogidze, P.B. Kuminov, A.V. Sergeev, and E.M. Gershenzon, *Sov. Phys. - Tech.Phys.Lett.* **25**, 47 (1999).
9. B.L. Altshuler and A.G. Aronov, *Modern Problems in Condensed Matter Science,* Eds. A.L. Efros and M. Pollac, North-Holland, Amsterdam and New York (1985), p.1.
10. M. Tinkham, *Introduction to Superconductivity*, 2nd ed., McGraw-Hill, New York (1996).

BROADBAND DIRECT DETECTION SUBMILLIMETER SPECTROMETER WITH MULTIPLEXED SUPERCONDUCTING TRANSITION EDGE THERMOMETER BOLOMETERS

Dominic J. Benford, Troy A. Ames, Jay A. Chervenak, S. Harvey Moseley, Rick A. Shafer, Johannes G. Staguhn†, George M. Voellmer
NASA Goddard Space Flight Center, Greenbelt, MD 20771, USA
† SSAI, Lanham, MD 20706, USA

François Pajot, Cyrille Rioux
IAS-CNRS, 91405 Orsay, France

Thomas G. Phillips
Caltech, Pasadena, CA 91125, USA

Bruno Maffei
University of Wales, Cardiff, CF24 3YB, Wales

Kent D. Irwin
NIST, Boulder, CO 80305, USA

Abstract

We present performance results based on the first astronomical use of multiplexed superconducting bolometers. The Fabry-Perot Interferometer Bolometer Research Experiment (FIBRE) is a broadband submillimeter spectrometer that achieved first light in June 2001 at the Caltech Submillimeter Observatory (CSO). FIBRE's detectors are superconducting transition edge sensor (TES) bolometers read out by a SQUID multiplexer. The Fabry-Perot uses a low resolution grating to order sort the incoming light. A linear bolometer array consisting of 16 elements detects this dispersed light, capturing 5 orders simultaneously from one position on the sky. With tuning of the Fabry-Perot over one free spectral range, a spectrum covering $\Delta\lambda/\lambda = 1/7$ at a resolution of $\delta\lambda/\lambda \sim 1/1200$ can be acquired. This spectral resolution is sufficient to resolve Doppler-broadened line emission from external galaxies. FIBRE operates in the 350 μm and 450 μm bands. These bands cover line emission from the important star formation tracers neutral carbon [CI] and carbon monoxide (CO). We have verified that the multiplexed bolometers are photon noise limited even with the low power present in moderate resolution spectrometry.

SCIENTIFIC MOTIVATION

Spectroscopy of distant galaxies in the far-infrared and submillimeter has lagged behind continuum studies at the same wavelengths (e.g., with SHARC at the CSO [1]) and spectroscopic studies at longer wavelengths (e.g. OVRO [2]). In large part, this is due to a relative lack of available instrumentation combining high sensitivity and large bandwidth. Observing an emission line from a typical galaxy with velocity-broadened linewidth of ~300km/s in the 350μm and 450μm atmospheric windows (850GHz and 650GHz, respectively) requires a spectrometer with a bandwidth of at least 0.5μm (1GHz). Additionally, detecting this line is easiest if the spectral resolution is approximately this width. Hence, a spectrometer with a spectral resolution of slightly more than 1000 is optimal for the detection of faint galaxies in the far-infrared and submillimeter.

To put this in perspective, shown below (Fig. 1) is a 9 GHz wide portion of the high resolution spectrum of Orion-KL taken at the CSO around the CO J=6→5 line near 690 GHz [3]. A coarse resolution spectrometer would miss the smaller features and blur the CO line, decreasing its contrast. A simulation of the spectrum of the nearby infrared-luminous galaxy M82 is shown in Fig. 2, over a 40 GHz wide portion from 790 to 830 GHz containing both the CO J=7→6 and CI transitions. Even at a spectral resolution of 1000, the lines are resolved.

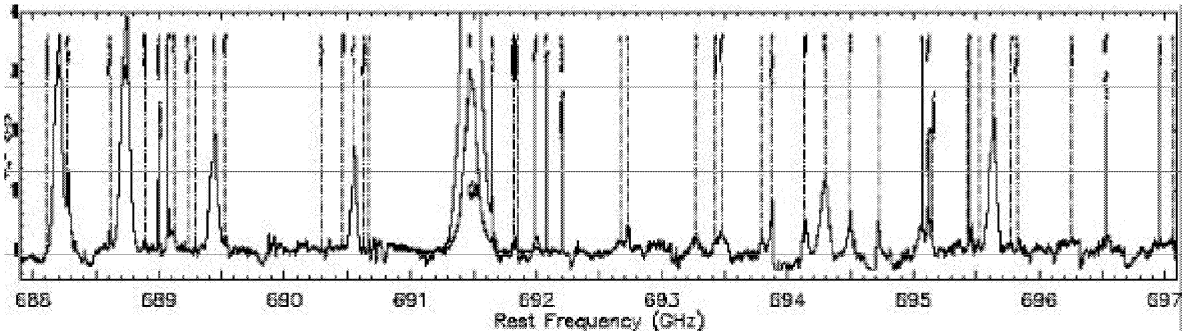

FIGURE 1. Spectrum of Orion between 688 and 697 GHz, showing many low brightness, narrow lines in addition to the dominant CO line.

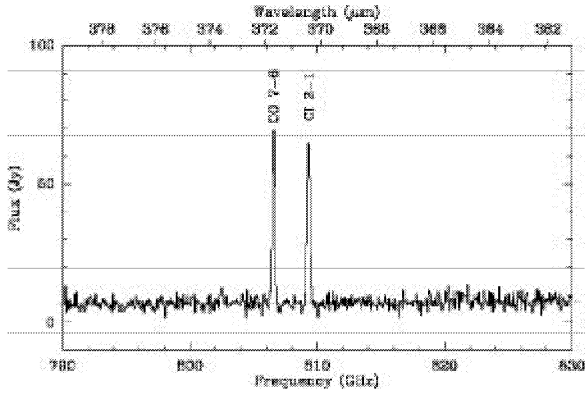

FIGURE 2. Simulated spectrum of M82 between 790 and 830 GHz, showing only the continuum and emission from CO and CI.

The Fabry-Perot Interferometer Bolometer Research Experiment, FIBRE, is an instrument designed to demonstrate a suite of advanced technologies suitable for sensitive detection of far-infrared light. This includes superconducting transition edge sensor (TES) bolometers, SQUID multiplexed amplifiers, and a cryogenic Fabry-Perot interferometer. These components are being developed for the SOFIA imaging Fabry-Perot spectrometer SAFIRE and for a complement of ground-based instruments.

Heterodyne spectrometers have been developed with noise only a few times the quantum limit at frequencies near 1THz. This is a noise temperature of order 100K. However, the photon noise from Mauna Kea in good weather using a spectral resolution of 1000 is about 46K. It is clear that in this case – indeed, whenever the instrument sees low photon occupation number – lower noise can be achieved with direct detection than with heterodyne detection [4].

INSTRUMENT DESIGN

Superconducting TES Bolometers and SQUID Amplifiers

The superconducting TES bolometer has been developed for use at wavelengths from the submillimeter to X-rays. It combines high speed with high sensitivity and can be read out by SQUID amplifiers, which are well suited to multiplexing. Unfortunately, the development of these detectors is too detailed to discuss at length here [5,6], but the overall technology was summarized at the 12th Terahertz Technology Symposium [7]. The FIBRE bolometers were used in the laboratory to demonstrate that multiplexed detection using the NIST-designed SQUID multiplexer of Chervenak et al. [6] was possible [8]. Further measurements, as presented by Staguhn et al. [9], have verified that the noise performance of these amplifiers is limited by detector Johnson noise contributions (e.g., amplifier noise is still below both phonon and photon noise in an appropriately designed detector) as predicted by theory.

FIBRE features two 1×8 monolithic bolometer arrays consisting of 1 mm×1 mm absorbers with a 50 μm×150 μm Mo/Cu bilayer TES. This is shown in Fig. 3.

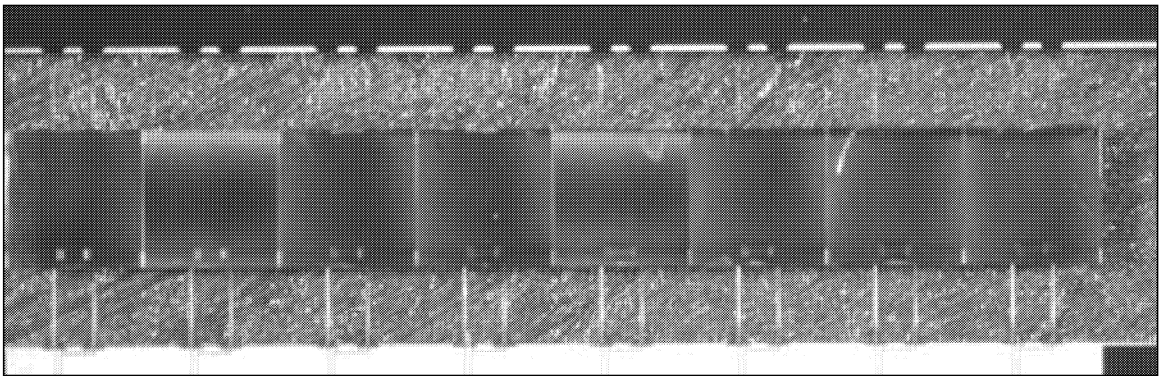

FIGURE 3. Photograph of a single 1×8 monolithic bolometer array. Each 1 mm×1 mm pixel is a 1 μm thick silicon membrane supported by 4 legs approximately 5 μm wide. The TES is the small pale rectangle at the bottom center of each detector.

The principal of operation of the superconducting bolometer is relatively straightforward, and similar to conventional semiconducting bolometers. A small, thermally isolated thermistor receives heat input from incident radiation and electrical bias power; the sum of these powers determines its temperature above the bath temperature (Fig. 4). The electrical bias power is simply $P=V^2/R$, where the resistance R depends strongly on the temperature, as shown in Fig. 5. When the incident radiation increases, the temperature rises and R increases dramatically. This causes the bias power to drop, sending the device back to the same temperature. This effect, called electrothermal feedback, is instrumental in improving the response speed, stability, linearity, and noise properties of superconducting bolometers. The noise can be made phonon-limited, where the noise equivalent power is $NEP^2=4kT^2G$. This noise power can be converted into a noise temperature using $T_N = NEP/(2kv\Delta v)$ [10]. We have tested bolometers yielding noise temperatures of ~30K at frequencies of ~1THz, when operated from a ^{3}He bath, and with response times of <2ms.

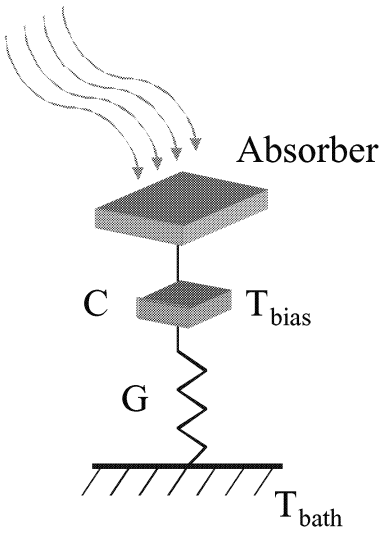

FIGURE 4. Diagram of the principal of operation of a bolometer.

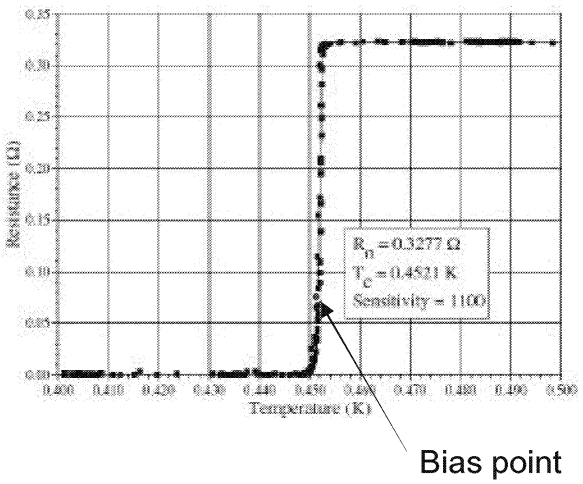

FIGURE 5. Operation of a superconducting thermistor with a sharp R vs. T curve.

Optical Design

The optical design uses a single Fabry-Perot etalon followed by an order-sorting grating [11]. The grating is blazed to operate in its first order, which is broad enough to transmit orders 40-45 of the Fabry-Perot for 350μm operation and orders 32-35 for 450μm operation. The grating disperses these Fabry-Perot orders along the array such that they are separated onto adjacent sets of pixels with only slight overlap. In this manner, a spectrum consisting of several orders of the Fabry-Perot is collected simultaneously. This configuration permits spectral multiplexing by using multiple detectors, since the detectors themselves have no spectral resolving power. By stepping the Fabry-Perot over one free spectral range, a complete spectrum is accumulated. The layout of the optics and a picture of the partially assembled optical system are shown in Fig. 6. The entire assembly is shown in Fig. 7, with the detector array package and all optical/magnetic baffles in place.

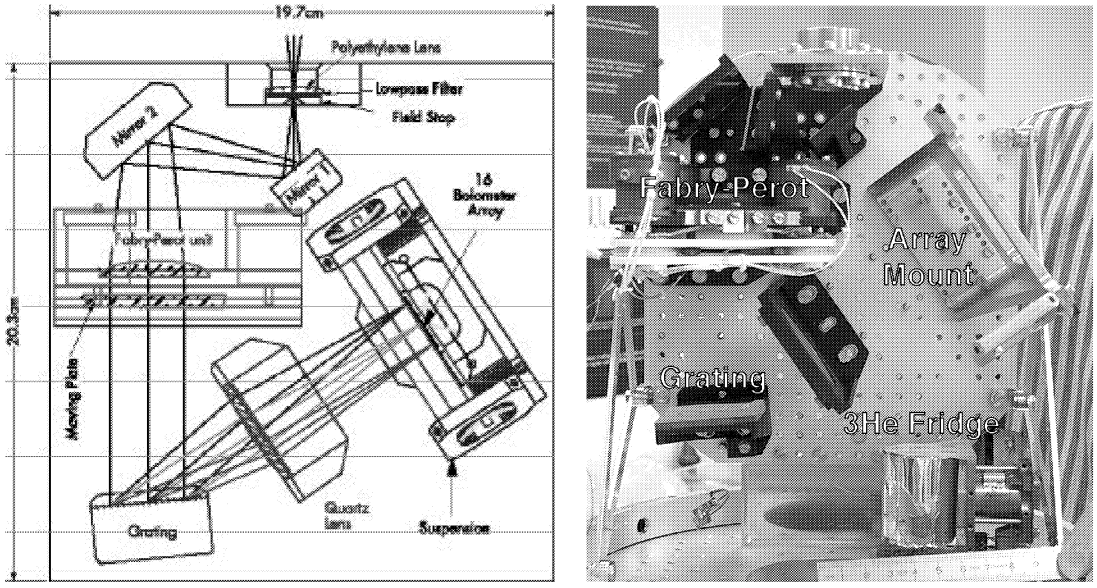

FIGURE 6. (Left) Diagram of spectrometer optics, showing three orders being dispersed onto the bolometer array. (Right) Optics being assembled, with the detector array and baffles yet to be added.

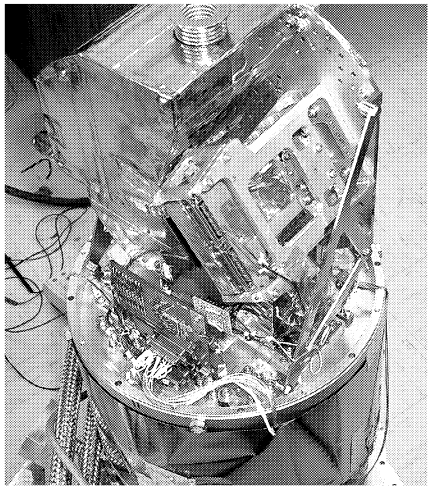

FIGURE 7. Illumination pattern of the Fabry-Perot/grating optics onto a 24-element detector array.

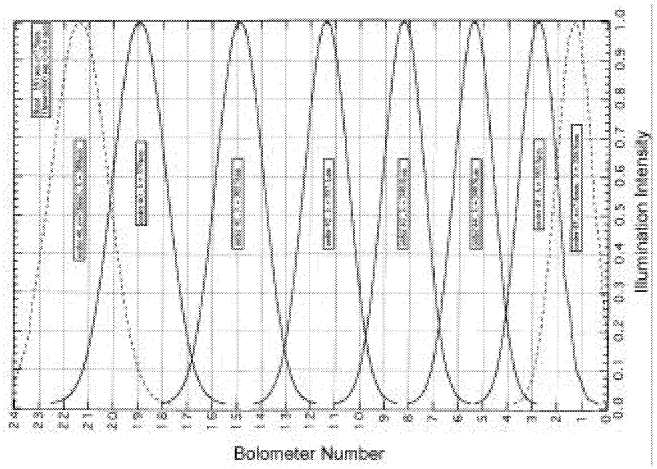

FIGURE 8. Illumination pattern of the Fabry-Perot/grating optics onto a 24-element detector array.

Instantaneously, the five to six orders are dispersed across the detector array. This illumination pattern is shown in Fig. 8. As the Fabry-Perot modulates the incident wavelengths, the peaks shift slightly, but less than two pixels width. The optics were designed to allow up to 24 pixels to be used, which cover either of the two observing bands as available from Mauna Kea. At the present, only 16 pixels are available in two groups of 8, with a gap of 3 pixels width between them. The array can be shifted in steps of 5 pixels to enable the entire band to be covered.

Commissioning Observations

FIBRE was delivered to the Caltech Submillimeter Observatory (CSO) on Mauna Kea, Hawai'i in May-June 2001. During six nights of poor weather, the instrument was operated and found to work very well. The bolometers were read out in multiplexed fashion (Fig. 9). This scan was taken while tuning the Fabry-Perot and observing a local oscillator source. The signal is seen strongly on one channel and weakly in others, demonstrating good optical performance for spectroscopy. The position of the Fabry-Perot is also shown. Those bolometers that were illuminated at a given Fabry-Perot tuning were found to have about 20 times the noise of the dark bolometers. The expected photon noise contribution is approximately 10 times the intrinsic (phonon + Johnson) noise of the detectors, so the system noise is near the theoretical performance and the bolometers are background-limited with a net NEP of 3×10^{-17} W/√Hz.

A spectrum (Fig. 10) was taken using a local oscillator source operating at 372μm (807GHz). The spectral resolving power was measured to be 1200, for a velocity resolution of 250 km/s, as predicted from the known performance of the Fabry-Perot. The Fabry-Perot spectrum follows an Airy function to within a few percent, with no detectable excess crosstalk. As seen in the illumination pattern in Fig. 8, there is some optical crosstalk induced by the grating.

The opacities at the zenith during the observing run were measured by skydips using both FIBRE and the CSO facility 350 μm taumeter. These measurements yielded zenith opacities of $\tau_{350\mu m}$~4 during most of the run. A representative skydip under the best conditions seen is shown in Fig. 11. In this case, we found $\tau_{372\mu m}$ ~3.0±0.3 measured using FIBRE operating at 372μm.

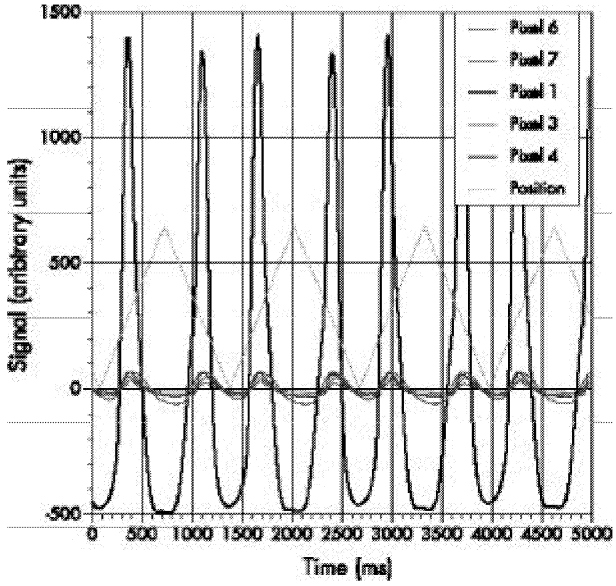

FIGURE 9. Multiplexed readout of the FIBRE bolometers.

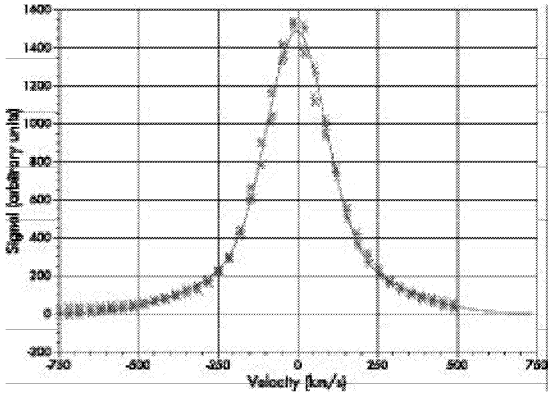

FIGURE 10. Velocity calibration spectrum at 372 μm (807 GHz).

No scientific data could be taken in such poor conditions, but in order to demonstrate a multiplexed detection using TES bolometers, we observed the limb of the Moon at 365μm. The secondary mirror was nutated to subtract the atmosphere, so we obtained a high signal-to-noise detection of the Moon emission despite a transmission of ~1% (Fig. 12). The signal was demodulated and a signal-to-noise measured for each of the 11 scan positions. Each data point contains 3 seconds of on-source time. When pointing at the limb of the Moon, the chopping demodulation results in a difference signal between the Moon and the background sky.

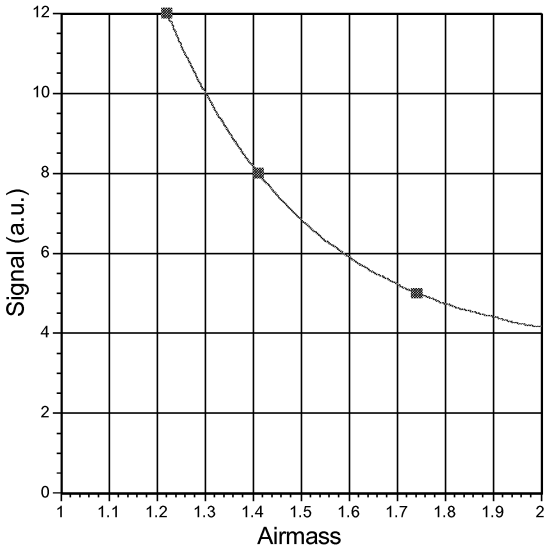

FIGURE 11. Skydip showing $\tau_{372\,\mu m}$~3.

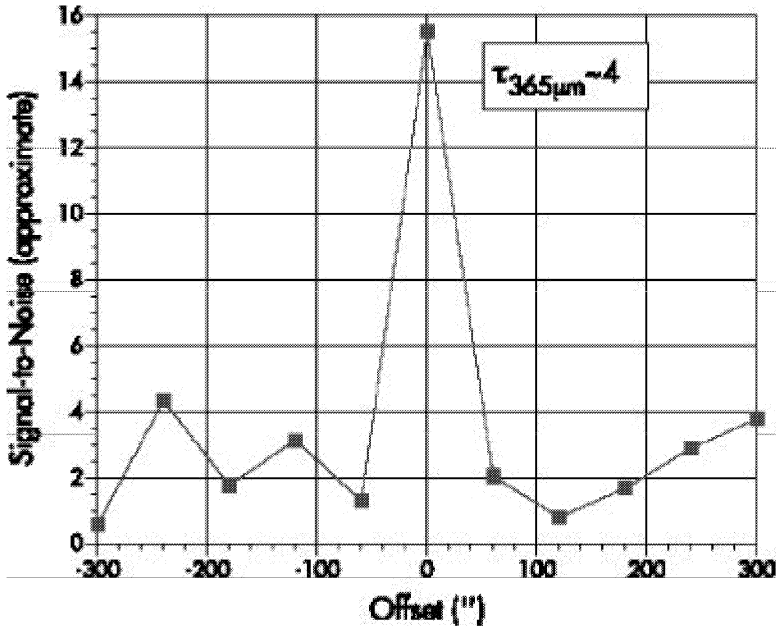

FIGURE 12. Detection of the limb of the Moon, taken while chopping so that a signal is seen only when exactly on the limb.

With the initial observations and instrument checkout, it is possible to predict the sensitivity of FIBRE to extragalactic line emission. First, a model of the atmosphere is used to estimate the noise equivalent flux (NEF) as a function of the 225 GHz opacity (Fig.

13). Second, assumptions about the total flux in a line from a galaxy is estimated, resulting in a minimum observation time calculation (Fig. 14).

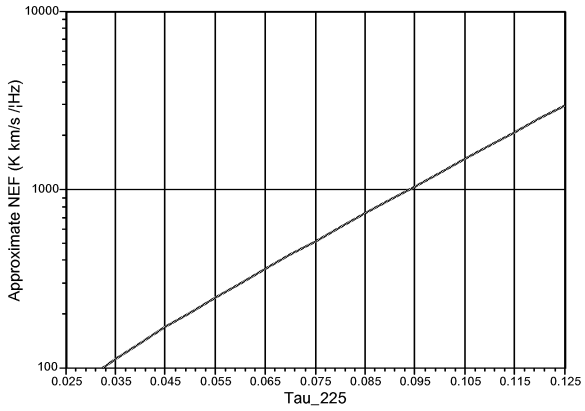

FIGURE 13. Prediction of the noise equivalent flux as a function of 225 GHz opacity.

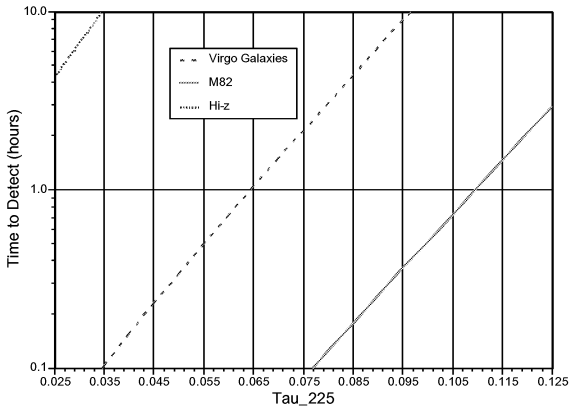

FIGURE 14. Time required to detect galaxy emission lines, as a function of 225 GHz opacity.

CONCLUSION

FIBRE achieved first light at the CSO, detecting the Moon at 365μm in bad weather with an atmospheric transmission of ~1%. The spectrometer was operating with a spectral resolving power of ~1200, and the signal amplitude and noise were consistent with expectations. The TES bolometer and SQUID multiplexer technology has been thus validated in an astronomical application. The use of a direct detector in a high resolution spectrometer permits the testing of detectors with lower noise than is required for ground-based continuum instruments, thereby validating technology more suitable for space-based instruments. This work is a first step in the direction of placing superconducting bolometer arrays on a cryogenic space telescope, with the promise of orders of magnitude improvement in science output over previous missions. Because this is only a first step, much work remains to be done on all aspect of the system. We anticipate future observations to study galaxies in the fine-structure line of CI and the CO rotational lines, and to continue to refine the multiplexed TES detectors in astronomical applications.

ACKNOWLEDGMENTS

We thank the staff of the CSO and our co-observers for making the observations described here possible; their support was crucial in the commissioning of FIBRE. We owe a debt of gratitude to many at NASA/GSFC, Caltech, IAS, and NIST for their contributions to FIBRE hardware and software.

REFERENCES

1. Benford, D.J., Cox, P., Omont, A., Phillips, T.G. & McMahon, R.G., ApJ L518, 65 (1999).
2. Blain, A.W., Frayer, D.T., Bock, J.J., & Scoville, N.Z., MNRAS 313 (3), 559-570 (2000).
3. Schilke, P., Benford, D. J., Hunter, T. R., Lis, D. C., & Phillips, T. G., ApJS 132, 281 (2001)
4. Zmuidzinas, J., in "New Concepts for Far-Infrared and Submillimeter Space Astronomy", Leisawitz & Benford, eds., in press
5. Benford, D.J. et al., ASP Conference Series 217, 134-139 (1999).
6. Chervenak, J.A, et al, Appl. Phys. Letters 74 (26), 4043 (1999).
7. Benford, D.J., et al., Proceedings of 12th International Symposium on Space Terahertz Technology, JPL Publication 01-18, p.122
8. Benford, D.J., et al., Int. J. IR MM Waves 21 (12), 1909-1916 (2000).
9. Staguhn, J.G., et al., in "Low Temperature Detectors", F.S. Porter et al., eds., AIP Conference Proceedings #605, p.321.
10. Phillips, T.G. 1988, in "Millimetre and Submillimeter Astronomy", Wolstencroft & Burton, eds., p.1
11. Maffei, B., et al., Infrared Physics & Technology 35, 321 (1994).

Critical Temperature Dependence of Heterodyne Mixing in Superconducting Nb based Hot-Electron Bolometers

I. Siddiqi and D.E. Prober
Department of Applied Physics, Yale University, 15 Prospect Street, New Haven, Connecticut 06520-8284

B. Bumble and H.G. LeDuc
Center for Space Microelectronics Technology, Jet Propulsion Laboratory, Caltech, Pasadena, California 91109

Nb hot-electron bolometers (HEBs) with critical temperature T_c = 5 to 6 K have previously demonstrated good heterodyne mixing performance at THz frequencies. HEBs with a lower critical temperature are predicted to have improved performance with lower noise. We present microwave (30GHz) mixing measurements on Nb HEB mixers with T_c between 1.4 and 5.3 K. The reduced T_c is obtained by application of a magnetic field, or by use of a bi-layer microbridge of Nb and Au with T_c = 1.6 K. The mixer output noise and voltage range of low mixer noise are observed to decrease approximately linearly with reduction of T_c. The Nb-Au mixer has a mixer noise temperature $\overline{T}_M$ = 50K (DSB) with reasonable dynamic range, and thus is promising for future single pixel and array receivers for THz spectroscopy.

Heterodyne spectroscopy at terahertz frequencies is a sensitive tool for identifying molecular species important in star formation and in atmospheric chemistry processes.[1] Hot-electron bolometer (HEB) mixers are well suited for such space-borne and ground-based astronomical applications. Unlike superconductor-insulator-superconductor (SIS) mixers, the HEB is not limited by the superconducting energy gap frequency and can operate at several terahertz.[2,3] Also, diffusion-cooled HEB mixers can have very large intermediate frequency (IF) bandwidths; up to 9 GHz has been demonstrated.[4] HEB mixers are considerably more sensitive than Schottky diode mixers, which have been used for higher frequency applications where SIS mixers are limited by the gap frequency or by RF losses.

The HEB mixer consists of a narrow, thin superconducting microbridge contacted with thick normal-metal films; see Fig. 1. The microbridge operates in the resistive state, due to application of local oscillator (LO) power and DC bias. When the RF signal is applied, the electron temperature of the microbridge (and thus the device resistance) oscillates at the IF. The IF bandwidth is determined by the inverse of the thermal relaxation time for cooling the hot electrons in the microbridge.[5,6] Diffusion-cooled Nb mixers use hot-electron out-diffusion for cooling.[6] These have demonstrated very low noise at 2.5 THz with receiver noise temperature T_R = 1800 K (DSB).[4] The mixer noise temperature T_M is estimated to be 350 K (DSB) for a similar device measured also at 2.5 THz.[7] NbN phonon-cooled mixers also have good performance.[3,8]

Diffusion-cooled HEB mixers consisting of a superconductor with lower critical temperature (T_c) are predicted to have improved performance.[9,10] In optimized HEBs, thermal fluctuation noise is

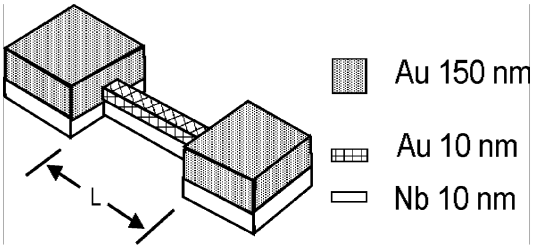

Figure 1: Superconducting mixer geometry for the Nb-Au HEB, device B. The thin layer of Au above the Nb lowers the T_c of the microbridge. The Nb HEB mixer, device A, has no gold layer on top of the microbridge.

the dominant noise source neglecting quantum effects. In this case, T_M is predicted to decrease linearly with T_c.[11] Another advantage of lowering the microbridge T_c is that the required LO power decreases. The LO power for a diffusion cooled mixer is predicted to be [12] $P_{LO} \approx (4\mathcal{L}/R)(T_c^2-T^2)$, where $\mathcal{L} = 2.45\text{x}10^{-8}$ W-Ω/K^2 is the Lorenz constant, R is the electrical resistance, and T is the temperature of the normal banks. For optimum performance one has $T << T_c$, and thus $P_{LO} \propto T_c^2$, being in the range 1 – 30 nW. Since output power from solid state LO sources at terahertz frequencies may be limited to μW, a mixer with a small required P_{LO} is desired, especially for space-borne missions and large format arrays.

A HEB mixer with reduced T_c should have improved performance, but will also be more susceptible to saturation effects that degrade T_M. Such effects can be important in a THz receiver but are negligible in the microwave measurements. T_M is given by T_M (DSB) = T_{out} / 2η, with η the conversion efficiency and T_{out} the output noise temperature. T_M is minimum only over a finite voltage range but then increases due to the decrease of η. Input saturation will occur when the absorbed RF background power is ~ 0.2 P_{LO} , as this reduces η.[13,14] Output saturation is due to RF background power downconverted to the IF which causes the voltage to deviate far from the optimum bias voltage. We characterize the voltage range for which T_M remains within a factor of two of its lowest value as ΔV_{opt}. Simulations we have conducted[13] using a discretized model for the microbridge[15] suggest that ΔV_{opt} will scale approximately linearly with T_c, for the simple case where the contacts to the microbridge do not perturb the superconductivity in the microbridge. This is the case for Nb devices. (In the case of Al HEBs,[13,16,17] the voltage range is further reduced due to contact effects.) The value $\bar{T}_M$ we report in the Table and Fig. 3 below is an average of T_M over the 20μV interval of bias voltage for which this average is lowest. This definition provides a more realistic value of the expected mixer noise temperature in a receiver where averaging due to background noise or bias variations might be present.

We report here on two Nb HEBs. The first, a Nb HEB, device A, was fabricated at JPL. Similar devices were previously measured in zero magnetic field at 20, 600, 1200, and 2500 GHz. [4,7,18-20] The dimensions are 0.08μm wide, 10 nm thick, and length L= 0.24μm. T_c in zero field is 5.3 K and is reduced to 1.4 K by applying a perpendicular magnetic field. The IF bandwidth is 1.4 GHz. The Nb-Au HEB, device B, was fabricated at Yale using double angle deposition.[21] A thin bilayer resist is used as the liftoff stencil. A thin (10 nm) Nb film is first sputter deposited at normal incidence, followed by Au which is sputter deposited at a 45 degree angle. A thick layer of gold deposits on the contacts, mak-

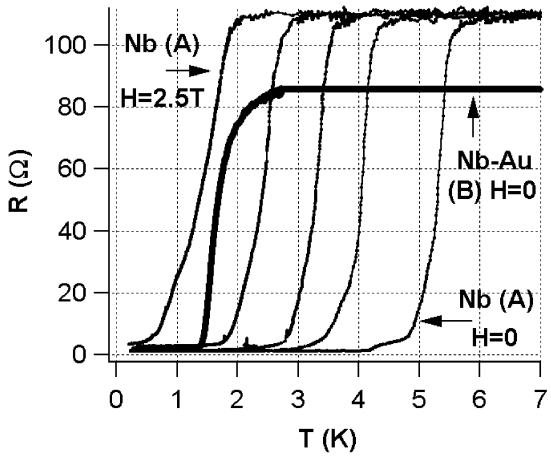

Figure 2: Resistance vs. temperature curves for the Nb HEB, device A, with H=0,1,1.5,2,2.5T and the Nb-Au HEB, device B, in zero magnetic field.

ing them non-superconducting, and a thin layer of Au (about 10 nm) deposits on top of the Nb microbridge, lowering its T_c. The Nb-Au HEB is 0.20 μm wide and L = 0.48μm. T_c in zero applied magnetic field is 1.6K. The measured IF bandwidth is 1.2 GHz, consistent with that predicted from the length and diffusion constant (determined from H_{c2}). R(T) curves are given in Fig. 2 for the Nb HEB, device A, in various magnetic fields and for the Nb-Au HEB in zero field, device B. A third device, a Nb HEB was also studied. Some of its properties were previously reported.[14] It followed the trends of device A. However, it displayed a two-step transition in zero field, which broadened dramatically with application of a field. Its noise was about twice that of the Nb HEB, device A, which we ascribe to the unusual transition shape. We therefore do not list that device. The measurements use a liquid ^{3}He cryostat equipped for microwave mixing measurements up to 40 GHz, at T = 0.2 K. Temperatures up to $(1/2)T_c$ could be used without significant performance degradation. For each value of T_c, the LO power and DC power is adjusted to optimize for the conversion efficiency. Microwave measurements are employed for their rapid turnaround, low background noise, and ease of calibration. Past studies of Nb devices[18] showed reasonable correlation between such microwave measurements and THz mixing results. A summary of the device parameters is presented in the Table. T_{out} and η are measured at 1.4 GHz, and values listed in Table I are those extrapolated to IF = 0 using the established frequency dependence. The values of $\bar{T}_M$ in the Table and Fig. 3 are at IF = 1.4 GHz.

Achieving low mixer noise is the key. The minimum $\bar{T}_M$ for both devices is given as a function of T_c in Fig. 3. For device A, $\bar{T}_M$ decreases linearly with the reduction of T_c, down to $T_c \sim 3$ K, and then increases for lower values of T_c. The decrease of $\bar{T}_M$ with reduction of T_c is consistent with theoretical expectations, and results simply from the reduction of thermal fluctuations if η is independent of T_c. Specifically, the theory in Ref. 11 predicts $T_M \sim T_c$ when operating with very small conversion loss and thermal fluctuations dominating all other noise processes. We observe a linear decrease in mixer noise temperature with T_c, as predicted, but with larger conversion loss (maximum conversion efficiency η = −11 dB). The reason for the increase of T_M for device A for $T_c < 3.3$ K is the reduction of η for applied fields of 2 and 2.5 T, for T_c = 2.4 and 1.4 K respectively (see Table). This reduction of η likely results from the very small critical currents obtained at the largest fields (0.5 μA at 2.5 T), indicating non-uniform superconductivity occurs at the largest fields. This can be seen in Fig 2, where the resistive transitions at 2 and 2.5 T are seen to

Table I: Nb HEB mixer parameters. The conversion efficiency and output noise reported are IF=0 values. The $\bar{T}_M$ listed is the minimum averaged over 20μV, as also in Fig. 4.

Device	T_c (K)	H (T)	$I_c(0)$ (μA)	T_{output} (K)	η (dB)	$\bar{T}_M$ (K)	ΔV_{opt} (μV)
(A) Nb	5.3	0	100	26	-11	170	200
	4.0	1.0	13	16	-11	110	135
	3.3	1.5	7	14	-11	95	130
	2.4	2.0	4	10	-15	180	90
	1.4	2.5	0.5	4	-20	250	40
(B) Nb-Au	1.6	0	14	3	-12.5	50	130

have very large fractional temperature widths. The small critical current at 2.5 T of device A, 0.5 μA, can be compared with the critical current of the Nb-Au device which has a similar T_c, for which I_c = 14 μA. For the Nb-Au HEB, larger conversion efficiency results and $\bar{T}_M$ = 50 K. P_{LO} for the Nb-Au HEB is 2 nW compared to 0.4nW for device A at T_c = 1.4 K. The resistive transition of this Nb-Au device, in Fig. 2, is more uniform and narrower than device A at 2.5 T. We believe that the relatively large critical current, low mixer noise, $\bar{T}_M$ = 50 K (DSB), and relatively good conversion efficiency (η = -12.5 db) are characteristic of a reduced-T_c device with a sharp transition. Another Nb-Au device has similar properties to device B.

For a practical mixer, low noise operation must be achievable over a reasonable operating range. The IV curve and T_M as a function of bias voltage are shown for the Nb-Au, device B, in Fig. 4. The IV curves are for P_{LO} = 0 and for P_{LO} = 2 nW, the absorbed power which gives the

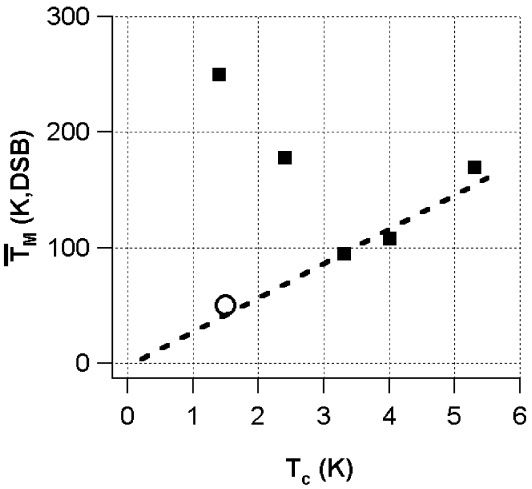

Figure 3: Mixer noise temperature from Table I for devices A (squares) and B (circle) as a function of T_c. T_{bath}= 0.2K. The dashed line is the expected linear decrease in noise temperature resulting from a decrease in thermal fluctuations.

minimum value of T_M. The critical current when increasing the voltage is 14 μA; small thermal hysteresis is seen in Fig. 4. The minimum T_M = 45 K, occurs just above 150 μV. We show data for T_M only for those voltages for which operation is completely stable. T_M remains below 90 K for voltages between 150 and 280 μV, giving a voltage range ΔV_{opt} = 130 μV. For P_{LO} between 2 and 4 nW, the minimum T_M remains below 50 K. For P_{LO} between 1 and 7 nW, T_M < 100 K. Thus, for array applications, small variations in the optimum P_{LO} for each element due to fabrication imperfections or pixel-to-pixel differences in the coupled P_{LO} should not result in a significant change in the noise temperature of each pixel. We list ΔV_{opt} and other microwave parameters for both devices at all fields in the Table. We see in the Table that ΔV_{opt} decreases approximately linearly with reduction of T_c for the Nb HEB.

We finally consider saturation issues. For Device A, ΔV_{opt} scales approximately linearly with T_c, as shown in the Table, in good agreement with numerical calculations.[14] These predict ΔV_{opt} ~ 100μV for a HEB with a uniform T_c = 1.6K along the length of the bridge. With the experimental value ΔV_{opt} ~ 130 μV, we estimate for the Nb-Au HEB the level of IF power which would begin to produce output saturation as approximately 40 pW at the IF. This corresponds to a background noise temperature T_{back} = 13,000 K with an IF bandwidth of 2 GHz, assuming η = -12.5 db (total RF bandwidth of 4 GHz due to both sidebands). Such a large level of background noise is not expected in typical applications.[22] Input saturation would result if the coupled broadband background noise power is comparable to P_{LO} = 2nW. For receivers with 200 GHz RF bandwidth, the incident background power is 0.5 nW for T_{back} = 200 K. The Nb-Au HEB should thus show no significant saturation effects. Overall, the Nb-Au HEB shows better performance than a Nb HEB in a magnetic field. In applications where the instantaneous RF bandwidth is very large (≥ 0.5 THz), Nb-Au devices with slightly higher T_c, for increased P_{LO}, can be used to avoid input saturation. Such devices can be produced with a thinner Au layer. Thus, the Nb-Au HEB looks very promising for THz applications with low mixer noise and very small required LO power, and should provide sufficient dynamic range for the anticipated applications.

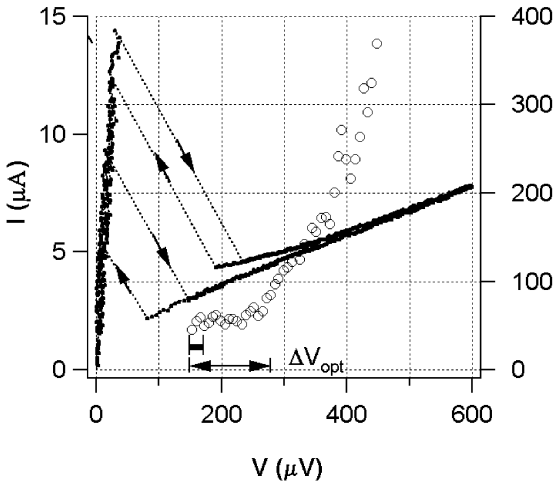

Figure 4: Mixer noise temperature and conversion efficiency for the Nb-Au HEB, device B, as a function of bias voltage. T_M is the mixer noise temperature at that voltage. The heavy bar shows the 20mV range over which the average of T_M ($\overline{T}_M$) is found.

We thank C.M. Wilson for assistance with metal deposition in the Nb-Au device fabrication, and B.S. Karasik and W.R. McGrath for useful discussions. This research was supported by the NSF AST 9618705 and the NASA Office of Space Science. Funding for I.S. was provided in part by a NASA Graduate Student Fellowship.

[1] T.G. Phillips and J. Keene, Proc. IEEE **80**, 1662 (1992).
[2] W.R. McGrath, B.S. Karasik, A. Skalare, R. Wyss, B. Bumble, and H.G. LeDuc, Proc. of the SPIE **3617**, (1999).

[3] A.D. Semenov, H-W. Hubers, J. Schubert, G. N. Gol'tsman, A. I. Elantiev, B. M. Voronov, and E. M. Gershenzon, J. Appl. Phys. **88**, 6758 (2000).
[4] R. A. Wyss, B.S. Karasik, W.R. McGrath, B. Bumble, and H.G. LeDuc, in *Proceedings of the 10th International Symposium on Space Terahertz Technology,* edited by T. Crowe and R.M. Weikle (University of Virginia, Charlottesville, VA, 1999), pp. 215-228.
[5] E. M. Gershenzon, G.N. Gol'tsman, I.G. Gogidze, Y.P. Gusev, A.I. Elantiev, B.S. Karasik, and A.D. Semenov, Superconductivity **3**, 1582 (1990).
[6] D.E. Prober, Appl. Phys. Lett. **62**, 2119 (1993).
[7] B.S. Karasik, M.C. Gaidis, W.R. McGrath, B. Bumble, and H.G. LeDuc, Appl. Phys. Lett. **71**, 1567 (1997).
[8] E. Gerecht et al., in *Proceedings of the 11th International Symposium on Space Terahertz Technology,* edited by J. East (University of Michigan, Ann Arbor, MI, 2000), pp. 209-218.
[9] B.S. Karasik and W.R. McGrath, in *Proceedings of the 9th International Symposium on Space Terahertz Technology,* edited by W.R. McGrath (Pasadena, CA, 1998), pp. 73-80.
[10] It is unclear if superconducting films are available to produce phonon-cooled mixers with lower T_c but also having adequate IF bandwidth. If such materials can be found, our arguments for reduction of T_c would also apply to these phonon-cooled devices.)
[11] B.S. Karasik and A.I. Elantiev, Appl. Phys. Lett. **68**, 853 (1996); the quantum mixer noise is $T_M^Q = h\nu/k = 48K * f(THz)$ and is negligible in the microwave experiments. HEB mixers are not yet quantum-limited in noise performance, and a decrease in noise temperature is thus predicted for devices with lower T_c, even when operating at THz frequencies where T_M^Q is larger than at 30 GHz.
[12] P.J. Burke, Ph.D. thesis, Yale University, 1997, available from authors.
[13] I. Siddiqi, A. Verevkin, R. Jahn, D.E. Prober, A. Skalare, W.R. McGrath, P.M. Echternach, and H.G. LeDuc, submitted to J. Appl. Phys. (7/2000).
[14] I. Siddiqi, D.E. Prober, B. Bumble, and H.G. LeDuc, in *Proceedings of the 12th International Symposium on Space Terahertz Technology,* edited by I. Mehdi (San Diego, CA, 2001), to be published.
[15] A. Skalare and W.R. McGath, IEEE Trans. Appl. Supercond. **9**, 4444 (1999).
[16] I. Siddiqi, A. Verevkin, D.E. Prober, A. Skalare, W.R. McGrath, P.M. Echternach, and H.G. LeDuc, IEEE Trans. Appl. Supercond. **11**, 958 (2001).
[17] A. Skalare, W.R. McGrath, P.M. Echternach, H.G. LeDuc, I. Siddiqi, A. Verevkin, and D.E. Prober, IEEE Trans. Appl. Supercond. **11**, 641 (2001).
[18] P.J. Burke, R.J. Schoelkopf, D.E. Prober, A. Skalare, B.S. Karasik, M.C. Gaidis, W.R. McGrath, B. Bumble, and H.G. LeDuc, J. Appl. Phys. **85**, 1644 (1999).
[19] A. Skalare, W.R. McGrath, B. Bumble, H.G. LeDuc, P.J. Burke, A.A. Verheijen, and D.E. Prober, IEEE Trans. Appl. Supercond. **5**, 2236 (1995).
[20] A. Skalare, W.R. McGrath, B. Bumble, and H.G. LeDuc, IEEE Trans. Appl. Supercond. **7**, 3568 (1997).
[21] P.M. Echternach, H.G. LeDuc, A. Skalare, and W.R. McGrath, in *Proceedings of the 10th International Symposium on Space Terahertz Technology,* edited by T. Crowe and R.M. Weikle (University of Virginia, Charlottesville, VA, 1999), pp. 261-268.
[22] In contrast to these results for Nb and Nb-Au, we find for Al HEBs that output saturation at the IF is a significant issue. A large fraction of the microbridge (up to 50%) is made non-superconducting even at T = 0 by the normal contacts, so that $\Delta V_{opt} < 10\ \mu V$ for a typical Al HEB. This is consistent with our simulations.

Terahertz Initiatives at the Antarctic Submillimeter Telescope and Remote Observatory (AST/RO)

Antony A. Stark, Adair P. Lane, Christopher L. Martin (SAO),
Richard A. Chamberlin, Jacob Kooi (Caltech),
and Christopher K. Walker (U. Arizona)

ABSTRACT

The Antarctic Submillimeter Telescope and Remote Observatory (AST/RO) is a 1.7-meter diameter offset Gregorian instrument located at the NSF Amundsen-Scott South Pole Station. This site is exceptionally dry and cold, providing opportunities for Terahertz observations from the ground. Preliminary analysis of recent site testing results shows that the zenith transparency of the 1.5 THz atmospheric window at South Pole frequently exceeds 10% during the Austral winter. Routine observations at 810 GHz have been conducted over the past two years, resulting in large-scale maps of the Galactic Center region and measurements of the ^{13}C line in molecular clouds. During the next two years, the observatory plans to support two Terahertz instruments:

1) TREND (*Terahertz Receiver with Niobium Nitride Device*—K. S. Yngvesson, University of Massachusetts, P. I.), and

2) SPIFI (*South Pole Imaging Fabry-Perot Interferometer*—G. J. Stacey, Cornell University, P. I.).

AST/RO could be used in future as an observational test bed for additional prototype Terahertz instruments. Observing time on AST/RO is available on a proposal basis (see `http://cfa-www.harvard.edu/~adair/AST_RO`).

I. The AST/RO Instrument

The Antarctic Submillimeter Telescope and Remote Observatory (AST/RO) is an instrument routinely used for the measurement of submillimeter-wave spectral lines over regions several square degrees in size toward the Milky Way and Magellanic Clouds. AST/RO is a 1.7m diameter offset Gregorian telescope, with optics designed for wavelengths between 200 μm and 3 mm. All of the optics in AST/RO are offset for high beam efficiency and avoidance of inadvertent reflections and resonances. The design of

AST/RO is described in Stark et al. (1997) . AST/RO site testing, logistics, capabilities, and observing techniques are described in Stark et al. (2001).

Currently, there are five heterodyne receivers mounted on an optical table suspended from the telescope structure in a spacious (5m $\times$ 5m $\times$ 3m), warm Coudé room:

1. a 230 GHz SIS receiver, 85 K double-sideband (DSB) noise temperature (Kooi et al. 1992);
2. a 450–495 GHz SIS quasi-optical receiver, 165–250 K DSB (Engargiola et al. 1994, Zmuidzinas & LeDuc 1992);
3. a 450–495 GHz SIS waveguide receiver, 200–400 K DSB (Walker et al. 1992, Kooi et al. 1995), which can be used simultaneously with
4. a 800-820 GHz fixed-tuned SIS waveguide mixer receiver, 950–1500 K DSB (Honingh et al. 1997);
5. an array of four 800-820 GHz fixed-tuned SIS waveguide mixer receivers, 850–1500 K DSB (the PoleSTAR array, see `http://soral.as.arizona.edu/pole-star` and Groppi et al. 2000).

Spectral lines observed with AST/RO include: CO $J = 2 \rightarrow 1$, CO $J = 4 \rightarrow 3$, CO $J = 7 \rightarrow 6$, HDO $J = 1_{0,1} \rightarrow 0_{0,0}$, [C I] $^3P_1 \rightarrow {}^3P_0$, [C I] $^3P_2 \rightarrow {}^3P_1$, and [^{13}C I] $^3P_2 \rightarrow {}^3P_1$. A proposal is currently pending to the Smithsonian Institution to purchase a local oscillator to cover 650–700 GHz, a frequency range which includes the ^{13}CO $J = 6 \rightarrow 5$ line. There are four currently available acousto-optical spectrometers (AOS), all designed and built at the University of Cologne (Schieder et al. 1989): two low-resolution spectrometers with a bandwidth of 1 GHz (bandpass 1.6–2.6 GHz); an array AOS having four low resolution spectrometer channels with a bandwidth of 1 GHz (bandpass 1.6–2.6 GHz) for the PoleSTAR array; and one high-resolution AOS with 60 MHz bandwidth (bandpass 60–120 MHz).

AST/RO has been open to proposals from the general astronomical community since 1997. AST/RO research is a three part effort, where approximately equal time is given to each of these initiatives:

1. large-scale surveys of regions of general interest: the Galactic Center and the Magellanic Clouds;
2. support of observations of special interest, through observing proposals solicited from the worldwide astronomical community;
3. support of technology development, by making the telescope available for installation and trial of novel detectors, especially detectors at Terahertz frequencies.

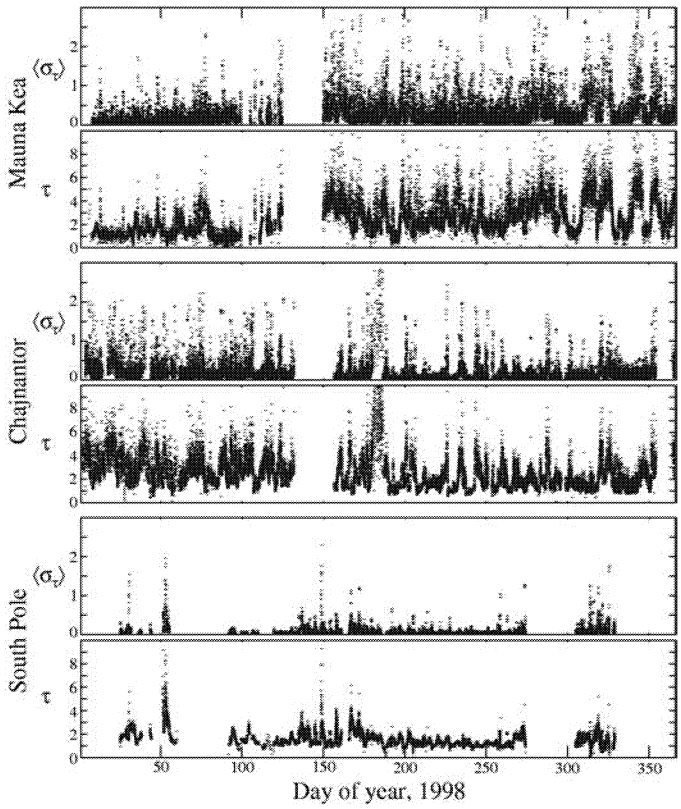

Fig. 1: **Sky Noise and Opacity Measurements at 350 μm from Three Sites.** These plots show data from identical NRAO-CMU 350 μm broadband tippers (Radford & Peterson, unpublished data) located at Mauna Kea, Hawaii; the ALMA site at Chajnantor, Chile; and South Pole during 1998. The upper plot of each pair shows $\langle\sigma_\tau\rangle$, the rms deviation in the opacity τ during a one-hour period—a measure of sky noise on large scales; the lower plot of each pair shows τ, the broadband 350 μm opacity. The first 100 days of 1998 on Mauna Kea were exceptionally good for that site. During the best weather at the Pole, $\langle\sigma_\tau\rangle$ was dominated by detector noise rather than sky noise.

II. Site Testing

The South Pole is an excellent millimeter- and submillimeter-wave site (Lane 1998, Chamberlin & Bally 1994, Chamberlin et al. 1997, Chamberlin 2002). It is unique among observatory sites for unusually low wind speeds, absence of rain, and the consistent clarity of the submillimeter sky. Schwerdtfeger (1984) has comprehensively reviewed the climate of the Antarctic Plateau and the records of the South Pole meteorology office. Chamberlin (2001) has analyzed weather data to determine the precipitable water vapor (PWV) and finds median wintertime PWV values of 0.3 mm over a 37-year period, with little annual variation. *PWV values at South Pole are small, stable, and well-understood.*

Submillimeter-wave atmospheric opacity at South Pole has been measured using skydip techniques. We made over 1100 skydip observations at 492 GHz (609 μm) with AST/RO during the 1995 observing season (Chamberlin et al. 1997). Even though this frequency is near a strong oxygen line, the opacity was below 0.70 half of the time during the Austral winter and reached values as low as 0.34, better than ever measured

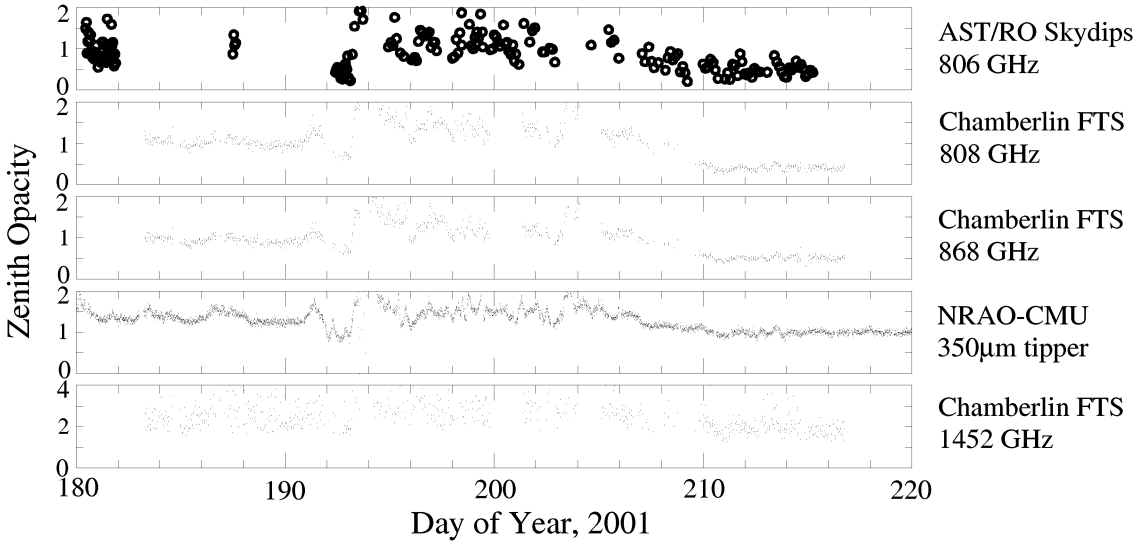

Fig. 2: **Simultaneous Opacity Measurements from Three Instruments at the South Pole.** These plots show data from AST/RO skydips, the NRAO-CMU 350 μm broadband tipper (Radford & Peterson, unpublished data), and a submillimeter-wave Fourier Transform Spectrometer (FTS, Chamberlin 2002) in July and early August of 2001. The AST/RO data are from skydips taken for calibration purposes during observations; they agree well with the FTS measurements at 808 GHz. The FTS measurements at 868 GHz are shown for comparison with the NRAO-CMU broadband measurements, which are centered at that frequency. Note that the NRAO-CMU tipper values are monotonically related to the FTS measurements, but show an offset and compression of scale. The bottom plot shows a preliminary reduction of FTS measurements at 1.452 THz, and indicates $\tau < 2$ for a significant fraction of the time. Usually August and September are the best months at the Pole; these observations unfortunately had to be stopped early because of insufficient liquid helium supplies.

at any ground-based site. The stability was also remarkably good: the opacity remained below 1.0 for weeks at a time. From early 1998, the 350μm band has been continuously monitored at Mauna Kea, Chajnantor, and South Pole by identical tipper instruments developed by S. Radford of NRAO and J. Peterson of Carnegie-Mellon U. and the Center for Astrophysical Research in Antarctica (CARA). Results from Mauna Kea and Chajnantor are compared with South Pole in Figure 1. *The 350μm opacity at the South Pole is consistently better than at Mauna Kea or Chajnantor.*

A new Fourier Transform Spectrometer developed by R. Chamberlin and collaborators was operational at the Pole during some of the winter of 2001. This instrument measures a broadband spectrum covering 300 GHz to 2 THz as a function of airmass

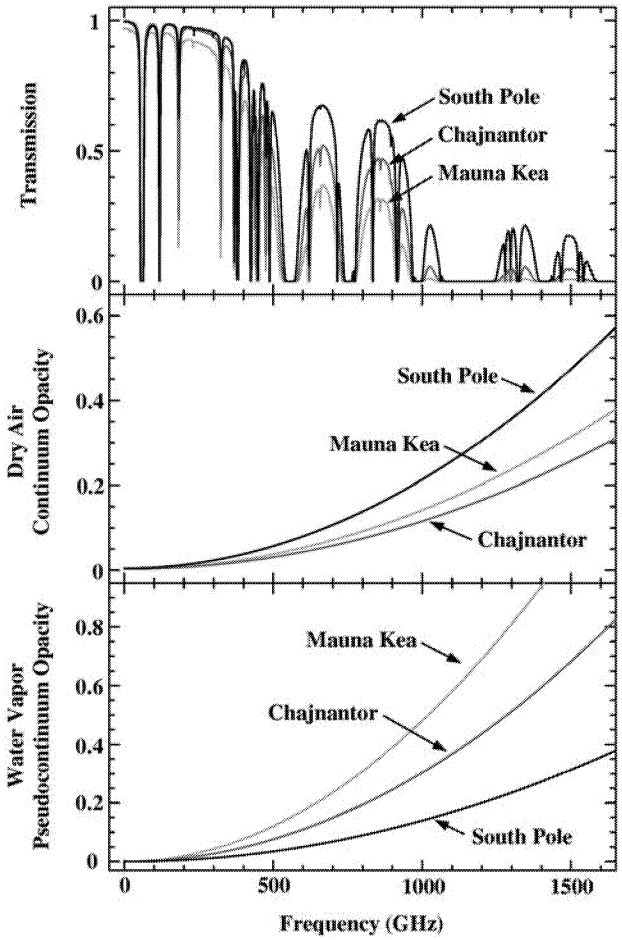

Fig. 3: **Calculated atmospheric transmittance at three sites.** The upper plot is atmospheric transmittance at zenith calculated by J. R. Pardo using the ATM model (Pardo et al. 2001). The model uses PWV values of 0.2 mm for South Pole, 0.6 mm for Chajnantor and 0.9 mm for Mauna Kea, corresponding to the 25^{th} percentile winter values at each site. Note that at low frequencies, the Chajnantor curve converges with the South Pole curve, an indication that 225 GHz opacity is not a simple predictor of submillimeter wave opacity. The middle and lower plots show calculated values of dry air continuum opacity and water vapor pseudocontinuum opacity for the three sites. Note that unlike the other sites, the opacity at South Pole is dominated by dry air rather than water vapor.

several times each hour. Some of these data are shown in Figure 2. The zenith transparency at 1.452 THz (near an important [N II] line) exceeded 10% for almost the entire first week of August 2001. *The observed relation between the NRAO-CMU tipper and the 1.452 THz measurements indicates that it will be possible to observe the* $\lambda 205\,\mu$m [N II] *line about 30 days each year.*

The South Pole 25% winter PWV levels have been used to compute values of atmospheric transmittance as a function of wavelength which are plotted in Figure 3. For comparison, the transmittances for 25% winter conditions at Chajnantor and Mauna Kea are also shown.

Sky noise is caused by fluctuations in total power or phase of a detector caused by variations in atmospheric emissivity and path length on timescales of order one second. Sky noise causes systematic errors in the measurement of astronomical sources. Lay & Halverson (2000) show analytically how sky noise causes observational techniques to fail: fluctuations in a component of the data due to sky noise integrates down more slowly

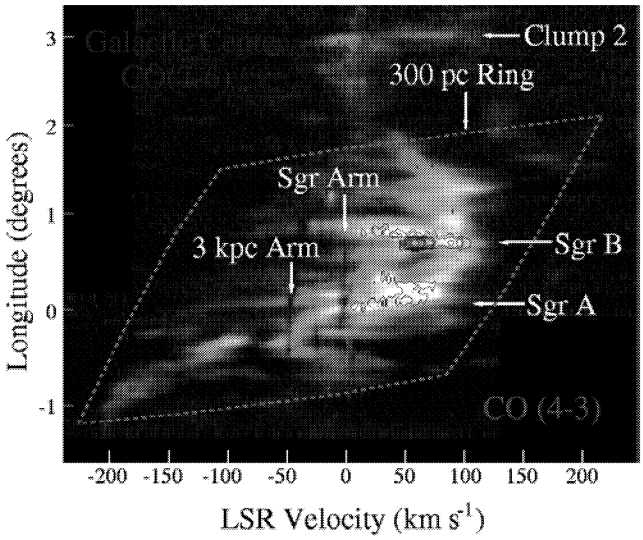

Fig. 4: **AST/RO observations of the Galactic Center Region** (from Kim et al. 2000). The CO $J = 4 \rightarrow 3$ (pseudo-color) and $J = 7 \rightarrow 6$ (blue contour) lines observed in an $l - v$ strip, sampled every $1'$, at $b = 0$. These data have been used in conjunction with CO and ^{13}CO $J = 1 \rightarrow 0$ data to determine the the density and temperature in the features shown here.

than $t^{-1/2}$ and will come to dominate the error during long observations. Sky noise at South Pole is considerably smaller than at other sites, even comparing conditions of the same opacity. The PWV at South Pole is often so low that the opacity is dominated by the *dry air* component (Chamberlin & Bally 1995, Chamberlin 2001, cf. Figure 3); the dry air emissivity and phase error do not vary as strongly or rapidly as the emissivity and phase error due to water vapor.

III. 810 GHz Observations at AST/RO

AST/RO has detected the isotopic [^{13}C I] $^3P_2 \rightarrow {}^3P_1$ fine-structure transition in three galactic regions: G 333.0-0.4, NGC 6334 A, and G 351.6-1.3. This is only the second time that this line have been successfully observed, the previous detection being a single spectrum obtained with the Caltech Submillimeter Observatory toward the Orion Bar (Keene et al. 1998). The [^{13}C I] line was observed simultaneously with the CO $J = 7 \rightarrow 6$ line emission at 806 GHz (Tieftrunk et al. 2001).

Essentially all of the NGC 6334 Giant Molecular Cloud was mapped in 492 and 810 GHz [C I] and the CO $J = 7 \rightarrow 6$ and $J = 4 \rightarrow 3$ spectral lines. The data show that high excitation temperatures exist throughout most of the cloud volume. Detailed modeling is in progress to account for the observed line intensities and ratios (Yan et al. in preparation).

An up-to-date bibliography of AST/RO publications can be found at the AST/RO website `http://cfa-www.harvard.edu/~adair/AST_RO`.

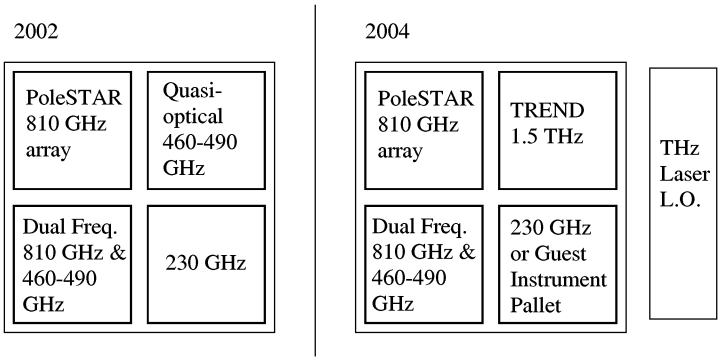

Fig. 5: **AST/RO Receiver Room Configurations.** On the left is the current configuration of pallets in the AST/RO receiver room, looking downwards to the Coudé focus. At right is a proposed configuration circa 2004, with the TREND 1.4 THz HEB mixer and its laser local oscillator installed. A "Guest Instrument Pallet" would permit testing of high-frequency prototypes.

IV. Terahertz Initiative

Two new short wavelength instruments are in development for use on AST/RO:

- Dr. G. Stacy and collaborators have developed the South Pole Imaging Fabry-Perot Interferometer (SPIFI, Swain et al. 1998), a 25-element bolometer array preceded by a tunable Fabry-Perot filter. This instrument was successfully used on the JCMT in May 1999 and April 2001 and is being modified with new instrumentation, cryogenics, and detectors for South Pole use. SPIFI is frequency agile and can observe many beams at once, but has limited frequency resolution (~ 100 km s^{-1}) and scans a single filter to build up a spectrum.
- Dr. S. Yngvesson and collaborators (Gerecht et al. 1999, Yngvesson et al. 2001) are developing a 1.5 THz heterodyne receiver, the Terahertz Receiver with Niobium Nitride Device (TREND). TREND has only a single pixel and is not frequency agile. Its HEB device requires high local oscillator power levels; we will use a laser local oscillator source which requires that the gas be changed in order to change frequencies. The frequency resolution of TREND is high (~ 2 MHz), limited by the stability of the laser.

In addition, Dr. D. Prober and collaborators are developing a low-noise, low-power 1.5 THz heterodyne receiver based on aluminum and tantalum HEB technology which may be tested on AST/RO.

Deployment of these technologies on a ground-based telescope is a path of technological development that has exciting prospects. On AST/RO, the $\sim 35''$ beam size and high spectral resolution (~ 0.4 km s^{-1}) of Terahertz receivers will allow the study of galactic star-forming regions and large-scale studies of nearby galaxies. In future, these detectors could be used on the South Pole Submillimeter Telescope (SPST), an 8-meter telescope (see NRC 2001), which would have a beamsize of $\sim 7''$.

V. Conclusion

We hope to begin ground-based Terahertz observations with AST/RO in 2003. Routine observations have been carried out in the 350 μm window over the past two years, and our experience has been that such observations are possible more than 100 days each year. Site testing with a new Fourier Transform Spectrometer, combined with long-term measurements from the NRAO-CMU tipper, indicates that observations in the 200 μm window should be possible about 30 days each year. Two Terahertz detector systems, SPIFI and TREND, are scheduled for installation in the next two years. We expect that after initial tests and observations these instruments will become available for astronomical use on a proposal basis. AST/RO is also open to proposals for tests of other prototype Terahertz instruments in the coming years.

We thank Simon Radford of NRAO and Jeff Peterson of CMU for the data shown in Figure 1. We thank Juan R. Pardo of Caltech for discussions on atmospheric modeling and for carrying out the calculations shown in Figure 3. The AST/RO group is grateful for the logistical support of the National Science Foundation, Antarctic Support Associates, Raytheon Polar Services Company, and CARA during our polar expeditions. This work was supported in part by United States National Science Foundation grant DPP88-18384, and by the Center for Astrophysical Research in Antarctica and the NSF under Cooperative Agreement OPP89-20223.

VI. References

Chamberlin, R. A. 2001, J. Geophys. Res., 106 (D17), 20101

Chamberlin, R. A. 2002, in ASP Conference Series, Vol. 266, Astronomical Site Evaluation in the Visible and Radio Range, ed. J. Vernin, Z. Benkhaldoun, & C. Mũnoz-Tuñon, (San Francisco: Astr. Soc. of the Pacific)

Chamberlin, R. A., & Bally, J. 1994, Applied Optics, 33(6), 1095

Chamberlin, R. A., & Bally, J. 1995, Int. J. Infrared and Millimeter Waves, 16, 907

Chamberlin, R. A., Lane, A. P., & Stark, A. A. 1997, ApJ, 476, 428

Engargiola, G., Zmuidzinas, J., & Lo, K.-Y. 1994, Rev. Sci. Instr., 65, 1833

Gerecht, E., Musante, C. F., Zhuang, Y., Yngvesson, K. S., Goyette, T., Dickinson, J., Waldman, J., Yagoubov, P. A., Gol'tsman, G. N., Voronov, B. M., & Gershenzon, E. M. 1999, IEEE Trans., MTT-47, 2519

Groppi, C., Walker, C., Hungerford, A., Kulesa, C., Jacobs, K., & Kooi, J. 2000, in ASP Conference Series, Vol 217, Imaging at Radio Through Submillimeter Wavelengths, ed. J. G. Mangum & S. J. E. Radford, (San Francisco: Astr. Soc. of the Pacific), 48

Honingh, C. E., Hass, S., Hottgenroth, K., Jacobs, J., & Stutzki, J. 1997, IEEE Trans. Appl. Superconductivity, 7, 2582

Keene, J., Schilke, P., Kooi, J., Lis, D. C., Mehringer, D. M., & Phillips, T. G. 1998, ApJ, 494, L107

Kim, S., Martin, C. L., Stark, A. A., & Lane, A. P. 2000, American Astronomical Society Meeting 197, BAAS, 32, 4.04

Kooi, J. W., Chan, M. S., Bumble, B., LeDuc, H. G., Schaffer, P. L., & Phillips, T. G. 1995, Int. J. IR and MM Waves, 16

Kooi, J. W., Man, C., Phillips, T. G., Bumble, B., & LeDuc, H. G. 1992, IEEE Trans. Microwaves Theory and Techniques, 40, 812

Lane, A. P. 1998, in ASP Conference Series, Vol. 141, Astrophysics from Antarctica, ed. G. Novak & R. H. Landsberg, (San Francisco: Astr. Soc. of the Pacific), 289

Lay, O. P., & Halverson, N. W. 2000, ApJ, 543, 787

National Research Council 2001, Astronomy and Astrophysics in the New Millennium, (National Academy Press)

Pardo, J. R., Cernicharo, J., & Serabyn, E. 2001, IEEE Trans. Antennas and Propagation, 49, 1683

Schieder, R., Tolls, V., & Winnewisser, G. 1989, Exp. Astron., 1, 101

Schwerdtfeger, W. 1984, Weather and Climate of the Antarctic, (Amsterdam: Elsevier)

Stark, A. A., Bally, J., Balm, S. P., Bania, T. M., Bolatto, A. D., Chamberlin, R. A., Engargiola, G., Huang, M., Ingalls, J. G., Jacobs, K., Jackson, J. M., Kooi, J. W., Lane, A. P., Lo, K.-Y., Marks, R. D., Martin, C. L., Mumma, D., Ojha, R., Schieder, R., Staguhn, J., Stutzki, J., Walker, C. K., Wilson, R. W., Wright, G. A., Zhang, X., Zimmermann, P., & Zimmermann, R. 2001, PASP, 113, 567

Stark, A. A., Chamberlin, R. A., Cheng, J., Ingalls, J., & Wright, G. 1997, Rev. Sci. Instr., 68, 2200

Swain, M. R., Bradford, C. M., Stacey, G. J., Bolatto, A. D., Jackson, J. M., Savage, M., & Davidson, J. A. 1998, SPIE, 3354, 480

Tieftrunk, A. R., Jacobs, K., Martin, C. L., Siebertz, O., Stark, A. A., Walker, C. K., & Wright, G. A. 2001, A&A, 375, L23

Walker, C. K., Kooi, J. W., Chan, W., LeDuc, H. G., Schaffer, P. L., Carlstrom, J. E., & Phillips, T. G. 1992, Int. J. Infrared and Millimeter Waves, 13, 785

Yngvesson, K. S., Musante, C. F., Ji, M., Rodriguez, F., Zhuang, Y., Gerecht, E., Coulombe, M., Dickinson, J., Goyette, T., Waldman, J., Walker, C. K., Stark, A. A., & Lane, A. P. 2001, in Twelfth Intern. Symp. Space THz Technology, (I. Medhi, Ed.), San Diego, CA, Feb. 14-16, 2001, p. 262

Zmuidzinas, J., & LeDuc, H. G. 1992, IEEE Trans. Microwave Theory Tech., 40, 1797

SMART: The KOSMA Sub-Millimeter Array Receiver for Two frequencies

U. U. Graf, S. Heyminck, E. A. Michael, S. Stanko, C. E. Honingh,
K. Jacobs, R. Schieder and J. Stutzki

KOSMA, I. Physikalisches Institut, Universität zu Köln, Zülpicher Straße 77,
50937 Köln, Germany. E–mail: *lastname*@ph1.uni-koeln.de

Abstract

We present the first results obtained with our new dual frequency SIS array receiver SMART[1]. The instrument is operational since September 2001 at the KOSMA 3m telescope on Gornergrat near Zermatt/Switzerland. The receiver consists of two 2×4 pixel subarrays. One subarray operates at a frequency of 490 GHz, the other one at 810 GHz. Both subarrays are pointed at the same positions on the sky. We can thus observe eight spatial positions in two frequencies simultaneously. For the first year of operation we installed only one half of each subarray, i.e. one row of 4 mixers at each frequency.

The receiver follows a very compact design to fit our small observatory. To achieve this, we placed most of the optics at ambient temperature, accepting the very small sensitivity loss caused by thermal emission from the optical surfaces. The optics setup contains a K–mirror type image rotator, two Martin–Puplett diplexers and two solid state local oscillators, which are multiplexed using collimating Fourier gratings. To reduce the need for optical alignment, we machined large optical subassemblies monolithically, using CNC milling techniques. We use the standard KOSMA fixed tuned waveguide SIS mixers with Nb junctions at 490 GHz, and similar Nb mixers with Al tuning circuits at 810 GHz.

We give a short description of the front end design and present focal plane beam maps, receiver sensitivity measurements, and the first astronomical data obtained with the new instrument.

Introduction

At last year's conference [1], [2] we introduced our design of a dual–frequency eight–pixel SIS–heterodyne receiver SMART[1]. SMART's unique feature is that it simultaneously measures in the 650 μm and the 350 μm atmospheric windows, thus combining and extending the frequency coverage of the other two currently installed submillimeter arrays CHAMP [3] and Pole STAR [4]. SMART is mainly intended for simultaneous mapping of the two fine structure transitions of neutral atomic carbon at 492 GHz and at 809 GHz. The large frequency coverage also allows to measure a variety of other spectral lines in this frequency range, for instance the carbon monoxide (CO) rotational transitions at 460, 807 and 880 GHz. The simultaneous measurements of different spectral lines in several spatial pixels enhances the data quality by eliminating a number of calibration and pointing uncertainties [5].

[1] **S**ub–**M**illimeter **A**rray **R**eceiver for **T**wo frequencies

Opto–mechanical Design

In order to fit into the limited space available at the KOSMA 3m telescope [6], the instrument was designed to be very compact. We therefore decided to place essentially all optical elements at ambient temperature. It is obvious that the thermal emission of these elements will degrade the receiver sensitivity to some extent. However, it turned out that the combined effect from a total of 14 warm surfaces only adds a very small amount to the receiver noise temperature.

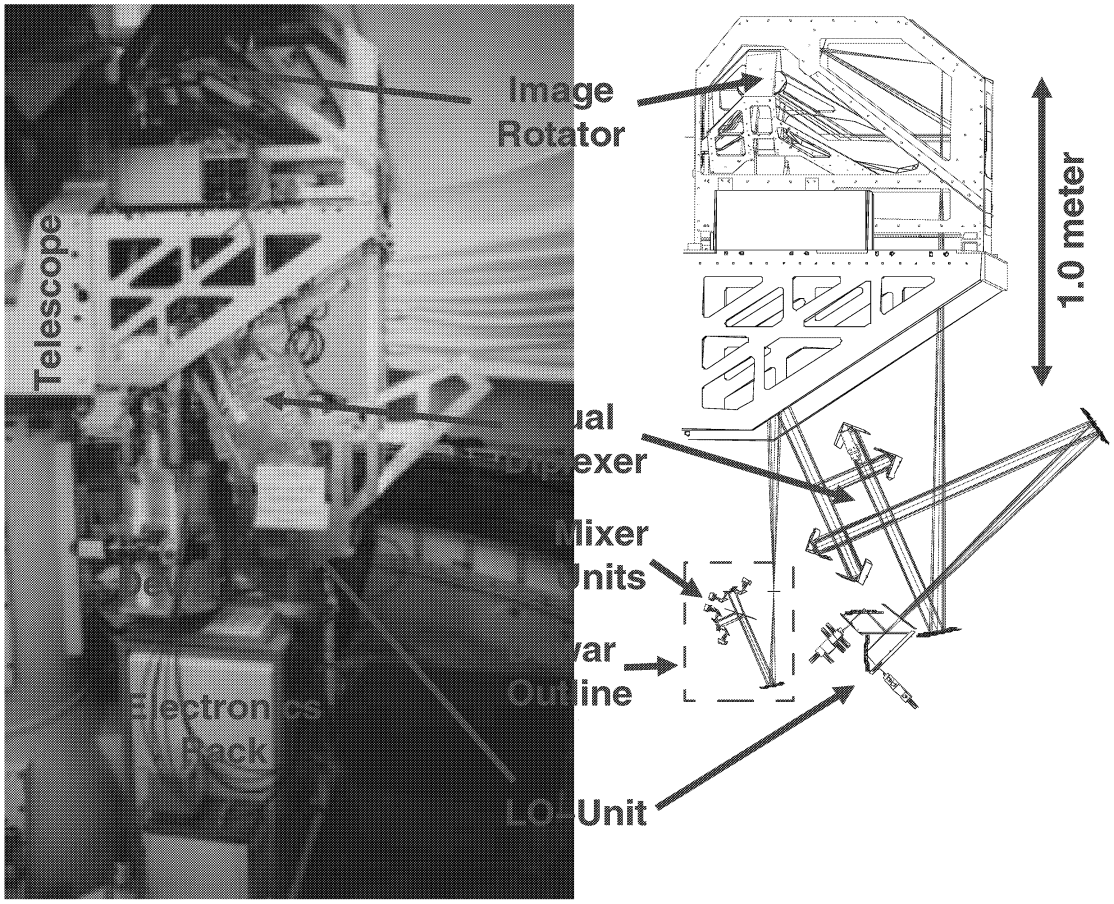

Figure 1: Photograph (left hand panel) and drawing (right hand panel) of SMART mounted at the KOSMA telescope.

Fig. 1 shows a photograph and a schematic drawing of the instrument mounted at the telescope. The main units of the receiver are:

- a K–type image rotator to compensate the image rotation introduced by the alt–az–mounted telescope when tracking an astronomical source,
- the diplexer assembly containing two identical Martin–Puplett–interferometers, which combine the signal beams and the LO–beams,

- the LO–unit, which produces the two LO–signals and splits them into eight beams, each,
- the dewar containing the mixer units, and
- the electronics rack with the instrument control electronics.

The imaging optics consist of two gaussian telescopes made of ellipsoidal and hyperboloidal mirrors. A first set of two mirrors reimages the telescope's focal plane to the optical center of the diplexers to create large beam waists in the diplexer. These waists are reimaged with a second gaussian telescope to the output waists of the mixer units. In order to minimize abberations, all reflection angles are kept small (24° or 32°) and all mirrors have long focal lengths (300 to 1900 mm). The dewar window has been placed between the mirrors of the second gaussian telescope, at the image of the telescope's primary mirror, where the total beam cross section is minimal.

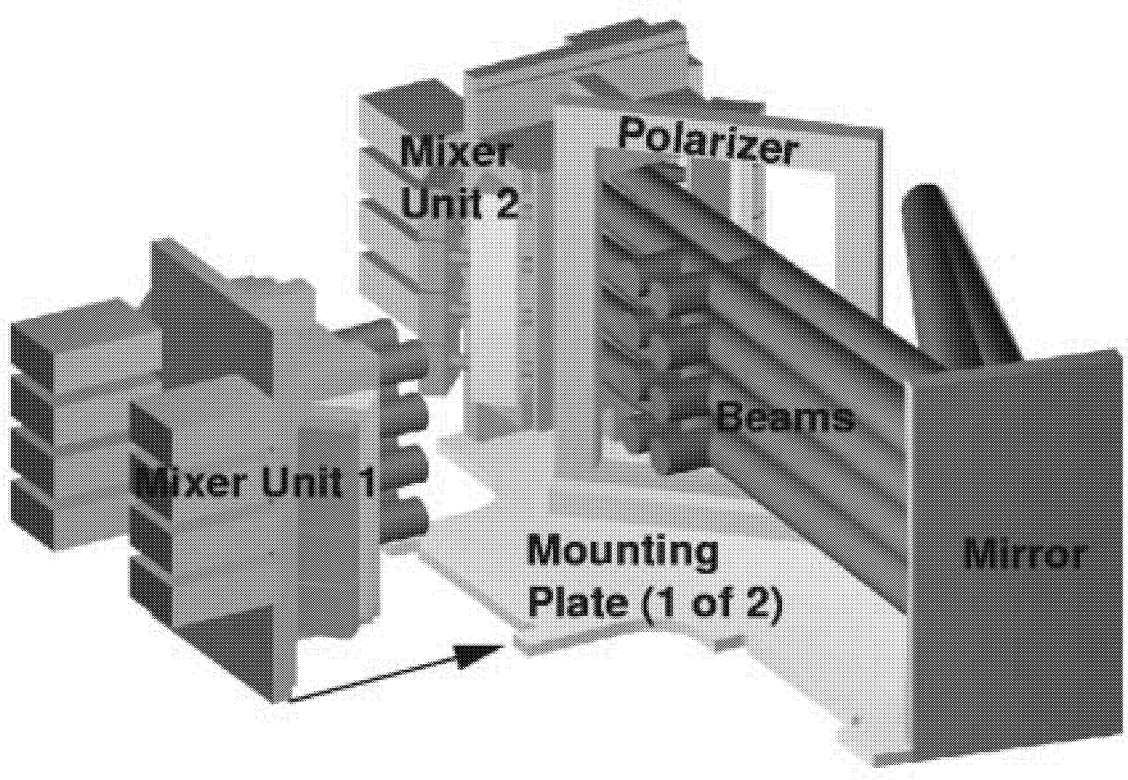

Figure 2: Assembly containing all optical elements inside the dewar. The mixer units (Fig. 3) together with a polarizer grid and a common imaging mirror are sandwiched between two identical CNC–machined plates.

Within the dewar (Fig. 2), the optics consist of the last mirror common to all mixers, a polarizer grid, and two similar mixer units. These mixer units (Fig. 3) are CNC–machined quasi–monolithic integrated optics components, each of which is

holding 8 mixers in two rows of four. Within the units, the mounting surfaces for the mixers and their collimating mirrors are machined in a single machining cycle with very high precision, thus eliminating the need for an individual alignment of the mixers. Similarly, all the optical elements inside the dewar are sandwiched between two precision machined plates, which hold them with high enough accuracy that no further alignment is required.

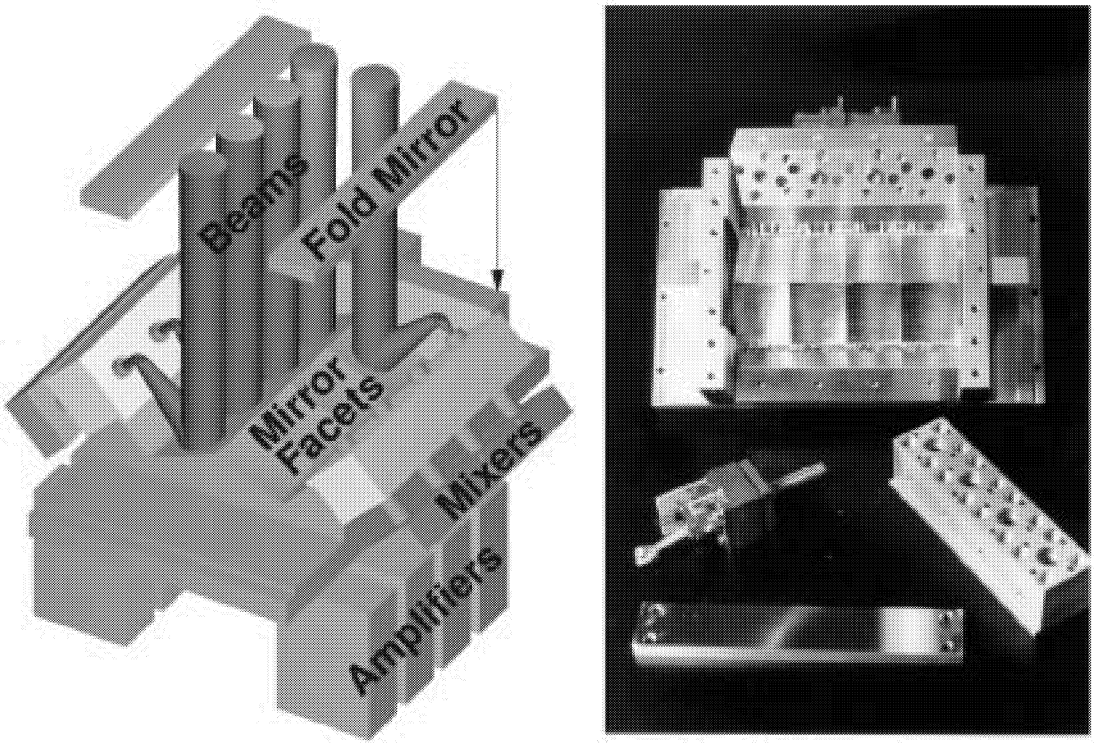

Figure 3: Drawing of the 490 GHz mixer unit (left hand panel) and photograph of the major components (right hand panel). It contains a facetted mirror to collimate the beams from the eight mixer horn antennas. The mixers are held by their feed horns, which are inserted in precision reamed holes in the mixer unit. The eight mirror facets cover an area of 84×42 mm^2.

The first optical element in the diplexer unit (Fig. 1) is a wire grid, which splits the polarization of the incoming signal beams to separate the optical paths for the two frequencies. At the same time, this grid couples the LO–beams onto the signal beams with orthogonal polarizations. The two Martin–Puplett–interferometers match the LO–polarizations to the signal polarizations. A second polarizer grid recombines the beams before they leave the diplexer unit.

We use two local oscillator chains with orthogonal polarizations. Each LO is split by a collimating Fourier grating (Fig. 4 [2]) into eight identical beams, matching the mixer arrangement. A polarizer grid combines the LO beams before injecting them into the diplexer unit.

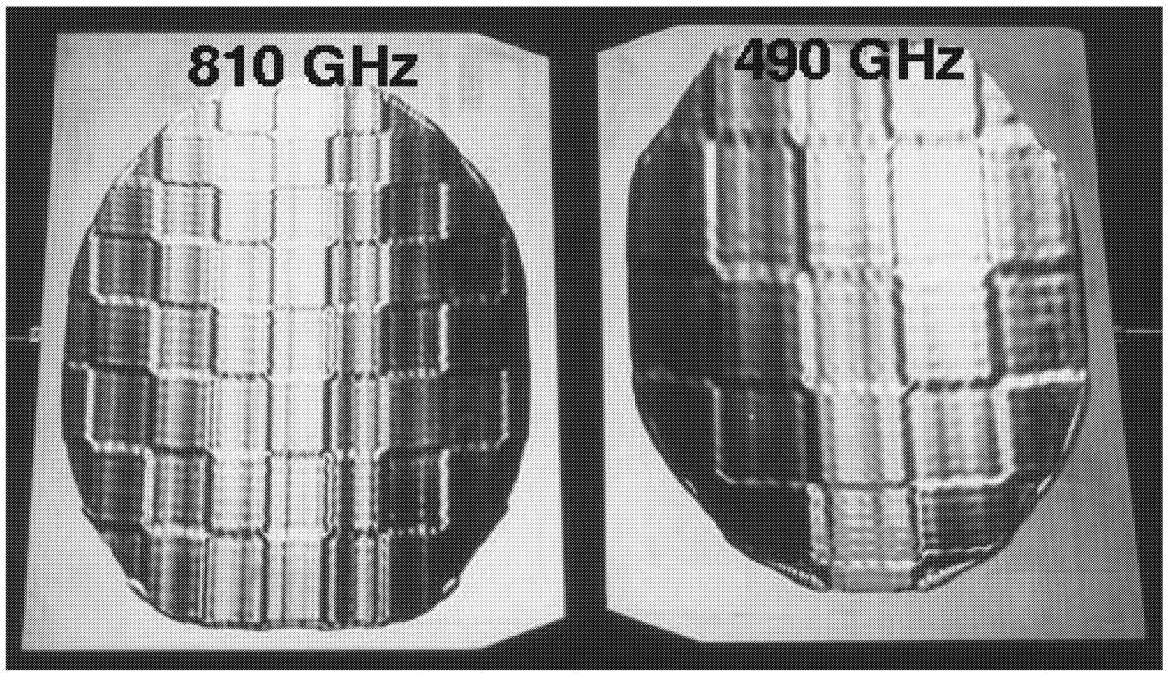

Figure 4: Photograph of the two collimating Fourier gratings used with SMART. Each grating collimates an incoming diverging LO beam and splits it into eight identical beams in a 2×4 arrangement. The grating on the left hand side with the smaller structure is for the 810 GHz frequency band, the one on the right hand side is for the 490 GHz band.

The image rotator is a computer controlled rotating arrangement of three mirrors in an asymmetric K–configuration. It allows to keep the receiver pixels aligned with respect to the astronomical source, while the image of the source is rotating in the telescope focal plane during long term measurements.

Cooling of the instrument dewar is provided by a closed cycle refrigerator [7], which keeps the SIS–mixers at a temperature of 4 K.

Mixers and Backends

In the 490 GHz frequency band we use the standard KOSMA Niobium SIS mixers with fixed tuned backshorts [8]. The mixer block design for the 810 GHz mixers is similar. The SIS devices, however, use a Nb–Al bilayer for the RF tuning circuit, in order to reduce the losses at frequencies beyond the niobium gap frequency.

The spectrometer backends used with SMART are the KOSMA array AOSs [9]. Each of the units combines four 1 GHz wide AOS channels in one opto–mechanical setup. The spectral resolution is approximately 1 MHz. Four array AOSs are required for the complete receiver.

Electronics

The instrument control electronics is described in more detail in Stanko et al. in this volume [10]. There we also present the control software and the automated receiver tuning procedure, which we developed to facilitate the operation of the instrument.

In addition to the control electronics, the receiver electronics also comprises the processing of the intermediate frequency mixer output signals, which requires the following functional units:

- amplifiers and filters for the receiver output
- frequency converters to shift the IF to match the AOS's input frequency
- variable attenuators to match the IF power level to the input level required by the AOS
- IF power monitors for receiver tuning and continuum observations
- switches to suppress the receiver output for AOS dark current measurements
- a frequency comb signal for the frequency calibration of the AOSs

We developed a compact IF processor for eight receiver channels, a photograph of which is shown in [10].

Receiver Performance

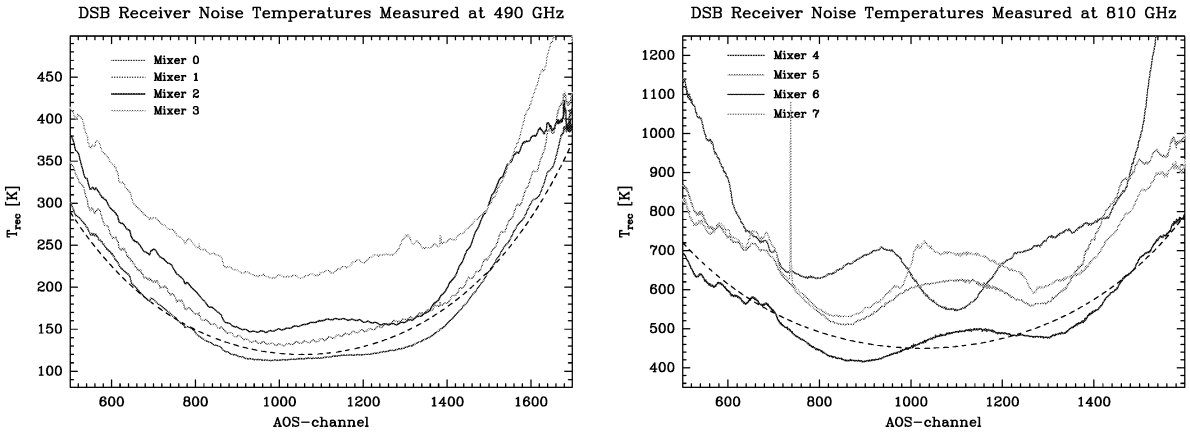

Figure 5: Receiver noise temperatures measured at the telescope. The dashed lines visualize the sensitivity loss caused by a room temperature diplexer calculated for intrinsic receiver temperatures of 120 K (at 490 GHz) and 450 K (at 810 GHz).

In Fig. 5 we show the receiver noise temperature at the telescope, simultaneously measured with all eight currently installed receiver channels. The figure shows the noise

temperature variation over the 1 GHz wide IF band plotted against AOS channels. Each backend channel is approximately 1 MHz wide. At 490 GHz the typical minimum noise temperature is around 150 K, at 810 GHz it is approximately 500 to 600 K. The most prominent feature in the plot is a curvature in the band. This loss in sensitivity toward the edges of the IF band reflects the transmission of the diplexer. The dashed lines in the noise temperature plots indicate the noise temperature functions one would get with an intrinsic receiver temperature of 120 K (at 490 GHz) or 450 K (at 810 GHz) looking through a room temperature Martin–Puplett interferometer. These curves represent well the measured values. At 490 GHz, where the effect is more prominent, we plan to increase the noise bandwidth by changing the IF center frequency to 4 GHz.

The most remarkable point in the noise temperature measurement is that, at 810 GHz, we do not see a difference between the receiver temperature measured at the telescope with the array and the noise temperatures measured with the same mixers in a single channel test dewar in the laboratory. Thus, SMART at least partly fulfills the most stringent request imposed on any array receiver: *"The noise performance of the arrays needs to be very close to that of single–pixel receivers if they are to compete"* (cited from [11]).

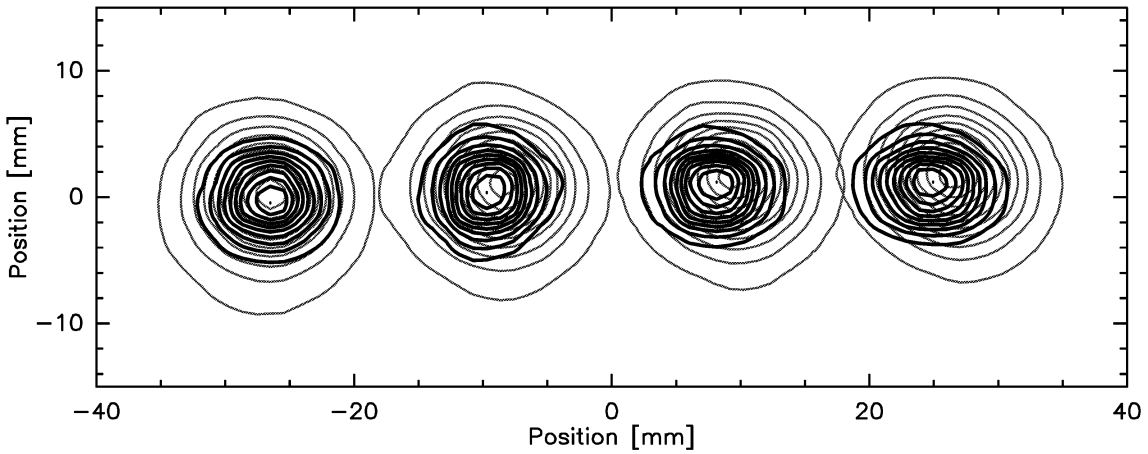

Figure 6: Receiver beam pattern measured at the location of the telescope's focal plane. The red contours are the 490 GHz beams, the black contours are the 810 GHz beams. Contour levels range from 5% to 95% of the peak intensities. The beam sizes and spacing fits well with the design values. The slight offset of the 810 GHz beams with respect to the 490 GHz beams results from a residual misalignment of the diplexer unit.

We measured the beam pattern by scanning the receiver beam in the focal plane using a chopped cold load (Fig. 6). The beams of the 8 mixers currently mounted are very clean and have the correct size and spacing. There is a slight offset between some of the 810 GHz beams and the corresponding 490 GHz beams, which is most likely due to a slight misalignment in the diplexer unit. However, the overlap between the beams is still very good.

First Astronomical Measurements

The power of the array receiver approach becomes evident with the astronomical data gathered. Even with only half of the mixers installed, SMART is a very fast instrument and allows to map extended sources in a short time. In Fig. 7 we show sample spectra obtained during a single integration of 160 seconds duration. With our IF frequency of 1.5 GHz we can measure the [CI] $^3P_2 \rightarrow ^3P_1$ line and the CO J=7→6 line simultaneously in opposite sidebands of the 810 GHz receiver branch. Thus the data contain a total of 12 spectral lines, 3 lines from each of 4 spatial positions.

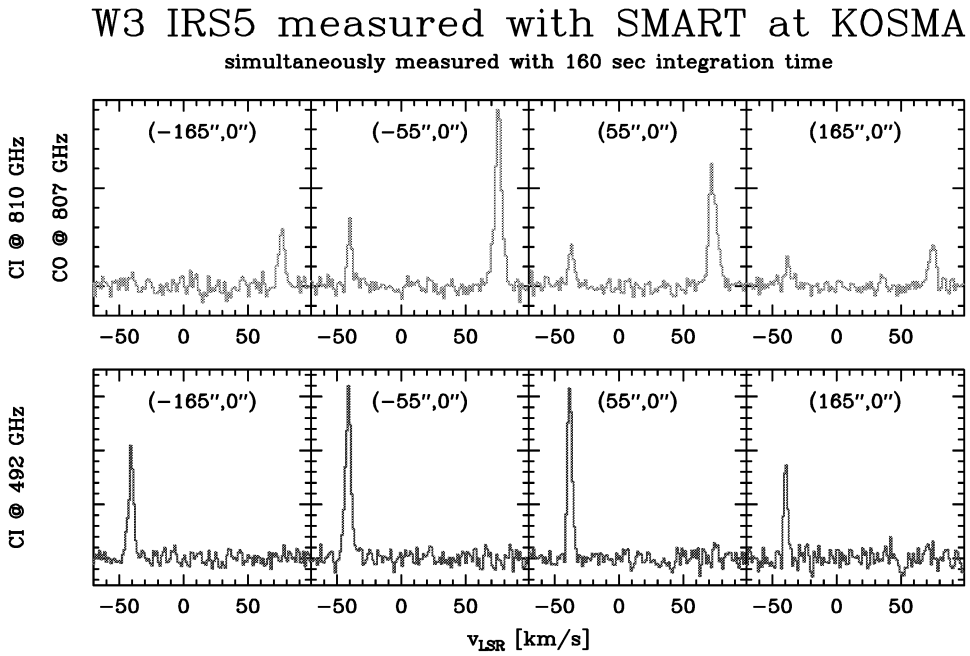

Figure 7: Sample spectra obtained simultaneously toward W3 IRS5 during a single 160 sec integration with SMART at the KOSMA telescope. The lower row of panels shows the 492 GHz fine structure transition of neutral atomic carbon (CI), the upper row shows the 810 GHz fine structure line of CI and the 807 GHz J=7→6 transition of CO. Pixel offsets are indicated in each panel.

Conclusions

We have built and installed the world's first dual frequency submillimeter heterodyne array receiver SMART. The optical alignment of the instrument is very simple because of the innovative integrated optics approach taken in the design. With its low receiver temperature and its good optical performance, SMART is a very powerful instrument for astronomical submillimeter spectroscopy.

Acknowledgments

This work was supported by the *Verbundforschung Astronomie* through grant 05

AH9PK1, by the *Deutsche Forschungsgemeinschaft* through grant SFB 494, and by the ministry of science of the state Nordrhein–Westfalen.

References

[1] U.U. Graf, S. Heyminck, E.A. Michael, and S. Stanko. KOSMA's 490/810 GHz Array Receiver. In I. Mehdi, editor, *Proceedings of the* 12th *International Symposium on Space Terahertz Technology*, 2001.

[2] S. Heyminck and U.U. Graf. Array–Receiver LO Unit using Collimating Fourier Gratings. In I. Mehdi, editor, *Proceedings of the* 12th *International Symposium on Space Terahertz Technology*, 2001.

[3] R. Güsten et al. CHAMP — the carbon heterodyne array of the MPIfR. In Thomas G. Phillips, editor, *Advanced Technology MMW, Radio, and Terahertz Telescopes*. Proceedings of SPIE Vol. 3357, 1998.

[4] C. Walker, C. Groppi, D. Golish, C. Kulesa, A. Hungerford, C. Drouet d'Aubigny, K. Jacobs, U. Graf, C. Martin, and J. Kooi. PoleStar: An 810 GHz Array Receiver for AST/RO. In I. Mehdi, editor, *Proceedings of the* 12th *International Symposium on Space Terahertz Technology*, 2001.

[5] J. Stutzki, U.U. Graf, S. Haas, C.E. Honingh, D. Hottgenroth, K. Jacobs, R. Schieder, R. Simon, J. Staguhn, G. Winnewisser, R.N. Martin, W.L. Peters, and J.P. McMullin. Atomic carbon in M82: Physical conditions derived from simultaneous observations of the [CI] fine–structure submillimeter wave transitions. *Astrophysical Journal (Letters)*, 477, 1997.

[6] C.G. Degiacomi, R. Schieder, J. Stutzki, and G. Winnewisser. The KOSMA 3–m Submillimeter-Wave Telescope. *Optical Engineering*, 34(9), 1995.

[7] Sumitomo Heavy Industries, Model SRDK–415.

[8] S. Haas, C.E. Honingh, D. Hottgenroth, K. Jacobs, and J. Stutzki. Low noise broadband tunerless waveguide SIS receivers for 440–500 GHz and 630–690 GHz. *Intl. J. IR mm Waves*, 17(3), 1996.

[9] J. Horn, O. Siebertz, F. Schmülling, C. Kunz, R. Schieder, and G. Winnewisser. A 4×1 GHz Array Acousto–Optical Spectrometer. *Exper. Astron.*, 9, 1999.

[10] S. Stanko, U.U. Graf, and S. Heyminck. Automatic Tuning of SMART, KOSMA's 490/810 GHz Array Receiver. In *Proceedings of the* 13th *International Symposium on Space Terahertz Technology*, Cambridge, Massachusetts, 2002.

[11] Richard Hills. Cost–Effectiveness of Array Detectors. In D.T. Emerson and J.M. Payne, editors, *Multi–Feed Systems for Radio Telescopes*. ASP Conference Series, Vol. 75, 1994.

BLAST - A NEW BALLOON-BORNE SUBMILLIMETER TELESCOPE

S. Dicker[3],
P. Ade[1], J. Bock[2], J. Cung[8], E. Chapin[5], M. Devlin[3], M.Griffin[1], J. Gunderson[4],
M. Halpern[8], P. Hargrave[1], D. Hughes[5], J. Klein[3],
C. Mactavish[6], G. Marsden[8], P. Mauskopf[1], B. Netterfield[6], L. Olmi[9],
M. Rex[3], D. Scott[8], G. Tucker[7], M. Truch[7], M. Viero[3]

[1]Cardiff University, Cardiff, UK
[2]Jet Propulsion Laboratory, Pasadena, CA, USA
[3]University of Pennsylvania, Philadelphia, PA, USA
[4]University of Miami, Coral Gables, FL, USA
[5]INAOE, Puebla, Mexico
[6]University of Toronto, Toronto, ON, Canada
[7]Brown University, Providence, RI, USA
[8]University of British Columbia, Vancouver, B.C. Canada
[9]University of Puerto Rico, San Juan, PR, USA

Abstract. *BLAST the Balloon-borne Large Aperture Sub-millimeter Telescope, will have three bolometer arrays operating at 250, 350, and 500 μm, with 149, 88, and 43 detectors respectively. The arrays will be cooled to 300 mK so that the receiver's noise (NEFD) will be dominated by photon shot noise and atmospheric emission. Because of the high (35 km) altitude of balloon observations, atmospheric noise will be low and we expect NEFDs less than 241 mJy/Hz$^{1/2}$ in all channels. A 2.0 m diameter spherical mirror will give diffraction limited resolutions of 30, 41, and 59" respectively.*

The first test flight, planned for early 2003, will last 6–24 hours across North America. Long-duration balloon flights from Antarctica will begin in late 2003 and will last 14 days. BLAST will yield data on astronomical problems as close as nearby stars and as far away as the beginnings of the Universe.

1. INTRODUCTION

The Balloon-borne Large Aperture Sub-millimeter Telescope (BLAST) is designed to produce wide (1–10 deg^2) maps of the sky at wavelengths of 250, 350 and 500 μm. Because of the dramatically increased atmospheric transmission at balloon altitudes, BLAST will be far more sensitive than existing bolometer arrays. Full advantage of the bolometric focal-plane arrays, being developed for the *Herschel* satellite [1], will be made. A 20 hour observation, during the planned long-duration balloon (LDB) flights, will map a square degree of sky to the confusion limit at each of BLAST's operating frequencies. The scientific goals [2] of these surveys include:

- The identification of galaxy populations responsible for the sub-millimeter background and measurement of their clustering on scales of 0.1–10 degrees.
- The measurement of the spectral energy distributions (SED) and colors of selected sub-millimeter galaxies to give their rest-frame luminosities and star formation rates.
- Placing constraints on evolutionary models and high red-shift star formation histories of starburst galaxies.

- Surveys of diffuse interstellar emission and dense star forming regions.
- Observations within the Solar system including planets, asteroids and Kuiper-belt objects.

Quick construction of BLAST was possible due to the use of detector assemblies and filters similar to those designed for the SPIRE instrument on *Herschel.* BLAST will provide the first "flight tests" of these critical components for the later satellite mission.

2. DETECTORS & ELECTRONICS

BLAST will have three focal plane arrays of spider-web bolometers [3]. The arrays will operate at 250, 350, and 500 μm and will have 149, 88, and 43 pixels, respectively. Each array is manufactured from a single wafer of silicon nitride and 10MΩ bias resistors are built into the array (Figure 1). The detectors have been optimized for the expected loading at balloon altitudes. Their predicted NEPs are 3×10^{-17} W/Hz$^{1/2}$, which is less than the expected photon shot-noise from the telescope. They have time constants between 5 and 20 ms, fast enough for efficient mapping. Each array is fed by close-packed 2fλ conical feedhorns with λ/4 backshorts for efficient coupling of the bolometers to the telescope. The field of view of each array is 13″ by 6.5″ and they observe the same patch of sky simultaneously.

The bolometers and the horn feeds are cooled to <0.28 K by a helium-3 absorption refrigerator [4] and are mounted in the SPIRE instrument's detector array assembly, shown in Figure 1. This assembly minimizes the heat load on the helium-3 refrigerator by suspending the detectors using Kevlar string from a 2K support structure. Heat conduction down the >300 wires needed to read out the bolometers is minimized using cables made of constantan traces deposited on a Kapton support structure.

Each bolometer is read out using the circuit shown in Figure 2. The bolometers are AC biased at 400 Hz. Spiderweb bolometers have a high impedance (10 MΩ when cold) so to prevent noise from stray capacitance in the wiring, a matched pair of cooled (120 K) JFET amplifiers with a gain of 0.98 is placed as close to each detector as possible. Room temperature electronics amplifies this signal and a 100 Hz wide bandpass filter removes excess noise. The signal is then digitized. A lock-in to the 400 Hz bias signal is carried out using software. To prevent RF from entering the cryostat, (which would then be dissipated as heat in the bolometers), the cables from the cryostat and the room temperature electronics lie in RF-tight conduit. RF filters separate the analog preamplifier circuits from the digital stages.

Because BLAST has 280 detectors wiring is non-trivial. The electronics and cabling are modular, each unit serving 24 bolometers. To save space in the cryostat, the JFET units are constructed from bare die, bonded to FR4 circuit boards. One such module is shown in Figure 2.

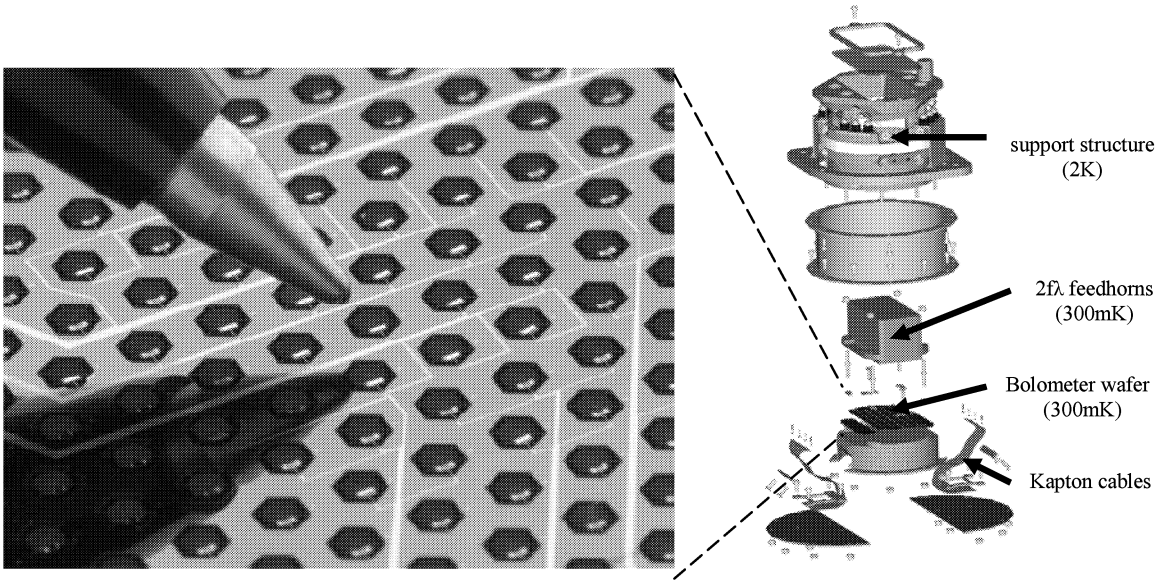

Figure 1. The array of 350 μm detectors to be used on BLAST is shown on the left and on the right is the SPIRE detector assembly that will house the wafer.

Band (μm)		250	350	500
Number of pixels		149	88	43
Beam FWHM	(″)	30	41	59
Background Power	(pW)	26	18	14
Background NEP	($\times 10^{-17}$ W/$\sqrt{}$Hz)	20	14	10
NEFD	(mJy/$\sqrt{}$s)	236	241	239
SCUBA's NEFD	(mJy/$\sqrt{}$s)	-	*1100*	*1001*
SOFIA's NEFD	(mJy/$\sqrt{}$s)	*550*	-	-
ΔS (1σ, 1hr, 1 deg^2)	(mJy)	38	36	36

Table 1. : Beam and sensitivity parameters for BLAST. The sensitivities obtainable by the SCUBA and SOFIA receivers have been added for comparison.

3. CRYOSTAT & CRYOGENICS

The blast cryostat has a 53.1 *l* nitrogen tank, a 30 K vapor-cooled shield and a 36.7 *l* helium tank. The expected hold time is 12 days, limited by the nitrogen. To achieve this hold time, essential for LDB balloon flights, the JFET modules are mounted on a G10 tube suspended from the nitrogen tank. In this way the ~3 mW of heat produced by the JFETs is dissipated to the liquid nitrogen. Dissipating this much heat to the helium bath would shorten the hold time to 4 days.

Since the total loading on the helium-3 refrigerator is estimated to be <30 μW it will have a hold time more than 40 hours. When exhausted, the refrigerator is recycled off a pumped helium-4 bath in a process that takes less than an hour. To conserve liquid helium, the main helium tank is not pumped. Instead, the helium-3 refrigerator is recycled off a small pumped helium pot connected to the main helium bath by a capillary [4].

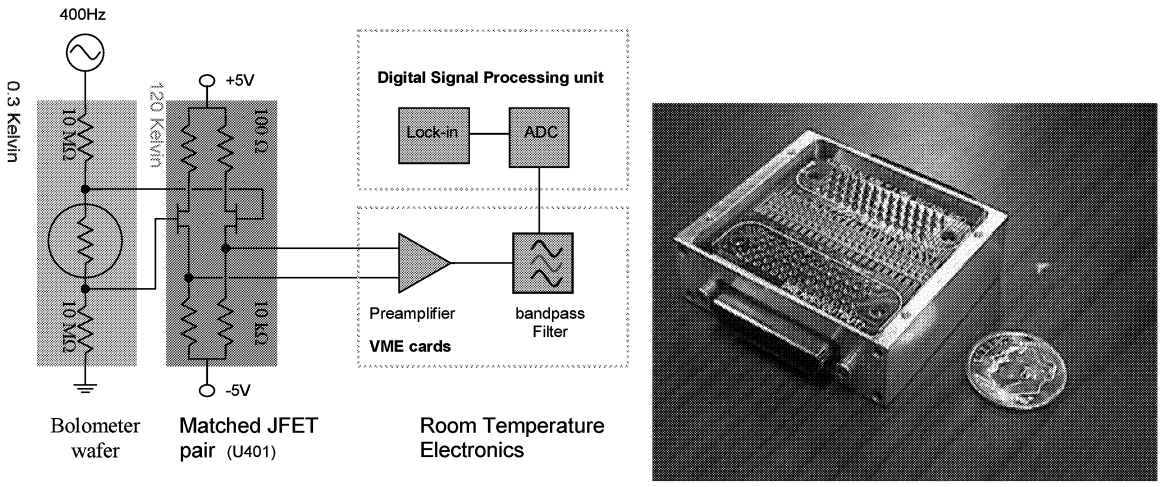

Figure 2. The electronics used to read out a single bolometer. To fit cold electronics for 255 bolometers in the cryostat, miniaturization was needed. On the right is a 24 channel JFET module.

4. OPTICS AND GONDOLA

BLAST is a Casigrain telescope with a 2 m primary mirror. The mirror, which is on loan to the project from NASA, is made of carbon fiber and weighs only 32 kg. The mirror has a f/2 spherical shape and a surface rms of 5 μm. The secondary mirror and reimaging optics in the cryostat correct for the spherical shape of the primary to give diffraction limited performance over a 14′ by 7′ field-of-view. To prevent spill-over from the ground only 1.9 m of the primary mirror is illuminated. The antenna efficiency is estimated to be over 80% and its emissivity is below 0.04. When the coupling efficiency of the bolometers and reflections from the filters are taken into account a telescope efficiency of 30% is achieved.

The BLAST reimaging optics, shown in Figure 3, are cooled to 2 K. All the mirrors and the detector arrays are mounted on a vertical "optics bench", enclosed in a light tight box. Where the beam enters the box, capacitive mesh filters define a band of 208 to 588 μm. The Casingrain focal plane is reimaged onto each array by two elliptical mirrors with a reflecting Lyot stop between them. After the second mirror, dichroic beam splitters (capacitive mesh) split the beam into the individual bands which are directed to their arrays via optical flats. Additional filters over each array are used to sharpen the edges of the bands. This design allows easy alignment before installation into the cryostat and shields the detectors from stray light.

The BLAST gondola consists of a precision-pointed inner frame on which the primary and secondary mirrors, a near-field baffle and the cryostat are mounted. The inner frame is supported by a stiff outer frame that is suspended from the gondola by four cables. Both frames are made of welded aluminum. The outer frame will be pointed in azimuth by a flywheel and an active pivot. The inner frame has an elevation mount with direct-drive

servo motors that turn it relative to the outer frame. Three orthogonally-mounted laser-ring gyros provide high bandwidth motion sensing, and a daytime CCD star camera, capable of seeing magnitude +7 stars, is used to update the gyros and provide pointing measurements to an accuracy of 4″ (after data analysis). Crude pointing of the outer frame will be provided by a combination of magnetometers and sun sensors. The whole gondola is surrounded by a sunshield made of mylar sheet stretched over an aluminum frame.

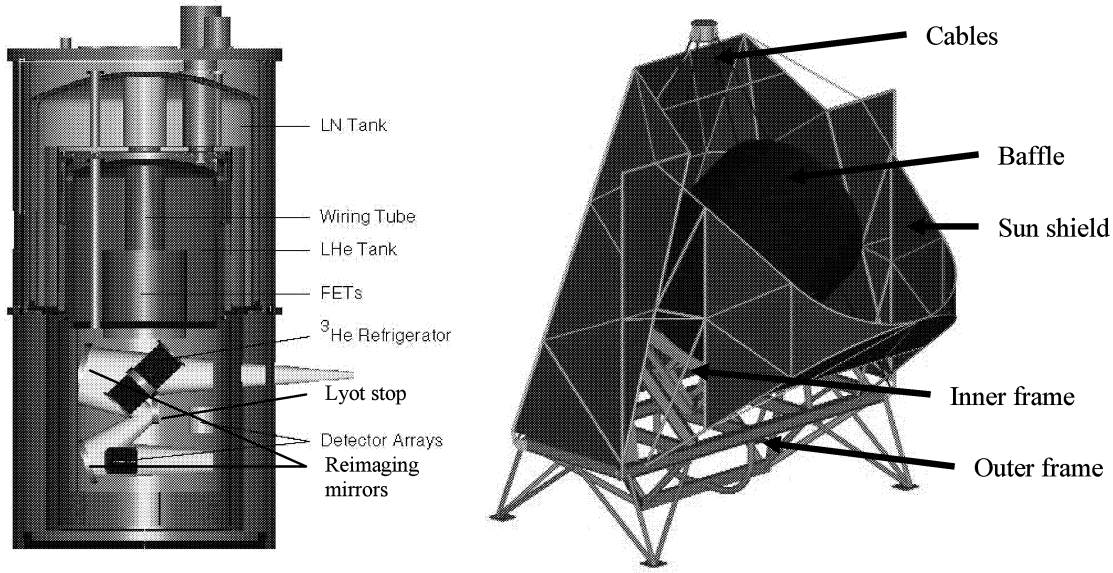

Figure 3. On the left is a cutaway view of the blast cryostat, showing the positions of the reimaging optics, the arrays and the helium-3 refrigerator. On the right the BLAST gondola is shown. The base of the gondola is 14 by 9.5 ft, the structure is 25 ft high, and the total mass is 4300 lbs (loaded).

5. CONCLUSIONS

BLAST will first fly overnight across N. America. Later Artic and Antarctic LDB flights will provide sub-millimeter maps much more cheaply and more quickly than those produced by the planned *Herschel* instrument. An upgrade to a 2.5 m mirror is also possible. BLAST will observe areas of the sky that are accessible by other lower frequency instruments such as SCUBA on the JCMT telescope. Such complementary observations will allow a greater range of science to be carried out. When SPIRE is launched BLAST observations will also be very useful for planning surveys.

REFERENCES

1. Griffin M.J., Swinyard B.M., Vigroux L. "The SPIRE Instrument for Herschel", in *The Promise of the Herschel space observatory*. Eds. G.L. Pilbratt *et al.*, ESA-SP 460, 2001
2. Scott D. *et al.*, "The Balloon-borne Large Aperture Sub-millimeter Telescope", in *The Promise of the Herschel space observatory*. Eds. G.L. Pilbratt *et al.*, ESA-SP 460, 2001
3. Bock J., *et al.*, "Silicon nitride micromesh bolometer arrays for SPIRE", Proc SPIE, Vol 3357, 297, 1998
4. Puchalla J., *et al.*, in preparation

Prospects for Terahertz Radio Astronomy from Northern Chile

R. Blundell, J.W. Barrett, H. Gibson, C. Gottleib, T.R. Hunter, R. Kimberk,
S. Leiker, D. Marrone, D. Meledin, S. Paine, D.C. Papa, R.J. Plante, P. Riddle,
M.J. Smith, T.K. Sridharan, C.E. Tong, and R.W.Wilson
Harvard Smithsonian Center for Astrophysics
60, Garden Street, Cambridge, MA02138, USA

M. Diaz, L. Bronfman, and J. May
Universidad de Chile

A. Otarola
European Southern Observatory

S.J.E. Radford
National Radio Astronomy Observatory

Abstract

The terahertz (THz) frequency range (1-3 THz, or 100-300 μm wavelength) provides an important window on the far-infrared Universe. Recent studies of the transmission spectrum of Earth's atmosphere reveal that windows centered at 1.03 THz, 1.3 THz, and 1.5 THz become significantly transparent from high altitude (> 5000m) sites in northern Chile. We are currently building a small radio telescope antenna in order to assess the feasibility of ground-based THz astronomy. The antenna, an 800 mm diameter paraboloid, has a surface accuracy of 3 μm rms and a beam width of about 1 arcminute at 1.5 THz. It will be coupled to HEB receivers, also under development at SAO. Initial astronomical tests will be carried out in the 850 GHz and 1.03 THz atmospheric windows. Receivers for the two higher frequency bands are currently under development and are expected to be deployed towards the end of 2002.

Introduction

Between the far infrared and the shortest radio wavelengths lies a region of the electromagnetic spectrum rich in astrophysical information, yet virtually unexplored. The dearth of scientific data in this spectral region is not due to lack of interest, for it provides unique targets for both interstellar chemistry and star formation studies. However, even though windows at 225 and 200 μm had been observed from Pikes Peak as long ago as 1971 [1], and it had been predicted that the South Pole may offer some atmospheric transmission in the far infrared [2], it has been generally accepted that 1 THz represents the upper frequency bound for radio observation from the ground [3]. Hence, this frequency regime has been left to a few groups with access to balloons or aircraft,

such as the Kuiper Airborne Observatory (KAO) [4], which was designed as a platform from which to make astronomical observations in the wavelength range 1 – 500 microns. Several groups have used the KAO to make spectroscopic measurements in the frequency range 1 – 3 THz, but it ceased operations towards the end of 1995. Since that time, radio astronomy observation above 1 THz has been relegated to the unenviable position of waiting for the 2008 launch of the Herschel Observatory [5], which will perform herterodyne spectrosopy in the frequency range from about 0.5 to 2 THz, or waiting for the KAO replacement, the Stratospheric Observatory For Infrared Astronomy (SOFIA) [6], which will carry a number of instruments and perform heterodyne spectroscopy to about 3 THz for approximately 20% of the time it operates.

Site selection and potential observations

In 1995, the National Radio Astronomy Observatory began a series of measurements to evaluate the feasibility of performing millimeter and submillimeter astronomical observations from Chajnantor, a plateau at 5,000 m altitude, in the Atacama region of northern Chile. It soon became apparent that this site offered excellent atmospheric transmission in both the millimeter and submillimeter, and is superior to any of the developed sites currently in use for radio astronomy. Largely as a result of the superior transmission offered at the Chajnantor site at 350 μm, we developed a purpose-built Fourier Transform Spectrometer (FTS) to evaluate the site for potential use for astronomical observation above 1 THz. The FTS continuously measures the sky brightness in order to determine the atmospheric opacity over the frequency range 350 GHz to 3 THz, and was installed at the Chajnantor site in the fall of 1997. Measurements made in the 1998 austral winter demonstrate that ground-based astronomical observations could be made from this site in the atmospheric windows centered at 1.03 THz, 1.3 THz, and 1.5 THz [7].

These windows provide unique targets to both interstellar chemistry and star formation studies. Put simply, cool interstellar clouds (10-15K) emit their strongest continuum emission in the 1.0-1.5 THz range. Also, in hot cores (50-200 K) where stars are currently forming, the high-*J* rotational transitions of common molecular species such as CO, CN, HCN, and HCO^+ emit their strongest rotational radiation in this frequency range. Near both young and evolved stars, molecules exist across a large range of excitation levels, with the more highly-excited states often lying closer to the exciting source or protostar. Surveys of objects in these lines will likely provide a good discriminator of the various stages of protostellar evolution, and for lines falling within the atmospheric windows, a ground-based telescope will offer substantial advantages over aircraft- and balloon-based platforms in terms of cost, logistics, and available observing time.

Figure 1 shows a selection of spectral lines falling within these windows, together with the measured atmospheric transmission from the Chajnantor site on the night of August 26th, 1998. In addition to lines from familiar molecules, there are many lines unique to

the terahertz range including the N^+ ground-state fine structure transition at 1.461 THz, and the NH^+ fundamental rotational doublet at 1.013 THz and 1.019 THz. These two

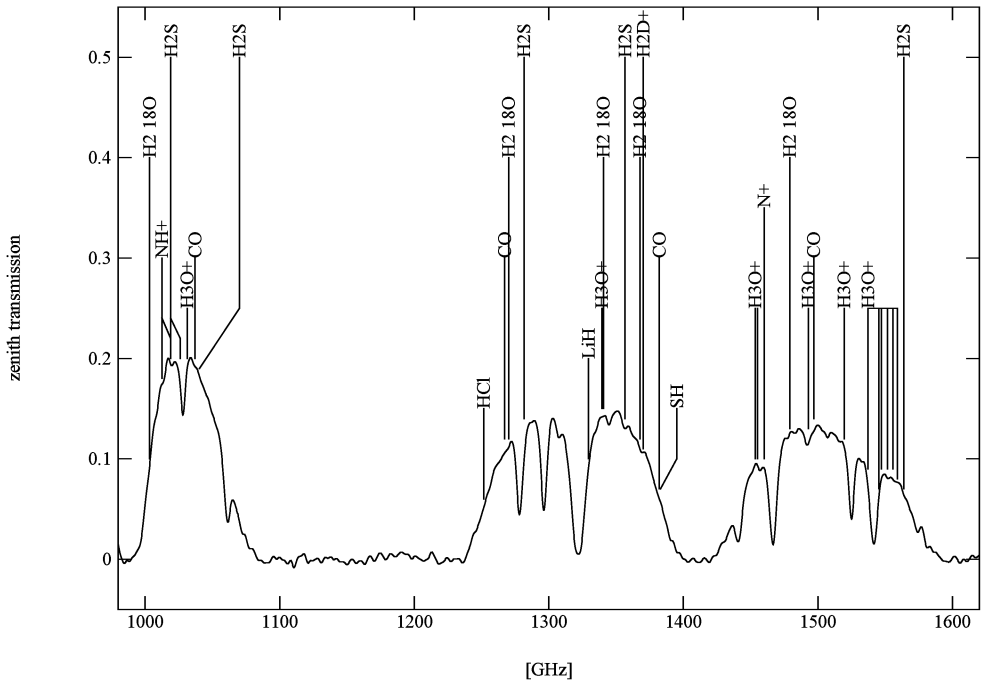

Figure 1 – Measured atmospheric transmission from the Chajnantor site on 1998 Aug 26, 06:00 UT, from a 10-minute FTS scan. The frequencies of selected molecular lines and the N^+ fine structure line are indicated for reference.

species are involved in the first steps of the theoretical synthesis chain for NH_3. The NH^+ ion has not been detected astronomically at any wavelength, despite its expected role in interstellar chemistry. Whereas the unresolved N^+ fine structure line is visible from the Galaxy in the COBE FIRAS spectrum, and an all-sky map with 7 degree angular resolution confirms that N^+ line emission will be widely detectable [8,9]. However, the kinematic information carried by this line, which can be studied in detail with heterodyne receivers, is not apparent from the COBE data. Also, and in contrast to optical lines of N^+, extinction effects by dust are insignificant at terahertz frequencies. Even a modest-sized terahertz telescope will offer better angular resolution than the COBE map by more than two orders of magnitude, and would be capable of detecting the N^+ line in nearby galaxies. The H_3^+ is an important species in ion-molecule chemistry in the interstellar medium, but it has no lines in the submillimeter. The H_2D^+ ion serves as a tracer for H_3^+, and its fundamental rotational transition at 1.370 THz is the best means of observing it in cool molecular clouds [10]. Of the metal hydride transitions shown in Fig. 1, HCl, LiH, and SH, the most important is likely to be the fundamental rotational transition of SH at 1.383 GHz. The only transitions of this molecule below 1 THz are at 867 GHz and 875 GHz, but have lower-state energy E/k = 527 K. Finally, a point not to be forgotten, the ability to perform line surveys in the terahertz windows will provide the potential to discover unexpected features of the interstellar medium.

In order to enhance our understanding of the weather above Chajnantor, SAO joined NRAO, ESO, and Cornell University in a collaboration to collect radiosonde data above the site [11]. Over the past three years, a number of radiosonde launches were under a variety of atmospheric conditions, including periods of excellent transmission, as determined by the FTS measurements. From the data, an example of which is given in Fig. 2, it appears that a layer of water vapor is often trapped above the site by a temperature inversion that is sometimes only several hundred metres higher. This implies that even a modest gain in altitude might result in a significant improvement in atmospheric transmission.

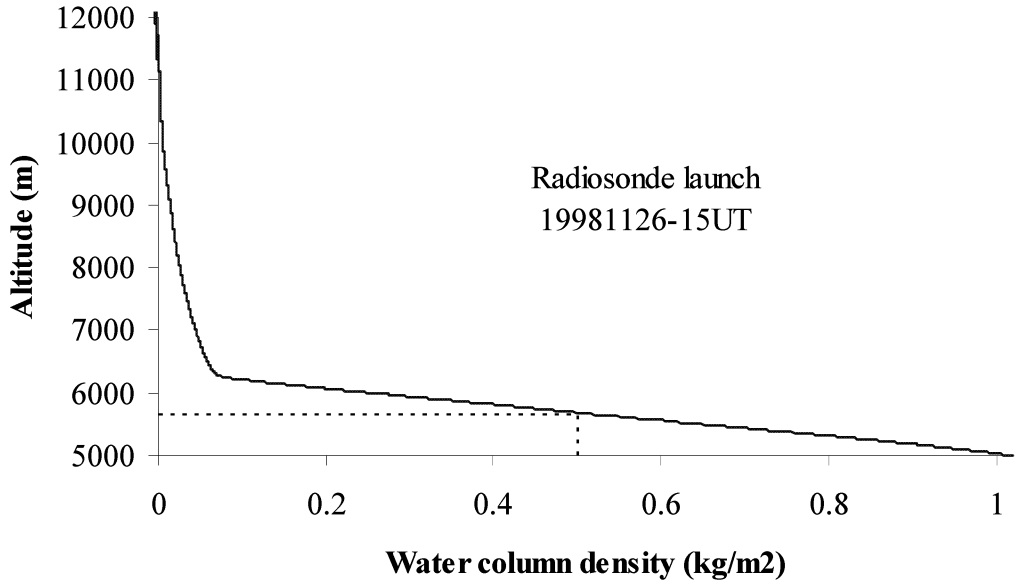

Figure 2 – Specific water vapor column density calculated from measured radiosonde data above Chajnantor. By ascending to just 650m above ground level, the water column density is reduced by half.

Following our measurements on Chajnantor, we deployed the FTS on a plateau, below the peak of Cerro Sairecabur, at 5,500 m altitude. In Fig. 3 we plot the cumulative distribution of opacities, from both sites in the 1.3 THz atmospheric window. The Chajnantor data was collected during the period from October 1997 to December 1999 and includes 37,000 spectra [12], and the data from Sairecabur was collected during the period October 2000 to January 2002 and includes 19,000 spectra. Both sets of data include periods of good and bad weather, and are considered to be representative samples of the four seasons. From the data we conclude that, on average, the opacity from Sairecabur is about 0.6 below that from Chajnantor. For example, we observe an atmospheric transmission of 8 % or better from the Chajnantor site 10% of the time; whereas from the Sairecabur site we observe a transmission of 15 %, again for 10% of the time, 24 hours/day, 365 days/year.

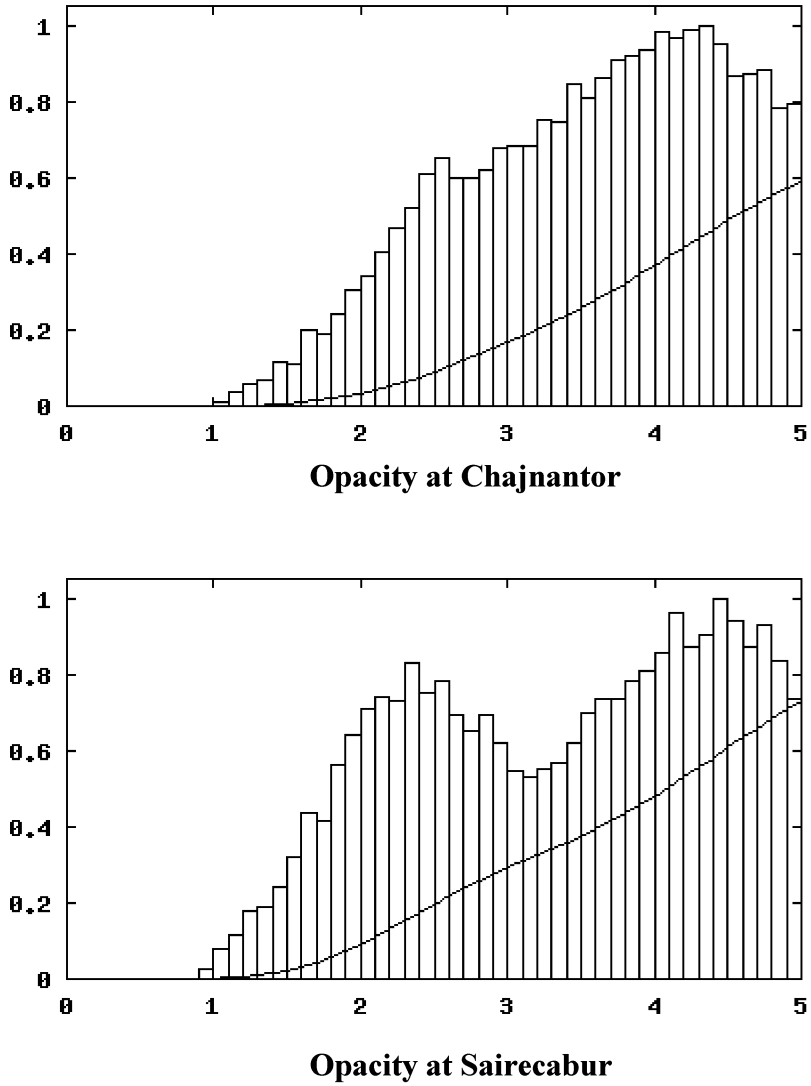

Figure 3 – Normalised histograms and cumulative distribution functions calculated for Chajnantor and Sairecabur. The Chajnantor data set represents 37,000 spectra taken between December 1997 and October 1999, and the Sairecabur data set represents 19,000 spectra taken between October 2000 and January 2002.

Instrument development

During the past several years there has been an effort to further develop heterodyne receiver technology, for the 1 – 3 THz frequency range, to be flown on future airborne and spaceborne astronomy missions. Superconductor-insulator-superconductor mixers are currently being developed to 1.4 THz, and a number of groups are working to develop the superconducting hot electron bolometer (HEB) mixer for use in the 1 – 3 THz spectral range.

Since 1995 we have been collaborating with the group at th Mscow State Pedagogical University to develop the phonon-cooled HEB mixer, and, since 1999, have successfully used this class of mixer for radio astronomical observations below 1 THz. In January 2000 we made the first fully resolved astronomical observation of CO at 1.037 THz from a ground-based site [13], and for the past two years have been working towards developing HEB mixers for use in the atmospheric windows above 1 THz. Figure 4 summarizes the current status of SAO HEB mixer receiver performance.

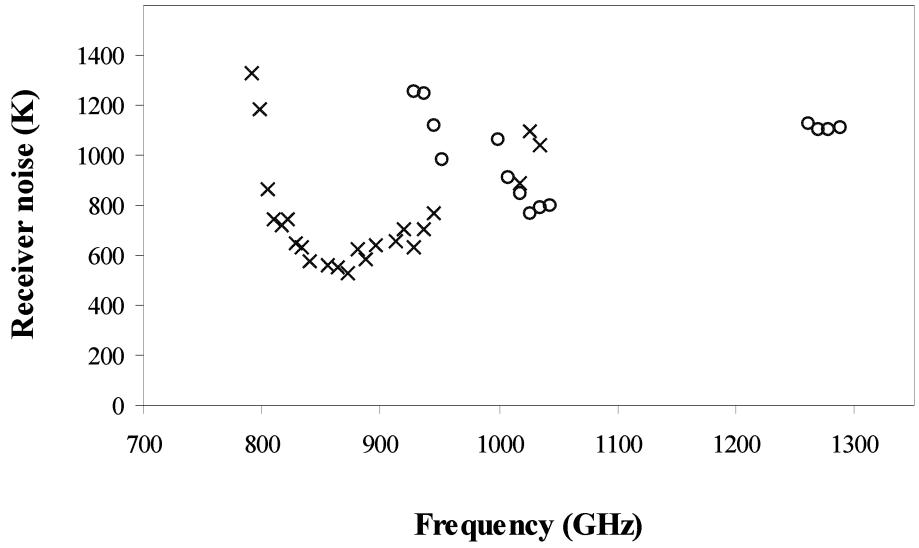

Figure 4 – Measured DSB receiver noise performance as a function of local oscillator frequency for two HEB mixer receivers developed at SAO. The lower frequency receiver covers the atmospheric windows centered at 850 GHz and 1.03 THz, the other is for use in 1.3 THz atmospheric window and provides redundancy at 1.03 THz. A third mixer, currently under development for use in the 1.5 THz atmospheric window, will provide redundancy at 1.3 THz.

If we assume that the mixers are double sideband, a reasonable assumption given the low intermediate frequency of the HEB mixer, we estimate single sideband receiver noise temperatures in the range 1,000 – 2,500 K for frequencies from 800 GHz to about 1,300 GHz. Suppose now that the average atmospheric transmission towards the source during an astronomical observation is about 10 %, we then calculate system temperatures of between 10,000 and 25,000 K which are similar to the receiver noise temperatures of heterodyne instruments previously flown on the KAO [14,15]. In other words, observations made from the Sairecabur site could be made with almost identical sensitivities as those made from the KAO. Such observations would be limited to the atmospheric windows shown in Fig. 1. However, a ground-based instrument will offer substantial advantages

over aircraft, balloon, and space -based platforms in terms of cost, logistics, and available observing time.

With one exception, all spectral line radio astronomy at frequencies in excess of 1 THz has been made using relatively small antennas. For example, the KAO antenna was 0.91 m in diameter, and the ISO reflector was only 0.6 m across. The Herschel satellite will incorporate a 3.5 m diameter antenna, and SOFIA will have an antenna 2.5 m across. For our test instrument we selected a reflector diameter of 0.8 m. This should permit scientifically interesting astronomical observation at reasonable cost. Since the aim of this work is only to evaluate the prospects for ground-based terahertz radio astronomy, it is important that any test facility should require only a minimum of infrastructure. We therefore decided to house the antenna on the top of a 20-foot shipping container that will also serve as a control room.

The reflector is made of a single piece of aluminum has an rms surface error of less that 3μm and supported on an alt-az mount with a standard coudee optical configuration. The azimuth and elevation axes are both driven by off-the-shelf brushless DC servomotors, followed by zero-backlash, high ratio reducers: a harmonic drive in the case of the elevation axis, and a worm drive for azimuth. The motors are driven by off-the-shelf intelligent PWM servo amplifiers, which provide electronic commutation. In addition, the commutation encoder is used to operate a velocity-feedback (speed control) loop in the amplifier itself. A DC velocity command is sent to each of the servo amplifers from a computer D-A card. High-resolution optical encoders with quadrature sine-wave outputs are mounted directly on each axis, and an interface PC card provides 1024 interpolation for each cycle, giving a total resolution similar to a 24-bit encoder. A simple position servo loop runs in the PC for both axes. With the velocity loop of the servo amplifer properly tuned, this provides an extremely smooth, well-behaved servo system, with a slew speed of up to 4 degrees per second and sidereal tracking errors less than 2 arcseconds.

Summary

We have demontrated that there exist new opportunities in terahertz astronomy from northern Chile. This spectral region is rich with scientific possibilities, and advanced receiver technologies, largely developed at SAO, will make sensitive heterodyne observations in this little explored region of frequency space possible.

References

1. W.G. Mankin, J.A. Eddy, R.M. MacQueen, R.H. Lee, and C.W. Querfeld, “Observations of Far Infrared Atmospheric Windows at 44 cm^{-1} and 50 cm^{-1} from Pikes Peak”, Nature Physical Science, Vol. 245, pp. 8-9, 1973.

2. C.H. Townes and G. Melnick, "Atmospheric Transmission in the FarInfrared at the South Pole and Astronomical Applications", PASP, Vol. 102, pp. 357-367, 1989.

3. J.E. Carlstrom and J. Zmuidzinus, "Millimeter and Submillimeter Techniques", Reviews of Radio Science, 1993 – 1995", Oxford University Press, 1996.

4. The Kuiper Airborne Observatory at http://spacelink.nasa.gov/NASA.Projects/ Space.Science/ Solar.System/Kuiper.Airborne.Observatory/

5. The Herschel Observatory at http://sci.esa.int/first/

6. The Stratospheric Observatory For Infrared Astronomy at http://sofia.arc.nasa.gov/

7. S.N. Paine, R. Blundell, D.C. Papa, J.W. Barrett, and S.J. Radford, "A Fourier Transform Spectrometer for Measurement of Atmospheric Transmission at Submillimeter Wavelengths", PASP, Vol. 112, pp. 108-118, 2000.

8. E.L. Wright, J.C. Mather, C.L. Bennett, E.S. Cheng, R.A. Shafer, D.J. Fixen, R.E. Eplee, Jr., R.B. Isaacman, S.M. Read, N.W. Bogess, S. Gulkis, M.G. Hauser, M. Janssen, T. Kelsall, P.M. Lubin, S.S. Meyer, S.H. Moseley, Jr., T.L. Murdock, R.F. Silverberg, G.F. Smoot, R. Weiss, and D.T. Wilkinson, "Preliminary Spectral Observations of the Galaxy with a 7 Beam by the Cosmic Background Explorer (COBE)", Ap. J. 381, pp. 200-209, 1991.

9. D.J. Fixsen, C.L. Bennett, and J.C. Mather, "COBE Far Infrared Absolute Spectrometer Observations of Galactic Lines", Ap. J. 526, pp. 207-214, 1999.

10. R.T. Boreiko and A.L. Betz, "A search for the Rotational Transitions of H_2D^+ at 1370 GHz and H_3O^+ at 985 GHz", Ap. J. 405, pp. L39-L41, 1993.

11. http://www.tuc.nrao.edu/alma/site/Chajnantor/instruments/radiosonde/

12. http://cfarx6.harvard.edu/

13. J. Kawamura, T.R. Hunter, C.E. Tong, R. Blundell, D.C. Papa, F. Patt, W. Peters, T. Wilson, C. Henkel, G. Gol'tsman, and E. Gershenzon, "Ground-based Terahertz CO Spectroscopy Towards Orion", submitted to Astronomy and Astrophysics, 2001.

14. A. L. Betz and R.T Boreiko, "Reversed Far-Infrared Line Emission from OH in Orion", Ap.J. 346, L101-L104, 1989.

15. H.P. Roser, "Heterodyne Spectroscopy for Submillimeter and Far Infrared Wavelengths", Infrared Physics, Vol. 32, pp. 385-407, 1991.

1400-1900 GHz Membrane Based Schottky Diode Triplers

Alain Maestrini, Goutam Chattopadhyay,
Erich Schlecht, David Pukala and Imran Mehdi

Jet Propulsion Laboratory, MS 168-314, 4800 Oak Grove Drive, Pasadena, CA 91109

***Abstract* — The membrane based planar Schottky diode process has been utilized to design a family of triplers to cover the astronomically important 1400 to 1900 GHz range. The design process involves a systematic study of the various parameters such as anode size, diode doping, circuit configuration, and circuit topology to name a few. A successful design necessitates that tradeoff space is established and the most *practical* circuit is selected keeping in mind the rather unpredictable task of final assembly. Simulations show that the designs being fabricated will produce output power in the microwatt range which ought to be enough to pump hot electron bolometer (HEB) mixers.**

I. Introduction

Recent progress in hot electron bolometer mixers has demonstrated very attractive sensitivities well into the THz regime. However, so far most if not all, of these mixers in the 1 THz range have been pumped with gas-based laser sources. For any flight applications it would be extremely important to develop solid-state sources that can pump these mixers. Fortunately, planar Schottky diodes have revolutionized the field of multiplied sources and in the last few years tremendous progress has been made towards implementing practical planar Schottky diode varactors in the THz range [1]-[6]. The present paper deals with the design of a family of triplers that cover the 1400 to 1900 GHz frequency range.

One possible approach based on a x2x3x3 chain driven by power amplifiers in the 92-106 GHz range will cover the astronomically important lines at 1.6 and 1.9 THz. Similarly, a x2x3x3 chain driven with a 80-92 GHz power amplifier will cover the 1.46 THz spectrum. The present paper deals with the design of the last stage triplers mentioned in the above scenarios. This paper will address some of the constraints that are placed on designs for the high frequency triplers and will address the methodology involved in designing circuits that can be implemented for robust LO chains.

II. Design Methodology

A common method employed to design and optimize diode multiplier circuits is to first optimize the diode parameters using non-linear codes (such as harmonic balance). The diode impedance is then properly matched to the input and output circuits utilizing linear circuit synthesis. This approach is relatively fast and has shown to work very well with balanced doublers in the sub-THz range [2,4,6], since the input and output circuits can be optimized independently. However, in our approach we have exclusively used non-linear codes to simultaneously optimize the input, output and the idler frequency for designing of the

triplers. Though, this places further burden on the computational hardware, it allows one to simultaneously optimize the diode physical structure along with the embedding circuitry for maximum advantage.

Diode model: A complete and accurate physical diode model that can predict device response at these frequencies is under development [7]. A practical approach is to use a simple model of the diode that can easily be described in commercial codes including significant efficiency limiting phenomena such as breakdown voltage and current saturation. Such an exercise has been carried out in [8] for doublers assuming very limited input power (0.1 mW). Based on this exercise doublers in the 1.9 THz range at room temperature should be designed according to:

$$R_s \times C_j(0) = 120\ \Omega.\text{fF} \qquad (1)$$

Where, R_s is the series resistance and $C_j(0)$ is the zero bias junction capacitance. Note that depending of the doping of the epy-layer the value of $R_s \times C_j(0)$ can vary: a lower doping level brings more resistance.

For the 1.4THz to 1.9THz triplers a zero bias junction capacitance of 0.6 to 1.2fF is assumed based on the wafer doping ($5\text{x}10^{17}$ cm^{-3}) and reasonable minimum dimensions consistent with the membrane fabrication process. Furthermore, the model was modified by introducing a linear frequency dependence of the RF series resistance. The series resistances of the high frequency triplers was chosen by extrapolating linearly the series resistances used to model an existing (and characterized) 1.2 THz balanced tripler [5] in accordance with (1).

Losses*:* At 1.9THz, losses in the circuitry are a major concern. Losses not only introduce a linear attenuation of the signals in a multiplier circuit, losses can also make the matching of the diode very inefficient. Simulations show that a diode with $C_j(0)$=1fF, pumped with 2.5mW at 633GHz, can transfer power to the third harmonic at 1.9 THz up to thirty times more efficiently when matched by an optimal and ideal circuit, than when matched by a circuit feasible with the state-of-the-art technology (with an ideal matching circuit the diode works in a true varactor mode, with a feasible matching circuit the same diode works mostly in a varistor mode). The losses must be included during the optimization of the circuit and not after. Matching circuits designed with no loss could be in practice "surprisingly" lossy and not fully optimum.

Topology limitation & accuracy*:* Another major difficulty encountered in the designing of terahertz multipliers is the limitation in the topology of the circuits. This limitation is mainly due to the RF losses that the metallic parts of the circuits can induce. Actually, to keep the losses acceptable, it is necessary to use matching elements made of sections of waveguides in which the currents flow with a low surface density. The rectangular waveguide, the coaxial waveguide or the suspended microstrip are usually good candidates for such a requirement. Unfortunately the topology of the circuits feasible with such

waveguides is pretty limited. In addition, the active devices are totally immersed in these waveguides, a fact that does not facilitate efficient modeling.

The accuracy of the fabricated circuits is also a concern when working at these frequencies. It is important to design the circuits to be as tolerant as possible to fabrication and assembly variations. To allow for machining tolerances in the waveguide blocks it is recommended to integrate on chip the critical matching elements in order to take advantage of the tighter tolerances associated with micro-photolithographic techniques. Circuits fabricated on thin dielectric membrane combine low loss and accuracy providing for a more stable and robust implementation.

Input power: Another practical constraint that must be acknowledged for any high frequency multiplier design is the fact that only limited amount of RF power will be available to drive the multiplier. When the pump power of a multiplier is small, the diode cannot be properly modulated. At the limit, the power conversion from the fundamental to the n^{th} harmonic follows a law that asymptotically tends to:

$$P_n \xrightarrow[P_1 \to 0]{} \alpha(f) \times P_1^n \qquad (2)$$

or in the logarithmic form :

$$Log(P_n) \xrightarrow[P_1 \to 0]{} \alpha'(f) + n \times Log(P_1) \qquad (3)$$

where P_n is the power produced at n^{th} harmonic, P_1 is the pump power, $\alpha(f)$ is coefficient that depends on the diode and the frequency. Equation (2) shows that for a tripler (n=3), dividing the pump power by two can divide the output power delivered by the diode by eight (and the conversion efficiency by four). This relationship is confirmed by simulating various multipliers with varying input power (see Figure 1).

Circuit configuration: When one has to choose between designing a balanced multiplier that requires at least two diodes, or an unbalanced multiplier that requires only one, the relation between the pump power and the efficiency of a diode has to be taken into account. The single diode of an unbalanced multiplier will receive twice the power that each diode of the simplest balanced multiplier will receive. In addition, the higher the order of multiplication, the bigger the difference in the conversion efficiency of the diode. On the other hand, balancing a multiplier considerably simplifies the matching circuit. In addition, there is the possibility to reduce the size of the anode to compensate the decrease of pump power (a smaller diode will be easier to modulate than a bigger one). In practice, this possibility is limited at high frequencies by the fact that a smaller anode presents a higher series resistance, and also by the fact that there is a minimum size for the anode.

Thus, for the 1.4 THz to 1.9 THz tripler designs both a balanced and an unbalanced approach was attempted. A generic block diagram of an unbalanced and balanced tripler are shown in Figure 2. An E-plane probe located in the input rectangular-waveguide couples the signal at the fundamental frequency to a suspended-microstrip waveguide that can propagate only the TEM mode. In order to keep this waveguide monomode, the dimensions of the channel in which the circuit is inserted have to be chosen with care. The diode(s) is (are) connected to an E-filed probe that couples the third harmonic of the funda-

mental to the output waveguide (the second harmonics is kept below cutoff). The matching of the diode is performed, both, by a succession of high and low impedance sections printed on chip and by the input and the output probes, with their respective backshort and waveguide step.

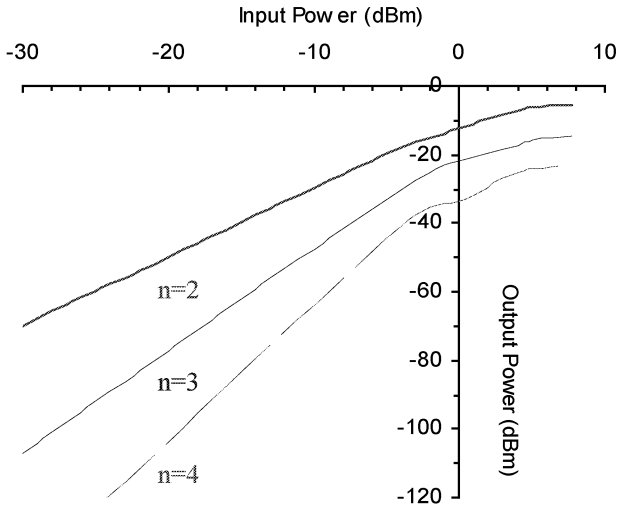

Figure 1: The calculated output power versus input power of an ideal frequency doubler (top), tripler (middle) and quadrupler (bottom) fits perfectly equation 3. The multipliers are optimized for an input frequency of 500GHz and an input power of 3.5mW. The diode is the same for all the multipliers – Cj(0)=1fF, bias fixed to zero volts.

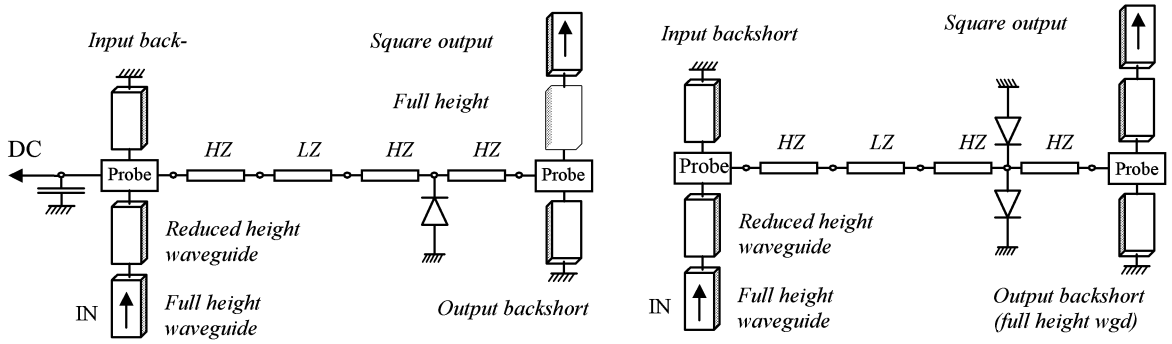

Figure 2: Generic block diagram of the unbalanced (left) and balanced (right) triplers. *HZ* stands for high impedance line, *LZ* stands for low impedance line.

III. A 1400 GHz tripler

The technology involved in fabricating these circuits has been discussed in [9]. The circuits are mounted in a gold-plated waveguide structure split into two precision-machined halves. Figure 3 shows the unbalanced and balanced designs inside the waveguide blocks. The diode of the unbalanced design has a very small mesa with a symmetrical anode that is grounded on both sides of the channel by two beam-leads. Each side of the mesa is connected to a high impedance line. One of them continues to the output probe. This structure is very compact. This design provides compactness but does slightly increase the parasitic capacitance.

The balanced tripler (Figure 3, bottom) has two diodes positioned on each side of the high impedance line. The diodes are connected in series at DC. One has its anode grounded at one side of the channel by a first beam-lead, the other has its cathode grounded to the other side of the channel by a second beam-lead. Due to the symmetry of the field at the fundamental frequency (TEM mode), the diodes appear in an anti-parallel configuration at RF. The second harmonic is trapped in a virtual loop [3] and cannot propagate in other parts of the circuit. This topology offers the advantage of a very small phase shift between the two anodes and the possibility to tune the matching at the idler frequency by adjusting the length of the beam-leads that ground the diodes. By reducing the mesa size from 10x10μm (minimum size used up to now at JPL) to 7x7μm, we could implement the two diodes in a channel of 64x25μm.

For these circuits the bias scheme is not a trivial problem. The unbalanced tripler can be biased through the input probe (that crosses the entire waveguide height) and the suspended microstrip line. A DC capacitor is implanted on chip to ground the RF signal. This solution can also work for the balanced designs but it is much more difficult to implement. Actually, two independent and opposite polarities have to be brought to the diodes. This can be done by implementing a small capacitor between the two mesas. The suspended microstrip has also to be divided into two insulated lines as shown in Figure 4. It is also possible to design the balanced circuit so that it is pretty much optimized for zero bias. We have included both designs in the current fabrication run.

We can compare the calculated performances of these multipliers with the performances of a diode that would be matched by an ideal circuit : at 1.46THz the balanced circuit is only about two times worse in terms of efficiency than an ideal circuit. Calculations show that 75% of the fundamental is coupled to the diodes. The remaining losses (another 25%) are shared between the second and the third harmonic. Simulated output power from the triplers is shown in Figure 5. For a given input power of 3.5 mW the balanced approach certainly seems to be the preferred approach. Considering that over 8 mW has already been demonstrated at 440 GHz it is possible that more input power will be available. Even with the limited input power a 3dB bandwidth of about 20% is achieveable. Moreover, considering that the HEB mixers might only require LO power levels at the one microwatt range the existing design ought to cover even a larger bandwidth.

IV. A 1900 GHz Tripler

The unbalanced and balanced designs for the 1.9 THz tripler are shown in Figure 6. At a first glance they would seem to be 'scaled' copies of the designs for the 1.4 THz tripler. Even though the basic topology of the two designs looks similar, a detailed design was done for both triplers because simple scaling from one design to the other does not work.

Compare to the 1.4THz triplers, the 1.9THz triplers have a narrower channel. The mesas have the same size but their spacing is reduced. Another difference: the anode of the un-

balanced design at 1.9THz is grounded on both sides of the channel by two wide beam-leads that come very close to the mesa.
For the balanced circuit, implementing the two diodes was very difficult due to space limitation, even with a mesa as small as 7x7 micron. The chip was designed using the tightest tolerances available with the current technology.

Biasing of the unbalanced design is not difficult. However, a biasing scheme for the balanced design is not trivial. The solution suggested for the 1.4 THz design will not work due to space restrictions. The current circuit has been designed with zero bias. This sacrifices some of the potential bandwidth but seems to be the only practical approach given the restrictions on technology.

An input power of 2.5mW at 633 GHz is assumed. This amount of power has not been demonstrated yet but certainly looks plausible given the recent results up to 400 GHz. Optimized simulations of both the balanced and unbalanced circuits are shown in Figure 7. The balanced configuration can provide twice as much power as the unbalanced design but only for a limited bandwidth. At the band edges both designs provide similar amounts of output power. The inability to further reduce the length of the beam-leads that ground the diodes of the balanced tripler is believed to be the main reason for this limitation.

We can compare the calculated performances of these multipliers with the performance of a diode that is matched by an ideal circuit. The balanced tripler design has one-eighth the efficiency as an ideal tripler using the same diode. Only 70% of the fundamental is coupled to the diodes. The low performance of this circuit is believed to be mainly due to a non-optimized idler forced by the current technology.

An interesting simulation is to see what happens to the performance of the multipliers as input power is reduced. As the input power drops below 1 mW the unbalanced circuit tends to outperform its balanced counterpart. One could argue that the designs have not been optimized for low power but in reality the anodes cannot be shrunk any more to off set the reduced input power level.

V. Conclusion

Triplers that work in the 1400 to 1900 GHz range have been designed and described. These circuits are based on the GaAs membrane process and are currently under fabrication. Simulations indicate that if the final stage triplers can be pumped with 2-4 mW of input power it will be possible to get sufficient output power to pump HEB mixers.

ACKNOWLEDGMENTS

The authors wish to acknowledge many helpful discussions with Neal Erickson, Peter Siegel, Suzi Martin, and John Gill. The research described in this publication was carried out at the Jet Propulsion Laboratory California Institute of Technology, under a contract with the National Aeronautics and Space Administration.

REFERENCES

1. N. Erickson, R. P. Smith, S. C. Martin, B. Nakamura, and I. Mehdi, "High Efficiency MMIC Frequency Triplers for Millimeter and Submillimeter Wavelengths," *IEEE MTT Symposium*, Boston, June 2000.
2. E. Schlecht, G. Chattopadhyay, A. Maestrini, A. Fung, S. Martin, D. Pukala, J. Bruston and I. Mehdi, "200, 400 and 800 GHz Schottky diode substrateless multipliers: Design and results," in 2001 IEEE MTT-S Int. Microwave Symp. Dig., Phoenix, AZ, May 2001, pp. 1649-1652.
3. J. Bruston, A. Maestrini, D. Pukala, S. Martin, B. Nakamura and I. Mehdi, "a 1.2 THz planar tripler using GaAs membrane based chips ",*proceeding of the 12th International Space Terahertz Technology Symposium,* San Diego, February 2001.
4. N. R. Erickson, G. Narayanan, R. M. Grosslein, S. Martin, P. Smith, I. Mehdi, M. Coulomb, G. DeMartinez, "Monolithic THz frequency multipliers," Proc. of the 12th Intl. Space Terahertz Techology Symp., San Diego, Feb. 2001, pp. 297-309.
5. A. Maestrini , J. Bruston , D. Pukala, S. Martin, I. Mehdi, "Performance of a 1.2 THz Frequency Tripler using a GaAs Frameless Membrane Monolithic Circuit", *IEEE MTT-S International Microwave Symposium,* Phoenix, Arizona, May 20-25, 2001.
6. G. Chattopadhyay, E. Schlecht, J. Gill, S. Martin, A. Maestrini, D. Pukala, F. Maiwald, and I. Mehdi, "A Broadband 800 GHz Schottky Balanced Doubler," IEEE Microwave and Wireless Components Letters, Vol. 12, no. 4, April 2002.
7. E. Schlecht, F. Maiwald, G. Chattopadhyay, S. Martin, and I. Mehdi, "Design considerations for heavily-doped cryogenic Schottky diode varactor multipliers," in Proc. 12th Int. Space Terahertz Technology Symp., San Diego, CA Feb 2001, pp. 485-494.
8. Neal Erickson, private communications, 2000-2001.
9. Suzanne Martin, Barbara Nakamura, Andy Fung, Peter Smith, Jean Bruston, Alain Maestrini, Frank Maiwald, Peter Siegel, Erich Schlecht and Imran Mehdi, "Fabrication of 200GHz to 2700GHz Multiplier Devices using GaAs and Metal Membranes", *IEEE MTT-S International Microwave Symposium,* Phoenix, Arizona, May 20-25, 2001.

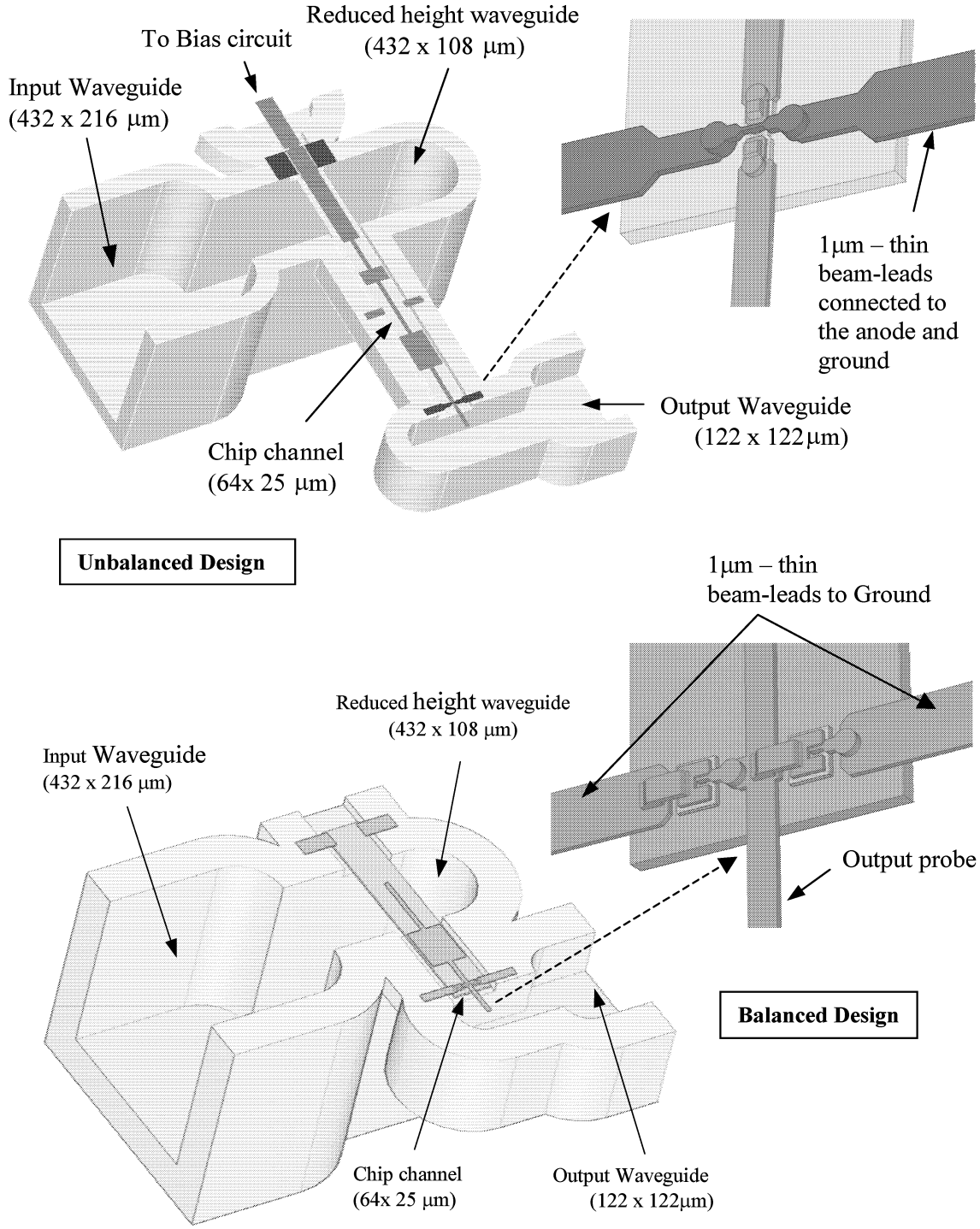

Figure 3: Unbalanced and balanced design of the 1400 GHz tripler.

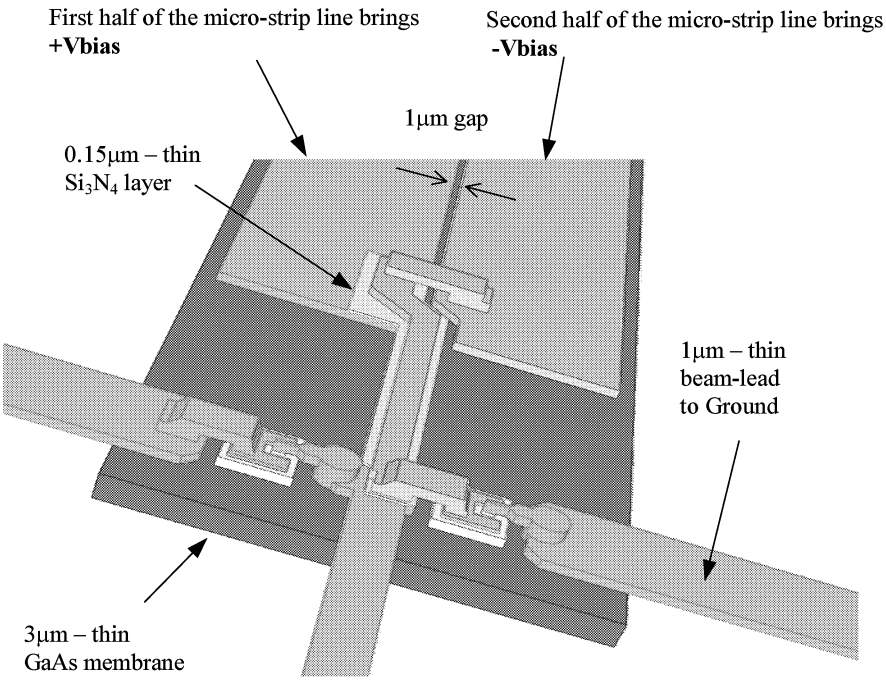

Figure 4: A possible approach for providing appropriate bias to a balanced tripler design.

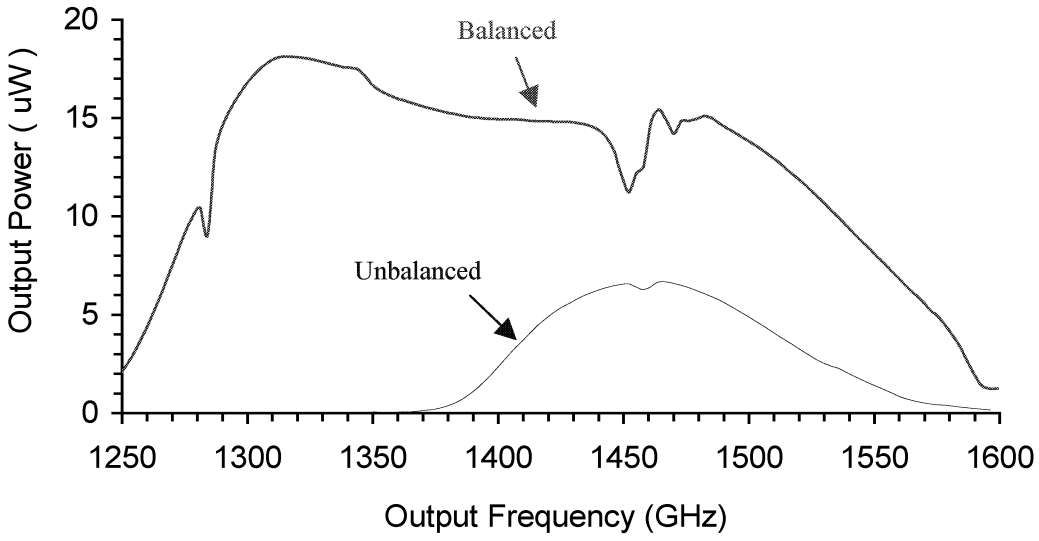

Figure 5: Calculated output power of the 1.4 THz balanced and unbalanced tripler. Input power of 3.5 mW is assumed in each case

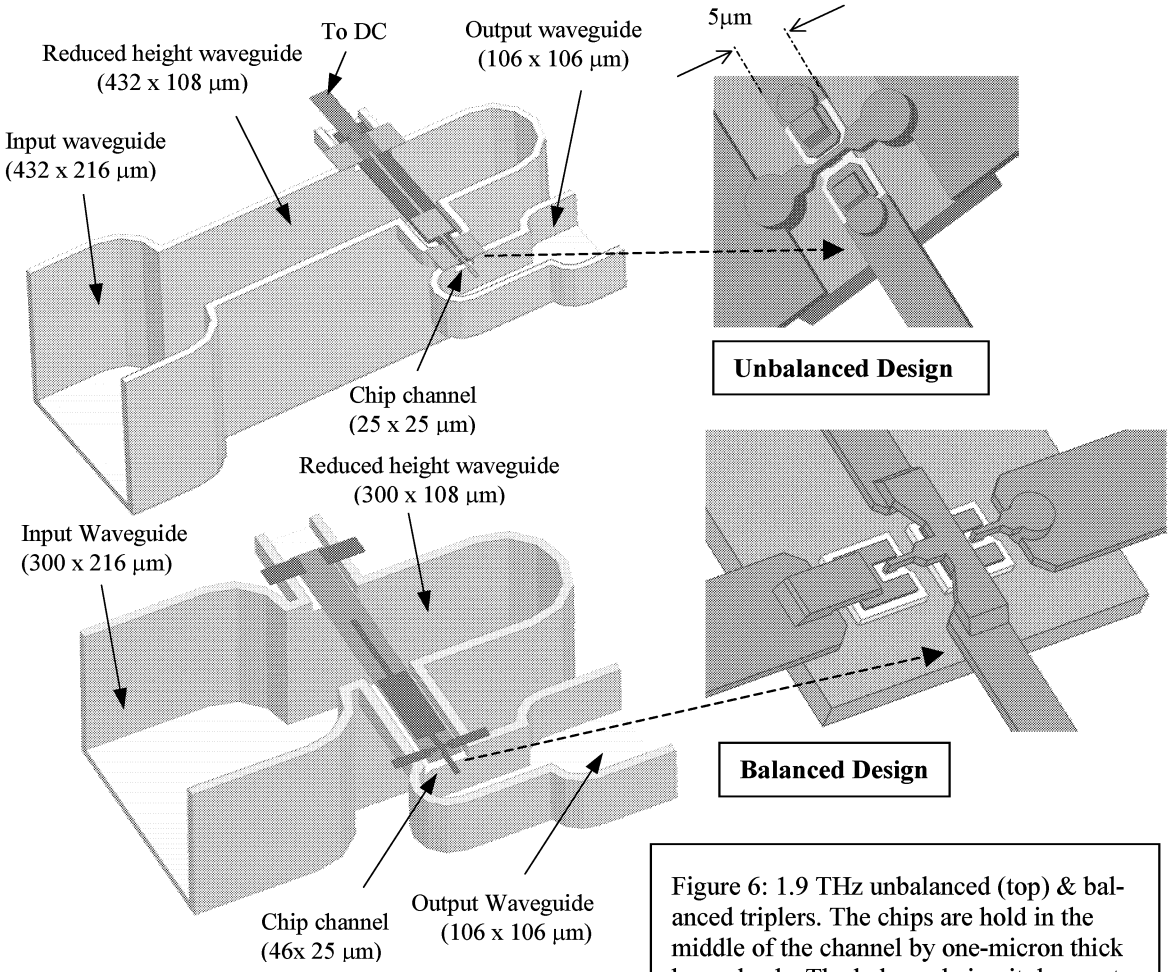

Figure 6: 1.9 THz unbalanced (top) & balanced triplers. The chips are hold in the middle of the channel by one-micron thick beam-leads. The balanced circuit does not allow to bias the diodes.

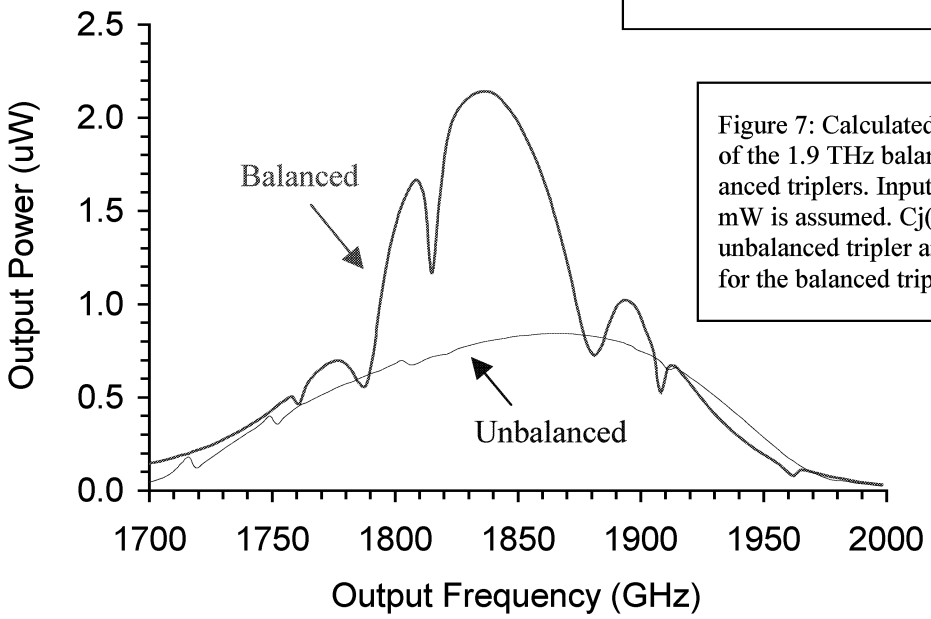

Figure 7: Calculated output power of the 1.9 THz balanced and unbalanced triplers. Input power of 2.5 mW is assumed. Cj(0)=1fF for the unbalanced tripler and Cj(0)=0.8fF for the balanced tripler.

1500 GHz Tunable Source Using Cascaded Planar Frequency Doublers

N. Erickson, G. Narayanan, R. Grosslein
Department of Astronomy
University of Massachusetts
Amherst, MA 01002

G. Chattopadhyay, A. Maestrini, E. Schlecht,
I. Mehdi, S. Martin
Jet Propulsion Lab
Pasadena, CA 91109

Abstract

A complete source for 1.5 THz has been built using a cascade of four planar doublers following a MMIC based HEMT power amplifier. This driver is in turn driven by a times nine multiplier so that the complete source may be synthesizer controlled. The source is intended for use at 120 K and has been tested at 60-90 K. The peak output powers of the stages are: first stage 53 mW, second stage 15 mW, third stage 2.0 mW and final stage 45 μW. The peak output was measured at 1484 GHz, although >1 μW is produced over the frequency range 1450-1620 GHz. Based on preliminary testing with lower power, it is expected that a power of 1 μW is sufficient to drive an HEB mixer.

Introduction

The heterodyne instrument on the Herschel (FIRST) space observatory will cover frequencies from 500 to 1900 GHz, presenting very demanding requirements on LO sources. The most challenging requirement is at the highest frequencies where LO sources with power >1 μW are needed in the 1.4-1.9 THz range with 10% tuning bandwidth. For best reliability, the source must use all-planar components with no mechanical tuning. While initially this appeared to be a very ambitious goal, planar diode technology has recently evolved to the point where this is possible. At this time, diode fabrication is relatively consistent, and multiplier designs work very well at nearly all required frequencies. Fairly complex circuits can be fabricated monolithically, on GaAs of any needed thickness. Efficiencies of many multipliers actually exceed expectations, and the operating bandwidth is near the goal. This paper describes a chain for 1.5 THz with sufficient output power over a 10% band to meet the system goal, although work remains to make this an optimal source. The entire LO system for Herschel is intended to be operated at a temperature of 120 K, so most of the data is measured at low temperatures.

The source uses a cascaded chain of four passive doublers (net x16 multiplication), with a high power driver in the 100 GHz range. The initial stage of the driver is a x9 multiplication to 89-106 GHz band, which is followed by amplification to a typical power

of 150 mW. The power amplifiers are GaAs MMIC's fabricated at TRW, and assembled into waveguide housings at UMass and JPL. The driver is a synthesizer or sweeper in the 10-12 GHz range, so frequency control is quite simple.

All of the final four doublers are balanced designs using planar diode arrays. The number and size of diodes used in each doubler depends on the required input power level. Most of these doublers have been described previously, but current results are better than previously reported and the full cascade of stages is entirely new.

First stage doubler

The doubler for 200 GHz was built at UMass using a 6 diode array. This doubler has been described previously [1,2,5], and is a balanced design using a diode array which is soldered in place, as shown in figure 1. The bias circuit is decoupled from the output with just a beam lead planar capacitor using a SiN film, and the diode is coupled to the output with a gold bond wire. The design bandwidth is 188-212 GHz output with a flat response, and the circuit seems to work well across this full band, as shown in figure 2. The optimum input power for this doubler is 150-180 mW. Limited input power at the highest frequencies causes the data be scattered, but the points with optimum drive show nearly constant efficiency. There is a substantial advantage to operating this doubler at low temperature as seen in the efficiency vs temperature curve of figure 3. The diodes use an epitaxial layer doping of $1x10^{17}/cm^3$, which gives a significant increase in carrier mobility at lower temperature, leading to lower series resistance and a 60% increase in efficiency at 80 K. At the expected operating temperature of 120 K, the efficiency should be 33%. Power was measured at all frequencies using a waveguide calorimeter having very flat frequency response from 75-2000 GHz [3,4].

A comparable design built at JPL uses beam leads rather than solder joints to mount the diode, and a bias structure which is fully integrated with the diodes. This integrated doubler appears to work about the same as the discrete design, although data is not quite as complete on this unit. This style of construction is preferred due to its easier and more repeatable assembly. However, the beam leads do lead to a larger temperature rise for the diodes.

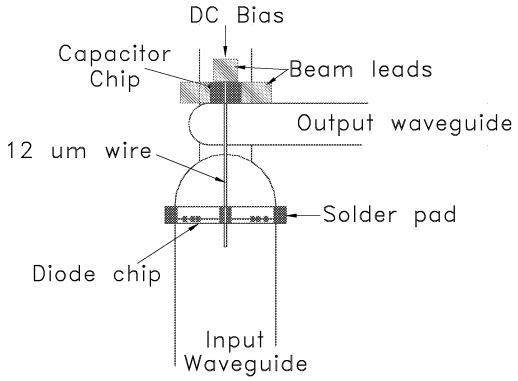

Figure 1. Schematic of the 200 GHz doubler showing just the inner region of the block. Outside of this area, waveguide steps provide the required wideband matching.

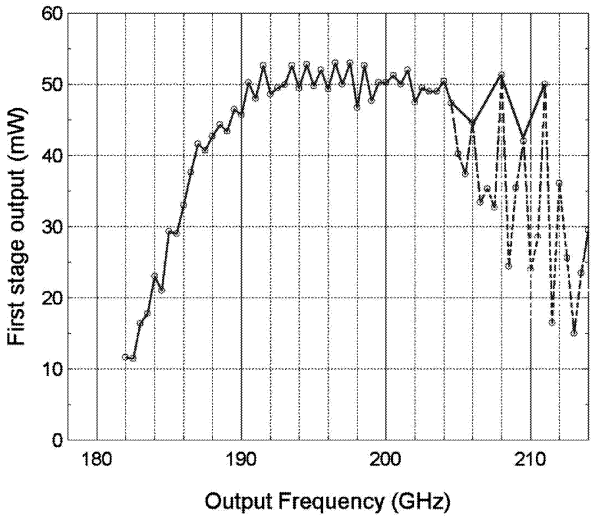

Figure 2. Output power of the first stage at 80 K with 140 mW input (up up to 204 GHz). The source power is too low for points on the dashed line, and only points on the solid line have 140 mW input.

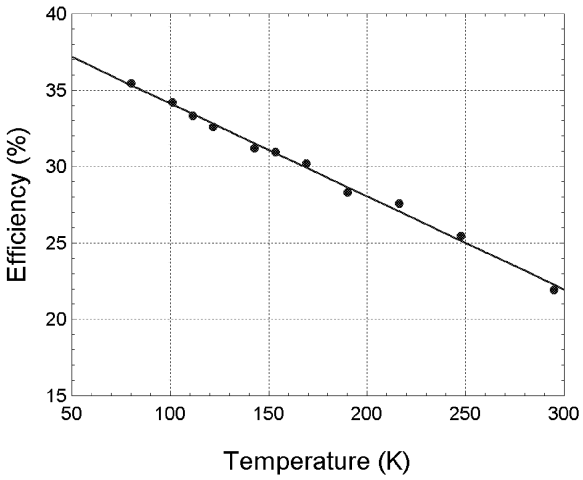

Figure 3. Efficiency of the 200 GHz doubler as a function of temperature.

Second Stage Doubler

The doubler for 400 GHz was designed and assembled at JPL using a 4 anode planar array. In concept it is identical to the 200 GHz doubler, but with a higher level of integration. The design is one with minimal substrate, consisting mostly of suspended metal with beam leads for mounting and grounding. It has been described previously [5]. The installation requires no soldering, or any difficult assembly. As with the 200 GHz doubler, the diode chip is quite simple, and much of the impedance matching over a wide band is done with machined waveguide steps. The view of one block with the diode installed is shown in figure 4.

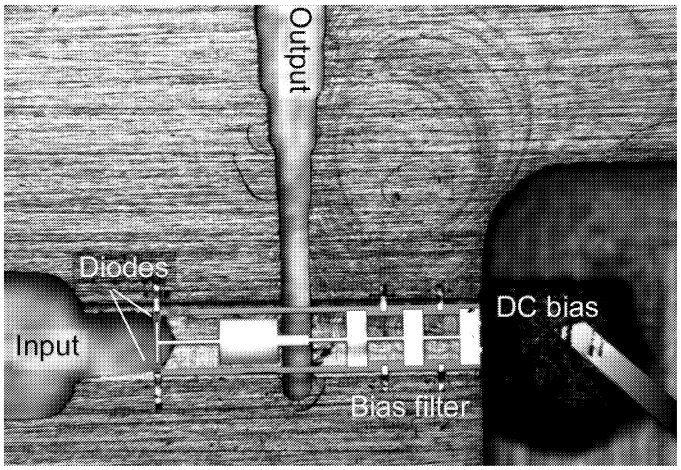

Figure 4. Internal assembly of 400 GHz doubler, using "substrateless" design.

This doubler was tested with drive from the 200 GHz doubler, with no isolator between stages. While isolators for this band are practical, and are planned for eventual use, one was not yet available suitable for vacuum operation at the needed power level. The resultant power vs frequency, shown in figure 5, shows a lot of ripple, which is likely to be mostly due to the interaction between stages. The room temperature efficiency is 16% and the 80 K efficiency is estimated to be 24%, with a diode epilayer doping of $2x10^{17}$. This doubler appears to be tuned a bit lower than its nominal design band of 375-425 GHz, and this is a typical problem with many multipliers designed for this work. Most of the effects of actual device fabrication seem to shift the frequency lower than the idealized models used for design purposes. No designs so far have been tuned high.

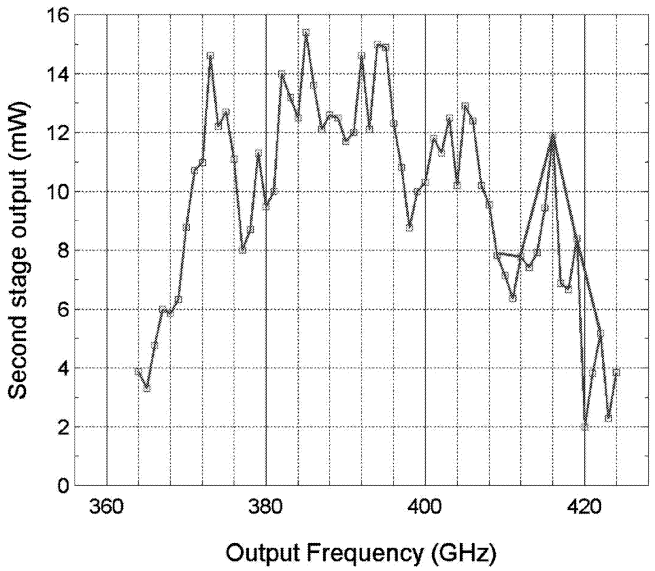

Figure 5. Output power of first two cascaded stages at 80 K. Input power to first stage is 140 mW below 408 GHz output. Above this frequency, only the upper curve has 140 mW input. No isolator is used between stages.

Third stage doubler (800 GHz)

The doubler for 800 GHz was designed at UMass with diodes fabricated at JPL. It is a balanced design as at lower frequencies, but just a pair of diodes is used, since the required power level is quite low. The diodes have a capacitance of 4.3 fF, which should be able to handle (as a pair) up to 10 mW input with a peak junction voltage below their 5.5 V breakdown. The previous stage works somewhat better than expected and its output exceeds this power by ~2 dB at some frequencies. The doubler chip is a very compact circuit on 12 μm thick GaAs, and uses beam leads for grounding the diodes and the bias bypass capacitor. The substrate is narrowed between the input and output waveguides to eliminate higher modes, which can cause a large difference in the coupling of the two diodes to the output waveguide. The circuit is simple to assemble except that diode chip is quite small, as can be seen in figure 6. Handling the chip is difficult because there is little GaAs that can be touched and the 1 μm thick beam leads are too fragile to pick up with tweezers. However, they can be picked up by simply touching a probe to them, and generally they stick. The diode is not attached to the block anywhere except at the bias terminal. This lead is connected to the bias circuit and the remaining beam leads are just clamped between the halves of the block. As with the other doublers the simple diode circuit is supplemented with waveguide steps to increase the bandwidth.

The output waveguide where the diode crosses is only 36 μm high, which is too small to cut with an end mill, so this waveguide was broached (scraped) with a tool having just the 36 μm width. This tool was ramped out of the block at a steep angle at the end of the cut to form the integral backshort. All other features were cut with end mills. All of the machining was done on an NC micromill [6].

A waveguide diagonal horn is integral to output of the doubler, since initial testing was to be of this as a final stage, and the waveguide seemed too small to flange reliably. This horn is an obstacle to using this as a driver for a following stage, but the horn may be eliminated for future use.

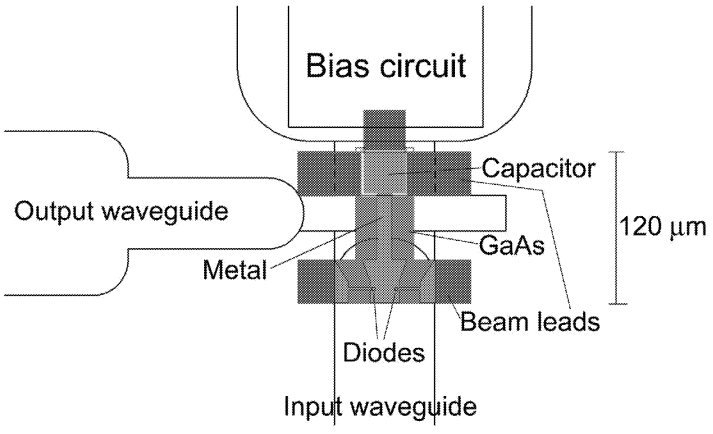

Figure 6. Cross section of 800 GHz doubler.

The output of these three cascaded stages is shown in figure 7, for room temperature and 80 K operation. There is more ripple than for the 400 GHz driver, and the ratio of maxima to minima is larger. In addition, this doubler, too, is tuned lower than designed, since it is intended to work from 780-860 GHz. The apparent tuning error is ~30 GHz, only a 3-4% shift relative to the design, but one that must be understood and corrected. The typical bias voltage is 1.5-2.5 V (reverse), with no systematic frequency dependence, and the bias current is very small.

The very large change in output power with cooling is mostly due to the change in input power, which may increase a factor of 2.4. The efficiency of this doubler is relatively temperature insensitive. The cold efficiency is about 11%, while at room temperature it is ~10%. The diode doping is $3x10^{17}$ which leads to minimal temperature dependence to the mobility. However, the efficiency rises with input power when it is underdriven, accounting for the very large increase in power at the higher frequencies at low temperature. It is notable that the maximum output power is ~20 times larger than that available at comparable frequencies using whisker contacted triplers, which were the best previously available multiplier technology.

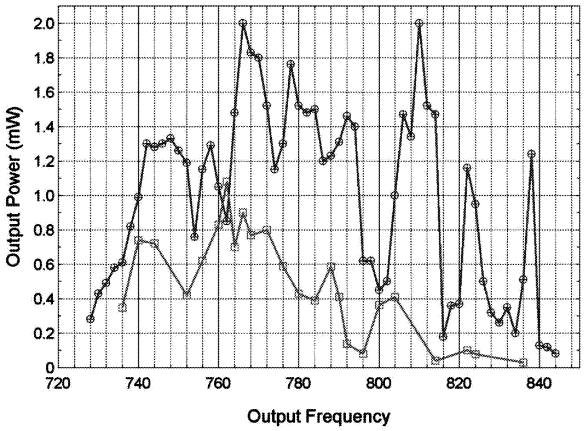

Figure 7. Output power of 3 cascaded stages at room temp (upper) and 80 K (lower). Input power for the cold data is 140 mW below 816 GHz. Input power at room temperature is 160 mW below 790 GHz. At higher frequencies input power may be significantly lower.

Fourth stage doubler (1.5 THz)

The 1.5 THz doubler uses a balanced design in a resistive mode. The circuits used in the lower frequency stages are not easily extended to this frequency because of the need to machine very low height output waveguide. However an alternate circuit geometry puts the diodes in series in the output waveguide, with a coupling probe to the full height input waveguide. The diodes may then be biased in series via an extension of the substrate and a SiN bias bypass capacitor. The circuit layout is shown in Figure 8. The overall diode construction uses a framed design with 50 μm thick frame and 3 μm substrate for active part of the circuit. This design has been described previously in preliminary tests with a laser pump [7].

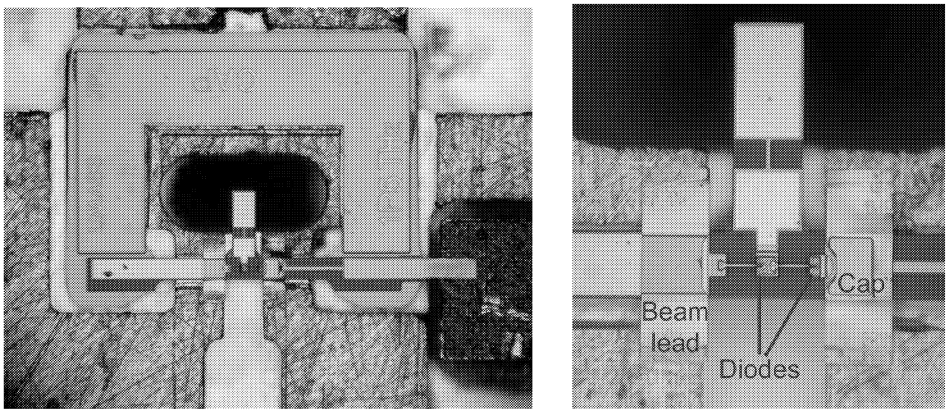

Figure 8. Overall view of the 1.5 THz doubler showing the frame and input waveguide, and detail showing just the electrically important part of the circuit.

The doubler is very easy to assemble, but the frame complicates the machining, because the input waveguide must plunge directly through the block. This waveguide does not need to be very long because a conical waveguide horn is integral to the input, and can be machined from the other side of the block. This block was designed for tests with a laser driver, before the complete chain was complete, so an input horn was desired. This horn has approximately the same dimensions as that on the 800 GHz doubler so coupling between them can be fairly good. although higher modes can also cause a large variation in coupling.

The complete four stage chain was tested at 60K over a wide band, and at room temperature over a more limited band. The chain as used at room temperature is shown in Figure 9. The setup for cold tests placed much of the chain at room temperature and just the final power amp stage and the four doublers at low temperature, as shown in Figure 10. In order to eliminate a lossy vacuum window on the output, the THz power sensor was placed inside the dewar, although it was maintained near room temperature through the use of an isolating section of stainless steel waveguide

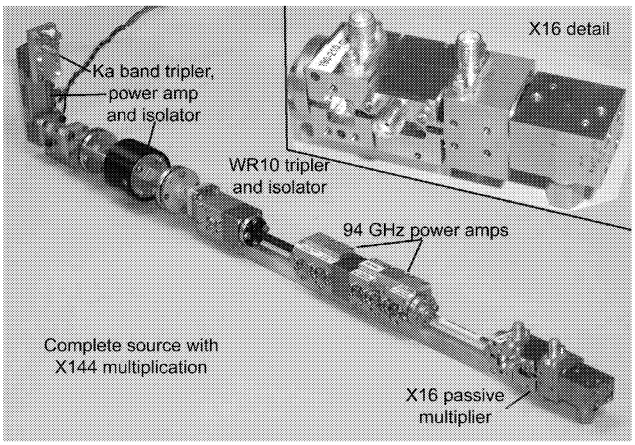

Figure 9. Complete source with x144 multiplication, using x9 stage followed by power amps and a x16 passive multiplier. The output is a small diagonal feed horn which points upward.

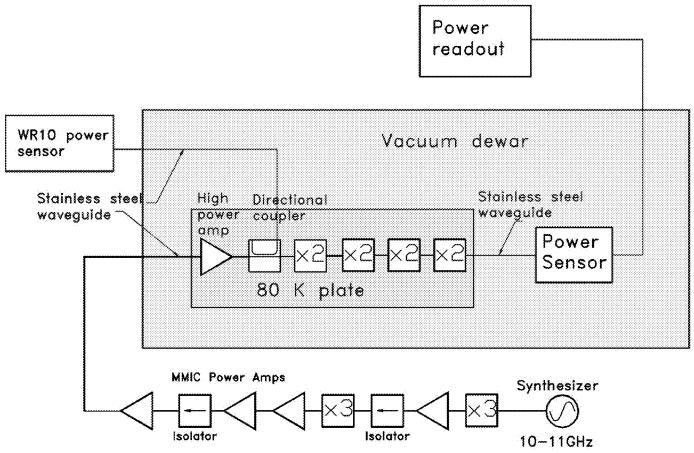

Figure 10. Setup for testing the complete X16 chain cold. Placing the power sensor in vacuum (at room temperature) eliminates the need for a window at 1.5 THz.

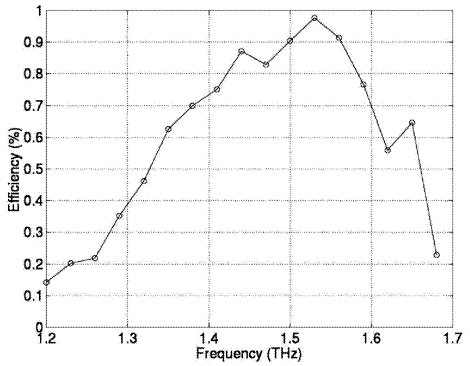

Figure 11. Predicted efficiency vs. frequency for the 1.5 THz doubler.

The predicted frequency response of the doubler is shown in Figure 11. The actual output power is shown in Figure 12, although this is convolved with a widely varying input power, making interpretation of the data difficult. One problem is the inherent variation in input power shown in Figure 7, but in addition, the horn-to-horn coupling adds a great deal of additional ripple due to mode conversion at some frequencies. It appears that this doubler does work at nearly the predicted frequency band, rolling off just 50 GHz lower than expected, but there is no data at low frequencies to show what happens. A few points were added using a different first stage doubler with lower tuning but this did not properly overlap the tuning of the first. This extended the range only slightly before the following stages began to roll off. Even with these problems we still can get >1 μW output power over 150 GHz, and the data sampling with 4 GHz spacing is equivalent to full coverage for the Herschel IF bandwidth of 4 GHz. Room temperature data is much more limited because of low input power, but still up to 10 μW can be obtained, making this a useful source for mixer testing. There is no good way to measure the efficiency either at room temperature or cold. It is impossible to know the true available power from the driver, or the interactions between two nonlinear devices. However, the cold efficiency, corrected for input mismatch, must be ~1-2%, given the peak driver stage output of 2 mW, and the

maximum cold output peaks of 20-45 μW. Room temperature efficiency is not expected to be much different given the high diode doping of $5x10^{17}$, and almost no temperature dependence to the mobility.

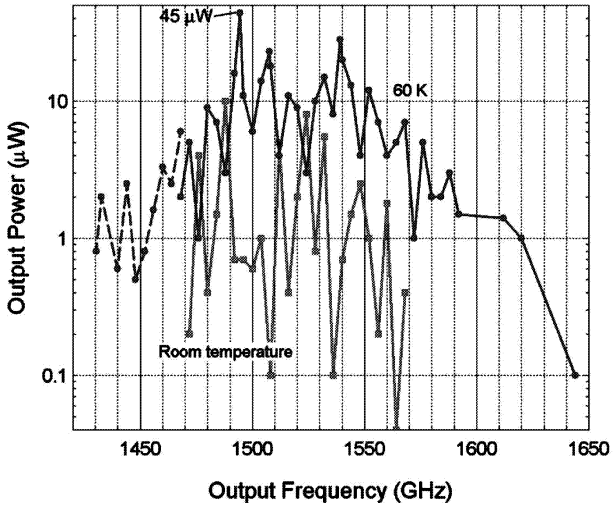

Figure 11. X16 output power with 160 mW into first stage. Upper data is at 60 K, lower data is at room temperature. Data on the dashed curve uses a different first stage doubler, but the same following stages.

HEB mixers are supposed to operate on extremely low LO power, and the Herschel specification is 1 μW for each mixer. There has been little data to support this, so this source was used to pump an HEB mixer at JPL. At the time of the test, the third stage doubler had not been optimized, so the source produced only 0.2 μW output, which pumped the mixer to within about a factor of two of the needed power. The IV curve of the mixer is shown in Figure 12 for this low power. No data was obtained with the higher power source in time for this paper, but there seems to be little doubt that with proper coupling the present power should easily drive the mixer at any frequency.

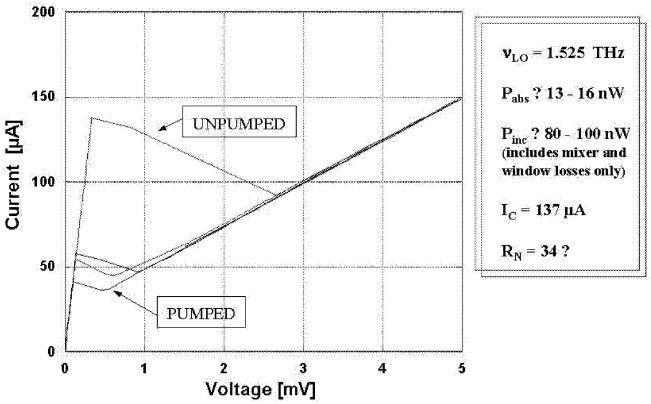

Figure 12. HEB mixer test at JPL with preliminary source with ~0.2 μW output.

Conclusions

A complete source has been built for 1.5 THz using a cascade of extremely high performance doublers. The output power of 45 μW is a record high for a solid state source at any nearby frequency. All of the stages work as well or better than expectations and the output power is sufficient to drive an HEB mixer over a wide band. All multipliers survive cooling to 60 K without problems and all work as well or better than at room temperature. The performance of this chain indicates that even higher frequency sources such as one at 1.9 THz as required for Herschel should be quite practical. The primary technical challenge at this point is getting the multipliers to work precisely at the needed frequency. All of the bands for Herschel are only 10-12% in fractional bandwidth, and at this time the tuning error for a given stage appears to be as much as 3-4%, although test data are not as complete as are needed for full diagnostic purposes.

References

1. N.R. Erickson, G. Narayanan, R.P. Smith, S.C. Martin, I. Mehdi, T.W. Crowe and W.L. Bishop, "Planar Frequency Doublers and Triplers for FIRST," *Eleventh International Symposium on Space Terahertz Technology*, pp. 543-551, May 2000.
2. N. Erickson, T. Crowe, W. Bishop, R. Smith, S. Martin, "Progress in Planar Diode Balanced Doublers," *Tenth International Symposium on Space Terahertz Technology*, pp. 475-484, Mar. 99.
3. N. Erickson, "A Fast and Sensitive Submillimeter Waveguide Power Meter," *Tenth International Symposium on Space Terahertz Technology*, pp. 501-507, Mar. 99.
4. Erickson Instruments LLC, Amherst, MA, Model PM1B submillimeter power meter.
5. A. Maestrini, D. Pukala, E. Schlecht, I. Mehdi and N. Erickson, "Experimental Investigation of Local Oscillator Chains with GaAs Planar Diodes at Cryogenic Temperatures," *Twelth International Symposium on Space Terahertz Technology*, pp. 495-503, Feb. 2001
6. G. Narayanan, N. Erickson, R. Grosslein, "Low Cost Direct Machining of Terahertz waveguide Structures," *Tenth International Symposium on Space Terahertz Technology*, pp. 518-528, Mar. 99.
7. N.R. Erickson, G. Narayanan, R.M. Grosslein, S. Martin, I. Mehdi, P. Smith, M. Coulomb and G. DeMartinez, "Monolithic THz Frequency Multipliers," *Twelth International Symposium on Space Terahertz Technology*, pp. 297-309, Feb. 2001.

HARMONIC BALANCE OPTIMIZATION OF TERAHERTZ SCHOTTKY DIODE MULTIPLIERS USING AN ADVANCED DEVICE MODEL

E. Schlecht, G. Chattopadhyay, A. Maestrini, D. Pukala, J. Gill and I. Mehdi

Jet Propulsion Laboratory, California Institute of Technology, Pasadena, CA 91109 USA

Abstract — Substantial progress has been made recently in the advancement of solid state terahertz sources using chains of Schottky diode frequency multipliers. The multiplier diodes are often simulated using a simple Schottky junction model plus a series resistance, R_S, because of the model's simplicity and ease of use in commercial harmonic balance simulators. The DC series resistance value is useable for R_S at low frequencies, but at high frequencies the R_S must be increased to match the measured RF performance. The junction properties are determined from forward I-V measurement.We have developed a harmonic balance simulator and corresponding diode model that incorporates many other factors participating in the diode behavior. These include time-dependent velocity saturation, carrier inertia and shunt capacitance in the undepleted active layer, tunneling through the Schottky barrier and heating of the junction at high powers. The model is calibrated using ensemble Monte Carlo calculations of material parameters, but otherwise no parameters are fitted other than to DC I-V measurements. The program can be used to optimize the doping concentration and diode dimensions for any multiplier, based on its frequency, input power and operation temperature. Optimizations are demonstrated for 200, 400 and 800 GHz doublers, and comparison between calculation and measurement will be shown. The match between them will be seen to be quite close. Further, the measurements include new, low-temperature measurements of an 800 GHz chain yielding a high 2 mW peak output power.

I. INTRODUCTION

Currently there is a demand for wide-bandwidth frequency multiplier chains [1-3] with outputs above 1 Terahertz for use in submillimeter wave heterodyne receivers. These space-borne radiometers are primarily intended for astrophysical observation. The Jet Propulsion Laboratory has developed and implemented novel technologies to produce robust, reliable and repeatable planar Schottky diode multipliers for these applications

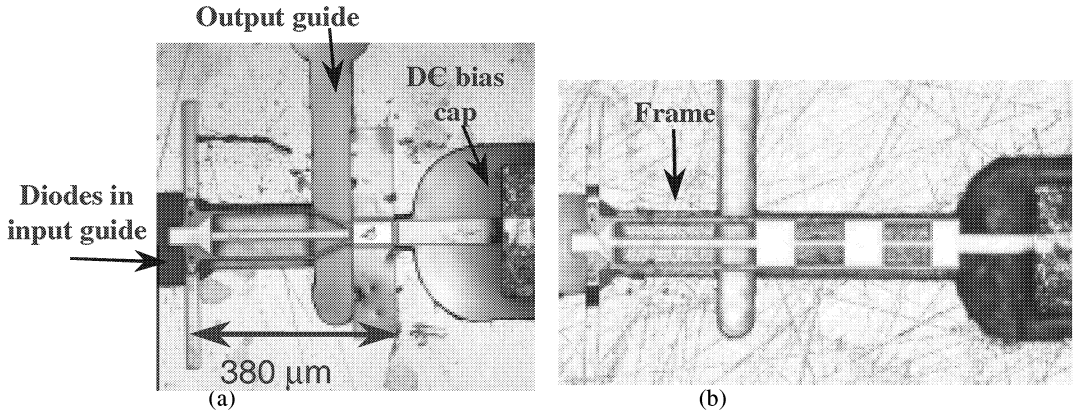

Figure 1. 800 GHz doublers mounted in block, both to the same scale. (a) is a version with on-chip bias capacitor, (b) uses a high-low transmission line filter for DC bias bypass.

[4]. In order to produce useable power at the final output frequency, the first stages in the chains are being pumped with high power levels of 200 mW or more at W-band [5]. Further, space missions such as the Herschel Space Observatory will be operated at low temperature, both for thermal margin and for improved multiplier performance [6]. There is a continuing effort at JPL to improve the modeling of the diodes, including

temperature, high frequency and high power effects. This paper will focus on a few recent additions to the diode modeling, as well as the results of optimization of diode characteristics for specific frequency/power/temperature combinations, and a comparison of multiplier simulations and measurements.

II. DESIGN AND ANALYSIS

The doublers consist of two components – nonlinear solid-state devices and surrounding passive circuitry. The devices are arrays of two to six Schottky diodes in a balanced configuration [7,8]. These are analyzed using a specially designed harmonic balance simulator. The surrounding passive input, output and impedance matching circuitry are analyzed using the HFSS finite element electromagnetic simulator. The circuit design process has been discussed previously [5,9-11], as has the fabrication [12]. An example of two versions of an 800 GHz doubler appears in Figure 1.

The harmonic balance simulator uses a modification of the reflection algorithm [13,14]. This method is can incorporate an arbitrary set of differential equations in the diode model. Additionally, since the solution of the harmonic balance equations is an iterative relaxation process [15], during the course of the convergence such external variables as the bias voltage and the material properties can be varied in a controlled way. This allows the normal difficulty the method has of requiring an artificial DC embedding resistance [16] to be circumvented by adjusting the fictitious bias voltage so that the real bias will be the correct value. Additionally, the change in material properties with temperature can be incorporated via a thermal model to investigate the effect of heating in the high power multipliers.

The thermal model itself, described in an earlier paper [17], is a simple one-dimensional thermal resistance model that takes into account heat flow through the GaAs frame and the gold metalization. The results are in the form of a profile of the temperature of the anodes versus the dissipated power and the block temperature. The data from the calculation can be fit to a version of the thermal resistance model that is quadratic in power:

$$T_{ANODE} = T_{BLOCK} + R_{T1}P_{DISS}\left(1 + R_{T2}P_{DISS}\right) \quad \textbf{(1)}$$

where R_{T1} is the low-power thermal resistance, around 2.05 K/mW and R_{T2} is the correction, around 0.012 mW^{-1}.

This equation can then be incorporated into the material properties of the diode model, and its effect included in the harmonic balance investigation of the multiplier's performance.

III. DIODE MODEL IMPROVEMENTS

Since the diode model will be included in the iterative harmonic balance simulator, it needs to be fast. Therefore, we are using a modified equivalent circuit model. Most of the elements of the model have been reported earlier [17–20], so only recent modifications to the model will be discussed. The junction capacitance model, $C(v)$ includes the effect of fringing [21] as well as a version of the flatband capacitance [22-24] modified for numerical stability.The undepleted epi model includes carrier inertia modeled as an inductance, L_i, and shunt displacement capacitance, C_d [18]. The spreading resistance, skin effect impedance and ohmic contact impedance occur in the highly doped n^+ region, and their models are as before [17,18,20]. They are affected by the mobility in the n^+ GaAs, however, and that has been changed as described below. Modifications to the model of the junction current, $i(v)$ will also be covered.

A. Buried n+ layer mobility. In an effort to track down all causes of reduced efficiency, the mobility of highly doped GaAs, especially as a function of temperature, was investigated. Several measurements were found [25-27], which indicated the mobility is

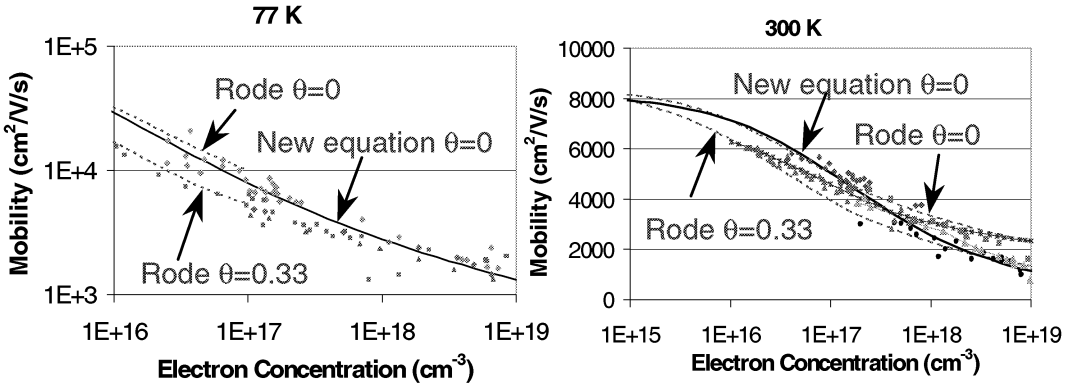

Fig. 2. GaAs Mobility at high doping concentrations. The broken lines are those of [40]. The solid line is the new formula. Dots are various measurements [25-27] (a) 77 K. (b) 300 K.

lower for doping concentrations above 5 X 10^{17} cm^{-3} than the values being used. The earlier equation [20] was based on the work of Rode and Knight [28,29]. A new equation was fitted, based on a combination of the measurements, Rode's work and others [30,31]. The results are indicated in Figure 2, which shows a combination of Rode's results, several measurements, and the new formula. The parameter θ is the compensation ratio of ionized acceptors to ionized donors, N_A^-/N_D^+.

B. Junction current. Another source of reduced efficiency not previously included in the model is the reverse current increase due to avalanche multiplication. Previous calculations of the junction current incorporating barrier tunneling plus thermionic emission [20,32] and avalanche multiplication [20,33] matched measurements of actual diodes well [20].

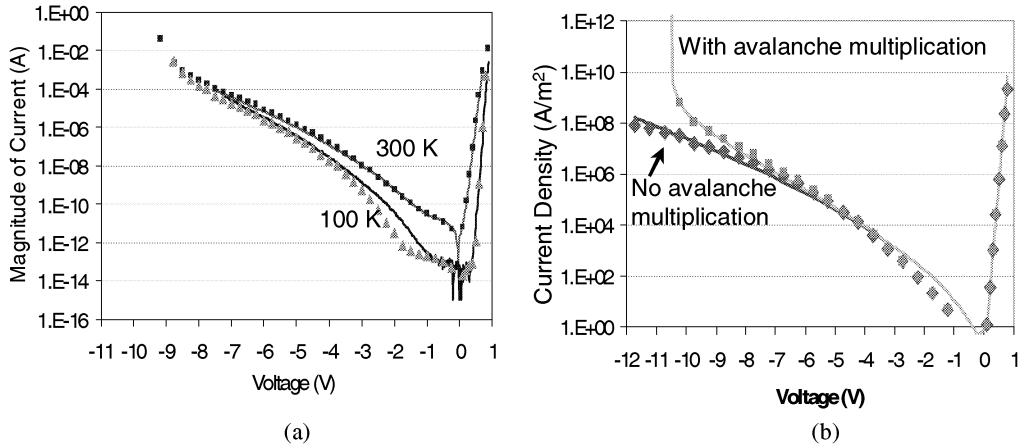

Fig. 3. Junction forward and reverse current magnitude. (a) Current measured for 45 μm^2 anode, $3X10^{17}$ cm^{-3} doping (solid) compared to quantum transmission matrix calculation (markers). (b) Representative fit of transmission matrix calculation (markers) to fitted formula (solid), with and without avalanche multiplication.

A representative plot of the junction current is shown in Figure 3. Figure 3a, reproduced from [20], compares the junction current measured and calculated. These

apply to a diode having an anode area of 45 μm^2 with an active layer doping of 3×10^{17} cm^{-3}, measured at 100 and 300 K. The junction current is calculated using the transmission matrix technique [32,34] and includes avalanche multiplication [33]. Since these calculations are too slow for the iterative solution required by the harmonic balance algorithm, the usual thermionic emission formula was modified to include reverse current

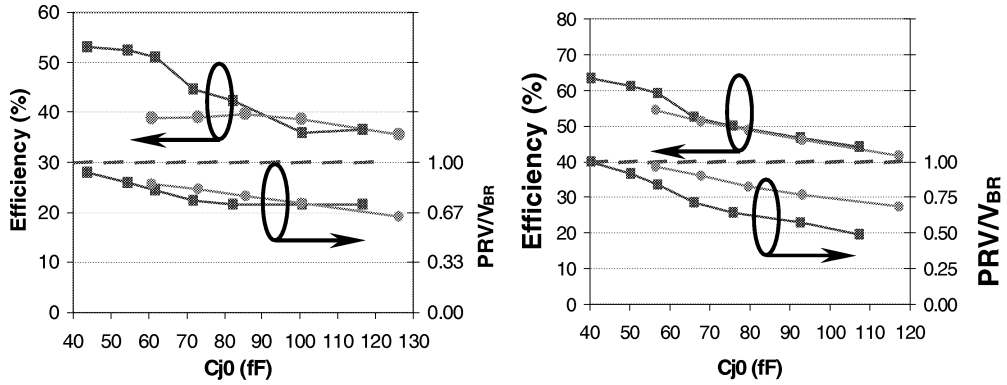

Fig. 4. Optimization of 200 GHz doubler. The input power is 33 mW per diode. Square markers reference $1X10^{17}$ cm^{-3} doping, round markers $2X10^{17}$ cm^{-3}. (a) 300 K block temperature. (b) 120 K block temperature.

[17]. It now has been further modified to include the current increase due to avalanche multiplication.

Figure 3b compares the transmission matrix calculation with the values from the

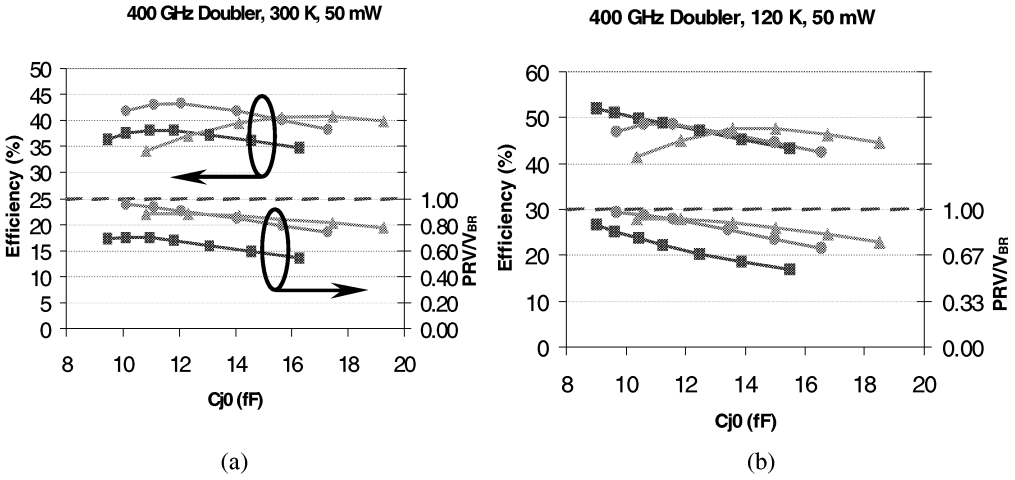

Fig. 5. Optimization of 400 GHz doubler. The input power is 7 mW per diode. Square markers reference $1X10^{17}$ cm^{-3} doping, round markers $2X10^{17}$ cm^{-3}, triangle markers $3X10^{17}$ cm^{-3}. (a) 300 K block temperature. (b) 120 K block temperature.

modified thermionic emission equation used in the harmonic balance simulator.

IV. Doping Optimization

One of the primary reasons for performing this work is to determine optimum doping for multipliers at various frequencies, temperatures and pump powers. During the

fabrication process only one or two doping profiles can be included in a process run at a time. Since a range of multipliers is fabricated in each run, the dopings selected must represent a compromise among the various optimum dopings.

Figures 4 through 6 depict diode efficiencies calculated at block temperatures of 120 and 300 K for 200, 400 and 800 GHz doublers using diodes with several dopings. The results are plotted as a function of diode junction capacitance at zero bias, C_{j0}, since that is more characteristic of circuit tuning with frequency than diode area.

Shown on each plot is both the calculated efficiency and the ratio of the peak reverse voltage (PRV) during the pump cycle to the breakdown voltage. The limitations on the diode efficiency are 1) the diode series resistance; 2) junction current, which represents a circuit loss; 3) current saturation; and 4) the bias voltage and pump power must be limited in order to prevent diode damage. Reverse current is more destructive at a given power level than forward current as discussed in [36]. Therefore, prudence dictates that the multiplier design include a safety margin between PRV and breakdown voltage, V_{BR}. Work is continuing at JPL to find an appropriate margin, but at this point it seems that the PRV/V_{BR} ratio should be less than about 0.8.

The results indicated in Figures 4 through 6 can be compared to the analytical optimum doping formulas given in [37]. These equations incorporate the limitations to diode multiplier performance due to junction breakdown and current saturation, both of which are functions of doping and temperature. Further, they assume a particular profile of the diode waveform during the pump cycle that is consistent with the results we have found. Since the formulas don't take account of the series resistance, they can't determine the achievable efficiency.

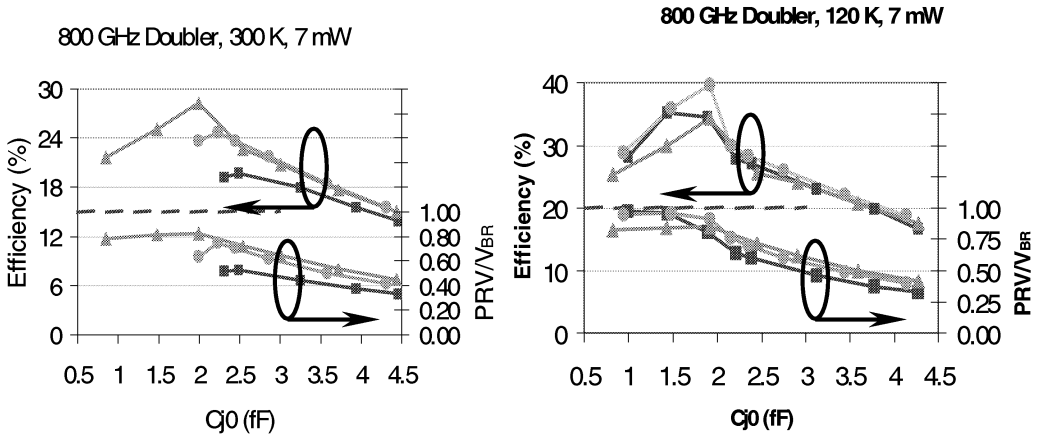

Fig. 6. Optimization of 800 GHz doubler. The input power is 3.5 mW per diode. Square markers reference 2X10^{17} cm^{-3} doping, round markers 3X10^{17} cm^{-3}, triangle markers 4X10^{17} cm^{-3}. (a) 300 K block temperature. (b) 120 K block temperature.

Assuming the active epi-layer is made just thick enough that the breakdown and depletion region punch-through occur at the same time, equations (1) and (2) of [37] can be combined with the standard expression for depletion width [38] to yield:

$$N_D(opt) = \frac{8 f_{out}^2}{v_{pk}^2} \frac{\varepsilon}{q} \left[V_{bi} - PRV(N_D, T) \right] \qquad \textbf{(2)}$$

where $N_D(opt)$ is the optimum doping, f_{out} is the multiplier output frequency, v_{pk} is the peak electron drift velocity, ε and q are the semiconductor permittivity and the electron charge respectively, and V_{bi} is the built-in voltage — about 0.8 V. Since the parameters are doping dependent, equation (2) must be solved iteratively. However, convergence is fast.

To determine a value for v_{pk}, it seems reasonable to expect that the optimum operating condition for the multiplier should be with the electric field across the undepleted epi no higher than that corresponding to the peak static electron velocity found from the Monte Carlo calculations. This is in the neighborhood of 4 to 5 kV/cm for donor concentrations above 1×10^{17} cm^{-3}. Looking at the results of the MC simulations, the transient peak velocities are generally around 1.25 to 1.4 times the static velocities for those field strengths. For example, for a step of 5 kV/cm the electron velocity peaks at about 15.6×10^{6} cm/s, after which it decays to the static value around 11.0×10^{6} cm/s in 4 or 5 ps, for a ratio of 1.4.

Table I. Optimum Doping, Simulation & Formula

Output Frequency	Block Temperature	Simulation N_D(opt)	Formula N_D(opt)
200 GHz	300 K	$\leq$1X10^{17}	1.1X10^{17}
200 GHz	120 K	$\leq$1X10^{17}	0.5X10^{17}
400 GHz	300 K	$\approx$2X10^{17}	2.0X10^{17}
400 GHz	120 K	$\approx$1X10^{17}	1.0X10^{17}
800 GHz	300 K	$\geq$4X10^{17}	6.9X10^{17}
800 GHz	120 K	$\approx$3X10^{17}	3.2X10^{17}

Using these values, the peak velocities are in the neighborhood of 15 to 20×10^{6} cm/s at room temperature, N_D between 10^{17} and 10^{18} cm^{-3}. At 120 K, the peak velocities are between 28 and 32×10^{6} cm/s, N_D being 5×10^{16} to 5×10^{17} cm^{-3}. In this case, for illustration, the safety margin mentioned earlier will be dropped, and V_{BR} will be used for the PRV.

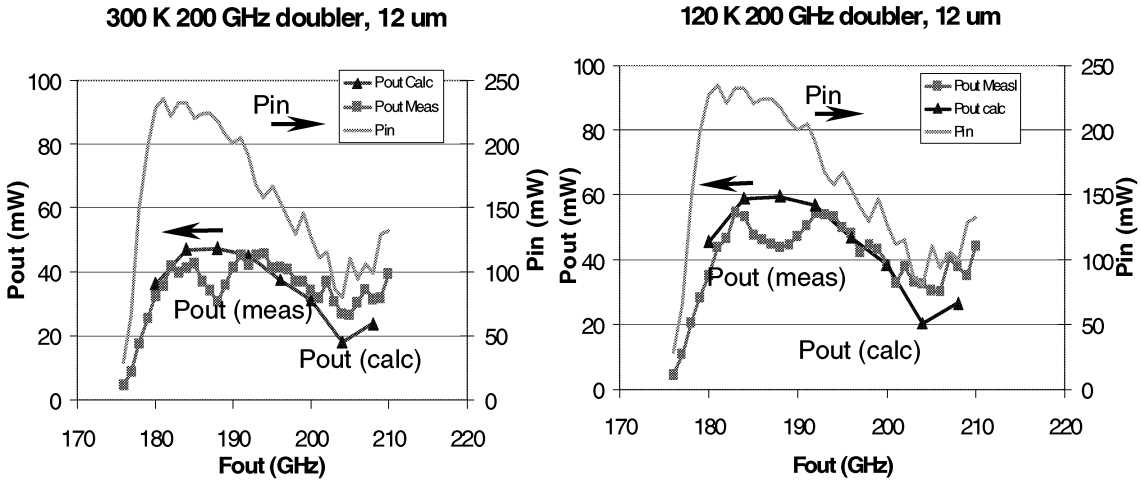

(a) (b)

Fig. 7. Plots of measured and simulated 200 GHz doubler efficiency. The doping is 2X10^{17} cm^{-3}. Anodes are 3 X 12 µm. Square symbols mark the measurements, triangles mark the simulations. (a) 300 K block temperature. (b) 120 K block temperature.

Table I compares the results from examining Figures 4 through 6 to those from the analytical formula. The agreement is good within the limits of what can be gleaned from the simulation plots.

V. DISCUSSION OF RESULTS OF IMPROVED MODEL COMPARED WITH MEASUREMENT

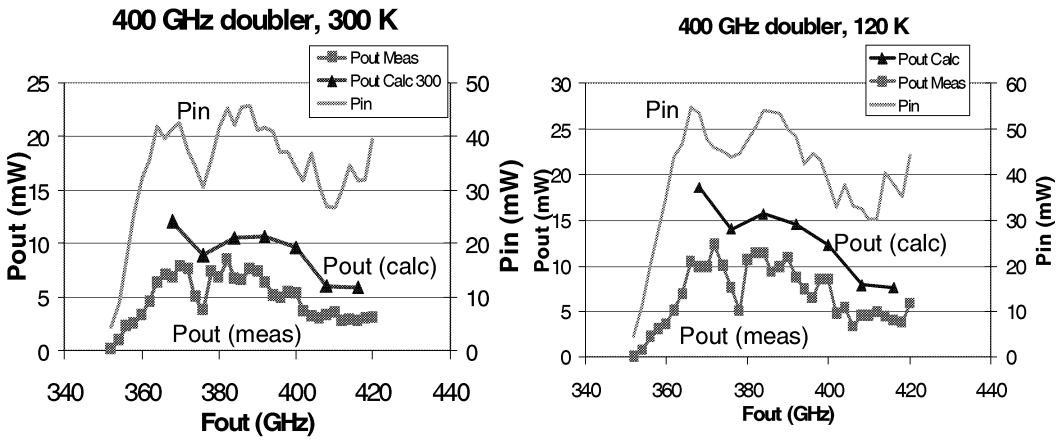

(a) (b)

Fig. 8. Plots of measured and simulated 400 GHz doubler efficiency. The doping is $2X10^{17}$ cm^{-3}. Anodes are 1.5 X 4.5 μm. Square symbols mark the measurements, triangles mark the simulations. (a) 300 K block temperature. (b) 120 K block temperature.

Using the same HB simulator, the existing designs for 200, 400 and 800 GHz doublers were also simulated. A representative photo of these designs appears in Figure 1. Three designs exist for the 800 GHz doubler [39], two variations of which include an on-chip MIM capacitor with Si_3N_4 for bias decoupling. The third variation was fabricated using a high-low transmission line low-pass bias filter. The 400 GHz doubler was only fabricated

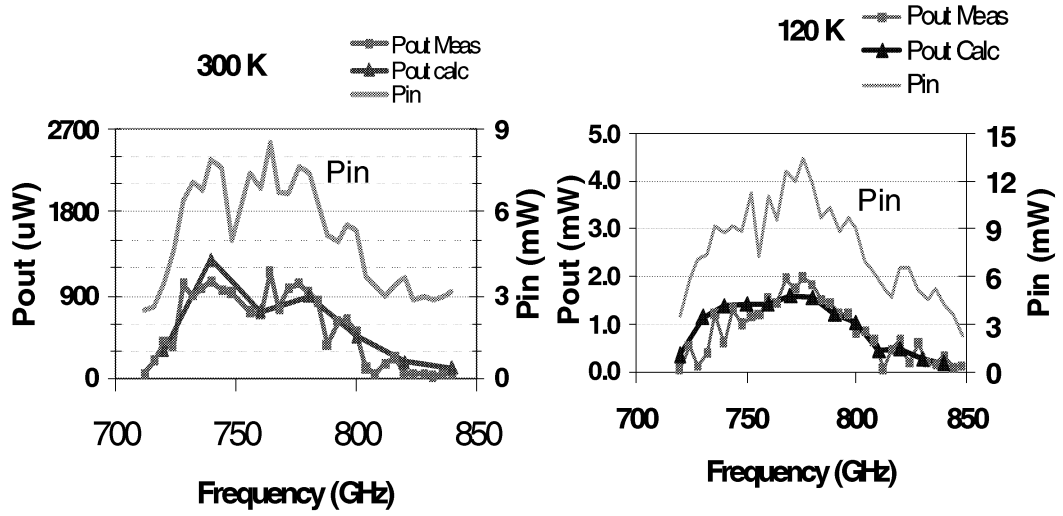

(a) (b)

Fig. 9. Plots of measured and simulated 800 GHz doubler efficiency. The doping is $3X10^{17}$ cm^{-3}. Anodes are 1 X 1.2 μm. Square symbols mark the measurements, triangles mark the simulations. (a) 300 K block temperature. (b) 120 K block temperature.

using the on-chip capacitor, whereas the 200 GHz doubler does its filtering with off-chip single-layer chip capacitors. The results of the simulations are compared to the measurements in Figures 7 through 9. The 800 GHz measured results for 120 K block

temperature have not been presented before, and represent the highest output power measured for an 800 GHz multiplier chain of which these authors are aware.

The agreement between mesurement and calculation is good, with one exception: When the input power is high at the lower frequencies, the simulator overestimates the efficiency. This is clear, for example in the range of about 188 GHz for the 200 GHz doubler, and below 400 GHz for the 400 doubler. It appears as if the simulator is analyzing multiplier power saturation incorrectly. The 800 GHz doubler does not exhibit this behavior because it is not driven near saturation.

To confirm this, a power sweep measurement was performed on the 200 GHz doubler, along with the corresponding simulation. The results presented in Figure 10 confirm this problem. The agreement between simulation and measurement are good at the low power end, but the multiplier actually saturates at a lower input power and produces a lower output power than the simulator would predict.

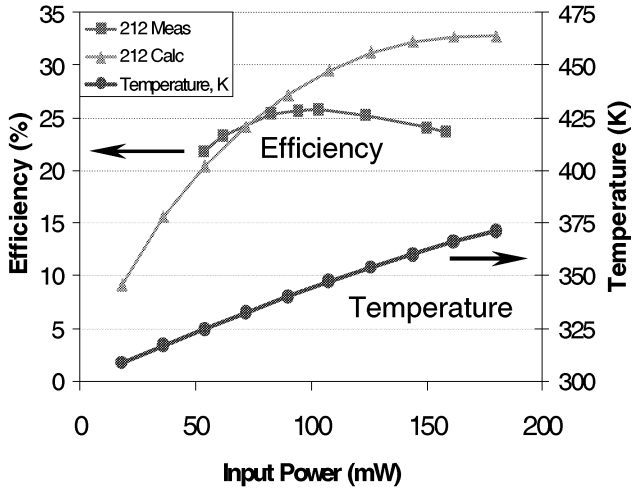

Fig. 10. Measured and simulated power sweep of the 200 GHz doubler. The frequency is 212 GHz. Square markers indicate the measurements, triangles indicate the simulation. Also shown is the simulated temperature.

An additional artifact of the modeling that appears in the optimization plots, especially Figure 6, is the kink at lower C_{j0}. This is due to a change in the width of the anodes at that point, give smaller diodes that can still be fabricated. The algorithm used to find the ohmic contact and spreading resistance for the rectangular diodes may be inaccurate for these small diodes. This needs to be investigated further.

VI. Conclusion

The improvements to the harmonic balance analysis and diode model that have been presented give results that match the measurements for 200, 400 and 800 GHz doublers very well. Further, low temperature measurements on one of the 800 GHz doublers have given a very high output power of 2 mW.

Nevertheless, there is room for improvement in the modeling, especially for multipliers running near saturation. Several possible improvements in the model will be tried. First, the way in which the harmonic balance simulator handles multipliers with several diodes will be made more realistic. Instead of assuming the power is equally divided, the diodes will receive power as determined by the circuit used, accounting for the coupling between them.

Second, at high input power there is some effect that is not accounted for. For example, the reverse current electrons at high reverse bias have a great deal of energy with respect

to the material in the undepleted epi. One could surmise that these electrons will also stay in the upper low-mobility valleys, and may in fact increase the series resistance without being part of the normal high-field current saturation mechanism. These possibilities will be investigated in further studies, including the further application of Monte Carlo methods.

REFERENCES

[1] E. F. van Dishoek and F. P. Helmich, "Scientific drivers for future high-resolution far-infrared spectroscopy in space," *Proc. 30th ESLAB Symp., Submillimetre and Far-Infrared Space Instrumentation 1996*, ed. E. J. Rolfe, ESA SP-388, pp. 3-12.

[2] G. Pilbratt, "The FIRST mission," *Proc. ESA Symp., The Far Infrared and Submillimetre Universe 1997*, ESA SP-401.

[3] N. D. Whyborn, "The HIFI Heterodyne Instrument for FIRST: Capabilities and Performance," *Proc. ESA Symp, The Far Infrared and Submillimetre Universe 1997*, ESA SP-401.

[4] I. Mehdi, E. Schlecht, A. Arzumanyan, J. Bruston, P. Siegel, R. Peter Smith, J. Pearson, S. Martin and D. Porterfield, "Development of millimeter and submillimeter-wave local oscillator circuits for a space telescope," *Proc. SPIE*, vol. 3795, pp. 329-337, *Terahertz and Gigahertz Photonics,* R.J. Hwu, K. Wu, Eds., October 1999.

[5] E. Schlecht, G. Chattopadhyay, A. Maestrini, A. Fung, S. Martin, D. Pukala, J. Bruston and I. Mehdi, "200, 400 and 800 GHz Schottky Diode "Substrateless" Multipliers: Design and Results," *IEEE Int. Microwave Symp. Digest,* pp. 1649-1652, Phoenix, AZ, May 2001.

[6] A. Maestrini, D. Pukala, F. Maiwald, E. Schlecht, G. Chattopadhyay, and I. Mehdi, "Cryogenic operation of GaAs based multiplier chains to 400 GHz, " *Eighth International Terahertz Conference*, Darmstadt, Germany, September 2000.

[7] B.J. Rizzi, T.W. Crowe, and N.R. Erickson, "A High-Power Millimeter-Wave Frequency Doubler Using a Planar Diode Array," *IEEE Microwave Guided Wave Lett.*, vol.3, pp. 188-190, June 1993.

[8] N.R. Erickson, "Diode Frequency Multipliers for Terahertz Local Oscillator Applications," *Proc. SPIE*, vol. 3357, pp. 75-84, *Advanced Technology MMW, Radio, and Terahertz Telescopes*, T.G. Phillips, Ed., July 1998.

[10] J. Bruston, R.P. Smith, S.C. Martin, A. Pease and P.H. Siegel, "Progress Toward the Realization of MMIC Technology at Submillimeter Wavelengths: A Frequency Multiplier to 320 GHz," *Proc. IEEE Intl. Microwave Symp. Digest*, Baltimore, MD, June 1998, pp. 399-402.

[11] D. Porterfield, T. Crowe, R. Bradley, N. Erickson, "An 80/160 GHz Broadband, Fixed-Tuned Balanced Frequency Doubler," *IEEE Int. Microwave Symp. Digest,* Baltimore, MD, June 1998, pp. 391-394.

[12] S. Martin, B. Nakamura, A. Fung, P. Smith, J. Bruston, A. Maestrini, F. Maiwald, P. Siegel, E. Schlecht and I. Mehdi, "Fabrication of 200 to 2700 GHz Multiplier Devices Using GaAs and Metal Membranes," *2001 Int. Microwave Symp. Digest*, pp. 1641-1644, Phoenix, AZ, May 2001.

[13] A.R. Kerr, "A Technique for Determining the Local Oscillator Waveforms in a Microwave Mixer," *IEEE Trans. Microwave Theory Tech.*, vol. 23, no. 9, pp. 828-831, Oct. 1975.

[14] P.H. Siegel, A.R. Kerr, W. Hwang, "Topics in the Optimization of Millimeter-Wave Mixers," NASA Technical Report NASA-TP-2287, NAS 1.60:2287, March, 1984.

[15] M.T. Faber, J. Chramiec, and M.E. Adamski, *Microwave and Millimeter-Wave Diode Frequency Multipliers,* p. 139, Artech House, Boston, 1995.

[16] S.A. Maas, *Nonlinear Microwave Circuits,* p. 114, IEEE Press, New York, 1997.

[17] E. Schlecht, G. Chattopadhyay, A. Maestrini, D. Pukala, J. Gill, S. Martin, F. Maiwald and I. Mehdi, "A High-Power Wideband Cryogenic 200 GHz Schottky "Substrateless" Multiplier: Modeling, Design and Results, " *Ninth International Conference on Terahertz Electronics*, Charlottesville, VA October 2001.

[18] T.W. Crowe, "GaAs Schottky Barrier Mixer Diodes for the Frequency Range 1-10 THz," *Int. J. Infrared Millimeter Waves*, vol. 10, no. 7, pp 765-777 (1989)

[19] J.T. Louhi and A.V. Räisänen, "On the Modeling and Optimization of Schottky Varactor Frequency Multipliers at Submillimeter Wavelengths," *IEEE Trans. Microwave Theory Tech.*, vol. 43, no. 4, pp 922-926, 1995.

[20] E. Schlecht, F. Maiwald, G. Chattopadhyay, S. Martin and I. Mehdi, "Design Considerations for Heavily-Doped Cryogenic Schottky Diode Varactor Multipliers, " *Twelfth International Symposium on Space Terahertz Technology*, San Diego, CA, February 2001.

[21] J.T. Louhi, "The Capacitance of a Small Circular Schottky Diode for Submillimeter Wavelengths," *IEEE Microwave Guided Wave Lett.*, vol. 4, no. 4, pp. 107-108, April 1994.

[22] P.H. Siegel, I. Mehdi, and J. East, "Improved Millimeter-Wave Mixer Performance Analysis at Cryogenic Temperatures," *IEEE Microwave Guided Wave Lett.*, vol. 1 no. 6, pp. 129-131, June 1991.

[23] I. Mehdi, P.H. Siegel, and J. East, "Improved Millimeter-Wave Mixer Performance Analysis Using A Drift Diffusion Capacitance Model," *1991 International Microwave Symposium Digest*, pp. 887-890, 1991.

[24] A. Jelenski, A. Grub, V. Krozer, H.L. Hartnagel, "New Approach to the Design and Fabrication of THz Schottky Barrier Diodes, " *IEEE Trans. Microwave Theory Tech.*, vol. 41, no. 4, pp. 549-557, April 1993.

[25] D.M. Szmyd, M.C. Hanna, and A. Majerfeld, "Heavily Dopde GaAs:Se. II. Electron Mobility," *J. Appl. Phys*., vol. 68, no. 5, p 2376-2381, 1 Sept. 1990.

[26] B. A. Sanborn, "Electron-electron Interactions, Coupled Plasmon-Phonon Modes, and Mobility in n-Type GaAs," *Phys. Rev. B* , vol. 51, no. 20, p 14256-14264, 15 May 1995.

[27] D. Lancefield, A.R. Adams, and M.A. Fisher, "Reassessment of Ionized Impurity Scattering and Compensation in GaAs and InP Including Correlation Scattering," *J. Appl. Phys*., vol. 62, no. 6, p 2342-2359, 15 Sept. 1987.

[28] D.L Rode, "Low-Field Electron Transport," in *Semiconductors and Semimetals Volume 10*, ed. R.K. Willardson, and A.C. Beer, Academic Press, New York, 1975.

[29] D.L. Rode and S. Knight, "Electron Transport in GaAs," *Phys. Rev. B.*, vol. 3, no. , pp. 2534-2541, 15 April 1971.

[30] J.G. Ruch and W. Fawcett, "Temperature Dependence of the Transport Properties of Gallium Arsenide Determined by a Monte Carlo Method," J. Appl. Phys. vol. 41, no. 9, pp 3843-3849, 1970.

[31] G.E. Stillman, C.M. Wolfe, and J.O. Dimmock, "Hall Coefficient Factor for Polar Mode Scattering in n-Type GaAs," J. Phys. Chem. Solids, vol. 31, pp. 1199-1204, 1970.

[32] U.V. Bhapkar and R.J. Mattauch, "Numerical Simulation of the Current-Voltage Characteristics of Heteroepitaxial Schottky Barrier Diodes," *IEEE Trans. Electron Devices*, vol. 40, no. 6, 1993.

[33] G.E. Stillman, and C.M. Wolfe, "Avalanche Photodiodes," in *Semiconductors and Semimetals Volume 12*, ed. R.K. Willardson, and A.C. Beer, Academic Press, New York, 1977.

[34] W.W. Lui and M. Fukuma, "Exact Solution of the Schrodinger Equation Across an Arbitrary One-Dimensional Piecewise-Linear Potential Barrier," *J. Appl. Phys*., vol. 60, no. 5, p 1555-1559, 1 Sept. 1986.

[35] J. East, "Monte Carlo Simulation of Schottky Barrier Mixers and Varactors," *Sixth International Symposium on Space Terahertz Technology*, pp. 442-457Pasadena, California, March, 1995.

[36] M. Schussler, V. Krozer, K.H. Bock, M. Brandt, L. Vecci, R. Losi, and H.L. Hartnagel, "Pulsed Stress Reliability Investigations of Schottky Diodes and HBTs," *Microelectron. Reliab.*, vol. 36 no. 11/12, pp. 1907-1910, April 2002.

[37] J.T. Louhi and A.V. Raisanen, "Optimization of the Schottky Varactor for Frequency Multiplier Applications at Submillimeter Wavelengths," *IEEE Microwave Guided Wave Lett.*, vol. 6, no. 6, pp. 241-242, June 1996.

[38] S.M. Sze, *Physics of Semiconductor Devices*, 2nd Ed., Chapter 5, Wiley, New York, 1981.

[39] G. Chattopadhyay, E. Schlecht, J. Gill, S. Martin, A. Maestrini, D. Pukala, F. Maiwald, and I. Mehdi, "A Broadband 800 GHz Schottky Balanced Doubler," *IEEE Microwave Guided Wave Lett.*, vol. 12 no. 4, pp. 117-118, April 2002.

Millimeter- and Submillimeter-Wave Planar Varactor Sideband Generators

Haiyong Xu, Gerhard S. Schoenthal, Robert M. Weikle,
Jeffrey L. Hesler, and Thomas W. Crowe

Department of Electrical and Computer Engineering
University of Virginia
Charlottesville VA 22903

***Abstract*--** In this paper, the design and optimization of a varactor sideband generator (SBG) is presented. The integration of the diode with the embedding circuit enhances mechanical robustness and makes the circuits easy to handle compared with a whisker-contacted diode structure. A nonlinear analysis was used to determine the optimum varactor diode parameters for use at 600GHz, yielding an anode diameter of 1.8 μm and an epitaxial layer doping of 1×10^{17} cm^{-3}. A 200 GHz SBG is also implemented as a proof-of-principle. The measured results for 200 GHz are presented. The measured upper sideband conversion loss is 7-10dB over more than 20 GHz tuning range.

Index Terms-- Conversion loss, epitaxial layer, millimeter- and submillimeter-wave sources, varactor sideband generator.

I. INTRODUCTION

Millimeter- and submillimeter-wave sources can be used for a variety of applications ranging from molecular spectroscopy to wireless communications. However, there is a lack of frequency tunable sources at these wavelengths. A sideband generator (SBG) can be used to generate frequency tunable sidebands from a fixed source, and is therefore a commonly used device.

The best Schottky diode SBG in a corner cube mount gave 10.5 μW of single sideband (SSB) output power with a conversion loss of 31 dB at 1.6 THz [1]. These results were improved dramatically with the application of varactor diodes as phase modulators. Two whisker-contacted varactor SBGs at 80 GHz and 1.6 THz were investigated by Kurtz [2], [3]. By switching to varactor diodes the conversion loss was improved to 14 dB at 1.6 THz. However, it has proved difficult to further develop these SBGs because of the difficulty in making the whisker-contact to the diode. This paper will describe a novel varactor-based SBG using planar diodes that overcomes the difficulties with previous designs. A proof-of-concept 200 GHz SBG is presented with measured results and a design of 600 GHz is discussed.

II. BASIC THEORY AND SBG LAYOUT

For a SBG, it is most appropriate to use a low frequency to pump the diode due to the lack of power at high frequencies. A typical IF microwave source can easily fully pump the varactor and the LO signal will cause negligible capacitance modulation of the varactor. Better conversion loss can be achieved by this design [4]. Different IF pumping signals will lead to different conversion loss as described by Kurtz [3]. Ideally, the best achievable conversion loss, 3.94 dB, can be obtained using a bipolar square wave 180 phase modulation,. The integrated varactor SBG circuit design is also based on this theoretical consideration. An open block photograph of the investigated SBG is shown in Fig. 1.

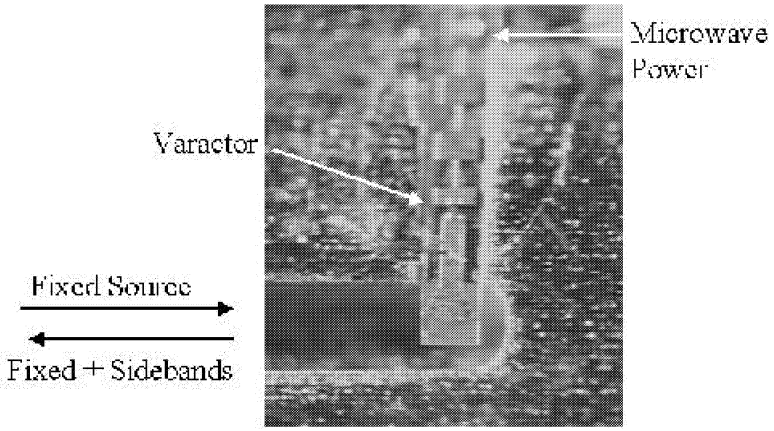

Fig. 1. Photograph of planar varactor circuit in SBG open block

The varactor and SBG circuitry are fabricated on a fused-quartz substrate, which is located in the microstrip channel. Waveguide-to-microstrip transitions are used to couple the high frequency signal from the waveguide and reflect its sidebands back to the waveguide. The microwave IF signal is applied to the varactor to control the LO signal phase shift. A low-pass microstrip filter is used to resonate the varactor and to block the LO signal.

III. SBG DESIGN AND SIMULATION

The SBG equivalent circuit model is shown in Fig. 2. The planar Schottky varactor is modeled by a junction capacitance C_j, a series resistance R_s, a finger inductance L_{fg}, a finger to pad capacitance C_{fp} and pad to pad capacitance C_{pp}. The main design goal is to determine the varactor parameters and load impedance to realize LO signal 180 phase modulation.

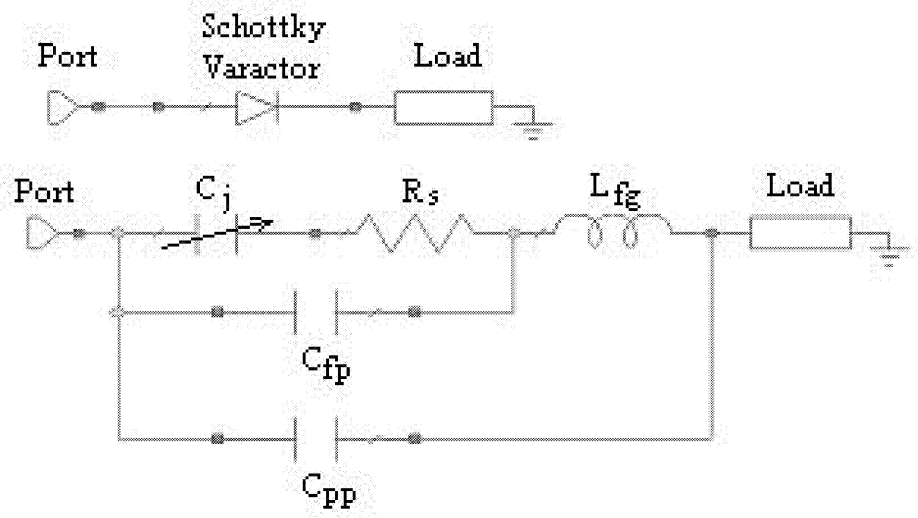

Fig. 2. Equivalent circuit of SBG

In order to achieve better phase modulation, the junction capacitance is initially set to resonate with the finger inductance at the LO frequency. The other varactor equivalent circuit parameters are first estimated based on previous simulations [5]. The L_{fg} and C_{j0} are optimized to give maximum phase shift for S_{11}. These values are translated into varactor dimension, such as anode size and finger length, according to typical formulas in [6]. The Ansoft High Frequency Structure Simulator (HFSS) is then applied to simulate the varactor integrated circuits. Coaxial ports were used at the anode junction, as described in [7]. Using this technique, all the varactor parasitic parameters including the filter circuit are analyzed in the HFSS. However, the nonlinear junction cannot be simulated since it changes with the pump. In order to include this nonlinear element, the three port S-parameter is exported into the microwave simulator package, Microwave Office, as a 3-port network. S_{11} is simulated again with the coaxial port terminated by a series junction resistor and capacitor, which is calculated based on anode size. This process is repeated to determine the varactor parameter, which will give a 180deg phase shift in reflection coefficient.

The 600 GHz Schottky varactor was optimized to have an epitaxial layer doping of 1×10^{17} cm^{-3} and an anode diameter of 1.8 μm. The finger length is set to 20 um. Since it is difficult to measure the S-parameters at 600 GHz, the 200GHz SBG was also designed to verify the theory. To make the fabrication simple, the same doping wafer is used. The anode size was chosen to be 4.3 μm with zero bias junction capacitance, $C_{j0} \approx 15\,\mathrm{fF}$. The theoretical reflection coefficients with varactor bias voltage varying from -10 V to 0.5 V are shown in Fig. 3. The predicted 200 GHz return loss is around 1dB, while the 600 GHz SBG is around 4 dB (with the microstrip and waveguide assumed lossless). The difference is due to the series resistance, which is determined by the anode size. The 200 GHz SBG junction

series resistance was calculated to be 6 Ω. The junction resistance for the 600 GHz SBG was calculated to be 18 Ω.

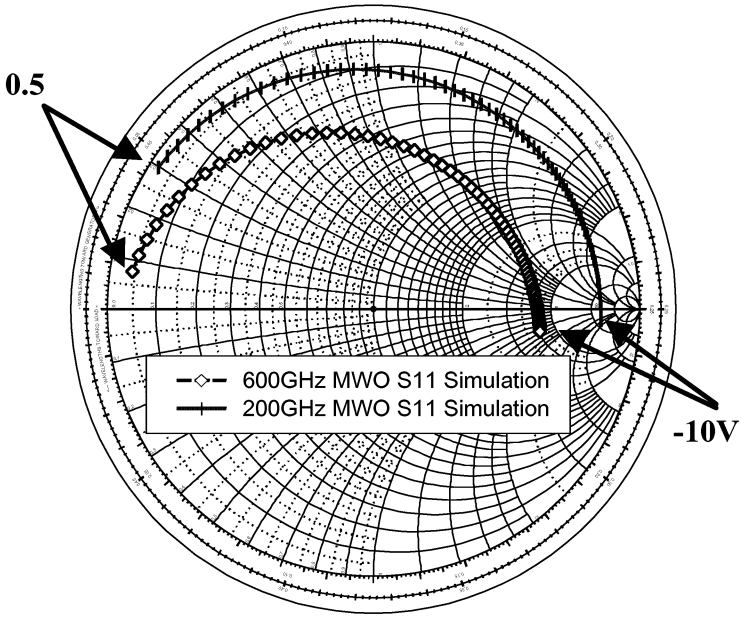

Fig. 3. SBG S_{11} phase variation with sweeping of bias voltage

IV. FABRICATION AND MEASUREMENTS

The integrated circuits were fabricated in UVA Semiconductor Device Lab according to the simulation results. The SEM photo of 600 GHz varactor is shown in Fig. 4.

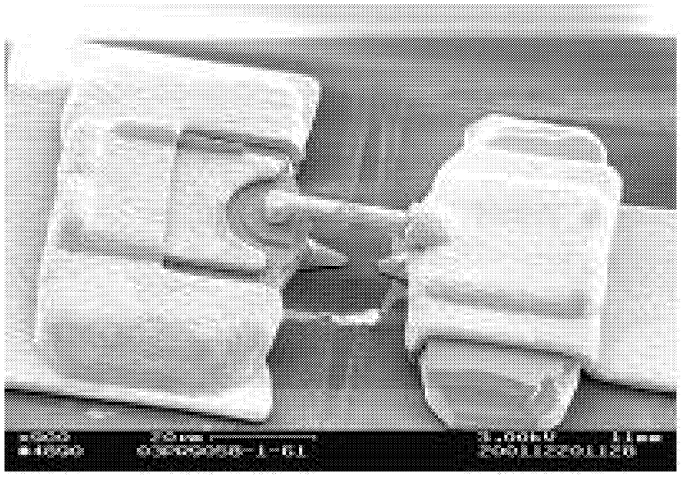

Fig. 4. SEM photo of 600 GHz SBG varactor structure

The varactor I-V curves and junction capacitances were measured, and were found to be similar to the simulation. The 200 GHz SBG blocks were first assembled and tested with

suitable circuits. The circuit S-parameters were measured with the Agilent 8510C Vector Network Analyzer (VNA) and an Oleson Microwave Lab WR-5 Extension (140-220 GHz). One of the reflection coefficients, S_{11}, corresponding to different varactor voltage biases was plotted in Fig. 5. The simulation result is also shown. The phase variation was nearly 180deg, which is quite similar to the design. However, the return loss is about 2 dB larger than the design. This increased loss is believed to be caused by dielectric and conductor losses, which are not considered in the simulation.

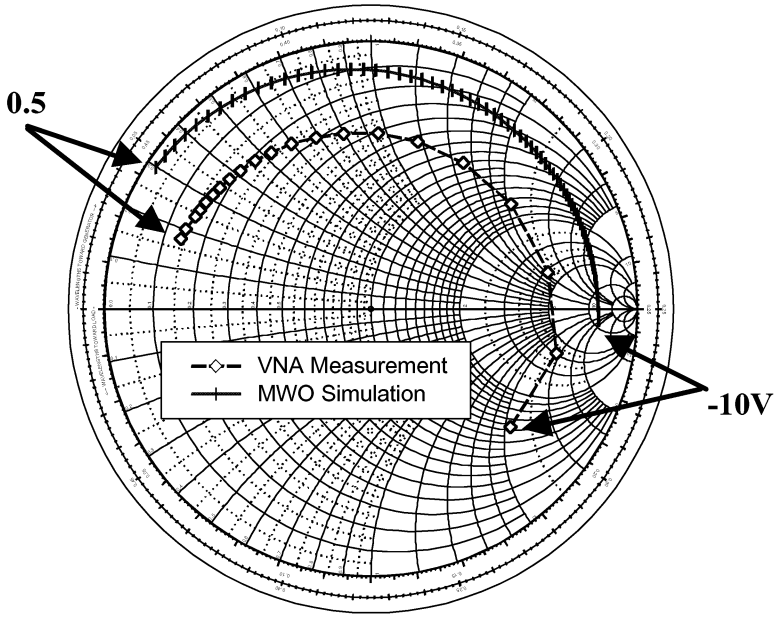

Fig. 5. Comparing S_{11} phase variation with different voltage bias

After the S-parameter measurement, the 200 GHz sideband generator conversion loss was tested. The test setup is shown in Fig. 6. It consists of WR-10 and WR-5 waveguides and components. A 100 GHz chain source is used to provide about 120 mW power. After a 100-200 GHz frequency doubler, the 200 GHz LO power is slightly more than 20 mW as measured by an Anritsu power meter. The WR-5 isolator is used to reduce the reflected signal effect. However, due to the large insertion loss of WR-5 isolator and WR-5 direction coupler, the SBG LO pump power at 200 GHz is about 1 mW. The modulating signal power is fixed at 15 dBm.

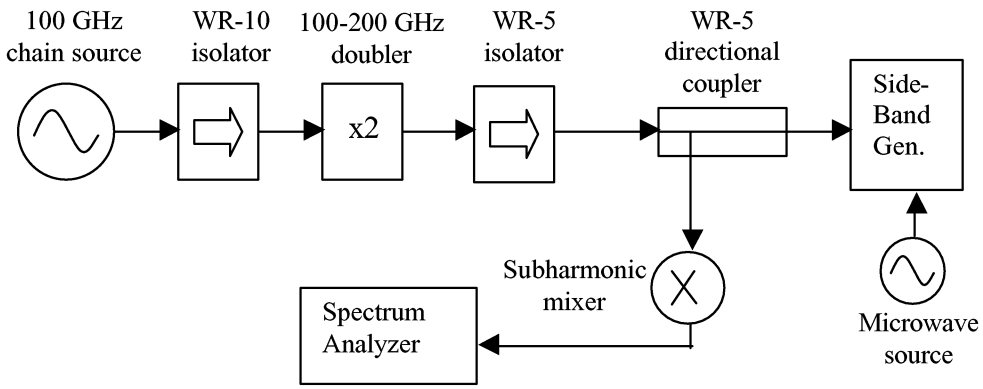

Fig. 6. The 200 GHz SBG conversion loss measurement setup

The reflected signals, LO and sidebands, are coupled into the coupling port of WR-5 directional coupler, and then sent to a 200 GHz subharmonic mixer RF port. The output IF signal from the mixer is sent to an Agilent 8565E spectrum analyzer. After calibrating out the mixer conversion loss and coupling loss, the SBG conversion loss is calculated, which is shown in Fig. 7. Over a 10 GHz frequency range, better than 10 dB conversion loss is achieved with 0 dBm input LO power.

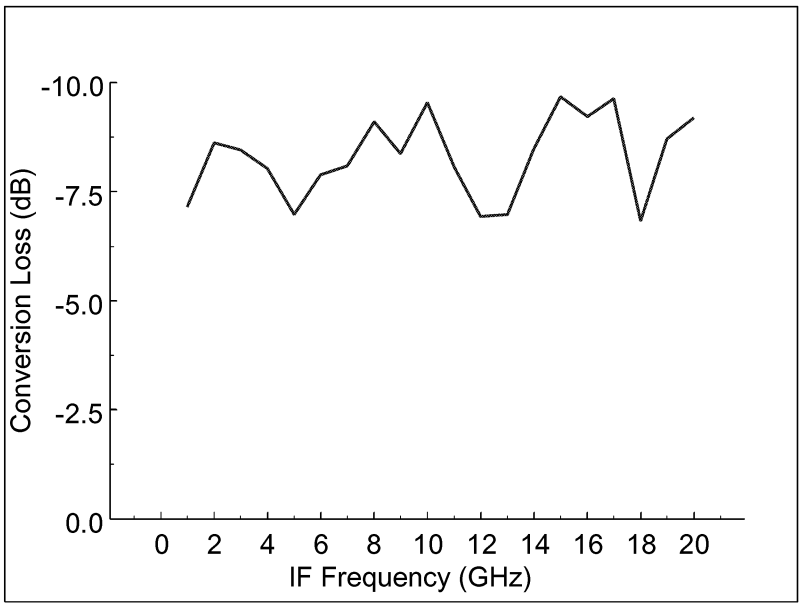

Fig.7. The test result of 200 GHz SBG conversion loss

V. CONCLUSION AND DISCUSSION

In this paper, an integrated varactor SBG is investigated. The 200 GHz SBG is implemented and tested. The reflection coefficient simulation agrees well with the test results, which provides practical instructions for higher frequency SBGs. Higher LO power, 10 mW, was also applied to the 200 GHz SBG. The upper sideband output power is about 1 mW, which indicates 10 dB conversion loss. The 600 GHz SBG will be tested using a solid state source and laser source. It's also expected that this SBG can be scaled to THz frequencies to provide a high power tunable source.

ACKNOWLEDGMENT

This research was supported by the US Army N.G.I.C. contract DASC01-01-C-0009.

REFERENCES

[1] E. R. Mueller and J. Waldman, "Power and Spatial Mode Measurements of Sideband Generated, Spatially Filtered, Submillimeter Radiation," *IEEE Trans. Microwave Theory Tech.,* vol. 42, No. 10, pp. 1891-1895, Oct. 1994.

[2] D. S. Kurtz, J. L. Hesler, T. W. Crowe and R. M. Weikle, "Millimeter- Wave Sideband Generation Using Varactor Phase Modulators," *IEEE Microwave and Guided Wave Letter,* vol. 10, No. 6, pp. 245-247, June 2000.

[3] D. S. Kurtz, "Sideband Generation for Submillimeter Wave Applications," Ph.D. Dissertation, Univ. of Virginia, May, 2000.

[4] P. S. Henry, "An Efficient Microstrip Upconverter for K_a Band," *IEEE MTT-S International Microwave Digest of Technical,* pp. 137-139, 1975.

[5] J. L. Hesler, "Planar Schottky Diodes in Sub-millimeter Wavelength Waveguide Receivers", Ph.D. Dissertation, Univ. of Virginia, January, 1996.

[6] R. F. Pierret, Semiconductor Device Fundamentals. Purdue University: Addison-wesley Publishing Company, 1996.

[7] J. L. Hesler, W. R. Hall, T. W. Crowe, R. M. Weikle, B. S. Deaver, Jr., R. F. Bradley and S. K. Pan, "Fixed-Tuned Submillimeter Wavelength Waveguide Mixers Using Planar Schottky Barrier Diodes," *IEEE Trans. Microwave Theory Tech.,* vol. 45, No. 5, pp. 653-658, May 1997.

A Photonic Local Oscillator for an SIS Mixer in the 100 GHz Band

T. Noguchi, A. Ueda, H.Iwashita, Y. Sekimoto, M. Ishiguro,
T. Ishibashi[†,1], H. Ito[†], and T. Nagatsuma[††]

Nobeyama Radio Observatory
[†]NTT Photonics Laboratories, NTT Corporation
[††]NTT Telecommunications Energy Laboratories, NTT Corporation

Abstract

We have developed a waveguide-mounted photomixer in the 75-115 GHz band with a uni-traveling carrier photodiode which is optically-pumped by two 1.55-μm lasers. We have successfully demonstrated to produce an output power of $\sim$2 mW at 100 GHz with an input laser power of $\sim$100 mW. An SIS mixer has been pumped by the photomixer as a local oscillator. It is found that in this configuration the photomixer can provide a sufficient local oscillator power required for optimum operation of the SIS mixer in the frequency band from 85 to 110 GHz. We have carried out similar experiment using a Gunn-diode local oscillator source and carefully compared the receiver noise temperature of the SIS mixer with those pumped by the photomixer. It is found that the receiver noise temperatures of the SIS mixer pumped by the photomixer is a little higher than those pumped by the Gunn oscillator.

Introduction

Millimeter- and submillimeter-wave heterodyne mixers based on the Superconductor-Insulator-Superconductor (SIS) junctions have used a local oscillator (LO) source which is a combination of a Gunn diode and multipliers. Since the LO source with the combination of a Gunn diode and multipliers has a mechanical complexity and poor frequency coverage especially at submillimeter wavelength, a compact and mechanically-simple LO source with broad frequency coverage is highly required for submillimeter-wave SIS receivers in the radio telescopes. Photomixers, which generate a difference frequency of two diode lasers at millimeter and submillimeter wavelength by photoconductive mixing, have been alternatively developed. Photomixers are so compact solid-state sources with broad frequency tunability that they can meet the requirement for the LO source of the SIS receivers at millimeter and submillimeter wavelengths.

It has been recently shown that photomixers using a uni-traveling carrier photodiode (UTC-PD) have a great potential for generation of millimeter-wave radiation with a bandwidth as high as 220 GHz [1]. Based on a simple analysis, it is expected that a 3-dB falloff bandwidth of the UTC-PD determined by carrier traveling time can be in a THz range [2]. The UTC-PD photomixer has emerged as one of the promising candidates to generate the millimeter- and submillimeter-wave radiation.

[1]Present affiliation: NTT Electronics Corporation

We have designed a new photomixer using the UTC-PD for generation of W-band radiation and successfully demonstrated to generate output power of $\sim$1 mW at 100 GHz by the photomixer.[3] Although the output power of the photomixer is thought to be enough to pump the SIS mixers as an LO of the usual receivers in this frequency band, noise characteristics of the photomixer have not been fully understood. At present, it is especially important to know the noise level of the photomixer when it is used to pump a low-noise SIS mixer as an LO. We have systematically measured noise temperature of an SIS mixer pumped by the photomixer as well as a Gunn diode as an LO. The measured noise temperature of those two cases are carefully compared to estimate the noise level of the photomixer in reference to that of Gunn diode.

In this paper, design and performance of the photomixer using the UTC-PD in the W band is briefly described. Then experimental results of measurement on noise temperature of SIS mixers using the photomixer as well as the Gunn diode as an LO are presented.

UTC-PD Photomixer

We have made a waveguide photomixer in the W-band using the UTC-PD. Detailed design of the UTC-PD and photomixer is described in Ref.[3]. A cross section of the photomixer mount is schematically shown in Fig. 1. Photographs of the mixer mount and the diode chip are also shown in Fig. 1.

Lasers ($\lambda = 1.5\mu$m) provided by two distributed-feedback (DFB) semiconductor laser-diodes are combined by a coupler into an optical fiber and then amplified by an optical fiber amplifier. The amplified lasers are focused onto the UTC-PD by a lens located in the photomixer mount. Schematic diagram of the photomixer experiment is shown in Fig. 2. The position of the lens is precisely aligned against the photodiode so that maximum power of millimeter-wave radiation is available at the output port of the photomixer mount. The output millimeter-wave radiation from the photomixer is detected by a spectrum analyzer with a harmonic mixer (HP11970) or a Schottky-diode detector.

In Fig. 3 output of the photomixer power measured by a Schottky-diode detector is plotted as a function of the photocurrent of the UTC-PD. It is noted here that the photocurrent of the UTC-PD induced by lasers is approximately proportional to the amount of laser power coupled to the diode in the experiment at lower frequency[4]. It is clear that the output power increases approximately in proportion to the photocurrent (or the input laser power) at lower photocurrent. At the photocurrent of 20 mA the output power reaches $\sim$2 mW, which is, as far as we know, one or two orders of magnitude higher than those generated by photomixers in this frequency band.[5]

In Fig. 4 a typical spectrum near 100 GHz of photomixer output is shown. Width of the output spectrum of the photomixer is less than 10 MHz, which is mainly governed by fluctuation of frequencies of the two lasers, since freely-running lasers are used in the experiment. It should be noted that no serious spurious peaks are found in this frequency range.

SIS Mixer Experiment

The photomixer was used as an LO source for SIS mixers in the 100 GHz band. The photomixer output and an RF signal are combined by a cross-guide coupler with a coupling efficiency of < -20 dB placed on the 4-K stage in the dewar and then coupled into the SIS mixer. This LO

coupling scheme is popularly used in low-noise receivers at millimeter wavelengths. Schematic diagram of a low-noise receiver employing SIS mixer associated with an LO source of the photomixer is shown in Fig. 5.

In order to compare noise of the photomixer with that of Gunn-diode oscillator, we have carried out similar experiment using a Gunn-diode LO source. Then, we carefully compared receiver noise temperatures of the SIS mixer pumped by the photomixer with those pumped by the Gunn-diode oscillator.

Results and Discussion

Pumped and unpumped I-V curves of an SIS mixer by the Gunn-diode oscillator and photomixer at 100 GHz as well as the hot (295 K) and cold (80 K) total IF power response are shown in Fig. 6(a) and (b), respectively. We have found that the photomixer is able to provide a sufficient LO power required to pump the SIS mixer in the frequency band from 85, which approximately corresponds to a cut-off frequency of the waveguide in the cross-guide coupler and mixer block, to 120 GHz. The frequency dependence of the achieved receiver noise temperature for the Gunn-diode LO as well as for the photomixer LO are shown in Fig. 7. It is found that no significant difference between the noise temperatures of the SIS mixer pumped with the Gunn diode and phtomixer is observed in this measurement. However, it is noted here that magnitude of the noise temperature of the SIS mixer is higher than those of usual SIS mixers in this frequency band. Since we suspected that the small amount of LO noise is deafened by the mixer noise, we carried out the same experiment using an SIS mixer with much lower noise temperature.

In Fig. 8, the receiver noise temperatures of the lower noise SIS mixer pumped with the photomixer LO and Gunn-diode LO are shown. In this case, the receiver noise temperature for the photomixer LO is systematically higher than that for the Gunn-diode LO. This result indicates that the photomixer has an "excess noise" with equivalent temperature from 15 to 25 K compared to the Gunn-diode oscillator.

It should be noted that photocurrent in the photomixer used in the second experiment is approximately half of that in the first experiment, when the same amount of laser power as that in the first experiment is applied. This is due to degradation of the photo-diode and/or poor alignment of optical system. As a result, output power of the photomixer was approximately 40 % of that in the first experiment.

We found that the "excess noise" increases as the laser power is decreased keeping the input power to the photomixer constant. We confirmed that noise figure (NF) of the optical fiber amplifier is approximately constant and independent on its gain. These results indicate that the "excess noise" is mainly dominated by the amplifier noise. It is expected that the "excess noise" can be suppressed by the increase of output power of the photomixer. We think the fact that the "excess noise" obtained in the first experiment is quite small is achieved by high output power of the photomixer.

Another noise source is harmonic oscillations generated in the photomixer, because sideband noise of the harmonic oscillations might be down-converted to the IF frequency in the SIS mixer. A recent experiment of an open-structured photomixer carried out by Hirata *et al.* [6] and indicates that significant amount of harmonic oscillations are excited in the photomixer. It is possible to eliminate the harmonic oscillations penetrating into the SIS mixer by adopting an

adequate low-pass filter in the output port of the photomixer. Although reason of the "excess noise" of the photomixer has not been fully understood yet, we are now studying the noise issue in the photomixer.

Summary

We have exploited a photomixer for generation of millimeter wave at W band using a UTC-PD and successfully demonstrated to generate millimeter-wave radiation with a power as high as 2 mW in the 100 GHz band. As far as we know, this is the highest output power ever generated by any kind of photomixers in this frequency band. An SIS mixer was pumped by the photomixer as an LO and we found that the photomixer can provide a sufficient power to drive the SIS mixer. It is found that the noise added to the SIS mixer by the photomixer is a little higher than that by a Gunn oscillator. Although origin of the additional noise of the photomixer has not been fully understood yet, we are studying to find the origin of the additional noise experimentally as well as theoretically.

Acknowledgment

The authors would like to thank S. Matsuura of Institute of Space and Astronautical Sciences (ISAS) for stimulative discussion. This work was supported by a Grant-in-Aid for Scientific Research from the Ministry of Education, Culture, Sports, Science and Technology.

References

[1] H. Ito, T. Furuta, S. Kodama, N. Watanabe, and T. Ishibashi, "InP/InGaAs Uni-Traveling-Carrier Photodiode with 220 GHz Bandwidth", *Electron. Lett.*, **35**, 1556–1557, 1999.

[2] T. Ishibashi, H. Fushimi, T. Furuta, and H. Ito, "Uni-Traveling-Carrier Photodiodes for Electromagnetic Wave Generation", *Proc. IEEE 7th Int. Conference on Terahertz Electron.*, pp. 36–39, Nara, Japan, Nov. 1999.

[3] T. Noguchi, A. Ueda, H. Iwashita, S. Takano, Y. Sekimoto, M. Ishiguro, T. Ishibashi, H. Ito, and T. Nagatsuma, 12th Int. Symp. Space Terahertz Technology, 3.2, San Diego, Feb. 14-16, 2001, Millimeter Wave Generation Using A Uni-Traveling-Carrier Photodiode.

[4] H. Ito, T. Ohno, H. Fushimi, T. Furuta, S. Kodama, and T. Ishibashi, "60 GHz high output power uni-traveling-carrier photodiodes with integrated bias circuit", *Electron. Lett.*, **36**, 747–748, 2000.

[5] P. G. Huggard, B. N. Ellison, P. Shen, N. J. Gomes, P. A. Davies, W. P. Shillue, A. Vaccari, W. Grammer, and J. M. Payne, ALMA Memo #396, "A Photonic MM-Wave Reference and Local Oscillator Source".

[6] A. Hirata, T. Nagatsuma, R. Yano, H. Ito, T. Furuta, Y. Hirota, T. Ishibashi, H. Matsuo, A. Ueda, T. Noguchi, Y. Sekimoto, M. Ishiguro, and S. Matsuura, "Output Power Measurement of Wide-band Photonic Local Oscillator at 100-800 GHz", *preprint*.

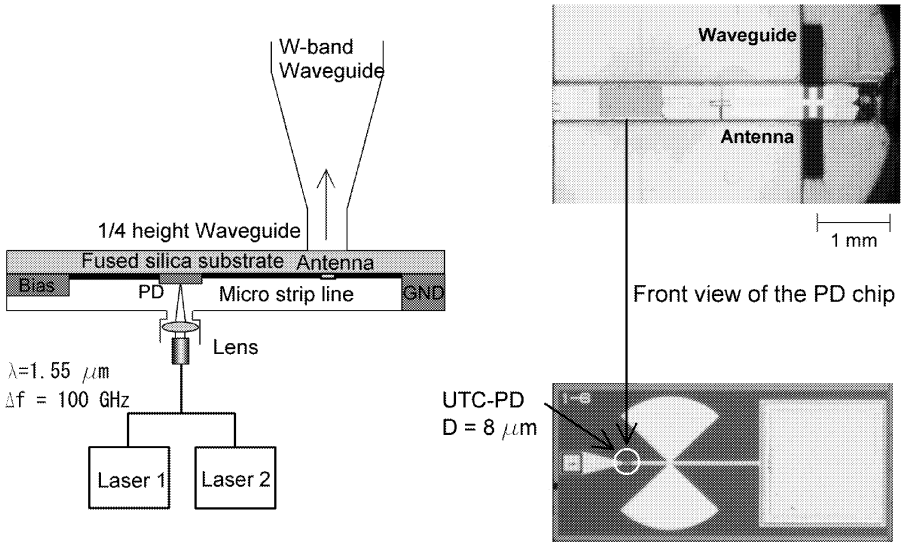

Fig. 1 Cross section of the photomixer mount (left), photographs of phtomixer mount (top right) and a UTC-PD chip (bottom left).

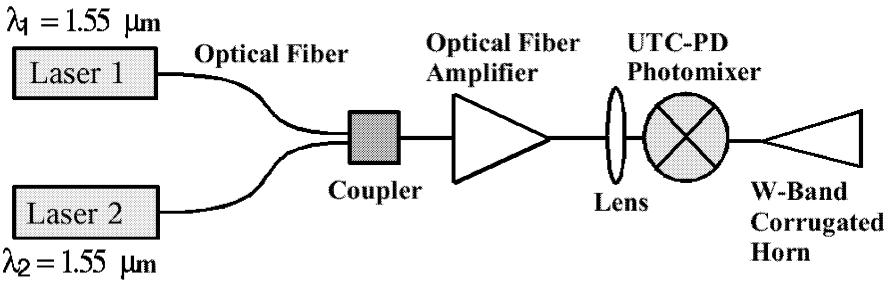

Fig. 2 Schematic layout of a photomixer oscillator.

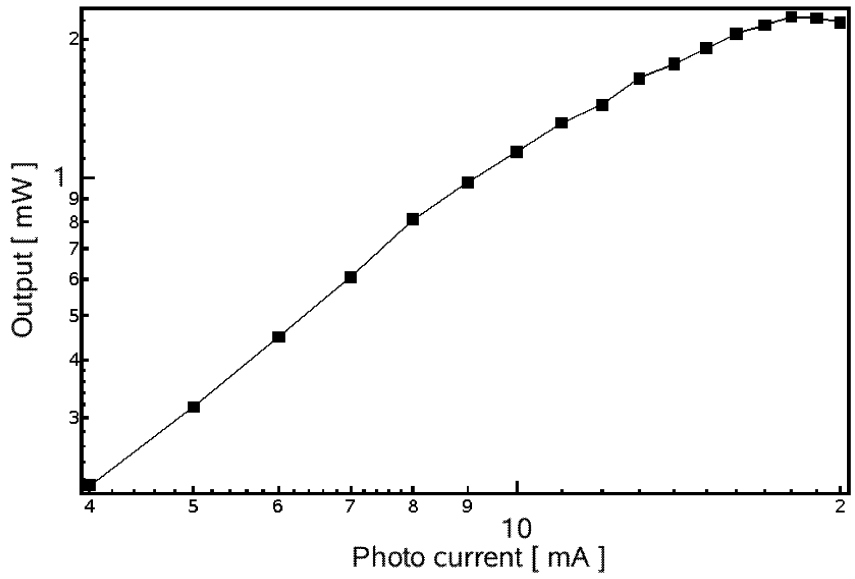

Fig. 3 Output power of the photomixer as a function of photocurrent induced in the photodiode by the laser irradiation.

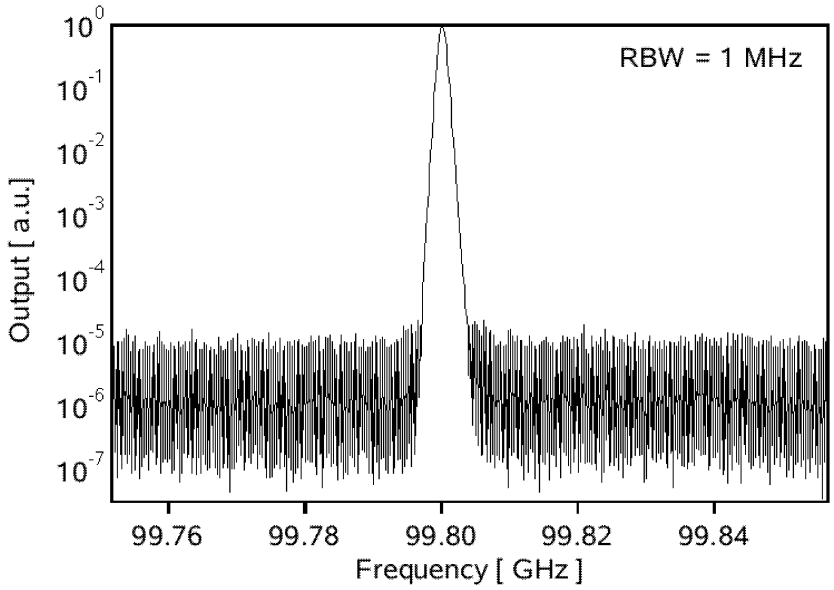

Fig. 4 Typical measured spectrum of the photomixer output.

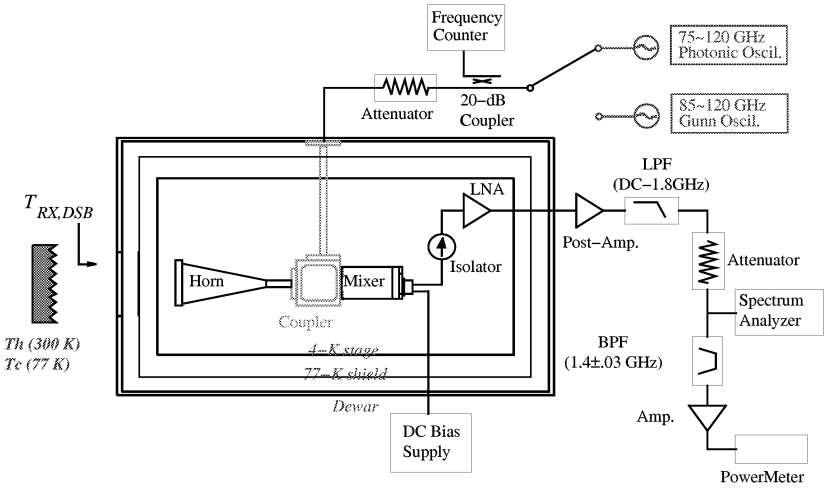

Fig. 5 Schematic layout of an low-noise SIS receiver with a phtomixer LO and Gunn-diode LO.

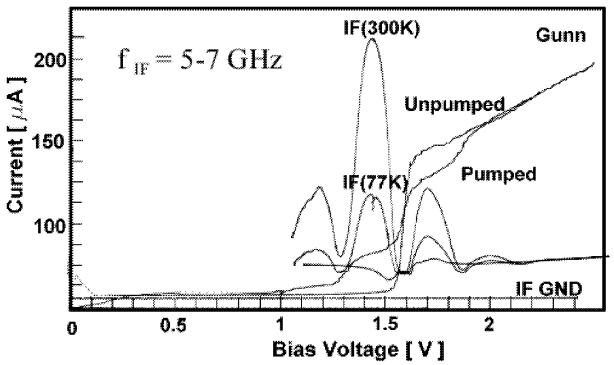

(a)

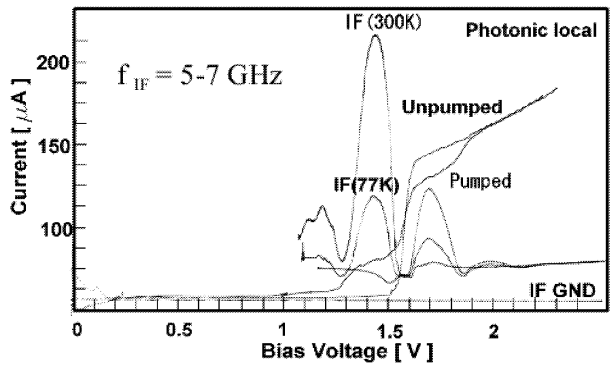

(b)

Fig. 6 Pumped and unpumped I-V curves and total IF power (a) by a Gunn oscillator and (b) by a photonic oscillator.

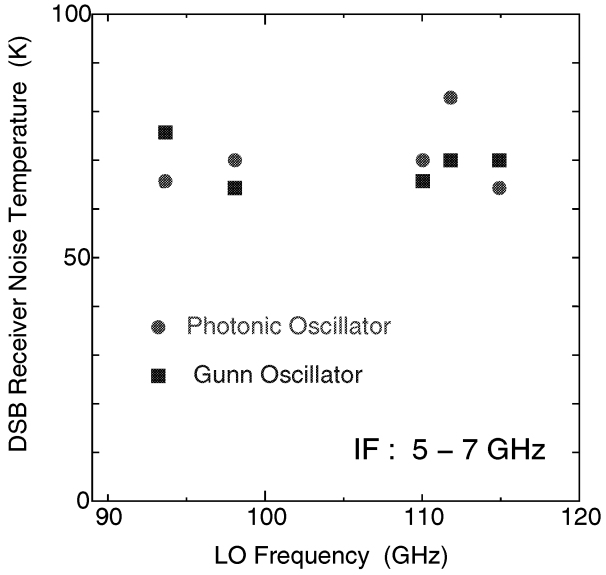

Fig. 7 Receiver noise temperature of an SIS mixer pumped with the photomixer and Gunn-diode oscillator as a function of frequency.

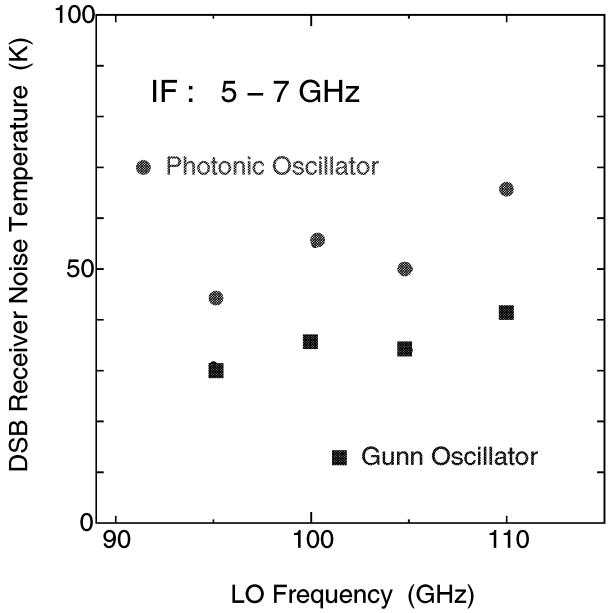

Fig. 8 Receiver noise temperature of an SIS mixer with good noise characteristics pumped with the photomixer and Gunn-diode oscillator as a function of frequency.

MILLIMETER- AND SUBMILLIMETER-WAVE ELECTRODYNAMIC PROPERTIES OF POLYMER ELECTRO-OPTIC MATERIALS

Mark Lee, Oleg Mitrofanov, and Howard E. Katz
Bell Laboratories, Lucent Technologies, 600 Mountain Ave., Murray Hill, NJ 07974

The bandwidth of commercial optical telecommunications technology has recently crossed into millimeter-wave frequencies (*i.e.* 40 GHz), and there is now a strong research effort aimed at extending these bandwidths deeper into millimeter-wave and perhaps even into submillimeter-wave frequencies. Materials with electro-optic optical non-linearities are inherent in such communications systems, since they allow a voltage signal to amplitude or phase modulate an optical carrier. Alternatively, an electro-optic material can be used in conjunction with optical interferometric techniques to form a phase-sensitive detector of THz waves. The ferroelectric perovskites most commonly used as electro-optic materials up to 40 GHz have crippling limitations that render them unusable at bandwidths exceeding 80 to 100 GHz.[1] Therefore, there has very recently been a resurgence of interest in the non-linear optical properties of conjugated polymer-based materials. The very fast and nearly lossless electron transfer along π-conjugated bonds in such polymers promise a very high intrinsic frequency response with little index dispersion over a very broad bandwidth. Also, recent progress in the chemical synthesis of electro-optic polymers[2] has resulted in materials with electro-optic coefficient as high as 75 pm/V, or greater than three times that of $LiNbO_3$, which is the most widely used electro-optic material today.

Using a combination of vector network analysis and pulsed THz time-domain spectroscopy, we have measured the real and imaginary dielectric properties of several different polymer host matrices and polymer electro-optic chromophores across the frequency range 0.05 to 600 GHz. All these polymer materials have very desirable properties for use as either electro-optic modulators or detectors at millimeter- to submillimeter-wave frequencies. The indices-of-refraction measured are all fairly low, in the range of 1.3 to 2.0 for all materials, and show very little dispersion up to at least 200 GHz and even up through 600 GHz in at least one case. Moreover, these index values are within approximately 15% of the corresponding optical indices at 1.5 μm wavelength for each polymer, making the engineering of high-efficiency velocity-matched collinear optical and millimeter-wave waveguides much simpler than with perovskite materials. Finally, these polymers have very small dielectric loss tangents up to at least 250 GHz. Typical loss tangents are comparable to, and in some cases smaller than, the loss tangent of a Teflon reference in this frequency range. Therefore, we expect negligible parasitic dielectric loss in millimeter-wave electro-optic devices made from these materials.

As an example of a very wide bandwidth electro-optic device, we have also designed, fabricated, and tested a prototype polymer optical modulator with optical response bandwidth exceeding 200 GHz.

---

[1]Mark Lee, Appl. Phys. Lett. **79**, 1342 (2001)

[2]Y. Shi, C. Zhang, H. Zhang, J. H. Bechtel, L. R. Dalton, B. H. Robinson, and W. H. Steier, *Science* **288**, 119 (2000)

THZ field generation and manipulation by coherent control over phonon-polaritons

T. Feurer, Joshua C. Vaughan, Nikolay S. Stoyanov, David W. Ward, Keith A. Nelson

Department of Chemistry, MIT, Cambridge, MA 02139

kanelson@mit.edu

Abstract: Here we present experimental demonstrations of coherent control over phonon-polaritons and the associated THz fields by employing spatial-only, temporal-only, and spatiotemporal pulse shaping to steer, focus, and amplify the propagating THz fields. In addition, we show that spatial-only control allows for the generation of specific excitation profiles, including circular excitation geometries that lead to focusing and increased peak amplitude/intensity levels. The polariton host crystals may be uniform or may be patterned into waveguide, resonator, polaritonic bandgap, and other structures. The capabilities enable multiplexed solid-state THz signal generation, signal propagation among specified addresses, signal manipulation, and signal readout, all without loss of bandwidth.

Mixed polar lattice vibrational and electromagnetic modes, called phonon-polaritons, which propagate at light-like speeds through their host crystals are unique and powerful sources of THz radiation. One way to excite them is by non-resonant impulsive stimulated Raman scattering using femtosecond laser pulses. New techniques in spatiotemporal imaging and spatiotemporal and spatial-only femtosecond pulse shaping and structuring of crystal materials have been developed to enable versatile spatiotemporal coherent control over the propagating phonon-polaritons and thereby over the associated THz fields.

Achieving control over propagating coherent responses places new demands on both the excitation and probing processes. In particular, it must be possible to generate excitation light fields that are specified functions of both time and position, and it must also be possible to monitor the time and position-dependent responses. Programmable spatiotemporal femtosecond pulse shaping, through which a single light beam with a single femtosecond pulse may be transformed into many spatially separated light beams, each of which has a specified time-dependent waveform, has been developed [1] and very recently improved [2] to achieve the high fidelity necessary for coherent control applications. Separately, spatiotemporal imaging of propagating, coherent lattice modes has been reported [3]. The combination of these two capabilities enables automated spatiotemporal coherent control over lattice waves that propagate at light-like speeds.

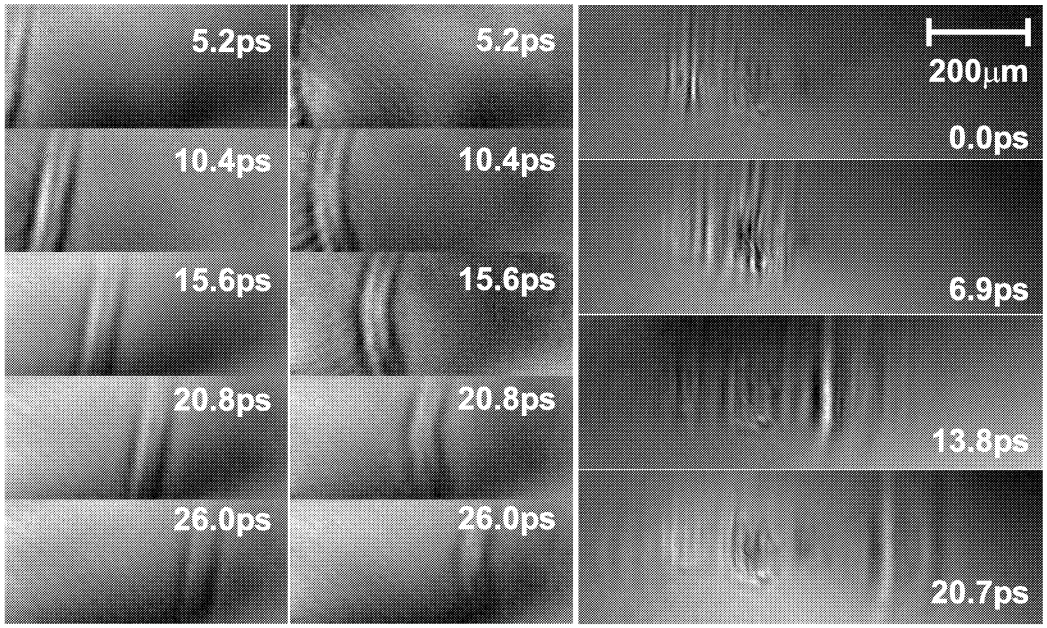

Fig. 1. Polariton responses to a series of about 20 spots, generated through spatiotemporal femtosecond pulse shaping. (LH column) Tilted polariton wavefronts resulting from pulses arriving at excitation spots separated along the vertical dimension at progressively later times, with a linear relation between temporal delay and spatial location of the spot. (center column) Polariton focusing specified through a parabolic relation between temporal delay and spatial location of the spots along the vertical dimension. (RH column) The excitation spots are horizontally arrayed. Excitation pulses arrive at the LH spot first and sweep toward the right, resulting in polariton amplification.

Figure 1 shows results of experiments conducted in $LiTaO_3$ crystals, using 800 nm spatiotemporally shaped excitation waveforms and variably delayed, 400 nm probe pulses. The images of the polariton responses were projected onto a CCD [3]. The LH column shows the result of a linear temporal sweep in which the uppermost excitation spot was irradiated first, then the spot below it, and so on. Different linear sweeps were used to steer polariton responses along selected directions. The center column shows the result of a parabolic temporal sweep in which the first pulses arrived at the top and bottom spots, the next pulses arrived at the adjacent spots, and so on, with the last pulses arriving at the middle spots. Polariton focusing with various focal lengths was conducted by varying the curvature of the parabolic temporal sweep. A combination of linear and parabolic delays was used for both focusing and steering, i.e. to direct focused polaritons to selected locations. The RH column shows polariton amplification, achieved with a sequence of pulses moving from left to right with temporal and spatial delays fixed to match the polariton group velocity. The phonon-polariton response propagating to the right is amplified substantially, while the unamplified responses propagating toward the left are only barely visible.

Besides active coherent control we demonstrate passive control over phonon-polariton propagation by laser-machining integrated waveguide structures on a $LiNbO_3$ platform. Because the wavelengths of phonon-polaritons is typically on the order of a few ten to a few hundred microns, femtosecond laser-machining offers a versatile tool to fabricate waveguides and more complex integrated waveguide structures.

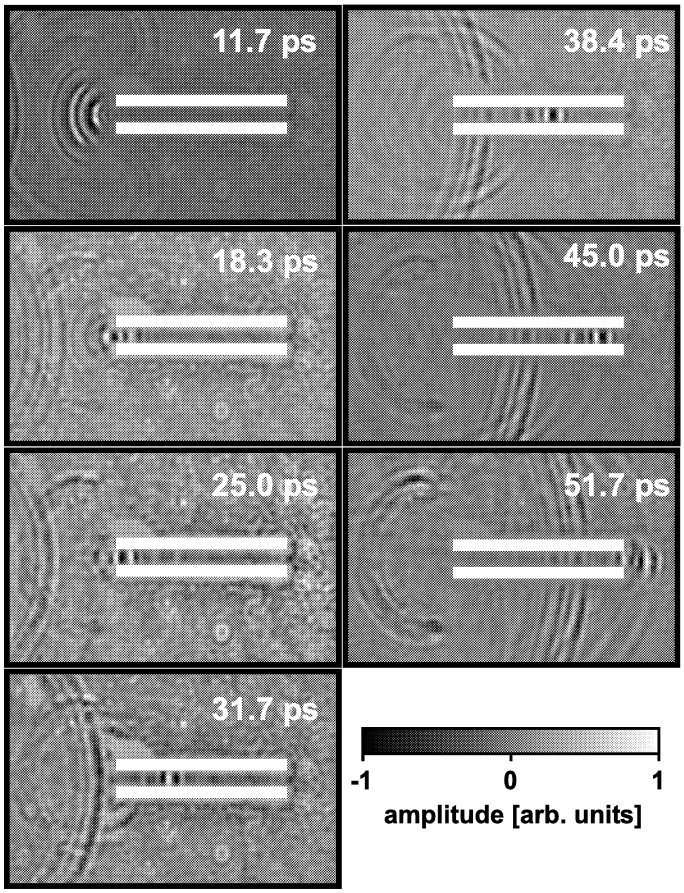

Fig. 2. Phonon-polariton propagation in a laser-machined waveguide structure.

Figure 2 shows a series of snapshots of a phonon-polariton being focused into a laser-machined waveguide structure. The waveguide is 0.2 mm wide and 1.7 mm long. The walls of the waveguide appear blurry, because the CCD camera was moved out of the image plane to achieve high contrast phase imaging. The white bars have been added by image processing and indicate the location and width of the waveguide walls. Immediately after entering the waveguide the phonon-polariton wavefront becomes perfectly plane and remains so until the phonon-polariton exits the waveguide. The last image shows the diverging phonon-polariton as it comes out of the waveguide.

More complex structures, for example an integrated Mach-Zehnder interferometer, have been

fabricated and their functionality has been shown.

Applications of our results include programmable generation of user-defined THz waveforms, nonlinear THz frequency spectroscopy, and THz-bandwidth signal processing applications.

Acknowledgement

This work was supported in part by National Science Foundation grant no. CHE97-13388 and MRSEC program award no. DMR98-08941, and Army Research Office grant no. DAAD19-99-1-0034. T. Feurer acknowledges financial support by the Max Kade Foundation.

References

1. R.M. Koehl, T. Hattori, K.A. Nelson, Opt. Commun. **157**, 57 (1998)
2. T. Feurer, J.C. Vaughan, R.M. Koehl, K.A. Nelson, Opt. Lett. **27**, 652 (2002)
3. R.M. Koehl, S. Adachi, K.A. Nelson, J. Phys. Chem. A **103**, 10260 (1999)

NOVEL TUNABLE SOURCE FOR GENERATION OF THZ RADIATION

L. Maleki, H. Javadi, and V. Ilchenko
Quantum Sciences and Technology Group
Jet Propulsion Laboratory
Pasadena, CA 91109

This paper describes a new approach aimed at the realization of a multi-channel spectrum analyzer for terahertz radiation. The approach is based on the novel technology of whispering gallery mode resonators that is inherently suitable for spacecraft instrumentation.

Photons at terahertz frequency are the most ubiquitous in the universe. Aside from cold interstellar clouds, and other cosmic sources, water, and all water bearing and cold (less than 600K) bio-matter emit terahertz radiation. The ability to sensitively detect terahertz radiation with a spacecraft instrument is a powerful technique for remote detection of extra terrestrial biotic and pre-biotic matter. Such an approach however requires the ability of wide-spectral and narrow-band receivers to realize the function of multi-channel spectral analysis.

Current technology for generating spectrally pure terahertz signals to realize coherent detection is grossly lacking in performance and suitability for spacecraft applications, as compared with millimeter wave technology. The most effective means to generate terahertz radiation involves lasers locked to modes of a high finesse optical cavity, and used for heterodyne frequency generation. This approach has a number of disadvantages, including the requirement for a bulky cavity and limitations associated with broad line-widths.

The technology of micro-resonators can be applied to this problem. In particular, novel microtorus resonators recently developed at JPL can be used to generate a comb of frequencies, separated by a desired amount (say, 100 to 400 GHz) over a range of 1520 to 1575 nm. Because of the high Q of the resonators ~9×10^9, the line-width of these lines are extremely narrow. With photomixing, such a comb can be used to synthesize a wide spectrum of terahertz frequency. We will also study and develop whispering gallery mode micro-resonators at terahertz frequency, to enable filtering and processing functions required for a spectrum analyzer.

Aside from applications to water and biomass detection, the development of sources and components mentioned above are extremely useful for terahertz astronomy, communications, and remote sensing of Earth. After completion of this seed effort, we anticipate funding from NASA and DOD for further development of this technology.

Generation of Millimetre and Sub-Millimetre Waves by Photomixing in a 1.55 μm wavelength Photodiode.

P. G. Huggard* & B. N. Ellison,
Rutherford Appleton Laboratory, Chilton,
Didcot, OX11 0QX, UK

P. Shen, N. J. Gomes & P. A. Davies,
Department of Electronics, University of Kent,
Canterbury, CT2 7NT, UK

W. P. Shillue, A.Vaccari & J. M Payne,
NRAO, Tucson, AZ 85721-0655, USA

Abstract: We report on the generation of radiation at frequencies from 70 GHz to above 600 GHz by photomixing in commercially available 70 GHz bandwidth photodiodes. The mm-wave and sub-mm-wave power was generated in W-band waveguide mounts by the beating of two 1.55 μm laser beams. Maximum optical to mm-wave power conversion efficiencies above 1 % were measured at frequencies between 75 GHz and 110 GHz, where an input power of +10 dBm yielded a non-saturated output power above -10 dBm. Measured output powers fell approximately as (frequency)$^{-4}$ above 140 GHz, so that a power of approximately -40 dBm was detected at 625 GHz. We remark that the waveguide mount is non-optimised for frequencies above 110 GHz, and so these measurements represent a lower limit on the generated power.

Introduction: Photomixer, also known as photonic, sources generate power at the difference frequency of two visible or near infrared laser beams by using ultrafast photoconductors or photodiodes. We have constructed photomixers based upon commercially available 1.55 μm photodiodes [1] which have a 70 GHz analogue bandwidth, our objective being the provision of photonic sources for use as phase references, phase calibrators, and local oscillators for heterodyne receivers in the ALMA telescope [2].

The work presented below has extended previous W-band measurements on the photodiodes [3] by incorporating modified devices into a waveguide mount. Advantages of this approach include the ability to provide optimised photodiode-embedding circuit impedance match conditions, e.g. by the use of stub tuners, and the ease of interface with standard waveguide components. The stub tuner approach is particularly useful in the case of photodiode mm-wave sources, as the effects of large and sometimes uncertain capacitance on the high frequency roll-off of the responsivity can be reduced. Our findings on the advantages of this waveguide mount approach have already been reported [4, 5].

* e-mail: p.g.huggard@rl.ac.uk

In what follows, we describe how the 1.55 μm wavelength photodiodes were adapted for use in the specially designed W-band waveguide mount. We further report how the cleaved single mode optical fibre was fixed in position with respect to the photodiode chip to form a compact and mechanically stable mm-wave source. Results are presented showing the dependence of mm-wave power on optical input power and on applied bias. Although the mount is optimised for W-band frequencies, i.e. from 75 GHz to 110 GHz, and the diode bandwidth is below 100 GHz, we have been able to measure powers at frequencies from 70 GHz up to the optical source imposed limit of 625 GHz. Finally, we demonstrate the reproducibility of the design by comparing the W-band characteristics of two photomixers for fixed backshort tuning.

The photomixing source and apparatus: The p-i-n photodiodes utilised are epitaxially grown on InP and are supplied as chips 2 mm in length and 500 μm in width. Incident 1.55 μm radiation is injected through an antireflection-coated facet and passes via a rib waveguide to the 5 μm x 20 μm photodiode [6]. The photodiode output contact is connected to the centre conductor of a short length of 50 Ω coplanar waveguide. Manufacturer's data indicates an external DC responsivity about 0.4 A/W at a reverse bias of 1V with a bandwidth of 70 GHz in a 50 Ω environment [6].

Our waveguide photomixer approach requires that the photodiode chip is enclosed in a metal channel. The cross-sectional dimensions of the supplied photodiode substrate are relatively large compared to the operational wavelength and longitudinal propagation of radiation in a waveguide mode may occur for frequencies above 94 GHz. Propagation of such a mode in the channel would represent a loss of power from the desired TE_{10} mode in the WR-10 output waveguide. To address this problem the chips were mechanically thinned to 200 μm and reduced in width to 380 μm: this modification increases the cut-off frequency of the undesired mode to 145 GHz.

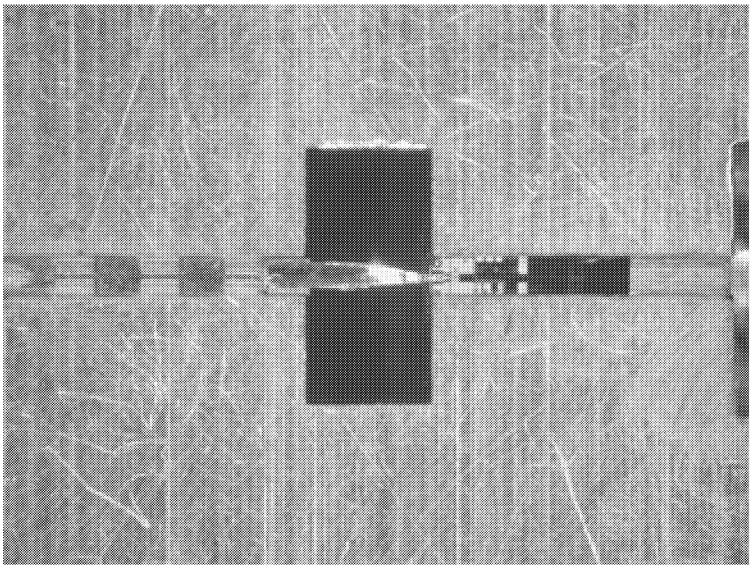

Figure 1: Photograph of u^2t photodiode chip (right centre) incorporated in a photonic mixer block**.**

A modified chip, appearing as the predominantly black area on the centre right of Figure 1, was fixed in the channel of a photomixer block. The dark rectangular area in the middle of the photograph is the end of the WR-10 waveguide. Constant voltage bias is applied to the photodiode by means of a radio frequency choke structure defined on a 200 μm thick quartz substrate. This is visible on the left hand side of Figure 1. A wedge shaped gold foil extends across the WR-10 waveguide to make contact with the output conductor on the photodiode chip. The electrical connection between the photodiode contacts and the foil probe is made by means of low melting point InSn solder.

A single mode optical fibre transports the 1.55 μm radiation to the photomixer. The stripped fibre enters the photodiode channel from the right-hand side as viewed in Figure 1 and its cleaved end is positioned about 40 μm from the chip facet. The fibre is glued into a stainless steel ferrule, which passes through a hole in the block and is then clamped to an x-y-z positioner. When alignment between fibre and chip has been optimised, the ferrule is fastened to the photomixer block by epoxy resin. After this has cured, the rigidity of the bond is such that light finger pressure on the exposed ferrule does not disturb the fibre to chip alignment.

In use, the photomixer block is capped with a metal lid through which the rectangular waveguide continues. A sliding backshort in this waveguide may be adjusted by means of a micrometer screw: Figure 2. To give an idea of scale, the rectangular block dimensions are 20 mm x 22 mm x 7 mm. The micrometer adjustment mechanism for the backshort could be eliminated in a future fixed backshort production device, considerable reducing the source height. This figure also shows the SMA bias connector and the epoxied stainless steel ferrule that supports the soft buffer coated fibre.

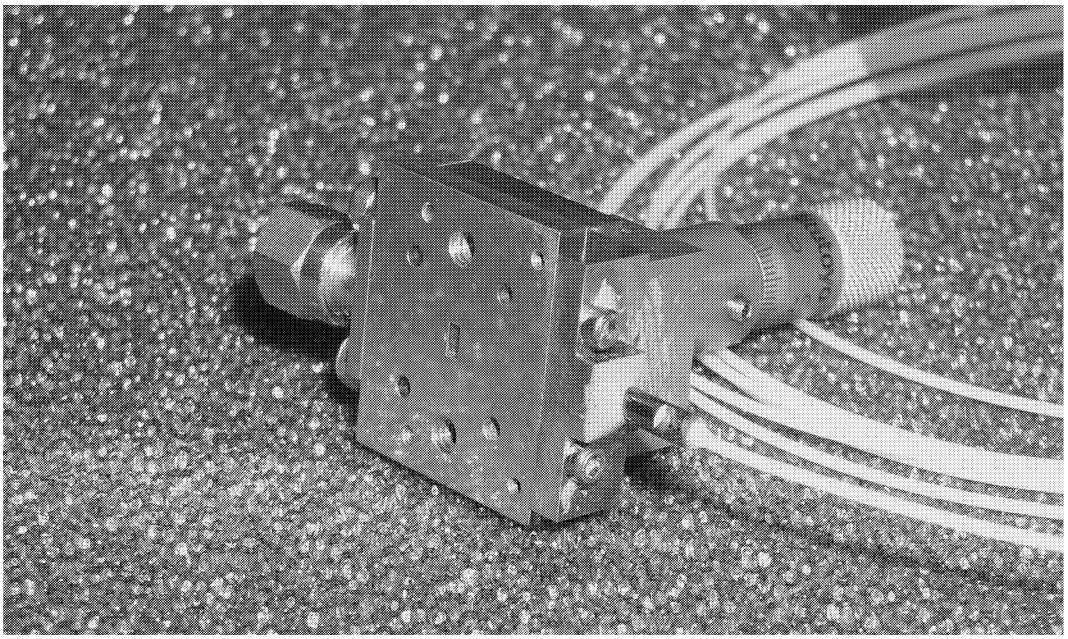

Figure 2: Photograph of completed photonic sources showing theWR-10 output waveguide and the stainless steel fibre ferrule cemented to the block. The block base dimensions are 20 mm x 25 mm.

Optical power is provided by two 1.55 μm diode lasers whose outputs are combined into a single mode fibre. The lasers and associated microprocessor driven control electronics have been packaged into a single microprocessor controlled 19" rack unit by NRAO. Frequency offsets from 1 GHz to 625 GHz and a combined output power above +10 dBm are available.

Methods used to characterise the generated mm-wave power depended on the frequency. An external W-band mixer connected to a spectrum analyser was used for frequencies from 75 GHz to 200 GHz. Measured in-band powers were verified to within 1 dB by means of a thermocouple power meter. At higher frequencies the radiation was coupled into free space by a rectangular feedhorn antenna. For power measurement the radiation was focussed into a calibrated Golay cell by a HDPE lens. Alternatively, for frequency verification outside the range of the spectrum analyser, the mm-wave signal was coupled into a Fourier transform spectrometer: this confirmed that the radiation was emitted at the difference frequency of the laser beams, and any higher harmonic components could not be discerned from the measurement noise floor.

Experimental results and discussion: The DC external responsivity of the photodiode was measured as 0.4 A/W for a reverse bias of 1.2 V, in good agreement with the manufacturer's specification. Figure 3 presents the dependence of the mm-wave power on optical power at frequencies of 75 GHz and 100 GHz for a reverse bias of –1.2 V. In both cases the expected square law response is observed, as indicated by the lines which have a slope of two. Respective maximum mm-wave powers of –7.7 dBm (170 μW) and –10 dBm (100 μW) are obtained for the maximum excitation power of +10 dBm (10 mW). These values correspond to a power conversion efficiency of at least 1%. The data shows no evidence of saturation and so mm-wave powers of at least 0 dBm would be expected if this behaviour continues to the optical power limit of +16 dBm (40 mW). For comparison purposes, powers of +10 dBm have recently been generated by strongly saturated uni-travelling-carrier photodiodes [7] driven by mode locked laser pulses. The pulse repetition frequency was 100 GHz and the average photocurrent was about 30 mA. Photomixing experiments in waveguide mounts with these photodiodes at the same frequency yields +3 dBm (2 mW) for an input of +23 dBm (200 mW) [8].

The bias dependence of the power at 100 GHz is shown in the Figure 3 inset for an optical power of +8 dBm. The signal initially increases strongly as the bias is changed from forward to reverse, and the power then saturates for reverse biases above 0.5 V. The total contrast available by varying the bias by 1.4 V is about 10 dB. Decreasing reverse bias increases the junction capacitance and possibly also increases the carrier transit time. Both these effects reduce the overall detector bandwidth – see below - and hence the mm-wave power at a given frequency decreases. This bias sensitivity offers the facility to remotely control photomixer output powers, a useful feature if the photomixer is to be used as a local oscillator for SIS mixers.

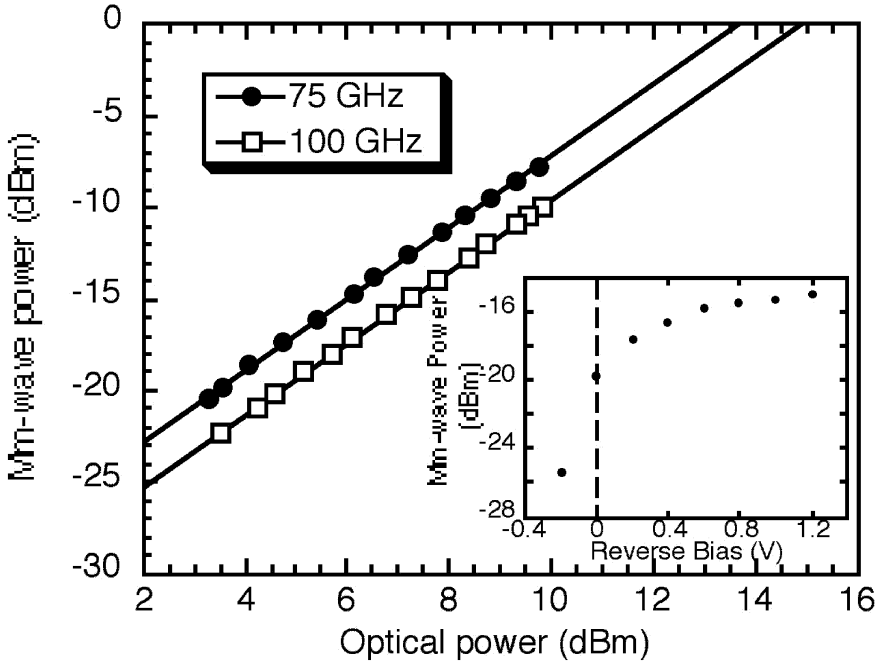

Figure 3: Dependence of mm-wave power on optical power at frequencies of 75 GHz (solid circles) and 100 GHz (open squares) for a reverse bias of –1.2 V. The lines indicate a slope of two. The inset shows the dependence of the mm-wave power on bias at a frequency of 100 GHz and an optical power of +7.8 dBm (6 mW).

While measuring the above power dependences, the position of the backshort was optimised at each frequency. Figure 4 displays the dependence of this maximised power as a function of frequency between 75 GHz and 625 GHz. The measurements were made at a reverse bias of 1 V and for a constant +10 dBm optical input power. The mm-wave power is found to peak at around –10 dBm for frequencies close to 100 GHz. A sharp dip is observed in the region of 120 GHz, above which the power recovers and then decreases approximately proportional to (frequency)$^{-4}$ so that the detected power above 600 GHz is about –40 dBm (100 nW).

The frequency response of the photomixer is determined by both photodiode properties and by the characteristics of the photomixer block and coupling structure. The photodiode bandwidth is a combination of the RC bandwidth (100 GHz) and the carrier transit time, τ_d, limited bandwidth (110 GHz) [6]. The expected dependence of microwave power on frequency, P(f), is thus a product of two terms, both varying as f^{-2} at high frequencies [9]:

$$P(f) \propto \frac{1}{[1+(2\pi f\tau_d)^2][1+(2\pi fRC)^2]} \qquad (1)$$

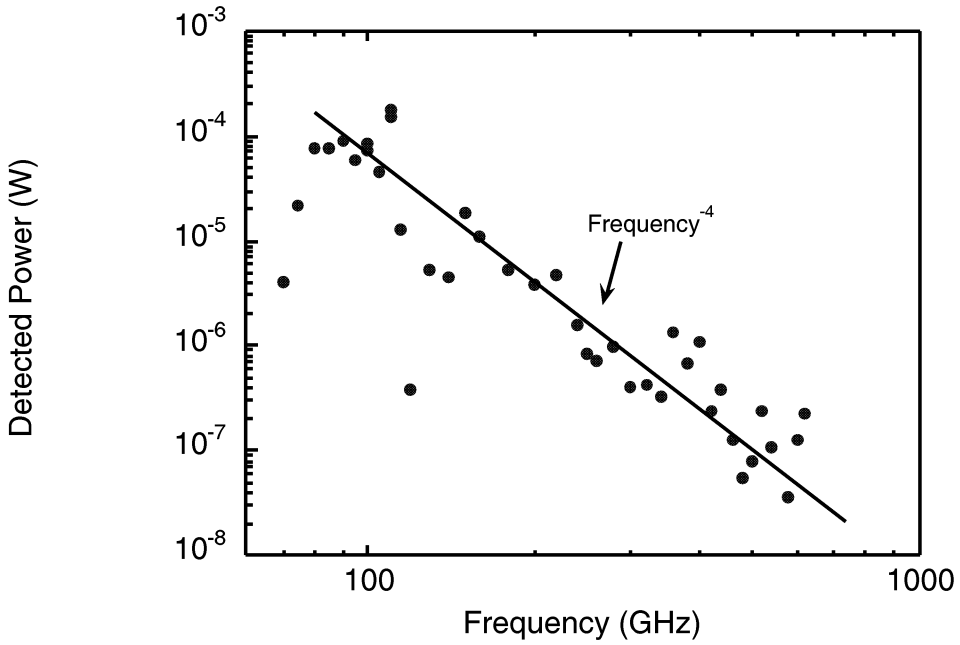

Figure 4: Dependence of mm-wave power on frequency for a constant excitation power of +10 dBm (10 mW). The line is a guide to the eye and indicates a $(\text{frequency})^{-4}$ dependence.

Within the band of the photomixer block, 75 GHz to 110 GHz, the effects of capacitance on the roll-off with frequency can be reduced by tuning the backshort appropriately. This tuning become less effective as the frequency rises and the waveguide becomes overmoded. HFSS calculations show that radiation can propagate in the photodiode and choke channels for frequencies above 150 GHz: this is a potential further loss mechanism. In addition the feedhorn beam pattern is unknown at high frequencies and the efficiency of coupling generated power to the Golay cell detector may therefore be lower. All these factors are tend to reduce the detected power and thus the data displayed in Figure 4 actually represents a lower limit on the available mm-wave power. We note that a power above –30 dBm is available at frequencies up to 300 GHz. This power level demonstrates the suitability of this non-optimised photomixer, when driven by an appropriately phase locked laser system, as a local oscillator source for an SIS mixer up to 300 GHz.

We mention that the sharp dip in the spectrum at about 120 GHz is probably a consequence of placing the photodiode close to the waveguide wall and contacting to it by means of a probe extending across the guide. The equivalent circuit of this geometrical arrangement is a series LC combination in parallel with the photodiode [10]. This LC circuit has a short circuit resonance in full height waveguide at approximately twice the cut-off frequency of the TE_{10} mode. For our WR-10 waveguide the cut-off frequency is about 59 GHz, and thus the dip position is consistent with this explanation. This undesirable drop in output power can be eliminated by reducing the height of the waveguide or by positioning the source centrally in the waveguide [11].

Finally, to demonstrate the reproducibility of our design, we compare the performance of two photomixers: Figure 5. This graph shows the performance of the two sources for

a fixed backshort tuning which maximised the 90 GHz power. One photomixer (red squares) was driven by the University of Kent laser system [4] and the second (blue circles) was used in the study with the NRAO source described above. The output spectra are similar in shape over most of the waveguide band, although some difference can be seen above 100 GHz. Output powers from the first mixer have been scaled by a few dB to achieve a better overlap of the curves. The discrepancy between curves is not surprising given differences between the laser systems, the responsivities of photodiodes and the manual assembly methods used to shape the probe, assemble the devices and position the fibre. We envisage that a production photomixer should incorporate a photolithographically defined probe on a quartz substrate which would present an impedance matched load to the photodiode. This should assist the production of photomixers with similar performances and with a lower W-band frequency dependence.

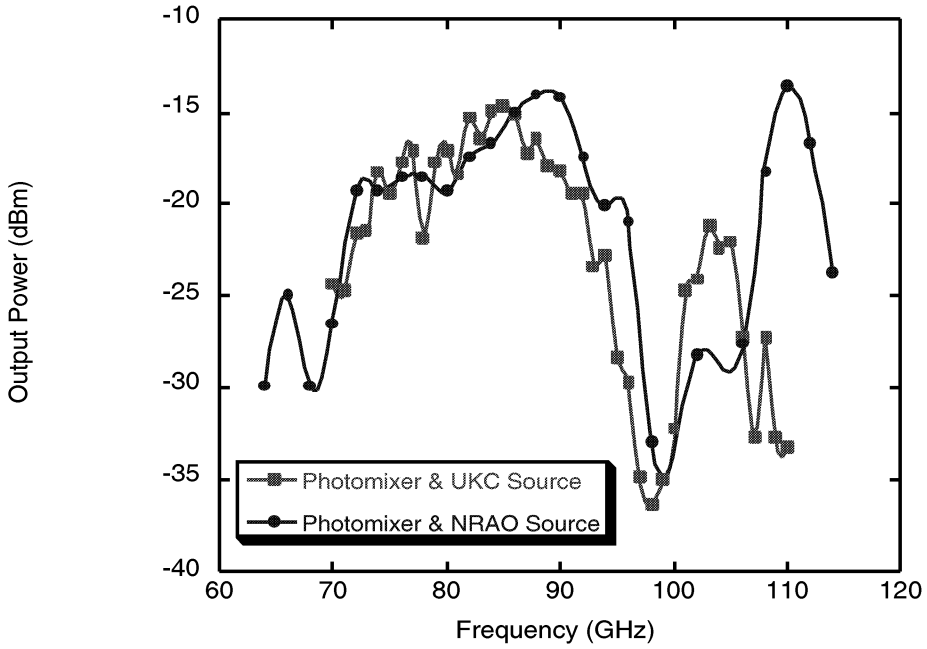

Figure 5: Comparison of the W-band tuning of two photomixers, both of which were fixed tuned for optimum power at 90 GHz. For comparison purposes the red data points have been scaled by a few dB to better overlap the blue points. The curves are a guide to the eye.

Conclusion: Ultrafast photodiodes have been coupled to rectangular W-band waveguide in a specialised mounting incorporating a tuneable backshort. Non-saturated peak powers above –8 dBm (-10 dBm) were generated at frequencies of 75 GHz (100 GHz) with power conversion efficiencies above 1%. The reproducibility of our design has been confirmed by comparing the performance of two fixed tuned devices. Output powers resulting from optimised tuning were found to decrease strongly with increasing frequency, dropping from about –10 dBm at 100 GHz to a level of –40 dBm at 625 GHz. The trend of the data indicates that the power depends approximately on $(\text{frequency})^{-4}$. Although the mount is not optimised for frequencies in the 200 GHz to 300 GHz range, we believe that the –30 dBm of power detected is already sufficient for the device to be used as a LO source for an SIS mixer.

References:

1: u^2t Innovative Optoelectronic Components GmbH, Tangermünder Weg 18, D13583 Berlin, Germany

2: J. M. Payne, W. P. Shillue and A. Vaccari, "Photonic Techniques for Use on the Atacama Large Millimeter Array", *Proc. Int. Topical Meeting Microwave Photonics*, Melbourne, pp. 105 - 108, IEEE (1999).

3: Bill Shillue, "Millimeter-wave RF Power measurements of a Commercial Photomixer", *ALMA Memo Series* #313: http://www.alma.nrao.edu/memos/index.html.

4: P. G. Huggard, B. N. Ellison, P. Shen, N. J. Gomes, P. A. Davies, W. P. Shillue, A.Vaccari and J. M Payne, "Efficient generation of guided millimetre-wave power by photomixing", *IEEE Photonics Tech. Lett*. **14**, pp. 197-199 (2002).

5: P. G. Huggard, B. N. Ellison, P. Shen, N. J. Gomes, P. A. Davies, W. P. Shillue, A.Vaccari and J. M Payne, "Generation of millimetre and sub-millimetre waves by photomixing in a 1.55 μm wavelength photodiode", *Electronics Lett*. **38**, pp. 327-328 (2002).

6: D. Trommer, A. Umbach and G. Unterbörsch "InGaAs Photodetector with Integrated Biasing network for mm-Wave Applications*", Proc. 10th Int. Conf. Indium Phosphide and Related Materials (IPRM'98),* Tsukuba, pp. 276 – 279, IEEE (1998).

7: T. Nagatsuma, T. Ishibashi, A. Hirata, Y. Hirota, T. Minotani, A. Sasaki and H. Ito: "Characterisation of a uni-travelling-carrier photodiode monolithically integrated with a matching circuit", *Electronics Lett.* **37**, pp. 1246 – 1247 (2001); H. Ito, Y. Hirota, A. Hirata, T. Nagatsuma and T. Ishibashi: "11dBm photonic millimetre-wave generation at 100 GHz using uni-travelling-carrier photodiodes", *Electronics Lett.* **37**, pp. 1225 – 1226 (2001)

8: T. Noguchi, A. Ueda, H. Iwashita, Y. Sekimoto, M. Ishiguro, T. Ishibashi, H. Ito and T. Nagatasmua, "A photonic local oscillator for an SIS mixer in the 100 GHz band", these proceedings.

9: E. R. Brown, F. W. Smith and K. A. McIntosh, "Coherent millimeter-wave generation by heterodyne conversion in low-temperature-grown GaAs", *J. Appl. Phys.* **73**, pp. 1480 - 1484 (1993).

10: A. R. Kerr, "Low noise room-temperature and cryogenic mixers for 80-120 GHz", *IEEE Trans. Microwave Theory Tech.* **43**, pp. 781 - 787 (1975).

11: T.H. Büttgenbach, T.D. Groesbeck, and B.N. Ellison, "A Scale Mixer Model for SIS Waveguide Receivers", Int J. Infrared Millimeter Waves **11**, pp. 1 -20 (1990).

PERFORMANCE OF TERAHERTZ HETERODYNE RECEIVER WITH A SUPERCONDUCTING HOT-ELECTRON MIXER

Alexei Semenov, Heinz.-Wilhelm Hübers, Heiko Richter
Institute of Space Sensor Technology and Planetary Exploration, DLR,
Rutherfordstr. 2, 12489 Berlin, Germany

Manfred Birk, Michael Krocka, Ulrich Mair
Institute of Remote Sensing Technology, DLR, 82234 Weßling, Germany

Konstantin Smirnov, Grigory Gol'tsman, Boris Voronov
Physical Department, State Pedagogical University, 119891 Moscow, Russia

Introduction

During the past decade major advances have been made regarding low noise mixers for terahertz heterodyne receivers. State of the art hot-electron-bolometer (HEB) mixers have noise temperatures close to the quantum limit and require less than a microwatt power from the local oscillator (LO). The technology is now at a point where the performance of a practical receiver employing such mixer, rather than the figures of merit of the mixer itself, is of major concern. We have incorporated a phonon-cooled NbN HEB mixer in a 2.5 THz heterodyne receiver and investigated its performance. This yields important information for future development of heterodyne receivers such as GREAT (German receiver for astronomy at THz frequencies aboard SOFIA) [1] and TELIS (Terahertz limb sounder), a balloon borne heterodyne receiver for atmospheric research [2]. Both are currently under development at DLR.

Mixer Design

The HEB was manufactured from a superconducting NbN film with a nominal thickness of 3.5 nm. The film was deposited by dc reactive magnetron sputtering on a 350 μm thick Si or MgO substrate [3]. The bolometer having a width of 2.4 μm and a length of 0.2 μm was located in the center of a planar feed antenna. Two types of feed antenna have been tested: logarithmic-spiral and double-slot. The logarithmic-spiral antenna was designed to cover the frequency range from about 0.5 THz to 6 THz, while the double-slot antenna was optimized for 1.8 THz. Due to processing the transition temperature (9 K) of the bolometer was lower than the transition temperature (10 K) of the film while the transition width and the square resistance slightly increased. The substrate with the HEB was glued onto the flat side of an extended hemispherical 12 mm diameter silicon lens with a Parylene antireflection coating, which was optimized for 2.5 THz [4]. The lens with the HEB was mounted in an Infrared Labs helium dewar with a wedged TPX pressure window and a cold

(77 K) quartz filter. The intermediate frequency (IF) signal was guided out of the mixer via the 50 Ω coplanar line. A circulator was used to feed the bias to the mixer and to transmit the IF signal to a 2 K low noise HEMT amplifier. The IF signal was filtered at 1.5 GHz with a bandwidth of 75 MHz, further amplified and rectified with a crystal detector.

Receiver Performance

Noise temperature and IF bandwidth

An optically pumped FIR ring laser [5] was used as a local oscillator. Signal radiation and LO radiation were superimposed by a 6 μm thick Mylar beam splitter. The double sideband

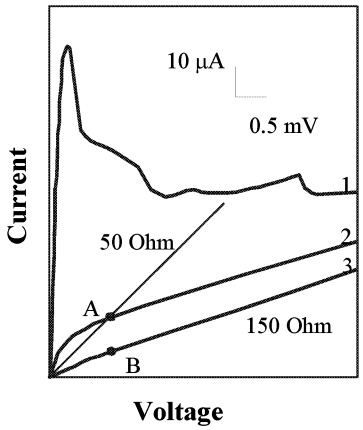

Figure 1 *IV-curve of the mixer (1: unpumped, 2: optimally pumped, 3 driven in the normal state) The lowest noise temperature is achieved in the point A.*

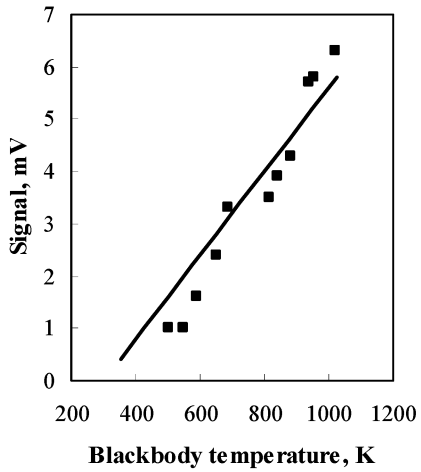

Figure 2 *Heterodyne signal as a function of the black body temperature.*

(DSB) noise temperature of the receiver was measured by the Y-factor method. Hot and cold loads (Eccosorb) at 293 K and 77 K alternatively covered the receiver beam. Output signals due to hot and cold loads were continuously readout by a computer, which performed statistical analysis of the signal and computed the noise temperature. Fig. 1 shows typical current-voltage (I-V) characteristics of the mixer recorded at different LO power. Minimal noise temperature is achieved in the vicinity of the operation point A. Applying an isothermal technique we estimated 100 nW power absorbed by the HEB at this optimal operation point. The best DSB noise temperature was about 2200 K at 2.5 THz frequency. We found that this figure does not noticeably decrease in the IF frequency range up to 2 GHz. This finding correlates with the expected 6 GHz noise temperature roll-off frequency for our HEB mixers [6].

Dynamic range and conversion losses

In order to evaluate the dynamic range of the mixer we measured the heterodyne response to black body radiation at 2.5 THz. We varied the black body temperature while keeping its aperture fixed. The receiver response (Fig. 1) was linear up to the black body temperature 1050 K. The beam-filling factor by the black body aperture was 10% [7]. This suggests a maximum non-saturating background temperature of ≈ 400 K at the receiver input. Since the signal shows no signs of saturation even at the largest black body temperature, we expect that the 3 dB compression would occur at a load temperature significantly larger than 400 K. The slope of the straight line in Fig. 2 corresponds to a conversion efficiency of -17 ± 1 dB. This figure includes optical coupling losses, conversion efficiency of the mixer, and losses in the IF chain from the mixer output to the input of the cold amplifier. The optical losses at 2.5 THz are 4±0.5 dB [3]. The IF losses were estimated comparing the noise signals originating from a 50 Ω resistor and the mixer driven into the normal state (point B in Fig. 1). This yields 4±0.5 dB IF losses (for details see Ref. 7). The remaining 9±1 dB loss are due to the conversion efficiency of the mixer. This is in agreement with the conversion efficiency calculated [7] in the framework of the uniform large signal model.

Beam pattern

The beam pattern of our hybrid antenna with a double-slot and a logarithmic-spiral feed is shown in Fig. 3. Patterns were measured at a LO frequency of 1.6 THz and 2.5 THz by moving a hot point like source in the far field of the receiver. The output heterodyne signal was registered as a function of the position of source. The solid lines represent Gaussian fit to the profile of the main lobe. At 1.6 THz a 3 dB beam width of 1.1° and 1.3° was found for the double-slot and logarithmic-spiral feed antenna, respectively. The side lobes were at –10 dB and at –6 dB, indicating that at this frequency the double-slot feed antenna is the better choice. However, this changes at higher frequencies where the dimensions of the double-slot antenna become comparable to the size of the HEB and the IF embedding circuitry. At 2.5 THz, we found higher side lobes and wider beam pattern for the double-slot feed.

Noise stability

Instantaneous noise of the output signal sets the minimum contrast of the source (source versus background) that can be distinguished by the receiver. If the output noise is completely uncorrelated (i.e. white) the radiometer equation states that the noise drops down as square root of the integration time. However, in practice the total noise of a receiver is a combination of white noise, $1/f$ noise and low frequency drift noise. The latter two do not integrate down. To choose the best observation strategy with particular

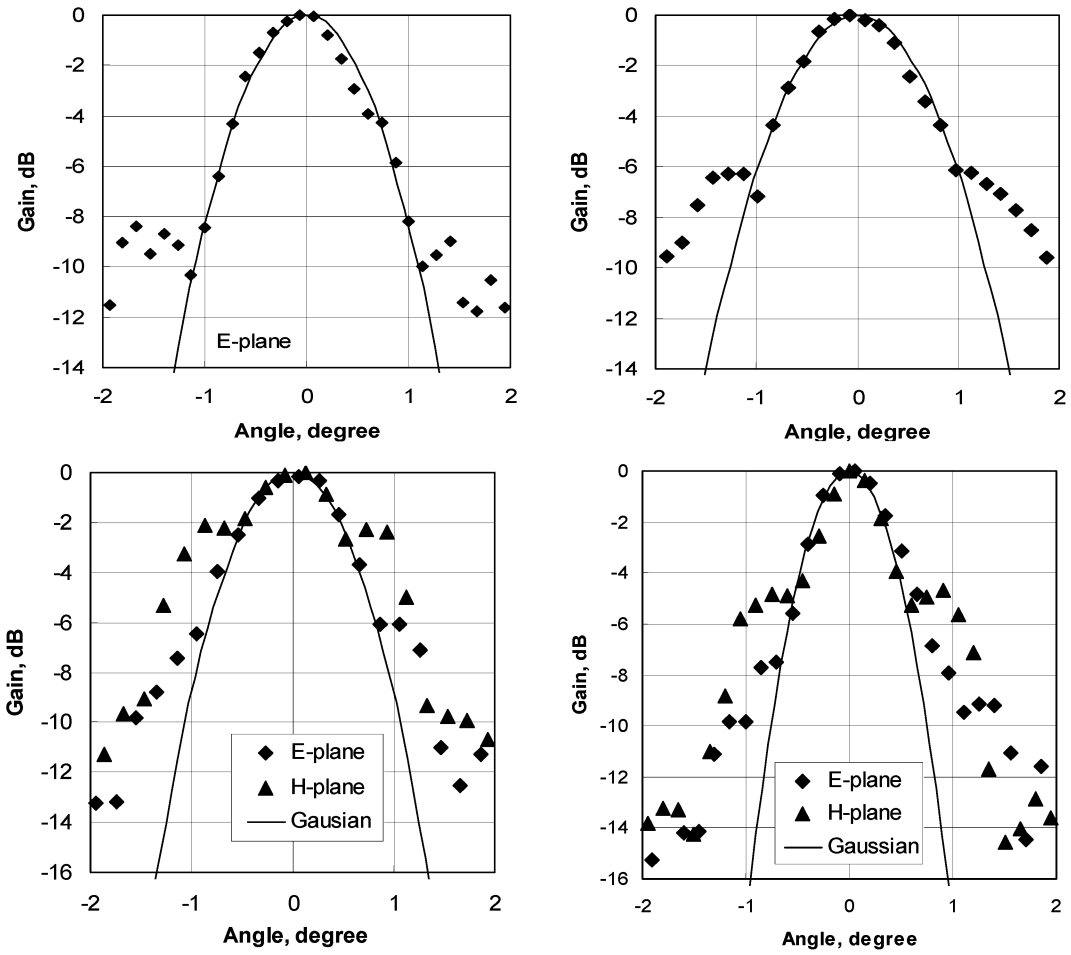

Figure 3 *1.6 THz (top row) and 2.5 THz (bottom row) gain pattern of hybrid antennas with double-slot (left) and logarithmic-spiral (right) feed on the 12 mm lens.*

receiver, it is useful to consider the "Allan" variance, σ_A, given by $\sigma_A(t)^2 = \sigma(t)^2/2$, where σ is the standard deviation of the signal [8] from the root mean square value. For a noise spectrum that contains white noise, 1/f and drift noise the "Allan" variance takes the form $\sigma_A(t)^2 = at^\beta + b/t + c$, where a, b, c and $\beta > 1$ are constants showing relative contribution of different noise types. They define an optimum integration time ("Allan" stability time), which is the crossover from the $1/t$ behavior due to the white noise to a plateau or an increase of σ_A caused by $1/f$ or drift noise, respectively. Fig. 4 displays the mean square output noise (σ_A) of our receiver as a function of integration time for two different bias regimes. For an operation regime in the linear part of the I-V characteristic (regime 1) the "Allan" time is 5 sec and the DSB noise temperature is 5500 K while in the nonlinear part (regime 2) this time is only 0.1 sec although the DSB noise temperature is much lower (1500 K). Indeed, the spectrum of the output noise in the regime 2 (Fig. 4, right panel) shows excess low frequency noise that is a mixture of the $1/f$ noise and drift noise.

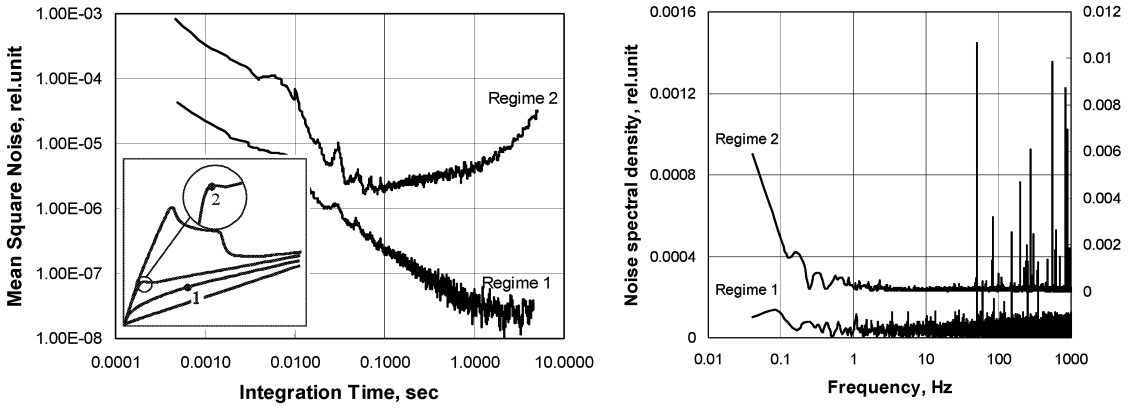

Figure 4 *"Allan" variance as a function of time (left panel) and spectrum of the output receiver noise (right panel) for two different operation points (see inset).*

Spectroscopy Test

As an overall receiver test we recorded a methanol emission line using a gas cell with 50 cm absorption length. The line was located in the upper sideband and was separated by 1.6 GHz from the 2.52278 THz methanol LO laser line. The gas was kept at ambient temperature. Behind the cell a 77 K blackbody was placed. An acousto-optical

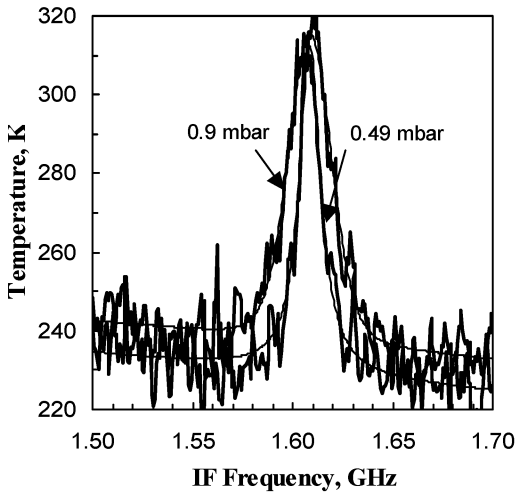

Figure 5 Methanol *emission line measured at the gas pressure 0.49 mbar and 0.90 mbar*

spectrometer was used as backend spectrometer. Fig. 5 shows spectra measured at two different gas pressures. The vertical scale corresponds to single sideband noise temperatures. The line was opaque in the center. Thus the signal should not be larger than 296 K. Larger experimental values may be due to the sideband ratio deviating from one or due to misalignment. The smooth line is a Voigt fit with a linear background. The line

full width at half maximum was 13 MHz at 0.49 mbar and 26 MHz at 0.90mbar that corresponds to the expected line width deduced from pressure broadening measurements at millimeter wavelengths.

Conclusion

We have demonstrated the practical usability of the terahertz heterodyne receiver with the NbN HEB mixer performing spectroscopy of a methanol emission line. The dynamic range of the receiver is large enough for applications in astronomy and atmospheric research. Both the noise temperature and noise stability of the receiver are strongly dependent of the operating point of the mixer. Thus, statistical analysis of the receiver noise, not only the noise temperature, is required for full performance characterization.

This work was partly supported by the INTAS (grant 99-0569) and the German Ministry of Science and Education (WTZ RUS-149-97).

1. R. Güsten, P. Hartogh, H.-W.Hübers, U. Graf, K. Jacobs, H. P. Röser, F. Schäfer, R. T. Schieder, R. Stark, J. Stutzki, P. van der Wal, and A. Wunsch: *GREAT: the First Generation German Heterodyne Receiver for SOFIA*, SPIE v. 4014, Airborne Telescope Systems, München 2000.
2. U. Mair, M. Krocka, G. Wagner, M. Birk H.-W. Hübers, H. Richter, A. Semenov, P. Yagoubov, R. Hoogeveen, T. de Graauw, H. van de Stadt, A. Selig, V. Koshelets, S. Shitov B. Ellison, B. Kerridge, D. Matheson, R. Siddans and J. Reburn: *TELIS – Development of a New Balloon Borne THz/Submm Heterodyne Limb Sounder*, 13th Int. Symp. on Space THz Technol., Cambridge, MA, 2002, in press.
3. A. D. Semenov, H.-W. Hübers, J. Schubert, G. N. Gol'tsman, A. I. Elantiev, B. M. Voronov, and E. M. Gershenzon: *Design and Performance of the Lattice-Cooled Hot-Electron Terahertz Mixer*, J. Appl. Phys. **88**, 6758 (2000).
4. H.-W. Hübers, J. Schubert, A. Krabbe, M. Birk, G. Wagner, A. Semenov, G. Gol'tsman, B. Voronov, and E. M. Gershenzon: *Parylene Anti-reflection Coating of a Quasi-Optical Hot-Electron Bolometric Mixer at Terahertz Frequencies*, Infrared Phys. and Technol. **42**, 41 (2001).
5. H.-W. Hübers, H. P. Röser, and G. W. Schwaab: *A Heterodyne Receiver for the Frequency Range 1-6 THz*, 30th ESLAB Symp. Submillimetre and Far-Infrared Space Instrumentation, ESA SP-388, p. 159, Nordwijk 1996.
6. A. D. Semenov, H.-W. Hübers, *Frequency Bandwidth of a Hot-Electron Mixer According to the Hot-Spot Model*, IEEE Trans. Appl. Superconductivity **11**, 196 (2001).
7. A. D. Semenov, H.-W. Hübers, H. Richter, M. Birk, M. Krocka, K. Smirnov, G. N. Gol`tsman, and B. V. Voronov, *2.5 THz Heterodyne Receiver with NbN Hot-Electron-Bolometer Mixer*, Proc. European Conf. on Appl. Superconductivity (2001).
8. R. Schieder, G. Rau, and B. Vowinkel, *Characterization and Measurement of System Stability*, SPIE v. 598, Instrumentation for Submillimeter Spectroscopy, 189 (1985).

NOISE TEMPERATURE FOR Nb DHEB MIXER RECEIVER FOR FAR-INFRARED SPECTROSCOPY

E. Gerecht, C. D. Reintsema, and E. N. Grossman

National Institute of Standards and Technology
Boulder, CO 80305

A. L. Betz and R. T. Boreiko

Center for Astrophysics & Space Astronomy, University of Colorado
Boulder, CO 80309

ABSTRACT **-** We are reporting a noise temperature measured on a diffusion-cooled hot electron bolometric (DHEB) mixer designed for a heterodyne focal plane array to study lines with frequencies of 2 THz and above. Our fabrication process utilizes selective ion milling techniques to produce Nb diffusion-cooled hot-electron bolometric mixers from a bilayer thin film of Au/Nb deposited on a silicon substrate. A microbridge of Nb 12 nm thick forms the HEB device. The devices are fabricated at the leads of a broad-band spiral antenna with a frequency response of up to 16 THz. A far-infrared (FIR) laser was used as the local-oscillator (LO) source at 2.52 THz (119 μm). A double-sideband (DSB) receiver noise temperature of 2500 K was measured. The IF frequency determined by the cold amplifier was centered at 1 GHz. This noise temperature result is not corrected for losses and mismatches and was performed at a bath temperature of 2 K. The device has a critical temperature (T_c) of 6 K and a 0.5 K transition width.

**** Publication of the National Institute of Standards and Technology, not subject to copyright.***

I. INTRODUCTION

Observations of spectral line have played a major role in expanding our understanding of the interstellar medium and planetary atmospheres. Heterodyne spectroscopy is capable of providing the required sensitivity and spectral resolution over the entire far-infrared spectral region. However, future observations will require more sophisticated receivers with quantum noise limited sensitivity and multiple mixer elements in the focal plane. Although small arrays have been demonstrated in millimeter wave receivers, none have been developed for

far-infrared receivers for the 1-5 THz band. An array as simple as 4 elements would provide a significant enhancement in line mapping capabilities, especially on airborne telescope such as SOFIA.

Until recently GaAs Schottky barrier diodes (SBD) were used almost exclusively for heterodyne receivers in the THz region. Below 1 THz, SIS (Superconductor/Insulator/Superconductor) mixer receivers have excellent noise temperature (only a few times the quantum noise limit). The noise performance is limited to frequencies below or about equal to the superconducting bandgap frequency. Hot electron bolometric (HEB) mixers, which use nonlinear heating effects in superconductors near their transition temperature [1], have become an excellent alternative for applications requiring low noise temperatures at frequencies from 1 THz to 5 THz. There are two types of superconducting HEB devices, the diffusion-cooled (DHEB) version [2][3] and the phonon-cooled (PHEB) version [4]. The two versions differ mainly by the cooling mechanism of the hot electrons. The devices under development here are DHEBs with a projected local oscillator (LO) power requirement of less than 100 nW and bath temperature of less than 2 K. The present state of the art of different THz receivers is compared in FIG. 1.

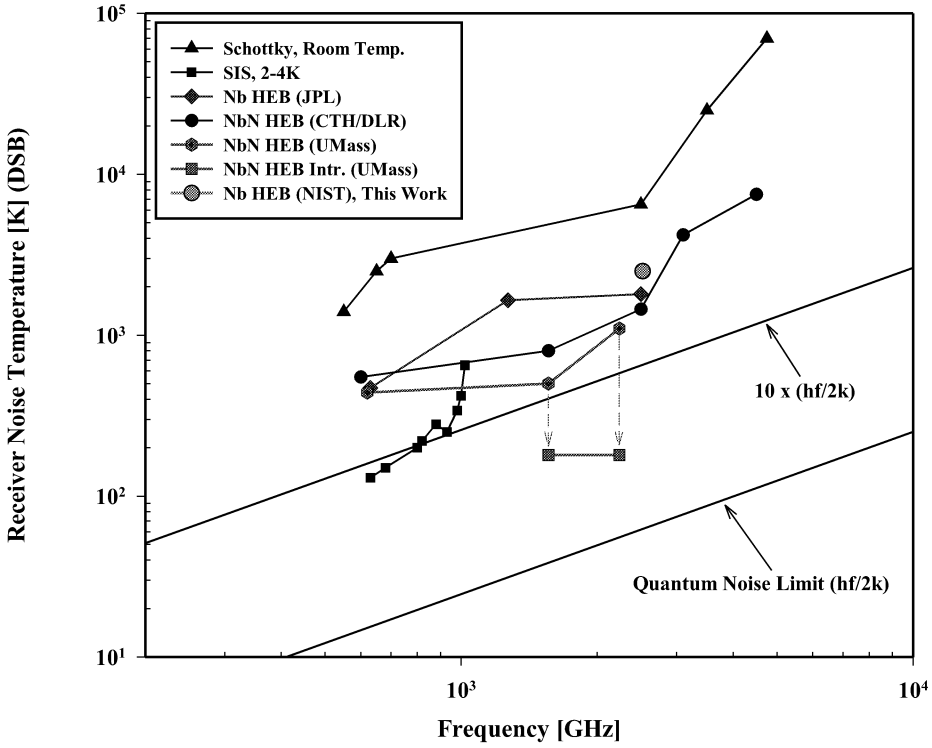

FIG. 1. Noise temperatures vs. frequency for receivers in the terahertz regime [5]-[8].

II. DEVICE DESIGN AND FABRICATION

A quasi-optical coupling design was chosen [9] for our work. The focal plane array is of the "fly-eye" configuration, with individual substrate lens for each of the 4 pixels. (Obviously, this configuration is suitable only for arrays of relatively small format.) The incoming energy couples to the device through an elliptical lens 4 mm in diameter, made from high-purity silicon and no AR coating, and a spiral antenna with a maximum frequency response of 16 THz [10]. The spiral wrap angle is 20 degrees, with a nominal separation of the feedpoints of 1.2 μm. The spiral design is self-complementary, implying an antenna impedance of 75 Ω. The array includes two antennas with 2 1/4 turns and two with 2 3/4 turns, which imply lower frequency limits of 520 GHz and 160 GHz, respectively. These approximate frequency limits are derived from the criterion that the antenna radius be equal to 1/4 of an effective wavelength. The radius of the inner edge of the antenna is used for the upper frequency limit and the outer edge for the lower frequency limit, with an additional quarter-turn left for engineering margin. The IF signal is coupled out of the HEB thru a 50 Ω coplanar waveguide (CPW), the center conductor of which contacts the center conductor of a microminiature K-type connector. The CPW groundplane is common to all four array elements, and directly contacts the body of the mixer block through an indium foil "gasket". The 4 element array configured with lenses and spiral antennas is shown in FIG. 2.

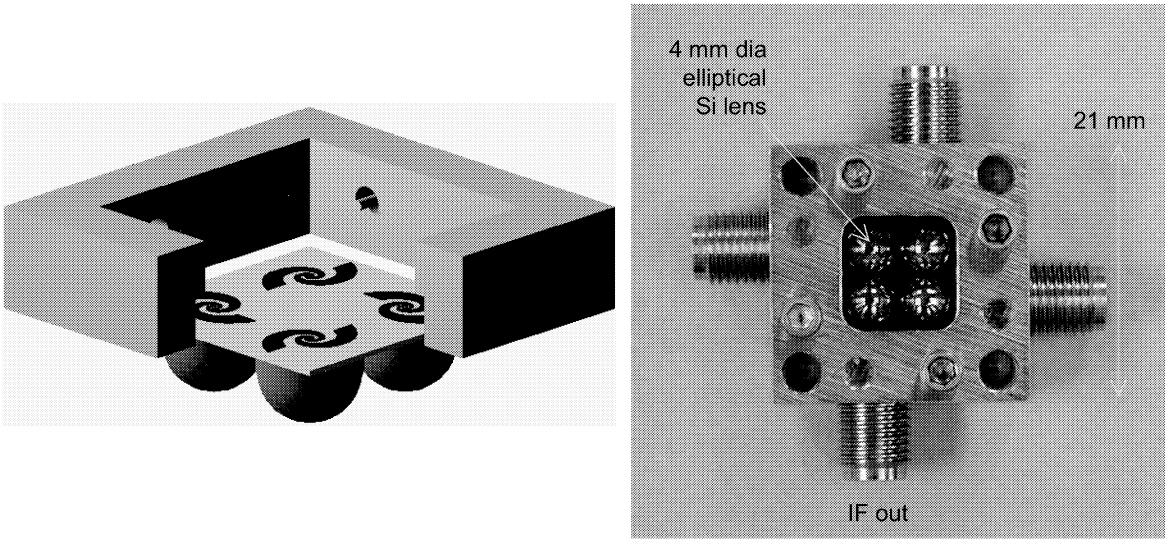

FIG. 2. Array configuration; on the left, a conceptual rendering showing the chip with four elements and substrate lenses, on the right, a photograph of the assembly.

A typical device fabrication begins with the deposition of a uniform bilayer metallic film across a silicon wafer that has been thermally oxidized to a thickness of 300 nm. The bilayer is composed of a 12 nm niobium base layer capped by 20 nm of gold (see FIG. 3). The films are deposited in-situ using DC magnetron sputtering. The HEBs are ultimately formed in the base Nb layer as the last step of the process. The gold cap layer is intended to protect the Nb during initial fabrication steps as well as to mitigate contact-resistance problems between the device and overlying metallic layers. Following the bilayer deposition, a gold layer 100 nm thick is deposited through a photoresist liftoff mask patterned by use of conventional UV lithography. This mask defines the log spiral antennas, ground plane, and the coplanar waveguide feed structure to the four array elements. The gold is deposited using thermal evaporation following a 1 minute Ar RF plasma cleaning step to treat the contact regions.

Since optical lithography is used for the antenna patterning, the lead separation at the feed of the antenna remains much too large (~2 μm) for the dimensions of useful HEB devices. Therefore, a second contact metallization step, using E-beam lithography (EBL), to define the length scale of the devices was performed. Again gold lift-off is used, but through an EBL-patterned PMMA mask in this case. Finally, 50 nm of Au are deposited with an electrode separation of between 80 and 100 nm at the antenna feed. The deposition process is the same as for the antenna layer.

The last few steps of the process have produced a structure, depicted in FIG.3(c), which includes a complete antenna structure over a blanket Nb/Au bilayer. The 20 nm Au bilayer cap is then removed in an Ar ion mill using the thick gold as a sacrificial mask. There is no additional patterning associated with this step. The 30 nm of the antenna and contact Au are sacrificed to clear the bilayer surface gold from the underlying Nb in the open field areas. The ion mill process has reasonable selectivity to Au as compared to Nb (>5:1).

At this point the device has a Nb layer underlying the entire structure as evident in FIG. 3(e). This Nb must be cleared everywhere except for the final device region. This is accomplished in a two-step reactive-ion etch (RIE) process. The first step uses optical lithography to pattern a mask that protects a 6 μm × 6 μm square region centered over each device. The chip is then subjected to a SF_6 RIE process to clear the Nb in the exposed field regions (see FIG.3(f)). The chip is then patterned one last time using EBL to leave a narrow strip of PMMA bridging the gap between the Au contacts and protecting the final device area. The width of this strip, nominally 10 to 20 nm, defines the final width of the HEB. There is a 10 μm × 10 μm window around this strip that fully encompasses the 6 μm × 6 μm Nb patch that was protected

during the first RIE step. The chip then undergoes an identical SF_6 RIE step to remove the last of the Nb. The designed final dimensions of a typical HEB are 80 nm length × 100 nm width × 12 nm thickness (see FIG.3(g)).

Following device fabrication, an elliptical Si lens is affixed to the backside of the substrate. The lens is positioned within a well etched into the backside of the substrate. The well position is registered to within ±5 μm of the device by means of an infrared backside contact aligner. This well is etched early in the process before device fabrication. The lens is affixed using purified bee's wax.

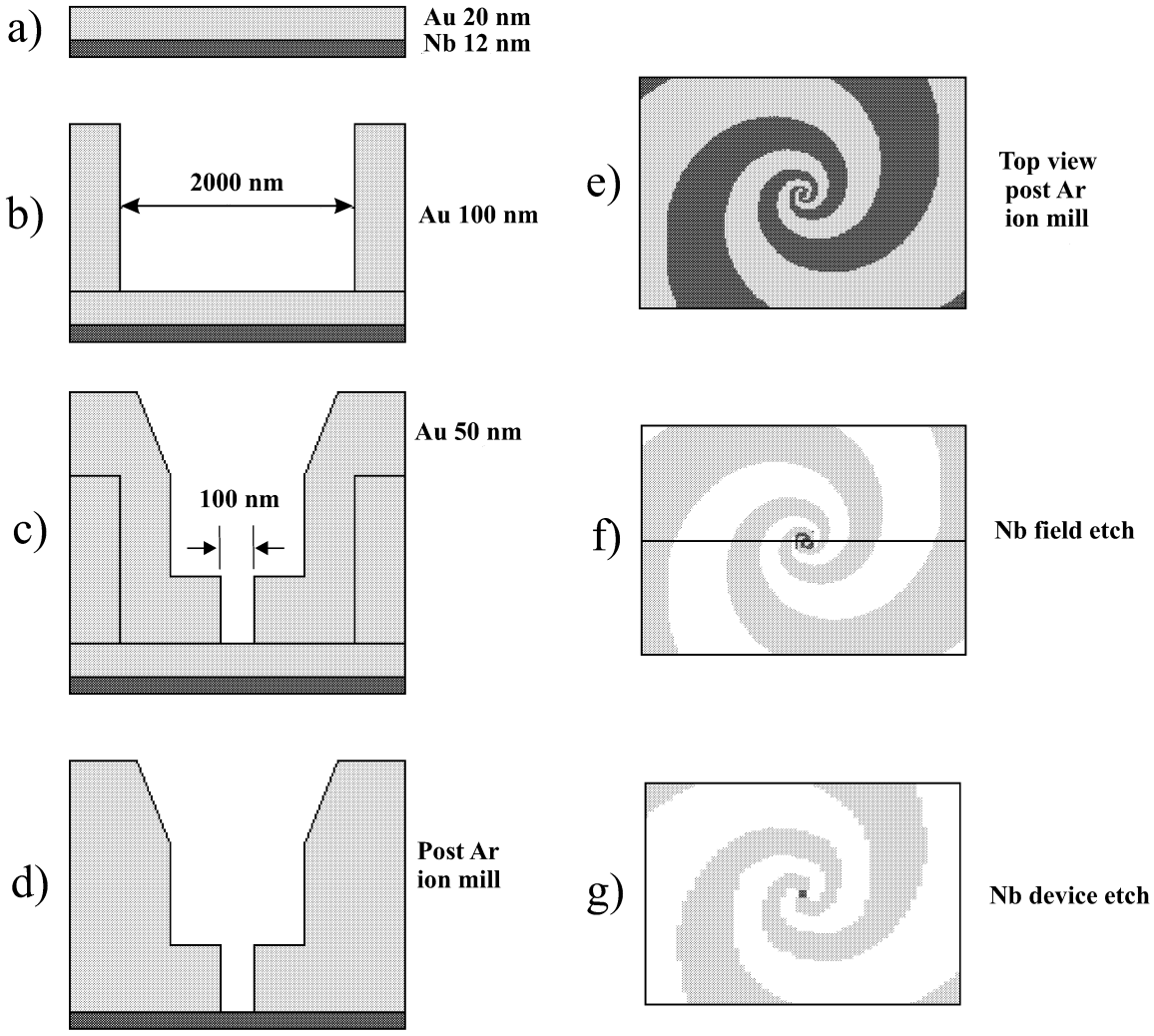

FIG.3. Device fabrication schematic.

III. OPTICAL LAYOUT

The apparatus for measuring noise temperatures is illustrated in FIG. 4. The mixer block is attached to an OFHC Cu pedestal on the cooled plate of a dewar. The base temperature is about 2 K, which is needed for Nb DHEB operation. The THz radiation enters the dewar through a quartz window and a reststrahl filter designed to block radiation above about 6 THz. The mixer is connected through a bias tee and a semi-rigid coaxial cable to a commercial cooled HEMT IF amplifier (L band) with a noise temperature of about 5 K.

The local oscillator signal is produced by an optically-pumped far-infrared laser. The laser is 1 m long and operates on most FIR laser lines between 30 and 300 μm. The polarization of the linearly polarized EH_{11} output mode can be rotated or converted to circular (if desired) by a polarization diplexer. The FIR laser and its CO_2 pump source run sealed off, but can be refilled with gas of any isotopic composition. The output power of the free-running FIR laser is stable to better than 1 % over a period of several minutes, but is normally actively stabilized to better than 0.01 % long term by a closed-loop leveling circuit. FIG. 4 shows the GaAs Schottky diode sensor used for power control. An error signal generated from the difference between the diode's output and a reference voltage is used to control the CO_2 pump laser frequency, and hence the FIR laser's output power.

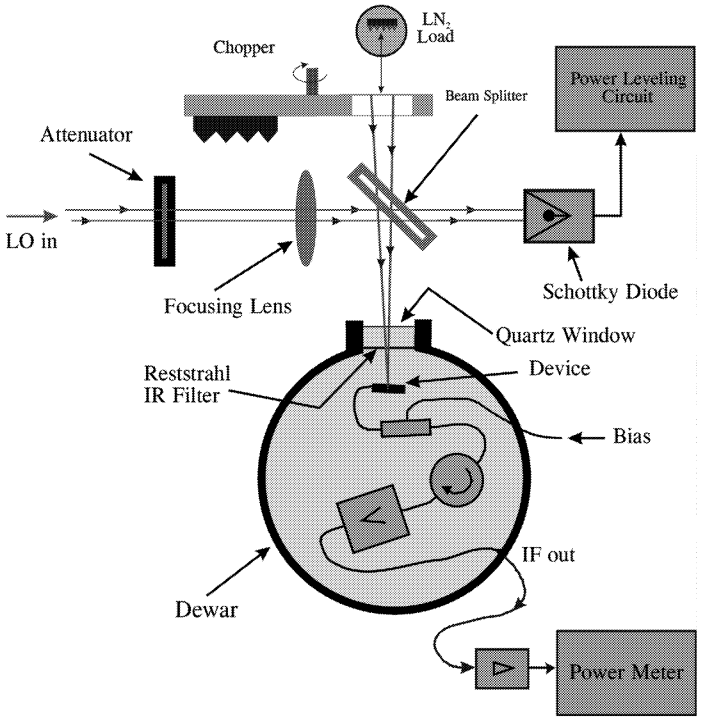

FIG. 4. Measurement setup for noise temperature.

IV. RESULTS AND DISCUSSION

Several DHEB devices were fabricated using the method described above. FIG.5(a) shows an SEM image of the device including the spiral antenna, whereas FIG. 5(b) shows an AFM image of the microbolometer at the antenna feeds. The gold banks of the antenna were aligned sufficiently well to accommodate the small microbolometer (~ 80 nm × 100 nm).

(a)

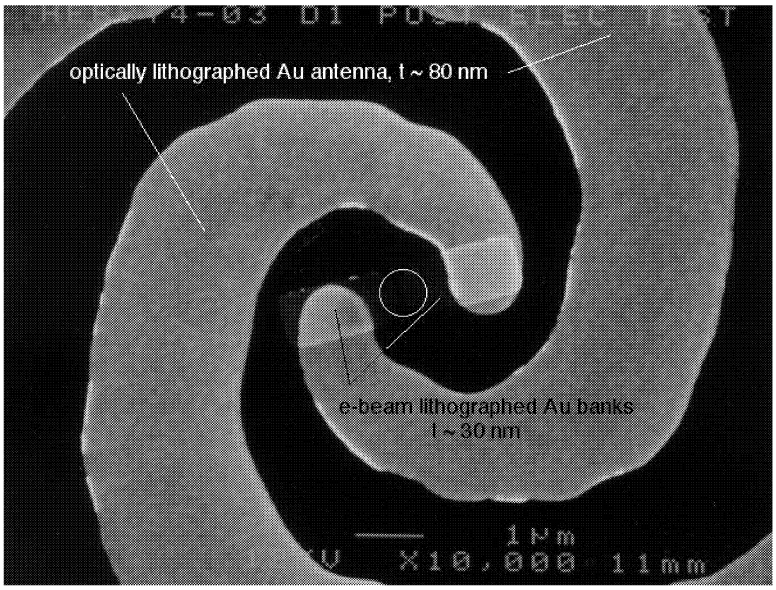

(b)

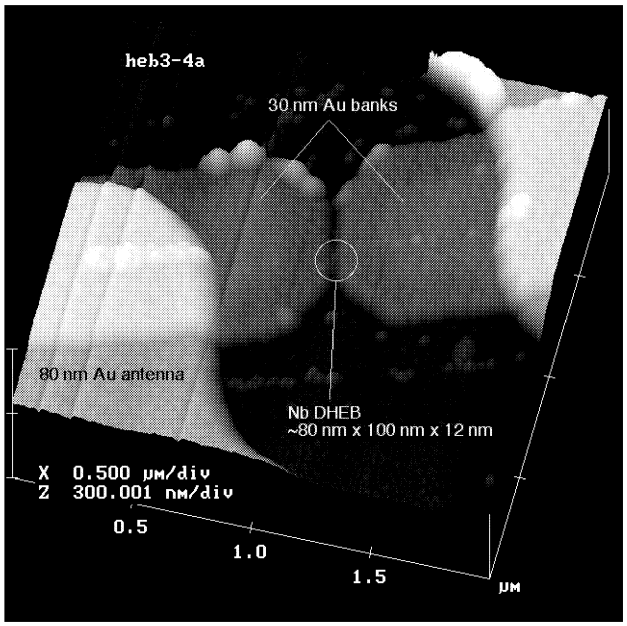

FIG.5. (a) SEM pictures of the DHEB, (b) AFM pictures of the DHEB.

The I-V characteristics of the device are shown in FIG. 6. The critical current is about 2.7 mA at a bath temperature of 2 K. The LO power centered at 2.52 THz (119 μm) was coupled to the device through a 6 μm beam splitter as illustrated in FIG. 4. The IF power was amplified by a cooled HEMT amplifier with 30 dB gain, a noise temperature of 5 K, and centered at 1 GHz. A room-temperature IF amplifier with a gain of 60 dB was used for additional amplification. Y-factor measurements between black body sources at room temperature and at N_2 (77K) were taken and Y-factors as high as 0.4 dB were observed. A reproducible double sideband receiver noise temperature of 2500 K was measured at the optimum bias point of 686 μV and 812 μA. This noise-temperature result was not corrected for losses and mismatches and therefore can be improved by better power coupling and IF matching circuitry. The power absorbed by the device was calculated from the constant resistance line (points (I) and (II) on FIG. 6), along which the hot electrons' temperature is constant, to be 4.9 μW. The total laser power of about 2.5 mW before the focusing lens and the beam splitter was not sufficient to pump the device optimally when a beam splitter with 8 % reflectivity was used. The total power coupling efficiency is estimated to be about 13 dB (~ 100 μW in front of the dewar) . The device was therefore LO starved, which implies that a better DSB receiver noise temperature was possible with more LO power. The need for high LO power is consistent with the rela-

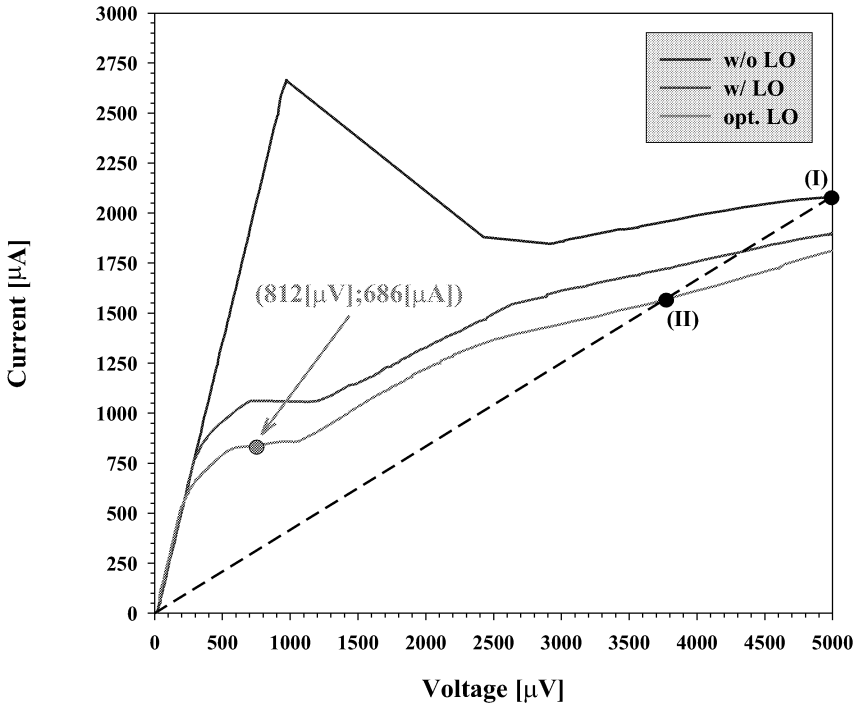

FIG. 6. I-V characteristics of the DHEB device.

tively high critical current. A microbolometer with a cross-sectional area of 100 nm × 12 nm cannot support such a high critical current. We attribute the high critical current to the larger 6 μm × 6 μm square area of Nb around the bridge that was not etched away entirely. Future efforts will correct this deficiency.

ACKNOWLEDGMENTS

This work was supported by the NASA Explorer/SOFIA Technology Development Program under Grant NAG5-8538.

REFERENCES

1. E. M. Gershenzon, G. N. Gol'tsman, I. G. Gogidze, Y. P. Gousev, A. I. Elant'ev, B. S. Karasik, and A.D. Semenov, "Millimeter and Submillimeter Range Mixer Based on Electronic Heating of Superconducting Films in the Resistive State", *Soviet Physics: Superconductivity*, 3, 1582, 1990

2. D.E. Prober, "Superconducting Terahertz Mixer Using a Transition-Edge Microbolometer," *Appl.Phys.Lett.*, 62, 2119, 1993.

3. R.Wyss, B.Karasik, W.R. McGrath, B. Bumble, and H. LeDuc, "Noise and Bandwidth Measurements of Diffusion-Cooled Nb HEB Mixers at Frequencies Above the Superconductive Energy Gap," *Proc. Tenth Intern. Space THz Technol. Symp.*, U.Virginia, March 1999, p. 214.

4. E. Gerecht, C.F. Musante, Y. Zhuang, M. Ji, K.S. Yngvesson, T. Goyette, and J. Waldman, "Development of Focal Plane Arrays Utilizing NbN Hot Electron Bolometric Mixers for the THz Regime," *Proc. Eleventh Intern. Space THz Technol. Symp.*, U. Michigan, May 2000.

5. A.L. Betz and R.T. Boreiko, "A Practical Schottky Mixer for 5 THz (Part II)," *Proc. Seventh Intern. Space THz Technol. Symp,* , pp. 503-510, Charlottesville, VA, March 1996.

6. P. H. Siegel, "Terahertz Technology", *IEEE Trans. on Microw. Theo.and Techn.*, Vol. 50, No. 3, 910-928, March 2002.

7. S. Cherednichenkoa , M. Kroug, H. Merkel, P. Khosropanah, A. Adam, E. Kollberg, D. Loudkov, G. Gol'tsman, B. Voronov, H. Richter, and H.-W. Huebers,"1.6 THz Heterodyne Receiver for the Far Infrared Space Telescope", *Europ. Conf. on Applied Supercond*., Copenhagen, August 2001.

8. A.D. Semenov, H.W. Huebers, J. Schubert, G. Gol'tsman, A.I. Elantiev, B. Voronov, and G. Gershenzon, "Design and performance of the lattice cooled hot-electron terahertz mixer", *J.Appl.Phys.* 88 (11), p.6758, 2000.

9. E. Gerecht, C. D. Reintsema, E. N. Grossman, A. L. Betz, and R. T. Boreiko, "Superconducting Nb DHEB Mixer Arrays for Far-Infrared Spectroscopy," *Proc. Twelfth Intern. Space THz Technol. Symp.*, JPL, February 2001.

10. E. N. Grossman, J. E. Sauvageau, and D. G. McDonald, "Lithographic Spiral Antennas at Short Wavelengths," *Appl. Phys. Lett.*, v. 59, p.3225, 1991.

TANTALUM HOT-ELECTRON BOLOMETERS FOR LOW-NOISE HETERODYNE RECEIVERS

Anders Skalare, William McGrath, Bruce Bumble, Henry G. LeDuc
Jet Propulsion Laboratory, California Institute of Technology, Pasadena, CA

ABSTRACT

We describe superconducting diffusion-cooled hot-electron bolometers that were fabricated from tantalum films grown on a thin niobium seed layer. The seed layer promotes single-phase growth of the Ta films, resulting in high-quality bolometers with transition temperatures up to 2.35 K and transition widths of less than 0.2 K. An S-parameter measurement set-up in a He-3 cryostat was used to measure device impedance versus frequency of a 400 nm long device at a temperature of 400 mK. It is shown that a 3 dB roll-off frequency of about 1 GHz can be achieved when the device resistance matches the impedance of the embedding network (no electrothermal feedback). This would lead to a prediction of 16 GHz for a 100 nm device, and indicates that a heterodyne mixer using a Ta HEB should be able to operate at several GHz even with a significant amount of electrothermal feedback.

INTRODUCTION

Superconducting hot-electron bolometer (HEB) mixers that are currently under development for observational platforms such as *Herschel* and *SOFIA* use either diffusion-cooled niobium devices with transition temperatures (T_C) of 5 to 7 K, or phonon-cooled niobium nitride devices with even higher T_C (an overview can be found in the references[1]). Since theory predicts that the mixer input noise should be proportional to T_C when an HEB mixer is limited by thermal fluctuation noise [2], it is of interest to study materials with lower-temperature transitions. A noise reduction of a factor of two can in some applications lead to a fourfold increase in data gathering capacity. The local oscillator (LO) power requirement is proportional to T_C^2, and can therefore also be reduced, which is advantageous at frequencies above 1 THz where solid-state sources are at present too weak for many applications. These advantages naturally have to be weighed against potential system disadvantages of the lower T_C, such as the increased complexity of cryogenic coolers and potential saturation effects in the mixer element itself. Only a few lower T_C mixers have been studied previously, such as niobium devices where the transition temperature has been suppressed by an external magnetic field [3], or by the proximity effect from thin gold coatings [3,4]. The predicted dependencies of noise temperature and LO power on transition temperature have been confirmed at microwave frequencies [3]. Aluminum-based bolometers ($T_C \leq 2K$) have also been investigated [5,6], but found to be unsuitable for THz mixers for a variety of reasons.

A superconductive material with a naturally lower T_C offers practical advantages compared to the use of magnetic fields and bi-layers. Here we investigate the usefulness of tantalum (Ta) for low-noise diffusion-cooled HEB mixers. Ta has superconducting properties that are similar to those of Nb, except for the T_C which is about a factor of 2 lower (for thin films: $T_C \approx 3K$ for Ta, versus 6-7K for Nb). Thus Ta should be a predictable material with the desired properties. Tantalum does however add some fabrication challenges, since it forms thin films that contain two lattice phases. This would be unacceptable for a practical device, since the additional electron scattering at the grain boundaries would tend to suppress the diffusion-cooling mechanism, and also because the different transition temperatures of the two phases leads to a broadening of the transition. The ultimate goals of this study can therefore be defined as:

Contact information for A. Skalare: anders.skalare@jpl.nasa.gov, Ph +1-818-354-9383

1) To demonstrate that high quality devices can be fabricated, with T_C between 2 and 3 K and transition widths (∂T_C) similar to niobium devices (0.1 to 0.2 K).
2) To verify that the diffusion-cooling mechanism is sufficient to produce intermediate frequency (IF) bandwidths that are useful in a typical receiver application (at least a few GHz).
3) To demonstrate that the mixer noise can be lower than for higher-T_C materials.
In this paper we will address the first two of these points, by describing the DC and microwave properties of our fabricated devices.

DEVICES

Based on previous experience, HEB devices with resistance values between about 20Ω to 100 Ω can be easily matched to microwave coupling structures, and provide the best mixer performance. For Ta, this can be achieved with microbridge lengths of 100–400 nm, widths of 100-200 nm and a film thickness of 10 nm. Our devices were fabricated on a silicon wafer by sputter deposition of a 10 nm Ta film on top of a 1.5 nm Nb seed layer. The purpose of the seed layer is to promote growth of the desired tantalum alpha-phase, giving higher superconducting transition temperatures and sharper transitions [7]. Thick gold pads serve to define the length of the microbridge and to prevent Andreev reflections from trapping heat in the device. We have utilized a modified version of our self-aligned processing method previously developed for Nb HEB devices [8] and found that it works well for Ta. The main modification is the use of SiO instead of Au as an etch mask, which improves the device definition and eliminates the need to remove the mask from the finished device.

The devices have transition temperatures of up to 2.35 K, a typical resistance-versus-temperature (R vs. T) curve is shown Fig 1. This device is 0.4 microns long and 0.2 microns wide, with a normal state resistance of about 80 Ω and a transition at 2.25 K. The R vs. T curve has a "foot" structure that is associated with the regions at the two ends of the device, similar to that seen in niobium bolometers. The curve clearly shows that the transition width of this device is similar to that of a niobium device, so that bolometric mixers with similar properties should be feasible.

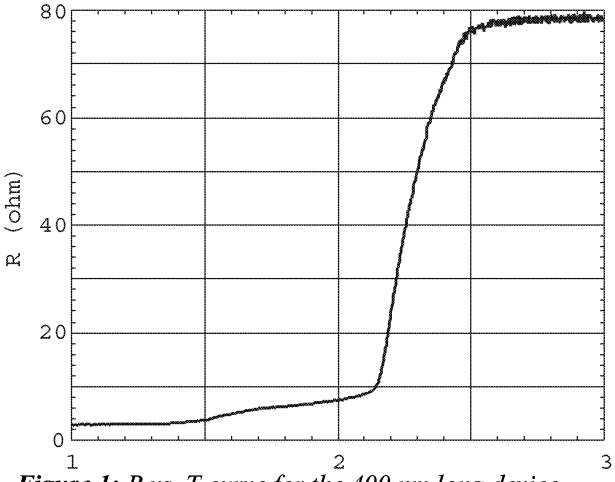

Figure 1: *R vs. T curve for the 400 nm long device that was used in the microwave measurements.*

IMPEDANCE MEASUREMENTS

To determine the thermal response time of tantalum HEB's, a He-3 cryostat was fitted with electronics for conducting microwave reflection measurements of the device, see Fig. 2. The set-up allows measurements at frequencies between about 200 MHz and 15 GHz, at temperatures down to 380 mK. This allows a more direct measurement of the device speed than for example a mixer bandwidth measurement, which is affected by input and output coupling variations with frequency. In the low-frequency limit the bolometer should have the same properties as at DC, and the device impedance should be equal to the differential resistance dV/dI at the bias point. At frequencies that significantly exceed the response roll-off frequency (but that are lower than the gap frequency of the superconductor) the device impedance should be the DC resistance V/I. A cross-over between these cases occurs near the roll-off frequency that is set by the thermal time constant at the DC bias point. An expression for the impedance as a function of frequency can be derived from a simplified lumped thermal model, where the device is represented by the electronic heat capacitance c_e that is heat sunk to the thermal reservoir by a heat conductance G :

$$Z(f) = R_0 \cdot \frac{1 + C + j \cdot 2\pi f \tau_0}{1 - C + j \cdot 2\pi f \tau_0} \qquad (1)$$

where R_0 is the resistance at the DC bias point, $\tau_0 = c_e/G$ is the thermal relaxation time of the device (excluding electrothermal feedback), and $C = I_0^2 \cdot (dR/dT)/G$ is the self-heating parameter at DC bias current I_0.

The device impedance as a function of frequency was measured for the three DC bias points that are marked on the IV curve in Figure 3. In order to estimate the device speed, equation 1 can be fitted to the data by adjusting τ_0 and C. The resulting thermal speed $f_0 = 1/(2\pi\tau_0)$ for the three points are 750 MHz, 1.13 GHz and 2.0 GHz. A possible reason that these numbers are not identical to each other is that the "lumped element" thermal model used is too simplistic to accurately describe this relatively wide thermal bias range of this distributed-temperature device. In addition to the measured curves, Figure 4 also shows the fitted curve for point B. Since bias points A and B best represent the device under realistic operating conditions as a mixer, a reasonable estimate of the speed for this 400 nm long device would be about 1 GHz.

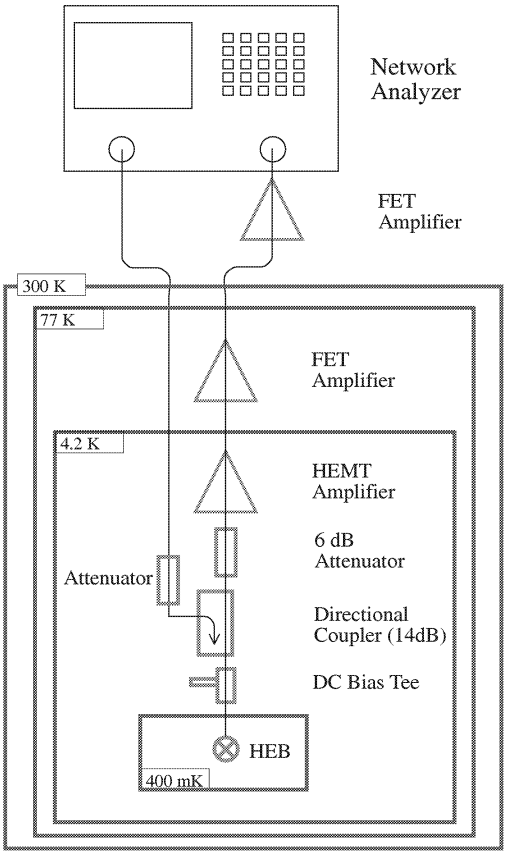

Figure 2: *Schematic of the impedance measurement setup. A helium-3 cryostat supplied by Infrared Laboratories is used to cool the Ta HEB to a temperature of 400 mK.*

CONCLUSIONS

Submicron-sized tantalum HEB devices with the desired transition temperatures and transition sharpness can indeed be fabricated using the niobium seed-layer technique. The sheet resistance is low enough to make devices that can be matched to antennas and other microwave coupling structures. The measured 400 nm long device can be expected to have a 3 dB mixer conversion efficiency roll-off at about 1 GHz, excluding electrothermal feedback. Due to the relatively small end effects (the "foot" structure in the R vs. T curve), it should be possible to use devices that are as least as short as 100 nm. Since the thermal relaxation time is proportional to the square of the device length [9,10] (diffusion-cooling), these would then have a "raw" speed of about 16 GHz. Since only a few GHz of bandwidth is needed for most mixer applications, this would indicate that Ta HEB devices will be fast enough even when including the slowing effects of electrothermal feed-back present in most bolometer mixer circuits.

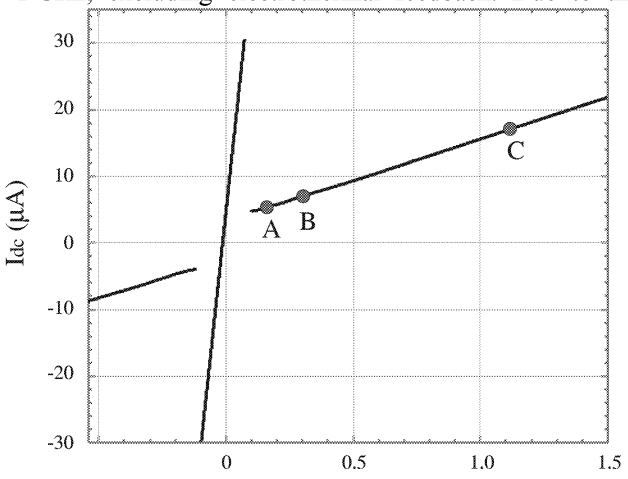

Figure 3: *Current-versus-voltage characteristic for a 400 nm long device as measured at 400 mK. The three markers (A, B, C) indicate the bias points that were used in the device impedance measurements.*

ACKNOWLEDGMENTS

The authors thank Dr. Sander Weinreb for the use of a low-noise wide-band HEMT MMIC amplifier, and Prof. Daniel Prober for many useful discussions. This work was carried out

by the Jet Propulsion Laboratory, California Institute of Technology under a contract with the National Aeronautics and Space Administration.

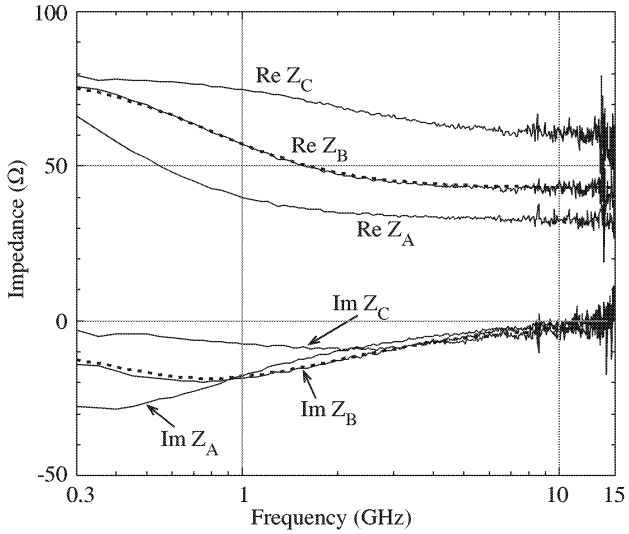

Figure 4: *Measured impedances (Z_A, Z_B, Z_C) curves for the three bias points in Figure 3. Also shown is a fitted theoretical curve for bias point B (dotted).*

REFERENCES

1. William McGrath, Anders Skalare, Boris Karasik, Dan Prober, Irfan Siddiqi, This Workshop Proceedings.

2. B.S. Karasik and A.I. Elantev, Appl. Phys. Lett. 68, 853 (1996); and Proc. 6th Int. Symp. Space Terahertz Technol., p.229, California Institute of Technology, March 21-23, 1995.

3. I. Siddiqi. D. Prober, B. Bumble, H. LeDuc, to appear in the Proceedings of the 13th Int'l. Symposium on Space Terahertz Technology, R. Blundell (ed), Harvard-Smithsonian Center for Astrophysics, Cambridge, MA, March 26-28, 2002. And Irfan Siddiqi, Ph.D. Thesis, Yale University, 2002 (available from Physics Department).

4. J.R. Gao, private communication

5. A. Skalare, W. McGrath, P. Echternach, H. LeDuc, I. Siddiqi, A. Verevkin, D. Prober, IEEE Trans. Appl. Supercond. 11, 641 (2001).

6. I. Siddiqi, A. Verevkin, R. Jahn, D. Prober, A. Skalare, W. McGrath, P. Echternach, H. LeDuc, J. Appl. Phys. 91, 4646 (2002).

7. D. W. Face and D. E. Prober, J. Vac. Sci. Tech. A, Vol 5, No.6, p.3408, (1987).

8. B. Bumble and H.G. LeDuc, IEEE Trans Appl. Supercon. 7, 3560 Part 3 (1997).

9. P.J. Burke, R.J. Schoelkopf, D.E. Prober, A.Skalare, W.R. McGrath, B. Bumble, H.G. LeDuc, *Appl. Phys. Lett*. 68, 3344 (1996).

10. R.A. Wyss, B.S. Karasik, W.R. McGrath, B. Bumble, H.G. LeDuc, Proceedings of the 10th Int'l. Symposium on Space Terahertz Technology, p. 214, Univ. of Virginia, March 16-18, 1999.

Improved Equivalent Circuit for Hot Electron Bolometer Mixers Fed by Twin Slots

Paolo Focardi, Andrea Neto, William R. McGrath, Bruce Bumble, Henry G. LeDuc

Abstract— **Series-fed coplanar waveguide embedding circuits are recently being developed for terahertz mixers using, in particular, superconducting devices as sensors. Although these mixers show promising performance, they usually also show a considerable downward shift in the resonating frequency, when compared with calculations using simplified models. This effect is basically caused by parasitics due to the extremely small details (in terms of wavelength) of the device and by the impedance of the remaining embedding circuit (in particular the RF filter). In this paper, we present an improved equivalent network model of such devices which agrees with measured results. We first propose a method to calculate the characteristic impedance and the propagation constant of the coplanar waveguide, etched between two semi-infinite media, that connect the receiving slot antennas to the superconducting device. In the formulation we take into account, for the first time, the radiation power leakage. We then describe the procedure to calculate the reactances due to the detailed geometry of the mixer device and circuit and we correct the input impedance, calculated with a commonly used simplified network. By comparing our results with a complete set of measured data, for seven mixers in the range between 500 GHz and 3 THz, we analyze the features of our model and propose further improvements. Indeed, based on the good results obtained with our improved equivalent network, a new set of THz mixers has been fabricated and is currently being tested. Useful guidelines for designing THz mixer circuits are also given.**

I. Introduction

SLOT antennas coupled to coplanar waveguides (CPW) are being developed for quasi-optical single-pixel heterodyne detectors for use in atmospheric and astronomical instruments in the submillimeter-wave/terahertz-frequency range. Hot Electron Bolometer (HEB) mixers ([1], [2]), for example, are often used at THz frequencies in such circuits placed at the focus of a dielectric lens ([3], [4]). HEB receivers are already finding use up to 1 THz on ground-based radiotelescopes [5], and similar receivers are being developed for frequencies up to 2 THz for the ESA/NASA Herschel Space Observatory, and up to 3 THz for NASA's SOFIA aircraft observatory.

P. Focardi, W. R. McGrath, B. Bumble and H.G. LeDuc are with the Jet Propulsion Laboratory, California Institute of Technology, 4800 Oak Grove Dr., Pasadena, 91109 CA.

A. Neto is with FEL-TNO, Den Haag, The Netherlands.

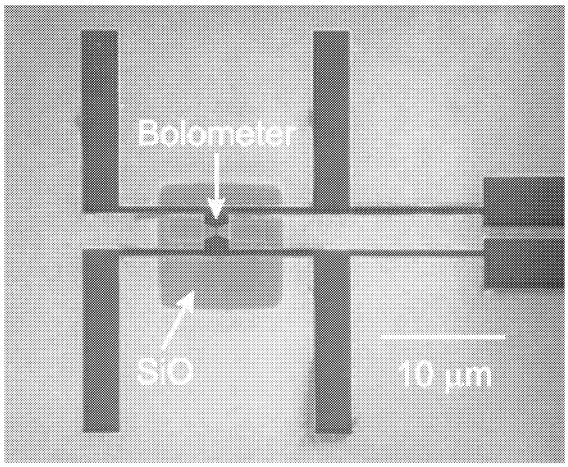

Fig. 1. Scanning Electron Microscope (SEM) photograph of an HEB mixer embedding circuit. The superconducting device is located at the center and coupled to the twin-slot antenna via CPW lines.

The prediction of the radiation pattern (up to 500 GHz) and of the resonating frequency (up to 100 GHz) for these mixer circuits has been found to be accurate, with respect to measurements, using a simplified network [6]. However, when the device is operated well into the THz regime (up to 2.5 THz), the measured resonant frequency (i.e. frequency of the peak response of the detector) is often significantly lower than that calculated with simple models ([2], [7]). This leads to significant increases (up to a factor 2) in

mixer noise due to the reduction in coupled signal power at the desired THz frequency. Thus, as previously reported [7], the accurate characterization of the entire mixer embedding circuit, including the parasitics associated with the geometry of the device, is needed to correctly design the circuit. Even though the geometry of these antennas, CPW lines, and devices is relatively simple, accurately simulating their performance in a THz circuit is not a straightforward matter. To the knowledge of the authors there are no commercial software tools to tackle this problem, even more so when the lens effect also has to be included [6]. A brute force approach based on a Method of Moments (MoM) analysis of the overall planar structure can be used, but since the device dimensions can be of the order of $\lambda_0/1000$, the numerical effort required for an accurate analysis becomes almost prohibitive, even for a single antenna. In [8] a dedicated MoM scheme for this kind of structure has been presented.

In this paper an equivalent network is presented that significantly improves the one presented in [6], though the lens effect is not included in order to concentrate the attention to the feed mechanism. The model is improved in the sense that the radiation leakage is accounted for in the calculation of the transmission line parameters. Additionally, the transition between the CPW and the bolometer is characterized via analytically evaluated lumped reactances. The emphasis is given to the physical interpretation rather than to the numerical solution (as in [8]), since this is what will be useful in future designs. A complete and detailed formulation of the improved equivalent network parameters has been presented in a recent publication [9]. In this paper we describe the procedure for calculating the above parameters, without getting into the mathematical details. In section II we first briefly describe the geometry of the detectors and circuits. Then, in section III, the formulation to calculate the parameters of the equivalent network is described. Before this work, the quasi-static approximations for these parameters were too inaccurate to correctly predict the actual performance of the circuits under investigation. The work in [10] accounts for a complex propagation constant in coplanar lines. However in [10] the attenuation was associated to losses in the conductor and in the dielectric rather than to the radiation effect which appears to be dominant in the case investigated in this paper.

A recent investigation [11] presents a direct integration method for the Green's Function (GF) of a microstrip. In [12] the method has been applied to slots etched between two semi-infinite dielectrics and provides, analytically in that case, the GF of a gap-excited slot placed between two different homogeneous dielectrics. In [9] the procedure is extended to coplanar waveguides in order to derive the circuit parameters mentioned above. Then we present a procedure that characterizes the strong reactive contributions associated with the transition between the bolometer and the coplanar waveguide. The lumped reactances we obtain are connected to the equivalent network that represents the overall antenna+detector circuit. This circuit is composed of the CPW equivalent transmission lines and of the active impedance of the slots; that is, the impedance of each of the two slots with the mutual coupling taken into account. In section IV, comparisons with measurements of submillimeter wave bolometric receivers show that the observed downward shift of the resonant frequency can be explained by the following: I) the reactances associated with both the "crowding" of the RF current and the fringing fields in the transition between the bolometer and the CPW (see fig. 2), and II) the phase shift caused by the imaginary part of the impedance of the RF bandstop filter used in the DC/IF line. In section V, some guidelines for future designs are provided and a new set of THz HEB mixers, that has been fabricated and is currently being tested, is presented. Finally, in section VI conclusions are drawn.

II. Receiver layout

The mixer circuit is located at the second focus on the back side of a silicon elliptical lens. Since the reflections due to the dielectric lens can be introduced separately, as discussed in [6], we assume the circuit under investigation to be located at the interface between two semi-infinite half spaces ($\epsilon_{r1} = 1$ and $\epsilon_{r2} = 11.7$). The spectral response and hence the center frequency of HEB mixers with six different twin-slot antenna designs have been previously measured with a Fourier-Transform Spectrometer [7]. The antenna slot lengths ranged from 26 μm up to 152 μm. Figure 1 shows a SEM photograph of a 2.5 THz HEB mixer.

The submicron-sized HEB device is connected to the twin slot-antennas via a CPW transmission line [1]. On the right, is located the RF band-stop filter structure (a total of eight high and low impedance sections were used). Figure 2 shows a detail of the transition between the CPW and the bolometer. The length of the transition region L and the width of the bolometer w_b are highlighted in the figure. The modeling of this structure could be performed with a full wave Method of Moment analysis as described in [8]. However in this paper we present an equivalent network model for the overall mixer embedding circuit. The first simplified equivalent network is shown in fig. 3.

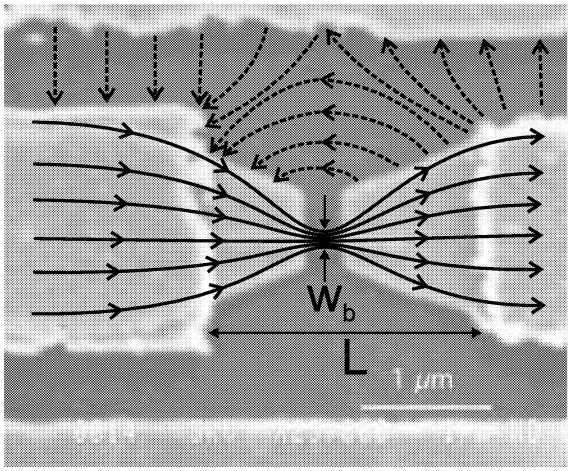

Fig. 2. Bolometer detail of a 2.5 THz design with a schematic representation of the electric field (dashed line) and of the RF current path (solid line).

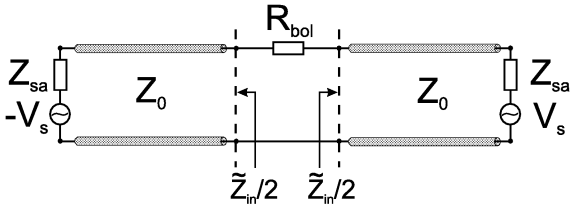

Fig. 3. Simplified equivalent network of the THz mixer circuit which includes the active slot impedance and the equivalent transmission lines.

The active slot impedances Z_{sa} are obtained by means of MoM simulations restricted to the receiving slots alone, while R_{bol}, Z_0 and V_s represent respectively the nominal DC impedance of the bolometer, the characteristic impedance of the CPW and the equivalent voltage source of the receiving antenna.

In the next section the transmission line parameters are presented, taking into account for the first time the power leakage in the two dielectrics. With the simplified equivalent network of fig. 3 we may then estimate the equivalent series load $\tilde{Z}_{in}$ seen by the bolometer. However, $\tilde{Z}_{in}$ must be modified to account for the reactances due the field deformations shown in fig. 2, which are associated with the CPW-to-bolometer transition. Analytical expressions for these reactances are available in [9]. Finally, as discussed in section IV, the effects of the RF filter must also be included to completely characterize $\tilde{Z}_{in}$.

III. Equivalent Network Parameters

The parameters of the CPW transmission line have been obtained using the formalism that has been presented in [12] for the case of a single slot etched in a perfect electric conductor between two semi-infinite dielectrics. In [9] the same formulation is extended to the case of an infinitely extended CPW whose geometry is shown in the inset of fig. 4.

A. Propagation Constant

The quasi-static approximation of the propagation constant is $\beta = \sqrt{\frac{k_1^2+k_2^2}{2}}$ [13], where $k_i = k_0\sqrt{\epsilon_{ri}}$ $(i = 1, 2)$, is the wavenumber in each semi-infinite dielectric (air and silicon) and k_0 is the free space wavenumber. Accordingly, the propagating mode is fast for the denser medium (i.e. silicon) and the mode is leaky. The unknown magnetic currents on the CPW are obtained from the direct solution of the pertinent Continuity of Magnetic Field Integral Equation (CMFIE) assuming, as in [11], the separability between transverse and longitudinal space functional dependence. In particular, the transverse electric field is assumed to be well represented by a unique edge singular function defined on each of the two slots composing the CPW. The procedure for finding the space domain magnetic current consists of: I) expanding via a Fourier Transform the transverse impressed magnetic field in spectral superposition of electric currents progressively phased by k_x; II) finding in analytical form, for each k_x, the 2D Green's Function

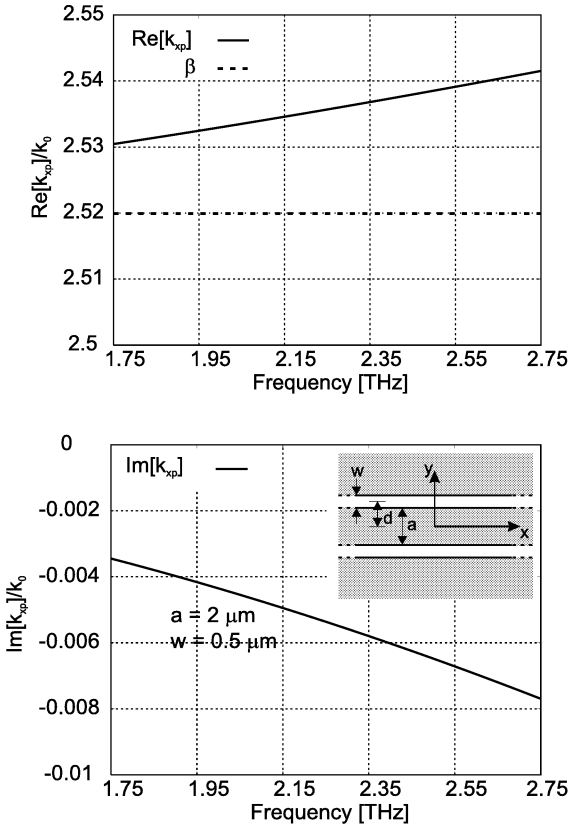

Fig. 4. Real and imaginary part of the propagation constant for a CPW with $a = 2\mu m$ and $w = 0.5\mu m$. Both graphs are normalized to the free space wavenumber. The real part also shows a comparison with the value of β (dashed line), obtained with the quasi static approximation.

(GF) by imposing the continuity of the magnetic field at the slot axis; and III) integrating in k_x all the 2D GF. Equating to zero the denominator of the spectral expression for the magnetic currents, a dispersion equation is obtained that, solved numerically, defines the propagation constant of the leaky mode supported by the structure.

In fig. 4 an example of the propagation constant is shown for a CPW with $a = 2\mu m$ and $w = 0.5\mu m$ (these are typical values for a THz circuit) as sketched in the inset. Both graphs are normalized to the free space wavenumber. In the upper graph, the real part of k_{xp} is shown, compared with the value of β (dashed line), obtained with the quasi static approximation. As the frequency increases the value of $Re[k_{xp}]$ tends asymptotically to the value of the propagation constant in the denser medium (silicon). In the lower graph the attenuation constant ($Im[k_{xp}]$) is seen to change significantly over the frequency range of 1 THz. Despite the amplitude of the real part (in the frequency range under investigation) being only slightly different from the value of the quasi static approximation, the important point is that now we have a frequency dependent function, and even more important is the fact that now we have an imaginary part that takes into account the power leakage.

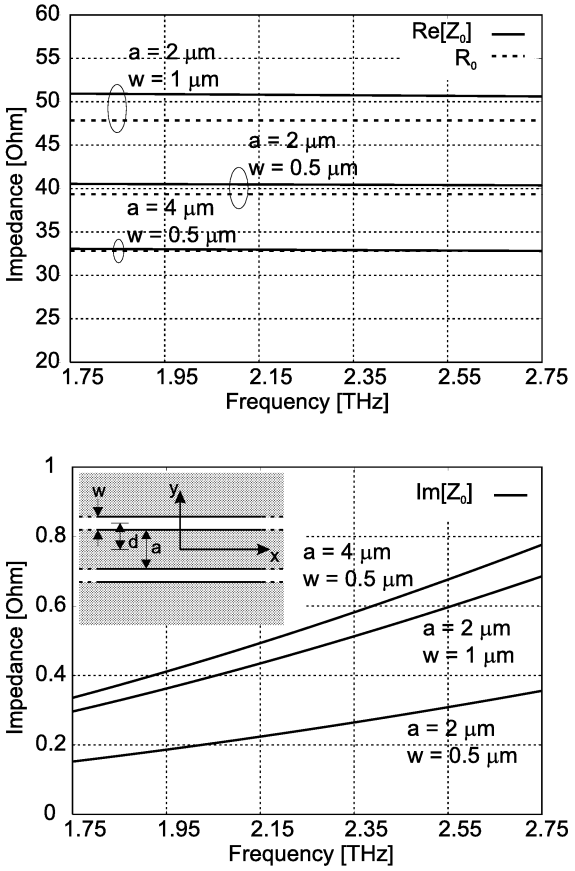

Fig. 5. Real and imaginary part of the CPW characteristic impedance for three different CPW geometries. Also shown in the upper graph, for the real part, is a comparison between the formulation of this paper (solid line) and the quasi static approximation (dashed line).

B. Characteristic Admittance

The definition of the characteristic admittance for a leaky line is a "hot topic" and has been

the subject of recent investigations; particularly promising is the one in reference [14]. In [9] we define the characteristic admittance at a specific transverse section as the ratio between current and voltage of the leaky wave launched by a source at finite distance. This avoids some of the ambiguities that arise with a leaky transmission line when the source is assumed to be at infinite distance. Indeed, since the propagating mode is exponentially attenuated in x, for x tending to infinity the major field contribution on the slot axis are due to fringe currents (that decay as $1/x^2$) rather than to the mode itself [12].

In fig. 5 the characteristic impedance of three different CPW's is shown, along with the values obtained with the quasi-static approximation formulated in [13]. Our formulation provides not only the imaginary part but also it can be seen that the quasi-static formula underestimates the real part of Z_0 when the width of the CPW slots grows with respect to the inner conductor a. In particular, this aspect significantly impacts the simulation results when introducing a transmission line model of the band stop filtering structure.

C. Reactances

The equivalent network in fig. 3 alone provides $\tilde{Z}_{in}$ which does not account for the electric and magnetic current crowding effects occurring in the transition between the bolometer and the CPW. Since the bolometer width is much narrower with respect to the CPW inner conductor, strong reactive energy is concentrated at this transition (see fig. 2). Our analysis accounts for the effect of the transition by correcting $\tilde{Z}_{in}$ via the introduction of two lumped reactances related to the lengths and widths involved in the transition. These two reactances are combined to represent a realistic model of the transition. In this way we can then calculate Z_{in} which is the actual embedding circuit series impedance seen by the bolometer.

With reference to fig. 6, the effect on the input impedance of the electric current crowding associated with an inner conductor reduction ($t_1 \rightarrow t_2$) can be represented as a series inductive impedance Z_s. An infinite slot, whose width is equal to L, is the canonical problem that best fits the geometry in fig. 6. The growth of inductive energy associated with the reduction of the inner conductor

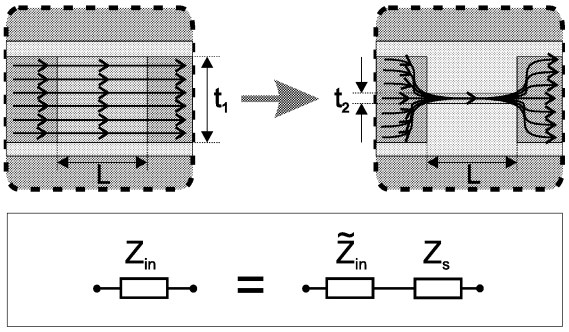

Fig. 6. Electric current crowding effect with the relevant dimensions indicated. In the upper part of the figure the electric current is sketched. In the lower part the connection of Z_s to the equivalent circuit is represented.

from t_1 to t_2 is assumed to be the same as that occurring in the selected canonical problem when the dimension of the source region is reduced accordingly. The complete formulation to derive Z_s is presented in [15] and applied in [9] to the case of a CPW. The series impedance Z_s grows linearly with the length L of the transition and it is also proportional to $ln(t_2)$ as t_2 tends to zero.

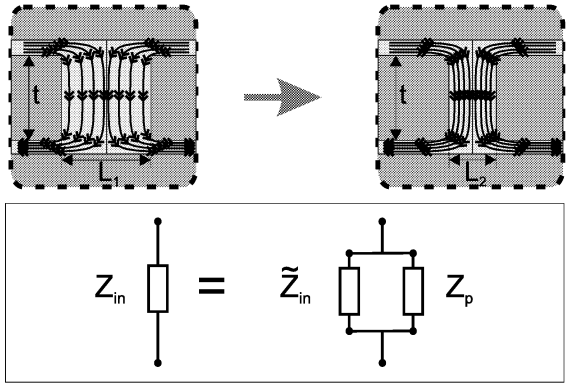

Fig. 7. Magnetic current crowding effect with the relevant dimensions indicated. In the upper part of the figure the magnetic current is sketched. In the lower part the connection of $Z_p = 1/Y_p$ to the equivalent circuit is represented.

With reference to fig. 7, the effect on the input impedance of the magnetic current crowding associated with a gap length shortening ($L_1 \rightarrow L_2$) can be represented as a parallel capacitive admittance Y_p. An infinite dipole printed between two semi-infinite dielectrics, whose width is equal to t, is the canonical problem that best fits the geom-

etry in fig. 7. The growth of capacitive energy in the fringing fields associated with a reduction of the gap from L_1 to L_2 is assumed to be the same as that occurring in this selected canonical problem when the dimension of the source region is reduced accordingly. Y_p is derived in reference [16], and explicitly formulated in [9] for the case of a CPW. The parallel admittance Y_p grows linearly with the width t of the transition. Again, it is proportional to $ln(L_2)$ as L_2 tends to zero.

In order to account for a more general transition we can combine the previous reactances in a staircase form, resulting in an equivalent network as shown in fig. 8. Note that all the parameters of the network are calculated with closed form expressions, provided that the largest dimensions of the transition are approximately less than $\lambda_{eff}/20$, where $\lambda_{eff} = 2\pi/\beta$ and β is the quasi static approximation of the propagation constant.

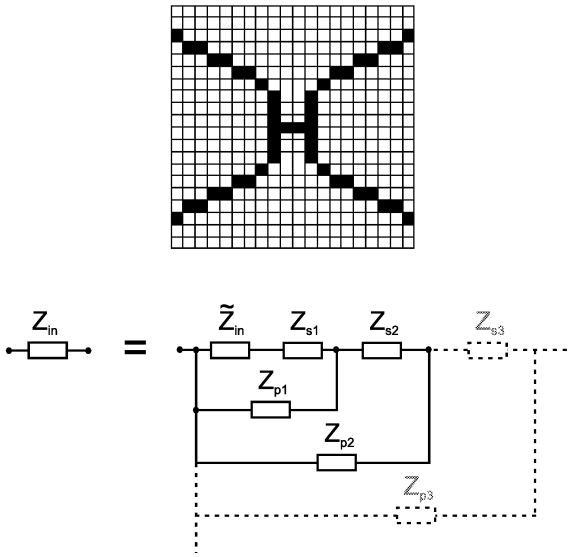

Fig. 8. Example of transition adopted to simulate the actual circuit geometry and of the equivalent network obtained resorting to a "staircase" shaped transition. The layout shown here is representative of the tapered transition region of Mixer No. 1. Each unit represents 0.1 μm.

IV. Numerical results

The parameters of the twin-slot mixers which have been measured and analyzed are shown in fig. 9, along with the bolometer device DC resistance, and in fig. 10 the relevant geometric parameters are indicated. Figure 11 shows the resonance

Mixer	L_a (μm)	W_a (μm)	S_a (μm)	a (μm)	b (μm)	R_{bol} T = 4°K	ν_c Measured (THz)
1	26	3	19	3	4	15	2.22
2	33	3	19	3	4	18	2.19
3	36.5	2	19	2	3	18	2.02
4	36.5	2	19	2	3	25	2.01
5	44	4	25	4.5	6	46	1.60
6	48	2.6	25	3	4.4	25	1.71
7	152	8.3	79.2	8	11	32	0.54

Fig. 9. Parameters of the different mixer circuits under investigation. R_{bol} is the HEB device DC resistance. Refer to fig. 10 for the meaning of the others parameters.

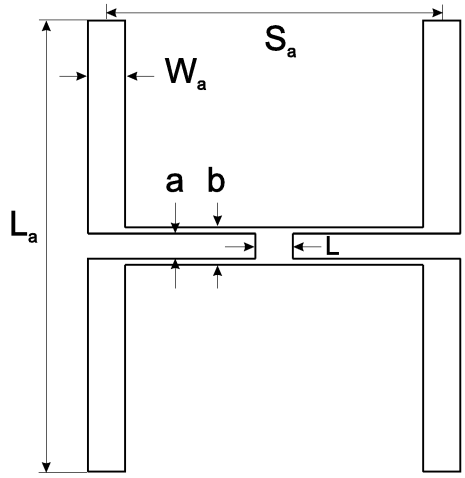

Fig. 10. Schematic layout of physical structure used in the simulations with the relevant dimensions defined.

frequency for the mixers under investigation. The measured results (dashed line with "prism" symbols) are compared with calculated curves that are obtained by using either the simplified network as it is ("plus" symbols) or corrected via the reactive current crowding contributions ("square" symbols). These latter are obtained assuming the flared transition between the bolometer and the inner conductor of the CPW such as in fig. 8, taking into account the actual dimensions of the mixer embedding circuits observed with the Scanning Electron Microscope. While the series inductance of fig. 6 tends to decrease the resonating frequency of the mixer, the parallel capacitance of fig. 7 tends instead to increase it. However, the overall effect, as shown in fig. 11 ("square" sym-

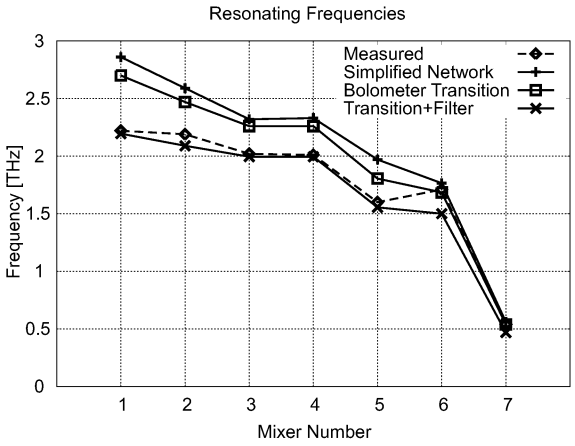

Fig. 11. Summary of measured and calculated resonating frequencies for the seven mixers under analysis.

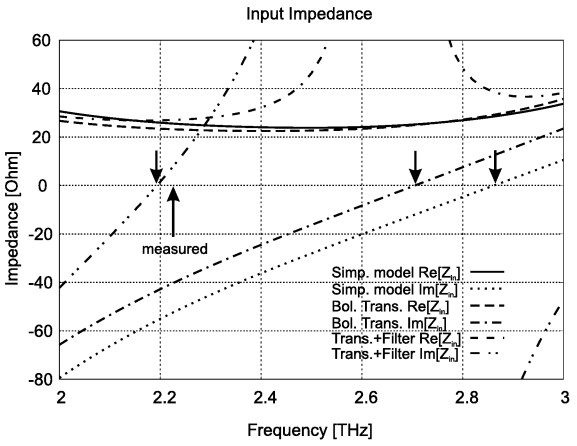

Fig. 12. Input impedance of mixer No. 1 calculated including: 1) simplified network, 2) simplified network + bolometer transition, 3) simplified network + bolometer transition + RF filter.

bols), is that the resonating frequency decreases, with respect to the simplified model. This means that the inductive part of the reactance we introduced tends to prevail.

The resonating frequency is even more strongly affected by the presence of the RF band-stop filter (see Section II). This latter has been modeled by simple transmission line theory where the relevant parameters are evaluated as in Sections III A and III B. Also shown in fig. 11 are the results ("×" symbols) obtained when the impact of the RF filter is included. It is apparent that the agreement between prediction and measurements is outstanding, except for the case of mixer No. 6. These results give strong support to our improved equivalent network, considering the extreme challenges associated with fabrication and measurement at 2.5 THz and the fact that the modeling of the filter does not account for the "step" transitions between the high and low impedance sections. However these latter can be considered higher order effects easily comparable with other phenomena that are not accounted for in the present analysis (i.e. internal reflections inside the lens, gluing of the silicon lens to the chip, fabrication tolerances, variation of metal thickness etc.). It is moreover clear from fig. 13, discussed in the following, that selecting the resonant frequency from the measured peak of the Fourier Transform Spectrometer (FTS) data is not a straightforward matter.

It is useful to refer to the percentage resonating frequency shift as the difference between the predicted and the measured frequency. We may highlight this shift by observing fig. 12 where a detail of the input impedance of mixer No. 1 is shown. Arrows indicate the resonating frequencies, for measured and predicted results, that occur when the imaginary parts of the impedance cross zero. Improving the simplified network with only the effect of the bolometer-CPW transition decreases the shift from 29% to 22%. By further introducing the effect of the filter, the resonant frequency shift decreases to 1%.

In the past the observed shift has been attributed to unknown lumped reactive effects associated to the superconducting bolometer itself (i.e. thermal gradients and skin effects). The present analysis attributes the dominant part of the observed shift to the embedding circuit modeled in this paper. From fig. 12 one can also outline the significant impact of the filter on the real part of the input impedance and the narrowing of the bandwidth due to the several high and low impedance sections used in the filter.

In fig. 13 the FTS direct detection responses of mixer No. 1, 3 and 5 are presented. For the same set of mixers, fig. 14 shows the predicted coupling efficiency, between input and bolometer impedance. These latter are obtained resorting to the following well known impedance-mismatch

expression:

$$\eta = 1 - \left| \frac{R_{bol} - Z_{in}}{R_{bol} + Z_{in}} \right|^2, \qquad (1)$$

where R_{bol} is the resistance of the bolometer and Z_{in} is the series impedance seen by the device in the equivalent circuit. The measured bandwidths appear larger than the calculated ones. This is basically due to the normalization adopted in the FTS curves: these are normalized to the maximum of the peak response while those in fig. 14 reflect the calculated mismatch between bolometer and input impedance. The ripples in the measured curve are due to several effects related to the quasi-optical FTS measurement system, in particular the lens internal reflections [6] and the thickness of the glue layer holding the chip to the lens.

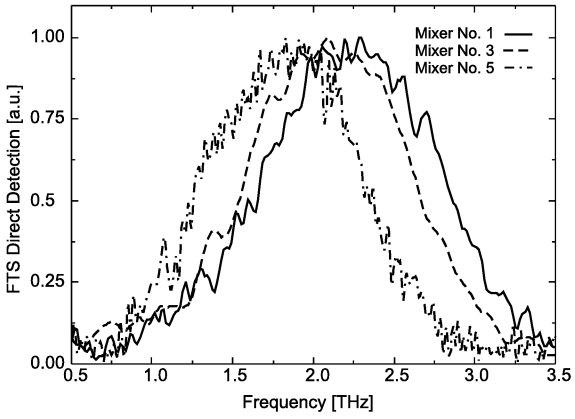

Fig. 13. Measured FTS direct detection responses for mixer No. 1, 3 and 5.

V. Design Considerations

Based on the previous results some guidelines for future design of CPW based twin slot bolometric mixers are now given.

In the past ([4], [6]), the main constraint in the design of such a mixer has been the overall beam pattern of the antennas+lens system, the emphasis being given to a gaussian shaped beam and consequently, good radiation efficiency. This goal was achieved operating the twin slot antenna at its second resonance. In this way a low real part of the input impedance for each slot was obtained

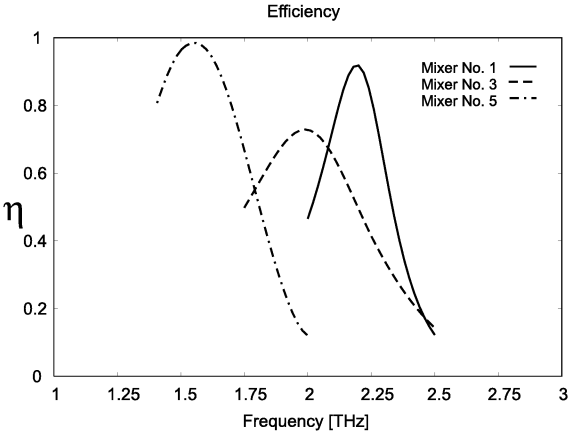

Fig. 14. Calculated coupling efficiency curves for mixers No. 1, 3 and 5.

and a good match to the characteristic impedance of the CPW could be achieved (each one in the order of 40 Ohms). More problematic instead was the matching between the bolometer impedance (typically low to obtain a fast response from the device) and the equivalent load represented by the CPW and slot antennas on each side of the bolometer. Moreover, the non zero reactance, provided by the RF filter, could significantly affect the impedance of the equivalent load of the slot connected to the filter itself. This latter effect and the CPW-bolometer transition play a dominant role in explaining the downward shift of the resonating frequency shown by the mixers under investigation.

As a result of the present investigation it seems more convenient to operate the slot antennas on their first resonance (half instead of a full wavelength long slots). Indeed, even though the overall radiation pattern could be slightly affected and different from the theoretical optimum, the input impedance of the radiating slots turns out to be higher (about 140 Ohms for the real part of mixer No. 1 at 2.5 THz). In this way the slot input impedance is more stable and the impact of the imaginary part of the filtering structure is less significant because it is in series to a high impedance.

To further motivate this choice it is worth mentioning that the previous studies on the beam efficiency [4] were based on Physical Optics (PO) calculations of the radiation patterns. There are presently on-going studies that include more so-

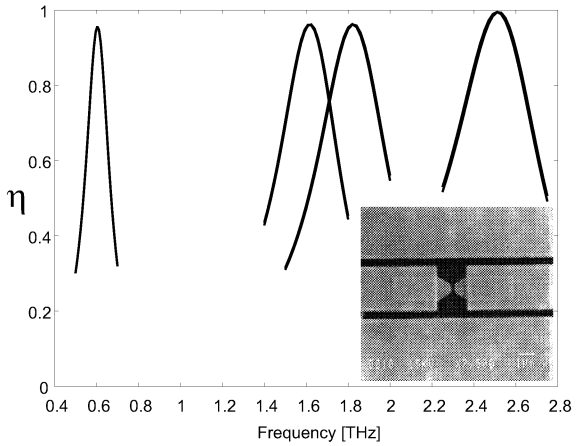

Fig. 15. Calculated matching efficiency between the bolometer resistance and the equivalent input impedance seen by the bolometer itself: new tapered designs.

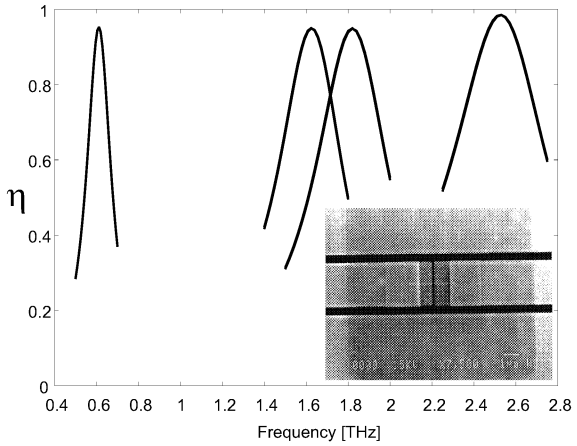

Fig. 16. Calculated matching efficiency between the bolometer resistance and the equivalent input impedance seen by the bolometer itself: new non-tapered designs.

phisticated diffraction mechanisms [17]. These latter could affect the calculation of the optimum beam efficiency for these kind of lenses. Additionally, when the slot antennas are operated on their first resonance, the slot impedance presented to the bolometer via a $\lambda_{eff}/4$ long CPW transmission line is much lower and typically about 20 Ohms. This way a good match of the real part of this impedance with that of the bolometer is straightforward, which results in a nearly optimum efficiency. It is true that in this configuration the impact of the lumped reactances associated with the CPW-bolometer transition are more relevant. However, observing the analytical expressions of the impedances presented in Section III C and explicitly formulated in [9], it is clear that the effect of this transition is much more negligible if the length of the transition L is reduced to the minimal realizable dimension without resorting to the flared transition of fig. 2.

Based on the previous considerations and on the good results obtained, a new set of THz mixers has been fabricated and is currently being tested. Different designs at four center frequencies have been carried out; in particular we aimed to have the center frequency at: 0.6, 1.6, 1.8 and 2.5 THz. The bolometer has been fabricated in Niobium and the microbridge is always 0.1 μm wide, while the length has been chosen to be either 0.1 or 0.2 μm. Moreover, with this new set of mixers we designed two different transitions between the CPW inner conductor and the bolometer: a tapered one, like in the previous measured devices, and a new non-tapered one. The choice of a non-tapered transition has been suggested by the formulation presented in [9] and is expected to give a much more negligible lumped reactance in the equivalent circuit and therefore a smaller down shift in the resonating frequency. Finally, also the filter section has been re-designed accordingly.

In fig.s 15 and 16 the calculated matching efficencies of the new designs are shown. In particular it is worth noting the example of the new non-tapered transition in the inset of fig. 16 and the very accurate and sharp profile of the 0.1 μm gap in the CPW inner conductor obtained with the fabrication process. These results, besides being very promising are also very useful for predicting the expected bandwidth of the receivers, even though other effects (such as the silicon lens effect) are not included in the model presented in this paper.

VI. Conclusions

In this paper we have presented an improved model for series fed coplanar waveguide embedding circuits that are used in bolometric THz receivers. We first calculated the complex propagation constant and characteristic impedance of the weakly leaky mode propagating in the CPW etched between two semi-infinite dielectrics. It has been found that for higher values of the charac-

teristic impedance the quasi static approximation is inadequate for an accurate design that aims to match the CPW impedance to the radiating slots or to the bolometer. We have also presented an improved model of the planar transition between the CPW and the bolometer.

Using these improvements, we have investigated seven mixers developed for real instrument applications and we have been able to explain the downward shift in the resonating frequency when comparing simplified predictions with the actual measurements. Higher order physical effects that can contribute to the input impedance of the circuit are still not taken into account. In particular, the bolometer impedance is accurately known only in DC and it is not necessarily real at 2.5 THz. Skin effects could have an impact on the overall circuit and other reactances could be associated with the vertical variation of the metal thickness between the CPW inner conductor and the superconductive metal of the HEB device. Finally, the transitions between high and low impedance sections of the filter should be taken into account.

Nevertheless the results obtained by our improved equivalent network are outstanding considering the extreme challenges associated with fabrication and measurement at 2.5 THz, and the predictions obtained for the new set of THz mixers presented in the last section of this paper are very promising.

Acknowledgments

This research was performed at Jet Propulsion Laboratory, California Institute of Technology, under contract with the National Aeronautics and Space Administration.

References

[1] B.S. Karasik, M.C. Gaidis, W.R. McGrath, B. Bumble, H.G. LeDuc, *Low noise in a diffusion-cooled hot-electron mixer at 2.5 THz*, Applied Physics Letters, 71, 1567, (1997).

[2] W.F.M. Gonzeules, J.R. Gao, W.M. Laauwen, G. de Lange, T.M. Klapwijlc, P.A.J. del Corte, *Direct and Heterodyne Response of Quasioptical Nb Hot Electron Bolometer Mixers Designed for 2.5 THz Radiation Detection*, Proceedings of the 11th International Symposium on Space Terahertz Technology, Univ. of Michigan, Ann Arbor, pp. 69-81, May 2000.

[3] D.B. Rutledge, D.P. Neikirk and D.P. Kasiligan, *Integrated Circuit Antennas*, in "Infrared and millimeter-waves", K.J. Button, Ed. New York: Academic, 1983, Vol. 10, pp. 1-90.

[4] D.F. Filippovic, S.S. Gearhart and G. M. Rebeiz, *Double-Slot Antennas on Extended Hemispherical and Elliptical Silicon Dielectric Lenses*, IEEE Trans. on Microwave Theory and Techniques, Vol. 41, Oct. 1993, pp. 1738-1749.

[5] J. Kawamura, T. Hunter, C.-Y.E. Tong, R. Blundell, D.C. Papa. F. Patt, W. Peters, T. Wilson, C. Henkel, G. Gol'tsman, E. Gershenzon, *Ground-based Terahertz Spectroscopy Towards Orion*, Accepted for publication in Astronomy and Astrophysics Letters, pp. XXX - XXX (2001).

[6] M. Van der Vorst, P.J.I. De Maagt, A. Neto, A. Reynolds, W. Luinge, R. Heres, M. Herben, *Effect of the Internal Reflection on the Radiation Properties and Input Impedance of Integrated Lens Antennas: Comparisons Between Theory and Measurements*, IEEE Trans. on Microwave Theory and Techniques, Vol. 49, No. 6, June 2001, pp. 1118-1125.

[7] R.A. Wyss, A. Neto, W.R. McGrath, B. Bumble, and H. LeDuc, *Submillimeter-wave spectral response of twin-slot antennas coupled to hot electron bolometers*, Proceedings of 11th Int. Symp. on Space THz Tech., Ann Arbor, MI, May 1-3, 2000.

[8] A. Neto, P.J.I. De Maagt, S. Maci, *Optimized Basis Functions for Slot Antennas Excited by Coplanar Waveguides*, Submitted to IEEE Trans. on Antennas and Propagation (April 5th, 2001, ID AP 0104-0156).

[9] P. Focardi, A. Neto, W. R. McGrath, *Coplanar Waveguide Based, Terahertz Hot Electron Bolometer Mixers: Improved Embedding Circuit Description*, accepted for publication on IEEE Trans. on Microwave Theory and Techniques, N. 0864, Dec. 2001.

[10] Joo-Hiuk Son, Hsi-Huai Wang, John F. Whitaker, Gerard A. Mourou, *Picosecond Pulse Propagation on Coplanar Striplines Fabricated on Lossy Semiconductor Substrates: Modeling and Experiments*, IEEE Trans. on Microwave Theory and Techniques, Vol. 41, No. 9, Page(s) 1574-1580, September 1993.

[11] D.R. Jackson, F. Mesa, M.J. Freire, D.P. Nyquist, C. Di Nallo, *An Excitation Theory for Bound Modes and Residual-Wave Currents on Stripline Structures*, Radio Science, Volume 35, Number 2, Page(s) 495-510, March-April 2000.

[12] A. Neto, S. Maci, *Green's Function of an Infinite Slot Printed Between Two Homogeneous Dielectric. Part I: Magnetic Currents*, Accepted for publication on IEEE Trans. on Antennas and Propagation, ID AP 0107-0350.

[13] K.C. Gupta, *Microstrip Lines and Slotlines*, Ramesh Garg, I.J. Bahl, Artech House 1979.

[14] N. K. Das, *A New Theory of the Characteristic Impedance of General Printed Transmission Lines Applicable When Power Leakage Exists*, IEEE Transactions on Microwave Theory and Techniques, Vol. 48, No. 7, Page(s) 1108-1117, July 2000.

[15] A. Neto, S. Maci, *Input Impedance of an Infinite Slot Printed Between Two Homogeneous Dielectric*, JPL Internal Report, D/21322.

[16] A. Neto, P.H. Siegel, *Equivalent Network Characterization for Series Fed Microstrip Lines on Thin Slabs*, Submitted to IEEE Trans. on Microwave Theory and Techniques (October, 2001, ID 0914).

[17] D. Pasqualini, F. Capolino, A. Toccafondi, S. Maci, *An Improved Evaluation of Radiation Pattern for Dielectric Lens Antennas*, IEEE Antennas and Propagation Symposium, Boston, July 2001.

GAIN BANDWIDTH OF PHONON-COOLED HEB MIXER MADE OF NBN THIN FILM WITH MgO BUFFER LAYER ON Si.

Yuriy B. Vachtomin, Matvey I. Finkel, Sergey V. Antipov, Boris M. Voronov, Konstantin V. Smirnov, Natalia S. Kaurova, Vladimir N. Drakinski and Gregory N. Gol'tsman

Physics Department, Moscow State Pedagogical University, Moscow 119435, Russia.

Abstract.

We present recently obtained values for gain bandwidth of NbN HEB mixers for different substrates and film thicknesses and for MgO buffer layer on Si at LO frequency of 0.85–1 THz. The maximal bandwidth, 5.2 GHz, was achieved for the device on MgO buffer layer on Si with a 2 nm thick NbN film. Functional devices based on NbN films of such thickness were fabricated for the first time due to an improvement of superconducting properties of NbN film deposited on MgO buffer layer on Si substrate.

Introduction.

In the last years, the development of HEB mixers has reached such a high level that these devices can be successfully utilized in heterodyne receivers of THz frequency range. Their high sensitivity and low LO power make them suitable for radioastronomic observations on space- and airborn platforms. An NbN HEB mixer seems to be a preferable mixing device now for such projects as FIRST (Far Infrared Receiver Satellite Telescope), GREAT (German REceiver for Astronomy Terahertz frequencies), or TELIS (TErahertz Limb Sounder). Heterodyne receiver based on this type of mixer is successfully used on the 10-m Heinrich Hertz Telescope on Mount Graham, Arizona [1]. The obtained values of noise temperature for a receiver based on NbN HEB mixer are 650 K at LO frequency of 1.6 THz and 1100K at 2.5 THz [2]. These noise characteristics amount to 5-10 times of the quantum limit.

Currently phonon- [3] and diffusion- cooled [4] HEB mixers are being developed. The main difference between the two modifications lies in the electron cooling mechanism. In the diffusion cooled HEB mixer, the electron subsystem is relaxed by the diffusion of nonequilibrium hot electrons to cold metal contact pads. The gain bandwidth in this case is

determined by the length of the active superconducting film and the electron diffusion coefficient and reaches 9 GHz for 80 nm long Nb microbridge [5].

In the case of the phonon-cooled HEB mixer, electron temperature is relaxed by electron-phonon interaction and later by the escape of non-equilibrium phonons to the substrate [6]. Gain bandwidth of this type of HEB mixer depends on electron-phonon interaction time τ_{eph} and on the non-equilibrium phonons escape time τ_{esc}. Currently, gain bandwidth of phonon-cooled NbN HEB mixers at the optimal operating point which yields the lowest noise temperature has achieved values of 3.6 GHz for the device on quartz substrate with MgO buffer layer [7], 4 GHz for Si [8], 3.7 GHz for sapphire [8], 4.5 GHz for MgO [2]. Further improvement of NbN phonon-cooled HEB mixers can be achieved through decreasing of τ_{esc}. Phonons escape time depends on film thickness and acoustic transparency of substrate-superconductor interface. In this work we studied the influence of MgO buffer layer on superconducting properties of NbN films of varied thickness. We also researched into gain bandwidth of the devices based on ultrathin NbN films deposited on MgO substrate and on MgO buffer layer on silicon substrate. A gain bandwidth of 5.2 GHz was obtained for a device fabricated from 2 nm thick NbN film deposited on Si substrate with MgO buffer layer.

Device design and fabrication.

In this work NbN HEB mixers on Si and MgO substrates and Si with MgO buffer layer were studied. MgO buffer layer, 200 nm thick, was deposited by e-beam evaporation from MgO pellet. The substrate temperature during the MgO deposition process was about 400 ^{o}C.

Ultrathin NbN films were deposited by reactive dc magnetron sputtering in the Ar + N_2 gas mixture. The maximum values of the critical film parameters (T_c and j_c) were reached at the partial Ar pressure of $5x10^{-3}$ mbar, the partial N_2 pressure of $9x10^{-5}$ mbar, the discharge current value of 300 mA, the discharge voltage of 300 V and the substrate temperature 850 ^{o}C. The deposition rate was 0.5 nm/s. It was defined as the ratio of the film thickness, measured with a Talystep profilometer-profilograph, and its deposition time. The film thickness varied between 2 and 10 nm according to deposition time. The quasioptical mixer was made by e-beam lithography and photolithography as illustrated in Fig. 1. For fabrication of the devices the central part of spiral antenna was formed using lift-off e-beam lithography based on Cr-Au metallization (Cr ~ 5 nm, Au ~ 70 nm). The gap between the gold contact pads that uncovered the active NbN film area in the mixer was 0.15 – 0.25 μm long and 1.5 – 2.5 μm wide. A SEM photograph of the central part for

one of the devices is presented in Fig. 2b. The next process was to fabricate the outer part of the mixer by lift-off photolithography based on Ti-Au metallization (Ti ~ 5 nm, Au ~ 200 nm) as presented in Fig. 2a. The last process was to remove the NbN layer by ion-milling in Ar atmosphere from the whole substrate surface except for the central part of the spiral antenna, which was protected by a SiO mask made by lift-off e-beam lithography.

An improvement of superconducting properties of NbN ultrathin films due to the presence of MgO buffer layer on silicon substrates is evident and reproducible. As can be seen from Fig. 3, NbN ultrathin films (even those 2 nm thick) deposited on MgO buffer layer have a higher T_c not only in comparison with NbN films deposited on silicon substrate but also with NbN films deposited on MgO substrate. We believe that this effect can be explained by the fact that surface properties of MgO buffer layers deposited on silicon substrate are better than those of MgO substrate itself. Silicon substrates can be polished more accurately than MgO ones but the discrepancy in thermal coefficient of expansion between silicon and NbN cause high mechanical stresses in the films, which explains worse superconducting properties of the NbN ultrathin films deposited on silicon.

Experimental Setup.

The HEB mixer output power versus intermediate frequency was measured at LO frequency in the range of 0.87-1 THz. The Experimental setup is presented in Fig. 4.

Two backward wave oscillators OB-44 were used as heterodyne and signal sources. Radio frequency (rf) radiation was focused using two Teflon lenses to create optimum patterns. After the attenuation by polarizers rf power was split by 50-μm Maylar beam-splitter and arrived into liquid-helium cooled vacuum cryostat through a Teflon window. After IR Zitex filter it fell on mixer block mounted on the cold plate of the cryostat. The mixer block consisted of a hyper-hemispherical lens fabricated from high-resistivity silicon with a mixing device positioned on the flat side of the lens. The device antenna was integrated with 50 Ohm coplanar line. The intermediate frequency signal was guided out of the HEB via a 50 Ohm microstrip line, which was soldered to an SMA connector. A bias tee was used to feed the bias to the mixer and to transmit the intermediate frequency signal to a room temperature amplifier. Because of a limited dynamic range of NbN HEB mixer and a comparably high noise temperature of ultra-wideband amplifiers we used two amplifying chains in the frequency range of 0.5–9 GHz (0.5-4 GHz 55 dB amplifying chain and 3.7-9 GHz 57 dB amplifying chain). The amplified signal power was recorded

by a power meter. The intermediate frequency was measured by a spectrum analyzer connected in a chain after the directional coupler.

When the output power was measured at low signal power versus intermediate frequency we had to use an amplifying chain that consisted of three amplifiers (about 65-80 dB in all frequency ranges). To prevent the noise power of the first amplifier after amplification from coming out of the dynamic range of the last amplifier, a tunable filter was inserted before the last amplifier. The filter had 20 MHz bandpass and the central frequency tuned in the range from 1.8 GHz to 12 GHz. Low input signal power measurements showed that output power about 65 dBm is within the dynamic range of the HEB mixer based on the ultrathin NbN film down to 2 nm thick.

Results and Discussion.

The output power vs. IF dependence was measured under varied operating conditions. The family of IV-curves for one of the devices is presented in Fig. 5. Operating point 1 yields an optimum noise performance of the device and is marked in the figure. Operating point 2 corresponds to the same LO power as operating point 1 and to a higher bias voltage. Measured output power vs. IF dependence of the device in the operating point 1 is presented in Fig. 6 by curve A. Curve B in Fig. 6 presents the measured IF dependence at operating point 2 of the same device. Operating at larger biases than the optimum can decrease a self-heating effect (positive electro-thermal feedback) and therefore expands the gain bandwidth. This can be described by the following equation [9]:

$$\Delta B = \Delta B_0(1+C(R-R_L)/(R+R_L)),$$

where R is the DC resistance of the sample at the operating point, R_L is the load resistance of the IF chain, and C is a self-heating parameter determined by the following equation:

$$C = (I^2(\partial R/\partial T)/c_e V)\tau_\theta ,$$

where I is the bias current, $\partial R/\partial T$ is the superconducting transition derivative of the resistance with respect to temperature, c_e is electron specific heat and V is active NbN film volume.

The experimental error of the obtained dependencies of the output power vs. intermediate frequency is not small enough due to residue resonances in the IF chain. To reduce this experimental error the output power ratio at two different operating points at each intermediate frequency was analyzed. This ratio IF dependence is presented in Fig. 6 by curve C. It is evident that residue resonance influence is decreased on the ratio curve.

This curve has two characteristic frequencies, corresponding to gain bandwidths of the device at two operating points.

Experimental results for devices based on 3.5 nm thick NbN film on MgO substrate and on MgO buffer layer on silicon substrate are presented in Fig. 7. The cut-off frequency for a device on MgO substrate is in good agreement with an independently obtained value [2]. As can be seen from the figure, the measured values of gain bandwidth for the devices investigated in this work and based on 3.5 nm NbN film are close to each other. The cut-off frequency for a phonon-cooled NbN HEB mixer is determined by electron-phonon interaction time τ_{eph} and non-equilibrium phonons escape time τ_{esc}. It is known from other papers [10] that the gain bandwidth of a device based on 3.5 nm thick NbN film partly depends on τ_{esc} that is determined by film thickness d and acoustic transparency between active superconducting film and substrate α as follows:

$$\tau_{esc} = 4d/\alpha u,$$

where u is the speed of sound in NbN. According to the result of Fig. 7, α can be assumed to be the same for MgO substrate and MgO buffer layer on Si substrate because in both cases all other parameters are the same. Consequently, the current MgO buffer layer on silicon substrate has good acoustic transparency to NbN ultrathin film (the same as has the MgO substrate itself) and better surface properties than other investigated substrates.

The noise bandwidth of a device based on 3.5 nm thick NbN film deposited on MgO buffer layer on Si was measured at LO frequency 0.6 THz in the Chalmers University of Technology. The obtained noise temperature vs. IF dependence is presented in Fig. 8. The Intermediate frequency with a noise temperature twice as high as the minimal value was about 5.5 GHz. This is in good agreement with gain bandwidth measurements.

The output power vs. IF dependence for a device based on 2 nm thick NbN film as obtained in this work is presented in Fig. 9. As can be seen from this figure, the gain bandwidth under optimal operation conditions achieved 5.2 GHz, while at higher bias voltage it reached 10.7 GHz. This latter value is in good accordance with the material limit provided by electron-phonon interaction time. This time τ_{eph} for NbN depends on temperature as follows [11]:

$$\tau_{eph} = 500 \cdot T^{-1.6}$$

The highest T_c of the devices based on 2 nm thick NbN ultrathin film achieves 9.2 K. According to the equation above, τ_{eph} is about 14.4 ps and provides an overall gain

bandwidth of 11.1 GHz. So, we can presume that in the case of NbN films 2 nm thick HEB mixer's cut-off intermediate frequency mostly depends on τ_{eph} and in its turn on the superconducting transition temperature.

References

1. C.-Y. Edward Tong, Jonathan Kawamura, Todd R. Hunter, D. Cosmo Papa, Raymond Blundell, Michael Smith, Ferdinand Patt, Gregory Goltsman and Eugene Gershenson "Successful operation of a 1 THz NbN hot-electron bolometer receiver", In 11th Intl. Sym. On Space Terahertz Technology, pp. 49-59, Ann Arbor, MI (USA), May 2000.
2. M. Kroug, S. Cherednichenko, M. Choumas, H. Merkel, E. Kollberg, H.-W. Huebers, H. Richter, D. Loudkov, B. Voronov, G. Gol'tsman "HEB Quasi-optical Heterodyne Receiver for THz Frequencies", In 12th Intl. Sym. On Space Terahertz Technology, pp. 244-252, San Diego, California (USA), 2001.
3. E. M. Gershenzon, G. N. Goltsman, I. G. Gogidze, Yu. P. Gousev, A. I. Elantiev, B. S. Karasik, A. D. Semenov "Millimeter and sub-millimeter range mixer based on electronic heating of superconducting film in the resistive state" Sov. Phys. Superconductivity **3**, p. 1582 (1990).
4. D. E. Prober "Superconducting terahertz mixer using a transition-edge microbolometer" Appl. Phys. Lett. **62**, pp. 2119-2121 (1993).
5. R. Wyss, B. Karasik, W. McGrath, B. Bumble and H. LeDuc "Resistive behavior of Nb Diffusion-cooled Nb Hot-Electron Bolometers". In 10th Intl. Sym. On Space Terahertz Technology, pp. 215-228, Charlottesville (USA), March 1999.
6. E.M. Gershenzon, M.E. Gershenzon, G.N. Gol'tsman, A.M. Lyul'kin, and A.D. Semenov. "Electron-phonon interaction in ultrathin Nb films". Sov. Phys. JETP, 70(3): 505-511, March 1990.
7. D. Meledin, C.E. Tong, R. Blundell, N. Kaurova, K.Smirnov, B.Voronov, G. Golt'sman. "Sensitivity and IF bandwidth of waveguide NbN phonon-cooled HEB mixers based on crystalline quartz substrate with MgO buffer layer." this conference proceedings.
8. S. Cherednichenko, P. Yagoubov, K. Il'in, G. Gol'tsman and E. Gershenzon "Large Bandwidth of NbN Phonon-Cooled Hot-Electron Bolometer Mixer on Sapphire Substrates" In 8th Intl. Sym. On Space Terahertz Technology, pp. 245-252, Cambridge, MA, 1997.
9. E.M. Gershenzon, G.N. Gol'tsman, A.I. Elant'ev, B.S. Karasik and S.E. Potoskuev "Intense Electromagnetic Radiation Heating of Electrons of a Superconductor in the resistive state" Sov. J. Temp. Phys.,14(7), 414-420, 1988.
10. S. Cherednichenko, M. Kroug, P. Yagoubov, H. Merkel, E. Kollberg, K. S. Yngvesson, B. Voronov, G. Gol'tsman "IF bandwidth of phonon-cooled HEB mixers made from NbN films

on MgO substrates", In 11th Intl. Sym. On Space Terahertz Technology, pp. 49-59, Ann Arbor, MI (USA), May 2000.

11. G. N. Gol'tsman, A. D. Semenov, Y. P. Gousev, M. A. Zorin, I. G. Gogidze, E. M. Gershenson, P. T. Lang, W. J. Knott and K. F. Renk "Sensitive picosecond NbN detector for radiation from millimeter wavelength to visible light", Supercond.: Sci. and Technol., vol. 4, 1991, pp. 453-456.

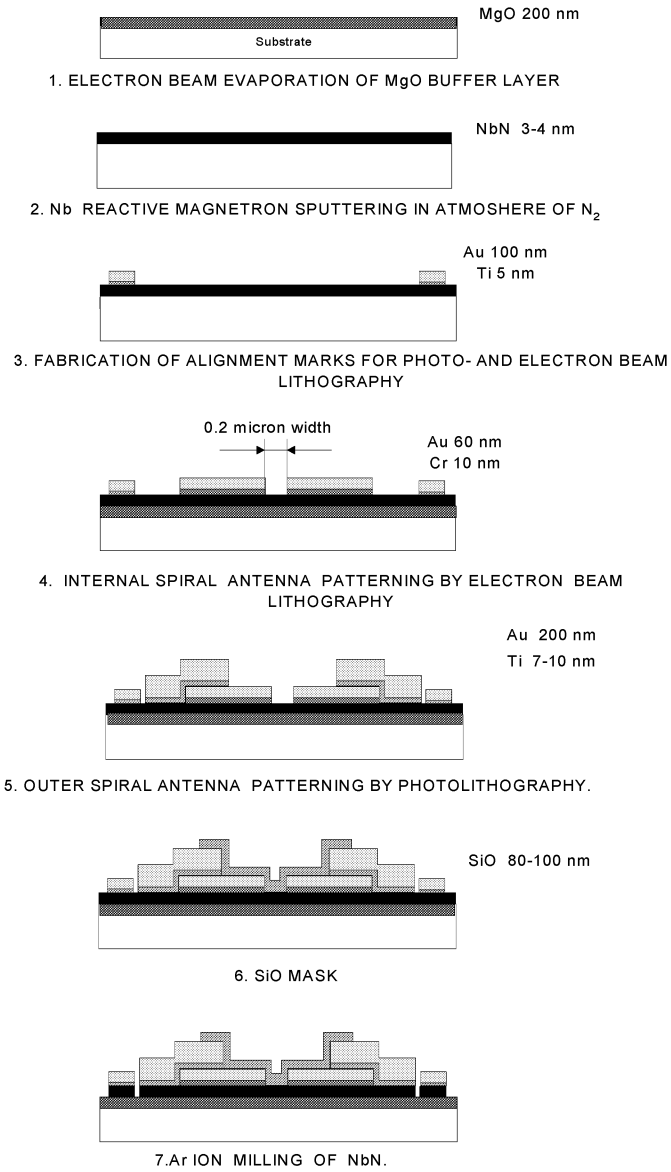

Fig. 1 Fabrication steps for NbN Hot-Electron Bolometer Mixer with MgO Buffer Layer

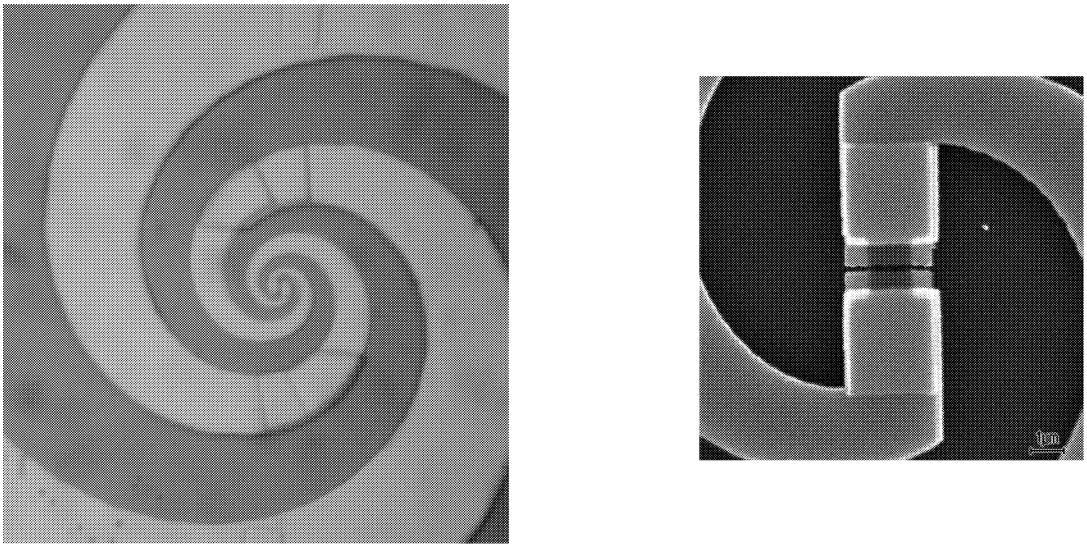

Fig. 2 Photograph of the spiral antenna integrated with the device (Left).
SEM photo of the central part of the antenna, showing the HEB device (Right)

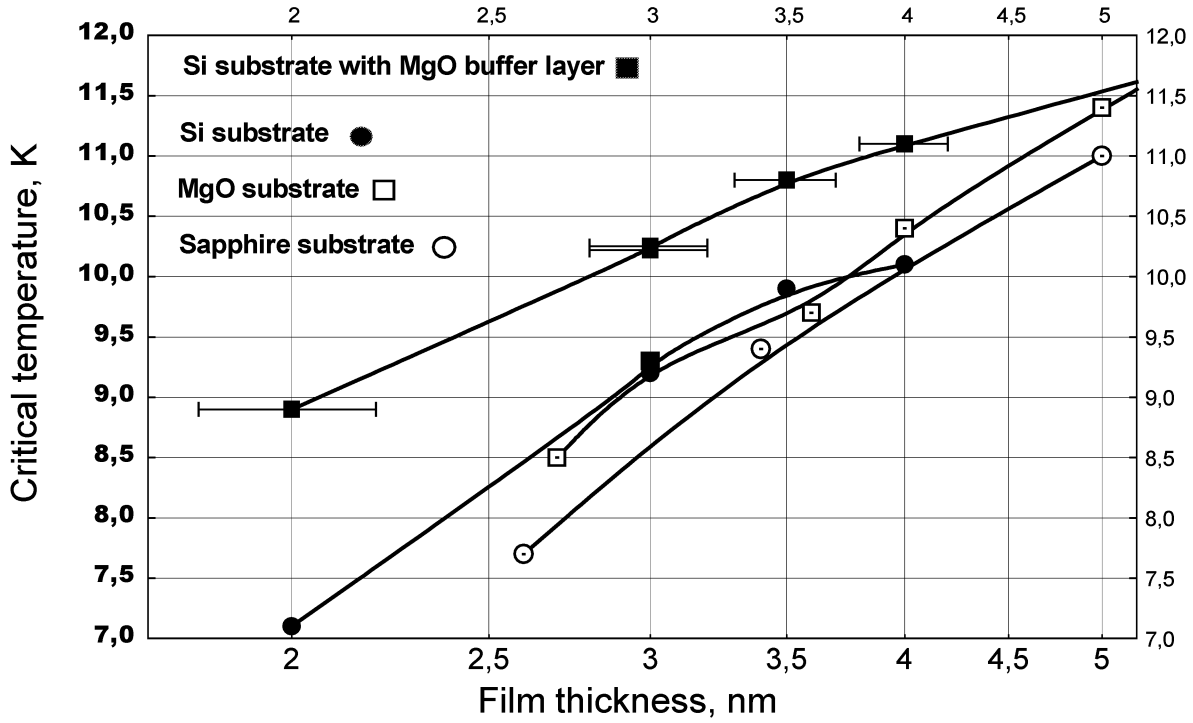

Fig. 3. Criticai temperature vs. film thickness for NbN films on different substrates.

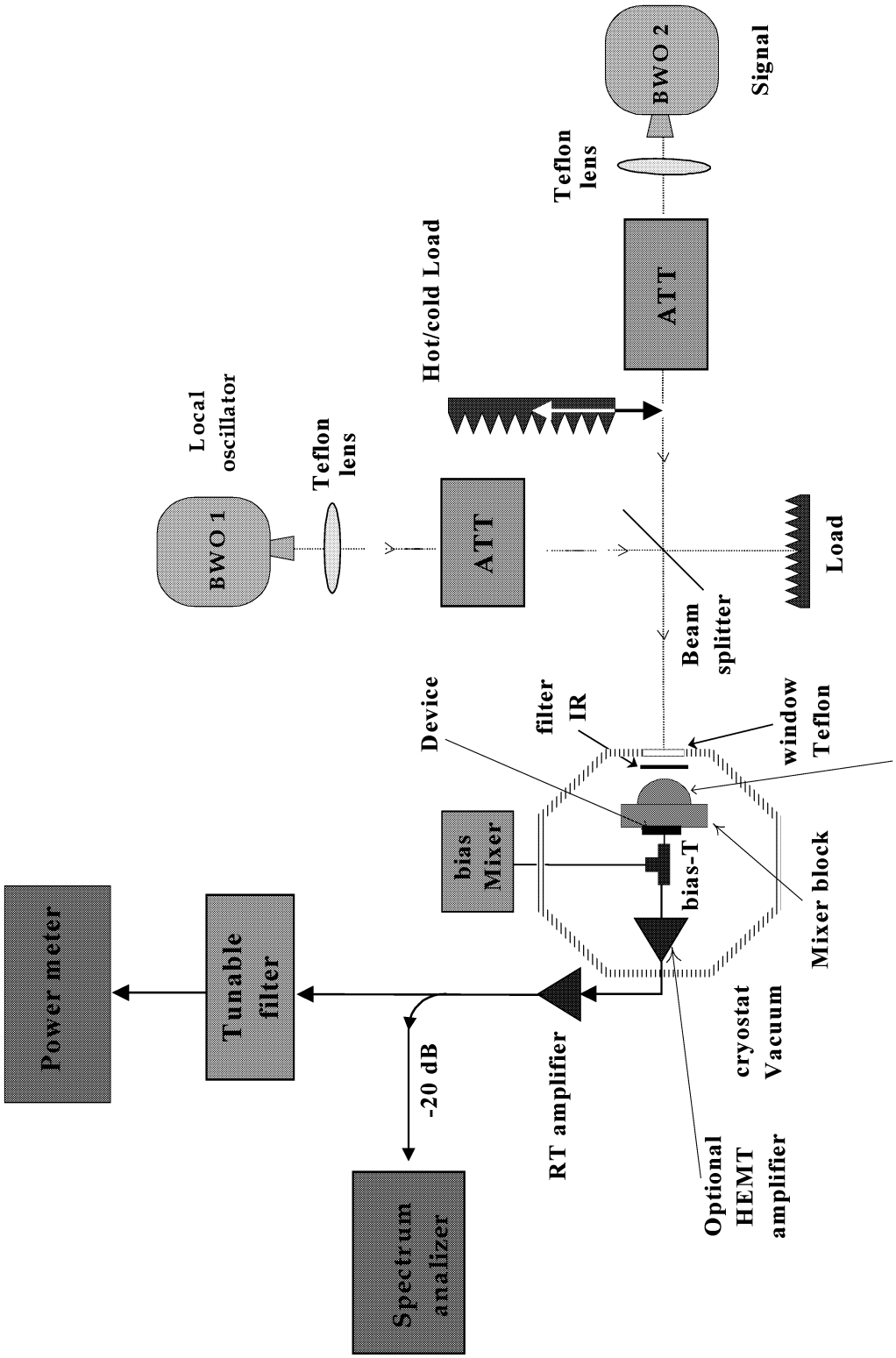

Fig. 4 Experimental setup

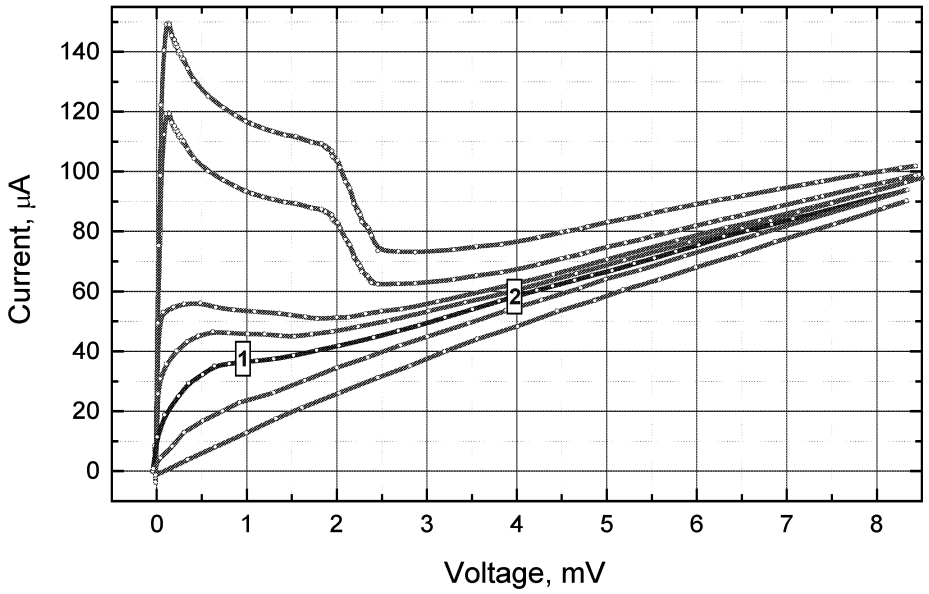

Fig 5. IV curves of device based on 3.5 nm thick NbN film on MgO buffer layer on Si substrate.

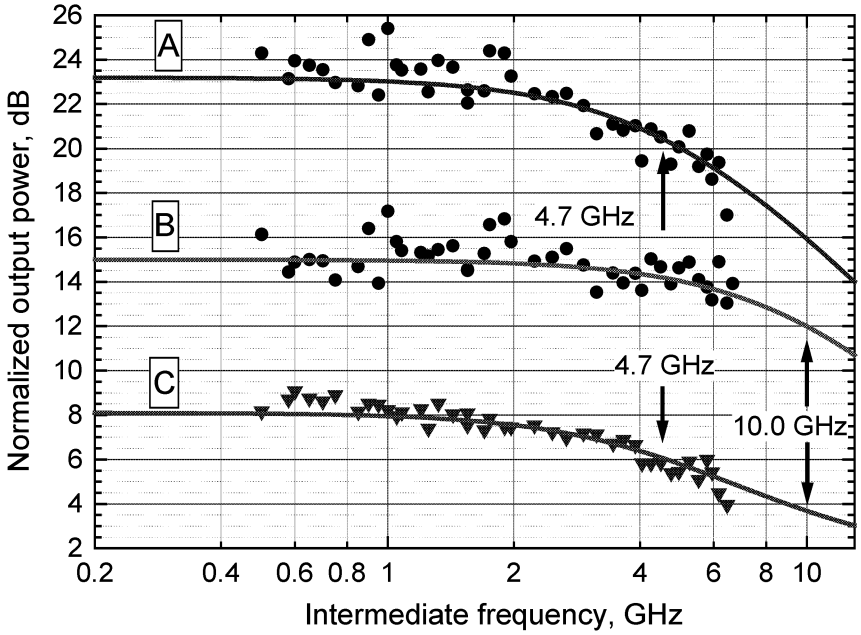

Fig. 6. Output power vs. intermediate frequency at two operating points mentioned on fig. 5 (curves A and B). Curve C presents output power ratio at each intermediate frequency

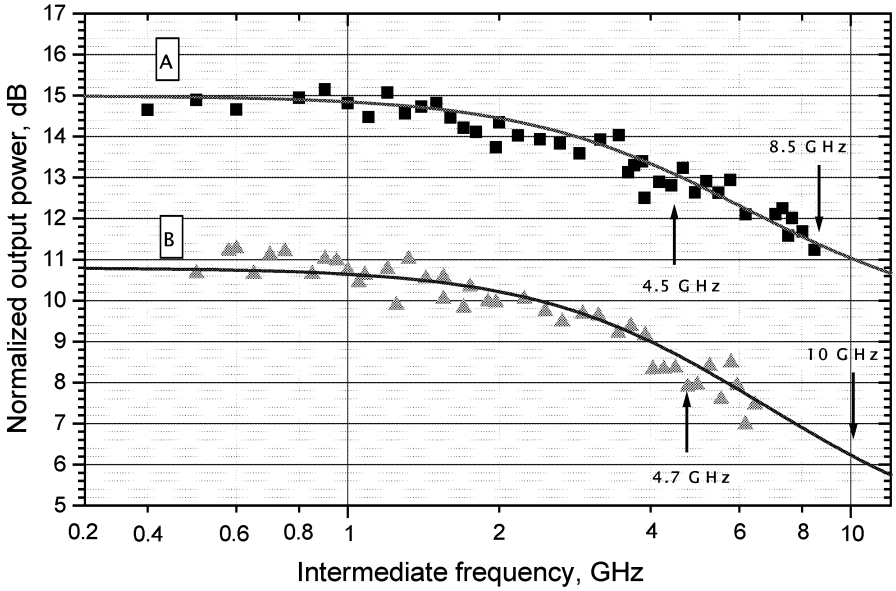

Fig. 7 Output power vs. intermediate frequency dependences for the devices based on 3.5 nm thick NbN film deposited on MgO substrate (A) and Si substrate with MgO buffer layer (B).

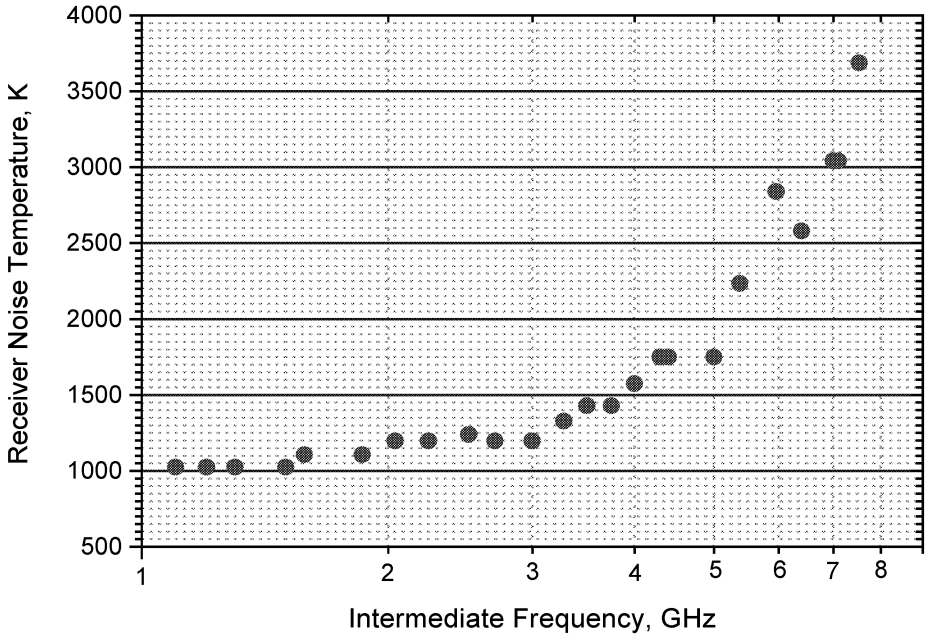

Fig. 8 Noise temperature vs. IF of a device based on 3.5 nm thick NbN film on MgO buffer layer on Si at 0.6 THz LO frequency.

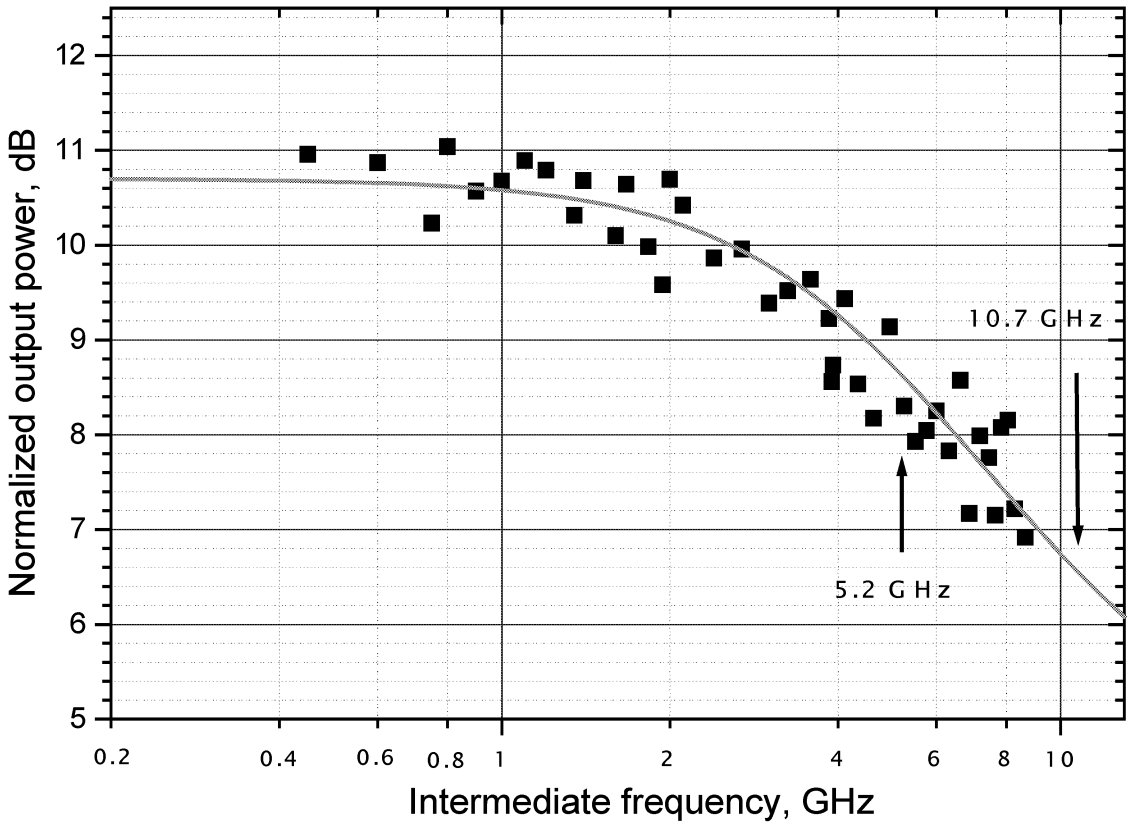

Fig. 9 Output power vs. intermediate frequency dependence for the device based on 2 nm thick NbN film deposited on Si substrate with MgO buffer layer.

Quasi-optical beam waveguide analysis using frame based Gaussian beam expansion

Torsten Bondo[1] and Stig Busk Sørensen
Ticra, Laederstraede 34, DK-1201, Copenhagen

Abstract

A frame based Gaussian beam expansion method which can be used for analysis of quasi-optical beam waveguides is presented. The method is tested for the scattered field of an ellipsoid at 321 GHz and 3.21 THz.

Keywords: Quasi-optics, Beam waveguide, THz, Gaussian beams, PO, frames.

Introduction

For reflector antennas and mirrors with diameters less than 250 wavelengths Physical Optics (PO) is a fast and accurate calculation method for determining the scattered fields. In optics where the diameter of the mirrors are much larger than a thousand wavelengths ray tracing methods as Geometrical Optics (GO) are efficient ways of determining the scattered fields. However, at Quasi-optical frequencies the mirrors are typically in the order of a thousand wavelengths in diameter and in this range neither PO nor GO methods suffice. The computational time for PO increases with the frequency to the fourth power and GO methods become inaccurate or impractical. A fast analysis method useful for this wavelength range is the Gaussian beam analysis method.

Imbriale et. al. [1] expand the field in a beam waveguide in Gauss-Laguerre beams, which are used to propagate the field from a reflector A to a reflector B. On the reflector B the currents are calculated by the PO approximation. The scattered field of the reflector B is found by making a new expansion in Gauss-Laguerre modes on an output plane in front of the reflector B. This involves the calculation of orthogonality integrals with respect to the reflected field which is unknown at this stage. By use of the reciprocity theorem the orthogonality integrals can be transformed to surface integrals on the reflector B that only involve the known surface currents. The method is fast, but it has the major disadvantage that the Gauss-Laguerre expansion is only accurate in the paraxial region so that diffractions from the reflector are not accurately described.

Parini et. al. [2] use a frame based expansion [4] consisting of fundamental Gaussian beam modes that are shifted and rotated in space. Reflector scattering is computed by GO and GTD using Gaussian beam diffraction techniques. This gives the scattered field on an output plane where a new frame expansion is made. In contrast to [1] the method is also able to compute non-paraxial fields since only the fundamental Gaussian beam modes are used in the expansion. The major drawback is the use of GO and GTD for computation of the scattered field which involves ray-tracing and may be inaccurate if the surface or rim has a complicated shape (e.g. a rectangular rim).

In this paper a method is presented which combines the features of [1] and [2] avoiding the major disadvantages of the two methods. The frame based expansion that consists of the fundamental Gaussian modes that are shifted and rotated in space is used to describe the field, and the reciprocity theorem is used instead of the GO+GTD analysis.

The method has been implemented in a computer program for analysis of a sequence of two 3D reflectors. If a sufficiently large number of expansion functions is included the accuracy of the new method is comparable

[1]Correspondence: email tb@ticra.com, web: www.ticra.com

to PO also outside the main beam but the computation time may then be longer than for PO. However, close to the main beam a good accuracy can be obtained with a small number of expansion functions and with a considerable saving of computation time in comparison to PO. Especially for computing the near-field at THz frequencies the method proves to be much faster than PO.

Frame based expansion

In [3] a uniform 2D aperture field is expanded in fundamental Gaussian beam modes that are shifted and rotated over the aperture plane. This method can be generalized to an arbitrary aperture distribution in 3D and will be used in the next section for an ellipsoidal reflector antenna. The mathematics of this method is described in [4] and involves the concept of windowed Fourier transforms and frame based expansion.

In 2D the expansion functions on the aperture plane are defined by:

$$g_{mn}(t) = \pi^{-1/4} e^{imp_0 t} e^{-\frac{1}{2}(t-nq_0)^2}. \tag{1}$$

This corresponds to Gaussian beams linearly shifted and rotated in space. n, m are integers that define the translation and the rotation of a gaussian beam, respectively and p_0, q_0 are characteristic constants that define the form of the function.

An arbitrary aperture field $f(t)$ can then be expanded in the series:

$$f(t) = \sum_{mn} c_{mn} g_{mn}(t) \tag{2}$$

where

$$c_{mn} =< \tilde{g}_{mn}, f >= \int_{-\infty}^{\infty} \tilde{g}^*_{mn}(t) f(t) dt. \tag{3}$$

The function $\tilde{g}_{mn}$ is the dual function to g_{mn} in this paper called the frame function. It can be computed from g_{mn} as described in [4].

In this way an arbitrary aperture field is expanded in Gaussian fundamental beams which can be propagated to the next reflector in the beam wave-guide.

Computation of the reflected field

A mathematical surface S is considered which provides an aperture plane and encloses the reflector currents $\bar{J}_1$, see Figure 1. $\bar{E}_1, \bar{H}_1$ are generated by the currents $\bar{J}_1$ and the fields $\bar{E}_2$ and $\bar{H}_2$ are Maxwellian fields propagating in a region with no sources. The fields $\bar{E}_2$ and $\bar{H}_2$ propagate in the opposite direction of $\bar{E}_1, \bar{H}_1$. Assuming that S is an infinite plane orthogonal to the z-axis at $z = 0$ the reciprocity theorem reduces to:

$$\oint_S (\bar{E}_1^t \times \bar{H}_2^t - \bar{E}_2^t \times \bar{H}_1^t) \cdot d\bar{s} = \int_R (\bar{E}_2 \cdot \bar{J}_1) \cdot ds \tag{4}$$

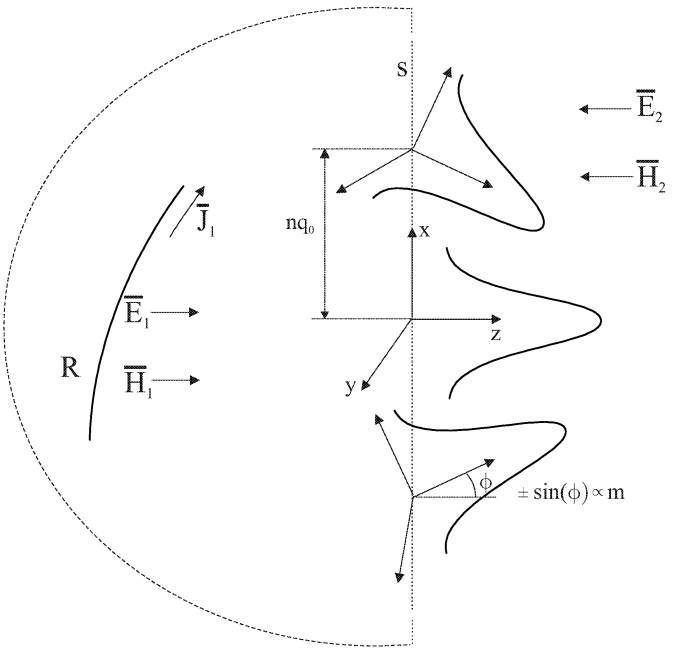

Figure 1: Illustration of the use of the reciprocity theorem and frame functions.

By a suitable choice of $\bar{E}_2$ and $\bar{H}_2$ the left hand side of (4) reduces to the integral in (3) such that the expansion coefficients c_{mn} can be computed from the right hand side of (4). The currents J_1 are the known PO currents on the reflector.

Hence, a method is constructed which uses the known PO currents on the reflector to compute a set of frame coefficients defined on an output plane by means of the reciprocity theorem. Once the coefficients are known the field value at any distance can be reconstructed as a sum of frame functions on the output plane weighted with the frame coefficients.

Results for a 3D ellipsoidal reflector

To evaluate the speed and accuracy of the frame based expansion method a comparison to PO at different frequencies and in different output planes is made.

A beam waveguide is considered which is operated at two frequencies 321 GHz and 3.21 THz. A coordinate system origin is placed at the reflection point of the ellipsoid where the centre ray combining the two focal points has a 90° reflection angle (see Fig. 2). In this coordinate system the two focal points are located in 63.5 mm along the negative x-direction and at 104.2 mm along the positive z-direction. The projection of the rim of the ellipsoid onto the plane orthogonal to the output direction along the z-axis, is a circle with diameter D=46.5 mm.

The product $p_0 * q_0$ must be $< 2\pi$ to ensure a stable expansion [4]. We have chosen $p_0 * q_0 = \pi/2$ with $q_0 = 1.5$ (see (1)) because it gives a simple frame function similar to the Gaussian fundamental function, but other values of p_0 and q_0 can also be used (and may prove to be more efficient - this will not be discussed in this paper).

The equations (1), (2), (3) must take into account the actual geometry of the system. Therefore, a scaling variable $x = Lt$ is introduced, where $L = w_0/\sqrt{2}$ and w_0 is the waist radius of the output beam. By this choice of scaling the width of the expansion frame functions matches the width of the output Gaussian beam in the waist. At the waist plane for 321 GHz, $L = 2.32$ mm and for 3.21 THz, L =0.245 mm. The input Gaussian

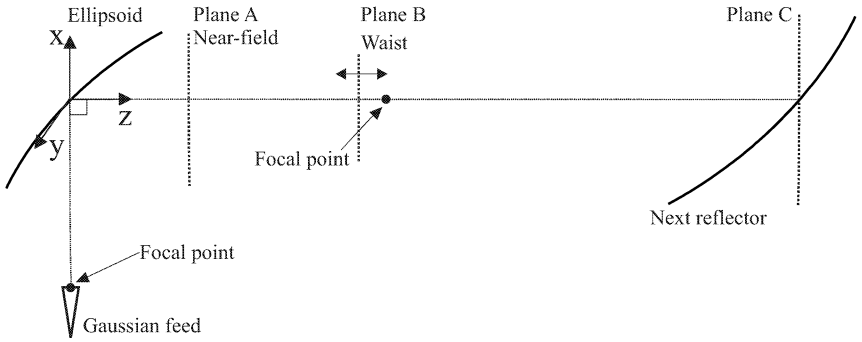

Figure 2: Geometry of the beam waveguide system.

beam has $w_0 = 2.12$ mm at 321 GHz and $w_0 = 0.212$ mm at 3.21 THz.

The Gaussian feed is radiating from 60 mm and 63.5 mm along the negative x-axis at 321 GHz and at 3.21 THz, respectively [1]. The beam is then scattered by the ellipsoid and the field is evaluated in three planes A, B and C (see Figure 2) :

A. The near-field plane of the reflector in a distance of 40 mm along the z-axis. The field is evaluated from $x = -25$ mm to $x = 25$ mm which is approx. the size of the projected diameter ($D = 46.5$ mm).

B. The plane located in the waist of the reflector which is placed at a distance of 88.7 mm for 321 GHz and in a distance of 103.9 mm for 3.21 THz along the z-axis. This is also the plane used to calculate the frame coefficients. The main lobe and approx. 4-5 side lobes are plotted for both frequencies along the x-axis.

C. The plane orthogonal to the ray along the z-axis at the reflection point of the next reflector in the beam waveguide at a distance of 240 mm along the z-axis. The field is evaluated from $x = -40$ mm to $x = 40$ mm which is the size of the projected diameter of the next reflector ($D = 80$ mm).

The speed of the frame method can be compared to the speed of the PO method by comparing the number of PO current elements to the number of frame coefficients.

A total of 3969 frame coefficients is used in the frame based expansion. In the expansion the n-number of the frame coefficients denotes the translation of the Gaussian beam and the m-number the rotation of the Gaussian beam (see (1) and Figure 1).

Therefore, the n-number must be chosen such that the Gaussian beams cover the field to be expanded. Furthermore, the m-number determines the degree of rotation of the Gaussian beams. By increasing or decreasing this number the area in which the radiated field is converged increases or diminishes.

[1] At 3.21 THz the Gaussian beam is radiating from the focal point

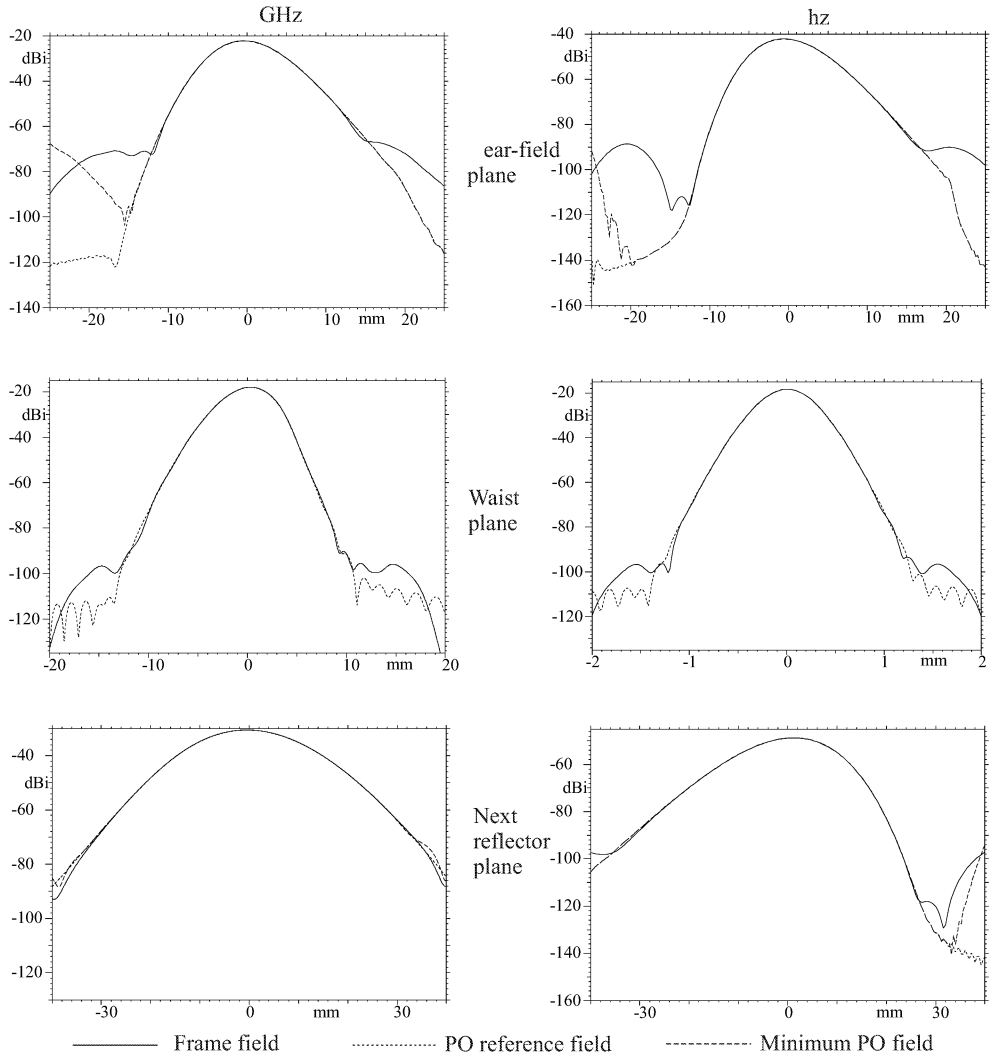

Figure 3: Near field at Plane A, waist field at plane B and field at the next reflector at plane C for 321 GHz and 3.21 THz (see Fig. 2 for set-up). Three types of fields are plotted: the frame field, a converged PO reference field and a PO field where the minimum number of PO points that ensures field convergence 45 dB below peak is used. The normalization of the curves is such that power flux in dB per unit area can be calculated by adding $20 \log_{10} k$. Only one PO curve is shown in Plane B, as the minimum PO solution and the reference PO curve overlap in this field region.

	Near field plane	Waist plane	Next reflector plane
PO 321 GHz	5186	961	315
PO 3.21 THz	507348	687	21377
Frame 321 GHz	3969	3969	3969
Frame 3.21 THz	3969	3969	3969

Figure 4: Table of the number of PO current elements for the minimum PO solution and the number of frame functions at 321 GHz and 3.21 THz that is used to obtain the results presented in Figure 3.

In Figure 3 the results of the tests are shown and table 4 contains the number of PO current elements and the number of frame functions at 321 GHz and 3.21 THz that are used to obtain the results presented in Figure 3. Two types of PO solutions are shown: The reference PO solution where a sufficiently large number of PO points is used to obtain field convergence over the whole output plane area and the minimum PO solution where the number of points are just sufficient for convergence down to -45 dB below the peak value.

The results show that a constant number of frame coefficient can be used for both frequencies on all output planes. In all cases the frame results are converged down to approx. -45dB below peak value. This stable results should be compared to PO where the necessary number of current elements is both frequency and position dependent. Especially in the near field at the high frequency a very high number of PO points must be used to make the field converge down to -45 dB. PO is, however, a fast method for computing the field in the waist of the beam waveguide, where the field is in phase. For the plane of the next reflector PO is very fast at low frequencies but becomes slow at high frequencies.

Conclusion

As a beam waveguide analysis tool at THz frequencies a frame based Gaussian beam method using a combination of two different techniques [1, 2] has been presented.

The method is frequency independent and only the number of the Gaussian beam functions determines the computational time. The accuracy of the method increases with m and n and can reach PO accuracy. However, for high m and n numbers the method can no longer compete with PO in speed. Also for simple field calculations where the field is in phase on the output plane, PO is a faster method.

For computing the near field the method proves to be very successful at THz frequencies, where PO is very time consuming when the near-field plane is close to the scattering object.

The method also has the advantage, that the fundamental Gaussian beam modes used in the expansion method are not limited to the paraxial region and a general reflector shape and rim can be handled in a beam waveguide system.

We believe that the frame based Gaussian beam method with the right tuning (eg. choice of the grid parameters p_0, q_0) can work as an intermediate accurate and stable alternative to the accurate, but in some cases slow method of PO and the fast and more unstable method of GO+GTD.

References

[1] *Recent Trends in the Analysis of Quasioptical systems,* W. A. Imbriale and D.J. Hoppe, Paper from "Davos Proceedings 2000", Switzerland email : william.a.imbriale@jpl.nasa.gov

[2] *Diffracted Gaussian beam analysis of quasi-optical multi-reflector systems,* C. Rieckmann, M. R. Rayner and C. Parini, Paper from "Davos Proceedings 2000", Switzerland email : m.r.rayner@elec.qmw.ac.uk

[3] *Alternative to Gabor's representation of plane aperture radiation,* D. Lugara and C. Letrou, Electronics letter 26th novemeber 1998 Vol. 34 No. 24

[4] *The wavelet Transform, Time-Frequency Localization and Signal Analyis,* I. Daubechies, IEEE Transactions on Information Theory,m vol. 36, no. 5, september 1990

A SUPERCONDUCTIVE PARALLEL JUNCTION ARRAY MIXER FOR VERY WIDE BAND HETERODYNE SUBMILLIMETER-WAVE SPECTROMETRY

F. Boussaha, Y. Delorme, M. Salez, M.H. Chung[2], F. Dauplay, B. Lecomte, J.-G. Caputo[3], V. Thevenet[1]

DEMIRM, Observatoire de Paris, 77 avenue Denfert-Rochereau, 75014 PARIS-France
[1]DASGAL, Observatoire de Paris, 77 avenue Denfert-Rochereau, 75014 PARIS-France
[2]Taeduk Radio Astronomy Observatory San 36-1, Whaam-dong, Yusong-gu Taejon 305-348, South Korea
[3]INSA-LMI-Rouen, Place Emile blondel B.P 08, 76131 Mont Saint Aignan Cedex, France

Abstract

The study of submillimeter-wave radiation in astronomy and atmospheric sciences requires increasingly performant receivers, in particular allowing extended spectral line surveys. To this end, we are developing a quantum-noise limited heterodyne receiver based on SIS junction parallel arrays with broad (larger than 30%) fixed tuned bandwidth. Simulations show that networks of junctions (N>2) of micronic size, embedded in a superconducting microstrip line, can provide a bandwidth in excess of the ultimate limit for a single or even twin-junction device. These circuits can be viewed as passband filters which have been optimized by varying the spacings between junctions. The results of simulations are confirmed by the first heterodyne measurements in the 480-650GHz bandwidth, and by preliminary FTS measurements beyond. The influence of the Josephson effect in these devices is also investigated.

I - Introduction

In the mid 90s, Shi et al [1,2] of Nobeyama radio-observatory presented a new mixer design based on the association of several parallel SIS junctions in order to increase the bandwidth. They succeeded with five then ten junction arrays, in which junctions are equidistant in superconductive microstrip line. In 1998, we simulated this type of circuits and identical results were obtained. Like Shi et al, we have noted widening bandwith but accompanied by ripples especially at high frequency. Extending the principle, we simulated a new structure with the same number of junctions but with a nonuniform distribution (fig. 1.). Nonuniform arrays make it possible to further improve both frequency response and sensitivity [3]. Since, Takeda et al [4] are also developping inhomogeneous distributed junction array.

On the basis of these simulations, we compared heterodyne performance of conventional single-junction and multijunction array coming from the same wafer which has about 4.5 kA/cm² current density. The single-junction is matched by one short inductive section of microstrip followed by Tchebytchev transformer . In the multijunction approch, the mixer, composed by N junctions connected in parallel within a superconductive microstrip, is optimized like passeband filter. In this case, the SIS junctions are represented by their intrinsic parameters (e.g., capacitance, normal resistance) and the different length microstrip sections by the induced inductances [3].

The devices use the same RF filter and the same antenna. Excellent I-V characteristics of 2 and 5 parallel junction (1 or 2 μm²) arrays were obtained, with current densities : 4, 6 and 13 kA/cm². The receiver performance for some of these devices has been

measered over the frequency range 480 GHz to 640 GHz, because of the availability of measurement equipments.

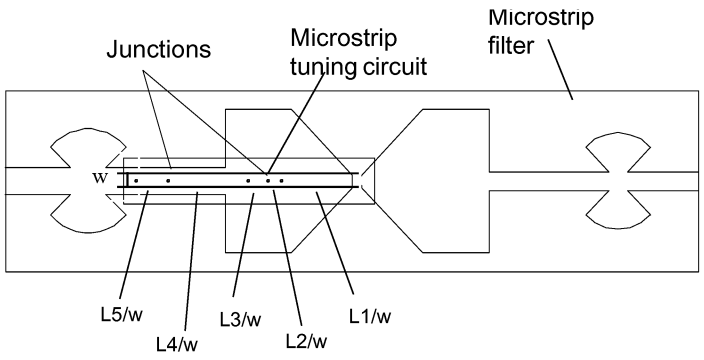

Fig. 1. Mask of non uniform distributed five junction array : L5/w=3.6, L4/w=8, L3/w=2, L2/w=1, L1/w=9.9 (w=5µm)

II-Parallel junction array fabrication process

Our process fabrication is based on "Selective Niobium Etching Process" (SNEP) [5,6]. A trilayer of Nb/Al-Al_2O_3/Nb film was first sputtered, using a DC magneton, on a 200 micrometer thick quartz quartz substrate. The first 200 nm thick Nb layer was deposited with a power of 600 W, at a rate of 2.2 nm/s ; In order to get a homogeneous layer of Al, it is necessary to let cool the substrate (1 hour in our case) before its deposit. The 10 nm thick Al layer was deposited with power of 100 W, at a rate of 0.5 nm/s. The tunnel barrier was built by thermal oxidation of the Al layer, using pure O_2 at pressure of 10^{-2} mbar during 30 mn. To prevent any damage of Al layer, The deposition of the 100 nm top Nb layer was performed at a reduced power : 300 W, 1nm/s. A positive S1828 photoresist was used to define the RF filters and DC lines. The Nb/Al-Al_2O_3/Nb film in excess was etched away with a reactive ion etching process : the SF_6 flow was 60 sccm with 60 W of RF power. The next step consists in the definition of junctions area. The photolithography process was accurately calibrated to get simultaneously several small junctions with same area, in confined space. The upper layer of Nb is etched with 20 sccm of SF_6 and 6 sccm of O_2 at a pressure of 3.10^{-2} mbar and a power of 60 W ; the etching rate was around 3 nm/s. To prevent short-circuits between the base electrode and the Nb contacts, the resist is etched by high pressure O_2 plasma at a flow of 80 sccm and 80 W of RF power. A 250 nm of SiO is evaporated to isolate the junctions area and the excess is removed by lift-off. After cleaning with an Ar RF plasma, the junctions are connected by a 400 nm film sputtered in four time at a rate of 1 nm/s and 300 W and patterned by lift-off.. Finally, a 200 nm gold film was evaporated follow-up the lift-off in order to obtain the electrical contact. The yield was about 80 %.

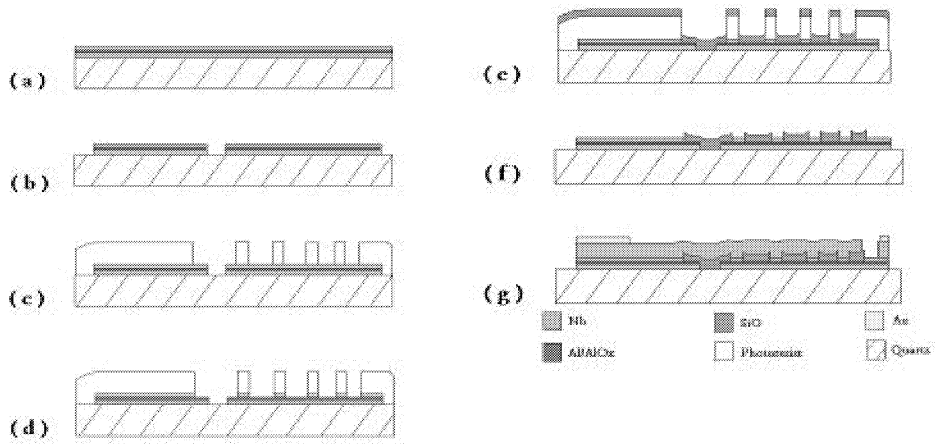

Fig.-2. Parallel junction array process fabrication (a) Sputtering Nb/ Al-Al_2O_3/Nb deposition (b) Trilayer etching : definition of RF filter (c) Definition of multijunctions (d) Upper electrode etching (e) Self-aligned deposition of SiO insulating layer (f) Appearance of multijunctions (g) Nb interconnection layer and gold contact pads

III-Results

All the devices were measured in the same mixer waveguide block at 4.2 K. DC and IF connections to the devices are made at one end through a SMA connector and at the other end via a ground return to the mixer block with gold wire. No IF matching circuit was used. The IF signal is amplified by a 4-8GHz cryogenic HEMT preamplifier. The double sideband (DSB) receiver noise temperature is obtained by measurement of the Y factor method.

The five parallel 1μm^2 junction array and 2μm^2 single-junction normal resistance were respectivily around 12 Ω and 30 Ω. We assumed that junction specific capacitance is 80 $fF/\mu m^2$. The IV characteristic pumped by 650 GHz LO radiation of multijunction array is shown in figure 3. A receiver noise temperature of 176 K DSB was meseared at this frequency. Over the frequency range 480 GHz to 640 GHz, the noise temperature of both single-junction and 5 junction array is shown in figure 4. With the multijonctions, we measured around 400 K noise temperature almost in all bandwidth, unlike single-junction response frequency which quickly degrades from 560 GHz, to reach average 1300K over the rest of the bandwith. Elsewhere, the noise temperature remains high because of the poorly matched IF output on one hand, and because of the large contributions of Rf quasi-optics noises (bad mixer block) on the other hand. The equivalent noise temperature of IF-chain was about 25 K. Using the "intersecting lines" method [8], we estimated the equivalent noise temperature of Rf contributions at all frequencies. For unkown reasons, we found very high values : average 250 K. The worst noise temperature was at 605 GHz LO. This same frequency corresponds to a dip in the FTS (fig. 5.) for jc=13 kA/cm^2 (heterodyne measurements not yet done). Possibly, this resonance is due to the mixer block and device independent.

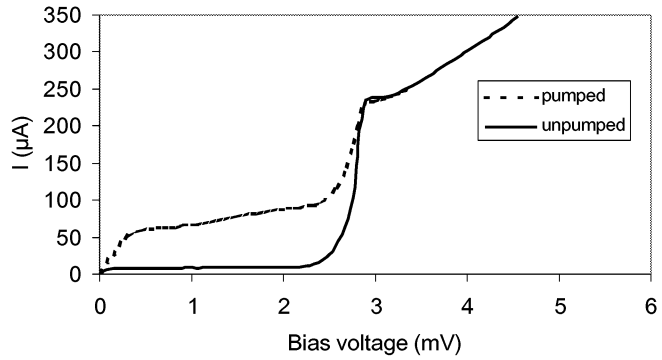

Fig. 3. Unpumped and pumped IV curves of 5 parallel junction arrays (4,5 kA/cm²) by applied microwave radiation at 650 GHz

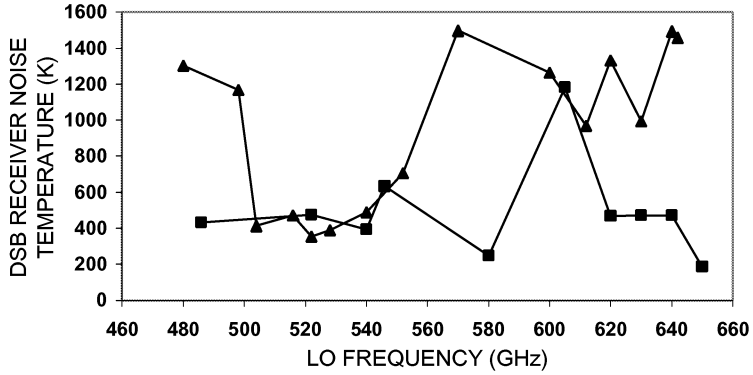

Fig. 4. Receiver noise temperature versus LO freqency for single junction (triangles) and for 5 parallel junction array (squares)

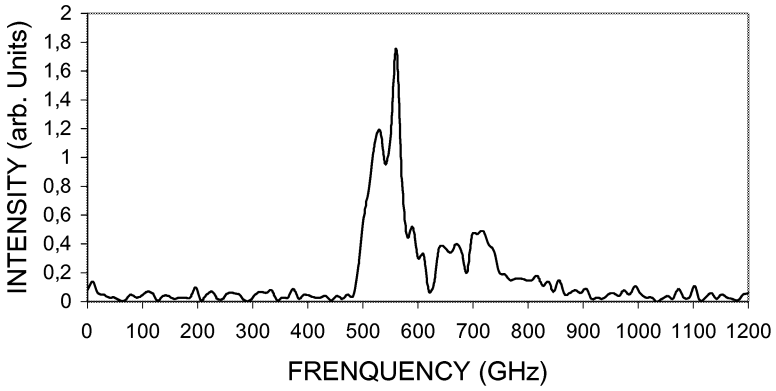

Fig. 5. FTS response of a 5 parallel junction array with jc=13 kA/cm².

Josephson effect

The figure 5 shows the evolution of critical current I_{max} at zero bias-voltage vesus applied magnetic field. The Josephson current cannot be supressed entirely and there remains a residual current about 2 to 5μA except for one value of the current in the coils (6.45mA).

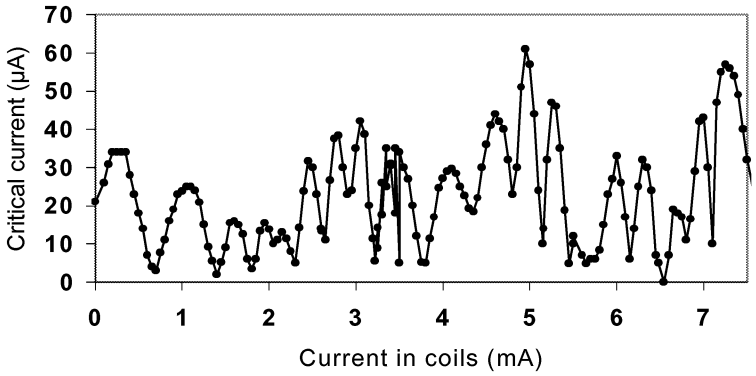

Fig. 5. Evolution of critical Josephson current versus magnetic field in multijunction array

In the 5 junction array, using a constant voltage bias, several steps and negative resistances have been observed in both the unpumped and pumped IV curves, as shown by figures 6-a and 6-b (for 542 GHz LO), enhanced or reduced by the magnetic field.

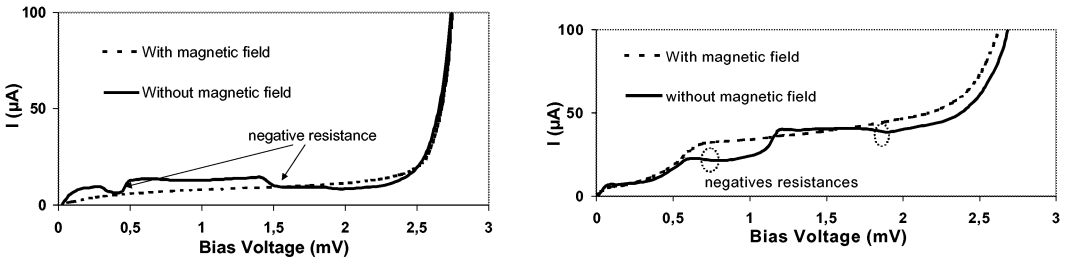

(a) (b)

Fig. 6. Multijunction array : negatives resistances in both (a) unpumped and (b) pumped IV by applied microwave radiation at 542 GHz LO

Although similar steps induced by Josephson pair tunneling, with or without LO, are a common feature of SIS mixers, those steps in 5-junction arrays have a qualitatively different look and behaviour. Their oddity is particularly striking when no LO nor any magnetic field is applied, as they strongly remind of the "zero field steps" (ZFS) seen in long Josephson junctions in which solitons propagate. Indeed, we observed three steps at 0.5, 1 and 1.35mV bias (fig. 8.).

If the multijunction structure, which is electrically equivalent to a long junction, can increase the mixer bandwidth, it also supports static and dynamic Josephson current modes different and more complex than the single junction. This was a theoretical expectation of ours, and more will be presented on this in another aticle. It potentially has consequences on mixer sensitivity. In the presence of LO, the steps are more difficult to suppress than in single-junction circuits.

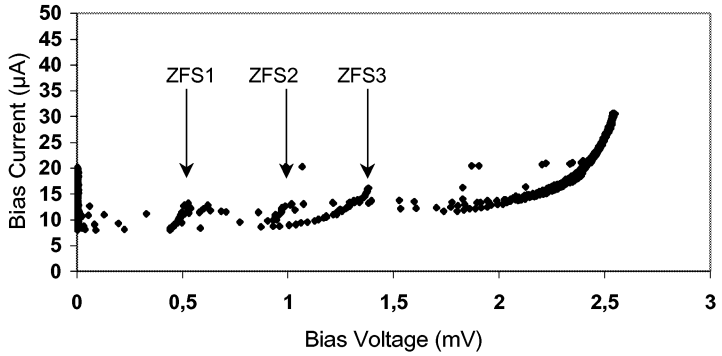

Fig. 8. ZFD apparition in multijunction array

The figure 9 shows the noise temperature measured with 5 junction array versus consumed OL power at 650 GHz. We note that there is an optimal power around 25-40 nW, but also that is another local minimum at higher power can exist. Thus, the LO power is not necessarily proportional to number of junctions. This result is important and was predicted by simulations based on Tucker theory [3,7]. In figure 10, each curve represents one junction. We note that a limited number of junctions provide the mixing while the others play a passive role.

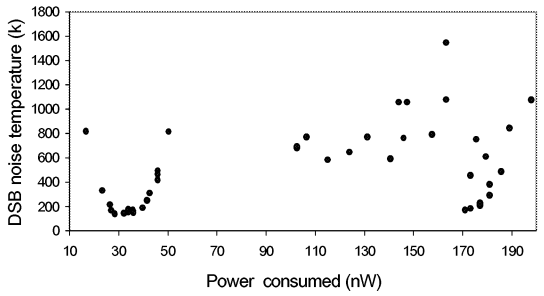

Fig. 9. 650 GHz LO power consumed by the 5 junction array

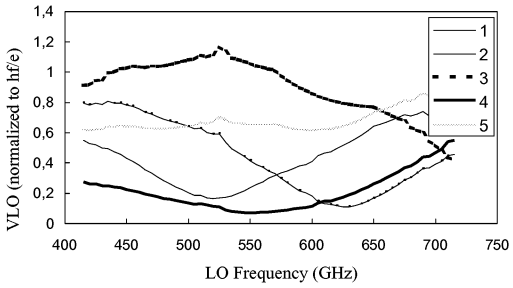

Fig. 10. Simulation of LO power consumed for each junction

IV-Conclusion

We succeeded to obtain high quality 5 junction array at medium and high current density (4.5,6 and 13 kA/cm²) in spite of the difficulty of fabricating arrays of rigorously identical junctions. The comparative heterodyne measurements of single junctions and distributed junction arrays confirm the simulations about widened bandwidth and average power necessary to drive the mixer. The Josephson current manifestation behavior is certainly more significant but does not seem to influence the SIS mixing operation.

Acknowledgment

The authors would like to thanks J.M. Krieg, G. Beaudin and Y. Viala for their continued support. We also thank B. Jackson from SRON for FTS measurement. The multijunction array development is funded by the french space agency (CNES, contract # 714/cnes/99/7759/00) and the Institut National des Sciences de l'Univers (INSU).

References

[1] S.-C. Shi, T. Noguchi and J. Inatani, 1997, "Analysis of the bandwidth performance of SIS mixers with distributed junction arrays", *Proc. 8th International Symposium on Space Terahertz Tech*. 81.
[2] S.-C. Shi, T. Noguchi, J. Inatani, Y. Irimajiri, and T. Saito, 1998, "Experimental results of SIS mixers with distributed junction arrays", *Proc. 9th International Symposium on Space Terahertz Tech*. 223
[3] M. Salez, Y. Delorme, M. H. Chung, F. Dauplay, "Simulated performance of multi-junction parallel array SIS mixers for ultra broadband submillimeter-wave applications", *Proc. 11th International Symposium on Space Terahertz Tech*. 343.
[4] M.Takeda, T.Noguchi and S.-C Shi, "Predicted Performance of superconductor-Insulator-Superconductor Mixers with Inhomogemous Distributed Junction Arrays", , Jpn. J. Appl. Phy., 39, PP.5095-5098 (2000).
[5] Yuda M, Kuroda K and Nakamo J 1987 Japan. J. Appl.Phys.26
[6] Gurvitch M, Washington M A, Huggins H A, Rowell TM 1983 IEEE trans. Mag 19 791
[7] J. R. Tucker and M. J. Feldman, 1985, "Quantum detection at millimeter wavelengths", *Rev. Mod. Phys*., **57,** 1055
[8] Qing Ke and J. Feldman " A Technique for noise measurement of SIS Receivers", 1994 IEEE trans. Mag 42, 752

WaFIRS, a Waveguide Far-IR Spectrometer:
Enabling Space-Borne Spectroscopy of High-z Galaxies in the Far-IR and Submm.

C.M. Bradford[1], J.J. Bock[1,2], M. Dragovan[2],
L. Earle[3], J. Glenn[3], B. Naylor[1], H. Nguyen[1,2], J. Zmuidzinas[1]

[1]Mail Code 320-47, California Institute of Technology, Pasadena, CA,
[2]Jet Propulsion Laboratory, Pasadena, CA,
[3]CASA, University of Colorado, Boulder, CO

Author Contact: bradford@caltech.edu

ABSTRACT

The discovery of galaxies beyond z~1 which emit the bulk of their luminosity at long wavelengths has demonstrated the need for high-sensitivity, broadband spectroscopy in the far-IR/submm/mm bands. Because many of these sources are not detectable in the optical, long-wavelength spectroscopy is key to measuring their redshifts and ISM conditions. The continuum source list will increase in the next decade with new ground-based instruments (SCUBA2, Bolocam, MAMBO) and the surveys of HSO and SIRTF. Yet the planned spectroscopic capabilities lag behind, primarily due to the difficulty in scaling existing IR spectrograph designs to longer wavelengths.

To overcome these limitations, we are developing WaFIRS, a novel concept for long-wavelength spectroscopy which utilizes a parallel-plate waveguide and a curved diffraction grating. WaFIRS provides the large (~60%) instantaneous bandwidth and high throughput of a conventional grating system, but offers a dramatic reduction in volume and mass. WaFIRS requires no space overheads for extra optical elements beyond the diffraction grating itself, and is two-dimensional because the propagation is confined between two parallel plates. Thus several modules could be stacked to multiplex either spatially or in different frequency bands. The size and mass savings provide opportunities for spectroscopy from space-borne observatories which would be impractical with conventional spectrographs. With background-limited detectors and a cooled 3.5 telescope, the line sensitivity would be better than that of ALMA, with instantaneous broad-band coverage. We have built and tested a WaFIRS prototype for 1-1.6 mm, and are currently constructing Z-Spec, a 100 mK model to be used as a ground-based $\lambda/\Delta\lambda$~350 submillimeter galaxy redshift machine.

1. Scientific Motivation

The advent of large-format bolometer arrays for wavelengths around 1 mm (SCUBA, MAMBO) had revealed a new class of galaxies which are likely at medium to high redshift. These sources are cosmologically significant – their counts reproduce much of the diffuse far-IR / submillimeter background radiation, representing the energy generated by all galaxies over the history of the universe (Blain et al.1999, Barger et al, 1999). These submillimeter galaxies are luminous systems similar to the nearby IR galaxies discovered with IRAS. Of the nearly 200 submillimeter galaxies discovered thus far, only a small fraction have confirmed spectroscopic redshifts and well-determined properties at other wavelengths. This is because the sources are very dusty with high extinction at short wavelengths, the optical and UV energy is almost entirely reprocessed and reradiated between $\lambda = 50$ μm and 1 mm, making the optical counterparts too faint to be detectable. While there are spectral features that could be used in the millimeter / submillimeter, the instantaneous bandwidth of heterodyne millimeter-wave receivers is currently a small fraction of unity, so searching for lines in sources with unknown redshifts is impractical.

The long-wavelength continuum source list will only increase in the next decade with new ground-based instruments (SCUBA2, Bolocam) and the confusion-limited surveys of HSO and SIRTF. The recently discovered submillimeter galaxies, and their soon-to-be-discovered far-IR cousins demonstrate the need for broad-band spectroscopy in the far-IR / submillimeter / millimeter bands. Long wavelength spectroscopy with large instantaneous bandwidth is the key to measuring these sources' redshifts, which constrain their luminosities, sizes, and masses. Moreover, the wide variety of spectral features in the mid- and far-IR provide information on the conditions in the interstellar medium and contrain the luminosity source(s). The types of spectral features include:

- Fine Structure Lines. Species include Ne^{+}, S^{++}, Si^{+}, C^{+}, C^{0}, O^{0}, O^{++}, with luminosities from 10^{-4} to 3×10^{-3} of the total bolometric luminosity. These lines also measure the gas conditions and UV field properties in regions where stellar or AGN luminosity is input into the ISM. Mid- and far-IR fine structure lines have been used to study the starburst conditions in nearby galaxies (Stacey et al., 1991, Lord et al, 1994, Colbert et al. 1999, Carral et al. 1994, Malhotra et al, 2001) and recently, in as an AGN / starburst discriminator in ULIGs (Genzel et al, 1998).

- PAH Bands. These features are very prominent in starburst systems, a well-studied redshift template with luminosities typically 1-4 % of L_{bol}. (see Helou et al., 2001, Tran et al., 2001.)

- Molecular Rotational Transitions. Millimeter and submillimeter CO rotation is the dominant coolant of molecular gas and a probe of its temperature and density. Mid- and high-J lines trace warm gas associated with UV or shock heating of dense molecular gas (Jaffe et al, 1985, Harris et al, 1993 Ward et al., 2002, Bradford et al., 2001). Though not energetically important, other abundant species such as OH and

CH, constrain molecular gas column densities and abundances through absorption transitions (Bradford et al, 1999, Smith et al, 2001, Fischer et al 2001). These lines also have potential as a redshift probe for extremely obscured sources (those weak in fine structure lines) like Arp 220.

Table 1 (below) examines the various ISM probes available in the far-IR and submillimeter. The redshift range is that which would be observable with a spectrometer operating from λ = 20 μm to 1 mm.

TABLE 1. Far-IR SPECTROSCOPIC PROBES

SPECIES	WAVELENGTH	DIAGNOSTIC UTILITY	REDSHIFTS
		IONIZED GAS	
O IV	54.9	Primarily AGN.	0 - 17
S IV	10.5	Probes of the gas density and	0.9 - 100
O III	51.2, 88.4	UV field hardness in star-	0 - 18
S III	18.7, 34.8	formation H II regions.	0 - 50
N III	57.3	Provides effective temperature	0 - 16
Ne II	12.8	of hottest stars.	0 - 75
N II	122, 205	Diffuse interstellar H II regions.	0 - 7
		NEUTRAL ATOMIC GAS	
C II	158	Density and temperature probes	0 - 5
Si II	34.81	of photodissociated neutral-gas	0 - 30
O I	63, 145	interface between H II regions	0 - 15
C I	370, 610	and molecular clouds.	0 - 1.7
		MOLECULAR GAS	
H2 rotation	28.1 and shortward	Arises in dense, 100 - 1000 K molecular gas - often shock heated. Coolant of first gravitational collapse.	0 - 100
CO rotation	2600 and shortward	Primary coolant of molecular gas - probes pressure and temperature. Isotopes provide column densities, total gas mass	0 - 3
		DUST	
PAH	7.7, 11.3	Indicates star formation	0.8 - 100

2. Sensitivity from Space

Unfortunately, though there are a wealth of diagnostics for dusty galaxies in the far-IR and submillimeter, the wavelength range is not generally accessible from the ground. The atmospheric windows shortward of λ~700 μm are accessible only occasionally from mountaintop sites. Between 30 and 200 μm, the atmosphere is completely opaque from all

terrestrial sites. While there are space missions planned to observe these wavelengths in the continuum (SIRTF, HSO), there is very limited spectroscopic capability planned for these wavelengths from space. The sensitivity attainable from a modest (diameter ~ 3.5 m) cool (T < 15 K) space telescope is dramatically better than what is currently planned between SIRTF and ALMA (see Figure 1). The effective line survey speed, proportional to the inverse of the sensitivity squared divided by the instantaneous bandwidth shows a more

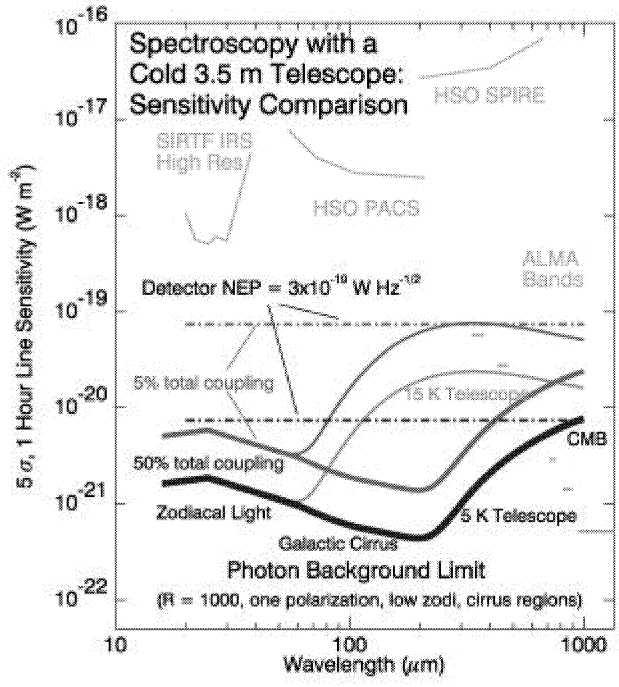

Figure 1. Spectral sensitivity on a cold 3.5 m space telescope. The 50% and 5% total couplings are conservative bounds to what might be achieved with a real spectrometer. Background noise is calculated from the fluctuation in the Zodical and cirrus backgrounds, toward patches of low intensity. If historical trends continue, background-limited performance at these frequencies will be possible, and gains of 2-4 orders of magnitude in sensitivity could be achieved.

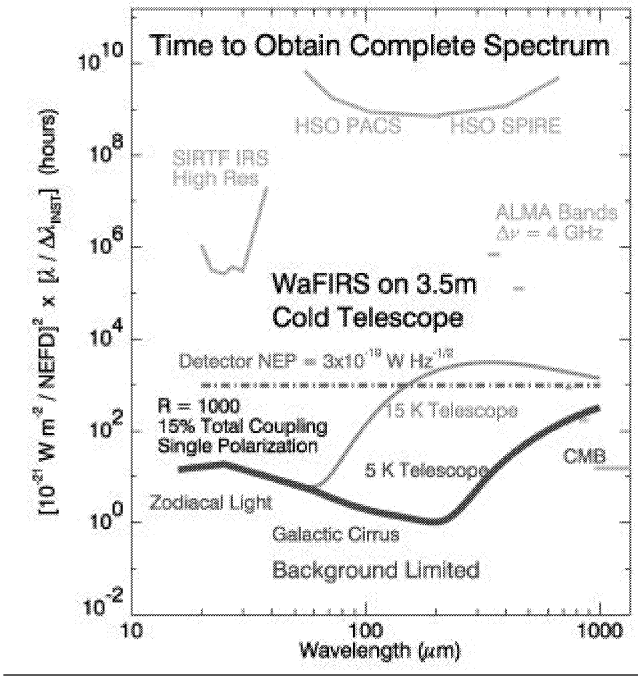

Figure 2. Sensitivity calculations similar to those of Figure 1, but including the effect of instrumental bandwidth. Under reasonable assumptions (15% efficiency, one polarization only), a broad-band spectrometer on a cold 3.5 meter telescope will have line survey speeds 6 or more orders of magnitude faster than the spectrometers of HSO, making far-IR line surveys practical. Such an instrument would be faster than ALMA for $\lambda<600$ μm.

dramatic gain of several orders of magnitude (see Figure 2). These large potential gains are possible in part because the raw sensitivity improves substantially by cooling the telescope to 15 K or lower (HSO is expected to operate at about 60 K). Another key aspect for observing sources with unknown redshifts is that the spectrometers on HSO are not optimized for line surveys. PACS is an imaging spectrometer with only a 1% instantaneous bandwidth, and SPIRE is a Fourier transform instrument with noise from the full band on the detectors at once. For an 8 meter class cold telescope such as SAFaIR, the sensitivity advantages are improved an additional factor of more than 5 beyond what is plotted in Figures 1 & 2.

3. Technical Background: Why a Waveguide Spectrometer

While there are a variety of options for a far-IR and submillimeter spectrometer, some are better suited to the science goals outlined above – observing high-redshift dusty galaxies with high sensitivity. Sources will be taken from preceeding continuum surveys, and will be spatially unresolved, so that imaging is not particularly important. In most cases, the redshifts will not be known in advance and the diagnostic lines are distributed over a broad spectral range, so a large instantaneous spectral bandwidth is critical. Given that in the far-

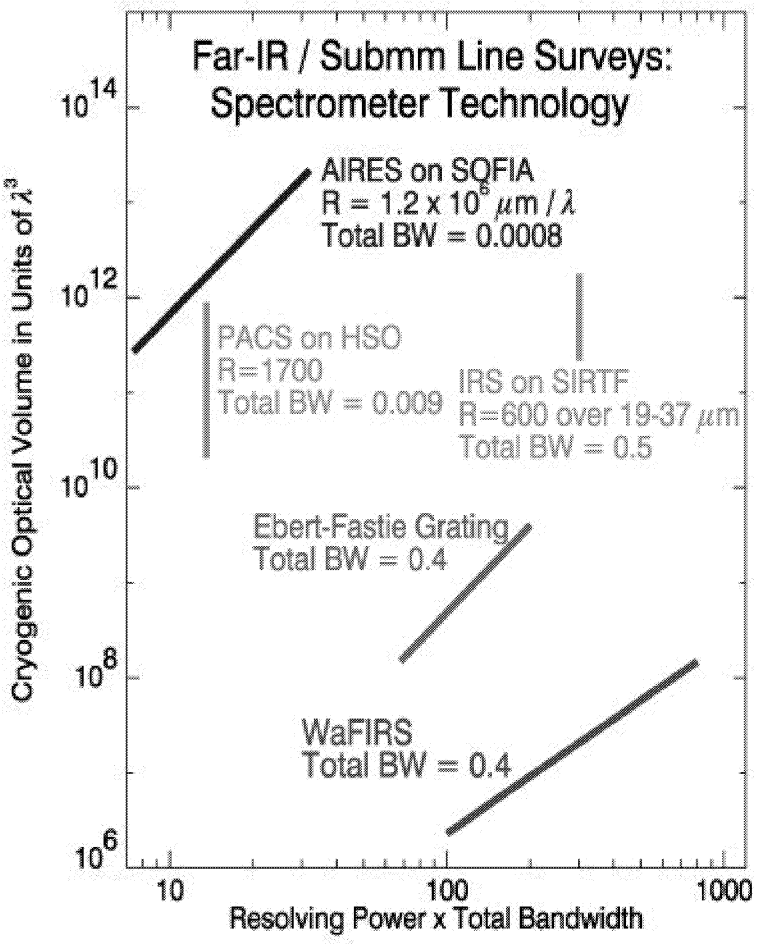

Figure 3. Sizes of existing spectrometer modules compared with their survey capability. The spectral survey capability of an instrument is given by its resolving power X total bandwidth. Modest resolution, broad-bandwidth systems exist (eg the SIRTF IRS modules) but are prohibitively large when scaled to far-IR and submillimeter wavelengths. WaFIRS offer a compact broadband system for longer wavelengths.

IR and submillimeter, the total number of detectors is typically a constraint, it therefore desirable to have the detectors arrayed spectrally rather than spatially, and an imaging monochromator such as a Fabry-Perot is not the instrument of choice. For ultimate sensitivity, a Fourier transform spectrometer (FTS) is not ideal because it places the entire spectral bandwidth and its associated photon noise onto a single detector. An FTS is appropriate only when using a detector which is not background-limited at the spectrometer resolution.

The obvious choice for background-limited point-source spectroscopy is a diffraction grating. Gratings have been used in astronomy for decades, and recently in the Infrared Space Observatory (ISO) as cryogenic, space-borne infrared spectrometers. When operated in first order, a grating naturally provides an octave of instantaneous bandwidth, and the resolution can be increased by increasing the grating size, roughly $d \sim \lambda \times R/2$. At far-IR and submillimeter wavelengths, this size quickly becomes prohibitively large, especially since real instruments are typically larger than the fundamental limit because they include collimating and imaging mirrors as well as order-sorting elements. For example, each of the spectrometer modules on SIRTF, measures about 40 x 15 x 20 cm, with a maximum $\lambda \times R$ product of 2 cm (R = 600 at 37 μm). To scale such an instrument up for a wavelength of 200 μm would result in a long dimension of over 2 meters, prohibitive for a space mission. Another example is the PACs spectrometer for HSO, an image slicing spectrometer which provides R=1500 out to 200 μm. The size of the cryogenic enclosure is quite large, roughly 80 cm x 80 cm x 30 cm, and because the instrument is designed for imaging spectroscopy; it only provides 16 spectral resolution elements, or 1% instantaneous bandwidth. The sizes of existing spectrometers are shown in Figure 3 in units of λ^3, plotted against the total number of spectral resolution elements.

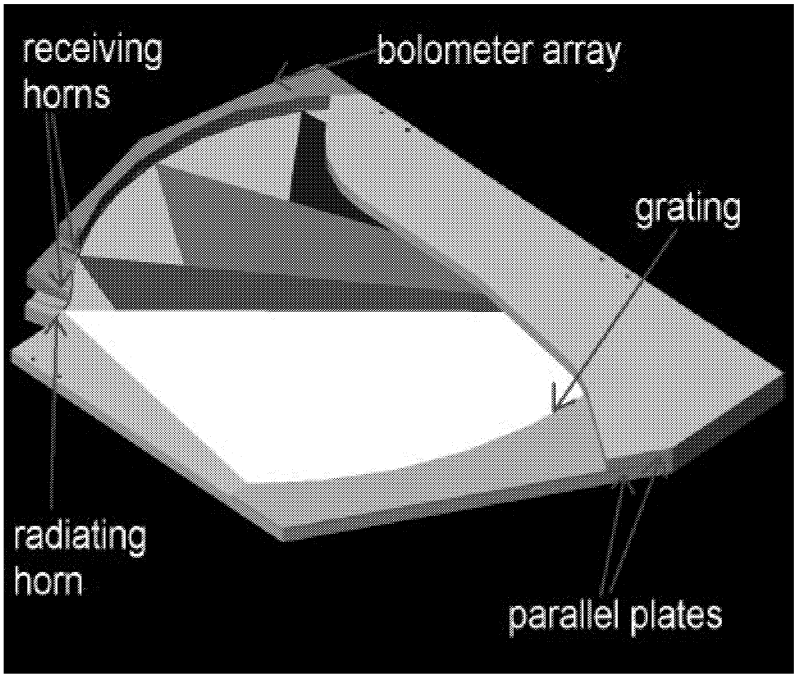

Figure 4. WaFIRS Concept: Rowland grating in parallel plate waveguide. The light enters the parallel plate medium from the radiating horn and illuminates the curved diffraction grating. Each facet of the grating is individually positioned. Bolometers are positioned behind receiving horns on the focal curve.

To provide spectroscopic follow-up capability for the continuum surveys and to provide the foundation for further spectroscopic study, we are developing a new technology for a compact, broad-band spectrometer for the far-IR and submillimeter. WaFIRS, the Waveguide Far-IR Spectrometer, consists of a curved diffraction grating, entrance feed horn and detector feed horns all inside a parallel-plate propagation medium (see Figure 4). The spectrometer need be only a few wavelengths thick due to the two-dimensional geometry. Several spectrometers could easily be stacked to provide multiple wavelength bands, multiple spatial pixels, or both. The curved diffraction grating is the most space-efficient grating configuration possible because it both disperses and focuses the light. The grating can be nearly as large as the largest spectrometer dimension, with very little overhead, thus providing the maximum resolving power for a given cryogenic volume. Furthermore, the grating is used in first order which provides up to an octave of instantaneous bandwidth for any given module. The dramatic reduction in volume relative to conventional spectrometers is illustrated in Figure 3. The design has no moving parts and, once assembled, is completely light tight. While the concept has not been applied in the far-IR or submillimeter before, similar systems have been produced for near-IR and optical applications. The compact, lightweight geometry and robust construction make WaFIRS extremely well-suited for airborne, ballon and space-based spectroscopy.

4. WaFIRS Technical Discussion:

WaFIRS is conceptually similar to the slit spectrometers with curved gratings used by Rowland, Wadsworth, Eagle and other shortly after Rowland made the first curved grating around the beginning of the 20th century (see Born & Wolf, 1999). Though WaFIRS uses the same basic layout, it is based on propagation of a single electromagnetic mode in a two-dimensional medium bounded by parallel, conducting plates. The propagation mode is analagous to the TE_10 mode in rectangular waveguide -- the electric field is normal to the direction of propagation, with a half-wave vertical profile which vanishes at the top and bottom. [The dispersion relation is that of waveguide, namely as the frequency decreases toward cutoff, the wavelength increases infinitely.] Light is injected into a WaFIRS module with a horn which provides a suitable illumination pattern on the grating. The grating is in first order, and diffracts the light to a circular focal curve which extends over nearly 90 degrees of arc, on which the feed-horn coupled bolometers are arrayed. Figure 4 shows a sketch of the WaFIRS concept.

We have designed and built a prototype for wavelengths of 1-1.6 mm. The spectral resolving power is between 180-250 and the overall size only 56 cm x 42 cm x 2.5 cm. The key to the design is the placement of each facet individually such that for two frequencies, the change in propagation phase from the input to the output is exactly 2π between two adjacent facets, providing perfect (stigmatic) performance at these two frequencies. In our λ=1-1.6 mm prototype, there are 400 facets, and the resulting grating curve has a length of 51 cm. To evaluate the spectrometer designs, we perform diffraction calculations which account for the amplitude and phase produced by the input horn at each facet, then sum the contributions from all the facets at each output location. The model therefore includes

diffraction and geometric optics, at a scalar approximation. The illumination of the grating is important -- a larger pattern from a smaller input horn produces higher spectral resolution, but lower efficiency, due to power which is lost beyond the edges of the grating. For the first prototype, we have chosen a 3.5 mm input horn which illuminates the grating with a power pattern of FWHM = 110 (180) facets at 1.0 mm (1.6 mm). The spectral resolution ($\nu / \Delta\nu_{FWHM}$) that results is 180 (250) at 1.0 (1.6 mm). Because the facet positions are individually calculated, the geometric aberrations are completely negligible, and the system is strongly diffraction limited.

4.1 Spectrometer Efficiency

Estimates of the spectrometer efficiency must include losses from: 1) Waveguide propagation with finite-conductivity plates, 2) diffraction efficiency into the proper order (i.e. blaze efficiency), and 3) illumination losses. Figure 5 plots our calculations of these contributions, and their product. The waveguide propagation loss is given by standard expressions (see Pozar, 1998), the 3 % loss for total propagation from input to detector can be achieved by polishing and gold-plating the parallel plates. In our prototype operated

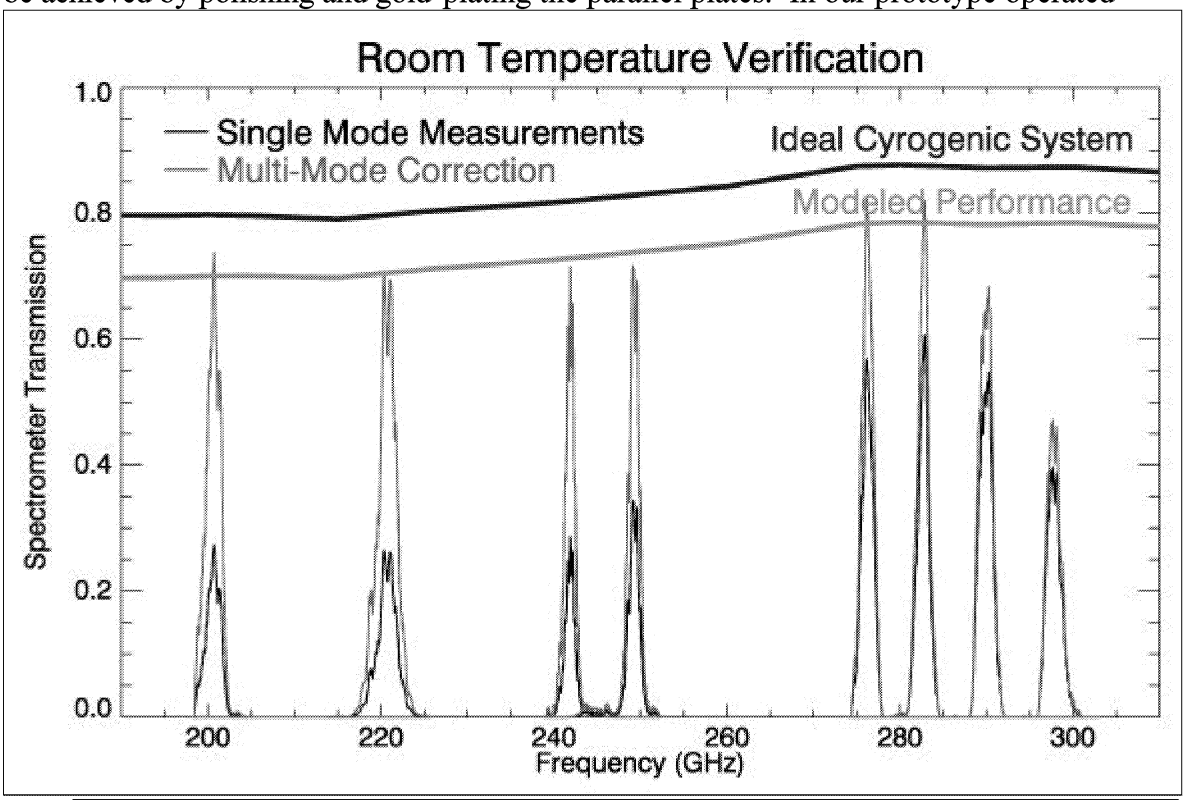

Figure 5. Testing of the first WaFIRS prototype. Measurements were made with a detector behind a single-mode feed, which does not couple all the power in the profile. Accounting for this coupling inefficiency produces the corrected curves which are close to performance predicted by the waveguide propagation loss, spillover loss. The high-frequency degradation is due to a blaze inefficiency, which will be corrected in future designs.

with only nickel coated plates and an aluminum grating, the propagation efficiency is somewhat lower. The blaze efficiency is calculated with commercially available software, applicable since with the waveguide propagation mode, the radiation is effectively in TE grating mode. These same calculations are the basis of our choice of a 29° blaze angle. Spillover losses are discussed above, they range from 89% to 94%. The net efficiency of a gold-plated cryogenic system is expected to be higher than 80% across our band.

4.2 Prototype Testing

We have measured the performance of our prototype using a backward wave oscillator (BWO) as a sweeping millimeter wave source (Figure 5,6, below). The power was measured with a diode detector in single-mode waveguide. At each frequency, a very small feed horn was used to measure the size of the intrinsic profile, then the total coupling as measured with a larger (but still single mode) feed is deconvolved using this profile. The results are quite close to our predictions over much of the band. We are investigating the reason for the loss in performance at the highest frequencies, it is likely a blaze efficiency.

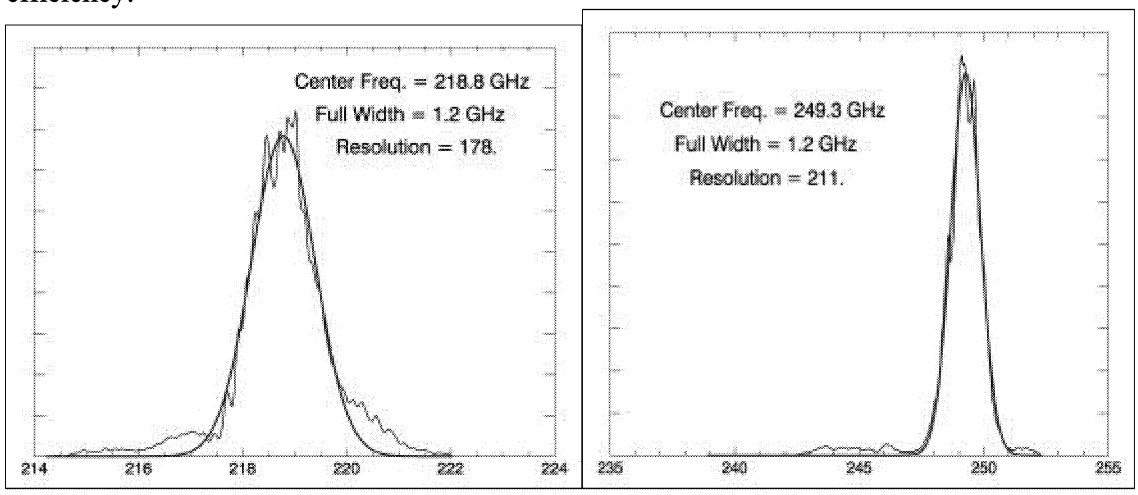

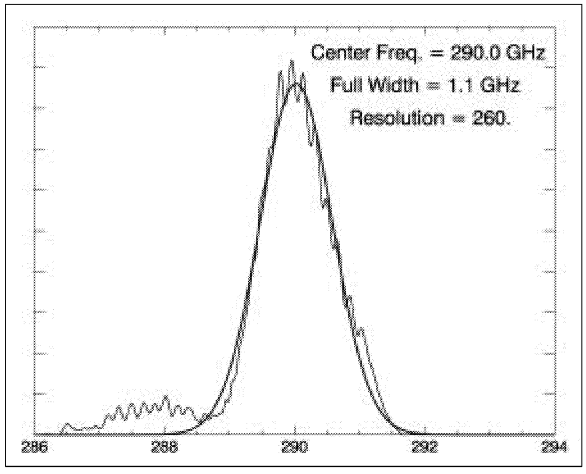

Figure 6 a,b,c .
Measured resolving power of the first WaFIRS prototype. To within the measurement uncertainties, profile widths are equal to those calculated in the design model. The second generation spectrometer will have resolving power between 250 and 400.

5. Scalability: Ground Based Observations and WaFIRS Modules for the Far-IR

In addition to our warm λ=1 mm prototype, we are constructing a cyrogenic version, Z-Spec for observations from ground-based submillimeter / millimeter observatories. Z-Spec will demonstrate the capability of WaFIRS to provide broadband spectroscopy with background-limited sensitivity at 1 mm. The instrument will measure the redshifts of submillimeter galaxies using the rotational CO lines. Also, we have produced designs with the same size and shape for a variety of shorter wavelengths, including a system which provides R=2000 at λ=100 μm. As wavelength is shortened, the number of facets and spectral resolution elements increases while the facet size and the physical size of a resolution element decrease. The grating remains in first order and the total fractional instantaneous bandwidth is constant. This extension to shorter wavelengths is possible because the design produces a stigmatic geometry for the grating, and geometric aberrations are small. The table below shows three examples of spectrometer designs:

Design Parameter	**1st Prototype**	**Z-Spec Module**	**Far-IR Module**
Frequency Range	195-310 GHz	195-310 GHz	1.9-3.0 THz
Stigmatic Frequencies	273, 204 GHz	296, 199 GHz	2.8, 2.0 THz
Number of Detectors	----------	160	~500
Number of Facets	400	500	4000
Resolving Power	180-250	250-400	1000-2000
Plate Spacing	2.5 mm	2.5 mm	0.6 mm
Spacing Tolerance	0.08 mm	0.04 mm	0.005 mm
Longest Dimension	50 cm	61 cm	55 cm
Illumination Efficiency	.87-.91	.78-.85	.9

6. References

Barger et al., 1999 AJ 117, 2656.
Blain et al., 1999. astro-ph /9906141
Blain et al., 2002, astro-ph /0202228
Born and Wolf, 1999. '*Principles of Optics*,' Cambridge U. Press. pp. 458-462
Bradford, C.M., PhD Thesis, Cornell University, 2001
Bradford, C.M., et al., 1999, in '*The Universe as Seen by ISO*,' Cox & Kessler, eds., ESA SP-427.
Genzel, R. et al., 1998, ApJ 498, 579.
Harris et al., 1991, ApJ 382, L75
Helou G., Malhotra, S., Hollenbach, D.J., Dale, D., Contursi, A.., 2001 ApJ 548, L73.
Jaffe, D.J. et al., 1985, ApJ 290, L59
Malhotra et al., 2001, ApJ, 561, 766.
Pozar, D.M. '*Microwave Engineering*.' J Wiley & Sons. Chap. 3.
Stacey, G.J. et al. 1991, ApJ 373, 423.
Tran, Q.D. et al., 2001, ApJ 552, 527.
Ward, J., Zmuidzinas, J., Harris A.I. Issac, K. 2002 ApJ, in press.

SUPERCONDUCTING HOT ELECTRON BOLOMETERS ON FREESTANDING SILICON NITRIDE MEMBRANE STRIPS USING FLIP-CHIP MOUNTING

M. Brandt, J. Stodolka, T. Tils, C. E. Honingh, K. Jacobs

KOSMA, I. Physikalisches Institut, Universität zu Köln
Zülpicher Strasse 77, 50937 Köln, Germany

ABSTRACT

We report on a novel fabrication scheme for 1.9 THz waveguide mixers for SOFIA, where Hot Electron Bolometer mixers (HEB) or SIS mixers are fabricated on 2 μm thick Si_3N_4 membrane strips. The strips are robust enough to be mounted on a separately fabricated Si support frame using an adapted flip-chip technology. Mounted onto the frame, the devices can be easily positioned and glued into a copper fixed tuned waveguide mount. Fabricating the large frames and the small Si_3N_4-strips separately requires significantly less space on the device wafer, allowing many more devices per wafer.

This concept is currently being tested in an 800 GHz prototype mixer with a HEB device. We have demonstrated that the cooling of the device via membrane and RF filter metallization is sufficient by comparing the resistance versus temperature measurements in Helium atmosphere and in vacuum. Heterodyne and Fourier transform spectroscopy measurements are currently being set up.

I. INTRODUCTION

Within the scope of the GREAT (4 Pixel, 1.6 – 2.0 THz) and STAR (4x4 Array, 1.9 THz) receivers for SOFIA we need low noise mixers with good coupling to the telescope. Waveguide mixers at THz frequencies demand considerably more technical effort than quasi-optical mixers, but they provide a set of advantages as :

- single mode Gaussian beam shape for optimum coupling to the telescope
- compact design for array and satellite applications
- intrinsic band pass filtering avoiding saturation

Scaling the fixed backshort mixer design that we have successfully used in submillimeter mixers to Terahertz frequencies is possible but obviously requires scaling of the substrate thickness. At 2 THz, a quartz substrate would be too thin to fabricate and handle. This paper describes our efforts to develop an alternative solution.

II. MIXER DEVICES ON MEMBRANES WITH SUPPORT FRAMES

The RF signal is coupled from waveguide to the device via the waveguide antenna probe. The substrate with antenna probe, HEB detector and IF filter has to be thin and narrow enough to prevent RF loss through the substrate channel. For 800 GHz mixers the standard procedure is to grind a quartz wafer down to 25 μm, which is almost the limit in quartz thickness that can be reliably fabricated and handled. To realize

considerably thinner substrate the general idea is to fabricate the mixer device on a thin (~2 µm) membrane layer deposited or grown on a bulk wafer. The membrane is then structured into the thin strips which are used as the substrates for the devices. By backside etching, the support wafer is taken away, leaving only the membrane strips and their frames of bulk material for support [1]. Materials tested were GaAs membranes on GaAs wafers with an AlGaAs etch-stop and Low Stress Silicon-Nitride on Silicon wafers. With both material combinations, frames with membrane strips have successfully been produced.

III. Separate Fabrication of Devices and Support Frames

One disadvantage of the frame/membrane concept is the relatively large wafer real estate occupied by the support frames. As the process for the THz mixer devices has only limited yield, the chances of producing a sufficient number of good and - important for array receivers- identical devices are comparably poor. This and some other points of concern led to a further optimization of the concept.

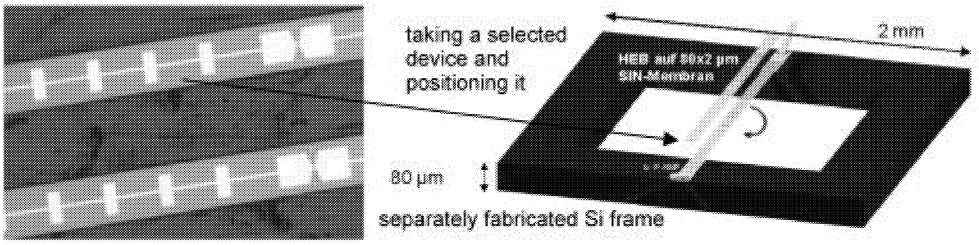

Fig. 1: "Flip-chip" concept

The mixers are fabricated on wafers with a membrane layer, and the support frames are produced on similar, but separate wafer. The finished devices on their thin membrane strip substrates then have to be mounted individually onto the frames, where they are electrically connected [2]. Of course, the mounting process is delicate and requires a special process. We therefore developed an adapted "flip-chip" process, taking advantage of an advanced microgripping station. With this process about 400 devices fit easily on a 1" wafer, about 20 times as many as with the conventional concept with typical quasioptical antenna circuits.

A second problem of producing the frames together with the devices is solved with this approach at the same time. Anisotropic etching of the frames from the back side is necessary to achieve a reproducible mechanical interface to the mixer mount. Most reasonably anisotropic etch processes with high etch rates only work well at temperatures above 80°C. At this process stage, the wafer already carries the delicate and temperature sensitive bolometer devices on the front side, so that etch protection is of utmost importance. We have not found a reliable way of protection for small wafers.

IV. Fabrication Process

The HEB devices are fabricated on a 2 µm thick, low stress Silicon Nitride (Si_3N_4) film deposited on a silicon wafer [3]. The process is the same as described in [4] with only minor changes. The IF bond pads, which are later used for the "flip-chip" bonding, consist of 300 nm Au for good electrical and thermal contact.

The HEBs are passivated with SiO_2 which also serves as an additional protection against the Silicon back etch solution. In the last step the Si_3N_4 membrane is cut into 80 µm strips with Reactive Ion Etching. For 1.9 THz these strips are scaled down to a width of 40 µm. During RIE, the HEBs are protected by a trilayer of resist/Cu/resist which can withstand the 12 minute silicon nitride etch. After RIE, a gold layer is deposited to cover the silicon area between the strips using the same photoresist for liftoff. This gold film protects the strips from being attacked by the etch solution when it breaks through from the backside. The wafer is diced into smaller pieces and the ground connections are cut to allow DC-testing of the devices while they are still supported by the bulk wafer.

The most critical part of the process is the final back-etching of the supporting Silicon wafer, leaving the devices on free standing silicon nitride strips. Obviously, this etch process does not have to be anisotropic. Still, all isotropic recipes with reasonable etch rates either use HF or need about 80°C process temperature. Long exposure to elevated temperatures deteriorates the bolometer characteristics. HF on the other hand attacks nearly any material or peels it off, making it difficult to find masking materials. We are now working with a room temperature solution using $Cu(NO_3)_2$ and NH_4F. In contrast to the standard HF/HNO_3 process, it is selective to SiO_2, so that SiO_2 can be used as an etch stop and passivation for the HEBs. The wafer is glued face down onto a subwafer with wax [5]. The reduced Cu precipitates on the Si surface and has to be removed with a polishing step. When the bulk Si is completely etched away, the gold between the strips is removed. Dissolving the wax results single devices on 80 µm x 1600 µm x 2 µm substrates.

V. "FLIP-CHIP" ASSEMBLY

For the support frames Si wafers are thinned down to 80 µm by lapping. After depositing Nb/Au bonding pads, the frames are etched with TMAH at 80°C using SiO_2 for masking. The anisotropic TMAH etch produces 70° side walls in <110> Si. The metallization on the frames could also be used to incorporate IF matching circuits.

For mounting on the frame, a selected device is removed from the storage box with the help of the KOSMA Micro Assembly Station (MAS) and is positioned onto the bond pads of the frame. The bond pads and IF filter metallization of the device are facing downwards. The device is ultrasonically bonded to the Au/Nb pad of the frame with a modified bond tool. When bonding the opposite substrate end, substrate strips that are slightly bent due to residual film stress can be straightened out. The resulting device/frame assembly can be easily handled and put into position by the micro-assembly station and electrically connected via the bond pads of the frame. Fig. 2 shows a finished device mounted into a 800 GHz copper waveguide block.

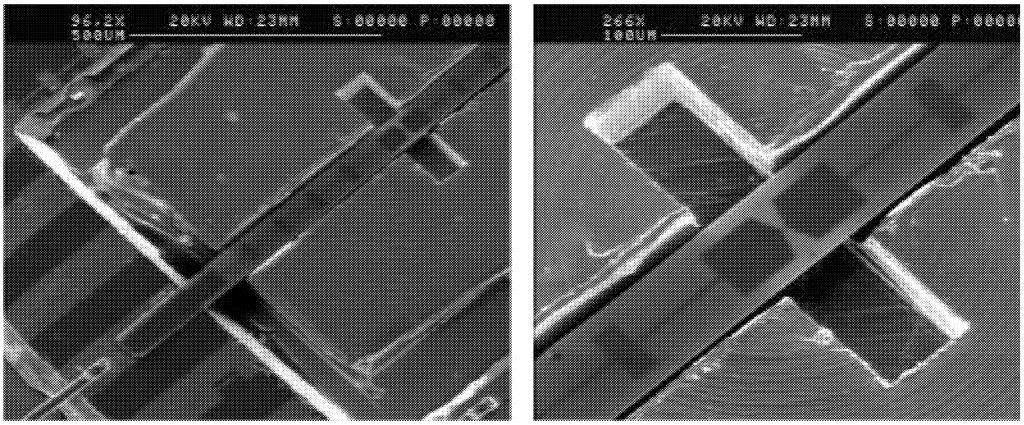

Fig. 2 SEM photo of "flip-chip" mounted HEB device. The left photo shows one part of the frame with the IF bond wire connection, the right photo shows a close-up of the RF waveguide and the freestanding device substrate. The substrate channel is 40 µm deep.

VI. DC Results

A point of concern for HEB devices on freestanding thin membrane substrates could be the cooling of the devices in vacuum. Fig. 3b shows a comparison of resistance versus temperature measurements in liquid Helium and in a vacuum dewar. The results show that there is no visible difference and that cooling via the gold wiring seems to be sufficient. The R/T and I/V characteristics are also very similar to devices fabricated on crystalline quartz.

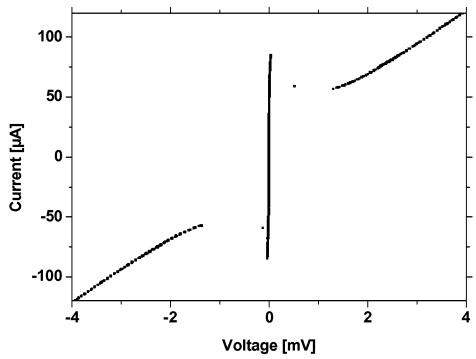

Fig. 3a I/V curve of HEB on freestanding membrane

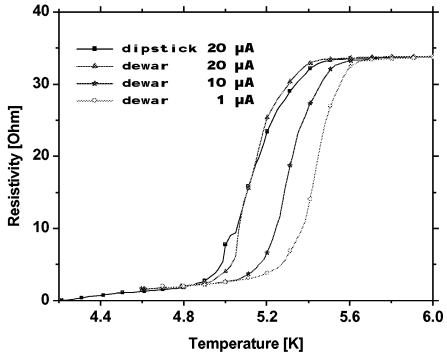

Fig. 3b R/T curves in liquid He (dipstick) and vacuum (dewar)

VII. RF Circuit Simulations

Compared to the standard designs, where the devices are on top of a 25 µm thick crystalline quartz substrate and face the horn antenna, the "flip-chip" devices are on the backside of a 2 µm membrane with a dielectric constant of 7.5 and face the backshort section of the waveguide. Simulations with CST MicroWaveStudio [6] show that sufficiently good coupling to the waveguide is still achievable (Fig. 4). Further optimization to reduce the inductive component and increasing the bandwidth appears to be feasible.

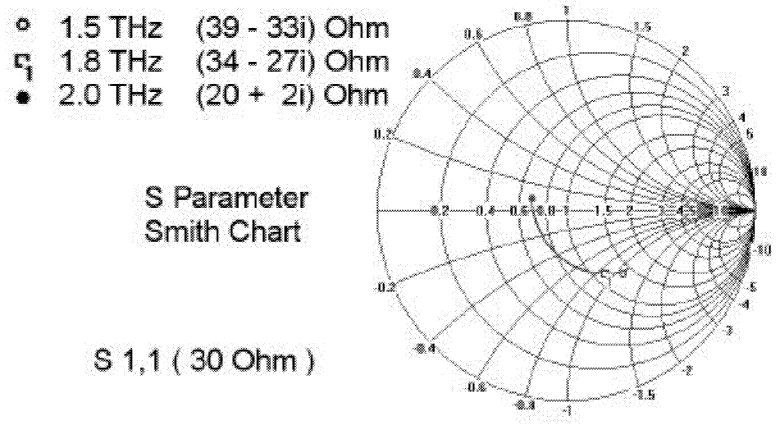

Fig. 4 S11 Smith Chart simulating the bolometer source impedance of a waveguide mixer for the 1.5 THz to 2.0 THz GREAT band.

VIII. CONCLUSIONS

Hot Electron Bolometers have been fabricated on freestanding silicon nitride membrane strips with DC device characteristics very similar to bolometers fabricated on quartz substrates. A modified flip-chip process is used to bond the devices to a separately fabricated silicon frame. The Si_3N_4 membranes with a thickness of 2 µm can be safely gripped and positioned with the KOSMA Micro Assembly Station. The "flip-chip" process shows a similar yield as our standard wire bonding and none of the "flip-chip" bonded devices lost its contact at 4.2 K.

IX. OUTLOOK

The 800 GHz design is a proof of concept for the mixers at 1.5 to 2.0 THz we are developing for SOFIA. Although the conventional copper "stamped backshort" waveguide mixer can still be fabricated at least at low Terahertz frequencies, we are working on novel methods to fabricate the waveguide mounts and the horn antennas with the help of micro-stereo lithography [7] and electroforming. These methods would allow scaling of the mixer designs to several Terahertz.

X. REFERENCES

1. P. H. Siegel, R. P. Smith, M. Gaidis, S. Martin, J. Podosek, U. Zimmermann, 1998: *2.5 THz GaAs Monolithic Membrane-Diode Mixer*, Proc. 9 th Int. Symp. on Space Terahertz Technology, Pasadena, CA, 147
2. J. Bruston, S. Martin, A. Maestrini, E. Schlecht, P. Smith, I. Mehdi, 2000:*The frameless membrane: A novel technology for THz circuits*, Int. Symp. on Space Terahertz Technology, Ann Arbor, MI, 277
3. Berkeley Microfabrication Laboratory, University of California, Berkeley
4. J. Stodolka, K. Jacobs,2001: *Fabrication and receiver measurements of a diffusion-cooled Hot-Electron-Bolometer at 800 GHz*, Proc. 12th Int. Symp. on Space Terahertz Technology, San Diego, CA, 47
5. W Wax by Apiezon
6. MicroWaveStudio, CST GmbH, Darmstadt, Germany
7. Micro-Tec, Dortmund, Germany

A Fast, Very Sensitive Calorimetric Power Meter for Millimeter to Submillimeter Wavelengths

Neal Erickson
Erickson Instruments LLC
316 Pine St.
Amherst, MA 01002
email: neal@ieee.org

Abstract

A calorimetric power meter is now commercially available having sensitivity and stability sufficient to measure a power level well below 1 μW. The Erickson model PM1B sensor has an input in WR10 waveguide, with a very well matched termination. The frequency response is believed to be flat throughout the submillimeter wave region. The response time of the sensor is 7 sec, but this time can be reduced through the use of thermal feedback, at the price of higher noise. An effective time constant of 1 sec is achieved with 0.15 μW rms noise, and 0.25 sec with 1 μW noise. The maximum input power is 200 mW, making the instrument useful with a wide variety of sources. The sensor head is quite small, yet well insulated from its environment.

Introduction

Calorimeters have long been used to measure power over extremely wide frequency bands. The method is very simple, just measuring the temperature rise of a well-matched wideband absorber in response to applied power. In principle, this technique is easily calibrated because the same absorber can be heated using a known amount of power applied through other means. In practice, the difficulty is in making a sensor with a fast response time and uniform load temperature, while maintaining acceptable sensitivity. It is important in this calibration that the reference heat produce the same response as the microwave power. In addition, drift due to ambient temperature variations is very difficult to control. The usual technique to reduce drift is to use a matched pair of sensors having nearly identical thermal environments, and to use one as the measurement sensor and the other as a reference. So long as the sensors are identical, they show no response to ambient temperature variations, but this requires extreme care in their fabrication.

In the simplest situation, the response time, τ, of the sensor is determined by the heat capacity of the sensor load, C, and the thermal resistance to thermal ground, ρ:

$$\tau = C \times \rho$$

while the temperature rise ΔT is given by:

$$\Delta T = \rho \times P, \text{ where P is the absorbed power.}$$

Since a large ΔT response is desired, ρ must be made fairly large, and the only way a fast response can then be achieved is by making the heat capacity (and thus the mass) of the

sensor as small as possible. However, a practical sensor can not be made arbitrarily small. A sensor must be large enough to be an efficient absorber with no frequency resonances. In practice this means that a slowly tapered load is required, and the load material must be thick enough that no power can pass through it. In addition the load must include a temperature sensor and a heater resistor for calibration.

This paper describes an improved calorimeter which has been designed to measure power levels below 1 μW with an acceptable time constant and with accuracy and reproducibility of ~2-3%. It is similar in many ways to the unit in [1] (which in turn uses concepts from earlier work [2,3,4]), but the improvements lead to nearly an order of magnitude increase in sensitivity, with faster response. This power meter is now available commercially as the Erickson Instruments PM1B.

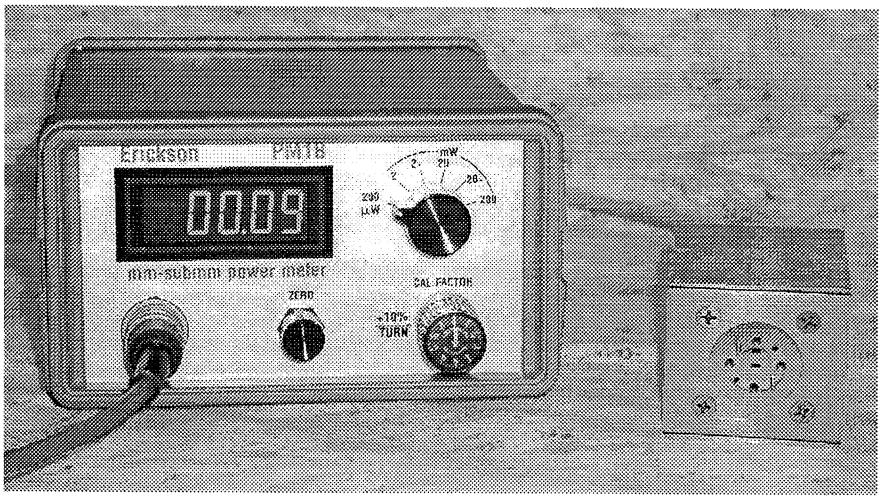

Figure 1. Complete PM1B. The sensor head is 5 cm square.

Calorimeter sensor construction

The geometry of the sensor used in this work is shown in figure 2. The input was chosen to be WR10 waveguide so that cross calibration could be done against other waveguide sensors, while being small enough to keep the heat capacity low. It is quite practical to couple from this waveguide into any smaller size using linear tapers. While many submillimeter sources are optically coupled, nearly all use waveguide internally, and are easily coupled back into waveguide using just a feedhorn. An unconventional waveguide termination geometry was chosen which places the load entirely on the outside of the waveguide, where it is easy to attach the thermometer and heater. The load itself is a rectangular slab of silicon with a thickness of 0.4 mm, having a 100Ω/ metal film on the inside. This load has very low mass and high thermal conductivity. The waveguide is cutoff at an angle of 10° to produce a VSWR better than 1.15:1 within the WR10 band. The expected VSWR at much higher frequencies (at least 2 THz) is comparable. All of the edges of the wafer are coated with conductive epoxy to eliminate loss of power, and the absorber is carefully sealed to the waveguide without any gaps where power can be lost.

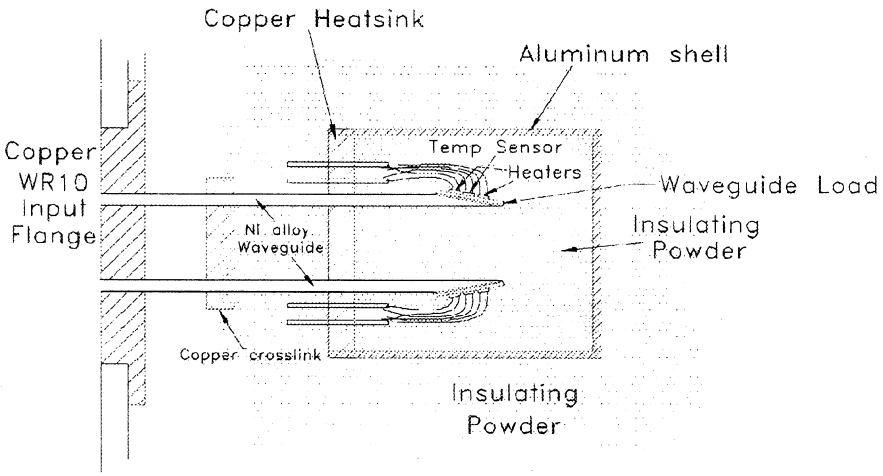

Figure 2. Diagram of the power sensor head, showing the waveguide loads, heaters and temperature sensors.

The waveguide is a low thermal conductivity Ni alloy having a thickness of 0.07 mm and a gold plated interior. The waveguide must be very thin so that it has sufficient thermal resistance in a short length, and so that its heat capacity is small. In this sensor the waveguide contributes ~1/3 of the total heat capacity of the load. The time constant of this sensor is 7 sec with a responsivity of ~180K/W. While this is faster than typical calorimeters, even faster response may be achieved as described in the next section.

The temperature sensors used must be very linear if the sensor is to work over a wide power range, and they also must have very low drift and noise. Thin film Pt resistance sensors (RTD's) have been found to be stable to <0.01 mK, with noise determined by the readout electronics. At an RTD bias of 0.5 V, the noise of the preamplifier is equivalent to ~.02 μW rms, and is less than typical drift levels. The bias resistors can add a very large amount of noise and the exact manufacturing process used seems to make a difference. Thin metal film resistors are best but some of these are still noisy, while the best add no detectable noise. Noise becomes quite important with the feedback circuit described later.

Drift in thermal sensors comes from two sources. In analogy with differential amplifiers, inputs can be considered common mode if a thermal influence is applied to both temperature sensors, and differential if it applies to one only. Common mode drift, as is caused by ambient temperature fluctuations, occurs because the sensors do not have matched response. The sensors show a linearity error of up to 3×10^{-3} which is equivalent to a common mode drift of 15 μW/K. The match of the sensors is trimmed with external resistors to bring this drift to a level ~2 μW/K (ambient), which leads to much improved stability for the sensor.

Differential drift due to external temperature fluctuations is a more difficult problem. The sensor response of 0.22 mK/μW means that differential influences must be very highly attenuated to measure power below 1 μW. The sensor's differential response is greatly reduced by connecting the waveguides together with copper plates at three points.

Any differential heat leaking in along the waveguides is short circuited at these points, and the mass of the last plate leads to a very slow propagation of this (mostly common mode) heat to the sensors. In the earlier sensors, the separation between waveguides was 10 mm, which has now been reduced to 5 mm. This helps considerably to reduce differential heat input. The total waveguide length to the load is 24 mm. Most of the length is used for thermal isolation and only 3 mm is used for power measurement. The sensors are isolated from differential heating from other directions by enclosing them in a metal shell, so that any external influence is nearly entirely common mode.

One subtle source of drift is heat generated in the temperature sensors due to the current used to measure their resistance. Convection currents from one load to the other cause drift which depends on the orientation of the sensors. This problem is potentially more serious as the sensors are moved closer together to reduce differential drifts. To eliminate this effect the sensors are thermally isolated from each other by filling the shell with a silica powder insulator, which almost completely blocks convection, and also has extremely low conduction. This same insulator fills the sensor housing surrounding the metal shell.

Feedback circuit for faster response

Improvement in the speed of response can be obtained electronically with the readout circuit. While in principle the readout response can be tuned to give an apparent increase in sensor speed, in practice this results in overshoot of the measured power, and very unpredictable responses while tuning. An alternative method is to use the readout circuit to maintain a nearly constant temperature for the load. This can be done by biasing the temperature of the loads (both sensor and reference) to a point somewhat above that which would be produced by the highest power that is to be measured. As RF power is applied, the heater power is reduced to maintain a constant temperature. Rather than measuring temperature rise, one then measures the change in heater power. If the feedback circuit maintaining the temperature has a gain, G, then the change in temperature for a given RF power is reduced by a factor of G, and the response time is decreased by the same factor. There is no problem in this case with spurious behavior in the indicated power, no matter how the RF power is varied, and arbitrarily fast response may in principle be obtained. However there are practical limits to speed because the sensor noise, for frequencies $> 1/\tau$, is increased by a factor of G, and also because the response can not be faster than the thermal equilibrium time within the load element (due to the thermal resistance between the heater and the thermometer). For the load used in these sensors, a gain of 30 is about as high as is practical, giving a predicted time constant of 0.25 sec. At this gain there is an overshoot in response to a power impulse of 1-2%. This gain leads to an rms noise level of ~1 μW and is only practical on the higher scales. At lower power levels the gain is reduced for lowest noise and highest stability.

A block diagram of the readout electronics is shown in Fig 3. The sensor uses a bridge circuit to measure the temperature imbalance of the two waveguide loads, with AC excitation of the bridge to minimize drift in the following amplifier. The AC imbalance signal is amplified and then synchronously detected to minimize noise. The reference

sensor is always heated with a power 5-10% above full scale input. A feedback circuit amplifies this error and heats the active sensor to approximately the same temperature as the reference. The feedback circuit is somewhat complicated because the error voltage from a linear temperature sensor applied to a heater resistor produces a feedback proportional to the error squared. Such a nonlinear loop response is difficult to compensate. To simplify the loop response and to provide a linear readout, an analog square root IC is included within the loop. These IC's (at the highest level of performance) are sufficiently accurate that their response has no measurable affect on the overall linearity of response. The feedback voltage (prior to the square root) is linear with input power, being largest with no input and decreasing to nearly zero at full scale input. After subtracting an offset this voltage is used for power indication.

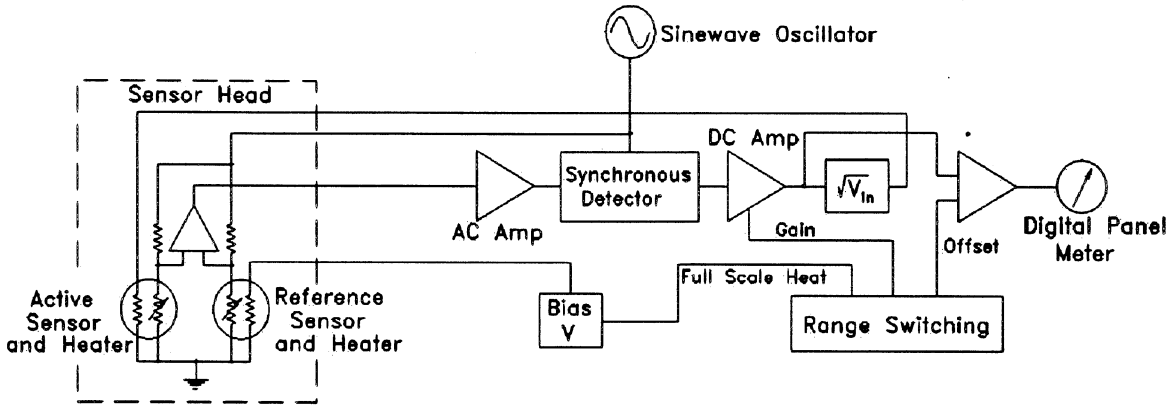

Figure 3. Block diagram of the readout electronics with feedback to increase the response speed.

The stability of this type of sensor depends critically on maintaining a constant heat path to thermal ground for both waveguide loads. Since the bias temperature is greater than full scale power, any variation in the thermal path will cause a significant zero drift. For this reason, it is necessary to change the bias heat when changing measurement scales so that the drift will be only a fraction of each full scale reading. Changing scales requires changing several gains and offsets in the electronics.

Performance

The meter has four ranges, 200 mW, 20 mW, 2.0 mW and 200 μW FS, using a $4^1/_2$ digit panel meter. The maximum power level of 200 mW is limited mainly by concerns for the sensor stability if operated continuously at higher temperatures, as is necessary due to the bias heat used. At the bias point, the sensor temperature is ~60 C. Table 1 shows the properties of the meter on the four ranges. Measurements typically require three time constants for a response to within 95% of the true input power, but the true sensor response is not a simple exponential due to multiple heat paths to ground with various intermediate

masses. The minimum readout noise is ±1 in the last digit of the meter, and this must be added to the rms noise of the electronics from the last column.

Scale	Gain	1/e time const.	95% response	rms noise
200 μW	none	7 sec	20 sec	~.02 μW
2.0 mW	5	0.9 sec	4 sec	~.15 μW
20 mW	30	0.25 sec	0.75 sec	~1 μW
200 mW	30	0.25 sec	0.75 sec	~0

Table 1

The 200 μW scale operates open loop for best stability, and has a drift level below 0.1 μW during a typical measurement interval, if the sensor is not thermally disturbed. However, most measurements introduce a differential thermal disturbance, and the drift becomes ~0.5-1.0 μW typically. This can be reduced if the sensor remains connected to the source for a time so that the transient dies out. Wrapping the sensor head in insulating foam significantly reduces drift. In one measurement, a power level of 0.2 μW at 1.5 THz was measured with confidence in a set-up where the source could be turned on and off without disturbing the sensor.

The large change in bias heat when changing scales leads to the only obvious difference in use between this meter and a more conventional power sensor. Upon changing scales, there is a large thermal transient that must die away before the sensor is stable once more. This stabilization time depends on the inherent time constant of the sensor element, and when switching scales to a lower power, at least five minutes are required for stabilization. This problem would be less if the two loads were perfectly matched so that they both settle at the same rate. When switching scales upward in power the settling time is quite short.

For some purposes, as when measuring the power from cryogenic components, it is useful to place the sensor in a vacuum to avoid the loss and calibration errors introduced by a vacuum window. This sensor works in vacuum (if the sensor case is provided with vent holes) with some minor changes in its properties. The open loop sensitivity increases by 30% (for the 200 μW scale), but on the higher ranges this error is reduced by feedback. Thus the sensitivity increase on the 2 mW scale is only 5%, and on the 20 and 200 mW scales only 1%. The exact changes can be measured in real time with the internal calibration. There is a change in the zero by ~70 μW, but otherwise operation is normal.

Accuracy

It is extremely hard to check the accuracy of a sensor such as this given the lack of power standards. In the case where the input loss is negligible, all of the power must appear as heat in the load, and this heat can be calibrated by heating the load with a known power. There is some uncertainty in this case because the load is not isothermal. The temperature gradient over the full length of the silicon load is ~15% of that within the waveguide. This can be largely resolved by placing the calibration heater in the same area

where most of the heat is expected to be dissipated. At lower frequencies the loss is primarily near the extreme end of the load (where the waveguide height becomes very low), and so the calibration heater is placed at this point. At very high frequencies the mode distribution may change this somewhat, but still the power tends to be dissipated in the same region. The uncertainty in the exact temperature distribution contributes an error of ~2% in power.

Calibration of waveguide loss is fairly simple in principle. The effective waveguide loss length is the full distance from the input to the last copper plate, plus half the distance from this point to the load. Assuming the waveguide loss is uniform over its length, and that the loss for all modes is not very large, this loss may be measured by inserting a piece of identical waveguide in front of the sensor and measuring the change in power. Standard coin silver waveguide has only slightly less loss than the plated waveguide used in the sensor and so a somewhat longer piece (~3 cm) may be used to measure this correction. In practice, the inaccuracy in the use of a calorimeter of this type is dominated by the much more uncertain loss in the tapers used to transition into WR10 waveguide. Within the 75-110 GHz band the input loss is small enough to introduce an uncertainty of only 1-2%. At 300-500 GHz the loss of a taper is ~1 dB, so the uncertainty is still acceptable. In direct comparisons of all meters with each other, relative errors never exceed 3%, in the test frequency range of 100-150 GHz.

Conclusion

A new ultra-broadband power meter with accuracy of ~3% has very high sensitivity, and a moderately fast response time. The sensitivity of under 1 μW is the highest ever achieved with a well calibrated thermal sensor. The unit is quite stable under typical ambient temperature variations, and is small enough to be used like a conventional microwave power sensor. The input is in WR10 waveguide but signals at any frequency above 70 GHz may be measured with appropriate tapers. Accuracy is expected to be good to >2 THz, and measurements may be made even in the visible.

References

[1] N. Erickson, "A Fast and Sensitive Submillimeter Waveguide Power Meter," *Tenth International Symposium on Space Terahertz Technology,* pp. 501-507, 1999.

[2] B. Volwinkle, "Broad-band Calorimeter for Precision Measurement of Millimeter and Submillimeter-Wave Power," *IEEE Trans. on Instrumentation and Measurement*, Vol 29, pp. 183-189, 1980.

[3] B. Vowinkel and H.P. Roser, "Precision Measurement of Power at Millimeter and Sub-Millimeter Wavelengths Using a Waveguide Calorimeter," *Int'l J. of Infrared and Millimeter Waves*, Vol 3, pp 471-487, 1982.

[4] A.C. Macpherson and D.M. Kerns, "A Microwave Microcalorimeter," *Rev. Sci. Instr.*, vol. 26, pp. 27-33, 1955.

FEASIBILITY STUDY FOR THE FOCALISATION OF THE NEW 40m RADIOTELESCOPE OF CENTRO ASTRONÓMICO DE YEBES

E. García[1], L. de Haro [1]*, J. A. López Fernández [2], F. Tercero [2], B. Galocha[1], J. L. Besada[1]

[1]*Grupo de Radiación. Dpto. Señales, Sistemas y Radiocomunicaciones.*

Universidad Politécnica de Madrid. Spain.

[2]*Centro Astronómico de Yebes (CAY). Ministerio de Fomento. Spain.*

Mail address: E.T.S. de Ing. de Telecomunicación. Ciudad Universitaria.

E-28040 Madrid (SPAIN)

Phone: +34 91 549 57 00 ext. 397 Fax: +34 91 543 20 02

e-mail: quique@gr.ssr.upm.es

Abstract: **This paper presents a first study of the focalisation of the new 40m. radiotelescope of Centro Astronómico de Yebes (Spain) which may operate at S, X, K and millimetre bands with a multiband feed system with minor mechanical changes on a classical Cassegrain type radiotelescope. The geometry of this Cassegrain antenna radiotelescope consists of a 40m paraboloidal main reflector with f/D=7.915.**

I. INTRODUCTION

In radioastronomy there are several scientific observation bands of interest, from 2 GHz up to higher than 300 GHz [1], [2]. It is necessary an individualized study of the problem for each observation band [1], [3], in order to design the feeds and the focalization elements such as lenses and conical or plane mirrors [1], [2], [3], [4], [5].This paper is related with the necessity of the focalization of the new 40 m Nasmyth-Cassegrain radiotelescope of the Centro Astronómico de Yebes in Spain with F/D ratio of 7.9 [6]. Our aim is to cover several bands from 120 GHz to 2 GHz. There is a dimension constraint in the receiver cabin for the situation of all the receivers, so it is suitable to share the maximum number of focalization elements for each observation band. In this paper it is verified, such as an example of the method, a possible solution to share an ellipsoidal mirror in three observations bands behind the Nasmyth M3 & M4 mirrors. In *Figure 1* the

receiver cabin and the physical dimension available for the situation of the receivers and their focalization elements are represented [6]. It can be seen that the cabin presents two Nasmyth asymmetric sections centered on M4 and M4' mirrors optical axis, that can be selected by means of Nasmyth mirror M3.

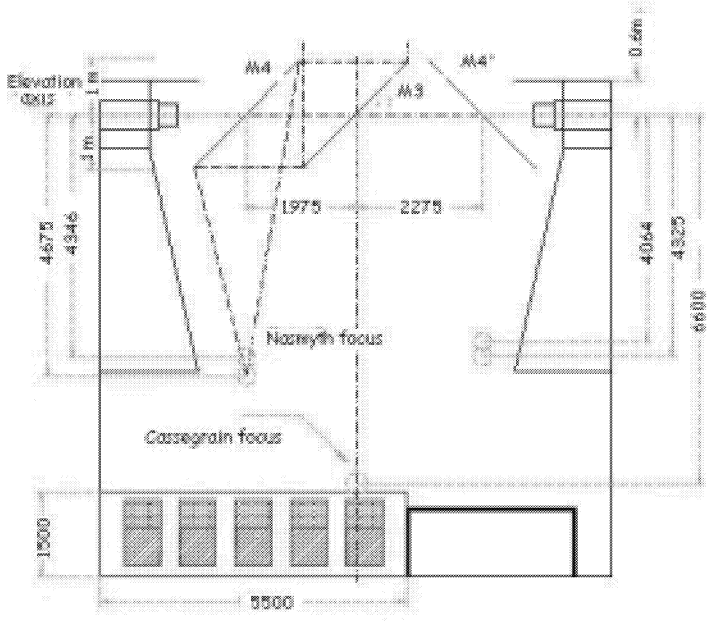

Figure 1: Radiotelescope receiver cabin.

II. FOCALIZATION PROBLEM

To deal with the focalization problem of the different radiotelescope bands, the quasi-optics theory (QO) is used in this paper [1], [7], [8], [9], [10]. In order to achieve the proper focalization of the radiotelescope two fundamental requirements are necessary: the first one is that the subreflector (and so the main reflector) has a suitable taper (illumination level in the edge), of 12 dB taper for an optimum aperture efficiency. The second requirement is to exist a perfect focalization, in terms of geometry optics (GO) [3], that feeders are situated in the system foci. In many observatories it is common to make independent focalization systems for each band, only sharing some plane mirrors to redirect the beams [11], [12], [13]. However, in this paper, a novel design procedure is proposed to focalize simultaneously several frequency bands with the minimum possible optic elements [11], [12], [13]. Moreover it has been applied to design Yebes focalization system at 42-48 GHz, 70-90 GHz and 92-120 GHz bands. This solution has a double improvements: a

reduction of the number of focalization elements and the total cost of manufacturing and a reduction of the density of optical elements on the receiver cabin allowing more free space for technical maintenance [1], [6] without reducing antenna performance.

Gaussian Beam analysis has been employed to study the behaviour of the fields reflected and subtended in the receiving cabin of the radiotelescope. Different solutions and combinations of ellipsoidal, hyperboloidal, paraboloidal and lenses are used to place the receivers in the limited size of the cabin. First, the main parameters of the fundamental Gaussian Beam Mode are calculated according to the desired horn in each band. Those non optimal solutions because of the sizes of the different focusing elements and the sizes of the feed horns are neglected. By doing so, with the optimal solutions for each band presented in this paper, it has been extensively employed to calculate the electromagnetic behaviour of the fields in the receiving cabin a study of the propagation of the higher order modes.

II. ANALYZED OPTICS

Defocused gaussian beam telescope geometry and its tolerance with the changes in the values of their lenses and focalisation distances are analysed. The gaussian beam telescope is very useful in systems that must operate over broad bandwidths. This device has particularly functional properties in Cassegrain radiotelescope focalisation systems. A pair of focusing elements separated by the sum of their focal lengths is called a gaussian beam telescope [1], [6]. This device has particularly useful properties in radiotelescope focalisation systems that must operate over broad bandwidths. Systems with such a structure are frequency independent. One of the best approaches to study the properties of this geometry, is the Quasi-Optical (QO) theory, which is explained in [1], [6], [9].

However, this frequency independence has several limitations if some quasi-optical parameters are analysed. If a corrugated horn is used as the feed, some dependence of the beam waist with frequency is expected. If it is desired to focalise an observation Cassegrain radiotelescope band [1], [6] with this kind of horn and with the gaussian beam telescope structure in a wide margin, it is necessary to defocus the geometry to achieve the right taper (edge illumination level in the subreflector and therefore in the main reflector) and focalise

the beam in the subreflector. In terms of QO, to achieve the right beam radius (w) and the radius of curvature (R) in the subreflector.

This paper deals with the necessity of focalising the new 40 m Cassegrain radiotelescope of the Centro Astronómico de Yebes in Spain. The F/D ratio of this radiotelescope has a value of 7.9 and there will be nine receivers from 10 GHz to 120 GHz bands, including also VLBI measurements in S/X bands. Making use of QO theory, this paper studies the behaviour of the radiotelescope in one observation central frequency (90 GHz) with the defocused gaussian beam telescope configuration geometry. Tolerance results with displacements of the separation distances among the optical elements and with variations in the focal distances of the lenses are considered.

The 90 GHz central frequency is selected to expose some tolerance results of the defocused gaussian beam telescope. The geometry and the parameters notation is shown in *Figure 2*. The selected feedhorn is a corrugated one. In terms of QO, it is possible to define the theoretical main dimensions of this horn knowing the beam waist of the quasi optical beam that it must generate [13] and the phase error over the horn aperture plane. One way to do that involves the use of three parameters. Two of them are related to the Cassegrain radiotelescope and to the beam that has to illuminate it: the F/D ratio and the taper at the angle defined by this F/D ratio. The third parameter is the phase error over the horn aperture plane.

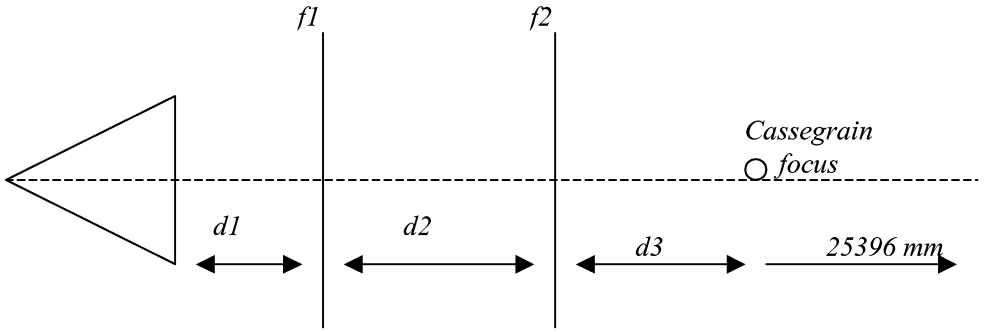

Figure 2: Defocused gaussian beam telescope geometry.

In this paper a F/D ratio of 1.5, a 12 dB taper and a phase error aperture of 0.24 are used. With these characteristics the physical implementation of the horn is guaranteed. The theoretical horn radius and slant length are equal to 6.85 mm and 29.37 mm, respectively.

This horn produces a beam waist of 3.74 mm, which is entirely inside of the paraxial approximation. To show the functional properties of the defocused gaussian beam telescope, the band from 70 to 110 GHz is studied.

The geometry formed by horn + ideal lens + ideal lens is used, but without preserving the values of the distances between the optical elements which would form the focused gaussian beam telescope. Some restrictions are imposed to the focalisation problem due to the design requirements of the Yebes radiotelescope. For a subreflector radius ($R_{subreflector}$) of 1640 mm and an edge taper (T) of 12 dB, it follows:

$$w_{subreflector} = R_{subreflector} \cdot \sqrt{\frac{20}{T \cdot ln(10)}} \tag{1}$$

Therefore the beam radius in the subreflector must take a value of 1395.3 mm. If the focalisation of the system is also required, the radius of curvature must be equal to the distance of the Cassegrain focus, f_s = 25396 mm in the radioastronomical observation band. Furthermore other important requirement has been included in the synthesis of the gaussian beam telescope. As the feed system will be a part of a radioastronomical receiver, a low noise level is essential. Noise level can be reduced cooling the optical system inside a cryostat. Only the horn and the first lens can be cooled due to physical considerations. In order to achieve that, several restrictions on the dimensions of the intermediate beam waist on the cryostat window are introduced. As the diameter of the cryostat window is 140 mm, the intermediate beam waist should be smaller than 35 mm. Finally, the beams in all the band are truncated to a 4w diameter [6], [9], so an accurate analysis in terms of QO theory is again guaranteed. The percentage error allowed to the beam radius and to the radius of curvature in the subreflector in all the band is 1% and 0.05%, respectively.

III. RESULTS

Quasioptical theory has been applied to design a defocused gaussian beam telescope. Geometry is optimised using the conjugate gradient method to achieve all the requirements exposed. Results are presented in *Figure 3* - *Figure 14*. The optimal value of the parameters are d1=79.57 mm, d2=86.56 mm, d3=268.00 mm, f1=86.08 mm and

f2=908.66 mm. Taper in all the band is between 12.25 and 12.3 dB, and defocusing is ±3λ, which are entirely suitable for Cassegrain systems. The two lenses are perfectly feasible [1], [9]. A tolerance study on the different physical dimensions of the gaussian beam telescope has been done. The aim of this study is to simulate the effects of little displacements between the components and errors on the manufacture of the lenses. The allowed tolerance is 5 mm for each physical dimensions. It has been found that the critical parameters for a designed system are the focal distance of the first lens and the distance between this lens and the aperture of the horn. In *Figure 5* - *Figure 6*, little variations of f1, due to contraction of the dielectric material of the lens inside the cryostat, for example, imply a strong variation of the beam radius on the subreflector. The radius of curvature varies too, but no so rapidly. Defocusing presented in radius of curvature figures, have two limits, one for ±3λ and other for ±10λ, which is still completely suitable in Cassegrain radiotelescopes with high F/D ratio. The same considerations can be applied to the tolerance study for d1, as it is shown in *Figure 9* - *Figure 10*. Finally, tolerance study on d2, d3 and f2, shows that both, beam radius and radius of curvature, are more robust with little variations of the parameters.

IV. CONCLUSIONS

Defocused gaussian beam telescope has been analysed with Quasi-optics theory. Variation tolerance in all the parameters of the geometry has been presented in several figures for the central band observation frequency of 90 GHz. Allowing a minimum percentage error of beam radius and radius of curvature over the subreflector, it is possible to achieve a right focalisation in a wide band with the defocused gaussian beam telescope geometry, which is demonstrated by the large band study realised from 70 to 110 GHz centred in 90 GHz. From the figures presented it follows that the radius of curvature tolerates the changes in the value of the telescope parameters better than the beam radius does. Therefore, the defocused gaussian beam telescope is more robust in focalisation than in taper (illumination) when there are variations in the geometry parameters.

V. ACKNOWLEDGEMENT

This work have been realized in the Grupo de Radiación of the Universidad Politécnica de Madrid (Spain) and in the Centro Astronómico de Yebes (Spain), as part of a contract for the electromagnetic design of the new 40 m radiotelescope of this Observatory.

VI. REFERECNCES

[1] P.F.Goldsmith, "*Quasioptical Systems,*" IEEE Press/Chapman & Hall Publishers Series on Microwave Technology and RF. New York 1997.

[2] Rohlfs K., Wilson T. L., "T*ools of Radio Astronomy*", *Springer, Third Edition, Astronomy & Astrophysics Library, 1999.*

[3] G. A. Deschamps, "*Ray tehcniques in electromagnetics*" *Proceeedings of the IEEE, Vol 60, No 9, Sep. 197, pp 1022-135.*

[4] Kraus J.D., *Radio Astronomy*, "2nd Edition, Cygnus Quasar Books, 1986.

[5] Burke F. B., Graham-Smith F., "An Introduction to *Radio Astronomy*", Cambridge University Press, 2000.

[6] López Fernández J. A. et al., "*Configuración óptica del radiotelescopio de 40 m del CAY*", Technical repport of OAN, 2001.

[7] J. Tuovinen, "*Accuracy of a gaussian beam*" *IEEE Transanctions on antennas and propagation, Vol 40, No 4, Apt. 1992, pp 391-398.*

[8] L. Empacher, W. Kasparek, "*Analysis of a multiple-beam waveguide for free-space transmission of microwaves*" *IEEE Transanctions on antennas and propagation, Vol 49, No 3, March 2001.*

[9] P.F.Goldsmith, "*Quasi-optical techniques*" *Proceeedings of the IEEE, Vol 80, No 11, Nov 1992,pp. 1729-1747.*

[10] R.J. Wylde, "*Millimetre-wave gaussian beam-mode optics and corrugated feed horns*" *IEEE Proceedings, Vol 131, Pt H, No 4,Aug. 1984, pp 258-262.*

[11] J.A.Murphy, "*Distorsions of a simple gaussian beam on reflection from off-axis ellipsoidal mirrors*", *International Journal of Infrared and Millimetre Waves, vol 8, pp 1165-1187, 1987.*

[12] A. Azeez, A. Rashed, B. Saleh,"*Decentered gaussian beam*", *Applied Optics, Vol 34, No 30, Oct 1995.*

[13] James W Lamb, "*Quasioptical coupling of gaussian beam systems to large Cassegrain antennas*", *International Journal of Infrared and Millimetre Waves, vol 7, No 10, 1986, pp. 1511-1536.*

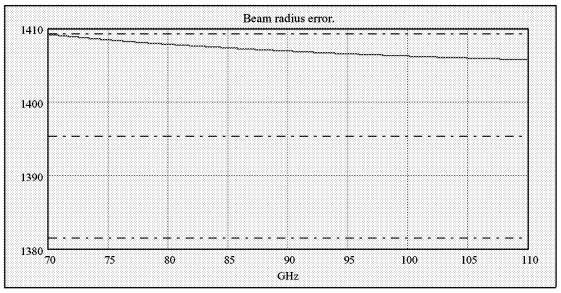

Figure 3: Beam radius in the observation band for optimised parameters

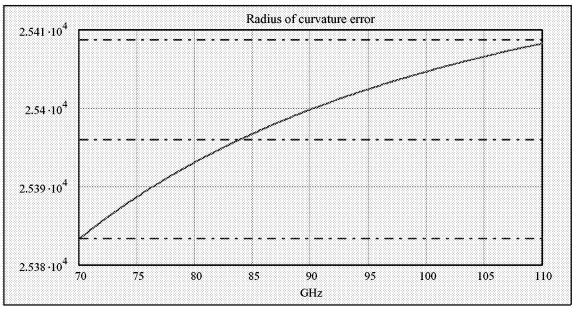

Figure 4: Radius of curvature in the observation band for optimised parameters.

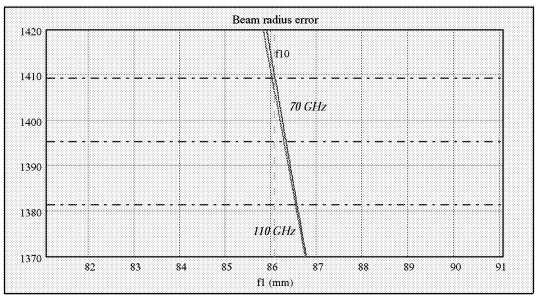

Figure 5: Beam radius for upper and lower frequencies of the band in function of the variation of f1. f10 is the optimised parameter.

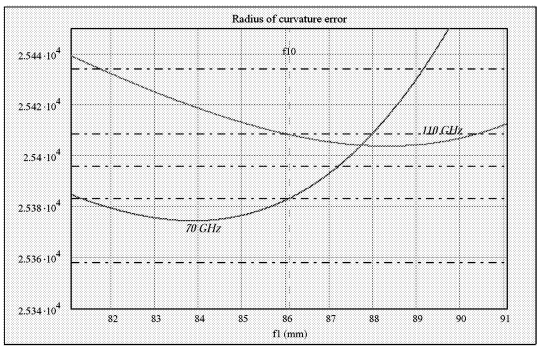

Figure 6: Radius of curvature for upper and lower frequencies of the band in function of the variation of f1. f10 is the optimised parameter.

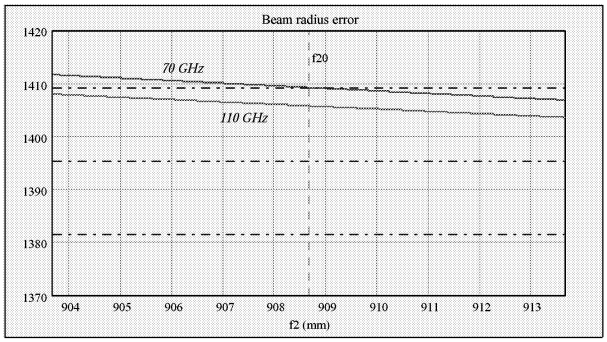

Figure 7: Beam radius for upper and lower frequencies of the band in function of the variation of f2. f20 is the optimised parameter.

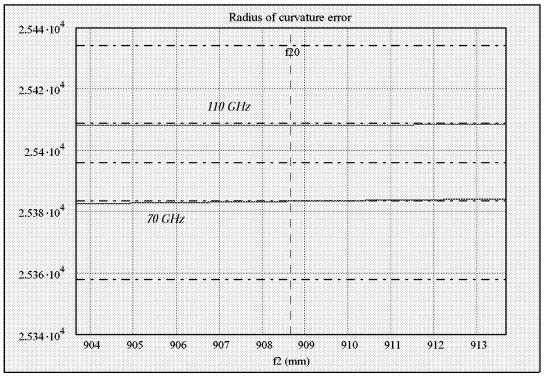

Figure 8: Radius of curvature for upper and lower frequencies of the band in function of the variation of f2. f20 is the optimised parameter.

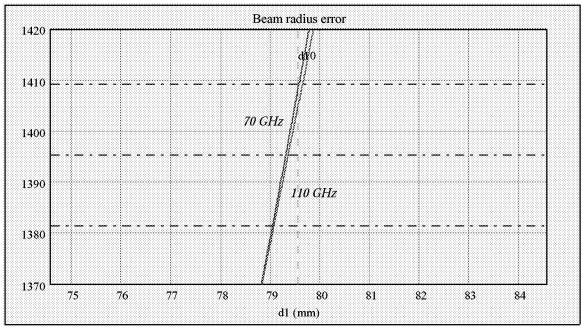

Figure 9: Beam radius for upper and lower frequencies of the band in function of the variation of d1. d10 is the optimised parameter.

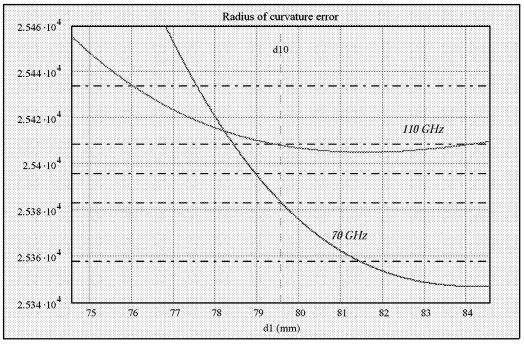

Figure 10: Radius of curvature for upper and lower frequencies of the band in function of the variation of d1. d10 is the optimised parameter.

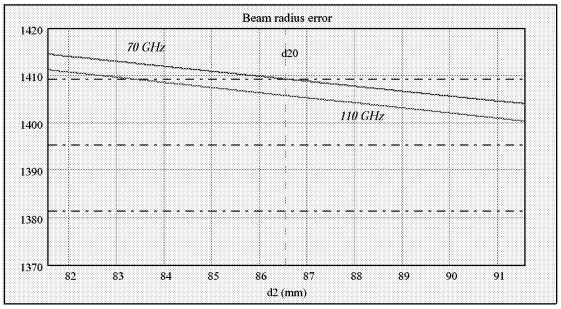

Figure 11 Beam radius for upper and lower frequencies of the band in function of the variation of d2. d20 is the optimised parameter.

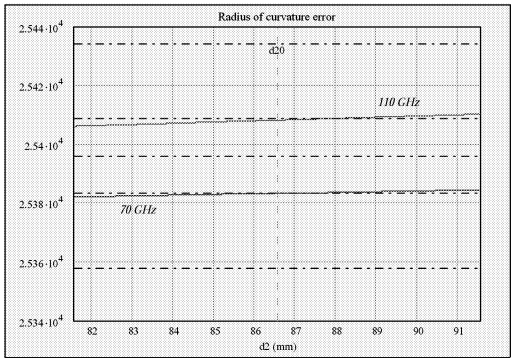

Figure 12: Radius of curvature for upper and lower frequencies of the band in function of the variation of d2. d20 is the optimised parameter.

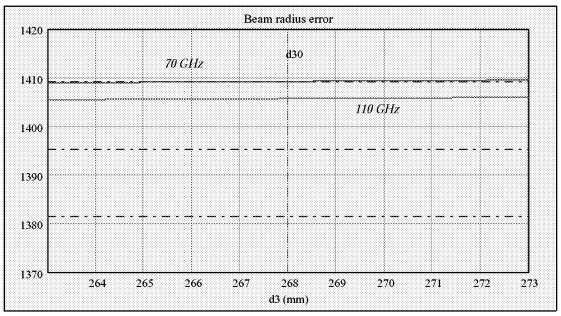

Figure 13: Beam radius for upper and lower frequencies of the band in function of the variation of d3. d30 is the optimised parameter.

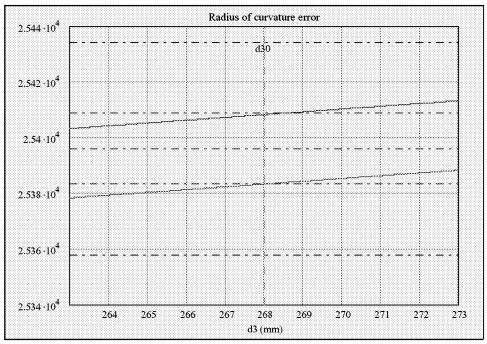

Figure 14: Radius of curvature for upper and lower frequencies of the band in function of the variation of d3. d30 is the optimised parameter.

NbN FILM DEVELOPMENT FOR PHONON-COOLED HEB DEVICES

E. Gerecht, A. K. Bhupathiraju, and E. N. Grossman

National Institute of Standards and Technology
Boulder, CO 80305

J. Nicholson, F. Rodriguez-Morales, D. Gu, and K. S. Yngvesson

Department of Electrical and Computer Engineering, University of Massachusetts
Amherst, MA 01003

ABSTRACT **-** Superconducting Hot-electron Bolometric (HEB) mixers employing thin films of NbN have become the devices of choice for heterodyne detection at terahertz frequencies. HEB mixers are inherently insensitive to the bandgap frequency of the superconducting material used in the device, in contrast to SIS mixers. We have developed a fabrication process for thin NbN films at the National Institute of Standards and Technology in Boulder, CO. A two-fold approach can be taken. The first is to maximize the critical temperature of the superconducting device by growing thicker films at the expense of IF bandwidth, whereas the second approach focuses on maximizing the IF bandwidth at the expense of the critical temperature. So far, we have developed a film-deposition process utilizing our DC reactive magnetron sputtering chamber. By current-biasing the RF plasma in a mixture of Ar and N_2, while using a Nb target, we can control the film stoichiometry and produce films with thicknesses of 5 nm. The films are deposited on MgO substrates that are heated to about 800 °C during deposition. A typical critical temperature (T_c) is about 10 K and the transition width is very small (0.5 K). The films are evaluated by measuring their superconducting characteristics as well as their thickness and surface roughness by means of AFM analysis.

Phonon-cooled HEB devices are fabricated from the films to study their performance as HEB mixers. The device fabrication process at UMass/Amherst involves lift-off lithography of the antenna (gold), and Reactive ion etching (RIE) or wet etching of the NbN. The I-V characteristics and noise temperatures of the devices were measured in order to determine their quality for PHEB applications.

**** Publication of the National Institute of Standards and Technology, not subject to copyright.***

I. INTRODUCTION

Heterodyne detection is the most sensitive spectroscopic technique over a broad frequency range that produces high spectral resolution in the THz region. A technological challenge is therefore to develop heterodyne receivers with the best possible sensitivity and bandwidth that are still compatible with such constraints as operating temperature and power available from existing local-oscillator (LO) sources. Hot-electron bolometric (HEB) detectors, with a thin film superconductor (NbN) as the active medium, have been under development for the last decade. NbN HEB detectors have demonstrated an increase in sensitivity of an order of magnitude and a decrease in LO power requirement by three orders of magnitude in the last few years. FIG.1 shows a survey of the noise temperature as a function of frequency for different types of detectors operating in the terahertz regime. A two fold approach can be taken for the development of HEB technology. The first is to maximize the critical temperature of the superconducting device by growing thicker films at the expense of IF bandwidth, whereas the second approach focuses on maximizing the IF bandwidth at the expense of the critical temperature. Here, we concentrate first on maximizing the critical temperature at the expense of the bandwidth. To conduct the investigation, we have developed a film-deposition process utilizing our dc reactive magnetron sputtering chamber. Then, PHEB devices were fabricated from the films. Preliminary results of the noise temperature measurements are presented.

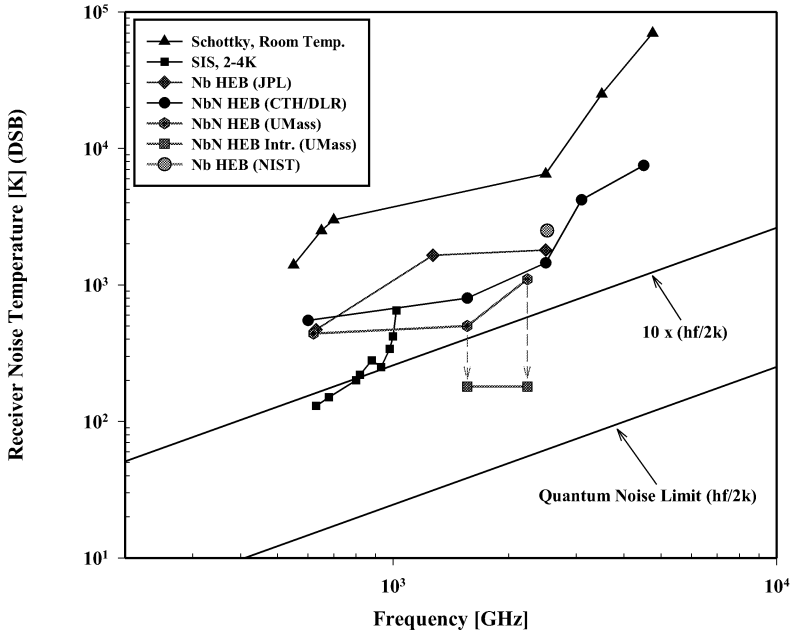

FIG. 1. Noise temperatures vs. frequency for receivers in the terahertz regime [1]-[6].

II. FILM AND DEVICE FABRICATION

NbN Films

NbN thin films were prepared by reactive sputtering from a Nb target in a nitrogen/argon atmosphere. The deposition chamber is cryopumped and achieves a base pressure of 1.5×10^{-5} Pa. Total pressure is controlled with a variable throttle valve on the cryopump and is measured with a capacitance manometer. UHP grade argon and zero-grade nitrogen are introduced into the chamber and their flow is controlled by needle valves. The partial pressure of nitrogen is determined simply by subtracting the initial Ar pressure from the total pressure of the mixture. The 75 mm diameter Nb sputtering target was specified to have a purity of 99.95%. The sample-to-target distance in our system is 10 cm. Crystalline MgO substrates, with (100) orientation, are cleaned in ambient temperature HF, followed by rinsing in organic solvents with ultrasonic agitation. The substrate was glued to a vacuum compatible heater block with silver paint and baked under a radiant heater for an hour prior to mounting in the deposition chamber.

The deposition sequence starts with cleaning of the target by sputtering Nb onto a dummy sample in an atmosphere of pure Ar, typically for five minutes. In the next step nitrogen is added and pre-sputtering continues for another five minutes, while equilibrium is reached with regard to the nitrogen content at the target surface.

As discussed at length in the literature [7], a feedback mechanism exists in the magnetron plasma during reactive sputtering of NbN. When the plasma is voltage or power biased, the feedback is positive, leading the target surface to be either completely covered with nitride or completely free of nitride. The plasma current-voltage (I-V) characteristic in this condition is hysteretic, and control of the stoichiometry of sputtered films is problematic. The films come out either nitrogen or niobium-rich, depending on the state of the target surface. However, under current bias the feedback is negative and the plasma I-V curve is single-valued, though it includes a region of negative differential resistance. Therefore, all NbN films described in this paper were grown with the plasma current-biased. FIG.2 shows the I-V curves for different pressures and gas compositions for our sputtering chamber.

While pre-sputtering, the MgO substrate was heated to 800°C and actively stabilized at that temperature. Substrate temperature was monitored by a thermocouple embedded in the body of the heater block. Experience with identical heater blocks used for high-temperature laser ablation of YBCO films indicates that a significant temperature gradient (probably 20 to 50 °C) exists between the thermocouple and the surface of the substrate. Once the films were

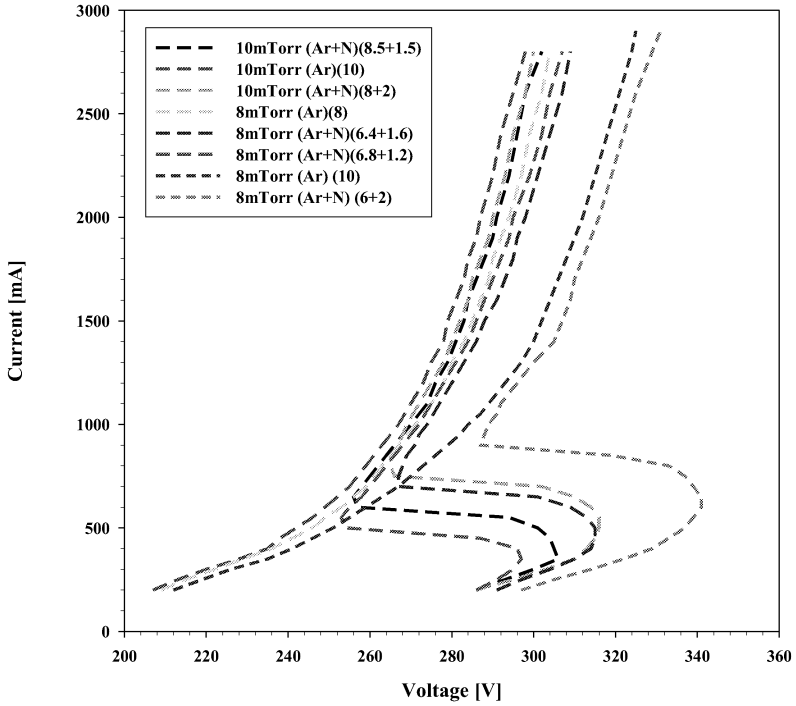

FIG. 2. I-V characteristics of the sputtering plasma.

deposited, the sample was cooled to ambient temperature in 1 atmosphere nitrogen background pressure.

Our highest critical temperature samples (T_c=11.2 K, ΔT_c=0.2 K) were obtained in a 15% N_2, 85% Ar mixture, at 1.33 Pa total pressure, an applied current of 1.2 A, and resulting voltage of about 275 V. Film thickness is measured with a commercial atomic force microscope (AFM). Typical deposition rates are around 0.25 nm/s. For the series of samples described here, a constant film thickness of 5 nm was desired. Accordingly, the deposition time for each film was adjusted under the assumption that deposition rate is proportional to power. Two optimization studies for maximizing critical temperature as a function of the plasma current and substrate temperature are shown in FIG.3.

Quasi-optical Design

The next step is to evaluate the films by fabricating Phonon-cooled HEB mixer devices, and to measure the noise temperature and IF bandwidth of these devices. A quasi-optical coupling design was used to couple the THz radiation into the device. A twin-slot antenna was photo-etched in a 200 nm gold layer that had been e-beam evaporated over the NbN film. Af-

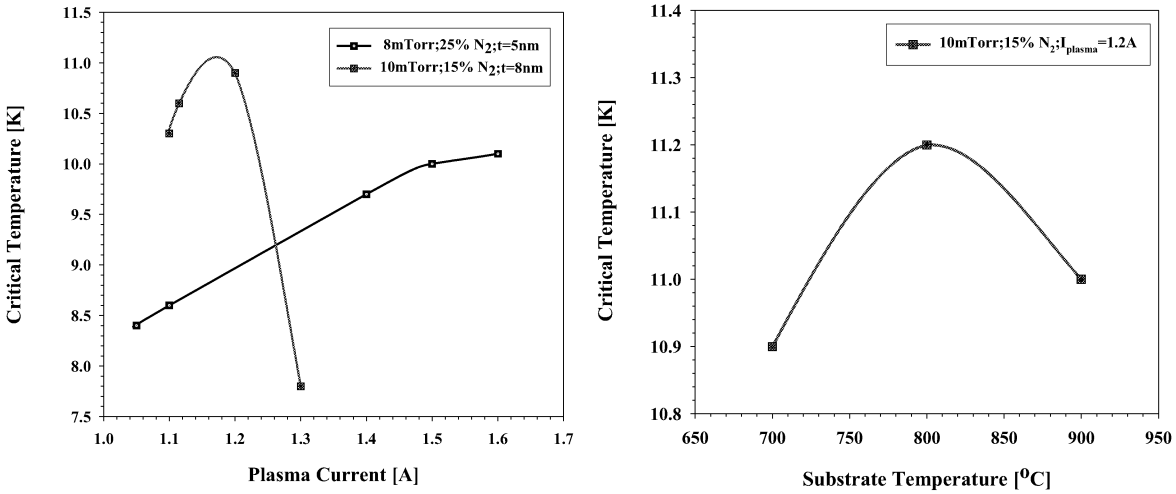

FIG.3. Optimizations of critical temperature as a function of substrate temperature and plasma current.

ter the gold layer was lifted off, the NbN film was wet-etched to define a HEB device with length of 1μm and width of 4 μm. The antenna response is centered at 1.5 THz, with a bandwidth of 1 THz to 1.9 THz. FIG.4 shows a photograph of the HEB device at the terminals of a twin-slot antenna. Following device fabrication an elliptical Si lens was affixed to the backside of the substrate. The lens was positioned using lines which had been accurately scribed on the lens side of the substrate and then affixed with purified bee's wax. The lens/substrate assembly was inserted into a mixer block, which also served as a bias tee. A three-section filter prevents THz radiation from escaping out the IF port. Four devices were fabricated, and one of these was tested successfully.

III. EXPERIMENTAL SETUP

The integrated antenna/HEB device and lens are attached to a copper post, which is thermally anchored at the other end to the liquid helium reservoir of a commercial dewar. The antenna is connected to the IF and bias system via a semirigid coax line. A cooled HEMT amplifier is also used inside the dewar. This IF amplifier has a pass band from 1000 to 2000 MHz with a noise temperature of about 5 K. The receiver noise temperature is measured with a CO_2 laser pumped FIR gas laser as the LO source. Mylar beam splitters with a thickness of 6 μm act

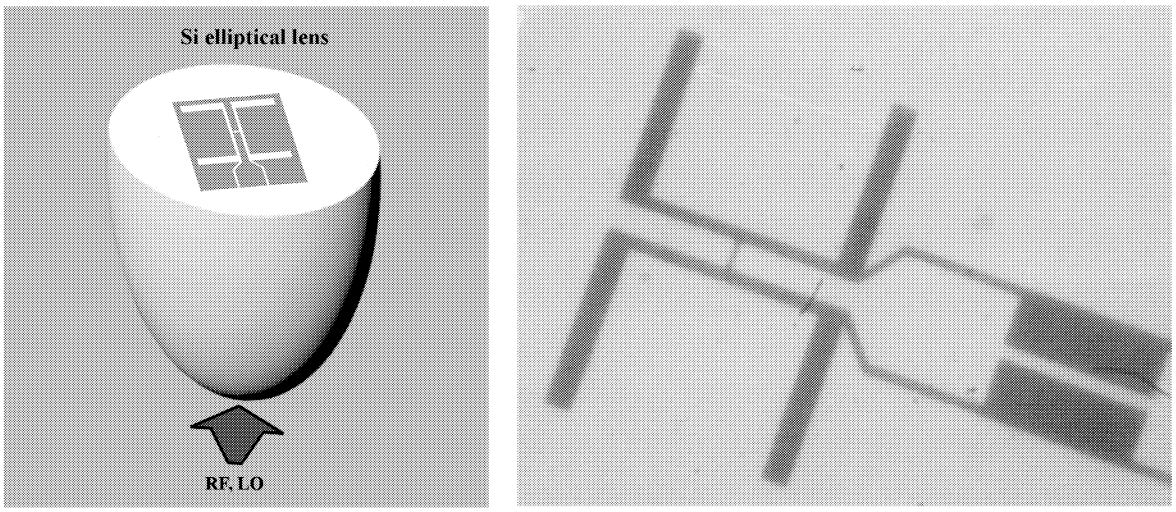

(a) **(b)**

FIG.4. (a) a quasi-optical design illustration; (b) a photograph of the twin-slot antenna. The PHEB device in the center is too small to be seen.

as diplexer between the LO and a chopped hot/cold noise source. The LO radiation is focused by a TPX lens.

IV. RESULTS AND DISCUSSION

The measured I-V curves are shown in FIG. 5. The top (black) curve was measured with no LO power applied, whereas the remaining curves were measured with different amounts of LO power applied at a wavelength of 184 μm (1.63 THz). The total receiver noise temperature, including the 6 μm thick mylar beam splitter, was about 6,000 K. The antenna and the lens were not optimally aligned in this preliminary experiment; therefore, we expect lower noise temperatures in future experiments. We base this on the excellent I-V curves (low critical current and a large reduction in the current at the resistive stage as shown in FIG. 5), which are similar to those of earlier devices that UMass/Amherst fabricated, and which had noise temperatures in the 500-1,000 K range. FIG.6 shows the measured IF frequency response. The 3 dB bandwidth is about 1.3 GHz, which is less than that for optimized films on MgO. Narrower bandwidths have typically been obtained in other laboratories for the first phase of a film growth program, so this is not too surprising. The preliminary results we have obtained so far are thus quite encouraging.

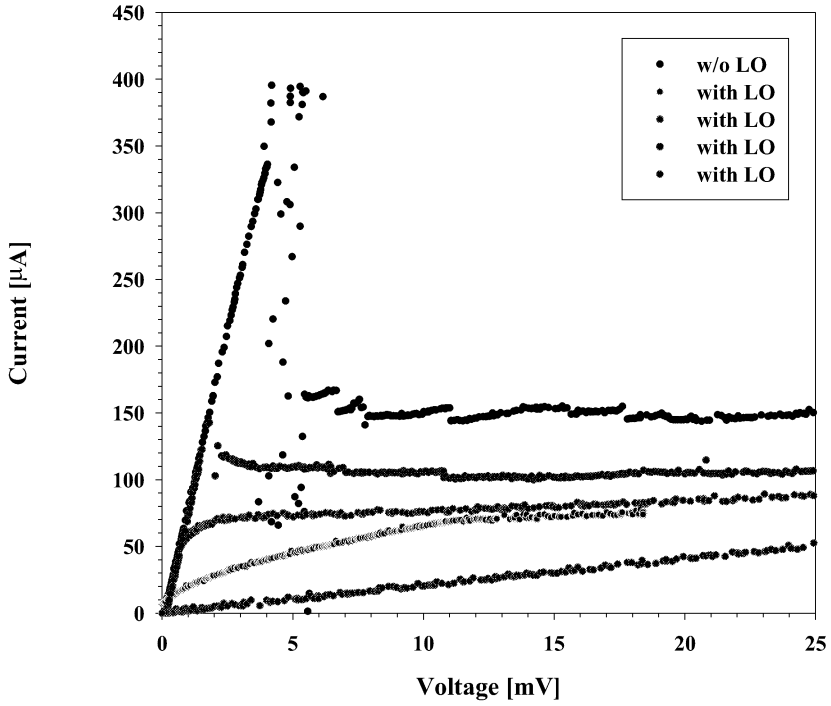

FIG.5. I-V characteristics of the device: the black curve was taken without LO power, showing the instability characteristics of an HEB device, whereas the blue through red curves were taken with increasing LO powers.

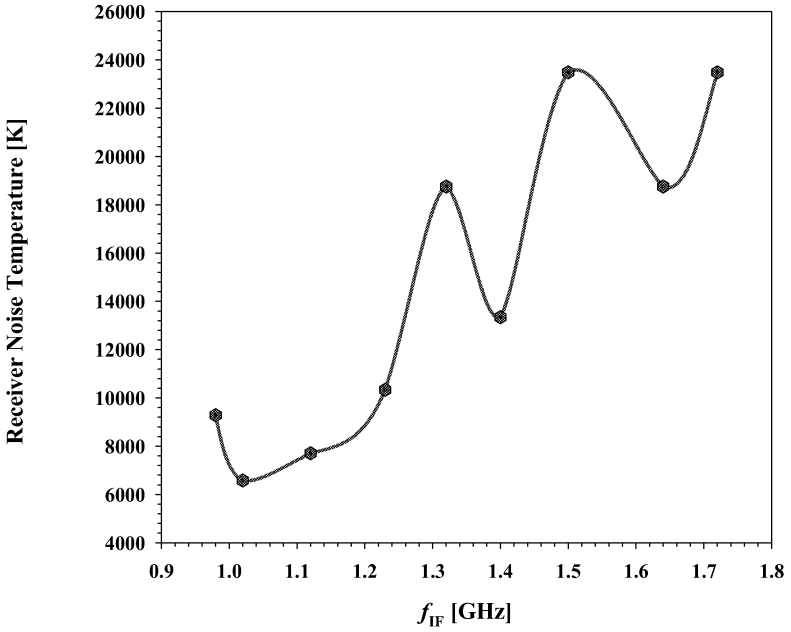

FIG.6. Noise temperature as a function of the IF frequency. The ripple in the frequency response is attributed to the IF filter circuitry.

ACKNOWLEDGMENTS

This work was supported by the NASA Space Astrophysics Research and Analysis Program.

REFERENCES

1. A.L. Betz and R.T. Boreiko, "A Practical Schottky Mixer for 5 THz (Part II)," *Proc. Seventh Intern. Space THz Technol. Symp,* , pp. 503-510, Charlottesville, VA, March 1996.

2. P. H. Siegel, "Terahertz Technology", *IEEE Trans. on Microw. Theo. and Techn.*, Vol. 50, No. 3, 910-928, March 2002.

3. S. Cherednichenkoa , M. Kroug, H. Merkel, P. Khosropanah, A. Adam, E. Kollberg, D. Loudkov, G. Gol'tsman, B. Voronov, H. Richter, H.-W. Huebers,"1.6 THz Heterodyne Receiver for the Far Infrared Space Telescope", *Europ. Conf. on Applied Supercond.*, Copenhagen, August 2001.

4. A.D. Semenov, H.W. Huebers, J. Schubert, G. Gol'tsman, A.I. Elantiev, B. Voronov, and G. Gershenzon, "Design and performance of the lattice cooled hot-electron terahertz mixer", *J. Appl. Phys.* 88 (11), p. 6758, 2000.

5. E. Gerecht, C. D. Reintsema, E. N. Grossman, A. L. Betz, and R. T. Boreiko, "Noise Temperature For Nb DHEB Mixer Arrays for Far-Infrared Spectroscopy," *Proc. Thirteenth Intern. Space THz Technol. Symp.*, Harvard Univ., March 2002.

6. E. Gerecht, C.F. Musante, Y. Zhuang, M. Ji, K.S. Yngvesson, T. Goyette, and J. Waldman, "Development of Focal Plane Arrays Utilizing NbN Hot Electron Bolometric Mixers for the THz Regime," *Proc. Eleventh Intern. Space THz Technol. Symp.*, U. Michigan, May 2000.

7. P. Yagoubov et al.,"The Bandwidth of HEB Mixers Employing Ultrathin NbN Films on Sapphire Substrate," *Proc. Seventh Intern. Space THz Technol. Symp,* Charlottesville, VA, March 1996.

A DUAL REFLECTOR FEED SYSTEM FOR A SUB-MM HOLOGRAM CATR

Janne Häkli, Tomi Koskinen, Juha Ala-Laurinaho, Jussi Säily, Anne Lönnqvist,
Juha Mallat, Jussi Tuovinen*, Antti V. Räisänen

MilliLab, Radio Laboratory, Helsinki University of Technology
*MilliLab, VTT Information Technology
email: janne.hakli@hut.fi

ABSTRACT – Manufacturing of large holograms for compact antenna test ranges can be facilitated with a modified hologram illumination. The relative quiet-zone size of the CATR can also be increased, which allows testing of larger telescope antennas with a fixed-sized hologram. The modified hologram illumination can be realized with a dual reflector feed system. In this paper, a simple ray tracing based synthesis technique for designing the dual shaped hyperbolic reflector feed system is described. Simulation results of a design example at 310 GHz are presented. The required accuracies in the reflector system assembly are also discussed.

INTRODUCTION

Several satellites carrying scientific instruments and antennas at sub-mm wavelengths (frequencies above 300 GHz) are scheduled for launch during this decade. The electrical testing of these telescopes is very demanding or even impossible with existing antenna measurement facilities. Conventional far-field antenna measurements are not applicable for large sub-mm wave antennas due to the required long far-field distance and the high atmospheric attenuations – the very reason for space-borne instruments. Near-field measurements are one option, but the measurements are very time consuming, as the required number of field samples is very large for accurate computation of the antenna radiation pattern. The compact antenna test range (CATR) is seen to be potentially the best antenna testing method at sub-mm wave frequencies [1].

In a compact antenna test range a collimating element forms the planar wave needed for antenna testing from a spherical wave radiated by a feed. The region, where the planar wave exists, is called the quiet-zone (QZ) of the CATR. Typically, the QZ is allowed to have at maximum 1 dB peak-to-peak ripple in amplitude and 10° in phase.

A set of reflectors, usually two reflectors, is commonly used as a collimating element in CATRs at microwave and millimeter wave frequencies up to 200 GHz. A binarized computer-generated amplitude hologram can also be used as a collimating element for a CATR [2]. The hologram pattern is manufactured by etching slots onto a copper-plated Mylar film. The hologram is a transmission type planar structure with inherently lower surface accuracy requirements than the requirements for reflectors. The hologram is tensioned into a frame to ensure sufficient surface flatness. The realization of a CATR based on a hologram is significantly more economical at sub-mm wave frequencies than the corresponding CATR based on reflectors, because the hologram manufacturing is less costly than manufacturing of large accurate reflector surfaces and only one hologram is needed for the CATR. An additional advantage is that the hologram is

lightweight, which allows the disassembly and transportation of the CATR to a different location. The basic structure of the hologram-based CATR is illustrated in Figure 1 with an example of the hologram pattern. Absorbers are placed around the CATR to reduce disturbances from the reflections from surrounding structures.

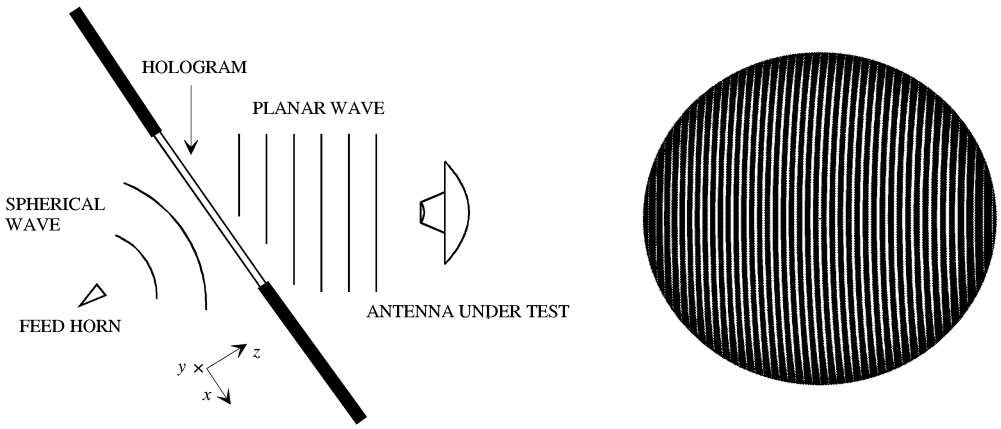

Figure 1. CATR based on hologram and an example of the hologram pattern

Testing of a large telescope requires a larger hologram than the telescope antenna aperture. The manufacturing of large sub-mm frequency holograms is the main challenge in the realization of a large hologram-based CATR. The large hologram patterns have to be combined from several separately etched hologram pieces that are soldered together as hologram patters cannot be currently etched on larger films than 1.5 meters by 6.0 meters. These seams cause disturbances to the QZ field. The slots in the hologram pattern are narrowed towards the hologram edges to realize an amplitude taper to the hologram aperture, which reduces edge diffraction disturbances to the desired plane wave. Etching of narrow slots (below 100 μm) is difficult for large surfaces.

The work described in this paper aims to decrease the size of the hologram needed for testing a telescope in a CATR with an improved feed system. In addition, the hologram fabrication is simplified by widening the narrow slots at the hologram pattern edges. These benefits can be achieved by introducing an amplitude taper with controlled phase into the hologram illumination. The improved illumination can be realized with a dual reflector feed system (DRFS). A DRFS design example for a 600 mm hologram operating at the frequency of 310 GHz is presented.

MODIFIED HOLOGRAM ILLUMINATION

Hologram manufacturing can be facilitated by modifying the hologram illumination to have an amplitude taper at the hologram edges. The amplitude taper reduces the need for narrowing the slots in the hologram pattern at the hologram edges. The resulting wider slots are easier to etch. One example of suitable incident amplitude in the hologram aperture is a rotationally symmetric Butterworth-type amplitude distribution function

$$E(\rho)=\frac{1}{\sqrt{1+\kappa\left(\frac{\rho}{\rho_0}\right)^{2N}}}, \tag{1}$$

where N is the order of the function, ρ is the radial distance from the hologram center and ρ_0 is the radial distance of the edge of the nearly flat part of function. The amplitude at this edge is determined with the parameter κ. The achievable relative quiet-zone size can be increased with the modified illumination. This allows testing of larger telescopes with a fixed-sized hologram. Holograms were designed for two test cases: for a large quiet-zone size and for more constant slot widths in the hologram pattern. The simulated quiet-zone for a 600 mm hologram at 310 GHz is shown together with the slots widths in the hologram pattern in Figures 2 and 3. In case 1 (Figure 2), the hologram was optimized for a large quiet-zone size. The illumination function used was (1) with N=3, ρ_0=300 mm and κ=4.01. The quiet-zone width is increased by 40 % and the narrowest slots are widened from 37.5 µm to 65 µm. In case 2, the hologram slot widths were chosen to be nearly constant over the hologram pattern, which facilitates the etching of the hologram pattern. The simulated QZ field amplitude together with the hologram pattern slot widths is shown in Figure 3. The illumination function (1) was chosen to have N=5, ρ_0=210 mm and κ=1. The slots in the pattern are 280–405 µm wide with the modified illumination.

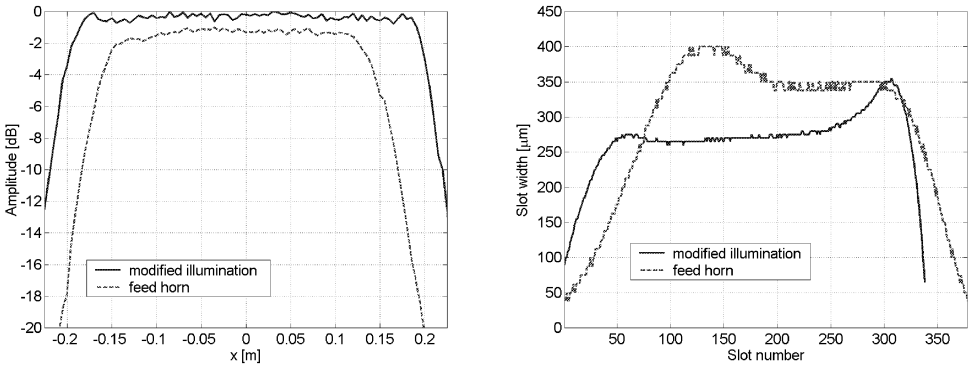

Quiet-zone amplitude *Hologram pattern slot widths*

Figure 2. Case 1: simulation results for a hologram optimized for large quiet-zone size compared to a hologram illuminated directly by the feed horn.

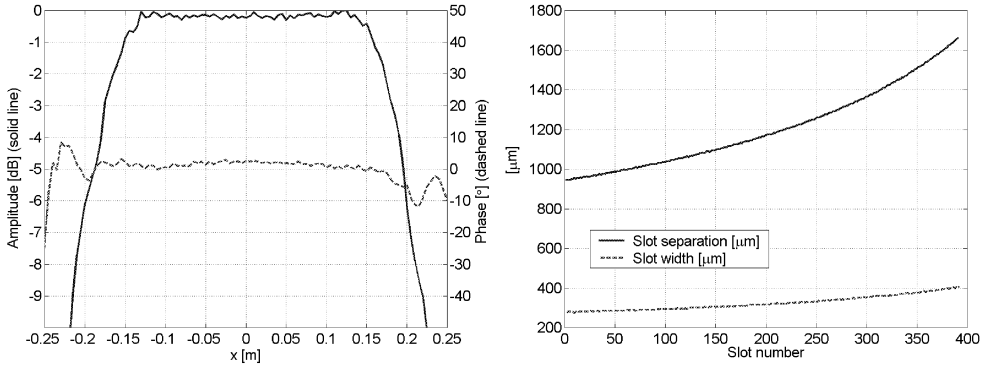

Quiet-zone amplitude and phase *Slot widths and slot separation*

Figure 3. Case 2: simulation results for a hologram with nearly constant slot widths.

SYNTHESIS OF A DUAL REFLECTOR FEED SYSTEM FOR THE CATR

Dual reflector feed system (DRFS) can be used to modify the hologram illumination. Two reflecting surfaces are needed to control both the illumination amplitude and phase. The hologram illumination is a shaped beam. The DRFS beam has an amplitude of a Butterworth-function (1) in the hologram aperture with the phase of a spherical wave originating from the hologram focus. The DRFS was chosen to have a dual shaped hyberbolic geometry. The basic structure for a 600 mm hologram is shown in Figure 4. The hyperbolic reflector surfaces allow a compact structure together with a wide shaped beam needed for the hologram illumination. The first, the subreflector, has concave shape and the second, the main reflector, is convex. The reflectors are fed with a corrugated horn.

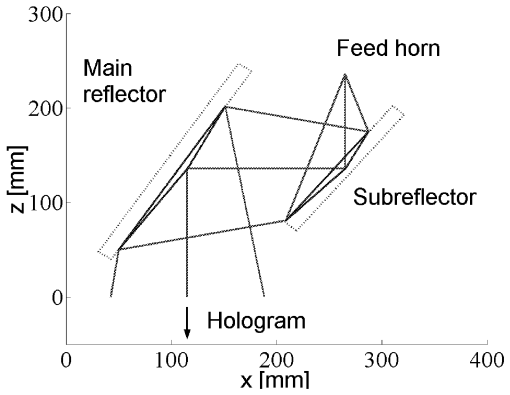

Figure 4. Schematic of the dual reflector feed system.

The subreflector center is located at the distance of 100 mm from the feed horn and the separation of the reflector centers is 150 mm. The design of the reflector surfaces is a dual shaped reflector synthesis problem. Shaped reflectors for shaped beam applications can be synthesized with several methods. Commercially available synthesis software are usually intended for satellite antenna applications with contoured beams. As the

hologram DRFS differs from the common applications, a simple specialized synthesis method was developed and implemented as MATLAB®-software. The used method is based on the method described in [3] with some modifications.

The synthesis of the hologram DRFS is based on ray-tracing, i.e., on geometrical optics (GO). The advantages of the GO method are that no initial surfaces are needed as in many diffraction synthesis methods and the method is straightforward and simple. The high frequency facilitates the use of a simple GO synthesis as the reflectors are relatively large in wavelengths. The main disadvantage of the method is that it does not take into account the diffraction effects. The GO synthesis is commonly used as the starting point for diffraction synthesis optimization in satellite communication antenna applications.

In geometrical optics, the electromagnetic fields are approximated with rays that propagate straight between the reflections. The rays in DRFS synthesis procedure were chosen to contain only the power density (amplitude) and phase information. The power is considered to propagate in flux tubes bounded by adjacent four rays. The ray path length determines the phase for each ray. The reflectors are assumed locally planar at the reflection points and the surface normal at each point is computed with reflection law (Snell's law) from the desired ray path.

The ray distribution in the hologram aperture, i.e., flux tubes, determine the illumination amplitude in the aperture. An even-angled ray distribution in spherical coordinates is used to describe the feed horn radiation. The ray distribution corresponding to the desired hologram illumination is solved in polar aperture coordinates from

$$P_{out} = P_{in} = \int_{\rho_1}^{\rho_2}\int_{\phi_1}^{\phi_2} \frac{E(\rho,\phi)^2}{C}\rho d\phi d\rho \,, \tag{2}$$

where $E(\rho,\phi)$ is the amplitude of the electric field and C includes all coordinate independent terms (for example the wave impedance). The electric field power density $E(\rho,\phi)^2$ is assumed to be piecewise linear in radial direction for easy solving of ρ_2 from (2) using the conservation of power within the flux tubes. The reflector surfaces are determined so that they transform the feed horn even-angled ray distribution into the ray distribution in the hologram aperture, which corresponds to the desired hologram illumination.

The synthesis procedure starts with the center ray path. This ray goes from the feed phase center to the sub-reflector center and reflects there to the main reflector center ending up at the hologram center. The center incident and reflected rays form 90° angles. The surface normal is then computed with reflection law from the incident and reflected rays. The surface tangent plane is easily determined from the normal vector for both reflector surfaces. The next ray is launched from the feed phase center towards the subreflector. The intersection point of this ray and the tangent plane is the next sub-reflector surface point. The new surface normal is calculated from the direction of reflected ray for the required ray path. The synthesis proceeds from the reflector centers towards the edges in counter-clockwise direction. Previously computed surface normal

at the closest known point in radial direction towards the reflector center from the current point is used to determine the local tangent plane at the current point. The main reflector is determined similarly by launching rays from the hologram focus to the hologram aperture (reflected rays) and using the rays from the corresponding subreflector points as incident rays. Finally, the phase of hologram illumination is corrected to the phase of a spherical wave originating from the feed horn phase center by moving the main reflector surface point along the ray path from the hologram focus to the hologram aperture. Additional optimization of the phase may be done with phase correction obtained from the simulated phase performance of the DRFS.

DESIGN EXAMPLE

The synthesized reflector surfaces for a 600 mm hologram at 310 GHz are shown in Figures 5 and 6. The hologram illumination function used was (1) with N=5 and $\rho_0 = 210$ mm. Simulated quiet-zone field and hologram pattern slot widths are shown in Figure 3. The direction of the incident radiation is different in Figures 5 and 6 to better illustrate the reflector surfaces. The subreflector is concave, i.e., the feed horn is below the surface in Figure 4, and the main reflector is convex with the hologram and the subreflector above the surface in Figure 5. The dimensions of the shaped reflector surfaces are approximately 166 mm × 119 mm × 2.7 mm and 122 mm × 83 mm × 4.6 mm for the main reflector and the subreflector, respectively. The edges of the shaped reflector surfaces are rounded to reduce edge diffraction and flat plates were added to the reflector surfaces to allow simulation of the surfaces milled out of metal plates.

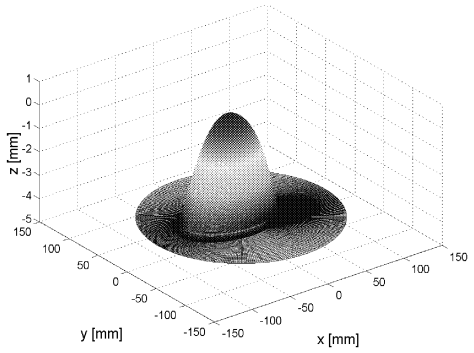

Figure 5. Subreflector surface (inverted).

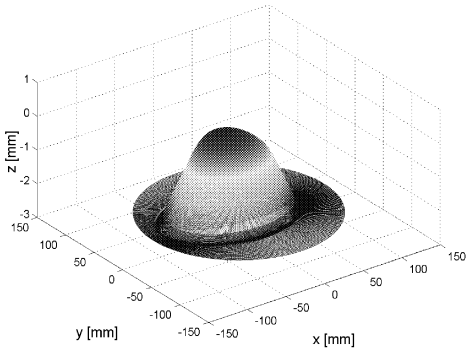

Figure 6. Main reflector surface.

The applicability of the GO synthesis method for the DRFS design was verified with simulations of the DRFS radiation. The simulations were done with commercial reflector antenna analysis software GRASP8W. Physical optics (PO) and physical theory of diffraction (PTD) were used to compute the DRFS radiation at the hologram aperture. The focal length of the hologram was 1.8 meters and the near-field radiation of the dual reflector feed system was computed at the corresponding distance from the DRFS. The simulated DRFS radiation is presented in Figures 7 and 8 for the horizontal amplitude cut and for the vertical amplitude cut of the hologram aperture field, respectively. The objective was the 5th–order Butterworth-illumination. The phase in the center crosscut of the aperture field compared to the desired ideal spherical wave is

shown in Figure 9. The simulated cross-polarized field at the hologram center is presented in Figure 10. Both of these aperture cuts are in the horizontal direction.

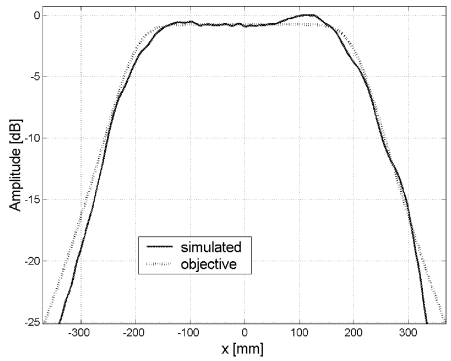

Figure 7. Amplitude in a horizontal cut.

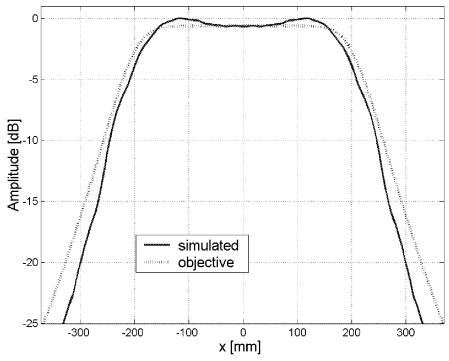

Figure 8. Amplitude in a vertical cut.

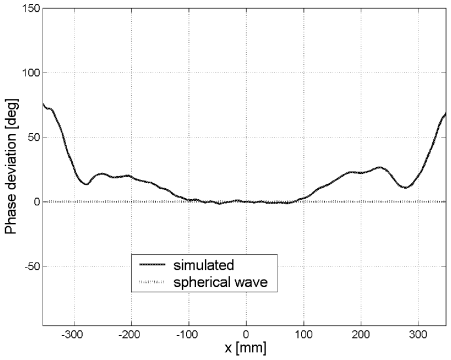

Figure 9. Simulated phase in a horizontal cut.

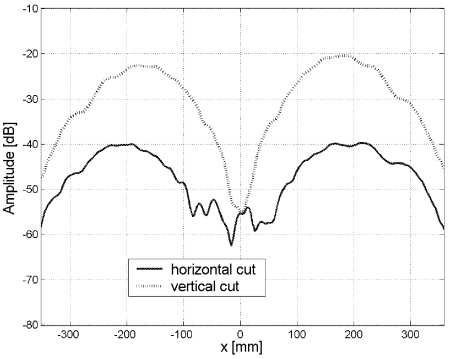

Figure 10. Cross-polarization.

The deviation of the simulated DRFS performance from the desired Butterworth-type illumination is mainly due to edge diffraction. The edge diffraction could be reduced with further optimization of the DRFS structure and with using lower edge illumination both in the hologram illumination (edge taper on the main reflector) and in the feed horn beam (edge taper on the subreflector). The 310 GHz corrugated horn used has a wide beam, which makes the reflector sizes inconveniently large for lower than –15 dB edge taper on the subreflector.

Manufacturing and assembling of the dual reflector feed system

Phase and amplitude errors in the incident field on the hologram cause errors to the QZ field, which are roughly of the same order of magnitude as the errors in the incident field. Therefore, to satisfy the QZ field quality requirement of 1 dB amplitude and 10° phase ripple (peak-to-peak), the hologram illumination ripples are allowed to be at maximum half of these. The main DRFS manufacturing related causes for the hologram illumination deviations from the desired are the accuracy of reflector surface milling and the potential misalignment of the reflectors.

Assuming the RMS-surface error in the milling to be of the order of 2 μm, the RSS-phase error caused by the two reflections in the reflector system can be estimated to be about 2°. If the phase errors caused by the misalignment of reflectors and the feed horn are independent of milling errors, the maximum allowed phase deviation due to the misalignments is about 4.5° for the total RSS-error of 5° in the hologram illumination. The total phase deviation caused by the misalignment can be estimated to be

$$\Delta\varphi_{misalignment} = \sqrt{\Delta\varphi_{feed}{}^2 + \Delta\varphi_{sub}{}^2 + \Delta\varphi_{main}{}^2}\,. \tag{3}$$

Assuming that the deviations caused by the feed horn ($\Delta\varphi_{feed}$), the subreflector ($\Delta\varphi_{sub}$) and the main reflector ($\Delta\varphi_{main}$) have an equal and independent contribution to the total phase deviation in the DRFS beam, the allowed phase deviation caused by each of them is approximately 2.6°. The effect of the reflector (or feed horn) dislocation and misalignment was studied with GRASP8W simulations. In the simulations, the other objects were kept at their correct locations and alignment, while the reflector (or horn) under investigation was moved or rotated. Simulation results for subreflector displacement in *z*-direction, i.e., when the subreflector distance from the feed is changed, are shown in Figures 11 and 12 in horizontal and vertical cuts at the center of the hologram aperture, respectively. The phase is compared to the beam of the perfectly aligned DRFS .

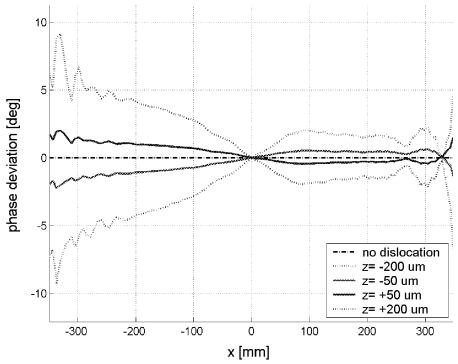

Figure 10. Phase deviation (horizontal cut).

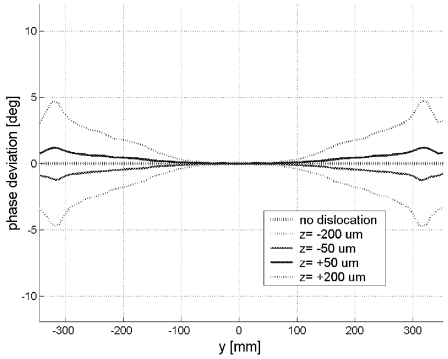

Figure 11. Phase deviation (vertical cut).

In the simulations with several examples of dislocations and misalignments, an approximately linear dependence between the amount of the misalignment and the resulting phase deviation was observed. The amplitude deviations were observed to correspond with the amount of the phase deviation in the simulation. The maximum allowed amplitude deviation could have been determined similarly to the phase deviations that were discussed here. The estimated location and alignment accuracies of the DRFS assembly are shown in Table 1. The rotation tolerance around the *x*-axis is estimated to be about the same as the tolerance of the *y*-axis rotation.

Table 1. Estimated accuracies required for the reflector (feed) locations and alignment.

	Dislocation in *x*-direction	Dislocation in *y*-direction	Dislocation in *z*-direction	rotation around the *y*-axis	rotation around the *z*-axis
Feed	<20 μm	<20 μm	<100 μm	<0.007°	<30°
Subreflector	<20 μm	<20 μm	<100 μm	~0.005°	~0.12°
Main reflector	<20 μm	<20 μm	<100 μm	<0.007°	<0.2°

The required accuracies for the reflector locations and alignment are quite high. Some of the misalignment effects can be compensated by rotating the whole reflector system in relation to the hologram, which eases the actual accuracy requirements. Nevertheless, the alignment of the reflectors is critical for satisfactory DRFS operation. To ensure sufficient accuracy the reflector system will be manufactured as an integrated system. The manufacturing and the mechanical design of the DRFS will be done by Thomas Keating Ltd in England.

Conclusions

The hologram based compact antenna test range can be improved with a dual reflector feed system. The relative quiet-zone size of the hologram CATR can be increased by modifying the hologram illumination with two shaped hyperbolic reflectors. The hologram manufacturing is facilitated when the modified illumination is used as very narrow slots are not needed at the hologram pattern edge. A simple geometrical optics based synthesis method was developed and implemented as an MATLAB®-software. The simulated hologram illumination agrees reasonably well with the desired illumination, which shows that the synthesis method is applicable to the dual reflector feed system design for the hologram CATR.

Acknowledgements

Individual authors are grateful to the Foundation for Commercial and Technical Sciences, the Foundation of Technology (Finland), the Foundation of the Finnish Society of Electronics Engineers, the Finnish Cultural Foundation, Jenny and Antti Wihuri Foundation and the Nokia Foundation for their support. This research is funded by ESA/ESTEC (ESTEC contract No.13096/98/NL/SB). VTT Information Technology is acknowledged for the use of GRASP8W software.

References

[1] Foster, P. R., Martin, D., Parini, C., Räisänen, A., Ala-Laurinaho, J., Hirvonen, T., Lehto, A., Sehm, T., Tuovinen, J., Jensen, F. , Pontoppidan, K., *Mmwave antenna testing techiniques - Phase 2*, MAAS Report 304, Issue No. 2, ESTEC Contract No. 11641/95/NL/PB(SC), December 1996.

[2] J. Ala-Laurinaho, T. Hirvonen, P. Piironen, A. Lehto, J. Tuovinen, A. V. Räisänen, U. Frisk, "Measurement of the Odin telescope at 119 GHz with a hologram type CATR", *IEEE Transactions on Antennas and Propagation,* Vol. 49, No. 9, pp. 1264–1270, 2001.

[3] P.-S. Kildal, "Synthesis of multireflector antennas by kinematic and dynamic ray tracing", *IEEE Transactions on Antennas and Propagation*, Vol. 38, No. 10, pp. 1587–1599, 1990.

MIXER DEVELOPMENT FOR HIFI BAND 2 (640 – 800 GHz)

C. E. Honingh, M. Justen, R. Teipen, T. Tils, K. Jacobs

KOSMA, I. Physikalisches Institut, Universität zu Köln
Zülpicher Strasse 77, 50937 Köln, Germany

We present a fixed tuned SIS waveguide mixer for 640–800 GHz. The waveguide and filter design has been done using 3D EM-Simulation to improve the accuracy of the design for the required large fractional bandwidth. In this frequency range we use standard Nb–Al_2O_3–Nb SIS junctions with an R_NA product of approximately 15 ohm-μm^2 , and areas between 1 μm^2 and 0.4 μm^2. The choice of tuning structure material is not directly obvious because the frequency range includes the niobium gap frequency at 700 GHz. Therefore devices with a NbTiN ground plane and as a choice with a niobium or an aluminum top electrode are used.

Current best noise temperatures are 300 K at the lower frequency end of the band and 450 K at the high end of the band, measured with the prototype HIFI mixer at 4–8 GHz IF frequency, for a device with a niobium top electrode.

Measurements and analysis of devices with different designs, and both integrated tuning structure top electrode materials will be presented. The accuracy of the RF mixer design will be evaluated.

The HIFI Focal Plane Unit

B.D. Jackson, K.J. Wildeman, and N.D. Whyborn
on behalf of the HIFI Focal Plane Consortium
SRON National Institute for Space Research
Postbus 800, 9700 AV Groningen, The Netherlands

ABSTRACT

The Heterodyne Instrument for the Far-Infrared (HIFI) is a heterodyne spectrometer being built for the European Space Agency's Herschel Space Observatory, with seven receiver channels covering the 480-1250 and 1410-1910 GHz frequency ranges. This paper provides an overview of the HIFI Focal Plane Unit (FPU) design, with particular emphasis placed upon an overview of the primary elements in the FPU's signal chain.

1. THE HERSCHEL SPACE OBSERVATORY

The Herschel Space Observatory (see Fig. 1) is a cryogenic space telescope being built by the European Space Agency to study the universe in the far-infrared and the submillimetre (60-670 um) [1-3]. To fulfil its scientific goals, Herschel will carry three scientific instruments: two imaging arrays with low-to-medium spectral resolution (PACS [4] and SPIRE [5]); and a high-resolution heterodyne spectrometer (HIFI) [6,7]. To maximize the sensitivity of these instruments, the Herschel telescope will be passively cooled to ~ 80 K, while a superfluid helium bath will cool the satellite's optical bench and the instruments' detector elements to 10-15 K and < 3 K, respectively. The instruments' warm control electronics, together with the satellite's command and control system and HIFI's intermediate frequency spectrometers, will be located in the satellite's service module, below the cryostat, while the HIFI local oscillator unit will be mounted on the side of the cryostat, with the local oscillator beams injected into the focal plane unit through windows in the cryostat.

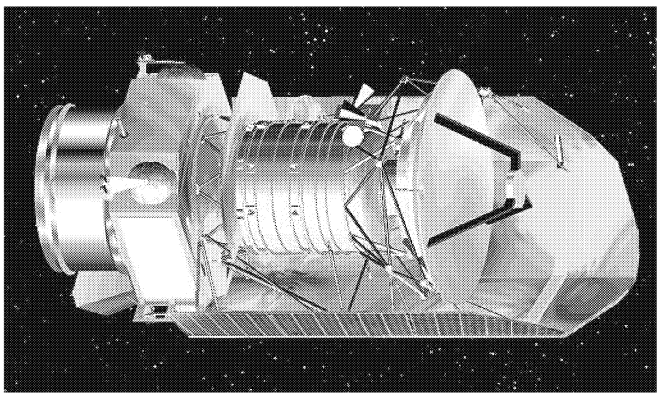

Fig. 1 – The Herschel Space Observatory

2. THE HETERODYNE INSTRUMENT FOR THE FAR-INFRARED (HIFI)

The Heterodyne Instrument for the Far-Infrared (HIFI) is a high-sensitivity, single-pixel heterodyne spectrometer that will be used to study a wide range of objects in the local solar system, our own galaxy, the interstellar medium, and both nearby and distant galaxies [6]. The primary characteristics of the HIFI instrument are:

- complete spectral coverage of 480-1250 (with 5 SIS mixer bands) and 1410-1910 GHz (with 2 HEB mixer bands);
- a spectral resolution of 0.14 to 1 MHz;
- high sensitivity, with $T_{N,rec} \sim 4hf/k_B$;
- a 4 GHz instantaneous band-width in both the upper and lower sidebands;
- dual polarization operation; and
- a calibration accuracy of at least 10% (with a goal of 3%).

As seen in Fig. 2, HIFI has five major sub-systems: the Local Oscillator Sub-System (LOSS); the Focal Plane Sub-System (FPSS); the Wide-Band Spectrometer (WBS); the High-Resolution Spectrometer (HRS); and the Instrument Control Unit (ICU).

Within the LO sub-system, a tuneable, spectrally pure 24-36 GHz signal is generated in the Local Oscillator Source Unit. This signal is then frequency-multiplied to 71-106 GHz, amplified, and further frequency-multiplied to the desired RF frequency in the Local Oscillator Unit. The result is a spectrally pure LO signal with a tuneable frequency and power level. Fourteen multiplier chains are used to cover the full HIFI spectral range, with two chains per Focal Plane mixer channel. The LO beams are fed into the Focal Plane through 7 windows in the Herschel cryostat.

Inside the Focal Plane Unit (FPU), the incoming astronomical signal is split into 7 beams. Each of these signal beams is optically combined with its corresponding LO beam, and then split into two linearly polarized beams that are coupled into 2 mixer units. Each of the mixer units generates an intermediate frequency (IF) signal that is amplified within the FPU prior to leaving the cryostat.

The IF output signals from the FPU are coupled into two IF spectrometers. The Wide-Band Spectrometer (WBS) is a four-channel acousto-optical spectrometer that samples the full 4-8 GHz output of the FPU with 1 MHz resolution, while the High-Resolution Spectrometer (HRS) is a high-speed digital auto-correlator that samples a narrower portion of the IF band with a higher resolution.

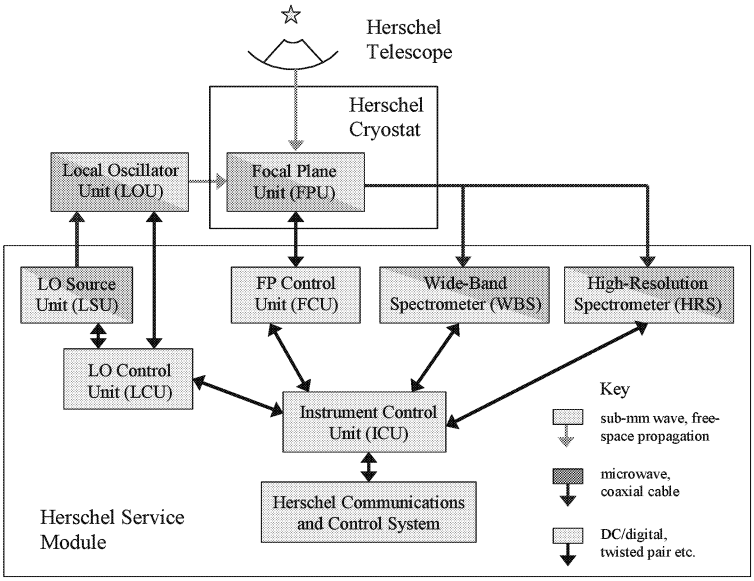

Fig. 2 – Block Diagram of the HIFI Instrument

Each of the 4 HIFI sub-systems includes a warm electronics unit. These four control units are, in turn, commanded by a single Instrument Control Unit, which also interfaces with the satellite's on-board command and control system.

3. THE HIFI FOCAL PLANE UNIT

The HIFI Focal Plane Sub-System consists of the Focal Plane Unit (the FPU, located on the Herschel optical bench) and the Focal Plane Control Unit (the FCU, contained in the satellite's warm service module).

The Focal Plane Unit (see Fig. 3) consists of six major assemblies: the Common Optics Assembly (COA); the Diplexer Assembly; the Mixer Sub-Assemblies (MSA's, of which there are 14); the second-stage IF amplifier box; the Focal Plane Chopper; and the Calibration Source Assembly.

The complexity of the Focal Plane sub-system is demonstrated by the large consortium of institutes that are contributing to its design, construction, and testing: ~ 20 groups from ~ 14 institutes (see Table 1, on the following page).

3.1 FPU Design Constraints

The design of the Focal Plane Unit is constrained by a number of important design requirements. In particular, the inputs to the FPU optical design are:

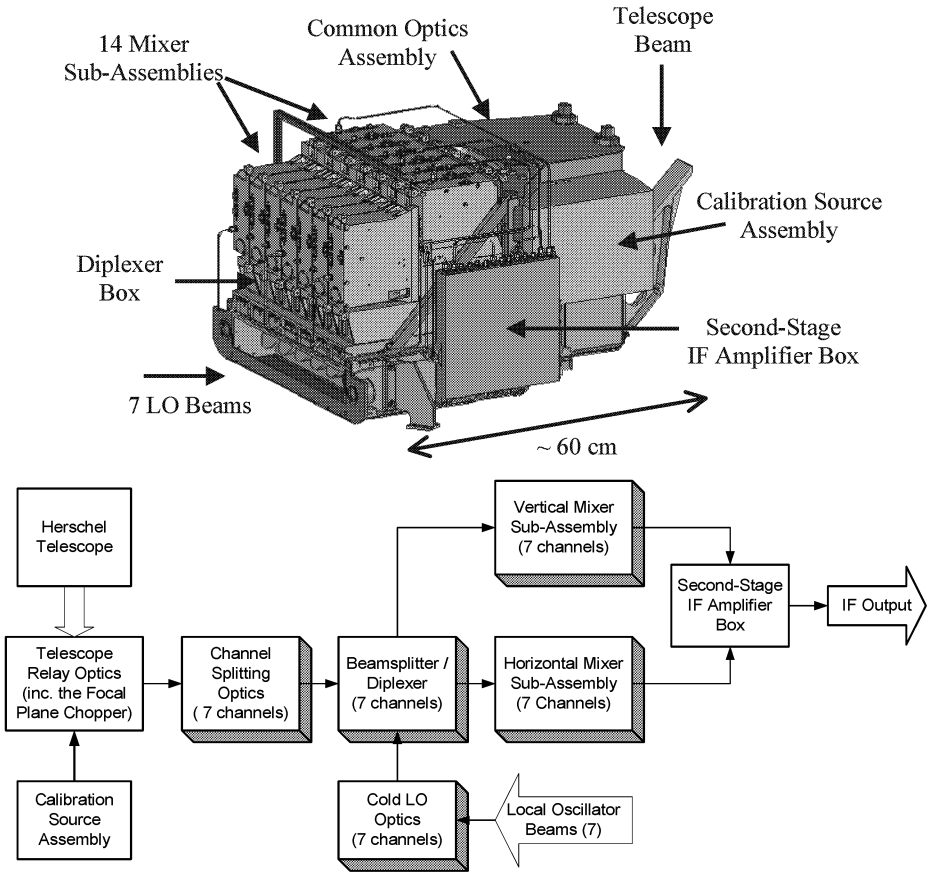

Fig. 3 – The HIFI Focal Plane Unit

Table1: The HIFI Focal Plane Sub-System Consortium

Country	Institute(s)	Responsibilities
The Netherlands	SRON	Management, System Integration and Testing, System Engineering, FCU, Mechanisms
	SRON, TPD, MECON	COA, Diplexer Box, MSAs, Calibration Source
	SRON, DIMES	Band 3 and 4 Mixers
France	LERMA, IRAM	Band 1 Mixer
Germany	KOSMA	Band 2 Mixer
	DLR (Berlin)	Band 6L Mixer Beam Measurements
USA	JPL/NASA	Band 6H Mixer, IF Amplifier HEMTS
	JPL, CalTech	Band 5 Mixer
Sweden	CTH	Band 6L Mixer, Band 1-4 MSA Beam Measurements, IF Amplifier Design
Spain	YEBES	First-stage IF Amplifier
Switzerland	ETH	Second-stage IF Amplifier, COA and MSA Construction
Ireland	NUI	Quasi-optical Design Analysis

- It is assumed that fundamental mode gaussian beams can approximate the RF beams produced by the mixers, the LOs, and the telescope.
- The Herschel telescope is a Ritchey-Chrétien telescope with a 3.5-m primary mirror and a 0.31-m secondary. The secondary is 1.6 m in front of the primary and 2.6 m from the telescope focal plane (yielding a geometrical F/D ratio of 8.68 for the edge-rays incident on the focal plane).
- The FPU produces seven optical beams (one per channel) that are spatially separated in the telescope focal plane, resulting in an angular separation of the optical beams on the sky.
- The telescope secondary is an aperture-stop in the optical system, truncating each of the HIFI signal beams at –11-dB (independent of frequency).
- The 7 LO beams enter from the back of the focal plane unit. Each beam has a 7.5 mm waist located ~ 200-250 mm from the input to the FPU, with the beams spaced by 50 mm.
- The optical imaging quality of the system should be high (a fundamental gaussian passing through the system should suffer distortion losses ≤ 1 %).

In addition to the optical interfaces, the mechanical and thermal interfaces to the spacecraft places the following constraints on the FPU design:

- The total FPU mass is ~ 46 kg.
- The total FPU volume is 50 x 70 x 40 cm^3.
- The average heat-load of the FPU on the cyrostat is ~ 20 mW on the instrument's 10 K level, 7 mW at 4 K, and 5 mW at 2 K (during operation).
- The FPU should survive the high vibration levels present during launch.

Finally, the HIFI model philosophy generates two additional, but related requirements:

- After integration of the FPU, it should be possible to repair or replace critical components within 1 month (i.e. mixers and mechanisms).
- After integration, it should be possible to upgrade the FPU if ongoing development yields a significant improvement in mixer sensitivity.

3.2 The Common Optics Assembly

The Common Optics Assembly (COA, see Fig. 4), is the basis of the FPU structure, and mounts directly on the Herschel optical bench. Its optical design consists of 3 blocks: the telescope relay optics, the channel-splitting optics, and the cold local oscillator optics.

The telescope relay and channel-splitting optics relay the instrument's seven signal beams from the Herschel focal plane into the diplexer box. This is done with 6 common mirrors (the telescope relay optics, shared by all channels), followed by 7 sets of three mirrors (the channel-splitting optics). The telescope relay and channel splitting optics have three primary functions:

- They produce an image of the telescope secondary on the fourth mirror in the chain, enabling the implementation of a focal plane chopper.
- They produce an image of the focal plane on the first mirrors in the channel-splitting optics. Because the instrument's seven beams are separated in the focal plane, this allows the beams to be split by seven isolated mirrors with different orientations.
- In each channel, they create an image of the telescope secondary within the diplexer box. This image is a frequency-independent waist that is relatively large, to minimize diffraction losses within the diplexers.

The waists of the seven beams entering the FPU from the LO unit are re-imaged by the

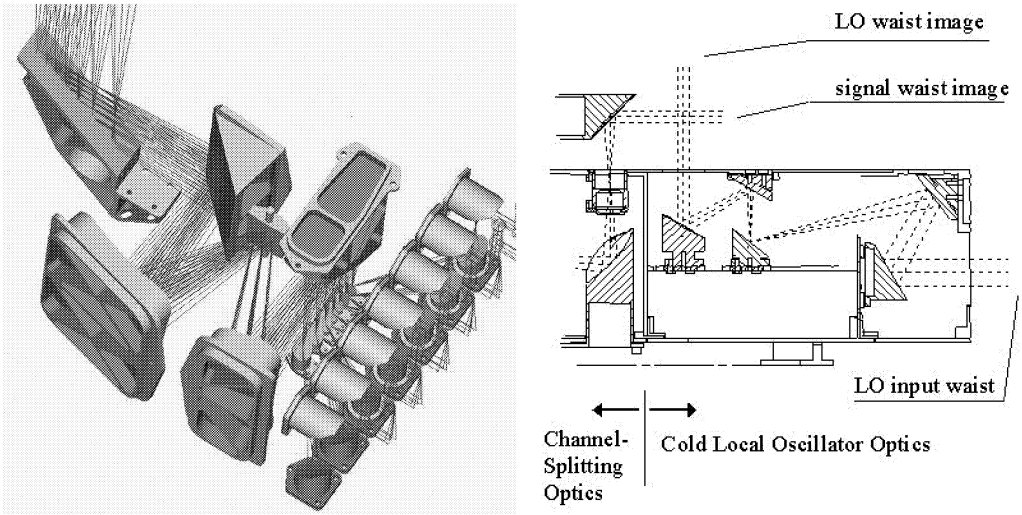

Fig. 4 – The Common Optics Assembly. The left-hand image shows the mirror configuration of the telescope relay optics (the first six common mirrors) and the channel-splitting optics (the 7 sets of three smaller mirrors). The right-hand image shows the layout of a single channel of the cold local oscillator optics.

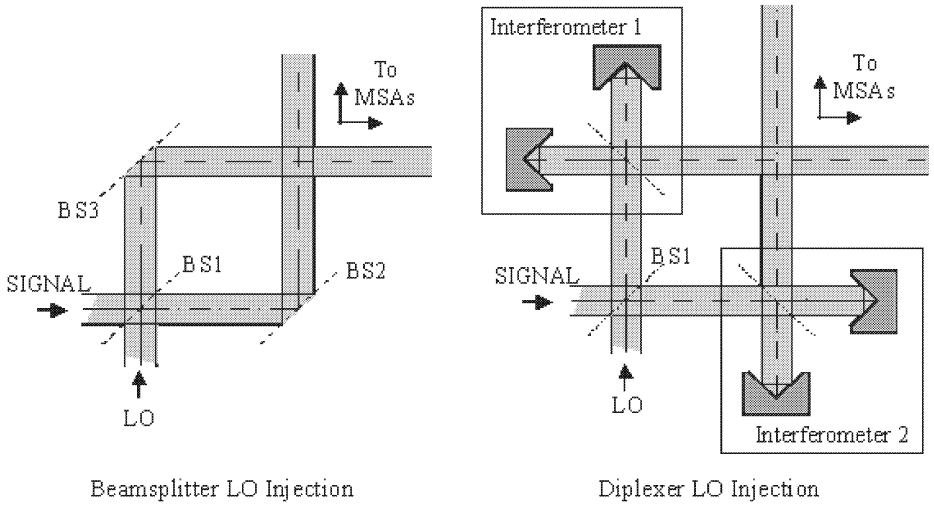

(a) (b)

Fig. 5 – Local Oscillator Injection Schemes

cold local oscillator optics, producing frequency-independent waists in the diplexer box that match the signal beam waists produced by the channel-splitting optics.

3.3 The Diplexer Assembly

Within the diplexer assembly, each of the 7 signal beams is combined with its corresponding LO beam, creating two linearly polarized output beams per frequency channel. Each linearly polarized beam is then directed into a Mixer Sub-Assembly.

At low frequencies, where relatively high LO powers are available, the combining is done with three polarizing beamsplitters per channel. As indicated in Fig. 5a, the first beamsplitter is placed at the intersection of the LO and signal beams, creating two mixed beams (one contains the "horizontally" polarized signal beam plus the "vertically" polarized LO beam, while the second contains the inverse). Each of the mixed beams then hits a second beamsplitter, whose polarization is defined to reflect 90 % of the signal power and 10 % of the LO power (the remaining signal and LO power are absorbed in a beam-dump). This 90%/10% coupling of signal and LO powers is achieved by setting the polarization of BS1 18° from the vertical, while BS2 is horizontally polarized and BS3 is vertically polarized. Increased coupling of signal power to the mixers can be achieved by rotating the polarization of BS1 closer to the vertical (although this also reduces the LO power coupling).

At high frequencies, where LO power is scarcer, a Martin-Puplett diplexer is used for LO injection (see Fig. 5b). Once again, the first beamsplitter creates two beams containing LO and signal power in orthogonal polarizations (the polarization of BS1 is vertical in this case). The following pair of beamsplitters in Fig. 5a are then replaced with a polarizing Michelson interferometer that rotates the polarization of the LO beam relative to that of the signal beam, creating a linearly polarized output (one interferometer is used for each mixer). In this manner, the coupling of both the LO and signal powers to the mixers are high, although mechanisms are needed to tune the interferometers for use at different frequencies.

3.4 The Mixer Sub-Assembly

Each of the 14 linearly polarized outputs from the diplexer box enters a Mixer Sub-Assembly (MSA) that includes:

- three mirrors that focus the optical beam from the diplexer into the mixer;
- a mixer unit (SIS mixers in bands 1-5 and HEB mixers in bands 6L and 6H);
- a low-noise IF amplifier (plus two IF isolators that suppress reflections in the cable between the mixer and the amplifier);
- low-frequency filtering for the mixer's DC bias lines; and
- a mechanical structure that isolates the 2 K mixer from the 10 K FPU

The resulting MSA design (see Fig. 6) is a densely packed ~ 5x12x15 mm^3 box. The design's complexity is driven by a number of factors, including the need for a compact design and the desire for a low-distortion, all-reflective optical design. In particular, this second requirement necessitates the use of at least two mirrors (the second mirror compensates for distortions introduced by the first mirror). In practice, a three-mirror system is used because it is more compact than a comparable two-mirror design.

3.5 The IF2 Box

Prior to leaving the FPU, the IF outputs of the 14 mixer sub-assemblies pass through a 14-channel second-stage amplifier (the IF2 Box). The extra gain provided by this additional amplifier is needed to overcome the losses in the IF cables between the FPU and the spectrometers (~ 5 m of stainless steel cable will be used to minimize the heat-load on the cryostat). In addition, the IF2 box has several extra functions:

- equalizing the output powers of mixers in different bands;
- offsetting the frequency-dependence of the IF cable losses; and
- combining the 14 mixer outputs into 4 cables to reduce the thermal load on the cryostat.

3.6 The Focal Plane Chopper

The fourth mirror of the telescope relay optics is the focal plane chopper. The chopper mirror is mounted on flex pivots that allow it to rotate around the centre of its optical

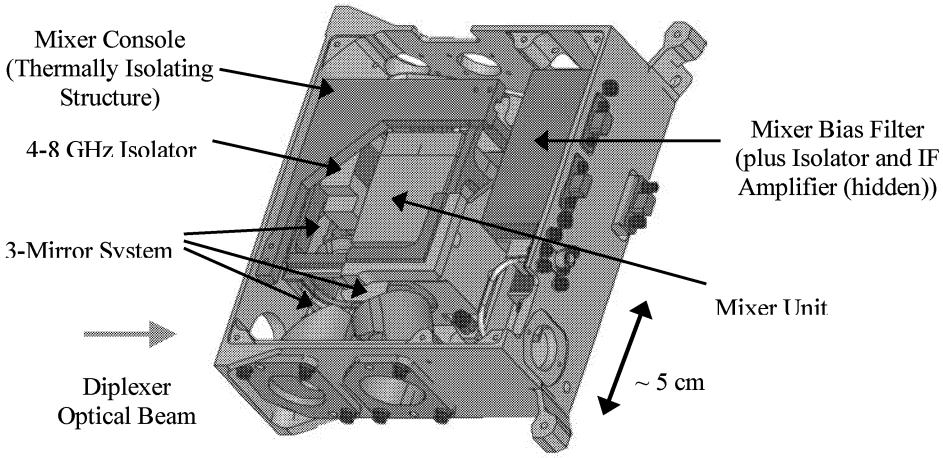

Fig. 6 – The Mixer Sub-Assembly

surface (in one direction). Because the mirror is located at an image of the telescope secondary, tilting the chopper results in a tilt of the beam on the sky. The primary uses of the chopper are to scan the beam on the sky (in one direction), and to redirect the instrument's optical beam into the on-board calibration source.

3.7 The Calibration Source Assembly

Mounted on the side of the COA, the calibration source assembly contains a lightweight blackbody cavity (the calibration source) that can be heated to 100 K, plus a set of mirrors that focus the optical beam from the FPU into the cavity. The calibration source assembly provides two stable blackbody signal loads that are used to verify the calibration of the instrument's sensitivity (one load is at ~ 10 K, while the second is at an adjustable temperature between 10 and 100 K). The HIFI signal beam is steered into the calibration source by using an extreme position of the focal plane chopper.

4. THE HIFI MIXER UNITS

4.1 Performance Requirements

The ultimate sensitivity of the HIFI instrument will be largely determined by the sensitivity of the SIS and HEB mixers at the heart of the FPU. For this reason, ambitious goals have been set for the performance of these mixers. In particular, with a goal of $T_{N,rec} \sim 4\ hf/k_B$ defined for the sensitivity of the integrated instrument, the goal sensitivities of the HIFI mixers are $T_{N,mixer+IF} \sim 3.5\ hf/k_B$ (including the noise contributions of the IF chains). In general, this goal has been achieved in SIS mixers at lower RF frequencies (below 700 GHz). However, the desire to achieve this sensitivity over broad RF and IF bandwidths, and at much higher RF frequencies, makes this a significant challenge. This is highlighted by the plot in Fig. 7 of the goal sensitivities of the HIFI mixers versus the best-reported sensitivities at the time of the submission of the HIFI proposal to ESA (in 1996).

Band	Frequency (GHz)	Mixer Type
1	480-640	SIS, WG
2	640-800	SIS, WG
3	800-960	SIS, WG
4	960-1120	SIS, WG
5	1120-1250	SIS, QO
6L	1410-1710	HEB, QO
6H	1710-1910	HEB, QO

Note: WG = waveguide mixer
QO = quasi-optical mixer

(a)

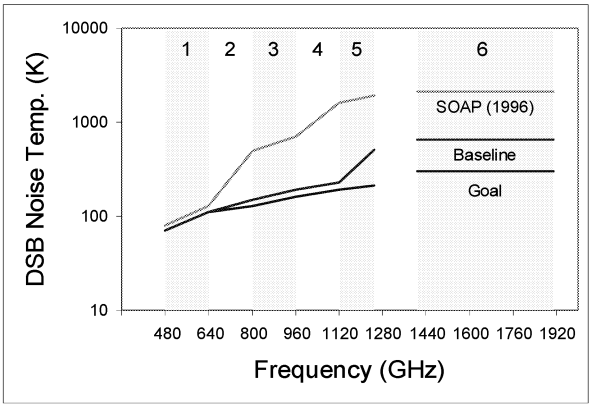

(b)

Fig. 7 – HIFI Band Definition and Mixer Sensitivity Goals. Note that the baseline and goal sensitivities are defined as the effective input noise of a receiver with loss-less optics (i.e. only the mixer and IF chain noise contributions are considered). Also, note that the 1996 State-of-the-Art Performance (SOAP) generally corresponds to narrow-band mixers at low IF. A clear split between the SOAP and Goal sensitivities is seen above 640 GHz.

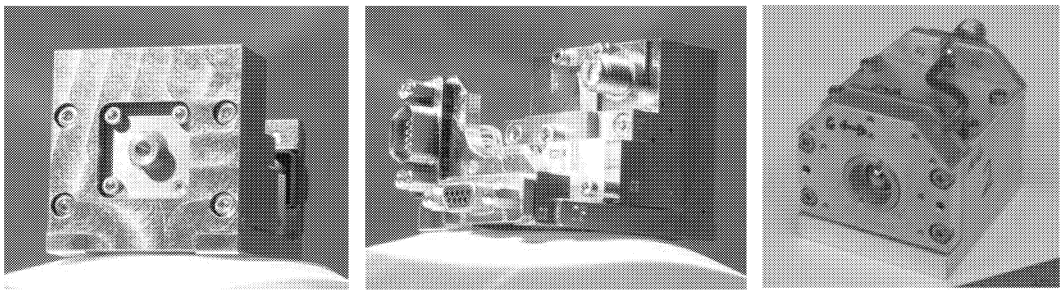

(a) (b) (c)

Fig. 8 – Two Prototype HIFI Mixer Units. (a) and (b) front- and rear-views of the band 4 mixer (from SRON), with its corrugated horn visible in (a), (c) is a front-view of the prototype band 6H mixer (from JPL/NASA), with its quasi-optical lens visible.

4.2 Interfaces and Other Requirements

The HIFI mixers are compact units with well-defined optical, mechanical, and electrical interfaces designed to facilitate rapid integration into the mixer sub-assemblies. This has required the inclusion of a number of features that are not present in laboratory-based SIS or HEB mixers. In particular, while a typical lab mixer includes:

- a RF beam-forming element (a waveguide horn or a quasi-optical lens-antenna);
- a SIS or HEB mixing element;
- a superconducting electro-magnet (for SIS mixers only); and
- an IF output connector that is also used as the DC bias connector,

a HIFI mixer will also include a number of additional features:

- a built-in bias-T to split the IF output from the DC bias input;
- a five-wire bias network (to allow the actual mixer bias to be monitored, while also providing ESD protection and EMC filtering on the bias lines);
- a resistive de-flux heater (for the SIS mixers only); and
- absolute alignment of the mixer's quasi-optical RF beam.

Furthermore, the mixer units must be rugged enough to survive 4-5 years of instrument and satellite integration and testing, the satellite launch, and 4-5 years of in-flight operations. This requires that the mixer units be able to survive, without suffering a loss of calibration, low-level ESD events, several days of vacuum bakeout at 80°C, a large number of thermal cycles to 2 K (~ 25 are foreseen for the flight units), high vibration levels, and irradiation by energetic particles.

Fig. 8 includes pictures of two prototype HIFI mixer units.

5. CURRENT STATUS AND EXPECTED DEVELOPMENT SCHEDULE

The HIFI instrument has a three-stage development program, including a development model, a qualification model, and a flight model.

At present, the mixer and IF amplifier development programs are wrapping up, with development model hardware deliveries scheduled for the spring of 2002. The construction and integration of the development model FPU is expected to be complete

by the summer of 2002 and will be followed by ~ 6 months of instrument-level testing in the second half of 2002.

The development model program will be followed by a qualification program, which will demonstrate the compliance of the as-built hardware with the requirements of space qualification (including, in particular, formal environmental testing of both individual units and the integrated instrument). At lower levels of integration (i.e. units that are deliverable to the FPU), the qualification program has already begun, with completion expected by the end of 2002. The qualification program for the integrated FPU will begin in mid-2002, and will last until the second half of 2003.

The construction of flight hardware will begin in the second half of 2002, with the units at a lower level of integration being delivered in mid 2003, so that the integration of the FPU can take place in the second half of 2003. Testing of the integrated instrument is planned for the second half of 2004.

6. ACKNOWLEDGEMENTS

The authors would like to thank the HIFI Focal Plane Sub-System consortium for their significant contributions to this project (see Table 1).

7. REFERENCES

1. G.L. Pilbratt, "The Herschel mission, scientific objectives, and this meeting," pp. 13-20 in Ref. [2].
2. G.L. Pilbratt, J. Cernicharo, A.M. Heras, T. Prusti, and R.A Harris, *SP-460 The Promise of the Herschel Space Observatory*, ESA, The Netherlands, 2001.
3. The Herschel web-site: http://astro.esa.int/herschel
4. A. Poglitsch, C. Waelkens, and N. Geis, "The Photodetector Array Camera & Spectrometer (PACS) for Herschel," pp. 29-36 in Ref. [2].
5. M.J. Griffin, B.M. Swinyard, and L. Vigroux, "The SPIRE Instrument for Herschel," pp. 37-44 in Ref. [2].
6. Th. de Graauw and F.P. Helmich, "Herschel-HIFI: The heterodyne instrument for the far infrared," pp. 45-52 in Ref. [2].
7. The HIFI web-site: http://www.sron.nl/divisions/lea/hifi

An Interferometric Microwave Comb Generator

R. Kimberk, C. E. Tong, H. Gibson, R. W. Wilson, R. Blundell, S. Paine, and T. R. Hunter
Smithsonian Astrophysical Observatory
60, Garden Street, Cambridge, MA02138, USA

Abstract

We have developed a scheme for generating a comb of radio frequencies, covering the microwave to millimeter spectral range. The system utilizes a single diode laser coupled to an optical interferometer and photodetector. Frequency modulating the laser at a rate of 2.154 GHz, we observe an electrical signal from the photodetector with a spectrum that is a comb that extends beyond the 40th harmonic of the fundamental modulation frequency. The line width of the electrical output is less than 2 Hz. We have compared the phase stability of an element of the comb with the output from a classical diode frequency multiplier (both driven from the same source) and have concluded that a phase-stable output can be generated. Finally, we have developed analytical and numerical models that suggest that our scheme may be used for frequency generation through the submillimeter.

Introduction

The design of photonic local oscillators for use with low noise heterodyne receiver systems has been motivated by the development of photo detectors with frequency response in the microwave and millimeter [1,2]. Attempts at producing a usable photonic local oscillator are usually based on the mixing of the outputs of two solid-state lasers in a photo detector. The poor line width and frequency stability of the simple heterodyne systems have led to more complex systems to control the phase and frequency of the resulting tone [3,4]. We have developed a single laser homodyne system. The operating principle is similar to the time delay / phase shift frequency discriminator used to demodulate frequency and phase modulated radio signals [5]. An angle modulated (either frequency or phase modulated) signal is demodulated and converted to an amplitude-modulated signal, through the use of an appropriate differentiator. In our device we incorporate a time delay frequency discriminator (interferometer) with the time delay set to recover a maximum number of harmonics of the modulation signal. The HP 11980A fiber optic interferometer is based on comparable techniques and other similar schemes have been used to measure laser chirp [6,7].

System description

The optical output frequency of a semiconductor diode laser is a function of its bias current. Modulating the bias current produces an angle modulated optical signal. In our scheme the sum of a DC bias and a microwave signal is used to set the operating point and modulate the optical output frequency of a Fabry-Perot laser diode. The diode is an SDL-5432 with a nominal output wavelength of 830 nm. The wavelength change is about 0.01 nm/mA, which is equivalent to a

frequency shift of about 4 GHz/mA. The DC bias current is set sufficiently above the threshold value for lasing to occur, so that at no time does the sum of the DC and microwave current fall below threshold. The angle modulated optical signal from the laser passes through an optical isolator and then is coupled to the input of a Mach-Zehnder interferometer. The interferometer is constructed from two Newport, F-CPL-S22855, 3 dB single mode fiber couplers. The first of these is used to split the laser output into two equal power components, one of these incurs an additional path length delay, δ, resulting in a time delay $\Delta t = \delta/c\sqrt{\varepsilon_r}$ before being recombined with the other at the output of the second coupler. Figure 1 is a diagram of this system.

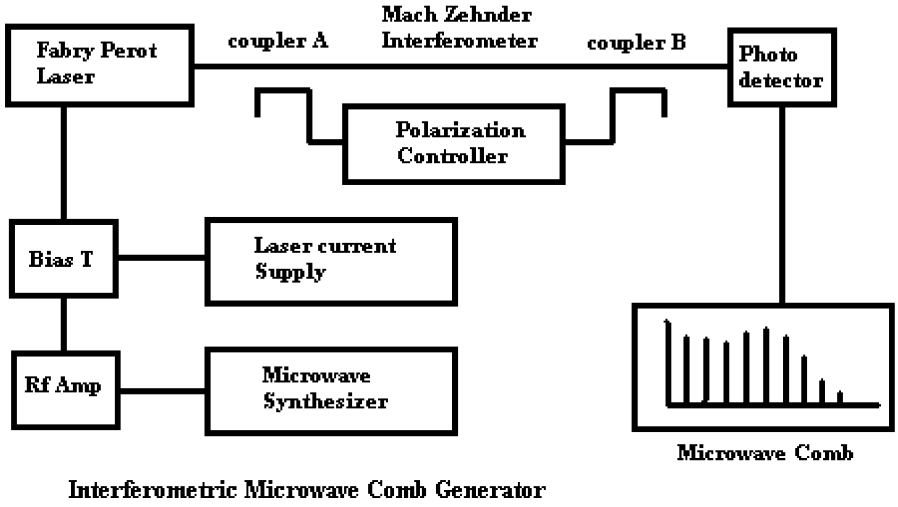

Figure 1. The system diagram

The time domain description of the angle modulated laser output may be written:

$$a(t) = \cos [\omega_c t + \beta \sin \omega_m t] \quad (1)$$

where ω_c is the carrier or optical frequency, ω_m is the modulation frequency, and β is the modulation index (the amplitude of $\sin \omega_m t$). β is equal, for the particular case of frequency modulation, to $\Delta\omega_c/\omega_m$: the maximum change in carrier frequency, $\Delta\omega_c$, divided by the modulating frequency, ω_m.

At the interferometer output we therefore have:

$$a_1(t) = A \cos [\omega_c t + \beta \sin \omega_m t] \quad (2)$$

and the delayed signal

$$a_2(t) = A \cos [\omega_c (t - \Delta t) + \beta \sin \omega_m (t - \Delta t)] \quad (3)$$

Setting the time delay equal to one half of the period of the modulating frequency, $\Delta t = \pi/\omega_m$, in order to maximize the resulting comb bandwidth, we have

$$a_2(t) = A \cos [(\omega_c t - \pi\omega_c/\omega_m) - \beta \sin \omega_m t] \quad (4)$$

The sum of expressions (2) and (4) may be written

$$a_1(t) + a_2(t) = 2A \cos(\beta \sin \omega_m t + \phi)\cos(\omega_c t - \phi) \quad (5)$$

where $\phi = \pi\omega_c/2\omega_m$

The output of the interferometer consists of an optical carrier

$$\cos(\omega_c t - \phi) \quad (6)$$

with a low frequency amplitude envelope given by

$$2A \cos(\beta \sin \omega_m t + \phi) \quad (7)$$

In equations (4) and (5) the bandwidth of the amplitude modulation is also maximized for additional delays of $2n\pi/\omega_m$ for n = 1,2,3 … In addition, to achieve the output described by expression (5), the two signals must also have the same polarization. A polarization controller is therefore placed in one arm of the interferometer and manually adjusted to maximize the interferometer output.

The interferometer output is coupled to a photodetector that produces an electrical signal whose amplitude is proportional to the square of the amplitude envelope, expression (7). The voltage output at the photodetector may be written:

$$V_{out} = k A \cos^2 (\beta \sin \omega_m t + \phi)$$

$$= k A [1+ \cos(2\beta \sin \omega_m t + 2\phi)] \quad (8)$$

where k is a constant related to the effective responsivity of the detector. In this study, the photodetector used was a New Focus model 1434. A 1 mW input at 1.06 μm produced an output power of –37 dBm from near DC to 25 GHz.

Examination of expression (8) shows that the action of the square law photodetector not only shifts the angle modulated optical spectrum to base band, but also generates a modulation index of 2β, twice the original index of expression (1). In the frequency domain, expression (8) is a comb of spectral lines separated by ω_m. Expression (8) can be expanded into a series

$$V_{out} = k A [1 + \sum_{-\infty}^{+\infty} J_n(2\beta) \cos (n\omega_m t + 2\phi)] \quad (9)$$

where $J_n(x)$ is the Bessel function of the first kind, of order n. As the modulation index is increased, the power is shared with more and more sidebands and the bandwidth of the signal increases. According to Carson's rule [5], 98% of this power is contained within a bandwidth of

$$(2\beta + 1)\omega_m \tag{10}$$

As an example, modulating our laser (with a modulation sensitivity of 0.01 nm/mA, or 4 GHz/mA) to a depth of 10 mA at a frequency of 10 GHz, yields $\beta = \Delta\omega_c/\omega_m = 4$, so the bandwidth of the microwave comb, given by expression (10), is 90 GHz.

Output Noise Power

The interferometric comb generator takes advantage of the temporal coherence of the laser to produce a more spectrally pure output than is possible with a heterodyne (two laser) mixing scheme. The temporal coherence of the laser is related to its line width and power spectral density. The line width specification frequently given by the laser manufacturer is the wavelength between the Fabry-Perot modes that are 3 dB below the dominant mode. This specification should not be confused with the line width (FWHM),$\delta\omega$, of any given mode, which is of order 0.1 MHz [9]. The power spectral density of a given mode has a Lorentzian distribution, parameterized by the center frequency and $\delta\omega$ of about 6×10^5 radian/s.

The intrinsic laser phase noise may be modeled as a random phase modulation of the optical carrier [8]. We implement this in our model by introducing a phase term, $\beta_n \sin \omega_n t$, that modulates the optical carrier.

$$a(t) = \cos [\omega_c t + \beta_n \sin \omega_n t] \tag{11}$$

The absolute value of the noise frequency ω_n can assume any value from zero up to a few times $\delta\omega$. Its mean value is $\delta\omega/2$. For a well behaved laser, the noise modulation index β_n, should be small ($\beta_n < 1$) and is a Lorentzian function of ω_n.

Equation (11) can be expanded in a series of Bessel functions:

$$a(t) = \sum_p J_p(\beta_n) \cos (p\omega_n t + \omega_c t) \tag{12}$$

Since β_n is small, we retain only the linear terms of the series

$$a(t) = \cos \omega_c t + \beta_n \cos (\omega_n t + \omega_c t) \tag{13}$$

Expression (13) implies that the noise power density at an offset ω_n from the optical carrier is β_n^2. Next, we investigate the effect of the extra phase noise term in the entire system. The analysis given in the previous section is repeated with the addition of the phase noise term:

$$a(t) = \cos(\omega_c t + \beta \sin \omega_m t + \beta_n \sin \omega_n t) \tag{14}$$

The interferometer output can be written as

$$a_1(t) + a_2(t) = 2A \cos[\beta \sin \omega_m t + \phi + \beta_n/2 (\sin \omega_n t - \sin \omega_n (t - \Delta t))] \cos[\omega_c t - \phi + \beta_n/2 (\sin \omega_n t + \sin \omega_n (t - \Delta t))] \tag{15}$$

The photodetector extracts the amplitude envelope of the interferometer output to yield

$$V_{out} = kA \cos^2[(\beta \sin \omega_m t + \phi + \beta_n/2 (\sin \omega_n t + \sin \omega_n (t - \Delta t))] \tag{16}$$

For a path length difference of 100 mm Δt will be equal to 5×10^{-10} s. Then $\delta\omega\Delta t$ will be about 3×10^{-4} and the product $\omega_n \Delta t << 1$. In the limit of small argument, $\cos(\omega_n \Delta t) \sim 1$ and $\sin(\omega_n \Delta t) \sim \omega_n \Delta t$ so that

$$[\sin \omega_n t + \sin \omega_n (t - \Delta t)] \sim \omega_n \Delta t \cos \omega_n t \tag{17}$$

V_{out} (expression (16)) can then be rewritten as

$$\begin{aligned} V_{out} &= kA \cos^2(\beta \sin \omega_m t + \phi + \beta_n/2 (\omega_n \Delta t \cos \omega_n t) \\ &= .5\, kA + 1/2\, kA \cos(2\beta \sin \omega_m t + 2\phi + \beta_n \omega_n \Delta t \cos \omega_n t)] \end{aligned} \tag{18}$$

the AC component of V_{out} may be expanded using a Jacobi – Anger series

$$\sum_{p=-\infty}^{+\infty} \sum_{k=-\infty}^{+\infty} J_p(2\beta) J_k(\beta_n \omega_n \Delta t) \cos[2\phi + p\omega_m t + k(\omega_n t + \pi/2)] \tag{19}$$

Since $\beta_n \omega_n \Delta t$ is small, we retain only the lowest orders of the series, i.e. k = -1, 0, and 1.

$$\begin{aligned} V_{out} = \sum_{p=-\infty}^{+\infty} \sum_{k=-\infty}^{+\infty} & J_p(2\beta) [\cos(p\omega_m t + 2\phi) \\ & + (\beta_n \omega_n \Delta t) \cos(p\omega_m t + 2\phi + \omega_n t + \pi/2) \\ & - (\beta_n \omega_n \Delta t) \cos(p\omega_m t + 2\phi - \omega_n t - \pi/2)] \end{aligned} \tag{20}$$

From the above expression we can say that associated with each discrete line in the comb of the photodetector output there is a noise sideband of power density $(\beta_n \omega_n \Delta t)^2$ at an offset of ω_n. Comparing this noise power density to that of the intrinsic laser noise given by equation (13), we note that the noise power density is reduced by a factor of $(\omega_n \Delta t)^2$.

At the mean offset of ω_n , equal to $\delta\omega/2$, the noise reduction is simply $(\delta\omega\Delta t/2)^2$. As $\delta\omega/2$ is equal to $1/\tau$, where τ is the coherence time of the laser, $(\delta\omega\Delta t/2)^2 = (\Delta t/\tau)^2$. The same result may be derived from the normalized autocorrelation function, referred to as the degree of temporal coherence.
For example, in our experiment the path length difference was set at 140 mm, which is equivalent to a path length delay of 7×10^{-10} s in glass fiber. For $\delta\omega$ of about 3×10^5 rad/s, we have

$$(\delta\omega\Delta t/2)^2 = ((7 \times 10^{-10}) \times (3 \times 10^5)/2)^2 \sim 10^{-8} \quad (21)$$

The noise power of the photodetector output is improved compared to that of the original laser output by about 80 dB.
Measured values of noise power for a comb line at 10.77 GHz are; - 80 dBc/Hz at 1 kHz offset, - 80 dBc/Hz at 10kHz, -100 dBc/Hz at 100kHz, and –110 dBc/Hz at 1 MHz. The shape of the noise pedestal of the comb matched the shape of the noise pedestal of the modulating signal. This suggests that the measured noise was predominately the noise of the modulating signal and not the laser phase noise.

Numerical Model

A numerical model has been developed to provide a theoretical framework through which a detailed understanding of the effect that various parameters, such as carrier frequency, modulation rate and index, phase relationship between carrier and modulating signal, dimensional changes within the interferometer, and interferometer type, have on the photodetector output. A large array is used to store a time domain sequence of the angle modulated laser output. Each array point is a time slice of the modulated waveform. The array length is chosen to be exactly 2^n long and we adjust the time slice such that exactly a whole number of carrier cycles and modulation cycles fit it. This arrangement can now be used as a circular buffer, as the beginning and end match up. For example, with a laser wavelength of 830 nm (361 THz), a modulating signal of 10 GHz and a buffer size of 4,194,304 we can fit 8 modulation cycles, with each carrier cycle sampled 14.52 times. Because the ends of the array match up, we do not need a windowing function and the Fourier transform is an ideal case, offering very low noise.

A Michelson interferometer may be modeled by moving through the array with two pointers, one offset by the path length delay from the other. The contents addressed by the two pointers are added together and stored in another array. A Fabry-Perot interferometer simulation uses multiple taps with a weighting factor appropriate to the reflection and finesse of the cavity. The circular buffer is essential in this mode, as one may use hundreds of taps. A square law detector may be modeled by simply squaring the contents of each array element. The model generates an output that is rich in phase, amplitude, power, time domain, and frequency domain information.

Experimental Results

An experiment was performed to verify the operation of the interferometric comb generator. The system parameters were:

a) Laser drive current 200 mA
b) Average output power of interferometer 8 mW
c) Microwave modulation frequency 2.154 GHz
d) Available microwave modulation power 16.8 dBm
e) Interferometer path length difference 14 cm

The New Focus 1434 photodetector has a nominal operating bandwidth of 25 GHz. Its output port is a SMA connector. The microwave comb output up to 26 GHz was observed directly with a spectrum analyzer. Between 26 and 46 GHz we connect a WR-28/K-connector transition to the photodetector. A HP 1197Q waveguide harmonic mixer was used as an external mixer for the spectrum analyzer. Because the photodetector's output is above the frequency limit of its SMA connector, power coupling is expected to drop above 32 GHz. As well, above 40 GHz, the efficiency of the harmonic mixer and the waveguide transition rolls off rapidly. For frequencies greater than 50 GHz, a K to V adapter, followed by a V-connector/WR-15 waveguide transition, and a Pacific Millimeter WR-10 harmonic mixer were connected to the spectrum analyzer as an external mixer. The power measurement was not calibrated in this frequency range. The noise floor of the power measurements ranged from –102 dBm to –110 dBm.

The output frequencies were all found at multiples of the microwave pump. From the pattern of the output power, we determined that 98% of the power in the comb is contained below about 40 GHz. This suggests that the angle modulation of the laser had a modulation index (β) of about 10. Figure 2 is a graph of the comb power versus frequency. Figure 3.a is the predicted response produced by the numerical model. Figure 3.b is the frequency modulated optical input signal to the interferometer as given by the numerical model.

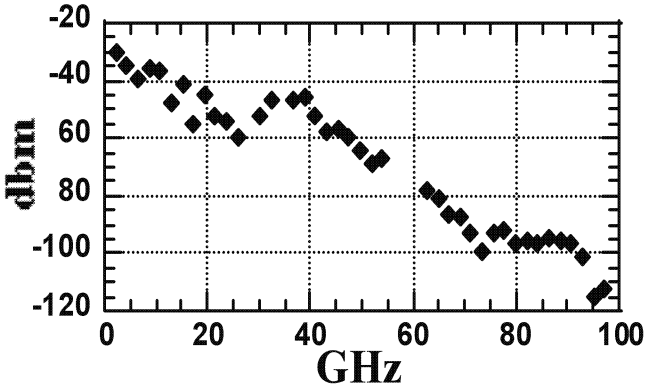

Figure 2. Graph of the microwave comb line power measured by the spectrum analyzer vs the frequency of the comb line. X-axis is frequency in GHz and Y-axis is power in dBm.

Both the numerical and experimental data sets display a similar sharp roll-off pattern above 40 GHz. We conclude that there is qualitative agreement between the numerical model and the experimental results. With one arm of the interferometer removed the output power dropped as much as –37 dB at 53.85 GHz, the highest frequency for which this effect was measured. The reduction in output power with one arm of the interferometer removed is less at lower frequencies due to gain switching of the laser. Gain switching is a nonlinear response of the amplitude of the laser to changes of the input current. Figure 4 is the spectrum of a comb line at 15.078 GHz (7^{th} harmonic).

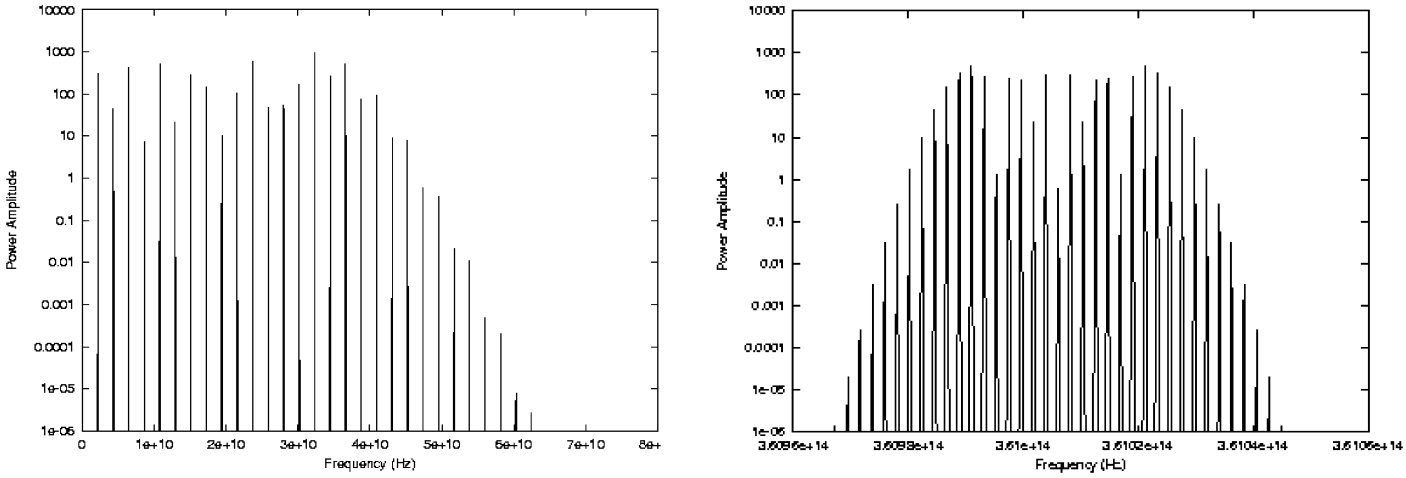

Figure 3. a) Numerical model prediction of comb output
b) Numerical model prediction of optical input to the interferometer

In a subsequent experiment we measured the increase of phase noise of the photodetector's output as a function of harmonic number. The ratio of phase noise power to carrier power of a given line in the photodetector's output should be n^2, where n is the harmonic number of the output line. The laser was modulated with a 100 MHz signal which was itself frequency modulated at 50 kHz to produce a pair of discrete sidebands. The interferometer output was therefore a comb of lines spaced at 100 MHz intervals, and each line had 50 kHz sidebands. The ratio of the power in the comb line and its associated sideband at 50 kHz offset was measured from 100 MHz to 1.8 GHz, the 17^{th} harmonic of 100 MHz, at the output of the photodetector. The excess phase noise (above the n^2 ratio) ranged from 0.5 dB at 300 MHz to 5 dB at 1.8 GHz.

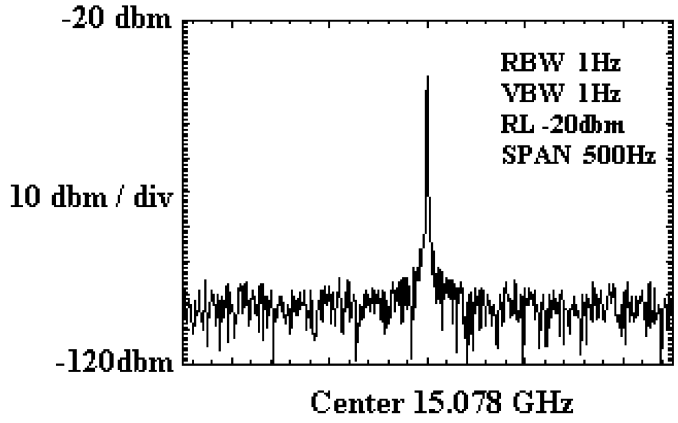

Figure 4. Spectrum of one of the comb lines

A third experiment was done to determine if the output was phase stable with respect to the modulating signal ω_m. The modulating signal was split with half going to the laser and the other half going to the input of a frequency multiplier. The output of the frequency multiplier was the same frequency as the comb line to be phase compared. The two frequencies after down conversion to 70MHz were inputs to a HP8508A vector voltmeter, with the frequency multiplier's output acting as the reference. Lines at 8.616 GHz and 17.232 GHz were examined. Over a 10 minutes time scale, measurements were taken. The 8.616 line was phase stable to about 1 degree rms, while the 17.232 GHz line had a short term stability of about 2 degrees rms with a drift of about 2 degrees. One degree at 17.232 GHz corresponds to about 48 microns in free space so some of the measured drift may be caused by the collection of cable and devices required for the test. For longer time scales the polarization stability of our interferometer became the limiting factor.

Conclusion

A simple photonic microwave comb generator has been demonstrated and mathematically modeled. The generality of the approach suggests that other means of producing an angle modulated output, and other types of interferometers, may be used to build better devices with higher power output to higher frequencies. Photodetectors are currently commercially available with a DC to 60 GHz frequency response. However, photodetectors with response to several hundred GHz are available in some laboratories. Furthermore, Phase modulators are available with a DC to 40 GHz frequency response and a $V\pi$ of 6 Volts (pi radians of phase shift with 6 Vrms input). Polarization preserving fiber couplers are also available. Given the interest in solid state local oscillators for heterodyne applications, it seems likely that our type of frequency generation scheme will be used throughout the submillimeter in the near future.

References

1. T. Noguchi, A. Ueda, H. Iwashita, S. Takano, Y. Ishibashi, H. Ito, and T. Nagatsuma "Millimeter Wave Generation Using a Uni-Traveling-Carrier Photodiode" Proceedings of the Twelfth International Symposium on Space Terahertz Technology (2001)

2. P.G. Huggard, B.N. Ellison, P. Shen, N.J. Gomes, P.A. Davies,W.P. Shillue, A. Vaccari, W. Grammer, and J.M. Payne "A Photonic MM-Wave Reference and Local Oscillator Source" Alma Memo #396

3. S. Verghese, E.K. Duerr, K.A. Mcintosh, S.M. Duffy, S.D. Calawa, C-Y.E. Tong, R. Kimberk, and R. Blundell "A Photomixer Local Oscillator For 630-GHz Heterodyne Receiver" IEEE Microw. Guid. Wave Lett. 9, 245 (1999)

4. J. M. Payne L.D. Addario, D.T. Emerson, A.R. Kerr, B. Shillue "Photonic local oscillator for the Millimeter Array" SPIE Vol. 3357

5. Ferrel G. Stremler "Introduction to Communication Systems" third edition Addison-Wesley Publishing Company

6. T. Bosch, S. Pavageau, D. d'Alessandro, N. Servagent, V. Annovazzi-Lodi, and S. Donti"A low-cost, optical feedback laser range-finder with chirp-control" IEEE Instrumentation and Measurement Technology Conference Budapest, Hungary, May 21-23, 2001

7. Chung E.Lee, William N. Gibler, Robert A. Atkins, and Henry F. Taylor "In-Line Fiber Fabry-Perot Interferometer with high-Reflectance Internal Mirrors" Journal of Lightwave Technology, Vol. 10, No. 10, October 1992

8. Ana Garcia Armada "Understanding the Effects of Phase Noise in Orthogonal Frequency Division Multiplexing (OFDM)" IEEE Transactions On Broadcasting, Vol. 47, NO. 2, June 2001Pallab Bhattacharya "Semiconductor Optoelectronic Devices" second edition Prentice hall 1997 page 268.

Development of the HIFI band 3 and 4 mixer units

G de Lange, B.D. Jackson, M. Eggens, H. Golstein, W.M. Laauwen, L. de Jong, S. Kikken, C Pieters, H. Smit, D. Van Nguyen

SRON National Institute for Space Research
Postbus 800, 9700 AV Groningen, the Netherlands

We describe the current status of the HIFI mixer units for Band 3 and Band 4. The mixer units cover the 800-960 GHz and 960-1120 GHz frequency range with a 4-8 GHz IF frequency band. The major requirements and design drivers are presented. Functional tests of the magnet, the de-flux heater and the corrugated horn were performed. Details of the mechanical design of the mixer units and the assembly procedure are described.

1 Introduction

The Herschel Space Observatory (launch date 2007) will fly two bolometer instruments (PACS and SPIRE) and the heterodyne instrument HIFI [1]. An international consortium led by the PI institute, SRON, is building HIFI [2]. Within HIFI, 7 frequency bands cover the spectral range from 480-1250 GHz (SIS mixers) and 1.41-1.91 THz (HEB mixers). During observations a single frequency band will be operational. SRON is also responsible for the development of the mixer units for band 3 (800-960 GHz) and 4 (960-1120 GHz). Each of these bands contains two tunerless waveguide mixers to measure both signal polarizations simultaneously. The mixer units are mounted on a 2 K platform in a mixer console that thermally isolates the mixer units from the Focal Plane Unit (10 K ambient temperature). Within the Focal Plane Unit, each of the mixer units is connected to a 4-8 GHz IF chain consisting of two isolators (one at 2K and one at 10 K) a low noise first stage IF amplifier close to the mixer unit, and a common second stage IF box. The second stage IF box provides further amplification, signal equalization, and finally power combining of the 14 separate IF channels into four coax lines that run between the cold and warm (outside the dewar) IF back-end. In the back-end a Wide Band Spectrometer and a High Resolution Spectrometer are available for IF spectral analysis. The LOs for the 7 bands are located in the LO-box, mounted on the outside of the dewar, and injected by either a wire-grid beam splitter (bands 1 and 2) or a Martin-Pupplet diplexer. [3]

During observations, the instrument will run in an autonomous mode. Optimal settings of the mixer units (bias voltage, magnet current, LO power) therefore have to be available from look-up tables. Further details on the HIFI focal plane unit are given in a paper by Jackson et al. [4]

The mixer unit development program is currently in the Qualification Model phase, where extensive environmental testing will prove the flight worthiness of the units. In this paper we present the current status of the mechanical layout of the mixer unit and experimental results of its functional behavior. Environmental qualification testing will be done in near future and may give rise to design changes in the mixer unit presented in this paper. Details on the current performance status and the SIS device design are presented in a separate paper by Jackson et al. [5,6].

2 Requirements

The specific requirements for a space mission and the unique opportunity for a space based heterodyne observatory determine to a great extent the performance and mechanical design drivers for the mixer units. A summary of the design drivers is given in Table 1.

T_{mix} DSB	Band 3		Band 4	
Frequency	*800 GHz*	*960 GHz*	*960GHz*	*1120 GHz*
Baseline	119 K	158 K	158 K	190 K
Goal	99 K	129 K	129 K	151 K

Sensitivities, excluding contributions from IF chain and optics losses

•Withstand shelf life, bake-out, launch and in-orbit operation (9 years)
•Mass < 75 grams
•Envelope 32x32x45 mm
•IF range 4-8 GHz, ripple < 2dB/1 GHz
•De-flux heater operating at current < 15 mA
•Magnet current < 10 mA for second minimum in the Fraunhofer pattern
•Beam quality
•Optical alignment tolerances (goal): x,y: 42 μm, tilt 0.2°
•ESD protection, EMC shielding
•Bias circuit isolation > 30 dB in IF range

Table 1 Summary of the main requirements of the HIFI band 3 and 4 mixer units

The two main requirements for the instrument are reliability and sensitivity. Note that the challenging goal sensitivities of the mixer units given in Table 1 are the sensitivities of the mixer unit only, without noise contributions from the optics and IF. Constraints on mass, envelope, magnet current, and heater current and are mainly determined by the need to minimize the dissipation and heat load on the 2 K and 10 K level. The choice of materials and procedures in the assembly of the unit is driven by the environmental conditions of the instrument during shelf-life (several years), bake-out (80 degrees for 72 hrs), thermal cycling (approximately 25 times), launch (vibration levels, 20 G rms in qualification) and in-orbit operation (>3 years). Procedures and materials commonly used in ground-based and laboratory receivers are not compatible with these environmental conditions (e.g. silver paint or low temperature crystal bond).
The instrument assembly and spare unit replacement philosophy determine the alignment tolerance on the position of the optical beam in the mixer unit. To allow for mixer unit replacement within the instrument (due to failure or significant performance improvement), a 'blind' replacement, relying on mechanical interfaces only, is foreseen. There are no adjustable mirrors within the instrument (mirrors will be shimmed once during assembly).
To allow the use of a magnet current look-up table it is necessary to be able to remove trapped flux from the SIS device and superconducting electrodes. A de-flux heater that can warm up the superconducting layers above their critical temperatures (in Band 3 and 4 this is about 15 K) is therefore implemented.
The potential high levels of electromagnetic fields within the instrument (specified as 2 mV/m in 3-9 GHz range, 2 V/m outside this range) require that the mixer units have proper shielding for EMC, especially in the 4-8 GHz IF range. Protective circuitry to avoid ESD damage during handling and operation is also required.

3 Main features

The current design of the mixer unit is shown in Figs 1 and 2.

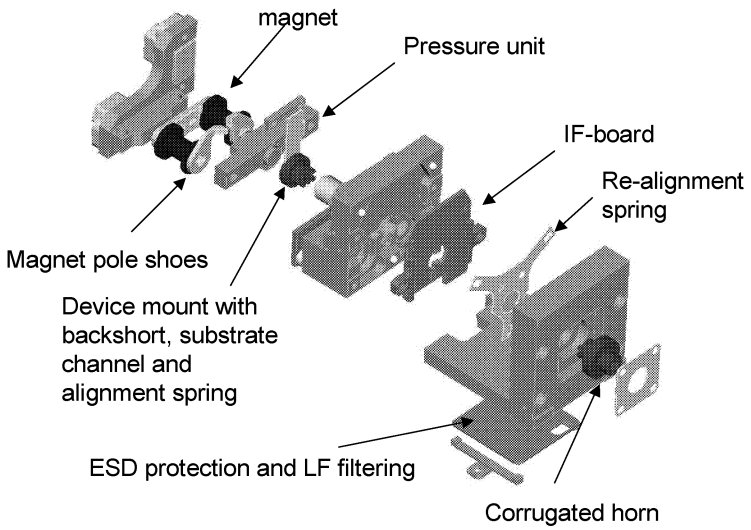

Figure 1 Exploded view of the mixer unit

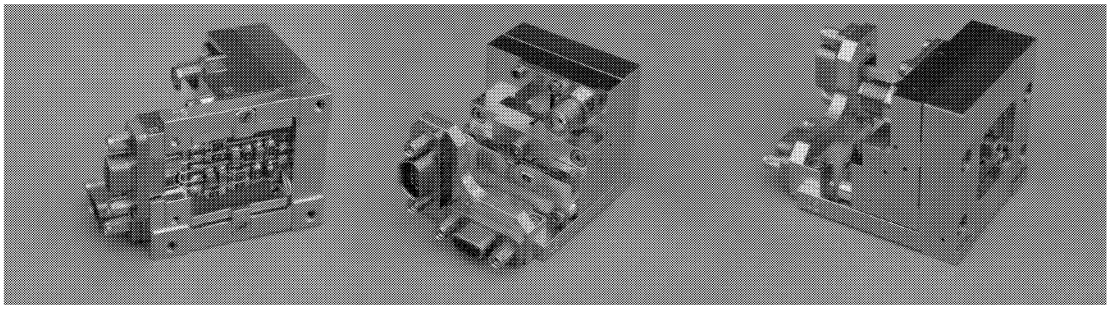

Figure 2 The QM prototype mixer unit

The unit consists of four sub-units:

- *The horn bracket.* This bracket holds the horn, the low frequency filtering and ESD circuit board, and the bias connectors (type: Cannon MDM 3401 9 pins). Also on the horn bracket are the mechanical reference planes that define the position of the bracket on the mixer console. The ESD/EMC filtering board is held in place with two aluminum springs. The board for the flight mixers will be made from alumina (FRP in the development unit shown here).
- *The IF-box.* This box houses the magnet, the IF circuit board, an auxiliary PCB, and the IF output connector (Radiall female bulkhead receptabel). The alumina IF circuit board is clamped with 2 Vespel springs into the housing
- *The device mount*. The SIS device and the heater are mounted in the device mount. Attached to the device mount is a leaf spring that is used for alignment purposes
- *The pressure unit.* This unit holds a pressure plate that is pushed forward against the device mount. Releasing a stack of washer springs inside the pressure unit applies a controlled pressure to the waveguide/device mount interface.

3.1 Corrugated horn

The mixer unit uses a corrugated horn antenna, tapering down to a reduced height waveguide of 300x75 μm (Band 3) or 240x60 μm (Band 4). The horn design is equal for all bands (except for a scaling factor). For the band 3 horn (with a center frequency of 880 GHz) the aperture radius is 1.6 mm and the horn slant length is 9.8 mm. At 880 GHz the far field

divergence angle is 8.46 degrees and the waist size is 0.729 mm. The band 3 and 4 horns are currently being fabricated at RPG and Thomas Keating. Results of amplitude measurements on an RPG horn at 890 GHz are shown in Figs. 3 and 4. The experiments show that horns with a well predicted and symmetric beam pattern can be fabricated at these high frequencies.

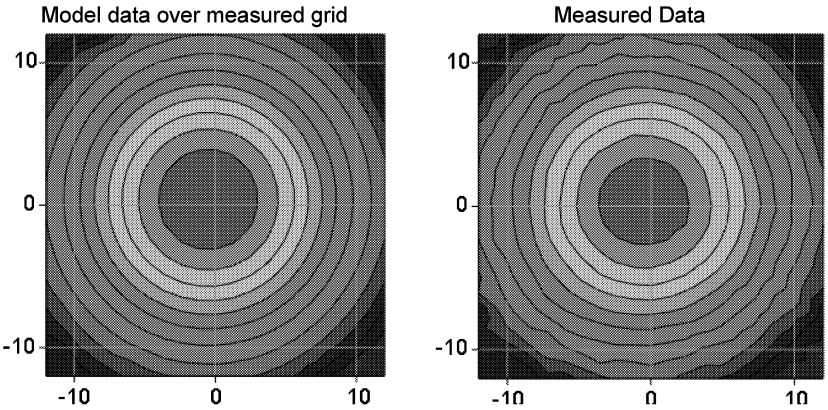

Figure 3 Model and measured data for a band 3 horn at 893 GHz

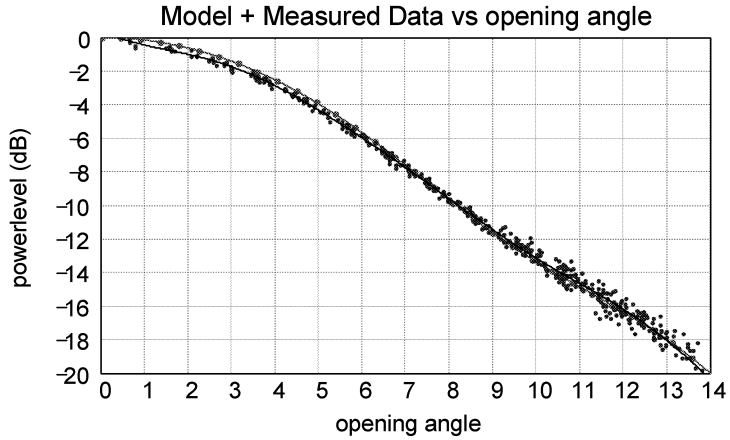

Figure 4 Comparison of model and experimental data of a band 3 horn at 893 GHz

3.2 Magnet

The magnet consists of two superconducting coils and a (multi-element) core of Vacuflux 50. The flight model coils will be fabricated using an ortho-cyclic winding technique by which the 64 μm diameter wires (fabricated by Supercon) on the coil are packed as densely as possible. The gap between the pole pieces at the position of the device is 1 mm. A 10 mA magnet current results in approximately 400 Gauss at the junction position. The amplitude of the Josephson super current versus magnet current for a single junction (approximately 1x1 μm) device is shown in Fig 5. The cause of the hysteresis has not been identified yet.

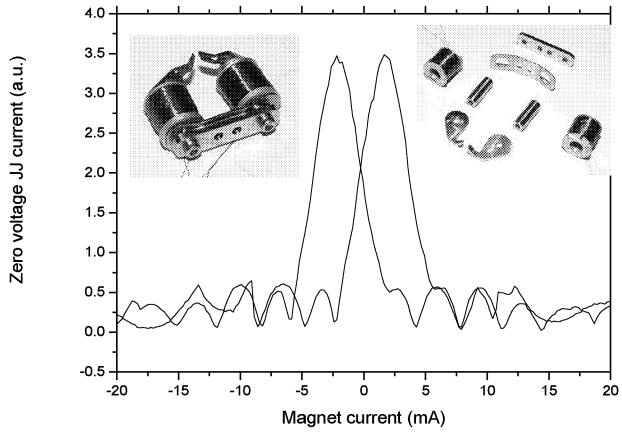

Figure 5 Zero-voltage supercurrent versus magnet current for a single junction device. The insets show the magnet parts and assembly

The best noise performance has been obtained with twin junction devices, with a 400 nm aluminum top electrode. To reduce the DC resistance of the top electrode we have added a 200 nm layer Nb on top of the aluminum. Due to proximity effects of the Nb on the Al this has the undesirable side effect that the two junctions form a SQUID loop. The super current versus magnetic field dependence for the twin junction device therefore shows a SQUID behavior (a rapid modulation on top of a Fraunhofer pattern). This makes the mixer unit very sensitive to magnetic field changes and flux trapping. Figure 6 shows an example of the supercurrent versus magnet current behavior of a twin junction device measured in a time span of an hour, before and after application of several heat pulses for flux removal. The magnetic field dependence varies considerably between the measurements. As one can see it will be difficult to give a single value magnet current for optimum Josephson effect suppression. Removing the top layer Nb locally, or not applying the extra Nb layer at all in future device fabrication runs, will avoid the SQUID type behavior of the device.

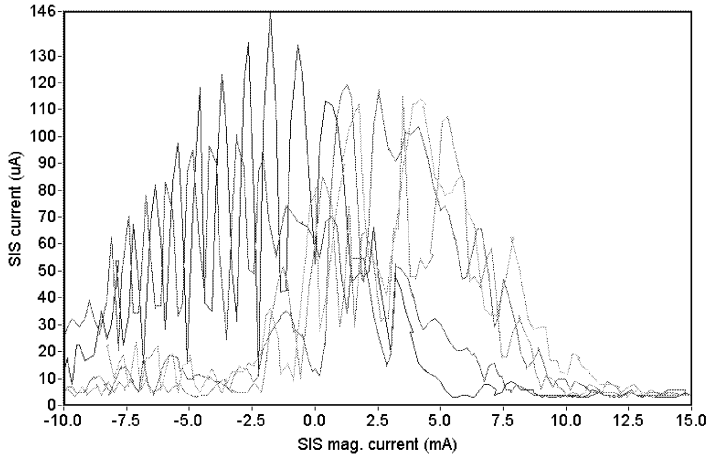

Figure 6 Magnetic field dependence of the zero voltage supercurrent in a twin junction device, after application of several de-flux heater pulses

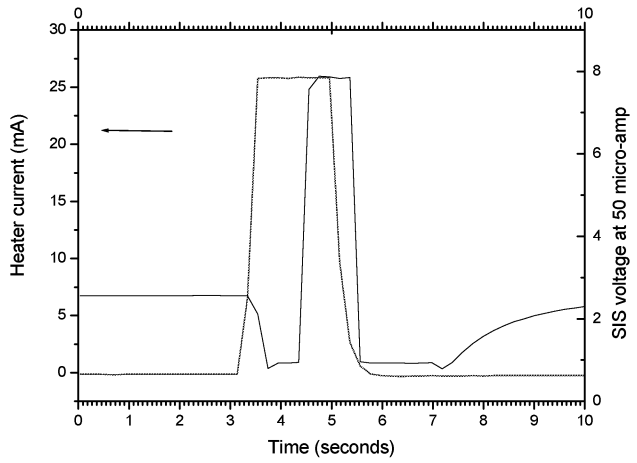

Figure 7 Heater current and junction voltage as a function of time.

3.3 De-flux heater

The de-flux heater consists of a 490 Ohm miniature resistor mounted with Apiezon T vacuum grease in a hole in the device mount. The heater resistor is in close proximity to the junction. To measure the heater characteristics we bias the device at a fixed current at the gap voltage.

A typical heater current and junction voltage versus time is shown in Fig 7. After applying the heater current (at t = 3 s) first the gap voltage decreases from 2.7 to 0 mV, then the Nb of the junction becomes normal conducting (at t = 4 s, T=9.2 K) and finally (at t = 4.3 s) the temperature reaches the transition temperature of the NbTiN. This is observed as a sudden increase of the device resistance because the NbTiN RF filter is no longer superconducting. The typical energy needed for heating the device to 15 K is 300-600 mJ. The actual effect of the de-flux procedure still has to be investigated in further detail. One has to insure that during cooldown no remnant magnetic fields are present which again could cause flux to be trapped.

3.4 IF circuit

The lay-out of the 625 μm thick alumina IF board and measured results of the bias-T isolation are shown in Fig. 8. The bias-T provides a 40 dB isolation between the DC and IF port within the 4-8 GHz IF range. The microstrip IF line is connected to the SMA output connector and the device via wire bonds. A 10 pF capacitor is used for DC blocking. We are currently investigating a planar 4-8 GHz bandpass filter for this purpose.

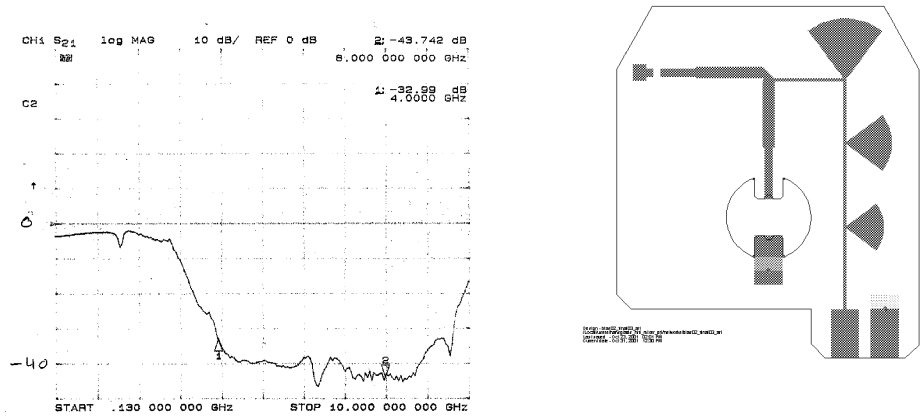

Figure 8 Lay-out of the bias-T circuit and the measured isolation of the bias-T.

3.5 ESD and EMC filter circuit.

An ESD and low frequency EMC filtering circuit is located in the bottom plate of the mixer unit (see Figs 2 and 9). The ESD circuit provides a 1000x protection. ESD tests on sample devices showed DC breakdown voltages in the range of 0.6 to 1.3 V.

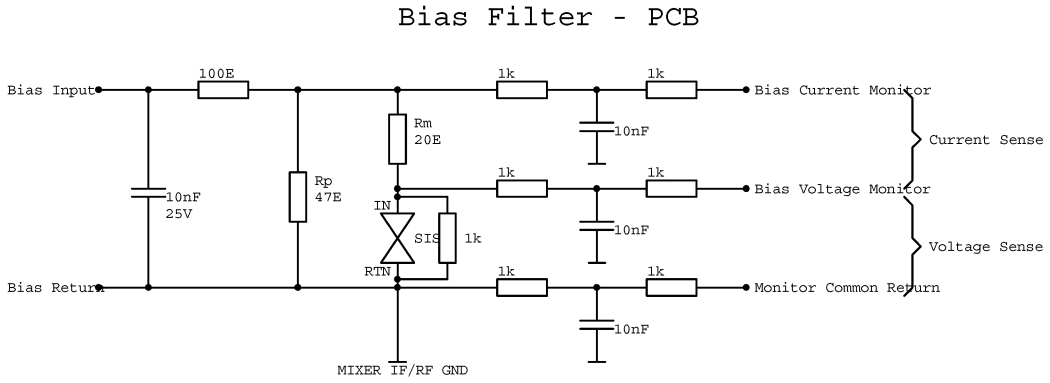

Figure 9 Schematic of the junction bias circuit, providing ESD and low frequency EMC protection.

4 Assembly procedures

The manufacturing and assembly procedures are chosen to comply with the environmental (e.g. aging, vibration, thermal cycling) and cleanliness (outgassing) requirements of a satellite instrument. Special attention is paid to the robustness of electrical interconnects (e.g. IF connector to IF board), electrical components, and component mounting methods with respect to thermal cycling and thermal bake-out.

4.1 Alignment:

We make use of in-situ alignment of the device mount to the waveguide of the corrugated horn. To do so, we attach the leaf spring on the device mount to a custom made x-y stage and

position the device mount while looking down the corrugated horn with a 100x magnification (see Fig. 10). After alignment, a spring (a stack of spring washers) inside the pressure unit is released and the device mount is pressed against the horn. The leaf spring attached to the device mount is then locked in position to the IF-box. This alignment method simplifies the manufacturing of the device mount considerably, since there is no need to position the waveguide and substrate channel very accurately within the device mount. Furthermore it adds flexibility in the device mounting procedure and IF design, since we do not need dowel pins or screws in the vicinity of the device. The IF-box and horn bracket are positioned with respect to each other by means of a three point alignment, making use of three alignment spheres in the IF box, and a Y-shaped alignment spring with three slits in the horn bracket (Fig. 10). The realignment accuracy of this method is better than 5 μm.

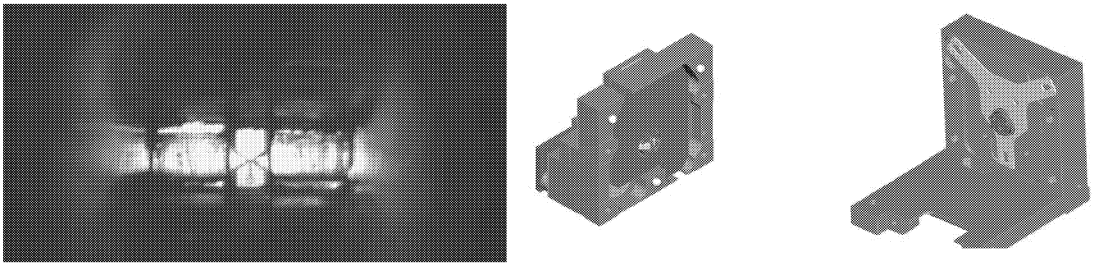

Figure 10 View of the device mount to waveguide(300x75 μm) interface as seen through the corrugated horn. Note that waveguide in the horn is slightly bigger than the waveguide in the device mount. The alignment of the horn bracket to the device box is defined by three spheres in the IF box, and an alignment spring with three slits in the horn bracket.

4.2 Device mounting

In our mixer designs at lower frequencies SIS devices are mounted into the device mount substrate channel with (super)glue, and electrical contact is made via silver paint or wire bonding on the device substrate. Direct bonding of 17 μm wires to the 40 μm contact pads on the thin (25 μm) substrates turns out to be a major cause of failure in the assembly procedure of the HIFI mixer units. We therefore develop an alternative mounting method in which the electrical contact to the device is made via silver epoxy (Epotek H20). The device is mounted with the silver epoxy on a gold patterned alumina carrier. The carrier is then mounted with Scotchweld 2216 to the device mount. Both Epotek H20 and Scotchweld 2216 have a flight record. Multiple wire bonds are used for the electrical contact from the contact pads on the carrier to IF-board circuitry (see Fig 11).

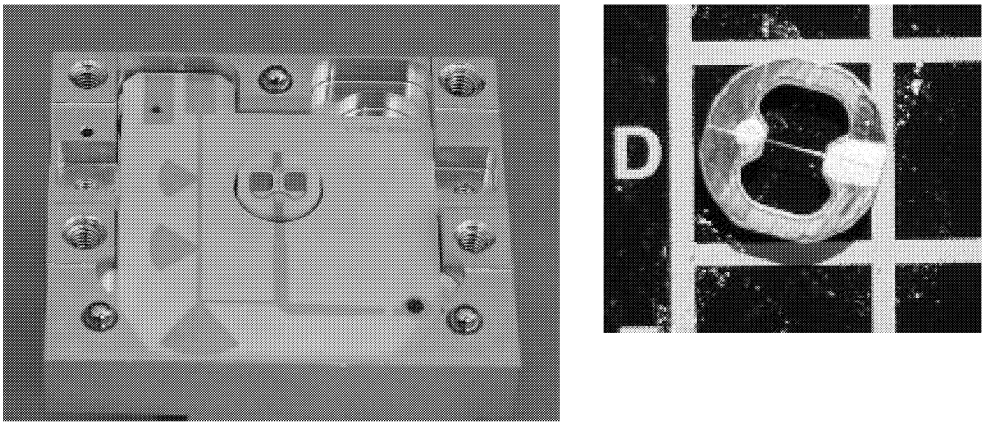

Figure 11 The IF box, with a (sample) alumina IF board and the device mount with an alumina mounting ring. On the right a prototype alumina mounting ring with a junction mounted with silver paint. .

During the test phase we make use of silver paint for the electrical contacting and (thermal) wax for the carrier mounting. The device and device carrier are easily removed from the device mount. This gives us the opportunity to characterize the device performance in a test unit and use the flight model mixer units only after a device has been selected.

5 Performance status.

The receiver Noise Temperature versus RF and IF frequency of one of the tested band 3 mixer units are shown in Figs 12 and 13. The instantaneous RF bandwidth observed in FTS and heterodyne measurements is sufficient to cover the 160 GHz HIFI specification, although this device is tuned too high in frequency to cover the actual band 3 frequency range. The overall

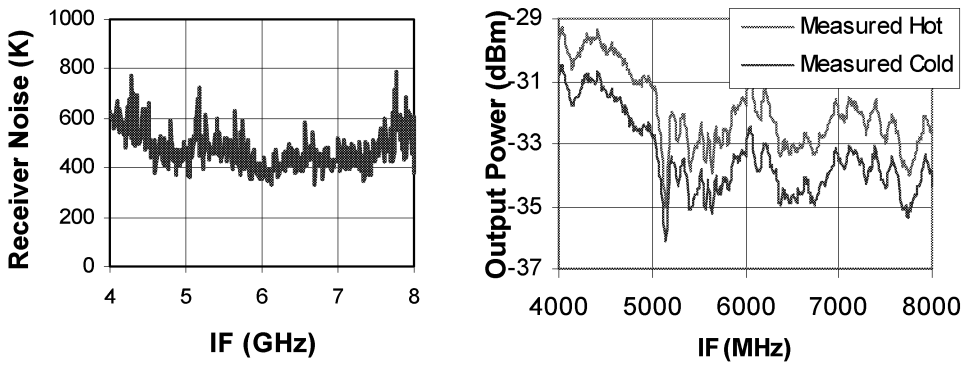

Figure 12 Noise temperature and IF output power for hot and cold input signals as a function of IF frequency

receiver noise temperature ranges from 400 to 1000 K DSB. The receiver noise temperature in HIFI will be considerable lower than our laboratory receiver, since HIFI will operate with a 10 K cooled diplexer and without vacuum windows or heat filters in the signal path. After correction for the optics losses (a room temperature beam splitter and vacuum window) the noise temperature ranges from 230-500 K. The variation of noise temperature within the 4-8 GHz IF band is still too large. We attribute the variations to the rather long wire bonds used for contacting the SIS device to the ground and signal line of the IF board.

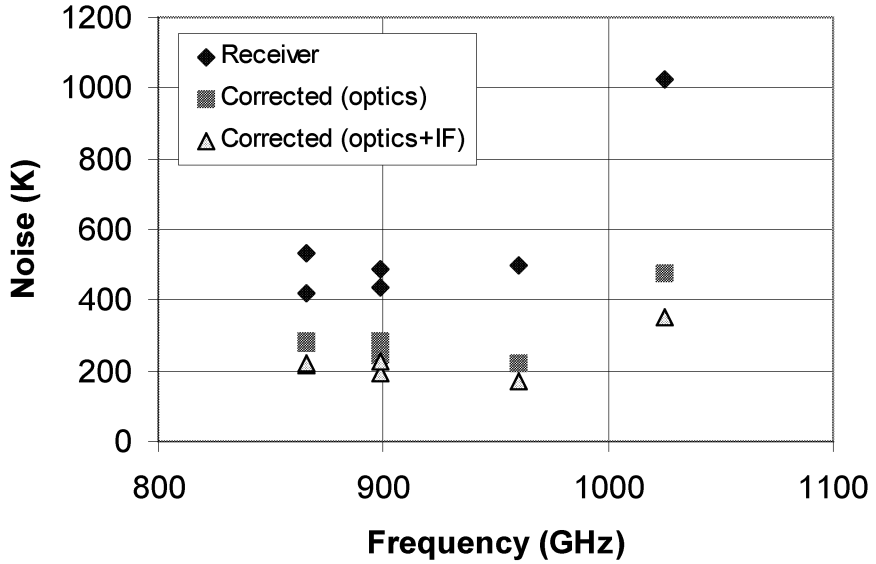

Figure 13 Receiver and corrected noise temperatures of a prototype band 3 mixer unit

5.1 Summary

In summary we have presented the current status of the band 3 and 4 mixer units for HIFI. The mixer unit is complying with the mechanical interface requirements. Measurements on the beam quality of the corrugated horn, the RF sensitivity in band 3 and the mixer unit bandwidth are very promising. The sensitivity at upper end of the band 4 has to be improved. Noise temperature variations within the 4-8 GHz IF bandwidth are still too large and the IF-output coupling circuit has to be optimized. The mixer magnet and de-flux heater are operating close to the required performance.

5.2 References

[1] Web site at : http://spdext.estec.esa.nl/home/herschel/

[2] Web site at: http://www.sron.nl/divisions/lea/hifi/

[3] Web sites at: http://www.sron.rug.nl/hifi_fpss/, http://www.sron.rug.nl/hifi_b34/

[4] B.D. Jackson, K.J. Wildeman, N.D. Whyborn, *The HIFI focal plane unit,* these proceedings

[5] B.D. Jackson, G. de Lange, W.M. Laauwen, L. de Jong, T. Zijlstra, N.N. Iosad, and T.M. Klapwijk, *THz SIS mixer development for HIFI*, these proceedings

[6] B.D. Jackson, A.M. Baryshev, G. de Lange, S.V. Shitov, J.-R. Gao, N.N. Iosad, and T.M. Klapwijk, *Low-noise 1 THz superconductor-insulator-superconductor mixer incorporating a NbTiN/SiO_2/Al tuning circuit,* Appl. Phys. Lett., vol. 79, no. 3, pp. 436-438, 16 July 2001.

DC and IF bandwidth measurements of superconducting diffusion-cooled hot electron bolometer mixers based on Nb/Au bilayer

X. Lefoul[1], P. Yagoubov[2], M. Hajenius[1], W. J. Vreeling[2], W.F.M. Ganzevles[1], J. R. Gao[2,a], P. A. J. de Korte[2], and T. M. Klapwijk[1]

[1]Department of Applied Physics and DIMES, Delft University of Technology, Lorentzweg 1, 2628 CJ Delft, The Netherlands

[2]Space Research Organization of the Netherlands (SRON), Sorbonnelaan 2, 3584 CA, Utrecht, The Netherlands

I. Introduction

Hot electron bolometer (HEB) mixers based on a superconductor-normal metal bilayer [1] are expected to improve the overall performance, in comparison with existing Nb or NbN mixers: lower mixer noise, larger intermediate frequency (IF) bandwidth, and in particular, lower LO power requirement. The bilayer takes advantage of the idea that one can engineer a superconducting layer with a required critical temperature and diffusion constant. We present measurements of IF bandwidth and DC resistance *vs* temperature using an Nb/Au bilayer HEB mixer, reporting the progress after work described previously (Ref. 1).

II. Nb/Au bilayer and mixer

The new concept is verified by using a combination of thin Nb and Au layers. Using a sputtered bilayer of a 5 nm Nb (bottom) and 5 nm Au (top), we obtain a T_c of 4.5 K and a sheet resistance of 10 Ω.

The IF bandwidth is measured with a mixer using a spiral antenna to couple the RF signal to the bridge. This design also allows a relatively simple fabrication process. We fabricate bilayer HEB mixers using a similar fabrication process as for Nb HEB's [2]. The process consists of: i) sputter deposition of a bilayer on a Si substrate, ii) thick Au cooling pads and antenna structure realized in the same step by evaporation and lift-off, patterned with e-beam lithography; iii) the narrow bridge defined by two etching steps using a thin Al strip as an etch-mask. The Au layer is etched with Ar RF sputtering, while the Nb is removed with a standard RIE etching using a gas mixture of CF_4/O_2. A SEM micrograph of a realized device is shown in Fig. 1.

The device used for IF measurements has a bridge length of 630 nm and a width of 200 nm, determined by SEM. The resistance *vs.* temperature of this device has been measured for temperatures down to 1.75 K (Fig.2). The T_c of the NbAu bridge is around 3.8 K, which is lower than an unprocessed bilayer, while the bilayer under the cooling pads does not become superconducting down to 1.75 K. The normal state resistance is 19

[a] Correspond author: j.r.gao@tnw.tudelft.nl

Ω. The temperature dependence of the resistance below 3.8 K seems to behave in a similar way as the Nb devices[3]. However, an analysis using similar structures shows that a substantial part of the dissipation is due to the superconducting proximity effect[4], which, in contrast to the previously proposed charge-imbalance model[3], allows for dissipation due to quasi-particles with energies smaller than the energy gap.

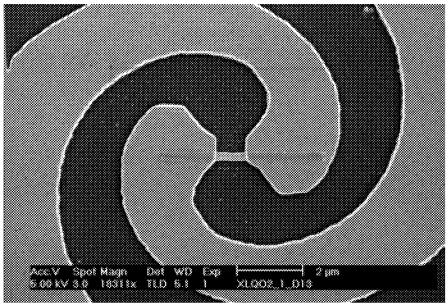

Fig. 1. SEM micrograph of an NbAu mixer. The NbAu bridge is located between the arms of the spiral antenna. The Au cooling pads are part of the antenna. The bar represents 2 μm.

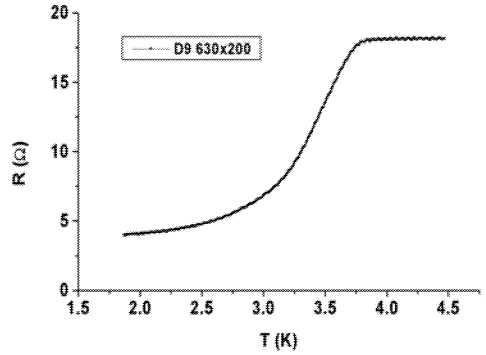

Fig. 2. The resistance as a function of temperature of the NbAu mixer used for the IF measurement. Bridge length: 630 nm and width 200 nm.

III IF bandwidth measurements

IF bandwidth measurements are done using a pair of submillimeter sources at frequencies around 650 GHz. A Miteq 0.1-8 GHz cryo-amplifier is used as the first stage amplification, followed by a room temperature amplifier and a spectrum analyzer.

The relative conversion gain *vs.* the IF (the frequency difference between two coherent sources) has been measured for a few DC bias voltages varying from 0.4 to 0.7 mV and at a bath temperature of 2.5 K. The IF bandwidth measurements together with the (un)pumped IV curves are given in Fig. 3. The one-pole Lorentzian fit to the data gives the $IF_{roll\text{-}off}$ (IF bandwidth) value varying from 0.4 GHz (0.4 mV) to 1.9 GHz (0.7 mV). Why the IF bandwidth increases by a factor of 5 for increasing bias voltage is not

fully analyzed. Assuming for the highest bias voltage that the measured value is intrinsic, without the influence of electro-thermal feedback, and that the superconducting bridge becomes fully normal, it should follow the out-diffusion model[5],

$$IF_{roll\text{-}off} = \pi D/2L^2$$

where D denotes the diffusion constant and L the length of the bridge. Having known the measured $IF_{roll\text{-}off}$ and L, we obtain a diffusion constant of 5 cm^2/s for this device, which is at least a factor of 3 higher than what we obtained in Nb HEB devices (1-1.5 cm^2/s). The higher diffusivity in the Nb/Au bilayer suggests the potential to improve the bandwidth obtained so far in Nb HEB devices.

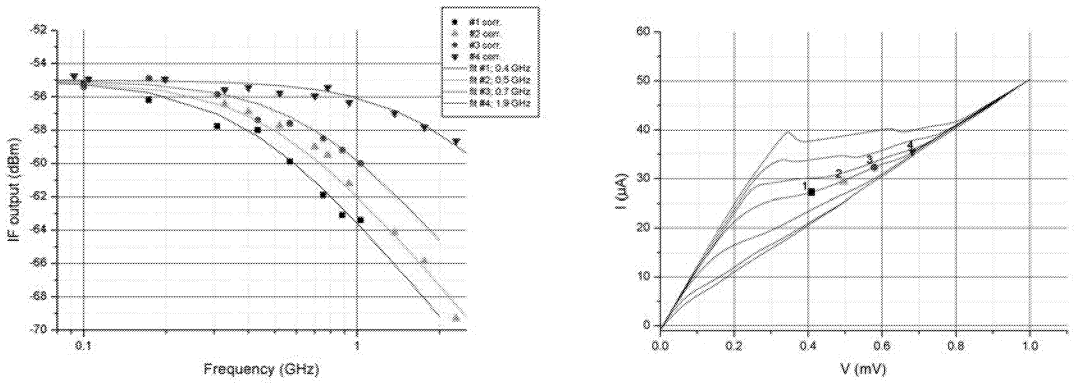

Fig. 3. Relative conversion gain as a function of IF frequency (difference between two coherent RF sources) for 4 different bias voltages (in the left-hand side). The unpumped and pumped IV curves of the same device with indications of the 4 bias points (in the right-hand side). The LO frequency in this case is about 650 GHz. The measurements are done at 2.5 K.

By simply assuming that the highly conductive Au layer dominates the sheet resistance (~10 Ω) of the bilayer, one would expect to have a much higher diffusivity value than observed. At this moment, it is not yet clear how to derive a reasonable value for the diffusivity from the resistance of a bilayer or to measure it directly, to compare to the value from the IF bandwidth measurement.

IV Sensitivity measurements

The IV curves pumped with different LO powers at 700 GHz have been measured at temperatures down to 500 mK using a ^{3}He cooler. No Y-factor could be measured with our current devices. We largely attribute this to the impedance mismatch between the low impedance bridge and the spiral antenna. To measure the Y-factor, we have to change the antenna design to a more suitable twin-slot antenna. A twin-slot antenna can also limit the RF bandwidth, reducing the direct detection effect in the Y-factor measurement. Another possible reason is that at the low bias voltages (see Fig. 3), the IF bandwidth is too low for the standard IF chain (1.5 GHz). It is worthwhile to mention that the recent

measurement[6] of a mixer using a similar bilayer at 30 GHz gives a maximum mixer conversion gain of an order of –10 dB, suggesting that Nb/Au mixers are indeed promising.

We also notice that the NbAu devices are more robust against electro-static discharge (ESD) in comparison with Nb HEB mixers studied in our labs. Several devices have been measured in both DC and RF setup, showing so far no change of the characteristics. This feature is important for real application.

V Summary

We succeeded in fabricating spiral antenna-coupled NbAu bilayer mixers. The largest IF bandwidth measured from a mixer with a 630 nm long bridge is 1.9 GHz, giving a diffusion constant of 5 cm^2/s for the bilayer. The IF bandwidth also shows a strong dependence on DC bias voltage.

Acknowledgements: The authors would like to thank Dr. E. W.J.M v.d. Drift for his support and advice on the fabrication. This work is supported partly by the European Space Agency (ESA) under Contract No. 11653/95/SRON STS-TDG-99/014.

References:

1. P. Yagoubov, X. Lefoul, W.F.M. Ganzevles, J. R. Gao, P. A. J. de Korte, and T. M. Klapwijk, "Development of Nb/Au bilayer HEB mixer for space applications", in Proceedings of 12th Int. Symposium Space Terahertz Technology, Feb. 14-16, 2001, San Diego, USA. Page 141.

2. W.F.M. Ganzevles "A Quasi-optical THz Mixer Based on a Nb Diffusion-cooled Hot Electron Bolometer", Ph.D. thesis, Delft University of Technology, May, 2002.

3. D. Wilms Floet, J. Baselmans, T.M. Klapwijk and J.R. Gao, "Resistive Transition of Niobium Diffusion-Cooled Hot Electron Bolometers", Appl. Phys. Lett., 73, 2826, 1998.

4. A.H. Verbruggen, T.M. Klapwijk, W. Belzig, and J.R. Gao, " The resistive transition of aluminium hot electron bolometer mixers with normal metal cooling banks", Proceedings of 12th Int. Symposium Space Terahertz Technology, Feb. 14-16, 2001, San Diego, USA. Page 42.

5. P. J. Burke, " High Frequency Electron Dynamics in Thin Film Superconductors and Applications to Fast Sensitive THz detectors", Ph. D. thesis, Yale University (1997).

6. I. Siddiqi and D. Prober, " Niobium-Gold Bi-Layer HEB mixers", This proceedings.

Broadband Fourier Transform Spectrometer (FTS) Measurements of Spiral and Double-Slot Planar Antennas at THz Frequencies

D. Loudkov[1], P. Khosropanah[2], S. Cherednichenko[2], A. Adam[2], H. Merkel[2], E. Kollberg[2], G. Gol'tsman[1]

[1]*Moscow State Pedagogical University, Department of Physics*
119435 Moscow, Russia

[2]*Chalmers University of Technology, Department of Microwave Electronics*
412 96 Gothenburg, Sweden

Abstract

The direct responses of NbN phonon-cooled hot electron bolometer (HEB) mixers, integrated with different planar antennas, are measured, using Fourier Transform Spectrometer (FTS). One spiral antenna and several double slot antennas, designed for 0.6, 1.4, 1.6, 1.8 and 2.5 THz central frequencies, are investigated. The Optimization of the measurement set-up is discussed in terms of the beam splitter and the FTS-to-HEB coupling. The result shows that the spiral antenna is circular polarized and has a bandwidth of about 2 THz. The frequency bands of double slot antennas show some shift from the design values and their relative bandwidth increases by increasing the design frequency. The antenna responses do not depend on the HEB bias point and temperature, as long as the device is in the resistive state.

I. Introduction

Hot electron bolometer (HEB) mixers currently have better performance as heterodyne receivers at THz frequencies, where SIS and Schottky mixers have worse sensitivity. It has been shown that NbN HEB mixers have noise temperature about $10h\nu/k$ [1,2], an intermediate frequency bandwidth close to 4 GHz [1,2], and require few hundreds of nW local oscillator power [3]. Among many factors, which affect the performance of mixers, the RF coupling is obviously crucial.

In order to couple the RF radiation to HEB, it is usually integrated with a planar antenna, which is specifically designed for the frequency of interest. Theoretically, this type of mixer is expected to operate up to 10 THz and even above. However, as the

design frequency increases, the size of the antenna decreases and it becomes difficult to estimate the antenna performance. Therefore it is inevitable to study the antenna frequency band experimentally. Fourier Transform Spectrometer (FTS) is usually used for this type of investigation in sub-millimeter range [4,5].

Log periodic spiral and double slot antennas are among the most commonly used planar antennas in sub-millimeter technology today. In order to characterize these antennas in THz range, we fabricated a set of NbN HEB mixers integrated with a spiral antenna and also with different double slot antennas, designed for 0.6 up to 2.5 THz. This paper presents the measured direct RF response of NbN HEB mixers, integrated with these antennas, using FTS.

II. Fourier Transform Spectrometer

The Fourier Transform Spectrometer (made by SPECAC LTD.) consists of a Michelson interferometer in vacuum chamber with a chopped Hg arc lamp and 50 μm Mylar output window. The source provides broadband radiation with the maximum intensity in the visible region, which is blocked by a black 0.2 mm thick polyethylene. The movable mirror has a maximum span of 200 mm with a minimum step size of 1.25 μm. The FTS is operated in a step-and-integration mode with an integration time of 1 sec. The measured interferogram is then apodized by cosine squared apodization function. Finally the Fourier transform of the apodized interferogram gives the spectrum of the response. The size and the number of steps determine the resolution and the maximum frequency of the spectrum. By choosing 200 steps with step size 7.5 μm one can achieve 90 GHz resolution up to 10 THz maximum frequency. Figure 1 shows the normalized measured spectrums, using 10 and 20 μm thick Polyethylene beam splitters. In both cases, Golay cell was used as a detector. The normalized calculated spectrums are depicted in the same figure. In this calculation, only the Fresnel's equations are used and the multiple reflections inside the beam splitter are taken in to account [6].

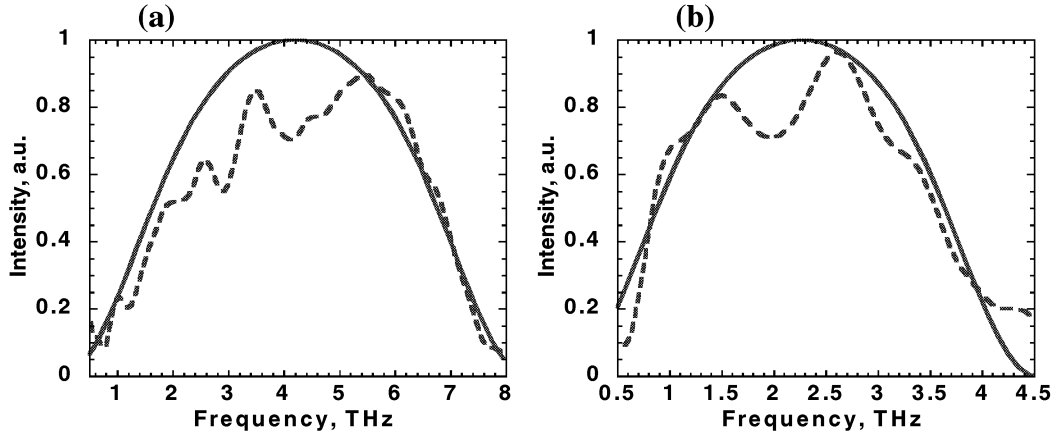

Figure 1. Measured (dashed lines) and calculated (solid lines) spectrums of the output signal from FTS, using (a) 10 μm polyethylene (b) 20 μm polyethylene beam splitters. A Golay cell was used as a detector.

The 10 μm thick polyethylene beam splitter can be used to study transmission properties of different materials up to 7.5 THz. For example, figure 2 shows the transmission spectrum of 1mm thick Teflon film. We can see that it is almost opaque for frequencies above 6 THz.

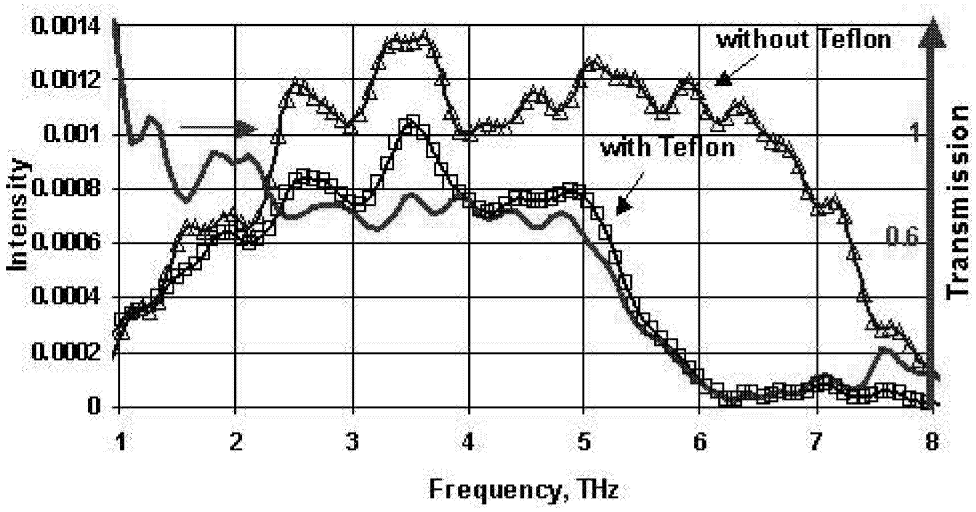

Figure 2. Study of transmission property of a 1 mm thick Teflon sheet. The triangle line is the response without the Teflon. The rectangle line in the response with Teflon. The solid line shows the Teflon transmission.

The 20 μm thick polyethylene beam splitter was used to measure the direct responses of the HEB mixers integrated with different planar antennas up to 4 THz.

III. Beam coupling

Characterizing the FTS output beam using a Golay cell indicates that it is divergent and quite wide (a few cm in diameter at the FTS output window). On the contrary, the main lobe of the receiver's radiation pattern is just few degrees wide [7,8,9] (for detailed description of the receiver see next section). Therefore, when the FTS output beam was directly coupled to the receiver, the response signal was very weak and noisy. In order to enhance the coupling, a parabolic off-axis mirror and a Teflon lense were tested between the FTS output and the receiver. Golay cell was used as a detector to investigate the effect of these two focusing tools. As it is shown in figure 3, better coupling was achieved via the mirror compared to the Teflon lense. By normalizing the curves (insertion in figure 3), we see that the Golay responses, with and without using the mirror, have the same spectra. The losses in Teflon cause attenuation above 2 THz. This indicates that the mirror is more suitable choice for wideband measurements.

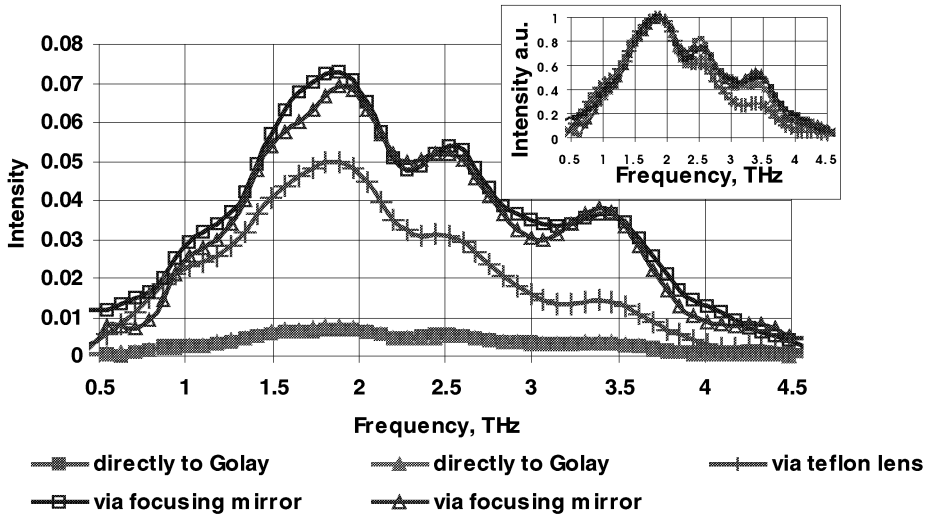

Figure 3. Study of a parabolic off axis mirror and a Teflon lens for collimating the FTS output beam. In these measurements, Golay cell was used as a detector. The insertion shows the normalized curves.

IV. Planar Antennas Measurements

The direct responses of NbN hot electron bolometers, integrated with different planar antennas have been measured. All the devices are made from 3.5 nm thick NbN films, sputtered on high resistive silicon substrates. The bolometers are 0.4 μm long and 4 μm wide. The chips were placed on a holder with 12 mm diameter silicon lens and mounted in a liquid Helium cryostat. The operating point of the device was controlled by DC bias and heating the mixer holder at the same time. A parabolic off-axis mirror was placed between the FTS output window and the cryostat. 20 μm thick Polyethylene film was used as a beam splitter in the FTS. All antenna measurements were done with 400 steps and a step size of 12.5 μm for movable mirror. This setting gives 30 GHz spectrum resolution (before apodization) and 6 THz maximum frequency.

Figure 4. SEM picture of the log periodic spiral antenna.

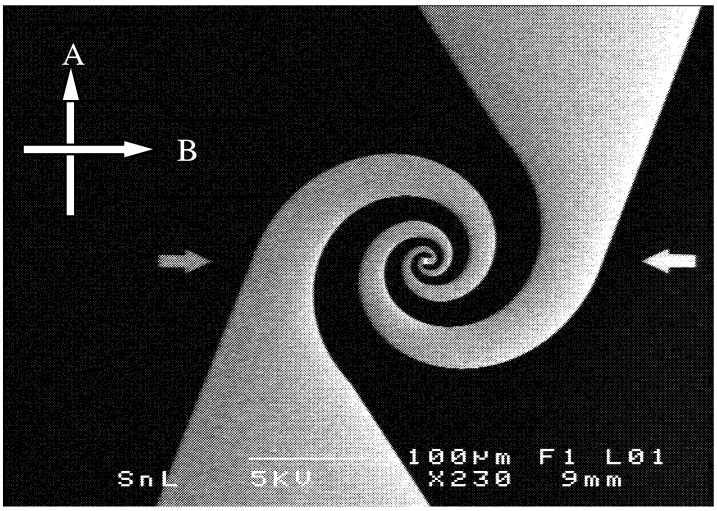

Two different types of planar antennas have been measured. One is log periodic spiral antenna and the other double slot antenna. Figure 4 shows a SEM picture of the spiral antenna. The spiral has inner and outer radii of 10 and 100 μm, respectively. The total antenna arm length is about 300 μm, which is calculated from its radii and the expansion rate (3.2 per turn) [10].

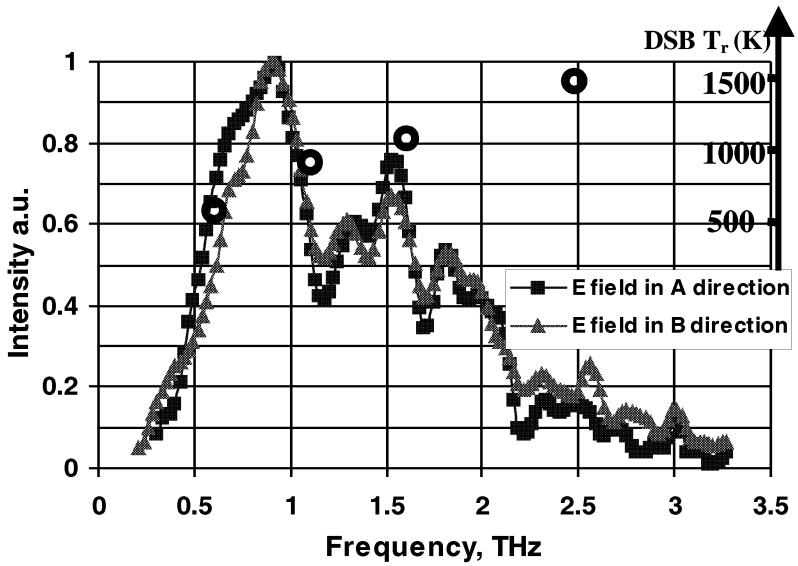

Figure 5. Normalized direct responses of the HEB, integrated with the spiral antenna. Direction A and B are shown in figure 4. Small circles show the measured double side band receiver noise temperatures at different LO frequencies.

The direct responses of the HEB integrated with the spiral antenna were measured with two different polarization of the incident beam. As we see in figure 5, the response spectrum of the spiral antenna did not show any polarization dependence. The bandwidth was about 2 THz, which is in agreement with estimated bandwidth of this type of Antenna in [11].

Figure 6 shows a SEM picture of a HEB, integrated with a double slot antenna, designed for 1.6 THz. Similar antennas have been fabricated for 0.6, 1.4, 1.8 and 2.5 THz. In all designs, the slot length (L) is $0.3\lambda_0$, the distance between slots (S) is $0.17\lambda_0$ and the width of the slots (W) is $0.02\lambda_0$, where λ_0 is the wavelength at design frequency in vacuum. The design rule was adopted from [12]. The dimensions of these antennas are summarized in Table 1. Note that the width of the coplanar line in the middle of the antenna is 4 μm and the same for all antennas.

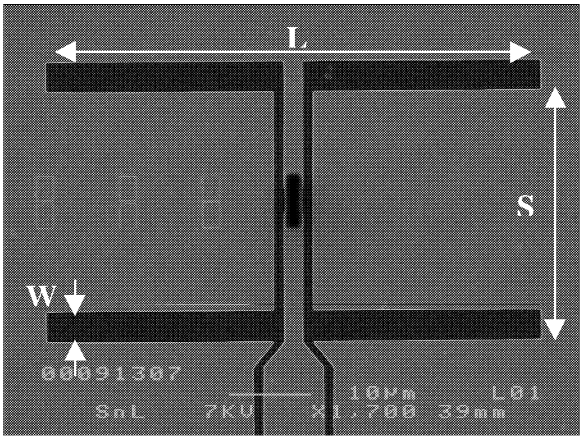

Figure 6. SEM picture of double slot antenna

	L (μm)	S (μm)	W (μm)
0.6 THZ	155	84	10,5
1.4 THz	64	36	4,6
1.6 THz	56	32	4
1.8 THz	50	28	3,6
2.5 THz	38,4	19,2	2,4

Table 1. Dimensions of the double slot antennas

The direct responses of the HEBs integrated with different double slot antennas are shown in Figure 7. The frequencies at which the local maximums and minimums occur are almost the same for all double slot antennas and also coincide with the strongest water absorption lines. We observe shifts between the bands of the antennas, designed for different frequencies. The higher is the design frequency, the wider is the relative bandwidth. This can be due to the fact that the width of the center coplanar line is the same in the middle of all the antennas and it is getting more comparable with the antenna size as design frequency increases (See table 1).

These results give important information about the optical losses in noise temperature measurements, which are usually done in air. For example in Figure 7(a), we see that although the antenna is designed for 2.5 THz, the response at 2.5 THz and 1.6 THz is almost the same. This can be the reason that the double side band receiver noise temperature of this mixer was measured 1700K, at both 1.6 and 2.5 THz LO frequencies.

Although it is difficult to see the center frequency of the antenna band directly, it can be estimated by fitting a parabola to the measured curve. Figure 8 shows the measured curves (solid line with squares) and the fitted parabolas (solid line) for 1.6 and 2.5 THz antennas. The calculated transmission of 30 cm air at 22°C and 30% humidity with 70 GHz resolution is depicted by the dashed line. Multiplying the parabolas with the atmosphere transmission factor gives a close approximation to our measured data (solid line with triangle). The conclusion is that the antenna responses are close to those parabolas mentioned above. We see that the response is down shifted from the design frequency, which has also been reported for antennas, integrated with Nb HEBs [4,5].

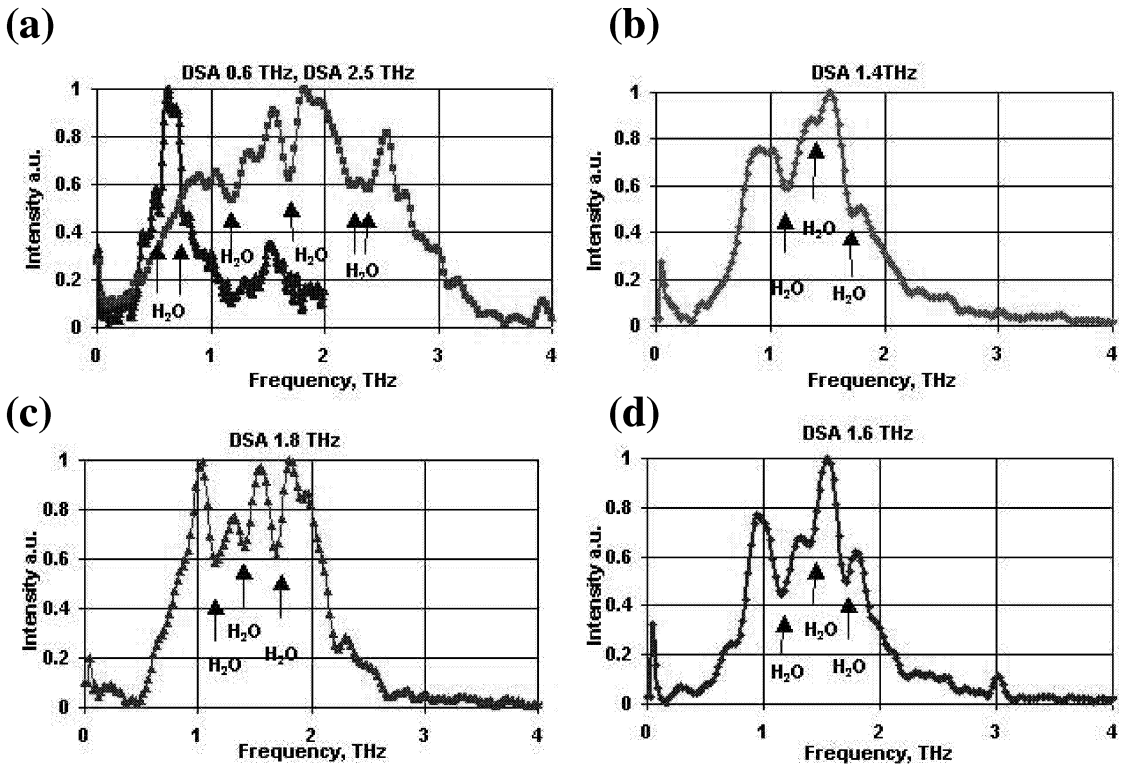

Figure 7. Direct responses of the HEBs integrated with different double slot antennas (DSA).

The direct responses were also measured at different operating conditions of the bolometers. The bias voltage was changed between 1 to 4 mV. We also changed the temperature of the mixer, within the range that the devices are stable and the DC characteristics of the bolometers were close to when they are used as mixers and pumped by a local oscillator. For all measured devices, the spectra did not change by varying either the bias voltage or the ambient temperature. This indicates that the direct responses are determined by the antenna structures and not by the bolometer operating condition, as long as it stays within the resistive state.

V. Conclusion

We have succeeded to extend the FTS frequency band up to 7.5 THz by using 10 μm polyethylene as a beam splitter. This set up can be used to study the optical property of material in THz range. For instance the transmission coefficient of 1mm thick Teflon sheet is measured. We see that it is almost opaque above 6 THz.

Our measurements show that the RF bandwidth of the spiral antennas is not strongly dependent on the radiation polarisation. The direct response of HEB integrated with different double slot antennas shows that the frequency bands of all antennas are down-shifted from their design values. Besides, the antenna bandwidth increases with increasing the design frequency.

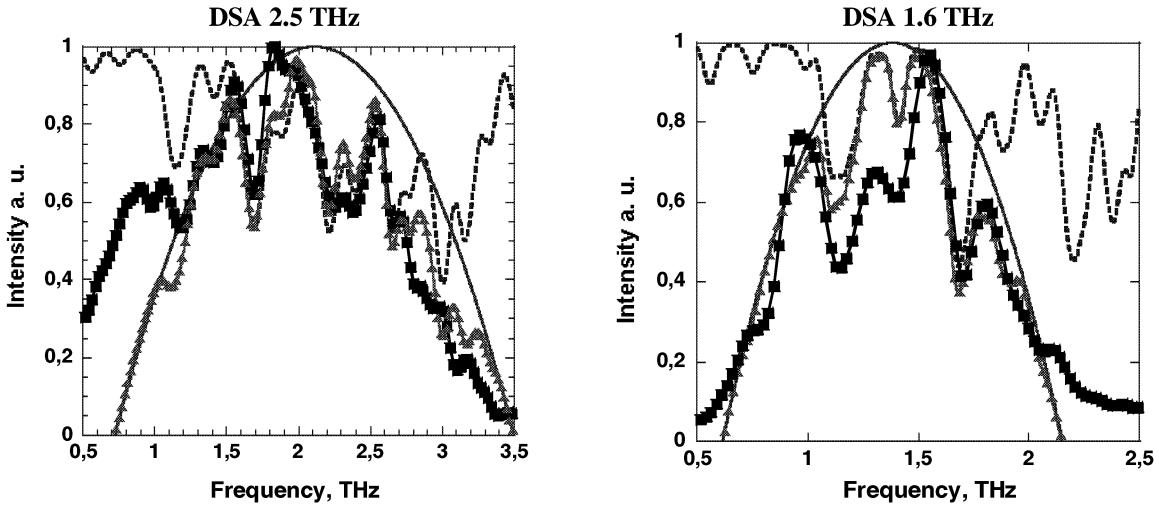

Figure 8. Calculated (solid line with triangles) and measured (solid line with squares) results for 1.6 and 2.5 THz antennas. The dashed lines show the air transmission coefficient. The parabolas (solid lines) are fitted to the measured curves.

For all measured mixers, changing the bias and temperature of the device, within resistive state, does not affect the result. This indicates that the measured spectrum is determined by the antenna response and not the intrinsic response of the bolometer. However, this might not be the case when the device is heated by a local oscillator (LO) instead of a heater. The temperature of the bolometer is not uniform when it is pumped by the LO. Therefore the response of the device might depend on the bias point and the absorbed LO power.

The interpretation of the antenna RF bandwidth from measurements is strongly affected by the water absorption. Vacuum measurements are required to characterise the planar antennas accurately. However, since the noise temperature measurements are usually done in air, the presented results are very informative.

VI. Acknowledgements

The authors would like to thank Dr. Scott Paine for providing software for calculating the atmosphere transmission. This project is partly supported by European Space Agency (ESA), Swedish National Space Board and the Swedish Foundation for Strategic Research.

References

[1] M. Kroug *et al*, **"HEB quasi-optical heterodyne receiver for THz frequencies"**, 12th International Symposium on Space Terahertz Technology, San Diego, February 2001, pp. 244-252

[2] M. Kroug *et al*, **"NbN hot electron bolometric mixers for terahertz receivers"**, IEEE Transactions on Applied Superconductivity, vol.11, no1, March 2001, PP. 962-965

[3] S. Cherednichenko *et al* **"Local oscillator power requirement and saturation effects in NbN HEB mixers"**, 12th International Symposium on Space Terahertz Technology, San Diego, February 2001, pp. 273-285

[4] R.A. Wyss *et al*, **"Submillimeter-wave spectral response of twin slot antennas coupled to hot electron bolometers"**, 11th International Symposium on Space Terahertz Technology, Ann Arbor, Michigan, May 2000, pp. 379-388

[5] W.F.M Ganzevles *et al*, **"Direct response of microstrip line coupled Nb THz hot-electron bolometer mixers"**, Applied Physics Letters, October 8, 2001,Volume 79, Issue 15, pp. 2483-2485

[6] P.F. Goltsmith "**Quasioptical systems**", IEEE Press, 1998, p. 204

[7] D.F. Filipovic *et al*, "**Double-slot antennas on extended hemispherical and elliptical silicon dielectric lenses"**, IEEE Transactions on Microwave Theory and Techniques, Volume 41, Issue 10, Oct. 1993, pp. 1738 –1749.

[8] P. Yagoubov *et al*, **"Characterization of an integrated lens antenna at Terahertz frequencies"**, 12th International Symposium on Space Terahertz Technology, San Diego, February 2001, pp. 193-204

[9] H.W. Hubers *et al*, **"Antenna pattern of the quasi-Optical hot electron bolometric mixer at THz frequencies"**, 12th International Symposium on Space Terahertz Technology, San Diego, February 2001, pp. 286-296

[10] P. Yagoubov *et al*, **"NbN hot electron bolometer mixers at frequencies between 0.7 and 3.1 THz"**, 10th International Symposium on Space Terahertz Technology, Charlottesville March 1999, pp. 238-246

[11] J. Kawamura *et al*, **"Spectroscopic measurements of optical elements for submillimeter Receivers ",** 7th International Symposium on Space Terahertz Technology, Charlottesville March 1996, pp. 349-355

[12] G.V.Eleftheriades *et al*, **"Self and mutual admittance of slot antennas on a dielectric half-space"**, Int. J. Infrared and MM Waves, vol.14, No.10, 1993, pp.1925-1946.

PROGRESS IN SIS DEVICE FABRICATION FOR HIFI MIXER BAND 2 AT KOSMA

P. Pütz*, S. Glenz, C. E. Honingh, K. Jacobs

KOSMA, I. Physikalisches Institut, Universität zu Köln
Zülpicher Strasse 77, 50937 Köln, Germany

ABSTRACT

We present our progress in device fabrication of Nb–AlO_x–Nb junctions embedded into low-loss tuning circuits. These integrated tuning circuits include a NbTiN ground plane and aluminum or niobium as top conductor materials. The junctions are defined by electron beam lithography down to areas of 0.4 μm^2. Instead of a lift-off process we use Chemical Mechanical Polishing (CMP) of the SiO_2 dielectric insulation to contact the junction top electrode.

Dipstick I/V measurements of devices with R_NA products around 15 $\Omega\mu m^2$ show a significantly higher gap voltage as compared to previously UV lithography / lift-off defined devices using otherwise identical fabrication parameters.

I. INTRODUCTION

Our goal is to develop the HIFI Band 2 SIS mixer for the Herschel Space Observatory [1]. The performance goals for HIFI are a mixer fractional bandwidth of 22 %, while complying to the mixer noise temperature specs of 110 K – 130 K (DSB) in the allocated frequency band between 638 GHz and 802 GHz. This corresponds to roughly only seven times the quantum limit $h\nu/2k$. Standard all-Nb devices cannot provide this performance above the Nb gap frequency of $2\Delta/h \approx 700$ GHz, so a low-loss tuning circuit material above the Nb gap has to be used. Although all-normal-conductor material tuning electrodes consisting of Al yield good-performance devices above 800 GHz [2], circuit simulations show that it is necessary to use an even lower-loss, superconducting, material especially for the low end of the targeted frequency band [3].

Because the fabrication of the Nb–AlO_x–Nb material combination is well-established and yields highly reproducible and high-quality tunnel junctions and the fact that the top of our frequency band is well below their theoretical mixing limit $4\Delta/h \approx$ 1400 GHz, our device design and fabrication baseline is to embed Nb–AlO_x–Nb junctions into a integrated tuning circuit with a NbTiN base and Nb or Al top electrode.

As NbTiN is the current choice for superconducting material above the Nb gap frequency, NbTiN thin film deposition techniques have been established for our junction fabrication and already have been integrated into HIFI Band 2 mixer fabrication in the past [4].

In order to achieve the performance goal the reproducibility of sub-micrometer-sized junction areas is the most critical fabrication parameter. Past mixer results and subsequent analysis show that a photolithographic defined junction area is not reproducible enough for HIFI Band 2 device development as a relative area reproducibility

* puetz@ph1.uni-koeln.de

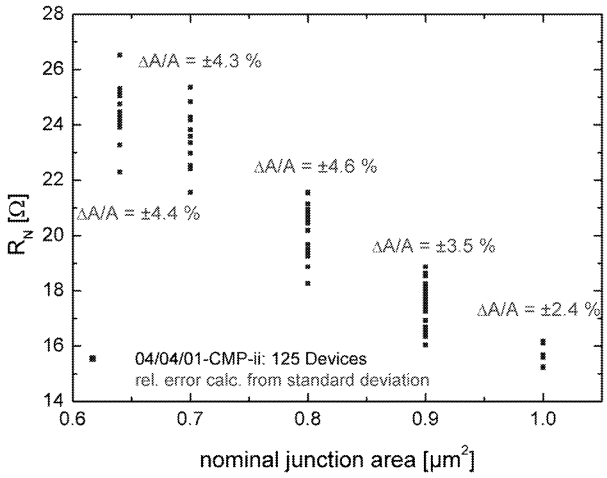

Fig. 1: Junction area reproducibility of simple Nb–AlO_x–Nb devices fabricated with our EBL / CMP process

$\Delta A/A < 10$ % (band center position) for junction areas of 0.5 μm^2 (RF matching) is required. Therefore we have integrated our electron beam lithography (EBL) / Chemical Mechanical Planarization (CMP) process scheme, which we developed in parallel for all-Nb devices, into junction fabrication for HIFI Band 2 mixer [5]. This process has proven its superior junction definition quality in the past yielding an area reproducibility complying to above design rule (Fig. 1).

We have decided to use EBL for junction definition while staying with standard photolithography for the likewise critical definition of the integrated top tuning electrode. We choose to do this because we encountered difficulties in achieving good RF performance of all-Nb mixers with the dual EBL and CMP process. We were able to trace the cause back to a resist related contamination problem during deposition of the integrated tuning top electrode. Good mixer results with photolithographic defined top tuning electrode reassured us that there is no inherent problem with our EBL / CMP process.

In this paper we present the current status of HIFI device fabrication at KOSMA and the advantages of the EBL / CMP process in comparison to our prior purely photolithographically defined batches.

II. Device Fabrication

Fabrication begins with the UV300 mask aligner definition of bilayer AZ7212 photoresist window structures on a 25 mm diameter and 285 μm thick INFRASIL fused quartz substrate. Through sputter-deposition of the metallization layer stack and subsequent lift-off these windows define the first half of the RF-blocking filter and waveguide-probe, the integrated tuning bottom electrode and the EBL alignment marks. The metallization consists of 350 nm NbTiN (tuning base electrode), 10 nm Au (diffusion barrier for the nitrogen and RIE etch stop, [6]), 100 nm Nb 1 (junction base electrode), 8 nm Al (for the AlO_x tunnel barrier) and 100 nm Nb 2 (junction top electrode) (Fig. 2). The Al layer is in-situ oxidized in the load-lock in a static pure oxygen atmosphere at 1.6 Pa using the Pa·s relationship [7] yielding a R_NA product of approximately 15 $\Omega\mu m^2$.

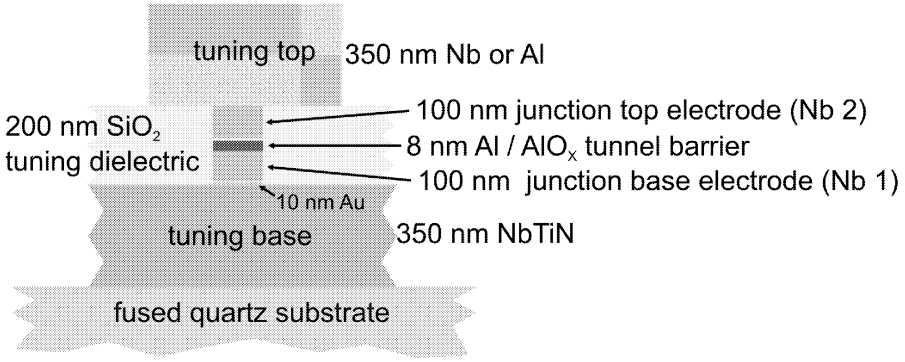

Fig. 2: Cross-section of HIFI Band 2 device layer stack

Then the junction area is defined via EBL in PMMA. Table 1 sums up the relevant process parameters. The use of an available 1 µm thick negative tone resist (MICRORESIST ma-N2410) would make a standard SNEP fabrication scheme possible but only works reproducible down to around 0.8 μm^2 junction area [8]. With a thin (positive tone) PMMA resist a self-aligned lift-off process for junction isolation is not possible.

Therefore we have integrated our EBL / CMP process into junction fabrication of our HIFI mixer. This processing scheme is based on the PARTS process [9] in which the junction isolation is not achieved by a self-aligned lift-off process (SNEP) but through planarization of a blanket layer of the dielectric material (Fig. 3). For pattern transfer during RIE, an etch mask is defined by sputter-deposition of 30 nm Al and 20 nm Au into the PMMA features and subsequent lift-off. The Au layer acts as a protection of the Al towards the alkaline developer during a subsequent photolithographic process. With this lithography step the area in which the Nb–AlO_x–Nb-layers are etched away is confined to the ground plane area of the tuning circuit.

The junction is then etched with several RIE steps. RIE of the Nb 2 and Nb 1 layers is performed with a mixture of CCl_2F_2 and NF_3 yielding an anisotropic etch behavior, while an Ar sputter etch is used to remove the AlO_x layer and the Au layer in a multi-cycle process [2],[4].

After removal of the remaining resist, 900 nm SiO_2 (tuning dielectric and junction isolation) is deposited onto the whole wafer with RF sputtering.

resist type	AR-P669.04 (PMMA 600k, 4%), ALLRESIST
resist thickness	220 nm
charge dissipation layer	6.5 nm Al sputter-deposited on PMMA
exposure dose	150 – 220 µC/cm^2 (proximity effect compensation)
e-beam current	14.0±0.2 pA
removal of Al layer	buffered phosphoric acid solution
development time	4 min AR600-56, ALLRESIST
stopper time	0.5 min AR600-70, ALLRESIST

Table 1: Electron Beam Lithography Parameters

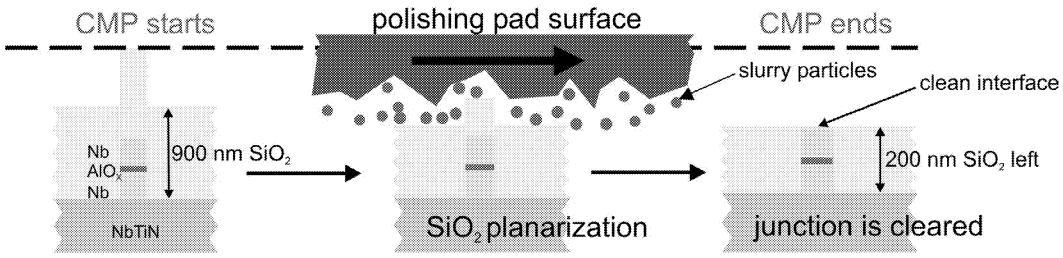

Fig. 3: Schematical explanation of the planarization process

The planarization efficiency during CMP is a function of feature size, with the generated topography of larger structures being planarized at a slower rate than smaller ones. This is due to deflection of the polishing pad and is in turn affected by the elasticity of the pad and the applied back pressure during polishing. Applied to our chip layouts this implicates that small features, such as the junction stack and waveguide probe, planarize faster than the large bond pad features at the other end of the RF-blocking filter structure. Dielectric thickness of the SiO_2 in the tuning circuit ground plane areas determines the end-point during polishing and thus terminates CMP before the contact area on the bond pad is cleared from the SiO_2. By defining additional holes in the dielectric layer during above photolithography contact problems are prevented.

During CMP the quartz wafer is glued onto a two inch silicon wafer with thin film wax for higher mechanical resilience during the polishing (Fig. 4, right). The CMP process has been transferred to a dedicated new polisher ([10], Fig. 4, left).

4 – 6 polishing steps are needed to complete the planarization and thinning of the dielectric each of typically 5 min duration. The remaining dielectric thickness must be 200±20 nm for the integrated tuning circuit to work as designed. End-point detection is realized by visually checking the color of the isolation dielectric under a microscope and profilometer measurements across the if structure relative to substrate level. The removal of the etch mask on top of the junction proves to be a very good additional indicator for clearance of the electrodes and can be performed without leaving any residue behind.

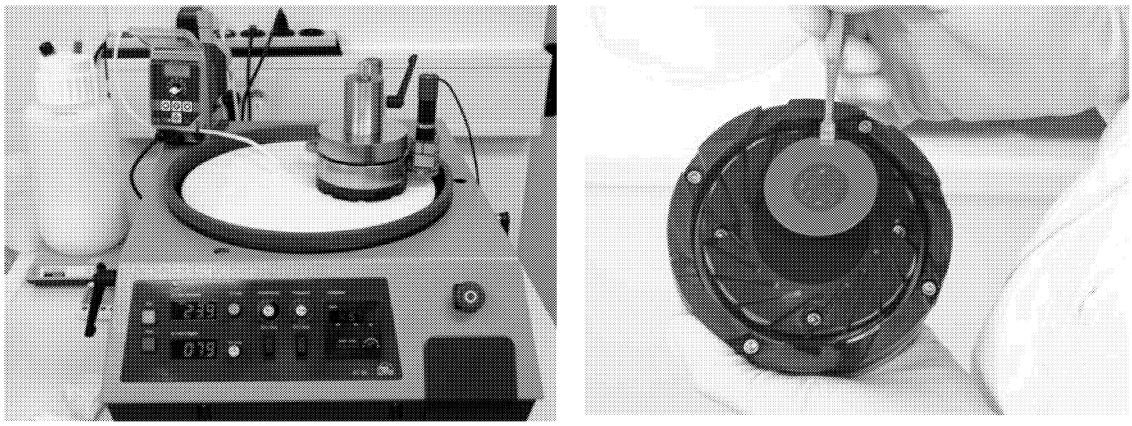

Fig. 4: CMP setup during processing (left photo) and quartz wafer glued onto a 2" silicon wafer prior to placement into the polishing head recess (right photo)

polishing pad	14" diam. IC-1000 / SUBA IV stack, RODEL CORP.
Slurry	ILD1200, diluted 1:4.3, pH = 10.5, RODEL CORP.
slurry feed	6 ml/min
jig rotation	22 rpm
pad rotation	20 rpm
relative velocity	0.37 m/sec
down force	26 N
wafer surface protrusion	approx. 100 µm, DF200 wafer backing, RODEL CORP.
typical bulk removal rate	30 nm/min

Table 2: Summary of important CMP processing parameters

The CMP process parameters have been adjusted to deliver local planarization of the junction area and best global uniformity of the tuning circuit dielectric thicknesses. After CMP the wafer surface is cleaned with a 2 % NH_4OH solution and PVA sponge. Table 2 sums up important CMP parameters.

Then follows the definition and sputtering of the integrated tuning top electrode, the missing half of the RF-blocking filter, the bond pad areas and alignment marks for dicing. This is done in two processing steps through UV lithography, sputter deposition of the metallization layers and subsequent lift-off. At first the Al-based integrated tuning top electrodes are defined with a 350 nm thick Al layer, supplemented by 70 nm Nb to eliminate series DC resistance. In the second step a 350 nm thick Nb layer, supplemented by 30 nm Au for bond adhesion, serves as the metallization layer for the Nb-based integrated tuning top electrodes, the other RF-blocking filters / waveguide probe halves, dicing marks and the bond pad areas of all devices.

To protect the integrated tuning top electrodes and the Al containing RF-blocking filters, a final UV lithography and lift-off step is needed for RF sputter-deposition of the 400 nm thick SiO_2 passivation layer.

III. DC I/V RESULTS

The inclusion of e-beam lithography and CMP into our HIFI mixer fabrication has a significant impact on device quality. An improvement of device quality is observed in two areas. First, junction area reproducibility has been significantly improved. Fig. 5 compares the junction area reproducibility of the first EBL / CMP scheme HIFI mixer batch with a previously defined UV300 / SNEP batch. The results are already close to those of past development runs with simple all-Nb devices (Fig. 1).

Second, the new process delivers junctions with systematically higher gap voltages than the old process. In Fig. 6 typical DC I/V curves of junctions from both fabrication schemes but otherwise identical fabrication parameters (e.g. layer stack, R_NA product, junction area) are compared. In this example the EBL / CMP processed device exhibits a gap voltage increase by over 0.2 mV (Fig. 6, left). In our interpretation the CMP leaves a very clean interface at the top of the junction electrode, thus enabling a better thermal contact of the junction to the integrated tuning top electrode and therefore better cooling of the tunnel barrier. We believe that our interpretation is also underlined by the fact that the gap voltage spread of a CMP produced batch is narrower when the junc-

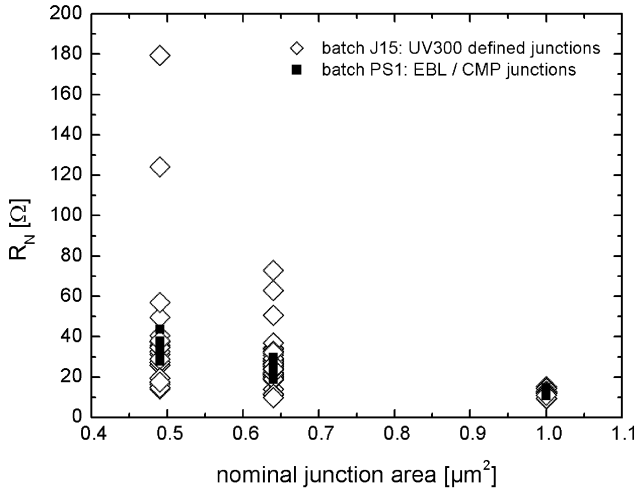

Fig. 5: Improvement in junction area reproducibility of a EBL / CMP fabricated batch in comparison to a past UV300 defined batch

tions of two differently processed batches are plotted as a histogram of their gap voltages (Fig. 6, right).

This underlines our past observation that it is very difficult to get a reproducibly clean junction top electrode interface after lift-off of the junction isolation during SNEP with embedded trilayer devices. With the UV300 / SNEP-based process we assisted the critical lift-off through a "short" chemical-mechanical polish on our prototype CMP setup.

Subgap current levels are not improved by the new process and are still at levels ($R_{sg}/R_N < 8$) significantly reducing mixer RF performance. As standard Nb–AlO_x–Nb devices of similar R_NA products routinely show R_{sg}/R_N ratios of 15 or better we conclude that this behavior is intrinsic to embedded trilayer devices of our junction fabrication. We have indication that the rough NbTiN base layer has an adverse affect on tunnel barrier leakage characteristics.

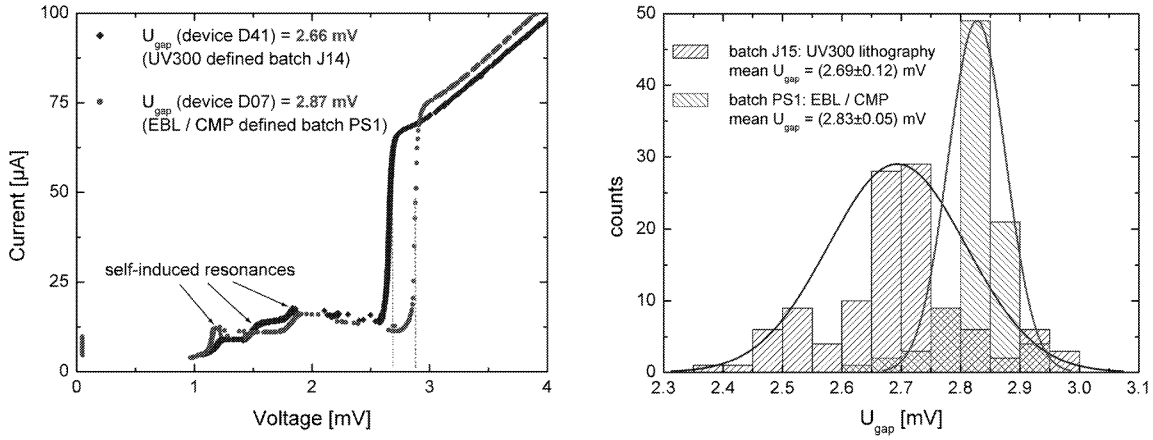

Fig. 6: Systematic increase and higher reproducibility of device gap voltage due to CMP. Comparison of two typical I/V curves (left) and histogram of gap voltage distribution (right) at 4.2 K

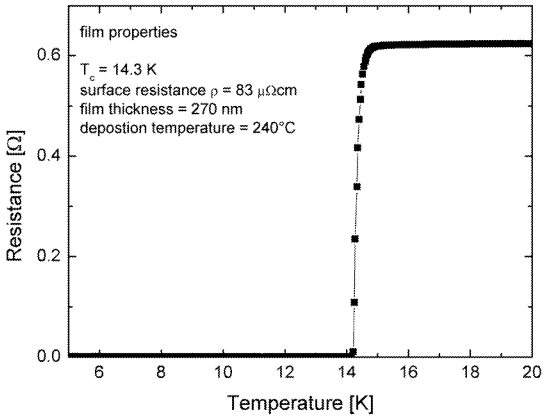

Fig. 7: R/T curve of a NbTiN thin film (van-der-Pauw structure), sputtered at an elevated substrate temperature of 240°C

NbTiN sputtered at an elevated substrate temperature is now available with our new sputtering machine for next fabrication runs. Van-der-Pauw measurements of NbTiN sputtered at 240°C show very promising results as they make low resistivity films for junction fabrication accessible without the penalty of high film stress (Fig. 7).

IV. SUMMARY

We have made progress in device fabrication for HIFI Band 2 mixer by integrating EBL and CMP for junction definition into the processing scheme. Junction area reproducibility has been greatly improved for junction areas below 1 μm^2 and the gap voltage been systematically increased through our EBL / CMP process.

R_{sg}/R_N ratios still have to be improved to achieve required device performance. We are narrowing down the cause for our low R_{sg}/R_N ratios.

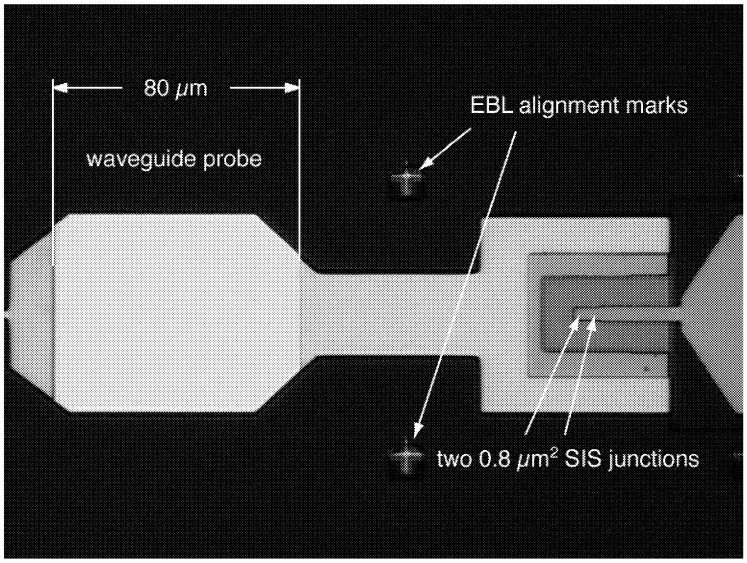

Fig. 8: Microscope photo of a recently fabricated EBL / CMP device for HIFI Band 2 mixer development (two junction integrated tuning circuit)

ACKNOWLEDGMENT

We thank Michael Schultz for dicing of the devices. This work was supported by DLR (Deutsches Zentrum für Luft- und Raumfahrt), Förderkennzeichen 50 OF 0001 2 and 50 OF 9902 4, by ESA (European Space Agency), CCN5 on ESTEC Contract 11653/95/NL/PB(SC) and by DFG (Deutsche Forschungsgemeinschaft), Sonderforschungsbereich 494.

REFERENCES

[1] FIRST HIFI homepage: http://www.sron.nl/divisions/lea/hifi/

[2] S. Haas, S. Wulff, D. Hottgenroth, C. E. Honingh, K. Jacobs, "Broadband Array SIS Mixers for 780 – 880 GHz with Aluminum Tuning Circuit, Proc. of the 11th Int. Symp. on Space THz Tech., Ann Arbor, MI, pp. 95 – 104, May 1 – 3, 2000.

[3] J. W. Kooi, J. A. Stern, G. Chattopadhyay, H. G. LeDuc, B. Bumble, J. Zmuidzinas, "Low-loss NbTiN films for THz SIS mixer tuning circuits", Proceedings of the 8th Int. Symp. on Space THz Tech., Boston, MA, pp. 310 – 319, March 25 – 27, 1997.

[4] S. Glenz, S. Haas, C. E. Honingh, K. Jacobs, "NbTiN Based Tuning Structures for Broadband Nb-Al_2O_3-Nb SIS Mixers from 640 GHz – 800 GHz", Proc. of the 12th Int. Symp. on Space THz Tech., San Diego, CA, pp. 1 – 10, Feb. 14 – 16, 2001.

[5] P. Pütz, K. Jacobs, "E-Beam SIS Junction Fabrication using CMP and E-Beam Defined Wiring Layer", Proc. of the 10th Int. Symp. on Space THz Tech., Charlottesville, VA, pp. 118 – 129, March 16 – 18, 1999.

[6] B. Bumble, H. G. LeDuc, J. A. Stern, and K. G. Megerian, "Fabrication of Nb/Al-N_x/NbTiN Junctions for SIS Mixer Applications", IEEE Trans. on Appl. Supercond., Vol. 11, No. 1, pp. 76 – 79, March 2001.

[7] A. W. Kleinsasser, R. E. Miller, and W. H. Mallison, "Dependence of Critical Current Density on Oxygen Exposure in Nb–AlO_x–Nb Tunnel Junctions", IEEE Trans. On Appl. Supercond., Vol. 5, No. 1, pp. 26 – 30, March 1995.

[8] I. Péron, P. Pasturel, and K.-F. Schuster, "Fabrication of SIS junctions for space borne submillimeter wave mixers using negative resist e-beam lithography", Proc. of the Applied Superconductivity Conference, ASC '00, Virginia Beach. Sept. 17 – 23, 2000.

[9] M. B. Ketchen, D. Pearson, A. W. Kleinsasser, C.-K. Hu, M. Smyth, J. Logan, K. Stawiasz, E. Baran, M. Jaso, T. Ross, K. Petrillo, M. Manny, S. Basavaiah, S. Brodsky, S. B. Kaplan, W. J. Gallagher, M. Bushan, "Sub-μm, planarized, Nb-AlO_x-Nb Josephson process for 125 mm wafers developed in partnership with Si technology", Appl. Phys. Lett., **59**, No. 20, pp. 2609 – 2611, 1991.

[10] IBS PT 350 Premium, I-B-S GmbH, Grafrath, Germany.

LOW NOISE CRYOGENIC IF AMPLIFIERS FOR SUPER HETERODYNE RADIOASTRONOMY RECEIVERS

Christophe Risacher*, Victor Belitsky

Group for Advanced Receiver Development (GARD), Radio & Space Science Department with Onsala Space Observatory, MC2, Chalmers University of Technology, 41296, Gothenburg, Sweden

Abstract

As part of Onsala Space Observatory instrumentation activities, a 3.4-4.6 GHz and a 4-8 GHz cryogenic low-noise amplifiers were developed. These amplifiers will be used as cold IF amplifier for mm and sub-mm wave receivers with SIS and HEB mixer (Onsala 7 channel 3mm array and APEX projects). The 2-stage 3.4-4.6 GHz amplifier was fabricated in 7 copies with consistently very similar performance at 12 K ambient temperature as follows: gain 28 dB with 2.8 K noise temperature using Mitsubishi MGFC4419G GaAs transistor, and 2.2 K noise when tested with Chalmers InP transistor at the first stage. The 2-stage 4-8 GHz LNA demonstrates 25 dB gain with noise temperature of 5.0 K with GaAs transistors, 4.0 K with Chalmers InP transistor at the input stage. These performances are in a very good agreement with simulations and are believed to be among the best-reported using GaAs transistors. The amplifiers design was carried using Agilent ADS, HFSS and Momentum CAD software. The amplifier input circuitry was measured separately and optimised for the best noise performance, while special care was taken about accurate modelling of passive components, bond wires and having accurate S parameters at cryogenic temperature for the transistor. In this paper we present details on the amplifier design, performances (modelled and measured) and also gain-stability comparison between GaAs and InP transistor based amplifiers.

Introduction

Millimetre and sub-millimetre wave receivers for high resolution spectroscopy in radio astronomy are usually of a super heterodyne type; the receiver employs frequency down-conversion based on superconducting SIS or HEB mixer operating at 4 K or lower ambient temperature; the sky signal transfers to an intermediate frequency (IF) signal of a few GHz and is amplified by a cryogenic low-noise amplifier. Nowadays, radio telescope receivers employ IF amplifiers with typically 1 GHz bandwidth centred either at 1.5 GHz or 4 GHz. But with the increasing interest for sub-mm observations, larger bandwidths are required for broader spectral line and continuum observations of extragalactic sources. Next generation of IF amplifiers will have 4 GHz bandwidth or even 8 GHz.

The first LNA presented here is designed for frequency band 3.4-4.6 GHZ [1], and is to be used as cryogenic IF amplifier for 3-mm wavelength 7 channel SSB receiver to be installed at Onsala 20m telescope. The other LNA is designed for the frequency band 4-8 GHz, and will be used as cold IF amplifier for our development of ALMA band 7 receiver (345 GHZ band) and also for APEX Project (to be built in Chilean Atacama desert end of 2002, and to be included in ALMA later on). The 4-8 GHz amplifiers will also be used as a front end for Onsala C band receivers on 20 m and 25 m antennas.

Amplifier Design

Design was carried out using Agilent ADS [2]. To achieve desirable accuracy of the modelling, the transistors were simulated using their S parameters at cryogenic temperature [3], and special attention was paid to develop adequate models of the passive components (resistors and capacitors). For example, the capacitor models include the series resistance and take into account series resonance as well as the first parallel resonance. The model consists of a series R-L-C circuitry with parallel R-C branch and the values were chosen to fit the manufacturer S-parameters data. In order to improve the stability and the input match, the bond wires, connecting the transistor source to the ground, and the resistors in the drain bias paths, provide the inductive feedback. The bonding wire model was developed using 3D EM simulation Agilent HFSS [4].

The most critical part in the design is the amplifier input stage where a 50 Ohm input line (from SMA connector) has to be transformed into a complex impedance varying with frequency and which should be as close as possible to the optimum noise match of the given transistors. The input stage uses a low impedance line, followed by a high impedance line with a tuning stub, to slightly increase the bandwidth, which is a part of the transistor gate bias line (Figure 1). This input stage was built as a separate test unit and precise measurement with a TRL calibration helped us to adjust performance of the entire amplifier for the optimum by changing the bypass capacitor location (±1 mm). The inter-stage and the output-stage were optimised for maximum gain, gain flatness and for the output match. The amplifier uses soft substrate, Duroid 6002, having excellent dielectric constant thermal stability and the coefficient of thermal expansion matched to that of copper. We use ATC chip capacitors of 100A series that show low series resistance and behave well at cryogenic temperature and surface mount series RC31 resistors. All the passive components are soldered using alloy 80In15Pb5Ag; for the substrate we used alloy 70In30Pb and the transistors are soldered using pure Indium. Bias lines are separated from the RF lines by a sidewall to avoid oscillations at low frequencies and the box resonance.

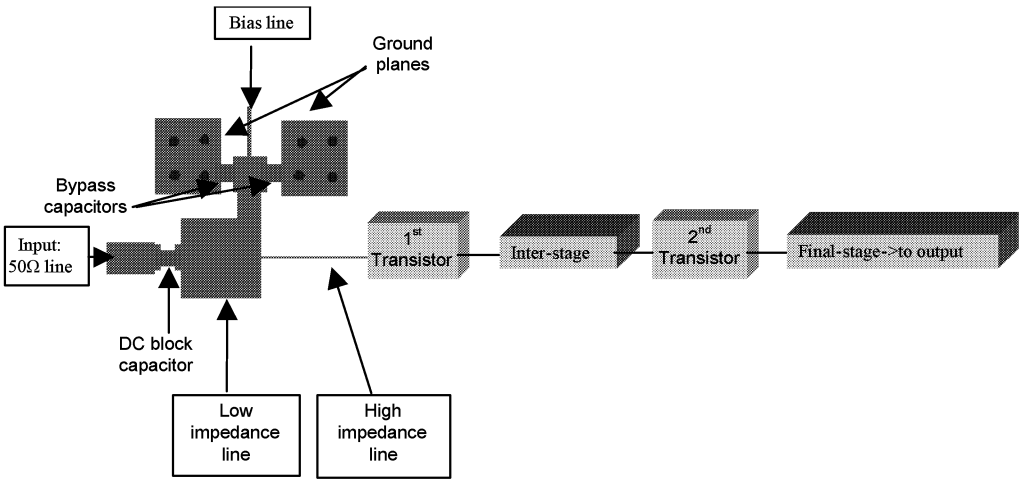

Figure 1. The amplifier block diagram and the input circuitry schematic.

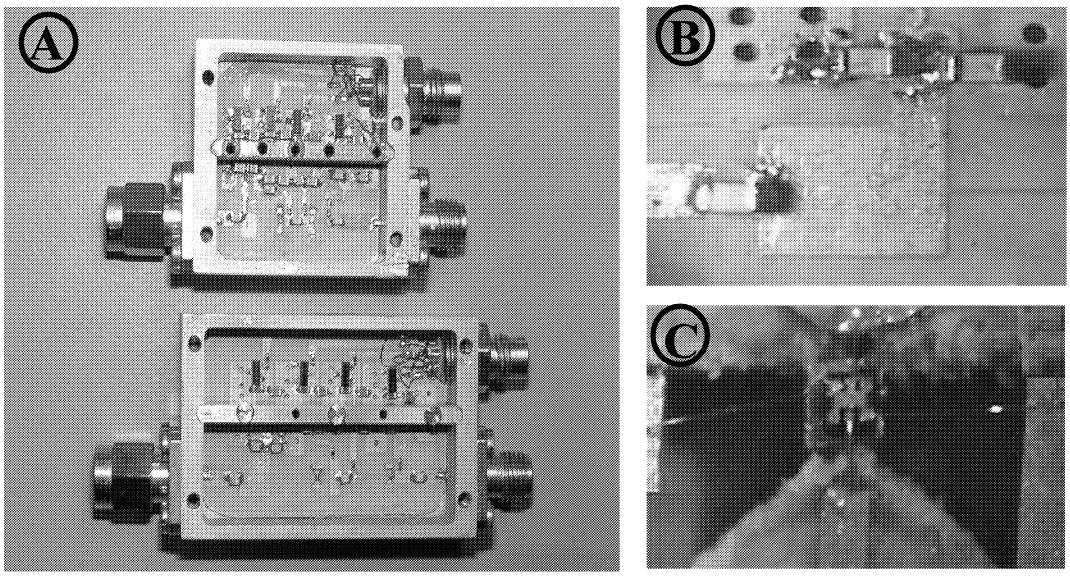

Figure 2. ***A:*** *Photograph of LNA 3.4-4.6 GHz (bottom one) with dimensions 65*26 mm and LNA 4-8 GHz (top one) with dimensions 50*26 mm.* ***B:*** *Magnified view of the input circuitry of LNA 3.4-4.6 GHZ. It consists of a low impedance wide line and a high impedance narrow line. Position of the capacitors provides a mean of tuning the noise performance.* ***C:*** *Magnified view of a GaAs HEMT chip transistor Mitsubishi MGFC4419G. Long bond wires from the source pads to ground provide inductive feedback and improves stability.*

We chose the option of having a cooled isolator at the input of the amplifier. This facilitates the design of the amplifier input circuitry, its input reflection coefficient is required to be only less than -5 dB. But the insertion loss of the isolator adds of about 10% to the noise when connected to the amplifier input.

Results

Two methods were used in our laboratory to measure the noise performance of the amplifiers: the variable load temperature (VLT) method and the cold attenuator (CA) method, both employing the Y-factor technique via connecting matched loads at different temperatures (T_{hot}, T_{cold}) at the input of the device, the amplifier under test (DUT), and to measure the output powers corresponding to the different load temperatures. As the DUT is assumed to be linear, the two measurement points are sufficient. The noise temperature T_e is then estimated as:

$$T_e = \frac{T_{hot} - Y \cdot T_{cold}}{Y - 1} \quad \text{, where} \quad Y = \frac{P_{hot}}{P_{cold}} \text{ measured at the output of DUT.}$$

VLT method (Figure 3) is a direct Y-factor measurement where we used a 50-Ohm load with a heater installed inside the cryostat on the cold plate and connected to the input of the amplifier through a short piece of a stainless steel coaxial cable providing thermal insulation. When the heater is OFF, the load is almost at the ambient cryogenic temperature 12 K (measured by a precision thermometer), whereas when the heater is ON the temperature up to 40 K can be reached.

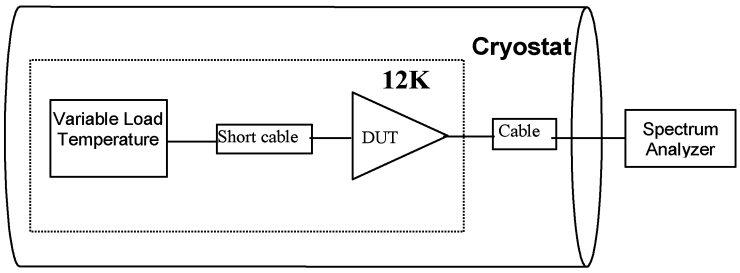

Figure 3. Variable Load Temperature Method

The CA method employs a cold attenuator and an external noise source, the noise diode HP346B with 15 dB ENR, operating together with the noise figure meter HP8970B. The noise signal from the diode is applied to the input of the amplifier under test via the precision 23 dB attenuator (Figure 4). By biasing the noise diode, the signal at the amplifier input can be changed from 50 K (9000 K from the noise source attenuated by the 23 dB cold attenuator) to 12 K when the noise source is OFF and the amplifier sees mainly the thermal noise from the attenuator at 12 K ambient temperature. The use of cold attenuator reduces the effect of the cable connecting the noise diode operating at room temperature to the attenuator at 12 K; the loss in the cable and its equivalent noise temperature can be only roughly estimated. The cold attenuator help also to improve the match of the noise source with the DUT, the noise diode impedance varies significantly between ON and OFF.

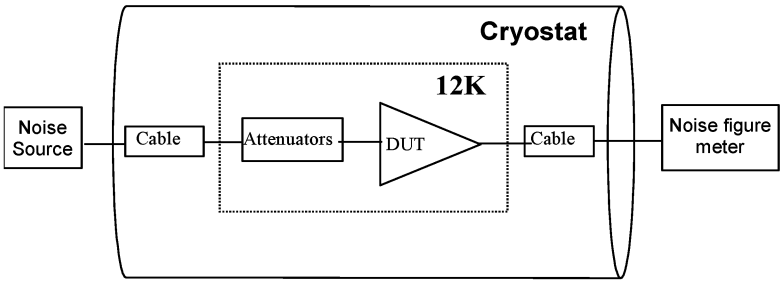

Figure 4. Cold Attenuator Method

The accuracy of amplifier noise temperature measurement was carefully investigated and estimated for both methods [2] for the given laboratory measurement setups and is of ±0.4 K for the VLT method and ±0.8 K for the CA method. Though being less accurate, the CA method is less time consuming than the VLT method, it is much more convenient for sweep measurements when optimising bias voltages. Therefore, results presented below were all taken with the CA method at cryogenic temperature of 12 K and moreover the few results with the VLT method are very consistent with the CA measurements.

3.4-4.6 GHz GaAs-based LNA (figure 5) gives 28 dB gain and the noise temperature of 2.8 K with total power consumption of 12 mW (optimised for the best noise performance). With a low power consumption of 4 mW, the amplifier has 26 dB gain and the noise temperature of 3.3 K, which is still very good. Replacing the first stage transistor with Chalmers InP HEMT [3] gives 28 dB gain with lower noise temperature of 2.2 K and total power consumption of 4 mW.

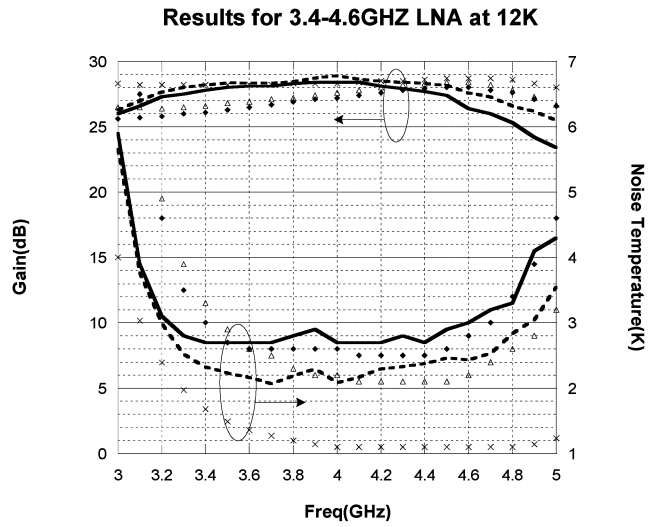

Figure 5. Simulations and measurement results for 3.4-4.6 GHz LNA: The bottom curves are noise temperature plots and the upper curves are gain plots. Continuous line is for measurement of GaAs MGFC4419G for both stages, dashed line is for measurement of the LNA by replacing the first stage transistor by Chalmers InP HEMT. The diamond marked line shows simulation results for GaAs-based LNA, the line with triangles is simulation results for Chalmers InP-based LNA, and the plot with crosses is simulation results for TRW InP-based LNA.

For the 4-8 GHz, (figure 6) GaAs based LNA gives 26 dB (±1.5 dB) gain and noise temperature of 5 K with a total power consumption of 15 mW. With a low power consumption of 4 mW, results are 23 dB gain and 6 K noise temperature. Replacing the first stage transistor with Chalmers InP HEMT gives 26 dB gain with a 4.0 K noise temperature and the total power consumption is 4 mW.

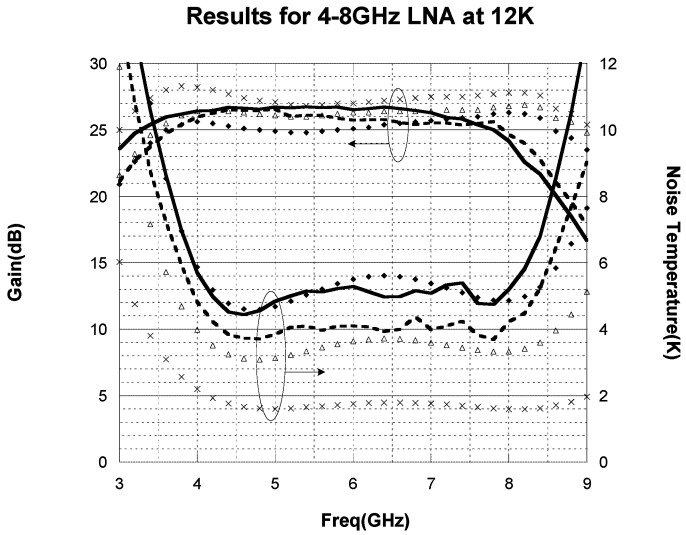

Figure 6. Simulations and measurements results for.4-8 GHz LNA: The bottom curves are noise temperature plots and the upper curves are gain plots. Continuous line is for measurement of GaAs MGFC4419G for both stages, dashed line is for measurement of the LNA by replacing the first stage transistor by Chalmers InP HEMT. The diamond marked line shows simulation results for GaAs-based LNA, the line with triangles is simulation results for Chalmers InP-based LNA, and the plot with crosses is simulation results for TRW InP-based LNA

The amplifier input match S11 is less than –5 dB, as expected, and the output match S22 is better than –12 dB for the both LNAs. At the cryogenic temperature (12 K), the measurement of the 3.4-4.6 GHz LNA together with a cooled isolator gives a noise temperature of about 3K, with slightly narrower bandwidth, which is still quite acceptable and within the specifications. The isolator shows almost a perfect match to 50 Ω for the frequency range 3.4-4.6 GHz and somewhat worse match outside this band but still much better to what could be achieved without the isolator. At room temperature the GaAs-based LNAs have 26 dB gain and 35 K noise temperature for the 3.4-4.6 GHz band and 24 dB gain and 35-40 K noise temperature for the 4-8 GHz band respectively.
The agreement between the simulation and the measurement is good, which is in part due to very accurate models for the transistors extracted by I. Angelov [5]. The simulations also show that with InP transistors from TRW, the noise temperature should drop to 1.0 K for the 3.4-4.6 GHz LNA and below 2.0 K for the 4-8 GHz LNA.

Gain Stability Measurements

A comparison between GaAs and InP HEMT transistors was carried out in order to estimate their relative gain stability. Two methods were used: the first method uses the Allan Variance [6-8] while the other method employs the power spectra of the noise (with FFT) and measures its normalized gain fluctuation value at 1 Hz [9].

A possible source of the gain instability is the variation of the ambient temperature; the low noise amplifiers under test were mounted on the cold plate of a 2-stage close cycle refrigerator providing the temperature of 12 K. The cold plate temperature was monitored continuously, and the temperature fluctuation due to the compressor cycle (1 Hz) was of about 5 mK; however, this is a lower limit of the measured temperature variations with fast fluctuations apparently filtered out because of the response time of temperature sensors; it was found that this has negligible effect on the gain of the LNA. Moreover no 1 Hz line was seen in the power spectra taken showing that our set-up is not sensitive to the compressor cycle, as opposed to the results in [8, 9]. The measurement procedure is described in [9] and employs a stable CW signal of 4.25 GHz, injected into the input of the amplifier with the output power monitored with a Boonton power detector. The power level was maintained constant to get 20 dBm at the input of the detector. The data was taken every 500 ms and we were looking at the gain instabilities in a narrow bandwidth around 4.25GHz. To avoid influence of the setup on the measurement results we calibrated the system alone, without the amplifiers under test; the calibration shows that it is stable to at least 50 s (see figure 7), which is sufficient for our tests.
The measurement presented here were taken with GaAs based 4-8 GHz LNA, with Vd=1.8 V and Id=5 mA for both stages, and the second InP-based 4-8 GHz LNA had the InP transistor at the first stage with Id=0.6 V and Id=3 mA and the GaAs transistor for the second stage.

Allan variance shows the relation between obtained sensitivity as a function of integration time. For ideal case when only white noise is present, Allan variance should follow a 1/T slope (radiometer formula). The different types of noise can be described by the following expression:

$$A\,\mathrm{var}(T) = c \cdot T^{\beta} \qquad (1),$$

where b = -1 is for white noise, b = 0 is for 1/f electronic noise, and b = 1 is for low frequency drifts. With this type of representation, one can easily identify the type of the noise present, and determine what is the optimum integration time to get the best sensitivity. This time limit is called Allan Time, integrating more would not give any improvement and could even degrade the signal to noise ratio.

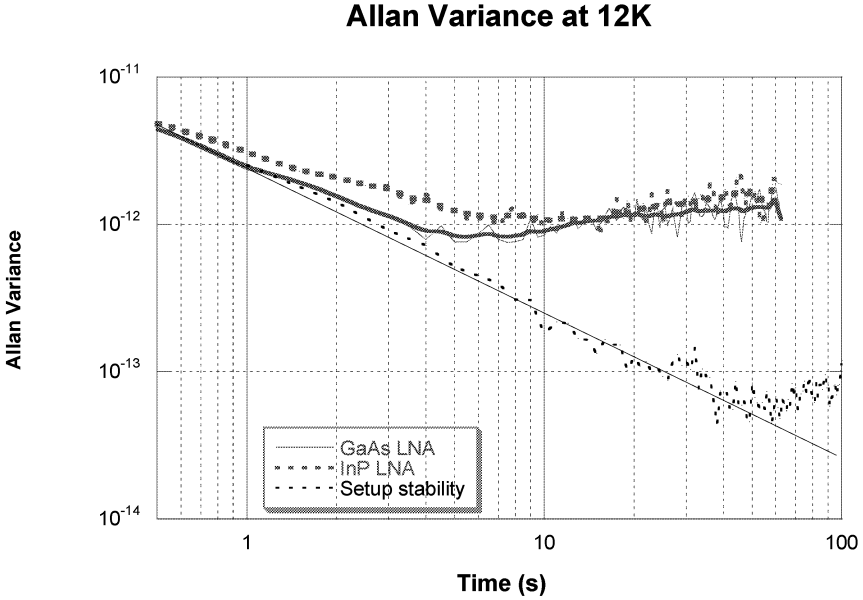

Figure 7. Solid line is for GaAs based LNA, and dashed line for InP based LNA. Already at 1s, there is a loss of integration efficiency and InP-based LNA deviates earlier than GaAs. At 7s 1/f noise become dominant for both amplifiers.

Figure 7 shows Allan variance plot; already at 1s there is a loss of integration efficiency, data points deviate from the ideal 1/T slope. This early deviation could be caused by some microphonic pickup noise on the LNA bias lines. At about 7s, 1/f noise becomes dominant, and Allan Variance stays at a constant level, slightly increasing due to the presence of some low frequency drift.

Taking the power spectra of the noise (with FFT) gives basically the same type of information as the Allan variance and shows the power spectra of different type of noises. The expression for the power spectral density of different type of noise is the following:

$$S(f) = b \cdot \left(\frac{1}{f}\right)^{\alpha} \qquad (2),$$

for the white noise $a = 0$, for the 1/f electronic noise $a = 1$, for the low frequency drift $a = 2$.
Figure 8 shows the normalized power spectra of the same data as in Figure 7. 1/f noise is clearly visible for frequencies < 1 Hz. Then the white noise becomes dominant for frequencies above 1Hz.

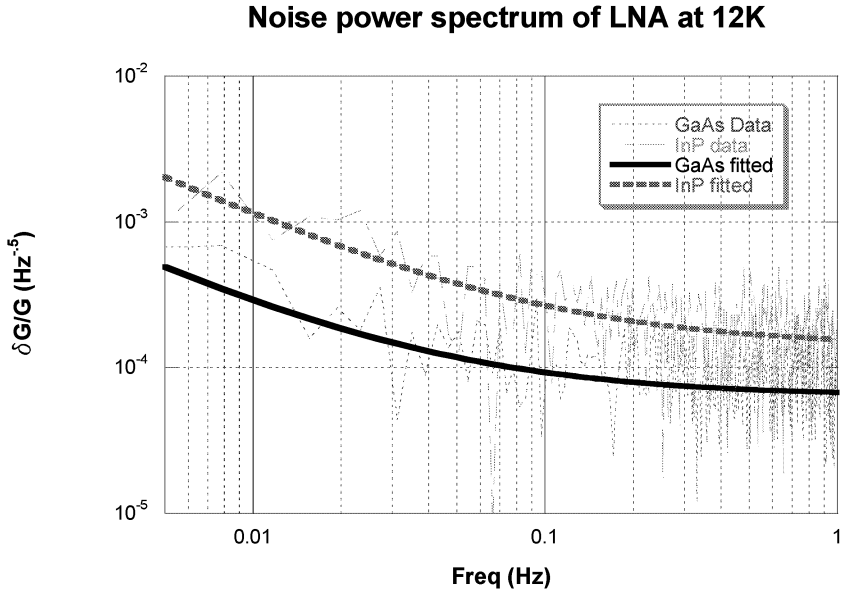

Figure 8. Normalized noise power spectrum for the same measurement as in Figure 4. Solid line is for the GaAs based LNA, dashed line is for the InP based LNA.

Here again, it is clearly seen that InP-based LNA has poorer stability than GaAs-based LNA. The values at 1 Hz are:

$$b_{GaAs} = 8 \cdot 10^{-5}\ Hz^{-0.5} \qquad b_{InP} = 15 \cdot 10^{-5}\ Hz^{-0.5}$$

It should be noted that no correction was applied to the data to subtract the measurement set-up intrinsic instability. Therefore the values above are the total instability of the LNA and the set-up itself.
Both methods give consistent results, showing that InP-based LNA are slightly worse than GaAs-based LNA for the gain stability. From Kraus [10], the gain instability degrades the sensitivity in a total power receiver as:

$$\delta T = T_{SYS} * \sqrt{\frac{1}{B * \tau} + \left(\frac{\delta G}{G}\right)^2} \qquad (3),$$

where T_{sys} is the system noise temperature, B is the effective bandwidth, t - the integration time, and dG/G the gain fluctuations of the receiver.

From this formula, it can be seen that for a large instantaneous bandwidth or large integration time, the stability of the receiver becomes an issue. If the LNA gain fluctuation is negligible compared to other gain fluctuations in the receiver like the SIS mixer conversion gain, then the LNA should have the lowest noise temperature to get the lower T_{sys} and therefore the lower δT. But if the LNA gain fluctuation is the dominant source of instability in the receiver, there is a trade-off to look for, and in some cases it could be worth using the more stable LNA, in spite of a slightly higher noise temperature.

Conclusion

3.4-4.6 GHz and 4-8 GHz low-noise 2-stage amplifiers based on GaAs HEMT transistors were designed and tested as part of our development work at Onsala Space Observatory. The amplifier design was carried out using Agilent ADS, HFSS and Momentum CAD and special attention was paid to model the passive components and the matching circuitry correctly and use accurate cold transistor S-parameters. The measured performance at cryogenic temperature of 12 K for the 3.4-4.6 GHz amplifier is 28 dB gain and 2.2 K noise temperature with Chalmers InP HEMT, and 2.8 K with MGFC4419G GaAs HEMT. For the 4-8 GHz amplifier, the performance is 25 dB gain and 4.0 K noise temperature with Chalmers InP HEMT and 5.0 K with the GaAs HEMT. These results represent the state of the art for these frequency ranges with the commercial GaAs transistors. The power consumption for optimum noise performance was in the range of 12-15 mW with GaAs and of the order of 4 mW with Chalmers InP; however the GaAs transistors can still be used with 4 mW power consumption with little performance penalties of 20% noise temperature increase and 2 dB gain drop.

The gain fluctuation measurement of the HEMT devices shows that GaAs-based LNA are slightly better than InP-based LNA in term of gain stability. In some cases, e.g., for receivers using large detection bandwidth or integration time in a single run, and having gain fluctuations mainly due to the LNA itself, a better receiver sensitivity could be achieved using GaAs based LNA rather than InP LNA, even despite having a slightly higher noise temperature.

Acknowledgements.

We would like to thank deeply N. Wadelfalk, I. Angelov, P. Starski, N. Rorsman, and H. Zirath Microwave Electronic Laboratory, Chalmers University for very useful discussions and possibility to test Chalmers InP HEMTs. Professor Roy Booth was always providing us with remarkable support and encouraged for successful completion of this work.

References

[1] Advanced Design System version 1.3, Agilent Technologies.

[2] C.Risacher, M. Dahlgren, V.Belitsky, "*A 3.4-4.6 GHz Low Noise Amplifier*" in Proceedings of Gigahertz 2001 Symposium, Lund, Sweden, November 26-27, 2001. Available at http://gard04.mc2.chalmers.se/homepage.htm

[3] I. Angelov and N. Wadefalk, private communication.

[4] High Frequency Structure Simulator version 5.6, Agilent Technologies.

[5] I. Angelov, N. Wadefalk, J. Stenarson, E. Kollberg, P. Starski, and H. Zirath, "*On the Performance of Low noise Low DC Power Consumption Cryogenic Amplifiers*", IEEE MTT-S 2000

[6] D W. Allan, "*Statistics of Atomic Frequency Standards*", Proc. IEEE,Vol. 54, No. 2, pp 221-230, 1969

[7] R. Schieder, "*Characterization and Measurement of System Stability*", SPIE, Vol 598, Instrumentation for Submillimeter Spectroscopy (1985)

[8] J.W.Kooi et Al., "*Noise in SIS receivers*", Int. J. of Infrared Millimeter Waves, vol. 21, no. 5, pp. 689-716, May 2000.

[9] J.D.Gallego, I.L.Fernandez "*Definition of measurements of performance of X band cryogenic amplifiers*", Technical Note ESA/CAY, 2000.

[10] J.D.Kraus, "*Radioastronomy*", New York cop. 1966

INTEGRATED NIOBIUM THIN FILM AIR BRIDGES AS VARIABLE CAPACITORS FOR SUPERCONDUCTING GHZ ELECTRONIC CIRCUITS

Matthias Schicke and Karl-Friedrich Schuster
Institut de Radio Astronomie Millimétrique (IRAM), 300, rue de la Piscine, 38406 St. Martin d'Hères, France

Abstract. Superconducting GHz electronics can be improved by variable tuning circuits. We present a low temperature (< 150°C) process for the fabrication of niobium (Nb) thin film air bridges as variable capacitors, which can be integrated in Nb superconducting electronics. These elements can be applied for on-chip adjustment of filters, resonators and tuning circuits. Measurements and calculations of the electrostatic actuation of the bridges will be compared.

1. INTRODUCTION

Variable tuning elements are of high interest for all high frequency applications. Waveguide backshorts are not integrable with planar filter structures, resonators and other superconducting electronic circuits. Electrostatically actuable air bridges can be fabricated on the same substrate as the circuits to be tuned. The bridges are actuated by applying a suitable voltage between the bridge and the ground electrode underneath it as shown in Fig. 1. Some recent developments on this type of elements, using normal conductors or silicon, has been presented by Rebeiz and Muldavin [1].

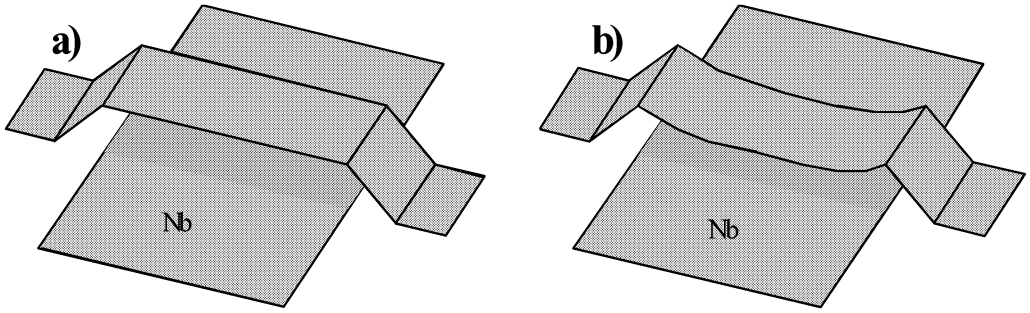

Figure 1. Schematic picture of an air bridge with electrode underneath for electrostatic actuation, a) without and b) with applied voltage.

In superconducting GHz electronic circuits the air bridges can be used for impedance matching, e.g. between the intrinsic capacitances of tunneling diodes and other parts of the circuit. In microstrip technology the air bridges can be implemented as tunable inductors, which broadens the range of application.

2. FABRICATION PROCEDURE

Most of the superconducting electronic circuits are based on superconducting Nb. Compared with galvanically grown bridge layers sputtered Nb air bridges have the advantage, that the same techniques can be used as for the other parts of the superconducting circuitry. As is depicted in Fig. 2a, in the first step the sacrificial layer, which defines the vertical shape of the bridge, is prepared. Here, the photoresist AR-4000/8 (ALLRESIST GmbH) was used, giving a resist thickness of 5 µm. Smooth rims of the sacrificial resist structures are necessary to avoid breaking of the Nb film at the edges of the structures. To obtain sufficiently smooth edges, the resist was baked in a convection oven before exposure and after development.

In the second step, the Nb layer was sputtered by DC-magnetron sputtering in steps of 9 s deposition and 5 min pause (Fig. 2b). The pauses are needed to reduce surface heating and thus deformation or polymerization of the resist layer.

The widths of the bridges are defined in the third step by a negative tone photoresist mask. For a good coverage of the structures, we used the same thick resist AR 4000/8 with a reversal process. Through this resist mask, which covers the surface of the Nb bridges, the non-covered parts of the Nb layer were etched by RIE (Reactive Ion Etching) as shown in Fig. 2c.

In the final step, the resist was washed away in 70°C hot acetone (Fig 2d).

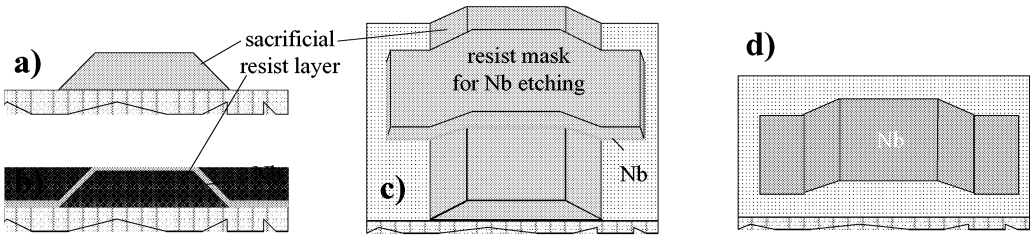

Figure 2. Fabrication process for sputtered Nb air bridges.

Air bridges with 200-700 nm thick Nb layers were fabricated with a typical length of 100 µm and widths of 50-300 µm (Fig. 3). The sputtered Nb films show tensile stress of 10…30 MPa. We tentatively explain this phenomenon with the expansion and shrinking of the sacrificial resist layer during deposition and cooling time, respectively.

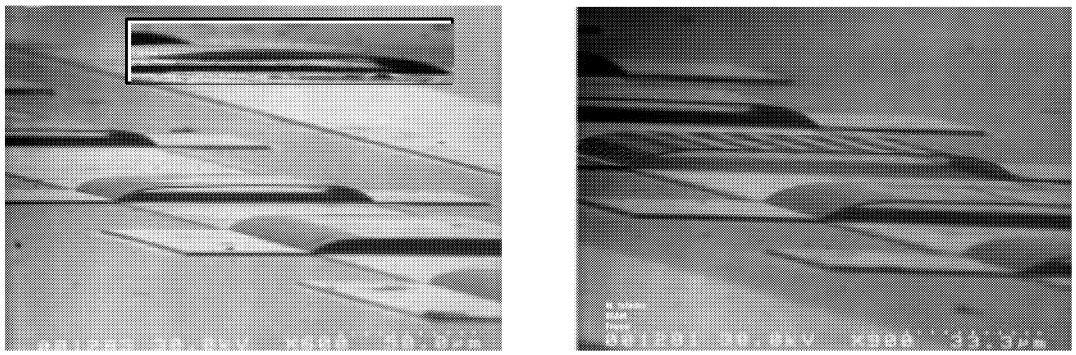

Figure 3. Nb air bridges, 5 µm high, 100 µm long, 100µm and 200 µm wide. The Nb film is 700 nm thick (240 nm in the inset). The inset shows the bending of the bridge layer and the reduced height due to stress in the Nb film.

Due to this stress, the released bridge shows a saddle structure (see inset of Fig. 3). This effect is more pronounced for thinner than for thicker Nb films and raises the zero-voltage capacitance of the device. Hence the zero-voltage capacitance can be adjusted by RIE of an initially too thick bridge layer. The Nb electrode underneath the bridge is produced with a standard lift-off process prior to the bridge fabrication.

3. PROPERTIES

Recent measurements on air bridges with 200-260 nm thick Nb bridge layers gave very promising results. These bridge layers were originally 330 nm thick before being thinned by RIE. The electrode underneath the bridge was covered by an AlN layer as a protection against RIE during the bridge layer etching. In the graph of Fig. 4 the measured voltage dependence of the capacitance is displayed for different bridges that are 100 µm long and 100 µm wide. Variations in the zero voltage capacitance can be explained by differences in the bridge height as described before. Standard formulas, found e.g. in [2], were used for the calculation of the mechanical behavior of air bridges with fixed ends. The deflection of the bridge was assumed to be parabolic and was iterated until the bending force was in equilibrium with the electrostatic force. In order to take into account the increased stiffness due to the saddle structure of the bridge layer, the calculations were done with an effective bridge layer thickness th_{eff}, being four to five times the Nb film thickness. Without applying a voltage, close to the posts the bridges were higher (h_p) than in the middle (h_m). Taking the Young modulus of bulk Nb (E = 105 GPa) and the mechanical parameters as indicated in the table, the theory confirms the measured values (Fig. 4). In the upper voltage region of some measurements the capacitance raised stronger than calculated with raising voltage. This effect can be explained with a flop-in effect of the saddle structure. An increase of more than 10% in capacitance was achieved applying 45 V. With improved geometries it seems possible to reduce this voltage to below 10 V.

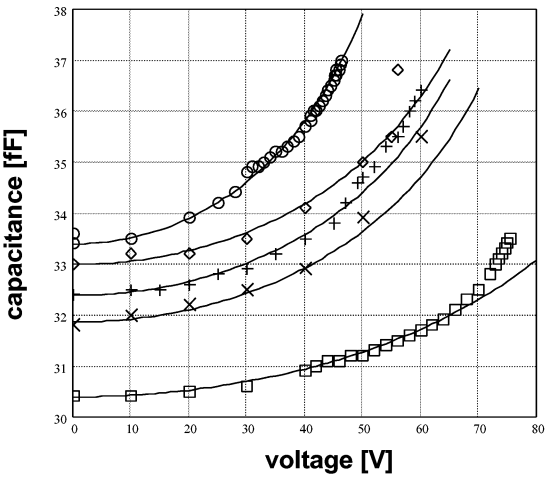

sample	h_p	h_m	th_{eff}	w_{el}
	µm	µm	nm	µm
?	4.0	1.36	990	60
?	4.0	1.75	1350	60
?	5.0	1.80	935	90
+	5.0	1.84	910	90
x	5.0	1.53	920	90

Figure 4. Graph: Measured voltage dependence of the capacitance for different air bridges. The lines are calculated taking the parameters given in the table. The height at the posts and in the center of the bridge are given by h_p and h_m, respectively. The thickness of the AlN on top of the electrode layer is named th_{AlN}, whereas th_{eff} is the effective thickness of the bridge layer. The width of the electrode underneath the bridge is called w_{el}.

4. CONCLUSIONS

Variable capacitors in surface mounted air bridge technology were fabricated with sputtered Nb for integration with superconducting electronic circuits. The measured voltage dependence of the capacitance corresponds with calculations and shows a 10% variability of the capacitance at 45 V. With improved geometries it seems possible to reduce this voltage to below 10 V. For 50…300 µm wide and 100 µm long air bridges capacitance values of 15…100 fF can be achieved. Further developments will include reduction of stress in the bridge layers.

References

[1] G. M. Rebeiz and J. B. Muldavin, "RF MEMS switches and switch circuits", IEEE microwave magazine, December 2001, pp 59-71.
[2] R. J. Roark and W. C. Young, "Formulas for Stress and Strain", McGraw-Hill, 1984.

SIMULATION OF THE PERFORMANCE OF A 5-JUNCTION ARRAY FOR 780-950GHz

S.C. Shi(1), M. J. Wang(2), and T. Noguchi(3)

(1) Purple Mountain Observatory, Nanjing, JiangSu 21008, China
(2) Institute of Astronomy and Astrophysics, Academia Sinica, Taipei, China (Taiwan)
(3) Nobeyama Radio Observatory, NAOJ, Nobeyama, Nagano 384-13, Japan

Abstract: The performance of a five-junction (Nb/AlOx/Nb) array is characterized in the frequency range of 780-950GHz for different wiring and ground layers of the thin-film microstrip lines of the junction tuning inductance and the associated impedance transformer. Three kinds of thin films (i.e., Nb, Al, and NbTiN) are taken for this investigation. The individual SIS junctions of the five-junction array have an area of $1\mu m^2$ and a critical current density of $10kA/cm^2$. The performance of parallel-connected twin junctions, which have the same junction parameters as those of the five-junction array, is also studied for comparison.

I. Introduction

As is well known, it is effective to enlarge the bandwidth of SIS mixers by increasing the critical current density of the SIS junction or adopting broadband mixing circuitry. However, the higher the junction's critical current density J_c is, the lower the junction quality (i.e., smaller $R_{sub}(2mV)/R_n$) becomes. SIS junctions of a small quality factor usually have low mixing conversion gain and high noise temperature, especially at submillimeter wavelengths. Hence it is of particular interest to develop submm SIS mixers with low-J_c junctions (say less than $10kA/cm^2$ for Nb ones) incorporating with broadband junction tuning circuitry. Distributed junction arrays have demonstrated broadband performance at frequencies below the gap frequency (~680GHz) of Nb SIS junctions [1-2]. It still remains unclear, however, whether they can perform well beyond the junction's gap frequency as far as the thin-film losses of the junction tuning inductance (longer than lumped cases) and the associated impedance transformer (usually with larger impedance transforming ratio [3]) are concerned.

To develop a 780-950GHz SIS mixer, we investigated the performance of a five-junction (Nb/AlOx/Nb) array and compare it with that of parallel-connected twin junctions. Different superconducting and normal-metal thin films such as Nb, Al, and NbTiN were adopted as the wiring and ground layers of the thin-film microstrip lines of the junction tuning inductance and the associated impedance transformer. We also

examined the effects of the junction quality and film thickness on the mixing performance of the two investigated tuning circuits.

II. Simulation Model

For both the five-junction array and the parallel-connected twin junctions, the individual SIS junctions were assumed to have an area of $1\mu m^2$ and a critical current density of $10kA/cm^2$. Note that the junction's specific capacitance and product of I_cR_n were taken as $90fF/\mu m^2$ and 1.95mV, respectively. We had two junction I-V curves of different quality factors, which were digitized from the real I-V curves of two SIS junctions (refer to sisiv-1 and sisiv-2 in Fig. 1). An impedance transformer was included for the two cases to have good RF matching between the junction tuning circuit and a real mixer block for 780-950GHz (scaled from a 660-GHz one [4]), whose embedding impedance (normalized to 35ohm) was calculated by HFSS [5] (refer to Fig. 2).

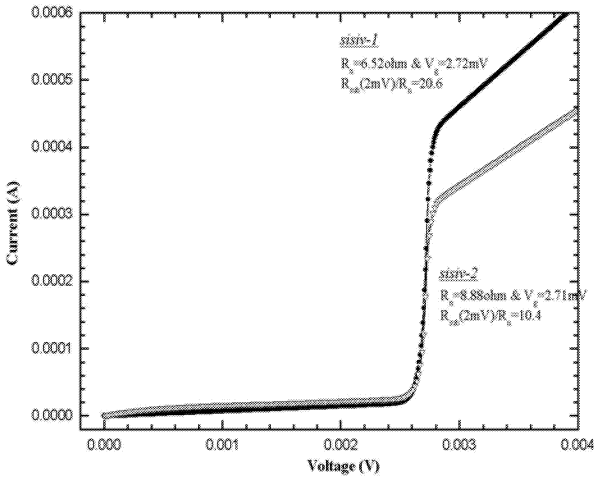

Fig. 1 Two digitized junction I-V curves (sisiv-1 and sisiv-2) used for simulation.

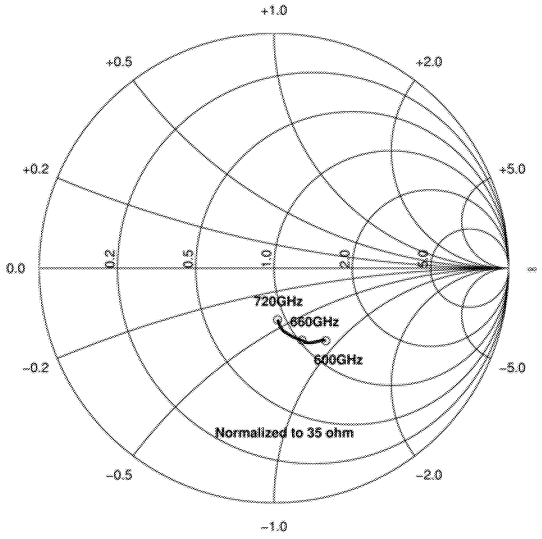

Fig. 2 Simulated embedding impedance for a 780-950GHz SIS mixer.

The mixing model of the five-junction array and parallel-connected twin junctions used here is almost the same as described in [1], except for the introduction of the loss effect of thin-film superconducting microstrip lines. At first, we calculated the local-oscillator (LO) voltage, including amplitude and phase, distribution among the individual SIS junctions, by assuming a fixed reduced LO voltage (α) for the last junction (according to the signal transmission direction). The equivalent conversion admittance matrix [Y] for the junction array was then obtained by combining the conversion admittance matrixes of the individual SIS junctions with the equivalent lumped impedance and admittance for the tuning microstrip line between two individual

junctions. We had the equivalent noise correlation matrix [H] for the junction array by transforming the noise currents (thermal and shot, at different small-signal sidebands) of the individual junctions to the input port of the junction array and then having an equivalent short-circuited noise current at the input port for all the noise contributions. With the equivalent mixing model, it is straightforward to simulate the performance of the junction array by means of the quantum theory of mixing.

As introduced before, three kinds of thin films (i.e., Nb, Al, NbTiN) were selected as the wiring and ground layers of the thin-film microstrip lines of the junction tuning inductance and the associated impedance transformer. Nb and NbTiN thin films had an energy gap and normal-state conductivity of Δ=1.45mV & σ_n=1.4e7Ω^{-1}m^{-1} (@ 9.2K) and Δ=2.47mV & σ_n=1.0e6Ω^{-1}m^{-1} (@ 20K) [6-7] respectively, while Al films had a ratio of σ_n/l_e=2.55e15Ω^{-1}m^{-2} [8]. The surface impedance of Al films was calculated according to Reuter-Sondheimer equation (nonlocal anomalous skin effect) [9], while those of Nb and NbTiN films according to Mattis-Bardeen theory [10]. The dielectric of the microstrip lines for the tuning inductance and impedance transformer had three layers, i.e., $Al_2O_3/SiO_2/Nb_2O_5$, which have respective dielectric constants and thicknesses of 9/0.09μm, 4/0.27μm, and 29/0.10μm (based on the fabrication process of Nb SIS junctions at Nobeyama Radio Observatory, Japan).

Given the fact that the effect of the spreading inductance around the SIS junctions, which is comparable to the junction tuning inductance at submm wavelengths, is no longer negligible, we assumed a short section of microstrip line (lossless, but with the same width as the tuning inductance) before and after each individual SIS junction as an equivalent spreading inductance [11]. For the simulated cases (5μm-wide tuning inducatnce and 1μm-wide junction), the length was found to be 0.7μm in terms of the modeling results for the 660-GHz SIS mixer (1μm) [12].

III. Simulation Results

Assuming an IF noise temperature of 15K and an SIS I-V curve as sisiv-2 (R_n=8.88ohm, V_{gap}=2.71mV, and R_{sub}(2mV)/R_n=10.4), we firstly simulated the receiver noise temperatures (SSB) of the five-junction array and parallel-connected twin junctions for 780-950GHz. Here we investigated five instances of different ground-/wiring-layers for the thin-film microstrip lines of the junction tuning inductance and associated impedance transformer, which are Nb/Nb, Al/Al, NbTiN/NbTiN, NbTiN/Al, and Nb/Al, respectively. Notice that the Nb and Al films were assumed to be 0.6μm thick for the wiring layer and 0.2μm thick for the ground layer, while the NbTiN film 0.6μm thick for the wiring layer and 0.3μm thick for the ground layer. The calculated results are shown in Fig. 3a-b. It should be pointed out that for each instance,

both the impedance transformer (width and length) and the tuning inductance (length only, of a fixed width of 5μm) were optimized for the lowest receiver noise temperature and the largest bandwidth (refer to Fig. 3), and the LO pumping level of the last junction was optimized at each frequency with all the individual SIS junctions dc-biased at a fixed voltage of 2mV.

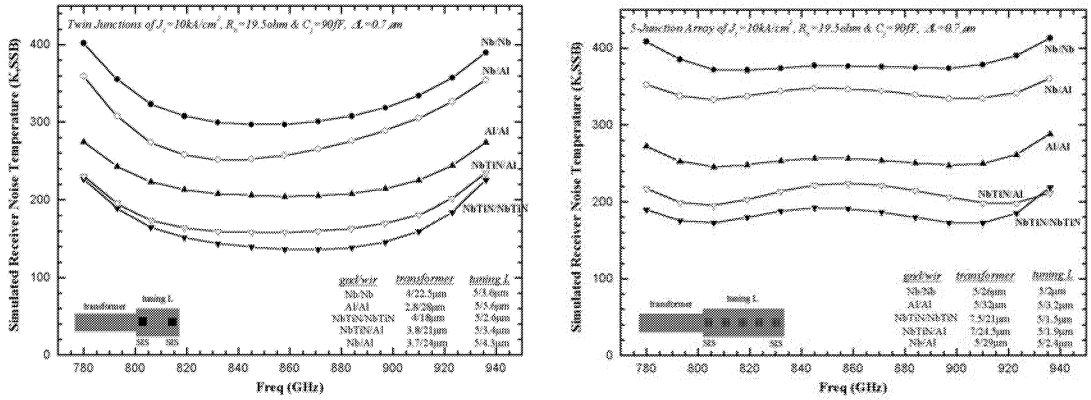

Fig. 3 Simulated receiver noise temperature as a function of frequency (with sisiv-2) for Nb, Al, and NbTiN tuning circuits, with a) for parallel-connected twin junctions (left) and b) for five-junction array (right).

We can see clearly from Fig. 3a-b that for all the simulated five instances, the five-junction array has a large bandwidth but a high receiver noise temperature in comparison to the parallel-connected twin junctions. The difference of the receiver noise temperature, however, becomes smaller for the instance with all NbTiN films, even for the instance just with a NbTiN film for the ground layer. Obviously, while having good bandwidth performance, distributed junction arrays still can have good noise performance beyond the junction's gap frequency if low-loss thin films (either superconducting or normal metallic) are adopted for the junction array's tuning microstrip line. It is also interesting to indicate that for both the five-junction array and the parallel-connected twin junctions, the instance of the Al/Al combination has much better noise performance than the Al/Nb one while the difference is not large between the NbTiN/Al and the NbTiN/NbTiN combination.

As the magnetic penetration depth of NbTiN superconducting films (~220nm) is much larger than that of Nb films (for all Nb junctions we used to have 200nm-thick ground layer), it is necessary to examine the effect of the thickness of the NbTiN ground layer on the mixing performance. Fig. 4a-b shows the simulated receiver noise temperature for the five-junction array and parallel-connected twin junctions for three different thicknesses of the NbTiN ground layer (i.e., 0.2, 0.3, and 0.4μm). Obviously, the frequency response of the receiver noise temperature does not change considerably

when the thickness is larger than 0.3μm.

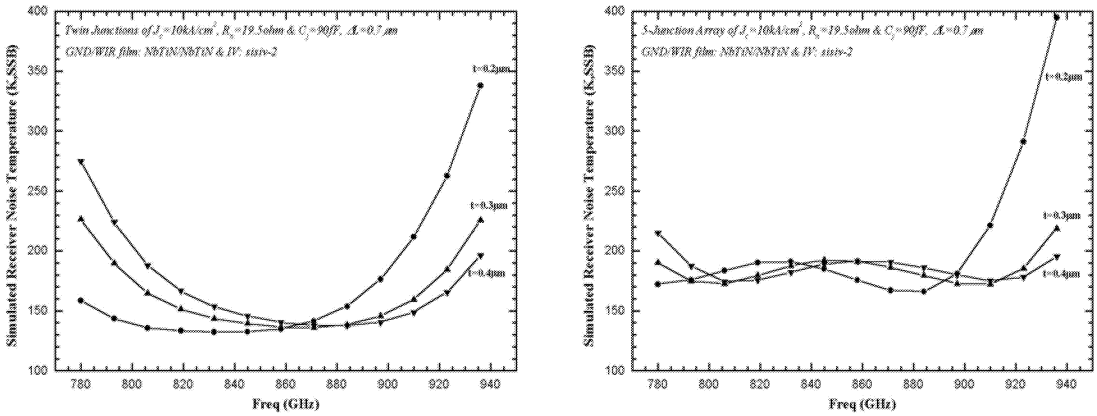

Fig. 4 Simulated receiver noise temperature as a function of frequency (with sisiv-2) for NbTiN tuning circuit of different ground-film thicknesses (0.2, 0.3 and 0.4μm), with a) for parallel-connected twin junctions (left) and b) for five-junction array (right).

By simulating the performance of the five-junction array and parallel-connected twin junctions with a new junction I-V curve of a larger quality factor (sisiv-1, also plotted in Fig. 1, R_n=6.52ohm, V_{gap}=2.72mV, and R_{sub}(2mV)/R_n=20.6), we tried to understand how the noise performance of distributed junction arrays changes with the junction quality. Three instances, i.e., Nb/Nb, Al/Al, and NbTiN/NbTiN combinations for the ground-/wiring-layer, were selected for this investigation. As demonstrated in Fig. 5a-b, the receiver noise temperature was improved significantly, especially for the instance of the Nb/Nb combination. It has been found that the improvement is due mainly to that of the mixer noise temperature as the mixer conversion gain varies less than 1dB.

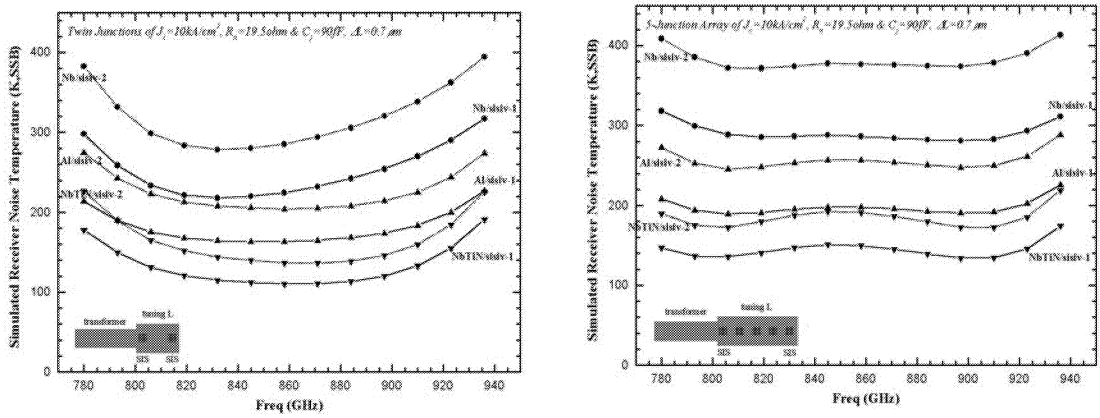

Fig. 5 Simulated receiver noise temperature as a function of frequency with different I-V curves (sisiv-1: solid & sisiv-2: dash) for Nb, Al, and NbTiN tuning circuits , with a) for parallel-connected twin junctions (left) and b) for five-junction array (right).

IV. Summary

The performances of a five-junction (Nb) array and parallel-connected twin junctions (Nb) have been thoroughly investigated in the frequency range of 780-950GHz for the Nb, Al, and NbTiN wiring and ground layers of the thin-film microstrip lines of the junction tuning inductance and the associated impedance transformer. It has been found that the five-junction array has a large bandwidth in general over the parallel-connected twin junctions and a comparable receiver noise temperature when employing NbTiN films. In addition, the receiver noise temperatures of the two junction tuning circuits with NbTiN films are less sensitive to the junction quality than with Nb films.

References

1. S.C. Shi, T. Noguchi, and J. Inatani, "Analysis of the bandwidth performance of SIS mixers with distributed junction arrays," in *Proc. 8th Int. Symp. on Space Terahertz Tech.*, Boston, USA, Mar. 1997, pp. 81-90.

2. S.C. Shi, T. Noguchi, J. Inatani, Y. Irimajiri, and T. Saito, "Experimental results of SIS mixers with distributed junction arrays," *IEEE Microwave & Guided Wave Letters*, vol. 8, no. 11, pp. 381-383, Nov. 1998.

3. S.C. Shi, C.C. Chin, and W. Zhang, "Characterization of Nb based superconducting microstrip lines around the gap frequency," *Int. J. IR & MM Waves*, vol. 21, no.12, pp. 2007-2013, Dec. 2000.

4. Tong C.-Y. E., Blundell R., Papa D.C., Barrett J.W., Paine S., and Zhang X., "A Fixed Tuned Low Noise SIS Receiver for the 600 GHz Frequency Band," in *Proceedings of the Sixth International Symposium on Space Terahertz Technology*, 1995, p. 295.

5. Ansoft High-Frequency Structure Simulator, Ansoft Corporation, Four Station Square, #200 Pittsburgh, PA 15219-1119, USA.

6. J. A. Stern, B. Bumble, H.G. Leduc, J.W. Kooi, and J. Zmuidzinas, "Fabrication and DC-Characterization of NbTiN Based SIS Mixers for Use between 600 and 1200GHz," in *Proceedings of the 9th International Symposium on Space Terahertz Technology*, Pasadena, CA, Mar. 1998, pp. 305-319.

7. B.D. Jackson, A.M. Baryshev, G. de Lange, J.-R. Gao, S.V. Shitov, N.N. Iosad, and T.M. Klapwijk, "Low-noise 1THz superconductor-insulator-superconductor mixer incorporating a NbTiN/SiO2/Al tuing circuit," *Appl. Phys. Lett.*, vol. 79, no. 3, pp. 436-438, July 2001.

8. M. Bin, M.C. Gaidis, J. Zmuidzinas, and T.G. Phillips, and H.G. LeDuc, "Low-noise 1THz niobium superconducting tunnel junction mixer with a normal metal tuning circuit," *Appl. Phys. Lett.*, vol. 68, no. 12, pp. 1714-1716, Mar. 1996.

9. A.B. Pippard, in Advances in Electronics and Electron Physics, edited by L. Marton, Academic, New York, 1954, p. 1.

10. Mattis D.C., and Bardeen J., "Theory of the Anomalous Skin Effect in Normal and Superconducting Metals," *Physical Review*, vol. 111, no. 2, p.413, 1958.

11. S.C. Shi, W.L. Shan, W. Zhang, C.C. Chin, M.J. Wang, and T. Noguchi, "Development of a 600-720 GHz SIS mixer for the SMART," in *Proceedings of 12th Int. Symp. on Space THz Tech*, San Diego, USA, Feb. 2001, pp. 215-222.

12. M. J. Wang, C. C. Chin, W. L. Shan, W. Zhang, H. W. Cheng, T. Noguchi, S. C. Shi, "Characterization of the Performance of a 600-700 GHz SIS Mixer," *these Proceedings*.

A SUPERCONDUCTING SPECTROMETER WITH PHASE-LOCKED JOSEPHSON OSCILLATOR

S. V. Shitov[1,2], V. P. Koshelets[1,2], P. N. Dmitriev[1], L. V. Filippenko[1],
An. B. Ermakov[1,2], V. V. Khodos[3], V. L. Vaks[3]

[1]Institute of Radio Engineering and Electronics, Russian Academy of Sciences (IREE RAS), Moscow, Russia

[2]National Institute for Space Research (SRON), Groningen, the Netherlands

[3]Institute for Physics of Microstructures, Russian Academy of Sciences (IPM RAS), Nizhny Novgorod, Russia

Abstract

A sensitive heterodyne spectrometer employing a superconducting local oscillator is demonstrated experimentally for the first time at 327 GHz. The research is continuation of the study on the concept of a superconducting integrated receiver (SIR). The sensor of the phase-locked receiver comprises a quasioptical double-dipole antenna SIS mixer ($T_{RX} \approx 250$ K, DSB), a Josephson-type flux-flow oscillator (FFO) and a twin-SIS harmonic mixer, all integrated on the same silicon chip of size 4 mm by 4 mm. An elliptical silicon lens is the only optical element focusing the beam. Room temperature PLL electronics is used along with a synthesized reference source at about 10 GHz. The effective bandwidth of the PLL circuit of about $\pm$ 10 MHz and the hold range of $\pm$ 2.5 GHz are estimated experimentally while locking at 32-th harmonic of the reference source. It was found that the optimum pump current of the SIS mixer can be adjusted within the range of 14…42 μA simply via change of the bias current of the FFO while it stays locked. The signal from a room temperature semiconductor harmonic multiplier driven by a second synthesizer is used to test the spectrometer; the spectral resolution as low as 10 kHz is estimated. The effect of broadening of a spectral line of SO_2 gas at 326867 MHz is measured for a laboratory gas cell at 300 K within the pressure range of 0.03-0.3 mbar demonstrating feasibility of the PLL SIR.

Introduction

Sub-millimeter wave spectrometers are currently of great interest for radio astronomy and for earth study by monitoring the atmosphere chemistry. Most of advanced spectrometers nowadays employ ultra-low noise SIS mixers at the temperature of liquid helium. A sensor of the SIS mixer is a thin-film integrated circuit fabricated with micron accuracy so the tiny circuit may contain many SIS junctions. In contrast, conventional local oscillators used with SIS mixers are room temperature semiconductor devices (usually a Gunn oscillators in combination with multipliers). This fact makes impossible integral packaging of the whole receiving system.

Josephson oscillators are devices fully compatible with technology of SIS mixers. There is a 1-microWatt level (moderate-power) type of Josephson junction oscillators, flux-flow oscillator (FFO), which is proven to be suitable for integration with a low-noise SIS mixer as a local oscillator (LO). Among the Josephson devices FFO has also an advantage of good tuneability in combination with relatively narrow free-running linewidth. Recent experimental study on phase-locking FFO up to 700 GHz [1] is the good support for the development of practicable submillimeter spectrometer. This paper deals with recent progress on experimental study of superconducting integrated receiver (SIR) with phase-locked (PL) FFO.

1. Chip design and measuring system

The microphotograph of the PLL SIR chip for 320-370 GHz band is presented in Figure 1. The equivalent scheme of the experimental chip containing the double-dipole single-junction SIS mixer, PLL feedback FFO and harmonic mixer (x35) is presented elsewhere [2,3]. A twin-SIS junction is used for the harmonic mixer, and there is no magnetic field supply, so the harmonic mixer is operating in the "mixed" mode employing both Josephson and quasi-particle nonolinearities. Figure 2 presents the general view of the pixel with three coaxial cables mounted. The microwave lens from silicon with antireflection coating is clearly seen. The chip mount is placed inside a magnetic shield as described in [4]. The block scheme of the experimental setup is described elsewhere [5]. We note here only that the phase detector system and the reference source are room temperature devices outside the cryostat.

2. Experimental results and discussion

The experimental devices are produced using our standard procedure developed for integrated receivers and described elsewhere [6]. The preliminary test of device at dc is performed using computer control measurement system IRTECON [7]. The test results are presented in Figure 3 as a quasi-3D graph of the mixer pump on all possible regimes of the FFO. Similar graphs are created for both SIS mixer and HM. The fact that the largest pump is achieved for SIS mixer and HM at a bit different frequencies, may mean some imbalance in the power split. This is possible for our microstrip T-junction splitter due to deviations in the fabrication process. Another important feature of the device is absence of Fiske steps within certain region below the boundary voltage of $V_g/3$. The permanent tuning is available in this region. This unusual behavior, which would mean normally high damping of the FFO caused by losses, can be explained here by very low reflection at the end of the long junction provided by the well matched output circuit. The phase-locking within such region of high damping is known to be difficult due to the wide initial linewidth associated with relatively high dynamic resistance [5].

The IV-characteristics of the twin-SIS harmonic mixer (HM) are presented in Figure 4. To obtain the optimal performance of the HM, it has to be pumped heavily that turns its IV-curve almost into a straight line. The IV-characteristic of the single-junction SIS mixer demonstrates no essential influence of the reference source at 10.1 GHz. The only effects seen when the reference source is switched on and off are partial suppression of the critical current (when FFO is off) and negligible change of the quasi-particle current (when pumped).

The Fourier transform spectrum (FTS) of the SIS mixer is obtained using Michelson interferometer and presented in Figure 5. The main peak of coupling is essentially narrower and higher in frequency than one predicted [2]. Careful calculations demonstrate that this effect can be explained by thinner insulation (190 nm instead of 250 nm). The inverse values of experimental heterodyne data (T_{rx}^{-1}) are plotted at the same graph demonstrating good fit to the FTS.

The heterodyne data were measured using standard hot/cold technique. The heterodyne response of the receiver is presented in Figure 6. Note that peak of the best sensitivity is within the region of high dynamic resistance of FFO that was discussed above. The emission spectrum of the free-running FFO measured at this frequency is quite wide being affected by the fine resonant structure that is typical for a rectangular-end FFO [8]. For this reason the left peak of FTS from Figure 5 was used for spectrometer operation. The IV-curve of FFO phase-locked at 325.5 GHz is presented in Figure 7. The oscillator is locked at 32-th harmonic of the reference source (f_{REF} = 10158.35917 MHz) assuming that the spectral line (f_2 = 326867.5 MHz) will be present at upper sideband (USB) relative to the frequency of the LO. The part of the IVC is magnified and presented in the inset demonstrating loosing and restoring of the locking regime. To obtain these data the bias current was changed manually within wide range while the feedback loop remained closed. The vertical portion of the curve presents the regime of nearly fixed frequency. The real PLL regime remains within the bias current range of 37…43 mA while the frequency lock is possible within range of 27.5…43 mA. The PLL regime initial parameters are: the control line current 25.2 mA, the bias current 40 mA, the bias voltage of FFO about 673 μV, PLL IF = 401 MHz, the dynamic resistance of the IVC, R_d = 0.0015 Ω. The hold range of ± 2.5 GHz can be estimated from the experimental data. The IV-curves of the SIS mixer pumped at 325.5 GHz by the phase-locked FFO are presented in Figure 8. The data are demonstrating possibility of adjustment of LO power to its optimum value via changing the bias current of the FFO while it stays phase-locked. To estimate the resolution of the spectrometer, the external signal source was used. The signal from synthesizer was applied to an external Schottky diode harmonic mixer, which worked as a multiplier producing a stable CW signal. The width of such spectrum, which has to include all system instabilities, was found of order of 10 kHz.

The photograph of our experimental setup for the spectral line detection is presented in Figure 9. The 1-meter gas cell was filled initially with SO_2 gas at pressure of a few mbar. Then the cell was pumping down to desired pressure within range of 0.03-1mbar. To be sure that the system is tuned properly, the test with the external harmonic mixer was performed prior to the gas line detection. The example of a SO_2 gas spectrum obtained using AOS is presented in Figure 10. The experimental data taken for different pressure were processed using Lorenz fit. The effect of the linewidth broadening is presented in Figure 11.

Conclusions

The superconducting spectrometer on the base of an externally phase-locked superconducting Josephson oscillator has been developed and demonstrated the capability of detection of low-pressure atmosphere contaminant like the SO_2 gas, which is the side product of metallurgy industry. The resolution of the spectrometer, according to the gas cell measurements, is not less than 1 MHz and can be as good as 10 kHz, as it

is demonstrated with CW source. To realize full potential of the new device, further improvements on both design and operation of FFO and coupling circuits are necessary. This study provides an important input for future development of a balloon-based 500-650 GHz integrated receiver for the Terahertz Limb Sounder (TELIS) scheduled to fly in 2004-2005.

Acknowledgments

The work was supported in parts by the Russian SSP "Superconductivity", RFBR projects 00-02-16270, the Nederlandse Organisatie voor Wetenschappelijk Onderzoek (NWO) and by INTAS grant 01-0367. The authors thank Dr. A. R. W. de Jonge for his help in setting up the AOS.

Reference

[1] V. P. Koshelets, P. N. Dmitriev, A. B. Ermakov, A. S. Sobolev, M. Yu. Torgashin, V. V. Khodos, V. L. Vaks, P. R. Wesselius, C. Mahaini J. Mygind, "Superconducting phase-locked local oscillator for submm integrated receiver," Presented at 13-th Int. Symp. Space Terahertz Techn., Harvard University, March 26-28 (2002) (this conference).

[2] S. V. Shitov, V. P. Koshelets, L. V. Filippenko, P. N. Dmitriev, A. M. Baryshev, W. Luinge, J.-R. Gao, "Concept of a superconducting integrated receiver with phase-lock loop," *Proc. 10-th Int. Symp. Space Terahertz Techn.,* Charlottesville, Univ. of Virginia (March 1999).

[3] S. V. Shitov, V. P. Koshelets, L. V. Filippenko, P. N. Dmitriev, V. L. Vaks, A. M. Baryshev, W. Luinge, N. D. Whyborn, and J.-R. Gao, *IOP Conf. Ser. No. 167*, 647 (2000).

[4] S. V. Shitov, V. P. Koshelets, A. B. Ermakov, L. V. Filippenko, A. M. Baryshev, W. Luinge, J.-R. Gao, "Superconducting chip receivers for imaging application," *IEEE Trans. Appl. Supercond.* vol. 9, pp. 3773-3776 (1999).

[5] V. P. Koshelets, S. V. Shitov, P. N. Dmitriev, A. B. Ermakov, L. V. Filippenko, V. V. Khodos, V. L. Vaks, A. M. Baryshev, P. R. Wesselius, J. Mygind, *Physica C*, **367,** pp. 249 - 255 (2002).

[6] L. V. Filippenko, S. V. Shitov, P. N. Dmitriev, A. B. Ermakov, V. P. Koshelets, and J. R. Gao, "Integrated superconducting receiver: fabrication and yield," *IEEE Trans. on Appl. Supercond.,* vol.11, No 1, pp. 816-819 (2001).

[7] B. Ermakov, S. V. Shitov, A. M. Baryshev, V. P. Koshelets, W. Luinge, "A data acquisition system for test and control of superconducting integrated receivers," *IEEE Trans. on Appl. Supercond.,* vol.11, No 1, pp. 840-843 (2001).

[8] V. P. Koshelets, A. B. Ermakov, S. V. Shitov, P. N. Dmitriev, L. V. Filippenko, A. M. Baryshev, W. Luinge, J. Mygind, V. L. Vaks, D. G. Pavel'ev, "Superfine resonant structure on IV-curves of long Josephson junction and its influence on flux flow oscillator linewidth," *IEEE Trans. on Appl. Supercond.,* vol.11, No 1, pp. 1211-1214 (2001).

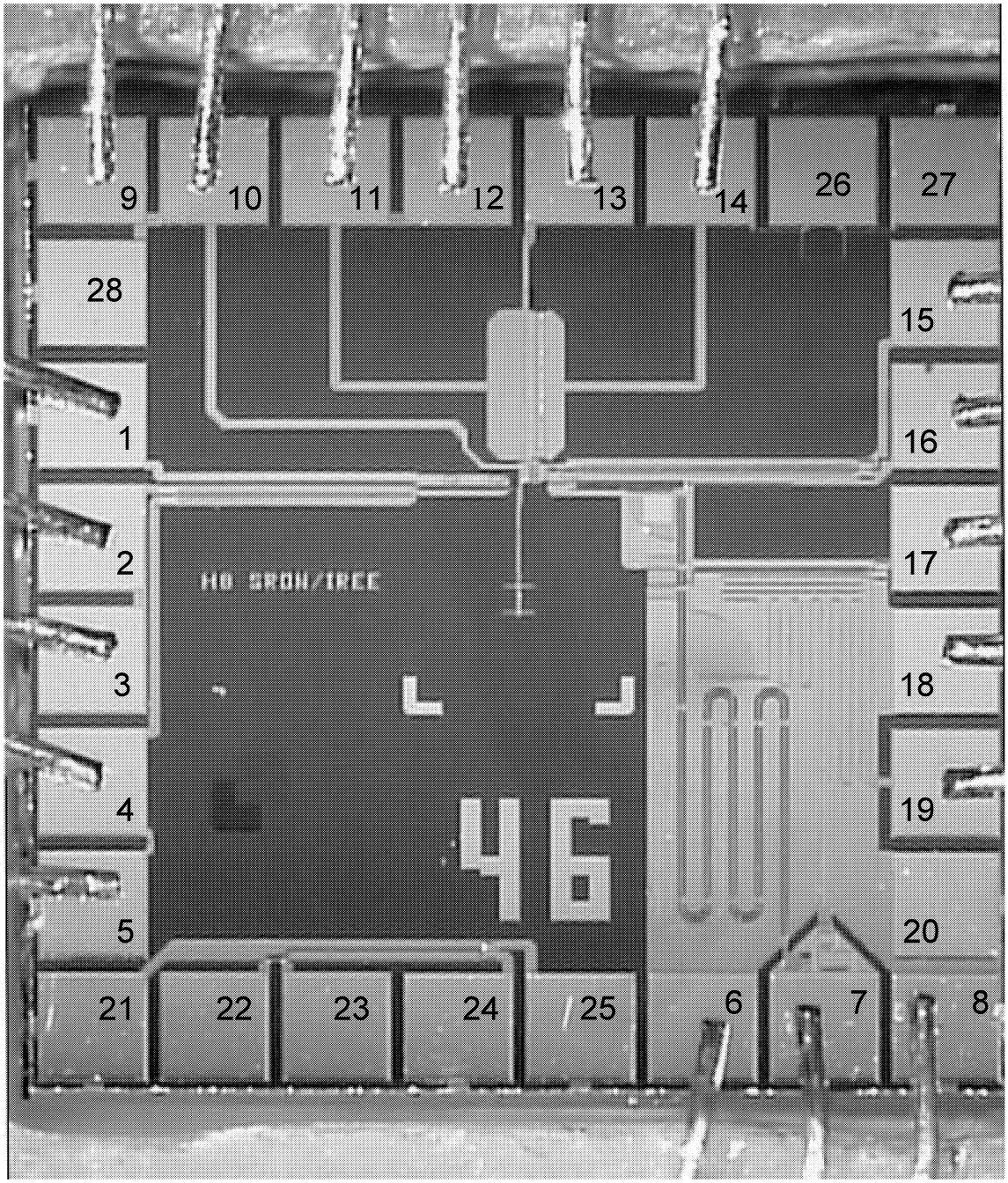

Fig. 1 Micro-photograph of the chip of the superconducting integrated receiver with phase-locked Josephson oscillator. The chip size is 4 mm by 4 mm. Contact pad destinations: (1), (2) SIS mixer bias / IF out; (3), (4) SIS control line; (5) bias for balanced mixer (optional); (6)-(8) reference signal input and bias input for harmonic mixer; (9), (11), (12), (14) FFO bias; (10), (13) FFO control line; (15)-(16) harmonic mixer control line; (17)-(18) SIS multiplier control line (optional); (19)-(20) SIS multiplier bias (optional); (21)-(27) test structures; (28) spare FFO grounding.

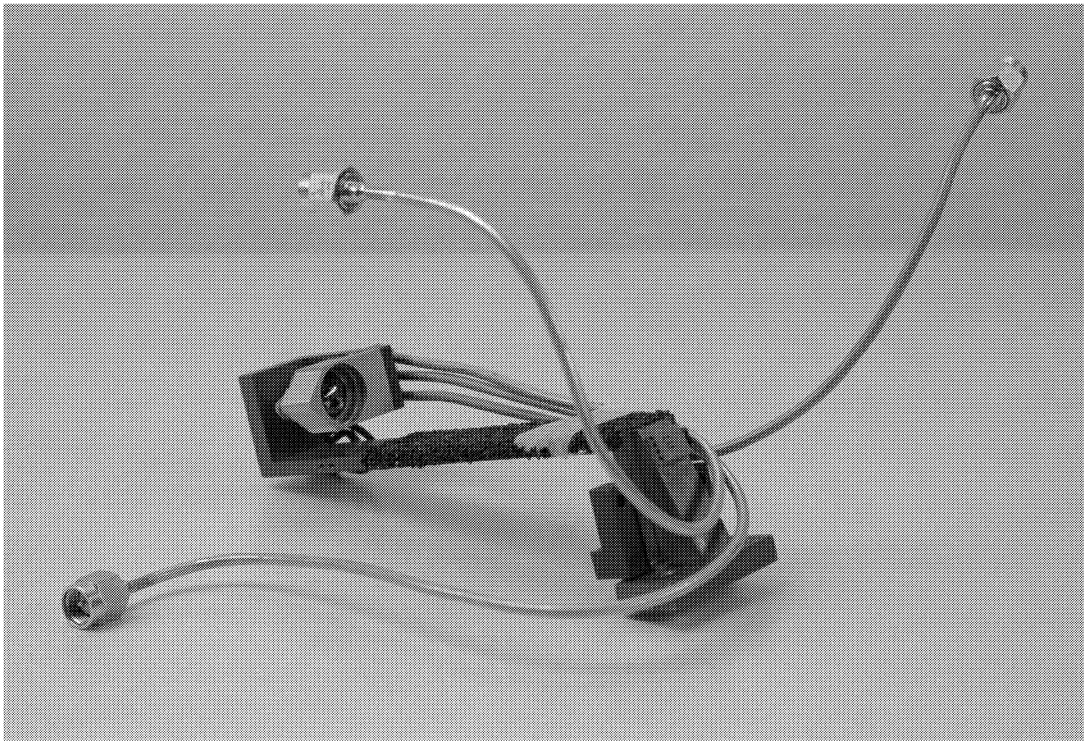

Fig. 2 General view of PLL SIR pixel. The mount of the imaging array is adapted. Three cables are connected to i) SIS mixer for IF/dc-bias, ii) FFO for PLL feedback, iii) harmonic SIS mixer for reference/PLL-IF/dc-bias.

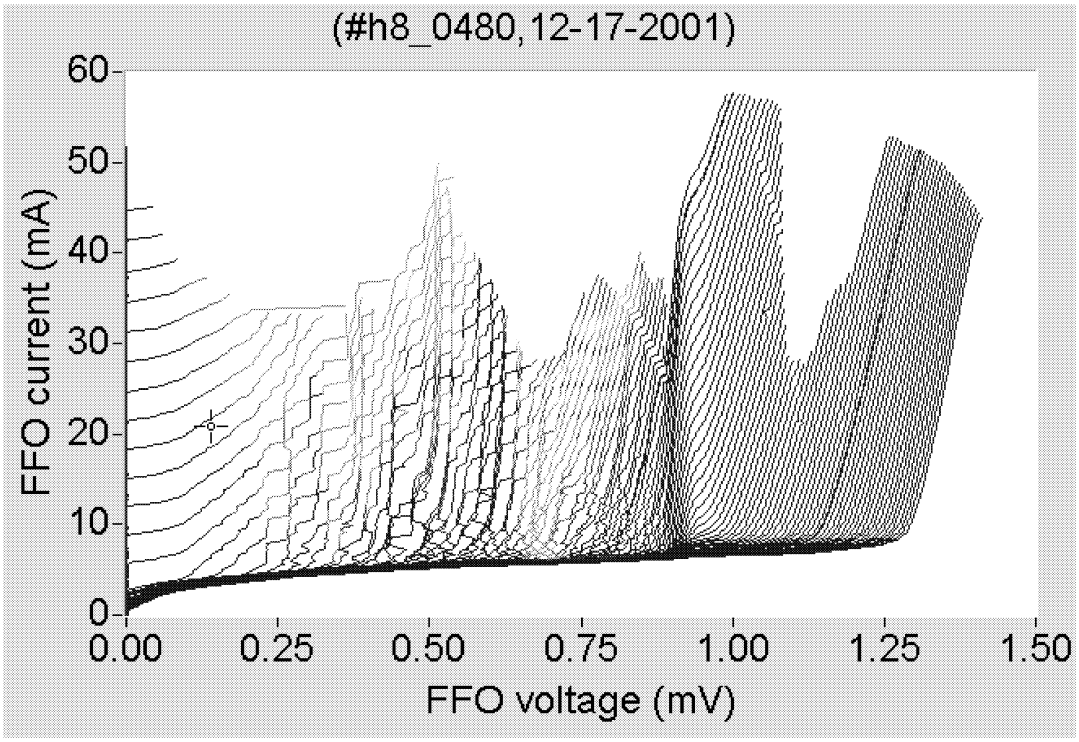

Fig. 3 Quasi-3D graph of the mixer pump on all possible regimes of the FFO.

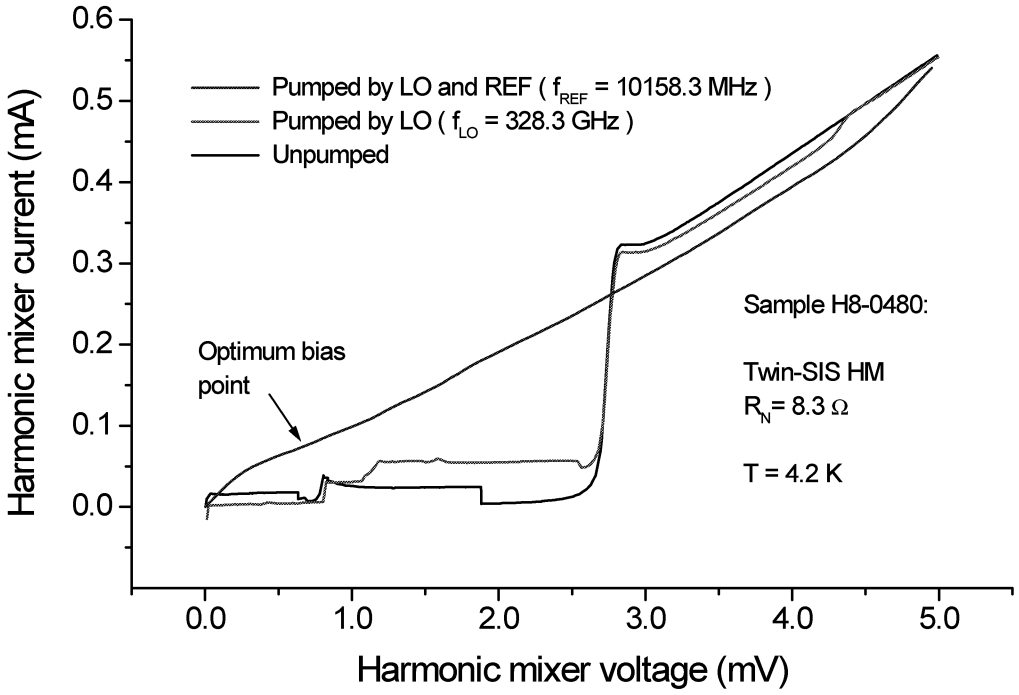

Fig. 4 IV-curves of harmonic mixer pumped with both FFO and reference source.

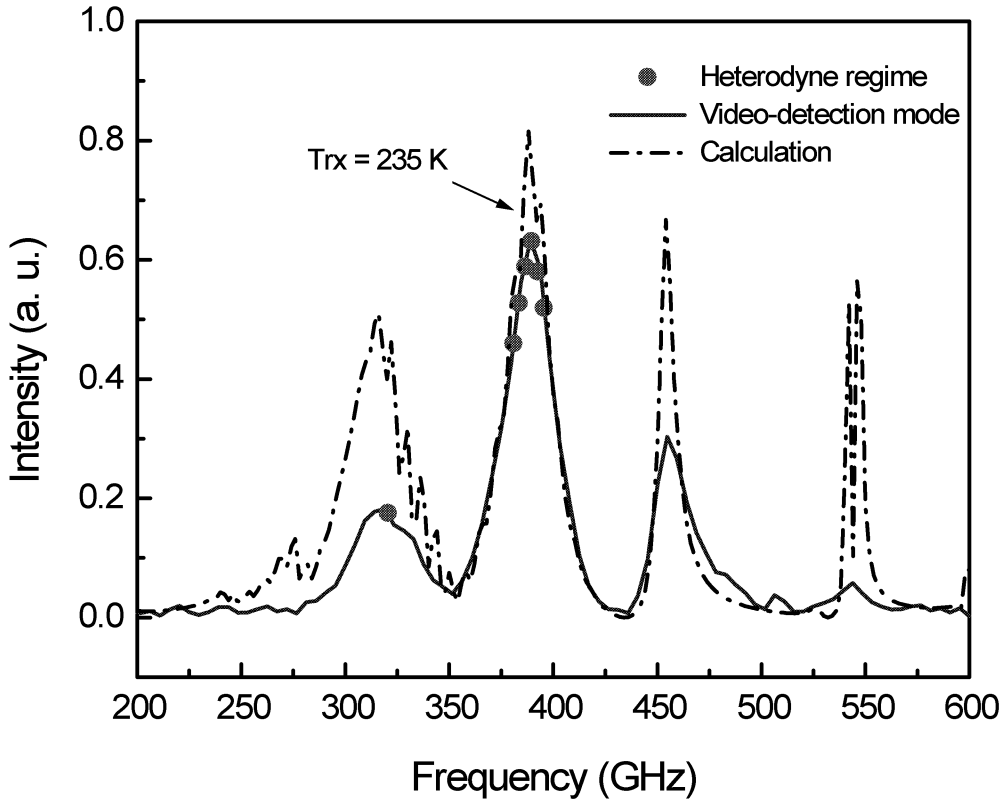

Fig. 5 Experimental FTS and heterodyne data along with best fit of calculated coupling between the antenna and the detector SIS junction.

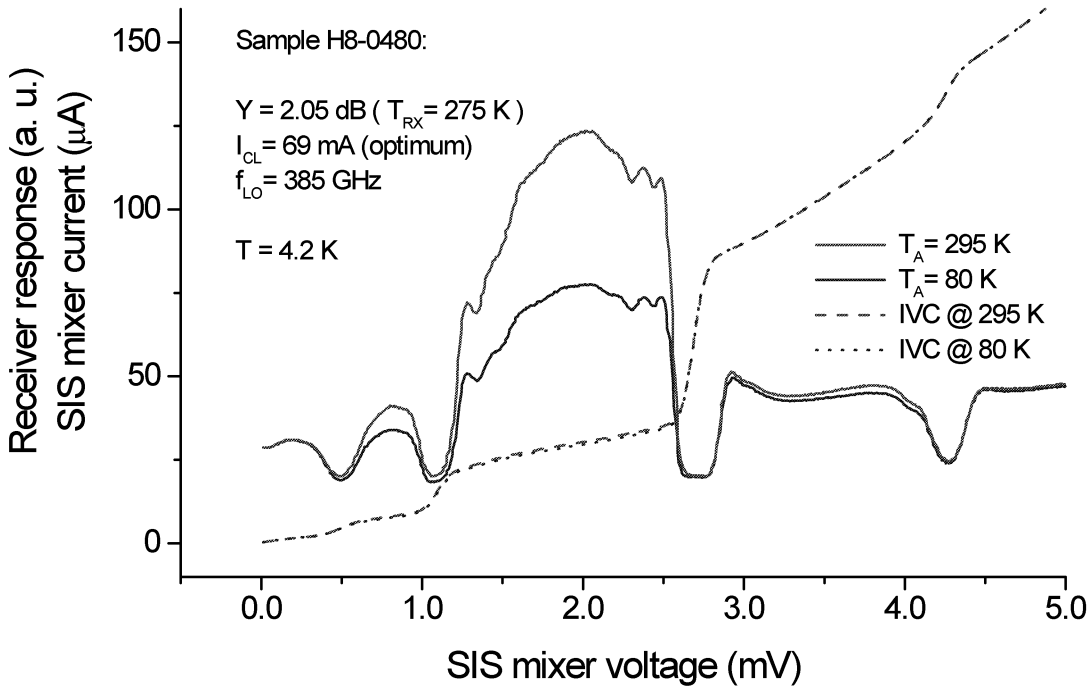

Fig. 6 Receiver heterodyne response at IF = 1.4 GHz and IV-curves of SIS mixer pumped by free-running FFO at about 385 GHz.

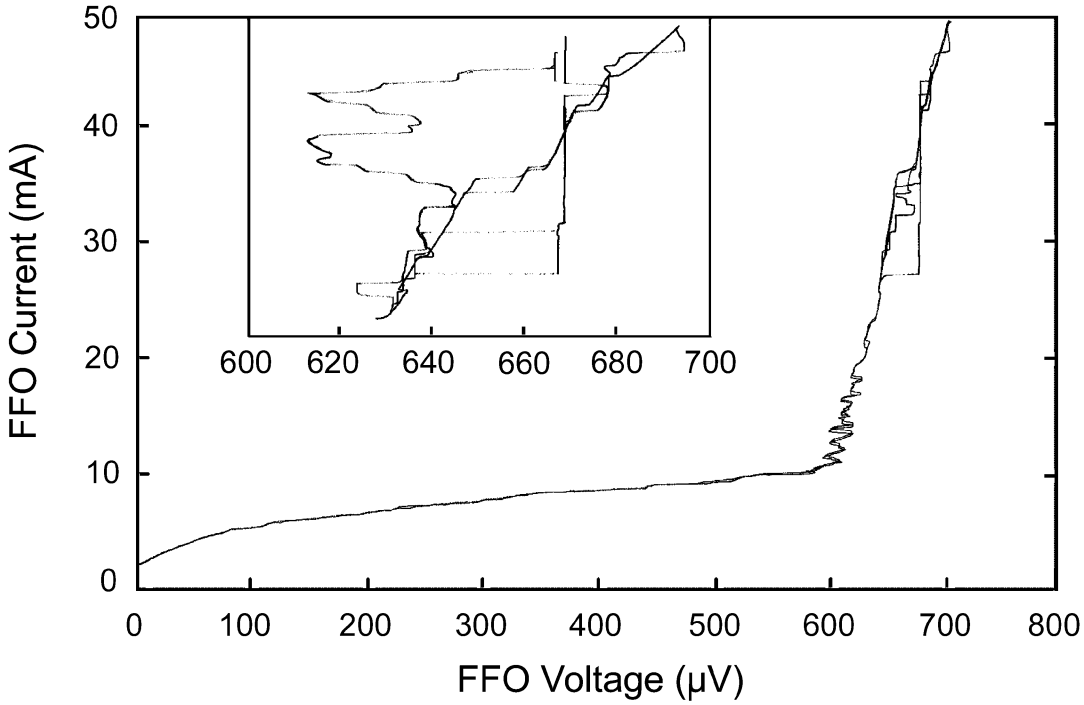

Fig. 7 IV-characteristic of FFO phase-locked at 325.5 GHz. The part of the IVC is magnified and presented in the inset demonstrating loosing and restoring of the locking regime for the PLL loop remains closed.

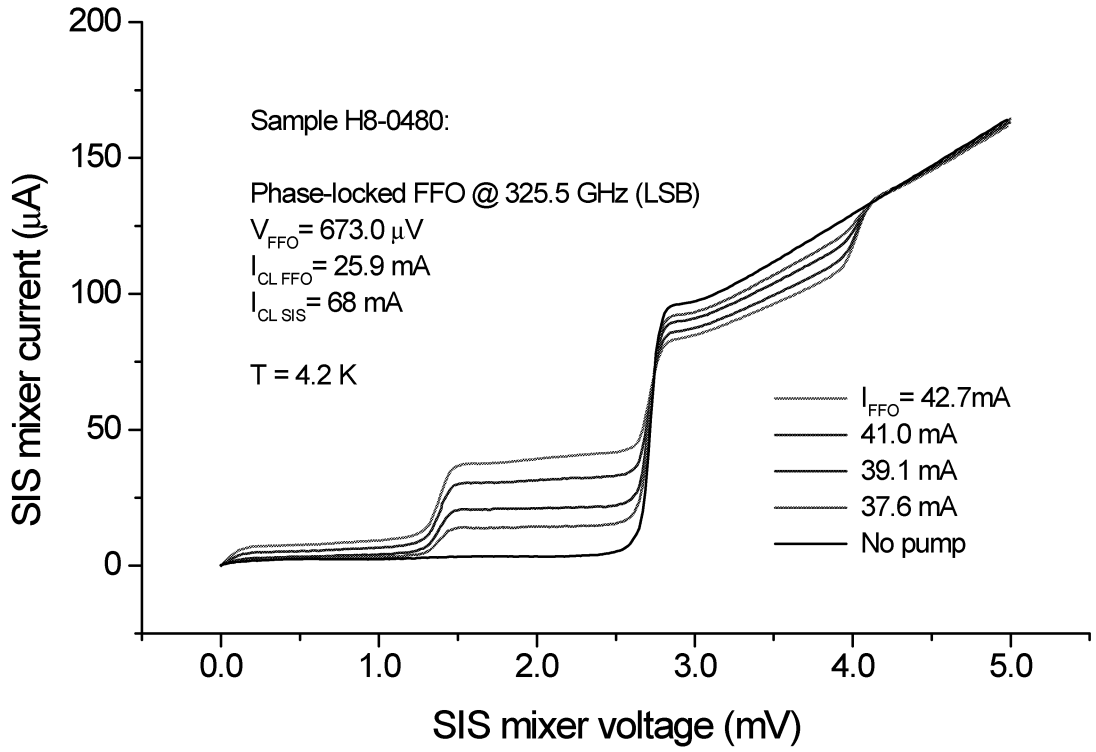

Fig. 8 IV-curves of SIS mixer pumped by phase-locked FFO. The pump level is being adjusted via simply changing the bias current of FFO while it stays phase-locked.

Fig. 9 General view of the gas cell setup.

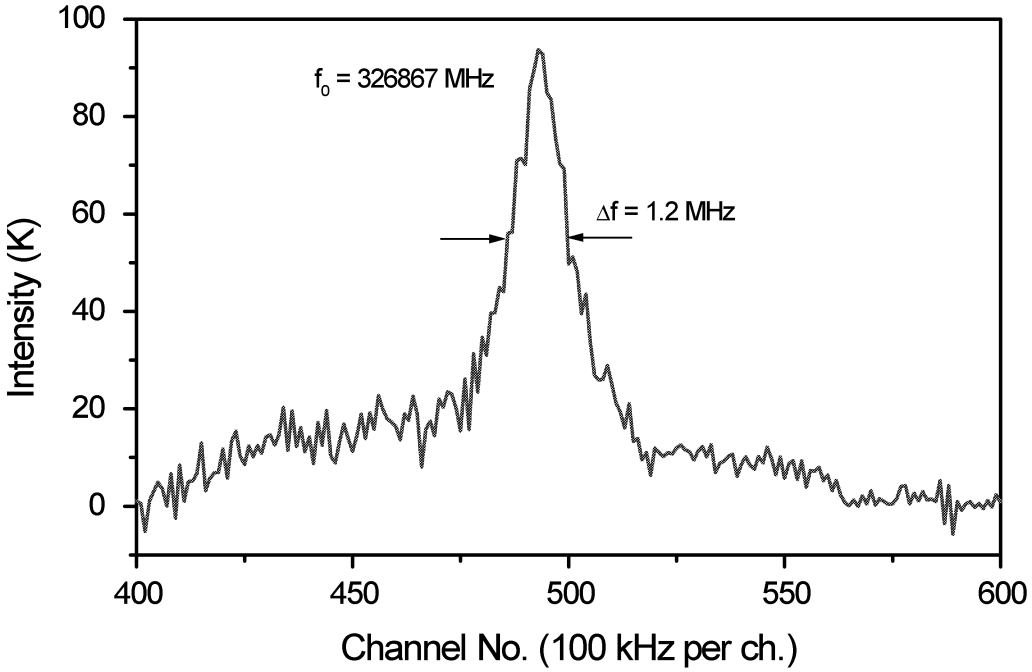

Fig. 10 Spectral line of SO_2 gas at pressure 0.03 mBar detected by superconducting integrated receiver with phase-locked Josephson oscillator (FFO). The data are processed using acousto-optical spectrometer.

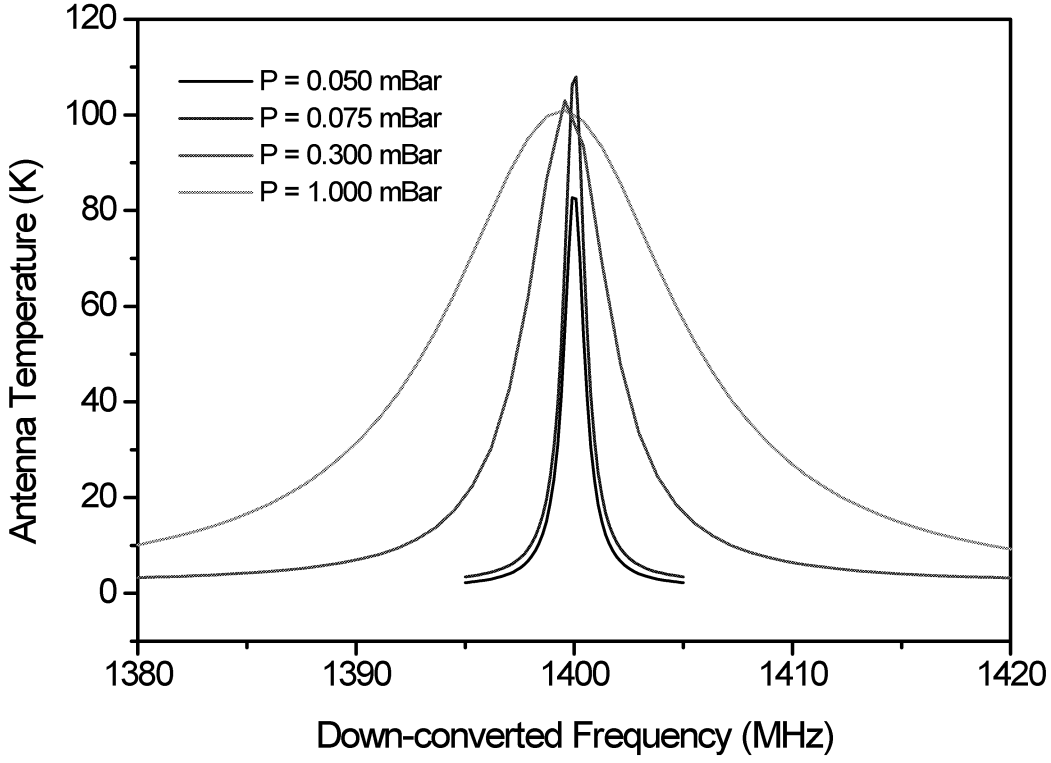

Fig. 11 Effect of broadening of SO_2 gas spectrum at 326.867 GHz measured by PLL superconducting integrated receiver.

Automatic Tuning of SMART, KOSMA's 490/810 GHz Array Receiver

S. Stanko, U. U. Graf, and S. Heyminck

KOSMA, I. Physikalisches Institut, Universität zu Köln, Zülpicher Straße 77, 50937 Köln, Germany. E–mail: *lastname*@ph1.uni-koeln.de

1 ABSTRACT

We describe the control system of SMART (Submillimeter Array–Receiver for Two–Frequencies), KOSMA's 490/810 GHz array receiver. All major electronic functions of the instrument such as mixer bias, magnetic field, PLL, and IF processing can be controlled either by computer or manually. The computer also monitors important status information.

Based on the hardware control system a procedure to automatically tune the array receiver has been developed. The automatic tuning is necessary to increase the duty cycle of the receiver and to avoid mistakes from manual operation of the complex tuning procedure.

To tune the 16 SIS (**S**uperconductor-**I**nsulator-**S**uperconductor) receiver channels, many parameters have to be optimized. Especially the magnetic field, which is applied to the junctions to suppress excess mixer noise caused by the Josephson effect, is very important and can not be set from look-up tables. An algorithm was developed to measure the relation between the strength of the Josephson effect and the applied magnetic field for each junction. Based on these data, the algorithm automatically finds and sets the optimum field strength and mixer bias.

2 INTRODUCTION

SMART, KOSMA's 490/810 GHz array receiver[1] currently consists of 8 SIS receiver channels. It has been installed in September 2001 on the KOSMA telescope[2] and has been operational since then. It will be upgraded to 16 channels in 2002, resulting in a 2×4 beam pattern on the sky, which is covered simultaneously in two frequencies. Besides the automatic mixer tuning its design includes innovative features like Fourier-gratings[3] for the local oscillator supply, integrated optics[4], and compact bias- and IF-electronics[5].

Although SMART is an array receiver, each of the channels has to be tuned individually, only the local oscillator tuning is done for each frequency channel

(i.e. for 4 to 8 mixers) at a time. In addition to the tuning algorithm and software, the automatic tuning requires specially designed hardware.

3 HARDWARE

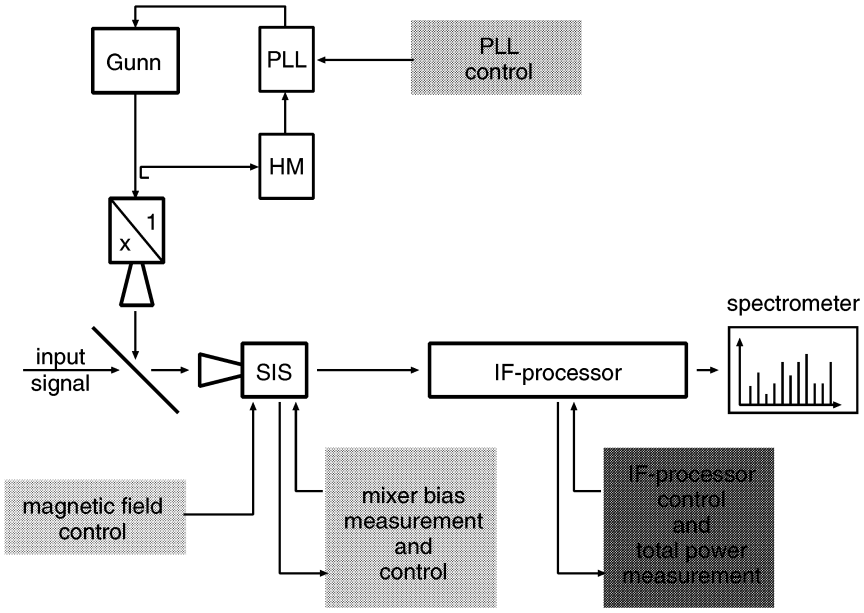

Figure 1: *Schematic drawing of the receiver electronics. Shaded boxes are computer controlled.*

Figure 1 shows the main elements of the electronics: the magnetic field control, the mixer bias measurement and control system and the IF-processor, in which the IF total power measurement is integrated.

The magnetic field control generates the current to establish a magnetic field which is applied to the junction to suppress the Josephson current (Figure 2) with its associated noise.

The mixer bias control unit is the primary power supply for the junctions. Additionally, their IV characteristics can be measured with this device.

The IF-processor amplifies and converts the IF signal of the junction. With this system we can also

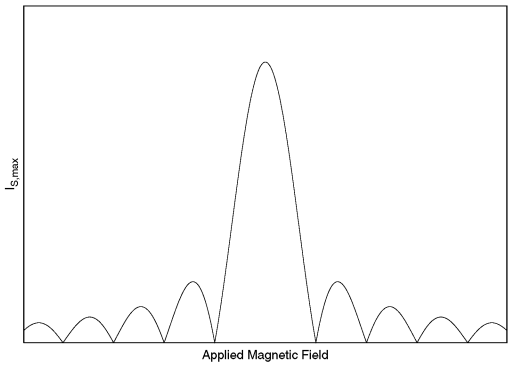

Figure 2: *Josephson current versus magnetic field (theoretical curve).*

measure a total power IF signal for laboratory and astronomical operation. In addition a 5 bit attenuator is integrated for each channel. A zero switch and a comb generator can be used for dark current measurements and frequency calibration of the acousto-optical spectrometer backends (AOS) [6].

An address bus connecting all units including the PC makes sure that all measurements and all modifications always refer to the same channel to avoid confusion.

3.1 RECEIVER RACK

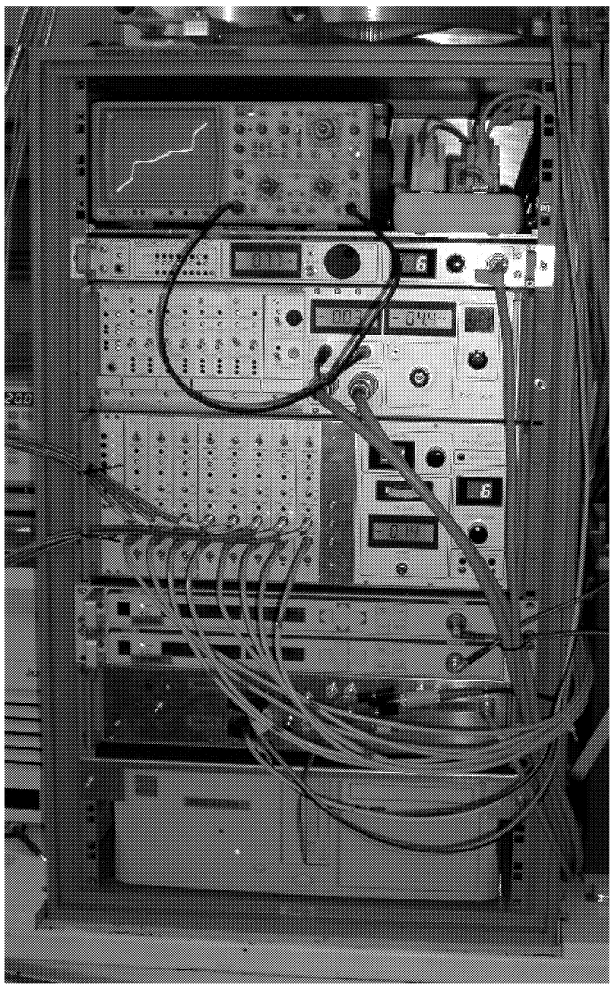

Figure 3: *Photograph of the SMART electronics rack containing magnet supply (beneath the oscilloscope), bias box, IF processor, two synthesizers, computer interface box and the control computer on the bottom.*

The receiver rack contains all the major electronics subsystems of KOSMA's array receiver. To automatically tune the receiver, a control PC has been set up, which is connected to all other subsystems through the PC interface. Using this interface the PC can read out all analog values of all channels directly. A 64 channel Analog-Digital-Converter card in the PC converts these values. The PC can also change all parameters in the subsystems to tune the junctions. All signals needed for this process have to pass the PC interface, where a manual/remote switch controls whether the PC is connected to the subsystems or not. Using this switch the PC can be put "offline", so the receiver can be tuned manually or pretuned values can be finetuned by the user. After this operation the computer can be turned "online" again.

The control PC runs under LINUX, which ensures reliable operation. All functions can be remote controlled through an Ethernet link. Additionally, changes of parameters and IV-curves as well as conversion curves are logged as housekeeping data.

3.2 ADDRESS BUS

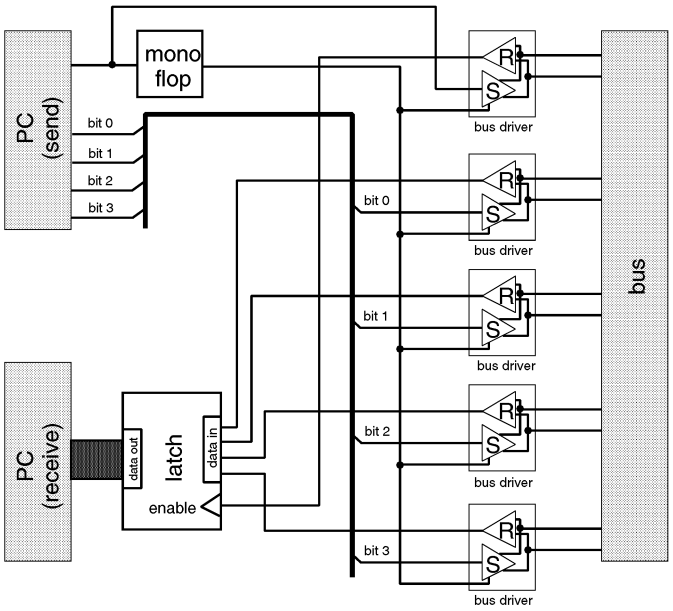

Figure 4: *Schematics of the address bus.*

An important part of the electronics system is the 5 bit address bus, which is connected to all subsystems including the PC interface. Each receiver channel is addressed by a unique number. Only the parameters of the channel selected in this way will be displayed and changed. This address can be set either by the PC or manually through any one of the control boxes. To avoid noise pickup from other telescope systems, a bus driver for each bit has been set up. Also the system avoids inconsistencies in case two or more subsystems attempt to set a channel, because all setting devices will read back the selected channel address.

3.3 DIGITAL POTENTIOMETER

One of the major requirements of the electronics was to give the operator the chance to correct or retune all parameters manually. This is useful for debugging and was needed to develop the algorithm for the automatic tuning. To ensure that both the operator and the computer can manipulate the same values, the digital potentiometer has been developed. A digital counter stores the value for each channel. It is connected to a DAC, which produces the desired voltage. Besides the advantage that the value can be manipulated either manually or under computer control, the voltage is independent of analog signals out of the computer so they are more immune against noise contamination from the computer hardware.

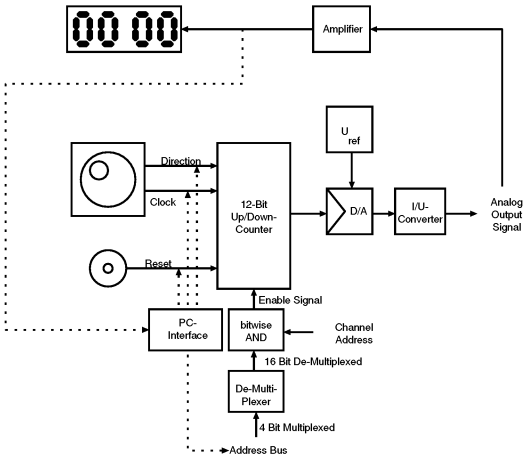

Figure 5: *The digital potentiometer.*

4 TUNING ALGORITHM

The tuning parameters are the local oscillator frequencies and pump levels, the mixer bias and the current for the magnetic field, which suppresses the Josephson current. LO tuning is done manually since it requires moving backshorts and it only needs to be done once per frequency.

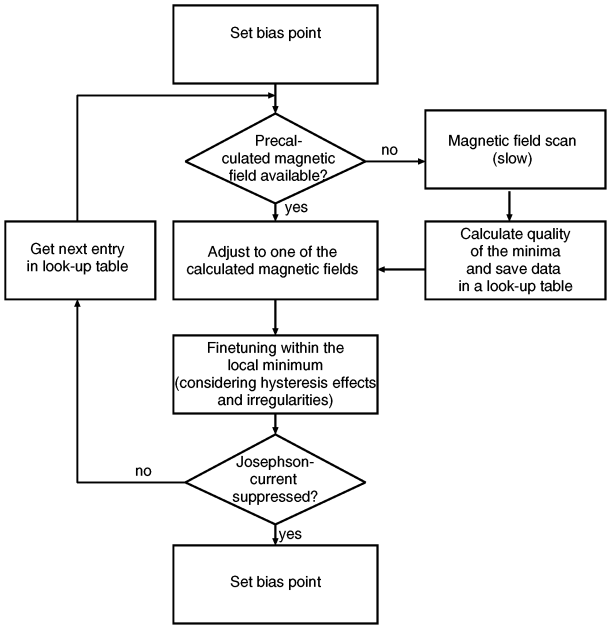

Figure 6: *Flow diagram of the tuning algorithm to tune bias voltage and magnetic field current.*

Figure 6 shows a flow diagram of the algorithm to tune the bias voltage and magnetic field for one receiver channel. In order to minimize the receiver temperature the noise caused by the Josephson current has to be measured. This

is done by scanning the conversion curve near the Shapiro step. So, initially, the bias point has to be set to that special voltage.

After that the optimum magnetic field strength to suppress the Josephson current has to be found. In general, a look-up table will provide a few rough estimates of suitable magnetic field coil currents. In this case a finetuning algorithm will optimize the current locally. If no table is available, or the values in the table are not good enough, a complete magnetic field scan is taken.

For tuning reasons the bias point was set near to the Shapiro step, where the conversion reacts very sensitively to a mistuned magnetic field. The optimum bias point for astronomical measurements is more robust and can be chosen from tabulated values.

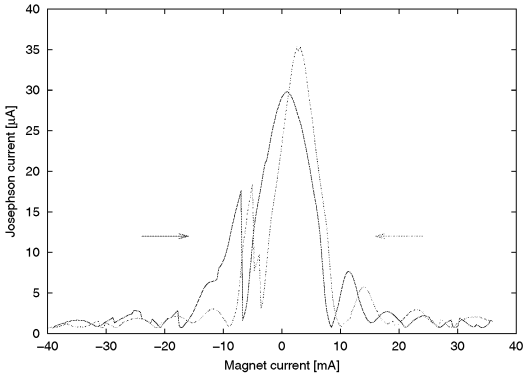

(a) Two magnetic field scans in different directions. A shift is visible which occurs due to the hysteresis of the field coil's iron core.

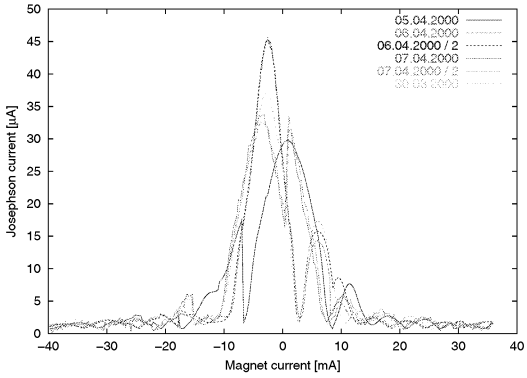

(b) Magnetic field scans measured on different days. There are remarkable changes so a tuning algorithm based on lookup tables can not be used.

Figure 7: *Hysteresis and statistical effects of the magnetic field scans.*

4.1 SETTING THE MAGNETIC FIELD

The main problem when tuning the receiver, is the setting of the magnetic field, which suppresses the Josephson noise, since the field required is not always reproducible due to external and statistical effects. Therefore magnetic fields can not be tuned by using a look up table. The correct magnetic field strength has to be calculated by measuring the IV-curve or the conversion curve.

As can be seen in figure 7 there are several kinds of disturbances (e.g. frozen flux, hysteresis) which have to be managed to find the optimum magnetic field current. First of all, hysteresis of the magnetic field leads to a shift between scans in different directions (Figure 7a). Changes in the magnetic environment may change the required field in a non-predictable way (Figure 7b).

To set the magnetic field to its optimum value the noise contribution by the Josephson current has to be estimated very precisely. This can be performed either by measuring the Josephson current on the IV-curve or the excess noise on the conversion curve. Using the conversion curve gives more precise information so this method is used for tuning.

The measured magnetic field scans are evaluated automatically in order to get the optimum magnetic fields for the junction. This is done by an algorithm which searches for minima and maxima separately (see Figure 8) and classifies the minima according to their expected usefulness in order to establish a new look-up table as input for the finetune algorithm.

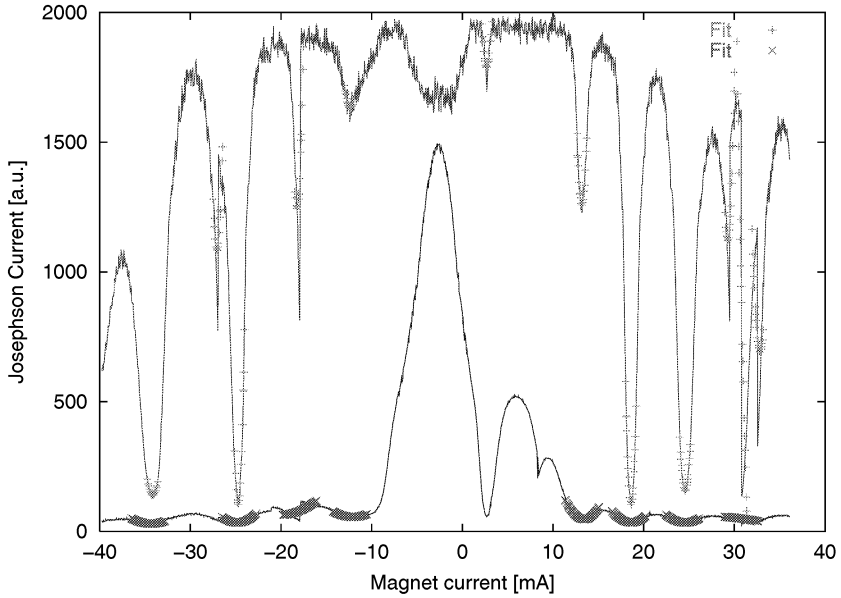

Figure 8: *Magnetic field scans. Outlined are the fitted minima. The Josephson noise was measured via the Josephson current in the IV-curve (blue line) or the excess noise on the conversion curve (red line). The algorithm finds minima in both cases.*

4.2 CALIBRATION OF THE BIAS VOLTAGE SCALE

To compute the proper bias point, first the IV-curve with maximum magnetic field is recorded. The gap voltage is derived to provide a preliminary scaling of the IV-curve. Now the shapiro step on the IV-curve without any applied magnetic field is determined. This yields a very accurate calibration of the voltage scale, which is required to set accurate bias points.

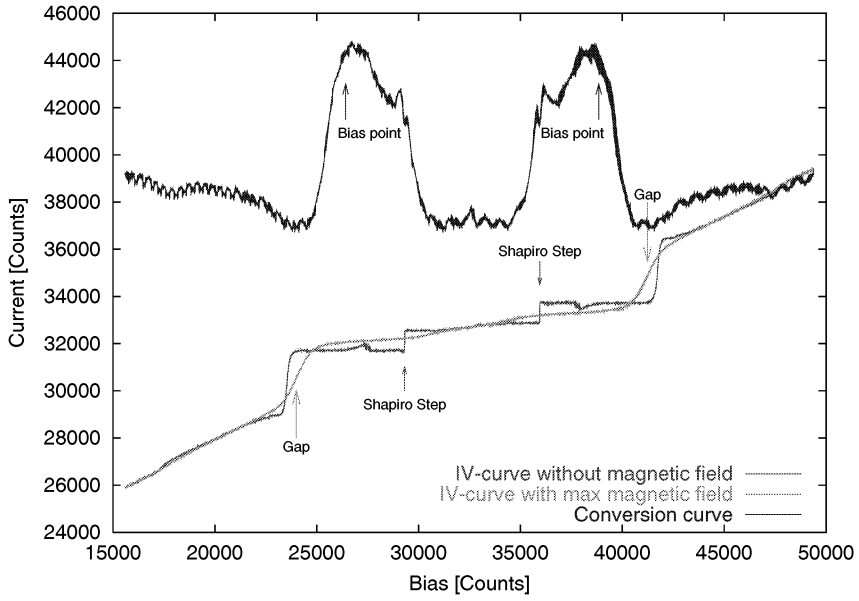

Figure 9: *Gap voltage and bias point derived from IV-curve with high magnetic field and without. The conversion curve is shown to demonstrate the bias point.*

5 PERFORMANCE

The noise temperature measurements shown in figure 10 where made at the KOSMA telescope with two 4 channel array acusto-optical spectrometers. Since we have no sideband filter in the array all temperatures are double sideband temperatures. The central part of the IF-band reaches DSB noise temperatures of 150 K to 250 K for the 490 GHz and 500 K to 700 K for the 810 GHz frequency band.

6 FUTURE PROJECTS

The immediate project is to expand the electronics and successively the software to tune and operate 16 instead of 8 receiver channels. This is no basic problem because, except for the local oscillator setting, all individual channels are treated as single SIS receivers.

Another step is to adapt the software to control future receivers such as STAR (SOFIA Terahertz Array Receiver) on SOFIA and possibly upcoming space missions, where manual tuning is impossible.

Implementation of an automated diplexer and LO-tuning will be part of a future project as well. Then LO pump levels can be tuned by the control PC.

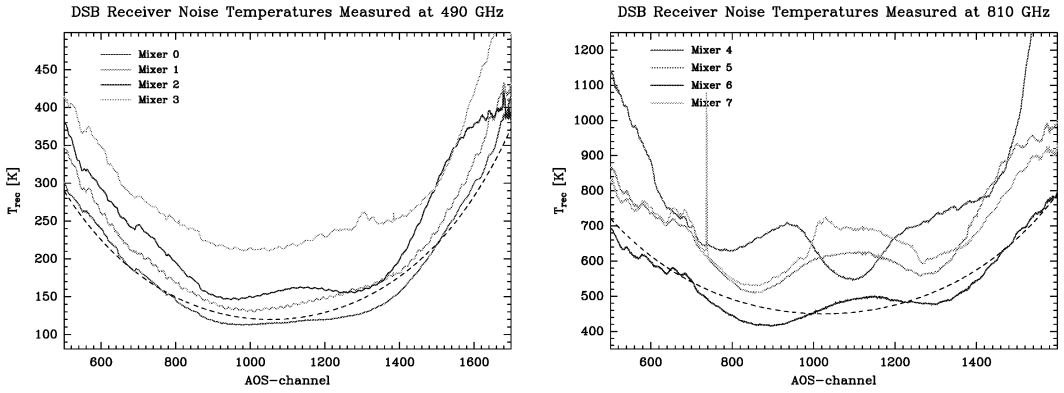

(a) 490GHz **(b)** 810GHz

Figure 10: *Measurement of the receiver noise temperature of the 490 GHz and the 810 GHz channels. The IF center frequency in both measurements is 1.5 GHz (AOS channel 1100) with 1 GHz nominal bandwidth (approx. 1000 AOS channels). The dashed line indicates the noise temperature function caused by the sinusoidal diplexer transmission assuming a 120 K (490 GHz) / 450 K (810 GHz) receiver.*

7 CONCLUSION

We developed the control electronics and algorithms to automatically tune an SIS receiver array. We also performed the first laboratory and astronomical measurements[7] which show high performance in terms of sensitivity and usability.

ACKNOWLEDGMENTS

This work was supported by the *Verbundforschung Astronomie* through grant 05 AH0PK1, by the *Deutsche Forschungsgemeinschaft* through grant SFB 494 and by the ministry of science of the State Nordrhein-Westfalen.

References

[1] U. U. Graf, S. Heyminck, E. A. Michael, S. Stanko, C. E. Honingh, K. Jacobs, J. Stutzki SMART: The KOSMA Sub-Millimeter Array Receiver for Two Frequencies.. in Proceedings of the 13th International Symposium on Space Terahertz Technology, Cambridge, Massachusetts, 2002.

[2] C. G. Degiacomi, R. Schieder, J. Stutzki, and G. Winnewisser. The KOSMA 3m submm telescope. in Optical Engineering 34(9), 1995.

[3] U. U. Graf, and S. Heyminck. Fourier Gratings as Submillimeter Beam Splitters. in IEEE Transactions on Antenna and Propagation, Vol. 49, No. 4, April 2001.

[4] D. Rabanus, et. al.. Techniques for Heterodyne Array Receivers. in USRA/NASA Det. Tech. Workshop, Monterey, Apr. 2002, in print.

[5] U. U. Graf, S. Heyminck, E. A. Michael, and S. Stanko. KOSMA's 490/810 GHz Array Receiver. in Proceedings of the 12th International Symposium on Space Terahertz Technology, San Diego, California, 2001.

[6] R. Schieder et al. The Cologne Acousto Optical Spectrometers. Experimental Astronomy Vol I, 1989.

[7] B. Mookerjea, C. Kramer, and J. Stutzki. Multiline study of star forming regions. Galactic Star Formation Across the Stellar Mass Spectrum Workshop, LaSerena, 2002.

Optical Modulation Spectrometer: A Concept Study

Volker Tolls[1] and Rudolf Schieder[2]

[1] Harvard-Smithsonian Center for Astrophysics, Cambridge, MA 02138, U.S.A.
[2] 1. Physikalisches Institut, Universität zu Köln, 50937 Köln, Germany

1 Abstract

The Optical Modulation Spectrometer (OMS) is a new type of spectrometer backend for heterodyne receivers with large bandwidth. It utilizes the high spectroscopic power of Fabry-Perot etalons for the analysis of IF signal from, e.g., a heterodyne receiver. This paper describes the underlying principle of an OMS and then presents the preliminary results of a concept study for an ultra-wideband (>10 GHz) OMS. The main advantages of the OMS are that it can provide the large bandwidth while being of small size, low weight, and low power consumption. These attributes make it a good candidate for future air-borne, balloon-borne, or space-borne applications where multiple spectrometers will be required for multi-frequency or array receiver systems.

2 Introduction

Broadband spectrometers will be required when heterodyne receiver systems operating from 1 to 3 THz go online. Large bandwidths are required to observe broad emission or absorption lines from extra-galactic objects at high redshifts, to perform spectral line surveys, and to observe planetary atmospheres. Many of these lines are pressure or velocity broadened with either large half-widths or line wings extending over several GHz. Current backend systems can cover the needed bandwidth only by combining the output of several spectrometers, each with typically up to 1 GHz bandwidth, or by combining several frequency shifted spectra taken with a single spectrometer. The ultra-wideband optical modulation spectrometer with at least 10 GHz bandwidth will enable broadband observations without the limitations and disadvantages of hybrid spectrometers.

The most commonly used backends for heterodyne detections systems are: (1) the Filterbank Spectrometer (FBS), (2) the Acousto-Optical Spectrometer (AOS), (3) the analog or digital Auto-Correlation Spectrometer (AACS or DACS), and (4) the Chirp Transform Spectrometer (CTS). The spectrometer application plot (Figure 1) shows the current state-of-the-art in bandwidth and resolution of single band spectrometers at 2 THz. To increase the bandwidth, hybrid spectrometers, the simultaneous parallel use of multiple spectrometers, can be used. However, in application where there are restrictions on power, size, or weight, like space borne or balloon borne observatories, single band spectrometers offer many advantages. An ultra-wideband OMS shows clear advantages where large frequency coverage and medium resolution are required.

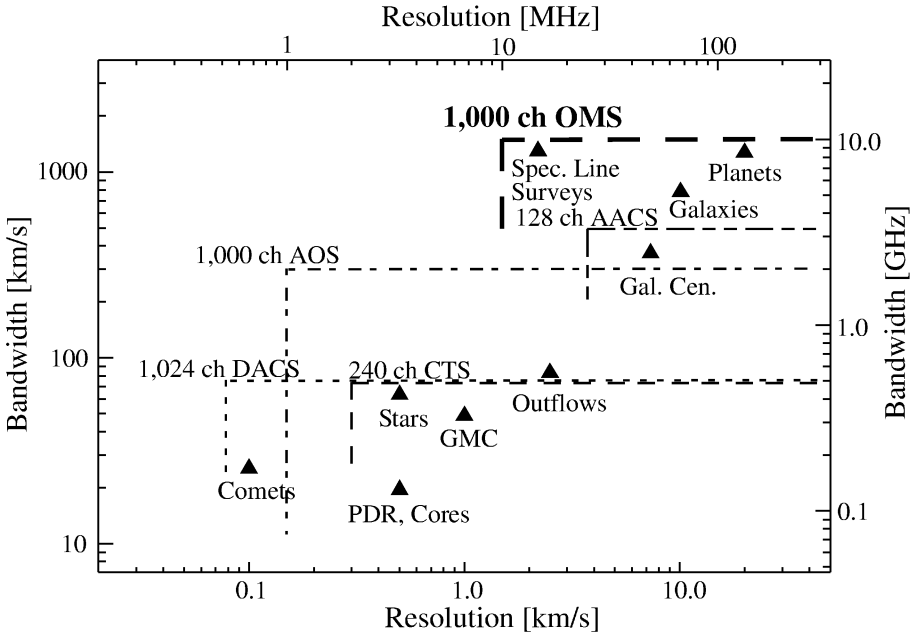

Figure 1: The spectrometer application plot shows the current state of the art in bandwidth and resolution of single band spectrometers. Also shown are the typical bandwidths and resolutions required at 2 THz ($150\mu m$) for a broad range of astronomical objects. The proposed 1000 channel OMS will offer both broad wavelength coverage and medium resolution. [adapted from Harris 1998]

3 Operational Principle

The OMS uses the high resolving power of Fabry-Perot etalons. Illuminated with divergent light with frequency f_0, the typical fringe system of bright rings of the Fabry-Perot etalon (see Figure 2, [Born 1989]) is converted into a linear system of bright lines by means of the illumination of the etalon and matching optics. The plotin Figure 2 shows the relative intensity I/I_0 as a function of the phase for two adjacent interference orders m and m+1. In the OMS (see Figure 3), laser light of frequency f_0 is modulated in an electro-optical modulator with a signal Δf (e.g., from a heterodyne receiver). The modulated light, $f_0 \pm \Delta f$, is fed into a Fabry-Perot etalon. The free spectral range (FSR) of the etalon needs to be FSR $> 2\ \Delta f$ in order to separate the upper $(f_0 + \Delta f)$ modulation sideband of the interference order m from the lower $(f_0 - \Delta f)$ modulation sideband of the order m+1. Now, through means of the illumination of the etalon, only the phase range corresponding to Δf is imaged onto a line detector array (effectively converting the phase or the corresponding frequency range into a space range). The intensities measured by the detectors are proportional to the input intensities to the modulator for a particular frequency interval within the input band. The detector read-out, A/D conversion and other spectrometer electronics are similar to the electronics of existing AOS's [Tolls 1992].

4 Design Goals

The design goals for the optical modulation spectrometer are summarized in Table 1. A first OMS

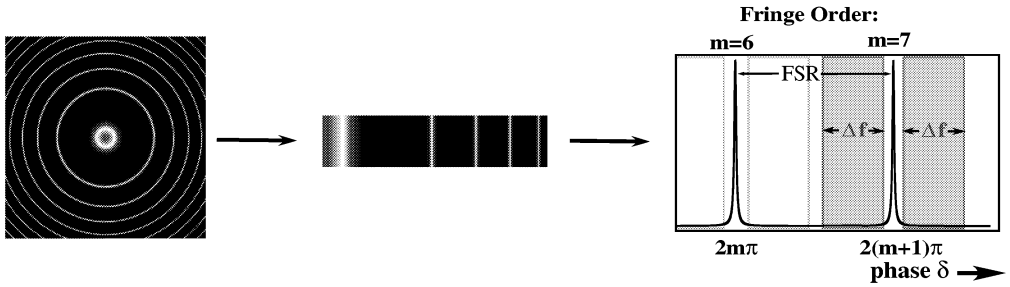

Figure 2: Schematic Fabry-Perot interference pattern for a divergent beam (left) and for a horizontally divergent and vertically parallel beam (center). When the beam is horizontally divergent and vertically parallel, the frequency is dispersed over many orders in the horizontal direction (center). In the proposed OMS (right), only a fraction of a single order (e.g., m = 7), denoted by the gray region with $f_0 + \Delta f$, is projected onto a linear CCD array.

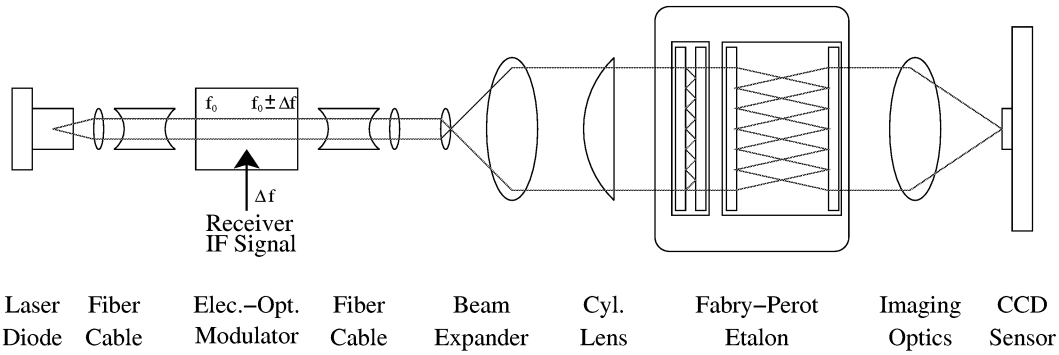

Figure 3: Optical schematic for an Optical Modulation Spectrometer: laser light is modulated by the IF signal from a heterodyne receiver and then spectrally analyzed in a double etalon and measured with a linear detector array.

instrument would have a bandwidth of 10 GHz (larger bandwidths are possible) with 10 MHz resolution. The mass, size, and power consumption are estimates (marked with *) derived from existing AOS spectrometers since the OMS incorporates similar optics and electronics (further improvement is possible but is undesirable for a first generation OMS). The specifications for the components will be refined once the design is complete and the components are selected. E.g., the modulator is listed with 10 GHz bandwidth, but modulators with 20 GHz bandwidth or more can be used as well since the final bandwidth is limited by the input signal (thus, by the currently available bandwidth of heterodyne receiver systems) and the etalon specification. The current design uses a Fabry-Perot etalon system with two matching solid glass etalons. The detector can be a linear CCD array or any other line detector depending on the laser wavelength and should have at least 1000 pixels.

5 Summary

The optical modulation spectrometer is a new kind of backend for applications which demand large bandwidth with moderate resolution, low power consumption, small size, and small weight. The last three design goals make the OMS a possible candidate for a single backend or array backends for future air-borne, balloon-borne, or space-borne heterodyne receiver systems.

Table 1: Specifications and key parameters of the proposed Optical Modulation Spectrometer. The values denoted with asterisks are estimates for a possible space flight configuration derived from the final specification of the SWAS AOS [Klumb 1994]. These values can be improved by further miniaturizing, making the mechanical setup as light as possible, and using highly integrated low power electronics.

Parameter	Design Specification
Bandwidth:	10 GHz
Resolution:	10 MHz
Resolving Power:	2 10^5 (in 2 THz heterodyne receiver system)
Spectroscopic Stability:	> 60 seconds for ON-OFF measurements
Mass*:	< 8 kg (optics, electronics, and RF components)
Size of Optics*:	5 x 5 x 30 cm^3
Size of Electronics*:	10 x 10 x 30 cm^3
Power Consumption*:	< 10 Watts

Component	Specification
Laser:	diode laser
Laser Wavelength:	1550 nm
Modulator:	electro-optical modulator
Modulator Bandwidth:	> 10 GHz
Fabry-Perot Finesse: Free Spectral Range:	Fabry-Perot Etalon system >2500 >22 GHz
Detector:	InGaAs IR line detector with 1024 pixel

Acknowledgment: This work was supported by NASA grant NAG5-10476.

6 References

M. Born and E. Wolf, "Principles of Optics", 6^{th} Ed., Pergamon Press, Oxford (1989)

A. Harris, K. Isaak, J. Zmuidzinas, "WASP: Wideband Spectrometer for Heterodyne Spectroscopy", Proc. SPIE Vol. 3357, 384 (1998)

M. Klumb et al., "Acousto-optical spectrometer for spaceborne application", Proc. SPIE Vol. 2583, 420 (1995)

V. Tolls, PhD. Thesis, University of Cologne (1992)

Design and Analysis of a Waveguide NbN-based SIS Mixer using a Tuning Circuit with Two Half-Wavelength Distributed Junctions for the 900-GHz Band

Yoshinori UZAWA, Masanori TAKEDA, Akira KAWAKAMI, and Zhen WANG

Kansai Advanced Research Center, Communications Research Laboratory
588-2 Iwaoka, Iwaoka-cho, Nishi-ku, Kobe 651-2492, Japan
e-mail: uzawa@crl.go.jp

Abstract

We designed a waveguide SIS mixer based on NbN for the 900-GHz band. The waveguide mixer block with an MgO substrate was designed using Hewlett Packard's High Frequency Structure Simulator (HFSS) and uses a waveguide-to-microstip transition. Simulation by HFSS showed that a source impedance of around 60 Ω can be achieved from 786 to 988 GHz by using an MgO substrate about 30 μm thick. The tuning circuit was proposed to reduce the current density of the NbN SIS junctions without impairing broadband operation; it consists of two half-wavelength distributed SIS junctions connected by a half-wavelength microstripline. Simulated mixer performance based on the experimental I-V curve of the NbN SIS junctions showed SSB receiver noise temperatures of below 150 K from 760 to 960 GHz, assuming a junction current density of 25 kA/cm^2.

1. Introduction

Millimeter- and submillimeter-wave SIS mixers with quantum limited noise sensitivity and wideband characteristics are needed in radio-astronomy projects such as the Atacama Large Millimeter Array (ALMA) and the Herschel space observatory. For example, the ALMA covers the frequency range from 30 to 950 GHz in ten bands. For most of the bands, waveguide Nb-based SIS mixers can be used because they satisfy demanding specifications. However, the highest band (band 10), from 787 to 950 GHz, is beyond the gap frequency of Nb (700 GHz). In band 10, Nb has a large RF loss due to pair-breaking. It would thus be very difficult to achieve the specified SSB noise temperature of about 440 K over band 10 by using conventional Nb-based SIS mixers. Although a few reported SIS mixers, consisting of Nb-based tunnel junctions and NbTiN- or Al-based tuning circuits, enable low-noise operation at frequencies above the gap frequency of Nb, they do not satisfy the specifications [1, 2].

Our approach for achieving low-noise operation above 700 GHz is to develop all-NbN SIS mixers that should in principle perform well up to a gap frequency of 1.4 THz, like all-Nb SIS mixers do. We previously developed NbN/AlN/NbN tunnel junctions and

NbN/MgO/NbN microstriplines that are epitaxially grown on single-crystal MgO substrates [3, 4, 5]. Using these technologies, we have demonstrated relatively low-noise performance and broadband operation in the 900-GHz band using a quasi-optical SIS mixer with a self-compensated distributed tunnel junction with a high current density (45 kA/cm^2) [6, 7]. To make these SIS mixers practical for such applications as the ALMA, further improvements are necessary. First, the quasi-optical coupling, which uses a self-complimentary log-periodic antenna, contributes a large input noise, as estimated using the standard technique. The coupling system must be improved to reduce this noise. Second, the high-current-density junction with usually poor quality, which is needed for broadband operation, degrades mixer performance. These junctions must be improved to obtain better performance.

We have now designed a waveguide all-NbN SIS mixer using an MgO substrate for application to ALMA band 10. We also proposed a broadband tuning circuit that enables junctions with lower current density and better I-V curve to be used. Numerical calculations of the receiver noise temperature based on Tucker's quantum theory of mixing show that broadband and low-noise characteristics can be achieved with this new mixer.

2. Waveguide design

Most of the reported SIS mixers use a waveguide coupling because of the availability of feed horns, such as corrugated horns and diagonal horns, which produce an efficient power coupling into the waveguide over a broadband and an excellent antenna beam pattern. In conventional waveguide SIS mixers, a greatly reduced-height waveguide effectively yield broadband RF matching between the waveguide and SIS junction [8]. However, it may be difficult to fabricate such a waveguide in the submillimeter-wave regime because the aperture is so small. One way to overcome this problem is to use a waveguide probe, which provides excellent power coupling using a waveguide-to-microstrip transition [9]. We designed a mixer block including a waveguide-to-microstrip transition for ALMA band 10.

Figure 1 shows the schematic layout of the waveguide mixer block, which we designed using Hewlett Packard's High Frequency Structure Simulator (HFSS) [10]. The mixer chip with MgO substrate, on which the SIS junctions, tuning circuit, impedance transformer, waveguide probe, and RF choke filter are integrated, is placed in a channel of the mixer block. The mixer chip is 70 μm wide, 1.4 mm long, and 32 μm thick. For simplicity, externally adjustable mechanical tuners are not used. A diagonal feed horn is buried in the block and connected to the input waveguide (0.1 mm high and 0.26 mm wide) through a tapered structure. The aperture and length are 2.5 and 16 mm, respectively.

The calculated feed-point impedance normalized to 60 Ω is shown in Fig. 2. The graph shows that an RF bandwidth of 21%, from 786 to 988 GHz, is available with our design. It also shown that ALMA band 10 is covered better than with −10 dB matching.

In designing the waveguide-to-microstrip transition, it is important to examine how the position of the waveguide probe affects the input coupling efficiency. Figure 3 shows the dependence of the S-parameters on the position of the waveguide probe. The S-parameters

were calculated assuming the input port of the input waveguide and the output port of the microstrip with a characteristic impedance of 60 Ω. The solid lines in Fig. 3 show the S-parameters when the waveguide probe was shifted 10 μm from the designed position toward the IF port, and the dashed lines show the S-parameters at the designed position. The bandwidth of the RF matching was not sensitive to the position of the waveguide probe. This is a benefit of mounting the mixer chip in the mixer block.

3. Tuning-circuit design

Recently proposed distributed mixers based on the nonlinear quasi-particle tunnel current in a SIS transmission line have demonstrated low noise and good tunablity at submillimeter wavelengths. Electrically long junctions (say, a few times the guided wavelength) need low-current density but a submicron line-width to achieve reasonably high impedance for ease of matching, so that electron-beam lithography is necessary [11]. To obtain high input impedance with a wide junction width with conventional photolithographic techniques, a resonant distributed SIS mixer (say, half or one guided wavelength) was proposed [12] and tested [6, 7, 13]. However, its fractional bandwidth is narrow when low-current-density SIS junctions are used because the bandwidth is largely governed by the Q-factor of the junction, like that of a conventional lumped element mixer. Using a conventional tuning configuration, consisting of a resonant SIS junction with a quarter-wavelength impedance transformer, we can control the matching bandwidth by adjusting only the current density of the junction. In sum, high-current density-junctions are needed to obtain wideband operation at submillimeter wavelengths.

The tuning method we proposed efficiently compensates for the reactance component of distributed tunnel junctions. According to simple transmission theory, the input impedance of an open-ended distributed SIS junction is expressed by

$$Z_{in} = Z_j \coth(\gamma_j l_j), \tag{1}$$

where Z_j, γ_j (=α+jβ), and l_j are, respectively, the characteristic impedance, propagation constant (α is quasi-particle loss and β is the phase constant), and length of the tunnel-junction transmission line. If the transmission line is low-loss (αl_j<<1), the equation can be rewritten as

$$Z_{in} = Z_j \frac{\frac{Z_j}{\alpha l_j}\cos(\beta l_j) + jZ_j \sin(\beta l_j)}{Z_j \cos(\beta l_j) + j\frac{Z_j}{\alpha l_j}\sin(\beta l_j)}. \tag{2}$$

This equation shows that the input impedance of an open-ended SIS tunnel junction is equivalent to that of a loss-less transmission line (α=0) end-loaded with a pure resistance of $Z_j/(\alpha l_j)$. Accordingly, the frequency-varying impedance of the SIS transmission line can be simply understood as the frequency-varying reactance component yielding in the loss-less transmission line. One solution for broadbanding by efficient reactance compensation is to use

a filter structure consisting of half-wavelength components, which can control the impedance characteristics to have a bandwidth within a prescribed tolerance.

The diagram in Fig. 4 is an example tuning circuit consisting of two distributed SIS junctions connected by a transmission line and an impedance transformer. The lengths of junctions and the line between them have half-guided wavelengths at the center frequency, and the length of the impedance transformer has a quarter-wavelength. The tuning circuit was designed for a source impedance of 60 Ω over ALMA band 10 centered at 870 GHz. The modeled SIS junctions and transmission lines are, respectively, the NbN/AlN/NbN tunnel junction and the NbN/MgO/NbN microstripline. These elements have been used in actual SIS mixers and have been well characterized.

The material parameters of the junctions and microstriplines used for the calculation are summarized in Table 1. The characteristic impedance of the 0.6-μm-wide SIS junctions with a symmetrical counter-electrode overhang of 1 μm on either side was about 2 Ω. The quasi-particle loss in the half-wavelength line (αl_j in equation (2)) for the given current density was of the order of 10^{-1}, so we can apply the model described by equation (2) to this circuit. The characteristic impedance of the microstripline between the SIS lines was about 27 Ω.

To match the impedance of the tuning circuit, which has a filter structure, to the source impedance, they are connected using a quarter-wavelength impedance transformer. A broadband matching of below –10 dB was obtained at frequencies ranging from 750 to 1000 GHz (fractional bandwidth of about 29%), as shown in Fig. 4. Also shown in the figure are the impedance loci toward the load at each position of the circuit. One can see that the reactance component was well compensated for with this tuning circuit. Compared to a roughly estimated fractional bandwidth of 10% from the $\omega C_j R_N$ products for a conventional mixer design, the improvement in matching was about three times.

4. Simulated noise performance

We numerically simulated the mixing properties of our distributed SIS mixer using Tucker's quantum theory of mixing [14]. Equivalent large and small signal models for the mixer were established by replacing the model of inhomogeneous junction arrays based on lumped elements [15] with a distributed element model as described by Tong et al. [16]. Each section of the tunnel junctions was divided into 16 cells, sufficient for analyzing quasi-particle nonlinear transmission lines [16]. In these lines, each cell must be driven by a different LO phase and amplitude. We assumed an LO drive strength with the zero phase at the open end of the mixer, then derived the conversion admittance matrices for each cell recursively according to transmission theory. The correlation matrices was derived from the LO amplitude only for each cell, based on the assumption that shot noise created at any point along a nonlinear transmission line is not correlated with shot noise generated at any other point [16]. We used a quasi-five-port approximation in which the fundamental frequency sidebands, the second harmonic sidebands, and IF frequency were taken into account [17]. The IF frequency was assumed to be 1.5 GHz, and the IF termination was 50 Ω. The dc characteristic of an actual

NbN SIS junction was used, as shown in Fig. 5. The subgap-to-normal state-resistance ratio at 4 mV was about 11.

We used simplified model without a quarter-wavelength transformer to calculate the mixing properties of the mixer. A constant source impedance of 5 Ω was assumed across the entire frequency band for a circuit consisting of half-wavelength components because the quarter-wavelength microstripline transforms a waveguide source impedance of 60 Ω to about 5 Ω at the center frequency. Figure 6 shows the calculated SSB receiver noise temperature. Note that the dc bias and LO strength across the last cell were optimized with respect to the receiver noise temperature at each simulated frequency by assuming a noise temperature of the IF amplifier of 2 K. One can see that there are two noise ripples, one at around 800 GHz, and another at around 930 GHz. In our simulation, this could be reduced by assuming a lower source impedance of 2 Ω, as shown in the figure, but the bandwidth became a bit narrow because the matching became worse. If we use junctions with a different width, the ripples can be reduced without impairing broadband matching.

To compare the performance of our mixer with that of other type mixers, we simulated the mixing properties of a full-wavelength resonant distributed SIS mixer with the same current density, 25 kA/cm^2. As shown in Fig. 6, the receiver noise bandwidth of our proposed SIS mixer was broader than that of the conventional mixer, as predicted from the design, whereas the total length of the distributed junction was the same. Thus, this tuning method using effective reactance compensation can reduce the current density and obtain broadband characteristics.

5. Conclusion

We designed a waveguide SIS mixer with an MgO substrate on which NbN-based SIS and microstrip are epitaxially grown in the 900-GHz band of the Atacama Large Millimeter Array. Simulation using Hewlett Packard's High Frequency Structure Simulator showed that the waveguide source impedance was around 60 Ω when a 32-μm-thick substrate was used. To achieve performance better than the previous results using high current density junction of 45 kA/cm^2, we proposed a broadband tuning circuit that enables the use of lower current density junctions, resulting in a smaller leakage current. It utilizes the efficient reactance compensation produced by two half-wavelength distributed junctions connected by a half-wavelength microstripline. Based on the design and simulated noise performance, we predict that a tuning circuit using NbN junctions with a current density of 25 kA/cm^2 can cover the whole 900-GHz band with a SSB receiver noise temperature below 150 K.

Acknowledgements

This work was supported in part by the ALMA Joint Research Fund of the National Astronomical Observatory of Japan.

References

[1] J. Kawamura, J. Chen, D. Miller, J. Kooi, J. Zmuidzinas, B. Bumble, H. G. LeDuc, and J. A. Stern, *Appl. Phys. Lett.*, vol. 75, pp. 4013-4015, 1999.

[2] B. D. Jackson, N. N. Iosad, G. Le Lange, A. M. Baryshev, W. M. Laauwen, J.-R. Gao, and T. M. Klapwijk, *IEEE Trans. Appl. Supercond.*, vol. 11, pp. 653-656, 2001.

[3] Z. Wang, A. Kawakami, Y. Uzawa, and B. Komiyama, *J. Appl. Phys.*, **79**, pp. 7837-7842, 1996.

[4] Z. Wang, A. Kawakami, and Y. Uzawa, *Appl. Phys. Lett.*, **70**, pp. 114-116, 1997.

[5] A. Kawakami, Z. Wang, and S. Miki, *IEEE Trans. Appl. Supercond.*, pp. 80-83, 2001.

[6] Y. Uzawa, A. Kawakami, S. Miki, and Z. Wang, *IEEE Trans. Appl. Supercond.,* vol. 11, pp. 183-186, 2001.

[7] Y. Uzawa, Z. Wang, A. Kawakami, and S. Miki, in *Proceeding of the 12th International-Symposium on Space Terahertz Technology*, Humphrey's Half Moon Inn, Shelter Island, San Diego, CA, 14-16 February 2001 (unpublished).

[8] C. E. Tong, R. Blundell, S. Paine, D. C. Papa, J. Kawamura, Z. Zhang, J. A. Stern, and H. LeDuc, *IEEE Trans. Microwave Theory Tech.*, vol. 44, pp. 1548-1556, 1996.

[9] S.-C. Shi and J. Inatani, *IEEE Trans. Microwave Theory Tech.*, vol. 45, pp. 442-445, 1997.

[10] *High Frequency Structure Simulator*, Hewlett-Packard Co., Palo Alto, CA 94303, USA.

[11] C. E. Tong, R. Blundell, B. Bumble, J. A. Stern, and H. G. LeDuc, *Appl. Phys. Lett.*, vol. 67, pp. 1304-1306, 1995.

[12] V. Yu. Belitsky and E. L. Kollberg, *J. Appl. Phys.*, vol. 80, pp. 4741-4748, 1996.

[13] T. Matsunaga, C. E. Tong, R. Blundell, and T. Noguchi, *IEICE Trans. Electron.*, vol. E85-C, pp. 738-741, 2002.

[14] J. R. Tucker and M. J. Feldman, *Rev. Mod. Phys.*, vol. 57, pp. 1055-1113, 1985.

[15] M. Takeda, T. Noguchi, and S.-C. Shi, *Jpn. J. Appl. Phys.*, vol. 39, pp. 5095-5098, 2000.

[16] C. E. Tong, L. Chen, and R. Blundell, *IEEE Trans. Microwave Theory Tech.*, vol. 45, pp.1086-1092, 1997.

[17] S.-C. Shi, J. Inatani, T. Noguchi, and K. Sunada, *Int. J. Infrared Millmeter Wave*, vol. 14, pp. 1273-1292, 1993.

Table 1. Parameters used in design.

NbN upper electrode thickness:	400 nm
NbN lower electrode thickness:	200 nm
MgO insulator thickness:	180 nm
NbN/AlN/NbN junction width:	0.6 μm
current density:	25 kA/cm^2
$J_C R_N A$ products	380 kVμm^2/cm^2
Specific capacitance:	120 fF/μm^2
AlN barrier thickness:	1 nm
$\omega C_J R_N$ products:	10 @870 GHz

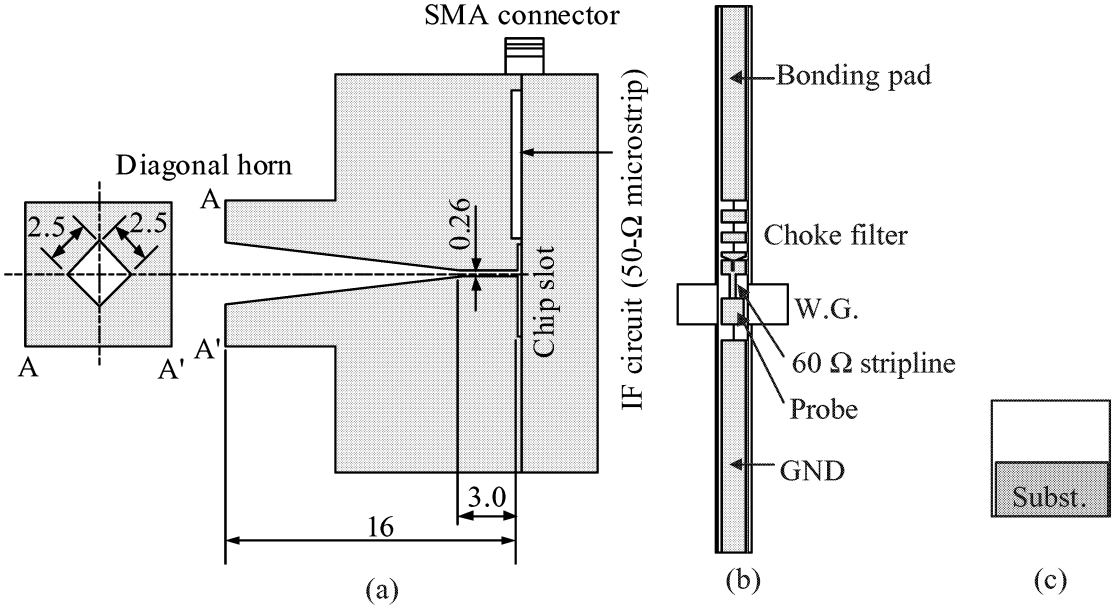

Fig. 1. Mixer mount layout showing diagonal horn section and mixer back piece. (b) View of chip slot from side of back piece. Waveguide is 0.1 × 0.26 mm, substrate is 0.07 × 1.4 × 0.032 mm. (c) Sectional view of chip slot, which is 0.073 × 0.073 mm.

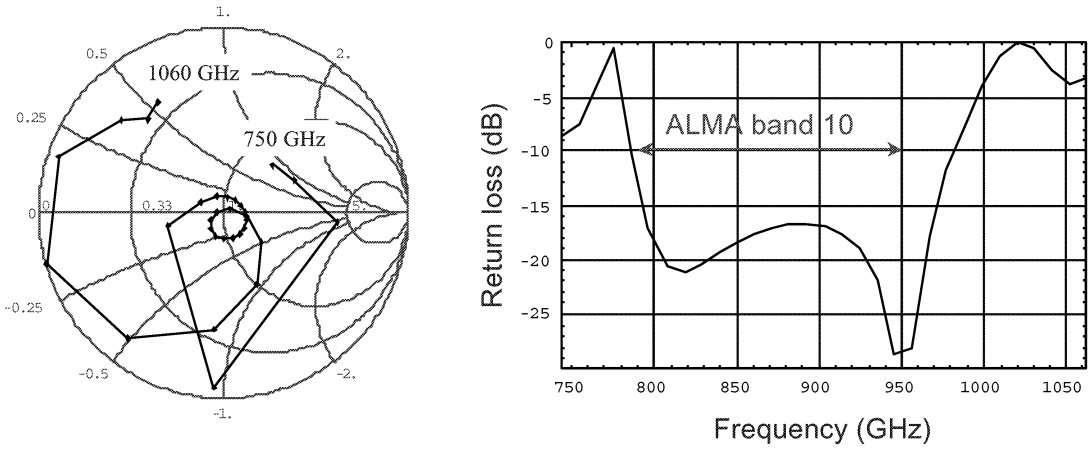

(a) (b)

Fig. 2. (a) Calculated feed-point impedance normalized to 60 Ω. (b) Return loss characteristics between feed-point and 60 Ω.

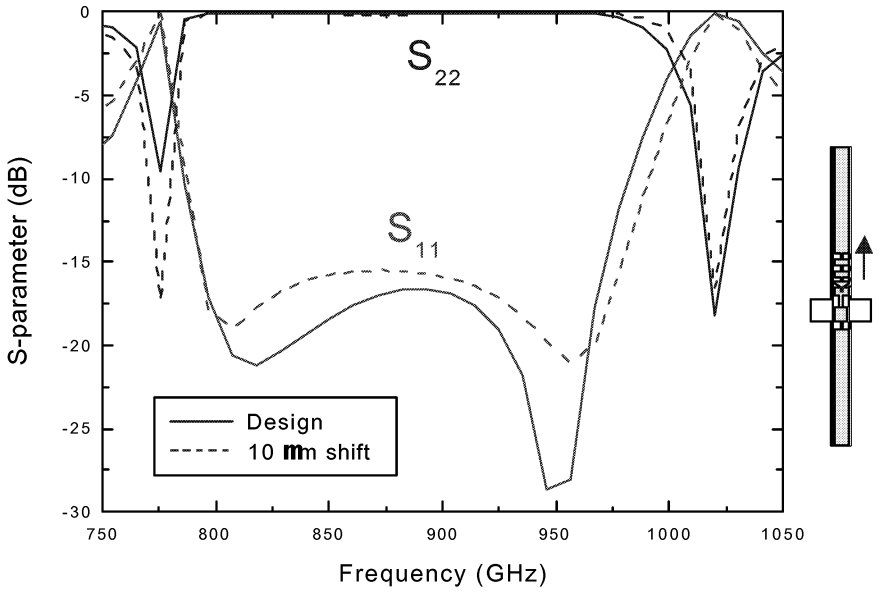

Fig. 3. Dependence of S-parameters on waveguide probe position. The 10-μm shift toward the IF port from the original position did not affect the characteristics.

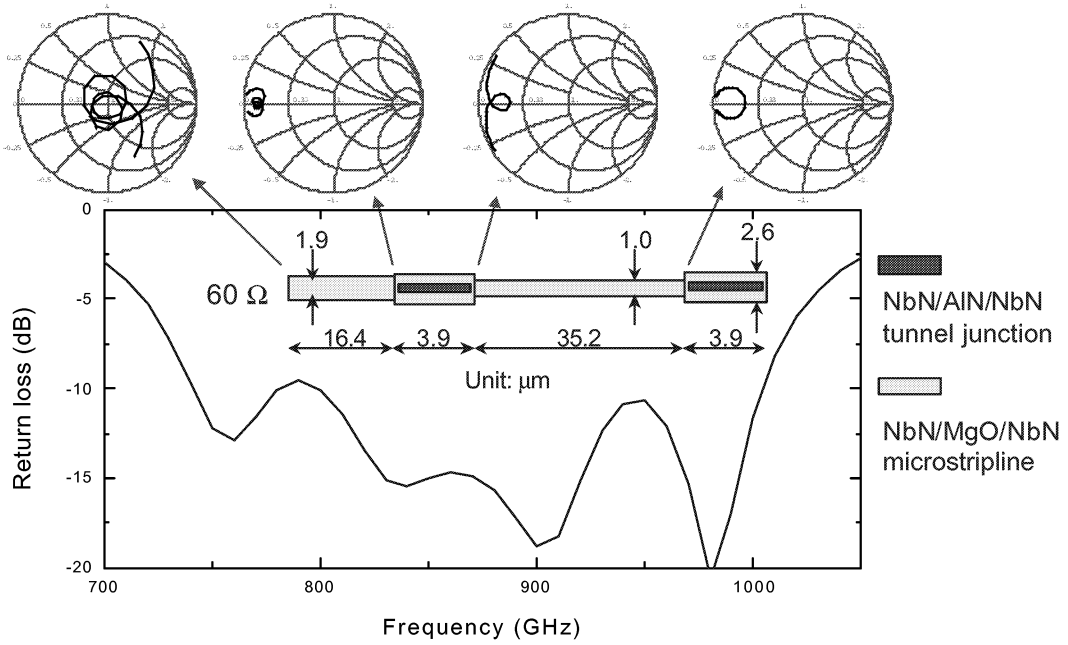

Fig. 4. Layout, theoretical return loss of tuning circuit, and impedance loci toward load at each position, normalized to 60 Ω.

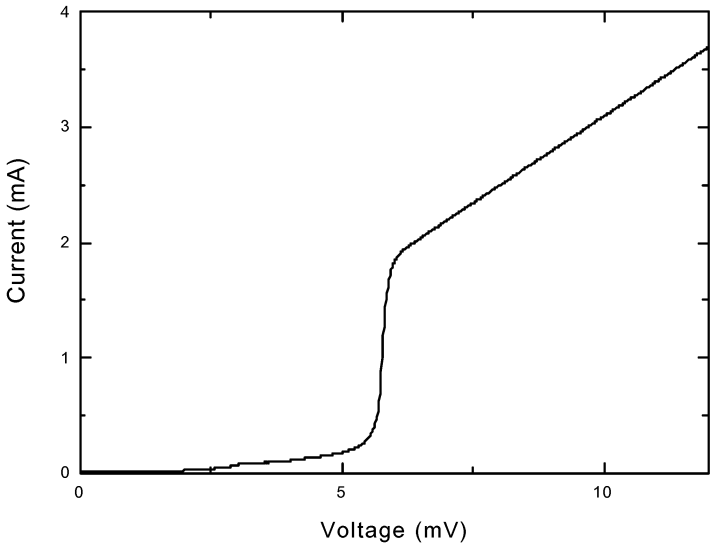

Fig. 5. Experimental I-V characteristics of NbN-based SIS junction. Subgap-to-normal state-resistance ratio was about 11.

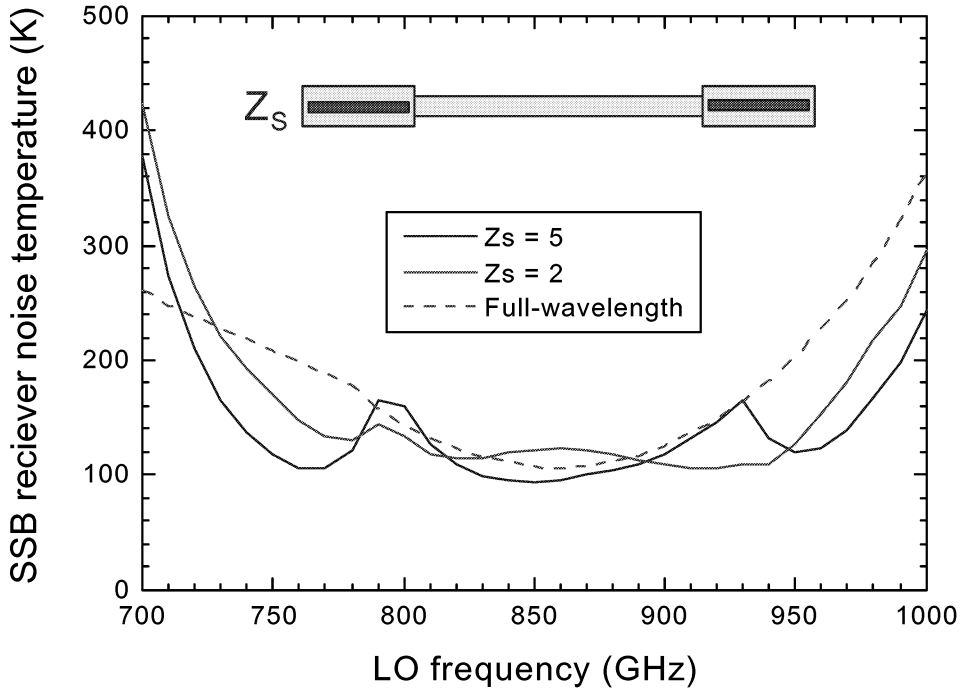

Fig. 6. Simulated SSB receiver noise temperature of two half-wavelength distributed junctions mixer. Also shown is the noise temperature of a conventional full-wavelength SIS mixer with the same current density.

Performance Characterization of a 600-700 GHz SIS Mixer

M. J. Wang[(a)], C. C. Chin[(b)], W. L. Shan[(c)], W. Zhang[(c)], H. W. Cheng[(a)], T. Noguchi[(d)], S. C. Shi[(c)]

(a) Institute of Astronomy and Astrophysics, Academia Sinica, Nankang, Taipei, China (Taiwan)

(b) Herzberg Institute, 5071 West Saanich Road, Victoria, BC, Canada

(c) Purple Mountain Observatory, Nanjing, China

(d) Nobeyama Radio Observatory, NAOJ, Nobeyama, Nagano 384-13, Japan

Abstract

A 600-700GHz SIS mixer with the twin-junction tuning circuit has been designed and fabricated [1]. The surface impedance of thin-film superconducting microstrip lines, based on Mattis-Bardeen theory [2], is included in the optimization of RF impedance matching. The receiver noise temperature measured in the frequency range of 630-660GHz is below 200K and the lowest receiver noise temperature of 181K is achieved at 656GHz. The FTS response of the SIS mixer shows a good RF coupling from 600GHz to 700GHz. Both the noise performance and the FTS response can be quantitatively described by numerical results using the quantum theory of mixing. Some detail considerations on the mixer model calculation, such as spreading inductance around the junction tuning structure and mixer's embedding impedance, are discussed.

Introduction

Nb-based superconductor-insulator-superconductor (SIS) mixers have been used very successfully in sub-mm wavelength detection. Their receiver noise temperature has reached to three times the quantum limit, ~3 hf/k_B, below the junction's gap frequency. However, at high frequency bands, Nb SIS mixers need to be designed carefully because the photon energy is close to or higher than the gap energy of Nb, Δ~1.4meV. When the frequency band covers the gap frequency of Nb, ~670GHz, the RF loss of Nb superconducting transmission lines increases dramatically and the surface impedance has strong frequency dependence. Usually, the RF properties of a superconducting transmission line can be described by the Mattis-Bardeen theory [2] in good accuracy. From results reported so far [4-9], the best receiver noise temperature is close to 5 hf/k_B in the band of 600-700GHz. Despite of the input loss contributed by the experimental setup, some other properties of SIS mixers should be taken into account. In this paper, we characterize the performance of a 600-700GHz mixer by comparing the experimental and simulated results.

Mixer design

The embedding impedance of the 600-700GHz SIS mixer was calculated by HFSS using the structure of the SMA mixer block and RF choke, which are designed by the receiver team at SAO, but with a substrate thickness of 30μm. Figure 1 shows the calculated embedding impedance over the interesting frequency band. Both the real and imaginary parts of the impedance vary remarkably in the band of 600-700GHz. This variation of the embedding impedance should be considered in the mixer performance calculation.

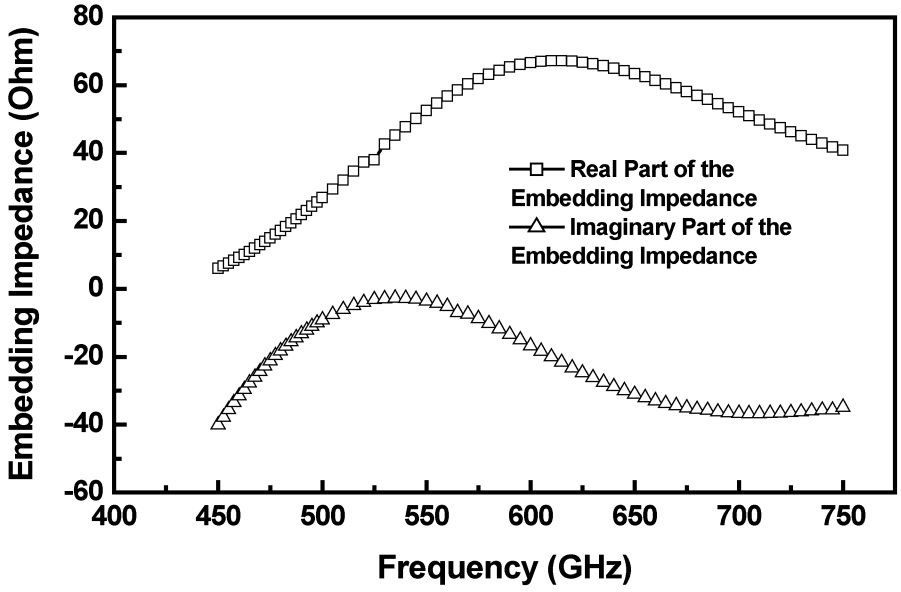

Fig. 1 Embedding impedance of the 600-700GHz SIS mixer calculated by HFSS.

The junction circuit design was based on a PCTJ (Parallel Connected Twin Junction) structure [10]. The designed parameters for the SIS junction as well as the transmission line structure are shown in Fig.2. To consider the capability and reliability of fabrication, the junction size was kept as large as possible, 1.2×1.2 μm^2 in this case. The designed J_C was 10 kA/cm^2 and the junction's specific capacitance was assumed to be 90 fF/μm^2. The superconducting transmission line was based on $Al_2O_3/SiO_2/Nb_2O_5$ trilayer dielectric with thickness of 900Å/2700Å/1000Å. In addition, the RF surface loss of superconducting films is no more negligible when photon energy is close to or higher than the gap energy of superconductor. For niobium-based devices, the gap frequency is near 670GHz (Δ~1.4 meV), which is just in the frequency band of interest. According to

Junction design parameters

Single Junction Parameters (design)

J_c=10kA/cm^2

A=1.2x1.2μm^2

C_j=1.44μm^2 x 90fF/μm^2=129.6fF

R_n=13.54Ω (by I_cR_n=1.95mV)

Impedance transformer

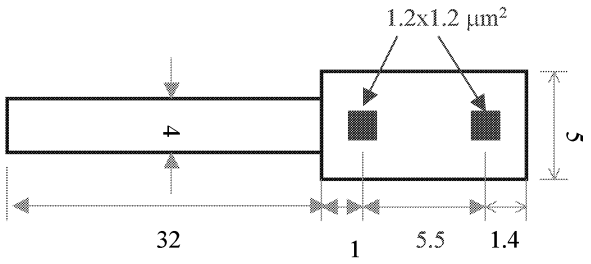

Fig. 2 Designed SIS junction parameters and the transmission line structure near junction, in μm unit. The J_C is 10 kA/cm^2 and the junction specific capacitance is assumed to be 90 fF/μm^2. Two 1.2×1.2 μm^2 junctions are connected by a 5.5μm wide superconducting transmission line to tune out the junction's geometric capacitance.

Mattis-Bardeen theory [2], the RF losses of the superconducting transmission lines were included during the optimization procedure of RF impedance matching [11].

Experiments

The SIS junction was fabricated by selective niobium etching process with additional anodization technique [12]. The Nb/AlO_x-Al/Nb (1000Å/70Å/2000Å) multi-layer was *in-situ* deposited on crystal quartz wafer with RF choke photo-resist lift-off pattern. The Al layer was exposed to 25 mtorr of Ar/10%O_2 mixture for 30 minutes to obtain critical current density (J_C) of 10kA/cm^2. The junction was defined by Deep UV source of mask aligner and top Nb was etched by RIE system using CF_4+O_2 mixture as processing gas. Before the deposition of the insulator layer, an additional anodization process was applied to anodize about 300Å thick Nb around the junction. An insulating layer of SiO_x/AlO_x (2700Å and 900Å) was deposited as the dielectric of the superconducting transmission lines. Before the deposition of a 6000Å thick wiring Nb film, the native oxide on top Nb surface was removed by applying Ar plasma. A 200Å/2000Å thick Ti/Au film was deposited on the contact pad of chip to reduce the contact resistance of DC/IF leads. Then, the quartz substrate was thinned by lapping machine and diced into individual chips, measuring 2mm (L) by 150μm (W) by 30μm (T).

The mixer performance was measured in a liquid He cooled dewar using typical hot/cold load technique. Fig. 3 shows the schematic drawing of the testing system. The LO source was generated by a multiplier (doubler+triplier) pumped by Gunn oscillator. Its frequency coverage is from 600GHz to 700GHz. The wire grid angle was set at 20° to couple enough LO power. However, it will increase the input RF noise temperature. Smaller grid angle was also tried to obtain lower receiver noise temperature in a narrow frequency range limited by insufficient LO power. The RF signal and LO power passed through a mylar vacuum window and Zitax IF filter, then were reflected by a cooled off-axis parabolic mirror into the corrugated horn of the mixer block. The IF signal was magnified by a cooled low noise amplifier (LNA) in the dewar and by a post amplifier at room temperature, then detected by a HP48xx power detector. Magnetic field by a superconducting coil was applied to reduce the Josephson tunneling effect. The hot/cold load was provided by a black body emitter at temperature of 295K/77K. The FTS measurement was done in the laboratory of National Astronomical Observatory of Japan at Mitaka. To get more reliable information, we used the same mixer block and junction in FTS and T_{rx} measurement.

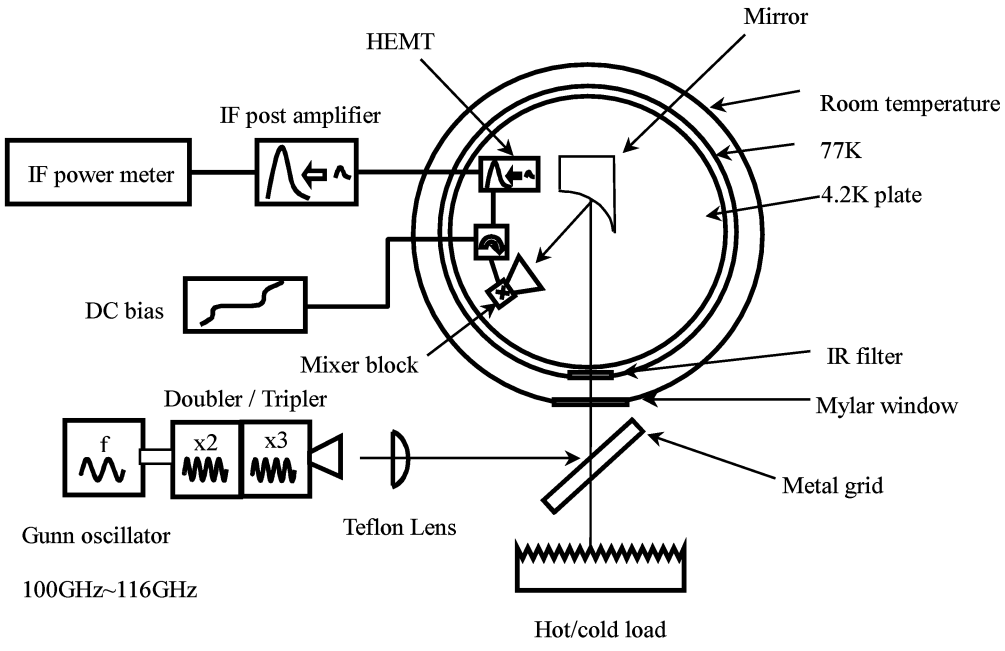

Fig. 3 Schematic drawing of the mixer performance testing system.

Results and discussion

The mixer noise performance is shown in Fig. 4. The solid circle is the simulated mixer noise temperature without any additional correction of the embedding impedance (simply assumed to be 35Ω here). Obviously, the center frequency is around 670 GHz. The data of sample Mixer A, Mixer B, and Mixer E (open square, down triangle and diamond points) are experimental results with a wire-grid angle of 20° . The un-corrected receiver noise temperature, T_{rx}, is below 300K in the frequency range of 600-680GHz. The center frequency of the mixer noise performance is shifted to 650GHz. The lowest T_{rx} is near 230K around 650GHz. It should be noted here that the quick rise of T_{rx} in the band edge was due to insufficient LO power. The solid triangle is exactly the same experiment of sample Mixer A, but with a wire-grid angle of 10° . The noise temperature is reduced significantly in the frequency range of 630GHz to 670GHz. The lowest noise temperature can reach to 181K at 656GHz. This performance improvement is attributed to the reduction of the RF input noise temperature from the wire grid. It can be roughly estimated from the power loss of the RF signal due to the

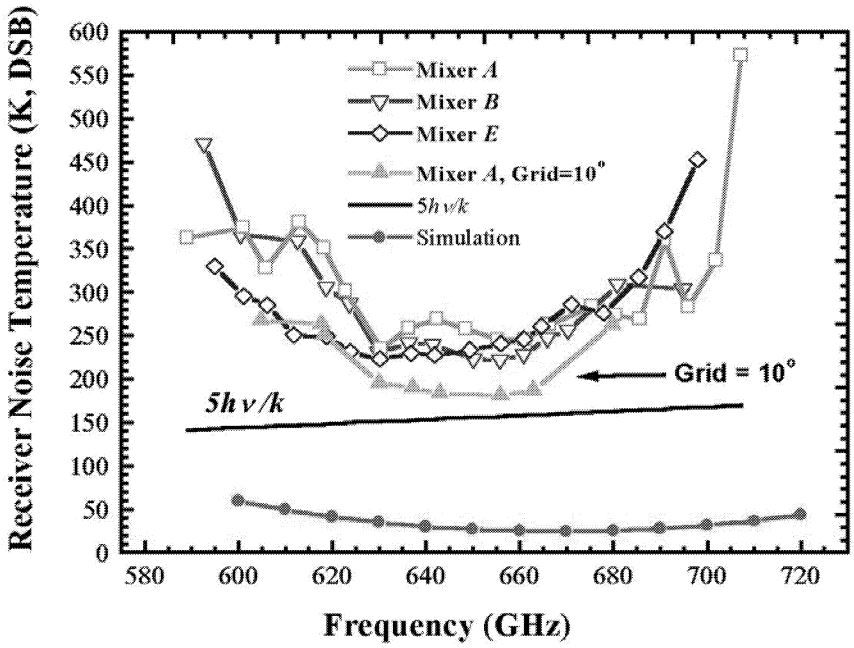

Fig. 4 Measured and simulated receiver noise temperature of the 600-700GHz SIS mixer. The solid circle is the simulated mixer noise temperature without any additional correction of the embedding impedance. The open square, down triangle and diamond points (Mixer A, Mixer B, and Mixer E) are the experimental results with wire grid at 20° . The solid triangle is exactly the same experiment of sample Mixer A but with wire grid at 10° .

misalignment between the waveguide polarization and the wire grid angle. The effective angles of the wire grid projected onto the waveguide polarization direction are about 25.8° and 13.8° for setting at 20° and 10° on the grid's holder, respectively. It is well known that the input noise of an object is equal to $T_{amb} \times \alpha$, where T_{amb} is the physical temperature of object and α is the absorption coefficient. Thus, the input noise temperature contributed from the wire grid is about 56K and 16K for the cases of the wire grid set at 20° and 10° on the grid's holder, respectively. The 40-K reduction of T_{rx}, due to the wire grid angle changed from 20° to 10°, is consistent with the experimental results.

The FTS experiment could reveal the relative coupling strength between RF signal and mixer. The measured time domain FTS response is shown in Fig. 5. The SIS mixer was biased at 1.9mV that is similar to the value for the T_{rx} measurement. The nice FTS response curve in time domain will give a more reliable frequency response after Fourier transformation.

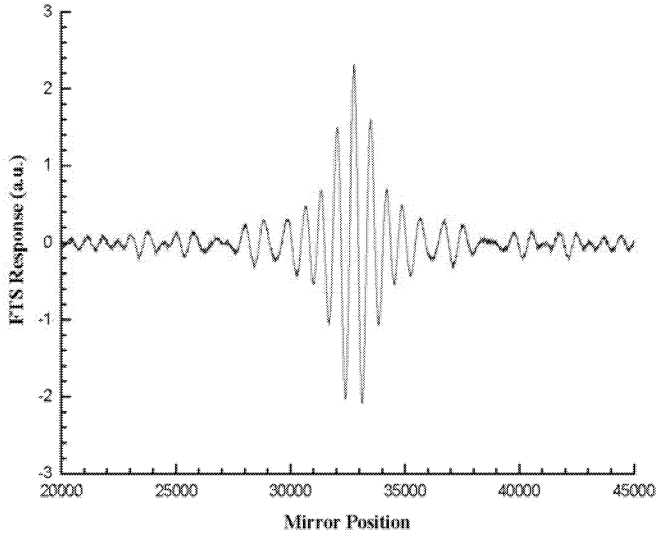

Fig. 5 Time domain FTS response measured for the 600-700GHz SIS mixer biased at 1.9mV.

Fig. 6 shows the FTS response of the 600-700GHz SIS mixer, the solid circle points, in a frequency range of 400GHz to 800GHz. The T_{rx} result of the same receiver is also plotted in the figure, down triangles, for comparison. The FTS response is relatively strong from 600GHz to 700GHz and from 470GHz to 510GHz. There is a strong absorption of water around 550GHz, which will reduce the FTS response. In general, the FTS response is consistent with the mixer performance result. The up-triangles are

the simulated result of the RF coupling. An additional length of 2x1μm (2ΔL) in tuning inductor, about 40% increase in length of the original design, was added during the simulation. We found that the FTS response can be described qualitatively by the simulation result. The origination of this additional inductance might be due to the spreading current effect near small SIS junctions because of their low impedance comparing with the transmission line. It may need more experiment to understand the contribution of this effect.

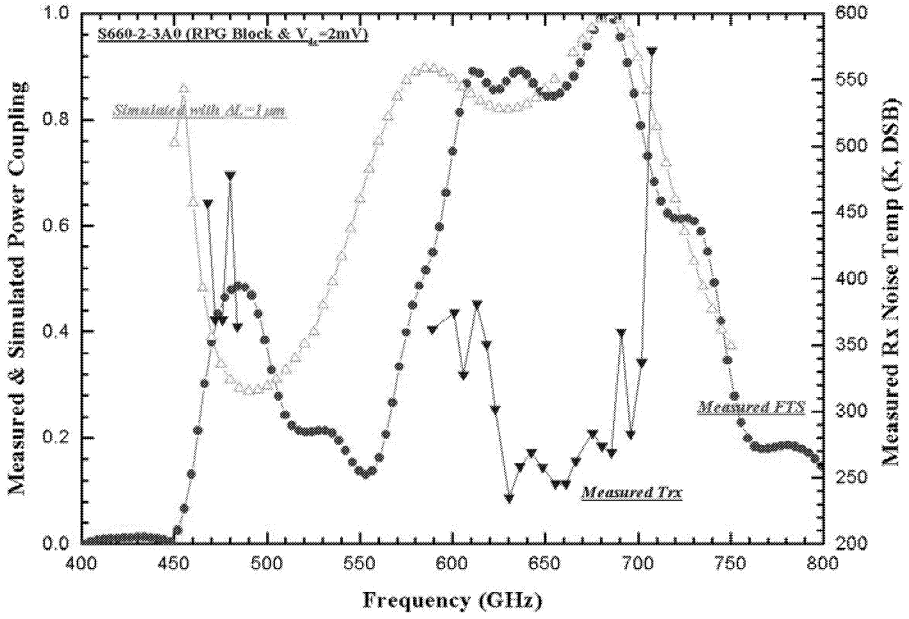

Fig. 6 Measured FTS response of the 600-700GHz SIS mixer, the solid circles. The down-triangles are the T_{rx} value of the same receiver. The FTS response is basically consistent with the performance of receiver. The up-triangles are the simulated results with additional 1mm of tuning structure. The FTS response can be qualitatively described by the simulation result. The additional inductance might be originated from the spreading current effect near SIS junction.

Conclusion

Low noise SIS receivers for 600-700GHz have been achieved using PCTJ type mixer. The un-corrected double-side-band noise temperature is below 300K in this frequency band. The variation of the embedding impedance and the RF loss of the thin-film transmission lines are taken into account in the simulation model. However, the lowest noise temperature is only close to $5hf/k_B$. The FTS result shows a consistent

frequency window of the RF coupling as T_{rx} experiment. The simulated RF coupling can qualitatively describe the FTS experimental result by adding an extra inductor. This additional inductor might result from the current spreading effect near the SIS junctions. More experimental results are necessary to clarify its origination.

Acknowledgement

We grateful appreciate the receiver team of SAO for providing the detail designs of the mixer block and RF choke. We also thank Dr. Matsuo for his help on FTS experiments and useful discussion.

References

[1] S.C. Shi, W.L. Shan, W. Zhang, C.C. Chin, M.J. Wang, and T. Noguchi, "Development of a 600-720 GHz SIS mixer for the SMART," in *Proceedings of 12th Int. Symp. on Space THz Tech*, San Diego, USA, Feb. 2001.

[2] D.C. Mattis and J. Bardeen, "Theory of the anomalous skin effect in normal and superconducting materials," Phys. Rev., **111**, 412, 1958.

[3] J. R. Tucker, IEEE J. Quantum Electron. **QE-15**, 1234, 1979.

[4] C.-Y. E. Tong, R. Blundell, D. C. Papa, J. W. Barrett, S. Paine, and X. Zhang, "A Fixed Tuned Low Noise SIS Receiver for the 600 GHz Frequency Band, " The Proceedings of Sixth International Symposium on Space Terahertz Technology, p. 295, 1995

[5] S. Hass, C. E. Honingh, D. Hottgenroth, K. Jacobs, and J. Stutzki, "Low noise broadband Tunerless waveguide SIS Receivers for 440-500GHz and 630-690GHz, " International Journal of Infrared and Millimeter Waves, 17(3), 493-506, 1996.

[6] C.-Y. E. Tong, R. Blundell, B. Bumble, J. A. Stern, and H. G. LeDuc, "Sub-millimeter Distributed Quasiparticle Receiver Employing a Non-Linear Transmission Line, " The Proceedings of Seventh International Symposium on Space Terahertz Technology, p. 47, 1996.

[7] J. W. Kooi, M. S. Chan, H. G. LeDuc, and T. G. Phillips, "A 665GHz Waveguide Receiver Using a Tuned 0.5 μm^2 Nb/AlO_x/Nb SIS Tunnel Junction," The Proceedings of Seventh International Symposium on Space Terahertz Technology, p. 76, 1996.

[8] T. Matsunaga, C.E. Tong, T. Noguchi, & R. Blundell, Proc. 12th Space THz Tech. Symp., San Diego, CA, (February 2001)

[9] accepted by International Journal of Infrared and Millimeter Waves, 2002.

[10] T. Noguchi, S. C. Shi, and J. Inatani, "An SIS Mixer Using Two Junctions Connected in Parallel," IEEE Transaction on Applied Superconductivity, **5**, p. 2228, 1995.

[11] S.C. Shi, C. C. Chin and W. Zhang, "Characterization of Nb-Based Superconducting Transmission Lines around the Gap Frequency," International Journal of Infrared and Millimeter Waves 21(12): 2007-2013; Dec 2000

[12] T. Noguchi, A. Sakamoto, S. Ochiai, "Fabrication of sub-micron SIS junctions," Technical Report of IEICE, SCE93-64, pp.43-48, 1994.

A Comparison of Power Measurements from 100 GHz to 600 GHz

Qun Xiao, Yiwei Duan, and Jeffrey Lee Hesler

University of Virginia

Introduction

The accurate measurement of absolute power at millimeter and submillimeter wavelengths is difficult, and different power meters can give substantially different results, thus complicating comparisons between measurements by different groups. This paper will present a comparison of measurements done using a variety of commonly used power meters over a frequency range from 100 GHz to 500 GHz.

Measurement

In the WR-10 frequency range we compare power measurements using two HP-437B power meters with W8486A diode power sensors [1], [2], and an Erickson PM1B calorimeter power meter [3]. Each of these meters is used to measure the power output from a Gunn oscillator.
In the WR-8 frequency band we compare an Erickson PM1B power meter with two Anritsu ML83A power meters with WR-8 thermistor power sensors. The power source is a WR-8 Gunn oscillator.
In the WR-3 frequency range, we compare the measurement results of the Anritsu ML83A power meter with both WR-3 and WR-8 power sensors and the Erickson PM1B power meter. The power source is a WR-10 to WR-3 frequency tripler. Finally, some power measurement results above the WR-3 frequency band are presented.

1.WR-10 measurement
In WR-10 frequency band, a Carlstrom Gunn oscillator is measured using a variety of power meters: an HP W8486A power sensor (which is borrowed from NRAO and is calibrated and traceable to NIST), an HP W8486A power sensor (which has not been recently calibrated), and an Erickson PM1B power meter.

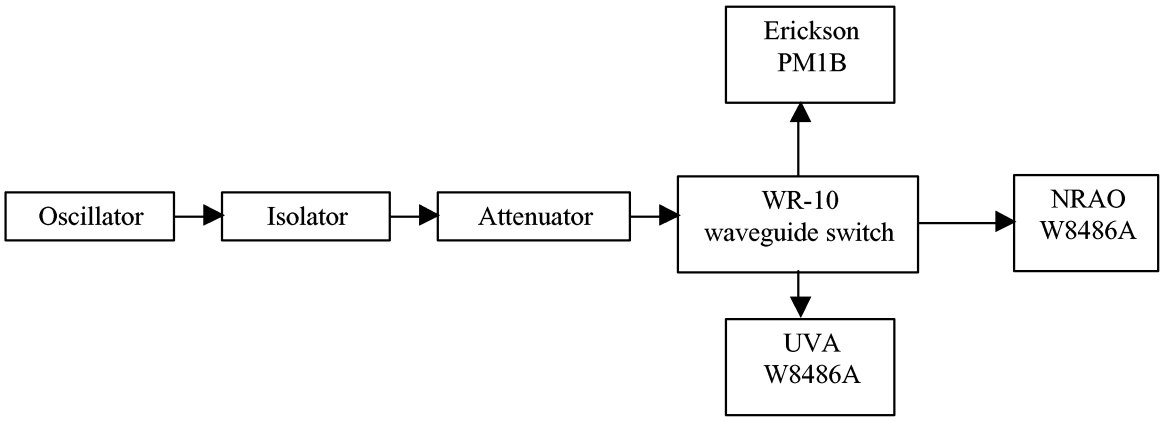

The following graph shows the measurement results. Figure 1 shows the power measured using the various meters and the calibration factors for the Erickson PM1B power meter and the UVA HP W8486A sensor.

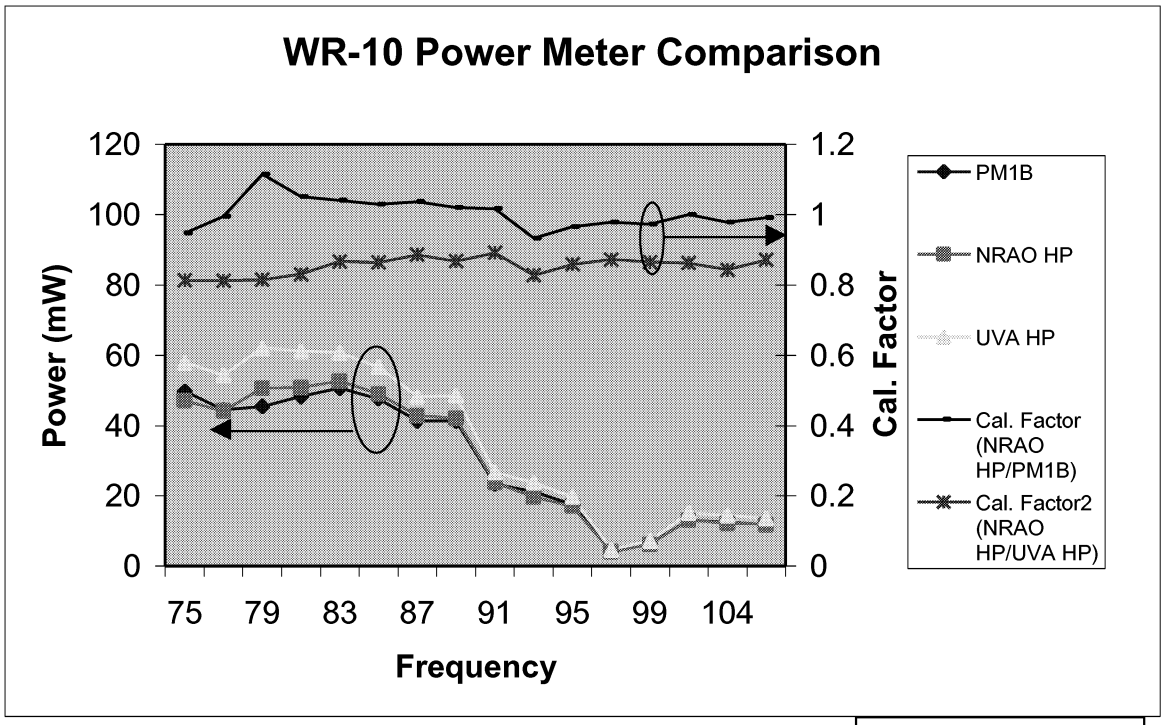

Figure 1

From Figure 1, we can observe that the reading of Erickson PM1B is quite consistent with that of NRAO HP power meter, with is calibrated and traceable to NIST. The reading of UVA HP power meter has a similar shape to that of NRAO HP power meter, but shifts to a higher level. We believe the reason is that this meter has not been recently calibrated.

We also checked the power meters' performance at lower power levels. The HP power meters can automatically select scale range. The Erickson PM1B needs to be set manually. The results are plotted in Figure 2. From Figure 2, we can observe similar behavior as we saw at higher power level. This means all power meters perform consistently on different power levels.

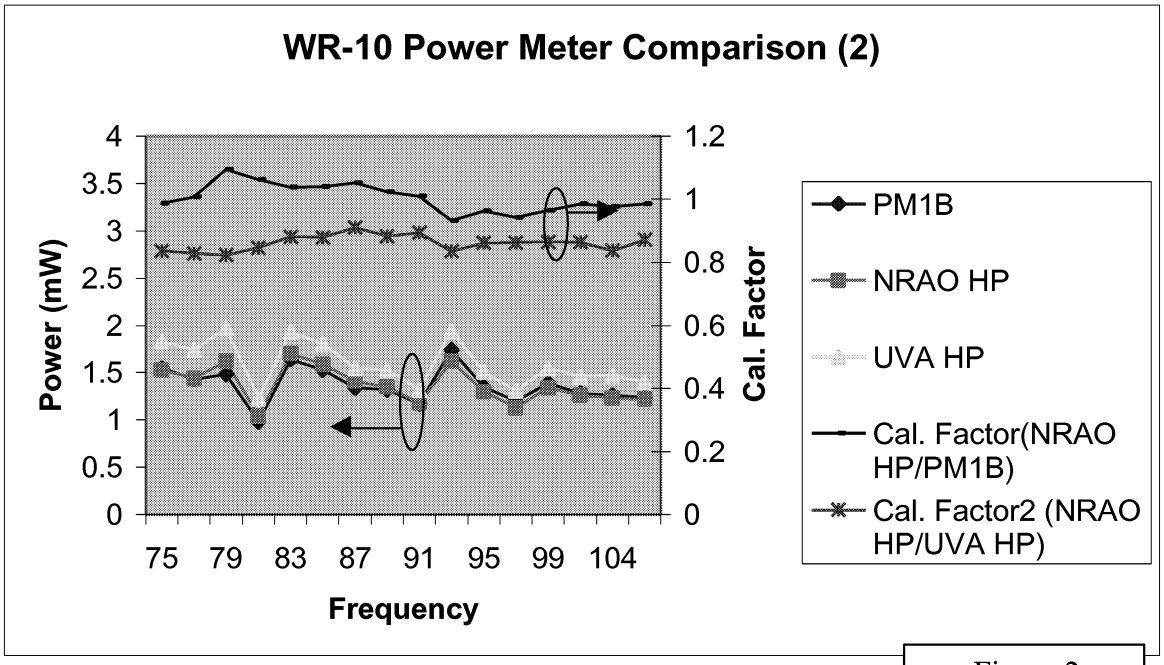

Figure 2

2. WR-8 measurement

In the overlap frequency band of WR-8 and WR-10, we compare the NRAO HP W8486A power sensor with Anritsu WR-8 power sensor.

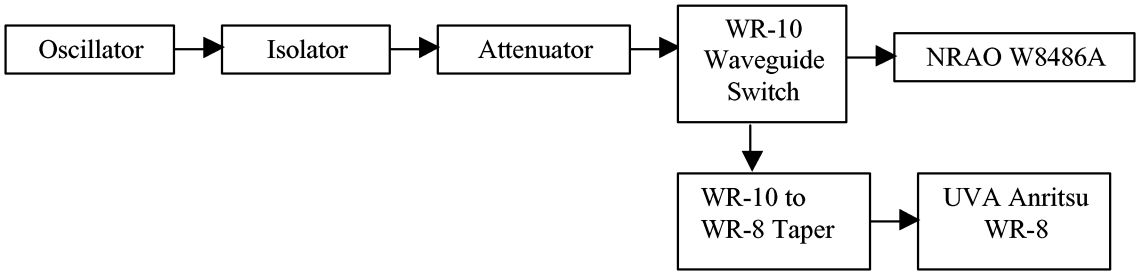

Measurement Setup for 90-110 GHz

The measurement result is plotted in Figure 3. We can observe that the reading of the Anritsu WR-8 is lower than the HP meter, but the scale factor is constant and remains between 1.25 and 1.35.

In the higher end of WR-8 frequency band we test the UVA Anritsu WR-8 power meter, the NRAO Anritsu WR-8 power meter, and an Erickson PM1B power meter. The results at lower power level are showed in Figure 4 and at higher power level in Figure 5.

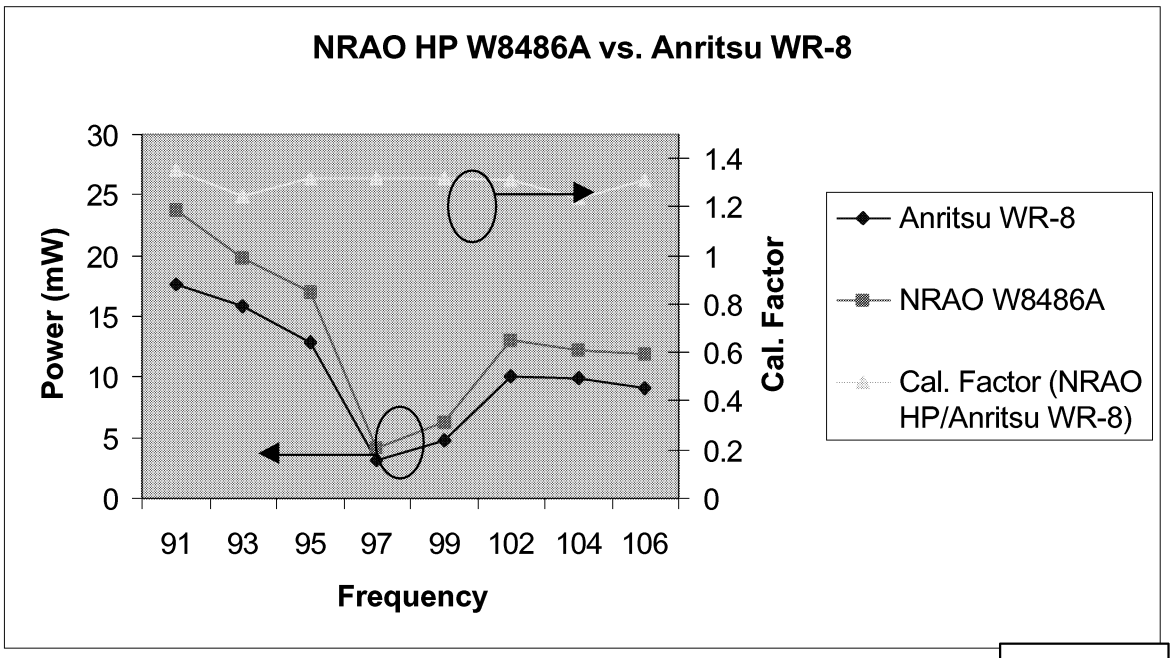

Figure 3

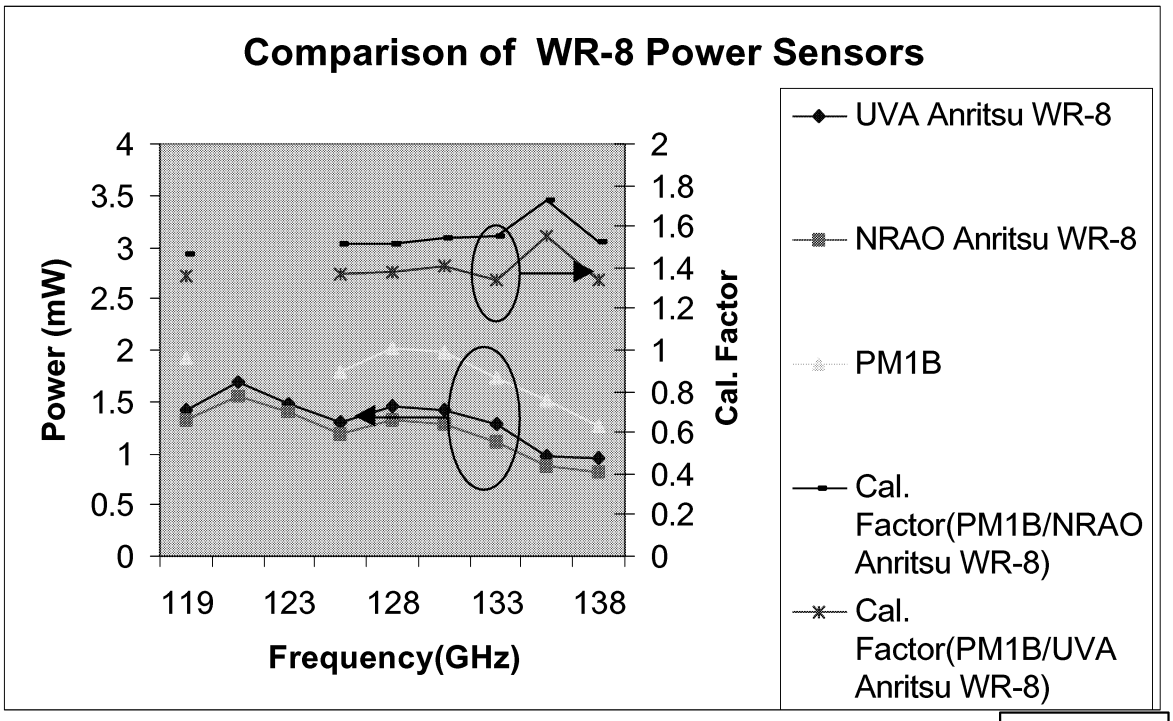

Figure 4

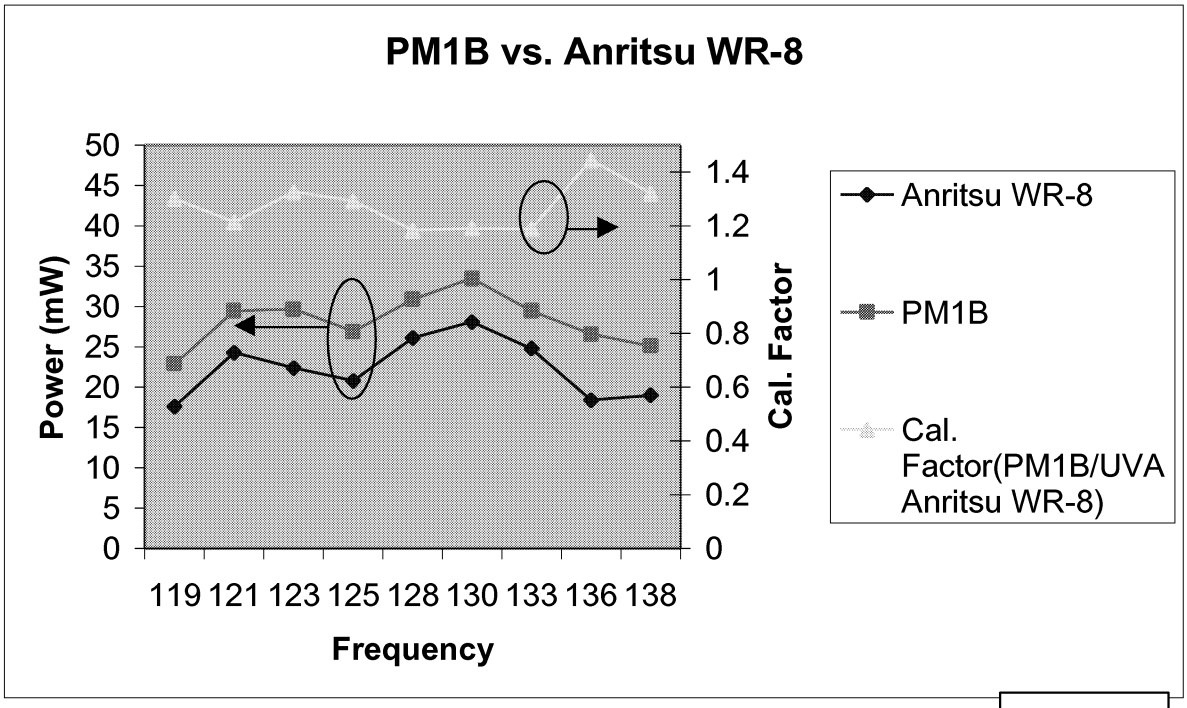

Figure 5

In the measurement shown in Figure 4 we use the Erickson PM1B with its scale range set to 2+ mW to measure the Gunn power. At 120GHz and 122GHz the reading is out of range, so those two points are omitted. The readings of the two Anritsu WR-8 power meters are very consistent to each other, but are lower than the reading from the Erickson PM1B.

3. WR-3 Measurement

In WR-3 frequency range, we compare 2 power measurement methods. They are an Anritsu WR-3 power meter and an Erickson PM1B power meter. We use a WR-3 to WR-10 tripler as the power source. When we use the PM1B power meter, we insert a WR-3 to WR-10 taper between the tripler and the power meter.

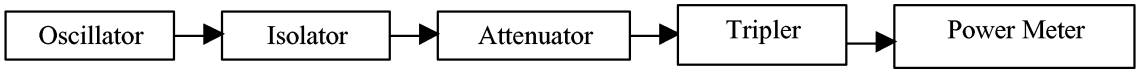

Measurement Setup for the WR-3 frequency range

The measurement results are shown in Figure 6.

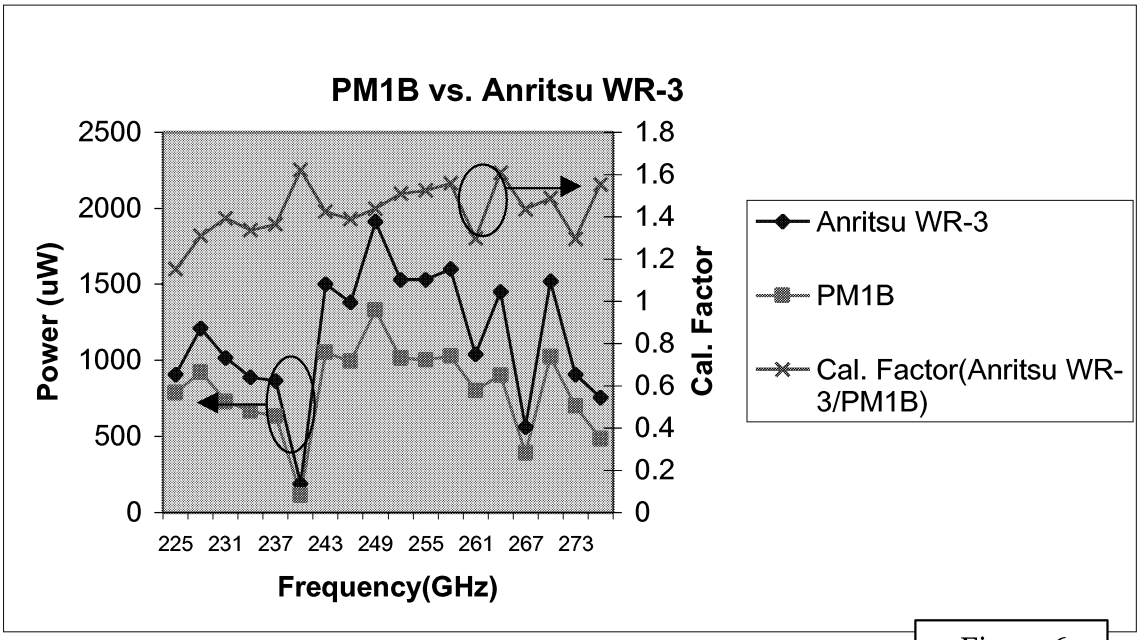

Figure 6

As shown in Figure 6, the Anritsu and Erickson meters track very well over this frequency range.

We also compare the Anritsu WR-3 power meter, an Erickson PM1 (borrowed from NRAO), and an Anritsu WR-8 power meter in the WR-3 frequency band.

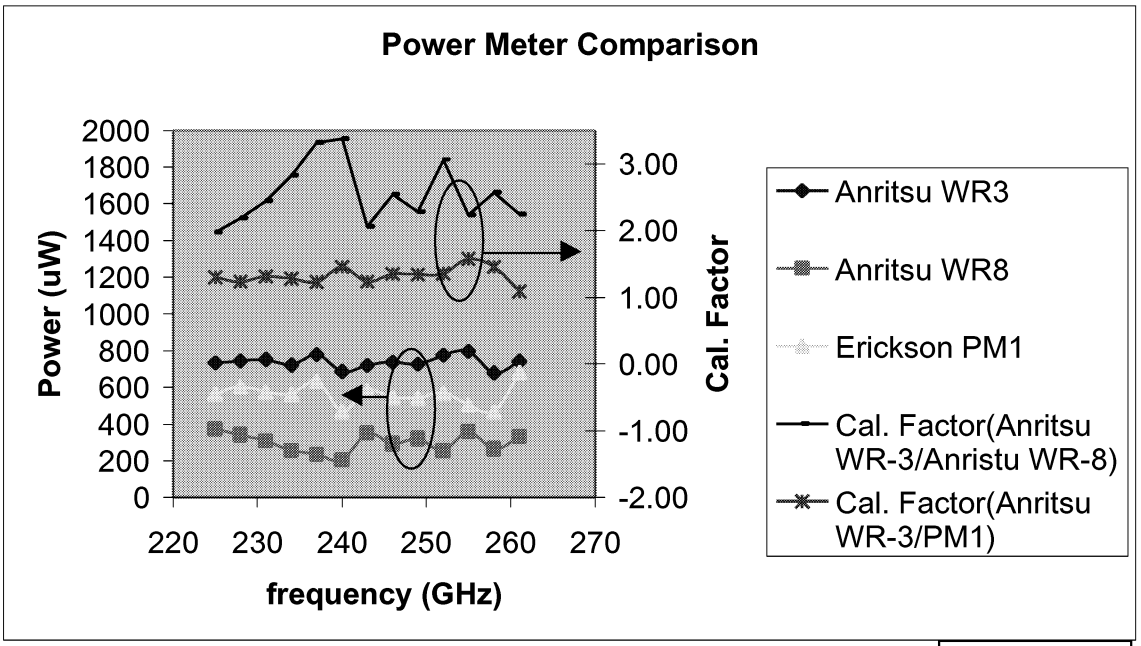

Figure 7

From figure 7, we can observe the Erickson PM1 power meter has almost same performance as Erickson PM1B, with a scale factor about 1.4 compared to the Anritsu WR-3 power meter. However, the scale factor for the Anritsu WR-8 power meter referenced to the Anritsu WR-3 power meter varies over a much larger range, from 2 to3.5. Also, this correction factor was found to vary significantly from measurement to measurement. This shows the problem associated with using a meter above band.

4. Power measurement above the WR-3 frequency band.
We also measured power in the 400 to 500 GHz range. The power source is a quintupler pumped by a Gunn oscillator.

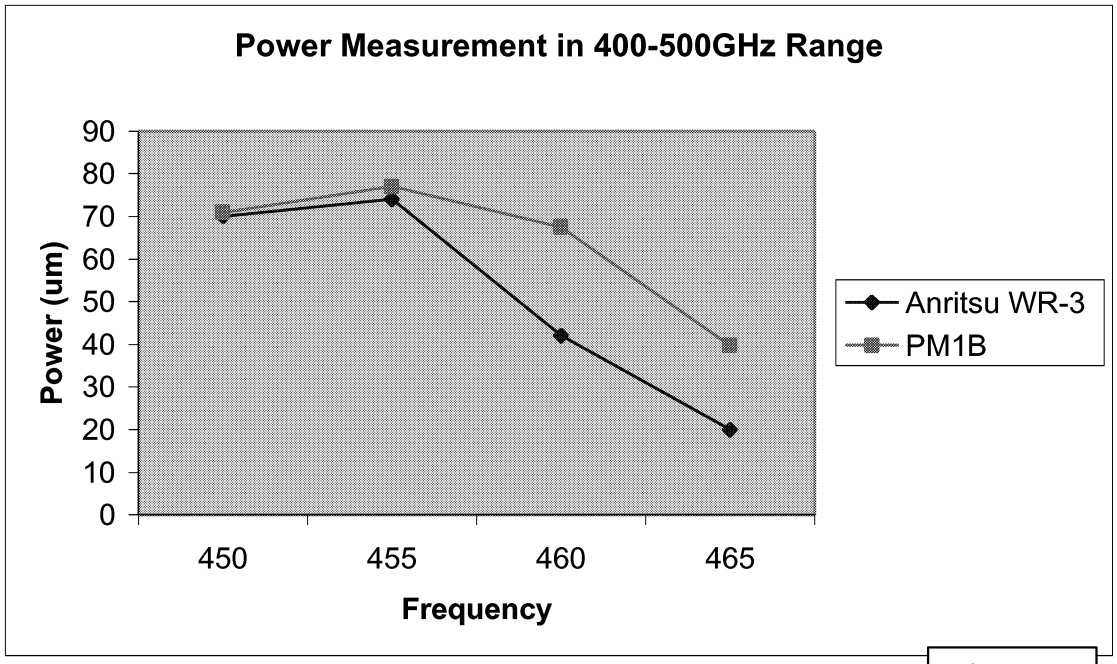

Figure 8

As found when using the WR-8 Anritsu power meter above band, the WR-3 Anritsu power meter shows significant deviation from the Erickson PM1B power meter above band.

Conclusion

In the WR-10 frequency range, the calibrated HP W8486A power sensor is the best choice because it is traceable to NIST and has a faster measurement speed compared with the Erickson PM1B power meter. The measurement result from the Erickson PM1B is very close to that of the W8486A.

In the WR-8 frequency range NIST has not set any power calibration standard yet. From the comparisons in the overlap frequency range of WR-8 and WR-10, we believe the Erickson PM1B power meter will be quite accurate over the WR-8 frequency range.

The use of the Anritsu power meter heads above their specified band was found to be prone to significant error and repeatability problems.

Up to the WR-3 frequency range, the measurement results of the Anritsu WR-3 power meter, the Erickson PM1, and the Erickson PM1B have very similar shape and with a scale factor about 1.4. Since Anritsu Corp. no long produces the WR-3 power sensor we have decided to use the Erickson power meter series PM1B as our power standard.

Reference

[1] EPM Series Power Meters E-Series and 8480 Series Power Sensors Technical Specifications, *Agilent Technologies*
[2] Choosing the Right Power Meter and Sensor Product Note, *Agilent Technologies*
[3] Operation Manual of Erickson PM1B Power Meter, *Erickson Instruments LLC*

Acknowledgement

The authors would like to thank Dr. Shing-Kuo Pan and Dr. Kamaljeet S. Saini in National Radio Astronomy Observatory for their help in power measurement and discussion.

PROGRESS ON *TREND* – A LOW NOISE RECEIVER USER INSTRUMENT AT 1.25 THZ TO 1.5 THZ FOR AST/RO AT THE SOUTH POLE

K.S. Yngvesson, J. Nicholson, Y. Zhuang, X. Zhao, D. Gu, R. Zannoni,
Department of Electrical and Computer Engineering, University of Massachusetts,
Amherst, MA 01003; yngvesson@ecs.umass.edu

E. Gerecht
Department of Astronomy, University of Massachusetts, Amherst, MA 01003, and
National Institute of Standards and Technology, Boulder, CO 80305;
gerecht@boulder.nist.gov

M. Coulombe, J. Dickinson, T. Goyette, and J. Waldman
Submillimeter Wave Technology Laboratory, University of Massachusetts at Lowell,
MA 01854

C.K. Walker
Department of Astronomy and Stewart Observatory,
University of Arizona, Tuscon, AZ …

A. Stark and A. Lane
Smithsonian Astrophysical Observatory
Cambridge, MA 02138

At the Twelfth International Symposium on Space THz Technology last year we introduced and described the ongoing *TREND* ("*Terahertz Receiver with NbN Device*") instrument development. *TREND* is a low-noise heterodyne receiver for the 1.25 THz to 1.5 THz frequency range. *TREND* takes advantage of the atmospheric attenuation window in this frequency range, as well as the availability of an excellent site, the US South Pole Station, and a 1.7 m diameter operational telescope (AST/RO) at that site.

Since last year's report, the local oscillator laser has been completed and tested. The output power is as high as 200 mW on the strongest line. The laser is now being integrated with NbN HEB mixer devices in a new mixer block design, which we will describe. A new twin-slot antenna design is being used. We will also discuss the plans for installation of the system on AST/RO which is anticipated to occur during the austral summer season of 2002/2003. The receiver will then be used for observations of NII and CO during the austral winter season of 2003.

DETECTION AND INTERPRETATION OF BISTABILITY EFFECTS IN NBN HEB DEVICES

Yan Zhuang and K. Sigfrid Yngvesson
Department of Electrical and Computer Engineering, University of Massachusetts, Amherst, MA, 01003

ABSTRACT- Characteristics of an umpumped NbN Hot Electron Bolometer (HEB) device, between the superconducting state and the resistive state, show that a negative differential resistance occurs in the region between the superconducting state and the resistive state. The device is potentially unstable in this region, and we have performed further observations of the periodic waveform which occurs for this case on a fast digital oscilloscope. In order to fully understand the physical processes in this region both device voltage and current need to be obtained simultaneously. We then use the established theory for bistabilities in superconductors [1] to calculate the rise time of the waveform, and the frequency of the relaxation oscillations at about 6 MHz, which we observe in a number of devices. We show that the above theory can provide a qualitative interpretation of this waveform. The calculated rise time and frequency of the relaxation oscillations do not agree very well quantitatively, however, indicating that the simplest model based solely on the thermal conduction equation is insufficient. We also suggest how this model might be modified in order to obtain better quantitative agreement.

I. INTRODUCTION

Observing the Current – Voltage Characteristics of an umpumped NbN Hot Electron Bolometer (HEB) device, a negative differential resistance occurs in the region between the superconducting state and the resistive state. The device is potentially unstable in this region, and we reported some results of studying this state at the 12th Space THz Technology Symposium [2]. We have made further observations of the periodic waveform which occurs for this case on an oscilloscope. In order to fully understand the physical processes in this region both device voltage and current need to be obtained simultaneously. We then use the established theory for bistabilities in superconductors [1] to calculate the rise time of the waveform, and the frequency of the relaxation oscillations at about 6 MHz, which we observe in a number of devices. We finally discuss our results in terms of the most recent models for PHEB mixer devices.

II. EXPERIMENTS AND RESULTS

The 3.5 nm thick NbN HEB device was mounted on a circuit board in a small metal box in order to shield it from outside radiation, and to minimize parasitics. A small resistor, r = 10 Ω, was used to enable us to measure the device current. The box was connected to two coaxial cables housed in a stainless steel tube "dipstick" to allow insertion of the device into liquid helium. The structure is shown in Figure 1. Two separate voltages, V_1

and V_2, can be measured by connecting each cable to one channel of a digital oscilloscope whose maximum frequency is about 1 GHz. In this situation both the voltage across the device (V_d) and the device current (I_d) can be measured simultaneously. This turned out to be very important for the interpretation of the data.

$$V_d = V_1 - V_2 \tag{1}$$

$$I_d = V_2 / r \tag{2}$$

The bias supply is constructed with OPAMPS and has a very low source resistance, accomplished through feedback. There are also OPAMP circuits for recording the voltage and current levels on digital multimeters, which can then be displayed on a computer through a LABVIEW program. The sampling rate is about 20 samples per second, so only very slow variations can be recorded at the bias supply. It is connected through a low-pass filter with a cut-off frequency of 2.5MHz. One typical voltage biased I – V characteristics of a HEB device is shown in Figure 2. As is well – known there are 4 different regions in the I – V curve: (1) the superconducting region; (2) a region in which slow (a few hundred Hz) oscillations occur, whose frequency basically is determined by characteristics of the OPAMP in the bias supply (slow enough to be picked up by the LABVIEW system); (3) a second negative differential resistance region where the oscillations are much faster, and can be observed on the oscilloscope; the DC voltage and current as recorded through LABVIEW are stable at any particular point in this region; we will primarily study the device behavior in region (3) in this paper; (4) a stable hotspot region, where a stable hotspot is formed and can expand when the bias voltage is increased. All recordings are stable in region (4). We have studied the bistability for a voltage bias situation.

It is possible that the device in its negative resistance region can be stabilized by adding a series resistor r_{stab}. The circuit will become stable when increasing r_{stab} to make the total resistance become positive as we showed earlier [2].

$$r_{stab} > \left| \frac{dV_d}{dI} \right| \tag{3}$$

The corresponding I – V curve is shown in Figure 3 that includes a curve without the stabilizing resistor to make a comparison.

In our paper at the 12th STT [2] we recorded the device current by measuring the voltage across a series resistor inside the voltage bias supply. Because of the slow response rate of the OPAMP in the voltage supply, the current appeared to be almost constant with a percentage change of only about 1%. This time we measure the device current directly, as shown in Figure 1, allowing us to record the instant current value for the HEB device. Figure 4 shows the simultaneous measurement of both voltage and current. The voltage waveform is almost the same as before. It has a very fast rise (rise time about 12 ns) and then performs periodic relaxation oscillations. The amplitude of the voltage peaks indicates that the device is in a totally normal state at the peak of the oscillation. We can show this by multiplying the average current (about 0.2 mA for the data in Figure 4) by the full normal

resistance (R_N = 150 Ω) of the device. We find a voltage of 30 mV, which agrees with the peak voltage amplitude in Figure 4. When the relaxation oscillations die out, the device returns to superconducting, as indicated by the voltage across it being zero. The corresponding current during the relaxation oscillations used in this estimate is the average current in the instability region. The current also shows (weaker) relaxation oscillations. When the oscillations vanish, and the device is temporarily back to being superconducting, the current gradually increases, reaches the critical value, and the cycle repeats. The repetition rate of the waveform increases with increasing bias voltage, as shown in Figure 5.

III DISCUSSION

We now discuss the measurement results in terms of a one – dimensional hotspot model.

The Superconducting State

It has been claimed that the main mechanism which determines the critical current in the superconducting state of an HEB device is vortex pinning. As long as the pinning force is larger than the Lorenz force, the device remains in the superconducting state. But our calculation concludes that there are no vortices available in the NbN film of an HEB device of a typical size. For example, in the simplest case, we consider a strip with width W = 5μm; length L = 1μm; thickness d = 4 nm; and total current I = I_C =500μA. The x-direction is along the device width. The H field in the x-direction (perpendicular to the current direction) is more or less independent of x, except for at the edges. Although the field has a singularity at the edges, this singularity is of no consequence when we integrate the field in order to obtain the total flux. We can then estimate that $B_x = \mu_0 H_x = \mu_0 I / 2W = 1.2\times10^{-4}$ Vs/m^2, and the total flux $\Phi = 3\times10^{-16}$Vs. However, a vortex must contain a minimum flux of one flux quantum, which is $\Phi_0 = 2\times10^{-15}$ Vs. *Thus vortices can not exist in this strip.* The critical current is probably determined by depairing of the Cooper pairs rather than by vortex pinning.

Instability Region

In earlier studies it has been found that the superconductivity can be destroyed by Joule self – heating even when the transport current is much lower than the critical current [1],[3],[4]. The cooling and heating mechanisms obey the heat balance equation:

$$Q(T) = W(T) \tag{4}$$

$$W(T) = \frac{h(T)}{d}(T - T_0) \tag{5}$$

Here Q(T) = jE(T) is the power of the Joule heat released per unit volume. W(T) is the specific power of heat transfer to the coolant kept at a bath temperature T_0, h(T) is the heat transfer coefficient, d =A/P, A is the area, and P is the perimeter of the cross section of the specimen. A bistability occurs when this equation holds for several temperatures, as shown

in Figure 6, where there are three intersection points between Q(T) and W(T). The step shape of the Q(T) curve is due to the stepwise increase of the resistivity ρ(T) around the critical temperature T_C. The stability of the three points 1, 2, and 3 with respect to a small perturbation is determined by the following criterion:

$$\frac{\partial W}{\partial T} > \frac{\partial Q}{\partial T} \tag{6}$$

From the above equation we can see that the states corresponding to the phases T_1 and T_3 are stable, and the state corresponding to phase T_2 is unstable. There is a simple method to decide the condition of stability that introduces the Stekly parameter α defined as:

$$\alpha = \frac{\rho_n j_C^2 d}{h(T_C - T_0)} \tag{7}$$

where ρ_n is the resistivity in the normal state, and j_C is the critical current at the bath temperature. It turns out that the differential conductivity can be expressed by α as:

$$\sigma(E) = (1-\alpha)\rho_n^{-1} \tag{8}$$

The condition for obtaining the above equation is $j_C >> E\rho_n^{-1}$ which is satisfied in thin superconducting films. For example, the typical value of j_C in our NbN devices is around 1-3 x 10^6 A/cm^2, and $E\rho_n^{-1}$ is about 10^5 A/cm^2 for NbN thin film material. The differential conductivity becomes negative when $\alpha > 1$, which indicates that there is a thermal instability in the resistive state. Obviously, the upper limit of the current density in order to get the thermal instability is j_C, while the lower limit j_m can be calculated by assuming that the temperature of the superconductor at $j = j_m$ is T_C; then j_m can be expressed as:

$$j_m = \left[\frac{h(T_C)T_C}{\rho_n(T_C)d}\right]^{1/2}\left[1-\frac{T_0}{T_C}\right]^{1/2} = j_C\alpha^{-1/2} \tag{9}$$

Here j_m depends on the characteristics of the superconductor and the coolant parameters, and can be much lower than the critical current j_C. Now the transport current density should be in the range $j_C\alpha^{-1/2} < j < j_C$ in order for Q(T) and W(T) to have three intersection points. Reference [1] shows that the lower limit is actually $j_P = \sqrt{2}j_m$. Outside this range the superconductor material will be in one of the stable states. In the case of NbN HEB devices, the value of α is usually much larger than 1. For example, typical values for a device such as the one used to obtain the data in Figures 3 and 4, are ρ_n=2x10^{-4} Ωcm, j_C=2x10^6 A/cm^2, d=5×10^{-5} cm, h=20 W/cm^{2}K, T_C=10K, T_0=4.2K. Substituting the above values in equation (7) we get $\alpha = 287 >> 1$. The lower limit for the current, I_P, is estimated to be 30 μA,

whereas Ic = 400 μA. The bistability is thus potentially very strong. We can interpret the behavior of NbN HEB devices that we observed in Figure 4 in terms of propagation of switching waves, which describes the movement of the domain walls between the two stable states: superconducting and normal states. The domain wall moves in one direction when transforming from one stable state to the other, or vice versa, depending on the value of j. The velocity c of the propagation can be expressed as in [5]:

$$c(i) = \left(1 + 0.561\alpha^{-1.45}\right)(M-1)/\sqrt{M} \tag{10}$$

$$M = \left(\alpha i^2 - 1 + \frac{i}{2}\right) \Big/ \left(1 - \frac{i}{2}\right) \tag{11}$$

Here c(i)= v/v_h, v_h= L/t_h, where L and t_h are the characteristic thermal length and time, and i= j/j_C is the dimensionless current density. The c value as a function of dimensionless current i is plotted in Figure 7. We also estimate $v_h = 10^4$ cm/sec. Our interpretation of the device behavior in region (3) can then be summarized as follows:

1) After j_c has been exceeded, a normal domain spreads with an initial normalized velocity c = 24. The expansion will slow as the resistance grows, and the current decreases, until the normal domain reaches the contacts. The average velocity during the initial expansion can be estimated to be $10 \times v_h = 10^5$ cm/s. The initial velocity is so high that it is close to the sound velocity in the film, which should act as an ultimate speed limit. The estimated time for a domain to cover half the length of the device is about .5 ns, a very short time, while we measured a value of 12 ns. The initial rise time is, however, also influenced by the response time of our measurement system, which we checked by a measurement using a fast (6 ns rise time) pulse generator substituting for the HEB device. The rise time was found to be 15 ns which confirms that we could not have measured the rise time of the HEB device waveform if it had been as fast as .5 ns.

After the initial transient, the voltage and current oscillate around an average current of about 200 μA. From the bistability theory, we would expect that for $j > j_P$, the domain would grow with increasing velocity until it reaches the contacts, and $R = R_N$. In region (3) there is not enough power available to sustain a stable hot spot, and the current has meanwhile decreased below j_P, which reverses the sign of the velocity, and the domain then decreases in size; the current subsequently increases above j_P again, leading to the domain oscillating back and forth until the device goes superconducting, etc.. The frequency of these relaxation oscillations can be found by estimating the time required for the domain to expand through about half the length of the device, and back again. We assume that the oscillations are sinusoidal. Also, the measured average current is 200 μA rather than the expected value of 30 μA, based on j_P, and $\alpha = 290$. The velocity curve for this larger average current value has also been plotted in Figure 4. It corresponds to $\alpha = 10$. If we assume that the oscillations occur around this current point, and use the measured peak current amplitude from Figure 4, we find a relaxation oscillation frequency of about 60 MHz, with a period of 16 ns. Instead, we measure the period of the oscillation to be roughly 160 ns, or a frequency of 6 MHz. In addition to the higher than expected average current, this seems to give us pretty clear evidence that one must include further physical

effects in the calculation of the propagation speed than the purely thermal effects (lateral thermal conduction and heat transfer to the substrate) which were included in the above calculation. Possible such effects are:

(a) The contacts are likely to be involved in the thermal balance, since the normal domain periodically reaches these. The contacts would add considerable heat capacity, and could have this effect.
(b) Recent modeling of phonon-cooled HEB devices while under LO illumination has shown bistable regions which may correspond to the bistability discussed here [6]. It has also been argued that the hotspot should be defined in terms of the critical current as a function of position in the device, rather than the electron temperature [7]. The latter paper also showed that Andreev reflection at the superconducting/normal boundary should have an influence on the temporal response of the device. A very preliminary calculation [8] of the oscillation relaxation frequency yielded 30 MHz, which is closer to the measured value than our simplified estimate above.
(c) The thermal healing length in the above calculation is about half the length of the HEB device, which will introduce some further error to the simple estimate of the relaxation oscillation frequency, which is based on an infinitely long strip.

We want to emphasize that the relaxation oscillation frequency has been determined to be independent of the external circuit, and must be related to the physics of the device itself. The theory may be better fitted by measuring a longer device, an experiment which we are now planning to perform.

2) The device is superconducting during a portion of the repetitive behavior measured in Figure 4. During this time no power can thus be dissipated. The current rises driven by the voltage supply, and we interpret the delay in reaching I_c as due to the effect of the time constant determined by the inductance in the LP-filter and the cable, together with resistance r. The measured inductance is 20 μH, which yields a time constant of about 2 μs, which agrees reasonably well with our measured waveform. This also explains that the repetition rate of the waveform increases with increasing DC voltage, as shown in Figure 5. Note that the duration of the part of the repetitive waveform when the relaxation oscillations occur, is more or less independent of the voltage.

3) In region 2, we also observe slower oscillations, at frequencies of the order of hundreds of Hz, which can be changed by adding elements to the external circuit. Substituting a simple bias supply consisting of a battery and a potentiometer, eliminates these lower frequency oscillations, and only the relaxation oscillations are observed. These are thus clearly the most fundamental phenomenon observed in the negative resistance region.

Consequences for device behavior in active mixer operation

The model we have used to estimate the rate at which a hot-spot domain can vary its size could also be used to analyze device models in the stable state, where LO power is applied to bring the differential conductivity to positive values. The modeling required for actual HEB mixer operation is likely to be much more complex, as shown in papers by Merkel et al. [6,7]. The advantage of our approach is that it is possible to test the models for the bistable regions and for the temporal response of hotspots with relatively simple measurements. Our experiments also detect higher frequencies in the GHz range, when the HEB device is measured in the bistable region through a low-noise cooled HEMT amplifier.

IV. CONCLUSION

In this paper we measured the voltage and the current of the NbN HEB device simultaneously in the bistability region. We conclude that no vortices can exist in a typical NbN HEB strip. The transition between the superconducting state and the normal state was interpreted qualitatively as the propagation of a switching wave. The calculated relaxation oscillation frequency based on the domain velocity is about ten times higher with the measured result. We expect that use of a more detailed model of the device will result in closer quantitative agreement with measurements in the future. Also, measurements on longer devices, which we plan to carry out, should facilitate better agreement between theory and experiment.

ACKNOWLEDGEMENTS

We would like to acknowledge stimulating discussions with Dr. Harald Merkel of Chalmers University of Technology. We would also like to acknowledge support from NASA Contract NAS1-01058 from NASA Langley Research Center.

REFERENCES

[1] A.VI. Gurevich and R.G. Mints, "Self-Heating in Normal Metals and Superconductors," Rev. Mod. Physics, **59**, 941 (1987).

[2] Y. Zhuang and K.S. Yngvesson, "Negative Resistance Effects in NbN HEB devices," 12th Intern. Symp. Space THz Technol, San Diego, CA, Feb. 2001, pp. 143-153

[3] V.A. Altov, V.B. Zenkevitch, M.G. Kremlev, and V.V. Sytchev, "Stabilization of Superconducting Magnetic Systems (Plenum, New York)", 1977.

[4] V.L. Newhouse, Applied Superconductivity (Wiley, New York), 1964

[5] L. Dresner, "Analytic Solution for the propagation velocity in superconducting composites", IEEE Trans. Magn. **15**, 328, 1979

[6] H.F. Merkel, P. Khosropanah, K.S. Yngvesson, S. Cherednichenko, M. Kroug, A. Adam, and E.L. Kollberg, "An Active Zone Small Signal Model For Hot Electron Bolometric Mixers,", 12th Intern. Symp. Space THz Technol, San Diego, CA, Feb. 2001, pp. 67-74

[7] H. F. Merkel, et al., "A Model for the Optimum Performance of NbN HEB Mixers", this symposium.
[8] H.F. Merkel, private communication.

FIGURES

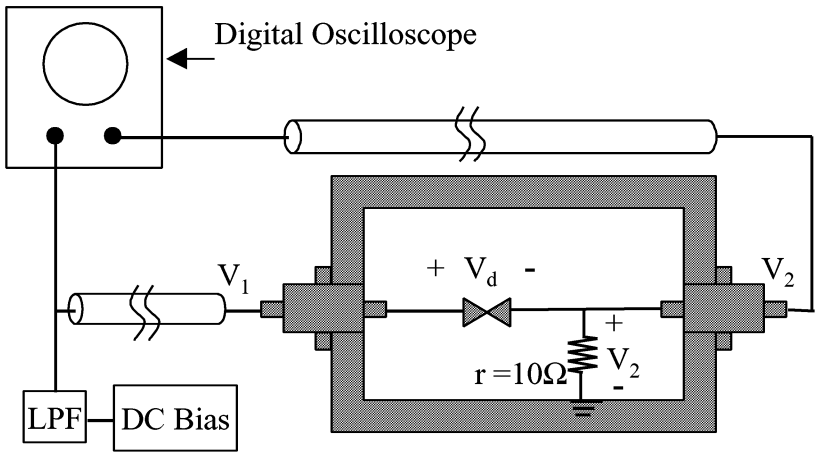

Figure 1: Experimental Setup for the current and voltage measurement of the NbN HEB device

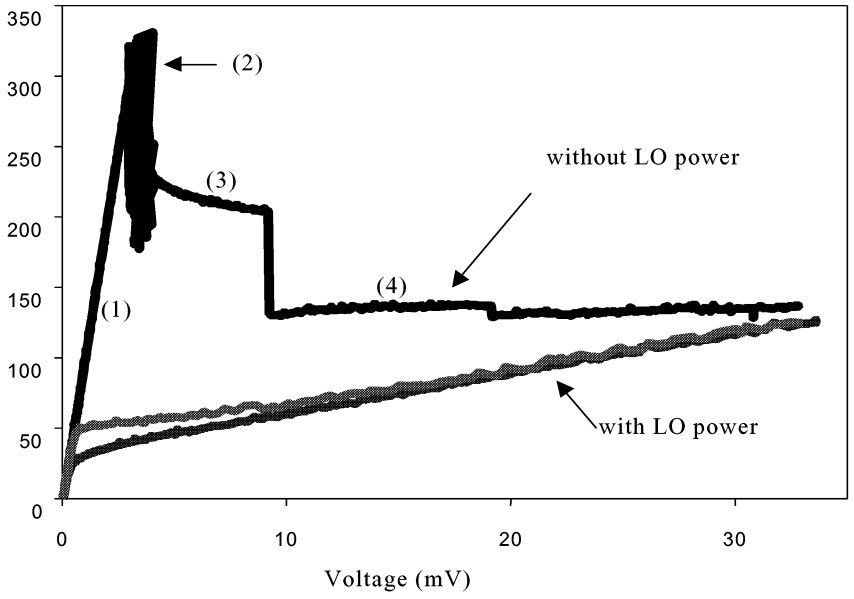

Figure 2 Typical voltage biased I – V characteristics of a HEB device

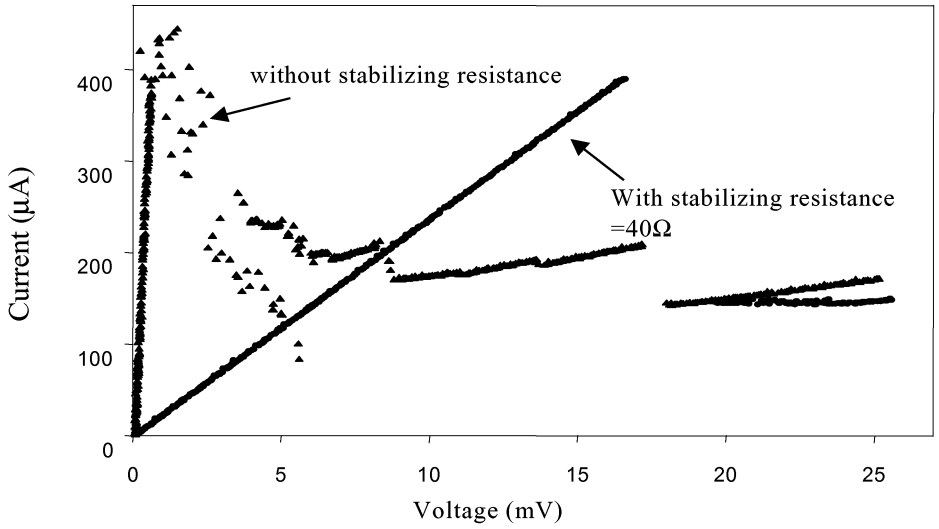

Figure 3: I –V characteristics of a HEB device with stabilizing resistor

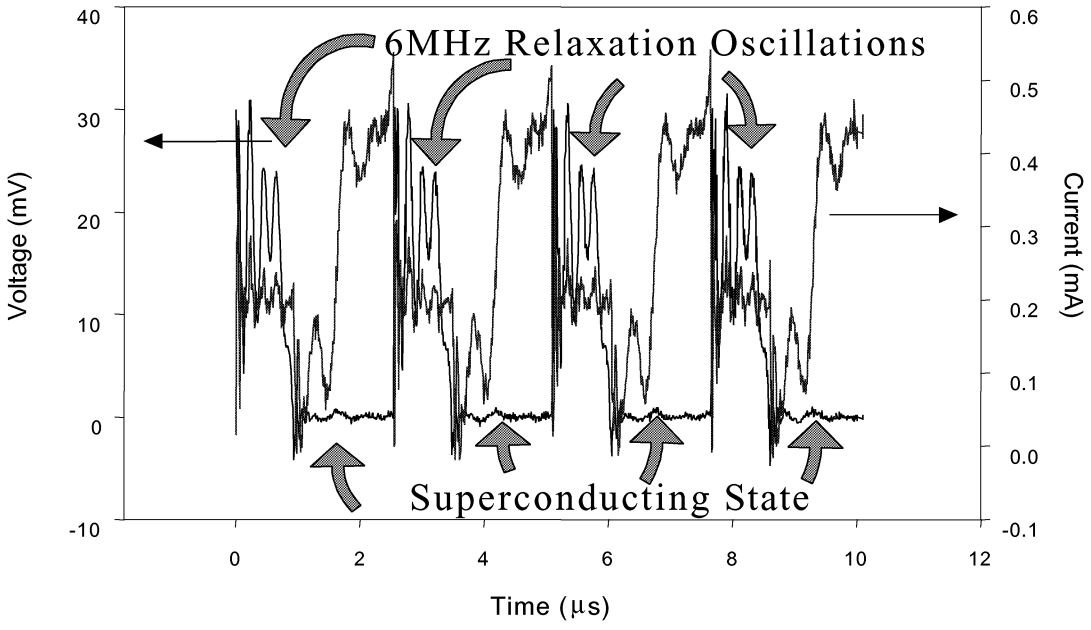

Figure 4: Voltage and Current waveform in the bistability region of the HEB device

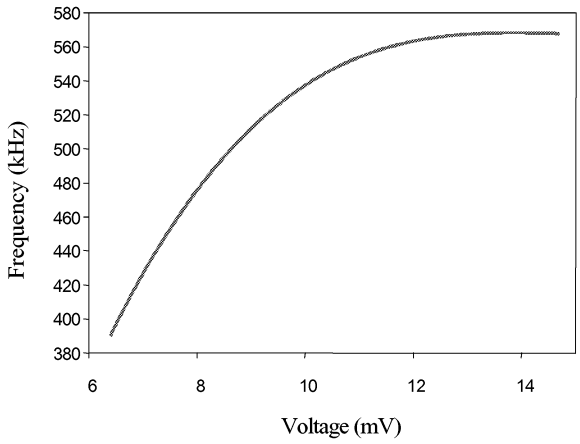

Figure 5: Repetition frequency as a function of the bias voltage

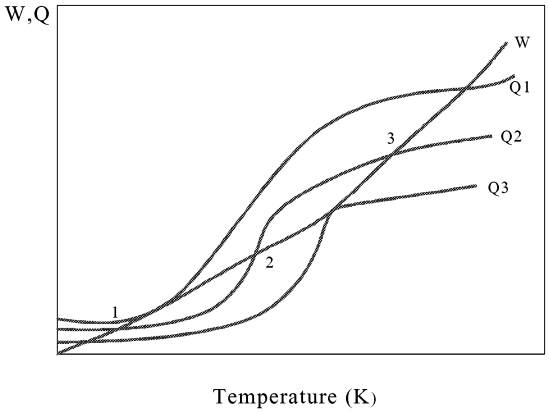

Figure 6: W and Q curves as a function of temperature

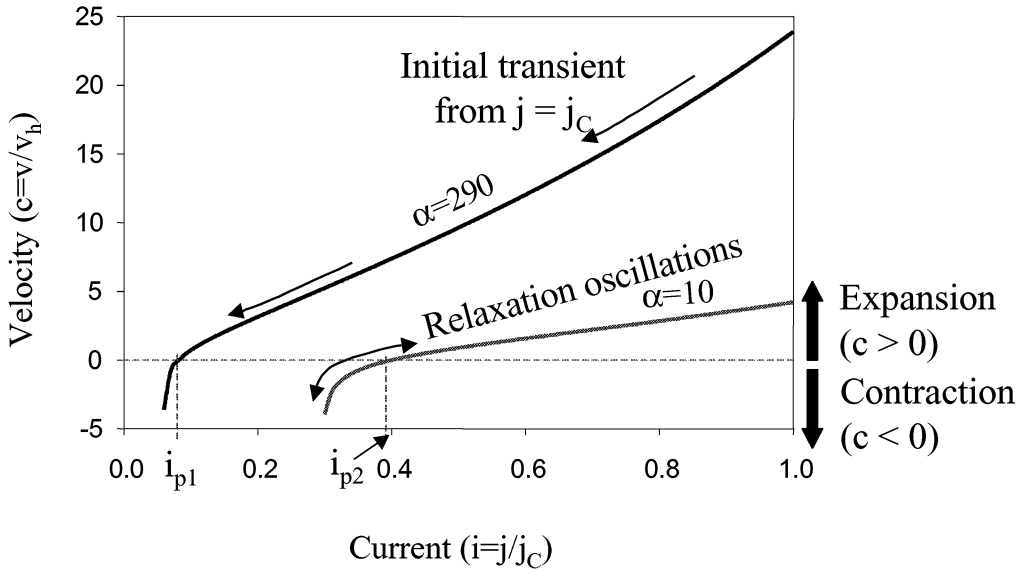

Figure 7: $c(i) = v/v_h$ as a function of $i=j/j_C$ for $\alpha = 290$ and $\alpha=10$

SUPERCONDUCTING PHASE-LOCKED LOCAL OSCILLATOR FOR SUBMM INTEGRATED RECEIVER*

V.P. Koshelets[1,2], P.N. Dmitriev[1], A.B. Ermakov[1], A.S. Sobolev[1], M.Yu. Torgashin[1], V.V. Khodos[2], V.L. Vaks[2], P.R. Wesselius[3], C. Mahaini[4] J. Mygind[4],

[1]Institute of Radio Engineering and Electronics, Moscow, Russia
[2]Institute for Physics of Microstructure, Nizhny Novgorod, Russia
[3]National Institute for Space Research (SRON), Groningen, the Netherlands
[4]Department of Physics, Technical University of Denmark, Lyngby, Denmark

ABSTRACT

Presently a Josephson Flux Flow Oscillator (FFO) appears to be the most developed superconducting local oscillator for integration with an SIS mixer in a single-chip submm-wave receiver [1, 2]. A receiver DSB noise temperature below 100 K has been achieved for a superconducting integrated receiver (SIR) operating with an internal FFO in the frequency range 480 - 520 GHz. The feasibility of phase locking a FFO to an external reference oscillator at all frequencies of interest has to be experimentally proved because it is vitally important for practical use of the SIR in high-resolution spectral studies. The increase of the intrinsic FFO linewidth due to the larger internal damping caused by Josephson self-coupling (JSC) effect at voltages $V > V_{JSC} = V_{gap}/3$ considerably complicates phase locking of the FFO. Comprehensive measurements of the FFO radiation linewidth have been performed using an integrated harmonic SIS mixer; the obtained FFO linewidth and spectral line profile have been compared to theory. The influence of the FFO parameters on the radiation linewidth, particularly the effect of the differential resistances associated both with the bias current and the applied magnetic field has been studied in order to optimize the FFO design. New FFO designs have resulted in a free-running FFO linewidth of about 10 MHz in the flux flow regime up to 712 GHz, limited only by the gap value of the Nb-AlOx-Nb junction. This narrow free-running linewidth along with the construction of a wide-band PLL system has enabled us to phase lock the FFO throughout the frequency range 490 – 712 GHz where continuous frequency tuning is possible. An absolute FFO phase noise as low as –73 dBc and –69 dBc at 100 kHz offset from the carrier has been achieved at 450 and 707 GHz, respectively. This satisfies the requirements for single dish radio astronomy missions and atmospheric monitoring.

*The work was supported in parts by the Russian SSP "Superconductivity", RFBR projects 00-02-16270, INTAS project 01-0367, the Danish Research Academy, the Danish Natural Science Foundation, the Hartmann Foundation, and the Nederlandse Organisatie voor Wetenschappelijk Onderzoek (NWO). Authors thank A. Baryshev, T. de Graauw, M. Khapaev, M. Kupriyanov, A. Pankratov, M. Samuelsen, S. Shitov, H. van de Stadt, A. Ustinov and N. Whyborn for fruitful discussions

Lightweight and compact ultra-sensitive submm Superconducting Integrated Receivers (SIR) [1, 2] with low power consumption are very suitable for both radio-astronomical research and remote monitoring of the Earth atmosphere. The SIR is a single-chip device, which comprises an SIS-mixer with a quasioptical antenna and a superconducting local oscillator. Presently, the Flux Flow Oscillator (FFO) [3] based on unidirectional flow of magnetic vortices in a long Josephson tunnel junction is the best choice for integration with an SIS mixer. Nb-AlO_x-Nb FFO's have been successfully tested as local oscillators from 120 to 700 GHz (gap frequency of Nb) providing enough power to pump an SIS-mixer (about 1 μW at 450 GHz). Both frequency and power of the FFO can be dc tuned [2, 4]. A receiver DSB noise temperature below 100 K has been achieved for a SIR with the FFO operated in the frequency range 480 - 520 GHz [2, 5]. The antenna beam, approximately f/9 with sidelobes suppressed below -16 dB [2], makes the integrated receiver suitable for coupling to a telescope. An imaging array of nine SIRs has been developed and tested [2, 5].

The frequency resolution of a receiver is one of the major parameters in spectral radio astronomy. In order to obtain the required frequency resolution of at least one part per million and to allow interferometric measurements the local oscillator must be phase-locked to an external reference. In order to study the conditions for phase locking of the FFO linewidth has been measured using a specially developed technique based on an integrated harmonic mixer [6]; see also [2, 4]. An unexplained superfine resonance structure on the FFO IVC was resolved by this technique [7]. This structure considerably complicates FFO phase locking. In order to avoid this structure and to realize permanent frequency tuning (at least along the Fiske steps) we have developed a new design of the FFO. The new FFO is tapered at both ends so that its width is decreased from 6 μm to 1.5 μm over a distance of 20 μm (see Fig. 1). As a result of this modification the resonant structure was almost suppressed. It should be noted that a tapered FFO has larger output impedance compared to the usual FFO of rectangular shape. This also simplifies the impedance matching to the microwave circuits.

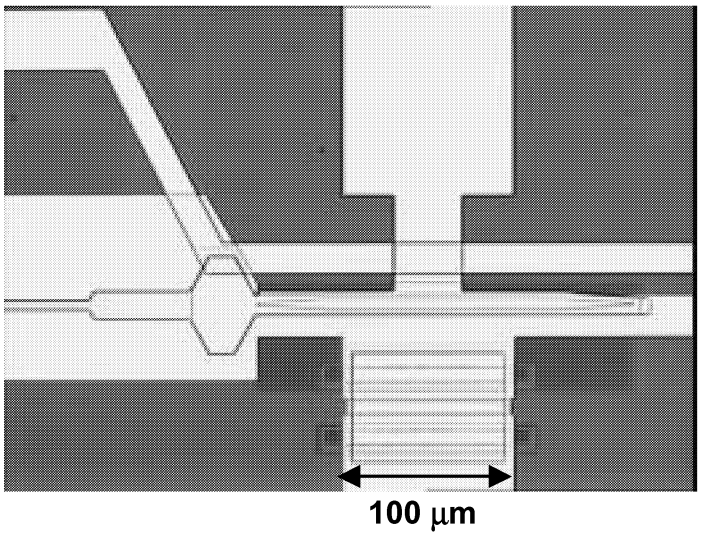

Fig. 1. Photo of the tapered FFO with separate control line for magnetic tuning.

The absence of the resonance structure enables detailed analysis of the free-running FFO spectrum. The FFO line profile has been measured in different regimes of FFO operation and compared to theoretical models. For this we use a frequency locking system with a relatively low loop gain (so called, frequency detector). Thus very low-frequency noise and drift is eliminated by the narrow-band feedback and the "natural" linewidth, determined by much faster fluctuations, can be measured. The shape of the FFO spectrum provides important information about the relationship between internal and external fluctuations as well as the spectral distribution of these fluctuations. According to theory [8, 9] the line shape is Lorentzian for wideband fluctuations, whereas the profile will be Gaussian for narrow-band external electromagnetic interference, e.g. EMI with frequencies smaller than the free-running FFO linewidth δf_{AUT}. A Lorentzian shape of the FFO line has been observed both at higher voltages on the flux flow step (FFS) [10] and at Fiske steps (FS's) [11] in the resonant regime. This means that the free-running FFO linewidth in all operational regimes is determined by wideband thermal and shot noise fluctuations. That is very different from traditional microwave oscillators where the "natural" linewidth is very small and the observed linewidth can be attributed mainly to external fluctuations.

According to theory [8, 9] the radiation linewidth of a small (lumped) Josephson oscillator is determined by the noise spectral power density, $S_I(0)$, of the bias current at low frequencies, $0 < f < \delta f_{AUT}$, where δf_{AUT} is the linewidth of the free-running junction. This noise spectral density is a nonlinear superposition of wide-band thermal and shot noise converted by the Josephson junction to low frequencies [8, 13]. The current noise is transformed into voltage (and consequently, frequency) fluctuations by the differential resistance, $R_d^B = \partial V/\partial I_B$, associated with the bias current I_B. The dependence of the calculate linewidth for the lumped tunnel junction is shown as curve 1 in Fig. 2. The experimental values of the FFO linewidth (asterisks in Fig. 2) are considerably larger than predicted [8, 13, 14]. Furthermore, there is a plateau where the linewidth does not decrease below a few hundreds of kilohertz while R_d^B decreasing below 0.003 Ω. To explain such behavior an additional noise contribution is needed; furthermore since the FFO line shape remains Lorentzian at FSs with small R_d^B we can conclude that this extra noise is wideband. Thus the standard noise model for lumped (short) tunnel junction is insufficient to explain the noise associated with the flux flow in the distributed long Josephson junction.

Recently an additional noise term, which accounts for the influence of the wideband noise in the bias current introduced via the magnetic field control line, has been added to form a phenomenological FFO model [11] (see also [15]):

$$\delta f = (2\pi/\Phi_0^2)\,(R_d^B + K*R_d^H)^2\, S_i(0), \qquad (1)$$

where $R_d^H = \partial V_{FFO}/\partial I_H$ is the differential resistance associated with the magnetic field , and K is a coefficient of the order of unity. Note that $R_d^H = (\partial V_{FFO}/\partial I_{CL})/M$, where M is the mutual inductance between the control line and the FFO, I_{CL} is the current in the control line. This model allows us to calculate quantitatively the FFO linewidth in the whole operational range (see Fig. 2 – solid line). The calculated dependence of the linewidth of the lumped tunnel junction [8, 13] for the case of wide-band fluctuations only via I_B ($K = 0$) is shown in Fig. 2 by the dashed line 1), the dependence for fixed values of $R_d^{CL} = 0.003$ Ω

and R_d^{CL} = 0.03 Ω are presented by the dotted and the dash-doted lines 2) and 3), respectively. The solid line is calculated for each experimental point taking into account all relevant parameters (I_B, V, R_d^B, R_d^{CL}, etc.). Indeed the calculations agree with the measured linewidth over the whole range of experimental parameters by using K =1 both on the Fiske steps and on the flux flow step. The fact that K =1 gives the best fit is not understood, but it may relate to the geometry of the junction and the control line. The increase of the intrinsic linewidth at the R_d^B value of about 0.01 Ω is related to the strong increase of the internal damping [12] caused by Josephson self-coupling (JSC) at voltages $V > V_{JSC} = 1/3*V_{gap}$ (V_{JSC} corresponds to 450 GHz for Nb-AlO_x-Nb FFO). As a result the FFO IVCs are deformed at V_{JSC} (see Fig. 4 below) and R_d^{CL} increases. The dependence of the FFO radiation linewidth on R_d^{CL} is shown in Fig. 3

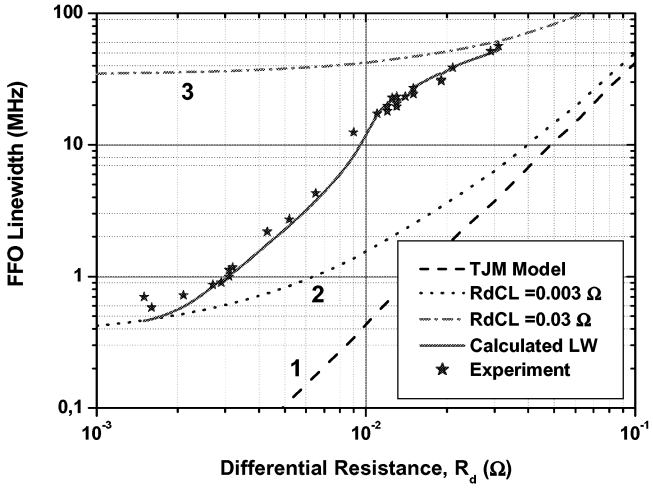

Fig. 2. Dependence of FFO radiation linewidth on the bias current differential resistance R_d^B. Curves 1 - 3 are calculated for the following parameters: V_{dc}= 1 mV, I_{qp}=3 mA, I_s=7 mA, T_{eff}= 4.2 K.

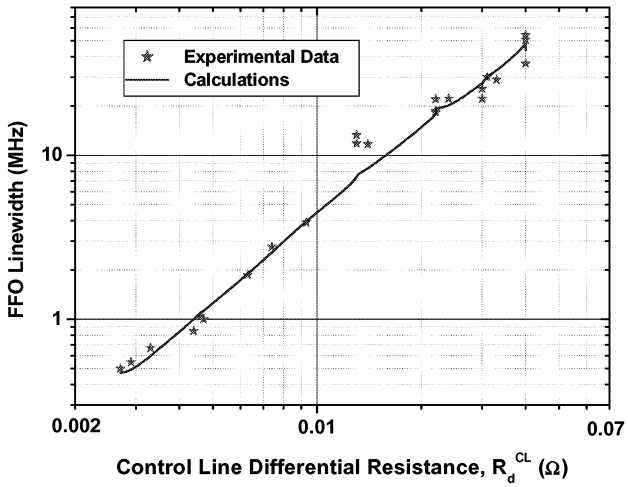

Fig. 3. Dependence of the FFO radiation linewidth on the control line differential resistance R_d^{CL}. The solid curve is calculated for each experimental point for measured parameters (I_B, V, R_d^B), T_{eff}= 4.2 K.

In order to phase lock the FFO one has to decrease the free running linewidth, which (in accordance to Eq. 1 and Fig. 2, 3) is mainly determined by R_d^B and R_d^{CL}. New designs of the FFO have been developed to achieve this, one design is shown in Fig. 1. A typical set of the corresponding FFO IVCs is shown in Fig. 4. Data were recorded with incremented magnetic field. Each IVC was measured for a fixed control line current, $I_{CL,}$ which is then incremented by $\Delta I_{CL} \approx 0.5$ mA before the next IVC is recorded. The dependence of the R_d^B and R_d^{CL} on the FFO voltage is shown in Fig. 5.

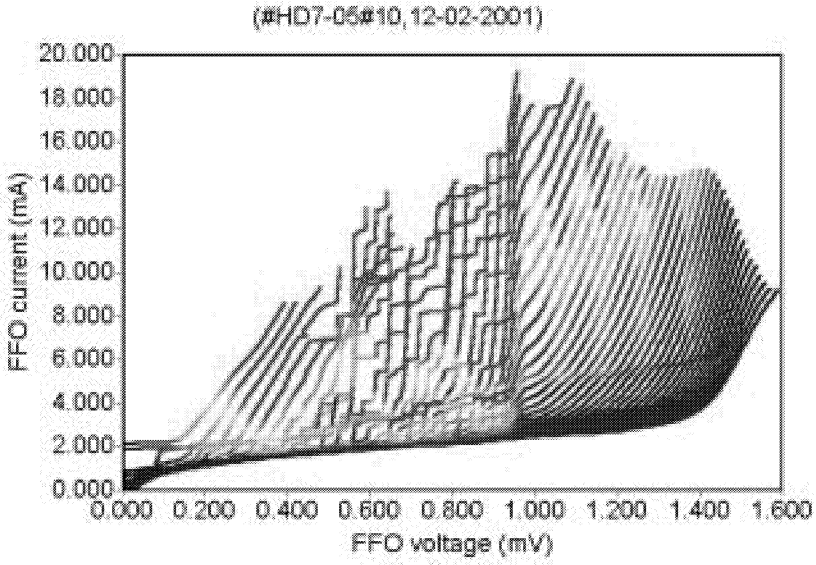

Fig. 4. IVCs of the FFO with new design, measured with incremented magnetic field (I_{CL} = 10–35 mA)

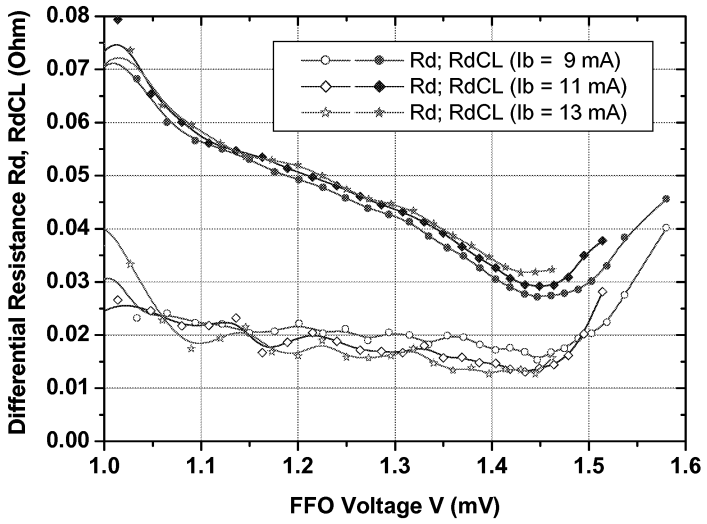

Fig. 5. Dependence of the differential resistances R_d^B and R_d^{CL} on FFO voltage, measured at different bias currents, I_B.

Fig. 5 shows a well-defined dependence of R_d^{CL} on bias voltage (FFO frequency). This has been observed for all tested FFO of very different designs and may be considered as universal and fundamental. Presumably it reflects the fact that introduction of an additional fluxon in the junction requires increasing control line current as the fluxon chain gets denser. One can see that R_d^{CL} has a minimum at 1.45 mV (corresponding to a FFO frequency of 725 GHz). The position of this minimum approximately coincides with $V_g/2$ and changes with temperature as V_g. At I_B = 11 mA the R_d^{CL} value increases considerably from 0.03 Ω (that results in free-running linewidth of about 5 MHz) to almost 0.08 Ω at 500 GHz (1.03 mV). The free-running FFO linewidth correspondingly increases almost 10 times that considerably complicates the phase locking of FFO. Note that the JSC effect is important only for 0.9 mV < V < 1.1 mV.

The FFO, as any Josephson junction, is a perfect voltage-controlled oscillator and hence its frequency can be stabilized and the FFO linewidth can be decreased by phase locking to an external reference source using a phase-lock loop (PLL) system with bandwidth larger than δf_{AUT}. Actually, a PLL system will effectively suppress the influence from external low frequency fluctuations and alter the differential resistances R_d^B and R_d^{CL} in the bias point. We have developed a special PLL unit utilizing an integrated SIS harmonic mixer to down-convert the FFO signal to a 400 MHz IF signal. After amplification the IF signal is compared to a 400 MHz reference signal in an analog phase detector, the output of which is fed to the FFO bias supply. All reference signals as well as the spectrum analyzer used to display the phase noise on the IF signal are phase-locked to a common 10 MHz reference oscillator. The PLL unit is optimized for operation with a low signal-to-noise ratio at a minimal time delay (measured delay of about 5 ns corresponds to a regulation bandwidth of 50 MHz). The bandwidth of the complete PLL system, Δf_{PLL}, is further limited to 15 MHz due to the delay in its 2 m long cables, but it still exceeds the free-running linewidth of the FFO with new design.

Earlier, phase locking of a Josephson oscillator was demonstrated in the frequency range 250 – 450 GHz [16] for a FFO biased on resonant Fiske steps. In this case the initial free-running FFO linewidth (FWHP, full width, half power) was only about 1 MHz due to the low dynamic resistance of the Fiske resonances. The new design of the FFO [10, 11] results in a decrease of the free-running FFO linewidth in the flux flow regime for $V > V_{JSC}$. Along with development of an improved wideband PLL system it enables us to phase lock FFO in the frequency range from 490 to 712 GHz, limited only by the gap value of the Nb-AlOx-Nb junction. Fig. 7 demonstrates the spectra of the frequency and phase locked FFO operating at 707 GHz. The wings at the curve "A" of Fig. 7a mark the frequency difference from the carrier at which the phase of the return signal from PLL system is shifted by π/2 that results in some increase of the phase noise.

The PLL system, of course, cannot change the wide-band thermal and shot noise fluctuations, but it can diminish both differential resistances (at frequencies $f < \Delta f_{PLL}$) to zero. This manifests itself as a constant-voltage step in the dc I-V curve of the FFO. Note that a similar step with finite slope and larger voltage and current span appears when the FFO is only frequency locked (see Fig. 6). The voltage locking range here is about 5 μV corresponding to a frequency range of about 2.5 GHz.

According to Eq. (1) the zero dynamic resistance created by the PLL system results in an infinitely sharp spectral line. Indeed, as seen in Fig. 7 b, a 1 Hz linewidth is measured at 707 GHz relative to the reference oscillator. The 1 Hz is an artifact caused by the limited frequency resolution of the spectrum analyzer. One can see that the residual phase noise is as low as 75 dB below the carrier. The dependence of the phase noise on the frequency offset from the carrier is shown with diamonds in Fig. 8. Even lower phase noise has been measured for a FFO in the resonant regime when biased on the steep Fiske steps, f = 450 GHz (see Fig. 8). In order to find the "absolute" (total) phase noise of the phase-locked FFO one should add the noise of the reference oscillator multiplied by n^2 where n is the harmonic number used in the harmonic mixing. The absolute FFO phase noise (solid lines in Fig. 8) is dominated by the reference oscillator noise for offsets < 1 MHz. Note that the measured phase noise already meets the requirements for single dish radio astronomy and atmospheric missions. It should be mentioned that the phase noise at large offsets probably is limited by the measuring system rather than by the FFO itself.

Since the free-running FFO line shape is Lorentzian, the FFO power inside the effective PLL regulation bandwidth can be calculated, see Fig. 9. From this figure one can see that the initial FFO linewidth should not exceed 3.5 MHz to insure that the phase-locked FFO oscillates with 90% of the total power. The present set-up has an effective PLL bandwidth of about 15 MHz. The "unlocked" rest of the total FFO power will increase both the phase noise (compare curves with different free-running linewidth in Fig. 8) and the calibration error. The calibration error of the spectrometer noise temperature will be approximately equal to the percentage of the unlocked FFO power. To overcome this problem an additional decrease of the FFO free-running linewidth (new designs with smaller R_d^B and R_d^{CL}) and an increase of the PLL regulation bandwidth are required. In this respect the ongoing design of a new ultra-wideband PLL system that can operates at cryogenic temperature seems very promising.

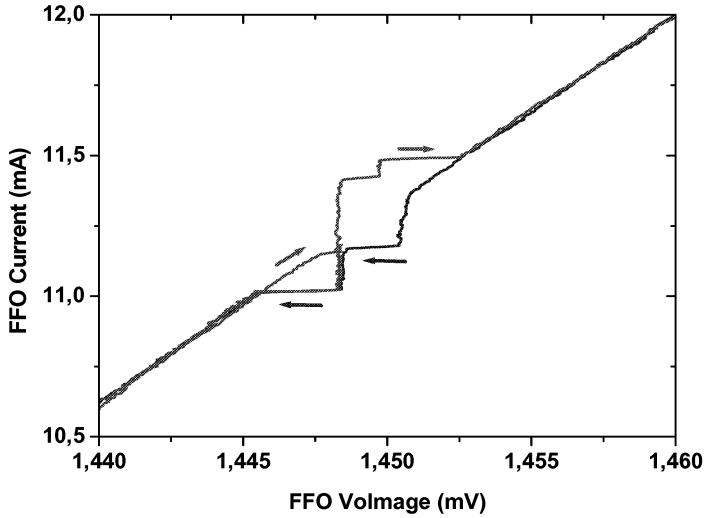

Fig. 6. IVC of a FFO, frequency locked at 700 GHz.

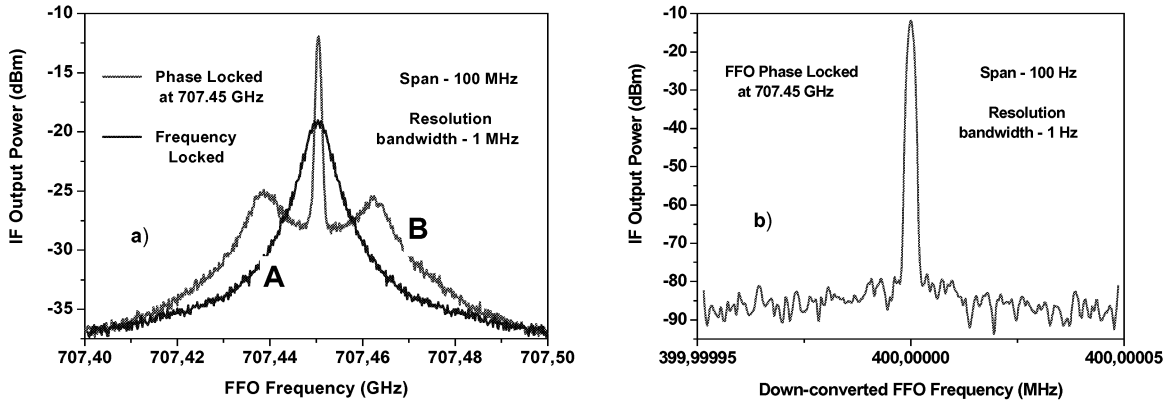

Fig. 7. Residual spectra of a FFO operating at 707.45 GHz. **(a)** Frequency locked FFO (A) and phase-locked FFO (B); the free-running linewidth is δf_{AUT} = 6.3 MHz, spectrum analyzer span 100 MHz. **(b)** Down-converted spectrum, span 100 Hz. T = 4.2 K

In order to resolve a weak signal adjacent to a strong line the PL FFO must have a well-defined line-shape. The dynamic range of the spectrometer is closely related to the ratio between the carrier and the spectral power density (FFO phase noise) at a frequency offset equivalent to the channel spacing of the spectrometer. The phase noise of the phase-locked FFO is about -80 dBc/Hz at the 1 MHz offset from the carrier for f_{FFO} = 700 GHz (see Fig. 8). For a 1 MHz channel this gives a dynamic range of 20 dB for the spectrometer. This figure exactly corresponds to the requirements for the HIFI wide band spectrometer (WBS).

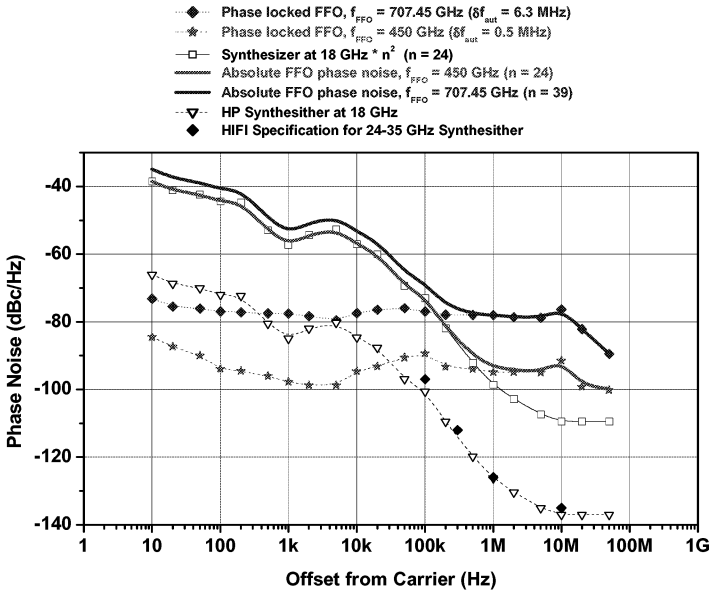

Fig. 8. **P**hase noise of a phase-locked FFO measured at different frequencies. Since the phase noise of the FFO is measured relative to the n^{th} harmonic of a synthesized oscillator, its noise, multiplied by a factor n^2, should be added to the residual FFO noise to get the total (absolute) FFO phase noise – solid and dash lines.

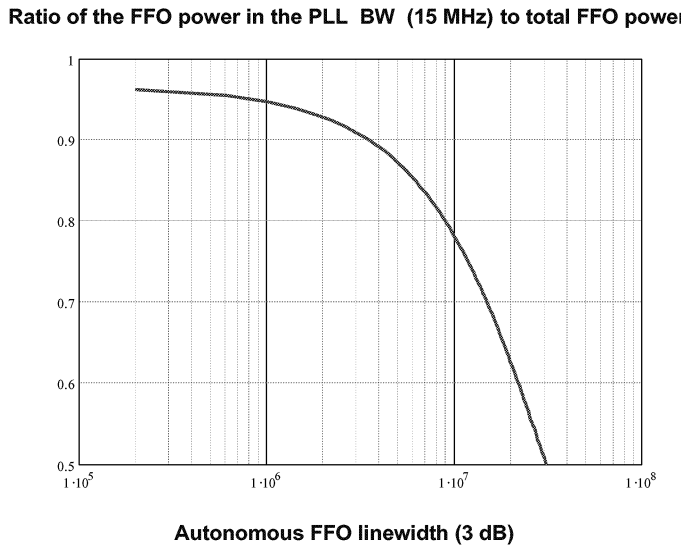

Fig. 9. Dependence of the ratio of phase-locked FFO power to total power emitted on the autonomous 3 dB linewidth, calculated for a Lorentzian line shape and an effective PLL BW = 15 MHz.

The noise level of a phase-locked FFO at an offset from the carrier equal to the receiver intermediate frequency (IF) will couple to the SIS mixer and raise the SIR noise level. Usually the IF (say, 4 – 8 GHz) is far above the PLL regulation bandwidth (< 100 MHz), the phase noise of the synthesizer and PLL will not contribute to the FFO noise. However, for safe calculations of the requirements for FFO noise at large offsets we may assume that this noise, T_{LO}, contributes less than 10% of the receiver noise (say T_R = 200 K at 650 GHz, so T_{LO} < 20 K). This value of T_R corresponds to a value of about $0.65*hf/k_B$ at f = 650 GHz, where h and k_B are Planck´s and Boltzmann´s constants, respectively. The carrier power can be estimated as the power required for pumping a SIS mixer at a specified frequency. The optimal FFO power delivered to the mixer at the LO frequency is

$$P_{LO}^{opt} = (\alpha * hf_{LO})^2/(e^2 * R_{rf}), \quad (2)$$

where R_{rf} is the SIS mixer high frequency resistance (approx. the normal state resistance, say 10 Ω) and α =0.8. For f_{LO} = 650 GHz P_{LO}^{opt} = 460 nW. The allowed noise/carrier ration (NCR) can be calculated as

$$\text{NCR} = 10 \log (T_{LO} * k_B) - 10 \log (P_{LO}^{opt}) = -152 \text{ dBc/Hz}. \quad (3)$$

Certainly such low phase noise cannot be directly measured by any available technique. Indirectly, however, we already did this when we compared the noise temperature of the integrated receiver pumped by an internal FFO and an external local oscillator and carefully estimated the receiver noise temperature budget. Within the accuracy of the measurements we can conclude that the FFO did not add to the receiver noise temperature more than 20 K at an IF = 1-2 GHz. It should be noted that balanced mixers reject the LO noise to some degree and will further diminish the LO noise.

In conclusion, a considerable narrowing of the free-running FFO linewidth (compared to all previous measurements) along with the construction of a wide-band PLL system have enabled us to phase lock a Nb-AlOx-Nb FFO in the frequency range 490 – 712 GHz where continuous frequency tuning is possible. An absolute FFO phase noise as low as –73 dBc and –69 dBc at 100 kHz offset from the carrier has been achieved at 450 and 707 GHz, respectively. This satisfies requirements for single dish radio astronomy missions and atmospheric monitoring.

References

[1] V.P. Koshelets, S.V. Shitov, L.V. Filippenko, A.M. Baryshev, H. Golstein, T. de Graauw, W. Luinge, H. Schaeffer, and H. van de Stadt, *Appl Phys Lett,* **68,** 1273 (1996).

[2] V.P. Koshelets and S.V. Shitov, Superconductor Science and Technology, **13,** R53 (2000).

[3] T. Nagatsuma, K. Enpuku, F. Irie, and K. Yoshida, *J Appl Phys,* **54,** 3302 (1983), see also Pt. II: *J Appl Phys* **56,** 3284 (1984); Pt III *J Appl Phys* **58,** 441 (1985); Pt IV *J App. Phys* **63,** 1130 (1988).

[4] V.P. Koshelets and J. Mygind, "Flux Flow Oscillators For Superconducting Integrated Submm Wave Receivers", Studies of High Temperature Superconductors, edited by A.V. Narlikar, NOVA Science Publishers, New York, vol. 39, pp. 213-244, (2001).

[5] S.V. Shitov, A.B. Ermakov, L.V. Filippenko, V.P. Koshelets, A.M. Baryshev, W. Luinge, and J-R. Gao, *IEEE Trans on Appl Supercond.,* **9,** 3773 (1999).

[6] V.P. Koshelets, S.V. Shitov, L.V. Filippenko, A.V. Shchukin, and J. Mygind, *Appl Phys Lett,* **69,** 699 (1996).

[7] V.P. Koshelets, A.B. Ermakov, S.V. Shitov, P.N. Dmitriev, L.V. Filippenko, A.M. Baryshev, W. Luinge, J. Mygind, V.L. Vaks, D.G. Pavel'ev, Proceedings of the 11th International Symposium on Space Terahertz Technology, University of Michigan, Ann Arbor. May 1-3, (2000), pp 532-541.

[8] K.K. Likharev, "Dynamics of Josephson junctions and circuits" *Gordon and Breach Science Publishers* (1986).

[9] A.N. Malakhov, "Fluctuations in auto-oscillating systems", Science, Moscow, 1968 (in Russian).

[10] V.P. Koshelets, S.V. Shitov, P.N. Dmitriev, A.B. Ermakov, L.V. Filippenko, V.V. Khodos, V.L. Vaks, A.M. Baryshev, P.R. Wesselius, J. Mygind, *Physica C*, **367,** pp. 249 - 255, (2002).

[11] V.P. Koshelets, A.B. Ermakov, P.N. Dmitriev, A.S. Sobolev, A.M. Baryshev, P.R. Wesselius, and J. Mygind, Extended *Superconductor Science and Technology,* **v. 14,** pp. 1040 - 1043, (2001)

[12] V.P. Koshelets, S.V. Shitov, A.V. Shchukin, L.V. Filippenko, J. Mygind, and A.V. Ustinov, *Phys Rev B,* **56,** 5572 (1997).

[13] A.J. Dahm, A. Denenstein, D.N. Langenberg, W.H. Parker, D. Rogovin, and D.J. Scalapino, Phys Rev Lett, **22**, 1416 (1969).

[14] M. Salerno, M.R. Samuelsen, and Y. Yulin, *Phys. Rev. B,* **v. 86**, pp. 5397-5399, **(**2001)

[15] A.L. Pankratov, *Phys. Rev. B*, **v. 65**, 054504-1-9, (2002).

[16] V.P. Koshelets, S.V. Shitov, L.V. Filippenko, V.L. Vaks, J. Mygind, A.B. Baryshev, W. Luinge, and N. Whyborn, *Rev of Sci Instr.,* **71,** 289 (2000).

On-Chip Detection of Radiation Power from Flux-Flow Oscillators with Epitaxial and High-J_C NbN/AlN/NbN Junctions

Satoshi KOHJIRO*, Zhen WANG**, Sergey V. SHITOV***, Shigehito MIKI****,
Akira KAWAKAMI**, and Akira SHOJI*
* National Institute of Advanced Industrial Science and Technology,
1-1-4 Umezono, Tsukuba, Ibaraki 305-8568, Japan
** Kansai Advanced Research Center, Communications Research Laboratory,
588-2 Iwaoka, Iwaoka-cho, Nishi-ku, Kobe 651-2492, Japan
*** Institute of Radio Engineering and Electronics,
Mokhovaya 11, 101999 Moscow, Russia
**** Graduate School of Science and Technology, Kobe University,
1-1 Rokkodai-cho, Nada-ku, Kobe 657-8501, Japan

Abstract

To develop an efficient local oscillator (LO) operating above 0.7 THz, the gap frequency of Nb, on a same chip with a SIS mixer, we have investigated the radiation power P of NbN-based flux-flow-type Josephson oscillators (FFOs). The designed and fabricated chip incorporates FFOs, SIS power detectors (DETs), and their coupling circuits. Both FFOs and DETs consist of epitaxial NbN/AlN/NbN junctions with high critical current density J_C ($15 < J_C < 78$ kA/cm^2). The most part of the coupling circuit consists of NbN/SiO_2/Al microstrip lines whose *rf*-loss is approximately 2-3 dB. It has been found P>200 nW, enough for the optimum pumping of a SIS mixer with *rf*-resistance of 50 Ω, is coupled to DETs in the frequency range of 0.5-0.9 THz. The coupling bandwidth is larger than 20% of its central frequency. In the band, the radiation frequency is tuned by the control current through the FFO in the range of 10-100 mA. The peak power >1 μW is detected at 0.76THz. In addition, the dissipated power in a FFO is smaller than 500 μW, which is less than 10^{-4} of that of semiconductor sources. These experimental results indicate that FFOs with high-J_C NbN/AlN/NbN junctions are applicable for an on-chip LO above 0.7 THz.

1. Introduction

For submillimeter-wave astronomy and global monitoring of atmosphere pollution, flux-flow oscillators (FFOs) [1, 2] based on the flux motion in long Josephson junctions

are suitable for a tunable, compact, and low-power consuming local oscillator (LO) on a same chip with a SIS mixer. Recently, Nb-based FFOs were successfully tested as an integrated receiver's LO up to the gap frequency of Nb, say 0.7 THz [3, 4]. To increase the operating frequency of FFOs beyond 0.7 THz, the material of electrodes should be changed. There are two candidates for such electrode material. One is NbTiN grown on several kinds of substrate materials and the other is epitaxial NbN on MgO substrates. Though reported surface resistance of NbTiN film is reasonably low [5] and successfully adopted for the tuning structure in SIS mixers [6, 7], it is difficult to get low dark current when junction electrode is replaced by NbTiN. Epitaxial NbN film [8-10] is suitable not only for the tuning structure [11], but also for NbN/AlN/NbN Josephson junctions with reasonably low dark current in the range of $5<J_C<127$ kA/cm^2 [12], where J_C is the critical current density of Josephson junctions. This feature of epitaxial NbN is an advantage for FFOs and corresponding integrated receivers operating above 0.7 THz. In this paper, we have studied the radiation power P of NbN-based FFOs and demonstrated they are applicable for an on-chip LO above 0.7 THz.

2. Device Design

Fig. 1 shows the top view and cross-section of the device. The designed chip incorporates FFOs, SIS power detectors (DETs), and their coupling circuits. Both FFOs and DETs consist of epitaxial NbN/AlN/NbN junctions with high critical current density J_C ($15<J_C<78$ kA/cm^2).

The FFO's length l_F is 39 or 500 μm, where the former can be used both operational regimes of Fiske resonant and real flux-flow [3, 4], while the resonant mode is completely suppressed above 0.3 THz for l_F=500 μm due to $\alpha l_F>1$, where α is the attenuation constant of electromagnetic wave in a FFO. The FFO's width is W_F=3 μm which does not satisfy the conventional requirement of $W_F<2\lambda_J$ [1] for $J_C>20$ kA/cm^2, where λ_J is its Josephson penetration depth. The reason for adopting W_F=3 μm is that we found in another experiment FFOs with W_F=2 μm become too insensitive to the applied magnetic field to be tuned the oscillation frequency in our interested region. Note that no degradation on characteristics has been experimentally observed for FFOs with $W_F>2\lambda_J$. To obtain steep current steps on its current-voltage characteristics, important both for higher output power and narrower oscillation linewidth, so called projection part with the length of 16 and 100 μm is introduced at the edge of FFOs [2] with l_F=39 and 500 μm, respectively. The bias current of the FFO I_{BF} is fed to the junction due to its overlap geometry, while the control current I_{HF} for applying the

magnetic field flows through the base electrode underneath the FFO.

The length of DETs is 2-3 μm, a half of wavelength in the junction at a certain frequency between 0.55 and 0.82 THz, where the junction capacitance is compensated by the inductance of junction electrodes [13]. The width of DETs is 0.5-2.0 μm to get the variation of their impedance. Both the bias current I_{BD} and the control current I_{HD} for suppression of its Josephson current are supplied to the DET due to its in-line geometry.

The coupling circuit used here is similar to that reported previously [14]. The circuit consists of impedance transformers, a *dc*-break, and *rf*-filters. An impedance transformer with a tapered NbN/SiO_2/Al microstripline matches the output impedance of a FFO (0.5 Ω) to the following circuits of 10-25 Ω. A *dc*-break composed of two microstrip stubs and a pi-slot line in an Al groundplane satisfies both <1 dB coupling loss for *rf*-signal and complete isolation for *dc*-bias between a FFO and a DET. *Rf*-filters are positioned at *dc*-connections for control currents on both DETs and FFOs to prevent the leak of *rf*-signal. The *rf*-loss of the total coupling circuit is estimated as approximately 2-3 dB from our experimental *dc*-properties of epitaxial NbN [10] and Al.

3. Device Fabrication

An epitaxial NbN/AlN/NbN junction sandwich was deposited on a (100) MgO single crystal of 20x20x0.5 mm^3 by an *rf*-magnetron sputtering method without intentional heating of the substrate. The fabrication process of junctions and their characterization were already reported in detail [12]. J_C was varied by the deposition time of the AlN barrier. Thickness of base and counter electrodes was 210-250 and 220-400 nm, respectively. After the sandwich formation, the base electrode was patterned and etched by a reactive ion etching (RIE) technique in CF_4 until the surface of MgO substrate was exposed. Before removing the photoresist, a 250-nm-thick SiO_2 radical absorber was deposited. The role of this radical absorber is explained later. Next, both FFOs and DETs were defined by the patterning and RIE of the counter electrode in CF_4. Since sidewall of base electrodes without the radical absorber was exposed to CF_4 gas plasma, the base electrode was considerably side-etched during the etching of counter electrodes. The above-mentioned SiO_2 radical absorber prevents this side etching, resulting in successful fabrication of 0.5-μm-wide base electrodes. After a 900-nm-thick SiO_2 film was deposited on a whole substrate for an insulation layer, the SiO_2 film was removed with chemical-mechanical polishing technique [15] until the surface of counter electrodes was exposed. This planarization has advantage of both sufficient step coverage over the edge of counter electrodes and ohmic contact between

the wiring and the counter electrode without the formation of small via holes on DETs. The sample was completed by evaporating a 300-nm-thick Al patterned by photoresist stencil lift-off. Typical *dc*-properties of NbN base electrode and Al wiring were as follows. The critical temperature and the normal-state resistivity at 20 K of NbN are 15-16 K and 50-60 μΩcm, respectively. The normal-state resistivity at 20 K and the ratio of resistivities at 300 K and 20 K of Al are 0.2-0.3 μΩcm and 10-20, respectively. These properties are same as those used in a SIS mixer operating above 0.7 THz [11].

4. Results and Discussion

4-1. *Dc*-Characteristics of a FFO and a DET

Current-voltage (I_{BF}-V_F and I_{BD}-V_D) characteristics of fabricated FFOs and DETs were measured at 4.2K with various control currents I_{HF} and I_{HD} for the applied magnetic field, respectively. Fig. 2 shows an example of I_{BF}-V_F characteristic of a FFO with J_C=58 kA/cm^2 and l_F=39 μm. In Fig. 2, current steps are appeared due to the flux-flow in the junction, where each step corresponds to each I_{HF} value. Since the height of current steps I_S is proportional to the generated power in the FFO and step voltage to the oscillation frequency, it is preferable for the higher step to be observed in the wider voltage region. As shown in Fig. 2, I_S >15 mA is clearly observed for 0.6-2.7 mV. It indicates the FFO with epitaxial NbN/AlN/NbN junctions oscillates internally for 0.3-1.3 THz, i.e. close to the gap frequency of the epitaxial NbN. The oscillation frequency is tuned by I_{HF} in the range of 18-86 mA which can be supplied easily from batteries or compact *dc*-power supplies. From I_{BF} and V_F of operating points in Fig. 2, the dissipated *dc*-power in the FFO is estimated <100 μW, since I_{HF} flowing through superconducting base electrode does not consume the power. No FFOs in our experiment consume *dc*-power >500 μW. This value is less than 10^{-4} of that of semiconductor sources such as Gunn diodes used with frequency multipliers.

Fig. 3 shows an example of I_{BD}-V_D characteristic of a DET with J_C=15 kA/cm^2 and the area of 2.9 × 0.5 μm^2. The Josephson current is successfully suppressed by I_{HD}. The solid line denotes the unpumped curve, while the dotted lines pumped ones when the coupled FFO is biased on a current step shown in Fig. 2. As shown, the photon-assisted tunneling (PAT) current is observed for a various bias voltage of coupled FFO V_F. The first PAT step is seen around V_D=1.8 mV. The frequency of the irradiated wave is related to the voltage of the first PAT step V_{PAT1} below V_G as $f_{PAT}=e(V_G-V_{PAT1})/h$, where V_G is the gap voltage of a DET, e the unit charge, and h Planck's constant. From V_G=5.4 mV and V_{PAT1}=1.8 mV, we got f_{PAT}=0.86 THz, which is

consistent with the oscillation frequency of the coupled FFO estimated from V_F as $f_F=2eV_F/h=0.85$ THz.

4-2. *Rf*-Coupling between FFO and DET

Based on the experimental unpumped I_{BD}-V_D curve, theoretical pumped curves are calculated [16] for various *rf*-voltages in the DET V_{rfD}. By fitting the theoretical pumped curve to the experimental one, we get V_{rfD}. From V_{rfD} and the normal resistance of the DET R_{ND}, detected power is calculated as $P=V_{rfD}{}^2/(2R_{ND})$. Fig. 4 shows the detected power as a function of frequency for 5 samples. Each sample has different values of J_C and thickness of SiO_2 insulator t_{SiO2} used in microstrip coupling circuits. For comparison, theoretical power required for the optimum pumping for a SIS mixer with *rf*-resistance of 50 Ω is also plotted as small dots in Fig. 4. As shown, the detected power is larger than the theoretical optimum pumping power between 0.5 and 0.9 THz. The 3dB-bandwidth of each sample is larger than 20% of its central frequency. The peak power of 1.3 μW is detected at 0.76 THz i.e. above the gap frequency of Nb, which indicates the advantage of NbN-based FFOs.

4-3. Optimum J_C

To be clear the preferable J_C values, in Fig. 5, we plot in closed circles the peak value of detected power as a function of J_C. As shown, the peak power increases with J_C and saturates around 70 kA/cm^2. The open squares denote the ratio of junction's subgap resistance at 2mV to its normal resistance R_{ND}, i.e. how small the dark current is. As shown, the normalized dark current is almost independent of J_C below 70 kA/cm^2. From these preliminary results, tentative optimum region of J_C is 50-70 kA/cm^2. This value corresponds to $\omega A_D C_S R_{ND}$ product at 0.7THz of 3-5, which is calculated from J_C-dependent specific capacitance C_S [12] and $J_C A_D R_{ND}=3.75$ mV which is experimentally obtained, where ω is the angular frequency and A_D the area of DETs. This $\omega A_D C_S R_{ND}$ value is also suitable for the design of SIS mixers on a same chip with FFOs. For practical application, further discussion on optimum J_C will be necessary from the view point of J_C-dependent oscillation linewidth of FFOs [17].

4-4. Upper Frequency Limitation

Fig. 6 shows the relation between the maximum coupling frequency f_{MC} and t_{SiO2} used in microstrip coupling circuits, where the inset shows the definition of f_{MC}. The

solid line denotes the designed value and triangles the experimental ones. As shown, the experimental f_{MC} is 10-20% smaller than the designed value. To study the reason of this discrepancy, in Fig. 7, we compare the experimental (triangles with line) and theoretical (solid curve) frequency-dependent power transmissions from a FFO to a DET, where two types of microstrip coupling circuits are adopted. The insets show the configuration of microstrip lines.

Fig 7 (a) shows the case of normal microstrip line used for our present design. The electric field in the line concentrates under the stripline. The contribution to the line capacitance of the free space behind the stripline is negligibly small because of its low dielectric constant (ε_r=1) though weak electric field exists in the free space. Note that a substrate behind the groundplane never contributes since the electric field does not exist in a substrate. Using this model for the calculation, we find the discrepancy between theoretical and experimental frequency responses.

Fig. 7 (b) shows the case of embedded microstrip line closer to our device configuration shown in Fig. 1 (b). A MgO substrate with ε_r=9.6 is attached not behind the groundplane but behind the stripline. Because of the electric field in the substrate, the substrate increases the line capacitance, i.e. decreases f_{MC} from the initial value of the normal type. As a result, theoretical value fits reasonably experimental one.

In Fig. 6, the designed f_{MC} based on embedded microstrip circuits is also plotted in open squares, which agree quantitatively with experimental value. These results indicate f_{MC} of the present experiment is determined not by FFOs but by microstrip parameters far from the optimum value. It suggests the future possibility of detection of required power for 0.9-1.3 THz after redesigning the coupling circuit based on the embedded microstrip model.

5. Conclusion

We have demonstrated the radiation power P>200 nW from NbN-based FFOs is detected by on-chip SIS detectors for 0.5-0.9 THz. The peak power >1 μW is detected above the gap frequency of Nb. The coupling bandwidth is larger than 20% of its central frequency. In the band, the radiation frequency is tuned by the control current through the FFO in the range of 10-100 mA. The dissipated power in a FFO is less than 500 μW. Higher J_C is preferable for larger P. The maximum detectable frequency is determined by parameters of microstrip coupling circuits. These experimental results indicate that FFOs with high-J_C NbN/AlN/NbN junctions are applicable for an on-chip local oscillator above 0.7 THz.

Acknowledgements

The authors would like to acknowledge M. Takeda in Communications Research Laboratory and T. Noguchi in Nobeyama Radio Observatory, Japan, for the guidance of the calculation of pumped *I-V* curves of DETs. They thank the members of Superconducting Devices Group and Microsystems Group in AIST for the management of facilities required for this work. J. Itoh is appreciated for continuous support and encouragement. This work is supported in part by the Ministry of Education, Culture, Sports, Science and Technology, Japan and a fellowship program by Japan Society for the Promotion of Science, as well as RFBR (Russian Foundation for Basic Research) projects 00-02-16270 and INTAS (INTernational ASsociation for Promotion of the Scientific Research in Russia funded by NATO countries) project 01-0367.

References

[1] T. Nagatsuma, K. Enpuku, K. Yoshida, and F. Irie "Flux-flow-type Josephson oscillator for millimeter and submillimeter wave region. II. Modeling", *J. Appl. Phys.* **56**, 3284-3293 (1984).

[2] T. Nagatsuma, K. Enpuku, K. Sueoka, K. Yoshida, and F. Irie "Flux-flow-type Josephson oscillator for millimeter and submillimeter wave region. III. Oscillation stability", *J. Appl. Phys.* **58**, 441-449 (1985).

[3] V. P. Koshelets and S. V. Shitov, "Integrated superconducting receivers", *Supercond. Sci. Technol.* **13**, R53-R69 (2000).

[4] V.P. Koshelets and J. Mygind, **"**Flux flow oscillators for superconducting integrated submm wave receivers", *Studies of High Temperature Superconductors*, edited by A.V. Narlikar, NOVA Science Publishers, New York, **39,** 213-244 (2001).

[5] J. W. Kooi, J. A. Stern, G. Chattopadhyay, H. G. LeDuc, B. Bumble, and J. Zmuidzinas, "Low-loss NbTiN films for THz SIS mixer tuning circuits", *Int. J. Infrared Millim. Waves* **19**, 373 (1998).

[6] J. Kawamura, J. Chen, D. Miller, J. Kooi, J. Zmuidzinas, B. Bumble, H. G. LeDuc, and J. A. Stern, "Low-noise submillimeter-wave NbTiN superconducting tunnel junction mixers", *Appl. Phys. Lett.* **75**, 4013-4015 (1999).

[7] B. D. Jackson, A. M. Baryshev, G. de Lange, J. R. Gao, S. V. Shitov, N. N. Iosad, and T. M. Klapwijk, "Low-noise 1THz superconductor-insulator-superconductor mixer incorporating a NbTiN/SiO_2/Al tuning circuit", *Appl. Phys. Lett.* **79**, 436-438 (2001).

[8] A. Shoji, S. Kiryu, and S. Kohjiro, "Superconducting properties and normal-state

resistivity of single-crystal NbN films prepared by a reactive rf-magnetron sputtering method", *Appl. Phys. Lett.* **60**, 1642-1626 (1992).

[9] Z. Wang, A. Kawakami, Y. Uzawa, and B. Komiyama, "Superconducting properties and crystal structures of single-crystal niobium nitride thin films deposited at ambient substrate temperature", *J. Appl Phys.* **79**, 7837-7842 (1996).

[10] S. Kohjiro and A. Shoji, "Surface resistance of NbN and NbC_xN_{1-x} films in the frequency range of 0.5-1.5THz", *Inst. Phys. Conf. Ser.* No **167**, IOP Publishing Ltd., 655-658 (2000). S. Kohjiro, S, Kiryu, and A. Shoji, "Surface resistance of epitaxial and polycrystalline NbCN films in submillimeter wave region", *IEEE Trans. Appl. Supercond.* **3**, 1765-1767 (1993).

[11] Y. Uzawa, Z. Wang, and A. Kawakami, "Terahertz NbN/AlN/NbN mixers with Al/SiO/NbN microstrip tuning circuits", *Appl. Phys. Lett.* **73**, 680-682 (1998).

[12] Z. Wang, H. Terai, A. Kawakami, Y. Uzawa, "Characterization of NbN/AlN/NbN Tunnel Junctions", *IEEE Trans. Appl. Supercond.* **9**, 3259-3262 (1999).

[13] V. Yu Belitsky, E. L. Kollberg, "Superconductor-insulator-superconductor tunnel strip line: Features and applications", *J. Appl. Phys.* **80**, 4741-4748 (1996).

[14] S. V. Shitov, V. P. Koshelets, L. V. Filippenko, P. N. Dmitriev, V. L. Vaks, A. M. Baryshev, W. Luinge, N. D. Whyborn, and J. R. Gao, "A superconducting integrated receiver with phase-lock loop", *Inst. Phys. Conf. Ser.* No **167**, IOP Publishing Ltd., 647-650 (2000).

[15] S. Kohjiro, H. Yamamori, and A. Shoji, "Fabrication of niobium-carbonaitride Josephson junctions on magnesium-oxide substrates using chemical-mechanical polishing", *IEEE Trans. Appl. Supercond.* **9**, 4464-4466 (1999).

[16] C. A. Hamilton and S. Shapiro, "Rf-induced effects in superconducting tunnel junctions", *Phys. Rev. B* **2**, 4494-4503 (1970).

[17] V. P. Koshelets, private communication.

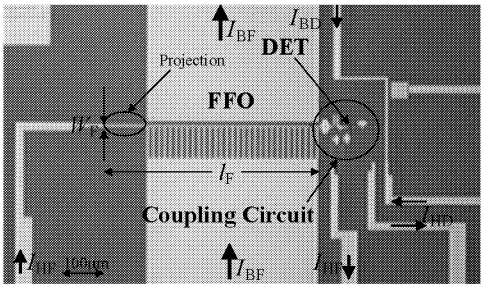

(a)

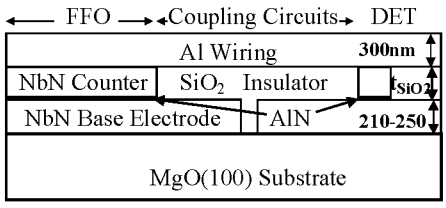

(b)

Fig. 1. Top view (a) and cross-section (b) of a FFO and a coupled DET. Al wiring is not shown in (a).

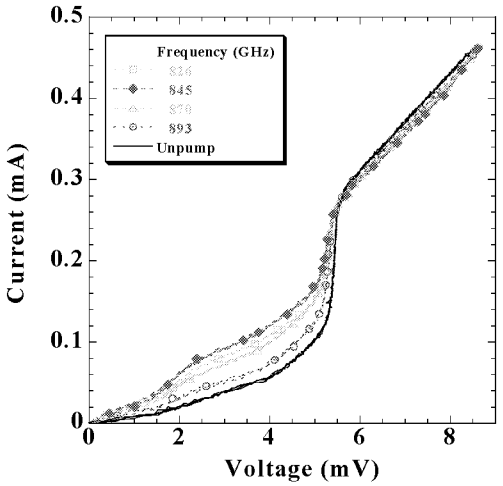

Fig. 3. I_{BD}-V_D curves of a DET with J_C=15kA/cm^2 and area of 2.9 × 0.5 μm^2 under various oscillation frequency of the coupled FFO.

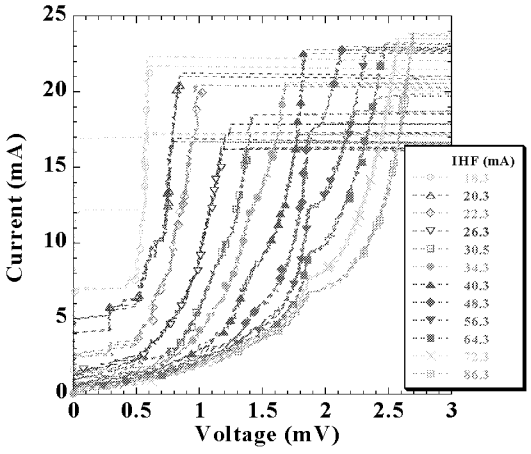

Fig. 2. I_{BF}-V_F characteristics of a FFO with J_C=58kA/cm^2, l_F=39 μm, and W_F=3 μm under various control currents I_{HF}.

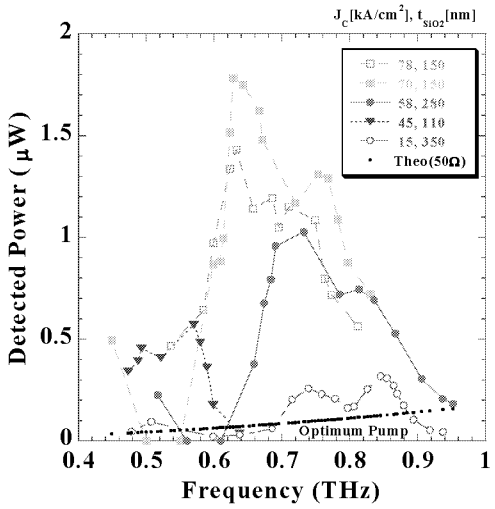

Fig. 4. Detected power P vs. oscillation frequency of FFOs. Experimental results on 5 samples with various J_C and t_{SiO2} are shown. Theoretical optimum pumping power for a SIS mixer with *rf*-resistance of 50 Ω is plotted in small dots.

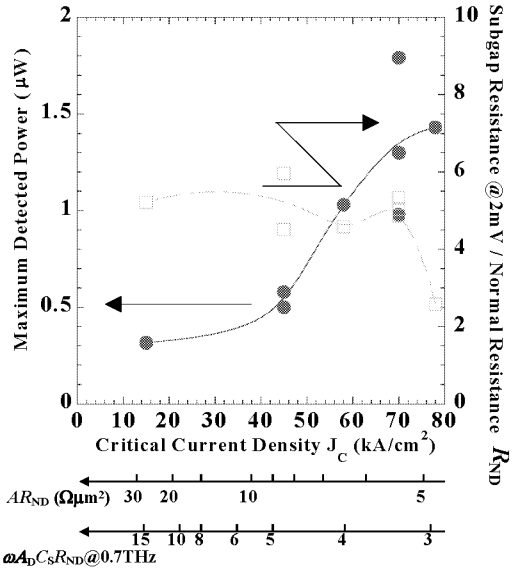

Fig. 5. Peak power (closed circles) and ratio of subgap resistance at 2mV to normal resistance (open squares) vs. J_C. The horizontal axis is also on scales of $A_D R_{ND}$ and $\omega A_D C_S R_{ND}$ products at 0.7THz.

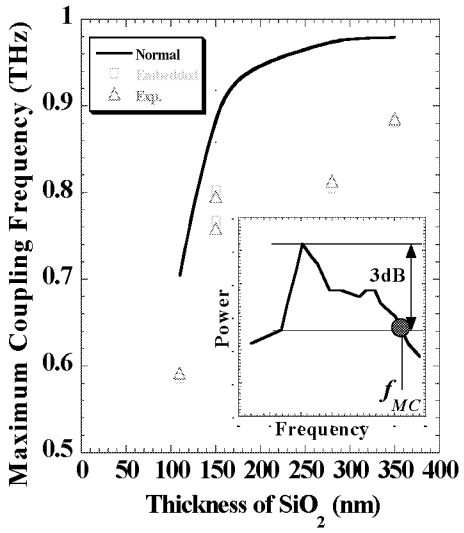

Fig. 6. Maximum coupling frequency f_{MC} vs. t_{SiO2} for designed and experimental (triangles) values. Designed f_{MC} is calculated both for normal (solid line) and embedded (squares) microstrip coupling circuits shown in Fig. 7. The inset shows the definition of f_{MC}.

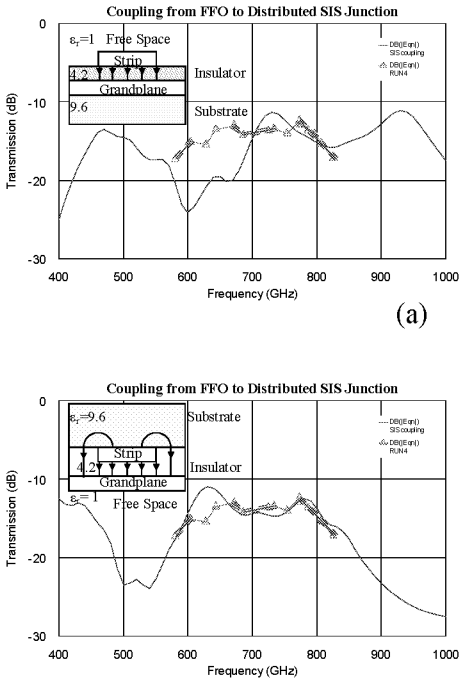

Fig. 7. Frequency dependence of power transmission from a FFO to a DET for designed (solid line) and experimental (triangles with line) values. Designed value is based on (a) normal and (b) embedded microstrip coupling circuits. Inset shows the configuration of microstrip lines.

Development of Backward Wave Oscillators for Terahertz Applications

Lawrence Ives, Jeff Neilson, Malcom Caplan, Nikolai Chubun, Carol Kory, Mike Read,
Calabazas Creek Research, Inc., 20937 Comer Drive
Saratoga, CA 95070-3753 USA
(408) 741-8680
Rlives@CalCreek.com

Steve Schwartzkopf, Ron Witherspoon
Ron Witherspoon Incorporated
Campbell, CA

Introduction

Calabazas Creek Research, Inc. (CCR) is developing advanced backward wave oscillators (BWOs) operating from 300 GHz to more than 1 THz. The BWOs will be used by the National Aeronautics and Space Administration as local oscillator sources in heterodyne receivers for low-background astronomy observations and remote sensing. Above 100 GHz, only BWOs have broad tunability (over 100 GHz) and high output power (~1 mW). The current program will reduce the weight, improve the efficiency, and extend the operating range of these devices.

CCR is working with Sandia National Laboratory to utilize advanced masking and etching techniques to reduce manufacturing cost and achieve unprecedented feature sizes. This will allow significant reduction in the periodicity of the BWO circuit, reducing the operating voltage and extending the operating frequency to more than 1 THz. Twenty six circuits can be made on a single 6 cm diameter wafer, significantly reducing the cost and improving reliability. The circuits will be manufactured using the LIGA process, and the results will determine what frequency range can be achieved. The current 600-700 GHz BWO requires feature sizes of approximately 20 microns, while LIGA is capable of producing feature sizes on the order of 5 microns. This indicates that frequencies approaching 2 THz may be achieveable. Circuits up to 1.9 THz are being manufactured for evaluation.

The output coupling into waveguide was redesigned to increase the amount of usable power by a factor of 5 in the 600-700 GHz BWO. Similar designs are now in progress to extend these techniques to the higher frequency BWOs. CCR is also investigating alternative coupling schemes to eliminate the requirement for waveguide output.

The current BWO utilizes an external permanent magnet to provide the 1.1 T field required for beam confinement. Recent research on W-Band sources developed techniques to confine electron beams using periodic permanent magnets within the vacuum envelope[1]. Research is underway to determine if such techniques can be applied to the BWOs. If successful, the weight of the BWO system would be reduced from approximately 20 Kg to a few hundred grams with a similar reduction in size.

Finally, the prototype BWOs will incorporate a single stage depressed collector for energy recovery from the spent electron beam. Simulations indicate that approximately 80% of

the energy can be recovered, significantly increasing the device efficiency. This will reduce the electrical power requirement and eliminate water cooling.

Circuit Design

Calabazas Creek Research is using Microwave Studio to model the BWO circuit. The configuration of the BWO circuit is shown in Figure 1. Initially, the existing 600- to 700-GHz circuit was modeled in an attempt to duplicate the performance of the BWOs at the Jet Propulsion Laboratory (JPL). In parallel with the Microwave Studio simulations, which use a finite difference mesh, an analytical code was developed that allows simulation of circuits in seconds of CPU time, rather than the tens to hundreds of minutes required for Microwave Studio.

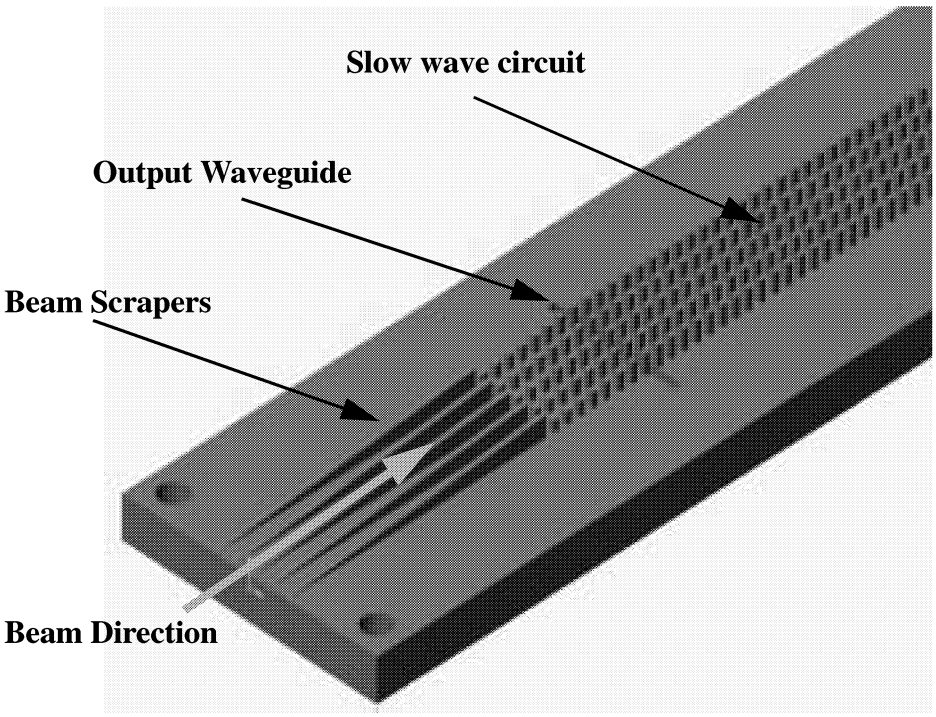

Figure 1. Layout of BWO circuit. The beam scrapers carves grooves in the rectangular electron beam for the slow wave structures downstream. The RF power is extracted through the base into rectangular waveguide.

The BWO circuit is periodic, so it is only necessary to model several periods. The geometry simulated is shown in Figure 2. The electron beam moves in the Z-direction, and there are five parallel rows of BWO posts, or pintles.

These efforts were successful in matching experimental measurements. Figure 3 compares the Microwave Studio analysis of the existing BWO with measured results at JPL. The agreement looks very good with the exception of two experimental points, which appear to be anomalous. The agreement is extremely good over the upper half of the band from 650 GHz to 700 GHz. The agreement with the measured results provides confidence in the accuracy of the model, which can then be used to calculate the magnitude of the electric fields, shown in Figure 4.

The model also allows analysis of potential competing modes. The simulation modeled the first five modes in the operating band. The predicted behavior of these modes in shown in Figure 5.

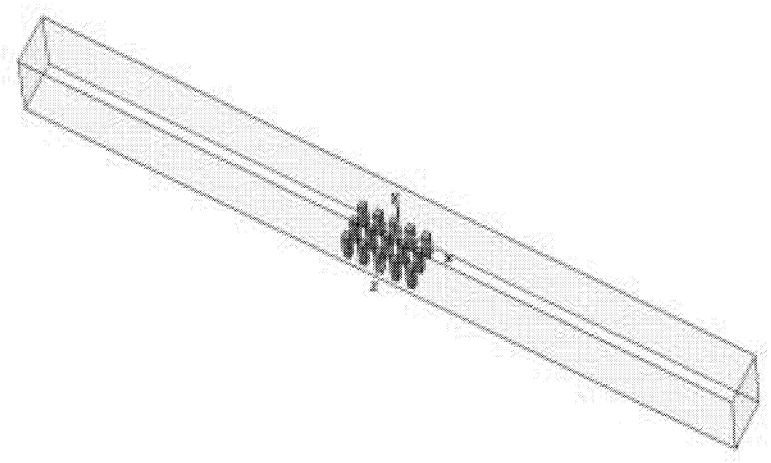

Figure 2. Periodic structure used in the Microwave Studio simulations. The enclosing box represents the size of the existing beam tunnel.

When the model was correctly predicting the observed performance, it was used to examine the effect of proposed changes in the circuit and beam tunnel configuration. The existing beam tunnel is 300μ high and 2,400μ wide. Apparently, the width was chosen for convenience by the current BWO manufacturer (Istok Co.) to facilitate manufacture. Using LIGA for manufacture allows simplification of the design to provide better performance. One of the first modifications proposed was to reduce the width of the beam tunnel from 2,400μ to 600μ. The new output coupler is approximately 600μ wide. It was necessary to determine if this change negatively impacts BWO operation. Figure 6 shows a comparison in the dispersion for this change as compared to the original design and measured results. The figure shows the proposed modification does not have a significant impact on BWO performance.

The interaction of the circuit with the electron beam is important to understand. As modifications are made to the circuit for higher frequency operation, there must be sufficient beam current density near the slow wave structure to initiate RF generation. As the frequency is increased, the required current density increases. Because the cathodes

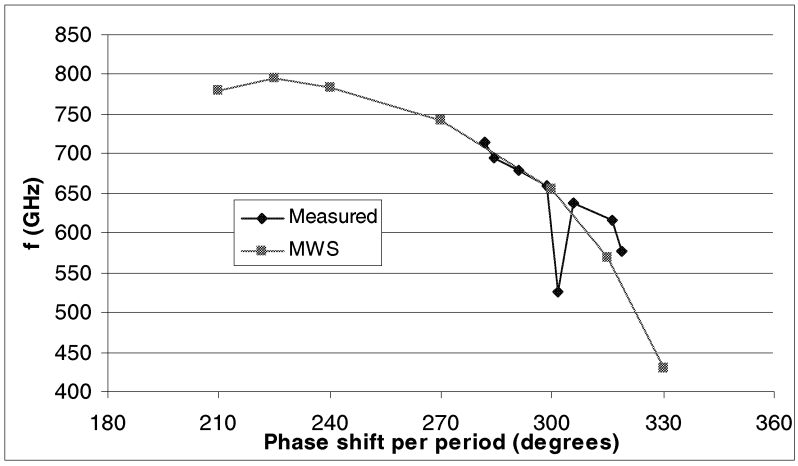

Figure 3. Comparison of measured and simulated dispersion of the 600- to 700-GHz BWO. Measured data is from NASA/JPL.

for the program are already purchased, it was necessary to determine how high in frequency they can operate. This will probably be the limitation in frequency until other cathodes are developed, because the LIGA process can produce circuit structures very high in frequency.

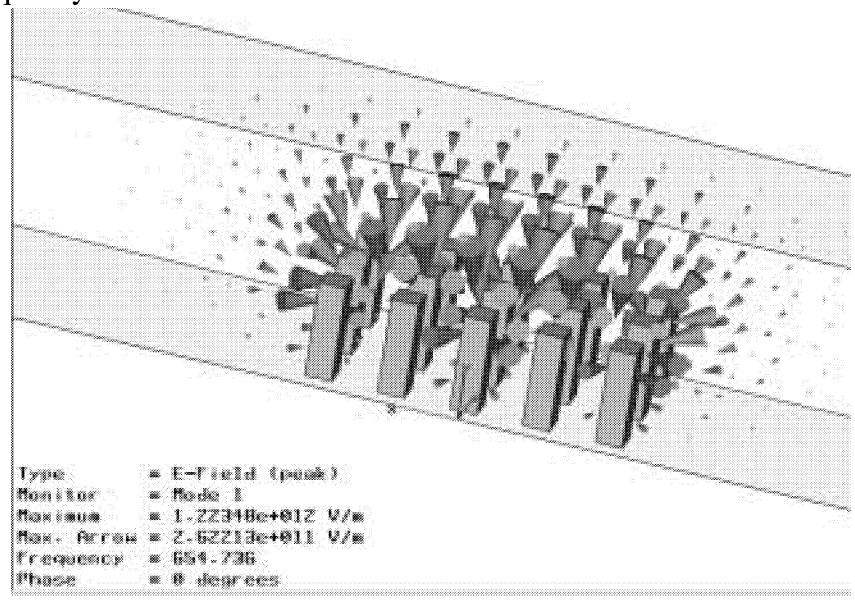

Figure 4. Arrow plot of the electric field strength at a phase shift per period of 300 degrees, f = 654 GHz. The size of the arrow is proportional to the electric field strength.

The relationship between the sheet electron beam and the circuit is shown in Figure 7, which is a cross section of the BWO looking in the Z-direction. The beam passes over the top and partially between the rows of pintles.

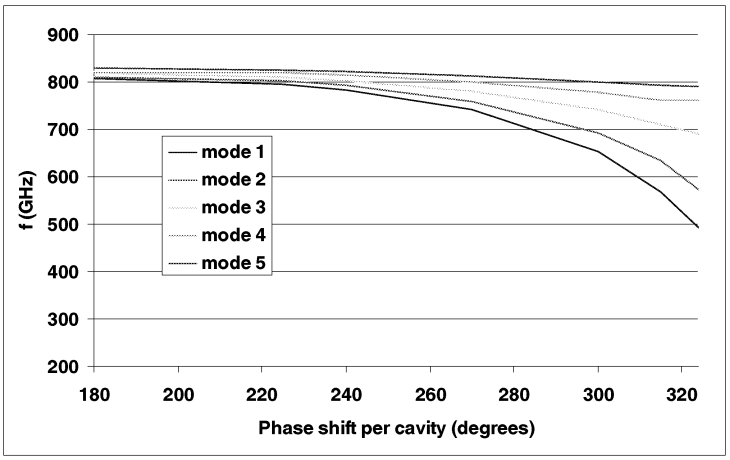

Figure 5. First five modes of the 600- to 700-GHz BWO

A plot of the electric field at various y-positions is shown in Figure 8. The peak fields occur at the tops of the pintles but significant field also extends into the region between the rows of pintles. this provides increased coupling to the electron beam.

When the magnitude of the fields is calculated, one can simulate impedance. The impedance is used to determine the ability of the electron beam to initiate oscillation. The impedance for both the existing BWO and a BWO with the reduction in beam tunnel width from 2400μ to 600μ were calculated. The greatest difference between the x = 2400μ

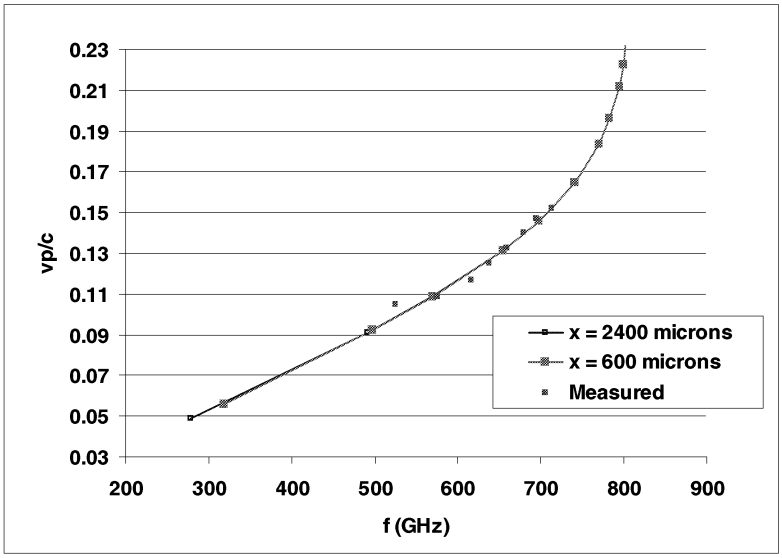

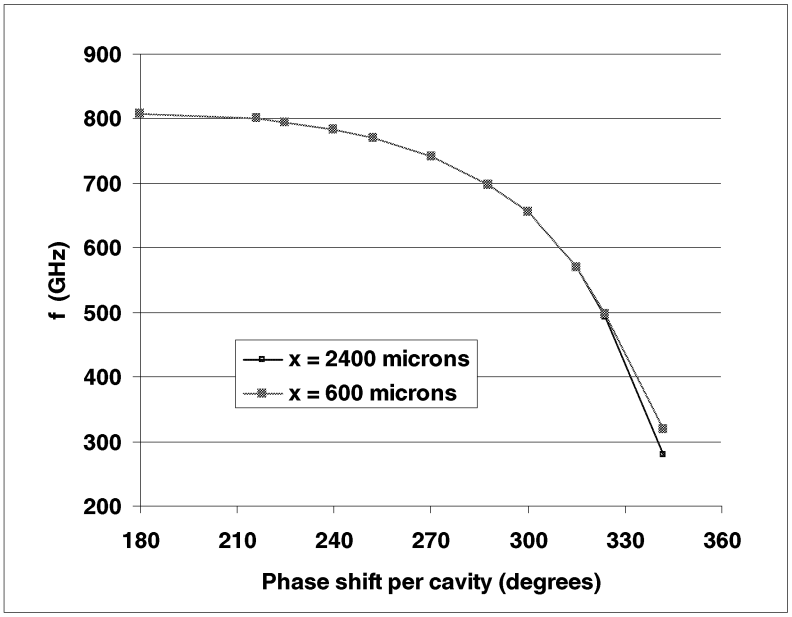

Figure 6. Top figure is simulated phase velocity versus frequency. Lower plot is comparison of frequency versus phase shift.

and 600μ cases is the behavior of the higher order modes. For the standard case, the next group of modes occurs much higher in frequency (approximately 10 THz). Reducing the x-dimension to 600μ causes this mode to shift down in frequency significantly (approximately 1 THz).

This reduction also places this mode in the vicinity of the second harmonic frequency of the operating mode, which might be problematic. To investigate this occurrence, the

impedance at a phase shift of 270 degrees as calculated for the first branch of these higher modes occurring at about 1500 GHz. We determined that the impedance is significantly lower than the operating mode frequency, which means the desired mode should oscillate at a lower current than the higher order mode.

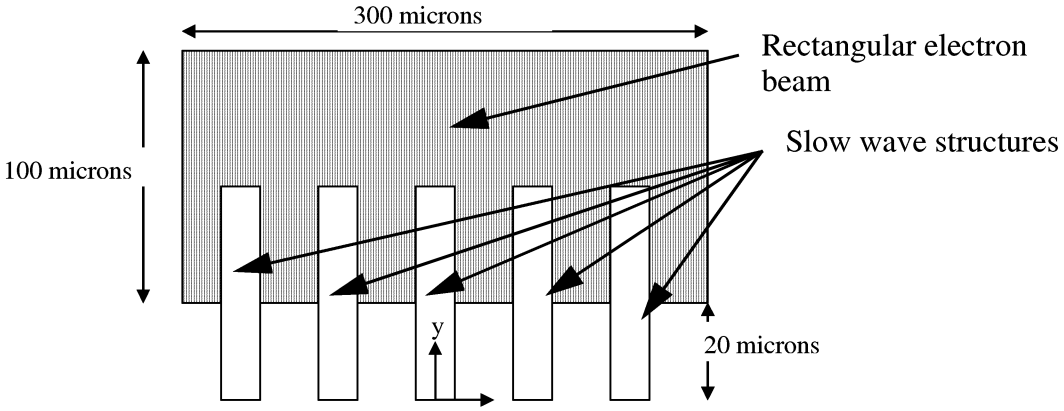

Figure 7. Schematic showing circuit coordinate system and electron beam.

Simulations are in progress to optimize the geometrical configuration for the 600-700 GHz BWO. Preliminary results indicate that the current spacing between rows of pintles (34μ) might not be optimal. In fact, the field structure appears more uniform with a spacing of about 10μ. Keep in mind, however, the requirement for beam transmission between rows. Reduced spacing may cause problems with beam alignment.

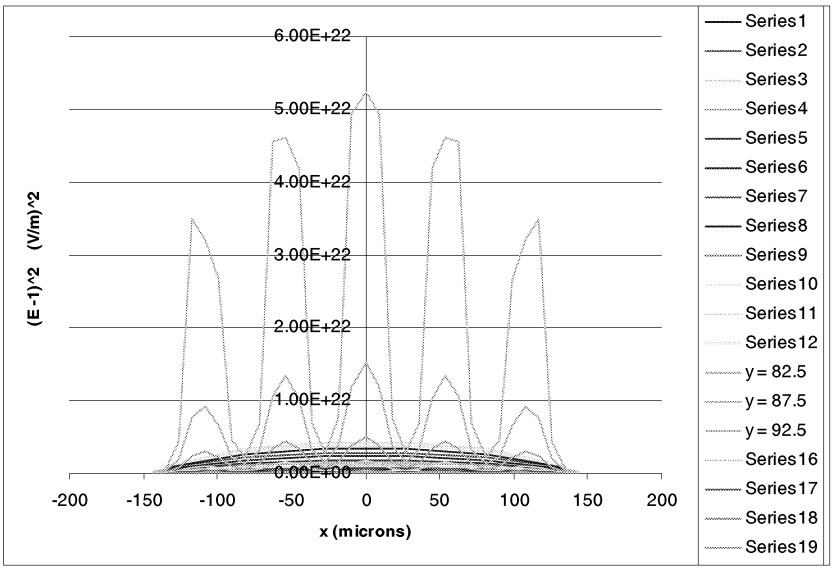

Figure 8. $|E_{-1}|^2$ as a function of x at several y locations for Beta L = 300 degrees (655 GHz) for standard case.

Higher frequency circuits were designed up to 1.9 THz. In theory, the circuit can be simply scaled by the frequency. Unfortunately, this requires an increase in the beam

current density to get equivalent coupling. Several cathodes are already procured, so the design must be analyzed to determine how high in frequency the design can go and still use these existing cathodes. If necessary, higher current density cathodes can be procured; however, high emission current density also means reduced lifetime. There is also a 2- to 3-month delivery schedule for additional cathodes.

The higher frequency circuit configurations were designed and transmitted to Sandia National Laboratory, where the wafer will be made using the LIGA process. The lithographic process was initiated and 26 circuits are scheduled for delivery in July 2002 operating from 530 GHz to 1.9 THz.

Output Coupler

The existing BWOs couple the output power from the circuit directly into overmoded rectangular waveguide. Calculations and measurements indicate that less than 10% of the RF power is coupled into the fundamental waveguide mode. Consequently, only a small fraction of the output power is usable by downstream instrumentation. The program investigated modifications to the output coupling scheme to reduce generation of spurious modes and radiate the power in a pure Gaussian mode.

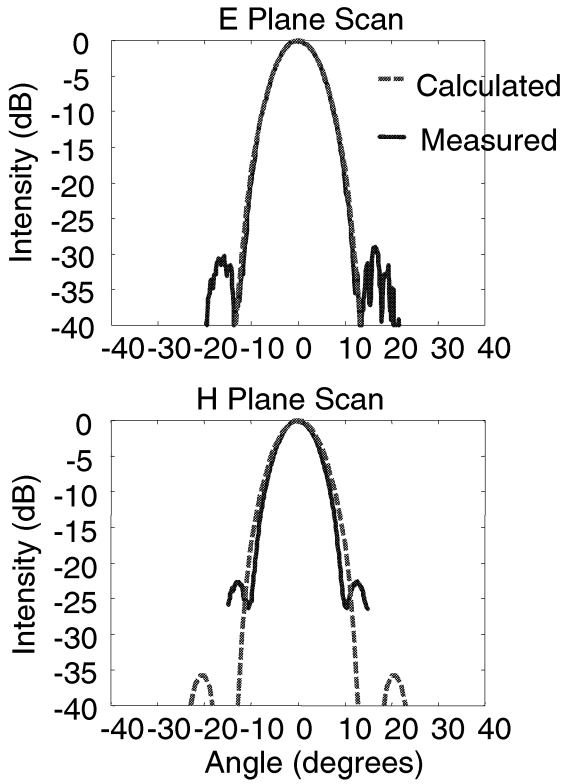

Figure 9. Measured performance of scaled output horn

The waveguide dimension were reduced at the slow wave circuit to only transmit the fundamental TE_{10} rectangular mode. A 2 micron iris was incorporated to match the waveguide to the RF circuit. A series of step transformers convert the TE_{10} rectangular mode into a TE_{11} circular mode in round waveguide. A non-linear horn is employed to generate a combination of TE_{11} and TE_{12} modes which, when combined together after a phasing section, radiate a 95% pure Gaussian free space wave.

A scaled version was built and tested at W-Band. Results of the measurements are shown in Figure 9. The spurious side lobes shown in the H-plane scan have since been eliminate following correction to the design code. A 600-700 GHz version of the output coupling system was manufactured and tested successfully at JPL.

Output Window

The current output windows consist of thin film glass mounted to stainless steel weld flanges. The new output design utilizes a dual mode horn to generate a Gaussian mode, so the guide wavelength is no longer the same. Fused silica is being investigated to provide half guide wavelength windows. Calculation indicate that the maximum VSWR in the operating band should be less than 1.4:1, which is considerably better than in the existing BWOs. It is anticipated that this will lead to reduced reflected power and better performance of the device.

Depressed Collector

The interaction efficiency of BWOs is typically less than a few percent, so most of the electron beam energy is dissipated in the collector. A single stage depressed collector was designed to recover this energy and improve the overall efficiency of the device. The power reduction also allows elimination of the water cooling required for the existing BWOs. A simulation of the depressed collector is shown in Figure 10. Electrons from the cathode pass through the slow wave circuit, across an insulating gap, and into a cavity designed to contain reflected and true secondary electrons. The cavity material is graphite to reduce the number of secondary and reflected electrons generate. Simulations indicate that approximately 85% of the beam power can be recovered. This will reduce the maximum power required for the BWO from 270 W to less than 50 W.

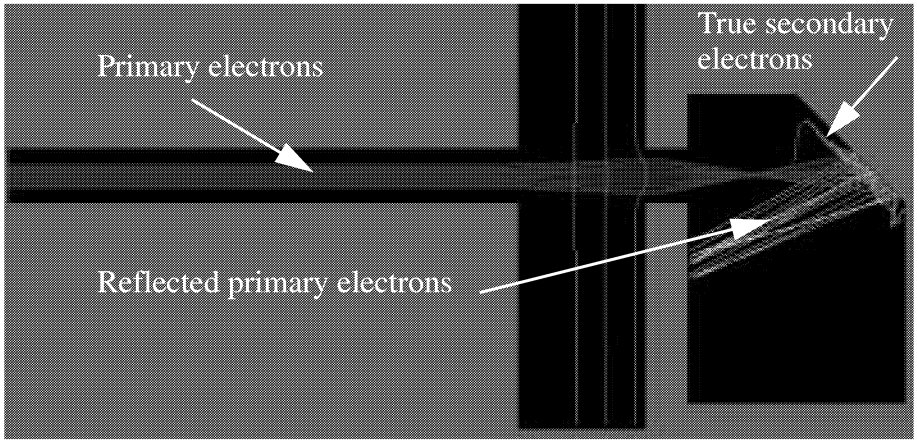

Figure 10. Simulation of sheet electron beam with single stage depressed collector. Primary electrons, reflected primary electrons, and true secondary electrons are indicated. Simulation is at 5,000 Volts, 30 mA.

Reduction of Magnet Size and Weight

Techniques are currently being developed to integrate permanent magnet focusing into W-band klystrons. This work is funded by the U.S. Air Force through the Multidisciplinary University Research Initiative (MURI), and CCR is involved with this program. The magnet research is being performed at the Stanford Linear Accelerator Laboratory.

Basically, permanent magnets and iron pole pieces are incorporated directly into the LIGA-produced structure to place the parts extremely close to the electron beam. This proximity reduces the magnetic field required and dramatically reduces size and weight.

CCR is investigating a similar technique for the BWOs. Because the BWOs use a sheet electron beam, permanent "wiggler" focusing is being considered. Preliminary calculations indicate that sufficient field strength can be generated using wiggler focusing adjacent to the electron beam and within the vacuum envelope. This procedure reduces the total weight of the BWO and magnet from 15 to 20 kG to less than 0.5 kG.

Implementation of permanent magnet, wiggler focusing requires a different type of electron gun. The current gun is totally immersed in the 1.1 T field, which provides the required focusing. Immersion will not be possible with permanent magnet, wiggler focusing, because the magnetic field will not extend into the gun region. Consequently, it is necessary to design an electrostatically focused, convergent gun. CCR currently has a Department of Energy SBIR grant to develop a sheet beam gun for an X-band klystron, so the actual gun design will not be a major task. Mechanical design of such a gun with the small size required could, however, be a significant development effort. One alternative being considered is a field emitter array (FEA) cathode. FEA cathodes do not require a heater and are theoretically capable of very high current densities—higher than available with the existing cathodes.

BWO Construction and Test

A solid model of the 600-700 GHz beam line assembly is shown in Figure 11. The main body assembly is approximately 2 cm X 2 cm X 4 cm and will be enclosed within a copper or glass vacuum envelope. The basic assembly is designed for compatibility with several of the LIGA circuits being manufactured. The output waveguide/ Gaussian mode antenna and window are frequency dependent, so these items must be designed for each particular frequency band. All circuits will have the same base structure so they will be interchangeable within the BWO body section. When the basic configuration is designed, it should be fairly straightforward to install various circuits and output components into a standard BWO body. This capability will reduce the design effort, manufacturing costs, and reliability while facilitating rebuilds.

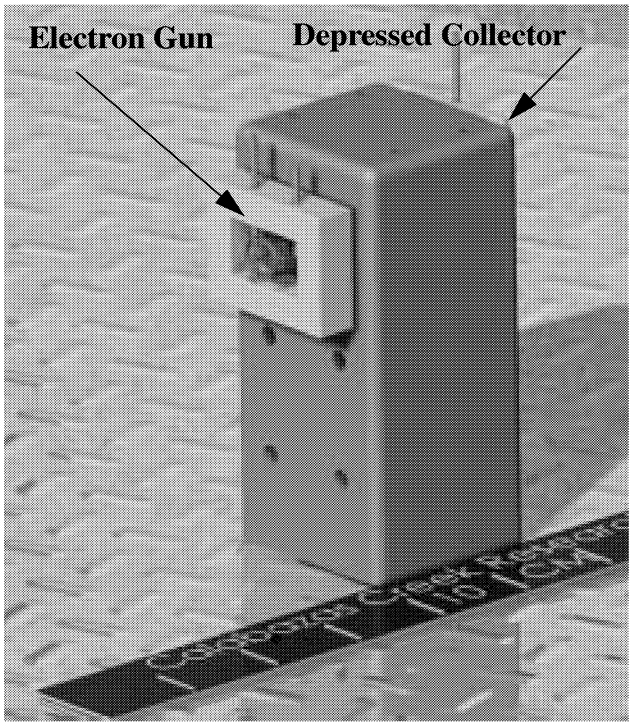

Figure 11. 600-700 GHz Beam Line Assembly.

The cathodes, magnet, power supplies, are completed. The LIGA circuits are currently being manufactured with delivery scheduled for early July. Drawings for the remaining parts, including the window, body, collector, electrical feedthroughs, and vacuum envelope are in progress. It is anticipated that final assembly of the prototype 600-700 GHz BWO will begin in July with completion in August. Testing will begin as soon as the prototype is completed.

Following successful test of the 600-700 GHz BWO, construction will begin for the next BWO in the frequency series which will operate from 650-900 GHz. Additional BWOs will be built and tested as time and funding allow.

Program Summary

A complete, theoretical understanding of the BWO circuit and interaction with the electron beam are essentially complete. This understanding will facilitate optimization of BWO performance and extension of the design to higher frequency, output power, and efficiency. Additional analysis is planned to improve understanding of RF coupling from the slow wave structure into the output waveguide slot.

Analysis to date, coupled with dramatic advances in micro-electro-mechanical systems and FEA cathodes, provides many possibilities for improvements in BWO performance, reduction in weight and power requirements, and reduction in size and weight.

1. Glenn Schietrum, A. Burke, G. Caryotakis, A. Haase, L. Song, “W-Band Klystron Research,” Pulsed Power Plasma Science 2001, 28thy IEEE Intern. Conf. Plasma Sci., June 2001, Las Vegas, NV.

This research is funded by National Aeronautics and Space Administration Small Business Innovation Research contract No. NAS3-01014.

NOVEL HETEROSTRUCTURE DEVICE FOR THZ POWER GENERATION

Z. S. Gribnikov[1, 2], N. Z. Vagidov[1], H. Eisele[2], V. V. Mitin[1], and G. I. Haddad[2]
[1]*Department of ECE, Wayne State University, Detroit, Michigan 48202*
[2]*Department of EECS, University of Michigan, Ann Arbor, Michigan 48109*

It has been shown that oscillations at THz frequencies can occur when carriers in a semiconductor device have a particular energy-wave vector dispersion relation with a section of a negative effective mass (NEM) like in Fig. 1. The device structures that have been investigated so far had one major disadvantage: These oscillations occur only at cryogenic temperatures and the generated RF output power is low [1]. The main reason for this is the range of energies where the NEM is present in the dipsersion relation. To overcome this disadvantage and to place this region within a more desirable interval (0.1–0.3 eV), a new heterostructure device is proposed. The main idea is the use of a structure that consists of two parallel channels of current conduction with different properties. In one of them, *i.e.*, the quantum well (QW) of Fig. 2, electrons, as the carrier chosen here, have a small effective mass, whereas in the other channel, *i.e.*, the superlattice (SL), the effective mass of electrons is several times higher. At $k_z = 0$ (where k_z is the component of the wave vector **k** along the growth direction of the SL), the electron wave function is localized almost completely in the QW. As k_z increases, the electron wave function expands further into the SL. As a result, electrons become heavier and heavier. Such a dynamic (quantum) real-space transfer (without any electron scattering) causes an NEM section to appear in the lowest subband of the QW. The position of this section relative to the conduction band edge, the width in energy of this subband, and its distance from upper subbands is determined by key parameters of the QW and SL. Several versions of such structures were investigated. The most promising choice is a configuration where the transverse motion of electrons in the SL is limited by an additional electric field. This electric field results from a *p*-type doping in the SL barrier layers and the *n*-type delta doping of the barrier layer on top of the QW. This electric field provides additional control over where the NEM section occurs in the dispersion relation. The QW and the top barrier layer with delta doping can be realized on the edge of the SL using the same method of cleaved-edge overgrowth in an MBE system as for T-shaped quantum wires. An alternative method is glancing-angle overgrowth in an MBE system. Numerical calculations were carried out for the proposed device structures and they yielded the best results for a fully strain-compensated SL of lattice-mismatched InGaAs/InAlAs on InP and a QW of InGaAs lattice-matched to InP.

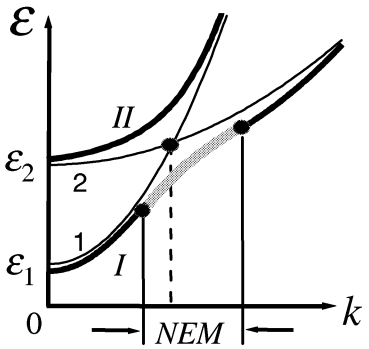

Fig. 1. The formation of an NEM region in the lowest branch *I* from the anti-crossing of the two initial dispersion branches 1 and 2.

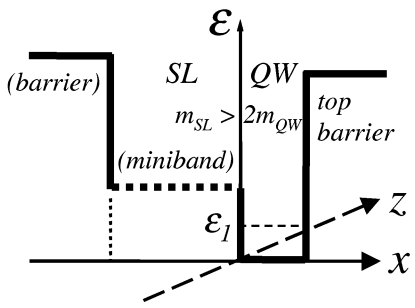

Fig. 2. Simplified heteropotential profile for one of the proposed device structures as used in the calculations.

[1] Z. S. Gribnikov, N. Z. Vagidov, A. N. Korshak, and V. V. Mitin, J. Appl. Phys. 87, 7466 (2000).

A Novel Full Waveguide Band Orthomode Transducer

Gopal Narayanan[1], and Neal R. Erickson

Department of Astronomy
University of Massachusetts
Amherst, MA 01003

Abstract

At millimeter and submillimeter wavelengths, cryogenically cooled receivers based on SIS and HEB technologies are approaching the quantum limit in noise temperature. Further increase in sensitivity can be obtained by using dual-polarized operation. One of the principal components of a dual-polarization receiver is a polarization diplexer or orthomode transducer (OMT). Traditionally the OMT used in radio astronomy receivers is the wire grid, which can be large and bulky. A waveguide based OMT, on the other hand, can be integrated with the mixer blocks and cryogenically cooled thereby reducing ohmic losses. A waveguide based OMT also lends itself well to integration into focal-plane array receivers. In this paper, we present the design of a novel OMT that can be constructed using conventional split-block techniques. The design is based on the proposed Bϕifot OMT by Wollack [1], but has been considerably modified to (a) make it easy to fabricate, and (b) make it scalable to $\sim$ 1 THz. The return loss is -20 dB or better over a full waveguide-band ($\sim 40\%$ bandwidth), and the cross-polarization and isolation are better than -70 dB. Design details of a W-band OMT are presented.

1 Introduction

An orthomode transducer (OMT) is a device that separates orthogonal polarizations within the same frequency band. In the literature, OMT's are called by various other names such as polarization diplexers, dual-mode transducers, orthomode junctions or orthomode tees. With receiver noise temperatures of waveguide-based SIS and HEB mixers approaching a few times the quantum limit, further increase in sensitivity can be obtained using dual-polarized operation. In radio astronomical applications, the conventional way to separate orthogonal polarizations is the wire-grid diplexer, which is a quasi-optical device that consists of free-standing parallel wires. The polarization with the E-field parallel to the wires is reflected, while the component orthogonal to the wires is transmitted through. However, the wiregrid polarization diplexer is large and bulky. If we desire the mixers for both polarizations to reside in one cryostat, the wiregrid should preferentially be inside the dewar, which correspondingly increases the size of the required dewar. A broadband waveguide-based OMT would be a preferable alternative as it would much smaller, and it would be a good match to available high-performance dual-polarized broadband corrugated feedhorns. A

[1]e-mail: gopal@astro.umass.edu

waveguide based OMT also lends itself well to integration into focal-plane array receivers. In this paper, we present the design of a full-waveguide band OMT for the W-band, which is scalable to 1 THz.

2 General Considerations for OMTs

With improved fabrication techniques [2,3,4], high-quality waveguide blocks can be made to 1 THz and beyond. One of the principal requirements in our design is the scalability of the design to terahertz frequencies. An OMT used for radio astronomy purposes should satisfy several important requirements: (1) A return loss of $\sim$ 20 dB or better for a full waveguide band ($\sim$ 40% bandwidth). (2) Isolation between the two orthogonal polarization ports of better than 40 dB. (3) Cross-polarization term should be less than 40 dB. Cross-polarization for a given polarization port is the amount of signal present from the orthogonal polarization. One of the driving goals of an OMT design should be that the cross-polarization introduced by the OMT should not exceed that produced by the optics and feedhorn that precede it in the system. (4) Low Insertion Loss. Since the OMT will be operated cryogenically the ohmic losses are less important that for room temperature operation. (5) The design should be scalable to 1 THz. The fabrication of the OMT should lend itself to established split-block techniques.

For any waveguide device, the broadband operation of the device is tied to its symmetry properties. Symmetrical or non-symmetrical transitions in waveguides produce higher order modes. Most of the higher modes are evanescent and do not propagate. However, uncompensated higher order modes store reactive energy which prevents the broadband operation of the device. What sorts of higher order modes are produced often dictates the broadband isolation and input match of waveguide devices. To design a broadband device, it is necessary to design the transitions such that only even-order higher modes are produced, because they are easier to compensate. A waveguide device is defined as symmetrical if different transitions cause the dominant mode to only generate symmetrical (even-order) higher modes. A device is defined as non-symmetrical if the dominant mode, in addition produces odd-symmetrical higher order modes.

Bϕifot classified waveguide-based OMTs into three groups [5,6] based on their increasing symmetry. Class I represents the simplest and most common approach, with one main arm for one mode and one orthogonal sidearm for the other mode. The main arm mode is symmetric while the sidearm mode is not. An example of such an OMT is that used in [7], where the H-bend in the sidearm breaks its symmetry, resulting in narrower percentage bandwidth ($\sim$ 20%). The Class II configuration OMT is more complex. Here there is one main arm, but the side arm is split into two symmetrical parts from the main arm. An example of this sort of device is that presented in [5] and implemented by Wollack [1]. In this device, the main arm mode sees a symmetrical device as in the Class I equivalent. In addition, the side arm also sees symmetrical splitting and combining junctions. The symmetrical nature of this splitting and combining makes it possible to achieve a good broadband match even for the side arm mode. The Class III OMTs are even more

complex, with both the main and side arms split into two symmetrical parts. The splitting junction essentially forms a classic turnstile junction whose matching properties have been well studied [8]. Since the splitting junction is symmetric both in the main and side arms, higher order symmetric modes will naturally be canceled in both arms, and thus these OMTs should have a natural broadbanded match and isolation performance. However, this class of OMT is very complex and hence expensive to fabricate.

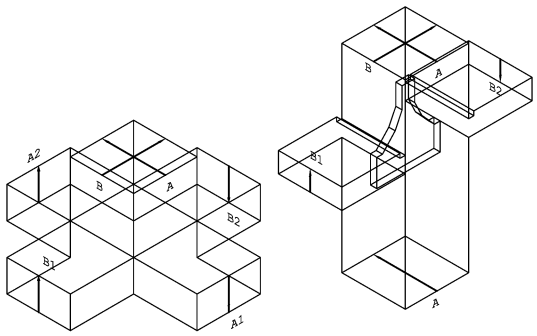

Figure 1: (a) The six-port Classic Turnstile Junction. A and B denote the two ports at the input for the orthogonal polarization. (b) Folded Turnstile Junction, which becomes a Class II OMT. Ports A1 and A2 are folded together.

The Bϕifot junction [5] is a Class II OMT, but it can be thought of as a turnstile junction where two of the ports have been folded parallel to the common port (see Figure 1). The two ports that form the main arm are separated by a metal septum, recombined into square waveguide and then transformed into a standard full-height waveguide. The two symmetric side arms remain the same as in the Class III turnstile-type OMT. For the polarization meant for the side arms, the septum can be thought of as back-to-back "mitered" bends which feeds the symmetric side arm ports. A WR-42 OMT based on the Bϕifot design was made and tested by Wollack [1]. In Bϕifot's design, pins are placed at the entrance apertures of the side arms. There are a pair of such pins for each sidearm. These pins act as capacitive posts. From the perspective of the main arm, these pins tune out the discontinuity of the holes created by the side arms in the main waveguide. From the perspective of the side arms, these pins along with the shape of the septum serve to tune out the dispersive reflective termination that is created by the septum in the main arm. While the pins provided adequate match for the OMT, their small diameters (0.127 mm for the 3 mm band) and the complexity of assembly of the pins in the block make them unsuitable for scaling the OMT to terahertz frequencies. In this work, we replaced the pins with capacitive steps at the side arm apertures (see Figure 1) which are easy to fabricate in-situ with the waveguide block, and work as effectively as the pins do.

3 OMT Design

3.1 Design Methods

Most parts of the OMT design was carried out using CST Microwave Studio (CST MWS) [9]. CST MWS is based on the finite integration (FI) method, which is a one-to-one translation of Maxwell's equations into a discrete space formulation without simplification or specialization. As a general approach its theoretical framework has been developed by the likes of particle accelerator designers for over three decades, and hence is a robust design tool. The FI method works explicitly in the time domain, and hence a full broadband simulation can be performed in one single solver run. MWS is well suited for electrically large structures and features a powerful, parametric drawing editor to lay out the structures. It also comes with a built-in optimizer which was used heavily to optimize the geometry of the septum and the dimensions of the capacitive waveguide steps. While most of the design was carried out in CST MWS, some critical portions such as the junction part of the OMT were also simulated with Agilent's HFSS [10]. The HFSS results verified the predictions of CST MWS, and hence the final results and optimizations were derived using the latter.

3.2 OMT Junction

The design of the complete OMT was done in several steps. First the OMT junction where the main and side arm waveguides meet was designed. The two orthogonal polarizations A and B (see Figure 1b) travel through the input square waveguide (WR-10 dimensions 2.54×2.54 mm). The septum lies in the split block plane at the junction. Polarization A travels straight through the main arm, while polarization B is split through the side arms and later recombined. The design and optimization of the septum and capacitive waveguide steps were carried out separately for both polarizations. Full symmetry considerations were used. Only one quarter of the structure shown in Figure 1b was simulated with magnetic and electric walls on the planes of symmetry being applied to reduce the problem size and solution times. The optimization was carried out for best input match over the 75 – 110 GHz for both polarizations by varying a variety of physical dimensions of the junction. The parameters that were varied included the size of the aperture for the side arm (the side arm waveguide height), length and width of the capacitive step, and several geometrical dimensions of the septum. The metal septum was treated as a perfect conductor. Both for simplicity of optimization and for fabrication ease, the septum was modeled as a simple shape with straight edges. Due to the requirements that the design be scalable to a THz, the design was pushed towards geometries where the thickness of the septum was greater. The final optimized design for the junction is shown in Figure 2. Figure 3 shows the input match at the OMT junction for the main arm and side arm polarizations for the chosen geometry.

The side arm waveguide is 0.813 mm (0.032") in height, with the capacitive step in the waveguide measuring 0.208×0.165 mm in dimension. The requirements of good input match for the two polarizations have an opposite dependence on the thickness of the sep-

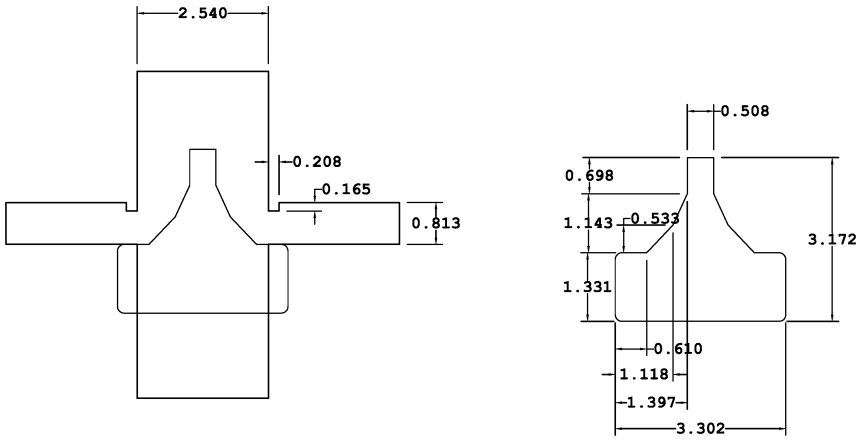

Figure 2: (a) Split-block view of the optimized OMT junction. All dimensions are in millimeters. (b) View of the Septum with some relevant dimensions. The septum is 0.254 mm thick for the W-band OMT.

tum. The bandwidth of good match for the side arm polarization (polarization B) increases with increasing septum thickness. For this polarization, increasing septum thickness makes the septum look more and more like back-to-back mitered bends. For the main arm (polarization A), the bandwidth of good match reduces with increasing septum width. A thin septum produces less discontinuity than a thick septum. The dimensions and geometry of the capacitive step acts as an additional variable in adjusting the match. The optimal thickness of 0.254 mm chosen here for the septum represents a good compromise for the two polarizations, while still remaining an easy enough junction to fabricate.

3.3 E-Plane Bend Across Split Block

In the main arm, polarization A travels through the 1:1 square waveguide and is then transformed into a full-height rectangular waveguide. The transformer is followed by an E-plane bend across the split-block to bring the port out orthogonal to the side-arm port. The square to rectangular transition is accomplished using a 3-section transformer. The transformer is immediately followed by the E-plane bend. The bend itself consists of two steps, both below the split block plane (see Figure 4). In the top block of the split-plane, a full-height rectangular waveguide brings out the main arm port to the outside world. The rectangular waveguide in the top block is hard to machine (it would have to be punched or fabricated as a cylindrical insert and pressed and soldered prior to milling the rest of the features in the top half). In view of this, we designed an oval waveguide which can be directly machined with an end-mill. The oval waveguide uses full-radius corners (0.635 mm), and has $a = 2.79$ mm (10% increased). Figure 4c shows that the reduction in bandwidth of match for using oval waveguide is minimal. The distance from the OMT junction shown in Figure 2 and the transformer E-plane bend shown of Figure 4 is 0.94 mm. This distance

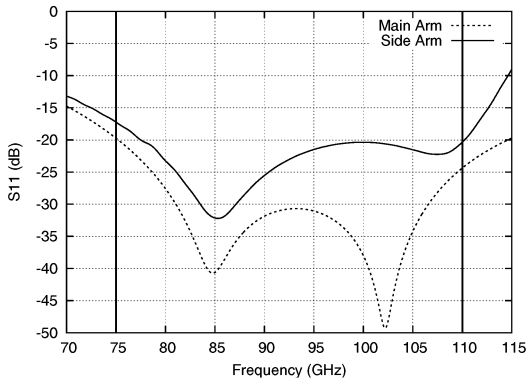

Figure 3: Input match (S11) in dB for the polarizations in the main and side arms for the OMT junction. The side arms match is worse because the side arm sees less symmetry than the main arm. Nevertheless, between 75 – 110 GHz, the match is seen to be at least as good as the required 20 dB.

was optimized in a linear circuit simulator [11] by using ideal rectangular waveguide transmission line sections between the de-embedded S-parameter equivalent networks from the OMT-junction and the transformer section.

3.4 E-Plane Combiner for Side Arm

The two side arms are made to bend around the main arm features through a pair of E-plane bends and are then recombined into a full-height rectangular waveguide which emerges on the opposite side of the square input waveguide of the block. A full-height to full-height waveguide E-plane power divider/combiner design has been recently presented by Kerr [12]. In the Kerr design, the two incoming full-height rectangular waveguides meet in a square waveguide section which is then transformed back into rectangular waveguide. The resulting combiner is physically quite long (~ 8 mm for W-band). We designed a very simple power combiner with excellent performance across a full waveguide band to combine two side arm waveguides (with a height of 0.813 mm each) to full-height waveguide. This combiner has the advantage that its length is quite small (2.54 mm). Figure 5 shows the cross-sectional view of the resulting combiner and its predicted performance.

At the junction of the combiner, the two waveguide arms are a little over half-height (0.762 mm high). There is a broad pedestal in the middle of the combining junction. Surprisingly in this reduced height guide, such a simplified geometry works as well as the more complex E-Plane Y junction shown in [12]. This combining junction, which can be thought of as an E-Plane Tee power divider can also be used for power division or combining for full-height to full-height waveguides. In Figure 5b, the input match for our E-Plane Tee power combiner is compared against the full-height Kerr Y combiner, and a slightly modified version of the E-Plane Tee combiner for full-height waveguide. Especially for power

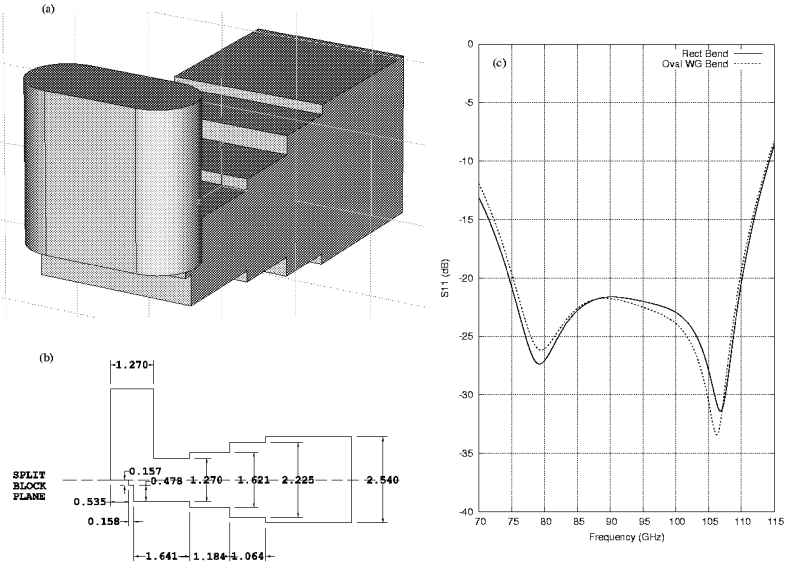

Figure 4: Square to rectangular transformer and E-plane Bend Across Split-block plane. (a) Isometric view of the transformer and E-plane bend; (b) Cutout view with dimensions. All dimensions are in mm; (c) Input match for the transformer and E-plane bend. The two curves show the change in the match from using rectangular and oval waveguides in the top half of the split plane.

combination in reduced height geometries, it can be seen that the E-Plane Tee is simple, compact, and has excellent performance. Even for full-height waveguides, the E-plane Tee has acceptable match over a full waveguide band.

3.5 OMT Predicted Performance

Figure 6 shows the isometric inside and outside view of the OMT with all the individual sections added together. A full simulation of the entire structure leads to the predicted performance curves shown in Figure 6c and d.

The input match is seen to be ≤ -20 dB across the 75 – 110 GHz band. Isolation and cross-polarization terms are more than 75 dB down across the band (not shown in the figure). We also simulated the effect of bending the septum or not having the septum properly centered in the center of the junction. Even when the septum is moved a full 0.127 mm (half its thickness) from the split-block plane, simulations show that the input match is only degraded by ~ 2 dB, while the isolation and cross-polarization terms are still better than 50 dB down. To gauge the effect of conductor losses in the OMT, the perfect conductors used in the simulation were replaced with a conductor of conductivity 2×10^7 S/m. This yielded a maximum insertion loss of ~ 0.1 dB and ~ 0.2 dB in the band, with a typical loss of ~ 0.06 dB and ~ 0.15 dB for the main arm and side arm polarizations

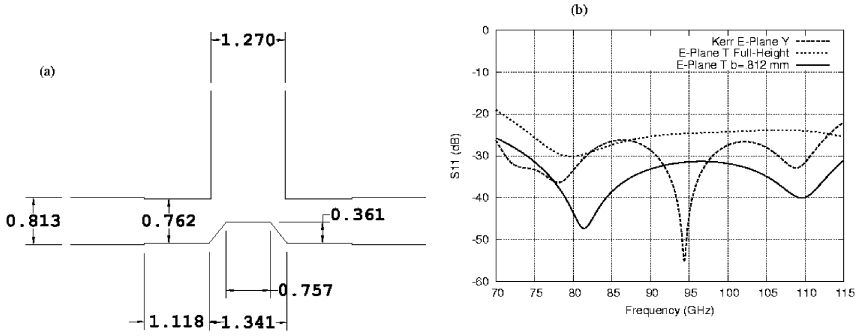

Figure 5: E-Plane Combiner Junction. (a) Dimensional details of split-block view of the E-plane Tee combiner. (b) Input match of the combining junction. Shown for comparison are two more S11 curves. The Kerr E-Plane Y combiner for full-height waveguide and our full-height E-plane Tee combiner design with one additional section added to transform the two input sides to full-height waveguide.

respectively.

At the time of this writing, the septum has already been made, and a test WR-10 block is being fabricated. Tests of the prototype OMT will be reported in a forthcoming ALMA memo.

4 A Scalable and Machinable Design

The Wollack NRAO OMT design had very tight mechanical tolerances and difficult assembly, and is not suitable for scaling much above $\sim$ 150 GHz. The new OMT design presented here avoids these problems. One of the significant advantages of this design is that the waveguide pins (0.127 mm for W-band) that was used in the Wollack design has been replaced with simple capacitive steps. The new design also has a septum that is over four times thicker than that used in the Wollack design, which considerably eases the task of assembly and handling of the septum. The compact split-block design is well suited to CNC machining. The design as presented for the W-band can be scaled to 500 GHz with little difficulty in machining. Slight modifications in the design and re-optimizations should yield machinable designs with acceptable performance even to 1 THz. In the OMT junction, some of the septum's geometrical parameters can be traded off against the waveguide step capacitor, whose dimensions at ~ 1 THz may pose some machining problems.

5 Conclusions

A novel full-waveguide band orthomode transducer has been designed. The design for the W-band has excellent matching, isolation and cross-polarization characteristics for the full design band of 75 – 110 GHz ($\sim 40\%$ bandwidth). The design is simple to fabricate and assemble and is scalable to frequencies of ~ 1 THz.

Research at the Five College Radio Astronomy Observatory is funded in part by a grant from the National Science Foundation.

6 References

[1] E. Wollack, "A Full Waveguide Band Orthomode Junction", Electronics Division Internal Report, National Radio Astronomy Observatory, Green Bank, WV, no. 303, May 1996.

[2] G. Narayanan, N. R. Erickson, and R. M. Grosslein, "Low Cost Direct Machining of Terahertz waveguide Structures," Tenth International Symposium on Space Terahertz Technology, pp. 518-528, Mar. 99.

[3] C. K. Walker, G. Narayanan, A. Hungerford, T. Bloomstein, S. Palmacci, M. Stern, J. Curtin, J., "Laser Micromachining of Silicon: A New Technique for Fabricating TeraHertz Imaging Arrays", Astronomical Telescopes and Instrumentation, SPIE Symposium, Kona, Hawaii, 1998.

[4] C. K. Walker, G. Narayanan, T. M. Bloomstein, "Laser Micromachining of Silicon: A New Technique for Fabricating Terahertz Waveguide Components", 1997, 8th International Symposium on Space Terahertz Technology, eds. Blundell and Tong, Harvard University.

[5] Bϕifot, A. M., Lier, E., and Schaug-Pettersen, T., "Simple And Broadband Orthomode Transducer", 1990, Proc. IEE, vol. 137, no. 6, pp 396-400.

[6] Bϕifot, A. M., "Classification of Orthomode Transducers", 1991, European Transactions on Telecommunication and Related Technologies, vol 2, no. 5, pp 503-510.

[7] Chattopadhyay, G., Philhour, B., Carlstrom, J. E., Church, S. Lange, A., and Zmuidzinas, J., "A 96 GHz Orthomode Transducer For Polatron", 1998, IEEE Microwave and Guided Wave Letters, vol 8., no. 12, pp 421-423.

[8] Montgomery, C. G., Dicke, R. H., and Purcell, E. M., "Principles of Microwave Circuits", Dover Publications, New York, 1948, pp. 459-466.

[9] Computer Simulation Technology (CST) Microwave Studio (MWS) v3.4, CST of America, Inc., Wellesley MA.

[10] High Frequency Structure Simulator (HFSS), v 5.6, Agilent Technology Inc., Palo Alto, CA.

[11] Advanced Design System (ADS), v2001, Agilent Technology Inc., Palo Alto, CA.

[12] Kerr, A. R., "Elements for E-Plane Split-Block Waveguide Circuits", 2001, ALMA Memo Series No. 381, NRAO.

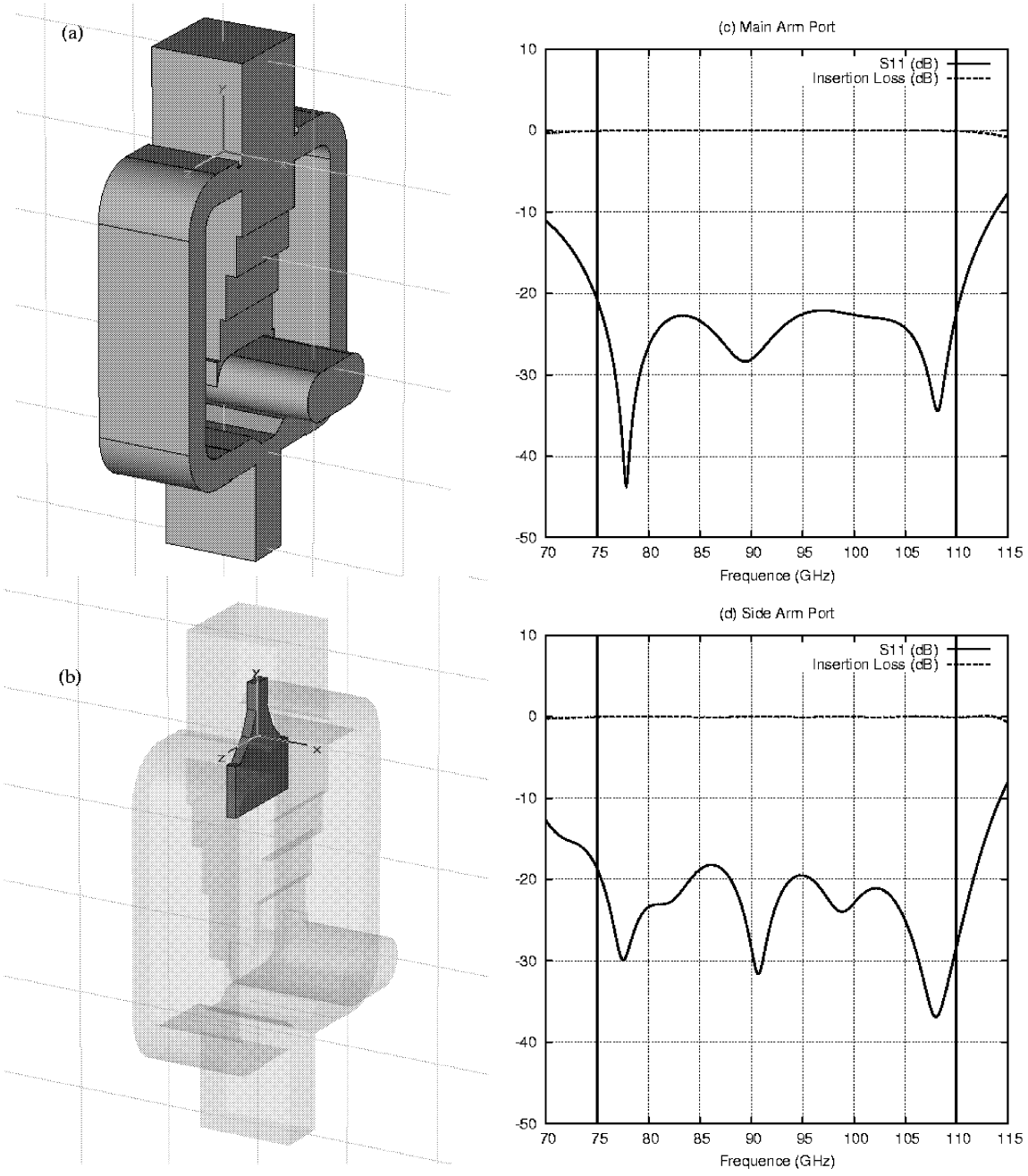

Figure 6: The full Orthomode Transducer. (a) Isometric view from the outside. The waveguide features of the OMT block measure $13.2 \times 7.6 \times 2.54$ mm. (b) Inside view showing the septum resting in the split block plane. (c) Simulated performance for the full structure for the main arm polarization. (d) Same as (c) for the side arm polarization port.

Phase and Amplitude Antenna Measurements on an SIS Mixer Fitted with a Double Slot Antenna for ALMA Band 9

M.Carter (IRAM), A.Baryshev, R.Hesper (NOVA); S.J.Wijnholds, W.Jellema (SRON);
T.Zijlstra (Delft University)

Introduction

Phase and amplitude antenna measurements are required to give a complete and comprehensive antenna beam pattern of receiver systems. Radio astronomical receivers in the past years have been becoming more complex and/or increasing in frequency. There are a number of multichannel receivers on telescopes now that are either multi-frequency, or multi-beam, with or without polarization diversity. These receivers, with the advent of projects like FIRST or ALMA, now go into the terahertz frequency bands.

The reason for phase and amplitude measurements over simple amplitude measurements is so that the entire antenna system can be properly measured in the laboratory environment

IRAM with its 2 radio astronomical sights at Pico Veleta and The Plateau du Bure have had for many years a phase and amplitude antenna test facility, which has worked up to frequencies of 350 GHz. This system has been upgraded to make measurements to the top of the ALMA frequency bands, of 1 THz for band 10

In this paper we show the schematic layout of the new system. Then we will proceed to show its properties at frequencies up to 700 GHz.

This will be followed by the measurements on crossed slot antenna fitted with an SIS junction in the ALMA band 9 frequency range 600-720 GHz.

Reasons for Phase and Amplitude Measurements.

There are a number of reasons to have a phase and amplitude antenna measurement facility over a simple amplitude measurement system. These can be listed as follows:

1. To measure all of the quasi-optical parameters of an antenna structure or system. These include the following:
   - The waist size and its position in the X, Y and Z directions with respect to a known reference.
   - To measure the angle of the beam from a known plane of reference.
2. To measure the efficiencies of the optical system, i.e. The side lobe levels the gains and the phase, and then be able to relate this to the theoretical models.
3. To find the efficiencies of coupling to further optical trains and telescopes

4. To be able to pre-align quasi-optical systems with optical systems such as laser alignment in order to be able to improve system efficiency.

The IRAM antenna facility

The antenna measurement facility was designed to work up to frequencies of 350 GHz, which are the maximum frequencies that the IRAM telescopes at Pico Veleta and the Plateau de Bure can reach. There are 2 different systems of taking the antenna beam patterns;

1. A far field antenna beam pattern system with an elevation over azimuth rotation stages.
2. An X and Y raster scan quasi-near field measurement system

The former system is mainly used for horn and horn lens systems, and the latter is for the more complex systems that would be difficult to rotate, due to size or complexity. It is possible to do a raster scan of about 450mm x 450mm. This latter was used for the measurements to be described. Both of these systems have a positional accuracy of about 0.5μm. The schematic diagram of the system is shown in figure 1 below. The receiver system for frequencies up to 350GHz is a homodyne system as described in reference 1. This system was not able to be increased in frequency for 2 main reasons;

1. The power from the harmonic mixer driving it from frequencies up to 36GHz was not enough to give enough dynamic range.
2. The system of multiplication of the reference level did not give a stable reference above a multiplication factor of 4.

This system has been modified to improve its performance at frequency ranges up to 1 Terahertz. The system shown in figure 1 has two phase locked Gunn and 6X multiplier sources. One as the local oscillator, Gunn2, which is directed onto the antenna under test and the mixer located in the dewar by means of a horn lens combination followed by a mylar beam splitter. The other is put on to the translation table. The horn used for the transmitter is an open-ended piece of waveguide of cross section 0.46 x 0.23 mm machined to a point. The signal is mixed with the LO to give an intermediary frequency, IF, of 4, or 1.5 GHz, depending which mixer is used for the experiments. This is amplified and filtered and bought into the mixing box A.

On each of the 2 oscillator chains before they are multiplied by 6, we have 2 directional couplers; 1 about-20dB used to phase lock the 2 Gunn oscillators from the 2 synthesizers 1 and 2. The other about –15dB, where there are 2 harmonic mixers. The signals are down-converted, filtered and amplified and then mixed together to have a reference signal which equals IF/6. This reference is multiplied by 6 and then, amplified, filtered and put into the other input port of the mixer box A.

In this mixer box a 3rd input from a 4th synthesizer at 1.5 GHz enters. This is split in 2. One part goes through a band pass filter to the reference port of the vector voltmeter, an HP8508A. The rest of the signal is mixed with the multiplied reference to a frequency of 2.5 GHz . This is filtered and amplified and mixed with the IF signal to give an input signal on the vector voltmeter of 1.5GHz. The 2 inputs to the vector voltmeter are phase coherent.

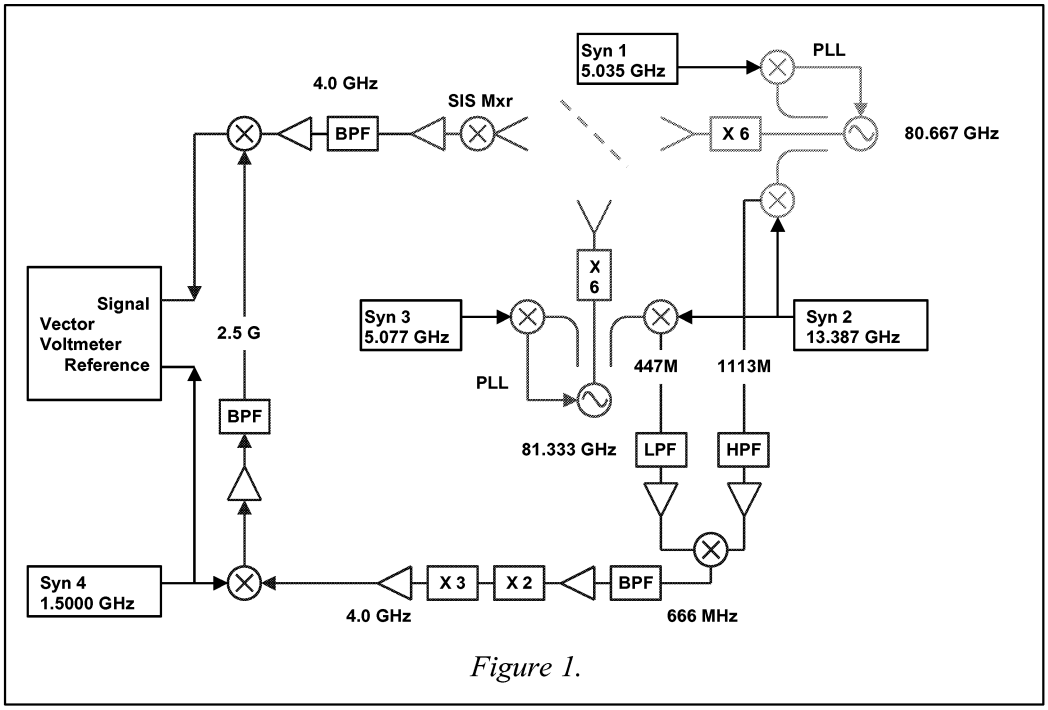

Figure 1.

This system has been modified from the lower frequency case in 2 major aspects:

1. The use of 2 Gunn oscillator / multiplier chains, one for the local oscillator (LO) and the other as the transmitter. At the lower frequencies a harmonic mixer could be used as a transmitting source. This has also meant the use of a first down converter on the reference.
2. The reference has to undergo the same number of multiplications as the transmitter. In this case a factor 6 was used. This has meant that the reference signal's signal to noise ratio was too low to lock the vector voltmeter. To get over this problem a further mixing scheme was required.

The equipment set up can be seen in the photographs in figures 2 and 3.

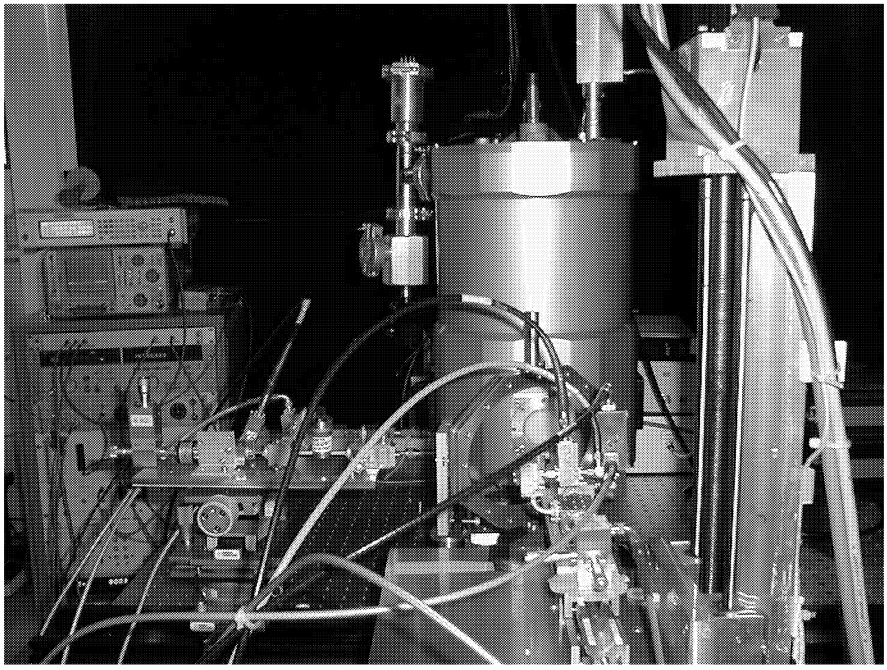

Figure 2 shows the view behind the transmitter with the Gunn and multiplier fitted onto the XY table. On the left can be seen the LO with the mylar beamsplitter in front of the Infrared Instruments dewar. Behind and to the left can be seen the rack of equipment holding the electronics, consisting of 2 of the synthesizers, The vector voltmeter and the reference multipliers, filters and amplifiers

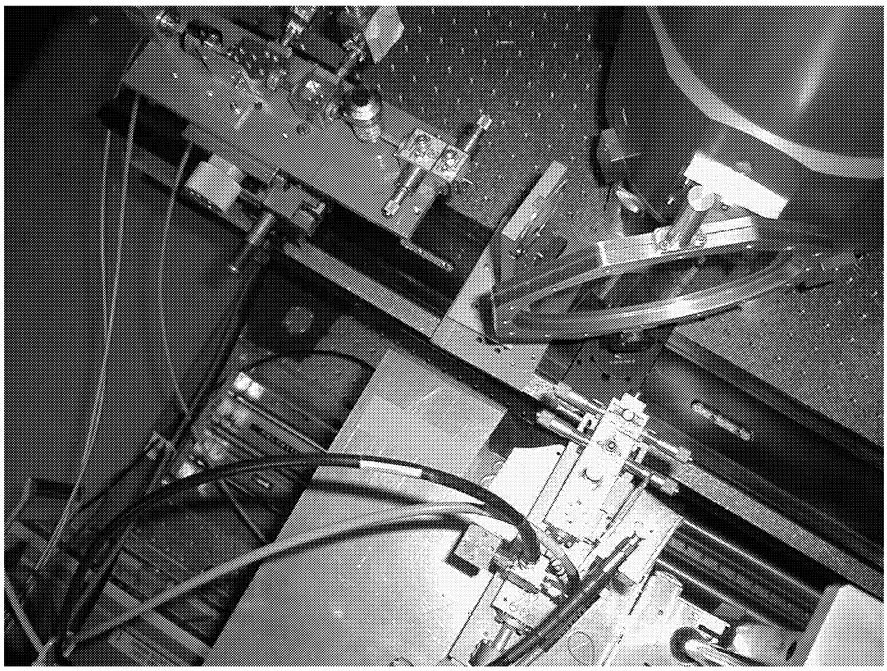

Figure 3 Shows a top view of the 2 Gunn multiplier chains. In the fore ground the transmitter on the XY table, and on the left the LO with the lens and the mylar beam splitter.

Performance

The system at present has been taken up to a frequency of 700GHz. The dynamic range as can be seen in fig 4 at a frequency of 630GHz is greater than 60dB.

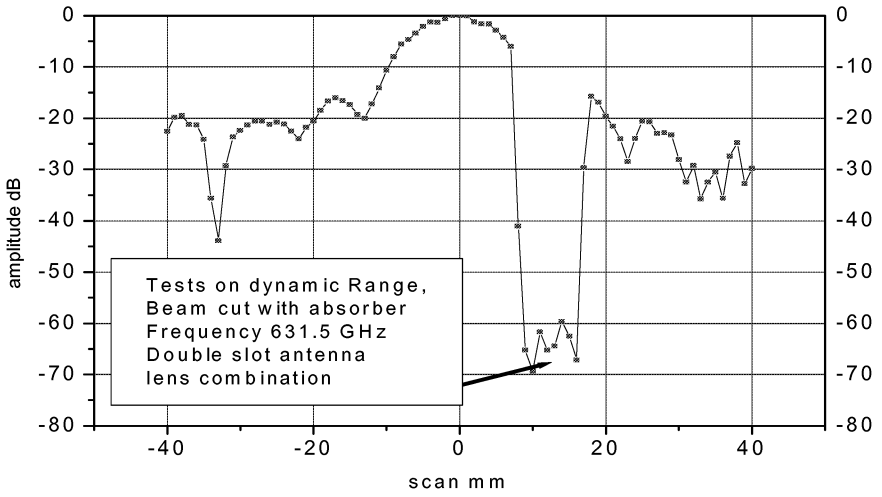

Figure 4 System dynamic range

The phase measurement shows that there is no loss of phase throughout its amplitude dynamic range. Figure 5 shows a plot of a diagonal horn at 634 GHz. The amplitude signal is to a level of –40 dB, but the phase can be unfolded all the way out to this level.

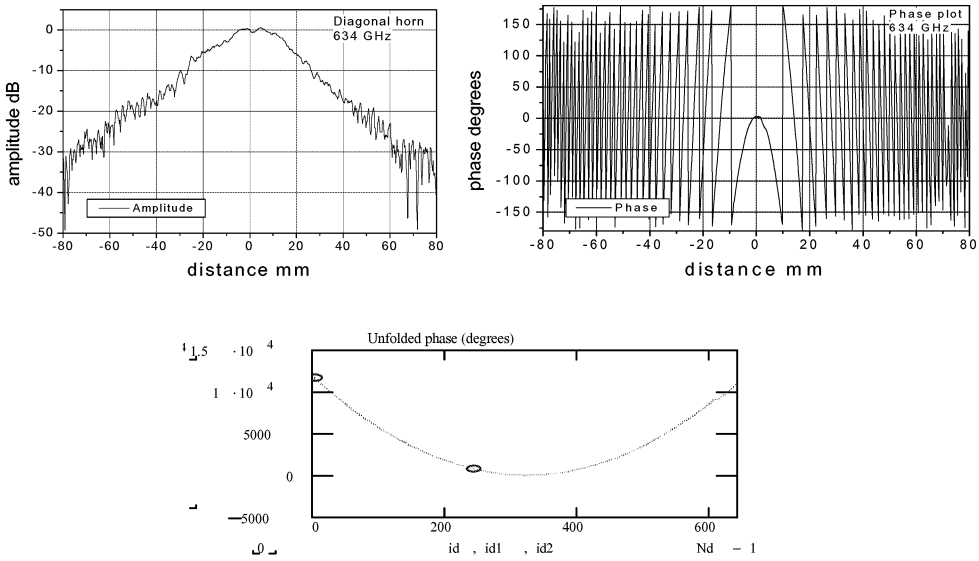

Figure 5 A measurement of a Diagonal horn at 634 GHz, showing the amplitude and phase plots, with the unfolded phase

One of the main problems encountered was the saturation of the SIS junction. Before each set of measurements checks had to be made to put the system into a linear measurement area. This was done by decreasing the transmitted signal in steps to see the effect on the polar pattern and then coming back to a level about 5 dB below the last point where there was not any change. This can be seen in figure 6.

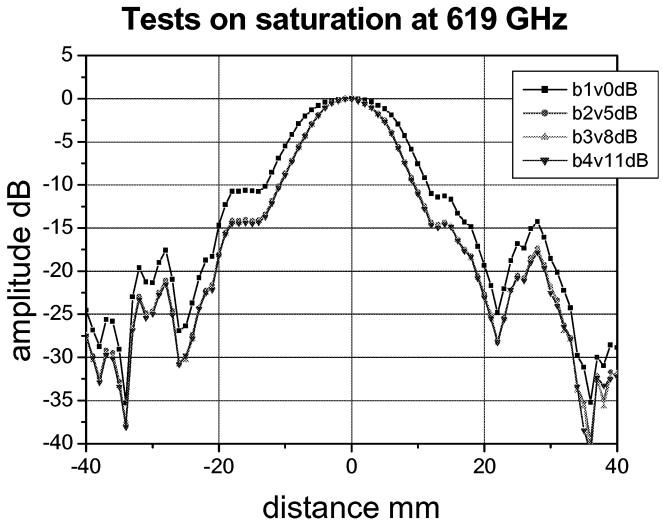

Figure 6 Saturation Experiments 0 dB,-5,-8,-11 transmitted power

Results

This equipment has been used to measure a double slot antenna mounted onto elliptical silicon lens, reference 2. The lens surface was matched with a stycast matching layer to reduce the reflection from the lens surface.

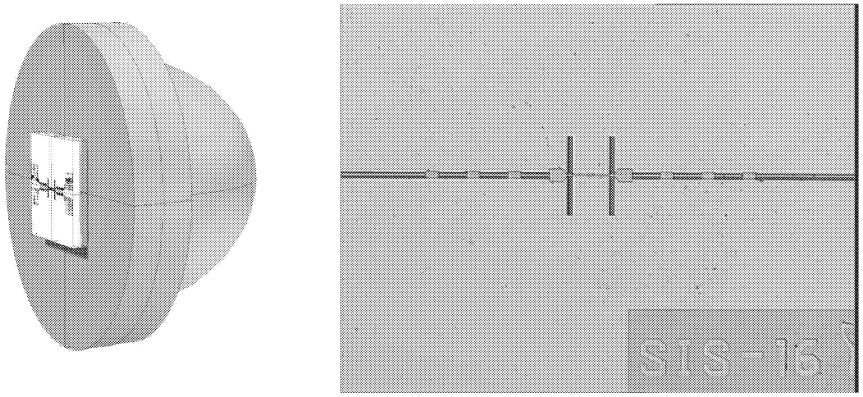

Figure 7 On the left a sketch of the antenna, and on the right a photograph

The measurements were made as described earlier, with the local oscillator injected through a mylar beam splitter. This meant that the transmitter had to be at the relatively large distance of 160 mm from the dewar.

Initial measurements in the 2 principle planes were made to align the antenna against the X-Y table, and to center the beam. This position was unfortunately lost during these measurements when the transmitter chains had to be changed.

The measurements were made in the quasi-near field of the elliptical lens. Cuts of +/- 40 mm distance with a step size of 0.25 mm were made in the 2 principal planes. These results are shown for 2 frequencies below at 604 GHz and 696 GHz.

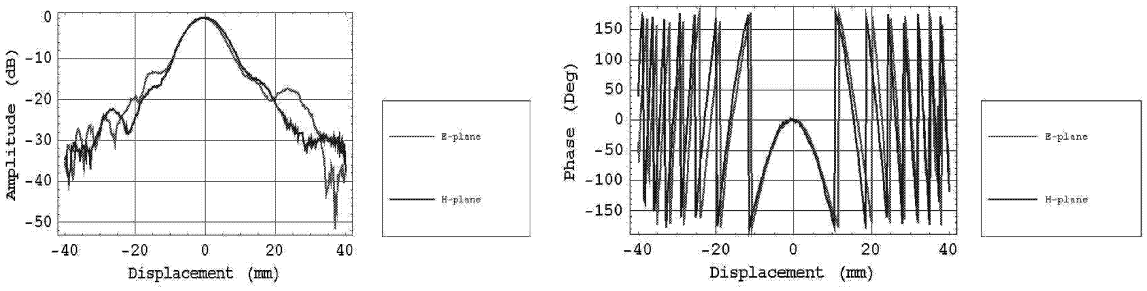

696 GHz measurements giving Woh = 3.78 and Wov =3.86

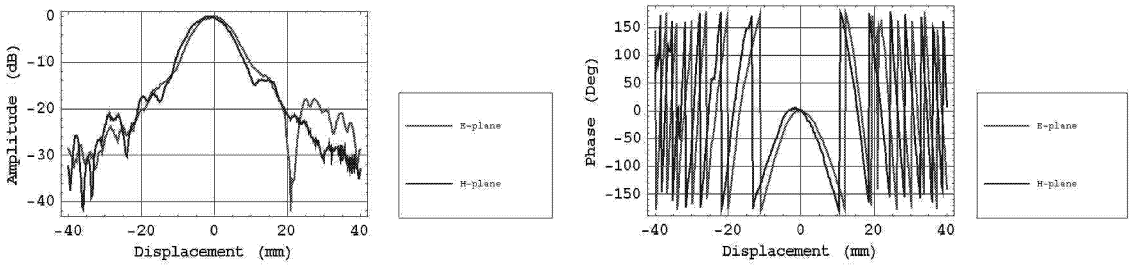

604 GHz measurements giving Who = 3.8 and Wov = 3.86

Figure 9 Crosscut measurements of the E-vertical and horizontal at 696 and 604 GHz

A series of these measurements were made over the frequency range. From the results of these measurements they were recalculated and put into the far field. These results can be seen below in figure 10. The results of these measurement show that there is a unique phase center for this antenna structure. The waist of this antenna structure is 3.9 +/- 0.2mm over the frequency measured and in both polarizations. The side lobe properties of this antenna have the first side lobes between –18 and -20 dB across the frequency range. The amplitude as the phase is perfectly symmetric and frequency independent. The 1-D Guassisity (overlapping integral with gaussian beam in Cartesian coordinate system) of this antenna was calculated over the frequency rang and found to be about 95-97%. However, the waist size Wv and distance |Zv for vertical direction are different from Wh and Zh in horizontal direction. This leads to slight degradation in 2-D Gaussitity which is about 89% across the measured frequency range.

A series of 2 dimensional scans were made at each frequency over an area of +/- 40 mm. To reduce the length of these measurements, the separation of the measurement points was increased to 2.5 mm x 2.5 mm, which has meant there is a reduction in the phase accuracy. An example of these measurements can be seen in figure 11.

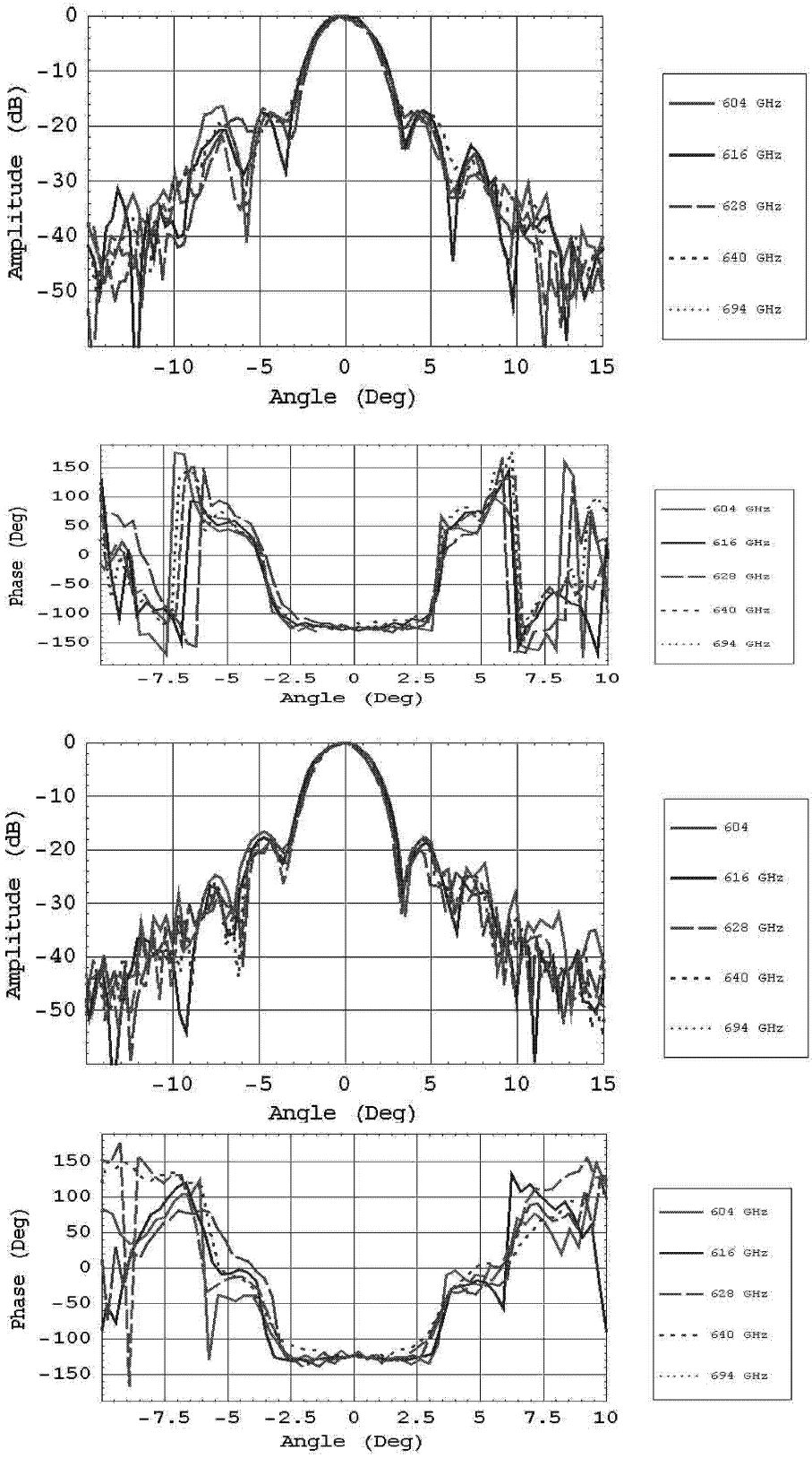

Figure 10 Far field results of the double slot antenna on a matched ellipsoidal lens above E-Vertical and below E-Horizontal

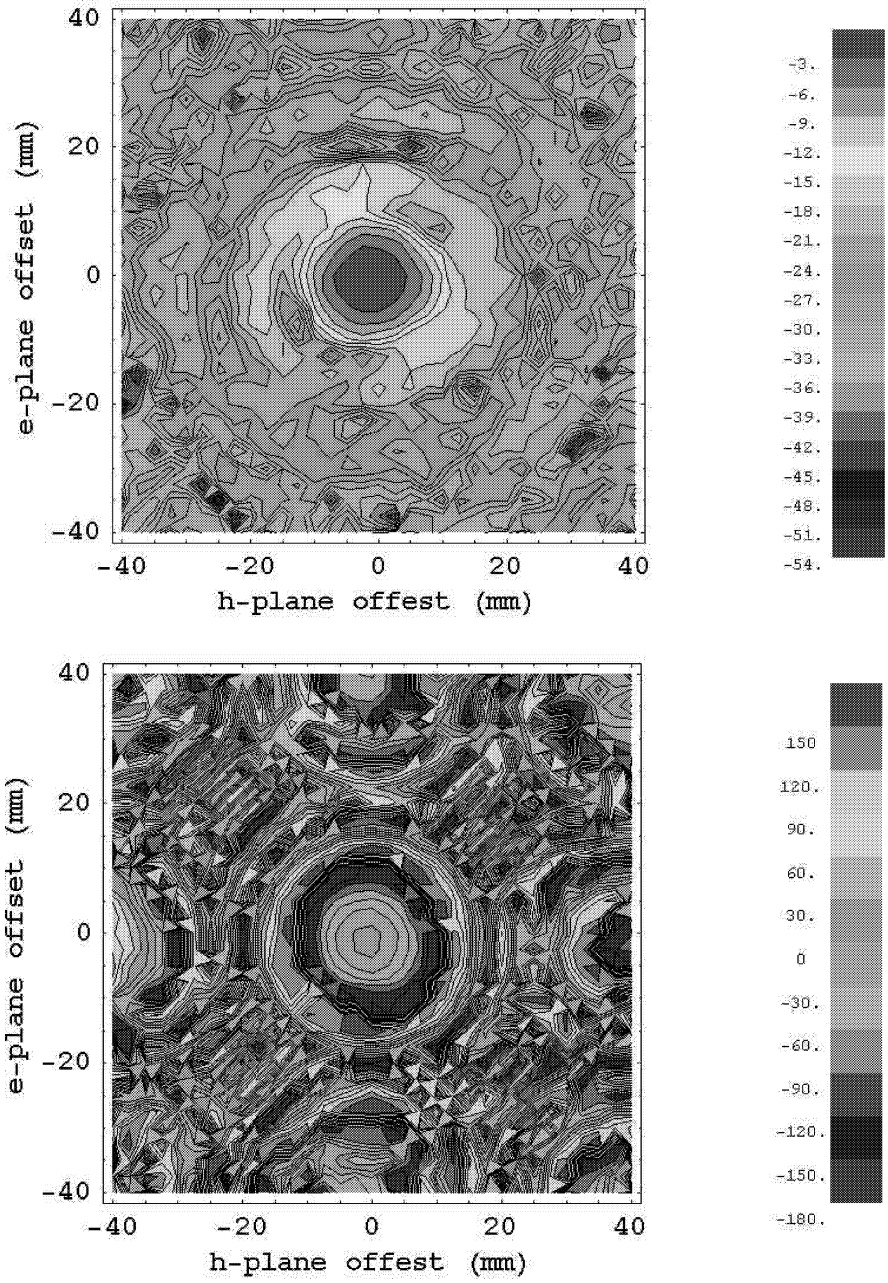

Figure 11 A 2 dimensional measurement pattern of the twinned slot antenna at 604GHz above the amplitude scale in 3dB steps, and below phase with the scale in 30-degree steps

Conclusion

In this paper we have shown a means of accurately measuring antenna and systems I the sub-millimeter wavelengths. The measurements shown were made at frequencies between 600 and 700 GHz. These measurements had a dynamic range of greater than 60dB, with a phase coherence over the entire dynamic range. With the measurement technique shown, this can easily be taken up into the Terahertz frequency ranges, without a degradation of performance.

With this equipment we have successfully measured in phase and amplitude a double slot antenna structure mounted on to a matched silicon ellipsoidal lens and fitted with an SIS mixer. This antenna is a possible candidate for the ALMA band 9 receiver. These measurements were made over a frequency range of 600 – 700GHz. The side lobe level was found to be at –18 to –20 dB over the frequency range. The beam was symmetrical and frequency independent. There was found to be a unique phase center for both major planes and a waist of 3.9mm. The Guassisty of the antenna was of the order of 89 % over the frequency range.

Acknowledgements;

We would like to thank the following people:

- At IRAM S.Halleguen, B.Lazareff, and F.Mattiocco for all of their help
- CNES for some of the funding of the equipment
- The observatory of Dwingalo for the loan of some of the equipment
- Harvard Smithsonian, R.Blundell and E.Tong for the loan of the high frequency transmitter

Reference;

1. M.Carter, S.Halleguen, B.Fouilleux, IRAM Antenna Test System Proceedings of the 5th International Workshop on Terahertz Electronics, Sept 1997, Grenoble France.
2. Van der Vorst, M.J.M.; De Maagt, P; Herben, M.H.A.J.; On the Design of Integrated Lens Antennas. 20th ESREC Antenna Workshop on Millimeter Wave Antenna Technology and Antenna Measurement; ESTEC, Noordwijk, The Netherlands; June 1997

FAR-INFRARED OPTICS DESIGN & VERIFICATION
Phase II

Ghassan Yassin[1], Stafford Withington[1], Créidhe O'Sullivan[2],
J. Anthony Murphy[2], Willem Jellema[3], Paul Wesselius[3],
Tully Peacocke[4] and Bruno Leone[5]

[1]Cavendish Laboratory, Madingley Road, Cambridge, UK
[2]National University of Ireland Maynooth, Co.Kildare, Ireland
[3] National Institute for Space Research, Groningen, the Netherlands
[4]UK Astronomy Technology Centre, Royal Observatory, Edinburgh, UK
[5] The European Space Agency (ESA), Noordwijk, the Netherlands

Abstract: In this paper we compare the performance of several commercial software packages (GRASP, ASAP, CODE V, GLAD) as well as the Gaussian beam mode method, in analysing the behaviour of submillimetre systems. The study was commissioned by the European Space Agency (**ESA**) and was carried out in two phases. In **Phase I** we allowed these packages to simulate the behaviour of carefully selected test cases in order to reveal their strengths and weaknesses. In **Phase II** we first investigate the ability of the packages to predict the performance of a whole submillimetre system. We also compare the simulated results with those predicted by near field amplitude and phase measurements.

1. Introduction

At present there is considerable interest in modelling the electromagnetic properties of submillimetre systems. For example, in the area of astronomical instruments, there are ongoing intensive activities to analyse the behaviour of optical systems corresponding to the projects "HARP", "ALMA" and the ESA missions "HERSCHEL" and "PLANK". The reasons for this increased effort may be summarised as follows:

- The continuous improvement in receiver technology and fabrication of optical components. This clearly invites comparable progress in the modelling and design tools.
- The availability of commercial software packages which can provide accurate, yet fast, modelling of optical systems at submillimetre wavelengths.
- The increased numerical processing speed of computers, which allows rigorous mathematical procedures to be incorporated into commercial software packages.

Based on this, ESA has launched a programme to investigate the ability of existing verification and design tools to predict the behaviour of quasi-optical systems in the submillimetre and far-infrared regions. The programme was planned in two phases. In **Phase I** we investigated the ability of several well known commercial software

packages to analyse the field scattered by optical components when illuminated by near or far field sources. The software packages that were chosen for this purpose were GLAD, GRASP, CODE V and ASAP. Occasionally, the package ZEMAX was also tested as well as a non-commercial Gaussian mode analysis software which was written by two of the authors. The single-component test cases were carefully selected in order to emphasise the strengths and the weaknesses of each package in providing reliable information which electromagnetically characterises a quasi-optical system. In particular, we wanted to assess the ability of the packages to simulate the following features:

- the near and far field radiation patterns,
- the vector nature of the electromagnetic fields (eg co-polar and cross-polar components),
- rigour versus speed of computation.

Our selected test cases also reflected the fact that we were interested in relating the simulations to the underlying electromagnetic computational method implemented by the packages. This, in many cases, helped us to understand the difficulties that some packages had in simulating common and simple cases. A complete description of the Phase I results have already been reported [1], [2].

The purpose of Phase II of the project is two-fold. After understanding the basic operation of the software packages we want to examine their ability to analyse the behaviour of a real submillimetre system. For this purpose we have chosen one of the HIFI channels of the ESA space telescope HERSCHEL. The analysis was carried out in the frequency range 480-640 GHz and focused on the ability of the packages to predict the near field patterns at the image plane of the system. The second major task in Phase II is the construction of a simplified version of the HIFI channel and a near field test system which is capable of measuring both the amplitude and phase of the radiated fields. The specifications of the test system were chosen in order to both compare the performance the packages and to assess the integrity of the best of them against experimental results.

2. Description of the Software Packages

We shall now provide a brief description of the basic operation of the packages mentioned above. Before that however, we would like to emphasise two issues. The first is that this presentation should not be considered as a full description of the package features or capabilities. The second is that since this work was carried out, some packages have either modified main features and/or added new ones. Clearly we are unable to comment on these modifications.

2.1 ASAP (Advanced Systems Analysis Programme): This package employs beam decomposition to form the aperture field distribution. The software samples the aperture either in the spatial domain or in the angular domain. The field distribution is then propagated using Gaussian ray Gaussian tracing. Our simulation results show that the software seems to experience difficulties whenever the scattering aperture is a few wavelengths across. This is to be expected, however, since rigorous analysis requires the full Gabor decomposition method where the Gaussian beams are both

displaced and rotated with respect to each other. To illustrate this point we show in Fig. 1 the computed far field pattern at 480 GHz for an ideal corrugated horn of aperture radius 2.5 mm and length 15.4 mm. The distance between the horn aperture and the plane of observation was 200 mm.

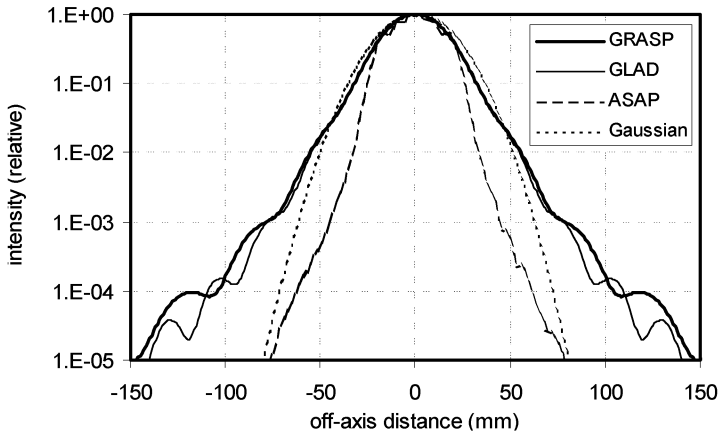

Figure 1. 480-GHz predicted far-field of an ideal corrugated horn of length 15.4mm and aperture radius 2.5mm. The calculations were made by ASAP, GRASP and GLAD and are compared with those of a Gaussain field.

From Fig. 1 it can easily be seen that the pattern calculated by ASAP is substantially narrower than those predicted by the other packages. In fact the results computed by ASAP did not improve even when the pattern was taken at the focal plane of a focusing element.

2.2 CODE V : This package employs both ray tracing and diffraction calculations. It performs Fraunhofer diffraction to calculate the far field and claims to use the angular spectrum method to calculate near fields. Our experience however showed that CODE V tends to have difficulties in producing accurate results in two distinct cases:

- near field diffraction from offset reflectors,
- far field diffraction when the pattern was viewed in a plane away from focus. We shall return to this point when we discuss the analysis of the HERSCHEL HIFI channel.

2.3 GLAD (General Laser Analysis and Design): The principle of operation of this package is based on a plane wave decomposition of the aperture fields [3]. The incident fields are expanded in terms of plane waves and the radiated field is found by integrating over all the spectral components. A two dimensional version of the method is illustrated in Fig.2

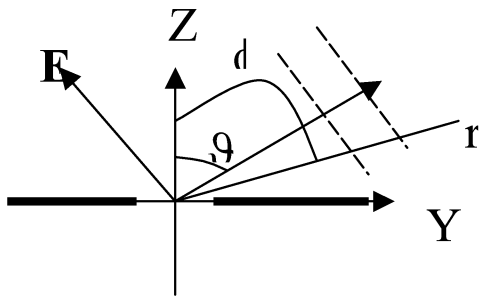

Figure 2 Plane wave decomposition in two dimensions

Here we show an electromagnetic wave illuminating a slit with the electric field in the plane of incidence. The field is therefore expanded for z>0 as:

$$\mathbf{E}(\mathrm{y,z}) = \int_{-\pi/2}^{\pi/2} E(\vartheta)[-\cos\vartheta\ \hat{\mathbf{y}} + \sin\vartheta\ \hat{\mathbf{z}}]e^{-ik(y\sin\vartheta + z\cos\vartheta)}d\vartheta$$

It can then be easily shown that the radiated near field in polar coordinates is given by:

$$\mathbf{E}(r,\phi) = \frac{1}{\lambda}\int_{\infty C}\left\{F(k\sin\vartheta)[\cos(\vartheta-\phi)\hat{\phi} + \sin(\vartheta-\phi)\hat{\mathbf{r}}\ ]e^{-ikr\cos(\vartheta-\phi)}\right\}d\vartheta$$

$$F(k_y) = \int_{-\infty} E_y(y,0)\,e^{-ik_y y}dy \qquad k_y = k\sin\vartheta$$

Similar expressions can be derived for the magnetic field. The contour of integration is shown in Fig. 3 where evanescent waves are also taken into account by integrating over the imaginary axes.

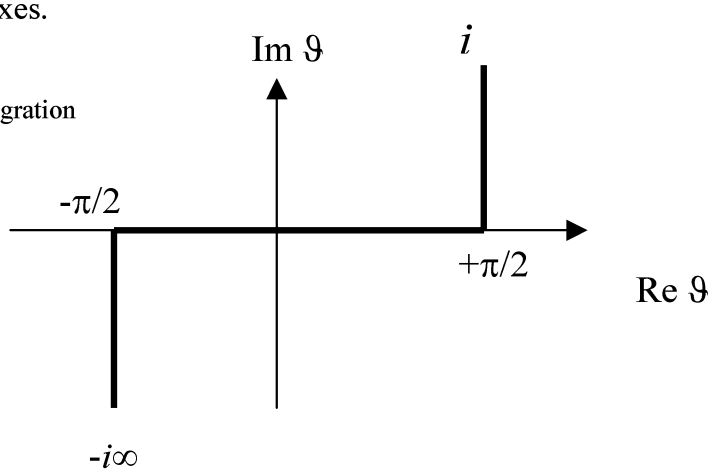

Figure 3 Contour of integration

It is interesting to note that the radiated field has both a longitudinal and transverse component, confirming the near field nature of this treatment. It can be shown that the radial component vanishes as the plane of observation is moved away from the aperture. Plane waves expansion is well known and has been treated by many authors [4]. However since the software package GLAD performed much better in our simulations than was initially anticipated, we list below some important features of this package.

1- The package is essentially scalar. Cross -polar components cannot be obtained.
2- Offset geometries are treated using the projected aperture method.
3- The co-polar calculations of this package were impressive. This also applies to scattering from offset apertures. Only in extreme near field cases did the accuracy of the results (when compared with our benchmark GRASP) start to deteriorate.
4- The package is able to handle a wide range of optical components and sources.

2.4 GRASP(General Reflector and Antenna Software Package): The operation of GRASP is based on the well known "Physical Optics" method [4]. Physical Optics (PO) scattering calculations are performed in two main steps:

1 Calculate the equivalent currents induced on the scattering surface using the physical optics approximation.
2 Calculate the fields radiated by those currents using the "Equivalence Principle.

To explain the principle of the PO approximation, consider first a plane wave illuminating a conducting surface. To calculate the currents at any point on the surface we attach a plane conductor tangent to the surface at that point. The induced equivalent electric and magnetic equivalent currents are given respectively by:

$$\mathbf{K} = \hat{\mathbf{n}} \times \mathbf{H}$$

$$\mathbf{K}^* = \mathbf{E} \times \hat{\mathbf{n}}$$

where E and H are the electric and magnetic fields respectively, and **n** is a unit vector normal to the surface at the point of interest. The principle of the PO approximation is illustrated in Fig. 4.

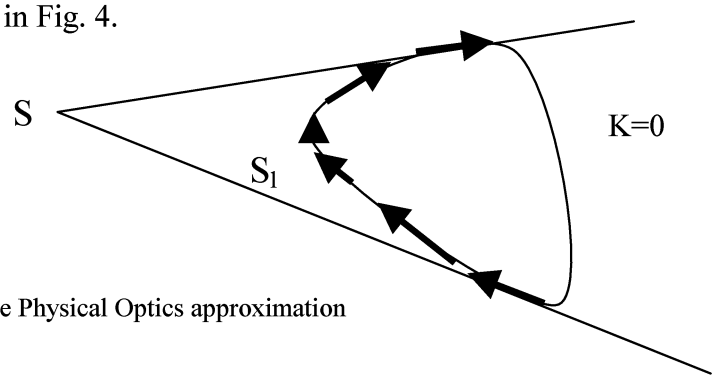

Figure 4 The Physical Optics approximation

Assume now that our scatterer is a perfect conductor illuminated by a point source. The induced currents in the PO approximation are found as follows. We made use of the fact that the tangential component of the electric field at the surface of a perfect conductor vanishes. Once the currents are known the corresponding vector potential can be calculated and subsequently the scattered fields, using the equivalence principle.

$$\mathbf{K}^{PO} = \begin{cases} \mathbf{n} \times \mathbf{H} = 2\mathbf{n} \times \mathbf{H}^i & \text{on } S_1 \\ 0 & \text{on the Shadow surface} \end{cases}$$

$$\mathrm{K}^{*PO} = 0 \quad \text{Everywhere}$$

The resultant electric field at a point a distance R from the origin is therefore given by

$$\mathbf{E} = \mathbf{E}^i - i\omega\mathbf{A} + \frac{\nabla\nabla \cdot \mathbf{A}}{i\omega\varepsilon\mu}$$

$$\mathbf{A} = \frac{\mu}{4\pi} \oiint_{S_l} \mathbf{K}^{PO} \frac{e^{ikR}}{R} dS$$

In the above equation $\mathbf{E}^i$ is the incident field, **A** is the vector potential and the integration is carried out over the illuminated surface of the scatterer. An equivalent expression could be written for the scattered magnetic field. At this stage two important aspects of this theory can be noticed:

- The PO approximation neglects the non-uniform currents near the edge of the scatterer. Our simulations however revealed that for practical aperture sizes, the effect of the non-uniform currents is only significant at very low levels (say below –40 db).
- Radiating the PO currents using GRASP is done rigorously according to Maxwell equations. No paraxial or scalar approximations are made. Both the electric and magnetic fields vectors are calculated.
- The information supplied by the output files of GRASP includes a full vector description of the scattered fields. All commonly required information (eg. co-polar and cross-polar components, spill-over, beam efficiency etc.) may be calculated using the information in the output files.
- GRASP takes care of the non-uniform edge-currents distribution using the "Physical Theory of Diffraction" (PTD) [5].

Our work in Phase I revealed that the PO method supplemented by the PTD correction yields solutions which are very close to the exact solutions of Maxwell equations. We arrived at this conclusion by comparing radiated fields simulated by GRASP using PO+PTD with those calculated by solving Maxwell equations using the method of moments. GRASP therefore was considered to be our benchmark for assessing results in Phase I. In Phase II of this project, we shall have the opportunity to compare the results simulated by GRASP with experimental results.

3. A Brief Discussion of Phase I Results

In what follows we shall present a summary of some important results from our work on Phase I. Some of these results are strongly related to the specific operation of the software packages but in many cases the results also reflect the nature of propagation and diffraction at submillimetre wavelengths. The following conclusions are related to scattering from single optical components illuminated by standard sources (point sources, plane wave, horns etc.).

1- Far field diffraction by an on-axis component: This is the simplest test case. All software packages, including ZEMAX, predicted the copular component reasonably well.
2- Near field diffraction from an offset reflector: here we can distinguish between two cases. In the practical case where the diameter of the aperture was more then 10λ and the plane of observation was more than 30λ away, GRASP and GLAD gave consistently good and similar main beam patterns. On the other hand only GRASP was able to handle diffraction reasonably when the distance between the aperture and observation plane was further reduced. The quality of ASAP and CODE V depended on the particular test case, hence could not be considered reliable.
3- Most of the difficulties that software package encounter in producing accurate diffraction calculations result from their paraxial nature rather than neglecting edge effects in calculating an aperture distribution. The success of the physical optics method should not therefore be attributed to the way PO currents are calculated but rather to the rigorous way those currents are radiated.

4- Only GRASP output files gave the full vector behaviour of the scattered field. It was also the only package that produced reasonable low sidelobe levels below (say below –40 dB). Consequently, it was considered as a benchmark for Phase II.

We shall finish this section by two illustrative examples. The first concerning near field diffraction form a circular aperture illuminated by a plane wave.

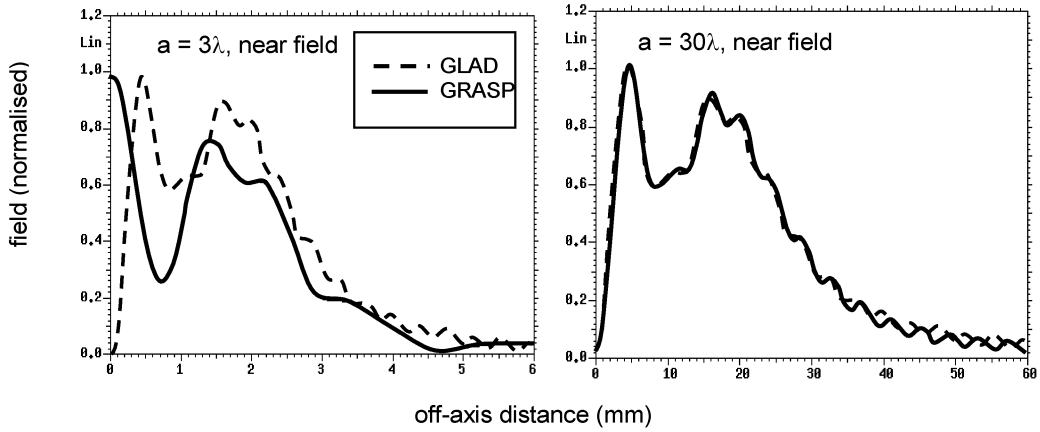

Figure 5 Beam amplitude in the near ($z_{out} = a^2/4\lambda$) field of an aperture of radius $a = 3\lambda$ and $a = 30\lambda$, calculated using GLAD and GRASP. GLAD is taken to be representative of the paraxial packages. λ = 1mm in both cases.

Noticed that despite the extreme change in geometry between the two patterns above, all the paraxial packages did was simply to scale the pattern.The pattern predicted by GRASP however changed substantially. We in fact verified that this faliure of the paraxial packages to predict the correct pattern has mainly resulted from incorrect prediction of the accurate longitudinal location of the Poisson spot.

The second example from Phase I is diffraction from an offset ellipsoid as shown in Fig. 6.

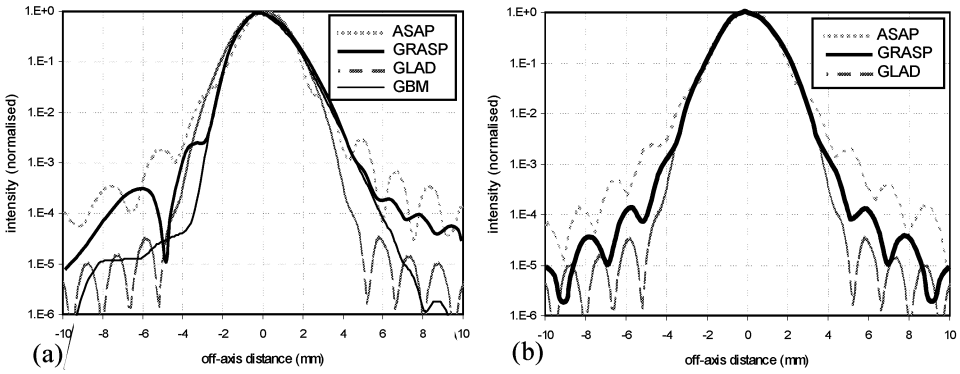

Figure 6 Intensity pattern at the output beam waist ($z_{in} = z_{out} = f$=12.57mm) for an ellipsoidal mirror of projected aperture $a = 1.5\times W$. (a) shows a cut in the plane of asymmetry, (b) in the plane of symmetry. λ = 1mm and W_{in} = 2mm in both cases. The beams were calculated using ASAP, GLAD, GBM & GRASP.

Notice the faluire of GLAD, ASAP, and GBM (Gaussian Beam Modes) to match the patterns predicted by GRASP, in particular in the plane of assymmetry. Substantial differences exist not only in the sidelobe level but also in the main beam. Notice that the faliure of GLAD to perform well in this test case must be the result of the strong aberrations intrinsic to this system.

4. Analysis of HERSCHEL HIFI Channel

A description of a simplified version of channel I of HIFI of the ESA space telescope HERSHEL (480-640 GHz) is shown in Fig. 7.

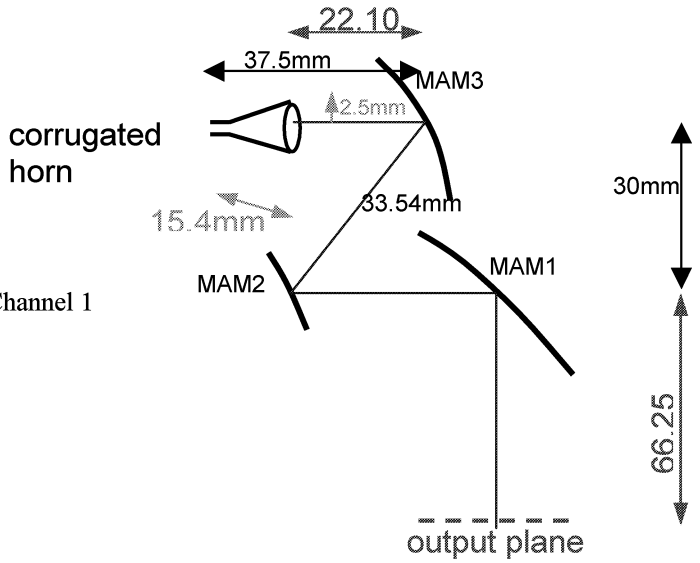

Figure 7 Layout of HIFI Channel 1

The system comprises a conical corrugated horn illuminating an off-axis ellipsoidal mirror. The beam is then focused onto a second ellipsoidal mirror before it is collimated by a 90 degrees offset parabolic reflector. Our plane of observation was located at the image of the telescope secondary mirror, 66.25 mm from the parabolic mirror MAM1. To emphasise the simulation differences between the packages, we carried out both focused simulations (0mm) and de-focused simulations by moving the horn aperture 5mm towards the mirror MAM3 (+5mm), 5 mm away from MAM3 (-5mm) and 10 mm away fromMAM3 (-10). The projected aperture diameters of the mirrors MAM1, MAM2, MAM3 were respectively, 25 mm, 16 mm and 28 mm. In the following simulations the corrugated horn was assumed to support an ideal HE_{11} mode which can be written as

$$E(r) = E_0 J_0\left(\frac{2.405}{a} r\right) e^{jk\left(\sqrt{R^2+r^2}-R\right)}$$

where R is the phase radius of curvature, *a* its radius and r is the radial coordinate of at the aperture. We have already shown a plot of the far field of this horn in Fig. 1. First we plotted both the symmetrical and asymmetrical cuts, at the output plane, when the horn was at the nominal focus. These are shown in Fig. 8

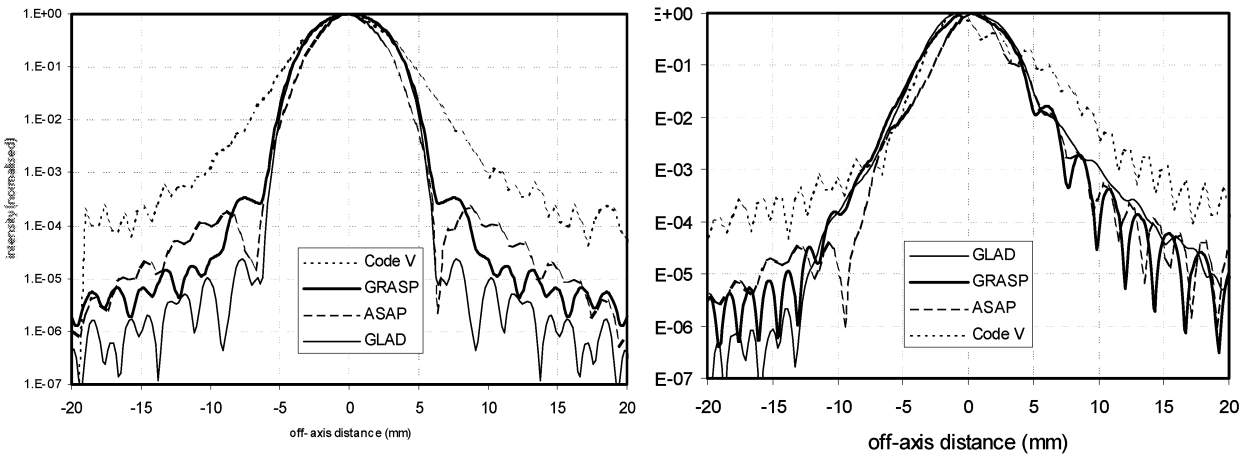

Figure 8 beam pattern predictions cuts in the plane of symmetry (left) and in the plane of asymmetry (right). The horn is at nominal focus.

Examining these results we notice that in the plane of symmetry, the agreement between GLAD and GRASP is good. ASAP does not do badly but the CODE V pattern is much wider than predicted by GRASP. The sidelobe level of GLAD seems too low, presumably as a result of under-estimating edge diffraction. A similar picture can be seen in the plane of assymetry. Based on this we should already be able to see big differences in the measured results between CODE V and other packages. To enhance the predicted differences between GRASP and GLAD we carried out defocused simultions as shown in Fig. 9.

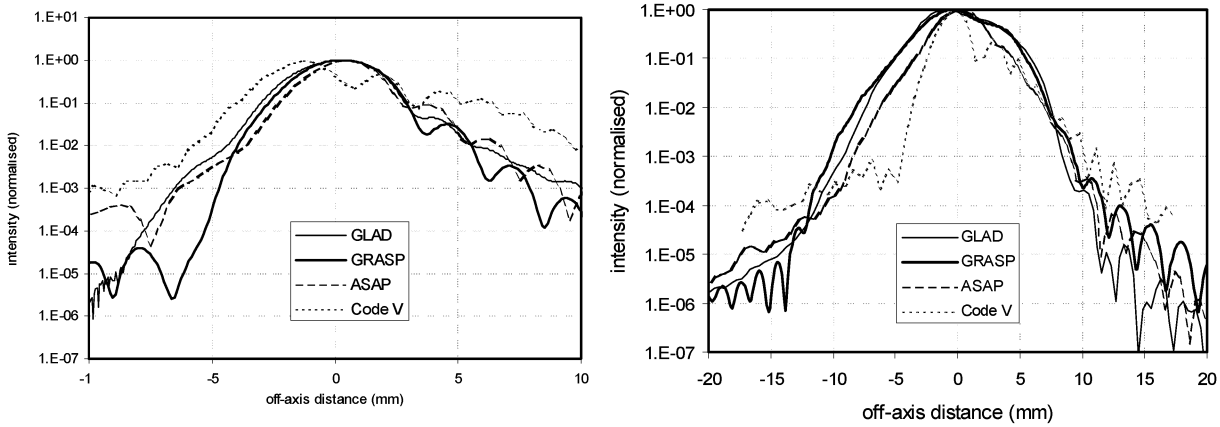

Figure 9 beam pattern predictions cuts in the plane of asymmetry . The horn is defocussed by 5mm away from the mirror MAM3 (right) or towards the mirror (left).

It can be seen that the radiation pattern differences between the various packages have become substantial. To distinguish between ASAP, CODE V and GRASP experimentally we only require a dynamic range of –25 db. For GLAD we will need an amplitude dynamic range of about –30 db. For assessing GRASP against experimental measurement we are likely to require a dynamic range better than –40 db.

Finally, we also compared the phase simulations as shown in Fig. 10. The left hand plot represents measurements when the horn was at the focus and the right hand plot when the horn was moved 5 mm towards the mirrors. The phase differences between the various packages are substantial and our experimental system will easily be able to detect those differences.

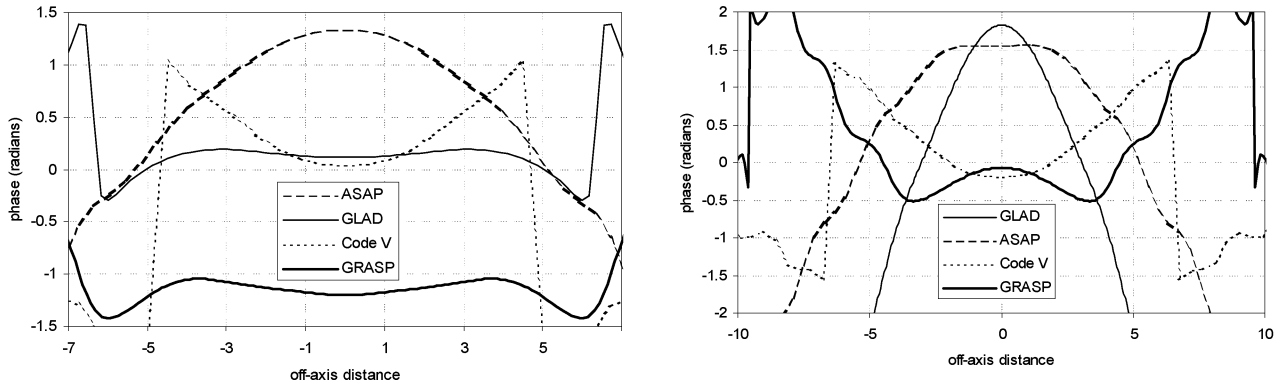

Figure 10 Main beam phase simulations (symmetric cut) when the horn is defocussed by 5mm towards the mirror MAM3 (right) and at nominal focus (left).

5.The Near Field Detection System

We have already stated that a major theme of our work on phase II is the construction of a near field detection system which will allow us to measure the amplitude and phase of our patterns. Both the detection system and the test channel will be constructed at SRON and work is already at an advanced stage. A schematic diagram of the detection system is shown in Fig.11.

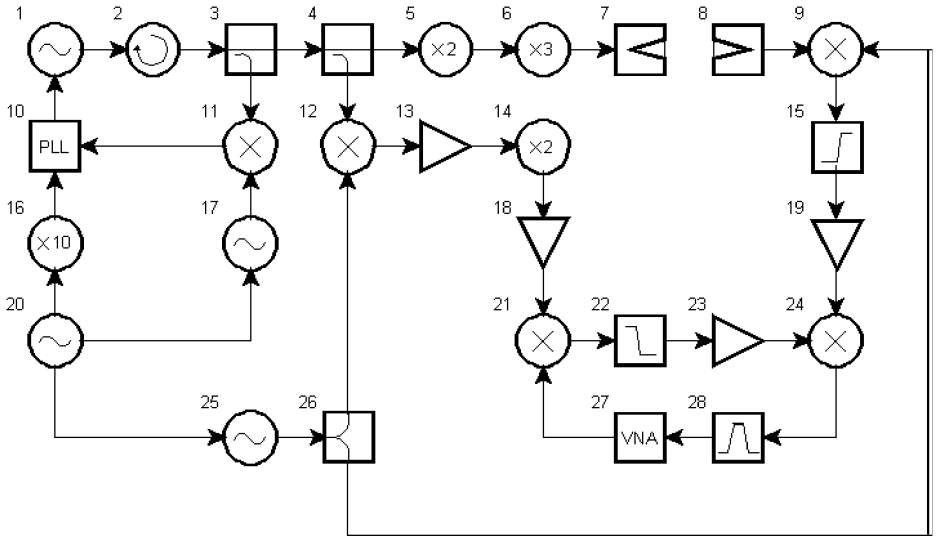

Fig. 11 The near field detection system

The detailed design of the 480 GHz near-field detection system (Fig. 11) was presented in the WP2-110 report.

Signal-to-noise calculations for the system gave a dynamic range of 33-55dB. 33dB was calculated for the worst case but the actual performance was expected to be better than this. The measured dynamic range (including also the coupling loss between the two horns, 7 & 8 in Fig. 11 was 40dB but the limitation was found to be a spurious

signal rather than ~~the~~ noise. We have already performed tests on the detection system by measuring the radiation pattern of the corrugated horn. Our preliminary results show indeed that we shall be able to obtain a dynamic range of –40 db. Together with phase measurements, the system will allow us to draw important conclusions regarding the quality of available commercial software for the analysis of submillimetre systems.

Acknowledgements

This work has been carried out as part of an ESA research contract (13043/98/NL/NB) Far IR Optics Design and Verification Tools'. The authors would like to acknowledge Peter de Maagt, Gert Ulbrich and Erico Armandillo of ESA for their useful comments.

References

1. Far-IR Optics Design and Verification Tools: Report on ESA research contract (13043/NL/NB).
2. O'Sullivan, C., *et al*: Far-Infrared Design & Verification, to appear in the July issue of Int. J. Infrared Millimetre Waves, 2002.
3. Jull, E. V.: Aperture Antennas and Diffraction Theory
4. Leo Diaz, : Antenna Engineering Using Physical Optics.
5. Shore, R.,A. and Yaghjian, A. D., : Incremental length diffraction coefficients for planar surface., IEEE Trans. Antenna and propagat. AP-36, pp. 55-70, 1988

ON THE DESIGN OF SUB-MM WAVE AMPLITUDE HOLOGRAMS FOR CATR

Tomi Koskinen, Juha Ala-Laurinaho, Jussi Säily, Janne Häkli,
Anne Lönnqvist, Juha Mallat, Jussi Tuovinen*, Antti V. Räisänen

MilliLab, Radio Laboratory, Helsinki University of Technology
P.O. Box 3000, FIN-02015 HUT, FINLAND
Tel: +358-9-4512255; Fax: +358-9-4512152
E-mail: tvkoskin@cc.hut.fi

*MilliLab, VTT Information Technology
P.O. Box 1202, FIN-02044 VTT, FINLAND

Abstract – A compact antenna test range (CATR) based on a 3 m hologram has been designed in order to measure the ESA ADMIRALS test antenna at 322 GHz. Also, a 650 GHz demonstration CATR based on a 0.97 m hologram has been designed. Both CATRs will be realized and tested later in 2002. In this paper, the design of the CATRs is discussed and simulation results are presented.

1. INTRODUCTION

Several ongoing projects (e.g., Planck and Herschel) aim to construct scientific or remote sensing satellites to probe the Universe at sub-mm wavelengths. These satellites will carry on board electrically very large reflector antennas, which should be tested before launch. The measurement of the antenna radiation pattern is perhaps the most essential test. Current measurement methods have significant weaknesses at sub-mm wavelengths, and hence a lot of work has and will be done in developing the current methods and inventing new ones.

The most suitable method to measure a full-radiation pattern at sub-mm wavelengths appears to be the compact antenna test range (CATR) [1]. This is because of its simple use in measurements. The radiation pattern of an antenna-under-test (AUT) can be measured directly as in the far-field method, which is widely used at lower frequencies. At sub-mm wavelengths, the far-field method is ruled out due to the very long measurement distance needed. For large reflector antennas, the distance may be even dozens of kilometers, which raises the atmospheric attenuation to a non-permitted level. One antenna testing method that can be used in the sub-mm wave range is a near-field scanning [2]. However, large amounts of near-field data have to be acquired that extends the measurement time very long (even to several days), and thus a high stability of measurement system is required.

In a CATR, a spherical wave radiated by a feed antenna, e.g., a horn is transformed to a plane wave with the use of a focusing element. The plane wave is used to measure the radiation pattern of the AUT. Since the dimensions of the range are relatively small, the CATR can be situated indoors and problems caused by the atmosphere are avoided. The AUT is placed into the quiet-zone (QZ), which is a region of the plane wave where the field quality satisfies certain criteria. Typical criteria for the plane wave in the QZ are that the amplitude and phase ripples do not exceed 1 dB and 10°, peak-to-peak, respectively.

In a conventional CATR, the focusing element is a reflector or a set of $2-3$ reflectors. In the sub-mm wave range, a strict surface accuracy requirement ($\sim\lambda/100$) makes the manufacturing of large reflectors very difficult and highly expensive. The focusing element could be also a lens, which has a lower surface accuracy requirement compared to a reflector (by a factor of $(\sqrt{\varepsilon_r}-1)/\sqrt{2}$ lower). However, finding an appropriate low-permittivity, high-homogeneity material is difficult.

2. HOLOGRAM BASED CATR

We use a hologram as the focusing element [3]. As the hologram is a transmission-type element its surface accuracy requirement ($\sim\lambda/10$) is much lower than that of a reflector. Layout of a hologram based CATR is shown in Figure 1. When the hologram is illuminated with a horn antenna it diffracts several beams into different directions. One of the beams is the desired plane wave used in antenna testing. The hologram is designed so that the plane wave propagates in an angle of 33° with respect to the normal of the hologram. This prevents the other diffraction modes produced by the hologram to disturb the QZ –field. Unwanted beams and the direct radiation of the horn antenna are eliminated by absorbers. Distance between the hologram and the horn is typically $2-5D$ (diameter of the hologram is D) and the QZ –field is optimized at a distance of $2-5D$.

The hologram used in a CATR is the interference pattern of a spherical wave and a plane wave coming from a certain direction (i.e., 33°). A binary amplitude hologram is a slot pattern, which has been etched onto a metal layer on top of a thin dielectric film. Holograms described more in detail later in this paper will be fabricated using the laser exposure of pattern and chemical wet-etching. High flatness is ensured by tensioning the hologram to a stiff frame. An example of a binary amplitude hologram is shown in Figure 2 where nearly vertical, radio-transparent slots are in white and metal stripes between them in black. The widths of the slots are less than 0.5λ. The slots have been tapered (narrowed) towards the edges of the hologram to prevent harmful edge diffraction.

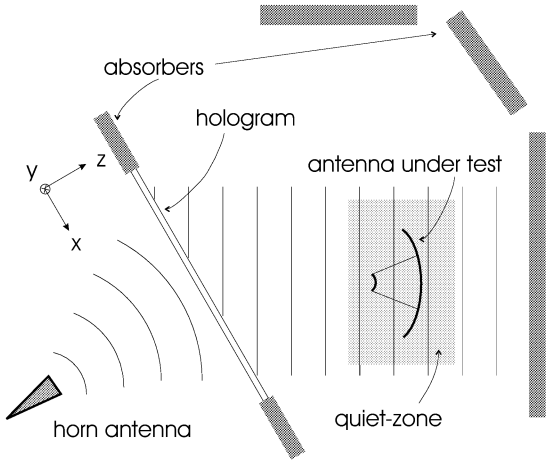

Figure 1. Layout of a hologram based CATR.

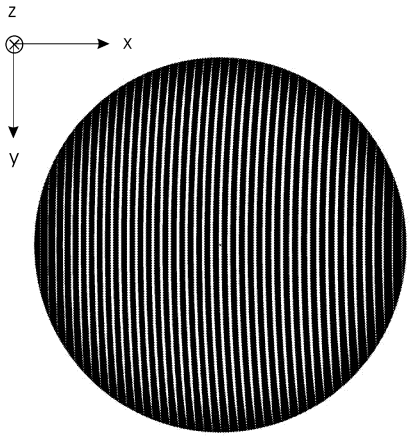

Figure 2. Binary amplitude hologram pattern.

The binary hologram pattern is generated with computer. Due to several non-idealities (e.g., a dielectric film, an edge diffraction and a non-ideal transmittance of slots), the initial hologram pattern does not directly produce a QZ adequate for antenna measurements. Therefore, the detailed electromagnetic behavior of the hologram structure has to be analyzed and the performance of the hologram optimized. Fields within the hologram structure and in the aperture are computed using the Finite-Difference Time-Domain (FDTD) method. The QZ –field is calculated from the aperture field using physical optics. If the QZ –field does not fulfill the requirements, the hologram pattern is modified appropriately and a new simulation is done. This iterative procedure is repeated until a satisfactory result is achieved. If the width of a slot is at max. 0.4λ, the transmitted power of a vertically polarized wave is a monotonically

increasing function of the width. Then, the amplitude of the QZ –field can be easily modified narrowing/widening the slots. The phase can be tuned moving the slots slightly. A local modification of the pattern affects (almost only) locally the QZ –field that makes the optimization of the QZ –field quite straightforward. The transmission coefficient of a slot is polarization dependent. For a horizontally polarized wave, the transmitted power is not a monotone function of the slot width, and hence it's very difficult to design holograms for the horizontal polarization. Therefore, holograms are always designed for a vertically polarized incident electric field.

Since the hologram is electrically very large, simulation of a whole hologram would be a too massive operation even for supercomputers. Comparisons between simulation and measurement results have shown that with a good accuracy the hologram pattern can be assumed to be infinite in the vertical direction when the QZ –field is examined locally along a horizontal cut. This is due to the gentle curvature of slots in the vertical direction. The assumption enables the use of a two-dimensional FDTD simulation, which reduces the computational burden to a fraction of the original one. Figure 3 illustrates the simplification of the analyzed structure. A hologram grid is generated at a certain y coordinate and the structure is assumed to be infinite in the y direction. Then, a two-dimensional FDTD simulation is done and the QZ –field is calculated at the same y coordinate. In a two-dimensional FDTD simulation, two cases can be studied separately: the incident electric field is either horizontally or vertically polarized. However, only an analysis for the vertically polarized electric field is usually done. [4]

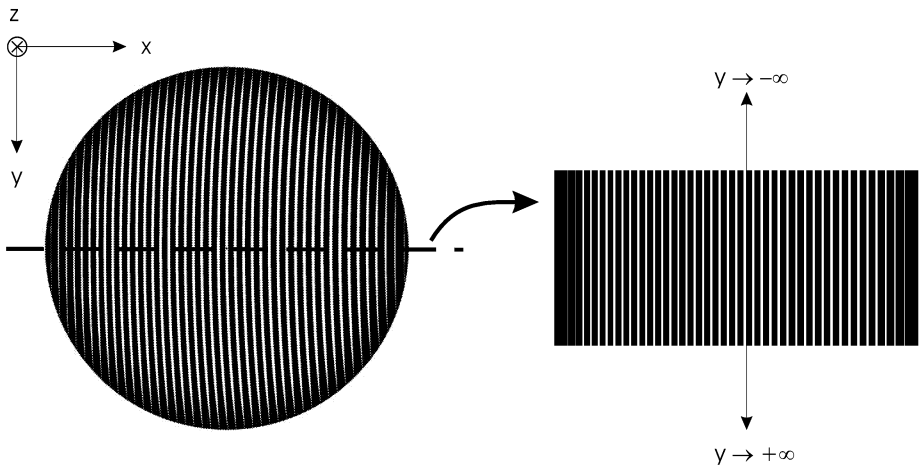

Figure 3. Simplification of a hologram used in FDTD simulations.

The simulation of cross-polarization is not possible when the simplification is done and the curvature of slots is omitted. The numerical simulation of cross-polarization has been examined in [5]. Results from FDTD simulations and

measurements agreed very well. The typical cross-polarization level of a hologram is about –20 dB near the edges of QZ. At the horizontal centerline, the cross-polarization is very small.

3. DESIGN OF HOLOGRAM BASED CATRs FOR 322 GHz AND 650 GHz

In our ongoing ESA project, two sub-mm wave CATRs based on binary amplitude holograms will be constructed. Both CATRs have been already designed and they will be realized and tested later in 2002. One of the CATRs is going to be used to measure the ESA ADMIRALS test antenna at 322 GHz. The diameter of the test antenna is 1.5 m. It has been estimated that to measure the antenna properly the diameter of the QZ has to be at least 1.8 m. The FDTD simulations show that a 3 m wide hologram produces a QZ larger than 1.8 m and is thus appropriate. Since there is no 3 m wide dielectric film available the hologram has to be composed of three 1×3 m^2 horizontal pieces. The pieces will be etched separately and then joined together by soldering. Numerous experimental studies carried out show that the soldering is the best choice to join pieces together. Also, taping and glueing were tested but the performance of the hologram was much worse with them. Furthermore, it has been noticed that a horizontal joint causes much less distortion than a vertical one. Careful alignment of the pieces is important to avoid an additional distortion. This hologram will be etched onto a 50 μm Mylar film covered with 17 μm thick copper layer. The distance from the horn to the hologram is 9 m and the QZ is optimized at a distance of 9 m from the hologram. The simulated QZ –field of the 322 GHz hologram at $y = 0$ at a distance of 9 m from the hologram is shown in Figure 4. Transversal displacement in the QZ is denoted by x. The width of the QZ is more than 1.95 m. The amplitude and phase ripples are less than 0.5 dB and 5°, peak-to-peak, respectively.

The other CATR is smaller and it will be used to demonstrate the feasibility of the hologram CATR at higher frequencies. The diameter of the hologram is 0.97 m and the operating frequency is 650 GHz. The diameter is limited by the maximum width of the suitable film. The hologram will be etched in a single piece onto a 25 μm Mylar film covered with 5 μm thick copper layer. The thickness of the film has to be reduced to 25 μm to avoid internal reflections inside the film. The distance from the horn to the hologram is 3 m and the QZ is optimized at a distance of 3 m from the hologram. The simulated QZ –field of the 650 GHz hologram at $y = 0$ at a distance of 3 m from the hologram is shown in Figure 5. The width of the QZ is more than 0.6 m. The amplitude and phase ripples are less than 0.5 dB and 5°, peak-to-peak, respectively.

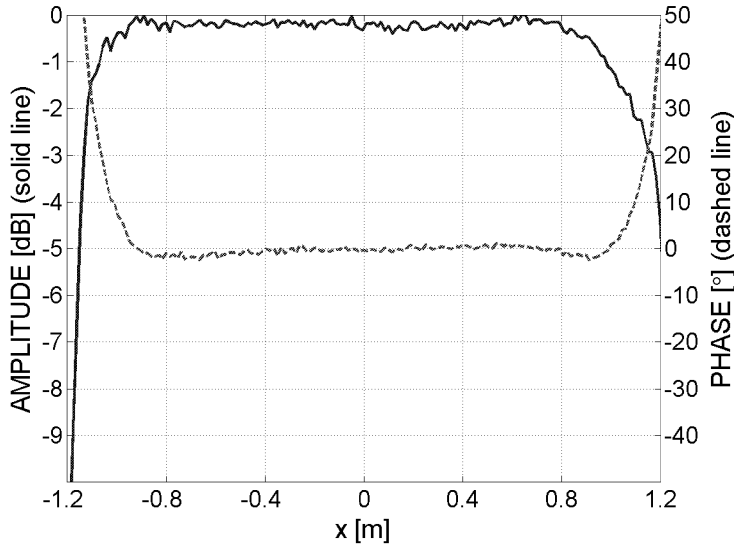

Figure 4. Simulated QZ –field of the 322 GHz hologram at y = 0 at a distance of 9 m from the hologram

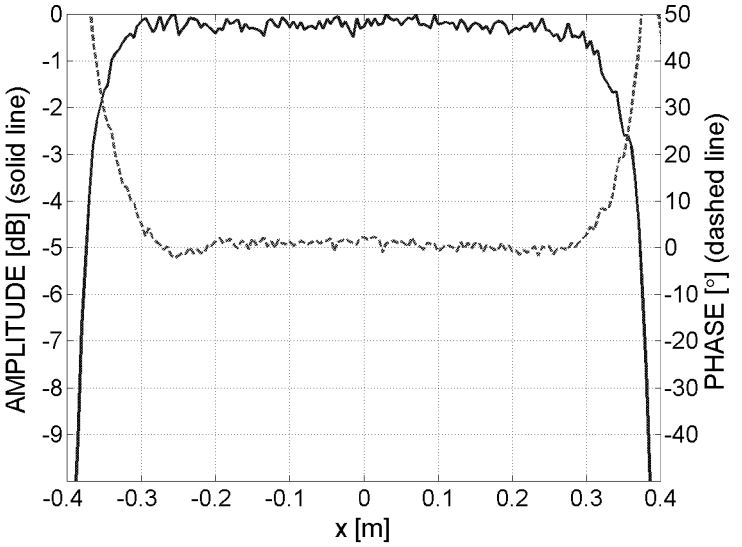

Figure 5. Simulated QZ –field of the 650 GHz hologram at y = 0 at a distance of 3 m from the hologram.

4. CONCLUSIONS

Two sub-mm wave CATRs based on binary amplitude holograms have been designed and simulated. They will be realized and tested later in 2002. The large CATR is based on a 3 m hologram and it will be used to measure the 1.5 m ESA ADMIRALS test antenna at 322 GHz. The other CATR is based on a

0.97 m hologram and operates at 650 GHz in order to demonstrate the feasibility of the hologram CATR at wavelengths under 0.5 mm.

ACKNOWLEDGMENTS

This work is supported by the Academy of Finland, ESA/ESTEC (Contract No. 13096/98/NL/SB) and the National Technology Agency (TEKES). Individual authors wish to thank the Finnish Cultural Foundation, the Finnish Society of Electronics Engineers, the Foundation for Commercial and Technical Sciences, the Foundation of Technology, Jenny and Antti Wihuri Foundation, Kaute Foundation and Nokia Foundation for their support. Also, CSC – Scientific Computing Ltd is acknowledged for providing their computer resources.

REFERENCES

[1] Foster, P. R., Martin, D., Parini, C., Räisänen A. V., Ala-Laurinaho, J., Hirvonen, T., Lehto, A., Sehm, T., Tuovinen, J., Jensen, F., Pontoppidan, K., *Mmwave antenna testing techniques – Phase 2*, MAAS Report 304, Issue No. 2, ESTEC Contract No. 11641/95/NL/PB(SC), December 1996.

[2] Erickson, N., Tolls, V., Near-field measurements of the submillimeter wave astronomy satellite antenna, *Proceedings of the 20th ESTEC Antenna Workshop on Millimetre Wave Antenna Technology and Antenna Measurements*, Noordwijk, The Netherlands, 1997, pp. 313−319.

[3] Hirvonen, T., Ala-Laurinaho, J., Tuovinen, J., Räisänen, A. V., A compact antenna test range based on a hologram, *IEEE Transactions on Antennas and Propagation*, Vol. 45, No. 8, 1997, pp. 1270−1276.

[4] Ala-Laurinaho, J., Hirvonen, T., Tuovinen, J., Räisänen, A. V., Numerical modeling of a nonuniform grating with FDTD, *Microwave and Optical Technology Letters*, Vol. 15, No. 3, 1997, pp. 134−139.

[5] Ala-Laurinaho, J., Sehm, T., Säily, J., Räisänen, A. V., Cross-polarization performance of the hologram compact antenna test range, *Microwave and Optical Technology Letters*, Vol. 27, No. 4, 2000, pp. 225−229.

A HOLOGRAPHIC MEASUREMENT SYSTEM FOR THE SMA ANTENNAS AT 680 GHZ

T. K. Sridharan, C. E. Tong, M. Saito, N. A. Patel, R. Blundell

Harvard-Smithsonian Center for Astrophysics
60, Garden Street, MS 78, Cambridge, MA 02138, USA.

ABSTRACT

We have set up a holographic measurement system for the in-field characterisation of the high frequency performance of the SMA antennas and optics. The SMA is a reconfigurable sub-millimeter array of 8 antennas operating down to a wavelength of $\sim$ 330 μm ($\sim$ 900 GHz), on Mauna Kea, Hawaii. For the holography system, the test signal is provided by a low-power phase-locked 682.5 GHz (440 μm) CW source mounted on the nearby Subaru Telescope building, in the near-field for the 6-m diameter SMA antennas. The source also emits multiple tones and has limited tunability. The complex beam pattern of the antenna under test is measured by raster scanning, with a second antenna of the Array providing the phase reference. Due to the small power output required, the signal source could be made compact and simple for reliable field use. In this presentation, we describe the design and charaterisation of the signal source and present preliminary measurements with the system. We used a novel power measurement scheme that allows measurement of low powers in the presence of multiple comb components, to characterise the signal source.

INTRODUCTION

The Sub-Millimeter Array which recently became partially operational on Mauna Kea, Hawaii, is a reconfigurable array of 8 antennas, each of 6-m diameter (Figure 1) [1]. It will carry out synthesis imaging

Figure 1: A view of the SMA on Mauna Kea. The Array will have 8 antennas when completed.

of celestial objects over the wavelength range $\sim$ 1700-330μm ($\sim$ 180 - 900 GHz). For efficient short wavelength operation, it is necessary that the surfaces of the antennas be measured and set to high accuracy. The

SMA specifications require an rms surface smoothness of 12 μm. Near-field holographic measurement at 232.4 GHz (1291 μm) is the primary method of achieving this goal. Near-field holography at high signal-to-noise allows accurate measurement and correction of panel-panel errors and panel flexures at a high spatial resolution of $\sim$ 10 cm. So far, we have set the surfaces of 5 of the antennas to within $\sim$ 20 μm rms of an ideal paraboloid, and one of them has been adjusted to an accuracy of 13 μm rms [2]. Three of the SMA antennas have now been equipped for operation in the 690 GHz band and in order to characterise the high frequency preformance of the antennas and optics, we have set up a holographic measurement system operating at 682.5 GHz. This system will help check the overall alignment of the optics at high frequencies directly and measure the illumination patterns realised. It will render insignificant the effects of diffraction due to the small subreflector (35-cm diameter) thus providing a better measurement of the surface smoothness. In addition, the system will also allow other useful tests of the Array (e-g., Array-wide phase stability measurements).

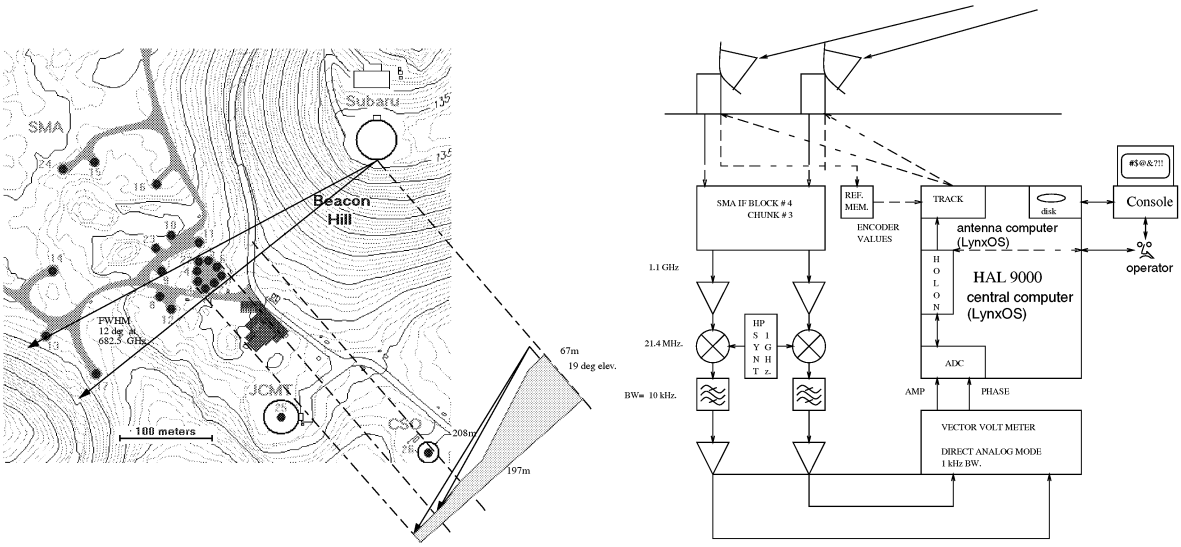

Figure 2: (a) The geometry for SMA near-field holography (b) The SMA holography system block diagram

THE SYSTEM

The holographic system is essentially same as the one used at 232.4 GHz [2], but for a higher frequency signal source. The signal-source is mounted on the cat-walk of the Subaru Telescope at a distance of 200-250-m from the antennas and at an elevation of $\sim 19^{\circ}$. For the 6-m diameter antennas, this is in the near-field for all our operating bands. During the measurements, the subreflector is positioned to focus on the near-field source. The system uses the standard SMA optics, recievers and IF electronics. Currently a vector volt-meter is used as the back-end to measure the complex beam pattern of the antenna under test. The geometry of the measurements is shown in Figure 2(a) and a block diagram of the system is shown in Figure 2(b). The measurements are made on-the-fly, typically mapping a 96$\times$96 raster with an elevation spacing of $11''$. The data are re-sampled off-line on to a regular grid and Fourier inverted to obtain the complex aperture domain field distribution.

SIGNAL SOURCE DESIGN & CHARACTERISATION

We first calculate the required power output of the signal source. With $T_{SYS,SSB} \sim 1200K$ at 680 GHz, the noise floor is $kTB = 2 \times 10^{-14}W = -107$ dBm, assuming conservatively B =1 MHz, for the Array correlator back-end. The measured noise-equivalent bandwidth of the vector volt-meter which we currently

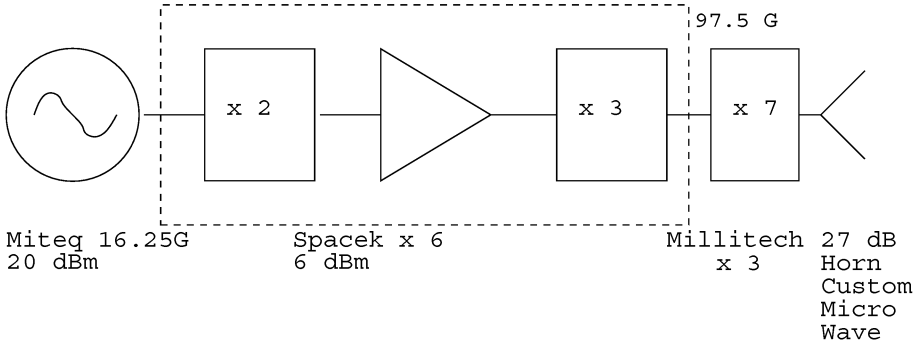

Figure 3: The block diagram for the 682.5 GHz singal source

use is 1 kHz. We require that the signal be detected at a signal-to-noise ratio of 40 dB. Based on our experience at 232.4 GHz, this will be adequate. Therefore, the required CW signal strength is $-107 + 40 = -67$ dBm. The beam coupling efficiency of a 6-m diameter antenna to a source at 220-m is -43 dB, when the antenna is focused on the source. We use a 2.5-mm square pyramidal horn with a gain of 27 dB. Therefore, the required output power of the transmitter is $-67 - 43 + 27 = -83$ dBm $\sim$ 10 pW. We conclude that 1 nW output power will be adequate with a big margin.

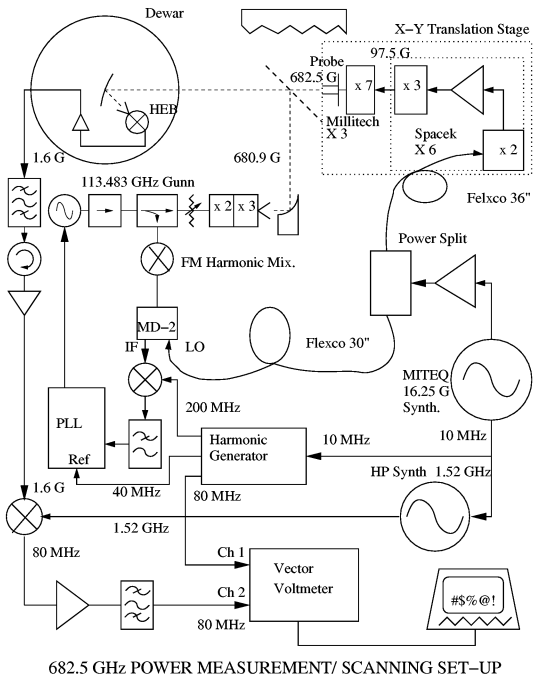

Figure 4: The system used for measuring the power output of the 682.5 GHz singal source

Figure 5: Test signal sources emitting phase-locked tones at 232.4 & 682.5 GHz, mounted on the cat-walk of the Subaru Telescope

Given the small power required, we use a scheme of multiplying up a phase-locked oscillator at 16.25 GHz, similar to the approach used for the 232.4 GHz signal source which has worked reliably for many years now. Such a source being simple, can be made compact and reliable and thus suitable for field use. In contrast, a Gunn oscillator based system, while providing more power, will be more cumbersome, requiring a PLL for the Gunn, and a somewhat stringent temperature control. As shown in Figure 3, a Miteq oscillator is multiplied up 6 times using a Spacek Labs active multiplier to produce 6 dBm at 97.5 GHz. This is used to pump a Millitech tripler. The tripler generates enough 7^{th} harmonic power output at 682.5 GHz which we use as our signal. In this scheme, a comb spaced 97.5 GHz is generated providing test tones at multiple SMA bands. A WR1.5 cut-off section at the horn input suppresses tones below 375 GHz. The 16.25 GHz synthesiser is tunable over the range 16.0-16.4 GHz, in steps of 50 MHz, allowing limited tunability of the final output. While this is not needed for the holographic measurements, it allows some flexibility in other tests of the Array. The square pyramidal horn used produces an elliptical beam with a horizontal major axis to optimally illuminate the central ring region of the Array, as seen projected from the signal-source. The source is locked to a 5 MHz internal crystal oscillator and has provision for an external reference input.

In order to measure the power output of the signal source, we use the system shown in Figure 4. It is based on the near-field scanning system of the CfA Reciever Laboratory used to characterise SMA recievers [3,4]. The test signal source, with an open waveguide probe replacing the pyramidal horn, is mounted on a translation platform which performs a 2-D raster scan in a plane perpendicular to the optical axis of a HEB reciever [5]. The LO for the HEB reciever and the test signal source are locked to the same reference which is also used to generate a reference signal for the vector volt-meter. The signal transmitted by the test source and recieved by the HEB receiver is down converted to feed the second channel of the vector volt-meter. Thus a map of the complex coupling between the probe and the reciever is measured. By integrating over this map, the coupling between the test-signal source and the reciever is estimated to be -30.6 dB, including the cosine profile across the probe aperture. The signal-to-noise ratio at the peak scanning position is measured to be 36 dB. Now, a calibration of the recieved power is carried out using the standard hot-cold Y-factor measuremnt. The derived $T_{RX,DSB}$ of 3000 K implies a noise floor power level of $2kTB = -130.8$ dBm with 1 kHz for B, the measured noise equivalent bandwidth of the vector volt-meter. With a peak signal-to-noise ratio

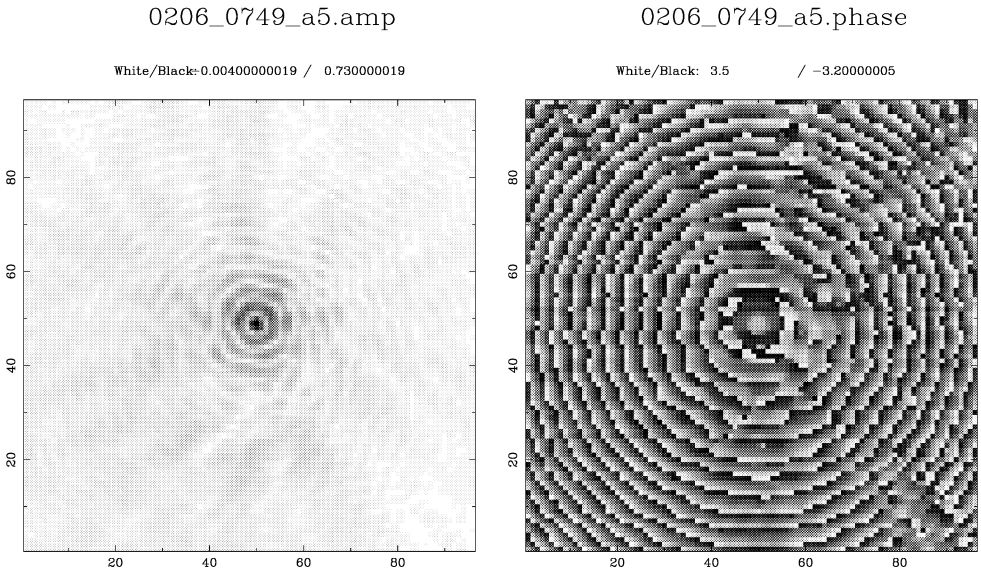

Figure 6: Beam domain amplitude and phase at 682.5 GHz obtained by raster scanning a 96×96 point grid, spaced 11″ and centered on the signal source.

of 36 dB, the CW power coupled is $-130.8 + 36 = -94.8$ dBm. Allowing for the probe-reciever coupling, the power *radiated* by CW test signal source is then $-94.8 + 30.6 = -64.2$ dBm $= 0.38$ nW. Based on our earlier calculations, this is sufficient. The method of power measurements we have used here has two

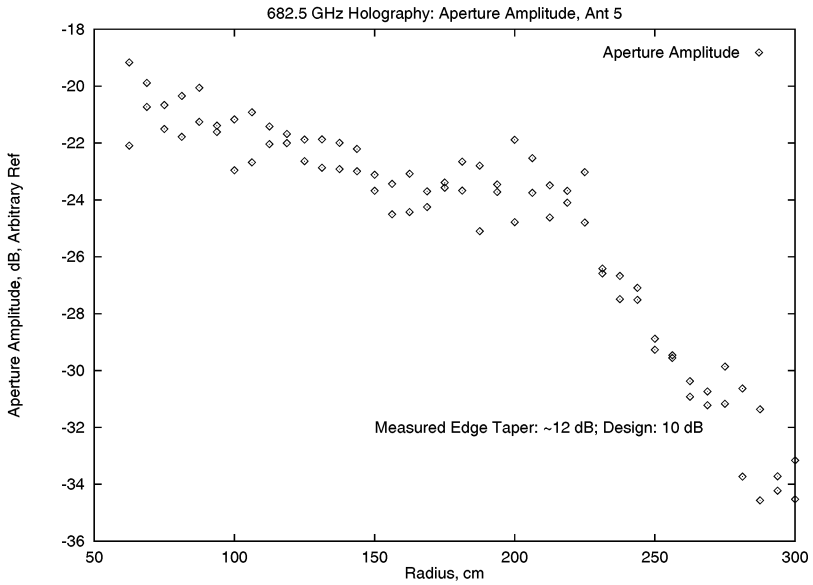

Figure 7: Measured radial illumination pattern for antenna 5. The aperture doamin amplitudes were averaged in azimuth to produce this plot.

advantages: (1) it can measure very low power levels, comparable to the thermal noise limit of the available recievers (2) it can measure the power in a single comb component as opposed to broad-band measurements.

PRELIMINARY RESULTS

We have built and installed a signal source of the above design on the cat-walk of the Subaru Telescope building, as shown in Figure 5. We have carried out preliminary antenna test measurements and the system is being curently debugged. Figure 6 shows complex beam domain maps made with this system. In the data we have so far, we are limited by phase fluctuations due to the atmosphere. Therefore, we are unable to derive surface error distributions or reliable illumination pattern after Fourier inversion. However, there is enough signal-to-noise ratio to measure the edge illumination as shown in Figure 7. Here, the amplitude in the aperture domain is plotted against the radial distance, after azimuthal averaging. This measurement suggests an edge taper of $\sim$ 12 dB to be compared with the design specification of 10 dB. These results show that we have a working system and after further debugging and tests under better weather conditions, we will be able to use the system to characterise the SMA high frequency antenna/reciever systems.

Acknowledgements
It is a pleasure to thank Donald Graveline, Richard Scovel & William Snow of the IF/LO Laboratory for help with the assembly of the system, Forrest Owens, Rob Christensen, Ferdinand Patt & Brian Keith of the Hilo Facility for help with installation and initial check-out and Ken Young for figure 2(a). We are grateful to the Subaru Telescope for hosting our instruments on their cat-walk and to Masao Nakagiri for arranging for smooth installation.

References

[1] Moran, J.M., "Submillimeter array", in *Advanced Technology MMW, Radio, and Terahertz Telescopes*, Ed. T. G. Phillips, Proc. SPIE Vol. 3357, p. 208-219, 1998.

[2] Sridharan, T.K., Saito, M., Patel, N., "Holographic Surface Quality Measurements of the Sub-Millimeter Array Antennas", URSI General Assembly, Maastricht, Aug 2002.

[3] Tong C.E., Paine S., and Blundell R., "Near-field characterization of 2-D beam patterns of submillimeter superconducting receivers", in Proc. 5th Int. Symp. Space THz Tech., Ann Arbor, MI pp. 660-673, May. 94.

[4] Chen M.T., Tong C.E., Blundell R., Papa D.C., and Paine S., "Receiver beam characterization for the SMA", in Proc. SPIE Conference on Advanced Tech. MMW, Radio, and THz Telescopes, Kona, Hawaii, pp.106-113, Mar. 98.

[5] Tong C.E., Stern J., Megerian K., LeDuc H.G., Sridharan T.K., Gibson H., Blundell R., "Performance of Niobium Titanium Nitride Hot Electron Bolometer Mixer Fabricated on Quartz with Aluminum Nitride Buffer Layer", in Proc. 8th Intl. Superconductive Electronics Conf., Osaka, Japan, pp. 77-78, June 2001.

Use of Subharmonically Pumped SIS Mixer with High Harmonics Number for Phase and Amplitude Antenna Measurements

A. BARYSHEV [1], M. CARTER [2], R.HESPER [1], S. J. WIJNHOLDS [3], W. JELLEMA [3], T. ZIJLSTRA [4]

[1] NOVA, University of Groningen, the Netherlands
[2] IRAM, Institut Radio Astronomique Millimetric, Grenoble France
[3] SRON-Groningen, Groningen, the Netherlands
[4] Department of Applied Physics (DIMES), Delft University of Technology

ABSTRACT

For the ALMA Interferometer and FIRST Mission a means of measuring accurately the phase and amplitude of horns and other antenna structure in the submillimeter bands is required to ensure good alignment and high coupling efficiencies to the telescopes.
This paper gives a means for making these measurements by using a SIS junction as a sub-harmonically pumped mixer. The measurements that are shown were made at 640 GHz, which is in the ALMA band 9, but they can be taken up to higher frequencies. A High harmonic number (>30) was used in these measurements and dynamic range of about 40 dB was achieved.
Any type of antenna structure connected to a SIS mixer could be measured. For these measurements a diagonal feed horn antenna was chosen. The mixer was mounted into a wet cryostat with a 1.2 GHz to 1.7 GHz IF. The cryostat was aligned against far field antenna measurement range. The transmitter moves in an X-Y raster scan in front of the cryostat window. The transmitter horn was a fundamental mode open-ended waveguide. The local oscillator in the range of 10-20 GHz was injected into the mixer by means of cold -20 dB directional coupler mounted into its IF chain. The phase locked Gunn multiplier chain was used as the transmitter. High harmonic of LO and Gunn chain output are combined to give an IF of 1.2 GHz. A homodyne phase and amplitude receiver was used for this measurement.
It is to be noted that no LO insertion was used at high frequencies. This has a great advantage for investigation of systems with wide beam because it does not limit the field of view taken up with optical local oscillator injection.
We will show the polar diagram, measured with this technique. The linearity of sub-harmonically pumped mixer was ensured by repetitive measurements of the same pattern with different signal levels. The IF output dependence from the SIS junction bias voltage will be presented. Optimal pumping power, signal level, operating bias point and conversion coefficient will be reported.

SUBHARMONICALLY PUMPED SIS MIXER

SIS junctions are widely used as detector element for quantum-limited mixers[1-6]. The high nonlinearity of SIS junction I-V curve allows making these mixers very efficient. The same high nonlinearity allows it to be used as a subharmonically pumped mixer. For instance, an SIS junction can be pumped with a local oscillator (LO) at microwave frequency F_{LO} to detect an input signal (RF) of a much higher frequency, F_{RF}, at an intermediate frequency (IF) $F_{IF} = F_{RF} \pm n \times F_{LO}$ where n is the harmonic number.

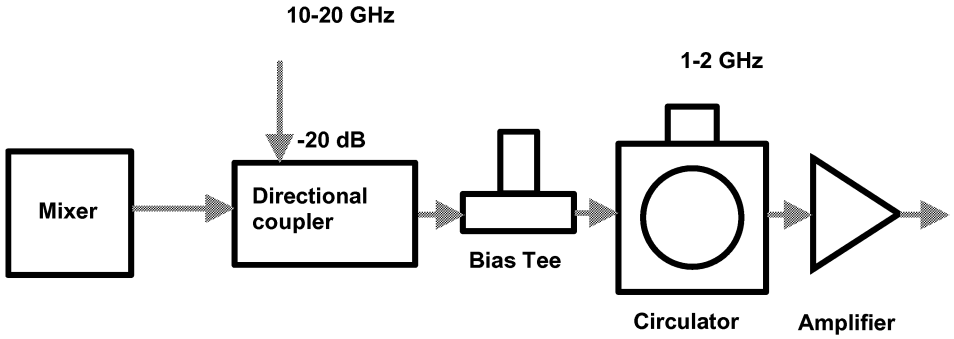

Figure 1: Scheme of mixer LO connection.

Subharmonically pumped SIS mixers for low harmonics number n = 2-5 were used by various groups [7]. Higher (n > 30) harmonic numbers were used in on-chip harmonic SIS mixers to study the linewidth and phase-locking of the Flux-Flow oscillator [8]. In this paper we present details of the operation of a subharmonically pumped SIS mixer for high harmonic numbers, and phase-and-amplitude antenna beam measurements using such a mixer.

The experimental mixer layout that was used to inject the LO is shown in fig. 1. The mixer was mounted on the cold plate in the vacuum space of a liquid helium dewar. The LO was injected through the –20 dB port of a directional coupler, providing at least 20 dB attenuation. The IF frequency, ranging between 1 and 2 GHz, was picked up through the main path of the directional coupler via a bias-tee and isolator, and amplified by a low noise Berkshire Technologies amplifier. The isolator provides good rejection of the LO signal to avoid damaging of the amplifier by the relatively high level of LO power. A waveguide mixer in the range of 450-520 GHz was used for studying the subharmonically pumped mixer operation. A Thomson carcinotron was used as RF source. To calibrate the conversion efficiency, the RF signal was injected through a 12 μm thick Mylar beamsplitter. A rotating grid was used to regulate the RF signal power. It was possible to pump the SIS mixer to alpha level $\alpha = 1.2$ during the experiment.

The IF output power was amplified by room temperature amplifiers with a total gain of 60 dB, and then connected through a tunable band-pass filter (30 MHz bandwidth) to a power detector. An automated measurement system [9] was used to record data.

The I-V curves of the measured SIS mixer are shown in fig. 2. The R_n value of the SIS junction is about 20 Ω. The junction's quality factor is about 30. The I-V curve with only LO power applied is shown by dotted line. Note that the LO power applied in this case is significantly smaller than the optimum LO power. No photon steps corresponding to 9.09 GHz are resolved in the picture. The dashed line represents the SIS junction pumped by the RF signal only. In this case the height of the photon-assisted tunneling step can be used as a measure of incident RF power. The junction's I-V curve corresponding to the optimum operation is shown as a continuous line. It looks like a "straight line", meaning that the mixer is "overpumped". The appropriate level of magnetic field was applied during the experiment to suppress the noise and conversion due to the Josephson effect.

The IF output power vs. mixer bias for these I-V curves is shown in fig. 4 for odd, and in fig 5 for even harmonic numbers. The output power has a periodical behavior with a period that is much larger than the width of the photon-assistant tunneling step

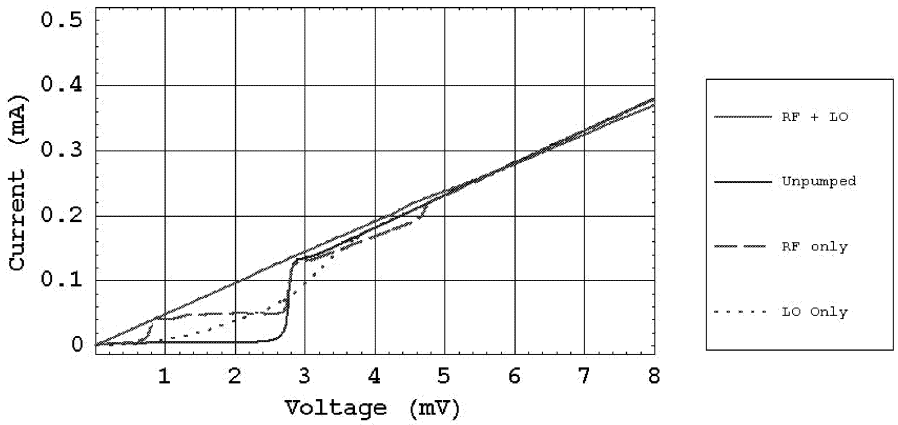

Figure 2: I-V curves of the SIS mixer 1) with neither RF or LO, 2) with RF only, 3) with LO only, 4) with RF and LO. Note that cases 3) and 4) have different LO power. $\boldsymbol{F_{RF}}$ *= 484 GHz,* $\boldsymbol{F_{LO}}$ *= 9.907 GHz*

corresponding to F_{LO}. The IF output has comparable amplitude for adjacent odd and even harmonic numbers. One should note that, due to the symmetry of the SIS junction's I-V curve, the odd harmonics have a zero in the output power at zero bias voltage while the even harmonics have a maximum at that point. The relative amplitude of the peaks in figs. 3 and 4 is changing nonlinearly as function LO input power. The estimated optimum LO input power was about –10 dBm, measured at the mixer-directional coupler interface. The loss due to mismatch between mixer and LO is not taken into account. It can also be seen that significant IF output power is produced, even for bias voltages far above the SIS junction's gap voltage of about 2.8 mV.

An additional measurement was made to check the linearity of a subharmonically pumped mixer with respect to the input RF signal. For this, the output power of the mixer was recorded while changing the mixer bias for different RF power levels. The RF power level was then calibrated by switching the LO off and measuring the height of the pumping step at a bias of 2 mV.

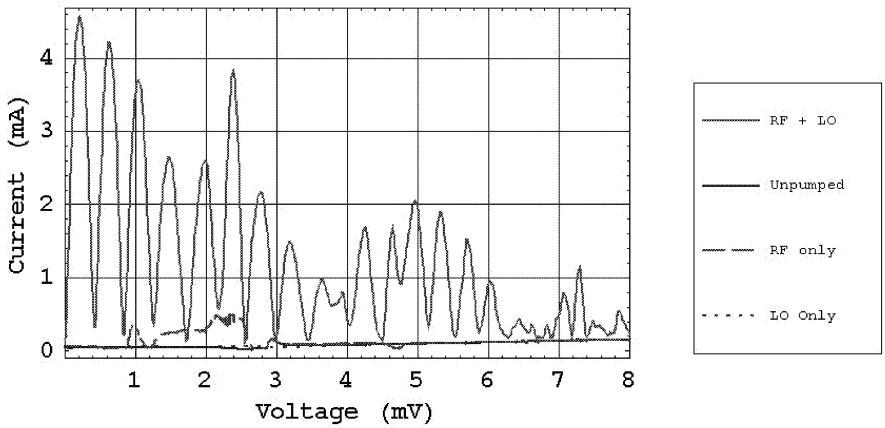

Figure 3: IF output power vs. SIS mixer bias for different operations regimes. $\boldsymbol{F_{RF}}$ *= 484 GHz,* $\boldsymbol{F_{LO}}$ *= 9.907 GHz,* ***49th*** *harmonic of synthesizer is used.*

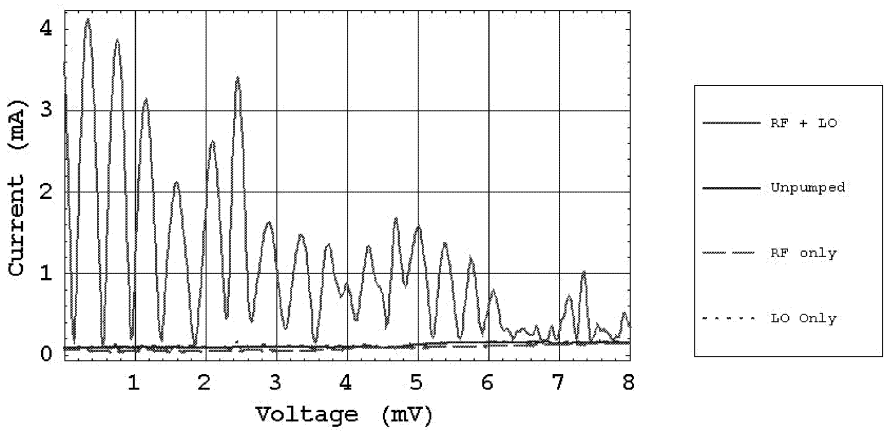

Figure 4: IF output power vs. SIS mixer bias for different operations regimes. F_{RF} *= 484 GHz,* ***50th*** *harmonic of synthesizer is used.*

For low pumping levels ($\alpha<1$) this current is proportional to the RF power coupled to the junction. We assume that, if the mixer is linear for such a high input power, that there will be no problem to use it for the much lower input powers that are typical for antenna beam pattern measurements.
The results of such a measurement procedure is presented in figs. 5 and 6. The mixer current of about 50 μA corresponds to the mixer pumping level $\alpha=1$. One can conclude that this mixer should only be used in the bias region close to zero, since the 1 dB compression point is highest there.

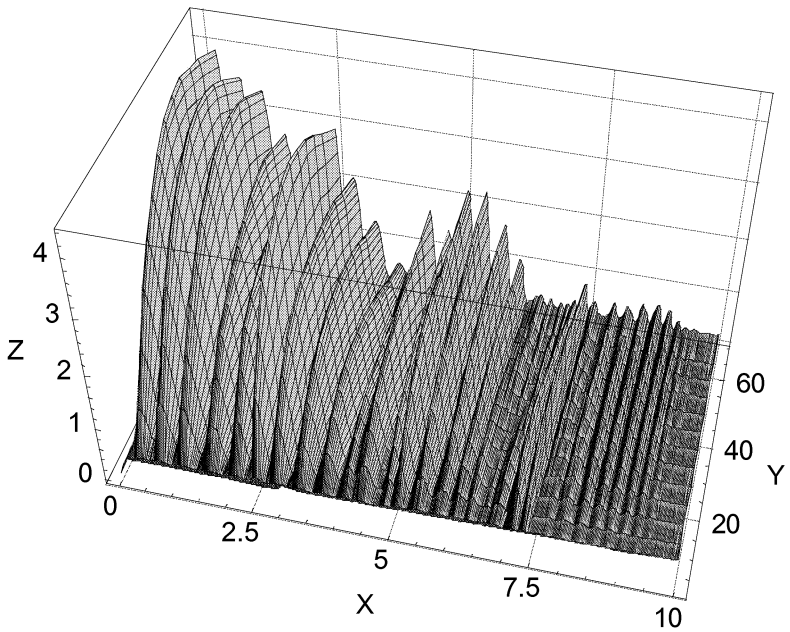

Figure 5: IF output power vs. SIS mixer bias for different RF signal power levels. F_{RF} *= 484 GHz,* ***49th*** *harmonics of synthesizer is used. X axis: SIS mixer bias voltage in mV, Y axis: SIS mixer bias current at 2 mV with LO switched off (proportional to input RF power) in μA, Z axis: IF output power (a.u.)*

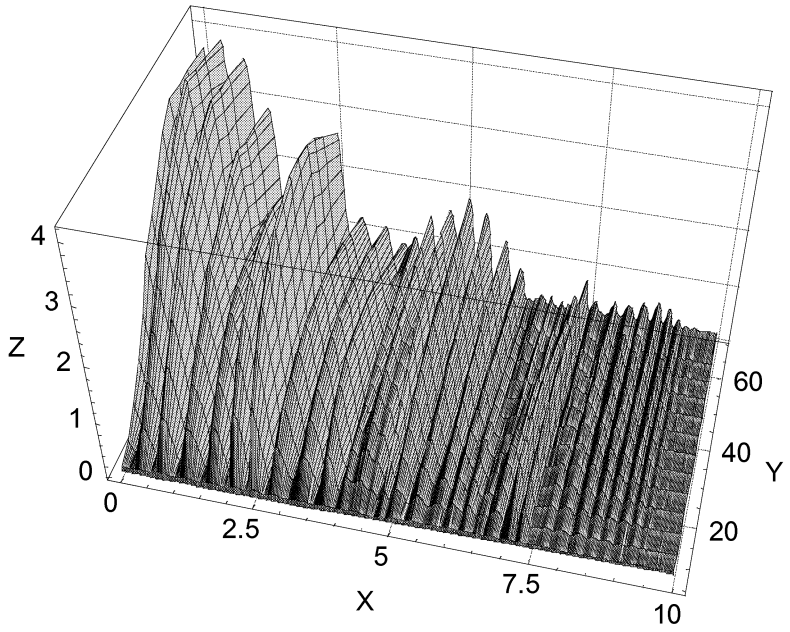

Figure 6: IF output power vs. SIS mixer bias for different RF signal power levels. F_{RF} *= 484 GHz,* ***50th*** *harmonics of synthesizer is used. X axis: SIS mixer bias voltage in mV, Y axis: SIS mixer bias current at 2 mV with LO switched off (proportional to input RF power) in μA, Z axis: IF output power (a.u.)*

ANTENNA BEAM PATTERN MEASUREMENTS

We used the waveguide SIS mixer, with diagonal feedhorn, described in [10] as subharmonically pumped mixer in our experiment. The mixer was mounted directly in front of the infrared radiation filter and the dewar window in such a way that its beam could be measured by a probe outside the dewar. The X-Y translation stage described in [11] was used for scanning. A tapered open-ended waveguide probe mounted on the multiplier chain was used as test feed.

The electrical connection scheme used in the experiment is shown in fig. 7. A phase-locked Gunn oscillator followed by a Shottky diode doubler and tripler was used as signal source. The signal (17 GHz) from a microwave synthesizer (G2) was used to pump both the SIS mixer and a harmonic mixer mounted between the Gunn source and the doubler. The IF output of the latter is filtered, amplified and multiplied by 6 to create a reference signal, coherent with the source signal, which is used to lock a vector voltmeter. The IF signal (1.2 GHz) from the SIS mixer was connected to the signal port of the vector voltmeter.

Since the RF frequency is in the range of 600-720 GHz, high multiplication numbers of the LO have to be used. That made the phase noise in the reference signal too high for the vector voltmeter to lock on it. However, since the same phase noise is also present in the SIS mixer IF signal, it can be subtracted by using the two-mixer chain shown in the bottom part of fig. 7. This scheme allows us to extend the measurement frequency even higher because it eliminates

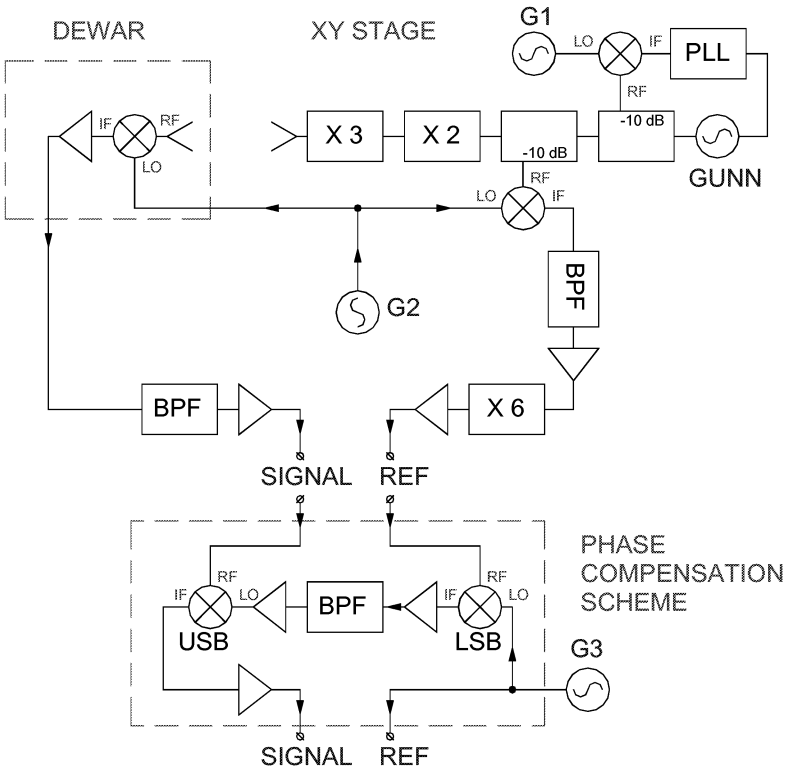

Figure 7: Scheme of the measurements and phase compensation scheme

the phase noise present in the source signal. A very narrow-band filter can be placed after the chain to further increase the signal to noise ratio of the system.
The antenna beam pattern for different signal source powers is presented in fig. 8. Some saturation at the 0 dB source level can be observed, but none is visible for source levels of –3, –6 and –9 dB. The small variations between the traces are due to slight changes in the effective signal path between the source and receiver due to different attenuator settings. A residual standing wave exists between source and detector, caused by imperfect matching of the source and detector elements. The measurements were done at 634 GHz RF using the 42nd harmonic of the LO signal source.

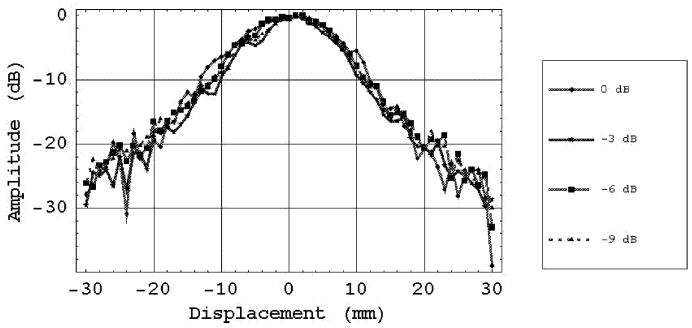

Figure 8: IF output power vs. source position for different source powers.

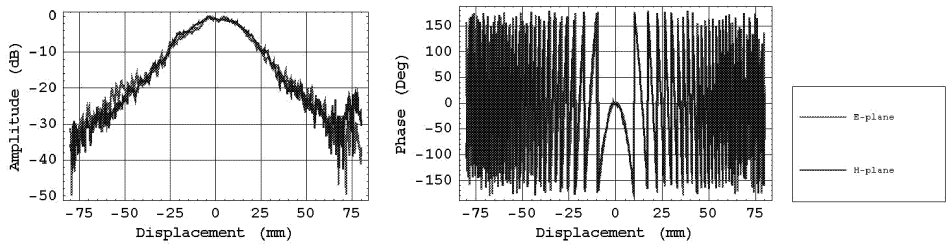

Figure 9: IF output power (left) and detected phase (right) vs. source position measured in the E and H planes.

The measured phase-and-amplitude antenna pattern of the diagonal horn, in both E and H direction, are presented in fig. 9. The signal to noise ratio of the system was about 45 dB. The phase is clearly detected even when the amplitude of the signal is close to -40 dB, due to the phase compensation technique described above. For all antenna beam patterns presented here, the subharmonically pumped SIS mixer was used at zero bias.
A comparison was made between the classical way of measuring the beam pattern by means of two RF sources (as described in [11]), and the subharmonically pumped SIS mixer. During the experiments, the system was switched over from one type of measurement to the other, while keeping all positions (including that of the beamsplitter) the same. The far field antenna beam pattern, calculated from the near field measurements is shown in fig. 10.

CONCLUSION

The operation of an SIS junction as a subharmonically pumped mixer with large harmonic numbers was studied experimentally. It was demonstrated that the conversion efficiency and linearity of such a mixer is good enough for using it in phase-and-amplitude antenna beam pattern measurements. A comparison was made between the conventional external-LO scheme and the one with the subharmonically pumped mixer, by performing antenna beam pattern measurements using both of them. The patterns were found to correspond to a high degree. The phase-noise compensating technique made it possible to use the system at very high frequencies.

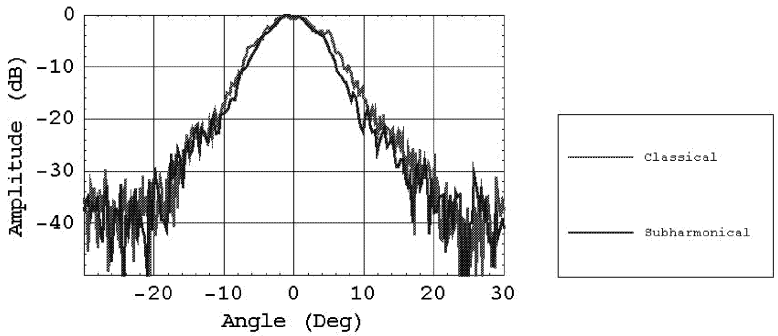

Figure 10: IF output power in the far field vs. angle for classical and subharmonically pumped measurements.

ACKNOWLEDGEMENTS

We would like to thank the following people:

- *At IRAM S.Halleguen, B.Lazareff, and F.Mattiocco for all of their help*
- *CNES for some of the funding of the equipment*
- *The observatory of Dwingalo for the loan of some of the equipment*
- *Harvard Smithsonian, R.Blundell and E.Tong for the loan of the high frequency transmitter*
- *Gerrit Gerlofsma and Duc van Nguen for technical assistance*
- *Wolfgang Wild and Herman van de Stadt for useful discussions*

REFERENCES

[1] Baryshev *et al.*, Proc of 12th Int. Symp. on Space Terahertz Technology, pp. 581-591, 2001

[2] Blundell *et al.*, IEEE Trans. Microwave Theory Tech., vol. 43, pp. 933-937, Apr. 1995.

[3] J. W. Kooi, *et al.*, Int. J. IR and MM Waves, vol. 16, pp. 2049-2068 1995.

[4] A.Karpov, J. Blondel, P. Pasturel, and K.H. Gundlach, IEEE Trans. Appl. Supercon. **7**, 1073 (1997)

[5] H. vand de Stadt, A. Baryshev, P. Dieleman, Th. De Graauw, T.M. Klapwijk, S. Kovtonyuk, G. de Lange, I. Lapitskaya, J. Mees, R.A. Panhuyzen, G. Procopenko, and H. Schaeffer, in Proc of the 6th Int. Symp. On Space THz Technol., CIT, PC, 66 (1995)

[6] M. Bin, M.C. Gaidis, J. Zmuidzinas, T.G. Phillips, and H.G. LeDuc, Appl. Phys. Lett. **68**, 1714 (1996).

[7] V.Yu.Belitsky, I.L.Serpuchenko, M.A.Tarasov, A.N.Vystavkin, Int. Conf. on mm waved and far infrared technology, Beijing, China, June 19-23, 1989, pp. 268-271

[8] V.P. Koshelets, S.V. Shitov, L.V. Filippenko, V.L. Vaks, J. Mygind, A.B. Baryshev, W. Luinge, N. Whyborn, Rev. of Sci. Instr., **v. 71**, No 1, pp. 289-293, (2000).

[9] A.B. Ermakov, S.V. Shitov , A.M. Baryshev, V.P. Koshelets, W. Luinge, Applied Superconductivity Conference ASC'2000, September (2000), Report 4EA10, *IEEE Trans. on Appl. Supercond.,* **v.11,** No 1, pp. 840-843, (2001).

[10] A. Baryshev, E. Lauria, R. Hesper, T. Zijlstra, W. Wild "Fixed-tuned waveguide 0.6 THz SIS Mixer with Wide band IF", this conference, to be published

[11] M.Carter, A.Baryshev, R.Hesper, S.J.Wijnholds, W.Jellema, T.Zijlstra," Phase and Amplitude Antenna Measurements on an SIS Mixer Fitted with a Double Slot Antenna for ALMA Band", this conference, to be published

Low noise SIS mixer with Nb tuning circuit for the frequency above 1 THz

A. Karpov, J. Zmuidzinas, F. Rice, D. Miller
J. A. Stern*, B. Bumble*, H. G. LeDuc*

California Institute of Technology, Pasadena, CA 91125, USA
* Jet Propulsion Laboratory, Pasadena, CA 91109, USA

We developed a SIS mixer for the 1.1-1.25 THz band of the heterodyne receiver of Herschel space observatory. The quasi-optical SIS mixer has two NbN/AlN/Nb junctions with the critical current 30-50 kA/cm^2 and the gap voltage of 3.4 mV. The tuning circuit integrated with SIS junction has the base electrode of Nb and a gold wire layer. This approach simplifies the SIS junction technology, compared to a design using NbTiN base electrode. The junction base electrode and the ground of the tuning micro strip circuit are formed in one step. The frequency of operation of the mixer is well above the gap frequency of Nb, and it behaves here as a normal metal. The epitaxial Nb film is gown at the sapphire substrate. The resistivity of Nb at the critical temperature of 0.2 μOhm cm is below the resitivity of the best normal metal films. This allows us to expect the loss of only 2 dB in the junction tuning circuit at 1.2 THz. The measured receiver noise temperature is below 600 K.

THz SIS Mixer Development for HIFI

B.D. Jackson, G. de Lange, W.M. Laauwen, and L. de Jong
SRON National Institute for Space Research
Postbus 800, 9700 AV Groningen, The Netherlands

T. Zijlstra, N.N. Iosad, and T.M. Klapwijk
Delft University of Technology, Department of Applied Physics (DIMES)
Lorentzweg 1, 2628 CJ Delft, The Netherlands

ABSTRACT

Low-noise THz SIS mixers are needed for the Heterodyne Instrument for the Far-Infrared (HIFI). Based upon the success of past work, in which NbTiN/SiO_2/Al tuning circuits were shown to enable the development of low-noise SIS mixers for frequencies up to 1 THz, a new waveguide mixer design is shown to be suitable for use in the 800-960 GHz band of HIFI. Potential modifications to this design that could improve its performance at higher frequencies are also discussed.

1. INTRODUCTION

The Heterodyne Instrument for the Far-Infrared (HIFI) [1] requires low-noise SIS mixers for frequencies between 480 and 1250 GHz. Below 700 GHz, the low-loss performance of Nb tuning circuits enables the development of SIS mixers with nearly quantum-limited sensitivities [2-4]. However, the RF losses in Nb increase significantly at higher frequencies [5], causing all-Nb SIS mixers to become increasingly less sensitive [6]. Past work has shown that the use of NbTiN-based tuning circuits can yield low-noise SIS mixers at frequencies up to at least 1 THz [7-9].[1] In particular, a quasi-optical mixer incorporating a NbTiN/SiO_2/Al tuning circuit and standard Nb SIS junctions has been shown to yield a receiver sensitivity of $T_{N,rec}$ = 253-315 K between 850 and 980 GHz [8]. Unfortunately, although previously demonstrated waveguide mixers offered similar peak sensitivities [9], their RF bandwidths were significantly smaller than that of the quasi-optical mixer. Furthermore, both types of mixer showed a loss of sensitivity above 1 THz, which was attributed to increasing RF losses in their NbTiN ground planes [8,9].

This paper presents a redesigned waveguide mixer incorporating a NbTiN/SiO_2/Al tuning circuit that is similar to that used previously. This mixer is shown to yield low-noise performance over a wide RF bandwidth, making it suitable for use in the 800-960 GHz band of the HIFI instrument. Potential design improvements are also discussed.

2. MIXER DESIGN

SRON is responsible for developing SIS mixers for bands 3 and 4 of HIFI (covering 800-960 and 960-1120 GHz, respectively). The design of these mixers is expected to fulfill a long list of optical, mechanical, thermal, and electrical interface requirements, plus requirements related to space qualification. A prototype of the band 4 mixer is seen in Fig. 1, and its design is described in detail elsewhere in these proceedings [10].

---

[1] Throughout this paper, NbTiN is used to represent $(Nb_{0.70}Ti_{0.30})_xN_{1-x}$, where x ~ 0.5.

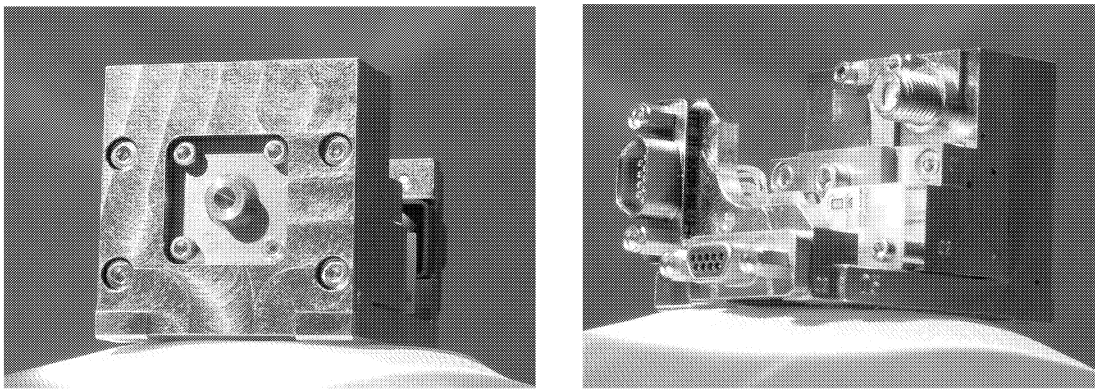

Fig. 1 – The demonstration model of the HIFI Band 4 Mixer Unit. The corrugated horn, plus the DC and IF connectors are all visible. The mixer unit is 32x32x45 mm^3.

The performance requirements for the HIFI mixers are derived from the baseline instrument sensitivity defined in the HIFI proposal (see [1]), resulting in a baseline mixer sensitivity requirement of $T_{N,mix} \sim 3.5\ hf/k_B$ across the mixers' full RF and IF bandwidths (4-8 GHz).[2] Based upon the results of past work [8,9], it is known that NbTiN/SiO_2/Al tuning circuits can yield mixers with high sensitivities up to at least 1 THz. However, the RF bandwidth of the previously demonstrated waveguide mixers was limited to ~ 100 GHz [9], due to the fact that the mixers' RF design had not been optimized. Instead, use was made of an existing full-height 1 THz waveguide mixer block and RF embedding circuit design (i.e. the designs of the waveguide probe and RF choke filter on the SIS chip) [11]. Furthermore, because the devices' on-chip tuning circuits were originally designed for use with an all-NbTiN tuning circuit, they were also non-optimal for the NbTiN/SiO_2/Al tuning circuit that was ultimately used.

The redesigned mixer incorporates a half-height waveguide, in place of the full-height waveguide used previously. The detailed waveguide, waveguide probe, and RF choke designs are all scaled from the design of a 600-700 GHz mixer that is in use at the James Clerk Maxwell Telescope (JCMT), in Hawaii [12]. In particular, the design of the JCMT mixer was scaled to the 880 and 1040 GHz centre frequencies of bands 3 and 4 of HIFI

	JCMT Mixer (650 GHz)	HIFI Band 3 (880 GHz)	HIFI Band 4 (1040 GHz)
Waveguide	400x100	296x74	248x62
Backshort Depth	140	103	88
Substrate Channel	100x70	74x52	62x42
Substrate	75x42	55x32	47x26

Note: all dimensions are given in μm.

Fig. 2 – Waveguide and substrate geometries for the mixers described here.

[2] Note that $T_{N,mix}$ is defined as the effective input noise temperature of the mixer plus a 4-8 GHz IF amplifier chain (with $T_{N,IF}$ = 10 K). It is estimated from the measured receiver noise by correcting for the RF losses in the receiver optics (i.e. beamsplitter, dewar window, and heat-filter(s)).

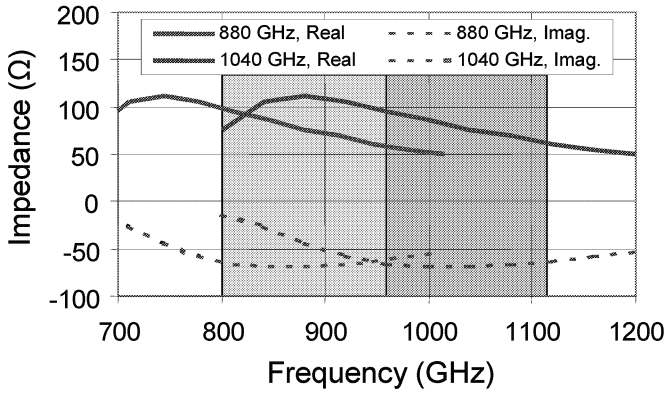

Fig. 3 – RF embedding impedances estimated for the 880 and 1040 GHz mixer designs. These are scaled from the calculated embedding impedance of the original 650 GHz design [13].

by assuming a 650 GHz centre frequency for the original design. The RF performance of the 650 GHz design was modelled in a 3-D electromagnetic simulator [13], to determine the RF embedding impedance seen at the input to the on-chip μ-strip tuning circuit. This frequency-dependent impedance was then scaled to estimate the embedding impedances of the 880 and 1040 GHz mixer designs (see Fig. 3).

The second stage of the mixer redesign was an optimization of the on-chip tuning circuit to maximize the RF coupling to the SIS junction(s) across the 800-960 and 960-1120 GHz bands. For the purposes of this design, two basic device geometries were used – a

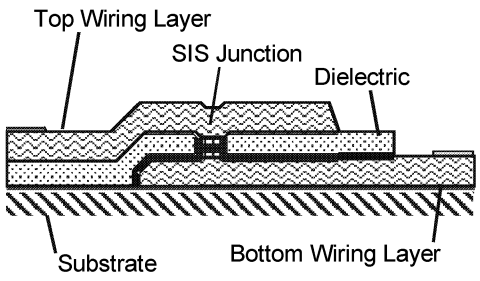

(a)

	Material	Critical Parameters
Substrate	fused quartz	200 μm thick polished to 20-30 μm
Ground Plane	NbTiN	300 nm T_c= 14.4 K $\rho_{n,\,16\,K}$ = 110 μΩ·cm
Dielectric	SiO_2	250 nm ε_r = 3.8
Wiring Layer	Al (+ Nb)	400 nm $\rho_{n,\,4\,K}$ = 0.4 μΩ·cm
Junction	Nb/Al-AlO_x/Nb	J_c = 7.5 kA/cm^2 A ~ 0.9 μm^2

(b)

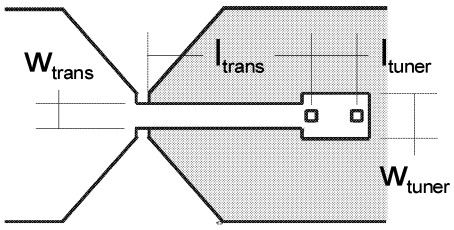

(c)

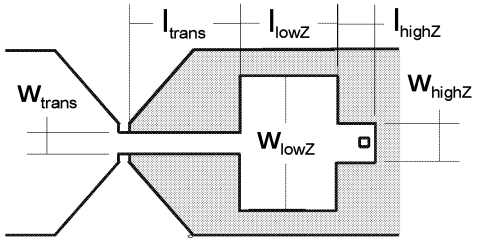

(d)

Fig. 4 – SIS Device Geometry. (a) a cross-section of a single-junction device, (b) the SIS device layer properties, (c) the twin-junction tuning circuit geometry, and (d) the single-junction tuning circuit geometry.

twin-junction design similar to that used previously at 1 THz [9], and a single-junction design that is similar to that in the 650 GHz JCMT mixer [12] (see Fig. 4 for schematic drawings of these tuning circuit layouts). Fig. 4 also summarizes the properties of the SIS junctions and the tuning circuit materials used for this design study.

For both basic device geometries, the coupling of radiation to the SIS junction(s) has been estimated by using the embedding impedances in Fig. 3 as the source impedance in a simple transmission line model of the μ-strip tuning circuit and a lumped element model of the SIS junction(s). In this model, the surface impedance of the Al wiring layer is calculated under the assumption that the Al is in the anomalous limit [14], while the surface impedance of the NbTiN ground plane is calculated using the Mattis-Bardeen formulation for the complex conductivity of a superconductor in the extreme anomalous limit [5] (using values of T_c = 13.0 and 14.5 K to model effective gap frequencies of 1.0 and 1.1 THz, respectively). The results of these calculations are summarized in Fig. 5 for the four basic designs (880 and 1040 GHz variants of the twin- and single-junction designs).

As seen in Fig. 5, the calculated responses of both the twin- and the single-junction designs can cover the full 800-960 GHz band, although the coupling the junction(s) is expected to be 20-30 % higher if a twin-junction design is used. In contrast, the performance of the 1040 GHz designs is critically dependent upon the effective gap frequency of the NbTiN ground plane (as simulated by the use of different values of the T_c of NbTiN). In particular, if the effective gap of the NbTiN is 1.1 THz, the 1040 GHz designs are expected to behave similarly to the 880 GHz designs. If, on the other hand, the effective gap of the NbTiN is ~ 1.0 THz (as was found to be the case in previous work [8,9]), the calculated performance of both designs drops significantly across the 960-1120 GHz band. In this case, an all-normal-metal tuning circuit would be needed to obtain significant sensitivity near the upper end of the band (see Fig. 5b).

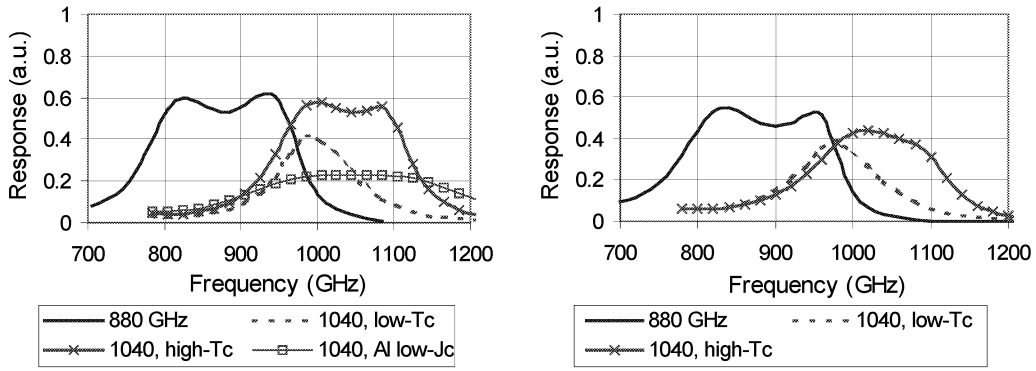

(a) (b)

Fig. 5 – Calculated RF coupling to the SIS junction(s) for the 880 and 1040 GHz twin-junction and single-junction designs (in (a) and (b), respectively). The twin-junction designs are estimated to be ~ 20-30 % more sensitive than the single-junction designs, while the responses of both types of 1040 GHz device depend strongly upon the T_c of the NbTiN ground plane (modelled by using different values of the T_c of the NbTiN ground plane).

3. DEVICE FABRICATION AND CHARACTERIZATION

Based on the results of the design study described in the previous section, three of the four basic device designs have been implemented in finished devices (twin- and single-junction 880 GHz devices, plus twin-junction 1040 GHz devices).

The fabrication process used to produce these devices is similar to that used previously for the fabrication of NbTiN-based SIS devices [9,15]. The NbTiN ground plane is deposited at room temperature, yielding a film with $T_c = 14.4$ K and $\rho_n \sim 110$ μΩ·cm [16]. The most significant modifications to the process described in Refs. 9 and 15 are in the definition of the SIS junctions – reactive ion etching of the Nb junction electrodes in $CF_4 + O_2$ has been replaced by reactive ion etching in $SF_6 + O_2$, and an extra O_2 plasma etch has been added to controllably shrink the resist pattern following the etching of the upper Nb electrode (prior to the Ar sputter etch of the junction barrier). These changes are intended to improve the reliability of the junction definition process.

After fabrication is complete, the devices are evaluated by first measuring their DC current-voltage characteristics (at 4.2 K) to identify promising candidates for RF testing. Selected devices are then mounted in a reduced-height mixer block, together with the appropriate corrugated horn, and the mixer block is mounted on the cold plate of a Helium cryostat. RF radiation is coupled into the cryostat through a 100-μm Mylar vacuum window and Zitex G104 infrared heat-filters mounted on the 77 and 4 K stages of the cryostat. The quasi-optical RF beam is focussed into the mixer by an off-axis elliptical mirror that is mounted on the 4 K stage of the cryostat. The 4-8 GHz IF output from the junction is decoupled from the DC bias with a planar bias-T circuit that is built into the mixer block. The mixer's IF output then passes through a 4-8 GHz Pamtech isolator and a low-noise 4-8 GHz YEBES amplifier [17] before leaving the cryostat. The total noise of the IF chain is ~ 10 K across the 4-8 GHz band.

The spectral response of the mixer is first measured with a Fourier transform spectrometer while operating the device as a direct-detector. Testing then proceeds with measurements of the heterodyne sensitivity of the receiver. For the results presented here, the response of the mixer is evaluated in a total power mode by measuring the full 4-8 GHz output of the receiver with a power meter. The noise and gain of the receiver, plus the noise contributions of the receiver optics, are evaluated using the Callen-Welton formulation for the signal power radiated by a blackbody load [18].

4. MEASURED DEVICE PERFORMANCE

The DC current-voltage characteristic of a representative 880 GHz twin-junction device is seen in Fig. 6, together with the IF output power of the device (both with and without the application of local oscillator power). The gap voltage of these devices is typically 2.6-2.8 mV and the sub-gap to normal-state resistance ratio is typically 10-15. (This is lower than is expected for 7-8 kA/cm^2 Nb SIS junctions, but is comparable to previous results obtained using Nb junctions integrated with NbTiN-based tuning circuits [8,9].)

As a test of the frequency-responses of the three basic tuning circuit designs, devices of each type have been tested with the Fourier transform spectrometer (see Fig. 7). As can be seen, both the single- and twin-junction 880 GHz designs yield strong responses across a wide RF bandwidth. In contrast, the responses of the 1040 GHz devices are

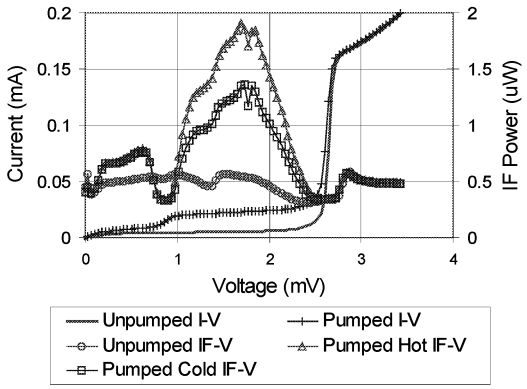

Fig. 6 – Current and IF output power vs. bias voltage for an 880 GHz twin-junction device measured at 4.5 K, both with and without applying 866 GHz LO power. The hot and cold IF output power curves correspond to 300 and 77 K blackbody signal loads and the sensitivity of this mixer is determined to be $T_{N,rec}$ = 420 K at 866 GHz.

much weaker than those of the 880 GHz devices. This is attributed to the fact that the response peaks of the 1040 GHz devices are tuned too high in frequency, so that their sensitivity is reduced by losses in the NbTiN ground plane above 1 THz. Evidence of this cut-off is also seen in the responses of the 880 GHz twin-junction devices, which are shifted above the 800-960 GHz band in which they are designed to operate. (They are actually sensitive from 850 to 1000-1050 GHz.)

The heterodyne responses of the four 880 GHz devices in Fig. 7 are summarized in Fig. 8. The twin-junction devices are seen to yield low receiver noise across the 850-970 GHz band, with optimum receiver sensitivities of 420 and 364 K measured at 4.5 and 2.5 K, respectively. Also shown in Fig. 8 are estimates of the effective input noise at the mouth of the waveguide horn (obtained by correcting for the estimated losses in the input optics). After this correction is applied, these mixers are found to offer sensitivities at

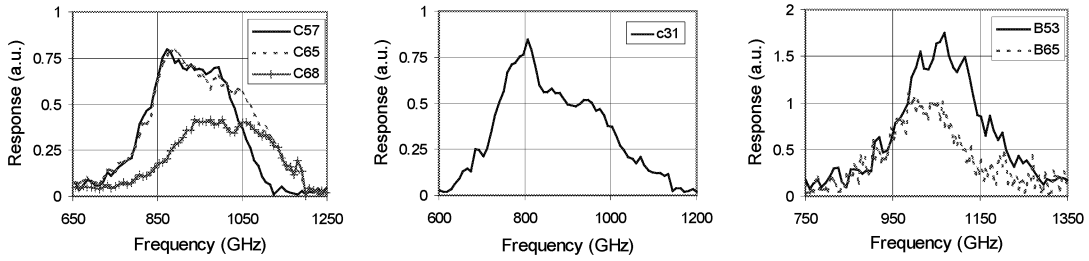

Fig. 7 – Measured FTS responses of: (a) three 880 GHz twin-junction devices, (b) one 880 GHz single-junction device, (c) and two 1040 GHz twin-junction devices. Both 880 GHz designs produce strong responses over a broad RF bandwidth. In contrast, the 1040 GHz devices produce very weak responses. The poor performance of the 1040 GHz devices is attributed to the fact that the devices' centre frequencies are tuned above the effective gap frequency of the NbTiN ground plane.

Chip	Design	Temp. (K)	Freq. (GHz)	$T_{N,rec}$ (K)	$T_{N,mix}$ (K)
c31	single	4.5	805	637	452
		2.5	805	506	351
c57	twin	4.5	866	420	284
c65	twin	4.5	890	440	293
		2.5	894	364	232
c68	twin	4.5	952	1260	430

(a)

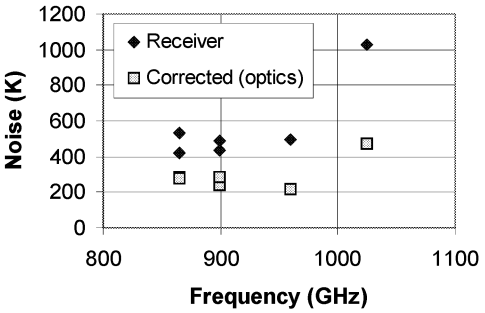

(b)

Fig. 8 – Measured receiver noise temperatures of the 880 GHz devices measured to-date (together with receiver noise temperatures that have been corrected for optical losses). (a) summarizes the peak performance of the four measured devices (note that the twin-junction devices, c57 and c65, are significantly more sensitive than the single-junction device, c31, as predicted in Fig. 5), while (b) summarizes the frequency dependence of the heterodyne response of c57 at a 4.5 K bath temperature. All noise temperatures are averaged over the full 4-8 GHz IF band.

2.5 K of $T_{N,mix} \sim 230$ K. Finally, with a peak sensitivity of $T_{N,rec} = 506$ K at 2.5 K, the one single-junction device measured to-date is ~ 30 % less-sensitive than the most sensitive twin-junction device, which is in line with the predictions of the tuning circuit performance presented in Fig. 5.

5. DISCUSSION

Based upon these results, it appears that the 880 GHz twin-junction device design performs as expected, yielding relatively low noise across a broad RF bandwidth. In particular, the measured sensitivity of $T_{N,mix} \sim 230$ K at 890 GHz approaches the baseline specification for the HIFI mixers (~ 170 K at this frequency). However, although some incremental improvements may be possible within the existing design and device geometry (i.e. if junctions with lower leakage currents and/or higher current-density (J_c) can be obtained, or if the resistivity of the Al wiring layer can be reduced), an improvement beyond this baseline would likely require a more major design modification. In particular, two potentially major changes can be identified:

A. The use of high-quality, high current-density junctions with AlN_x barriers [19,20] would reduce the loss in the NbTiN/SiO_2/Al tuning circuit [21] (which is estimated to be ~ 3 dB in the present twin-junction devices). See Fig. 9a for an estimate of the RF coupling improvement that could be obtained by using junctions with $J_c = 20$ kA/cm^2, in place of the 7.5 kA/cm^2 used currently.

B. Alternatively, the present waveguide + waveguide probe + RF-choke design yields a relatively large embedding impedance (see Fig. 3), which requires a high-Q tuning circuit to couple radiation to the SIS junction(s). In contrast, the use of a suspended-stripline design for the RF choke [22,23] or a single-sided waveguide probe [24] could yield a lower embedding impedance, and thereby reduce the RF loss in the tuning circuit.

More significant improvement is needed in the 1040 GHz devices, as the existing NbTiN ground plane does not appear to be of high enough quality for use at 1.1 THz. In particular, two options are seen as being the most likely to succeed:

A. Make use of the existing design and geometry, but with higher quality NbTiN films grown at elevated temperatures and/or on lattice-matched MgO substrates [25,26]. (Note that for a waveguide mixer, the elevated-temperature option is preferred because the MgO substrate would have to be thinned to ~ 15 μm to be electrically equivalent to the 25 μm thick quartz substrates used currently.)

B. Alternatively, the integration of an all-normal-metal tuning circuit with high-quality, very-high J_c SIS junctions based on an AlN_x tunnel barrier has been shown to yield low-noise mixers up to at least 1.2 THz [27].

The potential improvements in RF coupling that could be obtained by these two options are demonstrated in Fig. 9b.

Unfortunately, a number of these development options are not seen as realistic within the context of the pressing HIFI schedule. (The flight model mixers are needed by mid-2003, meaning that the flight model SIS devices are needed by the end of 2002.) For this reason, it is expected that the 880 GHz mixers for HIFI will be based upon the existing design (although some incremental improvements in the devices may be possible). For the 1040 GHz devices, the most likely solution will be the use of higher-quality NbTiN films (grown at elevated temperatures) in the existing device design and production process (since even a small improvement in the effective gap of the NbTiN should be enough to significantly improve the mixer performance in the 960-1120 GHz range).

6. CONCLUSIONS

A waveguide SIS mixer incorporating a reduced-height waveguide and a twin-junction NbTiN/SiO_2/Al tuning circuit is shown to yield low-noise performance over a broad RF bandwidth (850-1000 GHz), with a best-measured sensitivity of $T_{N,rec}$ = 364 K at 890 GHz. Correcting for the losses in the receiver optics, this corresponds to an input noise

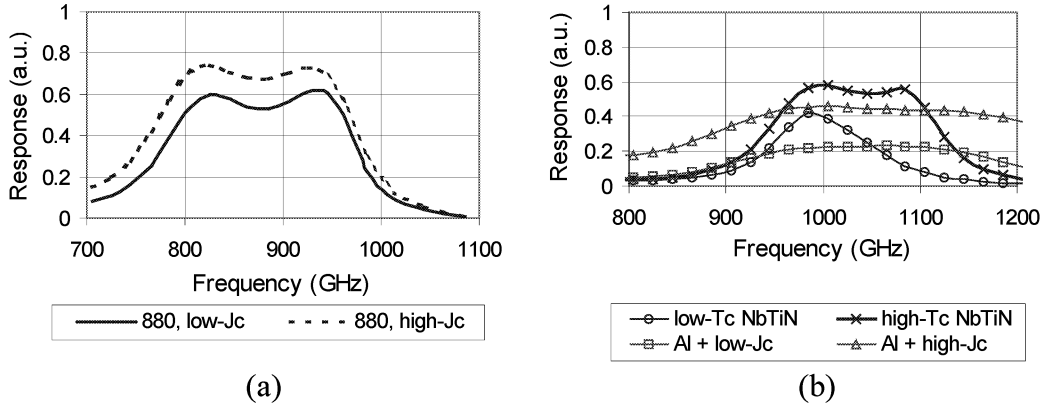

(a) (b)

Fig. 9 – (a) The simulated effect of increasing the junction J_c to improve the performance of the 880 GHz design. (b) The effect of modifications to improve the performance of the 1040 GHz devices (increasing the NbTiN gap frequency, or using an all-Al tuning circuit with low- or high-J_c junctions).

of the mixer together with the IF chain of $T_{N,mix} \sim 230$ K, which is approaching the baseline specification for the HIFI instrument (170 K at this frequency). Unfortunately, the performance of this mixer geometry drops significantly above ~ 1 THz, due to increasing RF losses in the NbTiN ground plane. It is hoped that this problem can be rectified by the integration of higher-quality NbTiN films with the existing device design and production process.

7. ACKNOWLEDGEMENTS

The authors would like to thank M. Eggens, H. Golstein, S. Kikken, B. de Lange, D. Nguyen, C. Pieters, H. Smit, and M. Zuiddam for their technical assistance, and J. Bruston, J.-R. Gao, Th. de Graauw, N. Honingh, M. Kroug, R. LeDuc, J. Stern, and J. Zmuidzinas for useful discussions. This work has been supported in part by ESA through ESTEC research contract #11653/95 SRON STS-TDG-99/014.

8. REFERENCES

[1] Th. de Graauw and F.P. Helmich, "Herschel-HIFI: The heterodyne instrument for the far-infrared," in: G.L. Pilbratt, J. Cernicharo, A.M. Heras, T. Prusti, and R.A. Harris (Eds.), *SP-460 The Promise of the Herschel Space Observatory*, ESA, The Netherlands, 2001, pp. 45-52.

[2] J.W. Kooi, M. Chan, B. Bumble, H.G. LeDuc, P. Schaffer, and T.G. Phillips, "230 and 492 GHz low noise SIS waveguide receivers employing tuned Nb/AlO_x/Nb tunnel junctions," *Int. J. IR and MM Waves*, vol. 16, no. 12, pp. 2049-2068, 1995.

[3] A. Karpov, J. Blondel, M. Voss, and K.H. Gundlach, "A three photon noise SIS heterodyne receiver at submillimeter wavelength," *IEEE Trans. Appl. Supercon.*, vol. 9, no. 2, pp. 4456-4459, June 1999.

[4] C.E. Honingh, S. Haas, D. Hottgenroth, K. Jacobs, and J. Stutzki, "Low-noise broadband fixed tuned SIS waveguide mixers at 660 and 800 GHz," *IEEE Trans. on Appl. Supercon.*, vol. 7, no. 2, pt. 3, pp. 2582-2586, 1997.

[5] D.C. Mattis and J. Bardeen, "Theory of the anomalous skin effect in normal and superconducting metals," *Phys. Rev.*, vol. 111, pp. 412-417, July 1958.

[6] G. de Lange, J.J. Kuipers, T.M. Klapwijk, R.A. Panhuyzen, H. van de Stadt, and M.W.M. de Graauw, "Superconducting resonator circuits at frequencies above the gap frequency," *J. Appl. Phys.*, vol. 77, pp. 1795-1804, Feb. 1995.

[7] J. Kawamura, J. Chen, D. Miller, J. Kooi, J. Zmuidzinas, B. Bumble, H.G. Leduc, and J.A. Stern, "Low-noise submillimeter-wave NbTiN superconducting tunnel junction mixers," *Appl. Phys. Lett.*, vol. 75, pp. 4013-4015, Dec. 1999.

[8] B.D. Jackson, A.M. Baryshev, G. de Lange, S.V. Shitov, J.-R. Gao, N.N. Iosad, and T.M. Klapwijk, "Low-noise 1 THz superconductor-insulator-superconductor mixer incorporating a NbTiN/SiO_2/Al tuning circuit," *Appl. Phys. Lett.*, vol. 79, no. 3, pp. 436-438, 16 July 2001.

[9] B.D. Jackson, N.N. Iosad, G. de Lange, A.M. Baryshev, W.M. Laauwen, J.-R. Gao, and T.M. Klapwijk, "NbTiN/SiO_2/Al tuning circuits for low-noise 1 THz SIS mixers," *IEEE Trans. on Appl. Supercon.*, vol. 11, no. 1, pt. 1, pp. 653-656, March 2001.

[10] G. de Lange *et al.*, these proceedings.

[11] H. van de Stadt, A. Baryshev, P. Dieleman, Th. de Graauw, T.M. Klapwijk, S. Kovtonyuk, G. de Lange, I. Lapitskaya, J. Mees, R.A. Panhuyzen, G. Prokopenko, and H. Schaeffer, "A 1 THz Nb SIS heterodyne mixer with normal metal tuning structure," in: J. Zmuidzinas and G.M. Rabeiz (Eds.), *Proc. of the 6th Int. Symp. on Space THz Technol.*, CIT, Pasadena, CA, March 21-23, 1995, pp. 66-77.

[12] A.M. Baryshev, L. de Jong, R. Hesper, H. Schaeffer, H. van de Stadt, W. Wild, T. Zijlstra, and M. Zuiddam, "Development of a 0.6 THz SIS Receiver for ALMA," in: I. Mehdi (Ed.), *Proc. of the 12th Int. Symp. on Space THz Technology*, CIT, San Diego, CA, Feb. 14-16, 2001, pp. 581-587.

[13] J. Kooi, private communications.

[14] R. L. Kautz, "Miniaturization of normal-state and superconducting striplines," *J. Res. Natl. Bur. Std.*, vol. 84, pp. 247-259, May-June 1979.

[15] N.N. Iosad, B.D. Jackson, T.M. Klapwijk, S.N. Polyakov, P.N. Dmitriev, and J.R. Gao, "Optimization of RF- and DC-sputtered NbTiN films for integration with Nb-based SIS junctions," *IEEE Trans. on Appl. Supercon.*, vol. 9, no. 2, pt. 2, pp. 1716-1719, June 1999.

[16] N.N Iosad, A.V. Mijiritski, V.V. Roddatis, N.M. van der Pers, B.D. Jackson, J.R. Gao, S.N. Polyakov, P.N. Dmitriev, and T.M. Klapwijk, "Properties of $(Nb_{0.35}Ti_{0.15})_xN_{1-x}$ thin films deposited on silicon wafers at ambient substrate temperature," *J. Appl. Phys.*, vol. 88, no. 10, pp. 5756-5759, 2000.

[17] I. Lopez-Fernandez, J.D. Gallego Puyol, A.B. Cancio, and F. Colomer, "New trends in cryogenic HEMT amplifiers for radio astronomy," presented at the Int. Science and Technology Meeting on the Square Kilometer Array, Berkely, CA, July 9-13, 2001.

[18] H.B. Callen and T.A. Welton, "Irreversibility and generalized noise," *Phys. Rev.*, vol. 83, pp. 34-40, July 1951.

[19] B. Bumble, H.G. LeDuc, J.A. Stern, and K.G. Megerian, "Fabrication of Nb/Al-N_x/NbTiN junctions for SIS mixer applications," *IEEE Trans. on Appl. Supercon.*, vol. 11, no. 1, pt. 1, pp. 76-79, March 2001.

[20] N.N. Iosad, A.B. Ermakov, F.E. Meijer, B.D. Jackson, and T.M. Klapwijk, "Characterization of fabrication process of Nb/Al-AlN_x/Nb tunnel junctions with low R_nA values up to 1 Ω μm^2," *Supercond. Sci. Technol.*, accepted for publication, 2002.

[21] J. Kawamura, D. Miller, J. Chen, J. Zmuidzinas, B. Bumble, H.G. LeDuc, and J.A. Stern, "Very high-current-density Nb/AlN/Nb tunnel junctions for low-noise submillimeter mixers," *Appl. Phys. Lett.*, vol. 76, pp. 2119-2121, Apr. 2000.

[22] R. Blundell, C.-Y.E. Tong, D.C. Papa, R.L. Leombruno, X. Zhang, S. Paine, J.A. Stern, H.G. LeDuc, and B. Bumble, "A wideband fixed-tuned SIS receiver for 200-GHz operation," *IEEE Trans. Microwave Theory Tech.*, vol. 43, no. 4, pp. 933-935, 1995.

[23] C.-Y.E. Tong, R. Blundell, S. Paine, D.C. Papa, J. Kawamura, X. Zhang, J.A. Stern, and H.G. LeDuc, "Design and characterization of a 250-350-GHz fixed-tuned superconductor-insulator-superconductor receiver," *IEEE Trans. Microwave Theory Tech.*, vol. 44, no. 9, pp. 1548-1556, 1996.

[24] S. Withington, G. Yassin, J. Leech, and K.G. Isaak, "An accurate expression for the input impedances of one-side microstrip probes in waveguide," in: T.W. Crowe and R.M. Weikle (Eds.), *Proc. of the 10th Int. Symp. on Space THz Technology*, U. of Virginia, Charlottesville, VA, March 16-18, 1999, pp. 508-518.

[25] J.A. Stern, B. Bumble, H.G. Leduc, J.W. Kooi, and J. Zmuidzinas, "Fabrication and DC-characterization of NbTiN based SIS mixers for use between 600 and 1200 GHz," in: R. McGrath (Ed.), *Proc. of the 9th Int. Symp. on Space THz Technology*, CIT, Pasadena, CA, March 17-19, 1998, pp. 305-313.

[26] N.N. Iosad, V.V. Roddatis, S.N. Polyakov, A.V. Varlashkin, B.D. Jackson, P.N. Dmitriev, J.R. Gao, and T.M. Klapwijk, "Superconducting transition metal nitride films for THz SIS mixers," *IEEE Trans. on Appl. Supercon.*, vol. 11, no. 1, pt. 3, pp. 3832-3835, March 2001.

[27] Karpov *et al.*, these proceedings.

ANALYSIS OF SUPERCONDUCTING COPLANAR WAVEGUIDES FOR SIS MIXER CIRCUITS

P. KITTARA, G. YASSIN AND S. WITHINGTON
Department of Physics, University of Cambridge,
Madingley Road, Cambridge CB3 OHE, UK

ABSTRACT In this paper we analyse the behaviour of the coplanar waveguide for SIS mixer circuits. In particular we present design curves for the propagation constant and the characteristic impedance of the transmission line, in addition to conduction, radiation and surface waves losses. The analysis is based on a conformal mapping method which rigorously takes into account the effect of metallisation thickness. We will show that the three loss mechanisms can be important, depending on the transmission line geometry and on frequency.

INTRODUCTION

A simple SIS chip requires three circuits: the feed circuit which couples power from the feed to the SIS device, the tuning circuit which tunes out the capacitance of the tunnel junction and the IF circuit which carries the low frequency signal. Conventionally, these circuits have been fabricated in microstrip, using Niobium in the superconducting state or Aluminium in the normal state. At frequencies above the gap however, the losses in both cases become substantial so that the noise temperature of the mixer becomes dominated by the circuit losses. Another problem that the mixer designer faces at high frequencies is that the length of the single stage stub become difficult to realise since its length becomes comparable to its own width and to the dimensions of the device. For example, at 700 GHz, taking a microstrip deposited on SiO of width w= 3μm dielectric thickness of h= 400 nm we find that the requited stub length which is requited to tune out the capacitance of a typical 1 μm^2 junction is about l=3μm. In this paper we shall present our work which addresses those difficulties, by introducing the superconducting coplanar waveguide (SCPW) as an alternative to the superconducting microstrip.

The coplanar waveguide is extensively used in printed circuit technology despite the the fact that at low frequencies and large dimensions it is known to have higher conduction losses than the microstrip. For example, a microstrip which consists of a copper strip of width w= 200μm, deposited on a substrate of dielectric constant ϵ = 12.9 and thickness h= 200μm has a characteristic impedance value of Z_0= 43 Ω and an attenuation constant of $\alpha = 0.025$ db/mm. On the other hand, a coplanar waveguide which uses the same material and substrate and having a gap of s=5 μm and a central conductor width w= 40 μm has a characteristic impedance Z_0= 21 Ω and an attenuation constant $\alpha = 0.3$

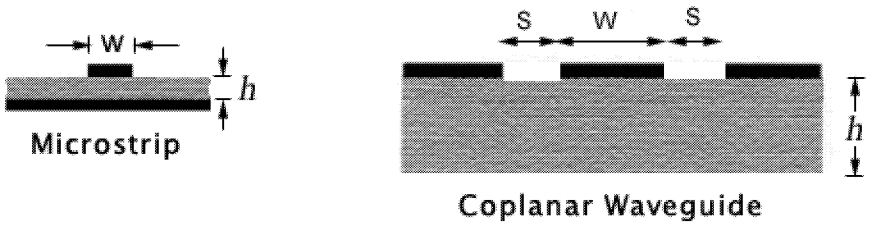

FIGURE I Geometry of the coplanar waveguide and the microstrip

db/mm. The situation however becomes completely different when SIS mixer circuits dimensions are employed. For example, a copper microstrip line at 900 GHz with $\epsilon = 5.8$, h= 0.4μm, w= 2 μm and film thickness $t = 0.4\mu$m gives Z_0= 21 Ω and an attenuation value of $\alpha = 33.9$ db/mm. In comparison, a copper CPW with the same film thickness and at the same frequency, having the same dielectric constant and h= 60 μm, w=100μm, s=2 μm, yields a characteristic impedance value $Z_0 \approx 37$ Ω and a much lower attenuation constant$\alpha = 2.5$ db/mm. For mixer circuits therefore, the conduction loss of the microstrip circuit is far larger than the loss of the coplanar waveguide. In addition, It is recognised that CPW have the following advantages over the microstrip:

- It offers a useful range of characteristic impedance values. As we shall see later, impedance values in the range of 50-200 Ω may be obtained for gap and central conductor width dimensions which are easy to fabricate.
- The electrical parameters are insensitive to the substrate thickness. This property is particularly important in SIS mixer circuits
- The central conductor and the ground planes are in the same plane. This means that only a single layer deposition is required, which could simplify the fabrication of the mixer chip a great deal.

  Despite the above obvious advantages, the SCPW is not commonly used in mixer circuits. Even at frequencies above the gap, the very lossy microstrip has been preferred. In fact it has been reported that in the few cases where attempts were made to use SCPW , the results were poor as a result of large losses. We attribute this problem to the fact that the design of these circuits was not based on rigorous theoretical procedure which took into account all the loss mechanisms. In this paper we shall describe design equations which take into account the various loss mechanisms in SCPW in particular radiation and surface waves losses. We will show that the contribution of each to the total loss is strongly dependent on the geometry.

METHOD OF CALCULATION

Comparison of various methods

Full wave analysis of CPW is very hard since this requires the calculation of the current density over the conductors for arbitrary film thickness and as a function

of frequency. This is particularly true in the case of mixer circuits where the metallisation thickness is comparable to some of the transmission line parameters such as the CPW gap. The need to include metallisation thickness in the basic formulation arises from the fact that the current density near an infinitely thin metal edge diverges to infinity as $r^{\frac{1}{2}}$ where r is the distance from the edge. Consequently the loss over a conductor with infinitely thin edges is unbound. To avoid laborious numerical procedures which add little to the accuracy of the final results we make use of the TEM approximation which requires that the cross section dimensions of the transmission line to be small compared to the wavelength . This allows us to derive analytical expressions for the characteristic impedance and the propagation constant for arbitrary film thickness, using a quasi-static approach. Methods that use this technique proceed usually as follows:

- Use Schwartz-Christoffel conformal mapping to map the CPW with thick metallisation in the z-plane to a CPW geometry with infinitely thin metallisation in the Z_1 plane. As a result of the symmetry, it is sufficient to work with half the cross section and consequently the resulting geometry in the Z_1 plane is a slot line with finite assymetric ground planes.

- The electrical parameters of the slotline in the Z_1 plane can now be found rigorously using standard computational techniques. However, following Heinrich approach (Heinrich, 1993), a quasi-TEM method combined with reasonable approximations is used to calculate the capacitance and inductance of the slotline using analytical formulas. Those expressions extend over several pages, hence are too long to include in this paper. The reader is therefore referred to the cited reference. The accuracy of Heinrich expressions is good as long as we satisfy the quasi-TEM condition:

$$\nu << \frac{c}{\sqrt{\epsilon_{eff}}} \frac{1}{w+2s}; \qquad h > 2(w+2s) \tag{1}$$

  where c is the speed of light in vacuum. Taking a cross section dimension of 50μm we find that $\nu \ll 3$ THz. It should be added however that when the gap is much smaller than the strip width and is comparable to the film thickness this condition could be relaxed since the fields will be confined to the gap and do not fringe much into the dielectric.

  It is also worthwhile noticing that a main difference between the expressions given in this paper and others is that here,the influence of the thickness is incorporated in the formulation of the problem while in other approximate treatments the effect of the thickness is taken as a correction to the zero-thickness case. We therefore believe that Heinrich expressions are more accurate, in particular for very thick metallisation as it is the case in mixer circuits.

- Whence the inductance and characteristic impedance are known the conduction loss is calculated using Wheeler's incremental method.

- After deriving expressions for the modal parameters, the superconducting values can then easily be calculated by replacing the normal conductivity with the complex conductivity given by Mattis-Bardeen equations.

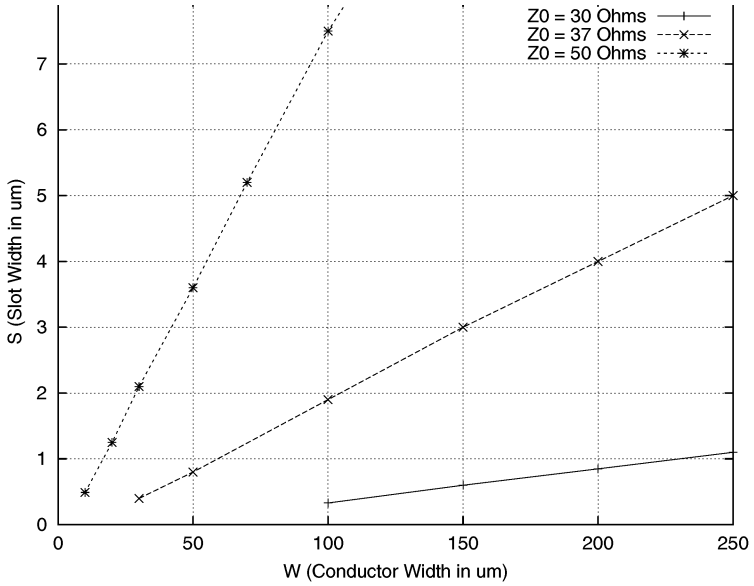

FIGURE II Design curves at 700 GHz for a Nb CPW in the normal state for three characteristic impedance values. The substrate dielectric constant ϵ_r=3.8, t= 400 nm and h= 60 μm

Finally, the electrical parameters computed by Heinrich theory are compared with those given by Whitaker *et al* (Whitaker, 1988), (Gupta, 1996) and the commercial package HP-EEsof. Whitaker *et al* uses approximate expressions based on conformal mapping and corrected by for the film thickness (Gupta, 1996). To make the expressions apply beyond the TEM limit they use a frequency correction factor which includes imperial parameters. We cannot therefore comment on the applicability of this correction for all CPW dimensions. We also found that HP-EEsof which uses similar formalism applies in the TEM interval only.

Calculation of the characteristic impedance

We start our computation by showing a design curve for three characteristic impedance values corresponding to a Niobium CPW (Fig. 2). The chosen film thickness, substrate height and Z_o values are typical to those found in mixer circuits. We would like to emphasise that superconductivity (unlike in microstrip lines) does not alter those values significantly. This is in contrast to microstrip geometry where the penetration into the strip, substantially modifies the modal parameters of the transmission line (Yassin and Withington, 1995). Another important observation which we can learn form Fig. 2 is that it is difficult to obtain low impedance values for convenient strip and gap dimensions. For example, to obtain a 38 Ω, for a gap $s = 2\mu$m we need a strip thickness w=100 μm which is too wide. Lower impedance values can only be obtained for much narrower gaps which increases the fabrication complexity. Values of 50Ω and above on the other hand are easily obtained. This is shown in Fig 3 where we plotted the impedance as a function of the strip width for several gap values.
The dependence of the propagation constant and the characteristic impedance for a CPW in the normal state on frequency are plotted in Fig. 4 and Fig. 5 respectively. It can be seen that our computations agree well with those given by

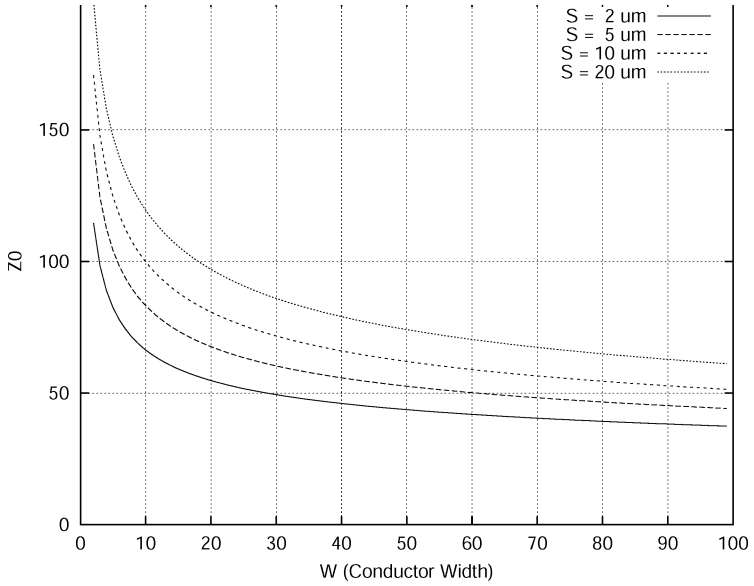

FIGURE III Characteristic impedance values for a CPW as a function of the strip width and gap. ϵ_r=3.8, t= 400 nm and h= 60 μm

Whitaker *et al* for frequencies below 1 THz. Above this frequency, the results start to depart slowly as a result of the frequency correction factor used by Whitaker. The equivalent plots for the superconducting state are very similar to those in Figs. 4,5 , hence are not plotted below.

Calculation of conductor losses

In Fig. 6 we compare the conduction losses of a SCPW when the modal values are computed by the three methods as a function of frequency. We also include the loss for a superconducting microstrip with the same metallisation (Niobium) and dielectric constant, having a width of 2μm and a substrate height of 400 nm (Yassin and Withington, 1995). It can be seen that in the frequency range below 1THz, there is close agreement between Whitaker *et al* and our methods both below and above the superconducting gap. In addition it is also shown that the conduction loss of the microstrip above the gap is substantially higher than that of the CPW. Notice that at frequencies above the gap, the losses of the SCPW become equal to those computed for the normal CPW. This is of course to be expected since at frequencies above the gap, Cooper pair-breaking becomes dominant.

RADIATION AND SURFACE WAVE LOSSES

In addition to the dielectric and ohmic losses, coupling of power to radiation and surface waves in coplanar lines contributes substantially to the total loss. those losses depend strongly on frequency and geometry. For thick substrates, radiation losses are dominant since the CPW radiates efficiently into the dielectric. For very thin substrates, radiation losses are small and surface waves are cutoff. In this case, conduction losses are dominant. As the substrate thickness increases, surface waves start to propagate resulting in steeply increasing loss as

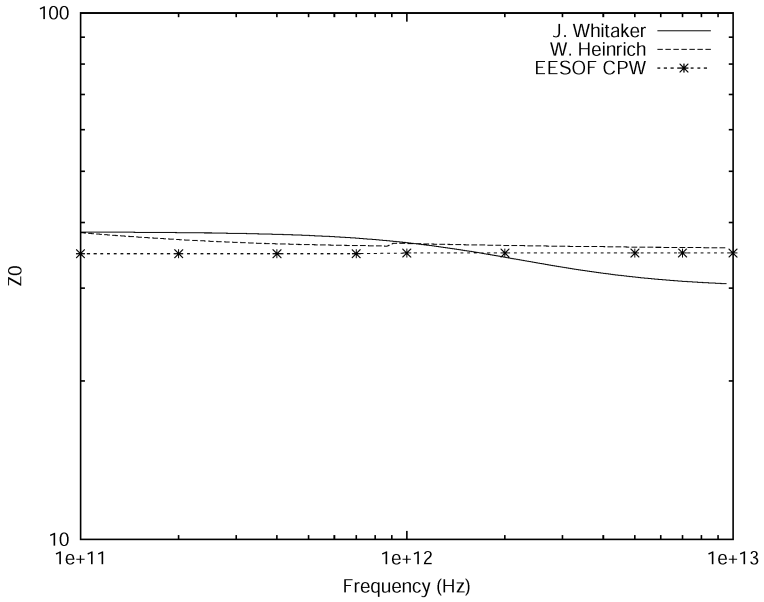

FIGURE IV Characteristic impedance as a function of frequency for a Nb CPW. ϵ_r=3.8, t= 400 nm, w= 100 μm and h= 60 μm

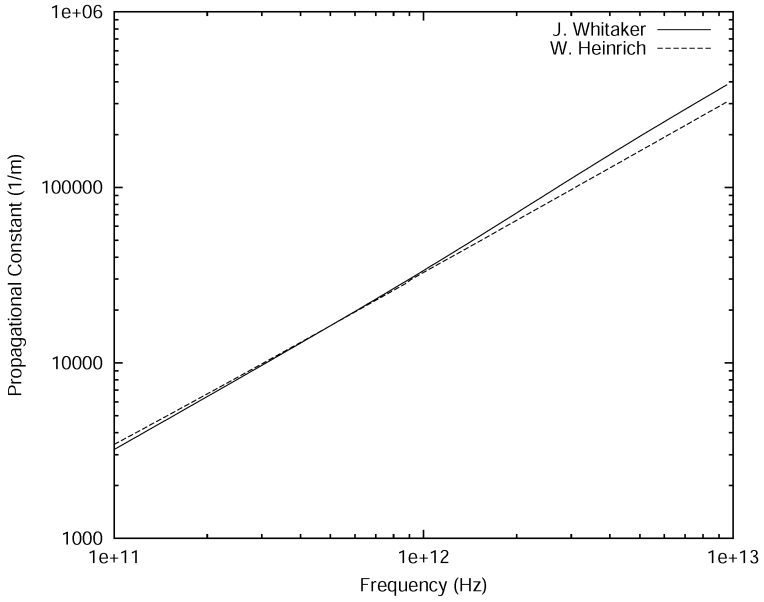

FIGURE V propagation constant as a function of frequency for a Nb CPW. ϵ_r=3.8, t= 400 nm and h= 60 μm, w= 100 μm

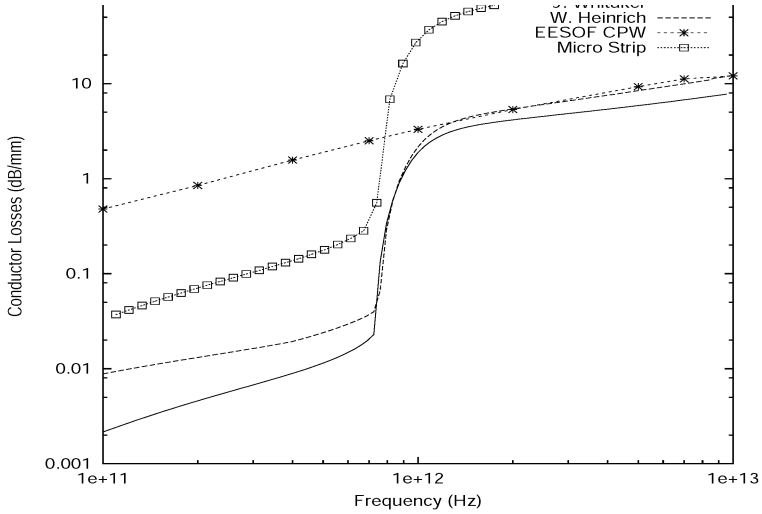

FIGURE VI Conduction losses as a function of frequency for for a superconducting Nb CPW and a microstrip. For the CPW: ϵ_e=3.8, t= 400 nm and h= 60 μm , w= 100 μm. For the microstrip: ϵ_r=3.8, t= 400 nm w=2 μ and h= 400 nm

shown in Fig. 8.

Thick Substrate

The radiation into the dielectric occurs because the phase velocity of the waves propagating along the transmission line is larger than the velocity in the dielectric. The radiation is emitted in a semi-cone of an angle ϕ_{rad} given by

$$\cos(\psi_{rad}) = \frac{k_z}{k_d} \tag{2}$$

where k_z is the CPW propagation constant and k_d is the propagation constant in the dielectric. Using the reciprocal method and quasi-static approximation, it can be shown that the attenuation coefficient is given by (Rutledge, 1983)

$$\alpha_{rad}^{CPW} = \frac{58.7(1-1/\epsilon_r)^2}{K(k)K'(k)\sqrt{1+1/\epsilon_r}} \frac{(w+2s)^2}{\lambda_d^3} \qquad \text{dB/m} \tag{3}$$

where k = s/(w+2s) and K(k) is the elliptic integral.

It can easily be seen that the radiation loss is proportional to the square of the total line width and to the cube of the frequency. At very high frequency, the quasi-static approximation breaks down and full wave analysis becomes necessary (Phatak, 1990).

Thin Substrate

Surface waves losses occur when elementary sources on thin substrates couple to surface waves. Those losses become important when the substrate is too thin for radiation losses but thick enough to make the propagation constant of the surface waves larger than that of the transmission line. When this happens, the

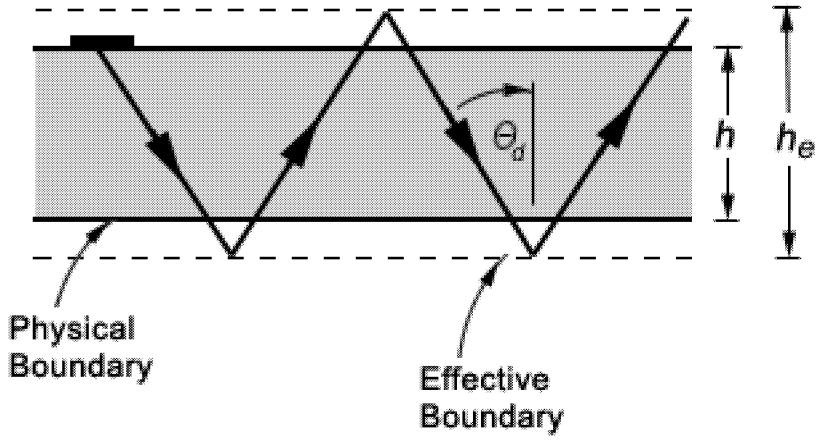

FIGURE VII Ray optics diagram for propagation in a dielectric waveguide.

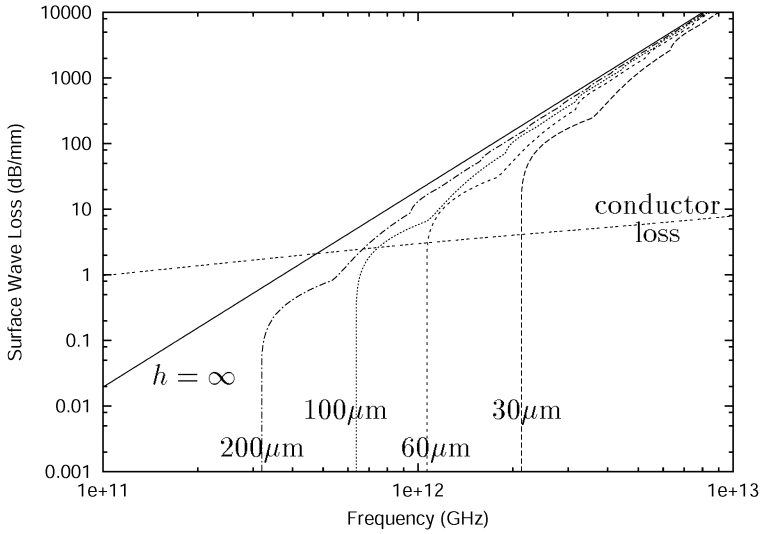

FIGURE VIII Radiation (solid line) and surface wave lossesfor a CPW with $s = 2\mu$m,$w = 100\mu$m and $\epsilon_r = 3.8$. Surface waves losses are plotted for several substrate thicknesses. Condctor losses are computed for Nb in the normal state.

transmission line begins to lose power at a rate which is determined by the angle ψ, given by:

$$\cos(\psi_{SW}) = \frac{k_z}{\beta} \tag{4}$$

where k_z is the propagation constant of the line and β is the surface waves mode propagation constant. Notice that the turn-on frequency is larger than the usual cut-off frequency of the dielectric slab guide.

Using reciprocity and quasi-static approximation for the impedance and field distributions, the attenuation coefficients due to surface waves can be written as (Rutledge, 1983)

$$\alpha_{SW}^{TE} = \frac{149.6}{\sqrt{1+1/\epsilon_r}} \frac{\sin(\psi_{SW}^{TE})\cos^2(\psi_{SW}^{TE})\sin(\theta_d)\cos^2(\theta_d)}{h_e^{TE} K K'} (\frac{w+2s}{\lambda_d})^2 \quad \text{dB/m} \tag{5}$$

$$\alpha_{SW}^{TM} = \frac{149.6}{\sqrt{1+1/\epsilon_r}} \frac{\sin^3(\psi_{SW}^{TM})\sin(\theta_d)}{h_e^{TM} K K'} (\frac{w+2s}{\lambda_d})^2 \quad \text{dB/m} \tag{6}$$

where θ_d is the angle of incidence on the dielectric-air interface as in Fig. 7 and h_e is the effective guide thickness given by

$$h_e = h + 2\delta \tag{7}$$

where h is the actual dielectric thickness and δ is the apparent ray penetration in the air region on the total internal reflection and can be calculated from

$$\delta^{TE} = \frac{1}{\sqrt{(\beta^{TE})^2 - k_0^2}} \tag{8}$$

$$\delta^{TM} = \frac{1}{\sqrt{(\beta^{TM})^2 - k_0^2}} \frac{1}{[(\frac{\beta^{TM}}{k_d})^2 - (\frac{\beta^{TM}}{k_0})^2 - 1]} \tag{9}$$

where $\beta = k_d \sin(\theta_d)$ is the dielectric guided propagation constant.

For the interfering zigzag plane waves to form a mode, the phase lag after reflection from top and bottom and return to the top must be a multiple of 2π :

$$-2k_d h\cos(\theta_d) + 2\phi = 2m\pi, \qquad m = 0, 1, 2... \tag{10}$$

$$\left.\begin{aligned} \phi^{TE} &= 2\tan^{-1}\left[\frac{\sqrt{\sin^2(\theta_d) - 1/\epsilon_r}}{\cos(\theta_d)}\right] \\ \phi^{TM} &= 2\tan^{-1}\left[\frac{\sqrt{e_r^2 sin^2(\theta_d) - \epsilon_r}}{\cos(\theta_d)}\right] \end{aligned}\right\} \tag{11}$$

where ϕ is the phase shift due to total internal reflection at dielectric-air interface (Ramo, 1994).

To calculate the attenuation we first find the angle of incidence θ_d for each mode, by solving the above simultaneous equations. From that the propagation constant and eventually the loss coefficient can be calculated. Clearly the total loss is the superposition of the loss contributions of all propagating surface waves modes. Note that TE_0 and TM_0 substrate modes can exist for very thin substrates.

CONCLUSIONS

A summary of coplanar waveguides losses discussed in this paper are computed in Fig. 8 and may be summarised as follows:

- For very thick substrates, the CPW is dominated by radiation losses in the frequency range relevant to high frequency SIS mixers.
- Surface waves loss is transformed into radiation loss as the substrate becomes very thick (see Fig. 8).
- The turn-on frequency of surface waves is a strong function of the substrate thickness. Whence turn-on occurs, surface waves losses become dominant.
- It is possible to find geometries where radiation and surface wave losses are negligible. For example, consider the CPW described in Fig. 8. Assuming that our operation frequency is 1THz, we choose a substrate thickness which is less than 60 μm to minimise radiation and surface wave losses, hence make our mixer performance limited by conduction losses (which are small for coplanar waveguides)

REFERENCES

Heinrich, W. "Quasi-TEM description of MIMIC coplanar lines including conduction loss effects," *IEEE Trans. Microwave Theory Tech.* MTT–41, no. 1, pp. 45-51, 1993

Whitaker J F et al"Propagation model for ultrafast signals on superconducting dispersive striplines", *IEEE Trans. Microwave Theory Tech.* MTT–36, pp. 277-285, 1988.

Yassin, G. and S. Withington, "Electromagnetic models for superconducting millimeter–wave and submillimeter–wave microstrip transmission line," *J. Phys. D: Appl. Phys.*, vol. 28 pp. 1983–1991, 1995.

Rutledge D B, Neikirk DP and Kasilingham D P, *Infrafed and Millimeter Waves,* vol 10, chapter II. Button K J,Ed. New York:Academic,1983.

Phatak D S, Das N K and Defonzo A P, "Dispersion fharacteristics of optically excited coplanar striplines: fomprehensive full-wave analysis," *IEEE Trans. Microwave Theory Tech.* MTT–38, no. 11, pp. 1719-1730 , 1990.

Ramo S, Whinnery J R and Duzer T V, *Fields and Waves in Communication Electronics* pp. 274-315, 1994.

Gupta K C *et al., Microstrip Lines and Slotlines.* Artech House, 1996.

Frankel M.Y.*et al.,* "Terahertz attenuation and dispersion characteristics of coplanar transmission lines", *IEEE Trans. Microwave Theory Tech.* MTT–39, no. 6, pp. 910-916, 1991.

Thirteenth International Symposium on Space Terahertz Technology

Authors and Registered Participants

Jack Barrett
Harvard-Smithsonian
Center for Astrophysics
jbarrett@cfa.harvard.edu

Andrey Baryshev
SRON/Kapteyu Institute
andrey@sron.rug.nl

Victor Belitsky
Onsala Space Observatory
belitsky@oso.chalmers.se

Dominic Benford
NASA/GSFC
dominic.bendford@gsfc.nasa.gov

Thomas Bertrand
Observatoire de Paris
bertrand.thomas@obspm.fr

Ray Blundell
Harvard-Smithsonian
Center for Astrophysics
rblundell@cfa.harvard.edu

Torsten Bondo
TICRA
tb@ticra.com

Faouzi Boussaha
Obervatoire de Paris
faouzi.boussaha@obspm.fr

Michael Brandt
KOSMA
brandt@ph1.uni-koeln.de

Matthew Carter
IRAM
carter@iram.fr

Goutam Chattopadhyay
CALTECH
goutam@submm.caltech.edu

Sergey Cherednichenko
Chalmers University of Technology
serguei@ep.chalmers.se

Chi Chung Chin
Herzberg Institute of Astrophysics
Chi-Chung.Chin@nrc.ca

Risacher Christophe
Onsala Space Observatory
risacher@oso.chalmers.se

Moon-Mee Chung
Taeduk Radio Astronomy Observatory
mhchung@trao.re.kr

Charles Cunningham
Herzberg Institute of Astrophysics
Charles.Cunningham@nrc.ca

Th. de Graauw
SRON
thijsdg@sron.rug.nl

Piet de Korte
SRON
dekorte@boulder.nist.gov

Gert de Lange
SRON
gert@sron.rug.nl

Simon Dicker
Univ. of Pennsylvania
sdicker@hep.upenn.edu

Erik Duerr
MIT Lincoln Lab
duerr@alum.mit.edu

Jack East
University of Michigan
jeast@eecs.umich.edu

Geoffrey Ediss
NRAO
gediss@nrao.edu

Neal Erickson
UMass Amherst
neal@ieee.org

Thomas Feurer
MIT
tfeurer@mit.edu

Paolo Focardi
JPL
focardi@achille.det.unifi.it

Jianrong Gao
SRON/Delft
j.r.gao@tnw.tudelft.nl

Enrique García
Universidad Politécnica de Madrid
quique@gr.ssr.upm.es

Eyal Gerecht
NIST
gerecht@boulder.nist.gov

Hugh Gibson
Harvard-Smithsonian
Center for Astrophysics
hgibson@cfa.harvard.edu

Gregory Gol'tsman
Moscow State Pedagogical Univ.
Goltsman00@mail.ru

Dazhen Gu
UMass Amherst
dgu@ecs.umass.edu

Janne Häkli
Helsinki Univ. of Technology
janne.hakli@hut.fi

Bill Hatch
JPL
william.A.Hatch@jpl.nasa.gov

Jeffrey Hesler
UVa
hesler@virginia.edu

Ronald Hesper
SRON/Kapteyu Institute
hesper@sron.rug.nl

Netty Honingh
KOSMA
honingh@phl.uni-koeln.de

Dr. Heinz-Wilhelm Hübers
DLR (German Aerospace Center)
heinz-wilhelm.huebers@dlr.de

Peter Huggard
Rutherford Appleton Lab
p.g.huggard@rl.ac.uk

Todd Hunter
Harvard-Smithsonian
Center for Astrophysics
thunter@cfa.harvard.edu

Brian Jackson
SRON
brian@sron.rug.nl

Hamid Javadi
JPL
hamid.h.javadi@jpl.nasa.gov

Alexandre Karpov
CALTECH
karpov@submm.caltech.edu

Jonathan Kawamura
JPL
jonathan.h.kawamura@jpl.nasa.gov

A.R. Kerr
NRAO
akerr@nrao.edu

Pourya Khosropanah
Chalmers University of Technology
pourya@ep.chalmers.se

Robert Kimberk
Harvard-Smithsonian
Center for Astrophysics
rkimberk@cfa.harvard.edu

Teun Klapwijk
Delft
klapwijk@tnw.tudelft.nl

Satoshi Kohjiro
AIST
s-kohjiro@aist.go.jp

Erik Kollberg
Chalmers University of Technology
Kollberg@ep.chalmers.se

Valery Koshelets
IREE (Russia)
valery@hitech.cplire.ru

Tomi Koskinen
Helsinki Univ. of Technology
tvkoskin@cc.hut.fi

Jean-Michel Kreig
Observatoire de Paris
kreig@mesiog.obspm.fr

Eugene Lauria
NRAO
glauria@nrao.edu

Bernard Lazareff
IRAM
lazreff@iram.fr

Jung-Won Lee
Herzberg Institute of Astrophysics
Jung-won.Lee@nrc.ca

Mark Lee
Bell Laboratories
markl@lucent.com

Steve Leiker
Harvard-Smithsonian
Center for Astrophysics
leiker@cfa.harvard.edu

Bruno Leone
European Space Agency
Bruno.Leone@esa.int

Alain Maestrini
JPL
alain.e.maestrini@jpl.nasa.gov

Dan Marrone
Harvard-Smithsonian
Center for Astrophysics
dmarrone@cfa.harvard.edu

Christopher L. Martin
Harvard-Smithsonian
Center for Astrophysics
cmartin@cfa.harvard.edu

Imran Mehdi
JPL
imran.mehdi@jpl.nasa.gov

Denis Meledin
Harvard-Smithsonian
Center for Astrophysics
dmeledin@cfa.harvard.edu

Harald Merkel
Chalmers University of Technology
harald@ep.chalmers.se

Dave Miller
Caltech
davem@submm.caltech.edu

Vladimir Mitin
Wayne State University
mitin@ece6.eng.wayne.edu

Jim Moran
Harvard-Smithsonian
Center for Astrophysics
jmoran@cfa.harvard.edu

Jean-Marie Munier
Observatoire de Paris
jean-marie-munier@obspm.fr

Gopal Narayanan
UMass Amherst
gopal@astro.umass.edu

Alessandro Navarrini
IRAM
navarrin@iram.fr

Tom Newman
Millitech LLC
Tnewman@Millitech.com

Takashi Noguchi
Nobeyama Radio Observatory
noguchi@nro.nao.ac.jp

Jean-Claude Orlhac
ASTRIUM
jean-claude.orlhac@astrium-space.com

Scott Paine
Harvard-Smithsonian
Center for Astrophysics
spaine@cfa.harvard.edu

Cosmo Papa
Harvard-Smithsonian
Center for Astrophysics
cpapa@cfa.harvard.edu

Ferdinand Patt
ASIAA - Hawaii
fpatt@sma.hawaii.edu

Brian Perkins
Brown University
Brian-Perkins@brown.edu

Patrick Pütz
KOSMA
puetz@ph1.uni-koeln.de

Michael Read
Calabazas Creek Research
mike@calcreek.com

Frank R. Rice
Caltech
rice@caltech.edu

Aric Sanders
Yale University
aric.sanders@yale.edu

Gerhard S. Schoenthal
University of Virginia
gss2r@mail.phys.virgina.edu

Alexei Semenov
DLR (German Aerospace Center)
Alexei.Semenov@dlr.de

Minghao Shen
Yale University
minghao.shen@yale.edu

Sergey Shitov
IREE, Russia
sergey@hitech.cplire.ru

Anders Skalare
JPL
anders.skalare@jpl.nasa.gov

Shing-Kuo Pan
NRAO
span2@nrao.edu

Dr Vijay Patel
SUNY at Stony Brook
vijay.patel@stonybrook.edu

John Pearson
JPL
John.C.Pearson@jpl.nasa.gov

Daniel E Prober
Yale University
daniel.prober@yale.edu

Antti Räisänen
Helsinki Univ. of Technology
antti@raisanen@hut.fi

Matthew Reese
Yale University
matthew.reese@yale.edu

Philippe Sabon
IRAM
sabon@iram.fr

Erich Schlecht
JPL
erichs@merlin.jpl.nasa.gov

Karl Schuster
IRAM
schuster@iram.fr

Andrei Sergeev
Wayne State University
sergeev@ciao.eng.wayne.edu

Sheng-Cai Shi
Purple Mountain Observatory
scshi@mail.pmo.ac.cn

Irfan Siddiqi
Yale University
irfan.siddiqi@yale.edu

Michael Smith
Harvard-Smithsonian
Center for Astrophysics
msmith@cfa.harvard.edu

Stig Busk Sørensen
TICRA
sbs@ticra.com

Antony A. Stark
CfA
aas@cfa.harvard.edu

Claude Stéphane
IRAM
claude@iram.fr

John Teufel
Yale University
john.teufel@yale.edu

Crowe Thomas
UVa
twc8u@virginia.edu

Sergey K. Tolpygo
SUNY at Stony Brook
sergey.tolpygo@sunysb.edu

Graf Urs
KOSMA
graf@ph1.uni-koeln.de

Joshua Vaughan
MIT
jvaughan@mit.edu

Martina Wiedner
Harvard-Smithsonian
Center for Astrophysics
mwiedner@cfa.harvard.edu

Qun Xiao
University of Virginia
qx9e@virginia.edu

Pavel Yagoubov
SRON
p.a.yagoubov@sron.rug.nl

Keith Yeung
Herzberg Institute of Astrophysics
Keith.Yeung@nrc.ca

T.K. Sridharan
Harvard-Smithsonian
Center for Astrophysics
tksridharan@cfa.harvard.edu

Stanko Stephan
KOSMA
stanko@ph1.uni-koeln.de

Matthew Sumner
CALTECH
sumner@its.caltech.edu

Patrick Thaddeus
CfA
pthaddeus@cfa.harvard.edu

Volker Tolls
CfA
vtolls@cfa.harvard.edu

Edward Tong
Harvard-Smithsonian
Center for Astrophysics
etong@cfa.harvard.edu

Yoshinori Uzawa
Kansai Advanced Research Center,
CRL
uzawa@crl.go.jp

Alexsandr Verevkin
Univ. of Rochester
verevkin@ece.rochester.edu

Wolfgang Wild
NOVA/SRON
wild@astro.rug.nl

Haiyong Xu
University of Virginia
hx4g@virginia.edu

Ghassan Yassin
Cavendish Laboratory
ghassan@mrao.cam.ac.uk

Sigfrid Yngvesson
UMass Amherst
yngvesson@ecs.umass.edu

Ric Zannoni
UMass Amherst
thezs@att.net

Jun-Hui Zhao
Harvard-Smithsonian Center for Astrophysics
jzhao@cfa.harvard.edu

Xin Zhao
UMass Amherst
zhao_hippo@yahoo.com

Yan Zhuang
UMass Amherst
yzhuang@ecs.umass.edu

Jonas Zmuidzinas
CALTECH
jonas@submm.caltech.edu